IAEA-TECDOC-957

Water reactor fuel element modelling at high burnup and its experimental support

Proceedings of a Technical Committee meeting held in Windermere, United Kingdom, 19–23 September 1994

INTERNATIONAL ATOMIC ENERGY AGENCY IAEA

The originating Section of this publication in the IAEA was:

Nuclear Fuel Cycle and Materials Section
International Atomic Energy Agency
Wagramerstrasse 5
P.O. Box 100
A-1400 Vienna, Austria

WATER REACTOR FUEL ELEMENT MODELLING AT
HIGH BURNUP AND ITS EXPERIMENTAL SUPPORT

IAEA, VIENNA, 1997
IAEA-TECDOC-957
ISSN 1011–4289

Printed by the IAEA in Austria
August 1997

FOREWORD

The reliable prediction of power reactor fuel behaviour constitutes a basic demand for safety based calculations, for design purposes and for fuel performance assessments. The ultimate goal of modelling is a description of fuel behaviour in both normal and abnormal conditions. From this knowledge, operating rules can be derived to prevent fuel failures and the release of fission products to the environment and, in extreme cases, to prevent escalation of fuel and core damage and the consequential hazard.

It is also fundamental to the future of nuclear power that reactors can be run economically to compete with other forms of power generation. As a consequence, the development of the understanding of fuel performance and the embodiment of that knowledge in codes allow for more realistic predictions of performance. This in turn leads to a reduction in operating margins, and improved operating economics.

The Technical Committee Meeting on Fuel Element Modelling at High Burnup and its Experimental Support was recommended by the International Working Group on Fuel Performance and Technology (IWGFPT). Its subject had been touched on in many of the IAEA's activities; however for the first time modellers and experimentalists were brought together to have an exchange of views on the research under way and to identify areas where new knowledge is necessary to improve the safety, reliability and/or economics of nuclear fuel. The timely organization of this meeting in conjunction with the second meeting of the Co-ordinated Research Programme on Fuel Modelling at Extended Burnup, in short "FUMEX", allowed fruitful participation of representatives of developing countries which are only rarely exposed to such a scientific event.

The thirty-nine papers presented covered the status of codes and experimental facilities and the main phenomena affecting the fuel during irradiation, namely: thermal fuel performance, clad corrosion and pellet-cladding interaction (PCI) and fission gas release (FGR).

The meeting was hosted by British Nuclear Fuel and AEA Technology, Windermere, United Kingdom, from 19 to 23 September 1994. Sixty-one participants from twenty-three countries or international organizations took part.

The IAEA wishes to thank BNFL and AEA Technology for the organization of the meeting and all the participants for their contributions to this publication. The officer of the IAEA responsible for the organization of the meeting and the compilation of this TECDOC was P.M. Chantoin of the Nuclear Fuel Cycle and Materials Section, Division of Nuclear Power and the Fuel Cycle.

EDITORIAL NOTE

In preparing this publication for press, staff of the IAEA have made up the pages from the original manuscripts as submitted by the authors. The views expressed do not necessarily reflect those of the governments of the nominating Member States or of the nominating organizations.

Throughout the text names of Member States are retained as they were when the text was compiled.

The use of particular designations of countries or territories does not imply any judgement by the publisher, the IAEA, as to the legal status of such countries or territories, of their authorities and institutions or of the delimitation of their boundaries.

The mention of names of specific companies or products (whether or not indicated as registered) does not imply any intention to infringe proprietary rights, nor should it be construed as an endorsement or recommendation on the part of the IAEA.

The authors are responsible for having obtained the necessary permission for the IAEA to reproduce, translate or use material from sources already protected by copyrights.

CONTENTS

Summary 7

STATUS OF CODES AND EXPERIMENTAL FACILITIES (Session 1)

Summary of the findings of the FUMEX programme 19
P Chantoin, W Wiesenack
Data for FUMEX: results from fuel behaviour studies at the
OECD Halden reactor project for model validation and development 39
W. Wiesenack
Development of a code and models for high burnup fuel performance analysis 55
M. Kinoshita, S. Kitajima
Calibration of the ENIGMA code for Finnish reactor fuel with support from experimental irradiations . . 75
S. Kelppe, K. Ranta-Puska
High burnup models in computer code FAIR 91
B.K. Dutta, P. Swami Prasad, H.S. Kushwaha, S.C. Mahajan, A. Kakodar
Computer modelling of the VVER fuel elements under high burnup
conditions by the computer codes PIN-W and RODQ2D 103
M. Valach, J. Zymák, R. Svoboda
Argentine nuclear fuels MOX irradiated in the Petten reactor:
Analysis of experience with the BACO code 117
A.C. Marino, E. Pérez, P. Adelfang
A fuel performance code TRUST V1C and its validation 141
M. Ishida, T. Kogai
Modification in the FUDA computer code to predict fuel performance at high burnup 151
M. Das, B.V. Arunakumar, P.N. Prasad
Modelling of the WWER-440 fuel rod behaviour under
operational conditions with the PIN-MICRO code 157
S. Stefanova, M. Vitkova, V. Simeonova, G. Passage,
M. Manolova, Z. Haralampieva, A. Scheglov, V. Proselkov
An overview of the fuels and materials testing programme at the OECD Halden reactor project 171
W. Wiesenack
Studsvik's fuel R&D projects 179
M. Grounes
Methods for acquiring data in power ramping experiments with
WWER fuel rods at high burnup 193
S.N.Bobrov, A.F.Grachev, V.A. Ovchinnikov, I.S.Poliakov, N.P.Matveev, V.V. Novikov

FUEL THERMAL PERFORMANCE (Session 2)

Thermal conductivity of fully dense unirradiated UO_2: A new formulation from experimental
results between 100°C and 2500°C, and associated fundamental properties 203
G. Delette, M. Charles
Thermal conductivity of hyperstoichiometric SIMFUEL 217
P.G. Lucuta, R.A. Verrall, H. Matzke
A proposal for a unified fuel thermal conductivity model
available for UO_2, $(U\text{-}PU)O_2$ and UO_2-GD_2O_3 PWR fuel 229
D. Baron, J.C. Couty
First steps towards modelling high burnup effects in UO_2 fuel 241
C. O'Carroll, K. Lassmann, J. van de Laar and C.T. Walker
Modelling of some high burnup phenomena in nuclear fuel 251
K. Forsberg, F. Lindström, A.R. Massih
Comparison of the ENIGMA code with experimental data on thermal performance,
stable fission gas and iodine release at high burnup 277
J C Killeen
MOX fuel irradiation behaviour in steady state (irradiation test in HBWR) 289
S. Kohno, K. Kamimura
A simulation of the temperature overshoot observed at high burnup in annular fuel pellets 303
D. Baron, J.C. Couty

Validation of the TUBRNP model with the radial distribution of plutonium in MOX fuel measured by SIMS and EPMA 313
C. O'Carroll, J. van de Laar, C.T. Walker

CLAD CORROSION/PCI AND TRANSIENT MODELLING (Session 3)

Modelling the waterside corrosion of PWR fuel rods 329
T.J. Abram
Modelling the gas transport and chemical processes related to clad oxidation and hydriding 347
R.O. Montgomery, Y.R. Rashid
INTEGRITY: A semi-mechanistic model for stress corrosion cracking of fuel 361
M. Tayal, K. Hallgrimson, J. MacQuarrie, P. Alavi, S. Sato, Y. Kinoshita, T. Nishimura
Transient fuel rod behaviour prediction with RODEX-3/SIERRA 381
M.R. Billaux, S.H. Shann, L.F. Van Swam
The elastic model for arbitrary radially cracked fuel implemented in COMETHE-4D 391
S. Shihab
Bi/Tri-dimensional effects observed in PWR fuel during transient conditions and their numerical simulation 403
B. Linet, N. Hourdequin

FISSION GAS RELEASE (Session 4)

Equi-axed and columnar grain growth in UO_2 419
R.J. White
Behaviour of large grain UO_2 pellet by new ADU powder 429
Y. Harada, S. Doi, S. Abeta, K. Yamate
Experiments to investigate the effects of small changes in fuel stoichiometry on fission gas release 443
P.S. Copeland and R.C. Smith
A fission gas release model 455
A. Denis, R. Piotrkowski
Fission gas release during post irradiation annealing of large grain size fuels from Hinkley Point B 467
J.C. Killeen

ADVANCED METHODS (Session 5)

Fuel rod analysis to respond to high burnup and demanding loading requirements: Probabilistic methodology recovers design margins narrowed by degrading fuel thermal conductivity and progressing FGR 483
R. Eberle, L. Heins, F. Sontheimer
Probabilistic fuel rod analyses using the TRANSURANUS code 497
K. Lassmann, C. O'Carroll, J. van de Laar
Modelling chemical behaviour of water reactor fuel 507
R.G.J. Ball, J. Henshaw, P.K. Mason, M.A. Mignanelli
A model for the oxygen potential of oxide fuels at high burnup 523
P. Garcia, J.P. Piron, D. Baron
Boron nitride coated uranium dioxide and uranium dioxide-gadolinium oxide fuels 539
G. Gündüz, I. Uslu, C. Tore, E. Tanker
A model for the description of the evolution of Pu agglomerates in MOX Fuels 547
E. Federici, P. Blanpain, P. Permezel

List of Participants 555

SUMMARY

1. INTRODUCTION

The Technical Committee Meeting on Fuel Element Modelling at High Burnup and its Experimental Support was attended by sixty-one participants representing twenty-three countries or international organizations.

The thirty-nine papers presented were split into five sessions covering: status of codes and experimental facilities, thermal fuel performance, clad corrosion/PCI and transient modelling, fission gas release and advanced methods of modelling. Uranium oxides, uranium-plutonium oxide (MOX) as well as gadolinia fuel were considered.

The technical discussions were conducted in four panel discussions including "Fission Gas Release", "Fuel Thermal conductivity", "Modelling of MOX Fuel" and "The Future of Fuel Modelling". The main points of discussion focused on the detailed models and interpretation of measurement of parameters which could limit the burnup extension of UO_2 fuel and MOX fuel, especially the "rim effect", the thermal conductivity degradation at high burnup and the fission gas release mechanism.

The main recommendations of this meeting were essentially to continue studying, through new experiments, fission gas release, the degradation of the thermal conductivity with burnup and to develop further the research on the rim structure and its effect on temperature and fission gas release. It was also considered that further efforts to develop more mechanistic models of the cladding evolution with burnup were needed. The good performance of MOX fuel was underlined; however, the necessity to enlarge the MOX database was emphasized.

The technical discussions are summarized below.

2. FISSION GAS RELEASE

It is recognized that thirty-seven years after the publication of Booth it is still difficult to predict accurately the amount of gas released from the fuel pellets during steady state and transient operations. The general understanding of the phenomenon has been the subject of many theoretical and experimental investigations. Nowadays it is based on the following scenario:

The gas atoms are created by fission in the fuel matrix. They then diffuse in the grains. Two different phenomena are involved: the thermal diffusion and the irradiation induced diffusion. Small intragranular bubbles with a diameter of 1 to 2 nm are observed in irradiated fuel. They are created in the wake of the fission spikes and then grow by diffusion. They are continuously destroyed by fission spikes (irradiation enhanced resolution). There is no bubble migration except at very high temperature.

The bubbles are out of equilibrium (quasi-crystallites). The intergranular bubbles act as sink for the gas atoms. They contribute to decrease the amount of gas available for release. This can be simulated by a reduction of an effective gas atom diffusion coefficient. The gas precipitates also on the grain faces. Lenticular pieces are created in that way. There is no migration of these intergranular bubbles. A fraction of the gas in these bubbles undergo irradiation enhanced resolution to the grain. The intergranular bubbles are out of equilibrium (quasi-crystallites). When a saturation concentration is reached on the grain face the surplus accumulates on the grain edge. Grain edge bubble interlinkage occurs when the saturation gas concentration on the edge is reached. The gas is then released to the free volumes.

Other phenomena contribute to increase the amount of released gas. At high temperature, mainly during power ramps, equi-axed grain growth can be observed. The grain boundaries then sweep both

the single gas atoms and the small intragranular bubbles. Athermal fission gas release occurs mainly at the periphery of the pellet by direct recoil and knockout.

During fast power transients micro cracks can appear and contribute to open the grain boundary.

At high burnup the pellet rim region restructures by grain subdivision and becomes highly porous (up to 30% porosity). Athermal fission gas release associated with that restructuring is observed.

DISCUSSION AND CONCLUSIONS

1. The diffusion of single atoms is correctly described using the diffusion coefficients derived by J.A. Turnbull (Ref. Turnbull, White and Wise, IAEA-TC-659/3.5, Preston).

2. The new burnup dependent fuel conductivity correlations (see Section 3) and the efficient thermal barrier of the pellet rim allow better understanding and interpretation of the fission gas release measurements.

3. The mechanistic scenario described above is adequate to explain the observations. There is no need to assume an acceleration of the diffusion kinetics resulting from the dissociation of chemical compounds of fission products, uranium and oxygen with increase of the oxygen potential.

4. The gaseous swelling and the fission gas release are two aspects of the same phenomenon and should be treated consistently in the models.

5. The thermal resolution of the gas present in the intragranular bubbles seems to be necessary to explain quantitatively the kinetics of release, but the mechanism of resolution is not yet fully understood.

6. The high density in the fission gas bubbles on the grain boundaries is confirmed by Electroprobe Microanalysis (EPMA).

7. It is not clear if the stresses in the fuel have an effect on interlinkage.

8. The effect of the grain size on athermal fission gas releases is limited, but can be important on thermal releases.

9. The elaborate models predict the experimental results better both in steady state and in transient conditions.

RECOMMENDATIONS

1. It is recommended that new in-pile and out-of-pile tests be conducted with well characterised fission gas measurements. Measurement or control of the fuel sample temperature is essential.

2. More research on the rim structure and on athermal release from the rim is necessary. Old tests should be re-evaluated taking advantage of new knowledge on the burnup dependent fuel conductivity and on the rim structure.

3. FUEL THERMAL CONDUCTIVITY

Fuel thermal conductivity as considered in this session is only one of the components in the thermal resistance of a fuel rod (the thermal conductivity-degradation of the fuel is shown in Fig. 1), gap conductance and the effect of thermal feedback (as illustrated in Fig. 2) and other effects such as axial gas transport were mentioned only briefly.

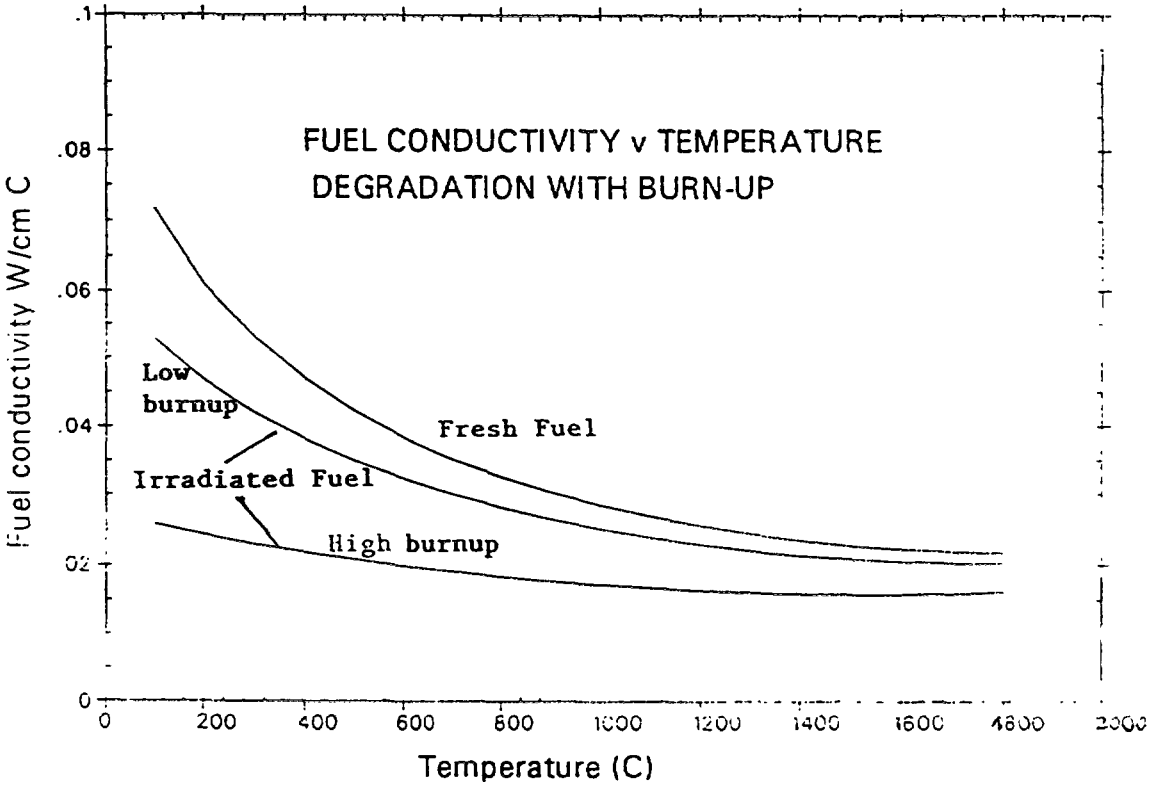

FIG. 1. Fuel thermal conductivity.

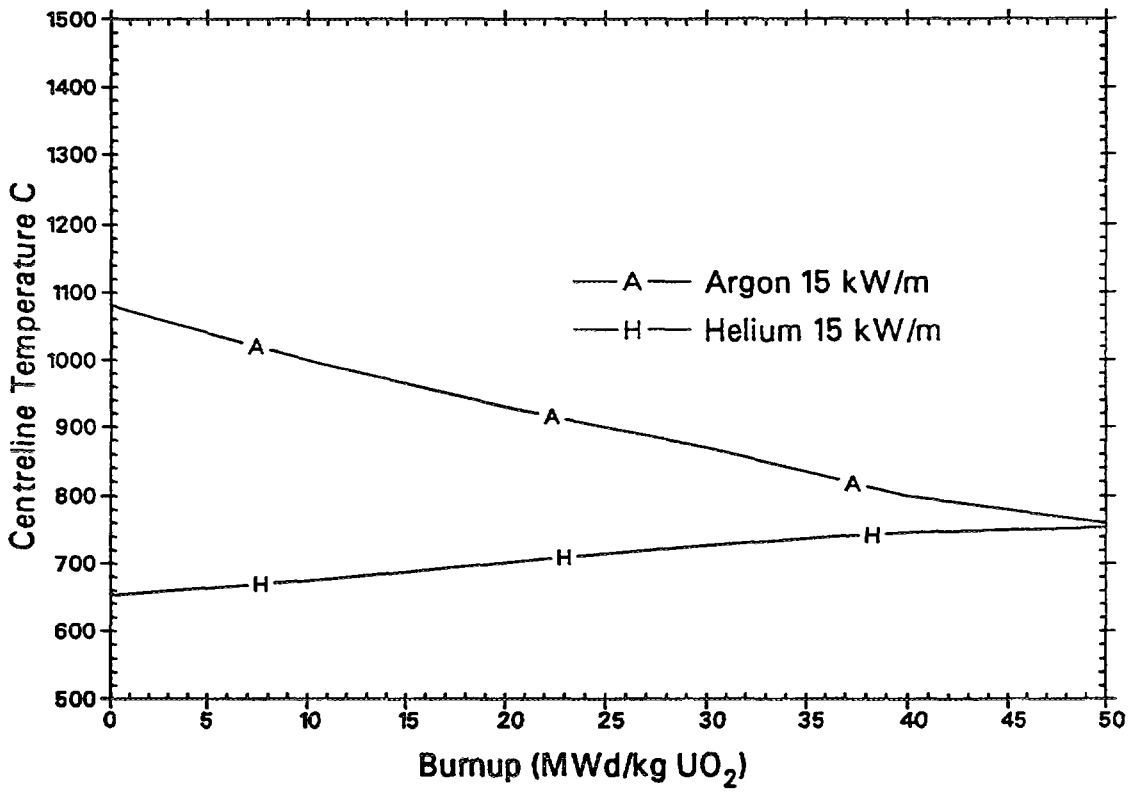

FIG. 2. Effect of gap composition on fuel temperature.

Discussion on the reason for the discrepancy between reported measurements concluded that there was probably an effect of manufacturing route, but the main contribution was due to different correction effects (e.g. porosity) and different experimental conditions, i.e. uncertainties as to stoichiometry.

Different formulations were discussed and it was agreed that the standard $k = (a+bT)^{-1}$ + additional terms was good and that it could be modified simply to treat UO_2 + additions (e.g. gadolinia) by modification of the parameters, principally 'a' and to a less extent 'b'. There was a suggestion that the standard equation for UO_2 could be applied without modification to MOX. An alternative formulation using a $\tan^{-1}$ function was also available and there was a suggestion that this may be better for UO_2 plus additives.

$$k^1 = k \tan^{-1} (2.4 \sqrt{k.x}) / 2.4 \sqrt{k.x}$$

where x is the mole fraction of additive.

It is now firmly established that UO_2 conductivity decreases with burnup at low temperatures and low exposure, this is due to irradiation damage and most codes assume a constant value of conductivity below 500°C. At high burnup the reduction is due to fission products residing within the lattice. This effect is most easily addressed by a simple modification to the standard phonon term which gives a formulation of the following type

$$K = \frac{1}{a(1+fBU) + bT} + \textit{smaller terms}$$

However it was suggested that this may not be adequate for high burnup and a modification to 'b' was required or, the simple expression should be replaced with the alternative $\tan^{-1}$ expression.

Sources of data on degradationof thermal conductivity were examined and it was clear that data from SIMFUEL lacked the influence of fission gases and as such represented an upper bound to irradiated fuel behaviour.

It is important to include effects of porosity and microstructural changes. It was clear that the current approaches can be regarded as 'recipes' and more accurate formulations must take time dependent effects into account.

So far there has been no consideration of the effect of burnup on temperature terms and, as there was evidence from studies on Nb_2O_5 doped fuel that there would be an effect, such changes are desirable for transient modelling.

Refinement of conductivity expressions could only take place with more data and the meeting considered that a priority should be placed on obtaining local data using laser flash techniques, or other techniques on irradiated fuel. However, in considering the various contributions to thermal conductivity, it is important to avoid double accounting.

4. MODELLING OF MOX FUEL

Discussions were organized around the following points:

Utilization of MOX fuel

- Experience in Belgium, France, Germany, Switzerland and Japan has shown good behaviour of MOX fuel up to burnups of 40 GWd/t (and higher in LTAs).

- Licensing has been performed by BN, BNFL, FGA, KWU, MHI and Toshiba with Vendor's code system.

- Large margins still need to be retained due to the smaller database for MOX than for UOX fuel.

Evolution of power

The radial power distribution of MOX (as shown in Fig. 3) may have beneficial effects at end of life (EOL) in reducing or delaying the onset of the rim effect.

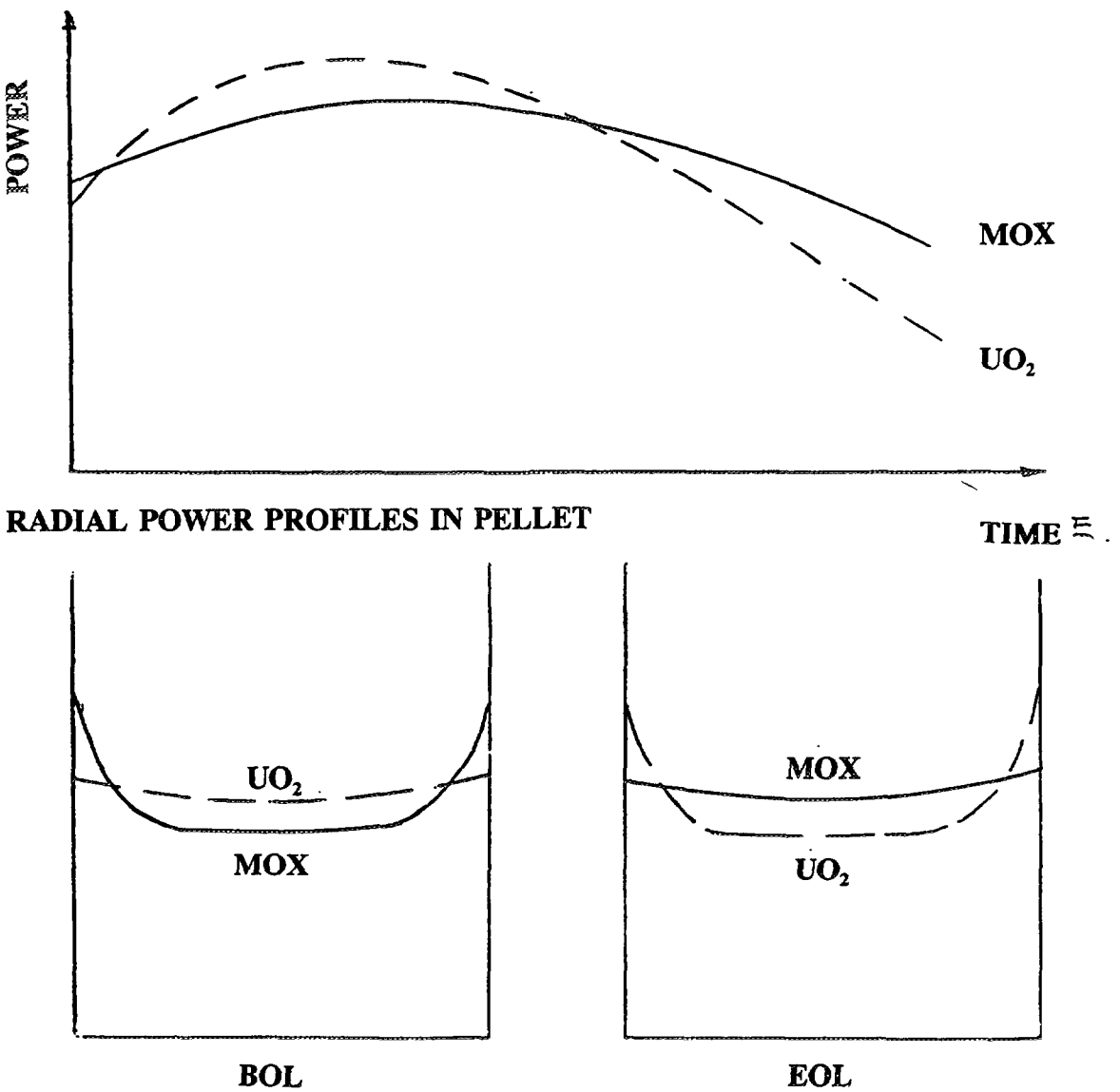

FIG. 3. Evolution of power.

Thermal conductivity

It seems reasonable to account for a weak Pu content effect, but of a lower magnitude than the 25% spread observed in the experimental database. The atypical structure of the specimens used in earlier experiments is probably masking the effect of Pu content. The database could usefully be refined or complemented in this area.

The degradation of thermal conductivity with burnup may be delayed in some type of MOX fuels due to the lower accumulation of fission products in the matrix for a given pellet burnup.

Experimental data are being generated to investigate the thermal conductivity degradation with burnup (in a proprietary programme).

Any effect of deviations in stoichiometry on the thermal conductivity at beginning of life (BOL) is likely to be small, because the fission product inventory is low. At EOL it appears that the buffering effect is real and can be relied upon.

The radial profile of oxygen/metal ratio (O/M) is a secondary effect under steady state operation but may become significant under some accidental transients.

Fission gas release (FGR)

The generation of helium in MOX may trigger enhanced fission gas release. The FGR is not only related to the heterogeneity, it also depends on the size of the Pu-rich particles relative to the fission spikes, on the enrichment of the particle, and on the temperature.

The terminology 'homogeneous and heterogeneous' is confusing. The paper by Federici entitled 'A model for the description of the evolution of Pu agglomerates in MOX Fuels' shows that some fission gas is retained in the 'heterogeneous' MIMAS fuel matrix while the paper by Kohno on MOX fuel irradiation behaviour in steady state shows that more homogeneous fuel gives lower gas release than the heterogeneous fuel, both prepared by the same process. The PNC process is distributing the Pu as PuO2 ('homogeneous' fuel) or as (U-50%Pu)O2 ('heterogeneous' fuel).

Pellet-cladding interaction (PCI)

The results presented by Marino in the paper on Argentinian experience with the BACO code did not fully support a PCI failure mechanism. More details of the failure condition and post irradiation examination (PIE) would be needed to confirm the failure as being due to PCI. Moreover the Pu content was low and this might be a contributing factor.

The internal chemistry of the MOX fuel could be important in explaining its improved PCI performance, as observed in Belgium, France and Germany. Also the Pu-rich agglomerates may act as accommodating volumes in the pellet; moreover, they may induce microcracks at the pellet periphery and so reduce pellet-cladding mechanical interaction (PCMI).

Modelling of MOX fuel

Specific models are needed for:

- development of radial power profiles
- thermal conductivity degradation
- fuel creep
- helium generation and release due to alpha activity
- distribution of the Pu in the matrix of heterogeneous fuel.

Experimental support is adequate for current licensing requirements but further data is needed to support future fuel duties.

CONCLUSIONS AND RECOMMENDATIONS

MOX fuel presents increased modelling challenges. From the discussion it appears that industry, with the support of utilities and national laboratories, have generated, and are using, an adequate database to support modelling of MOX fuel. Modelling codes developed and used for UOX fuel can represent MOX fuel, providing adequate MOX specific models are included.

As higher fuel duties and reduced uncertainty margins improve the economics of MOX fuels, it is felt important to enlarge the experimental database. The industry and utilities involved in MOX are undertaking programmes, and initiating new programmes, and PIE examination to achieve this objective.

5. THE FUTURE OF FUEL MODELLING

The discussion followed the headlines given in the Appendix. It concentrated on the two key aspects of the subject. The first was the acquisition of data and development of sub-models and the second aspect was the incorporation of these models into a mathematical model of the thermo-mechanical behaviour of a fuel rod.

Further developments in modelling are necessary in order to address the key issues of increased burnup and improved reactor cycles. There is a possibility that the current burnups may be close to the limit for current clad materials due to limitations imposed by waterside corrosion although improved clad designs and modified water chemistry are seen as realistic and promising options. Extensive test periods and improved access to data in these areas are needed. For example, although current models adequately cope with corrosion on existing materials, present knowledge is inadequate to extrapolate this for new materials.

To cover PCI under load following regimes there appears to be a need for improved models/treatments of clad creep and plasticity under stress reversal regimes and it was acknowledged that mechanical history played an important role in this. The effect of corrosion and hydrogen injection on cladding properties is also seen as an important issue. For some reactor systems there is a need for further information on low cycle fatigue.

Opinion is divided as to whether sufficient information is available on the fundamental processes of fission gas release although there is agreement that more data is needed for non-standard designs such as MOX and larger grain fuel and in the critical trans-interlinkage region. Further information is also needed for high burnup fuel and there is a perceived need for an international forum on the subject.

There was some debate on the efficacy of present solution methods and whether there was a need to push towards more advanced 2 or 3-D finite element codes. Although more accurate stress representations could be obtained the stochastic nature of pellet cracking and relocation does not guarantee that better results would be obtained unless the physical models themselves could be improved. The ideal solution would be for the twin processes of model development and numerical methods to be pursued in parallel.

Appendix
HEADLINES FOR DISCUSSION

1. The situation circa 1983

- Halden Project Code Comparison Exercise, Vaasky
  Temperature predictions varied by up to 600°C from code to code on relatively simple histories
- Riso-II Fission Gas Release Project
  Large gas releases in 'bumps'
  Postulated explanation that FGR started at 800°C.

2. Progress made - due to several high quality national and international programmes

- Thermal conductivity degradation identified by thermal experiments in Halden Reactor and the Riso-III fission gas release project.
- Wide variety of in-pile experiments conducted at the Halden, Riso and Studsvik Reactors on fuel thermal, fission gas release, clad deformation and PCI failures.
- High quality data originating from a number of 'clubs' such as NFIR, HBC, etc.
- The progress in fuel modelling has coincided with the advent of modern computer technology (hardware and software).

3. The way forward

3.1. Why we do it

- Safety
- Improved reactor cycle design without breach of technical limits of fuel.
- Economics

3.2. The challenge

- Increased burnup
- Load following/power cycling presents new technical obstacles
- Need to utilize improved cladding materials, new fuel designs, etc.

3.3. The problems

PCI (load following)
- swelling
- clad properties

Fission gas release
- operational
- transient
- high burnup (enhancement?)
- rim effect

LOCA/dryout
- fuel thermal properties
- clad degradation

Waterside corrosion, crud, hydriding
- clad variations

3.4. The methods

- New methods?
- Increased relevance of existing methods
  - FE (2d/3d)
  - Probabilistic analysis
- New concepts for submodels

3.5. Future experimental work

At the end of this session it was made clear that new experimental work is still needed.

- What needs to be done?
- Who is going to do it?
- Who is going to pay for it?

SESSION 1
STATUS OF CODES AND EXPERIMENTAL FACILITIES

SUMMARY OF THE FINDINGS OF THE FUMEX PROGRAMME

P. CHANTOIN
International Atomic Energy Agency,
Vienna

W. WIESENACK
OECD Halden Reactor Project,
Institutt for Energiteknikk,
Halden, Norway

Abstract

Description of fuel behaviour during normal, transient and accident conditions has always represented a most challenging and important problem. The ultimate goal is a description of fuel behaviour in all conditions to derive safety rules, improved design and economics. The FUMEX programme, promoted by the Agency with the support of the Halden project, is the second co-ordinated research programme in this area. The first step of FUMEX was to conduct a blind exercise which was carried out using 19 computer codes on 10 experimental rods irradiated in the Halden reactor. The results of this exercise are reported here and show an important improvement of modelling tools since 1984, especially due to the development of national and international parametric studies. However, shortcomings still exist and improvement in the evaluation of PCI, fuel temperature and fission gas release, especially during ramp, is not very well understood. The fuel clad gap modelling also requires further improvement.

1. INTRODUCTION

Reliable prediction of fuel behaviour constitutes a basic demand for safety based calculations, for design purposes and for fuel performance assessments. Therefore, due to the large number of interacting physical, chemical and thermomechanical phenomena occurring in the fuel rod during irradiation, computer codes were developed. The ultimate goal is a description of fuel behaviour in both normal and abnormal conditions. From this knowledge, operating rules can be derived to prevent fuel failures and the release of fission products to the environment, also, in extreme cases, to prevent escalation of fuel and core damage and the consequential hazard.

It is also fundamental to the future of nuclear power that reactors can be run economically to compete with other forms of power generation. As a consequence, the development of the understanding of fuel performance and the embodiment of that knowledge in codes allow for more realistic predictions of performance. This in turn leads to a reduction in operating margins, and improved operating economics.

Description of fuel behaviour during normal operation, transient and accident conditions has always represented a most challenging and important problem. This has been addressed by the Co-ordinated Research Programme (CRP) on Fuel Modelling at Extended Burnup (FUMEX) organized by the International Atomic Energy Agency. It started at the end of 1992, following a similar programme on fuel modelling called D-COM which had been proposed to Member States between 1982 and 1984. The FUMEX experiments were especially instrumented or examined (PIE) to study fuel behaviour in steady state at different power levels and different burn-ups (up to high burnups), fuel behaviour during power ramps up to high burnup, gap conductance and pellet-clad interaction.

In this CRP, 19 codes from 13 countries and one International Organization were involved. It has to be noted that this exercise was made possible thanks to the Halden Project which put at our disposal 6 irradiation experiments and the high competence of its staff. The enthusiasm and the work of all participants and of the supervising group also contributed largely to this performance.

The first part of the CRP, which consisted of a blind exercise carried out on irradiation experiments, is now completed. In this paper the first results of FUMEX will be presented showing some of the progress made since 1984.

2. THE D-COM BLIND PROBLEM

During the years 1982-1984 the IAEA sponsored a co-ordinated research program named "The Development of Computer Models for Fuel Element Behaviour in Water Reactors" (in short: D-COM). The list of participants is given in Table I. The detailed Consultants Report presenting the state-of-the-art in modelling the fuel rod behaviour and including a comprehensive review of fuel rod computer codes at that time is given in Ref. [1,2].

Table I: Participants of the D-COM Blind Problem

Country	Organization	Code
Denmark	RISÖ	Experiment
Argentina	CNEA	BACO
Belgium	BN	COMETHE III-L
Canada	AECL	ELESIM2.MOD10
Czechoslovakia	Rez	PIN/RELA
Germany/CEC	TU-Darmstadt/ITU	URANUS
Finland	VTT	FRAPCON-2
France	CEA-Grenoble	CREOLE
France	EdF	CYRANO-2
France	CEN-Saclay	RESTA
India	BARC	PROFESS
Japan	CRIEPI	FEMAXI-III
Sweden	Studsvik	GAPCON-SV
United Kingdom	BNFL	HOTROD
United Kingdom	UKAEA	MINIPAD-E
USA	Exxon	RAMPX2

As part of this program a code exercise was conducted [3], where the objective was to investigate the capability of fuel performance codes to predict fission gas release. The tests cases to be calculated by the codes consisted of three mini pins irradiated together (test HP 096) in the Danish DR 3 test reactor to a burn-up of 32000 MWd/tU. Two of the pins were finally bumped together with average heat ratings of 33.7 and 36.2 kW/m respectively at the end of bump. The blind code predictions were presented at the OECD-NEA-CSNI/IAEA Specialists' Meeting on Water Reactor Fuel Safety and Fission Product Release in Off-Normal and Accident Conditions, Risö National Laboratory, 1983 [4]. However, these results were not included in the proceedings, but some are given in Ref. [5].

The main conclusions from the exercise were:

a) Temperature

Temperature predictions showed a large spread.

b) Fission gas release

Fission gas release during the base irradiation was in fair agreement with experimental values. The fission gas release during the transient (bump test) was under-predicted by most of the codes.

c) Mechanical behaviour

Since the exercise concentrated on the thermal behaviour and gas release, many participants did not provide dimensional data. Of those codes which submitted mechanical data most codes predicted the cladding creep down reasonably well, mechanical data during the ramp was scarce and showed considerable spread.

The D-COM blind code exercise was considered by participants as very valuable in promoting discussions among modellers. A better knowledge of the centre line temperature during base irradiation was identified as an area of further development. It was also stated in the conclusions that basic phenomena such as gaseous swelling, transient gas release and grain growth should be better known during transients.

3. THE FUMEX BLIND EXERCISE

3.1 SHORT DESCRIPTION OF THE CODES USED

Within the current exercise 19 codes were applied (Table II); details of these codes will be given in the final publication. Only a general overview is presented here.

All codes use an axi-symmetric fuel rod representation and consist of three main parts:

i) Thermal analysis including gap conductance models which account for different pin pressures, gas compositions and gap sizes; standard correlations for the thermal conductivity of fuel and cladding are used. Standard numerical techniques such as FD and FE methods are applied.
ii) Mechanical analysis including cracking and relocation; in a few cases a simplified mechanical treatment of the fuel is adopted. However, most codes are based on an axi-symmetric, modified plane strain assumption. Two codes offer the capability of a two dimensional treatment. FD and FE methods are used.
iii) Physical models or empirical correlations are used for densification, swelling, fission gas release, grain growth etc.

Table II Participants of the FUMEX Blind Problem

Country	Organization	Code
Norway/OECD	Halden	Experiment
Argentina	CNEA	BACO
Bulgaria	INRNE	PIN micro
Canada	AECL	ELESIM.MOD11
Finland	VTT	ENIGMA 5.8f
France	EdF	TRANSURANUS-EdF 1.01
France	CEA/DRN	METEOR-TRANSURANUS
CEC	ITU	TRANSURANUS
India	BARC	PROFESS
India	NPC	FUDA
India	BARC	FAIR
Japan	NNFD	TRUST 1b
Japan	CRIEPI	EIMUS
China	CIAE	FRAPCON-2
Romania	INR	ROFEM-1B
Swiss	PSI	TRANSURANUS-PSI
Czech Republic	NRI Rez	PIN/W
United Kingdom	BNFL	ENIGMA 5.2
United Kingdom	NE	ENIGMA 5.8 D
Russia	IIM	START 3

Although the number of executable statements ranges from 2000 up to 30000 it is stated in the code descriptions that the codes represent the state-of-the-art in modelling. Two codes were specifically designed and validated for HWRs with a collapsible cladding and it is to be expected that these codes show some deficiencies in predicting an open gap situation.

3.2 BRIEF DESCRIPTION OF IRRADIATION USED

FUMEX irradiations were provided by the OECD Halden Reactor Project. They represent a selection of results from the Halden project's fuel testing programme which, for a number of years has focused on consequences of extended burnup on fuel operation. Rod characteristics utilized in FUMEX are given in Table III and simplified power histories in Figure 1. The six cases can be summarized briefly as follows:

FUMEX 1 This dataset represents the irradiation of production line PWR type fuel under benign conditions. Temperatures remained low but increased slightly with burn-up

FUMEX 2 This was a small diameter rod designed to achieve rapid accumulation of burn-up. Temperatures were estimated to remain low with assessment of internal pressure made with measured FGR by PIE.

FUMEX 3 This case consisted of 3 short rods equipped with centreline thermocouples each with a different gap and fill gas composition. After steady state irradiation to ~ 30 MWd/tUO_2, they were given a severe increase in power.

FUMEX 4 Two rods filled with 3 bar He and 1bar He/Xe mixture were irradiated to~33 MWd/kg UO_2. Both rods experienced a period of increased power part way through the irradiation.

FUMEX 5 The test case comprised a single rod base irradiated at low power to MWd/teUO_2 with a ramp and hold period at the end of life. The main purpose of this case was to assess PCMI and FGR under ramp conditions.

Table III Main features of FUMEX rods

	Diametral gap (μm)	Rod	gas pressure (bar)	Enrich (%wt)	Grain size (μm)	Fuel density (%TD)	Fuel diameter (mm)	Fuel stack length (mm)
FUM.1	130	He	10	3.5	10	94.1	8.09	810
FUM.2	130	He	10	13.0	7-10	94.3	5.92	443
FUM.3 rod1	100	He	1	10.0	3.4	95.0	10.70	140
FUM.3 rod2	100	Xe	1	6.0	20	95.0	10.70	140
FUM.3 rod3	50	Xe	1	10.0	3.4	95.0	10.75	140
FUM4 rodA	220	He	3	9.9	12.0	95.0	10.68	781
FUM4 rodB	220	He 92% Xe 8%	1	9.9	12.0	95.0	10.68	781
FUM.5	210	He	1	3.93	14.5	95.0	10.60	457
FUM.6	260	He	1	9.88	16.0	94.7	10.54	466

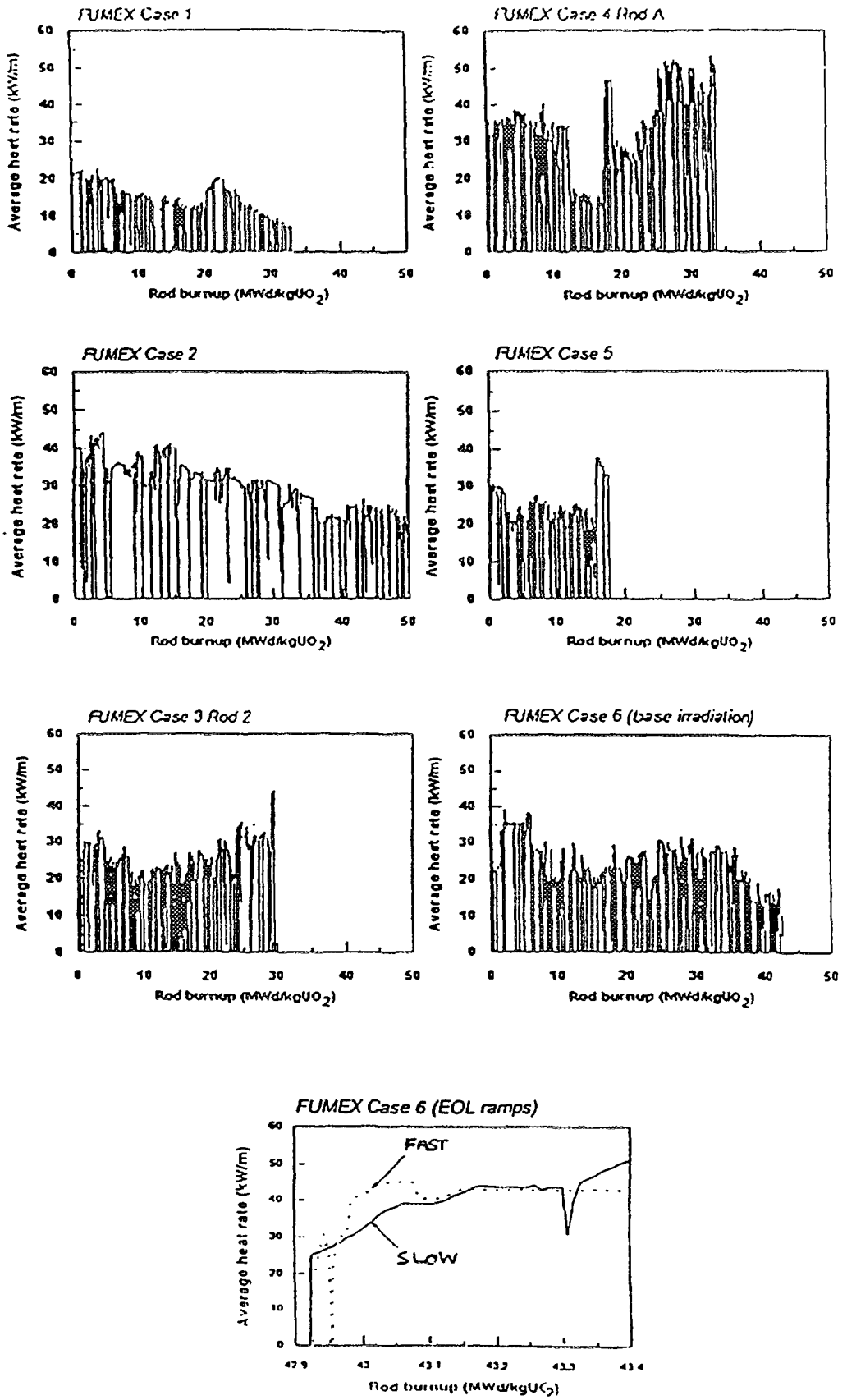

FIG. 1. Power histories of the FUMEX test cases

FUMEX 6 Two rods were base irradiated at low power. The rods were refabricated to include pressure transducers. Rod internal pressure was monitored during power ramps, one fast, one slow.

3.2.1 Irradiation conditions in the Halden Reactor

The Halden Reactor is a heavy water moderated and cooled boiling water reactor. The nominal operation conditions are 240°C coolant temperature and a corresponding saturation pressure of 34 bar. These conditions imply decreased uncertainties for some effects with an influence on experimental results and data evaluation:

- cladding creep-down is very small;
- cladding oxidation can be practically neglected;
- boiling conditions can be assumed for the entire length of the rod.

The reactor is operated with three major shut-downs per year for loading/unloading of driver fuel and experiments.

3.2.2 In-core instrumentation and experimental techniques

In-core instrumentation combined with suitable experimental techniques and test designs is the key to meaningful results for model development and validation. While PIE ascertains the state existing at the end of irradiation, in-pile instrumentation gives information on how phenomena developed during in-core service. The ten instrumented rods of the FUMEX cases thus provide a good basis for studying key parameters of fuel modelling. A summary of parameters recorded in each FUMEX rod is given in Table IV.

A general overview of instrumentation and experimental techniques applied in the Halden Project fuel testing programmes can be found in [6,7]. Those employed for producing FUMEX data are repeated below.

Table IV Measured parameters in FUMEX rods

	Fuel centre line temperature	Inside rod pressure	clad elongation	diameter change	FGR by PIE
FUM.1	X	X	X		X
FUM.2		X			X
FUM.3 rod1	X				
FUM.3 rod2	X				
FUM.3 rod3	X				
FUM4 rodA	X	X	X		
FUM4 rodB	X	X	X		
FUM.5		X		X	
FUM.6		X	X		X (end base irrad.)

Instrumentation

Fuel centre temperatures were measured with *refractory metal thermocouples*, the rod internal pressure was determined with *bellows pressure transducers*, and *elongation sensors* were used to obtain the length increase of the cladding. In FUMEX 4, the rods contained all three types of instrument, providing comprehensive information on the state of the fuel.

The *diameter gauge* is a two or three point contact feeler that can be moved along the length of a fuel rod during operation. Diameter changes can be detected with a micrometer resolution. FUMEX 5 is an example of application.

Re-instrumentation of irradiated fuel rods

Re-instrumentation of irradiated fuel rods is a method of shortening experiment execution times and costs. Since the instrumentation is exposed to irradiation for a shorter duration, the failure probability is decreased. FUMEX 6 is an example of re-instrumentation with a pressure transducer. The data obtained from this experiment gave a good indication of on-set and kinetics of fission gas release in response to a power increase.

Design features for simulation of burnup effects

Increasing burn-up in general incurs increasing uncertainties in data interpretation, e.g. fuel temperature changes can be effected by a combination of causes like fission gas release, changes in gap size and conductivity degradation. Test designs with controlled and known influential parameters therefore facilitate the assessment of separate effects.

FUMEX 3 and FUMEX 4 are examples where fission gas release was simulated by addition of xenon to the fill gas.

Xenon fill gas in combination with a small as-fabricated diametral gap (50 - 100 μm) simulates a high burn-up situation with a large amount of released fission gas and a closed gap due to fuel swelling and clad creep-down. Gap conductance models can be verified with measured data from tests with such a design without the uncertainties caused by high burn-up. FUMEX 3 is an example of this.

3.2.3 Error estimation of power and temperature data

At the first start-up of an experiment, assembly power is determined calorimetrically, resulting in a relation between total power and average neutron flux measured by neutron detectors. The calibration error is about 3% which has to be combined with a similar uncertainty for the distribution of total power to individual rods and local positions. The evaluation of start-up data of a large number of comparable HBWR experiments has indeed shown that the observed spread agrees with these considerations and is about 4%. During the course of irradiation, small local changes of the neutron flux distribution, which cannot be resolved with the arrangement of neutron detectors, will add another uncertainty. The combination of all sources leads to an error estimate for power data of about 5% for the time after the initial calibration. It is customary, however, to assign this uncertainty to temperature rather than power. In the FUMEX evaluation sheets, a 5% error on temperature above coolant temperature is indicated with a corresponding error bar.

3.3 MAIN RESULTS FROM THE FUMEX BLIND EXERCISE

The results of the exercise are outlined below and presented under specific topics. Each code has been given a number and the predictions are presented in the figures as a function of code number plotted as the abscissa. Where experimental data are available, these are given with their estimated accuracy.

3.3.1 Centre line temperature calculated at low burnup

The comparison between experiment and calculation is made on results from FUMEX 1, 3-1 and 4A at low or very low burnup, see Figure 2 for FUMEX 3-1. In FUMEX 1 at 5MWd/kg, shortly after the start of irradiation but subsequent to the major part of fuel densification, most of the codes under predicted the temperatures. However, *the majority of the predictions were within the limits of the experimental uncertainties* estimated to be about 50°C. For FUMEX 3-1, calculations of fuel temperature at 5 MWd/t were in good agreement with the experimental data, with the scatter within the experimental uncertainty. The same observation is applicable to FUMEX 4A where the comparison was made very early in life, before the fuel to clad gap has been affected by fuel densification.

3.3.2 Centre line temperature at low and high burnup

The comparison between experiment and calculation is carried out on FUMEX 1 between 5 and 20 MWd/kg, FUMEX 2 between 5 and 50 MWd/kg and FUMEX 3-1 between 5 and 36 MWd/kg.

According to the measured data in FUMEX 1, the temperature rise between 5 and 20 MWd/kg was approximately 30°C. Half the codes predicted this increase correctly whilst the others predicted decreasing temperatures. However the majority of codes give values lying just outside the experimental uncertainties. FUMEX 2 is purely an inter-code comparison as there were no experimental data for fuel temperatures. All early-in-life predictions of temperatures were within 600 to 750°C. The spread of predictions increased at high burn-up, 50 MWd/kg, particularly since some codes predicted increasing temperatures others predict decreasing temperatures as a function of burn-up. In FUMEX 3-1, Figure 3, the experimental evidence was for an increase in temperature of just under 300°C from 5 MWd/kg up to the start of the ramp. Several codes correctly reflected this increase in their predictions. Codes that did not predict increasing fuel temperatures with burn-up consequently severely under predicted the temperatures at high burn-up.

From these examples it can be deduced that if at intermediate burnup codes are underestimating the fuel temperature within acceptable limits it seems that the temperature calculations at high burnup substantially underestimate that temperature, likely due to an under-evaluation of the fuel thermal conductivity degradation with the burnup.

3.3.3 Influence of the gap conductance on fuel centre temperature

The three rods from FUMEX 3-2, 3-3, and 4B were filled with Xe or a mixture Xe-He.

The case FUMEX 3-2 employed a xenon filled rod which, at constant power, showed a progressive reduction of fuel temperature with burn-up. At the power chosen for the comparison, the reduction was about 300°C from 5 MWd/kg to the burn-up at the start of the ramp (32MWd/kg). This was in marked contrast to the helium filled rod employed in FUMEX 3-1, where, over a similar burn-up interval, the temperature increased by 300°C. At low burn-up many of the predictions were in agreement with the measured temperature of ~1350°C but *at the start of the ramp the scatter was somewhat increased*, Figure 4. It must be said that few codes provided simultaneously good prediction at both high and low burn-up.

Like FUMEX 3-2, FUMEX 3-3 is also a xenon filled rod but with a small grain size, 3.4 μm compared to 20 μm and a smaller fuel to cladding gap, 50 μm compared to 100 μm in case 3.2.

Most codes provided lower estimates for temperature at 5 MWd/kgUO_2 than for FUMEX 3-2 in keeping with the smaller gap. However, three codes gave higher temperatures at 5 MWd/kgUO_2 for FUMEX 3-3 as compared to FUMEX 3-2. *In these cases, the higher temperatures result from the calculation of large gaps generated by high densification on account of the small grain size fuel.* The experimental data showed a decrease in temperature by 100 to 150°C between 5 MWd/kgUO_2 and the time of the ramp. With few exceptions this was reproduced by the codes and the magnitude of this change was well predicted by some of the codes.

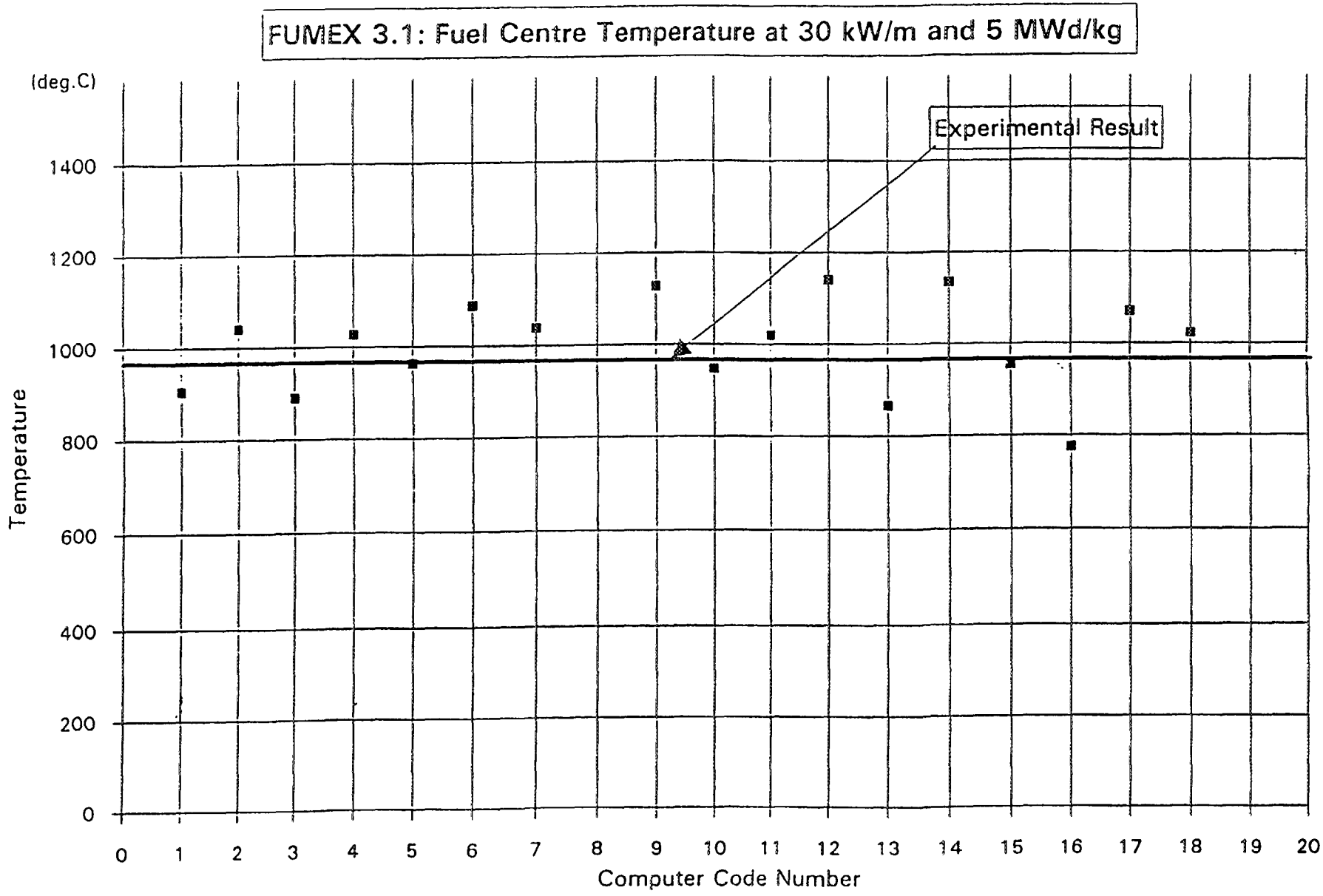

FIG. 2. *FUMEX 3.1: Fuel Centre Temperature at 30 kW/m and 5 MWd/kg*

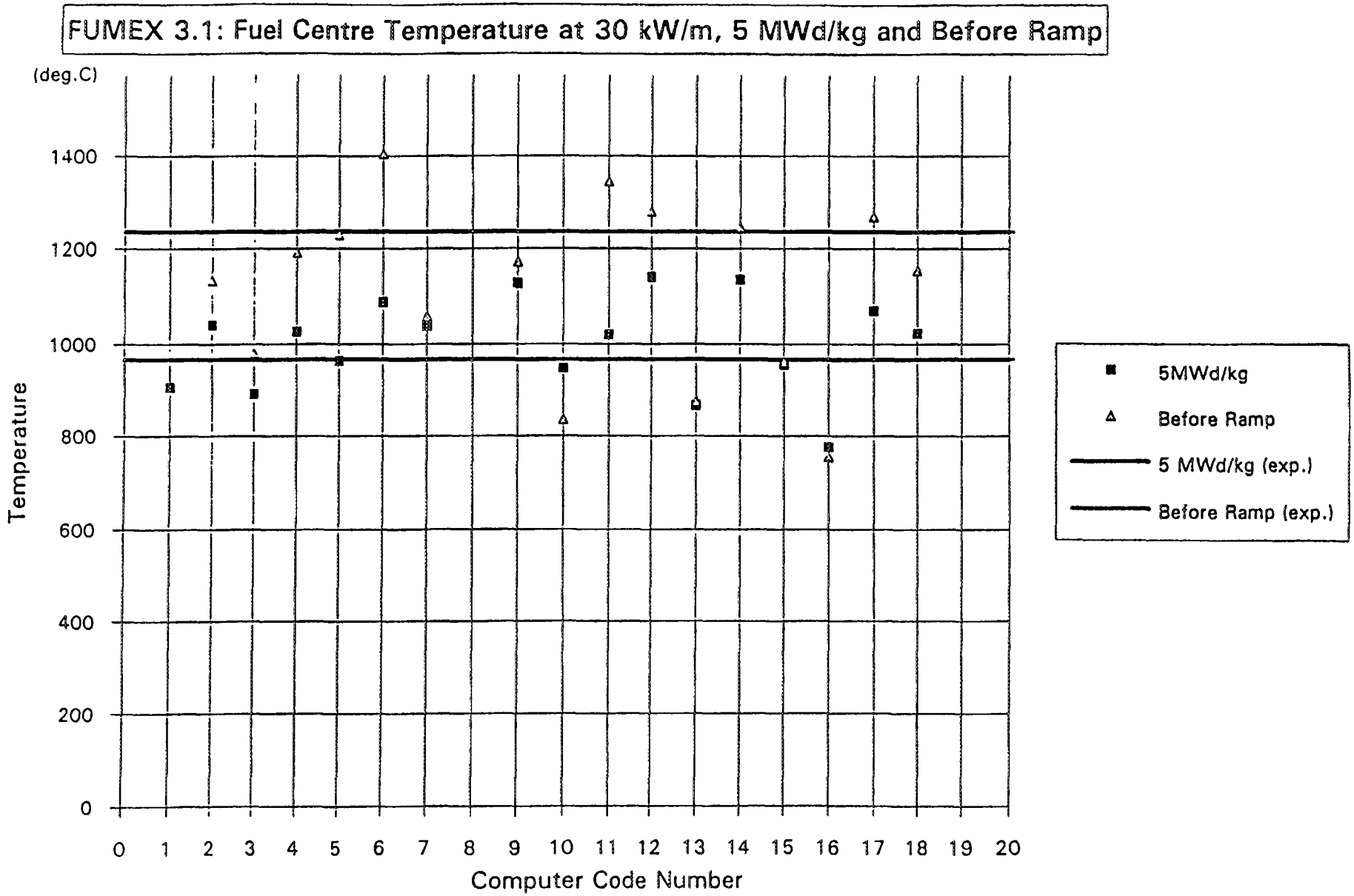

FIG. 3. FUMEX 3.1: Fuel Centre Temperature at 30 kW/m, 5 MWd/kg and Before Ramp

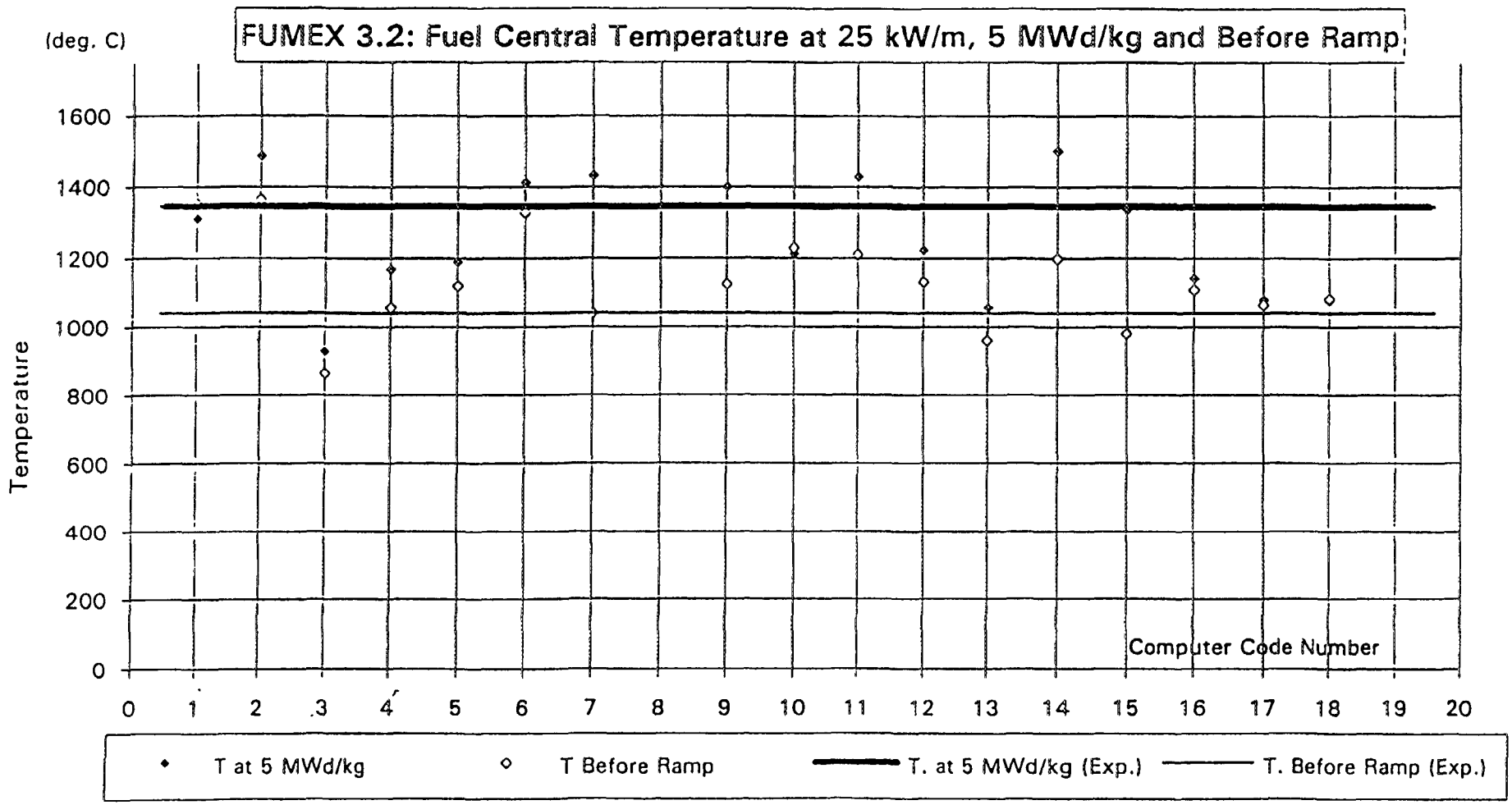

FIG. 4. FUMEX 3.2: Fuel Central Temperature at 25 kW/m, 5 MWd/kg and Before Ramp

FUMEX 3-2 and 3-3 are very sensitive tests of gap conductance models and prediction of gap size, as the poor conductivity of the xenon fill gas gives a very low gap conductance. This accounts for the high scatter of predictions between the codes.

For the 92% He/8% Xe filled rod of FUMEX 4B, the agreement between predictions and data was only fair during start-up. Discrepancies which are larger than that in the helium filled rod of FUMEX 4A are probably due to *the xenon content of the fill gas adding more sensitivity to predictions of the gap conductance models.*

3.3.4 Variation of fuel centre temperature during a power ramp

The power experienced by the 3 fuel rods of FUMEX 3 at the top of the ramp was very high, 60 kW/m. For FUMEX 3-1 and 3-2 *the majority of the codes over-predicted the maximum centre line temperature by about 300 °C*, see for example Figure 5 for FUMEX 3-1.

In FUMEX 3-3, apart from the prediction of 3 codes, agreement with data was good with a relatively small scatter compared with the experimental uncertainties. This is probably due to the codes predicting small, or in some cases a closed, fuel to cladding gap and hence a reduced influence on uncertainties in calculated gap conductance.

3.3.5 Fission gas release in steady state irradiation conditions

In FUMEX 1 and 2 the fractional fission gas release was respectively 1.8 and 3 %. This is a particularly difficult region for accurate predictions of gas release as it lies near the threshold for grain boundary saturation and small changes in materials and irradiation parameters lead to large variations in gas release. The difficulty is demonstrated by the under-prediction of the majority of codes in FUMEX 1 whereas in FUMEX 2 most codes over-predicted the release. However, despite this reservation, within the generally accepted accuracy of a factor of two, the predictions in FUMEX 2 were quite acceptable but somewhat conservative.

In FUMEX 6 at the end of the base irradiation the measured gas release was 16%. Most of the codes predicted significant quantities of release, typically 10 $\pm$ 5%, Figure 6.

3.3.6 Fission gas release during a power ramp

In FUMEX 3-3 the scatter observed in fuel temperature predictions is amplified in the scatter of fission gas release predictions. However, there is little correlation between error in temperature prediction and that for release. In some cases a high prediction of release is accompanied by a low prediction of temperature. *This is evidence of considerable variation in the predictive capabilities of the individual gas release models even with identical input parameters. Unfortunately this case has no measured value for release to validate the predictions.*

From pressure measurements, the fractional fission gas release, after the ramp, for both FUMEX 4A and 4B was in the range 20 to 25%, see Figure 7 for FUMEX 4A. After the ramp the predictions were scattered but typically in the range 20 $\pm$ 10%. By the end of life the predictions increased to 30-40% but with a similar scatter.

In FUMEX 5, before the ramp the fission gas release was very small. Most codes correctly predicted this. After the ramp there is a large scatter in calculated fission gas release with a tendency for over prediction. The shape of the curve for the experimental data is indicative of release by a diffusion controlled mechanism. It is to be noted that not all codes illustrate this behaviour.

For the slow ramped rod in FUMEX 6, the release was estimated from the pressure measurements to be in the region of 50%. There is a large scatter in predicted values but the majority of codes produced

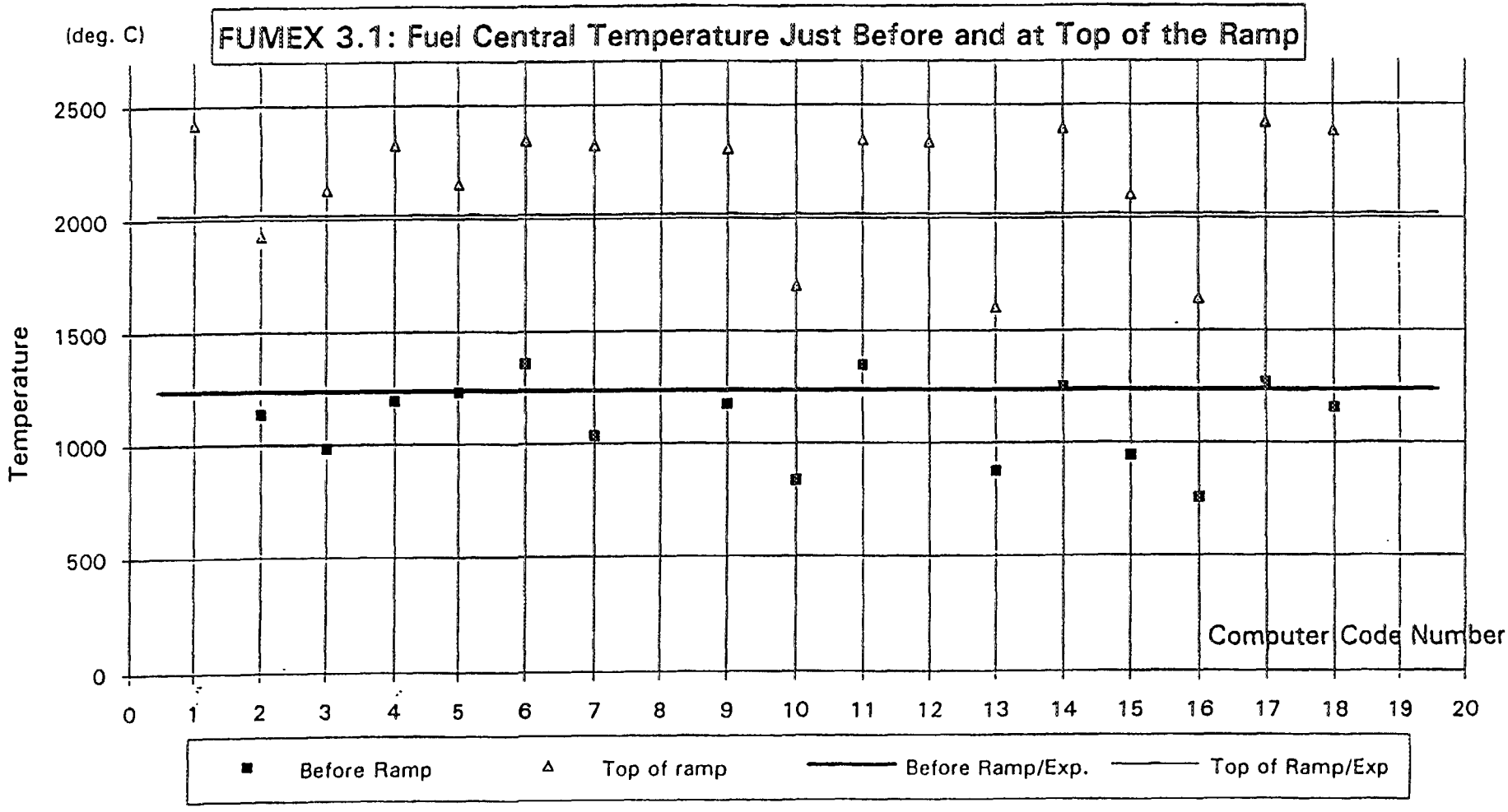

FIG. 5. *FUMEX 3.1: Fuel Central Temperature Just Before and at Top of the Ramp*

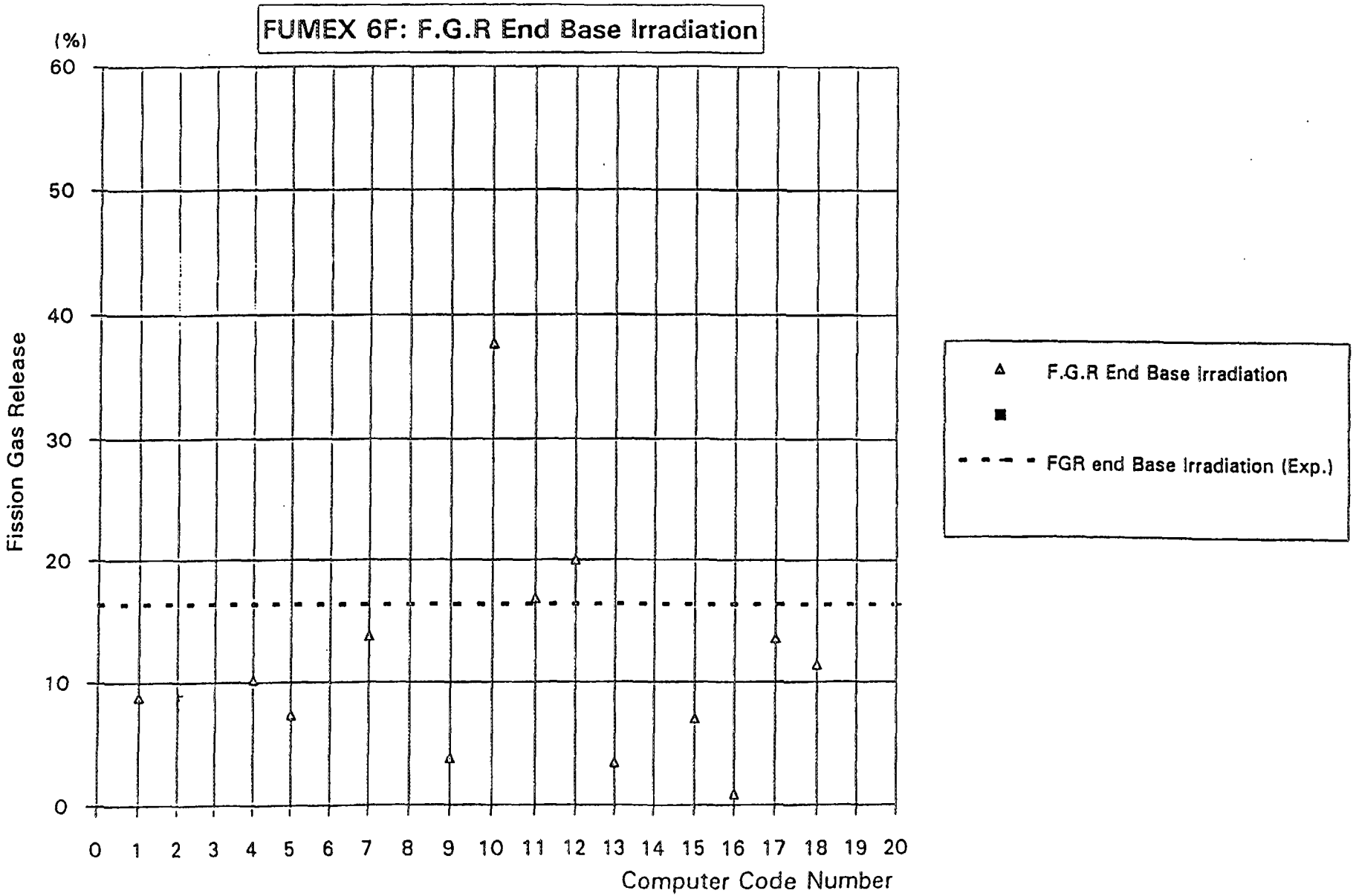

FIG. 6. *FUMEX 6F: F.G.R. End Base Irradiation*

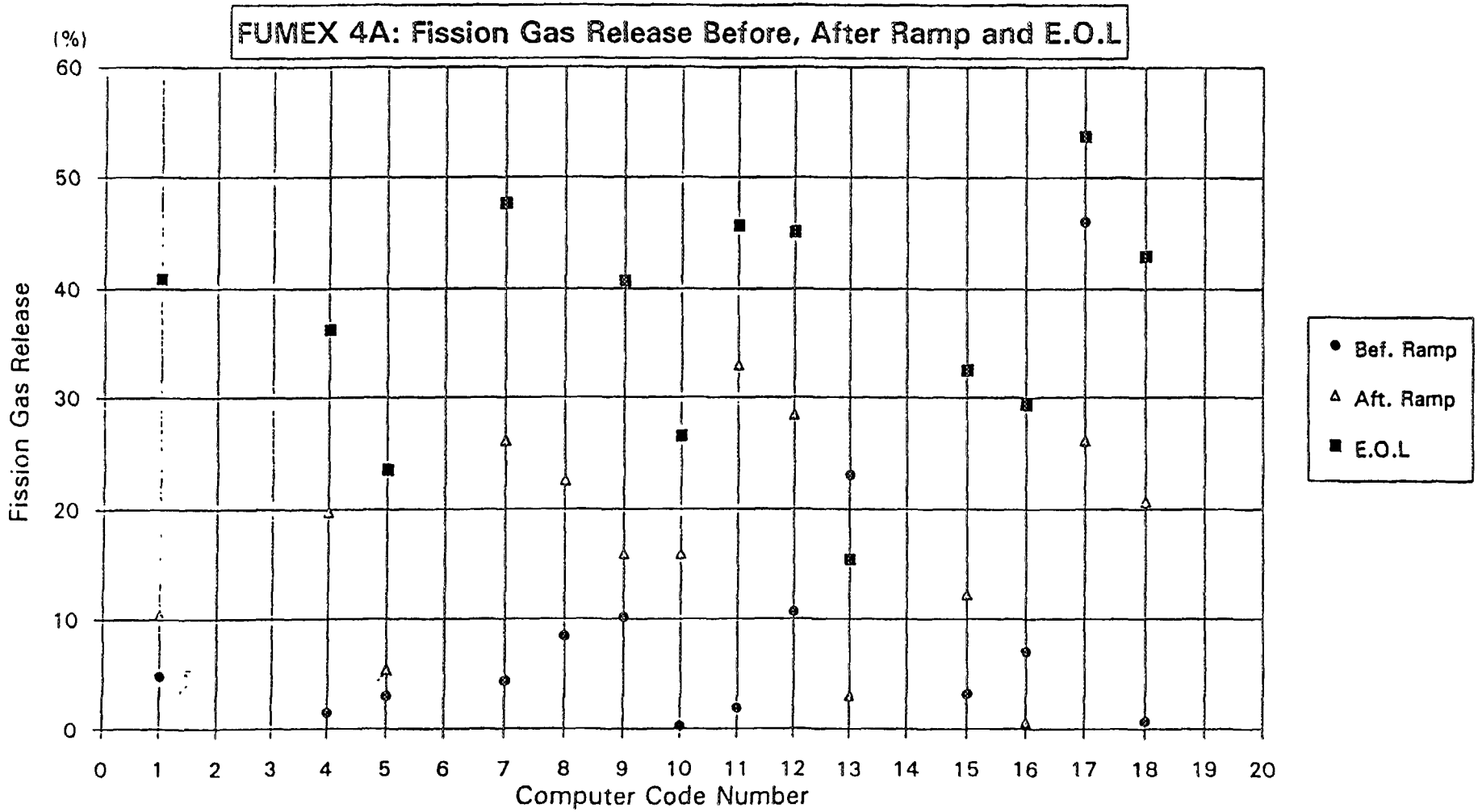

FIG. 7. FUMEX 4A: Fission Gas Release Before, After Ramp and E.O.L.

an under-estimate. For the rod subjected to a fast over power transient, the gas release estimated from the measured pressure was slightly lower at around 45%. This reduced release was duly reflected in lower predicted values although the actual scatter remained high.

3.3.7 Pellet Clad Interaction

FUMEX 1, 4A, 4B and 6 were equipped for clad elongation measurement as FUMEX 5 was monitored with a diameter measurement gauge.

In FUMEX 1 where predictions were presented, most codes provided reasonable estimates of clad elongations for free standing cladding due to thermal expansion. However, in contrast with the experimental data, where from measurements, fuel-clad mechanical interaction was evident above 15 kW/m at about 20 MWd/kg UO_2, no such predictions were made by any of the codes.

The experimental data for rod FUMEX 4B showed evidence of strong fuel-clad mechanical interaction, stronger than for the case of FUMEX 1. Of the codes that provided predictions of elongation as a function of power in the specified ramps, only the codes: ENIGMA 5.2 and 5.8D from the UK, the TRANSURANUS code used by PSI of Switzerland and the TRUST V1b code from NFD of Japan predicted such an interaction. ENIGMA 5.9B used by VTT of Finland gave predictions of only slight interaction. Even in these successful cases, the detailed evolution of length during the ramps was not reproduced correctly. This is not unexpected as the stochastic nature of the 'stick and slip' of the pellet column and the cladding makes modelling extremely difficult.

Predictions of diameter changes were requested at two axial positions during the course of the power ramp of FUMEX 5. Although there is much scatter in the predictions, the small increases are not dissimilar to the observed change in rod diameter. Apart from the predictions of one code, the scatter of predictions is very much as expected and reflect largely on the differences in radial temperature distribution in the fuel pellet. It is notable that many of the codes correctly predict the relaxation in diameter between the start and end of the over power period.

4. DISCUSSION CONCLUSION

i) The exercise has shown that modern codes can be run on state-of-the-art PCs without difficulty. This is a marked improvement over previous years where fuel performance codes were restricted to mainframe computers. This has been brought about principally through advances in PC technology but improvements in mathematical techniques and code organization have also played their part.

ii) Despite the complexity and degree of difficulty of the experimental cases chosen for this comparison, in general, the codes could handle the volume of data and required mathematical convergence without difficulty. However, it would appear that in a small number of instances, some stability problems remained.

iii) The most important contribution to the advancement of fuel behaviour analysis has been the ability to measure fuel centre line temperatures at the start of life and throughout irradiation to high burn-up. By carefully designed experiments, it has been possible to distinguish contributions to the temperature distribution made by the conductance of the fuel to clad gap and the thermal conductivity of the UO_2 pellet. The effect of gap size and fill gas composition is now well established.

Only recently however has it been recognized that the fuel conductivity decreases significantly with burn-up due to the accumulation of fission products. Quantification of this process is very important as it has significant implications on high burn-up performance, in particular the amount of fission products released and hence rod pressure in transients occurring towards the end of life.

These features are embodied in most of the codes that participated in the exercise but only some of them have an adequate representation. This is a very important step, as many of the physical processes modelled are exponentially dependent on temperature, and a good estimate of temperature is mandatory before further models can be developed successfully to describe other phenomena.

iv) The exercise has shown that there are difficulties with modelling fission gas release, and it is clear that the codes contain a variety of models, mechanistic and otherwise which, given identical conditions provide a wide spectrum of predictions. It is recognized that being a highly non-linear process, strongly influenced by temperature and feedback effects, accurate modelling is difficult over the whole range of release values 0 to 100%. In particular, the region around 1% is particularly difficult to predict accurately and this just happens to be the most important region above which gas release and rod internal pressure can run away. Although there is available the empirical Halden criterion relating fuel temperature to burn-up at which 1% release can be exceeded, and this is easily incorporated within any code, there is a need for further data refining the kinetics of release in this region.

v) It is apparent that the major lack of progress is in the area of mechanical interaction. Many codes cannot perform such calculations and even for codes which can, the predictions need further refining before details of the experimental data can be reproduced. However, it must also be recognized that there is not a universal need to calculate fuel-clad interactions, as only in a few countries are there any licensing restrictions requiring evaluation of clad strain and PCI failure. In which case it is a matter for individual code developers whether or not their code requires a detailed mechanical interaction model. Therefore the omission of mechanical interaction modelling should not be taken automatically as a failing of a code.

vi) With such a wealth of experimental data available, much of which is now accessible through open literature, there would appear to be a need to assemble a database against which codes can be developed and validated. A successful database includes not only a compilation of cases, but also a commentary on accuracy and inter-comparison. In this way 'rogue' and uncertain data are not used or at least are given weight according to their value. This could also be accompanied by a review of published models and their success so that new developments can capitalize on the work of previous studies. In this way, fuel performance modelling can achieve a maturity thus permitting safer and more economic use of the nuclear fuel cycle.

GENERAL CONCLUSION

The FUMEX exercise shows that much progress has been made since the D-COM CRP in the evaluation of fuel temperatures, degradation of the global thermal conductivity with burnup and an understanding of the impact on fission gas release. This progress was due largely to the strong development of national and international parametric studies. This exercise shows also that there was no room for complacency; efforts are still necessary to improve codes all over the world and consequently the economics and safety of nuclear energy.

REFERENCES

[1] GITTUS J., MISFELDT I., and ROLSTAD E., Water-Reactor computer-codes which model behaviour during normal- and transient-operation, Consultants Report, IAEA, International Working Group on Water Reactor Fuel Performance and Technology, Proceedings of a Specialists' Meeting, Bowness-on-Windermere (1984), IWGFTP/19, 15-62

[2] Gittus J.H., Development of Computer Models for Fuel Element Behaviour in Water Reactors, Survey report, IAEA-TECDOC-415 (1987)

[3] MISFELDT I. , The D-COM blind problem on fission gas release, IAEA, International Working Group on Fuel Performance and Technology for Water Reactors, OECD-NEA-CSNI/IAEA Specialists' Meeting on Water Reactor Fuel Safety and Fission Product Release in Off-Normal and Accident Conditions, Risö National Laboratory (1983), IWGFTP/16, 411-422

[4] INTERNATIONAL ATOMIC ENERGY AGENCY, International Working Group on Fuel Performance and Technology for Water Reactors, OECD-NEA-CSNI/IAEA Specialists' Meeting on Water Reactor Fuel Safety and Fission Product Release in Off-Normal and Accident Conditions, Risö National Laboratory (1983), IWGFTP/16

[5] INTERNATIONAL ATOMIC ENERGY AGENCY; Water-Reactor computer-codes which model behaviour during normal- and transient-operation, Consultants Report, International Working Group on Water Reactor Fuel Performance and Technology, Proceedings of a Specialists' Meeting, Bowness-on-Windermere (1984), IWGFTP/19, 63-165

[6] AARRESTAD O., Fuel Rod Instrumentation, Proceedings, IAEA Technical Committee Meeting on In-core Instrumentation and In-situ Measurements in Connection with Fuel Behaviour, Petten, The Netherlands, 1992.

[7] WIESENACK W., Experimental Techniques and Results Related to High Burnup Investigations at the OECD Halden Reactor Project; Proceedings, IAEA Technical Committee Meeting on Fission Gas Release and Fuel Rod Chemistry Related to Extended Burnup; IAEA TECDOC 697; Pembroke, Canada, 1992.

DATA FOR FUMEX: RESULTS FROM FUEL BEHAVIOUR STUDIES AT THE OECD HALDEN REACTOR PROJECT FOR MODEL VALIDATION AND DEVELOPMENT

W. WIESENACK
OECD Halden Reactor Project,
Institutt for Energiteknikk,
Halden, Norway

Abstract

Investigations of phenomena associated with extended or high burn-up are an important part of the fuel & materials testing programme carried out at the OECD Halden Reactor Project. The in-core studies comprise long term fuel rod behaviour as well as the response to power ramps. Performance is assessed through measurements of fuel centre temperature, rod pressure, elongation of cladding and fuel stack, and cladding diameter changes obtained during full power reactor operation. Data from fuel behaviour studies at the OECD Halden Reactor Project, provided for the IAEA co-ordinated research programme FUMEX, are used to elucidate short and long-term developments of fuel behaviour. The examples comprise: fuel conductivity degradation manifested as a gradual temperature increase with burn-up; the influence of a combination of small gap / high fission gas release on fuel centre temperature (situation at high burn-up); fission gas release during normal operation and power ramps, and the possibility of a burn-up enhancement; PCMI reflected by cladding elongation, also for the case of a nominally open gap, and the change of interaction onset with burn-up.

1. INTRODUCTION

Safe and economic nuclear power generation requires a fundamental knowledge of fuel behaviour in different situations. The research programmes carried out at the OECD Halden Reactor Project have for more than thirty years addressed areas of particular interest to the nuclear community and provided significant contributions to the understanding of LWR fuel behaviour. In this context, the Halden Project has valued the opportunity of participating in the IAEA co-ordinated research programme FUMEX (*FU*el *M*odelling at *EX*tended burn-up), promoting fuel modelling as one of the cornerstones of nuclear reactor safety.

Fuels testing at the Halden Project has for a number of years focused on implications of extended burn-up operation schemes aimed at an improved fuel cycle economy. The extrapolation of low burn-up experience to the envisaged exposure levels requires meaningful experimental data for model validation and development. While PIE ascertains the state existing at the end of irradiation, in-core instrumentation combined with expedient experimental techniques and test designs can give information on when and how phenomena occurred for the entire in-core service. Trends developing over several years, slow changes occurring on a scale of days or weeks, and transients from seconds to some hours can be captured by the same instrumentation, altogether making up the total picture of fuel behaviour. This is exemplified in this paper with irradiation data provided by the Halden Project for the FUMEX programme (Table 1). The examples elucidate short and long-term developments of, e.g. fission gas release, fuel temperatures and PCMI. However, the extent of the selections is limited by necessity and does in no way exhaust the amount of information and detail contained in the FUMEX data. It is nevertheless hoped that FUMEX participants will find this overview useful for their continued work.

Table 1: OVERVIEW OF FUMEX CASES

FUMEX	Instrumentation				Burnup	PIE	gap	Fill gas	Pressure	Comments
	Temperature	Pressure	Elongation	Diameter	MWd/kg UO_2		µm		bar	
1	X		X		35	X	130	Helium	10	benign irradiation conditions, moved at middle of life
2		X			51	(X)	100	Helium	10	thin rod for fast burnup accumulation
3-1	X				35		100	Helium	1	power ramp at end of life
3-2	X				30		100	Xenon	1	power ramp at end of life
3-3	X				28		50	Xenon	1	power ramp at end of life
4-A	X	X	X		35		100	Helium	3	ramp at middle of life, strong fission gas release and PCI
4-B	X	X			35		100	92%He,8%Xe	1	ramp at middle of life, strong fission gas release
5		X		X	18		210	Helium	1	in-pile diameter measurements during high power at EOL
6S		X	X		48	(X)	260	Helium	1 (25+)	re-instrumented, high power period after base irradiation
6F		X	X		47	(X)	260	Helium	1 (25+)	re-instrumented, high power period after base irradiation

2. IN-CORE INSTRUMENTATION AND EXPERIMENTAL TECHNIQUES FOR HIGH BURN-UP STUDIES

Investigations of fuel performance at high burn-up have to deal with a number of experimental problems:

- the time required for reaching the desired burn-up level;
- the demand on instrumentation to function reliably in a hostile environment for long times and high fluences;
- the need for a separation of an increasing number of phenomena which tend to become more interrelated and complex.

General overviews of instrumentation and experimental techniques applied in Halden Project fuel testing programmes have been given in [1,2]. Those of them which have been employed for producing the data provided for FUMEX, are briefly outlined below.

Instrumentation

Fuel rods can be instrumented with a variety of sensors which have shown a good performance in hundreds of irradiation applications in the Halden reactor. In the FUMEX cases, fuel centre temperatures were measured with *refractory metal thermocouples*, the rod internal pressure was determined with *bellows pressure* transducers, and *elongation sensors* were employed to obtain the length increase of the cladding. In FUMEX-4, the rods contained all three of these types of instrument, providing comprehensive information on the state of the fuel from start-up to unloading.

The *diameter gauge* is a two or three point contact feeler that can be moved along the length of a fuel rod during operation. Diameter changes can be detected with a micrometer resolution, and primary and secondary ridges are made visible. FUMEX-5 is an example of application.

Re-instrumentation of irradiated fuel rods

Re-instrumentation of irradiated fuel rods is a method of shortening experiment execution times and costs. Since the instrumentation is exposed to irradiation for a comparatively shorter duration, the failure probability is decreased. Experience with re-instrumentation exists for fuel centre thermocouples, cladding elongation detectors and pressure transducers. The techniques have been applied to rods pre-irradiated in the Halden Reactor as well as in commercial LWRs.

FUMEX-6 is an example of re-instrumentation with a pressure transducer. The data obtained from this experiment gave a good indication of on-set and kinetics of fission gas release in response to a power increase.

Design features for simulation of burn-up effects

Increasing burn-up in general incurs increasing uncertainties in data interpretation, e.g. fuel temperature changes can be affected by a combination of causes like fission gas release, changes in gap size (densification, swelling, clad creep-down), and conductivity degradation. Test designs with controlled and known influential parameters therefore facilitate the assessment of separate effects.

FUMEX-3 and FUMEX-4 are examples where fission gas release (an effect with considerable spread in model predictions as the FUMEX code evaluation has shown) was simulated by known additions of xenon to the fill gas. Fuel modelling codes must be able to predict the resulting change of the temperature - power relationship in a satisfactory manner.

Xenon fill gas in combination with a small as-fabricated gap (50 - 100 μm) simulates a high burn-up situation (large amount of released fission gas, closed gap due to fuel swelling and clad creep-down) which is quite important for safety assessments. Gap conductance models can be verified with measured data from tests with such a design without the uncertainties caused by high burn-up. FUMEX-3 is an example of this.

3. DISCUSSION OF SELECTED FUMEX DATA

Data from the Halden reactor are logged with a process control computer and administrated with the tailor-made Test-Fuel-Data-Bank system (TFDB) [3]. Results are permanently saved for every 15 minutes unless a more frequent acquisition and recording is required during special experimental phases. The original several hundred thousand records of FUMEX data contain information and details which to their full extent can only be appreciated by analyses reaching far beyond the limited selection put forth in the following sections. In general, the six FUMEX cases (actually ten fuel rods with distinct parameters) provide a good basis for elucidating fuel behaviour effects of continued interest.

3.1 FUEL TEMPERATURES

Fuel temperatures take a central position in fuel modelling because of their influence on many phenomena and material properties. A good prediction is therefore an essential requirement for any code. Measured temperatures are available for FUMEX-1, 3 and 4. The last two are the most interesting cases because they encompass two or three rods which allow a comparison within the same experimental set-up.

3.1.1 Influence of gap and gas composition

Contamination of the fill gas with some released fission gas is simulated in FUMEX-4 where rod B contains a mixture of 92% He / 8% Xe. The data of the first start-up (Fig. 1) show that temperatures in rod B are slightly higher than in rod A as is to be expected. A fine detail of difference is the shape of the curves: while the He filled rod A temperature curve has a small positive curvature, rod B with some Xe exhibits a nearly linear temperature - power relationship. The transition to zero and negative curvature with increasing xenon content is quite typical and can even be used to discriminate between temperature increasing due to fission gas release or conductivity degradation, as is further discussed in 3.2.1.

More extreme situations are tested with the three rods of FUMEX-3, where small gaps (100 and 50 μm) are combined with helium or xenon fill gas. These designs simulate gap closure with burn-up, with and without fission gas release. The start-up data (Fig. 2) show the characteristic shapes of the temperature - power relationship of rods filled with He (approximately straight) or Xe (curved down). Despite a much stronger initial increase, temperatures in the rod with 50 μm gap and Xe fill gas approach those of the helium filled rod at high power when the gap is closed. Even in this case with no uncertainty in gap size, calculated temperatures for Xe filled rods are very sensitive to variations in gap conductance model parameters like surface roughness, waviness factor and contact conductance contribution. The general experience with similar Halden Project temperature data (xenon or strong fission gas release together with closed gap by design or burn-up) indicates that gap conductance is better than models tend to calculate for this situation.

3.1.2 Thermal conductivity degradation

Conductivity degradation of UO_2 fuel has been manifested both with simulated and in-reactor burn-up [2,4,5] and is now generally accepted as an important effect to be considered in modelling of high burn-up fuel behaviour. A usable in-pile experimental set-up requires temperature measurements and the minimization of disturbing influences from changes of gap conductance. These conditions are best observed in FUMEX-3, rod 1 with helium fill gas and 100 μm gap. Fig. 3 shows indeed that temperatures normalized to a constant rating of 25 kW/m increase with burn-up. The step at 28 MWd/kgUO_2 is probably due to fission gas release (see further discussion in 3.2.1).

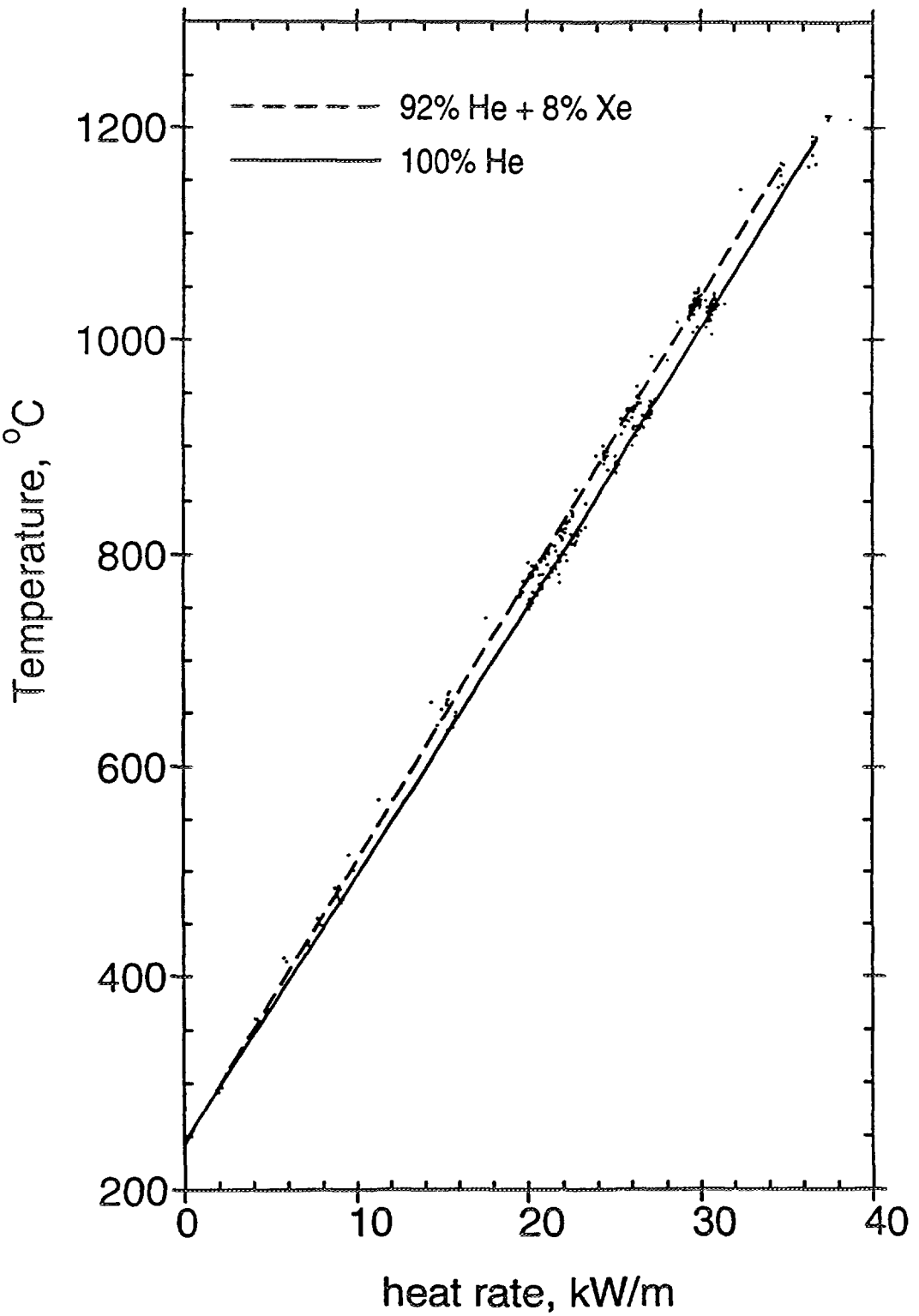

FIG. 1. *FUMEX 4 Start-up temperatures*

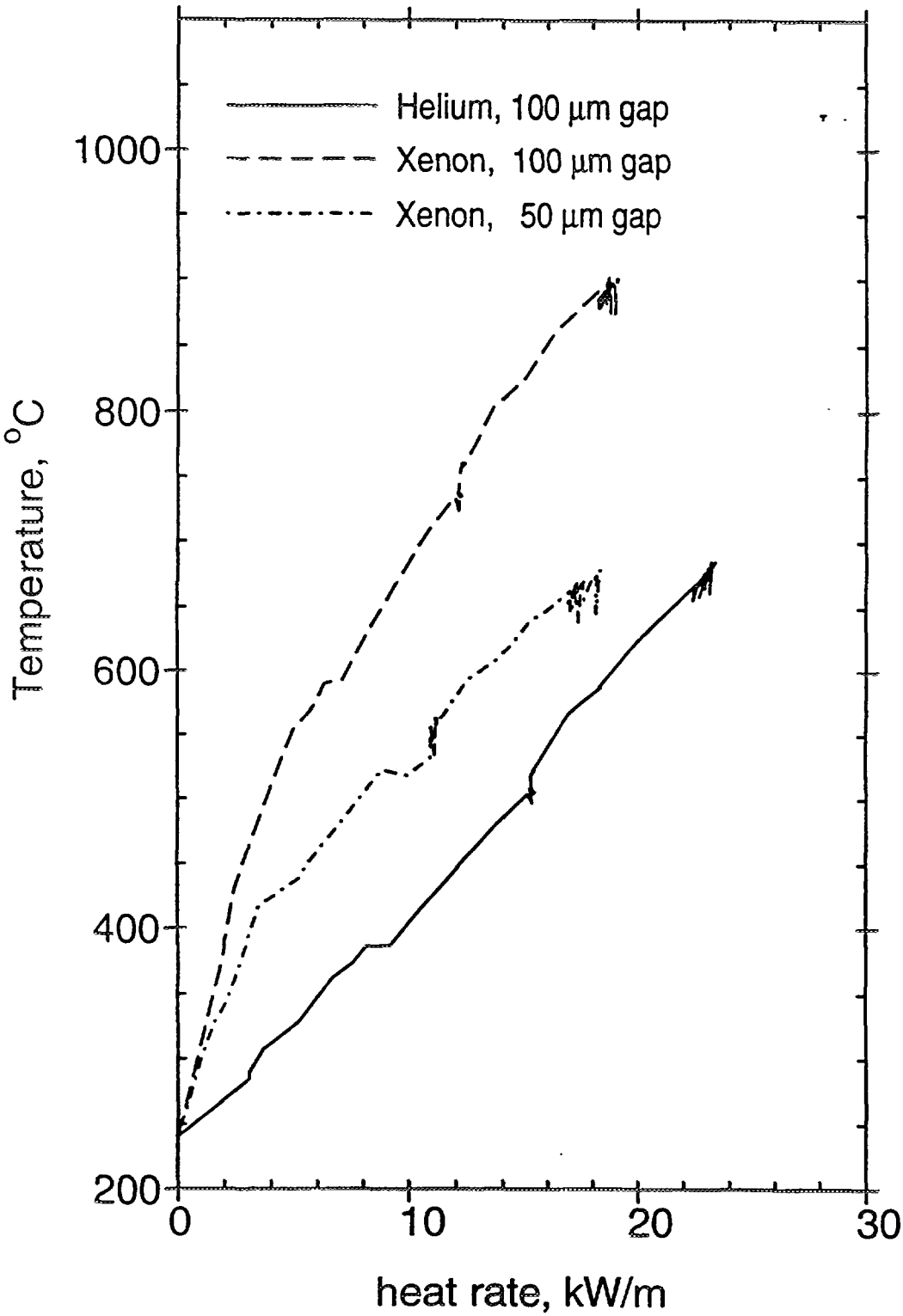

FIG. 2. FUMEX 3 Start-up temperatures

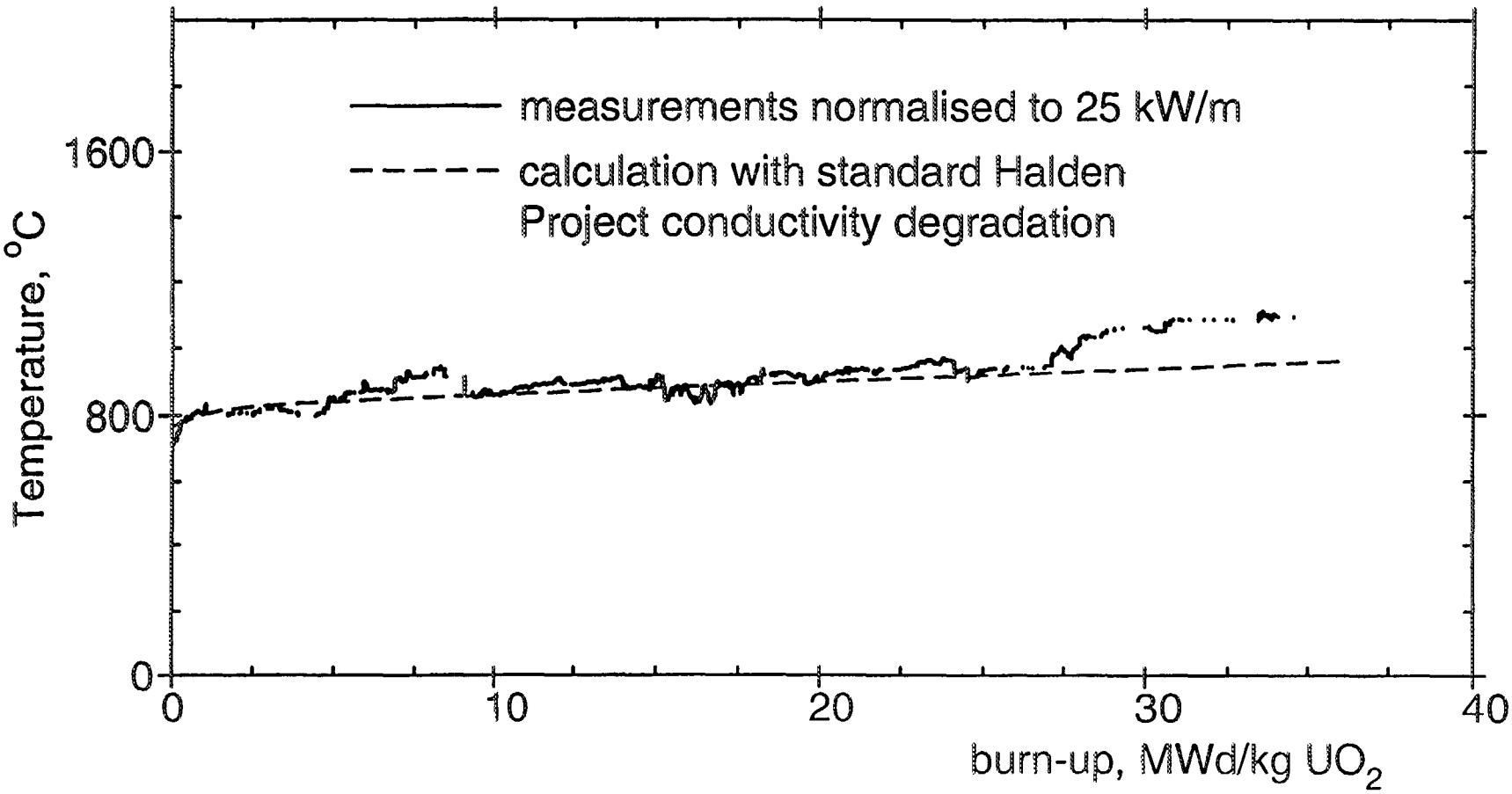

FIG. 3. *FUMEX 3 Rod 1 Temperatures at 25 kW/m*

The deduction of λuo_2 degradation from fuel centre temperatures requires a model to separate the total measured ΔT into the ΔT across the gap (influence of gap conductance) and the ΔT across the pellet (influence of λuo_2). Assuming a constant cold gap (swelling balanced by reverse relocation), the increase can be satisfactorily reproduced by a correction "c*Burnup" in the phonon term of conductivity:

$$\lambda phonon = 1/(a + b*T + 2.38*burnup)$$

The value of 2.38 ($m.K/(kW.MWd/kgUO_2)$) is in line with other Halden Project data and comparable to SIMFUEL results [4] where 1.94 was obtained. The difference is attributed to additional irradiation induced changes which cannot be simulated out-of-pile.

3.2 FISSION GAS RELEASE

The release of fission gases from UO_2 fuel has important consequences. The thermal behaviour of helium filled rods is affected through contamination of the pellet-clad gap with xenon, leading to a temperature rise which in turn will cause even more fission gas release. It has been postulated that rod overpressure and consequently clad creep-out may occur at high burn-up; licensing may require this effect to be considered for the safety case. Modelling therefore calls for a data base of fission gas release covering a range of burn-up and different operational situations. All FUMEX cases include information on this phenomenon, either directly through pressure measurements, more indirectly through its effect on fuel temperatures, or from PIE.

3.2.1 Release threshold

Halden Project data have shown that significant fission gas release ($> 1\%$) can be expected when a burn-up dependent temperature threshold is exceeded [6]. This can be associated with the formation of connections to the open surface of the fuel when intergranular porosity and fission gas bubbles interlink, a process which is also apparent in significant surface to volume ratio changes measured with Halden Project gas flow rigs [5].

The temperature data from rod 1 of FUMEX-3 confirm the threshold rule. Fig. 4 shows that measured fuel centre temperatures (in the middle of the 140 mm long segment) were below the threshold up to a burn-up of 25 $MWd/kgUO_2$. Then the threshold was just reached (slightly exceeded in pellets without the thermocouple bore). Later at 28 $MWd/kgUO_2$, the threshold was exceeded more clearly. Fig. 4 also shows an evaluation of start-up data which were fitted with second order polynomials. The first order coefficient (slope at zero power) increases approximately linearly until the point of postulated fission gas release is reached, while the second order coefficient (curvature) is constant for the same period. Then both coeffficients change, indicating that a new effect (fission gas release) is influencing fuel behaviour. This analysis thus discerns the causes of temperature increase: fuel effects (conductivity degradation) do not change the curvature, while gap effects (fission gas release) do. The point of transition in this case is at 26 - 27 $MWd/kgUO_2$, i.e. during operation close to or slightly exceeding the release threshold. Also the comparison with Fig. 3 confirms that temperatures started to increase at about 27 $MWd/kgUO_2$.

3.2.2 Release kinetics

Compared with temperature data, rod pressure measurements allow a more direct interpretation with respect to fission gas release. The two rods of FUMEX-6 (instrumented with pressure transducers after base irradiation to about 44 $MWd/kgUO_2$) are examples of release response to power increases of different speeds. The case 6S was presented in [2]; the onset of fission gas release was clearly detectable during the slow rise to high power. The case 6F (fast increase) is discussed below.

At end of base irradiation, about 17% FGR were determined during re-instrumentation. A feature of the base irradiation history is the operation at low power (16 - 19 kW/m) near the end; calculations indicate that fuel temperatures were 150 to 200 °C below the release threshold. This promotes re-sintering

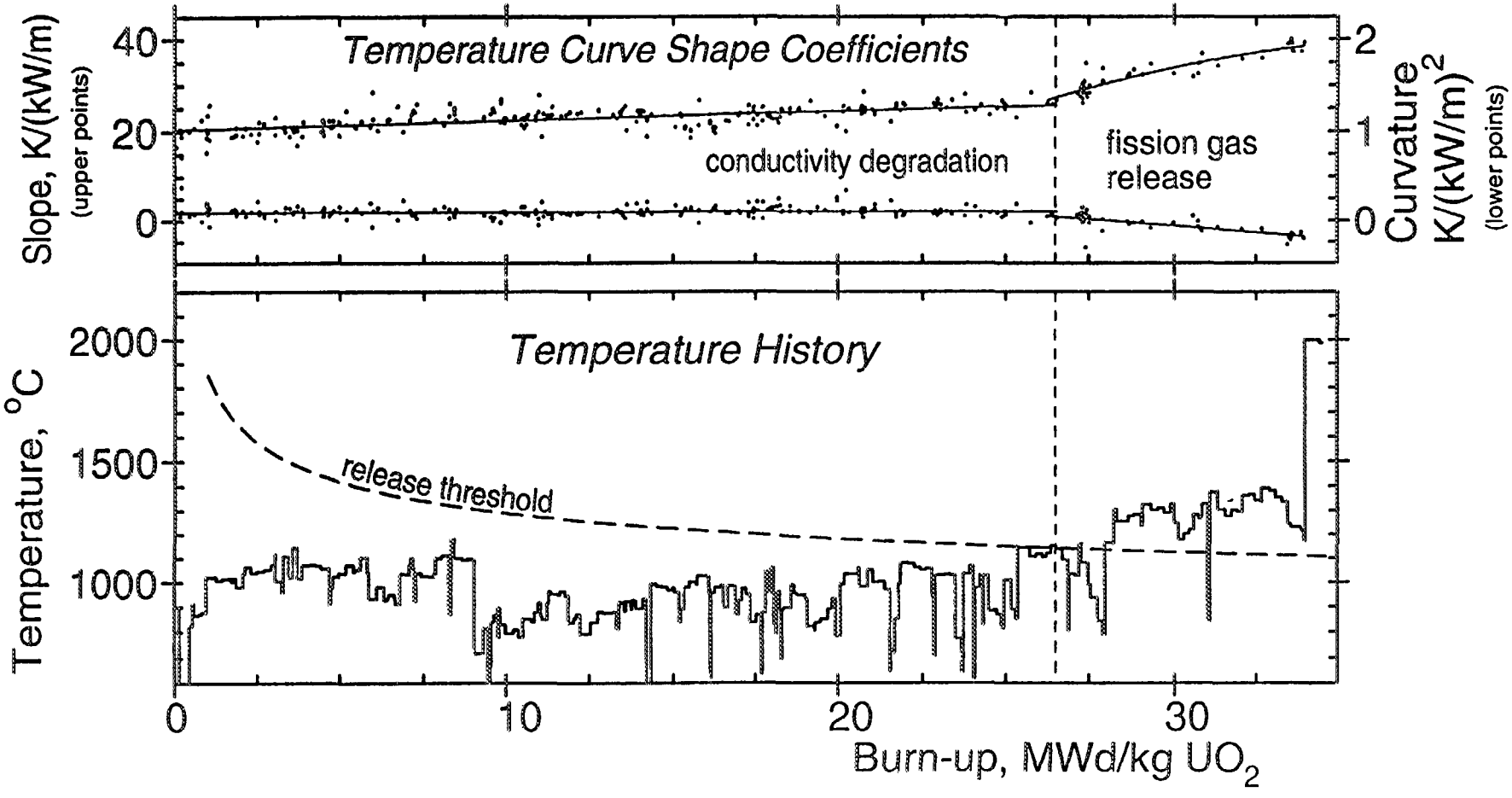

FIG. 4. *FUMEX 3 Rod 1 Temperature characteristics*

after previous FGR, gradually stopping further release, a pattern which is also apparent in surface to volume ratio measurements [5]. The final ramp with powers higher than at any time during base irradiation therefore would lead to release not only from peripheral parts of the fuel previously at too low temperatures, but also from central parts where fission gas again was accumulated. In addition, the rods were placed in the core after re-instrumentation in such a way that parts previously at lower power were at higher power during the final ramp and holding period.

The pressure increase during the final ramp (Fig. 5, data reduced to 0 power and 240 °C) shows a basic square root of time dependence. This means that release is diffusion controlled and driven by annealing of the concentration built up at lower temperatures (the approximation RELEASE $\approx 6.\sqrt{(\Omega/\pi)} - 3.\Omega/2$ of the diffusion equation solution for $\Omega = D.t/a^2 < \pi^{-2}$ can be assumed to hold for the entire time at high power).

3.2.3 Enhancement with burn-up

A possible enhancement of fission gas release with burn-up has been reported in several publications [7,8], but evidence for behaviour more "as expected" has also been presented [2,9]. An enhancement can be associated with two effects: the formation of a porous rim with increased athermal release, and higher fuel temperatures due to poorer conductivity of the rim as well as a general UO_2 conductivity degradation.

The HBWR has a lower epithermal flux than LWRs. Therefore the conversion of U-238 to Pu-239 is smaller and does not lead to a pronounced rim with high burn-up. This feature simplifies data interpretation as only the quantitatively understood effect of UO_2 conductivity degradation remains to be considered for improved temperature predictions if measurements are not available.

Although temperatures have not been measured for FUMEX-2, they can be estimated from instrumented co-irradiated sibling rods, indicating that they have been close to, but below the release threshold except for a short period at low burn-up. The pressure data normalized to zero power and 20 °C (Fig. 6) show that release must be small (< 3%) since the observed pressure increase can be explained by free volume reduction due to fuel swelling. Thus release from regions other than the rim seems to follow "normal" behaviour at least up to the burn-up reached with this test.

3.3 PELLET-CLADDING MECHANICAL INTERACTION

The rod of FUMEX-1 experienced a power increase at about 20 MWd/kgUO_2 because of loading to a more central core position. Cladding elongation for seven start-ups after moving the assembly is shown in Fig. 7. Most of the elongation is due to free thermal expansion, although the first start-up seems to deviate slightly from the following ones. A change of slope at the end of the power increases indicates pellet-cladding interaction where codes predict that the gap is still open. The point of interaction onset moves to higher powers with increasing number of start-ups; PCI starts at about the highest power reached during the preceding ramp for start-ups 2 and 3. It seems that the pellet fragments can be relocated inwards during the holding periods up to a certain limit. These details can hardly be reproduced by a conventional model assuming solid pellets concentric with the cladding. Cladding elongation can also provide information on the seemingly more important circumferential deformation due to radial expansion of the pellets. The close relation between hoop strain and axial strain, both in terms of magnitude and relaxation behaviour, was shown with Halden Project data comparing elongation and diameter changes obtained in-pile for the same rod [10], Fig. 8. Since axial cladding elongation can be measured more easily and frequently than diametral deformation, the data should not be neglected. However, the difficulties of modelling axial PCMI are recognized; they are probably the main reason why only few codes try to include the effect in a non-simplistic way.

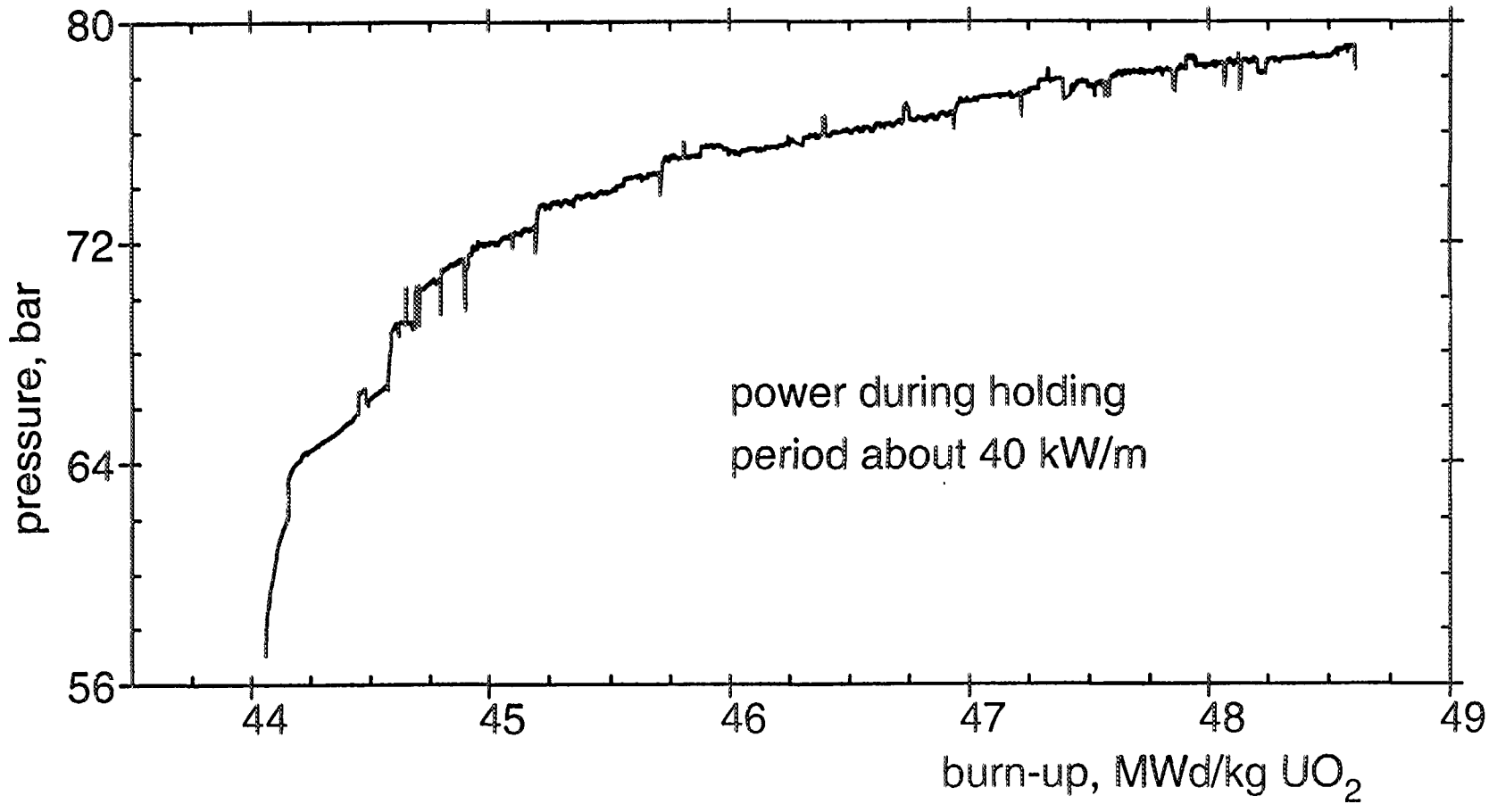

FIG. 5. *FUMEX 6F Pressure response to power increase*

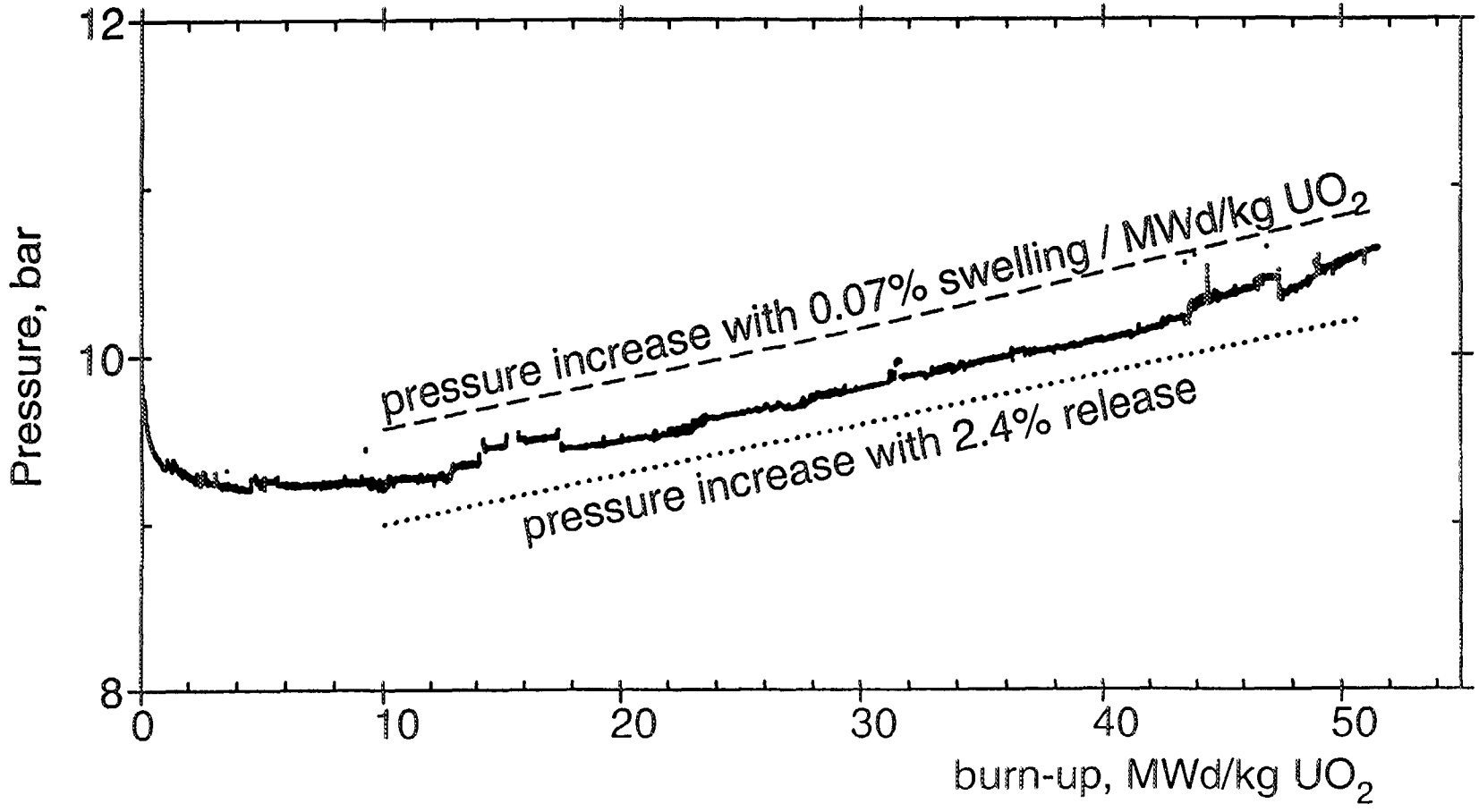

FIG. 6. *FUMEX 2 Pressure normalized to zero power and 20 °C*

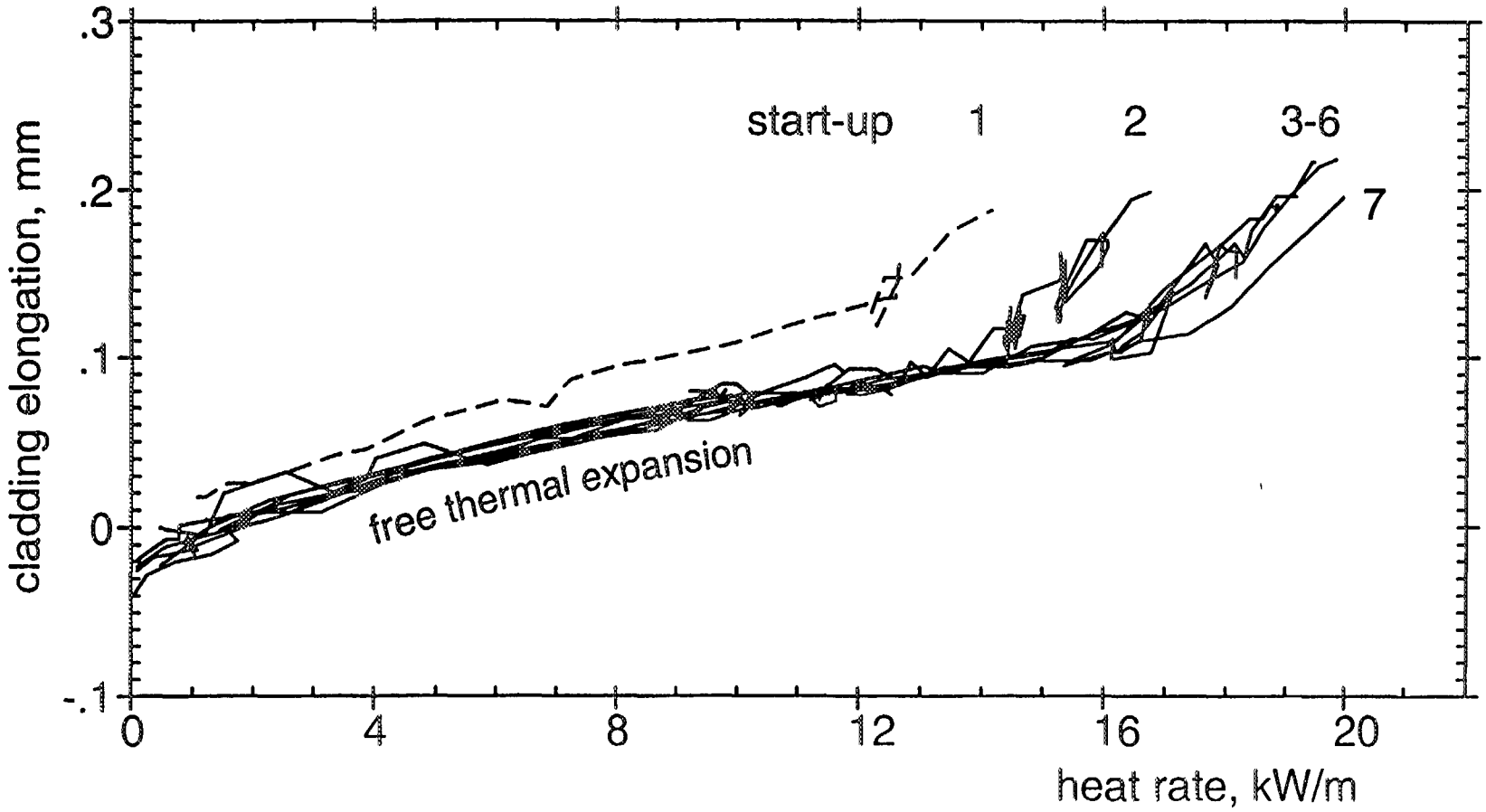

FIG. 7. *FUMEX 1 Start-up cladding elongation after reload*

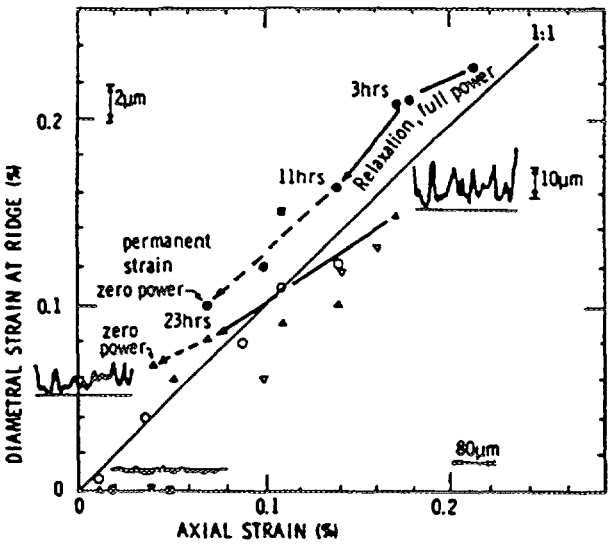

FIG. 8. Comparison of elongation and diameter changes in-pile

3.4 A COMPLEX DATA SET

The two rods of FUMEX-4 are the most instrumented of the tests included in the FUMEX study. Simultaneous measurements of cladding elongation, temperature and pressure provide a good insight into the behaviour of fuel and cladding. At middle-of-life, a power ramp was executed which led to considerable fission gas release (this ramp was not foreseen in the original experimental plan and the pressure sensors were not dimensioned for the rod pressure eventually occurring; an end-stop limited the compression of the bellows such that useable pressure readings are only available for some time into the high power period).

Fig. 9 shows the reaction of all three sensors during the high power period. It is not possible to provide a detailed analysis within the scope of this paper, but a few features can be pointed out:

- the general shape of the pressure increase again indicates diffusional release;
- steps in the pressure occurring at shut-downs point to restricted communication with the plenum at power;
- increasing temperatures also reflect the fission gas release;
- small temperature overshoots after start-ups may be the results of non-instantaneous mixing of helium and fission gas;
- considerable axial straining at start-ups is followed by relaxation (this behaviour is not well predicted by the codes participating in FUMEX).

Modelling of these details combining thermal and mechanical behaviour in a consistent manner is surely a challenge.

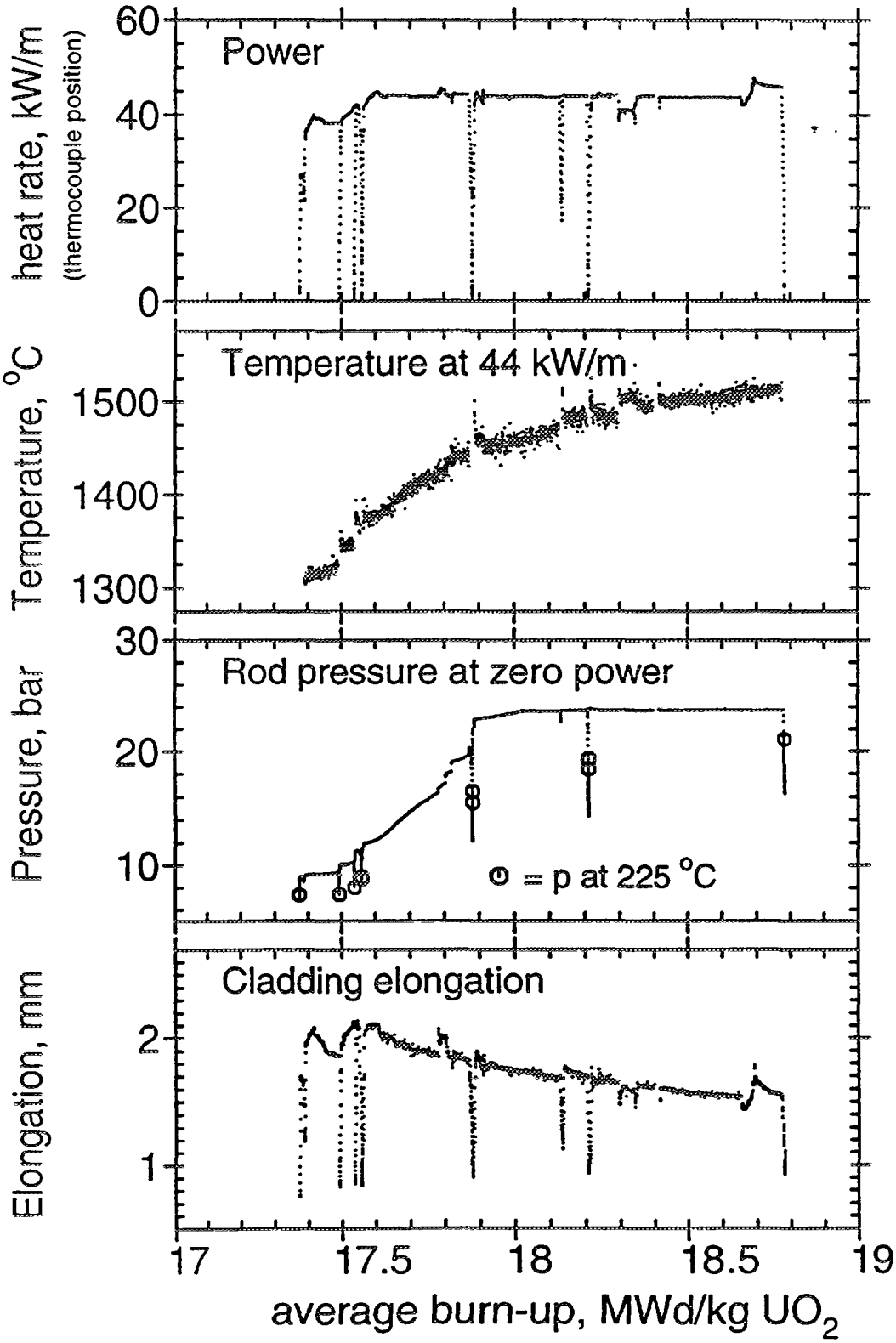

FIG. 9. FUMEX 4 Rod A Response after power ramp

4. SUMMARY

The data provided by the Halden Project for the IAEA co-ordinated research programme FUMEX constitute a comprehensive basis for fuel modelling and code validation. The examples selected in this paper illustrate fuel behaviour at different stages of irradiation:

- fuel temperatures influenced by design parameters and fission gas release;
- evidence for increasing temperatures due to conductivity degradation together with a quantitative analysis leading to a result in accordance with other published data;
- fission gas release at normal and high power operation, and the validity of a release threshold;
- cladding elongation behaviour providing evidence for pellet-cladding contact even for a nominally open gap, and the compliance and relocatability of pellet fragments.

REFERENCES

[1] AARRESTAD OLAV, Fuel Rod Instrumentation; IAEA meeting on "In-core Instrumentation and In-situ Measurements in Connection with Fuel Behaviour", Petten, The Netherlands, 1992.

[2] WIESENACK, W., Experimental techniques and results related to high burn-up investigations at the OECD Halden Reactor Project; IAEA Technical Committee Meeting on fission gas release and fuel-rod chemistry related to extended burn-up (IAEA-TECDOC-697), Pembroke, Canada, 1992.

[3] WIESENACK, W., Data acquisition and presentation tools at Halden; 30th EWGIT Plenary Meeting, CEN/SCK Mol, Belgium, 1988.

[4] LUCUTA, P.G., VERRALL, R.A., MATZKE, H., HASTINGS I. J., Thermal conductivity and gas release from SIMFUEL.

[5] KOLSTAD, E., VITANZA, C., Fuel rod and core materials investigations related to LWR extended burn-up operation; Journal of Nuclear Materials 188 (1992) 104-112.

[6] VITANZA, C., KOLSTAD, E., GRAZIANI, U., Fission gas release from UO_2 pellet fuel at high burn-up; ANS topical meeting on light water reactor fuel performance, Portland, 1979.

[7] MANZEL, R., EBERLE, R., Fission gas release at high burnup and the influence of the pellet rim; International topical meeting on LWR fuel performance, Avignon, France, 1991.

[8] FORAT, C. et al., Fission gas release enhancement at extended burnup: experimental evidence from French PWR irradiation; IAEA Technical Committee Meeting on fission gas release and fuel-rod chemistry related to extended burn-up (IAEA-TECDOC-697), Pembroke, Canada, 1992.

[9] KNUDSEN, P., BAGGER, C., MOGENSEN, M., TOFTEGAARD, H., Fission gas release and fuel temperature during power transients in water reactor fuel at extended burnup; ibid.

[10] VILPPONEN, K 0., In-pile measurements of pellet cladding interaction and relaxation; IAEA specialists meeting on "Fuel Element Performance Computer Modelling", Blackpool, U. K., 1980.

DEVELOPMENT OF A CODE AND MODELS FOR HIGH BURNUP FUEL PERFORMANCE ANALYSIS

M. KINOSHITA, S. KITAJIMA
Central Research Institute of the Electric Power Industry,
Tokyo, Japan

Abstract

Firstly the high burnup LWR fuel behaviour is discussed and necessary models for the analysis are reviewed. These aspects of behaviour are the changes of power history due to the higher enrichment, the temperature feedback due to fission gas release and resultant degradation of gap conductance, axial fission gas transport in fuel free volume, fuel conductivity degradation due to fission product solution and modification of fuel micro-structure. Models developed for these phenomena, modifications in the code, and the benchmark results mainly based on the Risø fission gas project is presented. Finally the rim effect which is observed only around the fuel periphery will be discussed focusing into the fuel conductivity degradation and swelling due the porosity development.

1. INTRODUCTION

Although nuclear power stations have non-cost based benefit, they are in competition with conventional power sources in commercial market. Therefore cost reduction efforts are taken in nuclear engineering. The high burnup extension of nuclear fuel is one of the most straight and significant methods to reduce the fuel cycle cost. It reduces the purchasing amount of fuel and also reduces storage space of the spent fuel as an example. Consequently the total mass flow of fuel cycle is decreased.

Research incentive

From the view of the technology development, the appreciated approach is to improve the fuel performance and induce the cost reduction. The high burnup extension is such a case and presently it is one of the major target of the industry. Also in the research of the LWR fuel performance, the front is the high burnup behavior.

The commercial reactor condition is specific in the following points: (1) The fluxes of neutron and gamma are relatively low compared to such as test reactors. This induces slow rated processes of irradiation damage. (2) The operating temperature is relatively low. Consequently the damage recovery rate is also low. (3) The dwelling time of the fuel is long such as for 4 to 5 years. This induces long-term damage accumulation. (4) These conditions result in micro-structure changes of fuel related materials such as fuel itself, cladding, and other parts of supporting grids, springs. At high burnup the last mentioned item (4) is in front of the research.

In general words this process could be expressed as "birth of new acting structure." For example, so called "fuel rim structure" is formed by superposing effects of fission damage accumulation and fission product accumulation and it seems to be in steady and stable structure. The other example is the cladding corrosion where structure of oxide and oxide/metal interface are in a steady state condition after initial break away of the protective layer.

These phenomena could be categorized as "complex" type. Here definition of the complex phenomena is that (1) it is composed of several individual phenomena, and (2) it is not just a linear-sum of the individual processes but a functional result of no-linear mutual interactions of different kinds of processes. These non-linearities cause many unexpected results. Therefore the control parameters, and controllability of the phenomena are in question. (If you find it you get commercial benefit.)

Use of codes

Computer modeling is the key to study these non-linear complex processes. And it is one of the front of the present advanced scientific tools. The objective of the codes are (l) simulation of the fuel behavior, and (2) analysis of the experimental data. For the former case the target of fuel models is to provide a computer based virtual fuel which integrates experimental results. Recent computer technology enable us to simulate every aspect of the fuel behavior. However as the processes are the complex ones, the usage of the code should be always parallel with experiments. When the process is non-linear the prediction of the code is not a simple logical process. The solution is dependent on initial conditions and other parameters. In high Burnup new micro-structure is organized by themselves. This non-linear situation is similar to the phase diagrams of the metallurgy and experimental parametric research is essential. The use of the code for the data analysis is to identify the macroscopic working condition of the fuel, such as local temperature, its gradient, stress/strain and burnup. Accurate estimation of these state-variables is the key to clarify the diagram of the complex phenomena.

The fuel reliability is closely related to threshold phenomena. Many of the remarkable processes have intrinsic threshold boundaries where the process become significant. The fuel temperature of 1200 °C is the typical one as all solid state transports are activated at this temperature in U02. The use of the fuel performance analysis code is to integrate the functional behavior of each process model and investigate the multi-dimensional parametric manifold. Final target is to identify the surface structure of the manifold to find out thresholds or boundaries related to the fuel reliability.

2. FUEL BEHAVIOR AND ITS BURNUP DEPENDENCE

The overall view of the fuel behavior is shown in Figure 1. The major performance controlling process up to around 40 MWd/kgM could be listed as follows;

(a) densification
(b) gas release (especially transient release)
(c) axial gas stacking/mixing
(d) pellet cracking
(e) relocation
(f) cladding creep down

The items of (a) to (c) are de-stabilizing phenomena of the fuel temperature. Especially (b) and (c) are dynamic and transient effects and short time response is important. The fuel temperature is the key of the non-linearity and it also may increase drastically non-proportional to the local power when the temperature positive feedback is occurred.

For higher burnup several processes are under investigation. Cladding corrosion might be a problem for reactors that coolant temperature is higher. The fission gas release might be a problem for reactors that fuel temperature is higher. Newly experienced phenomena is the rim effect which is due to accelerated burnup accumulation near pellet surface as a result of Pu build-up. There the original grains become assemble of smaller grains of around 100 nm diameter. The material property of this region is now in question.

3. BRIEF HISTORY OF THE CODE DEVELOPMENT

One of the main objectives of the code is to evaluate fuel reliability. It is to investigate the threshold phenomena and quantify the stable and safe region for design and operation. It is revised as new information comes out from experience.

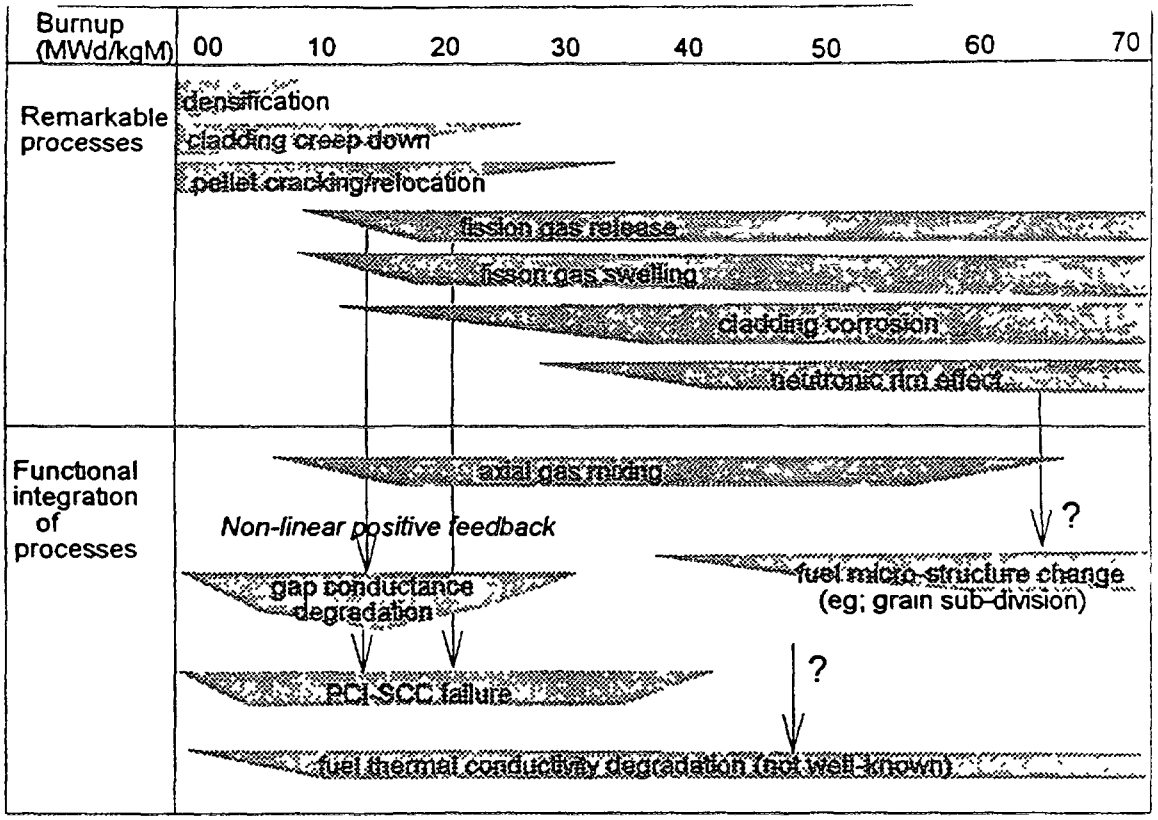

Fig 1 Major processes in fuel behavior

The code development was in parallel to the improvement of fuel. In 1970's PCVSCC failure was experienced. It was due to overlapping effects of initial insufficient experience on design/fabrication and reactor operation. The activity of the code development was increased to investigate the failure mechanism. The target was to evaluate (1) temperature increase due to gap conductance degradation in conjunction with fission gas release (temperature feed-back effect) and (2) cladding local stress due to PCMI. The code, such as the FEMAXI-III and its brothers in Japan, was utilized to assess the most prudent fuel temperature in operation and gave key information for the core and fuel design improvements [1]. Then the problem was fixed by (1) fabricate improved non-densifying fuel pellets, (2) pressurize the rod by Helium, (3) introduce zirconium barriered cladding. (4) reduce the linear heat rating of rod, (5) modify pellet shape to reduce the local ridge forming PCMI, (6) reduce reactor ramp rate to weaken the PCMI. Here the Helium pressurization was especially effective to achieve thermal stability. The last remedy was adapted by utilities and the fuel reliability was improved. These improvements became widely in commercial in 1980's.

The next decade of 80's was started as gradual move towards higher burnup. The target was around 50 MWd/kgU of the assembly averaged maximum. The elaborated test reactor experiments were conducted and some enhancement of fission gas release was observed. Especially analysis codes were utilized to investigate temperature and burnup dependence of the gas release. It was shown that at higher burnup such as at 30MWd/kgU and at the same calculated temperature, gas release was seems to be enhanced. However in these codes' sub-models of fuel thermal conductivity were not burnup dependent and consequently the calculated temperature was in question. Presently the key issue is the thermal conductivity degradation of fuel at high burnup. The main target of the code is now to clarify the state - variables, especially the temperature, at high burnup operation. On the other hand the burnup extension requires some design change. It is primarily an increase of enrichment and use of neutronic poison such as Gd added in the fuel material. The resultant heterogeneous core induces locally higher power. This situation gives some excess from commercially experienced power range. Therefore re-evaluation of the fuel performance at middle range of burnup is in interest. Therefore the performance at moderate burnup should be re-evaluated again and then the behavior at higher burnup should be analysed as the extension of that from the middle burnup.

4. IMPROVEMENT OF THE THERMAL MODEL

4.1 GASEOUS ENVIRONMENT AT LOCAL FREE VOLUME

Thermal stability

For the range of the moderate burnup the thermal stabilization should be re-analysed and it should be confirmed for the new design. Here we remind some detailed study concerning the temperature feedback in view of the high burnup extension.

As reviewed in Figure 1 the thermal feedback occurs when the pellet-cladding gap is present. Figure 2 shows fuel temperature increase due to the change of gas composition in the pellet-cladding gap calculated by FEMAXI-III for the initial stage of the irradiation. The residual radial gap of 30 μm is assumed. The effect of gas release is significant, around 300°C, even at such small gap condition. The ramp rate of the temperature is under the control of fission gas contamination rate at the gap volume.

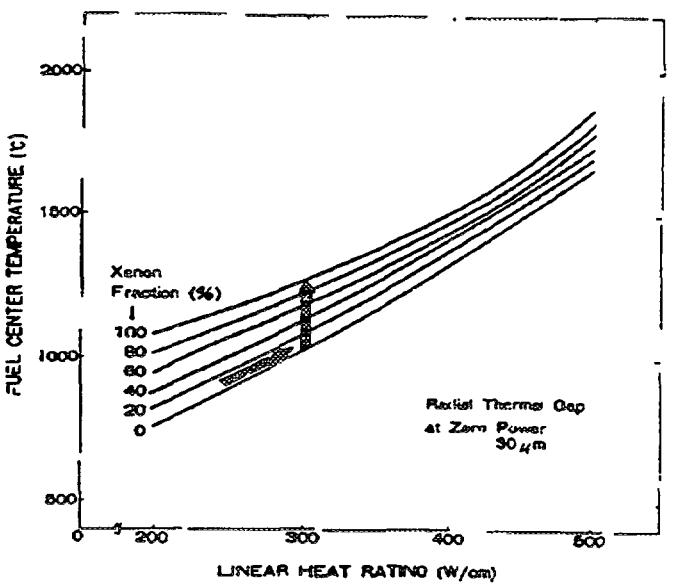

Fig.2 Temperature increase due to change of gas composition at P/C gap.

Axial gas transport

The detailed analysis of this thermal instability was performed introducing axial gas transport model. The several in-reactor experiments revealed that the instability is occurring as shown in Figure 3.

Here the fission gas is released at local region of high power or high fuel temperature. The released gas is transported by axial flow and mutual diffusion of Helium and fission gas. The local pressure increase is due to released gas volume, reduction of free volume due to thermal expansion, and increase of gas temperature. The rate of the axial flow is also dependent on the flow resistance at pellet/Cladding gap. The axial diffusion is dependent on the distance to the plenum and ratio of axial path cross section and the local free volume. The time constant of the diffusion is inversely proportional to the square of the rod length and the mixing is slow in long commercial fuels. One of such analysis is shown in Figure 4 and Figure 5 [2].

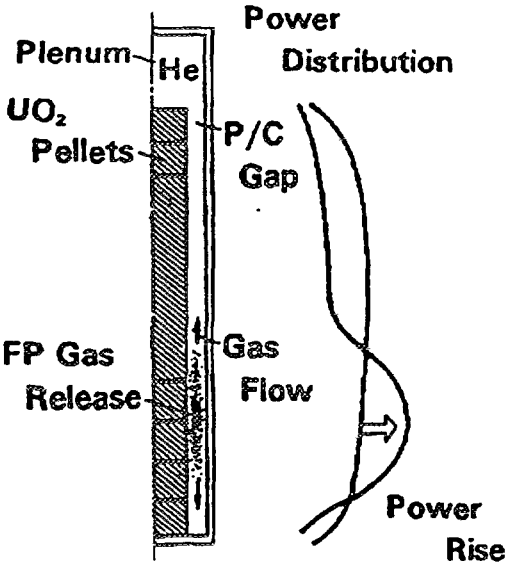

Fig.3 Axial fission gas flow and inter-mixing with filled Helium [2]

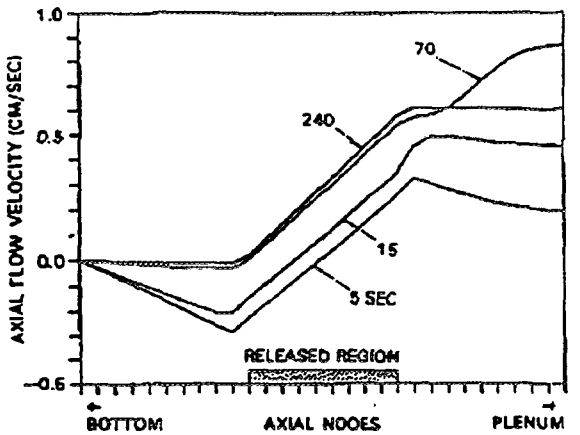

Fig.4 Axial gas flow at transient gas release.

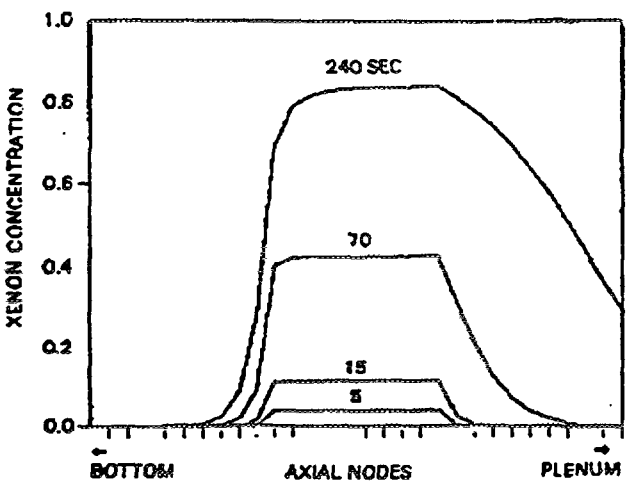

Fig.5 Axial concentration increase at transient gas release.

For the moderate burnup the results of detailed analysis of the thermal feedback effects could be summarized as follows;

(1) The beneficial effect of Helium pressurization and that of local free volume such as at pellet end-dish was confirmed by the analysis.
(2) The thermally stable, non-densifying pellet fabrication is very effective. There is a threshold of the allowable densification which is suppressing the instability.
(3) The pellet with improved gas release characteristic is appreciated. Prevent burst releases which is in time scale of minutes, and achieve slow release which is in time scale of hours are essential. There is a threshold of the gas release rate to induce the instability.
(4) The thresholds of (2) and (3) are dependent on heat rating and rod/pellet geometry.
(5) The load follow type of operation introduces axial flow and increase axial transport of the released gas. This enhances mixing and prevents thermal feedback. Therefore at least lower burnup up to 20MWd/kgU, as stated later, load follow type of operation is beneficial for the thermal stability.

4.2 FUEL THERMAL RESISTANCE MODEL

To analyse the thermal stability as burnup increases, the analysis model for fuel thermal resistance should be improved. Figure 6 illustrates our schematic view of fuel thermal resistance during irradiation.

The cause of the increase of fuel thermal resistance could be categorized as two parts [3,4]. (1) the effect of fission product solution in fuel matrix, and (2) the remaining part consisted of different mechanisms. The first part is dependent only on burnup and it has no potential to induce thermal instability (static character). The remaining part of the resistance could be dependent on other state variables such as gaseous component in the free volume, pellet radial relocation, mechanical restraint caused by PCMI (dynamic character). The concerned background mechanism of this portion is pellet cracking and relocation, grain boundary separation due to gas accumulation and applied thermal stress, and planar defects caused by gaseous precipitation (Fig.6). Although contribution of point defects and dislocations could be also important, these effects are not modelled in this paper.

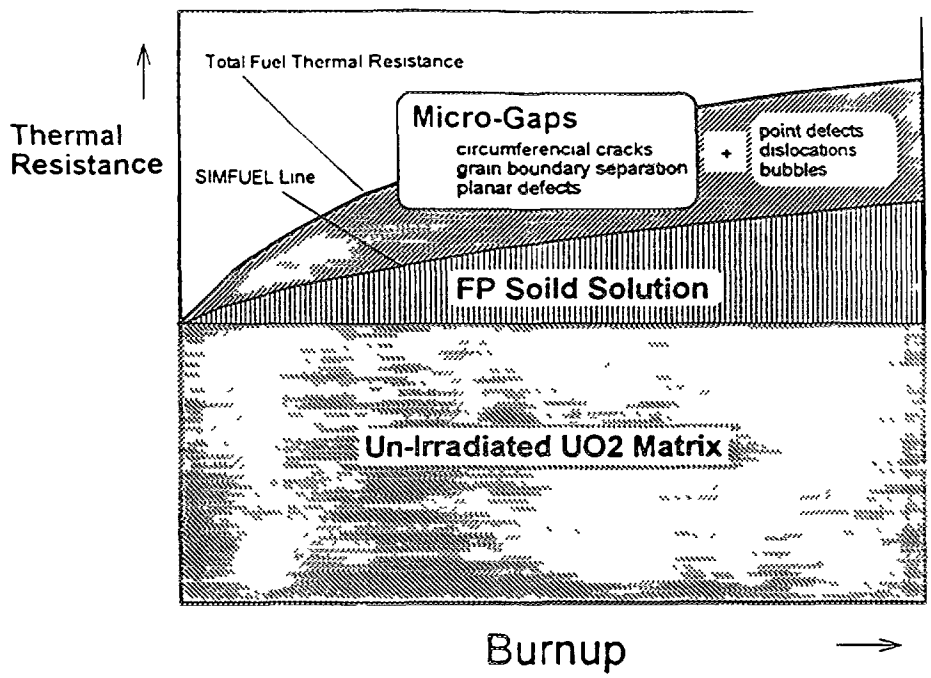

Fig 6 Schematic view of components of fuel thermal resistance during irradiation

(1) Effect of fission product solution

Most of the produced solid fission products may be in solution at normal LWR fuel condition. The quantity of the solid solution is proportional to the burnup, and it reduces the thermal conductivity of UO2 matrix. The solute atom induces lattice distortion and heat conduction is reduced by the phonon scattering. This effect was theoretically analysed by Klemens [5]. Ishimoto adapted the equation for UO2 [6], that is given by,

$$\lambda'_p = \lambda_p \frac{\tan^{-1}(2.40\sqrt{\lambda_p \cdot x}}{2.40\sqrt{\lambda_p \cdot x}} \qquad (1)$$

Here λ_p is the thermal conductivity of UO2 matrix with solute atoms and λ_p is that of unirradiated UO2 matrix. And x is concentration of the solute fission products. We assumed that the increase rate of the concentration is 0.1% per 1MWd/kgUO2. This assumption is that all solid fission products are in solution. Therefore it may give the upper limit for the conductivity degradation by this mechanism.

(2) Microgap model

The remaining part of the change of fuel resistance could be modelled by the microgap. Because the thermal conductivity of gas is less than that of UO2 matrix, any kind of internal gas gap causes degradation of effective thermal conductivity. Originally we introduced this model to simulate cracks and then extended to consider separated grain boundaries and now we intend to include effects from micro-structures which has planar shape with gas phase.

At the first stage of the irradiation, pellets are cracked into several fragments by thermal stress. This may take place at reactor startup and subsequent power cycling. At the lower burnup while pellet-cladding gap is still open, pellet relocation, that is a movement of the gap volume into the pellet internal, is the dominating mechanism of the decrease of effective fuel conductance (Fig. 1). Therefore even at condition of p/c gap closure, thermal resistance due to inner gap is still present. This model is expected to evaluate the potential of the thermal instability at the range of middle burnup where local power may increase due to higher enrichment adapted for burnup extension.

At high burnup the fission gas accumulates at grain boundary and its separation may take place when tensile thermal stress is brought out. This may caused by reactor shut-down or rapid power cycling as it induces stress reversal and may develop micro-cracks. If the separated grain boundaries are connected to the rod free volume, these open space may have the same pressure as that of plenum gas. However the gas composition is in question as the diffusional mixing is slow as (1) the path to the free volume is very narrow, and gas release from grain retards counter diffusion of gas from the free volume.

At higher burnup when pellet-cladding has tight contact, other mechanism that is the effects of newly developed fuel microstructure could be dominant. Irradiation damage is accumulated combined with precipitation of fission products. Our model covers one of them, that is planar defects with gaseous precipitation.

Simplified model

For use in analysis codes simplified model is necessary. Therefore some assumptions were made as follows [3];

(1) Microgap is uniformly distributed in pellet. Radial distribution such as due to the temperature induced microstructural change is ignored.
(2) Direction of defects are mapped into two components that are radial and circumferential directions. And the thermal barrier due to the radial component is ignored.
(3) Microgap width was set 0.6 11 m as a constant. This distance was determined by code benchmarking for temperature data from test fuel rods.

(4) Gas component in microgap is assumed as 100% fission gas (Xe+Kr).

(5) Gas pressure in microgap is assumed to be the same as gas pressure at free volume, such as plenum. In this model the key of the heat resistance is at the interface of the U02 matrix and the gas phase. The transfer loss of momentum energy at the interface induces the solid-gas temperature jump as shown in Figure 7.

In irradiated fuel pellet circumferential cracks are observed at PIE. These cracks are perpendicular to the heat flux. The number of the cracks is dependent on pellet property and development of internal stress which is function of pellet cladding interaction and power history such as number of cycles. The radial cracks are parallel to the heat flux and it has no effect on the increase of the thermal resistance.

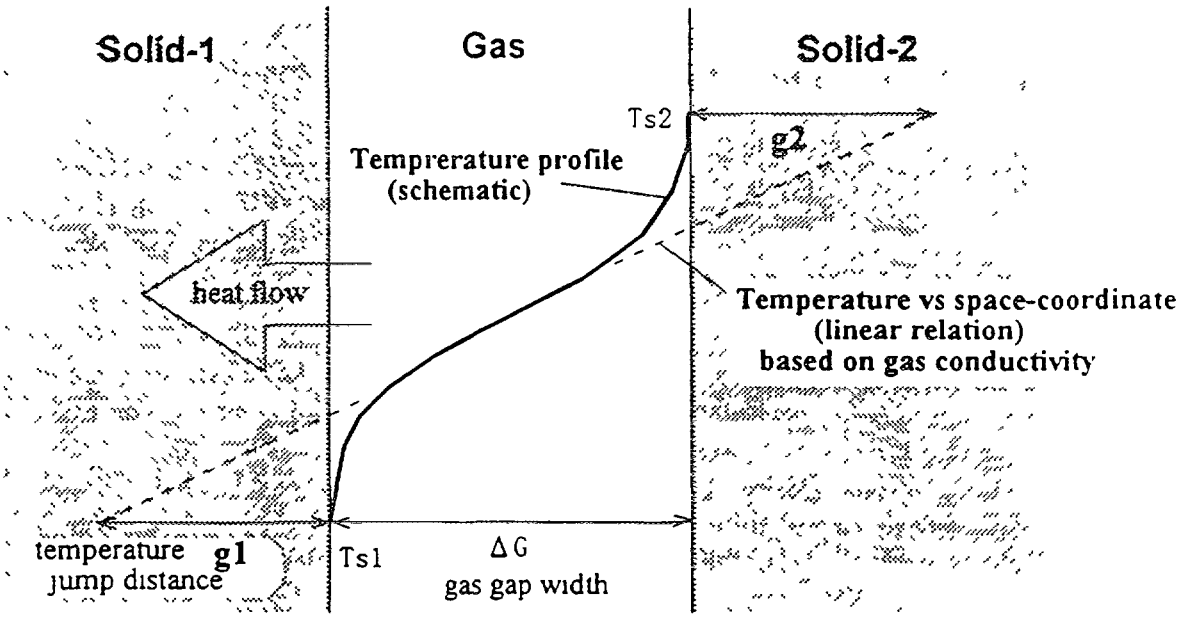

Fig 7 Temperature jump distance at gas-solid interface

The thermal conductance, which is inverse of the resistance, at circumferential microgaps, h_{mc}, is given by

$$h_{mc} = \frac{\lambda_{gas}}{g1 + g2 + \Delta G} \tag{2}$$

where ΔG is a microgap width and g1 and g2 are temperature jump distances (TJD) of mixed gas at UO2 matrix interface and they are given by,

$$g_{1,2} = \frac{5}{8}\pi^{0.5}\left(\sum_j X(j)\left(\frac{Ma}{M(j)}\right)^{0.5}\left(\frac{52}{25\pi} + \frac{1}{2}(1 - \alpha(j))\right)\cdot ac(j)^2\right.$$

$$\left. + \frac{1}{2}\cdot\frac{\left(\sum_j X(j)\left(\frac{Ma}{M(j)}\right)^{0.5}(1 - \alpha(j)\cdot ac(j))\right)^2}{\sum_j X(j)\left(\frac{Ma}{M(j)}\right)^{0.5}\cdot ac(j)}\right)\cdot Lm \tag{3}$$

$$ac(j) = \frac{\lambda g(j)}{\lambda ga}\left(\frac{M(j)}{Ma}\right)^{0.5}\frac{1}{X(j) + \sum_{j \neq k}\Phi(j,k)X(k)} \quad (4)$$

$$\Phi(j,k) = \left(\frac{1 + \left(\frac{\lambda g(j)}{\lambda g(k)}\right)^{0.5}\left(\frac{M(j)}{M(k)}\right)^{0.25}}{2^{1.5}\left(1 + \frac{M(j)}{M(k)}\right)}\right) \times\left(1 + 2.14\frac{(M(j) - M(k))(M(j) - 0.142M(k))}{(M(j) + M(k))^2}\right) \quad (5)$$

where $X(j)$ is fraction of j gas, Ma is an average mass of gases in microgaps ($Ma = \sum X(j)M(j)$). $a(j)$ is the accommodation coefficient between UO2 matrix and j gas. The conductivity of mixed gas, λ_{gas}, and the mean free path of the mixed gas, Lm, are given by,

$$\lambda_{gas} = \sum_j\left(\frac{\lambda g(j)}{1 + \sum_{j \neq k}\Phi(j,k)X(j)/X(k)}\right) \quad (6)$$

$$Lm = \frac{4}{5}\lambda_{gas}\frac{Tg}{Pa}\left(\frac{Ma}{2k \cdot Tg}\right)^{0.5} \quad (7)$$

where Tg is a gas temperature in microgaps, Pa is a gas pressure in microgaps and k is a Boltzman constant. The adapted model of TJD was from theoretical analysis by Loyalka [7]. The TJD is inversely proportional to gas pressure, and also function of gas component and temperature. In equation (2) the width of microgap is set to be very narrow, that is 0.6 μm. The effective thermal conductivity of pellet is given by,

$$\lambda_{eff} = \frac{R_{po} + \Delta G \cdot N_{mc}}{\frac{R_{po}}{\lambda'_p} + \frac{N_{mc}}{h_{mc}}} \quad (8)$$

where R_{po} is the pellet radius and N_{mc} is the total number of microgaps in pellet radius. We implemented these models in the fuel performance evaluation code, EIMUS, and applied the models for verification. The number of microgaps was estimated from the temperature data obtained at the OECD Halden Reactor Project. The data indicated that fuel central temperature decreases as rod internal gas pressure is increased. This temperature decrease becomes more significant as burnup increases. We evaluated this behavior utilizing the modified code and estimated the number of microgaps. Figure 8 shows calculated examples of modeled thermal conductivity. In this case we assumed that the normal pellets which density is 95%TD, irradiated at 1000C until 50MWd/kgUO2. The quantities of the thermal conductivity decrease due to fission product solid solution is nearly equal to the decrease due to the microgap models.

4.3 VERIFICATION OF TEMPERATURE CALCULATION

The RISØ project was conducted by RISØ national laboratory of Denmark to investigate fuel behavior, especially the temperature and fission gas release, up to burnup around 40MWd/KgUO2. The project phase-3 comprised totally 15 rods of both PWR and BWR designs and they were supplied for transient tests. PWR designed rods were fabricated by Advanced Nuclear Fuels (ANF) and BWR designed rods were fabricated by General Electric (GE) and also by RISØ National Laboratory. Nine rods were re-fabricated at the RISØ laboratory after base irradiation, and were instrumented with thermocouples and pressure transducers to measure fuel central temperature and rod internal pressure during transient tests.

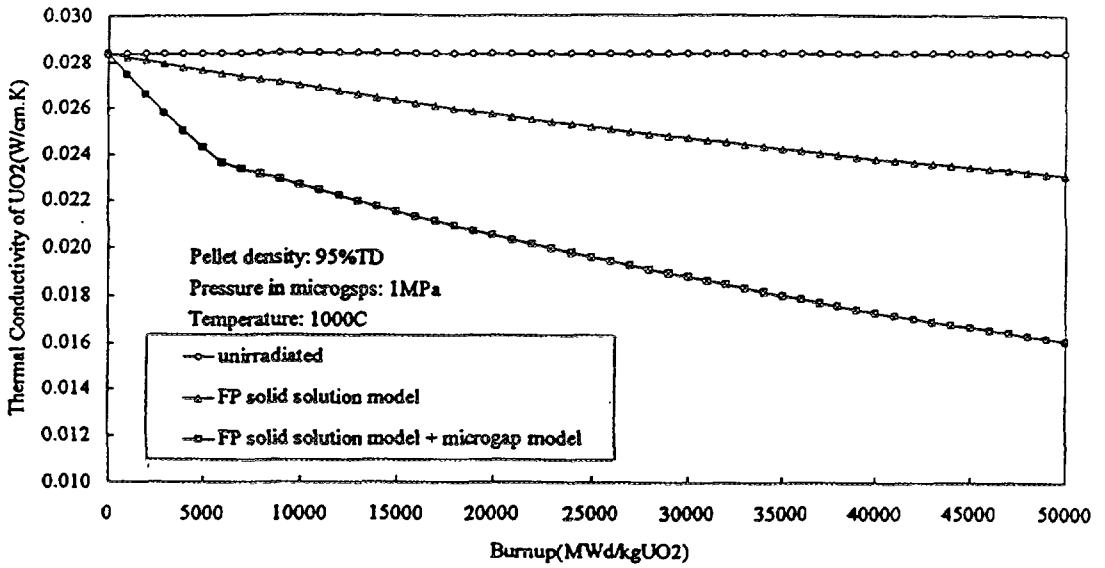

FIG. 8. *The comparison of the thermal conductivity which were calculated utilizing the thermal conductivity degradation models.*

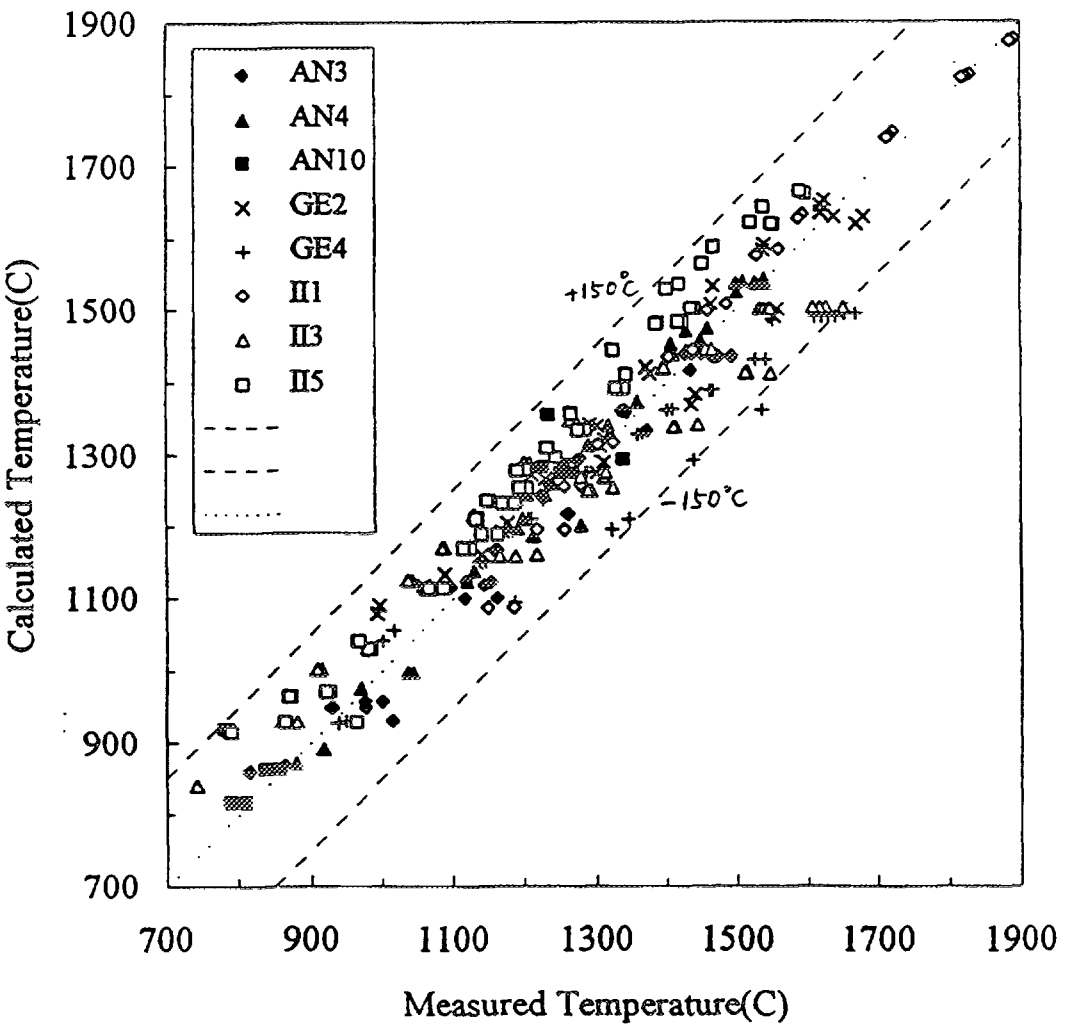

FIG 8a *Comparison of measured and calculated temperature.*

Refabrication data and irradiation conditions are shown in Table 1. Almost all of the re-fabricated rods were filled with Helium. Only one ANF rod and one RISØ rod, which failed during a transient test, were filled with Xenon gas. The initial gas pressure of Xenon filled rod were relatively lower than Helium filled rods. The burnup of ANF rods are around 38MWd/kgUO2. On the other hand GE fuels had a burnup range from 14 to 42MWd/kgU02.

TABLE 1 REFABRICATION DATA AND IRRADIATION CONDITIONS

Rod Name	Rod Type (Fabricator)	Filled Gas (MPa)	Burnup (MWd/kg UO2	Grain Size (μm)	Pellet diameter
AN1	PWR(ANF)	He 1.33	36.3	6.0	0.905
AN3	PWR(ANF)	He 1.47	36.5	6.0	0.905
AN4	PWR(ANF)	Xe 0.092	37.8	6.0	0.905
AN10	PWR(ANF)	He 0.641	39.3	6.0	0.905
GE2	BWR(GE)	He 0.66	37.9	18.9	1.040
GE4	BWR(GE)	He 0.66	19.0	32.6	1.040
II1	BWR(RISØ)	Xe 0.101	35.5	10.0	1.264
II3	BWR(GE)	He 0.68	13.9	19.0	1.089
II5	BWR(RISØ)	He 0.641	42.0	10.0	1.264

The diameter measurements indicated that ANF rods (AN3, AN4, AN10) experienced hard PC contact during transient tests as a result of large creep down of around 100 11 m during base irradiation. RISØ rods (II1, II5) experienced hard PC contact during base irradiation because of high heat rating. On the other hand, GE rods (II3, GE2, GE4) did not experience hard PC contact of thermocouple position at least, except II3 which failed during a transient test.

ANF and GE fuels showed little fission gas release during base irradiation. However RISØ fuels experienced fission gas release during base irradiation as a result of high heat rating. At similar temperature, ANF fuels released more fission gas than GE and RISØ fuels during transient tests. And only ANF fuels were showed gas release of approximately 6% at very low heat rating, that is below 170W/cm. The different behavior of GE and ANF rods could be due to own characteristics of the pellets. Time dependence of the measured rod internal pressures indicated that fission gas release to the free volume dose not follow the diffusion rule in fuel matrix and the burst release occurred when the power goes down rapidly for a short time (power dip). This behavior can be interpreted by the two stage mechanisms. The fission gas diffusionally moved from UO2 matrix to grain boundary. The grain boundary becomes large storage for the gas especially if pellets are constrained by large hydraulic pressure due to hard PC contact. This grain boundary corresponds to the microgap which has little or no connection to the open volume. Analysing the measured fuel central temperatures, they are higher than predicted if the thermal conductivity of the unirradiated UO2 is used for the calculation. The analysis results indicate that the effective thermal conductivity of pellet decreases about 25% at 40 MWd/kgUO2.

We calculated fuel center temperature of 8 rods which were measured temperatures during transient tests. Figure 8 shows the comparison of measured and calculated temperature of the rods. The figure indicate that different between calculated and measured fuel center temperatures are less than 150°C.

AN4 and II1 were Xenon filled rods which were instrumented with a thermocouple. The calculated temperatures agree well with the measured ones at a broad range of heat rating. This result induces that the assumed thermal conductivity is reasonable for a Xenon filled rod at a broad temperature range.

AN3 and AN10 rods have the same pellets as Xenon filled AN4. The measured temperatures of AN3 and AN10, having much better thermal conductance at PC gap, are lower than that of AN4 at all range of heat rating. For these Helium filled rods, we assumed that microgaps are completely filled with fission gas during whole tests because diffusion mixing in microgaps could be negligible if the gas release is continuously taking place. On the other hand, fission gas of a pellet-cladding gap could be mixed with plenum gas which has large fraction of Helium filled at refabrication. Calculated temperatures agree well with measured temperatures in general. The results indicate that the assumption of gas composition in microgaps is valid for AN3 and AN10.

We analysed BWR designed GE and RISØ fuels. Although GE fuels have a similar diameter as ANF fuels, RISØ fuels have a larger diameter than ANF fuels. The calculation was made assuming the microgaps are filled only with fission gas as previous calculations for ANF fuels. The calculated temperatures agree with the measured temperatures at high heat rating before the first power dip. In this condition the released fission gas could be enough to fill the microgaps. These results are indicating that the code with microgap model is able to predict fuel temperature at high heat rating for different sources of fuel fabrication. However, for GE fuels at low power and at the fission gas burst release, calculated results have some discrepancy. In general the fuels for this benchmarking have a burnup range between 15~45 MWd/kgUO2, it is confirmed that the modified code can predict the observed burnup dependence of fuel temperature.

The calculated temperature of II5 is higher than the measured temperature about 100C. It is supposed that this discrepancy is caused by a large pellet diameter of II5. Here we calculated a fuel temperature of II5, assuming the microgap number per pellet radius of RISØ fuel is approximately the same as that of ANF fuels.

The calculated temperatures of AN3, AN4, AN10 and GE2 are in good agreement with the measured temperatures in the range from low power of 200W/cm to the maximum power of 400W/cm. The measured rod diameters for these rods indicate that they had pellet-cladding contact at the thermocouple position even at low power during transients. Therefore the diffusion mixing of the gas in microgaps could have been very slow and the gas in microgaps were only fission gas during the transients. On the other hand, the calculated temperatures of GE4 and II3 are notably lower than the measured temperatures at low heat rating. The measured rod diameters indicated that these fuels did not have a hard pellet cladding contact at the thermocouple position. In these rods, fission gas in microgaps was partly mixed with Helium which was filled at re-fabrications. This analysis indicates that the fast mixing between microgaps and free volume may take place when mechanical PC contact in not significant.

In these analyses, we assumed that the microgap have an uniform distribution in pellet radial cross-section. However the microgaps may develop significantly around the pellet rim region at high burnup. In such a case the radial temperature profile will become more flat near pellet center. And the code, with uniformly distributed microgap model verified against central hole temperature, may over-estimate the center temperature of solid pellet.

5. FISSION GAS RELEASE MODEL AND VERIFICATION

We assumed that the matrix diffusion coefficient of fission gas in UO_2 is not affected of burnup. The diffusion coefficient is described to sum ones of three temperature regions and the total diffusion coefficient is given by;

$$D_{MAT} = D_1 + D_2 + D_3$$

[High Temperature Region]

$$D_1 = 2 \times 10^{-21} \cdot \exp\left(- \frac{1.0 \times 10^5}{1.986} \left(\frac{1}{T} - \frac{1}{1280} \right) \right) \quad (9)$$

[Middle Temperature Region]

$$D_2 = 2 \times 10^{-40} \cdot F \cdot \exp\left(- \frac{2.76 \times 10^4}{1.986} \left(\frac{1}{T} - \frac{1}{1300} \right) \right)$$

[Low Temperature Region]

$$D_3 = 2 \times 10^{-40} \cdot F$$

where T is a absolute temperature of UO2 matrix and F is a fission rate. At low temperature the fission gas release mainly by knock-on of fission fragments. At middle and high temperature the fission gas release under a diffusion law. Figure 9 shows the matrix diffusion coefficient of UO2 in the EIMUS code. On the other hand the diffusion in irradiated fuel is affected as a result of gas atom trapping by intra-grain bubbles. The effective diffusion coefficient in irradiated UO2 grain is given by [9],

$$D_{eff} = \frac{bD_{MAT}}{b + g} \quad (10)$$

where

$$b = 2\pi R^2 \cdot F \cdot L_F$$

$$g = 4\pi D_{MAT} \cdot R \cdot C_B$$

$$C_B = \frac{L_a}{\pi L_F \cdot R^2}$$

$$R = \left(R_0^4 + \frac{1.7 \times 10^{-28} \cdot C_{AV} \cdot D_{MAT}}{\pi \cdot F \cdot L_F} \right)^{0.25}$$

R_0 is initial intra-bubble radius, C_{av} is gas averaged atom concentration in grain calculated in gas release model, L_α is 7 and LF is 6×10^{-6}. Because C_{av} increases until the grain boundary is saturated by gas atoms, the effective diffusion coefficient is affected by burnup increase at lower burnup range less than ~20MWd/kgUO2.

We calculated fission gas release about 13 rods which were supplied to RISØ project phase-3 and measured by puncture tests at end of irradiation. Table III shows fabrication data, irradiation conditions and fission gas release rate of rods which were not re-fabricated at end of base irradiation. The comparison of measured and calculated fission gas releases of the rods are shown in Fig. 10. Calculated fission gas releases agree with measured ones within +25%, except GE4 and II5 rods. However the measured fission gas release of GE4 is about 2.5 times larger than the calculated value. Oppositely the fission gas release of II5 is about 2.5 times larger than the measured value. These discrepancies could be due to variances of the calculated temperatures compared to the measurements. The calculated temperature of GE4 is about 100 °C lower than the measurement and the calculated temperature of II5 is about 100°C higher than the measurement as they are shown in Fig 9.

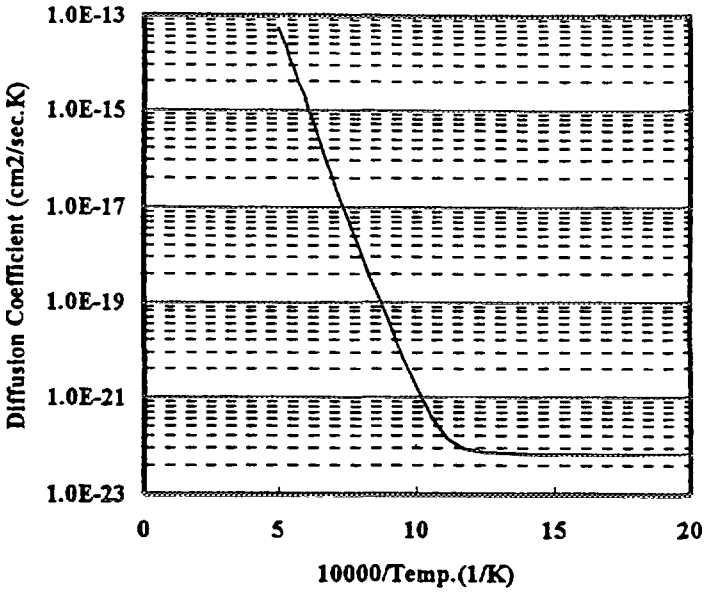

FIG. 9. The intrinsic diffusion coefficient versus the inverse of absolute temperature

TABLE II CONDITION OF PELLET-CLADDING CONTACT AFTER BASE IRRADIATION AND FP GAS RELEASE

Rod Name	PCMI at TC Position	FP Release (%)
AN1	-	36.5
AN3	hard	35.5
AN4	hard	40.9
AN10	hard	26.9
GE2	soft	23.0
GE4	soft	27.8
II1	soft	16.0
II3	-	17.4
II5	hard	10.6

TABLE III FABRICATION DATA, IRRADIATION CONDITIONS AND FISSION GAS RELEASE RATE.

Rod Name	Fabrication	Filled Gas (MPa)	Burnup (MWd/kgUO2)	Grain size (μm)	Pellet diameter (mm)	FP gas release (%)
AN2	ANF(PWR)	He 2.5	36.9	6.0	0.905	29.0
AN8	ANF(PWR)	He 2.5	36.3	6.0	0.905	14.1
GE6	GE(BWR)	He 0.5	45.9	18.9	1.041	29.7
GE7	GE(PWR)	He 0.3	22.6	18.9	1.041	12.9

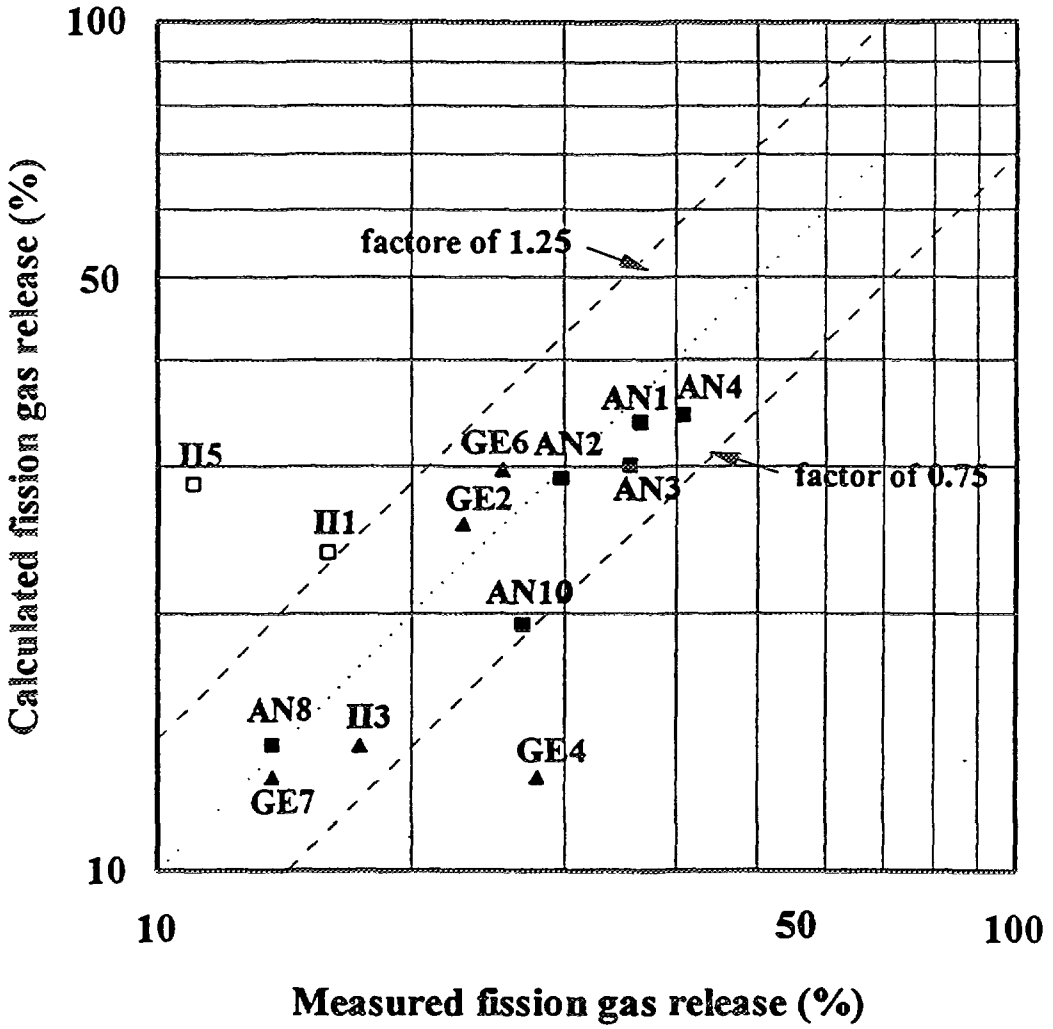

Fig 10 Comparison of measured and calculated fission gas release.

As the calculational results for fission gas release is in good agreement with the experiments, the assumed diffusion constants and fission gas release model seems to be reasonable for these burnup. And the estimated temperature is in consistent with the gas release observations.

6. PLANAR BARRIER MODEL AT HIGHER BURNUP

The analysis of the RISØ data indicates that the total resistance of the model is reasonable. The total is sum of effects of the fission product solution and the remainder. The latter part was described by the planar barrier model. At higher burnup this remainder part could be more essential. Here we propose advanced thermal model based on micro-structural change.

Experimental observation

(I) *Planar defect*

In ceramography etched fuel shows needle like appearance around outer region of the pellet (Fig. II). This was found for the fuel burnup from around 30 MWd/KgU pellet average (three reactor cycles). From SEM and TEM observations and etching susceptibility it is thought to be planar defects. Thomas found disk like defects by TEM which had vacant volume. The volume could be filled by fission gas

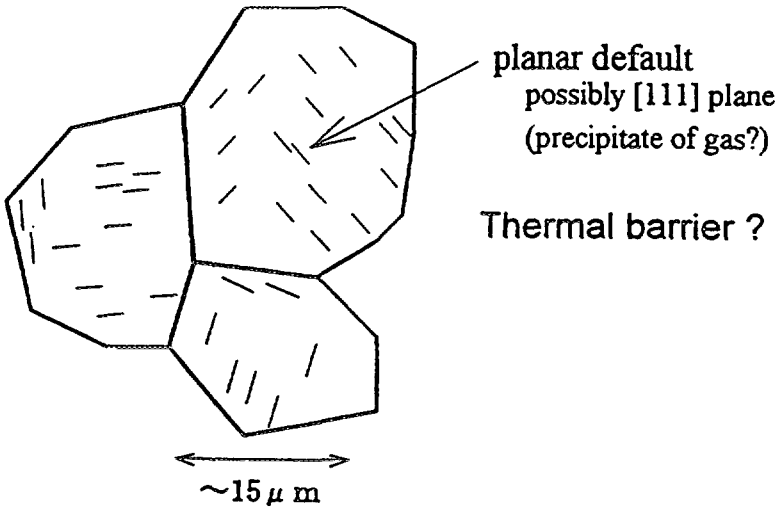

Fig.11 Planar defect in fuel grain

before the specimen preparation. Volatile FP elements such as Cs might be also present. The plane was parallel to [111] plane of U02 which has the highest planar density in Fluorite structure [10,11]. Nogita and Une found significant vacancy concentration and dislocation density around the rim region [12]. Therefore very high stress seems to be present with these defects. As the [111] plane could be the weakest plane to break, this structure could be formed by cleavage. And coherent precipitation of Xenon in planar form could be possible [13]. This planar defect could be a thermal barrier as the same mechanism of cracked pellets, that is the temperature jump distance.

The gas filled planar defect may grow and crack may propagate. This may induce increase of heat resistance. This process may occur when the temperature increases rapidly and induce increase of gas pressure. The stress reducing effects such as irradiation creep of fuel may contribute to cease the process. The local tensile stress may also contribute the growth.

The fuel temperature at the planar structure is low compared to the intra-bubble formation described below. And the structure is made by stress. The process of this structure formation is not temperature driven but it could be internal stress driven. The stress accumulation could be due to high concentration of (1) point defects, (2) dislocations, and (3) fission gas bubbles. The planar defect could be planar precipitin mode of fission gas assisted by the build-up stress by the point defects and dislocations.

(2) ***Intra-grain gas bubbles***

There is another remarkable structure change. That is development of intra-grain gas bubbles (Fig. 12).

This structure is observed at inner position of the pellet than that of the planar structure [15]. This has very exclusive character that its presence has very sharp radial dependence. This indicates that the formation process is very sensitive to the temperature. Retained gas analysis by EPMA shows that the fission gas release starts at the position where this structure is formed. [RISØ] These observations indicate the temperature of this structure formation may correspond to the threshold temperature of the atom movements at the surface and at grain boundaries. This threshold temperature is the fuel material property and it could be 1100 ~ 1200°C. On the contrary to the planar defect formation this structure formation is temperature driven.

(2)Intra-grain gas bubbles

There is another remarkable structure change. That is development of intra-grain gas bubbles (Fig. 12).

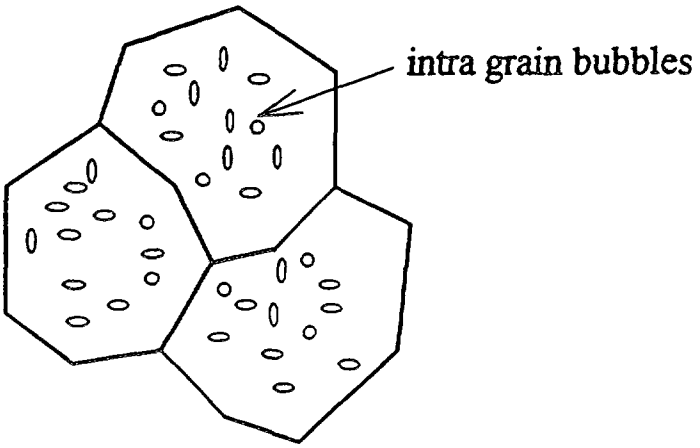

Fig.12 intra-grain gas bubbles.

(3) Rim structure

The neutronic rim effect which is Pu-239 build up at pellet rim due to the epithermal neutron absorption by U-238 induces higher fission rate at this area. Consequently higher burnup is achieved at the rim area and there significant structural changes were observed [16, 17]. The observations are (1) loss of original grain structure which is result of reduction of grain size down to sub-microns, (2) decrease of content of Xenon measured with EPMA, (3) significant formation of porosity which is mostly closed to the open space. The effect of this structure to the thermal property is not known. Although the porosity fraction is large the shape is spherical and the effect could be insignificant. Especially after formation of this structure the small sized grains have potential to throw out internal defect and fission products, the thermal resistance may only come from the increased area of grain boundary. The solid fission products, gases are localized as large individual precipitates. Therefore thermal barrier due to well-developed rim structure might be in-significant. However in the area just at the preceding stage of the structure formation, the defect density is very high at the saturated level and the resultant thermal resistance could be significant.

Planar defect model

The objective of planar defect model in the analysis code is to evaluate local thermal resistance in pellet. The thermal conductance at the defect is

$$h_{mc}^{defect} = \frac{\lambda_{gas}}{2g1} \qquad (11)$$

At the area where planar defects are present the effective thermal conductivity is

$$\lambda_{eff}^{defect} = \frac{1}{\frac{1}{\lambda'_p} + \frac{n_{mc}^{defect}}{h_{mc}^{defect}}} \qquad (12)$$

Here n_{mc}^{defect} size is radial number density of planar defect. This value is function of defect and its volumetric number density.

In order to analyse the experimental observation of microstructural change, the radial temperature profile is in question [18]. The model could be utilized to assess local conductivity degradation and to estimate local temperature profile especially from pellet edge to the inside where intra-bubble formation is observed.

7. DISCUSSION INSTABILITY

For the future study, the analysis codes will be utilized to evaluate fuel reliability at various operational conditions. The allowance for the fabrication quality is also the question. To assess fuel design and operational regulations identification of the various thresholds of remarkable processes and evaluation of possible instabilities are necessary. At the present level of the high burnup extension, effects of fuel microstructural change could be the main concern. Fig.13 shows schematic view of the inter-relations.

When the fuel temperature changes the micro-structures also change. The formation of new macrostructure, such as growth of planar defect by crystal cleavage, increase of intragas bubble density and its diameter increase, may change the thermal resistance.

Therefore the most important direction of the next research could be: (1) confirm the nonpresence of instability at the applied design, (2) identify the thresholds of remarkable processes in terms of local variables such as burnup, temperature and its gradient, stress. (3) Identify the thresholds in terms of engineering variables such as heat rating, rod burnup, rod geometry. The temperature gradient, dT/dr, may accelerate the process of microstructure change. The effect of mechanical constraint is also important. It may cease the growth of defects. If constraint is released, such as by P/C gap opening the swelling potential of fuel could be larger. In order to evaluate this feedback process it is essential to develop a thermal resistance model which is the non-solid solution part of the resistance increase at high burnup.

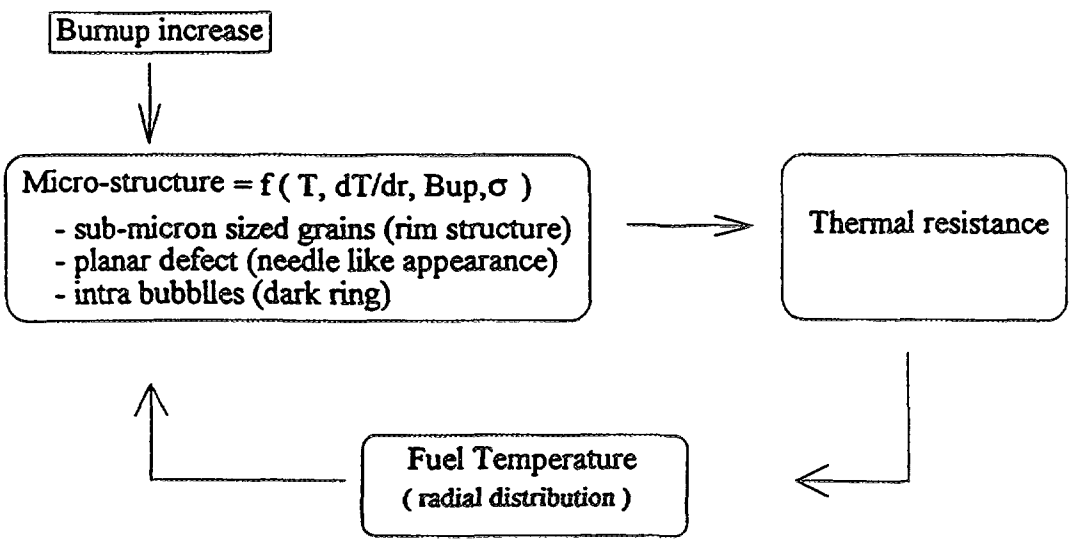

Fig. 13 Effect propagation of remarkable processes in high burnup fuel.

Threshold

The significance of the high burnup fuel is its variety of the micro-structure changes. There are thresholds for these changes and the research should be concentrated into the identification of thresholds. The fuel performance analysis code is the necessary tool and its accuracy should be improved. Therefore right experimental data are necessary to improve the code. As different microstructures are observed at radial local area of pellet, the model of the code should be detail enough to evaluate radial variation of properties such as thermal resistance. The proposed planar defect model of the resistance is the first step in this direction. However the work for code benchmarking and verification could be increased. And experimental data, especially well-characterized PIE data, is necessary and this is also work consuming. Therefore in order to move towards this direction, international collaboration is necessary.

8. CONCLUSION

To achieve high burnup extension preservation of fuel reliability is the main concern. At lower burnup we had experienced the thermal feed-back effect, which is one of non-linear complex phenomena and thermal instabilities. As the local power is increased due to the adapted higher enrichment, the performance at middle burnup should be re-analyzed especially for fuel with high temperature design. Adapting improvements of design and operation the non-linear instability, which deteriorates fuel reliability, must be avoided.

Focusing the analysis of such instability the performance analysis code, EIMUS, was improved to estimate high burnup fuel temperature implementing thermal resistance models of the fission product solid solution and the microgap formation. The RISØ data of temperature and gas release was utilized to verify the models and the results were satisfactory.

The planar defect model was proposed to model thermal resistance due to microstructure change at low temperature circumferential area of high burnup fuel. This may contribute to estimate radial temperature profile more accurately.

As remarkable processes are observed in microstructural change in high burnup fuel, we have to investigate the threshold of their formation and quantitative effects on fuel performance. For the future study, code improvements should be with detailed PIE. And in parallel codes should be utilized to analyze PIE data to identify above mentioned problems. These are work intensive and international cooperative efforts should be taken in systematic and rational manner.

Nomenclature

λp: thermal conductivity of unirradiated UO2 matrix.
x: fraction of the fission product solid solution.
λgas: average thermal conductivity of mixed gas in microgaps.
$g1,g2$: temperature jump distance.
ΔG: microgap width.
Rpo: pellet radii.
Nmc: number of microgaps
$M(j)$: mass of j gas.
Ma: average mass of mixed gas in microgaps ($Ma = \sum X(j)M(j)$).
$X(j)$: existence rate of j gas.
$\alpha(j)$: accommodation coefficient between UO2 matrix and the gas in microgaps.
Tg: gas temperature in microgaps.
Pa: gas pressure in microgaps.
k: Boltzman constant.
T: absolute temperature of UO2 matrix
F: fission rate.
D_{MAT}: diffusion coefficient of fission product in UO2 matrix.

REFERENCE

[1] KINOSHITA, M., Development of LWR Fuel Performance Analysis Codes, Journal of Nuclear Science and Technology Vol.30, No. 1, pp.1~17 January 1993.

[2] KINOSHITA, M., Evaluation of Axial Fission Gas Transport in Power Ramping Experiment, IAEA Specialists' Meeting on Water Reactor Fuel Performance Computer Modelling, Windermere, England, April (1984), also published in Res.mechanica, 19(3)1986.

[3] KITAJIMA, S., KINOSHITA, M., Evaluation of Measured High Burnup Fuel Temperature at RISØ Project Phase 3, presented at IAEA Technical Committee on Fission Gas Release and Fuel Rod Chemistry Related to Extended Burnup,1992 Pembroke, Ontario, Canada.

[4] KITAJIMA, S., MATSUMURA, T.,KINOSHITA, M., Reduction of Effective Thermal Conductivity in High Burn-up Fuels, IAEA Technical Committee Meeting on Fuel Performance at High Burnup for Water Reactors, Nykoping, Sweden, 5-8 June, 1990.

[5] KLEMENS, P.G., Physical Review,119,507(1960).

[6] ISHIMOTO, S., HIRAI, M., AND ITO, K., The Twelfth Japan Symposium on Thermophysical Properties, A304(1991).

[7] LOYALKA, S.K., Nuclear Technology, A Model for Gap Conductance in Nuclear Fuel Rods,Vol.53,220,May(1982) .

[8] TURNBULL, J.A., APPLEHANS, A.D., OECD Halden Reactor Project, Fuel Behavior inferred from Internal Gas Flow and Temperature Measurements made at the Beginning-of-Life of IFA-504, HPR273,(1981).

[9] TURNBULL ,J.A., J. Nucl. Mater. 38(1971)203-212

[10] THOMAS, L.E., EINZIGER, R.E, WOODLEY, R.E.; "Microstructral Examination of Oxidized Spent Fuel by Transmission Electron Microscopy", Journal of Nuclear Materials 166(1989)243-251

[11] THOMAS, L .E , BEYER, C. E. , CHARLOT, L. A., "Microstructural analysis of LWR spent fuels at high burnup", J. Nuc. Mater. 188(1992)80-89

[12] UNE, K., NOGITA, K., KASHIBE, S., AND IMAMURA, M.; "Microstructure change and its influence on fission gas release in high burnup UO2", J.Nuc. Mater. 188(1992)65-72

[13] MATZKE; "The rim effect in high burnup UO2 nuclear fuel", paper presented at 8th CIMTEC, Firenze, June 29-July 4,1994.

[14] NOGITA, K. AND UNE, K.; "Thermal Recovery of Radiation Defects and Microstructural Change in Irradiated UO2 Fuels", J. Nucl. Sci. and Tech.,30[9]pp (1993).

[15] MANZEL, R., COQUERELLE, M., BILLAUX, M.R., "Fuel Rod Behavior at extended burnup," pp335,ANS International Topical Meeting on Light Water Reactor Fuel Performance, West Palm Beach, Florida, April 17-21, 1994.

[16] KAMEYAMA, T, MATSUMURA, T, KINOSHITA, M.; "Analysis of Rim Structure Formation in Battelle High Burnup Effects Program", ANS/ENS International Topical Meeting on LWR Fuel Performance, Palais des Papes, Avignon, France, April 21-24,1991.

[17] WALKER, C.T., KAMEYAMA, T., KITAJIMA, S., KINOSHITA, M., "Concerning the microstructure changes that occur at the surface of UO2 pellets on irradiation to high burnup", J. Nucl. Mater., 188(1992)73-79.

[18] BAGGER, C., MOGENSEN, M., WALKER, C.T.; "Temperature measurements in high burnup UO2 nuclear fuel: Implications for thermal conductivity, grain growth, and gas release", J.Nucl. Mater., 211(1994)11-29

CALIBRATION OF THE ENIGMA CODE FOR FINNISH REACTOR FUEL WITH SUPPORT FROM EXPERIMENTAL IRRADIATIONS

S. KELPPE, K. RANTA-PUSKA
VTT Energy,
Jyvaeskylae, Finland

Abstract

Assessment by VTT of the ENIGMA fuel performance code, the original version by Nuclear Electric plc of the UK amended by a set VVER specific materials correlations, is described. The given examples of results include analyses for BWR 9x9 fuel, BWR fuel irradiated in the reinstrumented test of an international Risø project, pre-characterized commercial VVER fuel irradiated in Loviisa reactor in Finland, and instrumented VVER test fuel irradiations in the MR reactor in Russia. The effects of power uncertainty and some model parameters are discussed. Considering the fact that the described cases all mean prototypic application of the code, the results are well encouraging. The importance of the accuracy in temperature calculations is emphasized.

1. INTRODUCTION

The developments in the fuel operation strategies, including those leading to higher discharge burnups, have posed growing requirements for the understanding of the fuel behaviour phenomena and their analytical comprehension. As a part of improving its capabilities to perform up-to-date fuel performance analyses, VTT Energy (a division of the Technical Research Centre of Finland) made a licence contract with the Nuclear Electric Company (NE) of the UK for the use of the ENIGMA code [1]. The essential parts of this code have been developed or reviewed and updated during the past several years by NE and BNFL resulting in a set of models that was determined to represent the most recent experience and experimental findings with respect to high burnup fuel.

In Finland, the reactor types in use are the Russian VVER and the Swedish BWR. VVER fuel considerably differs from the rest of PWR fuel types. For the BWR, in turn, a succession of fuel concepts ranging from 8x8 to10x10 and being shared by two suppliers ABB Atom and Siemens have been introduced. These facts have provided a challenge to the users and analysts - and also to the acquired ENIGMA code, as it has been written and validated mainly for PWR (and AGR) applications.

The Finnish utilities have been active in accumulating qualified performance data from their fuels. Use of the pool-side examination facilities found at both of the reactor sites has yielded great amounts of representative measurements, supplemented by participation in international efforts on fuel irradiation testing. Features of data available to and being used by VTT for the first validation of ENIGMA is given in Table I.

A summary on the first validation the ENIGMA code against VVER and BWR data is the subject of this report.

2. RESULTS FOR SIEMENS 9 X 9 BWR FUEL WITH SUPPORT FROM THE RISØ FGP3 RESULTS

2.1 DESIGN AND OPERATIONAL DATA

TVO, the operator of the two ABB Atom BWR units has carried out series of pool side examinations for several fuel types. Among the most recent ones, 21 Siemens 9x9-1 type rods from three discharged

TABLE I. Data being used by VTT for ENIGMA validation

SOURCE	Irr. Condit.		In-Pile Data				PIE Data				REMARKS
	Fuel Type	Reactor	Temp	dL	pre	misc	FGR	Dim	PCI	misc	
Lovlisa pre-char.rods	VVER	Lo2					Kr85	prof dL	prof gap	gam	
TVO poolside	Ste 9x9	TVO I					Kr85			gam	
SOFIT-1.1	VVER	MR	TC				punc	prof	cera	gam	
SOFIT-1.2	VVER	MR	TC	X			punc	prof	cera	gam	PIE being done
SOFIT-1.3	VVER	MR	TC	X			punc	prof	cera	gam	PIE to be done
SOFIT-1.4	VVER	MR	TC	X			punc	prof	cera	gam	PIE to be done
HALDEN IFA-563	Special	HBWR	TC			S/V GF	punc MA				Isothermal
HALDEN IFA-562	Special	HBWR	ETM		X		punc				'Ultra-High' burnup
HALDEN IFA-533	HP	HBWR	RTC							cera	Reinstrum.
Risö FGP 2	ANF, GE	Comm/ RISÖ			X		punc EPMA XRF	prof	cera	QIA SEM TEM	Reinstr. press.
Risö FGP 3	ANF, GE	Comm/ RISÖ	RTC		X		punc EPMA XRF	prof		QIA SEM TEM	TC+P in same rod
HBEP/TVO	ABB 8x8	TVO II					punc EPMA XRF	prof	cera prof	SEM cera	
HBEP (others)	Several	Several					EPMA				

TC Thermocouple
RTC Re-instrumented thermocouple
GF Gas flush
ETM Expansion Thermometer
LVDT Linear var. differential transformer
EPMA Electron probe micro analysis
XRF X-ray fluorescence
SEM Scanning electron microscopy
QIA Quantitative Image Analysis
gam Gamma scanning
S/V Surface-to-volume determ
MA Micro analysis

assemblies (A,B and C) were measured. The assemblies were chosen to include power histories that are demanding with respect to fission gas release. Assembly discharge burnups were 32.8, 32.0 and 32.4 MWd/kgU. The rods were gamma scanned and the fission gas release fractions in the rods were nondestructively determined from ^{85}Kr peak intensities at the rod plena.

The assemblies A and B were irradiated for four cycles (years). Their power histories and axial power distributions were influenced by movements of an adjacent control blade. The assembly C was irradiated for three cycles in positions away from control bodies. The power level was higher leading to a discharge burnup comparable to that of the other two in spite of the shorter residence. Within the assemblies, enrichments of 1.30 to 3.40 w/o ^{235}U have been used. The rods A3, B3 and C5 are absorber rods containing 2.8 to 3.0% of Gd_2O_3. In assembly B, there is an axial blanket of 150 mm natural uranium in both ends of the fuel stack. Otherwise the fuel design data are quite similar.

The rod power histories were provided by the fuel supplier. From the assembly histories based on core surveillance data, rod power histories calibrated with the measured relative burnups were deduced. The rod average burnups range over 30.1 to 43.6 MWd/kgU.

The ENIGMA standard Zry-4 materials properties were used. These were judged to adequately describe the fully annealed Zr-2 cladding of the rods in question except for the creep. While creep was determined not to play an important role in the examined cases, a slight adjustment to a model parameter was made to tune the calculated creep to more closely match with the average of creep-in figures measured in other campaigns.

2.2 BASIC CALCULATION

The first round of calculations was made with standard values and ENIGMA default models. The gadolinia-bearing rods were simulated by decreasing the thermal conductivity of the oxide by one third over the history and leaving away the standard burnup dependency.

In Fig.1, the fission gas release results of the base case calculation are shown in comparison with the measured. The latter range from 0.0 to 18.8%. In the figure, an underprediction of fission gas release is obvious. One may conclude that the deviation is less severe for the assembly C, the one irradiated away from a control position.

More detailed results are given as an example for rod C1 in Fig. 2. The calculated release history is in accord with the often-referred release threshold due to C. Vitanza of the Halden project (Vit) logically reflecting the role of Halden data in the release model development. Also apparent is the model's tendency to accumulate the fission gas release early from the matrix at the grain boundaries, whereas a moderate temperature increase late-in-history effectively liberates larger amounts of gases. In other words, the final part of irradiation, and therefore uncertainty the in the heat rate, is very important as to the degree of release. In this case, a typical underprediction of release is seen (5.5 vs. 12.2%).

2.3 EFFECT OF UNCERTAINTY IN POWER

To show the power dependency the calculations were repeated with powers of 110%, 115% and 120% of the nominal. For the above rod C1, the result is seen in Fig. 3. One can notice that 10% power increase about doubles the calculated release and the experimental value would be reached with perhaps 13% overpower. It is remarked that the results shown are as a function of time, so in addition to the power effect, they contain an explicit burnup dependency, as well, which was separately shown to be clearly a non-zero portion of the whole.

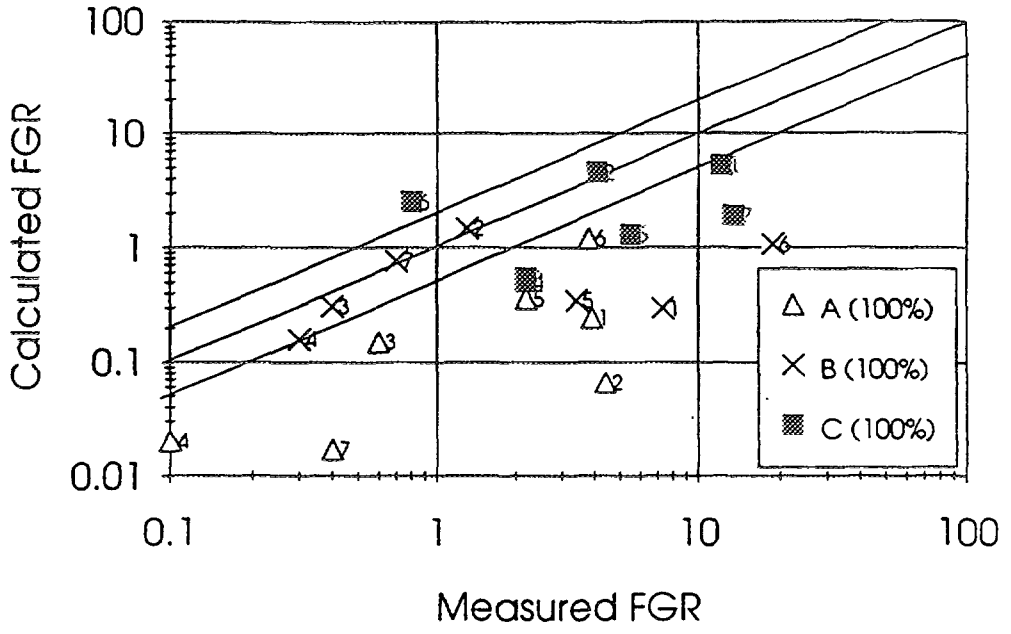

FIG. 1. *Comparison of the fission gas release fractions with the measured in the nominal case*

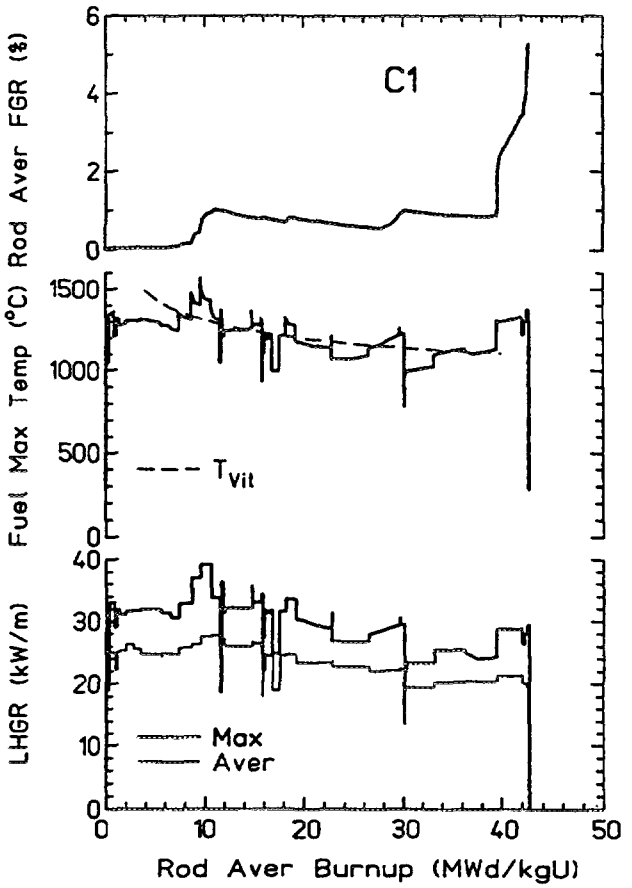

FIG. 2. *Rod LHGR, temperature and FGR in C1 (EMIGMA/VTT)*

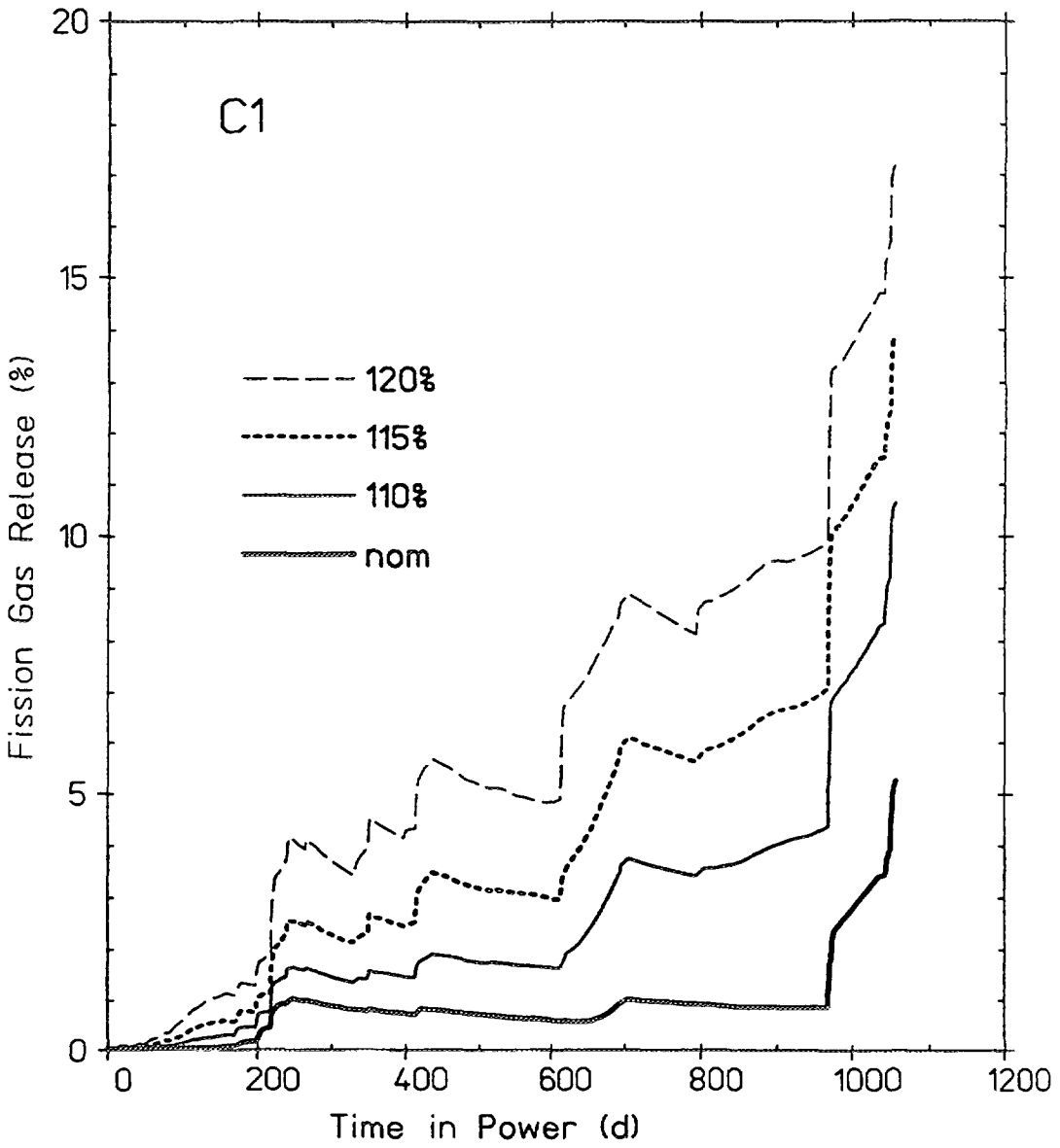

FIG. 3. FGR history with different power levels for rod C1

Results of the calculations repeated for all of the rods with the three increased power levels are shown in Fig. 4. Overpower of 10% is sufficient, in general, to remove the average underprediction. Hardly any underprediction remains with 20% power increase. One of the points that still deviate considerably is in the low release, or athermal regime and largely independent of power; the other is surprising with its 4.1% measured release and the power remaining below 25 kW/m except for a very short time early-in-life.

2.4 BENCHMARKING AGAINST RISØ FGP 3 MEASUREMENTS

The experience from the above comparison suggested more studies on the causes of the underprediction and attempts were made to fix the results with the measurements from the highly characterized experiments of the Third Fission Gas Project (FGP3). Fuel centerline temperatures measured with instruments re-installed in high burnup rodlets were largely well reproduced in ENIGMA calculations. However, in some BWR cases with mid-range burnups, the gap model fails to give the right trend when progressively higher powers are approached. This appears at the evolution of a hard pellet-to-clad contact

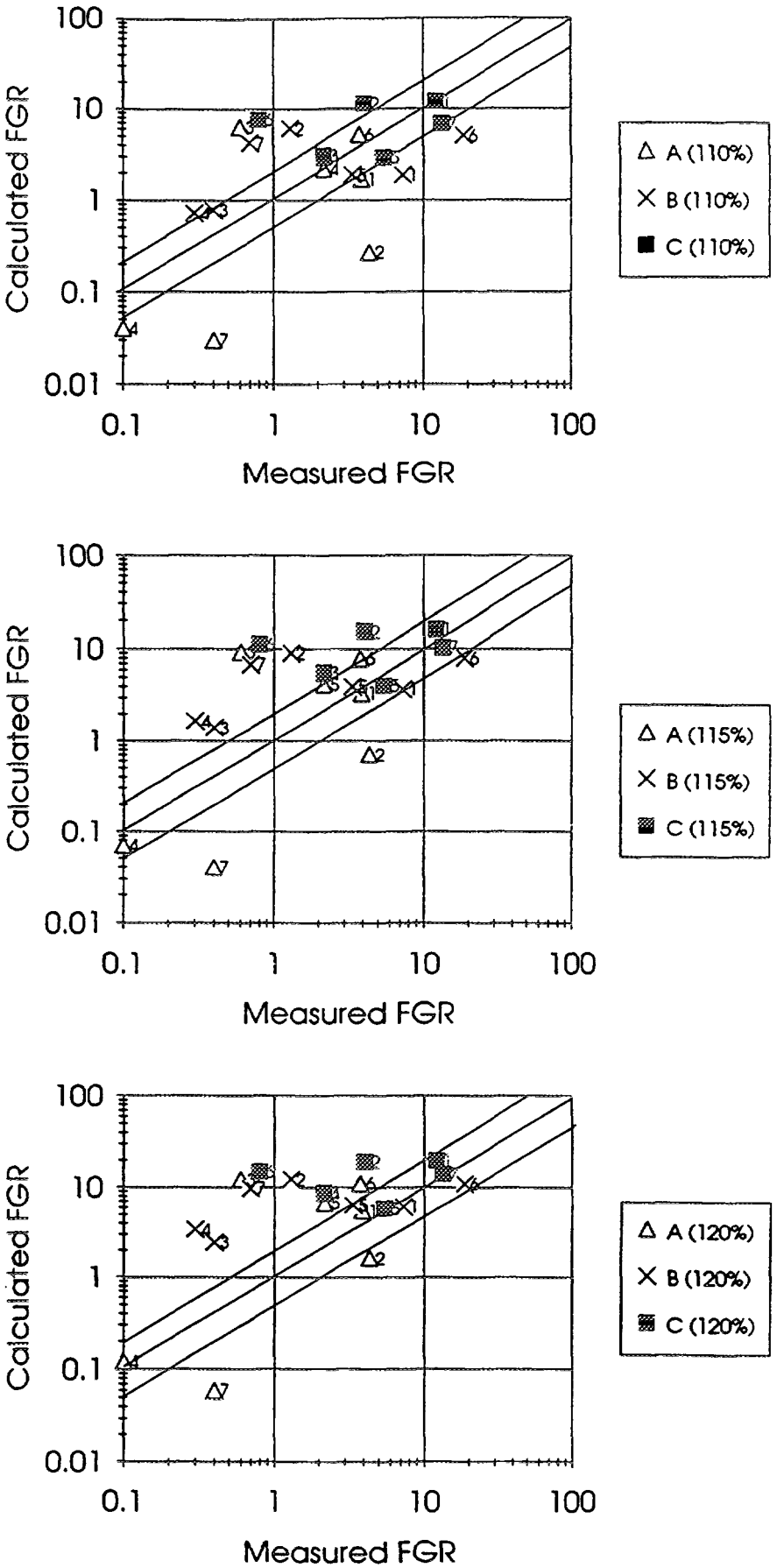

FIG. 4. *Comparison of measured and calculated fission gas release fractions at varied power levels of 110, 115, and 120% of the nominal in the calculation*

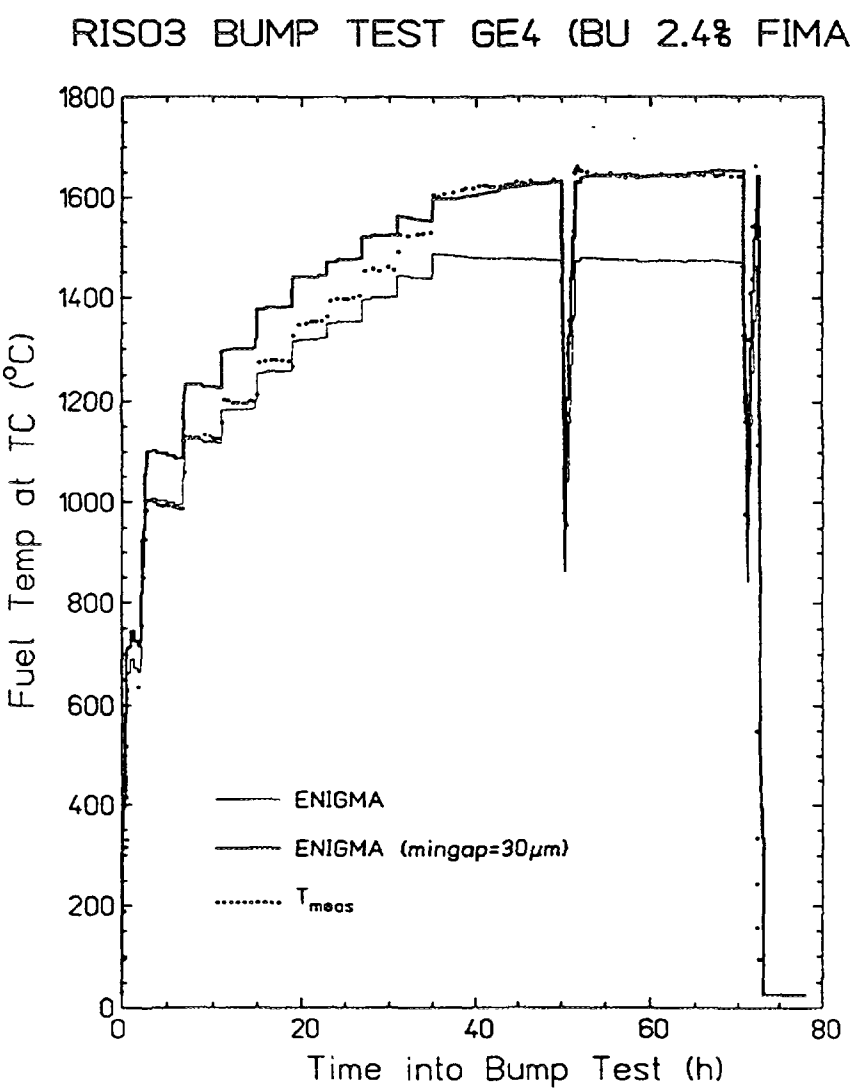

FIG. 5. Risø GE4 temperatures

when the solid contact portion of the heat transfer takes over leading to excessively high gap conductance values. The situation is described in Fig. 5. Just to make the top-of-ramp temperature match, a model parameter that sets the efficient gap at 30 μm is used. The effect of the parameter change is further illustrated in the graphs of Fig. 6 showing radial distributions of retained xenon in several FGP3 BWR rod cross sections. One sees that when the ramp terminal level temperatures are adjusted to the right level, the calculated xenon distributions come remarkably close to the observed. This gives reliance to the fission gas release model and stresses the importance of the temperature calculation.

Applied back to the above TVO/Siemens cases, an improvement in the prediction is reached. From Fig. 7, one concludes that the average underprediction is removed; the overall effect is much of the same as that of using 10% overpower in the calculations.

3. RESULTS FOR QUALIFIED VVER FUEL IRRADIATIONS

Experimental data bases for western PWR fuel types are not directly applicable to modelling purposes for VVER fuel. Of the differences the triangular lattice geometry, clad Nb-alloying and the annular pellets are to be mentioned above all. Together with the VVER fuel supplier and Russian research organizations the IVO utility has carried out several long-term campaigns for accumulating experimental data and operational experience of the VVER fuel.

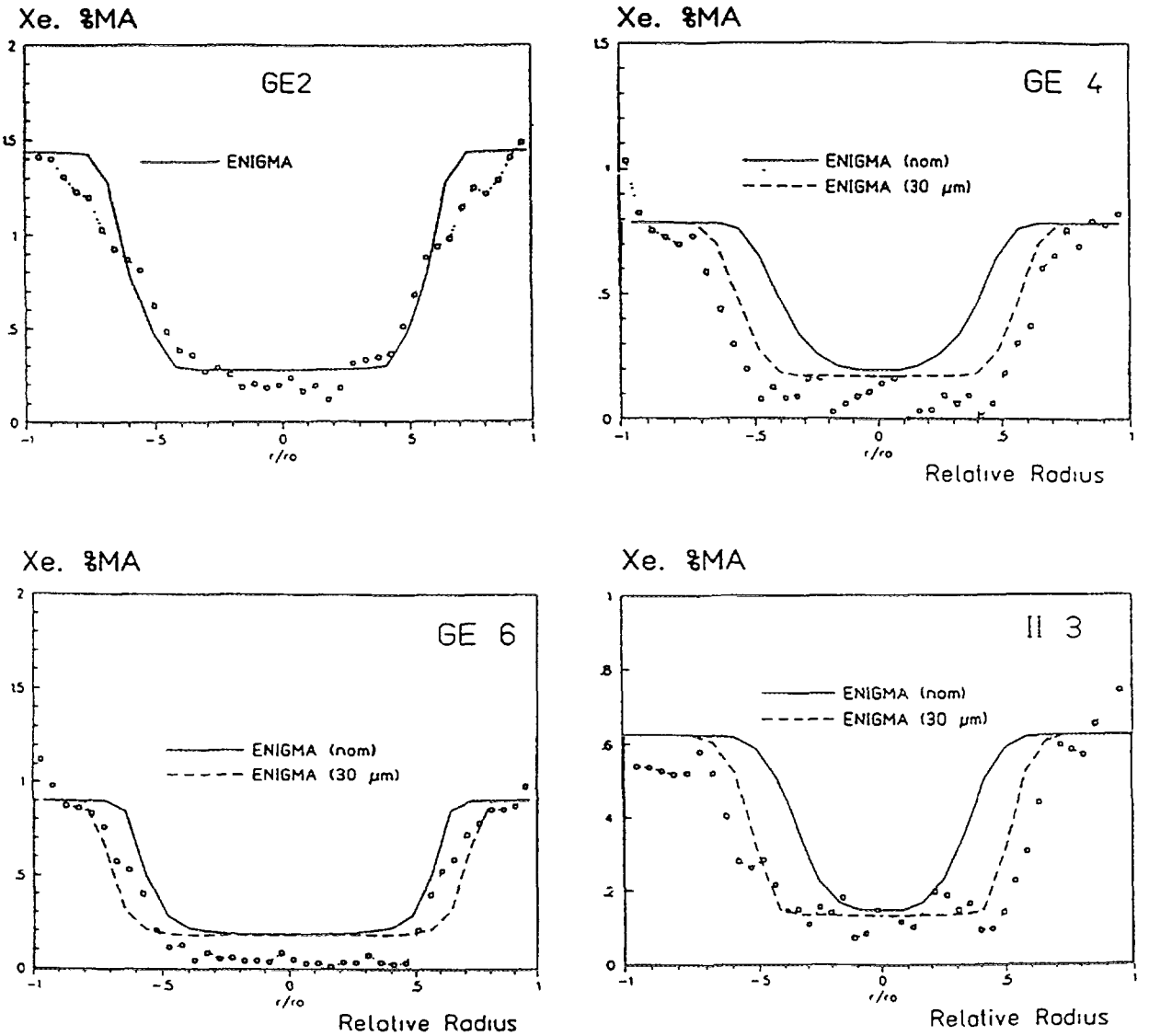

FIG. 6. *ENIGMA results on radial distribution of fission gases in Risø GE tests. Effect of two values of a gap parameter displayed*

A subtask in the Finnish-Russian co-operation on VVER fuel research, named the SOFIT programme, has comprised of fuel rod irradiations in the MR test reactor of the Kurchatov Institute/ IRTM in Moscow. One of the objectives of the programme is to calibrate fuel performance codes in both countries for the VVER fuel. In the test assemblies several fuel rods were equipped with fuel centre thermocouples. Instruments to measure fuel stack and clad length changes were available as well.

Recently, results became available from a campaign in which discharged Loviisa VVER fuel rods that had been pre-characterized in detail were non-destructively measured in the pool-side facility at the Loviisa plant [2].

Below, analyses and applications with the data from these sources, are described.

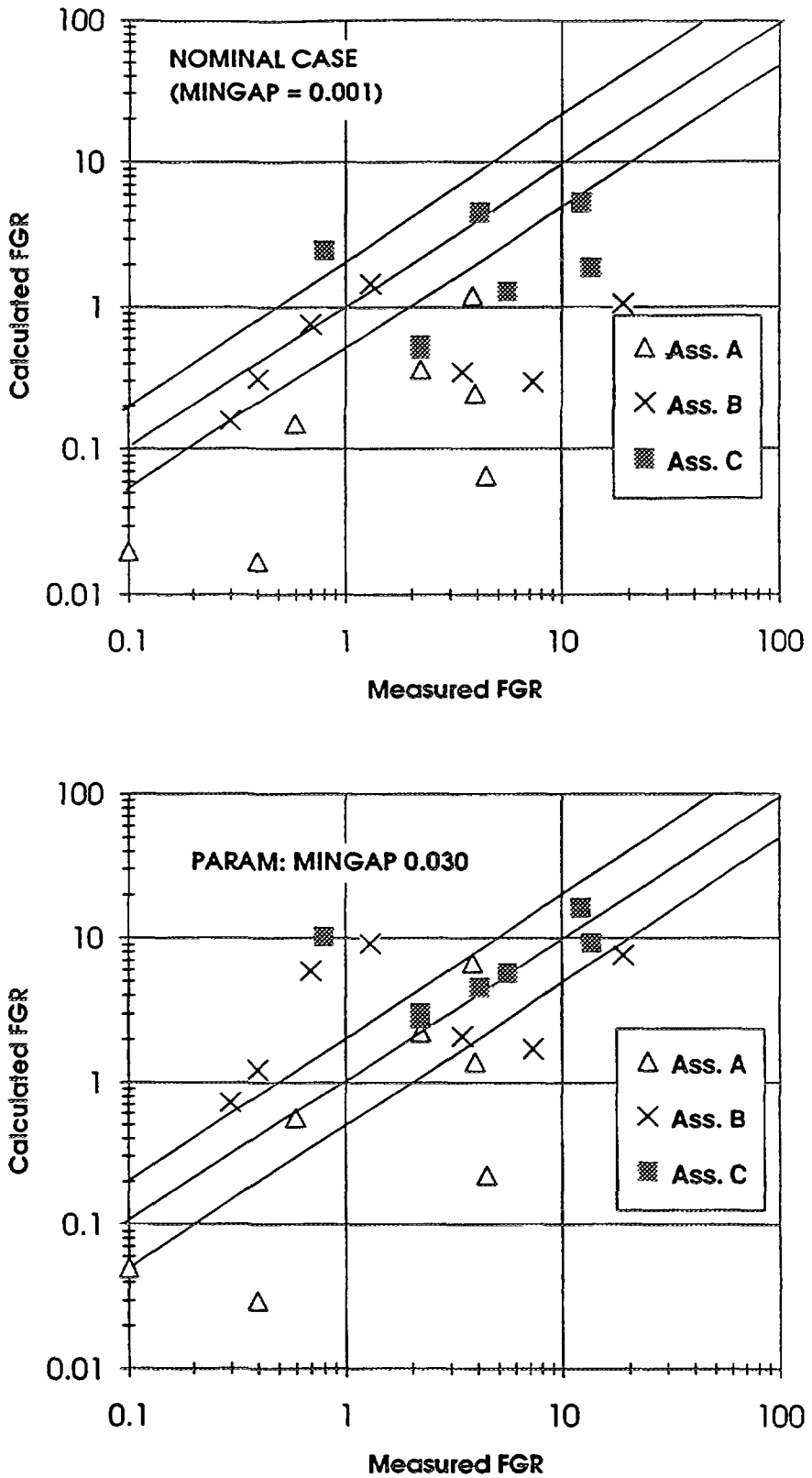

FIG. 7. *Comparison of measured and calculated FGR fractions. Effect of a gap parameter*

3.1 DESIGN DATA AND REVIEW OF THE AVAILABLE CORRELATIONS

3.1.1 Cladding material correlations

Features of the Zr1%Nb cladding material are its lower yield strength and greater uniform strain above $\sigma_{0.2}$ value as compared to Zy-2 or Zy-4. The material is partially recrystallized and hence less susceptible to creep-down than cold worked material at operating temperatures. Studies suggest that Nb-alloying impedes the cladding irradiation growth. Physical properties, like thermal conductivity and specific heat are practically those of Zircaloy.

At VTT, the materials properties required for ENIGMA calculations have been reviewed and several cladding material correlations based on tests and research by the manufacturer and IRTM were incorporated in the code. In spite of the amount of test results, there are no particular VVER correlations for the effects of irradiation on the mechanical characteristics (plasticity, fatigue, cracking, corrosion), for which one needs to rely on Zircaloy properties. The cladding material is comparatively resistant to waterside corrosion. Together with relatively low coolant temperatures of the VVER-440 reactors (264 - 298 °C) this keeps the oxidation of cladding practically negligible.

3.1.2 UO_2 material characteristics

The current type VVER fuel is characterized by compressed pellets, with chamfered pellet ends and with pressurization to 0.6 MPa. In Loviisa, the enrichment is 3.6 % ^{235}U and the initial density can range between 10.45 g/cm^3 and 10.60 g/cm^3. In the instrumented test irradiations, however, fuel fabrication parameters have been varied within broader limits in search for parameter effects. As an example, the diametral fuel-to-clad gaps from 0.140 mm to 0.290 mm have been studied. Mean linear intercept grain size is typically 4 to 7 μm. Significant volume of the UO_2 porosity is embodied in large pores of up to 100 μm in diameter. For the properties of UO_2, code default correlations are used in the calculations.

3.2 ANALYSES OF SOFIT EXPERIMENTS

3.2.1 Fuel temperature

At zero burnup the governing phenomena are mainly well understood. Consequently, the temperature increase at the start-up is well predicted by the code. The larger the initial gap the more demanding the case will be, because of the magnified effect of cracking, relocation and densification on the fuel temperature.

Fig. 8 compares the measured and calculated early-in-life temperatures. The temperature points were picked from the first day of irradiation of rods with differing as-fabricated densities and other parameters. Only a marginal underprediction is observed over the temperature scale of 200 - 1500 °C suggesting that modelling of the gap and initial relocation is appropriate for the VVER fuel. Naturally, the deviation from the measurement is smallest for the small gap rods.

Longer-term temperature records are available from among a few instrumented rods; the maximum burnup was about 14 MWd/kgU. Maximum rod rating reached 350 W/cm (near the thermocouple tip). Coolant inlet temperature was 310 °C. These represent conditions that are more severe than those in the Loviisa power reactors. There the maximum allowable linear (peak pellet) power is 325 W/cm and the coolant temperature is below 300 °C.

In Fig. 9 one finds the measured temperature history of a nominal gap rod together with the calculated temperature. The temperatures are well predicted by using default gap models. The available limited range of burnups leaves the verification of the temperature calculation and the probably necessary calibration of the models uncompleted. High burnup data is expected from the follow-up parts of the joint VVER irradiation programme.

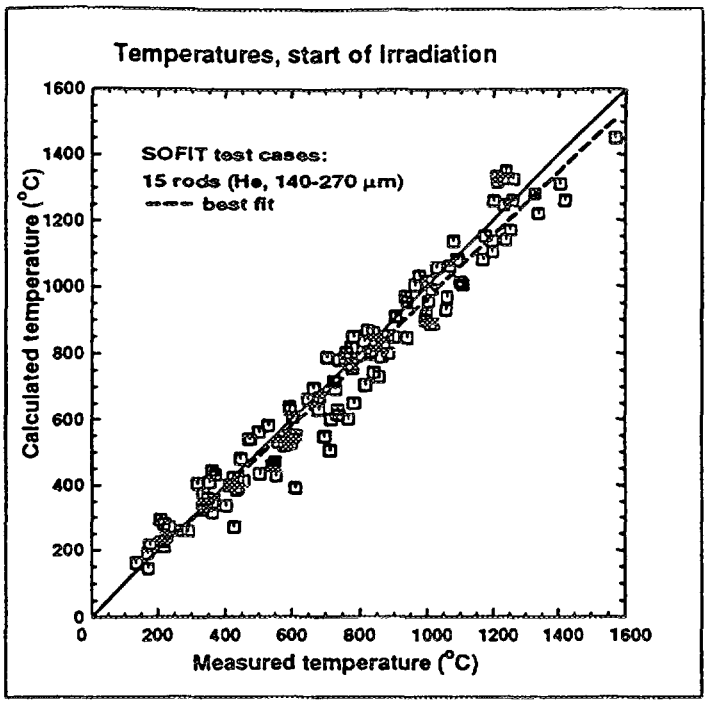

FIG. 8. *Calculated versus measured temperature for the SOFIT rods during first day of irradiation*

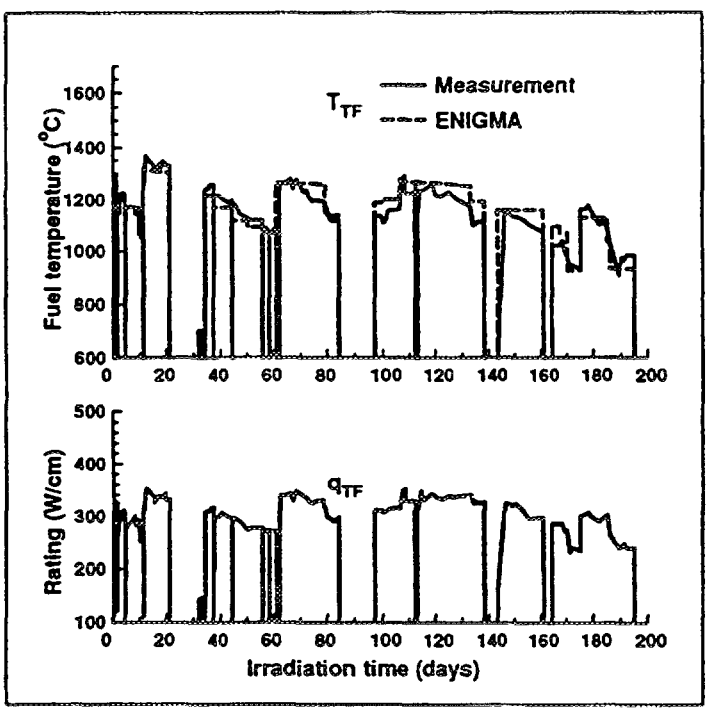

FIG. 9. *Longer-term power and temperatures of a nominal gap rod (Gap = 0.210 mm, helium fill pressure = 0.1 MPa.)*

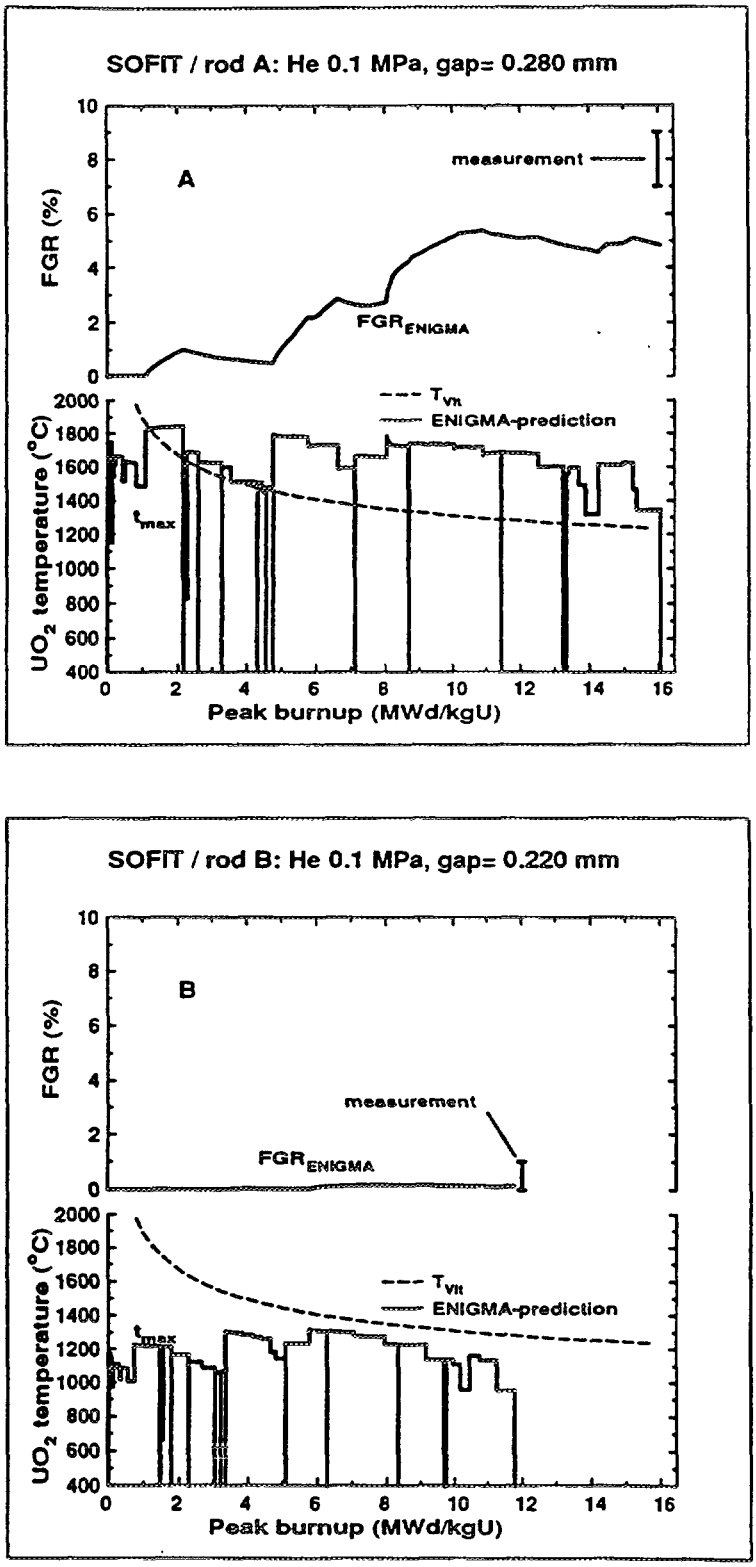

FIG. 10. Fission gas release, the SOFIT test irradiations

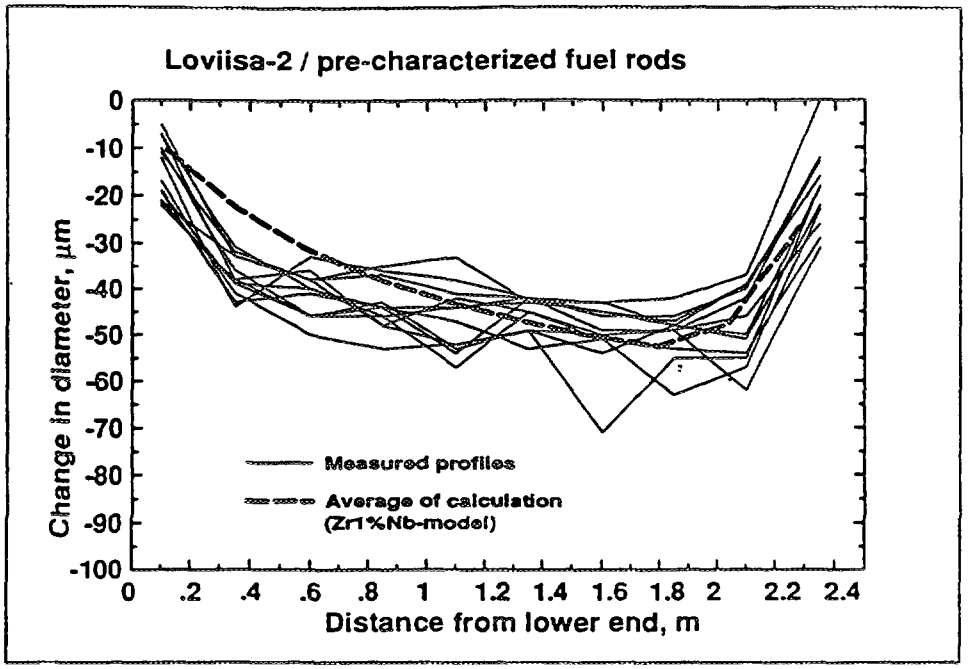

FIG. 11. *Measured and calculated creep-down of Loviisa power reactor fuel rods*

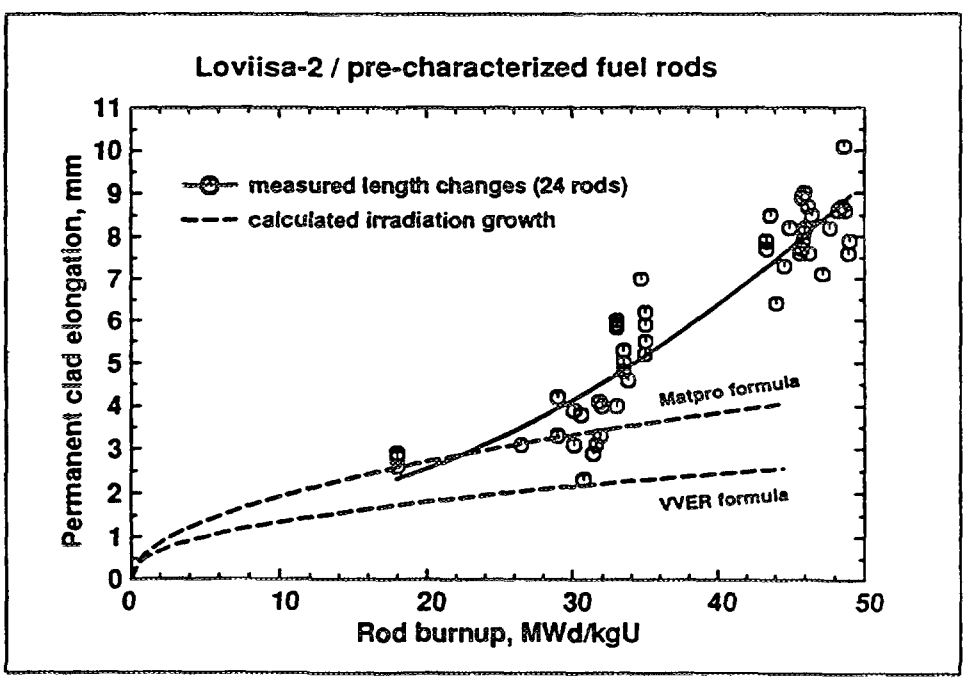

FIG. 12. *Measured clad length increase compared to calculated irradiation growth*

3.2.2 Fission gas release

If the temperatures are high enough, as in the test rod A shown in Fig. 10, fission gas release is triggered. The final fission gas release fraction of the calculation becomes 5 % - clearly a non-zero value while slightly less than the measured 7-9 %. For rod B the temperature threshold was not exceeded, and neither measurement nor calculation evidence thermally activated fission gas release.

Non-destructive examinations of rods irradiated in Loviisa-reactors have consistently indicated low fission gas release. Lately, the pool-side measurements of ^{85}Kr activity in plenum of high burnup fuel rods (43 - 49 MWd/kgU) suggested lower than 2 % gas release [2], which is in line with the code predictions for these rods.

3.3 ANALYSES OF PRE-CHARACTERIZED POWER REACTOR RODS

3.3.1 Clad creep and diameter changes

Pool-side profilometry has provided data for the verification of creep models. A creep formula specifically developed for VVER Zr1%Nb material was applied in the calculation. In Fig. 11 twelve measured full length creep-down profiles are plotted together with the calculated (average) profile. The calculated maximum creep is close to the measured values. There is, however, some underprediction over the lower third of the rods. In the creep model, temperature seems to be a dominant factor under the existing fast flux and stress conditions of the reactor. The measurement profiles point to a somewhat weaker dependence on the clad temperature and may show a closer association to neutron fluence distribution.

3.3.2 Rod permanent elongations

Clad permanent elongation results from two mechanisms. Of the total end-of-life length increase, approximately one third is concluded to be caused by irradiation growth, while two thirds arise from fuel-cladding interaction. This can be inferred from Fig. 12 where true rod lengths are compared with a Zr1%Nb irradiation growth curve. The Matpro-11 zircaloy irradiation growth curve is included for a reference.

Enhanced elongation, exceeding the irradiation growth, appears after ~ 30 MWd/kgU. By using typical fuel swelling assumptions, effectual onset of PCMI cannot be reproduced by the code. With strong interaction, one would expect clear ridging, which we do not see. Therefore, this may be related to some kind of wedging phenomena or another pellet stack effect, and would deserve closer examination. Nevertheless, for the new type of Loviisa fuel rods (pressed pellets, 0.6 MPa pressure) the average length change within a large set of high burnup rods has been only 6.5 mm (0.007 % per MWd/kgU). Although higher than calclulated, this small amount of lengthening has not seen to cause any disturbance in operation.

4. CONCLUSIONS

The ENIGMA code, developed by the British companies NE and BNFL and accuired and installed by VTT in Finland, was applied in a variety of calculations. Data from commercial and test reactor fuel irradiations were used for the first assessment of the code for BWR and VVER applications. The options for material properties in ENIGMA were supplemented with a reviewed set of VVER specific correlations. Sensitivity of the results was examined with some parameter studies. In the applications so far, the ENIGMA code has proven to be very flexible in use and has already become a frequently needed tool, while it is acknowledged that development of a fuel performance code needs to be a continuous task.

Comparison of the fission gas release results with those deduced from non-destructive ^{85}Kr determinations of a BWR (Siemens 9x9) fuel type shows the right trend, while there is a considerable, yet perhaps typical, scatter around the ideal fit. Some of that scatter unavoidably results from uncertainties in determination of the powers of single rods. These inaccuracies are not easy to quantify. Apart from that, some general underprediction of the gas release is apparent. The results suggest this being sometimes the

case for both athermal and diffusion release. In the future, the possible effect of the rim area in high burnup pellet should be studied and appropriate model refinement is recommended. Comparison with characterized test reactor results (Risø FGP3) suggests a good performance of the gas release model once temperatures are correct. The importance of accurate temperature calculation is much emphasized, and the efforts to study phenomena that contribute to that at high burnups, like thermal conductivities and gap heat transfer, need to be continued.

Results for the VVER fuel show satisfactory agreement with the measured data for cladding diameters. This suggests successful description of the clad creep as well as the ENIGMA models' adequacy for gap closure. Comparison with the VVER fuel behaviour measured in the MR test reactor is very satisfactory in the low burnup range studied so far. The observed fission gas release in Finnish VVERs is low; also in the ENIGMA results there is a wide margin to thermal release in these cases. The observed permanent end-of-life elongations of the VVER rods are larger than calculated. Early axial interaction and essentially non-existent ridge formation call for more studies on the possible effects of the pellet stack configuration.

In the current status of modelling, code assessment and calibration against fuel type specific data remains a necessity. The availability of sufficiently well-characterized data will place limits on this final phase of code development. Non-destructive pool-side examinations can provide highly useful data for such purposes the most valuable feature being the close representativeness as to design and irradiation conditions.

ACKNOWLEDGEMENTS

The Siemens company and the Kurchatov Institute prepared and generously provided the BWR rod power histories and the VVER materials properties data, respectively, for the use of the work summarized above.

Parts of the work have been funded by the Finnish utilities Imatran Voima Oy and Teollisuuden Voima Oy.

REFERENCES

[1] KILGOUR, W.J. et al., "Capabilities and Validation of the ENIGMA Fuel Performance Code.", International Topical Meeting on Light Water Reactor Fuel Performance April 21-24 1991 (Proc. Int. Conf. Avignon France, 1991), ANS/ENS, pp. 919-928.

[2] LÖSÖNEN, P., RANTA-PUSKA, K., "Pool side inspections and performance evaluation of VVER-440 fuel rods", 1994 International Topical Meeting On Light Water Reactor Fuel performance (Proc. Int. Conf. West Palm Beach), ANS, Illinois 1994, pp. 113-118.

HIGH BURNUP MODELS IN COMPUTER CODE FAIR

B.K. DUTTA, P. SWAMI PRASAD, H.S. KUSHWAHA,
S.C. MAHAJAN, A. KAKODAR
Bhabha Atomic Research Centre,
Trombay, Mumbai,
India

Abstract

An advanced fuel analysis code FAIR has been developed for analysing the behaviour of fuel rods of water cooled reactors under severe power transients and high burnups. The code is capable of analysing fuel pins of both collapsible clad, as in PHWR and free standing clad as in LWR. The main emphasis in the development of this code is on evaluating the fuel performance at extended burnups and modelling of the fuel rods for advanced fuel cycles. For this purpose, a number of suitable models have been incorporated in FAIR. For modelling the fission gas release, three different models are implemented, namely Physically based mechanistic model, the standard ANS 5.4 model and the Halden model. Similarly the pellet thermal conductivity can be modelled by the MATPRO equation, the SIMFUEL relation or the Halden equation. The flux distribution across the pellet is modelled by using the model RADAR. For modelling pellet clad interaction (PCMI)/stress corrosion cracking (SCC) induced failure of sheath, necessary routines are provided in FAIR. The validation of the code FAIR is based on the analysis of fuel rods of EPRI project "Light water reactor fuel rod modelling code evaluation" and also the analytical simulation of threshold power ramp criteria of fuel rods of pressurized heavy water reactors. In the present work, a study is carried out by analysing three CRP-FUMEX rods to show the effect of various combinations of fission gas release models and pellet conductivity models, on the fuel analysis parameters. The satisfactory performance of FAIR may be concluded through these case studies.

1. INTRODUCTION

India has adopted Pressurized Heavy Water Reactors as the mainstay of its nuclear power programme in the current stage. Since our natural Uranium resources are limited, our power programme has placed considerable emphasis on Plutonium recycle. Further, we are endowed with large resources in terms of Thorium and we, thus, have a strong interest in exploitation of Thorium for our nuclear electricity production.

At the present time, the Indian PHWR fuel bundles are used to an average burnup of 8000 to 10000 MWD/ton and peak burnup is of the order of 15000 MWD/ton. Due to our limited resources of natural Uranium, there is a strong desire to improve the burnup significantly to utilize this resource optimally. Various alternatives through advanced fuel cycles, based on MOX fuel and Thorium are being considered for this purpose. In parallel we are in the process of developing an Advanced Heavy Water Reactor System (AHWR) to facilitate the utilization of Thorium through thermal reactor cycles. This also would need fuel capable of achieving high burnup. One of the important necessities for design of high burnup fuel is to have a validated fuel analysis code with different up to date models. The development of computer code FAIR (Fuel Analysis for Indian Reactors) [1] has been done with this objective in mind.

2. GENERAL FEATURES OF FAIR

The computer code FAIR is a mechanistic code for the fuel analysis of water cooled reactors with multiple modules for analysing different features of a fuel pin based on latest literature. The code is specially designed for analysing high burnup fuels by selecting different modules typically suited for this purpose. Special feature has been introduced for collapsible clads to make it suitable for PHWR fuel pins also. The mechanics of the pellet and clad (thermal as well as deformations) is solved by using 2-D

axisymmetric finite element analysis. The thermal module can handle steady state as well as transient cases considering change in material properties with temperature. The variation in gap conductance between pellet and clad is considered by coupling the thermal module with the mechanical module to obtain convergence on physical gap for a given time instant. The mechanical module is a thermal-elastic-plastic module with the consideration of material properties as a function of temperature and creep strain. Special creep laws for UO_2 pellet and Zircaloy clads have been incorporated.

Other general features of FAIR are typical of a fuel analysis code. These are, consideration of densification, swelling, relocation, grain growth, cracking of pellets, etc. Gap conductance is calculated using Ross and Stout model with the more accurate modelling for the conductivity and extrapolation length for pellet-gas and gas-clad interfaces.

In the following sections, the four important modules of code FAIR, which are specially incorporated for the analysis of high burnup fuels, are described in detail.

3. HIGH BURNUP MODELS IN FAIR

3.1 CONSIDERATION OF CONDUCTIVITY DEGRADATION WITH BURNUP

Accurate computation of pellet temperature is of utmost importance for a fair prediction of overall mechanistic behaviour. One of the important inputs to temperature computation module is the pellet conductivity. The expression characterizing variation of UO_2 conductivity as a function of porosity and temperature is generally well established and is available in standard documents, such as, MATPRO [2], etc. However, understanding of degradation of conductivity with burnup, is still evolving. Besides having burnup independent conductivity expression from MATPRO, the computer code FAIR has two burnup dependent conductivity expressions. The first expression is based on the experimental results available from Halden [3]. In this model the burnup dependent phonon contribution to conductivity is represented by

$$\lambda_{UO2}^{phonon} = 1/(A + B.T + C \times \text{burnup}) \quad (1)$$

where A, B and C are tuning coefficients to match experimental data. The second expression for conductivity is based on the findings with simulated high burnup fuel, SIMFUEL [4]. The correlation is given by

$$\lambda = [0.053 + (0.016 \pm 0.0015)b] + [2.2 - (0.005 \pm 0.002(b) \times 10^{-4}\, T \quad (2)$$

where b is the burnup (at%), T is the temperature in K and λ is the UO_2 conductivity.

3.2 HIGH BURNUP FISSION GAS RELEASE MODEL

The fission gas release model is an important routine for any fuel analysis code. The accurate determination of fission gas release is important to calculate fission gas pressure and dilution of filler gases. This in turn affects the gap conductance and pellet temperature. The computer code FAIR has got three independent fission gas release models, specially suited for high burnup fuels. These are as follows.

The first model is the physically based model considering diffusion, sweeping, resolution of gas atoms in the grain matrix and saturation of grain boundaries for ultimate release [5]. The apparent diffusion coefficient (D′) is given by

$$D' = D\, b'/(b' + g) \quad (3a)$$

where, D is the single gas atom diffusion coefficient given by

$$D = 7.6 \times 10^{-10} \times \exp(-7 \times 10^4/RT) + S^2 J_v V + 2 \times 10^{-40} F \qquad (3b)$$

where S is atomic jump distance, J_v is jump frequency of vacancy, F is fission rate. The factor g is the probability of a gas atom in solution being captured by intragrannular gas bubbles and b′ is the probability of a gas atom within intragrannular bubble being redissolved. The expressions for b′ and g can be derived using bubble concentration, mean bubble radius, fission range, the range of influence and equation for Van der Wallis gas.

The grain boundary saturation limit is found out by using the expression for density of gas atoms over the grain boundaries at saturation. This is given by

$$N_f^{max} = \frac{2r_f f_r(\theta)}{3\, k\, T \sin^2\theta} f_b \left(\frac{2\gamma}{r_f} + P_{ext} \right) \qquad (4)$$

Where r_f is the radius of grain face bubble, θ is the semi dihedral angle, k is the Boltzmann constant, γ is the free surface energy and P_{ext} is the external force. The physically based model of code FAIR has been tested against experimental results for isothermal pellets up to high burnups quoted in the literature.

Besides the physically based mechanistic model, the code FAIR has got two more fission gas release models based on empirical relations. These are the standard ANS 5.4 model [6] and the Halden fission gas release model [7]. In the Halden model, the incubation period, up to which the fission gas release is less than 1%, is calculated by

$$buh = 5 \times \exp(9800/T) \qquad (5)$$

The fractional fission gas release is calculated using the following relations:

$$fgr = 0 \quad \text{if bu} < \text{buh} \qquad (6a)$$

$$= (T/1800)^5 \quad \text{if bu} > \text{buh and T} < 1800\,^{\circ}C \qquad (6b)$$

$$= 1 \quad \text{if bu} > \text{buh and T} > 1800\,^{\circ}C \qquad (6c)$$

The athermal release of fission gas is computed using the ANS 5.4 model. The prediction of Iodine release is very important for calculating the damage to the sheath of the fuel pin because of stress corrosion cracking. The iodine release calculations are performed in the code FAIR based on MATPRO [2].

3.3 MODEL FOR RADIAL FLUX DISTRIBUTION AT HIGH BURNUP

The radial power density profile across the pellet of fuel rods operating in a thermal reactor exhibits flux depression, which changes with the burnup due to build up of plutonium in a thin later near the pellet surface. In computer code FAIR, the well known RADAR (Rating Depression Analysis Routine) model [8] has been implemented for this purpose.

3.4 MODEL FOR STRESS CORROSION CRACKING OF SHEATH DUE TO PCMI

The prediction of stress corrosion cracking in the sheath due to PCMI at high burnup and high temperature is an important information to improve the performance of fuel bundles. This is more important for collapsible clad fuel rods used in PHWRs where the sheath has to follow the pellet during the entire operation of reactor. A special module has been implemented in the code FAIR to predict the stress corrosion cracking (SCC) induced sheath failure during the history of fuel rod operation. This model is based on the work of reference [9]. The important inputs for this module are the sheath strains, the material properties, especially the decrease in ductility. The first step in this methodology is to check whether sheath strain is more than the threshold to initiate a crack. This is given by

$$\Sigma = exp\left[\frac{1}{K6} \times log\left[\frac{-K_5}{\log\ (I/I_2)}\right]\right] \qquad (7)$$

where I is the threshold Iodine required for intragrannular failure, I_2 is the effective Iodine available and K_5, K_6 are constants.

Once this strain is exceeded, the next step is to calculate the rate of iodine penetration to the crack tip by using the expression

$$\frac{dI}{dt} = \frac{h}{w}\left[\exp\ (-Q/KT)\left[I_{eff}\ \exp\ (-K_5/\varepsilon^{K_6}) - I\right]\right] \qquad (8)$$

If the Iodine concentration at the crack tip exceeds the threshold for intergrannular stress corrosion cracking or transgrannular stress corrosion cracking, the crack propagates further. In this case a redistribution of the stress and strain in the clad is to be carried out for the new length of the crack, which is done analytically based on the hoop stress and moment equilibrium. The ultimate rupture of the sheath exceeds the ductile rupture strength of the material. This ductile rupture strength of the sheath material decreases due to irradiation and triaxiality at the crack tip.

4. EXERCISES

The performance evaluation of a fuel analysis code is a difficult task due to limited availability of experimental data in the open literature. The individual models of the code FAIR have been tested against the standard bench mark cases quoted in the literature. However, the performance evaluation of this code as an integral fuel analysis code was done against the following case studies.

The Electric Power Research Institute (EPRI) sponsored a research project (397-1) to evaluate six fuel rod modelling codes as a step towards a more effective utilization of these codes by the electric utility industry. The findings of this project were reported in an EPRI report [10]. The major conclusion of this research project was that the COMETHE-III J code was the most versatile code among all the participating codes. All the cases reported in that report were used as bench mark cases to evaluate the computer code FAIR. The results for case-C of this report as computed by code FAIR have been shown in Fig. 1 along with the results quoted by the other participating codes and experimental values. The results of the code FAIR can be seen to be more in agreement with those of COMETHE-III J, which incidentally deviated from the experimental values. The end of life fission gas release was calculated as 5.83% by FAIR, as against the value of 5.6% reported by the code COMETHE-III J.

The code FAIR was used for analytical simulation of the threshold power ramp criteria (P_c, ΔP_c curves) for a PHWR fuel rod. These curves have been originally generated based on the experimental results. For generating these curves, it is necessary to reach a particular burnup before subjecting the fuel rod to a ramp. The fuel rod can reach a given burnup through many combinations of power maneuvering. Hence in analytical simulations, different routes are assumed to reach a given burnup by specifying different constant initial power ratings. After reaching a particular burnup, the fuel pin is subjected to power ramps of varying magnitude. The fuel pin is assumed to reside at this power for a time long enough to consider the dwell period to be more than 2.5 hours. By using the PCMI model of the code FAIR, the maximum ramped power was computed which did not cause the sheath failure. This threshold peak power as a function of burnup and different initial power ratings is plotted in Fig. 1. along with the experimentally generated points quoted in reference [11].

The code FAIR recently participated in a co-ordinated research project FUMEX conducted by IAEA [12]. The project consisted of the blind code comparisons of different fuel performance parameters computed by different participating agencies, with the experimental results obtained in the Halden reactor.

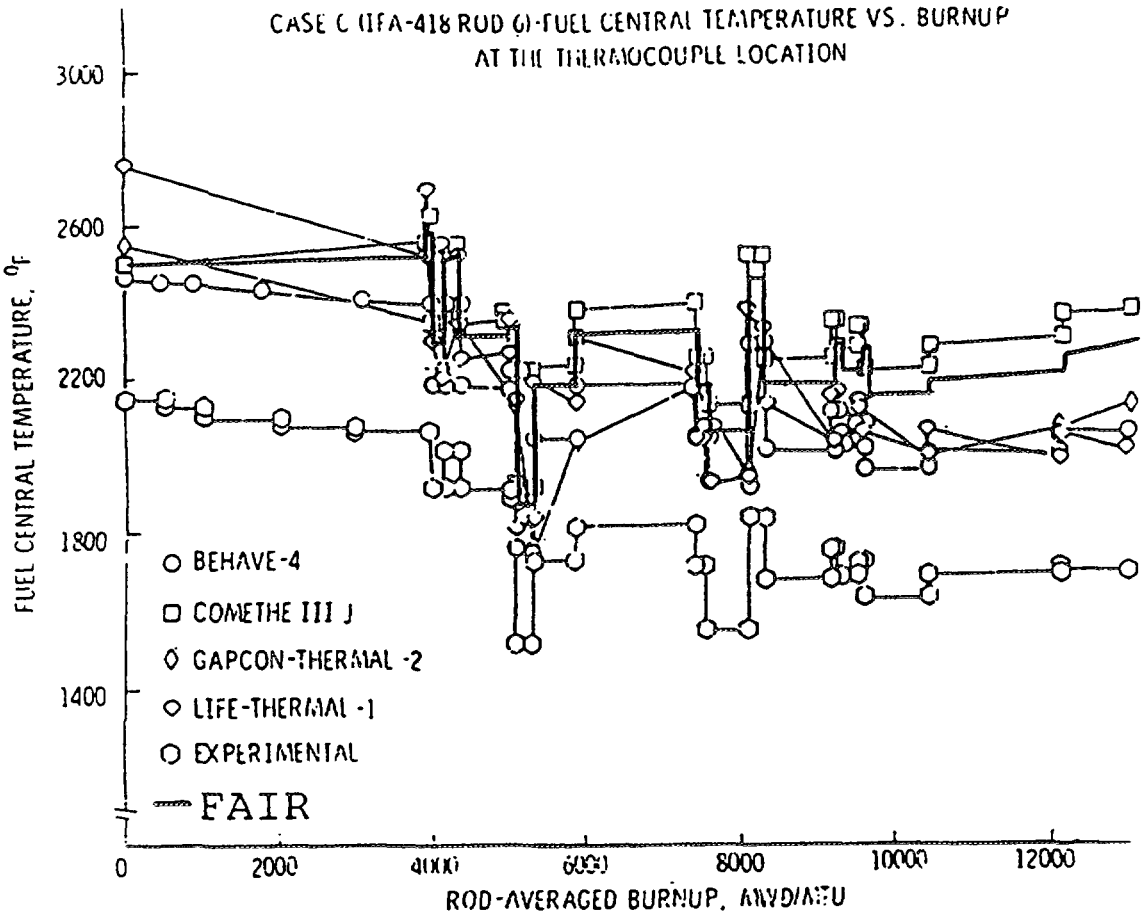

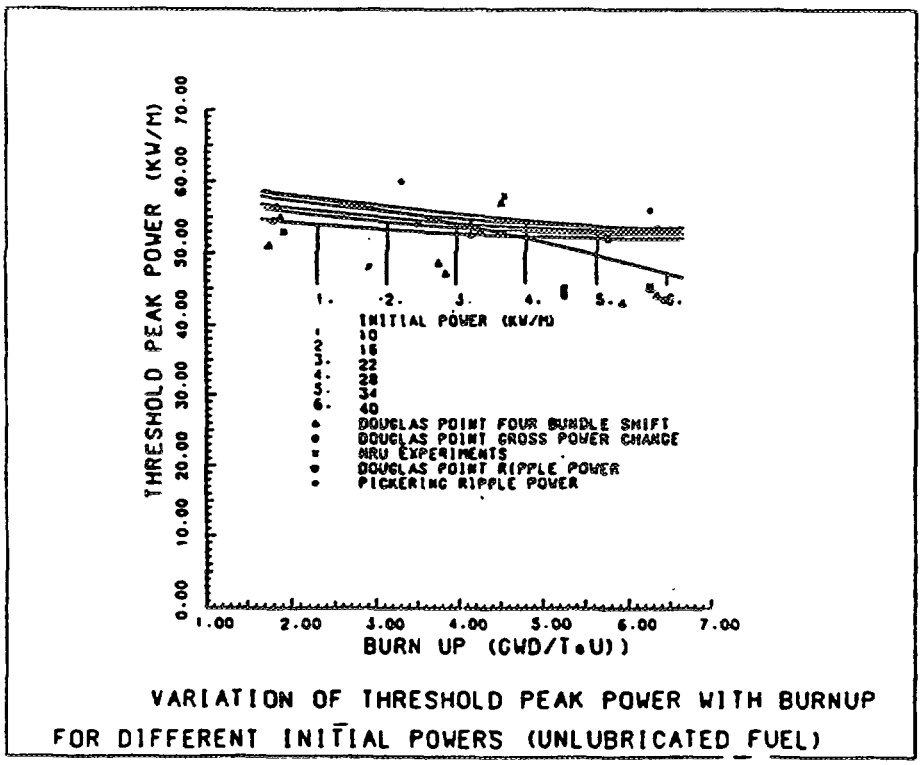

FIG. 1. Results of the case studies to evaluate code FAIR.

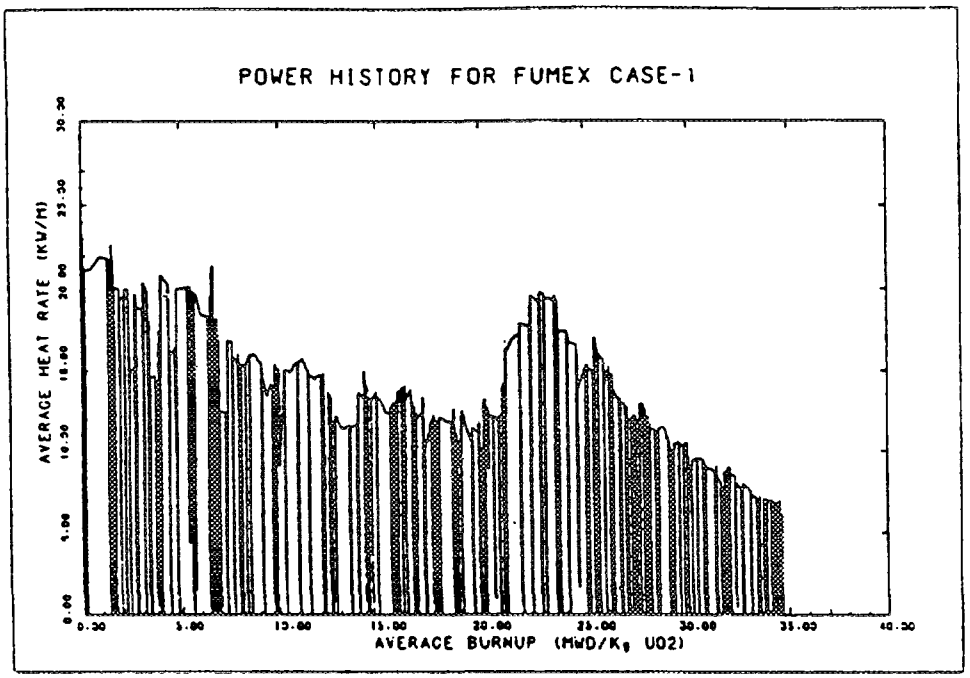

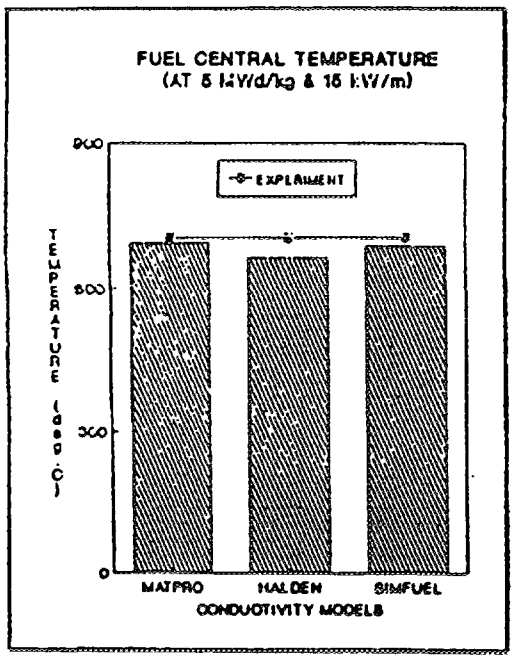

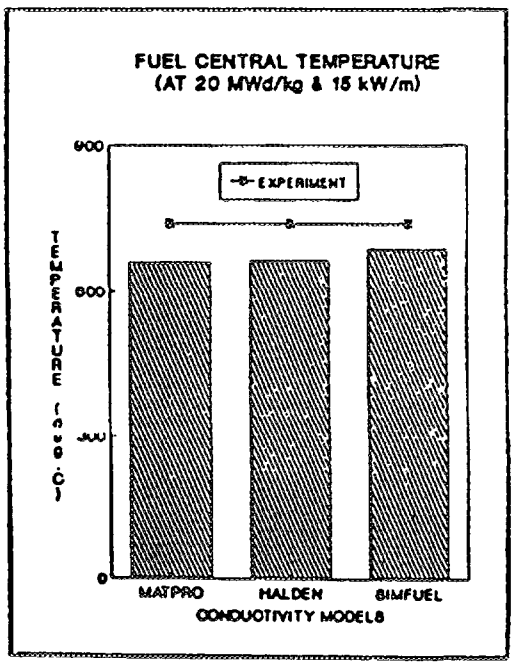

FIG. 2. Inter comparison of conductivity models for FUMEX case-1.

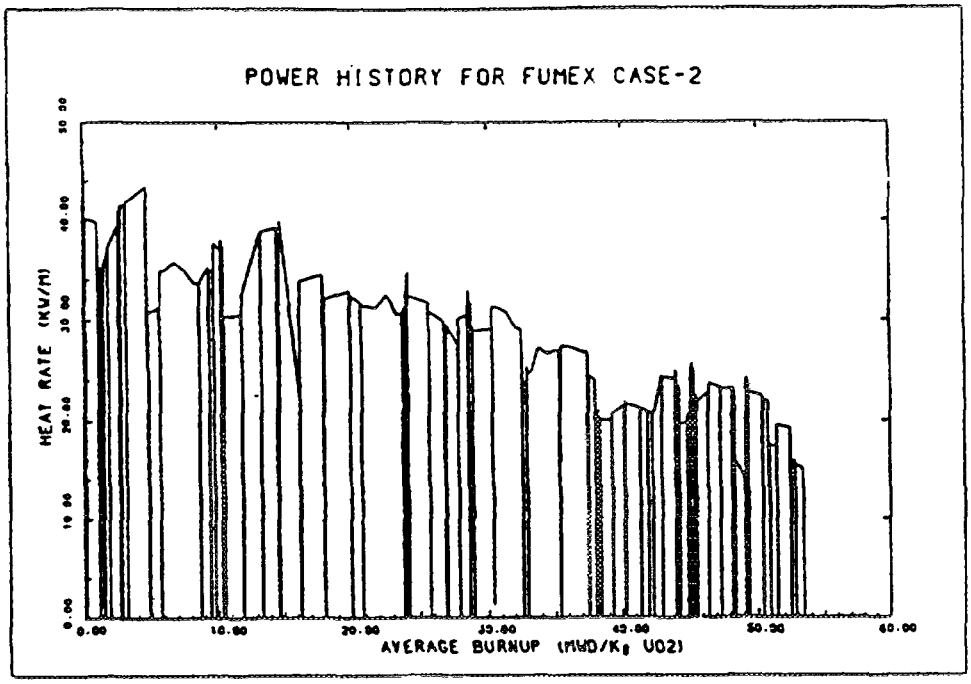

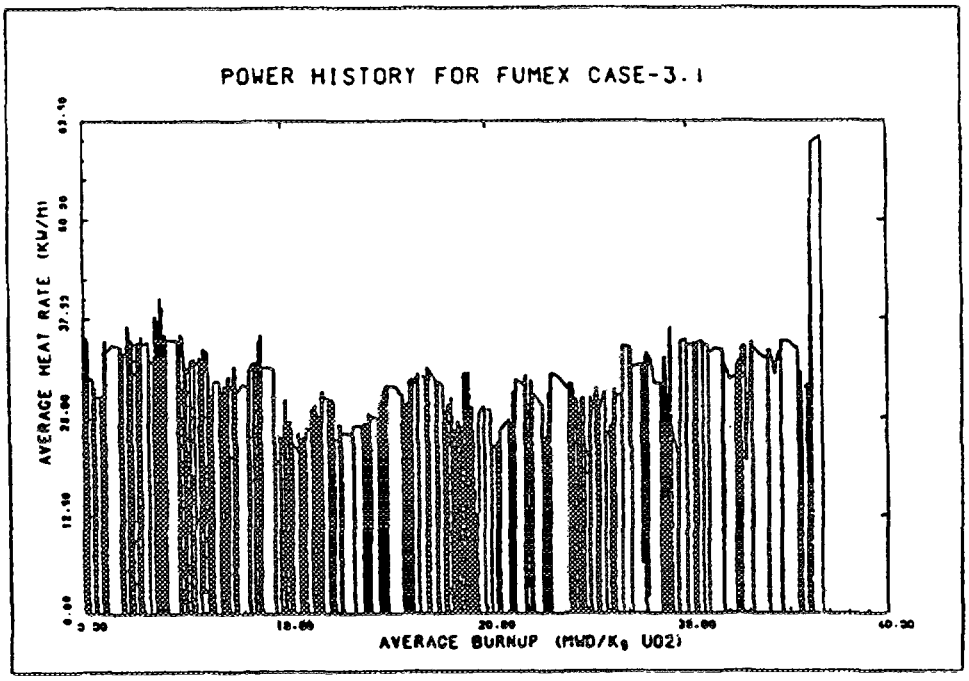

FIG. 3. Power histories for FUMEX case-2 and FUMEX case-3.1 [12]

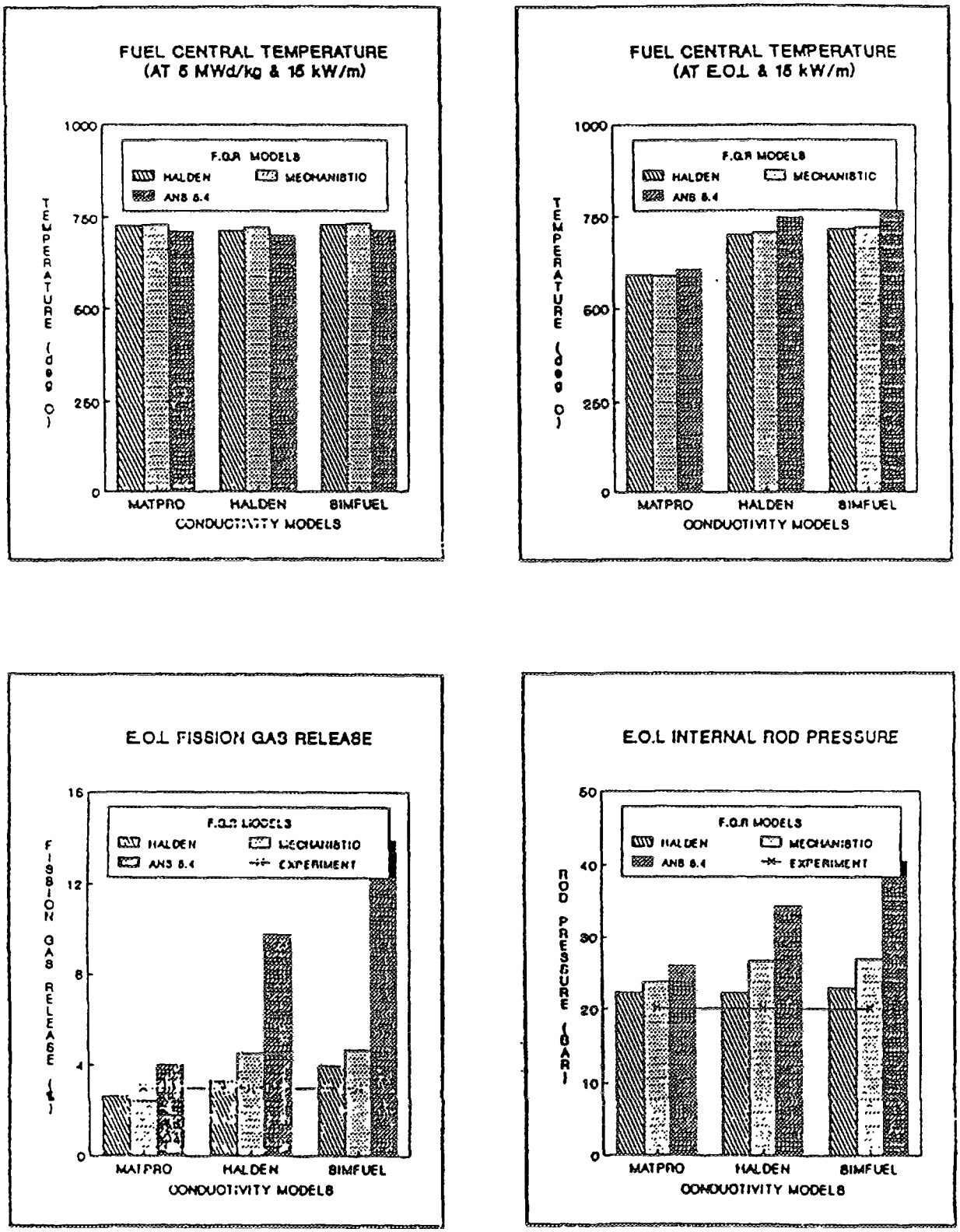

FIG. 4. Inter comparison of conductivity and F.G.R. models for FUMEX case-2.

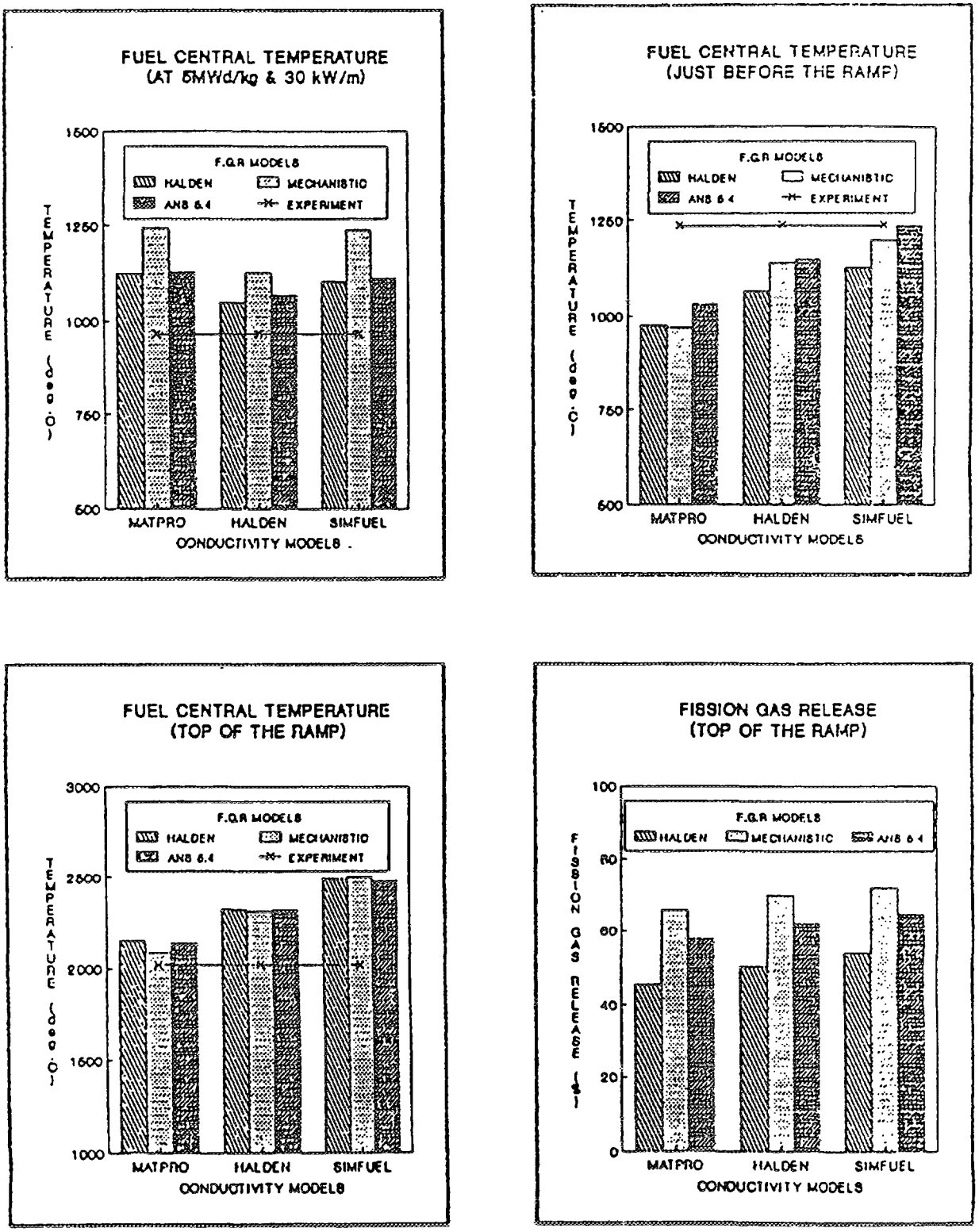

FIG. 5. Inter comparison of conductivity and F.G.R. models for FUMEX case-3.1.

The results computed by the participating codes and the experimental results are being published in an IAEA document to be presented in the present conference.

We have used three cases of this CRP for further study. These are FUMEX-1, FUMEX-2 and FUMEX-3 Rod 1. The study consists of computation of results by three burnup dependant conductivity models and the three fission gas release models implemented in the code FAIR. The conductivity models are based on MATPRO (burnup independent), HALDEN and SIMFUEL models. The fission gas release models are Halden model, ANS 5.4 model and mechanistic model of code FAIR. Each of the above three FUMEX cases is run for nine different combinations and the results obtained along with the power histories [12] are shown in Figs. 2-5.

5. CONCLUSIONS

From the performance analysis of various fuel rods using FAIR, the following conclusions can be drawn.

i) The code FAIR computed consistent results for all the cases analysed.

ii) The results computed by FAIR for the case-C of EPRI project show close match with the results quoted by using COMETHE-III J, for both temperature and fission gas release values.

iii) The threshold peak power curves simulated analytically using FAIR, have a good match with the experimentally generated data of PHWRs.

iv) The performance of various conductivity models implemented in the code FAIR, with respect to the cases analysed show the following:
   a) SIMFUEL model computes temperatures higher than the Halden model at high burnups.
   b) As MATPRO model does not consider the degradation of pellet conductivity with respect to burnup, the temperatures computed by MATPRO model are the lowest among the temperatures computed by all the three models of code FAIR.

v) The performance of various fission gas release models implemented in the code FAIR, suggest the following:
   a) The Halden model computed the lowest fractional fission gas releases among all the three models.
   b) For power histories devoid of severe power transients, the ANS 5.4 model computed the highest releases among all the three models.
   c) During severe power transients, the increase in the fractional release computed by using the mechanistic model of FAIR is the highest compared to the other two models.

REFERENCES

[1] SWAMI PRASAD, P. et al., Fuel performance analysis code FAIR, BARC report no. BARC/1994/E/013.

[2] HAGRMAN, D.L., et al., MATPRO-Version 11 (Rev.2), A handbook of material properties for use in the analysis of light water reactor fuel rod behaviour, NUREG/CR-0497, TREE-1280 Rev. 2, Aug 1981.

[3] WIESENACK, W., Experimental techniques and results related to high burnup investigations at the OECD Halden reactor project, IAEA-TECDOC-697, pp.118-123.

[4] LUCATA, P.G., et al, Thermal conductivity and gas release from SIMFUEL, IAEA-TECDOC-697, pp. 165-171.

[5] WHITE, R.J., TUCKER, M.O., A new fission gas release model, J. Nuclear Material. 118 (1983) 1 - 38.

[6] Background and derivation of ANS 5.4 standard fission product release model, NUREG/CR-2507, Jan. 1982.

[7] NORDSTROM, L.A., OTT, C., An approach to modelling fuel behaviour using data from some international high burnup fuel programmes, IAEA-TECDOC-697, pp.219-224.
[8] PALMER, I.D., et al., A model for predicting the radial power profile in a fuel pin, light water reactor fuel rod computer modelling, (Gittus, J.H. Ed.) 1983, 321-335.
[9] JAMES YU-CHEN YAUNG, A model of pellet cladding interaction to simulate operational ramp failure of water reactor fuel, University of California, Los Angeles, Ph.D. 1983.
[10] Light water reactor fuel rod code evaluation, EPRI report no: EPRI NP-369, 1977.
[11] PENN, W.J., et al., Candu Fuel - power ramp performance criteria, Nuclear Technology 34, July 1977, 249-268.
[12] Agreement on FUMEX cases between IAEA and India, agreement no: IAEA/IND/7348.

COMPUTER MODELLING OF THE VVER FUEL ELEMENTS UNDER HIGH BURNUP CONDITIONS BY THE COMPUTER CODES PIN-W AND RODQ2D

M. VALACH, J. ZYMÁK, R. SVOBODA
Nuclear Research Institute Řež plc,
Řež, Czech Republic

Abstract

This paper presents the development status of the computer codes for the VVER fuel elements thermomechanical behaviour modelling under high burnup conditions at the Nuclear Research Institute Řež. The accent is given on the analysis of the results from the parametric calculations, performed by the programmes PIN-W and RODQ2D, rather than on their detailed theoretical description. Several new optional correlations for the UO2 thermal conductivity with degradation effect caused by burnup were implemented into the both codes. Examples of performed calculations document differences between previous and new versions of the both programmes. Some recommendations for the further development of the codes are given in conclusion.

1. INTRODUCTION

Development of the modernized computer codes, describing the thermomechanical behaviour of fuel elements during steady-state and transient operation of the VVER-440 type reactors, is supported by the ČEZ utility, NPP Dukovany and the Czech Nuclear Safety State Office. Process of safety upgrading and modernization of the originally designed Russian reactors and nuclear cores brings with also some important questions related to the fuel performance under higher burnup conditions. Discussion about introducing the 4 and 5 year reloading cycles for the VVER-440 reactors postulated also requirements connected with the fuel safety parameters (fuel centerline temperatures, fission gases release and inner pressure at EOL, etc.). The process of fuel vendors diversification for the Dukovany NPP (VVER-440) as well as for the Temelin NPP (VVER-1000) became a reality in the Czech Republic. Main reason for the innovation of the computer code PIN and development of a new code RODQ2D is the necessity to preserve the gained experience and to establish a national capacity for the independent safety assessments and evaluations of nuclear fuel behaviour.

2. BRIEF CHARACTERIZATION OF THE CODES

PIN computer code is based on the Gapcon-Thermal-2 methodology (Fig. 1). Physical models are based on semi-empirical approach and verified on the Russian experimental data. The code is able to predict the fuel temperature field, pellet-cladding gap thermal conductivity, fission gases release and internal rod pressure under steady-state conditions. The programme does not include any fuel cladding failure criterion. Main goal of its innovation is to expand the code capabilities for the standard PWR-type fuel rods. The PIN-W version includes the interactive screen graphic output of the main modelled parameters.

RODQ2D is originally based on the STOFFEL code, written by Reinfried (ZfK Rossendorf, Germany) in PLl language. The code was reprogrammed into Microsoft FORTRAN by B. Golomysov (IAE Moscow, Russia). In the frame of the NRI Řež and Kurchatov Institute cooperation the following changes were incorporated: the iteration scheme for the gap conductance calculation was changed to allow arbitrary gas composition, more time-effective method was used to compute fuel and cladding creep, the material properties library for the cladding material ZrlNb was included (Fig.2).

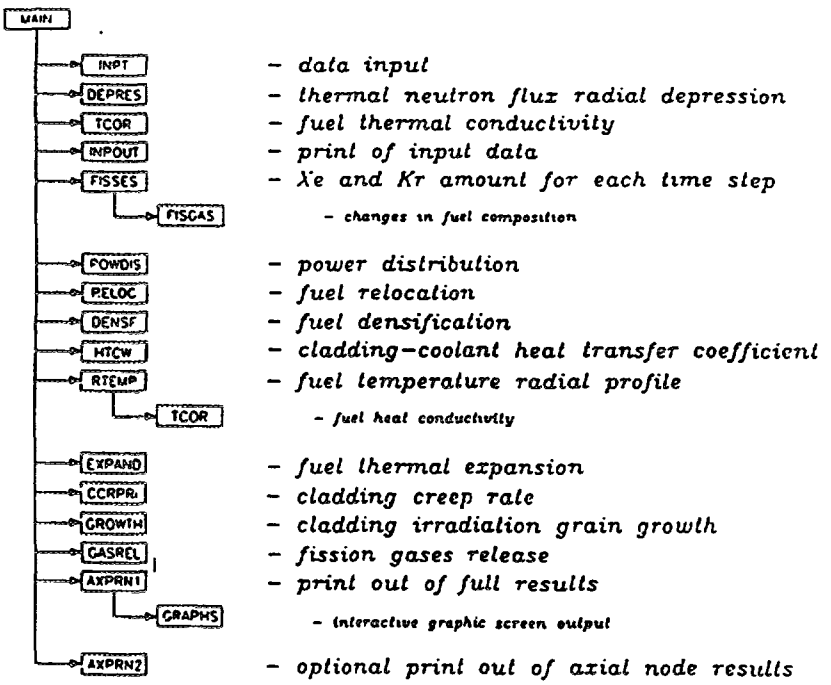

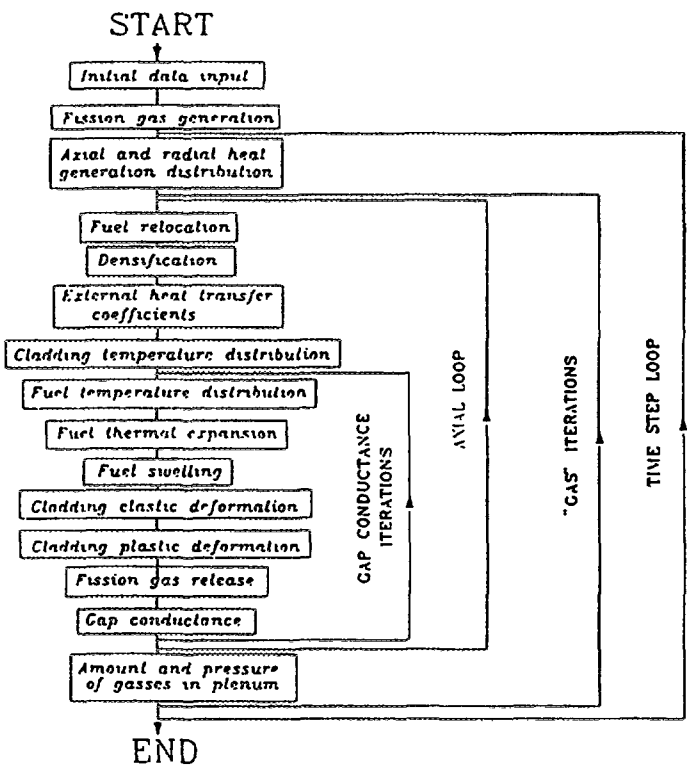

FIG. 1 *Structure of the code PIN-MICRO*
Flow chart of the code PIN-MICRO

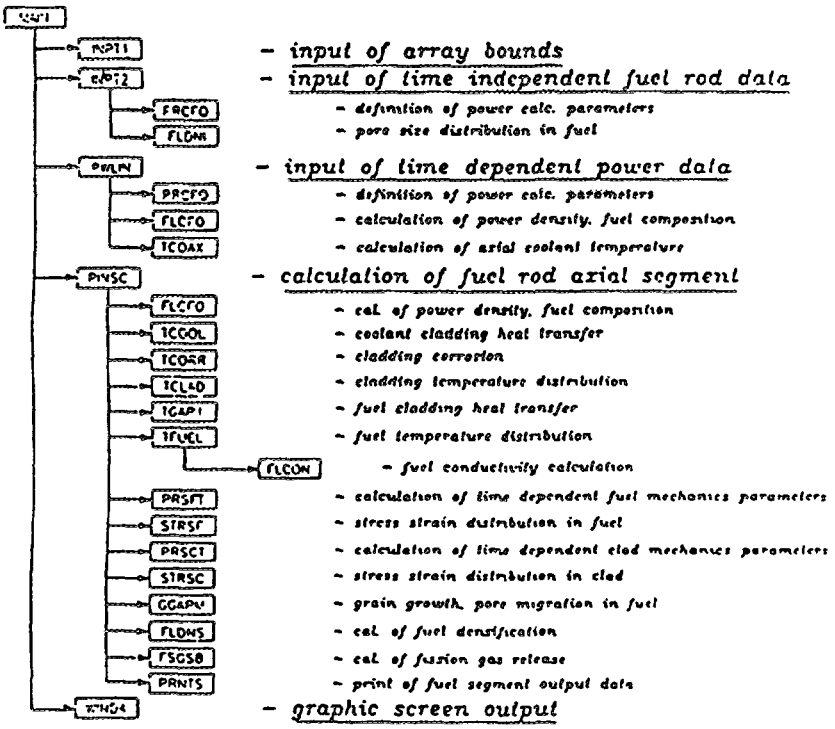

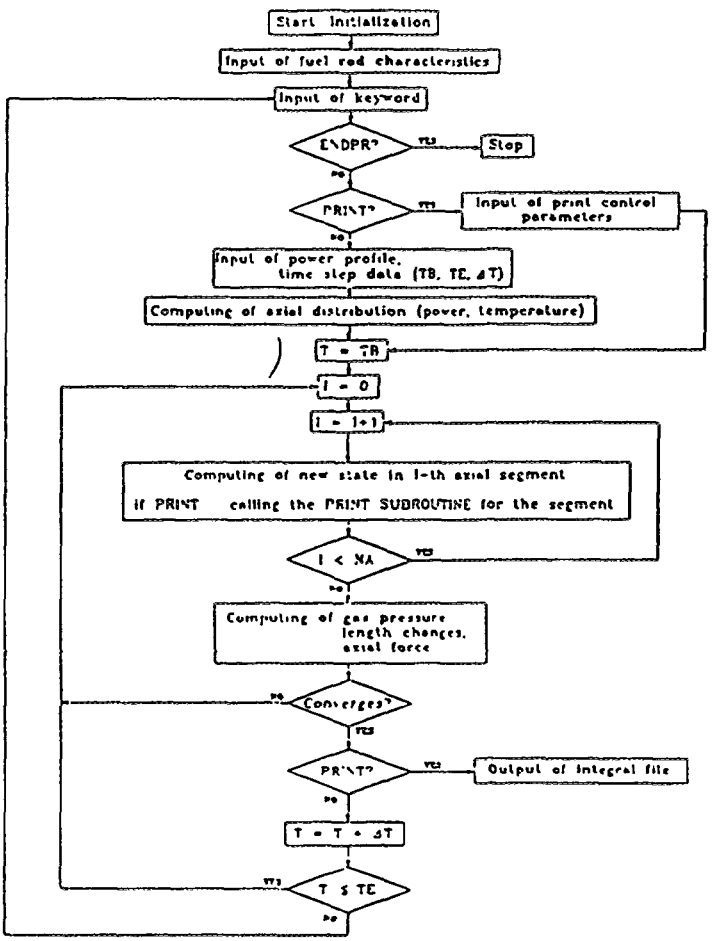

FIG. 2 *Structure of the code RODQ2D*
Flow chart of the code RODQ2D

The code belongs among the quasi two-dimensional integral codes. It is designed to predict the in-pile behaviour of a cylindrical water-cooled oxide fuel rod during quasistationary operation. The code enables also the calculation of power ramps with various ramp rates. Models for fission gas behaviour, densification and power density distribution are based on simplified mechanistic approach.

The numerical solution comprises geometrical nodalization into the axial and radial segments for using of finite differences method. The one-dimensional equation for radial heat conduction and Lame's equation for the strain-stress distribution are solved at each axial node. The coupled effects of the response parameters are treated by iterating to convergence at each power-time step. There are no restriction in the number of nodes or power-time steps.

During the last period of development the code was completely rewritten from the numerical, programming and physical point of view as well. In contradiction to the PIN-W, the RODQ2D is based on more "analytical approach", above all in the mechanical part. After finalization of this first version, more realistic modelling of gap changes during transients have to be the main attribute and advantage of the RODQ2D in comparison to the PIN-W possibilities.

The inner structure of the code is designed very flexibly (Fig. 2). The modern programming approach, based on Lahey FORTRAN, was used with some FORTRAN 90 features. The restart option and interactive graphic output is the standard feature of this version. The RODQ2D code was developed as a computer platform independent software. The transfer from the Lahey development environment (IBM-PC) to workstations with the UNIX and Windows NT was tested.

3. BASIS FOR THE PARAMETRIC CALCULATION

Participation of the NRI Řež plc in the OECD-HRP and in the IAEA FUMEX Blind problem strongly supports the process of the codes testing and validation. Open access to the unique experimental data-base of the OECD-HRP enabled preparation of the input data packages consistent for both codes.

3.1 DESCRIPTION OF THE EXPERIMENTAL DATA

The OECD-HRP Test Case (experiment IFA-432) and IAEA FUMEX exercise were found as a suitable data basis for the parametric simulations [1], [4], [5]. The IFA-432 can be characterized as a "high temperature experiment" with pronounced FGR (high level of linear power) and the FUMEX 1 exercise as a "low temperature experiment" with very long irradiation time and burnup related degradation effects. Calculations were performed by both codes from the beginning of this year. The submodels of relocation and fuel conductivity were modified for the codes tuning. The centerline fuel temperatures were used for the code to code and codes to the experiment comparison.

3.2 RELOCATION MODEL

The PIN-W empirical relocation model [6]:

$$\delta R = (A*(B/(1 + B) + C*P + 3)*G/100$$

where:

δR [inch] - fuel radius change, P [kW/ft] - linear power
G [inch] - fuel-cladding gap, $B = \exp(-4*Bu^{0.25})$
Bu - burnup, A and C - parameters.

Model can be used in the conservative or best-estimate version.

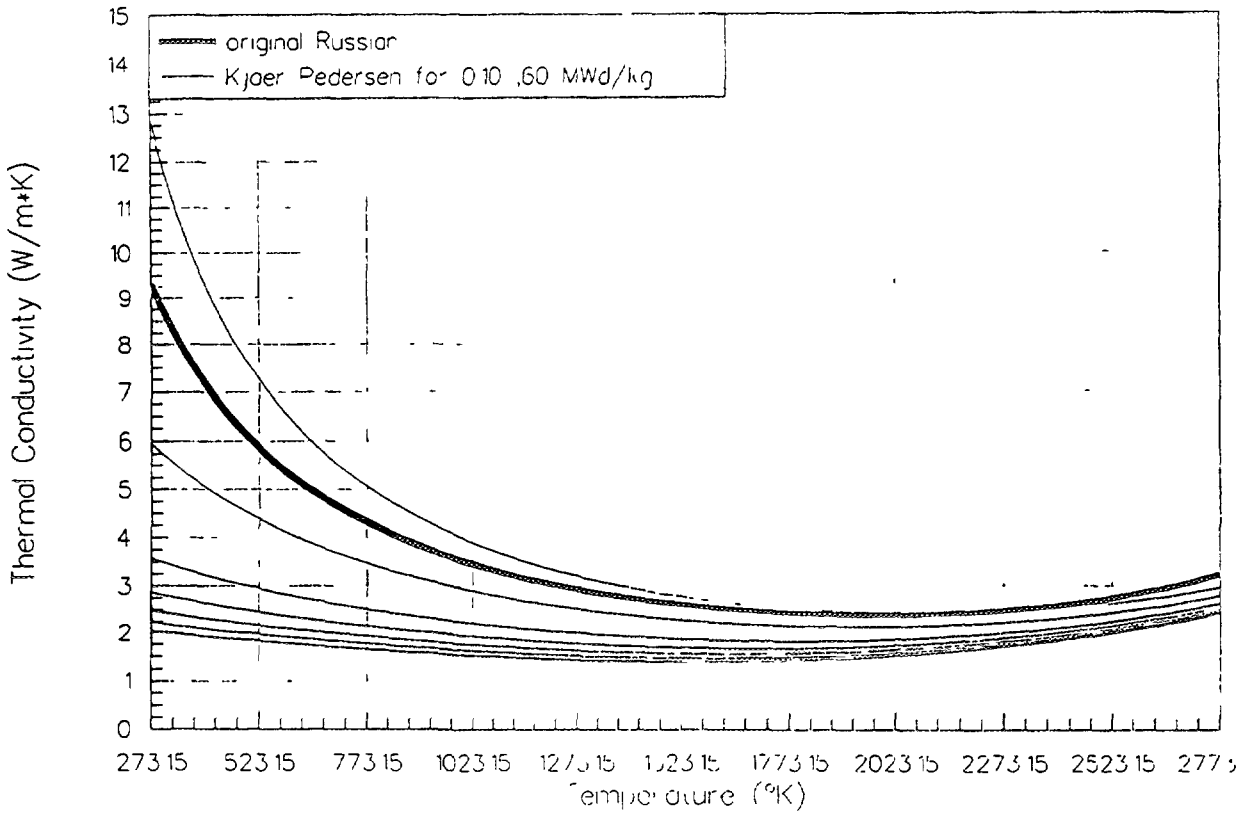

FIG. 3 Thermal conductivity UO_2

3.3 FUEL THERMAL CONDUCTIVITY MODELS (FIG.3)

Original Russian model [6]:

$$K = 1./(A*T+B) + C*T + D*T^3 *\exp(E*T)$$

where:

K [W/cm/K] - thermal conductivity
T [K] - fuel temperature, A, B, C, D, E - parameters.

HRP Vitanza-Kosaka model [3]:

$$K = 1 / (A + B*T + (C*Bu - D*B^2)) + E*T^3$$

where:

K [kW/m/°C] - thermal conductivity
T [°C] - fuel temperature, Bu [MWd/kg] - fuel burnup
A, B, C, D, E - parameters.

Kjaer-Pedersen model [2]:

$K = 93 / (0.0224*T + 1.1 + 56*P + 3*F(Bu)) + 2.5*10^{-14} *T^4$

where:

K [W/m/K] - thermal conductivity, T [K] - fuel temperature
Bu [MWd/kg] - fuel burnup, P [1] - fuel porosity
for Bu < = 10 MWd/kg $F(Bu) = (Bu/10)^2$
for Bu > 10 MWd/kg $F(Bu) = ((Bu - 7.5) / 10)^{0.5}$

4. CALCULATIONS

Calculations were performed at the NRI on the PC-486/66 MHz computers. Both codes used the same geometry nodalization. IFA-432 experiments were modelled by 10 axial and 20 radial segments. The CPU time for the PIN-W code was around 55 s and for the RODQ2D code up to 240 s. The FUMEX test cases were modelled by 8 axial and 20 radial segments. The PIN-W code consumed 1100 s of CPU time and RODQ2D 1300 s for one test run.

4.1 MATRIX OF CALCULATIONS

conductivity		relocation
Russian	PIN-W	original Russian conservative
Russian		hrp '93, coefficient C changed
Kjaer Pedersen		hrp '94, coefficient A changed
Russian	ROD-Q2D	no relocation
Russian		original Russian conservative
Russian		hrp '93, coefficient C changed
Kjaer Pedersen		no relocation
Kjaer Pedersen		original Russian conservative
Kjaer Pedersen		hrp '93, coefficient C changed

4.2 SUMMARY OF THE RESULTS

The calculation variants A2 and Al represent the IFA-432 rod No_1 and No_3 respectively. Fuel centerline temperature measurements for both rods and internal pressure for the A2 case were available [1], [6].

Fig. 4 shows IFA-432.1 recalculation by the PIN-W, Fig. 5 shows comparison against experimental data, Fig. 6 and 7 show results of the RODQ2D.

Fig. 8 and Fig. 9 include results of both codes for FUMEX-1. Two representative cases with the combination of the relocation and fuel conductivity models are presented. Both codes were relatively stable during calculations with different models.

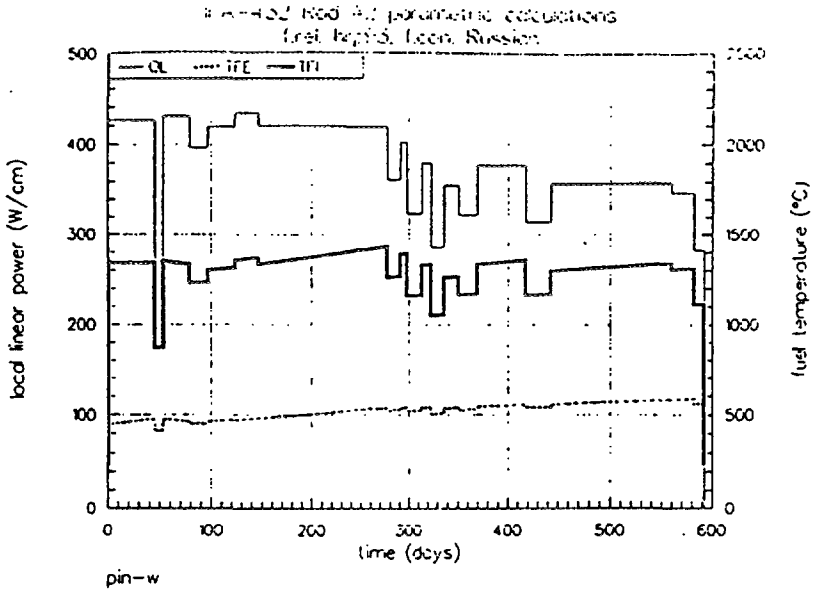

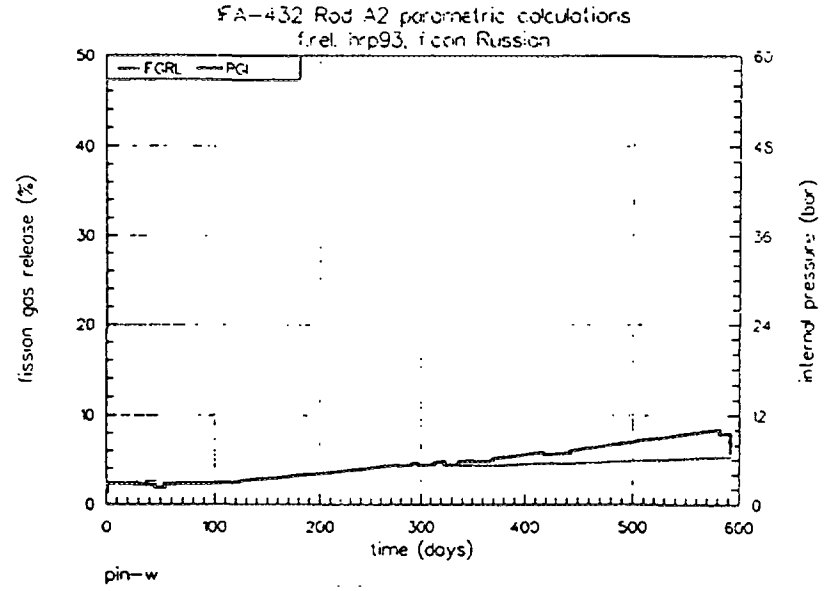

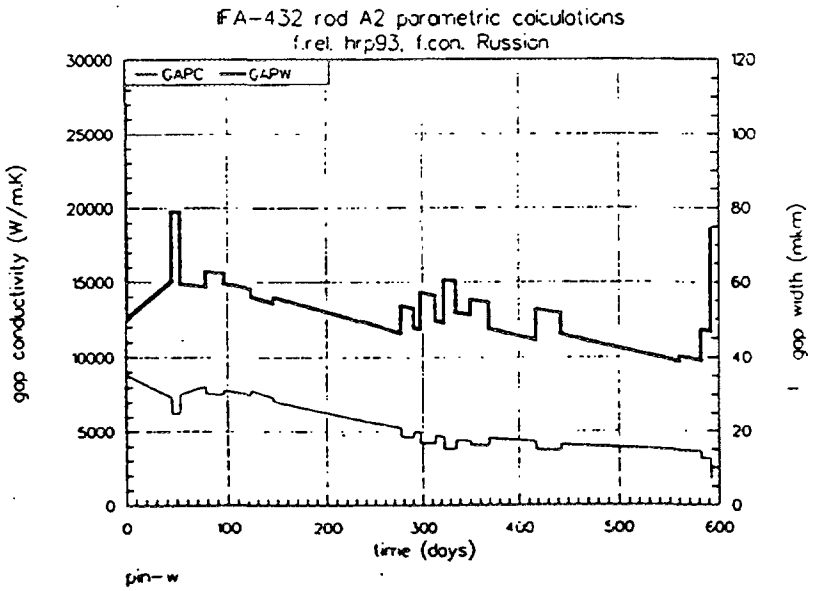

FIG. 4 *IF-432 rod A2 parametric calculations*

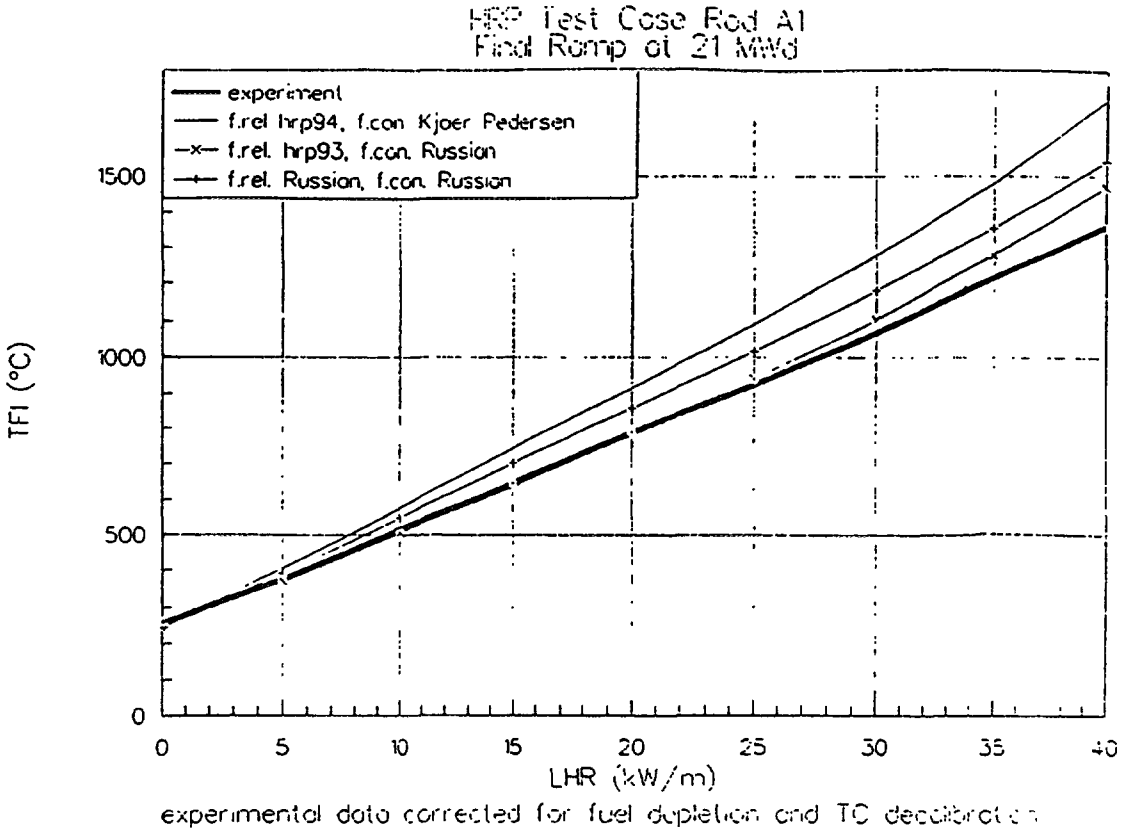

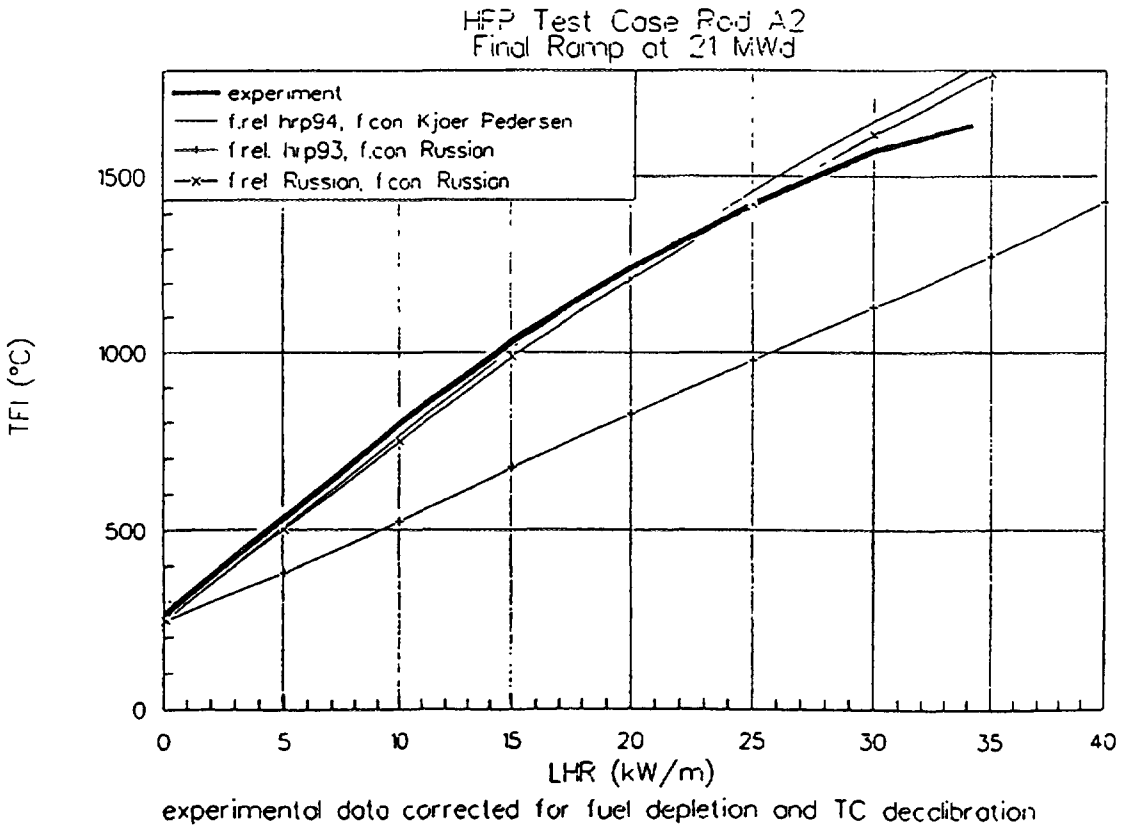

FIG. 5 ***HRP Test Case Rod A2 - Final ramp at 21 MWd***

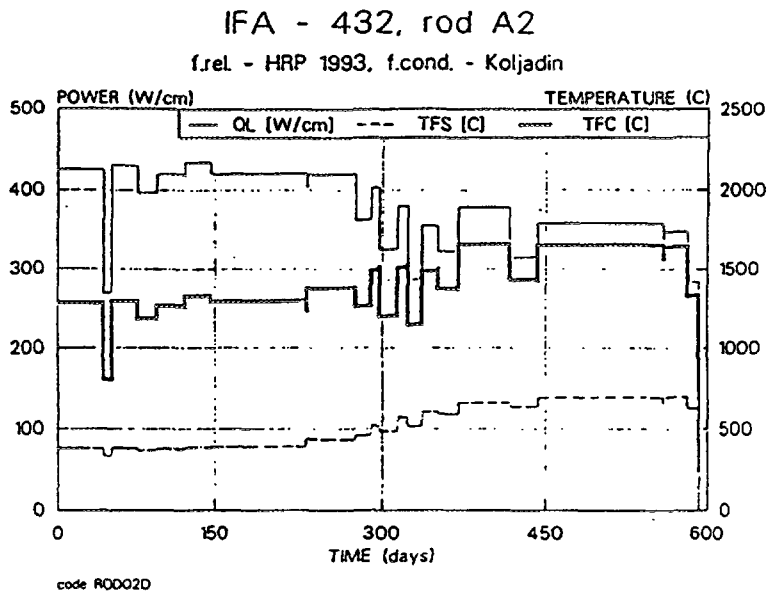

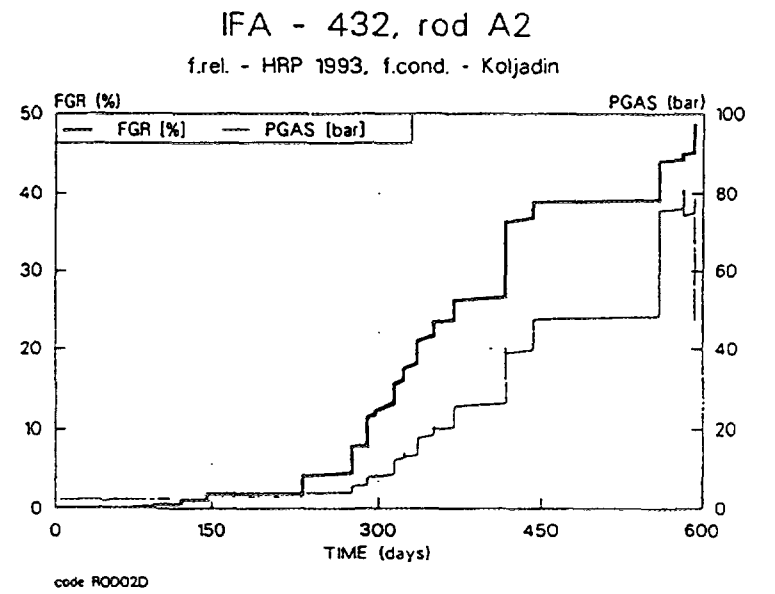

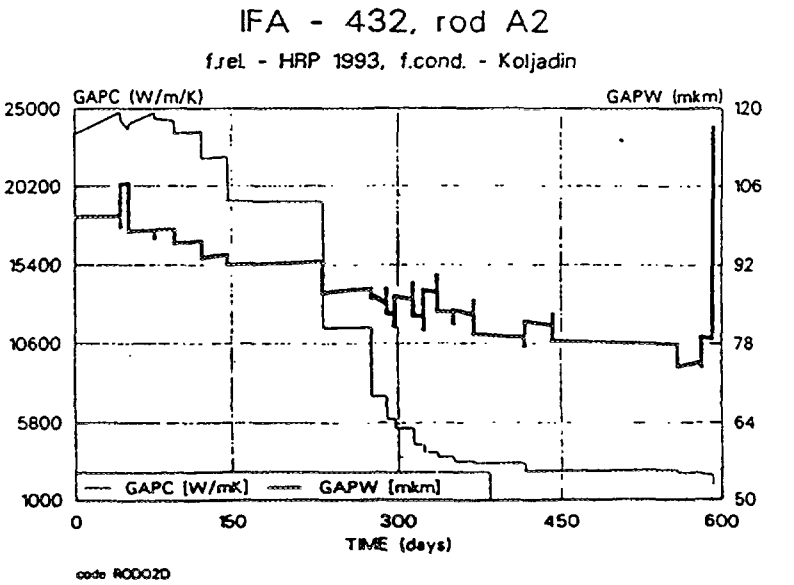

FIG. 6 *IFA-432 rod A2*

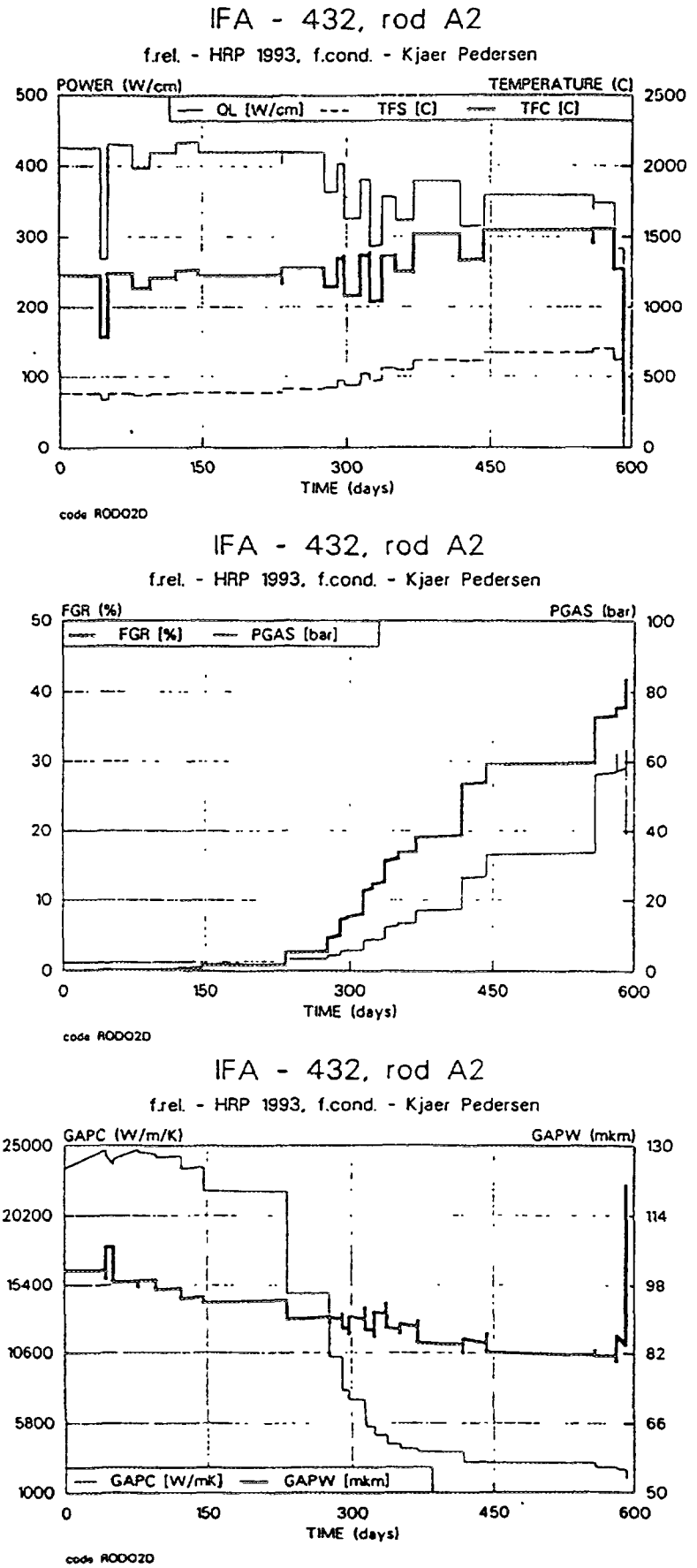

FIG. 7 *IFA-432 rod A2*

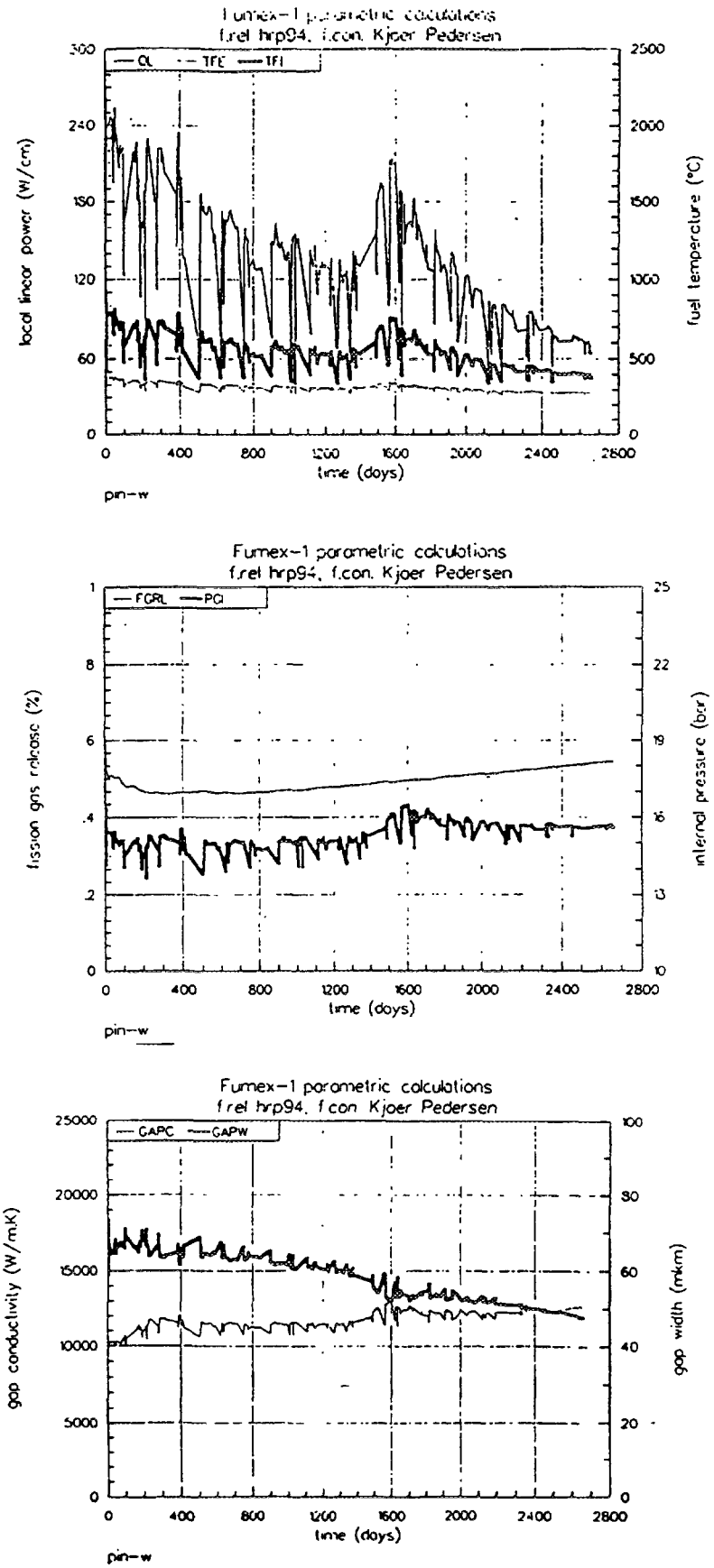

FIG. 8 *Fumex-1 Parametric calculations*

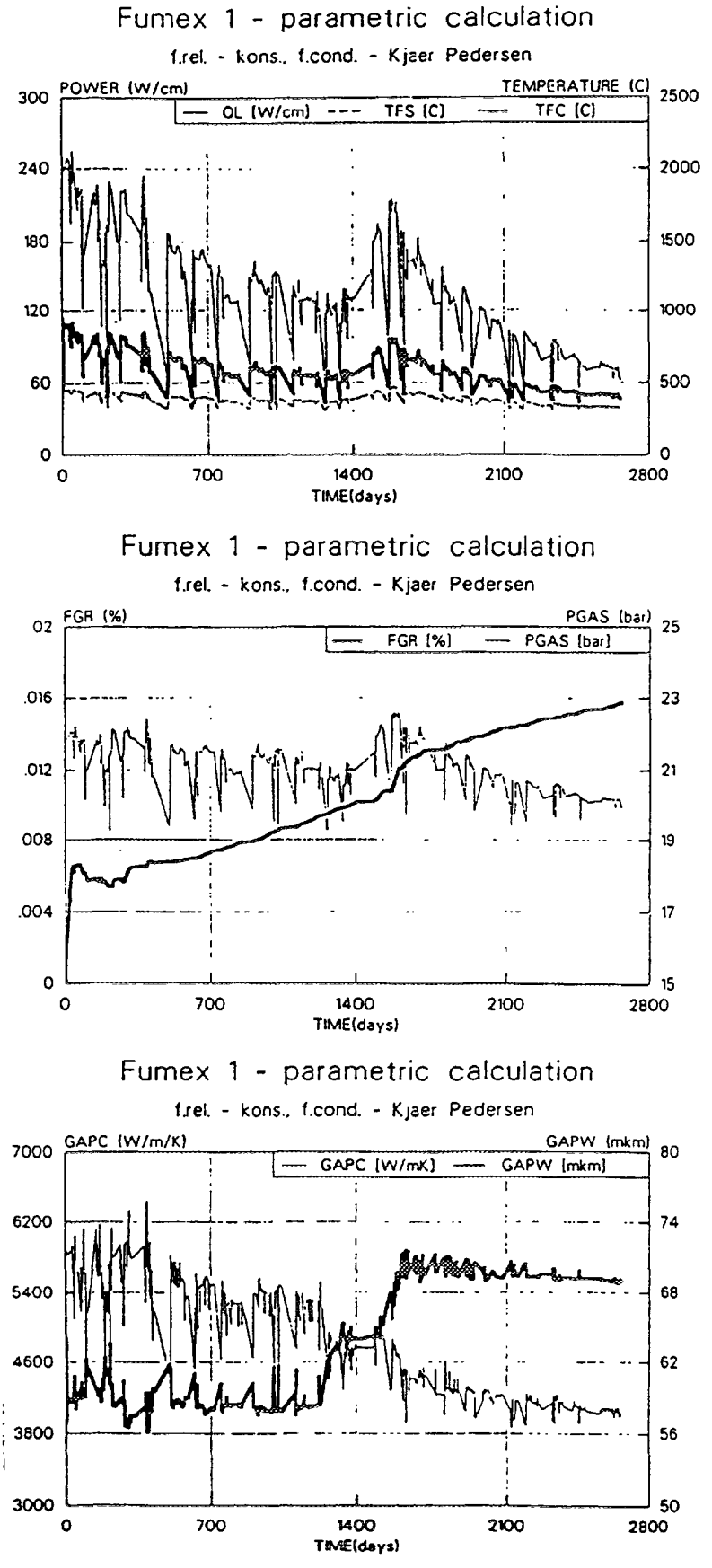

FIG. 9 *Fumex-1 Parametric calculations*

5. DISCUSSION

During the tuning of the relocation model on the IFA-432 rod A1 (small gap) and A2 (large gap) better confidence level for A2 case was obtained (Fig.5). Differences between PIN-W and RODQ2D in centerline temperature are probably caused by the extensive fission gas release in RODQ2D. Fig. 6 and 7 document small influence of the conductivity degradation during this low burnup and high power experiment.

The FUMEX-1 has relatively low measured temperatures. There are no significant differences between codes predictions, except much smaller fission gas release in the RODQ2D (Fig.8 and 9). The FGR predicted in this case by both codes were strongly underpredicted against the experimental value. This is probably caused by the inadequacy of the low-temperature FGR model or by the specific HBWR irradiation history.

6. CONCLUSION

The results of performed parametric calculations indicate, that the innovation of the fuel conductivity and fuel relocation models is not sufficient to reach satisfactory predictions of the codes. Nevertheless the centerline temperatures in best-estimate variants agrees with experimental results, the fission gases release is underpredicted. Correct prediction of the high burnup experiments by the codes PIN-W and RODQ2D (e.g. FUMEX 1) needs more realistic modelling of the fission gas release in the low temperature region, taking into the account other coupled effects (swelling, rim effect, fuel cracking, etc).

REFERENCES

[1] Reactor Fuel Performance Modelling Workshop, Vaaksy, Finland 14-19 June, 1982. OECD-HRP, January 1983, HWR 81.

[2] KJAER-PEDERSEN, N: Rim Effect Observations from the Third Ris Fission Gas Project. Fission Gas Release and Fuel Rod Chemistry Related to Extended Burnup. IAEA, April 1993, IAEA-TECDOC-697.

[3] KOSAKA, Y.: Thermal Conductivity Degradation Analysis of the Ultra High Burnup Experiment (IFA-562). OECD-HRP, February 1993, HWR-341.

[4] VALACH,M., SVOBODA, R., ZYMÁK, J.: Presentation of work performed in the frame of research agreement No.7344/CF between IAEA and NRI Řež plc. as a part of IAEA FUMEX coordinated programme. ÚJV-9990 T, 1st RCM on FUMEX, Halden, Norway, 28th June to 1st July 1993.

[5] VALACH,M., SVOBODA, R., ZYMÁK, J.: The first year's experience of the NRI cooperation with the OECD-HRP in the High Burn-up Fuel Performance, ÚJV-9884 T,M, March 1993.

[6] PAZDERA,F.,STRIJOV, P.,VALACH, M., et al.: User's Guide for the Computer Code PIN-micro, ÚJV 9517-T, Řež, November 1991.

ARGENTINE NUCLEAR FUELS MOX IRRADIATED IN THE PETTEN REACTOR: ANALYSIS OF EXPERIENCE WITH THE BACO CODE

A.C. MARINO, E. PEREZ, P. ADELFANG
Argentine Atomic Energy Commission,
Buenos Aires, Argentina

Abstract

The irradiation of our first prototypes of MOX nuclear fuels fabricated in Argentina began in 1986 [1]. These experiences had been made in the HFR-Petten reactor, Holland. The six rods were fabricated in the α Facility (GAID-CNEA-Argentina) [2]. The first rod has been used for destructive pre-irradiation analysis in the KFK (Kernforschungszentrum Karlsruhe), Germany. The second one was a pathfinder for calibrating systems in the HFR [3]. Another two rods included doped pellets based on iodine. One of them included CsI and auxiliary components. The second one included elemental iodine. The concentration of iodine was intended to simulate 15 MWd/ton(M)of burnup [4]. We defined the power histories with the BACO code. We assumed a cycle of 15 days that included interaction treatments of cladding and pellet due to the power cycling. The last ramp is let run until stress corrosion cracking (SCC) is induced. The experience named BU15 was done with the last two rods. The final burnup was 15 MWd/ton(M), and a final ramp test was arranged for one of them. This burnup is the same as the previous two rods. The power level during irradiation was low and without major solicitations, only the normal shutdowns of the HFR. The ramp was similar to that used for the iodine test [5]. We attempt to see the correct correspondence between the BU15 and the doping test. The pathfinder had an excellent behaviour in the HFR reactor. The presence of microcracks inside the cladding was observed in the iodine test as we predicted with the BACO code. The post-irradiation tests of the BU15 experience has just ended. The development of the ramp was interrupted due to an increase of activity in the system. We presumed the presence of a failure in the rod. The visual inspection of the rod shows an atypical failure for this kind of fuel, i.e. they found a small circular hole. We use the BACO code for the behaviour analysis of the fuel rods. We take special care in the stress analysis of the rod and the inventory of the fission gases. The maximum power levels reached in the defective zone of the MOX rod were found similar to the threshold value to induce stress corrosion cracking (SCC) or pellet-cladding interaction (PCI) failures. Additional post-irradiation analyses show that the hole in the BU15 rod was an SCC failure. That is in good agreement with BACO [6]. In this paper, we give a description of the different MOX fuel rod tests and we repeat the previous design work made with the BACO code, but now using the real power histories. We present the final results of the comparison between experience and code behaviour.

1. INTRODUCTION

1.1. BACO CODE

The BACO code (BArra COmbustible) simulates the fuel rod behaviour under operation conditions in a nuclear reactor. BACO code includes the following calculus and models: strain-stress state of the cladding and pellet system and cladding and pellet thermal-elastic-plastic analysis, pellet cracking, fission gases inventory, grain growth, porosity histogram evolution, creep, swelling, cladding anisotropy, etc. [7, 8, 9].

The BACO code development began in 1974 in CNEA. A new version of the code is due to the hardware and software new tools along with new behaviour models, a new set of experience, and new requirement of design.

The IAEA CRP FUMEX[1] about fuel modelling at extended burnup, required preliminary work with the BACO code in order to verify, to correct and to change models, calculus structuring and convergence analysis. From that work we obtained the BACO version 2.20. The job schedule is a

[1] Co-ordinated Research Programme (CRP) on Fuel Modelling at Extended Burnup (FUMEX)

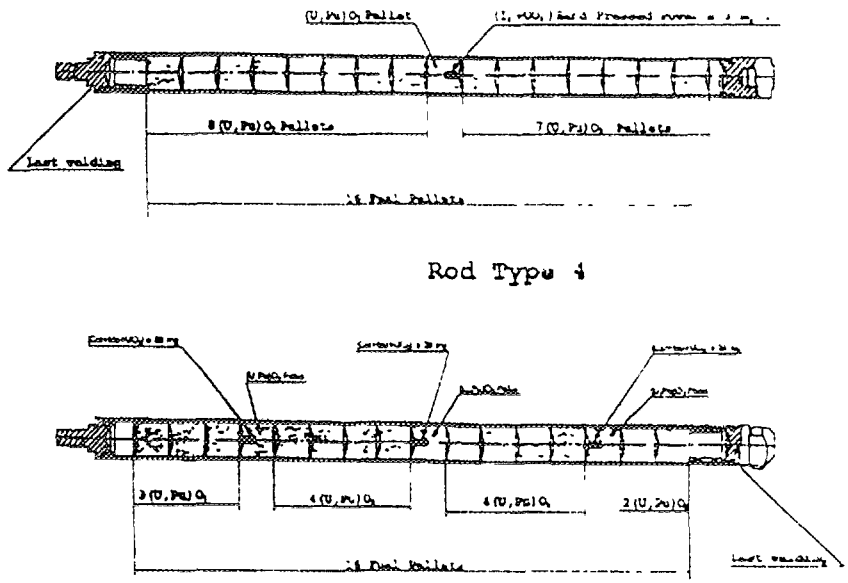

FIG. 1. MOX fuel pins type A.3 and A.4

MOX fuels irradiated at Petten reactor
Table 1 : Fuel rods characteristics (U/Pu mixed oxide).

Table 1.a : Fuel rods type A.1, A.3 y A.4.

Rod	A.1	A.3	A.4
Length [cm]	24.1	17.9	17.95
Pellets number	21	16	16
Compensating pellets number	1	-	-
Doped pellets number	-	1	3
Dope material	-	I	ICs Mo
Dope material [mg]	-	3.	6.604 ± 017 1.373 ± 0.036
Simulated burnup [MWd/ton(M)]	-	13761 ± 4933	14800 ± 390
Filling gasses	He	He	He
Filling pressure [atmosphere]	1.15	1.15	1.15
Cladding	Zry-4	Zry-4	Zry-4

Table 1.b : Pellets

Density	10.52 ± 0.04 gr/cm^3
Pellet height	11.2 ± 0.1 mm
Pellet diameter	10.40 ± 0.01
$Pu_{as}/U+Pu_{mz}$	0.53 %
Enrichment (U^{235}+Pu)	1.25 %
O/M relation	2.00
Dishing volume	25. ± 5. mm^3

feedback work. That is to say, we use the code to define the experience of irradiation and, in the next stage, we use these outputs in order to upgrade the code. Due that, we prefer to present this paper in a chronological way. We illustrate the steps that have improved the BACO code with each irradiation.

The emphasis in this paper is put in *Plots, Figures* and *Tables.*

1.2. FUEL RODS DESCRIPTION

The original design of the rods was made for utilization of the MZFR reactor (Karlsruhe, Germany). The decommissioning of that reactor compelled us to find another place to make the irradiation tests.

We realised the experiences in the HFR-Petten reactor. We modified the rods in two ways. First, some rod dimensional changes. These were the fuel length and the plug design compatible with the HFR assemblies. Second, a new definition of the original experience. We intended to emulate extended burnup with Iodine doped pellets.

Figure 1 shows the rods and indicates the position of the doped pellets. Table I presents the characteristics of doped rods.

2. PATHFINDER IRRADIATION

2.1. IRRADIATION TEST AND CALCULUS DESCRIPTION

The first irradiation was with the A.1.4 rod. We intended to calibrate the HFR reactor instruments. That experience verified the response of the HFR reactor detection systems with our MOX rod.

The duration of the irradiation was about 100 hours. It included a final ramp test. The maximum power level reached was similar to the next rods.

The A.1.4. rod behaviour was excellent. There were no fabrication failures and it was not necessary to do extra calibration in the reactor instrumentation.

We used the BACO code considering only one axial section and we included two cases [10]:

1) All the rods at the average linear power,
2) All the rods at the maximum linear power.

We assumed that the output with the maximum linear power informs us the behaviour of A.1.4 fuel rod at greatest demand. Using the average linear power history we obtained the standard values for this first irradiation.

2.2. RESULTS

Table II shows some input-output parameters. Table IIa gives the maximum values for the average and maximum power histories used and obtained during irradiation. Table IIb includes some final output parameters.

The plot presents the average power history (Fig. 2). It includes a steady state condition with a brief cycling and a final power ramp.

The central and surface pellet temperatures were acceptable.

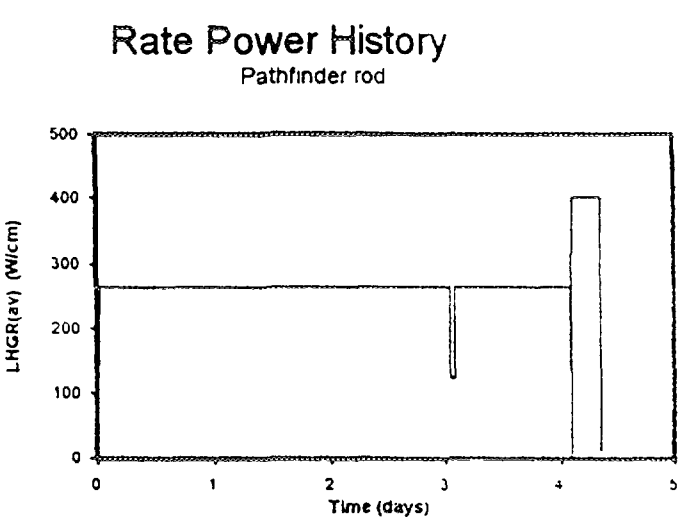

FIG. 2. Power history for the A.1.4 pin

MOX fuels irradiated at Petten reactor. Pathfinder rod.
Table 2 : BACO output using average and maximum[1] power histories.

Table 2.a : Maximum values reached during irradiation.

	Ql(average)	Ql(max)	Units
Linear power	403.	439.	W/cm
Pellet central temperature	1330.	1458.	°C
Pellet surface temperature	403.	409.	°C
Hoop stress	178.	190.	MPa
Contact pressure	36.	39.	MPa
Pellet centre von Misses' equivalent stress	150.	150.	cm
Surface crack scope	0.245	0.245	cm
Cladding radial strain	0.201	0.273	%
Cladding axial strain	0.137	0.134	%

Table 2.b : Reached values at final irradiation and zero power.
Time = 4.35 days.

	Ql(average)	Ql(max)	Units
Pellet radius	0.5202	0.5202	cm
Cladding inner radius	0.5213	0.5216	cm
Cladding outer radius	0.5837	0.5840	cm
Stack length	24.048	24.047	cm
Associated cladding length	24.020	24.018	cm
Radial cladding strain	-0.133	-0.094	%
Axial cladding strain	0.085	0.076	%

[1] $Ql_{(average)}$. Averaged linear power.
$Ql_{(max)}$ Maxim linear power. Peak factor = 1.14

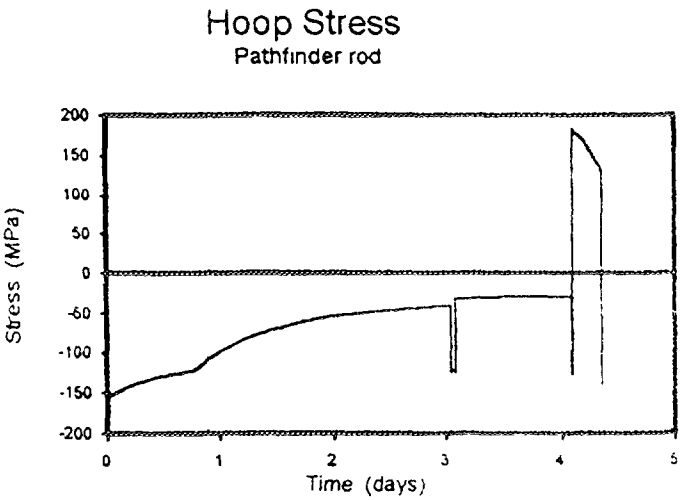

FIG. 3. Hoop stress for the pathfinder pin

The small diametrical gap used induced a pellet-cladding contact conditions in the first stage of the irradiation. The radial stresses between pellet and cladding was strong (see Table II).

There was no stress reversal during the cycling before the final ramp (Figure 3). The tangential stress in the inner surface of the cladding *(hoop stress)* reached the values corresponding with stress corrosion cracking (SCC) threshold limit for the Atucha-I fuels The burnup (and the fission gases inventory) is low in order to induce these kinds of failures at beginning of life (BOL).

Also, we analysed an additional power history including the cycle but without the shutdown previous to the final ramp (see Fig. 2). The output reached the same values as the previous observances. That means the influence of shutdowns in these kinds of analyses is irrelevant.

2.3. CONCLUSIONS

According with the disponible experimental information there was a good agreement with the code.

From here, we recommend a post-irradiation examination, in the cladding inner surface. We intend to find the presence of microcracks into the cladding. In order to compare with the next irradiation.

3. DOPED MOX FUEL RODS A.3 (WITH IODINE) AND A.4 (WITH CSI)

3.1. INTRODUCTION

The experiment started with the irradiation of two fuel rods similar to pathfinder, both containing Iodine compounds as dope to simulate the effect of extending burnup [1].

Fuel rods A.3 and A.4 have been employed for this second experiment. This irradiation, carried out during 15 days consisted of a power cycling between 120 and 290W/cm and a final ramp to reach 400 W/cm [11]. This final power level lead to a "hoop stress" of about 170 MPa which is likely to induce microcracks in the inner surface of the cladding, representing an incipient defect produced by stress corrosion cracking, without reaching the failure threshold of the tubing.

BACO code was employed to design the power history. The experimental power history was in good accordance with the proposed power history. Rod A.3 and A.4 behaved as expected:

- there were no failures in the cladding,
- no fabrication defects have been detected, and
- microcracks in the inner surface of the cladding were detected during PIE.

3.2. EXPERIMENT DESCRIPTION

During the fission of UO_2 or PuQ some of the fission products produced are volatile and corrosive. Once they come out of the fuel pellet they can react with the cladding during irradiation. Besides the chemical interactions there are possible mechanical interactions between pellet and cladding. As long as the burnup increases the gap between pellet and cladding becomes smaller and can reach the contact, these mechanical interactions are more important during power ramps because the fuel pellet expands faster than the cladding as long as temperature increases.

For safety reasons it is worth knowing how the Zry-4 cladding of the fuel rods behaves towards this combination of mechanical and chemical interactions during power ramps.

Both inpile and out of pile experiments indicate that a failure in Zry-4 tubing due to SCC may only occur when:

1. A certain stress threshold is reached in the tube, and
2. After reaching a certain burnup. Besides stresses it is necessary a critical concentration of fission products in the pellet-cladding gap.

In order to reduce the irradiation time needed to generate fission products, the fuel oxide can be doped with simulated fission products, employing only those considered mainly responsible for the chemical interactions with the cladding.

The fission product considered responsible for the failures in Zry4 tubing during power ramps is iodine, which has to be introduced in the fuel rod in an adequate chemical state.

Thermodynamics considerations and results of PIE, indicate that Iodine should be combined with Cs, which is present in excess in the fuel rods as CsI, which has no influence on the mechanical properties of Zry4 as it indicated by experimental results.

However, in the presence of oxygen, CsI can dissociate in Cs oxide and gaseous iodine, depending on the oxygen potential and the possible formation of ternary Cs oxides [12].

CsI can also dissociate by radiolysis [13]. Production of Cs uranate and Cs molybdate also lead to a great iodine potential.

Due to these mechanisms, after a certain burnup, a chemical condition can be reached in the fuel rods of a LWR or a HWR that can lead to partial pressures of iodine capable of inducing failures due to SCC in Zry-4 tubing. To simulate these conditions, besides CsI, elemental Mo should be added.

The iodine inventory, corresponding to 20 % of an EOL burnup of 15000 MWd/ton(M), was calculated using Table II of Reference 14.

Rod A.4:

CsI and Mo were mixed with UO_2, the mixture was introduced in central holes drilled in three pellets and hand pressed. The whole amounts were:

m(CsI) = 6.604 ± 0.17 mg
m(Mo) = 1.373 ± 0.036 mg
Corresponding to a simulated burnup of:
Bu = 14800 ± 390 MWd/ton(M)

Rod A.3:

Pure iodine was introduced in one pellet with the aim of comparing its effect on the cladding with that of combined iodine (CsI).

The simulated burnup was:
Bu = 13761 ± 4933 MWd/ton(M)

3.4. RESULTS

The BACO input data correspond to direct measurements made during fabrication and quality control stage. Then we had some discrepancies with dates provided for design planes and references, of course ever with the tolerances[15].

MOX fuels irradiated at Petten reactor
Table 3 : **BACO outputs for the doped rods (A.3 and A.4) using average and maximum power histories[2].**

Table 3.a : **Maximum values reached during irradiation.**

	A.3		A.4	
	$Ql_{(aver.)}$	$Ql_{(max)}$	$Ql_{(aver.)}$	$Ql_{(max)}$
Potencia lineal [W/cm]	418.	446.	352.	423.
Temperatura central del pellet [°C]	1392.	1487.	1168.	1408.
Temperatura superficial del pellet [°C]	413.	417.	402.	414.
Hoop stress [MPa]	193.	196.	160.	192.
Presión de contacto [MPa]	39.	40.	34.	39.
Tensión equiv. de von Misses en Rp(0) [MPa]	150.	150.	150.	216.
Radio de Alcance de las fisuras (out) [cm]	0.243	0.243	0.277	0.243
Deformación radial de la vaina [%]	0.18	0.22	0.08	0.19
Deformación axial de la vaina [%]	0.11	0.11	0.13	0.11

Tabe 3.b : **Reached values at EOL, cero power and S.T.P.[3] conditions (days=15.27 days).**

	A3		A.4	
	$Ql_{(aver.)}$	$Ql_{(max)}$	$Ql_{(aver.)}$	$Ql_{(max)}$
Pellet radius [cm]	0.5201	0.5188	0.5186	0.5189
Cladding inner radius [cm]	0.5207	0.5208	0.5203	0.5208
Cladding outer radius [cm]	0.5830	0.5831	0.5825	0.5830
Gap [µm]	6.	20.	17.	19.
Pellets stack length [cm]	17.973	17.971	17.979	17.973
Asociated Cladding length [cm]	17.986	17.984	17.994	17.987
Cladding radial strain [%]	-.266	-.247	-.339	-.250
Cladding axial strain [%]	-.077	-.088	-.036	-.074

[2] $Ql_{(aver.)}$: Averaged linear power
$Ql_{(max)}$: Maxim linear power. Peak factor = 1.063 (B.C. A.3)
Peak factor = 1.202 (B.C. A.4)
[3] S.T.P. : Standard Temperature and Pressure
T = 300 K
P = 1 atmosphere

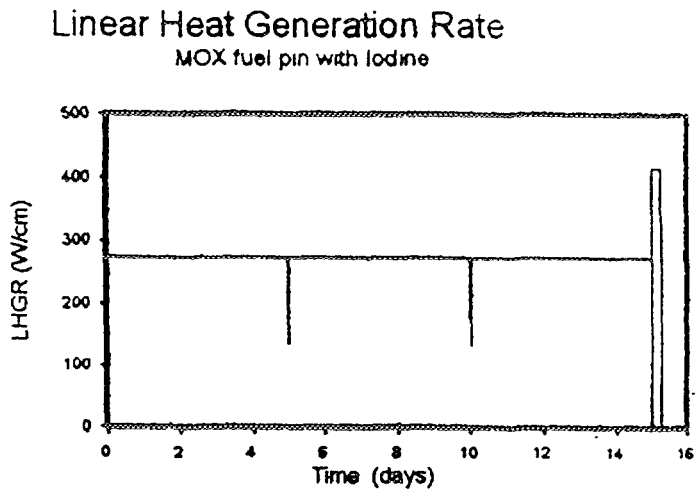

FIG. 4. *Average power history for the A.3 rod. Iodine as doped material.*

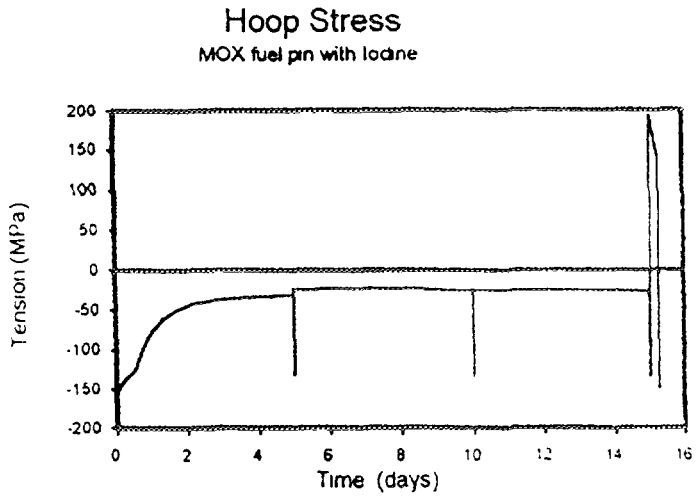

FIG. 5. *Hoop stress for the A.3 fuel MOX with Iodine*

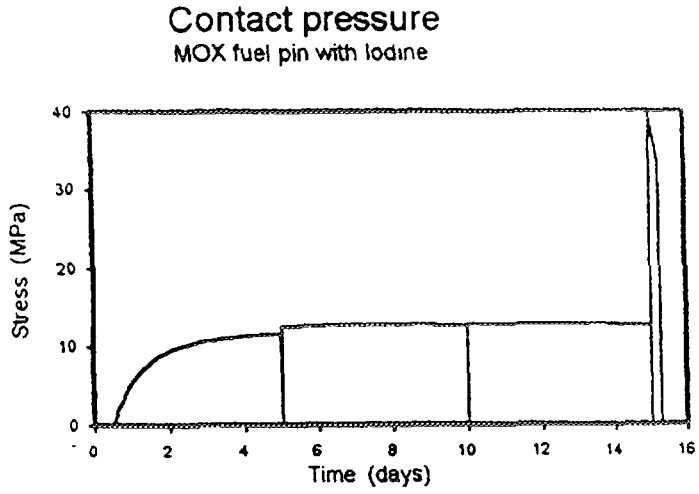

FIG. 6. *Radial stress between pellet and cladding A.3 pin*

We used the BACO code calculating with just one axial section [11] as follows:

1) All the rods at rate linear power,
2) All the rods at maximum linear power

We resumed the calculus with four BACO final outputs, two of each rod.

First, we defined a new scheme for the mesh point distribution in the code.

Table III shows some parameters of BACO output.

The plot in Figure 4 shows the averaged power history.

We have no post-irradiation information about the temperatures reached in the rods. The code shows that temperatures in gap and pellet were acceptable. The gap between pellet and cladding closed in the start-up and it was opened with each power-down cycle. BACO determined an open gap of 20 μm at EOL. (End Of Life) and STP conditions (Standard Temperature and Pressure). Post-irradiation determined an open gap of 20 μm for the A.3 rod, and 20-30μm for A.4 rod [15].

There was no stress reversal during the cycling in the steady state stage (Figure 5).

The stresses between pellet and cladding were strong (Fig. 6). The hoop stress reached the threshold for SCC [21]. The corrosive fission gases inventory simulated with Iodine is enough to induce SCC. The inner surface showed microcracks appeared during irradiation [15]. See pictures included in Figures 25 and 26.

We calculated a grain growth from 6.2 μm to 7.2 μm. There are good agreements between post-irradiation and BACO code output, specially about stress analysis and gap dimension.

4. BU15 EXPERIENCE: A1.2 AND A.1.3 MOX RODS BEHAVIOUR ANALYSIS

4.1. INTRODUCTION

The third irradiation experiment was carried out with fuel rods A.1.2 and A.1.3, both similar to the pathfinder. A burnup of approximately 15000 Wd/ton(M) was reached in both rodlets. This required 531.5 irradiation days. Rod A.1.3 was submitted to EOL power ramp.

Rods A.1.2 and A.1.3 behaved during the stationary phase as was expected:

- no rod failures were detected,
- no fabrication defects were evident.

During the EOL power ramp, rod A. 1.3 behaved as follows:

- a maximum power of 390 W/cm was reached,
- the power ramp had to be finished earlier than planned due to an increase in activity in the coolant circuit,
- visual inspection of the fuel rod revealed the existence of a small circular hole in the cladding
- this kind of failure is likely to be produced by SCC.

The aim of this step of the experiment was to study the stresses in the rod submitted to the power transient in order to determine the causes of the failure.

4.2. IRRADIATION POWER HISTORY

The power history for this irradiation test was proposed after the completion of calculus made with the BACO code. The target duration of the irradiation was an averaged burnup of 15000 MWd/ton(M), more or less the twice of final burnup for Atucha I. The scheduled preconditioned power level was 200 W/cm with a final ramp at high power level of 420 W/cm max. [16].

The real power history includes the normal cycle operation, it means, reactor shutdowns, variations from the planned average power in the fuel rods of approximately 100 W/cm and a final ramp test for one of the fuel rods (A.1 .3 fuel rod) interrupted at 52 minutes from the started time.

The total time for this test was of 1020.2 calendar days, corresponding to 26 irradiation periods (531.5 days) and 26 periods on which the fuel rods were not irradiated due to changes of irradiation capsules, reactor shutdowns or non availability of a suitable in core position.

After the pre-irradiation time the A.1.3 fuel rod was cooling for 49 days and 9 hours before starting the preconditioned irradiation period and the final ramp test.

The preconditioned test starting with an increased power rate of around 7.2 W/cm.min, during 42 minutes until reaching an average fuel rod power of 250/260 W/cm, where it remained in that condition for 39 minutes. After that the fuel rod power is reduced during 5 minutes at a power rate of 48 W/cm.min until reaching an average fuel rod power of 10 W/cm. After 10 minutes the ramp test started with an average ramp rate of 43 W/cm.min which, maintained for 8 minutes, gave a final average rod power of 350/360 W/cm. This power was held during 52 minutes.

At 28 minutes operation at the ramp power level an increase of the activity of the primary water was detected. This activity peak had a total duration of 6 minutes coming back to the previous level. As this event gave reason for assumption of a fuel rod failure the experiment was 24 minutes after the start of the activity release shutdown with a power rate of 175 W/cm.min lasting 2 minutes for that operation.

It is noteworthy that at beginning of life, the A. 1.2 and the A. 1.3 fuel rods reached maximum peak fuel rod power of 430 W/cm and 380 W/cm respectively. The average for the assembly was 330 W/cm. These maximum peak power levels, during that pre-irradiation period, were higher or equal to the maximum power reached during the final ramp test for the A.1.3 fuel rod.

For the calculus with BACO we consider four different cases:

- The individual power histories of A.1.2 and A.1.3 fuel rods.
  For these cases we used the maximum values of power reached during the irradiation (Figs. 7 and 8). With this assumption we supposed to have the worst irradiation condition for both fuel rods.

- We suppose that both fuels rods were assembled to form a single rod. It is considered the averaged behaviour of this assembly for the pre-irradiation periods and it is included the final power ramps. In this case we obtained the standard values for the third test of our MOX rods (See Fig. 9).

- For the fourth case, we analysed the real situation of the A.1.3 fuel rod. All the values considered corresponded to the physical location of the defect produced during the ramp. It means, the minimum values during the pre-irradiation phases and the peak values during the ramp test. That was due to the axial core position fixed for the fuel rod during the test. See Figures 10, 11 and 12, these plots show the defect location. Figure 13 includes the A.1.3 power history.

4.3. RESULTS

Table 4 shows some BACO output parameters, refer to it in each case.

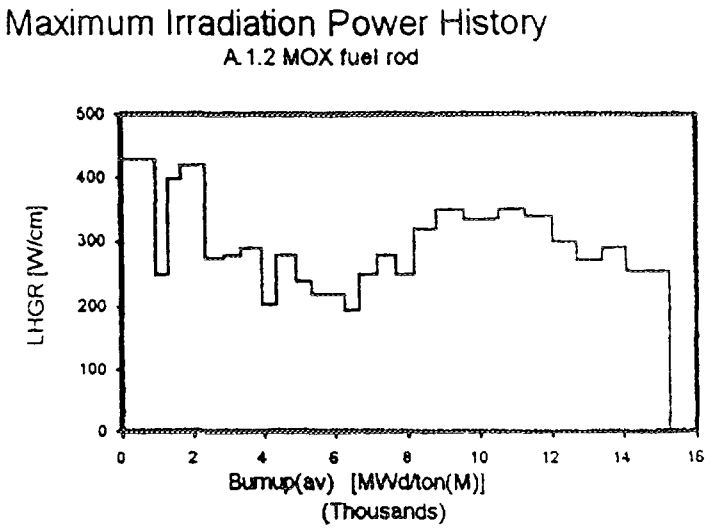

FIG. 7. *Maxmum power irradiation history for the A.1.2 rod*

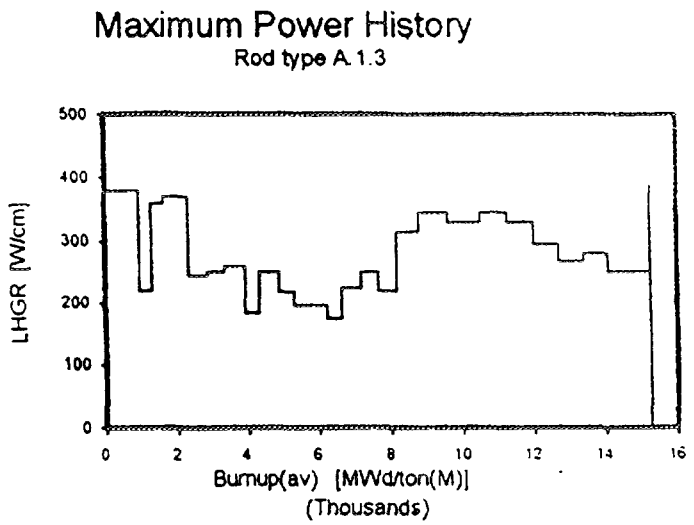

FIG. 8. *Maximum power irradiation history for the A.1.3 rod*

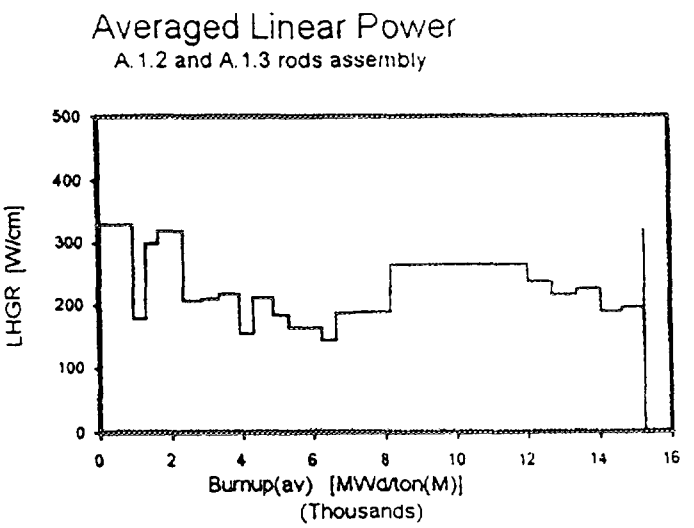

FIG. 9. *Averaged power irradiation history for the assembly*

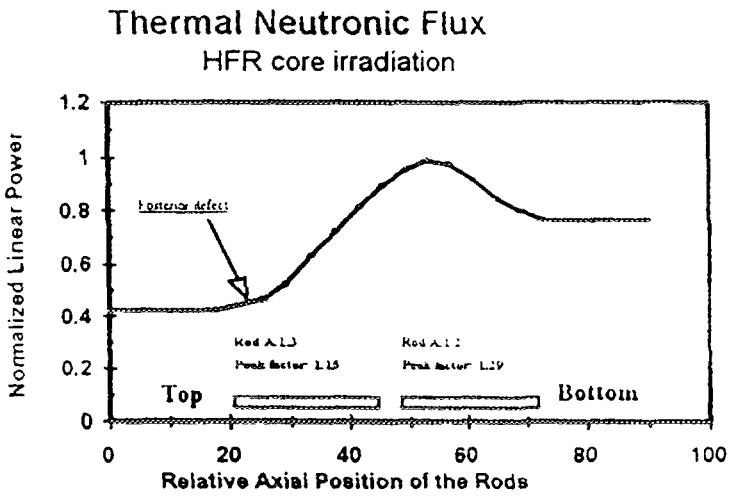

FIG. 10. *Thermal neutronic flux distribution for the assembly in the HFR core*

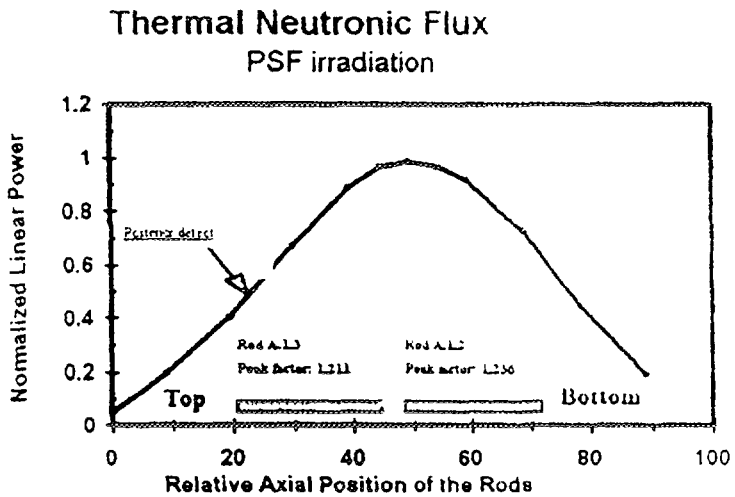

FIG. 11. *Thermal neutronic flux distribution for the assembly in the Poolside facility (PSF)*

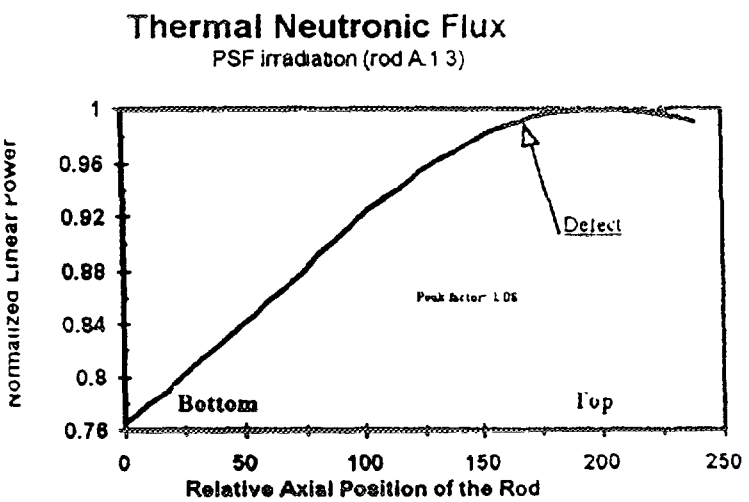

FIG. 12. *Thermal neutronic flux distribution for therod A.1.3 in the Poolside facility (PSF). Pre-irradiation and final power ramp stages.*

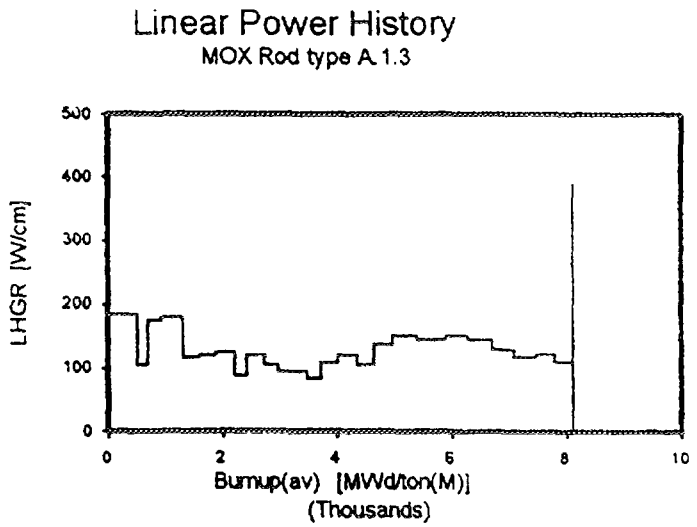

FIG. 13. Minimum power irradiation history and maximum power ramp for the A.1.3 rod.

MOX fuels irradiated at Petten reactor
Table 4 **: BACO outputs for the BU15 experience using average, maximum and minimum power histories[4] . (A.1.2 and A.1.3. rods).**

Table 4.a **: Maximum values reached during irradiation. BU15 experience.**

	Assembly	A1.2.	A1.3.	
	$Ql_{(aver.)}$	$Ql_{(max)}$	$Ql_{(max)}$	$Ql_{(min)}$
Linear power [W/cm]	360.	430.	389.	389.
Pellet centre temperature [°C]	1182.	1505.	1322.	1264.
Pellet surface temperature [°C]	419.	421.	432.	422.
Hoop stress [MPa]	134.	91.	135.	207.
Contact pressure [MPa]	32.	26.	32.	43.
von Misses' equivalent stress at pellet centre [MPa]	240.	248.	168.	222.
Surface crack scope [cm]	0.4848	0.4854	0.4854	0.4507
Cladding radial strain [%]	0.1113	0.3433	0.2254	0.0803
Cladding axial strain [%]	0.1105	0.1138	0.1107	0.1138

Table 4.b **: Reached values at EOL, cero power and STP conditions. BU15 experience.**

	Ensamble	A1.2.	A1.3	
	$Ql_{(aver.)}$	$Ql_{(max)}$	$Ql_{(max)}$	$Ql_{(min)}$
Pellet radius [cm]	0.5197	0.5180	0.5185	0.5180
Cladding inner radius [cm]	0.5193	0.5184	0.5196	0.5180
Cladding outer radius [cm]	0.5825	0.5814	0.5825	0.5913
Gap [μm]	10.8	4.4	10.9	0.00
Pellets stack length [cm]	23.852	23.861	23.850	23.969
Asociated cladding length [cm]	23.851	23.868	23.850	23.925
Cladding radial strain [%]	-0.3488	-0.528	-0.338	-.5522
Cladding axial strain [%]	-1.045	-0.972	-1.046	-.0733
Gas pressure [MPa]	0.183	0.150	0.232	0.374
Fission gases released fraction [%]	1.44	0.62	2.47	2.58
Released gases STP Volume [cm^3]	1.23	0.53	2.09	1.23
Gases STP volume at GB [cm^3]	30.90	32.18	31.44	12.21

[4] $Ql_{(aver.)}$: Averaged linear power
$Ql_{(max)}$: Maxim linear power
$Ql_{(min)}$: Minim linear power at the steady state ard Maximum power ramp increase.

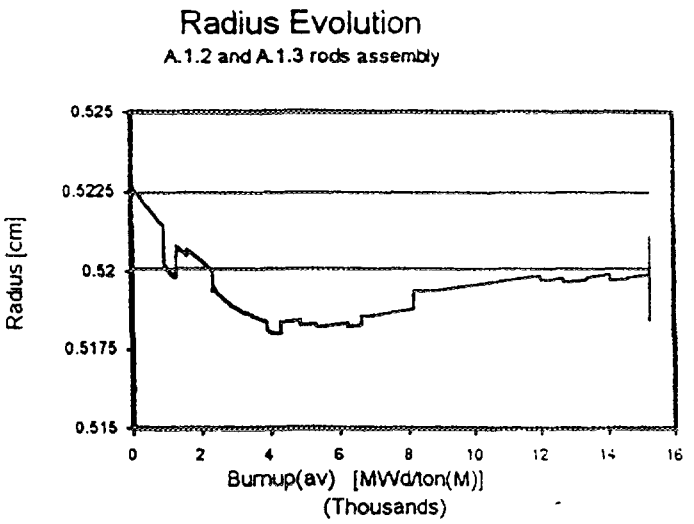

FIG. 14. *Radius evolution. Pellet and inner cladding initital radius as a reference point. Pellet and cladding are in contact.*

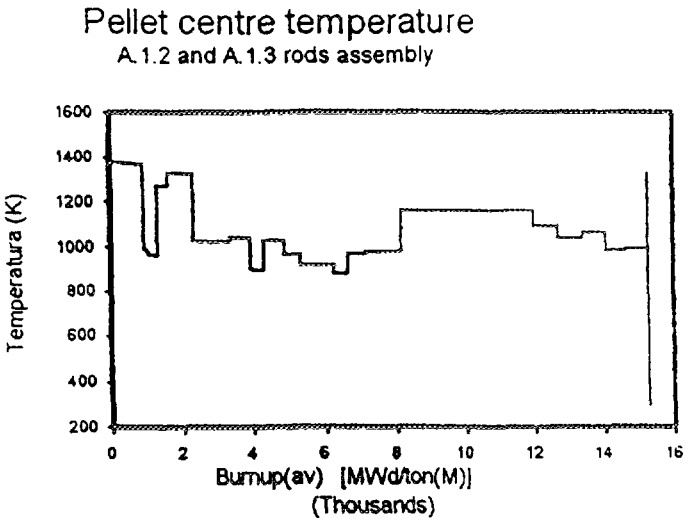

FIG. 15. *Pellet centre temperature for the assembly*

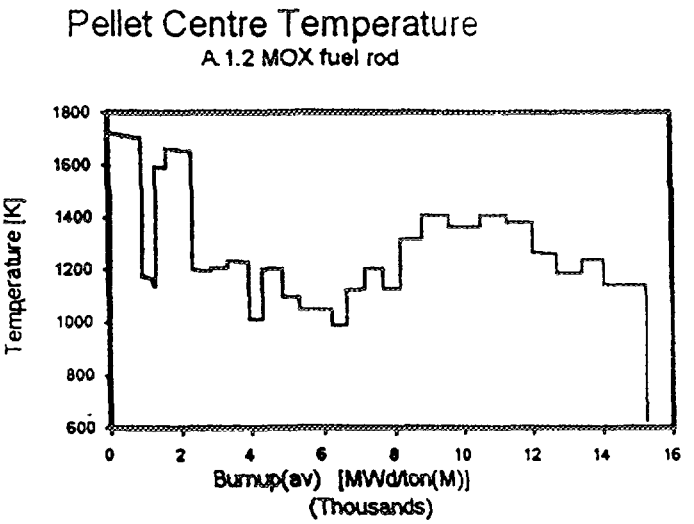

FIG. 16. *Pellet centre temperature for the rod A.1.2*

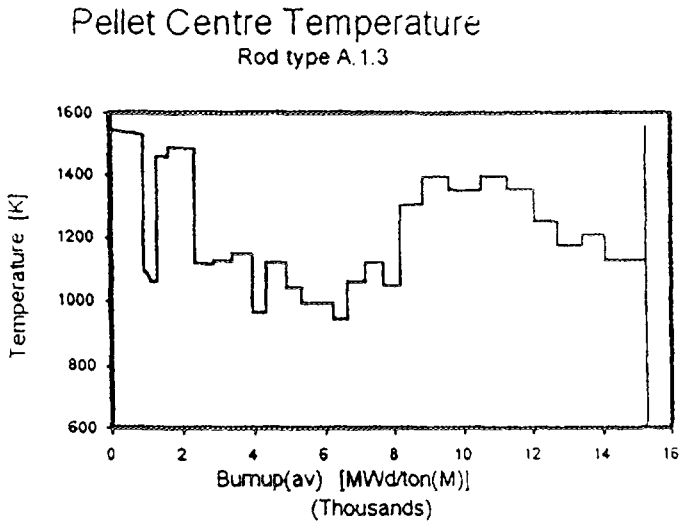

FIG. 17. Pellet centre temperature for the rod A.1.3

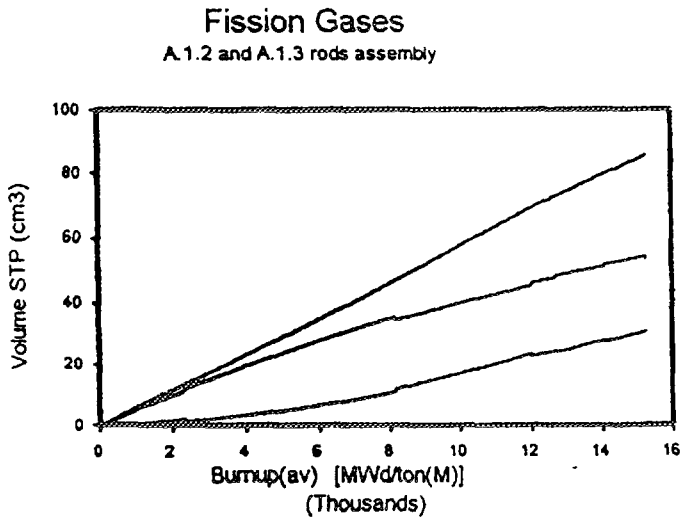

FIG. 18. Fission gas inventory evolution in the assembly

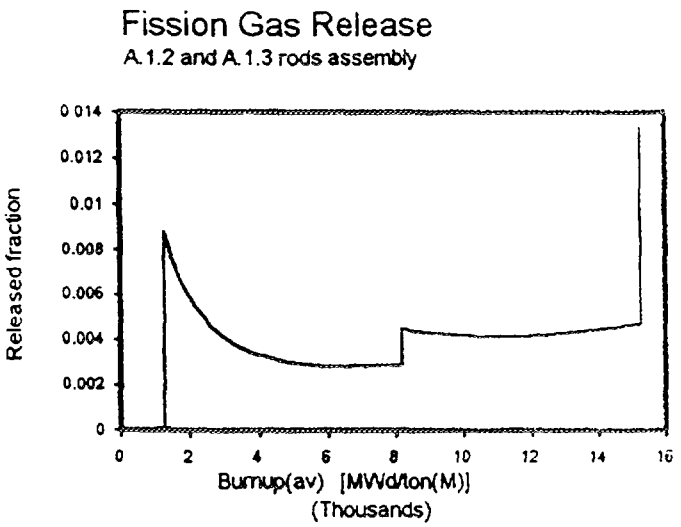

FIG. 19. Fission gas release fraction in the assembly

We had pellet and cladding contact in the first days of irradiation due to the small gap and high power condition. The gap was opened when shutdowns take place. It was easy to identify the densification and swelling behaviour (Figure 14).

Pellet centre and cladding inner surface temperatures were acceptable. As an example of the difference between the studied cases (see Figure 15) with centre temperature for the assembly, Fig. 16 for the A.1.2 rod and Fig. 17 for the A.1.3 rod. The temperatures are in Kelvin. We have not post-irradiation temperature analysis.

Figure 18 shows the fission gas inventory evolution. That was equivalent for all the cases. We discriminate:

- produced fission gases (upper curve),
- released fission gases (lower curve, just above the x axis),
- fission gases trapped in the UO_2 matrix, inside the grain (medium upper curve), and
- fission gases kept in grain boundary (medium lower curve)

There was a tendency to saturate the grain boundary.

Figure 19 completes the above information with the released gases fraction. The fraction released for the A.1.3 rod was 2.5%. The fraction for the A.1.2 rod was 0.6%. The difference is due to the A.1.3 last ramp. We can see that the ramp is more important than the steady temperature for fission gas release.

There was stress reversal with the assembly and the individual rods due to the shutdowns (Figures 20 and 21). The hoop stress maximum was 135 MPa in the A.1.3. rod. That is lower than SCC threshold [21]. The hoop stress of the A.1.3 rod with the real power history was equal to 207 MPa. That corresponded to the defective zone and we can assume a direct relationship. The defective zone supported the strongest mechanical solicitations and the value reached for the hoop stress is practically the SCC threshold. The bigger power increment was the last ramp:

$$Ql(end) - Ql(initial) = 290.W/cm$$

The radial contact stress between pellet and cladding was very strong too.

The final pressure in the rod due to free gases was about 0.2 MPa.

We calculated a growth in the grain size in the central zone of the pellet from R_g (initial) = 6.2μm to R_g(end)= 16μm.

The original MOX pins were not pressurised. The claddings were from MZFR reactor, that is a little thicker than Atucha-I claddings. BACO solves correctly Atucha I and Candu fuels. That means that the MOX rods are an intermediate case from the previous ones due to pressure filling gases, cladding thickness and structure. From here we have a set of combined exigencies and that is a good improvement in the BACO code.

The above set of calculus is to analyse the correspondences with some approximations using simplified power histories and to fit the code sensibility.

The post-irradiation and the next detailed study validate the above simplifications showed.

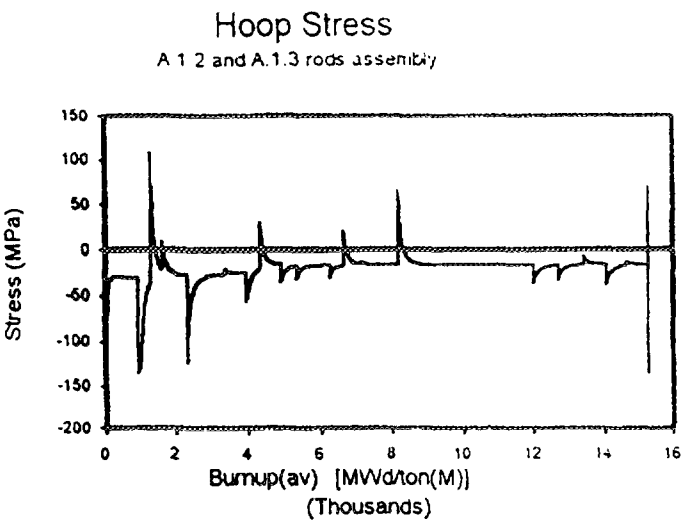

FIG. 20. Hoop stress for the assembly

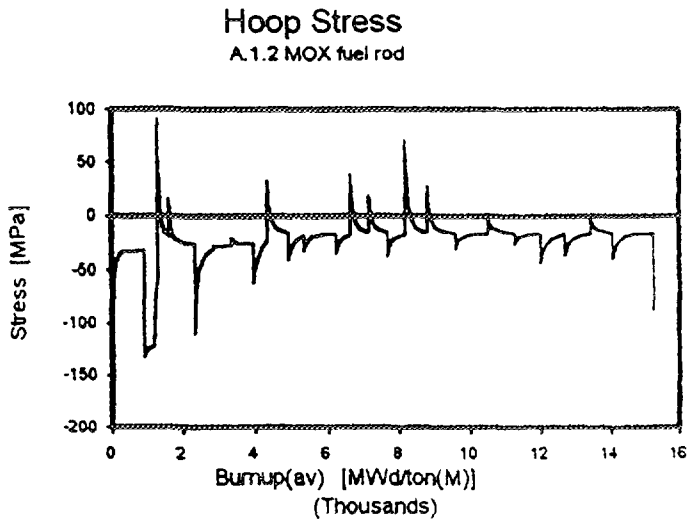

FIG. 21. Hoop stress for the rod A.1.2

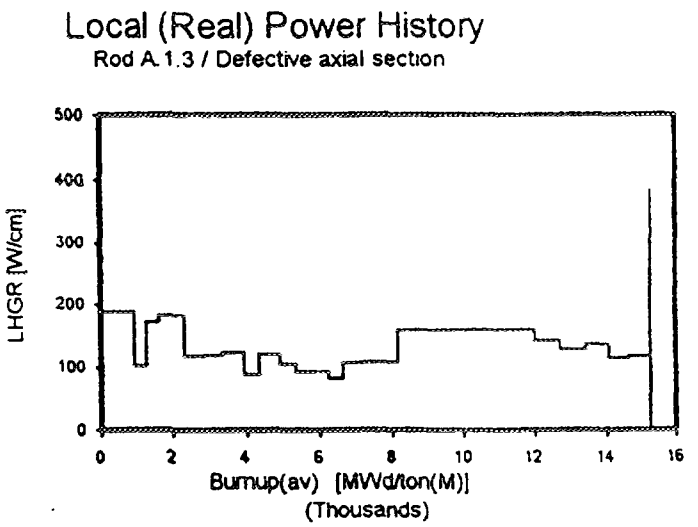

FIG. 22. BU15 experience. Real power history for the rod A.1.3 in the defective zone

MOX fuels irradiated at Petten reactor
Table 5 : **BACO outputs for the A.1.3. pin.**

Table 5.a : **Maximum values reached during irradiation for each axial section.**

	Axial section				
	1	2	3	4	5
Linear power [W/cm]	356.	337.	367.	383.	384.
Pellet centre temperature [°C]	1243.	1109.	1203.	1255.	1260.
Pellet surface temperature [°C]	409.	414.	420.	423.	423.
Hoop stress [MPa]	124.	164.	195.	202.	206.
Contact pressure [MPa]	30.	35.	41.	42.	42.
Tensión equivalente de von Misses' equivalent stress at pellet centre [MPa]	185.	151.	151.	191.	213.
Surface crack scope [cm]	0.208	0.242	0.243	0.277	0.278
Cladding radial strain [%]	0.170	0.086	0.084	0.082	0.081
Cladding axial strain [%]	0.110	0.114	0.112	0.114	0.114

Table 5.b : **Reached values for each axial section EOL, cero power and STP conditions**

	Axial section				
	1	2	3	4	5
Pellet radius [cm]	0.5203	0.5200	0.5195	0.5188	0.5182
Cladding inner radius [cm]	0.5203	0.5200	0.5195	0.5190	0.5185
Cladding outer radius [cm]	0.5835	0.5832	0.5827	0.5822	0.5818
Gap [μm]	0.0	0.0	0.0	1.5	3.5
Active stack length [cm]	4.779	4.780	4.783	4.789	4.792
Cladding length [cm]	4.769	4.771	4.775	4.780	4.783
Cladding radial strain [%]	-0.168	-0.227	-0.304	-0.397	-0.467
Axial cladding strain [%]	-1.076	-1.030	-0.938	-0.841	-0.780
STP Produced gases volume [cm^3]	22.62	19.89	17.11	14.20	11.90
STP Released gases volume [cm^3]	0.25	0.28	0.28	0.25	0.22
STP Trapped gases volume [cm^3]	12.25	11.62	10.78	9.69	8.18
STP Fission gases volume at grain boundary [cm^3]	10.12	7.99	6.05	4.26	3.49

Table 5.c : **Reached values for the rod at EOL, cero power and STP conditions.**

		Units
Active stack length	23.923	cm
Cladding length	23.877	cm
Axial cladding strain	-0.925	%
Gases pressure	0.405	MPa
Fraction gas release	1.5	%
Produced gases volume (STP)	85.716	cm^3
Released gases volume (STP)	1.287	cm^3
Trapped gases volume (STP)	52.520	cm^3
Fission gases volume at grain boundary (STP)	31.909	cm^3
% He	60.	%
% Xe	34.	%
% Kr	6.	%

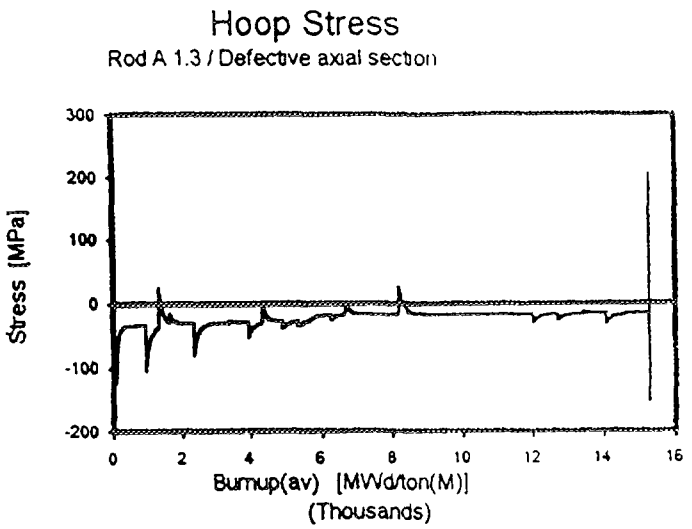

FIG. 23. Hoop stress for the rod A.1.3 in the defective zone

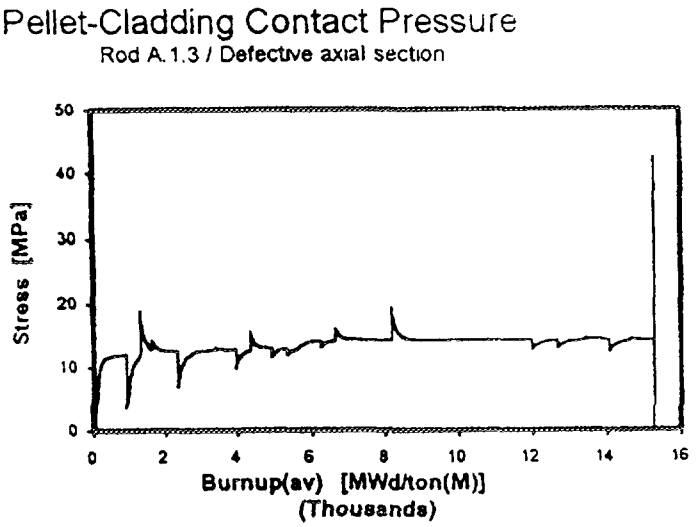

FIG. 24. Radial pellet-cladding contact pressure. Defective zone in the rod A.1.3

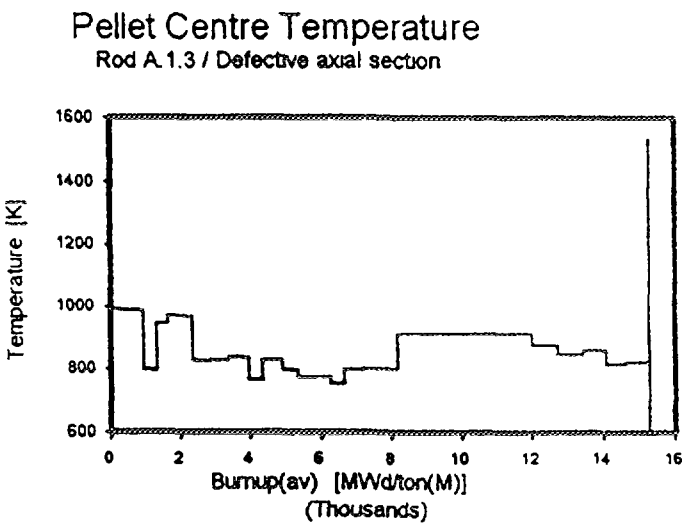

FIG. 25. Pellet centre temperature. Defective zone in the rod A.1.3

5. BU15 EXPERIENCE: A. 1.3 MOX RODS BEHAVIOUR ANALYSIS

5.1. POWER HISTORY

The proposed irradiation would induce a failure similar to the Iodine Doped Test. The real irradiation produced a defect in the A. 1.3 cladding (Fig. 22). We made an additional calculus with BACO code using a complete set of A.1.3 rod data. It means a detailed analysis of the defective rod. The post-irradiation showed that the hole found was due to SCC failure [17] See Figures 28 and 29.

The power axial profile was obtained from Figure 2 in Ref.18 (pre-irradiation stage), the figure 2 from Ref 19 (pre-irradiation ramp stage) and from Figure 2 Ref. 20 (power ramp). We "cut" the MOX pin in 5 axial sections. There was correspondence between the axial section choice and the defective zone. We saw maximum peak level in the failured section power.

5.3. RESULTS

Table 5 shows the parameters calculated with BACO code. We repeat the general observations made with the averaged power histories (See the corresponding tables). Due to the lower power, the final burnup for the A.1.3 pin was lower than the assembly, and of course the local burnup in the defective zone was the lowest.

We observed some direct correlation between one averaged power calculus and some axial section. We determined that the maximum hoop stress was a success in the axial section corresponding with the failure (Fig. 23 and 24). We show in Figure 25 the relative low temperature during pre-irradiation period and the increase in temperature in the final ramp.

There are good agreements between experience and BACO code predictions with this complete calculus, especially with the relationship between the hole failure and the mechanical solicitations predicted.

6. POST-IRRADIATION ANALYSIS

The irradiation-induced effects were studied in detailed post-irradiation examination which was performed at the HFR site in Petten and later at the hot cells of the Karlsruhe Nuclear Research Center [15, 22 and 23].

We do not give too much detail about this aspect of the experiment because the aim of the report is about BACO code comparison. We indicate only the main post-irradiation analysis made with the pins as follows:

- Visual inspection (Fig. 28 shows the hole in the A 1.3 rod)
- Eddy current check
- Neutron radiography
- Gamma scanning
- Betatron-radiography
- Dimensional control
- Sectioning diagram
- Ceramography (Fig. 27 shows the rod A.4)
- Scanning Electron Microscopy (Fig. 26 y 29 show the microcracks inside the A.3 cladding and the microcracks inside the rod.

The post-irradiation checks followed the BACO calculus for all the experiences.

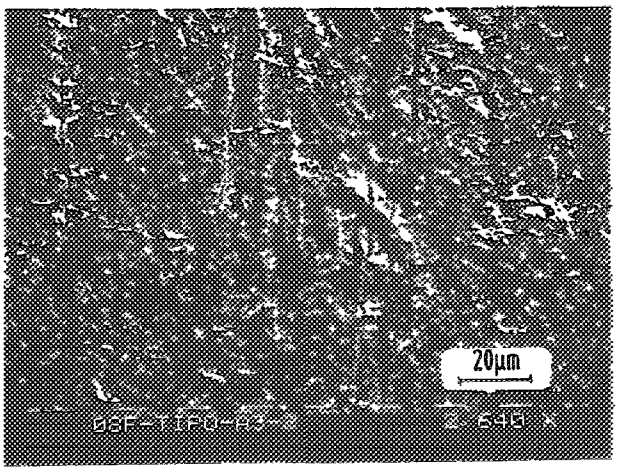

FIG. 26. *Rod type A-3 showing the microcracks inside the tubing*

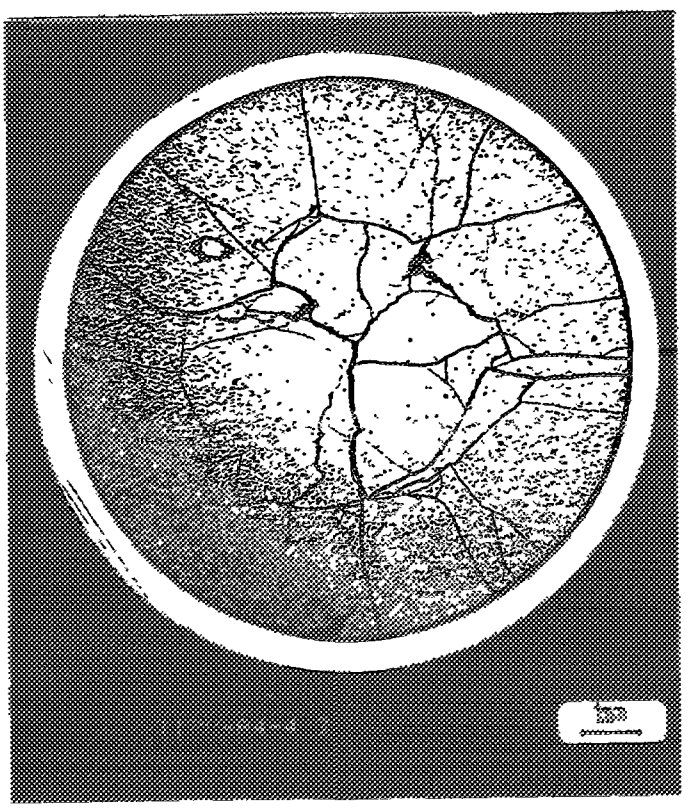

FIG. 27. *Ceramography of the rod type A-4 showing the crack pellet pattern*

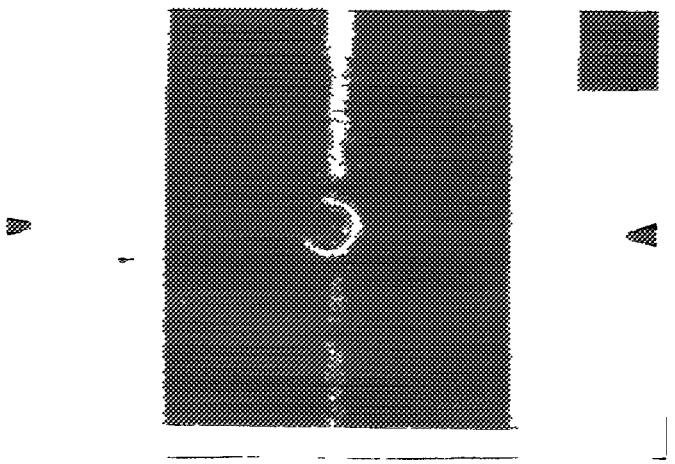

FIG. 28. *Rod type A.1.3 showing the hole in the cladding*

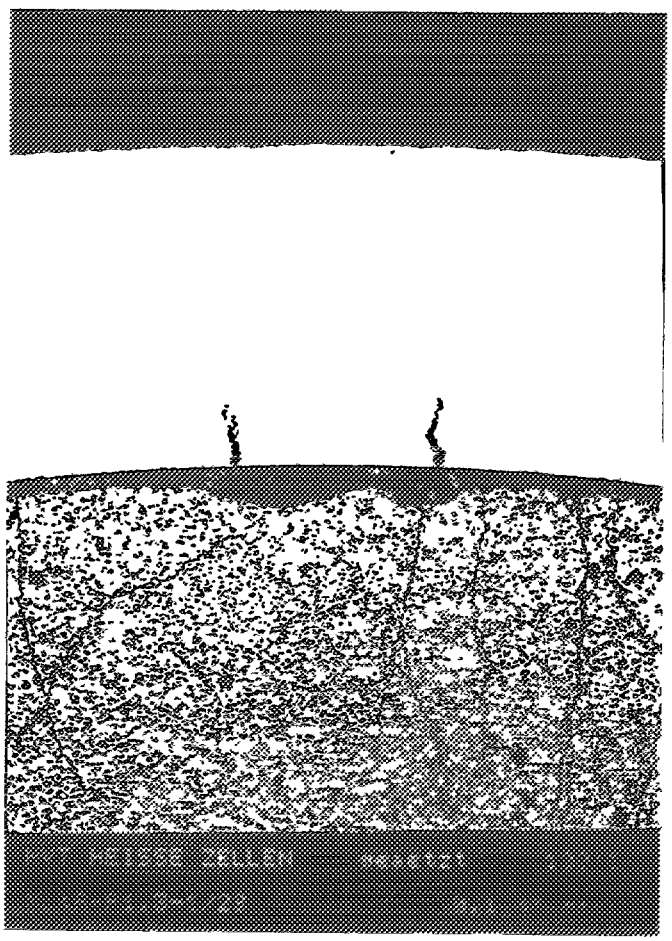

FIG. 29. *Rod type A.1.3 after ramp showing the microcracks depth in the cladding*

7. CONCLUSIONS

7.1. BACO code

We included some new improvement in the BACO code.

- We changed the mesh point scheme.
- We checked the creep and fission gases release models.
- We verified the mathematical convergence of the code.
- We developed a new set of tools with a Windows basis to processes the initial BACO output.

7.2. MOX rods

- The absence of fabrication failures is a good achievement in our MOX program development.
- The presence of microcracks inside the cladding indicated a good BACO code evaluation.
- The pathfinder rod and the BU15 rods have similar structures. That indicates the convenience of an additional methalographic post-irradiation with the pathfinder rod, in order to evaluate the inner surface of the cladding.
- The defective zone of the A.l .3 rod had the bigger mechanical solicitations. The calculated hoop stress was $\sigma_v = 207$ MPa. That value indicates that SCC was a possible way to produce the failure. The defect and the hoop stress previously calculated with BACO show a good prediction of the code.
- We can say that BACO code had a good performance in the two aspects of calculus: thermal and mechanics.
- Finally, we expect a post-irradiation analysis of fission gases for the two rods in the BU15 experience in order to check the predictions of our code.

REFERENCES

[1] MARINO A., ADELFANG P., SPINO J., "Experiencias cona oxitos mixtos (U,Pu)O2. Irradiaciones en los reactores MZFR y HFR-Petten, XIV Reunión Científica de la AATN, Córdoba, 1986 (59).

[2] OROSCO et al; "Fabricación y control de barras combustibles de óxidos mixtos (IJ,Pu)O_2, para ensayo de irradiación en el reactor HFR-Petten", XIV Reunión Científica de la AATN, Córdoba, 1986 (60).

[3] MARINO A. C., "Barras Combustibles MOX irradiadas en Petten. Análisis del comportamiento de la barra A.1.4 ("pathfinder")", Informe interno GACC-DPGT No. 002.09/93

[4] MARINO A. C., "Barras Combustibles MOX irradiadas en Petten. Análisis del comportamiento de las barras A.3 (con Iodo) y A.4 (con CsI)", Informe interno GACC-DPGT No. 002.10/93

[5] MARINO A C., PÉREZ E.,"Barras Combustibles MOX irradiadas en Petten. Análisis del comportamiento de las barras A.1.2 y A.1.3 (Experiencia de quemado extendido BU15)", Informe interno GACC-DPGT No. 002.13/93

[6] MARINO A C.,"Barras Combustibles irradiadas en Petten. Análisis del comportamiento de la barra A.1.3 (Experiencia de quemado extendido BU15)", Informe interno GACC-DPGT No. 002.16/93

[7] HARRIAGUE A- S., COROLI G., SAVINO E., 5th SMiRT Conf. (1979), Paper Dl/l.

[8] HARRIAGUE S., COROLI G., SAVINO E., - BACO (BArra COmbustible), a computer code for simulating a reactor fuel rod perfomance" Nuc. Eng. & Des. 56(1980)91.

[9] HARRIAGUE S, AGDÜERO D., LOPEZ PUMAREGA I., MARINO A. C. - "Prediction of the influence of rnaterial properties on fuel rod behaviourr -IAEA-TC-578/13

[10] MARKGRAF J. et al., "Technical Memorandum HFR/87/4627"

[11] MARKGRAF J. et al., "Technical Memorandum HFR/87/4663"

[12] HOFFMANN, SPINO, "Determination of conditions in a LWR fuel rod under which CsI can cause S.C.C. failure of Zircaloy tubing", Journal of Nuclear Material 127(1985)205-220.
[13] KONASHI et al., ''Fuel-cladding chemical interaction due to iodine induced by irradiation", Trans. Am. Nucl. Soc. Vol 45, Oct-Nov 1983, p. 275.
[14] HOFFMANN P., HFR Report 2785(1979).
[15] GEITHOFF D., "CNEA Fuel Pin Experiement A3/A4 Results of the Post-Irradiation-Examination", Primärbericht-PSB-Ber. IV 775 (ECI. IV).
[16] MARINO A., RUGGIRELLO G.,ADELFANG P., "Comparación entre los resultados calculados con el código BACO y los obtenidos de ensayos posirradiación para la primera irradiación de barras combustibles de $(U,Pu)O_2$. Análisis de la segunda propuesta de irradiación", XVI Reunión Científica de la AATN, Mendoza, 1988 (63).
[17] MARKGRAF, FISCHER et al., "Technical Memorandum IT/9214960".
[18] MCALLISTER, MARKGRAF et al., "Technical Memorandum HFR/92/4914".
[19] MCALLISTER, MARKGRAF et al., "Technical Memorandum HFR/92/4927".
[20] MCALLISTER, MARKGRAF et al.,"Technical Memorandum HFR/92/4948".
[21] ROBERTS, JONES, CUBICCIOTTI et al, "A Stress Corrosion Cracking Model for pellet-cladding interaction failures in Light-Water Reactor fuel rods", ASTM STP 681 (pp. 285-305).
[22] ADELFANG P., RUGGIRELLO G., OBRUTSKY L., "Resultados parciales de los ensayos posirradiación luego de una rampa de potencia, de una BC de oxidos rnixtos $(U,Pu)O_2$ con quemado simulado por productos de fisión sintéticos", XVI Reunión Cientffica de la AATN, Mendoza, 1988 (62).
[23] ADELFANG P., PÉREZ E., "Irradiación de BBCC de óxidos rnisxtos $(U,Pu)O_2$. Descripción de las experiencias y ensayos posirradiación no destructivos iniciales", XXI Reunión Cientffica de la AATN, Mar del Plata, 1993 (26).

A FUEL PERFORMANCE CODE TRUST V1C AND ITS VALIDATION

M. ISHIDA, T. KOGAI
Nippon Nuclear Fuel Development Co. Ltd,
Ibaraki-ken, Japan

Abstract

This paper describes a fuel performance code TRUST Vlc developed to analyse thermal and mechanical behavior of LWR fuel rod. Submodels in the code include FP gas models depicting gaseous swelling, gas release from pellet and axial gas mixing. The code has FEM-based structure to handle interaction between thermal and mechanical submodels brought by the gas models. The code is validated against irradiation data of fuel centerline temperature, FGR, pellet porosity and cladding deformation.

1. INTRODUCTION

TRUST is a computer code to analyse thermal and mechanical LWR fuel rod behavior throughout its life. The code has been developed to simulate high burnup fuel behavior, especially in terms of FP gas release and pellet gaseous swelling as observed in international ramp tests. Accordingly, the code has models depicting the FP gas behavior in fuel rod including axial gas mixing. As a result, the gas models greatly increase the mutual interaction between thermal and mechanical models through, for instance, the FP gas release dependency on pellet stress, thus make the calculation more difficult. To bring an accurate numerical solution efficiently to the problem, a new code structure is devised and the gas models are assembled on the structure. This paper gives an overview of the TRUST code, validation bases and some characteristic results.

2. CODE STRUCTURE

2.1 GEOMETRICAL CONFIGURATION

TRUST code has a FEM-based structure on which thermal, mechanical and gas models are assembled. Figure 1 shows how a fuel rod is depicted by finite elements in the TRUST code. Fuel rod is divided into axial zones, and each zone is divided into radial ring elements. The thermal and mechanical models commonly use the element configuration. At the pellet and cladding gap, an element is placed per axial zone to handle mechanical contact and heat conductance. To depict FP gas concentration in free volume with axial gradient, two elements are adopted per axial zone so that a connection node comes at the center of axial zones. FP gas concentration in upper plenum is expressed by one element as well as in lower plenum, if any. A spring or sleeve element, which is only mechanical, can be inserted in upper plenum.

2.2 SOLVING SCHEME

The overall flow of the TRUST code is shown in Fig.2. After accepting data for fuel specifications and irradiation history, the TRUST code repeats the finite element assembling and global equations solving procedure, and yields results step-by-step for entire irradiation history. In the single loop iterative procedure to resolve the non-linearity of the fuel rod behavior, the assembled equations are solved simultaneously, and no inconsistency is left between fuel temperature, its deformation, and FGR over next time step. The scheme has enabled the code efficiently handling submodels related to both temperature and stress, since good communication between thermal and mechanical models are ensured in the iterative procedure to resolve the demands from both models.

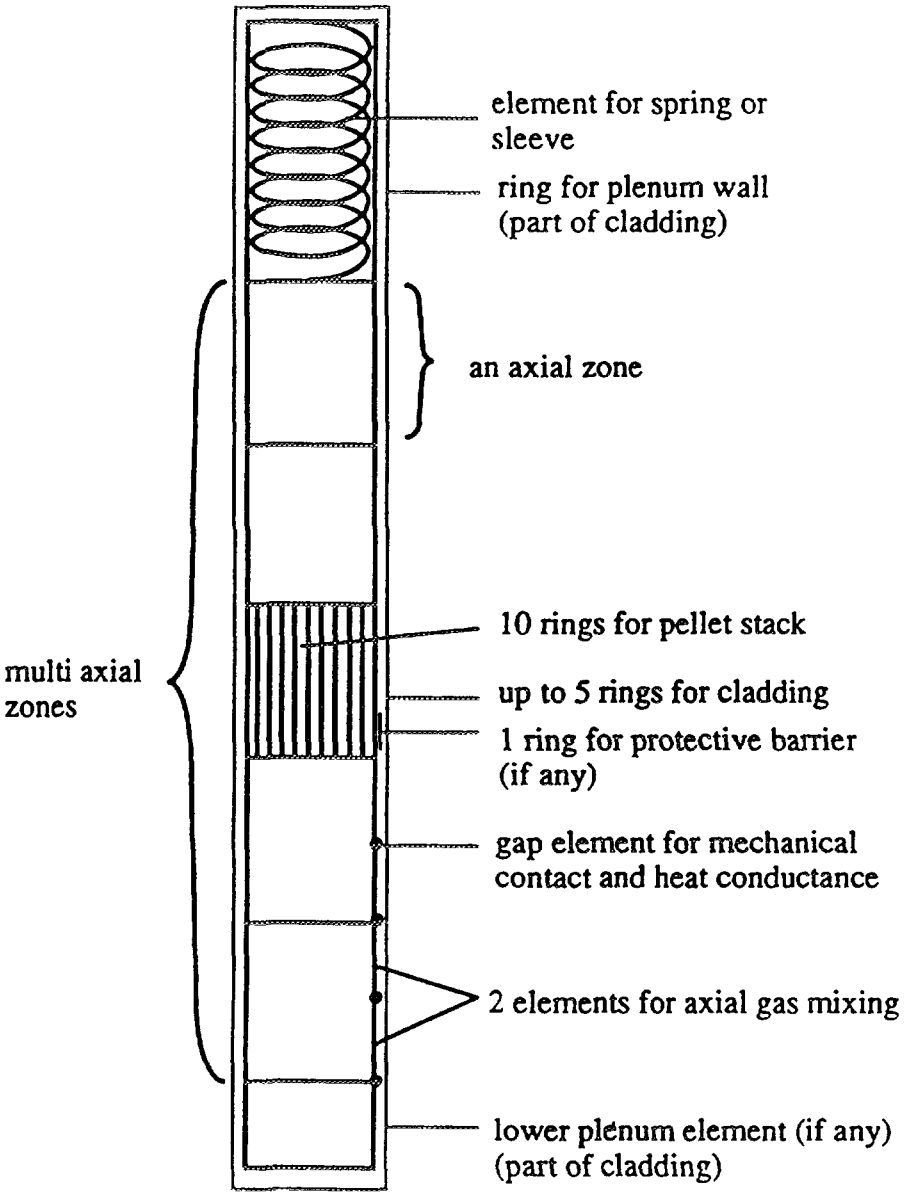

FIG. 1. Finite element configuration of the TRUST code

2.3 THERMAL MODEL

In the thermal model, a pellet thermal conductivity model depicts its reduction by accumulated soluble fission products[1], irradiation defects, and gaseous bubbles. The gap conductance is given by Ross and Stout model[2], based on the gap width, local FP gas concentration, and contact pressure implicitly written in the thermal equations. The values for them are determined in the process of solving the simultaneous equations. Radial heat generation distribution in pellet is given by a modified RADAR[3] model.

2.4 MECHANICAL MODEL

The mechanical model depicts fuel thermal expansion, creep, plasticity, pellet densification, swelling, crack, relocation, pellet-cladding contact, axial slipping, cladding irradiation growth, and resulting stress in pellet and cladding. Since most of the mechanical properties are temperature dependent,

the TRUST code uses linear expansion form of inelastic strains to make direct reference to fuel temperature change, i.e.,

$$\{\varepsilon\}^{j+1} = \{\varepsilon\}^{j} + \left[\frac{\partial\varepsilon}{\partial T}\right]^{j} \delta T^{j+1} \tag{1}$$

where j is iteration number $\left[\frac{\partial\varepsilon}{\partial T}\right]^{j}$ temperature sensitivity vector and δT^{j+1} temperature increment in an iteration. The stress dependency of the strains is treated likewise.

Pellet-cladding mechanical interaction is handled as illustrated in Fig.3. Radial pellet relocation at the initial startup is simulated by translating the whole pellet rings radially. Afterwards, the pellet crack opened by the relocation is considered to be compliant and diminish its width by circumferential stress.

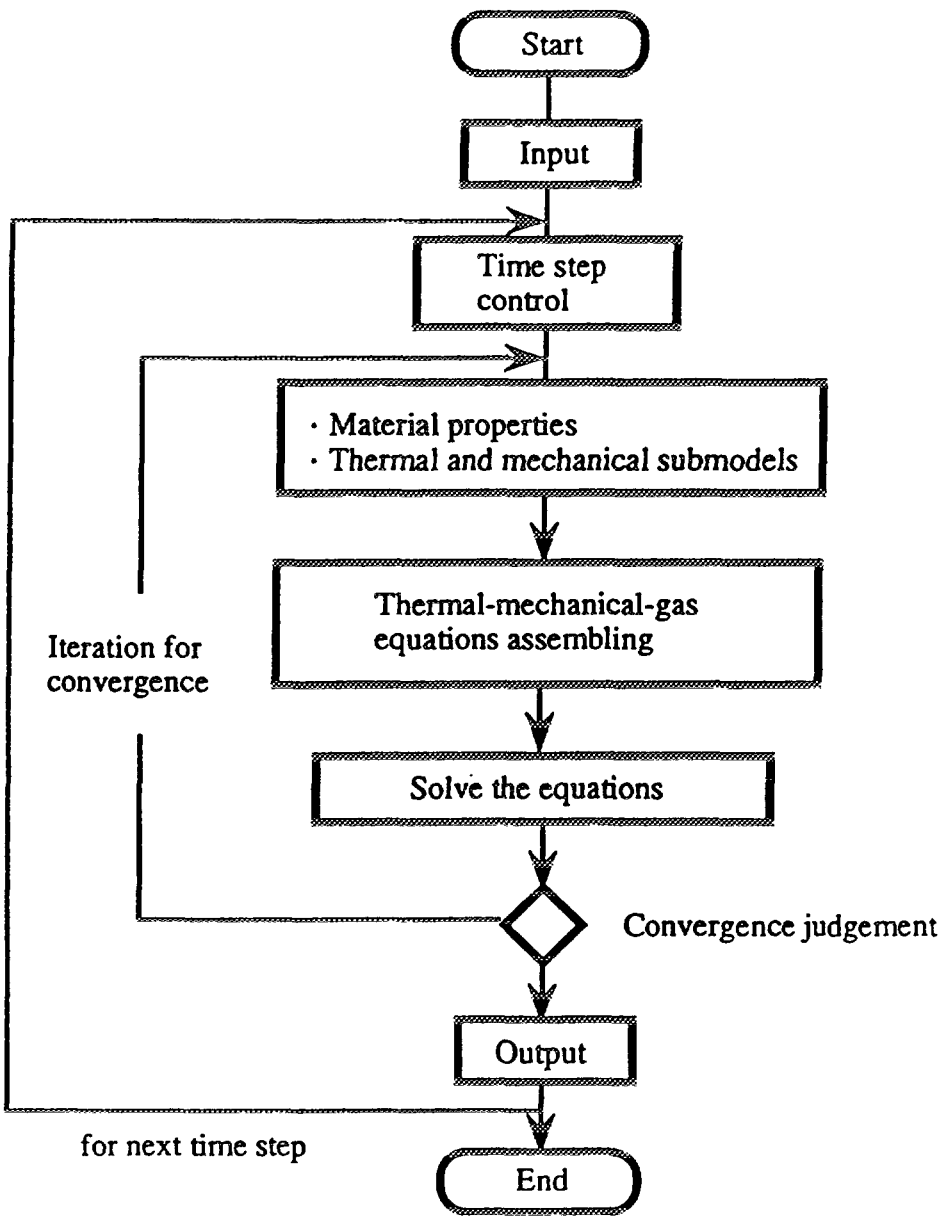

FIG. 2. Flow diagram of the TRUST code

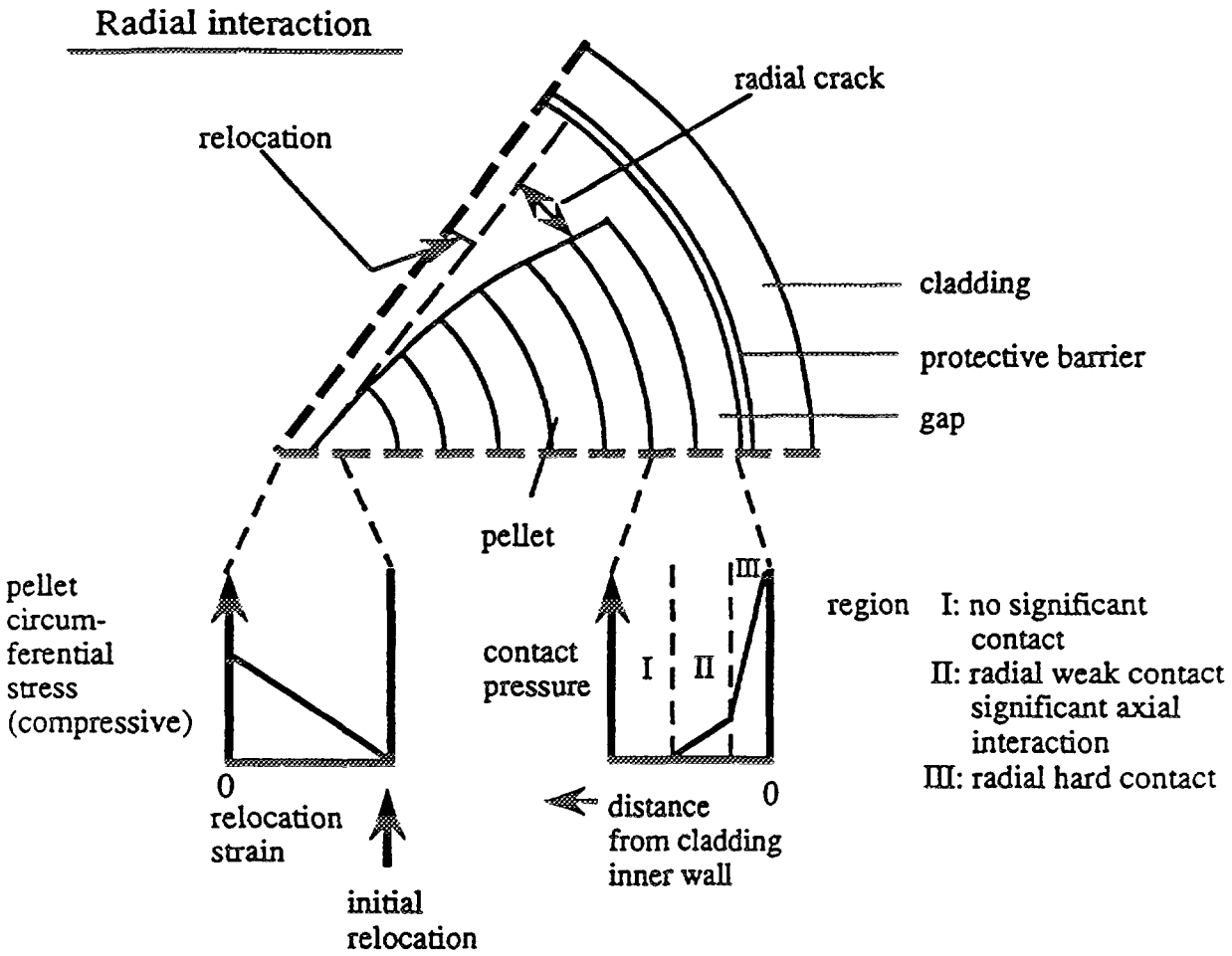

FIG. 3. Mechanical model for the TRUST code

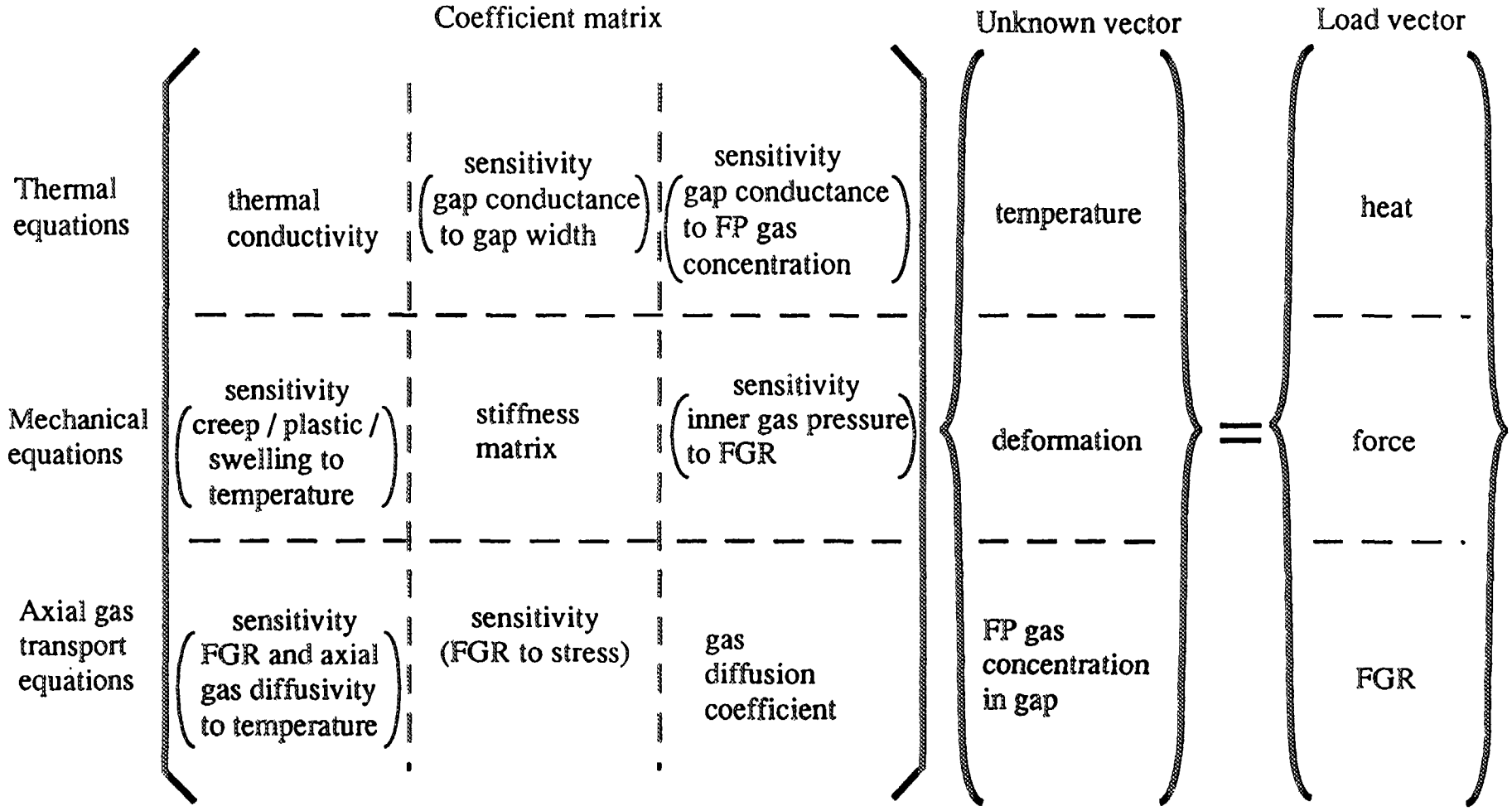

FIG. 4. Thermal/mechanical/gas equations assembling diagram

Pellet-cladding gap is modeled as though it is filled with three layers of compliant material. The innermost layer, depicted as region I in Fig.3, is made very soft to be compressive virtually without resistance. The second is made harder to elongate cladding axially under Coulomb friction. The third is for direct radial push of cladding by the pellet, having largest stiffness. The layers convey force to the cladding element as the pellet surface comes close to it, simulating the effect of the pellet fragmentation. The distance between the pellet and cladding elements is considered as the circumferentially averaged gap width in the actual fuel rod, and is used for evaluating the thermal gap conductance.

An axial force in fuel is conveyed by means of FEM connection nodes placed at the boundaries of the axial zones. To allow axial slipping between pellet and cladding, there are one connection node for cladding and the other for pellet. The pellet is stuck on the cladding if the axial force does not exceed the Coulomb friction force. While the pellet elements are made to cease conveying axial force when it transversely cracks, the cladding elements are permanently connected with adjacent ones. The model gives cladding stress as to be accumulated in the lower part of the fuel rod by the friction with pellet stack.

2.5 FP GAS MODELS

The process of FP gas diffusion in grain and on grain boundary is modelled to give FP gas release, and lenticular bubbles on grain boundary to give gaseous swelling of pellet.

Simple effective diffusion coefficient model is employed to give the FP gas transfer speed in grain radial direction. At the start of irradiation, the coefficient is set at the value measured at Harwell for UO_2 specimen[4]. The coefficient is made to be increased as the burnup proceeds in order to account for the measured FGR from irradiated rods.

The lenticular bubble is assumed to grow or shrink according to the stress field around the bubble, which is expressed in a formulation proposed by Hull and Rimmer[s]. Stress also plays a role in suppressing the FP gas transfer from the lenticular bubbles to the free volume.

Released FP gas is slowly mixed with fill gas and axially diffuses. Since pressure equilibrium throughout the rod is assumed in the gas mixing model, axial bulk gas flow occurs upon the gas release and the temperature change in free volume. The numerical instability associated with the bulk gas flow has been overcome by making the finite element boundaries movable in accordance with the bulk gas flow so that the gas does not cross the element boundary in a time step. The modified element accepts the relatively large time increment used in thermal and mechanical models, thus can be used to form a part of the simultaneous equations.

The FP gas diffusion speed in axial direction is determined by the shape of the free volume in pellet stack. Pellet central hole provides a fairly large and straight diffusion path. For the non-holed pellet stack, however, diffusion path has complicated shape due to pellet cracking. The TRUST code estimates the averaged path length and its width based on the simplified crack and gap geometry given by the mechanical model.

2.6 FINITE ELEMENT ASSEMBLING

Figure 4 is a diagram showing how the set of global equations are assembled in the TRUST code. The left hand side of the equation is the product of unknown field vector and coefficient matrix. The vector elements are chosen to be the fuel temperature and deformation as well as the FP gas concentration in gap. Thermal conductivity, fuel stiffness, and FP gas diffusion coefficient reside in the diagonal part of the coefficient matrix. In the off-diagonal part are the cross terms such as gap conductance sensitivity to gap width, and they bind the three subset of equations - thermal, mechanical and axial gas transport equations - together. The right hand side of the equations stands for the load vector consisting of fuel heat generation, external force and FGR. After assembling, the equations are handed to a solver which is designed to do the job in maximum efficiency.

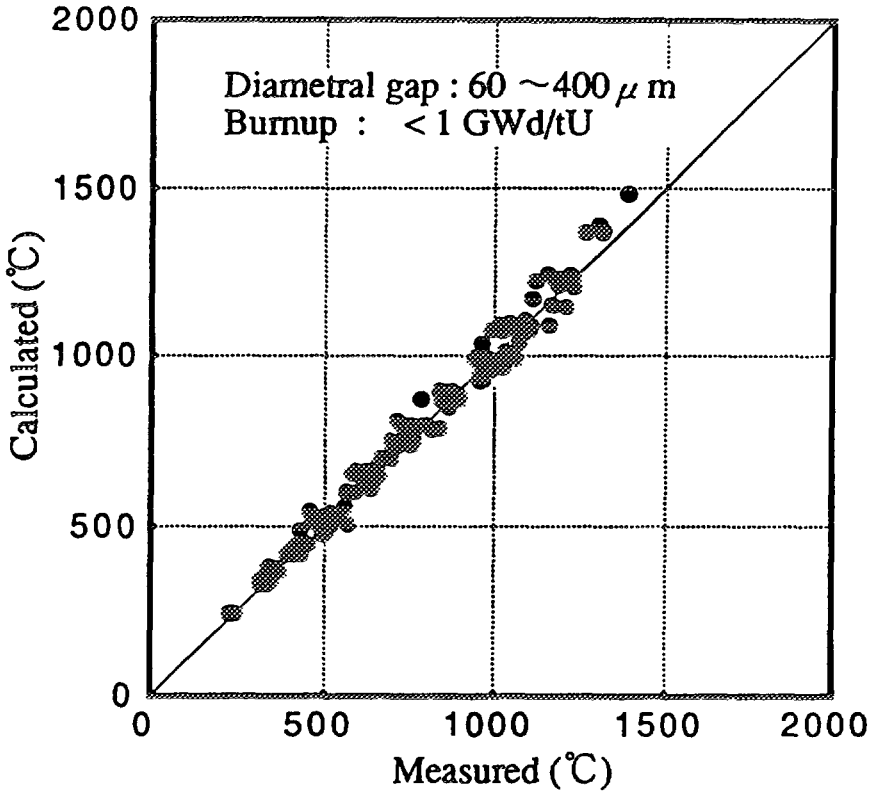

FIG. 5. *Comparison of fuel centreline temperature at the beginning of irradiation*

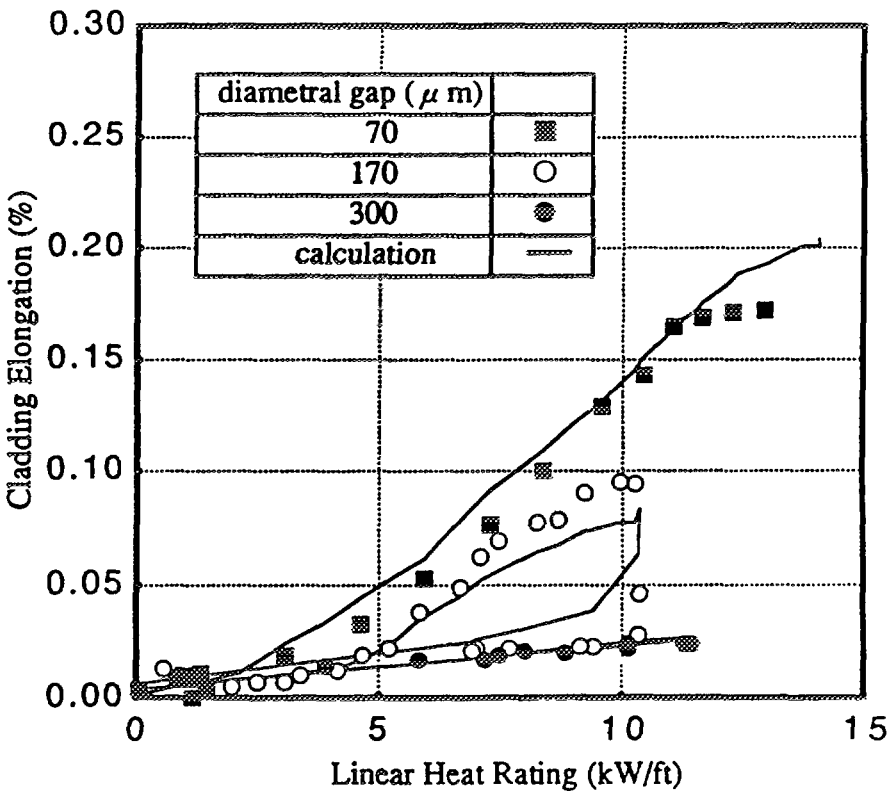

FIG. 6. *Gap size dependency of cladding elongation*

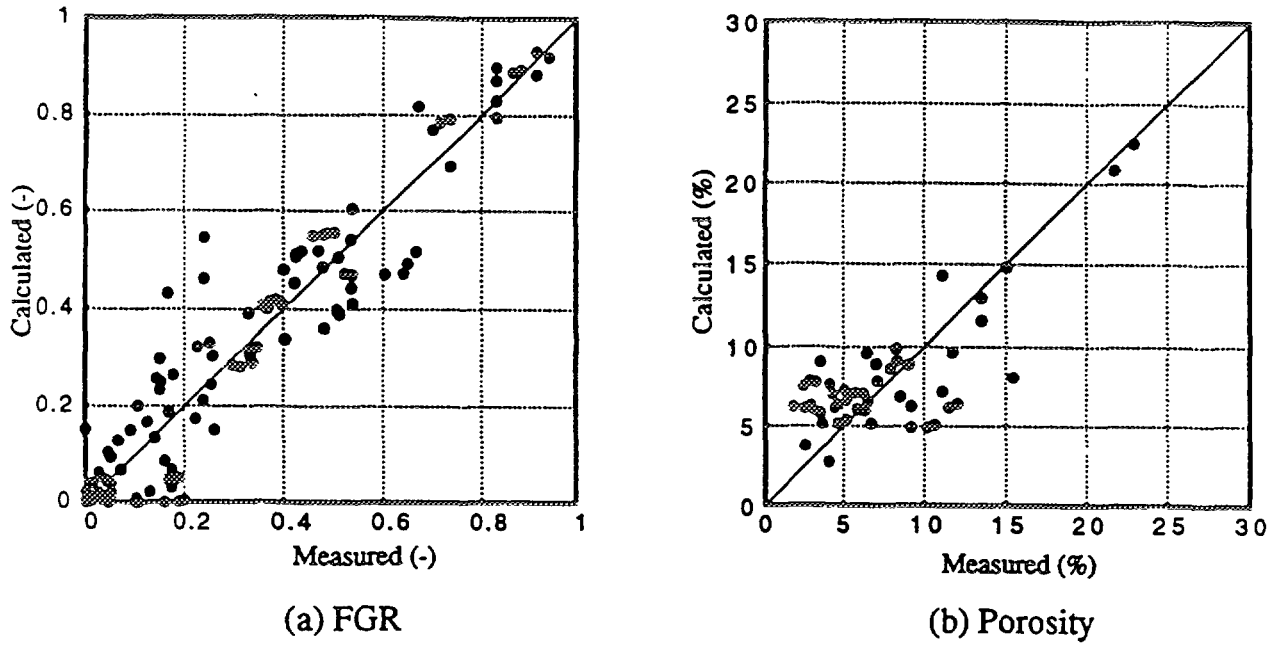

FIG. 7. *Comparison of FGR and porosity (Fission Gas Release and Gaseous Swelling Model)*

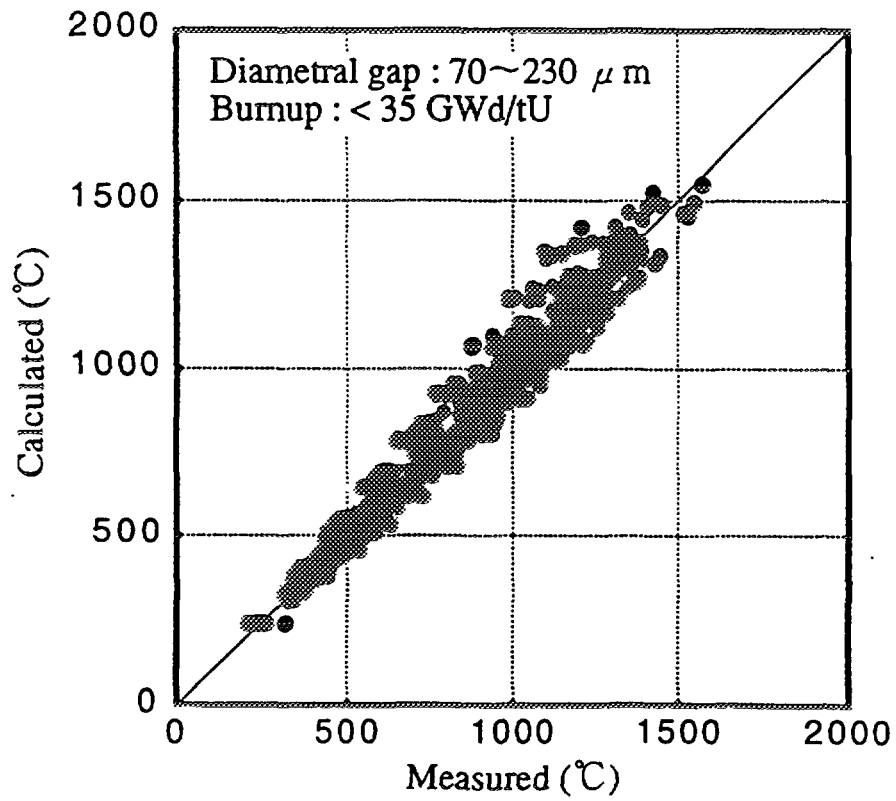

FIG. 8. *Comparison of fuel centreline temperature to high burnup*

3. VALIDATION DATABASE

The TRUST code has been validated through the comparison of its predictions with on-power and PIE data. The on-power data comprise fuel centerline temperature, rod internal pressure and cladding elongation. The PIE data employed are FGR, cladding permanent elongation, diameter change, pellet xenon retention, porosity and grain size. The data are from Halden irradiation test programs and other international projects, and PIEs for rods from commercial reactors carried out in NFD. Major design parameters of the fuel rods cover the manufactured diametral gap of 60 to 400μm, pellet stack length of 30 to 360cm, and initial fill gas pressure of 1 to 25atm.

4. RESULTS OF THE CODE VALIDATION

The validation of the TRUST V1c has been performed by separating the irradiation period into at the beginning of life and throughout the life, since fission gas release complicates fuel rod behavior.

The effects of initial gap size on fuel centerline temperature and cladding elongation has been firstly examined. Figure 5 compares the TRUST code predictions and the experimental data as for fuel centerline temperature at the startup, and they are in good agreement in a gap size range from 60 to 400μm. On the other hand, cladding elongation versus gap size at the startup is shown in Fig. 6. The rods with a medium and a narrow (70μm) gap size appear to become contact with cladding at 5kW/ft (160W/cm) and 3kW/ft (100W/cm), respectively, and the behavior is well simulated by the code. In addition to the effects of gap size, those of axial power profile (contact at the upper portion of a fuel rod elongates the cladding to a larger extent), pellet stack length and pellet shape on the cladding elongation has also been validated.

Prior to the code validation throughout the rod life, the fission gas release and gaseous swelling submodel has been verified independently using more than thirty cases in which sample temperature is measured. Figures 7 (a) and (b) show the comparison between calculated and measured of FGR and pellet porosity from rod ramp tests[6], UO_2 out-of-pile annealing tests[7,8], and UO_2 isothermal irradiation tests[9]. The figures show that fission gas behavior is appropriately simulated by the model.

As the most influential parameter to the fuel rod performance, validation of fuel centerline temperature has been carried out. Figure 8 compares the code predictions and measurements of fuel centerline temperature up to 35GWd/tU for the fuels with gap size of 70 to 230μm. The figure shows that the predictability of fuel temperature of the TRUST code is satisfactory.

5. CONCLUSIONS

1. A fuel performance code TRUST V1c for analyzing LWR fuel rod behavior has been successfully developed.

2. The fission gas release and gaseous swelling submodel in the TRUST code has been verified against rod on-power pressure data, UO_2 out-of-pile annealing test data and isothermal irradiation test data.

3. The code has been validated against on-power and PIE data from not only test reactors but commercial reactors. An extensive comparison of calculated fuel centerline temperature with measured has shown that the code predicts satisfactorily the fuel temperature up to high burnup.

REFERENCES

[1] ISHIMOTO, S. et al.: "Effects of Soluble Fission Products on Thermal Conductivities of Nuclear Fuel Pellets", J.Nucl.Sci.Technol. 31[8](1994)796.

[2] ROSS, A.M. and STOUT, R.L.: "Heat Transfer Coefficient between UO_2 and Zircaloy-2", AECL-1552(1962).

[3] PALMER,I.D.,HELKETH,K.W. and JACKSON,P.A: "A Model for Predicting the Radial Power Profile in a Fuel Pin", WATER REACTOR FUEL ELEMENT PERFORMANCE COMPUTER MODELLING, Ed. by J.Gittus, Applied Science Publishers(1983)321.

[4] TURNBULL, J.A. et al.: "The Diffusion Coefficients of Gaseous and Volatile Species during the Irradiation of Uranium Dioxide", J.Nucl.Mater. 107(1982)168.

[5] HULL, D. and RIMMER, D.E.: "The Growth of Grain-boundary Voids Under Stress", Phil.Mag. 4(1959)673.

[6] The Third Risø Fission Gas **Project: "Final Report:** The Project", RISØ-FGP3-FINAL,Pt.1(1991).

[7] UNE, K. and KASHIBE, S.: "'Fission Gas Release during Post Irradiation Annealing of BWR Fuels", J.Nucl.Sci.Technol. 27[11](1990)1002.

[8] UNE, K., KASHIBE, S. and ITO, K.: "Fission Gas Behavior during Postirradiation Annealing of Large Grained UO_2 Fuels Irradiated to 23GWd/t", J.Nucl.Sci.Technol. 30[3](1993)221.

[9] ZIMMERMANN, H.: "Investigations on Swelling and Fission Gas Behavior in Uranium Dioxide", J.Nucl.Mater. 75(1978)154.

MODIFICATION IN THE FUDA COMPUTER CODE TO PREDICT FUEL PERFORMANCE AT HIGH BURNUP

M. DAS, B.V. ARUNAKUMAR, P.N. PRASAD
Nuclear Power Corporation,
Mumbai, India

Abstract

The computer code FUDA (FUel Design Analysis) participated in the blind exercises organized by the IAEA CRP (Co-ordinated Research Programme) on FUMEX (Fuel Modelling at Extended Burnup). While the code prediction compared well with the experiments at Halden under various parametric and operating conditions, the fission gas release and fission gas pressure were found to be slightly over-predicted, particularly at high burnups. In view of the results of 6 FUMEX cases, the main models and submodels of the code were reviewed and necessary improvements were made. The new version of the code FUDA MOD 2 is now able to predict fuel performance parameter for burn-ups up to 50000 MWD/TeU. The validation field of the code has been extended to prediction of thorium oxide fuel performance. An analysis of local deformations at pellet interfaces and near the end caps is carried out considering the hourglassing of the pellet by finite element technique.

1. INTRODUCTION

The Computer Code FUDA (Fuel Design Analysis) [1] is used to carry out design calculations and analyses for licensing submissions. The code is also used for fuel performance evaluation of operating pressurized Heavy Water Reactors (PHWRs) and feed back to designs [2,3]. Additionally the code is used for optimizing the fuel design and fabrication parameter for improved performance. Earlier the validation field of the FUDA code was limited upto a maximum burnup of about 15,000 MWD/TeU as obtaining in a PHWR for different parameters like fuel centre temperature, surface temperature, fission gas release, internal pressure, sheath stresses and strains.

FUDA-MOD 1 is originally based on FUDA MOD 0 [4]. The code is written in FORTRAN 77. It is running on Unix operating system on i860 workstation, on SINTRAN-III operating system on Norks Data Computer and as well as on PC-386/ 486 with MS.DOS operating system. The code consists of about 2000 lines. It can be linked with graphic package for pre and post processing. The code offers several options like different pellet geometries, different fuel and sheath materials, applications for PHWRs and LWRs, and analysis for load following or base load operations.

2. CODE DESCRIPTION AND MODELS

The computer code FUDA uses Finite Difference Method for temperature, thermal expansions, and sheath stress calculations. Local stresses and ridge analysis are carried out by finite element technique.

Fuel expansion is calculated using a two zone model in which the stresses in UO_2 are ignored. The model assumes that above a certain temperature, the UO_2 deforms plastically and below that temperature, it cracks radially and behaves as an elastic solid. The extent of plasticity is governed by the temperature of the UO_2, the stress imposed on it by sheath strength and the coolant pressure and is a function of time. In case of PHWR fuel element which uses a collapsible sheathing with low diametral clearances, the firm contact between the pellet and the sheath due to external pressure and diametral expansion, limits the relative fuel movement [5].

The fission gas generated is a function of burnup. The fission gas generated for each radial burnup zone is calculated as suggested by Southier [6]. A simple steady state and Transient Gas Release Model URGAS developed by K. Lassmann has been used for this analysis [7].

Fission gas pressure is calculated based on mass of the fission gas release, mass of the fill gas, available void volumes and temperature of storage locations.

Global sheath stresses and strains due to fuel thermal expansion, swelling and densification are calculated [8]. The creep and stress relaxation in the time zone at constant power operation is calculated using semi-empirical formula considering athermal and thermal creep including effect for irradiation. Fuel sheath interfacial pressure is then calculated based on gas pressure and strains. This shows whether the expanded fuel is touching the sheath or gas gap exists between them.

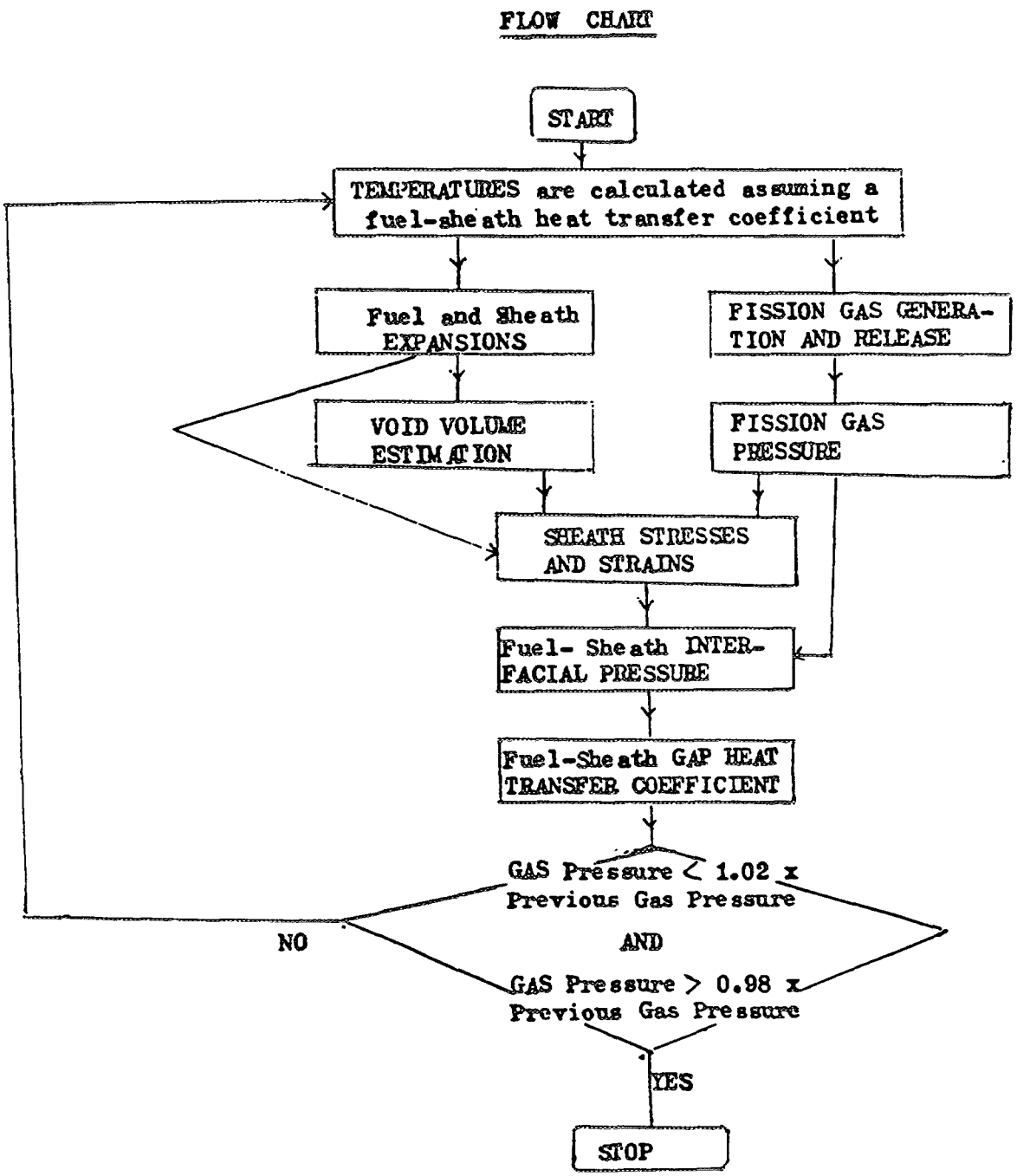

FIGURE - 1

Using global diametral changes, local deformations of the pellet and sheath are calculated considering hourglass phenomenon of the pellet. Finite element method using axisymmtric 8-noded isoparametric elements is used for calculating deformation, stresses and strains in pellet and in sheath [9].

The radial temperature distribution across the pellet and sheath are calculated for the given inputs of linear heat rating, coolant temperature and heat transfer coefficient. The components of the fuel-sheath heat transfer coefficient across the gas filled fuel-sheath gap through the solid-solid contact points are calculated using Ross and Stoute equation [10]. The gap conductance model URGAP by K. Lassmann has been referred for this purpose [11].

Using the new fuel-sheath heat transfer coefficient, new temperature distribution across fuel and sheath are calculated and the cycle is repeated iteratively. The iteration is terminated when two successive calculations of internal gas pressure agree within 5%. For any power change, the above iterative procedure is repeated for a given time zone till the required convergence is obtained. For improving accuracy, the pellet is divided into 100 rings radially and all the parameters are calculated for each ring. The radial flux depression in the element is taken into account in estimating powers in different rings. For radial flux depression calculation two options are available. The first one is using Bessell function with an inverse diffusion length, kappa value. The second option is using an equation fitted to the results of the neutron-physics code. This takes into account variation with burnup. Axial flux gradient in the fuel element can be handled by splitting the element into a number of equal lengths and considering each as being at an uniform power output [3] (Fig.1).

The following are the main models used in the code:

2.1 Flux depression in the pellet: The local flux perturbations affecting fuel design are radial flux depression through the bundle and flux peaking at the interface between adjacent fuel bundles in a channel. The radial distribution of flux is a function of pellet diameter, UO_2 enrichment and burnup and plutonium build up. Two options are included in this model viz., (i) Bessel function based and (ii) Based on PHWR physics codes which varies with burnup.

2.2 Film heat transfer co-efficient: Depending on the coolant condition and environment, sheath-to-coolant heat transfer is calculated. For forced flow through rod bundles, Dittus-Boelter equation is used. For BWRs, Jens-Lottes correlation is used.

2.3 Fuel-sheath gap heat transfer coeff.: Pellet clad gap conductance is calculated by Ross and Stoute model taking care of the physical gap existing between the pellet and the clad. Pellet-clad gap conductance consists of three parts

$$hg = hs + hf + hr$$

a) Conduction through solid-solid contact points (hs)

b) Convection through solid-gas interface (hf) and

c) Radiation exchange between pellet outer surface and clad inner surface (hr)

URGAP, a gap conductance model developed by K. Lassmann has been made use of for this analysis [11].

The heat transfer coefficient between the sheath and the pellet is a function of:

- radial gap/contact-pressure between the pellet and the sheath;
- the composition of gases inside the fuel element and gas pressure and
- the initial roughnesses of the surfaces of the sheath and of the pellet.

However, all these quantities are time-dependent, and consequently the quantitative data are uncertain because:

(1) Gap width and contact pressure are determined by uncertain fuel densification and swelling effects as well as by relocation effects (displacement of broken fuel fragments), apart from thermal expansion;

(2) gas pressure and gas composition depend on fission gas release, which is also uncertain.

(3) the surface characteristics change due to creep effects and chemical reactions, again in a manner which cannot be specified accurately.

In view of uncertain input parameter, more complicated models would not provide any better quantitative information. URGAP model is a simplistic heat transfer model for use in fuel rod modelling. URGAP model has been used in TRANSURANUS code. This model consists the gases helium, argon, krypton, xenon, nitrogen, hydrogen, oxygen, carbonmonoxide, carbon dioxide and water (steam). It considers the fuel surfaces UO_2, (U, Pu)O_2, UC, (U, Pu)C, UN,(U, Pu)N and the cladding surfaces Zr, ZrO_2, Fe, fuel, Fe_3O_2.

2.4 Fuel Thermal Conductivity: Thermal conductivity variation with temperature and porosity is considered. The low temperature radiation damage is considered by assuming the UO_2 conductivity below 500°C as constant. Pellet temperature profile is calculated by dividing pellet into a number of concentric rings, normally 100. Temperature is calculated from surface to centre using finite difference method.

2.5 Fission Gas Release: There are two models incorporated in FUDA for fission gas release.

i) Temperature dependent release mechanism.

ii) Physical model based on diffusion and grain growth mechanism - Both equiaxed and columnar grain growth are treated. Equiaxed grain growth is calculated based on local temperature, UO_2 enrichment and grain size. Fission gases are assumed to diffuse through UO_2 grains, the amount of diffusion being dependent amongst others on local temperature and grain diameter. The bubbles accumulated on the grain boundary grow in size and coalesce before releasing to the gap through the tunnels/cracks [12].

URGAS, a Simple steady state and Transient Gas Release Model by K. Lassmann has been used for numerical treatment and implementation of diffusion model of fission gas release [7]. URGAS is a simple gas release model based on the concept of an effective diffusion coefficient. The model is defined by an incremental algorithm that can accommodate temperature and burnup dependent diffusion parameters as well as a variable power history. By choosing the appropriate effective diffusion coefficient gas release from all fuels like oxide, mixed oxide, carbide, nitride can be modelled. It is in reasonable agreement with the ANS-5.4 model which has been validated against a large data base, but overcomes the problem of large storage requirements faced by ANS-5.4.

In view of the results of the FUMEX (Fuel Modelling at Extended Burnup) cases, the above modified models were implemented in the code. In particular fission gas release model URGAS by K. Lassmann is made use of to take into account the higher burnup effects based on physically based models. The code resulting from the implementation of these modification, namely FUDA-MOD 2, is now able to predict fuel performance parameters for burnups upto 50000 MWD/TeU.

3. VALIDATION

Validation field consists of different parameters like fuel centre temperature, surface temperature, fission gas release, sheath strain (plastic upto a burnup of 50,000 MWD/Te U against end of life

parameters measured after irradiation experiments. Variation of fission gas pressure with burnup is compared with available instrumented data from irradiation experiments. The different parameters are also compared with results obtained with other similar computer codes like ELESIM, ELESTRES etc.

The validation is based on, power reactor data, comparison with other codes, literature on results of inpile experiments conducted abroad and inpile experiments conducted in India and post irradiation examination.

Special irradiation experiments were carried out in power reactors with various design and fabrication variables such as fully annealed cladding, high grain size UO_2 pellets upto 400 microns and thorium bundles [13,14,15]. The validation field of the code has also been extended to these special irradiations including predictions of thorium oxide fuel performance. Thorium is being irradiated in research reactors DHRUVA and CIRUS. In KAPP-1 35 bundles of Thorium dioxide have been introduced into initial core for the purpose of flux flattening. Before this, ThO_2 bundles were test irradiated in MAPS-1 reactor to prove the design of the bundles. The calculations and analyses for licencing submissions for thorium bundles were also carried out using FUDA.

4. CONCLUSIONS:

1. FUMEX bench marking exercise for fuel performance codes has helped considerably in improving various models and submodels used in FUDA.

2. The gap conductance model URGAP by K. Lassmann has been used for prediction of fuel-sheath heat transfer coefficient in modified version of FUDA, viz, FUDA-MOD 2.

3. The Fission Gas Release Model URGAS by K. Lassmann has been used for prediction of fission gas release by diffusion mechanism.

4. The code has been updated, with improved models, to predict fuel performance parameters for burnups upto 50000 MWD/TeU.

5. With new version of the Code FUDA-MOD 2, the accuracy of Prediction of parameters compared to experimental results of FUMEX benchmarking exercises has been significantly improved.

6. The validation field of the code has been extended to special irradiation experiments in power reactors including thorium oxide fuel.

REFERENCES

[1] DAS, M., BHARDWAJ, S.A. "Fuel Design Analysis Code - FUDA", PPED internal report, 1981.

[2] DAS, M., "Design Aspects of PHWR Fuel For Improved Performance", Second Annual Conference on Nuclear Power Advanced Fuel Cycles, Indian Nuclear Society, Bombay, 1990.

[3] DAS, M., et.al. "Fuel Design Manual, MAPP", PPED internal report, 1983.

[4] PRASAD, P.N., SHYAM PRASAD, K., DAS, M., "Computer code for fuel design analysis FUDA - MOD 0, NPC internal report, 1991.

[5] DAS, M., RUSTAGI, R.S., "Mechanical Design Considerations for a Collapsible Fuel Cladding", Proc. of 4th International Conference on Structural Mechanics in Reactor Technology, San Fransisco, USA, Vol.D, 1977.

[6] SOUTHIER, NOTLEY M.J.F "Effect of power changes on fission product gas release from UO_2 fuel" NUCL.APPL. 5, 1968 (AECL-2737).

[7] DAS, M., "Fuel Element Performance for Indian PHWRs and Future Design and Development Programme", Proc. of International Seminar on Mathematical/Mechanical Modelling of Reactor Fuel Elements, San Fransisco, USA, 1977.

[8] NOTLEY, M.J.F., et.al. "The Longitudinal and Diametral Expansion of UO_2 Fuel Elements", AECL-2143 (1964).

[9] NOTLEY, M.J.F. "A Computer Program to predict the performance of UO_2 Fuel Elements", NUCL, APPL. Technology 1, 195 (1970).

[10] ROSS, A.M., STOUTE, R.L., "Heat Transfer Coefficient between UO_2 and Zr-2", AECL-1552, 1962.

[11] LASSMANN, K., HOHLETELD, F., "The revised URGAP model to describe the gap conductance between fuel and cladding", print from Nuclear Engineering and Design, 1986.

[12] NOTLEY, M.J.F "A Microstructure - Dependent Model for Fission Product Gas Release and Swelling in UO_2 fuel", Nuclear Engineering Design 56, 1980.

[13] DAS, M., BHARDWAJ, S.A., PRASAD, P.N., "Fuel Performance Experience in Indian Pressurized Heavy Water Reactor", 3rd International Conference on CANDU Fuel, 1992.

[14] DAS,M., "Design and Irradiation Experience with Thorium Bundles in MAPS", Ind-Japan Seminar on Thorium Utilization, Bombay, India, 1990.

[15] DAS, M., "Design and Irradiation Experience with Thorium Based Fuels in PHWRs", Third International Conference on CANDU Fuel, 1992.

BIBLIOGRAPHY

M. Das, S.A. Bhardwaj, O.P. Arora, "Fuel Behaviour Under Accident Conditions - Clad Ballooning and Fission Gas Release", Proc. of Symposium on Power Plant Safety and Reliability, BARC, India 1979.

M. Das, "Design Aspects of PHWR for Improved performance", Material Science Forum Vol. 48 & 49, Trans Tech Publication, Switzerland, (1989).

P.B. Desai, V.G. Date, M. Das, P.N. Prasad, K.S. Prasad, "Ballooning and Rupture Behaviour of PHWR Fuel Cladding", Third International Conference on CANDU Fuel, 1992.

K. Lassmann, "URGAS: A Simple Steady State and Transient Gas Release Model", 1984.

MATPRO - Version 11, Handbook of Material Properties for use in the Analysis of LWR Fuel Rod Behaviour, 1979.

R.S. Rustagi, M. Das, "Design Considerations for Nuclear Fuel Elements to Suit Reactor Operating in Small Electrical Grids:, Proc, of 3rd International Conference on Structural Mechanics in Reactor Technology, London, Vol. -C, 1975.

M. Tayal, "Modelling CANDU Fuel under Normal Operating Conditions: ELESTRES Code Description", AECL-9331, 1987.

MODELLING OF WWER-440 FUEL ROD BEHAVIOUR UNDER OPERATIONAL CONDITIONS WITH THE PIN-MICRO CODE

S. STEFANOVA, M. VITKOVA, V. SIMEONOVA,
G. PASSAGE, M. MANOLOVA
Institute for Nuclear Research and Nuclear Energy,
Sofia, Bulgaria

Z. HARALAMPIEVA
National Electric Company Ltd,
Kozloduy, Bulgaria

A. SCHEGLOV, V. PROSELKOV
Institute of Nuclear Reactors,
RSC Kurchatov Institute,
Moscow, Russian Federation

Abstract

The report summarizes the first practical experience obtained by fuel rod performance modelling at the Institute for Nuclear Research and Nuclear Energy, Bulgarian Academy of Sciences. The results of application of the PIN-micro code and the code modification PINB1 for thermomechanical analysis of WWER-440 fuel assemblies (FAs) are presented. The aim of this analysis is to study the fuel rod behaviour of the operating WWER reactors. The performance of two FAs with maximal linear power and varying geometrical and technological parameters is analysed. On the basis of recent publications on WWER fuel performance modelling at extended burnup, a modified PINB1 version of the standard PIN-micro code is shortly described and applied for the selected FAs. Comparison of the calculated results is performed. The PINB1 version predicts higher fuel temperatures and more adequate FGR rate, accounting for the extended burnup. The results presented in this paper prove the existence of sufficient safety margins for the fuel performance limiting parameters during the whole considered period of core operation.

1. INTRODUCTION

Fuel performance modelling and analysis in Bulgaria began less than two years ago. Calculated results and analysis of the thermomechanical behaviour of selected WWER-440 fuel assemblies (FAs) are presented in this paper. These results must be considered as preliminary, because of the insufficient experience of the Bulgarian authors in this field.

The calculations for the fuel rods (FRs) with highest power in the chosen FAs, are performed with the PIN-micro code [1] and with a modification of the code PINB1. The aim of these calculations and analyses is to determine the extreme values of the limiting parameters accepted for the normal reactor operation and to prove the existence of sufficient safety margins.

2. SHORT DESCRIPTION OF THE PIN-MICRO CODE

The PIN-micro code is a steady-state, quasi-two-dimensional code, developed on the base of the GAPCON-THERMAL-2 code [2]. It has been improved and verified against WWER FRs by introduction of specific correlations [3]. The consideration of the calculated results such as linear power, fuel burnup, fuel and cladding temperatures, gap gas composition and pressure, fuel and cladding deformations, caused by irradiation and depending on burnup, allows the FR behaviour to be analysed during its whole core-life.

The PIN-micro code cannot be applied to predict behaviour of the FR at fast transient and accident conditions.

2.1 INCORPORATED MODELS

The models and correlations included in the PIN-micro code describe: the radial temperature distribution in fuel and cladding, the gap size or pellet-to-cladding contact pressure, the radial deformation of the fuel pellets due to thermal expansion, relocation, densification and swelling, fuel grain growth and restructuring, the radial deformation of cladding due to thermal expansion, creep and irradiation growth, the axial elongation of fuel and cladding, the fission gas release (FGR), the gas composition and pressure.

2.2 CODE VERIFICATION

The PIN-micro code is verified in the framework of international experiments, as well as on Russian and Czech experiments, specific for WWER. The Russian experiments are performed in the MR reactor in the Kurchatov's Institute [3]. The behaviour of WWER-440 and WWER-1000 FAs has been investigated through comparison of measured and calculated results.

At present some Russian, Czech and Bulgarian specialists are applying their own PIN versions to improve and verify them in the framework of the IAEA CRP "FUMEX -- Fuel Modelling at Extended Burnup" against the Halden reactor extended burnup irradiation data.

3. THE MODIFIED PINB1 VERSION

Aiming to improve the user's convenience and partly to overcome some little lacks, a modification PINB1 of the PIN-micro code has been prepared on the basis of recent Russian publications and local considerations [4, 5, 6].

Compared to PIN-micro, the PINB1 includes the following modifications: FGR model for very low and extended burnup [4]; relocation and swelling models to account for fuel creep, which is not modeled; open gap and contact heat conductivity model [5, 6] and fuel thermal conductivity correlation [7]. The approach to the burnup determination is modified in accordance with the possible pellet chamfering, dishing etc., on the base of measured results for initial fuel debris [5, 6]. The burnup accumulation between two time steps in PINB1 does not depend on power during the next, but during the previous time step. The radial flux depression correlation is also modified [5]. The fast neutron flux determination dependent on burnup is based on the correlations from [4].

4. INPUT DATA PREPARATION

The most important input data, such as power history, power axial and radial distributions and peaking factors have been taken from [8]. The geometrical representation of the FR is performed through 10 axial and 20 radial segments.

4.1 GEOMETRICAL AND TECHNOLOGICAL PARAMETERS

For the calculations of the chosen two FAs, three variants of characteristic sets are defined: the case AVER representing the set of the most probable average values of all parameters; the case MAX, representing the most conservative from the central temperature point of view, conjunction of the fuel lowest density and maximal initial radial fuel to cladding gap; and the case MIN with maximal fuel density and minimal gap size, representing also a conservative conjunction of parameters leading to the earliest

Table I. Geometrical and technological parameters for the selected variants

Parameter		Variants		
		AVER	MIN	MAX
Central hole diameter,	mm	1.6	2.0	1.2
Fuel outer diameter,	mm	7.565	7.54	7.59
Cladding inner diameter,	mm	7.76	7.72	7.80
Cladding outer diameter,	mm	9.15	9.10	9.20
Gap,	mm	0.195	0.180	0.210
Gas inner pressure,	MPa	0.6	0.75	0.45
Fuel density,	g/cm^3	10.6	10.8	10.4

PCI. For the cases MAX, MIN it must be kept in mind that they are to be considered only as of very low probability to occur only locally within few FRs. The most important geometrical and technological parameters for the selected variants are given in Table 1.

5. CALCULATED RESULTS

The calculations for the chosen FAs are performed with the standard version of the PIN-micro code.

All presented graphical results are for the AVER case except for Fig. 6 and Fig.12, where results obtained and compared for the MAX and MIN variants are given.

5.1 FUEL ASSEMBLY 1

The calculated results for the FA 1 performance, variant AVER, during a three-year operational period in core and for a prognosed fourth cycle are presented in Fig.1 -- 6. Its reshuffling positions are "out-in-out". This FA has the highest power (25 kW/m) during the second year of operation, compared with the first and the third year (about 20 kW/m).

The maximum fuel temperature during the whole period remains lower than 1000 C. The FGR and the gas pressure are very low, less than 0.4% and 25 bar at the end of the predicted fourth cycle respectively, because of the low temperatures typical for the WWER-440 reactors.

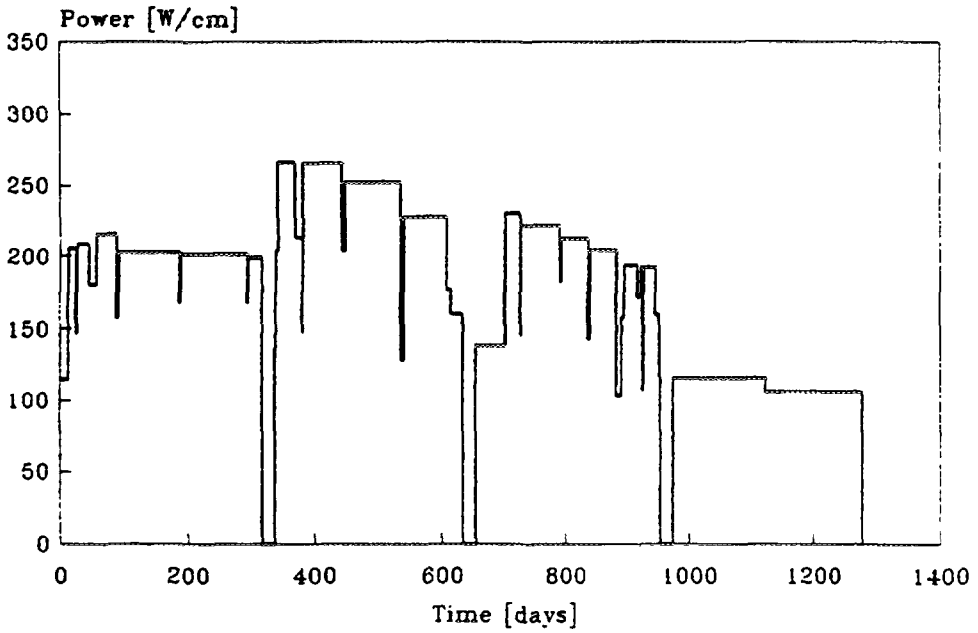

FIG. 1. Power History WWER-440, Assembly 1

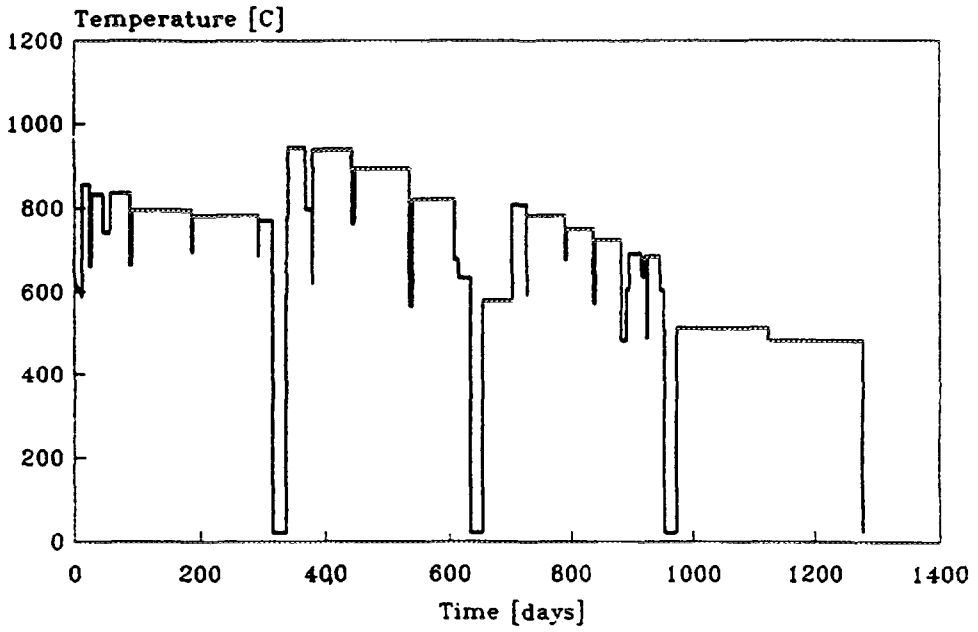

FIG. 2. Fuel Central Temperature WWER-440, Assembly 1

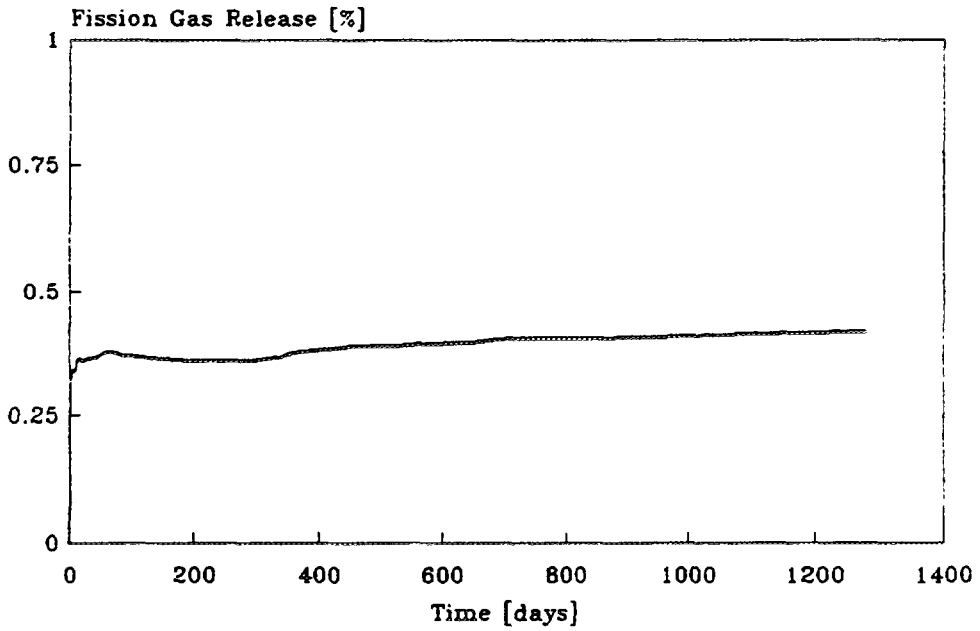

FIG. 3. Fission Gas Release WWER-440, Assembly 1

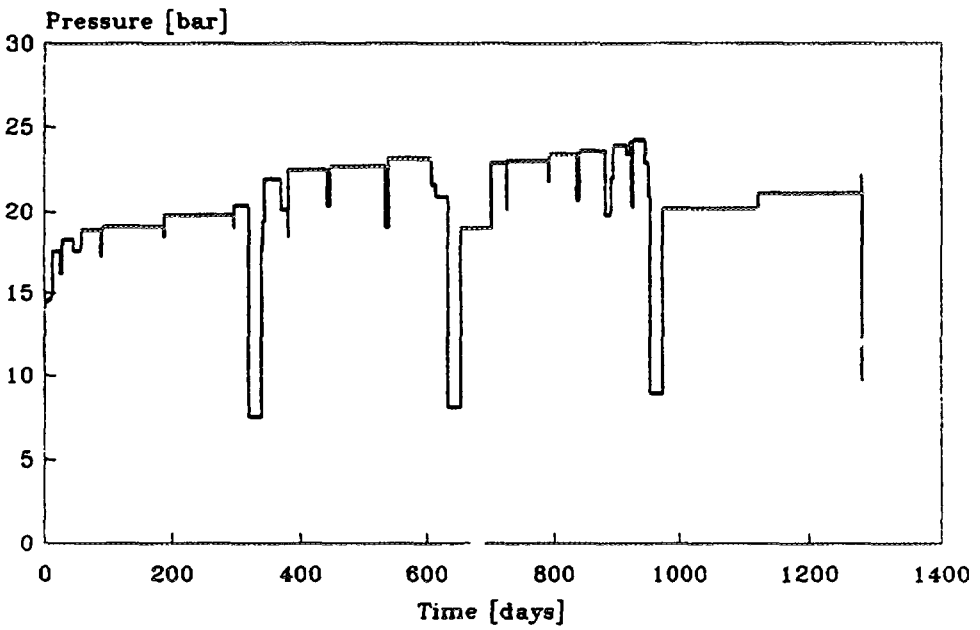

FIG. 4. Gas Pressure WWER-440, Assembly 1

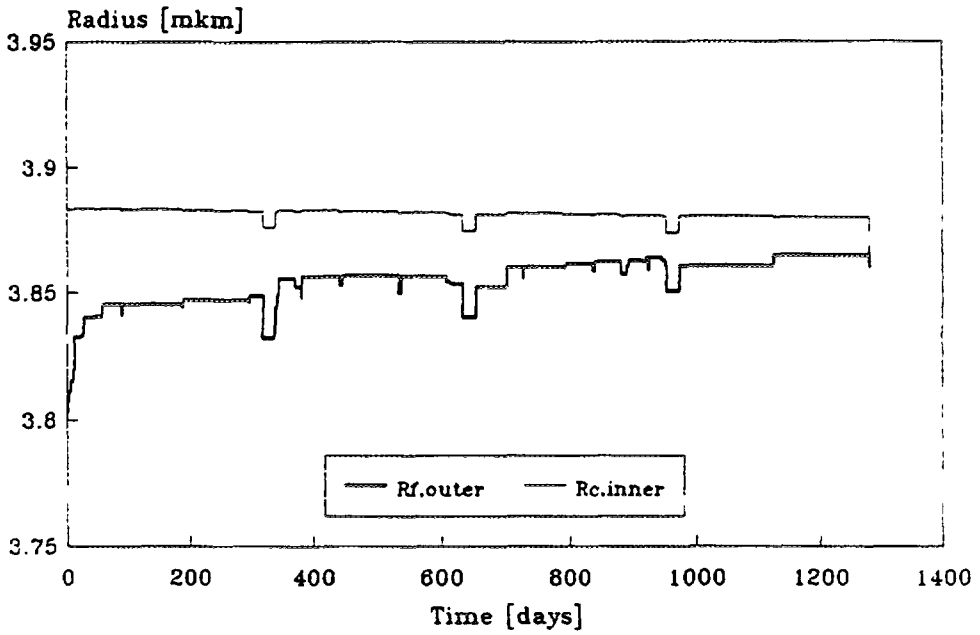

FIG. 5. Fuel & Cladding Radii WWER-440, Assembly 1

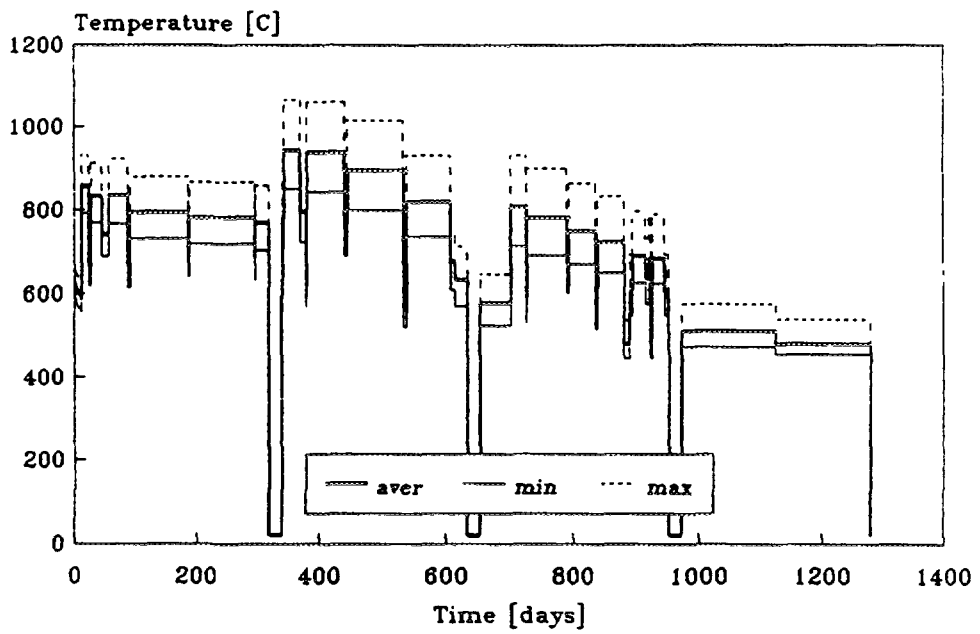

FIG. 6. Fuel Central Temperatures WWER-440, Assembly 1

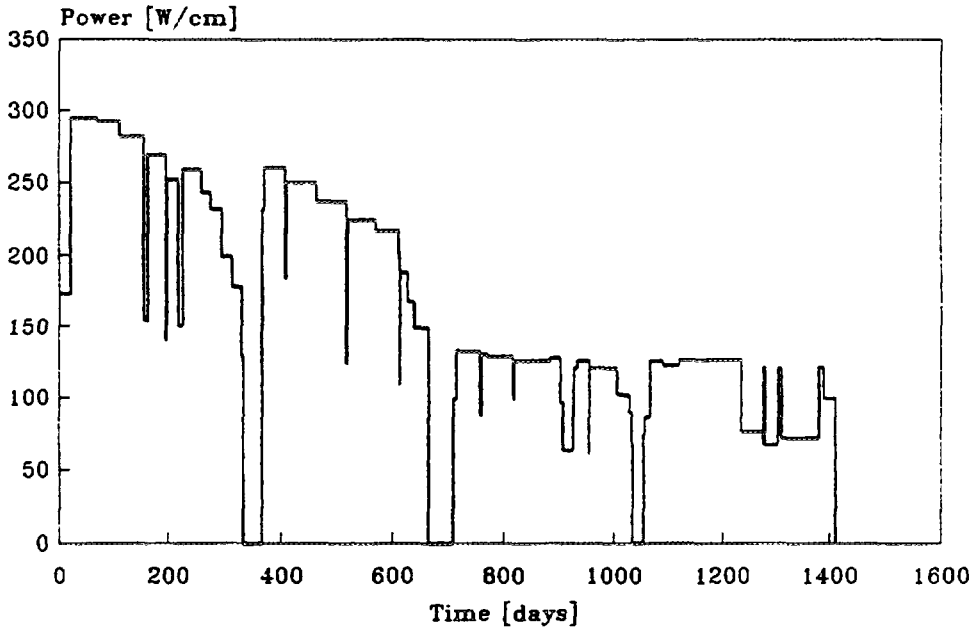

FIG. 7. Power History WWER-440, Assembly 2

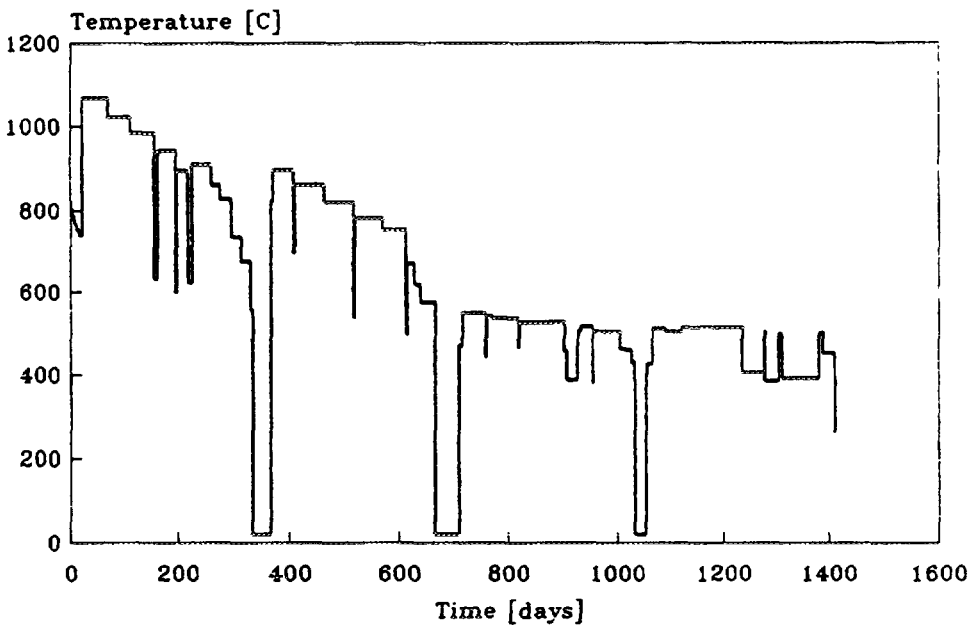

FIG. 8. Fuel Central Temperature WWER-440, Assembly 2

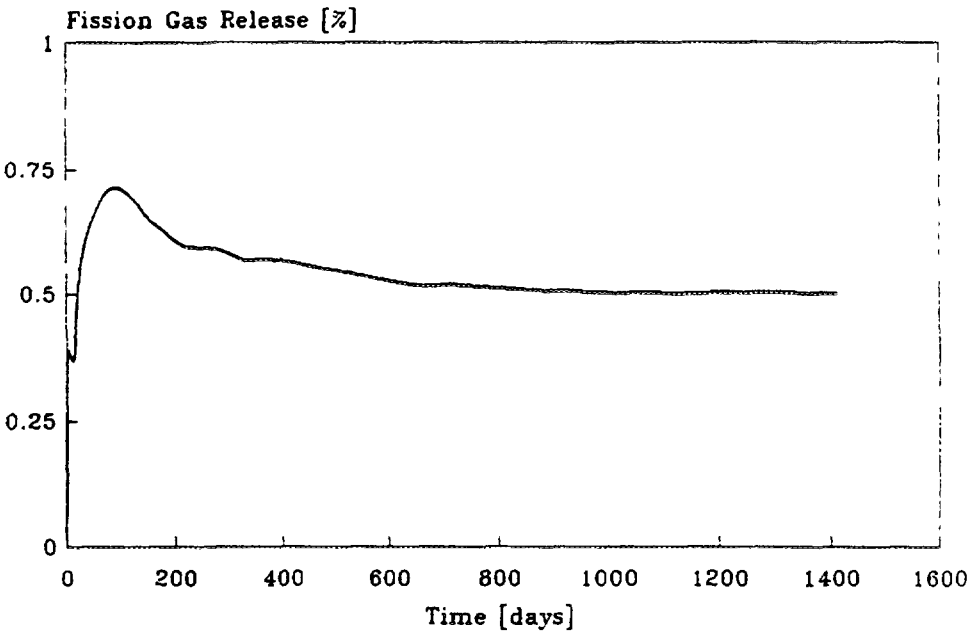

FIG. 9. Fission Gas Release WWER-440, Assembly 2

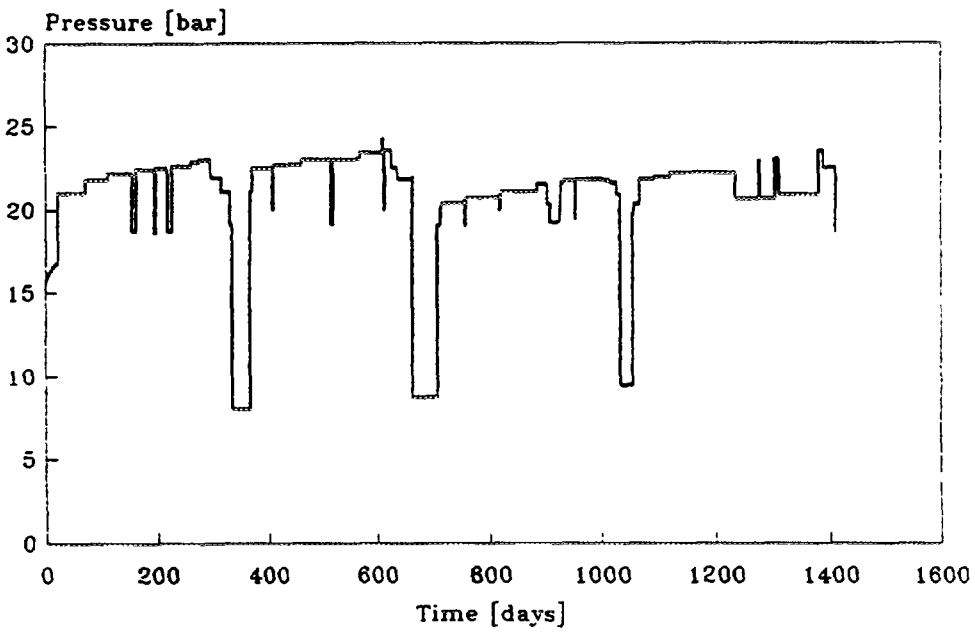

FIG. 10. Gas Pressure WWER-440, Assembly 2

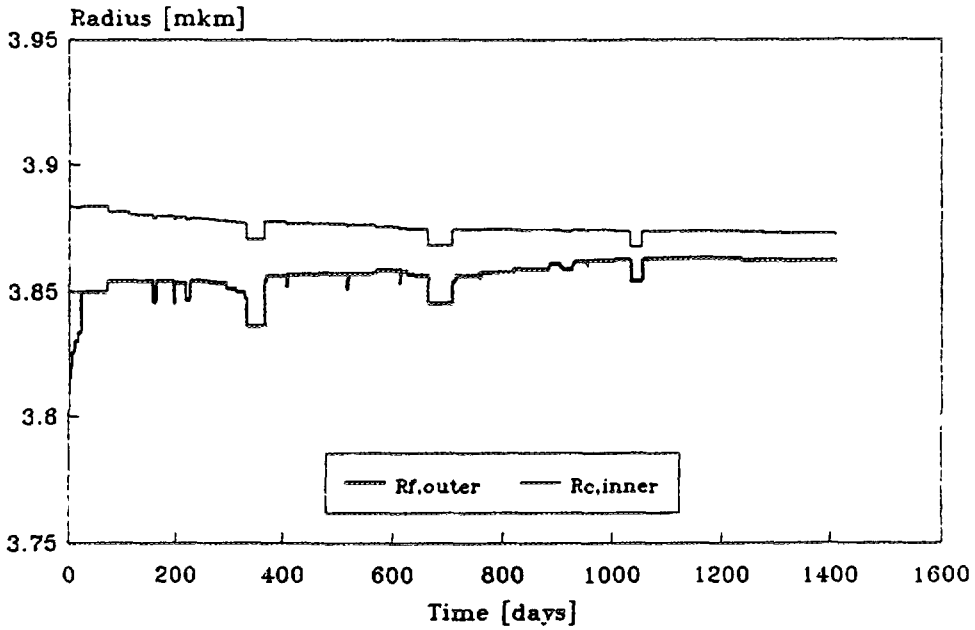

FIG. 11. Fuel & Cladding Radii WWER-440, Assembly 2

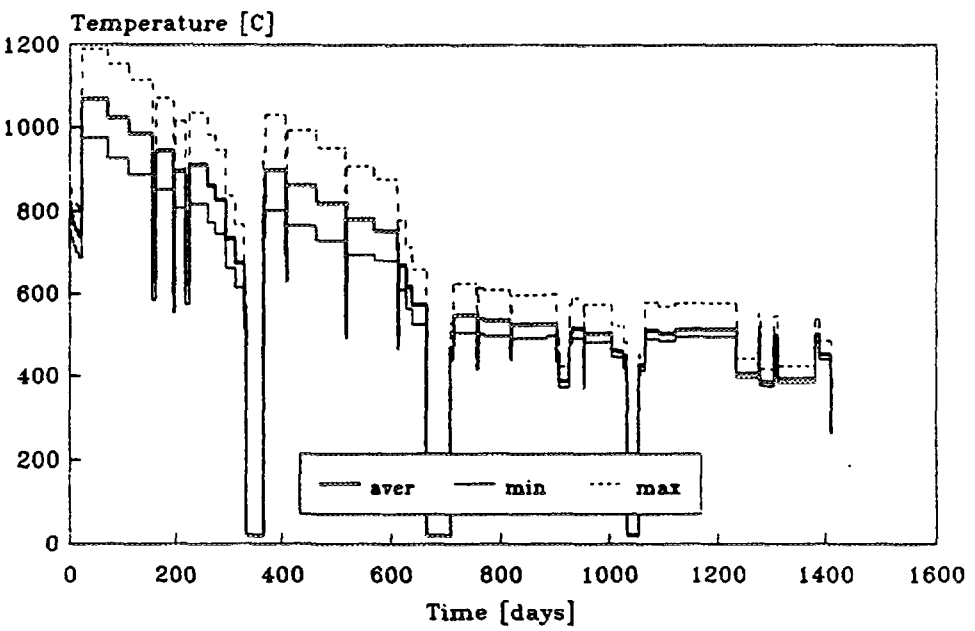

FIG. 12. Fuel Central Temperatures WWER-440, Assembly 2

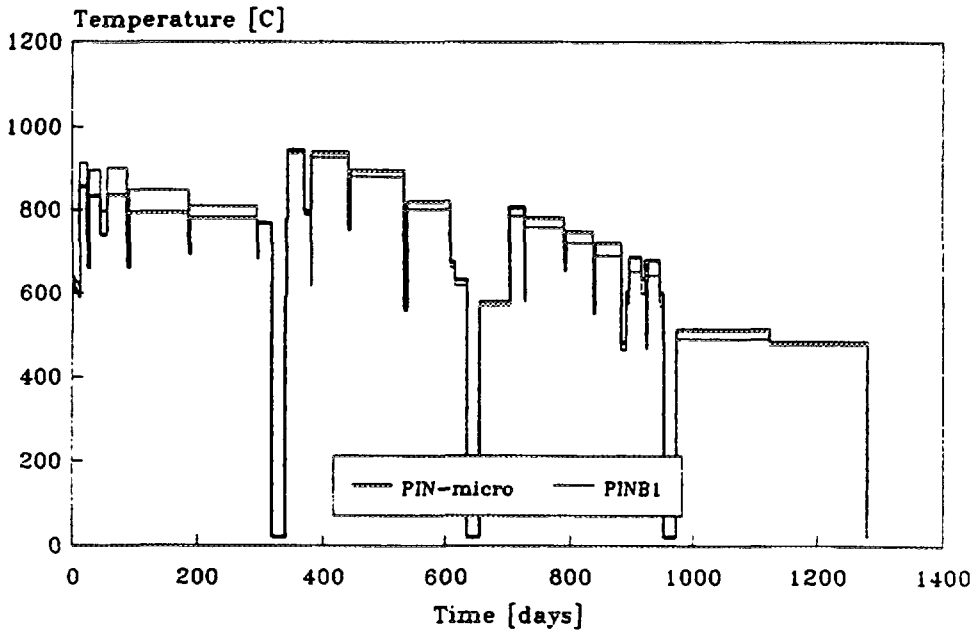

FIG. 13. Fuel Central Temperatures WWER-440, Assembly 1

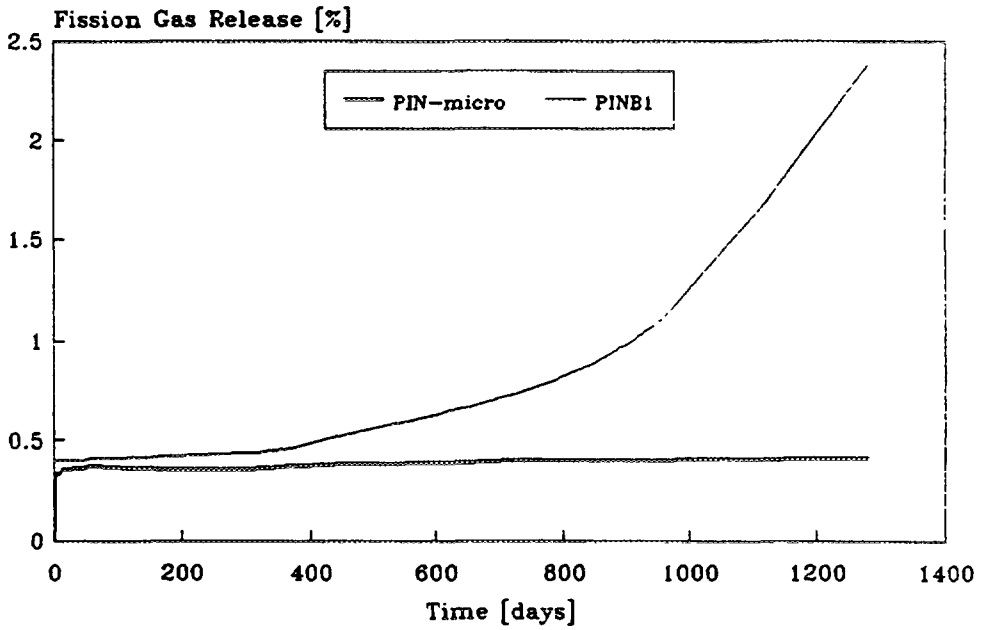

FIG. 14. Fission Gas Release WWER-440, Assembly 1

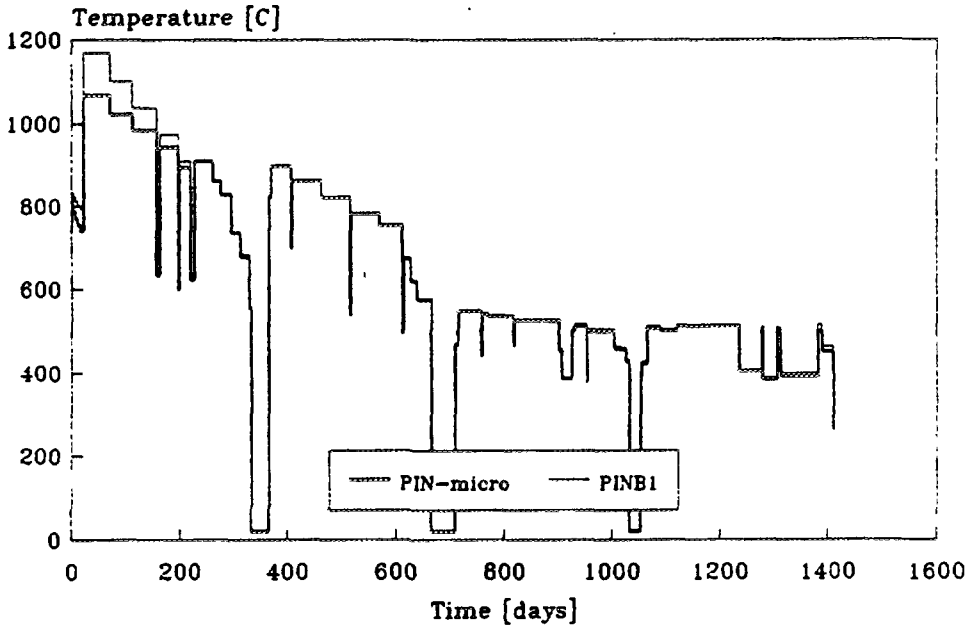

FIG. 15. Fuel Central Temperatures WWER-440, Assembly 2

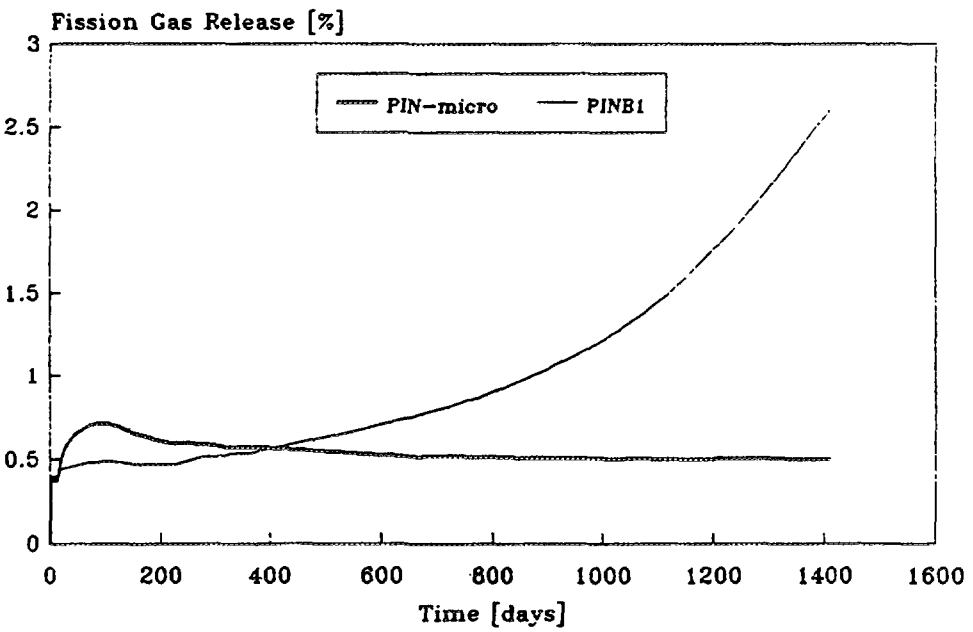

FIG. 16. Fission Gas Release WWER-440, Assembly 2

The results for the fuel and cladding radii are given in Fig. 5 and 6. For the cases AVER and MAX the gap closes gradually due to fuel swelling and fuel and cladding creep and comes to thermal contact during the third cycle. For the case MIN the gap closes at the beginning of the third cycle, but no mechanical contact occurs. The results for the fuel central temperatures for the formulated three variants of input data are given in Fig.6.

The analysis of the FA 1 predicted results show, that the FA has significant safety margins to operate for a fourth cycle in the reactor core.

5.2 FUEL ASSEMBLY 2

The calculated results for FA 2, variant AVER, are shown in fig.7 -- 12. This FA has worked successfully during 1177 effective days and the cladding tightness measurements have given very good results. The reshuffling positions for this FA have been "in-in-out". The linear power during the first and the second cycles is relatively high for WWER-440, about 30 kW/cm and 25 kW/cm, respectively. The maximum fuel temperature is 1050 C for the first year and about 800 C for the second. Because of the low temperatures, the FGR rate remains lower than 0.5% and the gas pressure is less than 23 bar at the end of core life. The results for the fuel and cladding radii and for the gap size show fuel-to-cladding thermal contact occurrence at the middle of the third cycle. For the MAX variant no mechanical contact occurs as well as for the MIN variant up to the end of the core life. The results for the fuel central temperatures for the formulated three variants of input data are given in Fig.12. The threshold temperature for intensive FGR has been reached only for the MAX variant during the first year.

The analysis of the FA 1 results proves its successful and reliable performance and the existence of significant safety margins during the whole core life.

5.3 COMPARISON OF THE PIN-MICRO AND THE PINB1 CALCULATED RESULTS

Some results obtained with the standard PIN-micro and the modified version PINB1 are compared in Figs.13 -- 16. Differences mainly in central fuel temperature and FGR values can be observed. The higher fuel temperatures correspond to the FGR, fuel thermal conductivity and other model modifications, leading to more adequate description of the processes within the fuel rod, accounting for burnup extension.

6. CONCLUSIONS

The presented results allow us to draw the following conclusions:

1. The PIN-micro code predicts adequately the thermal and mechanical behaviour of the WWER fuel rods at the steady-state operational conditions. The original code and its modification have been successfully applied to analyse regimes with extended burnup.
2. The comparison of the calculated results obtained by PIN-micro and the modified version PINB1 show higher fuel temperatures, particularly at low burnups, higher burnups due to the correction of the calculation approach, more adequate FGR, accounting for the first power ramp and for the regimes with extended burnup. The PINB1 version has to be verified against WWER experimental data.
3. The main thermomechanical characteristics predicted by the PIN-micro code prove successful performance of the selected WWER-440 FA 1 and FA 2 for. Sufficient safety margins for the accepted limiting parameters are present during the whole considered period of core operation.

REFERENCES

[1] PAZDERA F., VALACH M. "User's Guide for PIN: A Computer Program for Calculating the Thermal Behaviour of an Oxide Fuel Rod", Report UJV -- 6124T (1982).

[2] BEYER G.E. et al., "GAPCON-THERMAL-2: A Computer Program for Calculating the Thermal Behavior of the Oxide Fuel Rod", BNWL -- 1898 (1975).

[3] STRIJOV P. et al. "Research of VVER-440 Type Fuel Rods in MR Reactor" IAEA International Symposium on Improvements in Water Reactor Fuel Technology and Utilization, Stockholm, Sweden (1986).

[4] SIDORENKO V., SCHEGLOV A., "Neutron-Physical Characteristics of WER Reactor Core Affecting the Fuel Rod Performance", Atomnaya Energiya, Vol.74 (6), (1993).

[5] SCHEGLOV A., PROSELKOV., et al., "Thermophysical Characteristics of Fuel Rods Irradiated at VVER1000 of the Novovoronezh NPP", Atomnaya Energiya, Vol. 74 (5) (1993).

[6] YAMNIKOV V., MALANCHENKO L., "Thermal Conductivity of the Gaseous Mixture Under the Cladding and Its Change With Burnup", Atomnaya Energiya, Vol. 42 (4) (1977).

[7] LUCUTA P., VERRALL R. et al., "Thermal Conductivity and Gas Release From SIMFUEL:", Proceedings of a Technical Committee Meeting, Pembroke, Ontario, Canada (1992)

[8] HARALAMPIEVA TZ., ANTOV A., et al. "Core Design Neutron-Physical Parameters of Kozloduy NPP, Unit 1, 17th Fuel Cycle", National Electric Company, Kozloduy NPP (1994)

AN OVERVIEW OF THE FUELS AND MATERIALS TESTING PROGRAMME AT THE OECD HALDEN REACTOR PROJECT

W. WIESENACK
OECD Halden Reactor Project,
Institutt for Energiteknikk,
Halden, Norway

XA9744797

Abstract

The fuels and materials testing programme of the OECD Halden Reactor Project is aimed at investigations of fuel and cladding properties at high burnup, water chemistry effects and in-core materials ageing problems. For the execution of this programme, different types of irradiation rigs and experimental facilities providing typical power reactors conditions are available. Data are obtained from in-core sensors developed at the Halden Project; these are shortly described. An overview of the current test programme and the scope of the following years are briefly presented.

1. INTRODUCTION

The OECD Halden Reactor Project was established in 1958 as a joint undertaking of the OECD Nuclear Energy Agency through an agreement between nuclear centres of OECD countries sponsoring an experimental research programme with the Halden Boiling Water Reactor (HBWR), which is owned and operated by the Institutt for Energiteknikk, Norway. Following the first agreement, eleven more have been entered into, the present one ending in December 1996. Some joint programme and bilateral test plans reach well beyond that date already now and provide the starting point for further agreements. The reactor, which is continuously renewed and technically upgraded, has a life-time to beyond 2015, making it a reliable facility for execution of the most long-ranging test plans. This is also underlined by the increasing number of member states (15 at present) and the expressed interest of a number of countries to join the Halden Project.

The early research programmes were aimed at demonstrating the operability of HBWR type reactors and included extensive physics and dynamics studies. Then the emphasis gradually shifted to performance investigations on light water reactor fuels and materials and the development of computerised supervision and control systems. The main areas of activity defined in the present three years programme from 1994 - 1996 are

- high burn-up fuel performance, safety and reliability;
- degradation of in-core materials and water chemistry effects;
- man-machine systems research.

From the beginning, fuel performance and reliability investigations were supported by the development and perfection of in-core rod instruments. The measurement capabilities are expanded through development of experimental rig and loop systems where reactor fuel and material can be tested under light water reactor conditions, including prototypic PWR and BWR water chemistries.

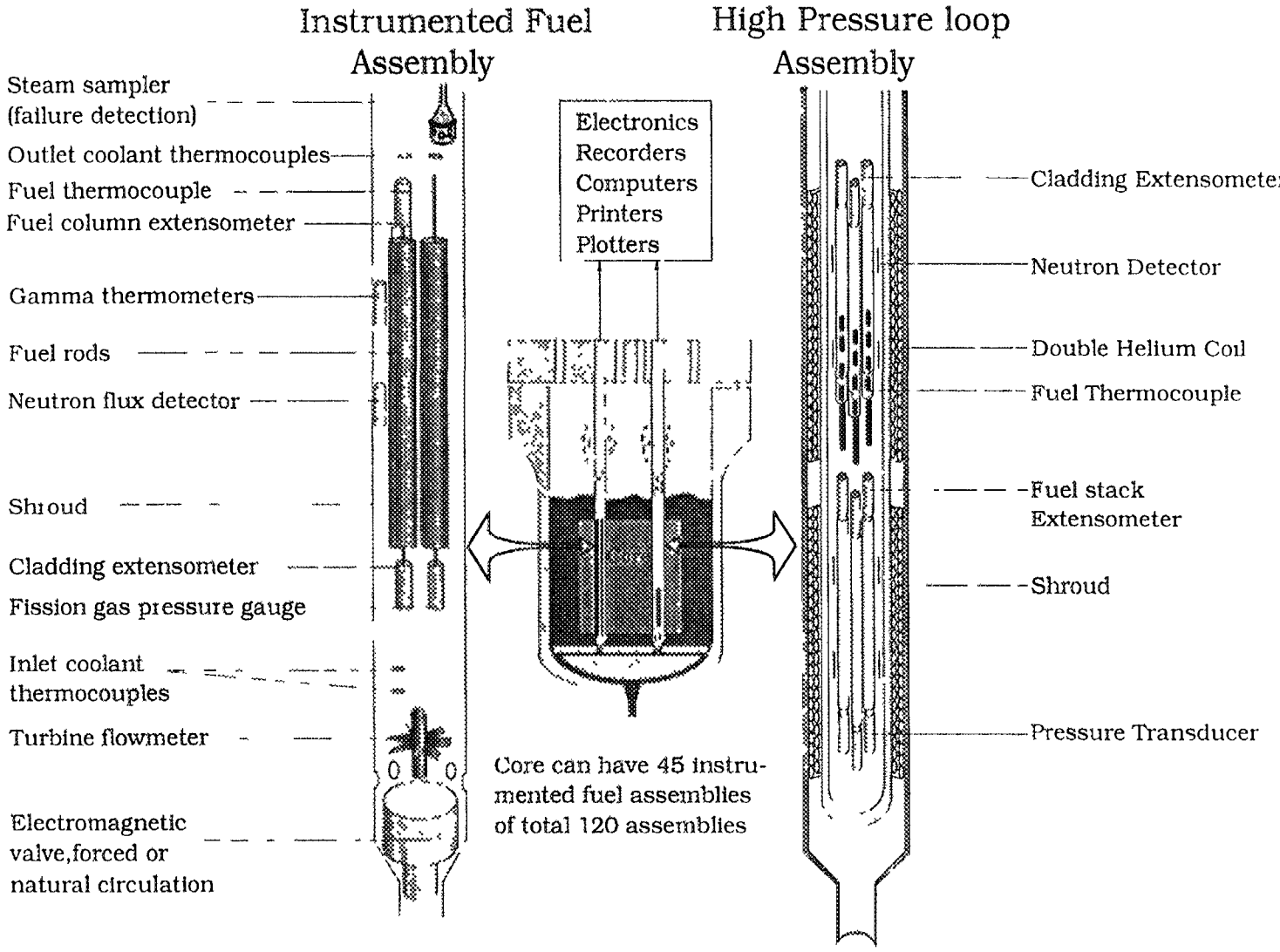

Fig 1 Principal layout of the HBWR with instrumented fuel assemblies (IFAs) The HBWR is a natural circulation boiling heavy water reactor with a maximum power of 25 MW The coolant water temperature is 240 °C corresponding to an operating pressure of 33 6 bar

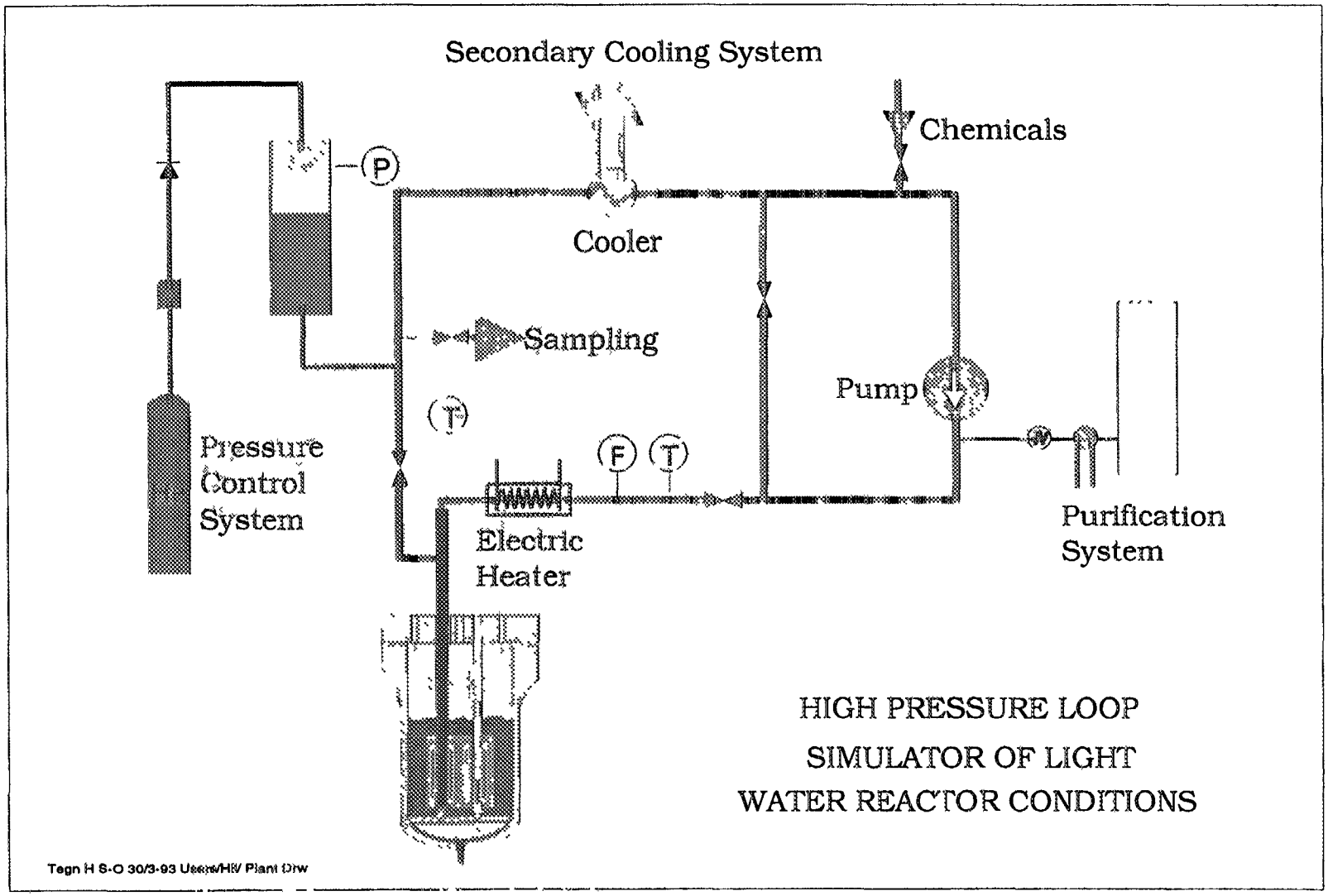

Fig. 2: Schematic representation of a BWR/PWR high pressure light water loop in the Halden Reactor

2. PROGRAMME BASIS

2.1 THE HALDEN REACTOR

The Halden reactor is a heavy water moderated and cooled boiling water reactor. Normal operating conditions are 34 bar system pressure and an associated saturation temperature of the coolant of 240 °C. This is close enough to BWR/PWR conditions for most types of fuel testing. Cladding creep and corrosion are negligible, facilitating the interpretation of experimental results.

About 30 - 35 coolant channels can be occupied by test assemblies, some of them contained in high pressure loops providing thermo-hydraulic and chemistry conditions typical of modern LWRs (Fig. 1). In general, the Halden reactor provides versatile means to simulate conditions prevailing in planned and existing commercial nuclear power plants.

2.2 INSTRUMENTED FUEL ASSEMBLIES AND IRRADIATION RIGS

A number of heavily instrumented rigs to suit different test objectives have been developed. Some of them are illustrated in Fig. 2 or described below. Many other types of rig not further explained here have been utilised over the years. They are associated with testing of fuel from special reactors, e.g. advanced gas-cooled reactor, advanced thermal reactor.

Base irradiation rigs are used mainly for burn-up accumulation prior to specific testing in other rigs.

In the *diameter measurement rig*, a diameter gauge can be moved along the fuel rod during operation. The change of cladding diameter in response to various modes of operation and burnup can be obtained with a micrometer precision. This type of test can also be executed in a high pressure loop as is currently the case with the Halden Projects BWR/PWR Zircaloy creep experiment.

Ramps and overpower tests are effected in various ways: by moving rods from low to high flux positions during operation, using (movable) neutron absorptions shields, depressurising coils with helium-3, or combinations of these. Also daily load following and frequency control modes of operation can be executed with these designs and have in fact been investigated.

The *gas flow rig* allows the exchange of fuel rod fill gas during operation. The gap thermal resistance and its influence on fuel temperatures can thus be determined. It is also possible to analyse swept out fission products for assessment of fuel structural changes and fission gas release [1]. This is an important experimental technique for the high burnup programme currently being executed.

The designs of instrumented fuel assemblies differ largely with specific testing purposes and requirements. Rods can be heavily instrumented with thermocouples, pressure transducers and elongation detectors, and stacked in several clusters.

2.3 INSTRUMENTATION CAPABILITIES

While PIE ascertains the state existing at the end of irradiation, in-core instrumentation provides

- a full description of performance history,
- cross correlation between performance parameters,
- on-line monitoring of the status of the test,
- direct comparison between different fuels and materials.

Trends developing over several years, slow changes occurring on a scale of days or weeks, and transients from seconds to some hours can be captured by the same instrumentation.

The Halden Project has more than thirty years of experience in performing in-core measurements, and a variety of sensors have been developed for this purpose. Most of them are designed and produced in-house, while a few - such as thermocouples and selfpowered neutron detectors - are acquired commercially. They are typically applied in fuel performance investigations:

- *fuel thermocouples* or *expansion thermometers*, which measure the fuel centre temperature;
- *bellows pressure transducers*, which provide data on fission gas release by measuring the rod inner pressure;
- *fuel stack elongation detectors*, with which densification and swelling behaviour can be assessed;
- *cladding diameter gauge* to determine radial deformations as function of power, holding time after ramping, and burn-up;
- *cladding elongation detectors*, which provide data on the onset and amount of pellet - cladding interaction, permanent deformation as well as relaxation capabilities of fuel and cladding as function of power and burn-up.

Fuel thermocouples, pressure transducers and cladding elongation detectors can be utilised for re-instrumentation of fuel segments previously irradiated in LWRs. This techniques has been applied in a number of tests and become more and more important for the investigation of high burnup fuel performance [2].

3. FUELS AND MATERIALS TESTING

The experimental programme carried out at the OECD Halden reactor Project is aimed at providing information and experience which will assist in enhancing safety and reliability of today's reactors as well as contributing to the continued development of present and next generation nuclear power plants. The programme is defined in close interaction with the Halden Projects participants and reflects the nuclear community's interests especially in the areas of extended burnup, degradation of in-core materials and water chemistry effects.

3.1 EXTENDED BURNUP FUEL PERFORMANCE

Fuel performance is in general the result of a complex interrelation of many different phenomena. With their extensive in-pile instrumentation, the tests at the Halden Project provide a unique data source for a mechanistic understanding. Attention was focused during the last years on the behaviour of standard UO_2 fuel; the current programme also includes studies of gadolinia bearing fuel which is increasingly utilised in commercial plants for achieving high burnup.

UO_2 Conductivity degradation is being studied in a number of tests by evaluating the change of fuel centre temperature occurring with increasing burnup. The results of a dedicated experiment have been reported in [2]. A goal of continued irradiation is to explore whether additional mechanisms arise above 70 MWd/kg UO_2, i.e. a general grain subdivision and depletion of xenon as already observed in the high burnup rim of LWR fuel.

Fission gas release is investigated with emphasis on retention/release properties at high burnup ($>$ 60 MWd/kg UO_2). The release behaviour of fuel variants is explored at different temperatures under isothermal conditions.

INSTITUTT FOR ENERGITEKNIKK
HALDEN REACTOR PROJECT

Double Cantilever Beam (DCB) Specimen Geometry

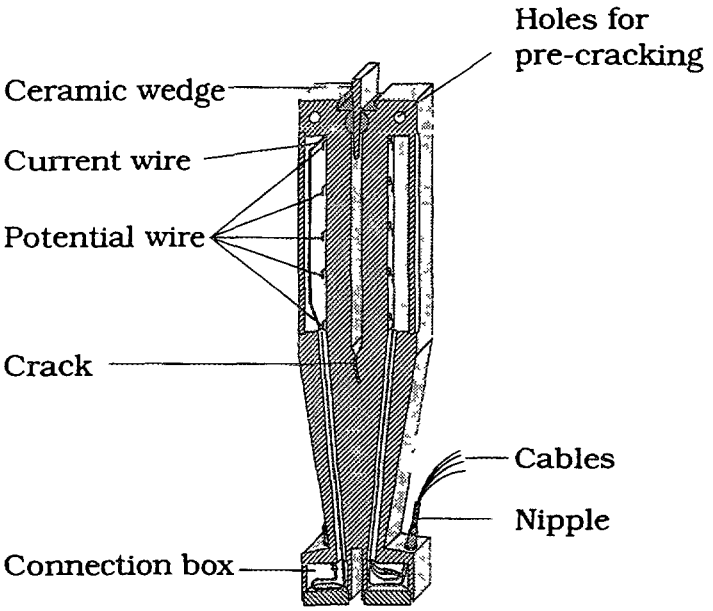

Each of the fatigue pre-cracked DCBs is loaded to a stress intensity of 37.4 MPa $\sqrt{m}$ by means of a ceramic wedge.

The DCBs are instrumented for on-line crack propagation monitoring by the DC potential drop method.

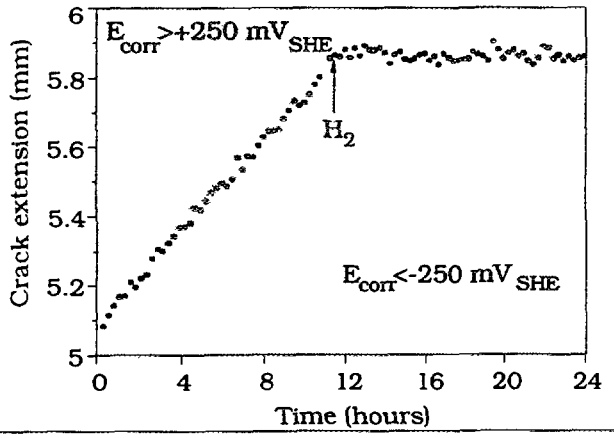

The benifits of hydrogen in mitigating crack propagation are clearly apparent. An example is illustrated in the figure which shows the crack propagation rates recorded for thermally sensitised 304 SS under NWC and HWC conditions.

Fig. 3: Instrumented Double Cantilever Beam (DCB) specimen used in Irradiation Assisted Stress Corrosion (IASCC) studies. Crack propagation is much slower in hydrogen water chemistry compared to normal water chemistry.

Fuel dimensional changes affect thermal properties and may together with cladding creepdown increase the mechanical loading on the rod during service. High burnup swelling behaviour is also relevant to the rod overpressure/lift-off criterion. The most direct measurements of fuel dimensional changes and PCMI are obtained with fuel stack and cladding elongation detectors. Complementary information from a number of tests is available through temperature and pressure measurements and PIE (Kjeller hot lab).

Cladding creep is measured in-pile on BWR and PWR rods as function of stress level and direction. The repeated occurrence of primary creep after stress reversals has been established with this test.

3.2 DEGRADATION OF IN-CORE MATERIALS AND WATER CHEMISTRY EFFECTS

In-core materials are subjected to a variety of influences affecting their properties. The impact on safe and reliable operation of nuclear power plants is therefore an important licensing consideration. Aspects and mechanisms of in-core materials performance as influenced by irradiation and chemistry effects are thus studied in a number of experiments at the Halden Project. The tests are conducted in several light water reactor loops providing typical and prototypical BWR/PWR conditions.

Zircaloy cladding corrosion has been investigated in a series of tests aimed at assessing the effect of water chemistry variables and operating parameters on the corrosion performance of different zirconium alloys under BWR conditions. The PWR facilities at the Halden Project have been used to assess the influence of thermo-hydraulic conditions and high lithium concentrations on Zircaloy cladding corrosion, using segments pre-irradiated in a commercial reactor [3].

Water chemistry effects are also studied with the objective to reduce primary system radiation levels and the personal doses in nuclear power plants [4]. Crud deposition and water chemistry investigations are supported by the development of methods for local electro-chemical potential measurements and the characterisation of the water chemical status.

In-core materials degradation is being addressed in consecutive experiments were irradiation assisted stress corrosion cracking of several in-core materials is investigated [5]. The specimens have the shape of Double Cantilever Beams (DCB, Fig. 3) and are instrumented for on-line crack propagation monitoring by the DC potential drop method. The beneficial influence of hydrogen (lower ECP) in mitigating crack propagation are clearly apparent (Fig. 3).

Hydriding and hydrogen migration affecting cladding mechanical properties, and the possible synergism between corrosion and hydrogen pick-up is an expanding field of experimental activity at the Halden Project. A test foreseen for 1995 will include standard and low-tin Zry-4 as well as fresh and irradiated material.

REFERENCES

[1] KOLSTAD, E., VITANZA, C.: Fuel rod and core materials investigations related to LWR extended burn-up operation; Journal of Nuclear Materials 188 (1992), pp 104-112

[2] WIESENACK, W.: Experimental techniques and results related to high burn-up investigations at the OECD Halden Reactor Project; IAEA Technical Committee Meeting on fission gas release and fuel-rod chemistry related to extended burn-up (IAEA-TECDOC-697), Pembroke, Canada, 1992

[3] KARLSEN,T., VITANZA, C.: Effects of pressurised water reactor (PWR) coolant chemistry on Zircaloy corrosion behaviour; Zirconium in the nuclear industry: tenth international symposium, ASTM STP, Philadelphia, 1994

[4] SYMONS, W.J., KARLSEN, T., GUNNERUD, P.: Materials degradation and activity transport studies at Halden; International symposium on activity transport in water cooled nuclear power reactors, Ottawa, Canada, 1994

[5] VITANZA,C. KARLSEN, T.: In-pile IASCC test programme in the Halden reactor; Sixth international symposium on environmental degradation of materials in nuclear power systems - water reactors; Sand Diego, California, 1993.

STUDSVIK'S FUEL R&D PROJECTS

M. GROUNES
Studsvik Nuclearr AB,
Nykoping, Sweden

Abstract

The report reviews some recently performed, ongoing and planned fuel R&D projects, executed by Studsvik Nuclear AB, a subsidiary of Studsvik AB. Data from these projects are used as experimental support for fuel modelling at high burnup. Much of Studsvik Nuclear's R&D work has been concentrated on fuel testing, which can be made in the R2 test reactor with high precision under realistic water reactor conditions. This type of work was started in the early 1960s. The fuel testing projects executed at Studsvik have been organised under three different types of sponsorship:

- International (multilateral) fuel projects: jointly sponsored internationally on a world-wide basis, with project information remaining restricted to the project participants throughout the project's duration and for some pre-determined time after project completion.

- Bilateral fuel projects: sponsored by one single organisation, or a few co-operating organisations, with project information remaining restricted to the sponsor, sometimes published later.

- In-house R&D work: sponsored by Studsvik Nuclear.

The fuel testing activities can be divided into a number of well-defined steps as follows:

- Base irradiation, performed in a power reactor, or in Studsvik's R2 test reactor.

- Power ramping and/or other in-pile measurements, performed in Studsvik's R2 test reactor. Non-destructive testing between different phases of an experiment, performed in Studsvik's R2 reactor pool, or in Studsvik's Hot Cell Laboratory.

- Destructive post-irradiation examinations, performed in Studsvik's Hot Cell Laboratory, or in the sponsor's hot cell laboratory.

Fuel testing in the R2 reactor is usually performed on fuel segments (rodlets) of 300-1000 mm length. However, tests have also been performed on full-size demonstration reactor fuel rods with up to 2.5 m length. In those cases only the lower 0.6 meters were irradiated. Irradiation at constant power is performed in boiling capsules (BOCA rigs) in fuel element positions, or in pressurised water in-pile loops operating under BWR or PWR pressure and temperature conditions. Fuel examination can also be performed on standard (full-size) fuel rods from power reactors, which are investigated in the Hot Cell Laboratory. If required, some types of tests could also be performed on such fuel rods in the R2 test reactor. Short fuel rodlets, suitable for ramp testing and other on-line measurements in the R2 test reactor, can now be fabricated from irradiated full-size power reactor fuel rods by the STUDFAB refabrication process. The following types of projects will be reviewed: ramp resistance studies; rod overpressure studies; defect fuel degradation studies; new types of fuel tests.

SUMMARY

A review of some bilateral fuel R & D projects and the following international projects, conducted under the management of STUDSVIK NUCLEAR since 1975, is presented: INTER-RAMP, OVER-RAMP, DEMO-RAMP I, DEMO-RAMP II, SUPER-RAMP, SUPER-RAMP EXTENSION, SUPER-

RAMP II/9x9, TRANS-RAMP I, TRANS-RAMP II, TRANS-RAMP III, TRANS-RAMP IV, ROPE I, ROPE II, DEFEX, DEFEX II and ULTRA-RAMP. A number of new prospective fuel R & D projects are also discussed.

1. INTRODUCTION

Since the early 1970's, a long series of bilateral and international fuel R&D projects, primarily addressing the PCI/SCC (Pellet-Clading Interaction/Stress Corrosion Cracking) failure phenomenon have been conducted under the management of STUDSVIK NUCLEAR. These projects have been pursued under the sponsorship of different organizations: the bilateral projects mainly by fuel vendors and the international projects by different groups of fuel vendors, nuclear power utilities, national R&D organizations and, in some cases, licensing authorities in Europe, Japan and the U.S. In most of the projects the clad failure occurrence was studied under power ramp conditions utilizing the special ramp test facilities of the R2 test reactor. The current projects are not limited to PCI/SCC studies but some of them also include other aspects of fuel performance, to be discussed below. During the late 1970's and 1980's the series of international PCI ramp projects branched out in two directions. One series was initially concentrated on the PCI phenomena under normal operational conditions in different types of BWR and PWR fuel rods subjected to increased burn-up under normal operational conditions. These projects were in a broad sense aimed at decreasing the fuel costs by increases in fuel utilization and reactor availability. Most of the bilateral fuel projects fell into this category. The other series of international projects was concentrated on more safety-oriented issues, aimed at providing data for fuel-related safety considerations. The first-mentioned series of international projects includes the INTER-RAMP, OVER-RAMP, DEMO-RAMP I, SUPER-RAMP, SUPER-RAMP EXTENSION and SUPER-RAMP II/9x9 projects. The second series includes the INTER-RAMP, DEMO-RAMP II, TRANS-RAMP I, TRANS-RAMP II, TRANS-RAMP III and TRANS-RAMP IV projects.

Presently a new international project combining the features of these two series, is under discussion: the ULTRA-RAMP project.

In later years two other types of fuels R&D project have been introduced: end-of-life rod overpressure studies and defect fuel degradation experiments. The end-of-life overpressure projects were designated ROPE I and ROPE II (Rod OverPressure Experiments). The defect fuel degradation projects are designated DEFEX I and DEFEX II.

Furthermore other types of projects are also under discussion. An overview of the 11 international projects that have been completed and 7 of the projects that are currently in progress or planned is given in Tables I and II.

It should be noted that reports of both the existence of bilateral projects and data from such project are only published when the sponsors agree to such reporting. All bilateral project information mentioned in this report has been published by the sponsors (some- times in co-operation with Studsvik Nuclear) in the open literature.

2. RAMP RESISTANCE - BWR FUEL

A quite large number of early ramp tests of ABB Atom (then ASEA-ATOM) BWR rods have been reported in the literature[1]. Early tests on fuel rods for the Italian CIRENE reactor were also reported[1].

Experiments with a large number of fuel rodlets in connection with the development of GE's barrier fuel have been described in the literature [1-4].

In connection with U.S. DOE's Fuel Performance Improvement Program, FPIP, manged by ENC (now Siemens Power), a number of fuel rodlets were ramp tested in R2 [5].

Table I.
Overview of STUDSVIK NUCLEAR's Completed International Power Ramp Test Projects 1975-93

Project (duration)	Fuel Type (No of rods)	Base Irradiation (MWd/kg U)	Research Objectives
INTER-RAMP (1975-79) treatment, Modeling data	BWR (20)	R2 (10-20)	Failure threshold & mechanism, Clad heat
OVER-RAMP (1977-80)	PWR (39)	Obrigheim (10-30) BR-3 (15-25)	Failure threshold, Design parameters, Modeling data
DEMO-RAMP I (1979-82)	BWR (5)	Ringhals I (15)	PCI remedies (annular, niobia doped pellets)
DEMO-RAMP II (1980-82)	BWR (8)	Würgassen (25-29)	Failure threshold, PCI damage by over-power transients
SUPER-RAMP (1980-83)	BWR (16)	Würgassen (30-35) Monticello (30)	Failure threshold, High burn-up effects, PCI remedies, Safe ramp rate, Gd fuel
	PWR (28)	Obrigheim (33-45) BR-3 (28-33)	Design parameters, Modeling data
SUPER-RAMP EXTENSION (1984-86)	BWR (9)	Oskarshamn 2 (27-31)	Safe ramp rate
	PWR (4)	Obrigheim (30-35)	Resolve unexplained failure resistance
TRANS-RAMP I (1982-84)	BWR (5)	Würgassen (18)	Failure boundary, Crack initiation & propagation, Structural changes, Fission gas release, Modeling data.
TRANS-RAMP II (1982-86)	PWR (7)	Zorita (30)	Failure boundary, Crack initiation and propagation, Structural changes, Fission gas release, Modeling data

Project (duration)	Fuel Type (No of rods)	Base Irradiation (MWd/kg U)	Research Objectives
SUPER-RAMP II/9x9 (1987-90)	BWR (4)	Dresden (30)	PCI performance
ROPE I (1986-93)	BWR (4)	Ringhals (36)	Investigate clad creep-out as a function of rod overpresssure
TRANS-RAMP IV (1989-94)	PWR (7)	Gravelines (20-25)	Influence of non-penetrating cracks on PCI failure resistance

Table II.
Overview of STUDSVIK NUCLEAR's Ongoing and Planned International Fuel R&D Projects

Project (duration)	Fuel Type (No of rods)	Base Irradiation (MWd/kg U)	Research Objectives
ROPE II (1990-94)	PWR (6)	Ringhals Obrigheim (> 40)	Investigate clad creep-out as a function of rod over-pressure
DEFEX (1993-95)	BWR (6)	No	Study secondary damage formation in fuel rods with simulated fretting defects
TRANS-RAMP III 1995-97)*) penetrating cracks on PCI	BWR (ND)*)	ND	Same as TR IV but BWR (NS, fuel: Influence of non-failure resistance
DEFEX II 1995-97)	BWR PWR (ND)	ND (10-20)	Same as DEFEX but (NS, irradiated fuel.
SUPER-RAMP III/10x10 (NS, 1995?)*)	BWR (ND)	ND*) (40)	PCI performance
Enthalpy determination 1995?)	BWR PWR different fuel types	ND (10-40?)	Determine differences in (NS, stored energy between (ND)
Post DO/DNB behavior (NS,1996?)	BWR PWR (ND)	ND (10-40?)	Determine ramp resistance after short periods of Post DO/DNB operation.

*)
NS = Not yet started
ND = Not decided

As part of joint programs sponsored by Hitachi and Toshiba with NFD and Japanese BWR utilities and in some cases ASEA-ATOM (now ABB Atom), in some cases GE, a large number of segmented fuel rods were irradiated in Swedish and U.S. power reactors and then ramp tested in R2 [6-9].

In a Japanese national program sponsored by Hitachi, Toshiba and NFD, a number of fuel rodlets from a Japanese power reactor have been ramp tested in R2 [10].

The first of STUDSVIK NUCLEAR's international fuel projects, INTER-RAMP, was executed in 1975-79 under the sponsorship of 14 organizations from 9 countries. The results have been described [11,12]. The main objectives of the program were to investigate systematically the failure propensity and associated phenomena of well-characterized BWR fuel rodlets when subjected to fast-overpower ramps under relevant and well-controlled experimental conditions.

The DEMO-RAMP I project was executed in 1979-82. The results have been described [13]. The main objective of this program was to investigate the effects of two PCI remedies, annular pellets and niobia doping of the UO_2, on the ramp behavior, especially the fission-product release and the pellet-cladding mechanical interaction (PCMI), of 8x8 type fuel rodlets.

The SUPER-RAMP project was executed in 1980-83. The results have been described [14, [15]. The main objective of this project, which was co-sponsored by 20 organizations from 11 countries, was to make a valid contribution to the general understanding of the PCI phenomenon for commercial type LWR fuel rods at high burnup levels under power ramp conditions.

For the BWR subprogram[2] the more specific objectives were to

- Establish the PCI failure threshold for standard type test fuel rods on fast power ramping at burnup levels exceeding about 30 MWd/kgU.
- Identify any change in failure propensity or failure mode as compared to the failure behavior at lower burnup levels.
- Establish a failure-safe reduced power ramp rate for passing through the PCI failure region.

In the SUPER-RAMP EXTENSION project, which was executed in 1984-86 further ramp tests were performed.

In the SUPER-RAMP II/9x9 project, executed in 1987-90, the failure boundary of 9x9 type fuel rodlets, irradiated in a commercial power reactor to a burnup of 25 MWd/kgU, was determinad [16].

3. RAMP RESISTANCE - PWR FUEL

In a joint program sponsored by MHI and Japanese PWR utilities fuel rodlets were irradiated in R2 and then ramp tested [17]. In another program sponsored by MHI, NFI and Japanese PWR utilities fuel rods, previously irradiated in the closed down BR3 reactor, were irradiated further in R2 and then ramp tested. Some results have been reported [18].

In a recent program sponsored by NFI in Japan and BWFC and other organizations in the U.S., segmented PWR fuel rods, irradiated to a high burnup, above 60 MWd/kgU, were ramp tested in R2 19.

---

[1] A list of references can be obtained from the author.

[2] The PWR Subprogram of the SUPER-RAMP project is discussed in Section 3 below.

The second of STUDSVIK NUCLEAR's international fuel projects, OVER-RAMP, was executed in 1977-81. The results have been described 20, 21. The overall objective was to increase the general understanding of the PCI phenomenon for commercial type PWR fuel rods under power ramp conditions. The main technical objectives were to

- Establish the power ramp failure threshold as a function of burnup.
- Determine the influence on the failure threshold of various design, material, pre-ramp irradiation and ramp testing parameters.
- Characterize failure mechanisms and pre-stages of fuel failure.
- Provide data for PCI failure analyses and predictive fuel modeling.

In the SUPER-RAMP project, already discussed in Section 1 above, there was also a PWR subprogram. The objectives of that subprogram were to

- Establish the PCI failure threshold for standard type PWR test fuel rods on fast power ramping at burnup levels exceeding about 30 MWd/kgU and preferably 40 MWd/kgU.
- Identify any change in failure propensity or failure mode as compared to the failure behavior at lower burnup levels.
- Establish any possible increase in failure resistance of selected candidate PCI remedy designs.

In order to investigate the difference between the various types of fuel further rods were investigated in the SUPER-RAMP EXTENSION project, discussed in Section 2 above.

There has been a considerable interest in the ramp resistance of PWR fuel after still higher burnups, above 40 or even above 55 MWd/kgU. "Pre-project" discussions regarding the prospective ULTRA-RAMP project are currently in progress (see Section 8).

4. SAFETY-ORIENTED RAMP RESISTANCE STUDIES

As part of early LOCA-oriented domestic programs, the redistribution of volatile fission products was studied 22. In recent years this type of studies have continued with fuel rodlets with successively higher burnups 23-25.

In a series of international fuel research projects (the INTER-RAMP, DEMO-RAMP II, TRANS-RAMP I, TRANS-RAMP II and TRANS-RAMP IV projects) it was demonstrated by means of power transient tests (intentionally interrupted power ramp tests) that when LWR test fuel rods were exposed to overpower ramps of increased severity, they exhibited a regular Pellet-Clad Interaction (PCI) failure progression. A higher transient peak power level resulted in an earlier fission product outleakage from the fuel rods. Stress corrosion cracks (SCC) initiated promptly on fast upramping, i.e. within the order of seconds and penetrated the cladding wall within about a minute. Depending on the actual power "over-shoot" and the time spent beyond the failure threshold, the transient passed consecutively through a number of power-time regions defining the progressive steps of the failure process.

Some of the LWR fault transients of the types that might be expected to occur once in a reactor year or once in a reactor lifetime carry a potential for causing PCI fuel clad damage or failure (i.e. through-wall crack penetration) on surpassing the PCI failure threshold. A question of prime concern is then whether a fast single transient of the type mentioned will result in fuel failure due to PCI, eventually followed by a release of radioactivity to the coolant.

In the INTER-RAMP (IR) Project, executed during 1975-79 11, 12, BWR fuel rods were subjected to power transients of varying "over-power" levels beyond the PCI failure threshold, where cladding failure and fission product release occur after a sufficient time. The results demonstrated a systematic time dependence of the fission product release to the coolant from the failed fuel rods. An increase in the power "over-shoot" of 5 kW/m caused a decrease of the time to fission product release by a factor of about 10.

In the DEMO-RAMP II (DRII) Project, 1980-1982 26, BWR fuel rods of intermediate burnup levels were subjected to intentionally interrupted short-time power transients at linear heat ratings a few kW/m above the PCI failure threshold. No cladding failures were detected after the transients but a large number of non-penetrating (incipient) cracks were observed. They had been formed very rapidly, within a minute. These cracks could be observed by destructive post-irradiation examinations only. The crack depths ranged from 10 to 60 percent of the cladding wall thickness.

In the TRANS-RAMP I (TRI) Project, 1982-1984 27, BWR fuel rods of intermediate burnup levels were subjected to simulated short time power reactor transients of a wide range of "over-powers" but at characteristic very fast ramp rates, in the range of 10 000 W/cm,min. The test results were similar to the DR II results and permitted a tentative interpretation of the PCI failure progression in terms of well-separated power/time boundaries defining 1) crack initiation at the inside surface of the cladding, 2) through-wall crack penetration and 3) out-leakage of fission products to the coolant water.

In the TRANS-RAMP II (TRII) Project, 1984-1986 28, PWR fuel rods of higher urnups, approximately 30 MWd/kgU, were subjected to short power transients corresponding to a steam line break event in PWRs. The PCI failure progression diagram obtained was quite similar to the one obtained from the TRI project for BWR fuel rods, indicating comparable times to failure for the two fuel designs, i.e. approximately one minute.

The crack initiation and penetration processes can only be detected by special hot cell laboratory or test reactor techniques. The delay of the fission product release indicates that in power reactors cladding failures that occur during fast transients and terminate before any outleakage of fission products may go undetected until manifested in later operational manoeuvers.

In the TRANS-RAMP IV (TRIV) project, still confidential, the influence of non-penetrating (incipient) cladding cracks on the PCI failure resistance during an anticipated subsequent transient occuring later in life was studied 29.

Experience from the earlier STUDSVIK projects mentioned, as well as from power reactor operation, shows that non-penetrating cladding cracks form readily during certain short-time power transients and cracks initiate already within 5-10 seconds. However, it is conceivable that these non-penetrating (incipient) cracks will not propagate further during continued operation, owing to some passivation effect. The main purpose of the TRANS-RAMP IV project was to investigate experimentally the propensity for through-wall crack penetration of such initially non-penetrating (incipient) PCI cracks following a second power transient.

A corresponding BWR project, TRANS-RAMP III (TRIII), is contemplated but is awaiting the publication of the TRIV project.

STUDSVIK NUCLEAR has also initiated some in-house R&D activities in this connection. There is a need for an improved LWR fuel design, resistant not only to operational power maneouvers but also to off-normal high power transients. STUDSVIK NUCLEAR has been working on such a potential remedy design, rifled cladding, for many years 30, 31. One approach, using a combination of rifled cladding and graphite coated fuel pellets under otherwise normal design conditions has so far demonstrated 100% failure resistance under very severe power transient test conditions. Although the test results are few so far, the remedy approach adopted seems promising. Fuel modeling has also indicated superior behavior in this and other respects 32, 33.

5. STUDIES OF "LIFT-OFF" PHENOMENA

When LWR fuel is used at higher and higher burnups the question of how the fuel might behave when the end-of-life rod internal pressure becomes greater than the system pressure attracts a considerable interest.

On one hand end-of-life overpressure might lead to clad outward creep and an increased pellet-clad gap with consequent feedback in the form of increased fuel temperature, further fission gas release, further increases in overpressure etc. On the other hand increased fuel swelling might offset this mechanism.

In connection with such considerations STUDSVIK NUCLEAR initiated a limited in-house R&D activity in order to investigate the ability to detect the phenomena of interest: the ROPE Pre-project 34. This was followed by the two international Rod OverPressure Experiments (the ROPE I and ROPE II projects).

The purpose of the first of the international projects, ROPE I, was to investigate the behavior of BWR fuel rods. ABB-ATOM 8x8 fuel rods, irradiated in the Ringhals 1 reactor to a burnup of about 35 MWd/kgU were tested. The rods were refabricated and pressurized to give hot internal overpressures during R2 irradiations of approximately 0, 4 and 14 MPa respectively. The clad creepout and the time dependent changes in fuel rod conductance were investigated as functions of rod overpressure.

The fuel rods were irradidated one at a time during three 3-day cycles in an instrumented rig in an in-pile loop in the R2 reactor. During these cycles the fuel rod thermal response was determined on-line by noise analysis. Between the 3-day cycles the rods were irradiated together for a total of six 15-day cycles without the on-line measurements mentioned. In the intermissions between these cycles, profilometry measurements were performed in the R2 reactor pool. After irradiation, the rods underwent non-destructive and destructive examinations. The rod with the highest overpressure had a measured diametral cladding outward creep strain of 11 m after 1634 hours irradiation, with no apparent primary creep. This exceeded the expected pellet diameter increase attributable to fuel matrix swelling, since the average swelling rate measured in the fuel would only have resulted in a pellet diameter increase of 3.2 m, after 1634 hours. Thus it was successfully demonstrated that a BWR fuel rod with an internal overpressure in excess of the pressure causing a cladding creepout rate as fast as the fuel solid swelling rate, can be operated at a linear heat rating up to 22 kW/m for more than 2 months without any apparent detrimental effect.

In the second of these international projects, ROPE II, PWR fuel is being investigated in the same manner 35. Data from this project have not yet been reported.

6. STUDIES OF DEFECT FUEL BEHAVIOR

Early defect fuel experiments, in the 1970's, consisted of irradiation of fuel rodlets with artificial defects (drilled holes or PCI type defects) [36]. Examinations of failed BWR power reactor fuel rods were also performed, both earlier [37] and recently [38, 39]. Later such experiments were also performed with GE barrier fuel [1-4].

In recent years two series of short-time fuel irradiation experiments were sponsored by Swedish nuclear organizations [40-41]. In these experiments, performed at a constant LHGR of about 45 kW/m, a total of seven liner and non-liner 8x8 BWR type fuel rodlets with varying design parameters were irradiated. The main aim has been to study the impact of simulated primary defects on the fuel behavior and to identify possible phenomena behind the ensuing degradation process. In particular the onset and progression of secondary defects by hydriding attracts attention. A special test technique was applied in which hydriding conditions are promoted in short length fuel rodlets. On-line fuel rod elongation measurements, neutron radiography and metallographic examinations have provided conclusive information. An interpretation of the test results suggests that secondary defects in the form of incipient

massive hydride precipitates may form already within a few hours of operation. Depending on the particular gap gas conditions these hydrides may grow or dissolve on prolonged operation. Unconstrained axial gas communication tends to suppress massive hydride formation by making more steam available.

On the basis of the experience gained from these experiments an international project, DEFEX, was started and is still in progress. In the DEFEX project a series of previously unirradiated 8x8 BWR type fuel rodlets with different types of cladding (standard, liner and rifled cladding) are irradiated. The primary defect is simulated by a special device at the top end of the fuel rodlet. This device contains an enclosed small reservoir of liquid water in an "extension plenum". This extra plenum is connected with the normal plenum volume of the rodlet through a tiny tube in such a manner that only water in the form of steam will communicate with the ordinary plenum volume and the interconnected void space of the interior of the rodlet. Heat is transferred to the enclosed water reservoir from the surrounding pressurized loop water at the start of the operation until the pressure and temperature of the whole system are in balance.

An important experimental feature of this arrangement is the possibility of post-irradiation puncture and subsequent collection of released fission gases and hydrogen from the closed system of the individual rodlets being irradiation tested. The test fuel rodlet is subjected to a modestly peaked axial power profile and the linear heat generation rate (LHGR) is maintained constant during the test period (one reactor cycle of about 16 days). The LHGR is kept sufficiently high to effectively close the fuel pellet/clad gap over the power peaked length section of the fuel rodlet. The simulated single defect is located in the top plenum region where the steam is let in. By this arrangement the diffusional migration of H_2O and H_2 in the axial direction will be constrained to such an extent that axial gap gas concentration gradients and partial pressure gradients can build up and be maintained more or less effectively at a steady LHGR level until the termination of the test period. Hydriding is consequently expected to initiate and to progress in the lower part of the fuel rodlet.

An on-line elongation detector measures the fuel rod length changes with high precision during operation. This device provides information on the length changes associated with massive hydriding, gas flow, diffusion and oxidation processes within the fuel rodlets. Non-destructive measurements performed before and after the irradiation phases include profilometry, eddy current measurements and neutron radiogaphy. According to experience, blister type hydrides can easily be detected. Gap squeeze measurements are performed to detect any imposed changes of the gap size as a result of pellet oxidation or swelling. Measurements of residual free hydrogen contained within the closed fuel rod system will yield useful information. The small releases of fission gases are also measured.

A continuation of this project is foreseen: the DEFEX II project, where irradiated fuel rodlets, in part refabricated from full size power reactors fuel rods, with a burnup in the range 10-20 MWd/kgU, will be used.

7. STUDIES OF FULL-SIZE POWER REACTOR FUEL RODS

Since the commissioning in 1972 of the first Swedish power reactor, Oskarshamn 1, STUDSVIK has been involved in the post-irradiation examination of full-length fuel rods and other assembly components, e.g. spacer grids from the Swedish, and also to some extent the Finnish power reactors.

The programs, which have mostly been proprietary, have been primarily directed to the verification of the fuel performance at all levels of burnup and, in the case of rods defected during operation, the determination of the cause of failure. Some of the work performed on ABB Atom rods has been published[1].

ABB Atom authors have described an unusual full scale in-core ramp experiment performed in the Oskarshamn 1 BWR during 1975 [42, 43]. A control rod had intentionally been left half-way in the core for some time and was then withdrawn in three fast steps with one hour hold time between each step.

It should be noted that this control rod withdrawal was rather extreme compared to the events during normal operation. Shortly afterwards the reactor was shut down for the annual refuelling. Leak testing revealed that 14 assemblies in the vicinity of this control rod had failed due to this ramp. The maximum LHGR reached was 38 kW/m. A total of about 40 rods were considered as failed. A number of these were investigated in STUDSVIK's Hot Cell Laboratory. In most of the cases the failures were not detectable during visual inspection and the failure location had to be determined by eddy current inspection. Metallographic inspection revealed narrow SCC cracks. It was concluded that the failures agreed well with the ramp test results on shorter fuel rodlets in the R2 reactor.

Imatran Voima Oy, Finland, operates the two Loviisa reactors, PWR units of the VVER-440 type of Soviet origin. Data from fuel inspection programs which included investigations of both a whole fuel bundle and individual rods in STUDSVIK's Hot Cell Laboratory have been published [44, 45]. The fuel bundle, with a rod average burnup of 32 to 48 MWd/kgU, was disassembled and assembled in the large cells. Since the fuel design is quite different from that of other PWRs new or modified techniques and equipment had to be developed.

8. UP-COMING INTERNATIONAL FUEL R&D PROJECTS

8.1. TRANS-RAMP III

The prospective TRANS-RAMP III project was discussed in Section 4 above.

8.2. DEFEX II

The prospective DEFEX II project was discussed in Section 6 above.

8.3. ULTRA-RAMP

The question of the ramp behavior at high burnup (above 50 MWd/kgU) has been widely discussed in recent years as regards both normal and off-normal ramp rate conditions. However, only limited experimental information seems to be available so far.

The concern addressed appears to relate to the impact of changes in the physical properties of the fuel pellets at high burnup and their effects on the ramp behavior of the fuel rods. The fuel pellets tend to crack up in minor fragments and may no longer behave as solid bodies. Will they become ejected and dispersed in the reactor coolant water as particles on clad failure? The fission gases will be entrapped in a magnitude of small bubbles and might cause fuel rod swelling on up-ramping. Other concerns relate to the loss of thermal conductivity and the impact of the rim zone on fuel ramp behavior and fission gas release.

In the SUPER-RAMP project a substantial fuel rod diameter expansion was observed (> 1 %) at burnup levels of 45-50 MWd/kgU on up-ramping by 100 W/cm.min to about 50 kW/m. The transient tests performed in the TRANS-RAMP I and II projects indicated very short times to failure at ramps rates of approximatly 1000 W/cm.min up to above 40 kW/m.

The prospective ULTRA-RAMP project would consitute a combination of the two roups of ramp projects, discussed in Section 1. Thus the ramp resistance in current fuel types would be studied both under normal operating conditions ("slow" ramps, e.g. 100 W/cmmin) and under off-normal operating conditions ("fast" ramps corresponding to ANSI Class II and III events, e.g. 1000 W/cmmin).

According to our present plans a number of very high burnup fuel rods of BWR or PWR types, or both, would be exposed to fast and slow ramp rates to preselected terminal power levels in the R2 test

reactor or to clad failure. The main objective is to identify any adverse or inadequate fuel rod behavior as for example abnormal fuel rod swelling, fast failure of the cladding, loss of fuel integrity on clad fracturing (causing dispersion of fuel particles in the coolant water), etc. Detailed non-destructive and destructive examinations (including advanced types of ceramography) would follow. These plans are quite flexible and depend on the feed-back we receive from discussions with prospective participants.

8.4. SUPER-RAMP III/10x10

In the new types of 10x10 BWR fuel the linear heat rate is lower than in earlier types of fuel and the PCI resistance is presumed to be correspondingly improved. However, some utilities using zirconium liner with earlier types of fuel have raised the question whether the lower linear heat rates in 10x10 fuel really make the added resistance against PCI failure, achieved with zirconium liner fuel, unneccessary. As far as is known no ramp tests have ever been performed on 10x10 fuel.

Thus the proposed SUPER-RAMP III/10x10 project would be similar to the earlier SUPER-RAMP II/9x9 project. It is planed to start in 1995 and be completed in 1996.

8.5. ENTHALPY DETERMINATIONS

The stored energy in fuel rods, the enthalpy, depends on the fuel design (dimensions, materials) and also burnup. This quantity is an important parameter in connection with safety considerations such as LOCA evaluations.

STUDSVIK's R2 test reactor is well suited for scram experiments where the thermal response of different types of fuel rods can be compared. The measurements can be performed in two ways: by use of the R2 reactor's calorimetric rod power measurement system and by noise analysis [46, 47].

Currently evaluations of some earlier test data are in progress. As soon as those evaluations are completed a project proposal will be circulated.

8.6. POST-DO/DNB RAMP RESISTANCE

Early experimental data in power reactors and test reactors have shown that short periods (less than about a minute) of Post-DO/DNB operation have not caused fuel failures (defined as leaking fuel rods). The question whether such operation might cause incipient (non-penetrating) fuel cracks and a decrease in ramp resistance has never been investigated.

STUDSVIK has planned an experiment where fuel rodlets would be exposed to short (20-30 sec) periods of Post-DO/DNB operation along a short part of their length (at the location of the highest linear heat generation) and then later ramp tested in the same in-pile loop.

REFERENCES

[1] DAVIES, J.H. et al., Barrier Fuel Ramp Tests at 14 to 20 MWd/kgU. Trans ANS 35(1980), p 203-204.

[2] ROSENBAUM, H.S. et al., Resistance of Zirconium Barrier Fuel to Pellet-Cladding Interactions. Trans ANS 38(1981), p 270-272.

[3] DAVIES, J.H. et al., Irradiation Tests on Barrier Fuel in Support of a Large-Scale Demonstration. ANS Topical Meeting on LWR Extended Burnup - Fuel Performance and Utilization. Williamsburg, Va, USA, 4-8 April 1982. Vol 2, p 5-51 to 5-67.

[4] DAVIES, J.H. et al., Fuel Pellet Cladding Interaction in Light Water Reactors. Proc. ASEE Annual Conference 1984, p 529-538.

[5] KJAER-PEDERSEN, N., WOODS, K.N., Ramp Tests on Fuel Rods Containing Solid Pellet, Annular Pellet and Sphere-Pac Particle Fuel. Proc. ANS Topical Meeting on Light Water Reactor Fuel Performance. Orlando, Fla, USA, 21-24 April 1985. ANS, LaGrange Park, Ill 1985. (DOE/NE/34130-1, Vol 2, p 6-35 to 6-51).

[6] INOUE, K. et al., BWR Fuel Performance and its Development in Japan. Proc. ANS Topical Meeting on Light Water Reactor Fuel Performance. Orlando, Fla, USA, 21-24 April 1985. ANS, LaGrange Park, I11 1985. (DOE/NE/34130-1,Vol 1, p1-17 to 1-33).

[7] INOUE, K. et al., An Overview of the Joint Development Work on PCI Remedy Fuel. Proc. ANS Topical Meeting on Light Water Reactor Fuel Performance. Orlanda, Fla, USA, 21-24 April 1985. ANS, LaGrange Park, I11 1985. (DOE/NE/34130-1, Vol 2, p 6-1 to 6-16).

[8] WAKASHIMA, Y. et al., Multiple Ramp Tests of Zirconium Liner Fuel. Proc. ANS Topical Meeting on Light Water Reactor Fuel Performance. Orlando, Fla, USA, 21-24 April 1985. ANS, LaGrange Park, Ill 1985. (DOE/NE/34130-1, Vol 2, p 7-79 to 7-91).

[9] AOKI, T., KOIZUMI, S., UMEHARA, H., OGATA, K., Fission Gas Release Behavior of High Burnup Fuels During Power Ramp Tests. IAEA Technical Committee Meeting on Fission Gas Release and Fuel Rod Chemistry Related to Extended Burnup, Pembroke, Ont, Canada, 27 April-1 May 1992.

[10] OHARA, H. et al., Fuel Behavior During Ramp Tests. Proc. 1994 International Topical Meeting On Light Water Reactor Fuel Performance. West Palm Beach, Fl, USA, 17-21 April 1994, p 674-686.

[11] THOMAS, G., The Studsvik INTER-RAMP Project: An International Power Ramp Experimental Program. J Nucl Materials 87(1979), p 215-226. Also Proc KTG/ENS/JRC Meeting on Ramping and Load Following Behaviour of Reactor Fuel. Petten, The Netherlands, Nov 30 - Dec 1, 1978. H Röttger, (Ed.) (EUR 6623 EN, p 95-106).

[12] MOGARD, H. et al., The Studsvik INTER-RAMP Project - An International Power Ramp Experimental Program. ANS Topical Meeting on LWR Fuel Performance. Portland, Oregon, USA, April 29 - May 3, 1979, p 284-294. (DOE/ET/34007-1).

[13] FRANKLIN, D.G., DJURLE, S., HOWL, D., Performance of Niobia-Doped Fuel in Power-Ramp Tests. Nuclear Fuel Performance. Stratford-upon-Avon, UK, 25-29 March 1985. Proc. BNES, London 1985. Vol 1, p 141-147.

[14] MOGARD, H., HECKERMANN, H., The International SUPER-RAMP Project at Studsvik. Proc. ANS Topical Meeting on Light Water Reactor Fuel Performance, Orlando, Fla, USA, 21-24 April 1985. ANS, LaGrange Park, Ill 1985. (DOE/ NE/34130-1, Vol 2, p 6-17 to 6-33).

[15] DJURLE, S., Final Report of the SUPER-RAMP Project. U.S. Department of Energy 1985. (DOE/ET/34032-1).

[16] HOWE, T., DJURLE, S., LYSELL, G., Ramp Testing of 9x9 BWR Fuel. Fuel for the 90's. International Topical Meeting on LWR Fuel Performance. Avignon, France, 21-24 April, 1991. Vol 1, p 828-837.

[17] BABA, T. et al., Power Cycling and Ramp Test in R-2 and Mihama Unit 2 for MHI PWR Fuels. IAEA Specialists' Meeting on Power Ramping and Cycling Behaviour of Water Reactor Fuel.

Petten, the Netherlands, 8-9 September, 1982. (IAEA IWGFPT/14, p 72-78). Also Res Mechanica 16(1985), p 231-240.

[18] SUZUKI, S., MURAKAMI, K., TAKAHASHI, T., Burnup Extension and Improved Reliability. Proc. 1994 International Topical Meeting On Light Water Reactor Fuel Performance. West Palm Beach, Fl, USA, 17-21 April 1994, p 352-359.

[19] WESLEY, D.A., MORI, K., INOUE, S., Mark - BEB Ramp Testing Program. Proc. 1994 International Topical Meeting On Light Water Reactor Fuel Performance. West Palm Beach, Fl, USA, 17-21 April 1994, p 343-351.

[20] DJURLE, S., The Studsvik OVER-RAMP Project. Studsvik Energiteknik AB, Sweden 1981. (STUDSVIK-STOR-37).

[21] HOLLOWELL, T.E., KNUDSEN, P., MOGARD, H., The International OVER-RAMP Project at Studsvik. Proc ANS Topical Meeting on LWR Extended Burnup - Fuel Performance and Utilization. Williamsburg, Va, USA, 4-8 April 1982, Vol. 1, p 4-5 to 4-18.

[22] FORSYTH, R., BLACKADDER, W.H., NILSSON, B., Volatile Fission Product Behaviour in Reactor Fuel Rods under Accident Conditions. Proc Specialists' Meeting on the Behaviour of Water Reactor Fuel Elements Under Accident Conditions, Spåtind, Norway, 13-16 September 1976, paper No. 14.(CSNI Report No. 13).

[23] LYSELL, G., SCHRIRE, D., Fission Product Distribution at Different Power Levels. IAEA Technical Committee Meeting on Fuel Performance at High Burnup for Water Reactors. Studsvik, Sweden, 5-8 June 1990. (IAEA IWGFPT/36, p 132-139).

[24] SCHRIRE, D., LYSELL, G., Fuel Microstructure and Fission Product Distribution in BWR Fuel at Different Power Levels. Fuel for the 90's. International Topical Meeting on LWR Fuel Performance. Avignon, France, 21-24 April, 1991. Vol 2, p 518-527. Also Studsvik Nuclear, Sweden. 1990. (STUDSVIK/NF(P)-90/79).

[25] LYSELL, G., BENGTSSON, S., Fission Product Redistribution after a Power Bump at High Burnup. Proc. 1994 International Topical Meeting On Light Water Reactor Fuel Performance. West Palm Beach, Fl, USA, 17-21 April 1994, p 328-334.

[26] MOGARD, H., KNAAB, H., BERGENLID, U., LYSELL, G., The International DEMO-RAMP II Project at Studsvik. Nuclear Technology 69(1985): 2, p 236-242.

[27] MOGARD, H. et al., The International TRANS-RAMP I Fuel Project. Fuel Rod Internal Chemistry and Fission Product Behaviour. Technical Committee Meeting, Karlsruhe, FRG, 11-15 November, 1985. Proc. (IAEA IWGFPT/25, p 157-167).

[28] MOGARD, H., HOWL, D.A., GROUNES, M., The International TRANS-RAMP II Fuel Project - A study of the Effects of Rapid Power Ramping on the PCI Resistance of PWR Fuel. ANS Topical Meeting on LWR Fuel Performance. Williamsburg, Va, USA, 17-20 April 1988, p 232-244.

[29] MOGARD, H., DJURLE, S., GROUNES, M., LYSELL, G., KJAER-PEDERSEN, N., Effects of High Power Transients on the Operational Status of LWR Fuel - Experimental and Analytical Investigations at Studsvik. Proc. International ENS/ANS Conference on Thermal Reactor Safety "NUCSAFE 88". Avignon, France, 2-7 October 1988, p 181-190.

[30] MOGARD, H. et al., Irradiation Testing of an Advanced Fuel Cladding Designed for Load-Follow and Extended Burnup Operation. Studsvik Energiteknik AB, Sweden 1986. (STUDSVIK-86/1). (Expanded version of A.5.1.2).

[31] MOGARD, H., KJAER-PEDERSEN, N., Improved PCI and FGR Performance of LWR Fuel using Rifled Cladding. Technical Committee Meeting on Fuel Peformance at High Burnup for Water Reactors. Studsvik, Sweden, 5-8 June 1990. (IAEA IWGFPT/36, p 147-159).

[32] KJAER-PEDERSEN, N., KINOSHITA, M.Y., MOGARD, H., Comparative Studies of Axial Gas Mixing in Fuel Rods with Standard and Rifled Cladding. IAEA Technical Committee on Power Ramping, Cycling and Load Following Behaviour of Water Reactor Fuel. Lyon, France, 18-21 May 1987.(IAEA IWGFPT/28, p 25-32 and IAEA-TC-624/13).

[33] MONTGOMERY, R.O., RASHID, Y.R., KJAER-PEDERSEN, N., Theoretical Evaluation of Rifled Cladding for LWR Fuel. Nucl Eng & Des 132(1992), p 309-316.

[34] SCHRIRE, D., Rod Overpressure Experiment (ROPE) - Pre-Project. Studsvik Energiteknik AB, Sweden 1987. (STUDSVIK/NF(P)-87/43).

[35] GROUNES, M., TOMANI, H., Tying up Fuel Rod Overpressure Problems with ROPE I and II. Nuclear Engineering International 37(1992):451, p 30, 32.

[36] BLACKADDER, W.H., FORSYTH, R.S., MALÉN. K., RÖNNBERG. G., Fission Product Release to Loop Water from Operating Intentionally Defected Fuel. IAEA Specialists' Meeting on the Behaviour of Defected Zirconium Alloy Clad Ceramic Fuel in Water Cooled Reactors. Chalk River, Canada, 17-21 September 1979. (IAEA IWGFPT/6, p 171-177).

[37] FORSYTH, R.S., JONSSON, T., Experimental Study of Defect Power Reactor Fuel, Final Report, SKI Projects B3/81 and B30/82. Studsvik Energiteknik AB, Sweden. 1982. (STUDSVIK/NF(P)-82/72).

[38] JONSSON, Å., HALLSTADIUS, L., GRAPENGIESSER, B., LYSELL, G., Failure of a Barrier Rod in Oskarshamn 3. Fuel for the 90's. International Topical Meeting on LWR Fuel Performance. Avignon, France, 21-24 April, 1991. Vol 1, p 371-379.

[39] SCHRIRE, D. et al., Secondary Defect Behavior in ABB BWR Fuel. Proc. 1994 International Topical Meeting on Light Water Reactor Fue Performance. West Palm Beach, Fl, USA, 17-21 April 1994, p 398-409.

[40] MOGARD, H., GROUNES, M., TOMANI, H., LYSELL, G., Studies in the R2 Test Reactor of Secondary Damage Formation in LWR Fuel Rods with Simulated Defects. IAEA Technical Committee Meeting on Fuel Failure in Normal Operation of Water Reactors: Experience, Mechanisms and Management. Dimitrovgrad, Russian Federation, 26-29 May 1992. (IAEA-TEC DOC-709, p 184-191).

[41] MOGARD, H., GROUNES, M., LYSELL, G., TOMANI, H., Experimental Studies of Post-Failure Degradation of BWR Fuel Rodlets. Proc. 1994 International Topical Meeting On Light Water Reactor Fuel Performance. West Palm Beach, Fl, USA, 17-21 April 1994, p 423-434

[42] JUNKRANS, S., VÄRNILD, O., ASEA-ATOM Research on PCI. ANS Topical Meeting Water Reactor Fuel Performance. St Charles, Ill, USA, 9-11 May 1977, p 219-229. Also IAEA Specialists' Meeting on Pellet Cladding Interaction for Water Reactors. Vienna, Austria, 27 June - 1 July 1977. (IAEA IWGFPT/1, Paper No. 23).

[43] JUNKRANS, S., NERMAN, H., ASEA-ATOM results on PCI Experiments on Fuel Rods; A Review. J Nucl Materials 87(1979), p 247-250. Also Proc KTG/ENS/JRC Meeting on Ramping and Load Following Behaviour of Reactor Fuel. Petten, The Netherlands, 30 Nov - 1 Dec 1978. 1979. (EUR 6623 EN, p 159-162).

[44] MOISIO, J., PATRAKKA, E., Fuel Examination Techniques Experience at Finnish Nuclear Power Plants. IAEA Specialists' Meeting on Post-Irradiation Examination and Experience. Tokyo, Japan, 26-30 November 1984, Paper FIN-1.

[45] MOISIO, J., TERÄSVIRTA, R., RANTA-PUSKA, K., Experience from Examinations of Fuel Rods Irradiated to High Burnups in Loviisa Reactors. Technical Committee Meeting on Fuel Performance at High Burnup for Water Reactors. Studsvik, Sweden, 5-8 June 1990. (IAEA IWGFPT/36, p 78-84).

[46] OGUMA, R., SCHRIRE, D., BERGDAHL, B-G., Fuel Rod Thermal Performance Studies Based on Noise Analysis. Studsvik Energiteknik AB, Sweden. 1986 (STUDSVIK-NF(P)-86/08).

[47] OGUMA, R., BERGDAHL, B-G., SCHRIRE, D., Application of a Recursive Identification Technique to Noise Analysis for Fuel Performance Study Specialists' Meeting on Reactor Noise (SMORN-V), Munich, FRG, 12-16 October 1987. Prog in Nuclear Energy 21 (1988), p 351-360.

METHODS FOR ACQUIRING DATA IN POWER RAMPING EXPERIMENTS WITH WWER FUEL RODS AT HIGH BURNUP

S.N.BOBROV, A.F.GRACHEV, V.A. OVCHINNIKOV,
I.S.POLIAKOV, N.P.MATVEEV
Research Institute of Atomic Reactors,
Dimitrovgrad

V.V. NOVIKOV
Institute of Inorganic Materials,
Moscow

Russian Federation

Abstract

A programme on in-pile tests which involve fuel burnup up to 60 MWd/kg and up to 12 fuel rods in the experimental rig is considered. Testing methods with reference to the MIR-M1 reactor are reported. Power ramping regime can be realized either by an increase of the total reactor capacity or by displacement of the nearest to the experimental cell control rods or by combination of these two ways. A total thermal capacity of the fuel rod cluster is determined by means of the thermal balance technique. The thermal capacity of each separate fuel rod can be estimated from the distribution of their relative activity within the accuracy range 5-10%. The important condition for this procedure is to keep the initial distribution of the fuel rod heating during power ramping. Means of instrumentation are described. They are standard detectors of loop facilities and transducers installed both in the irradiation rigs and fuel rods. Different ways of processing data on the fuel rod loss of integrity are reported. When the time of fuel rod loss of tightness is placed in correspondence with its capacity, processing can be made either on the maximum fuel rod heat load or on that at crack location. The information acquired in the experiments on the burnup values, heat rating distribution, kinetics of fission product gas emission, fuel rod elongation, fuel rod diameter changes, crack availability and fission products migration is used for the development and verification of calculation codes.

1. INTRODUCTION

One of the main phenomenon inferred from operational experience of water-cooled nuclear power plants (NPP) and producing an effect on fuel serviceability is power ramp at which an increase in power rate is significantly greater than that of fuel stress relaxation.

Without special measures aimed at limiting an amplitude and the rate of power increase, even a single ramp can result in fuel failure. As the burnup rises, upper safe range of linear heat generation rate (LHGR) becomes lower but the degree of fuel degradation and the amount of fission product release can give an essential rise in the event of fuel failure.

Presently, the reactor projects with improved safety having the maximum design burnup up to 65 MWd/kg are being developed. In this connection the study of fuel rod behaviour at high burnup under different operational modes is a subject of great importance. Fuel rods with high burnup can be characterized as follows:

- absence of gap between fuel and cladding;
- change in plasticity both of fuel and cladding, existence of corrosion damage;
- enhanced fission gas emission;
- release of long-lived fission products into the coolant increases in the case of fuel element loss of tightness. The present paper discusses the features of the experiments conducted in the MIR

reactor. Results of these tests are applied for making the appropriate recommendations on fuel rod operational conditions and also can be used for verification and modification of calculational codes capable for prediction of fuel behaviour.

Study of WWER- 1000 fuel rod behaviour under power ramping conditions is performed at the MIR reactor (RIAR, Dimitrovgrad). The reactor design and its experimental possibilities are described in details in Ref. [l].

2. TEST PROGRAMME

resently, RIAR and VNIINM have been conducting the combined study of WWER-1000 fuel rods behaviour at burnup up to 65 MWd/kg in accordance to the test programme which includes the following types of experiments:

- power ramp to elucidate a dependence of permissible ramps against fuel burnup;
- comparative tests for fuel rods with different modifications of fuel and cladding, involving power ramping and transient-repeated-mode operation tests at different values of burnup (cladding from zirconium alloy with Sn, Nb and Fe additions; bimetallic cladding; plasticized fuel; mixed U-Pu fuel; fuel with Gd addition);
- special tests after repeated irradiation of refabricated and full-scale fuel rods up to high burnup;
- study of failed fuel rods and fission products release;

By this time, five tests named "Power Ramp " (R) have been carried out,including refabricated fuel rods with length 1 m at burnup value of 46 MWd/kg (R-3).

Presently, the complex examinations of 8 from 10 fuel rods after the test R-3 have been terminated. The two fuel rods left after the power ramp, together with the fuel rods of the same design but not subjected to the ramp, have been loaded into the MIR reactor in order to get so much higher values of burnup. This is a preparatory stage for the future tests. The following experiments are planned to be carried out: Ramp-5 to compare different clad materials, Ramp-6 for joint testing both refabricated and full-scale spent WWER-1000 fuel rods. The results of this experiment are believed to confirm the possibility of using the full-scale fuel rods (when contacting fuel and cladding) for power ramping tests at high burnup, i .e . excluding the refabrication stage. Figure 1 illustrates the main stages of the test programme.

3. FEATURES OF POWER RAMP TECHNIQUE

3.1 OBJECT OF TESTING

As an object of being tested the following types of fuel rods can be utilized or are planned for

- refabricated, length 0.25 m and 1.0 m;
- previously irradiated in the MIR reactor,length 0.25 m and 1.0 m;
- spent full-scale WWER-1000 and WWER-440 fuel rods (beginning in 1994 end).

To perform power ramping test with WWER fuel rods at burnup higher than 20 MWd/kg, it becomes more beneficial to apply refabricated or spent full-scale fuel rods but not previously irradiated in the MIR reactor, if it is proved that refabrication does not distort the result of the test.

3.2 EXPERIMENTAL EQUIPMENT

The research reactor MIR has several loop facilities (LF) for provision experimental study of WWER- 1000 fuel rod behaviour, which features are presented in Table I. These LFs provide for the long-term repeated irradiation under WWER operational conditions of the refabricated and full-scale fuel

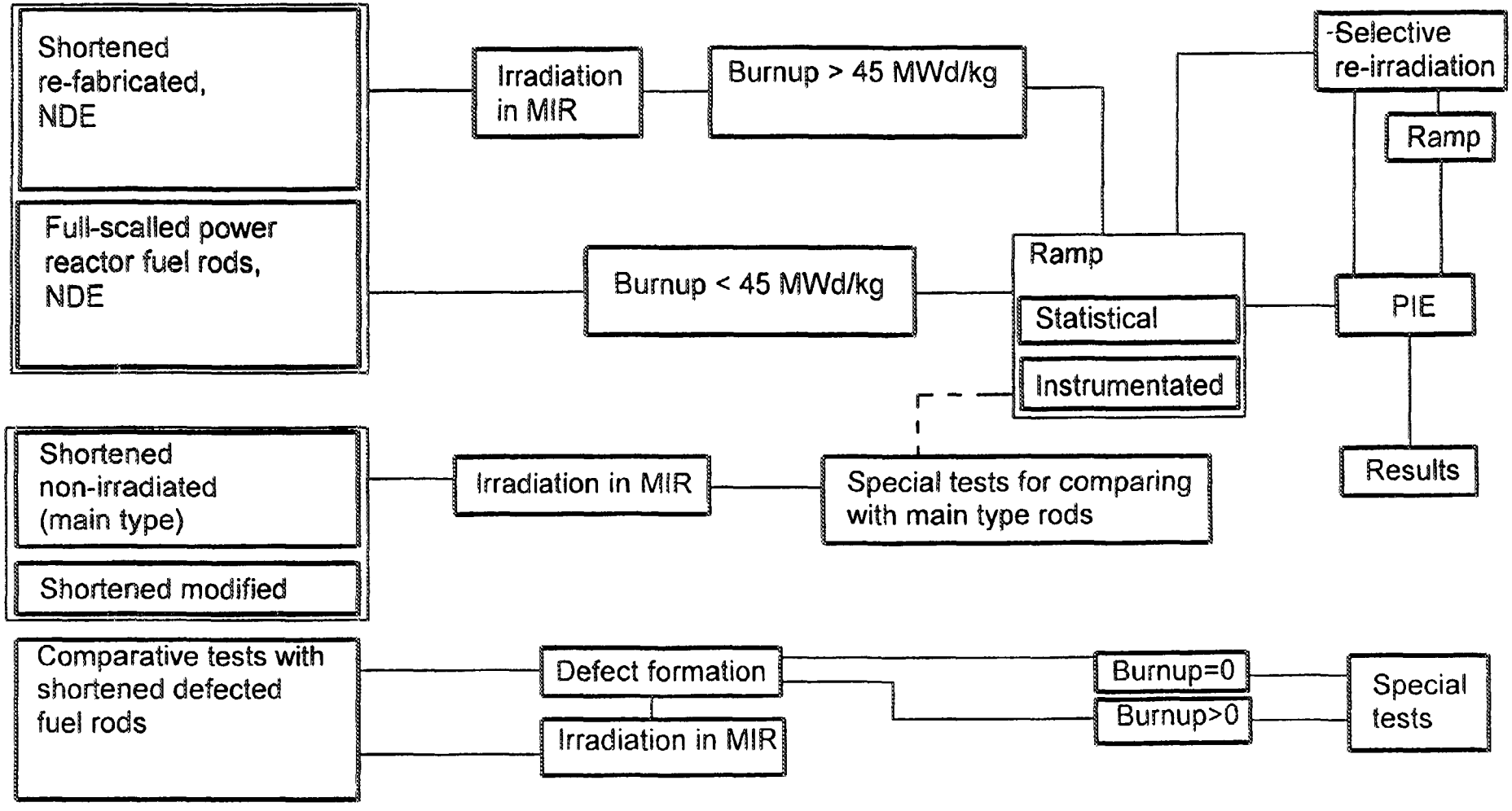

Fig. 1. Test programme

Table I. Technical features for the MIR Reactor Loop Facilities

	PV-1,2	PVK-1,2	PVP-1	PVP-2	PG-1
Coolant	water	water, steam	water, steam	water, steam	helium, gas mixture
Max pressure, MPa	20	20	8.5	20	20
Max coolant capacity, kW	2000	2000	100	2000	160
Max coolant temperature outlet, °C	340	340	500	500	550 (1000 in the core)
Max coolant flow rate, kg/h	16000	14000	675	1000	1000
Max activity, Bq/kg	3.7×10^{7}	3.7×10^{7}	3.7×10^{7}	3.7×10^{10}	3.7×10^{10}

Footnote: a. Neutron flux :

$E < 0.68$ eV - $(3 - 5) \times 10^{14}$ cm^{-2} s^{-1}

$E > 0.1$ MeV - $(2 - 4) \times 10^{13}$ cm^{-2} s^{-1}

b. Maximum inner diameter of the channels - 74 mm.

rods up to high burnup when required, and also make it possible to conduct the subsequent power ramping tests or others. Different types of irradiation rigs (I) can be used for the tests:

- dismountable IRs consisting of from 6 up to 12 non-instrumented refabricated rods or/and previously irradiated in the MIR reactor fuel rods (to be used for statistical tests);
- instrumented IRs for monitoring fuel rod length and gaseous fission products changes.

The instrumented IRs of many-times-use design are being developed to support this experimental programme. In addition to thermocouples and self-powered detectors, these rigs are furnished with fuel rod elongation sensors and fuel rod internal pressure sensors. Moreover, the rigs provide for replacement of any fuel rod by another one by installing either fresh or refabricated rods in order to perform monitoring of the fuel rod elongation and/or internal gas pressure. As a result of their utilizing, a data base on kinetics of cladding elongation and fission gas release in power ramping experiments at high burnup will be available.

3.3. METHODS FOR FUEL ROD POWER CHANGE PERFORMING

Power ramp can be conducted using the following three ways:

- reactor power increase;
- local power increase around the experimental rig with the help of withdrawal of the nearest control rods, total reactor power is kept constant when ramping;
- displacement of the fuel rods along the experimental rig from the low- to the high-neutron flux region.

All these ways have been approbated by this time. The advantages of the first one will be considered in more detail. In this case, the initial heat generation distribution both along the fuel length and between the fuel rods is maintained constant during the test. The results of calculational predictions are checked up by comparison with experimental data of post-irradiation gamma-scanning on short-lived fission products (Zr, Ba and La) inside the shielded cell. The total fuel rods thermal capacity is sufficiently large and can be reliably defined by the thermal balance technique. Error of LHGR determination is about 6 %.

While using such a way of power ramp executing, a single test comprising the fuel rods with different burnup and enrichment values can ensure a definite LHGR range, involving in LHGR limit, for example. Figures 2 and 3 show the primary results of the test R-3 performed in the MIR reactor in October 1993 with refabricated fuel rods, produced from the spent WWER-1000 fuel assembly of about 46 MWd/kg burnup, and power increase rate of 100 W/min.

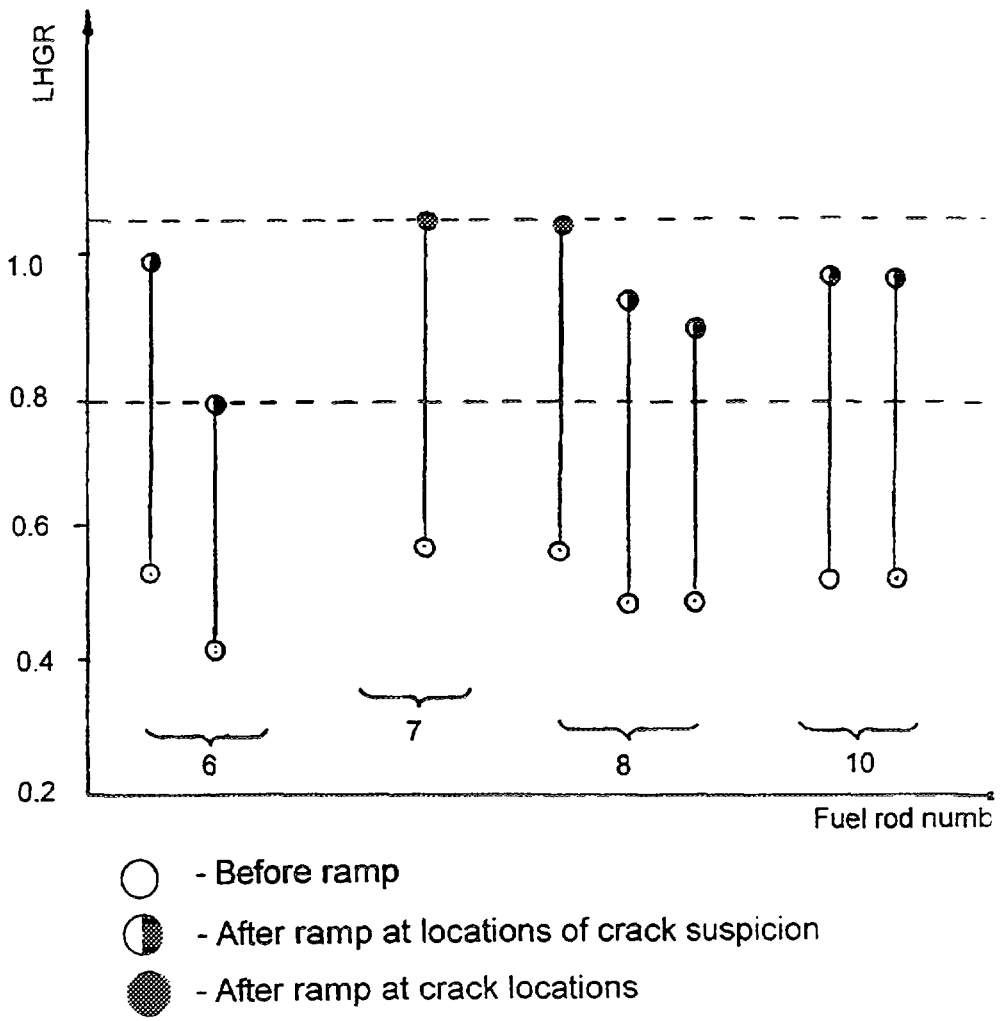

Fig. 2. LHGR at crack locations before and after power ramp

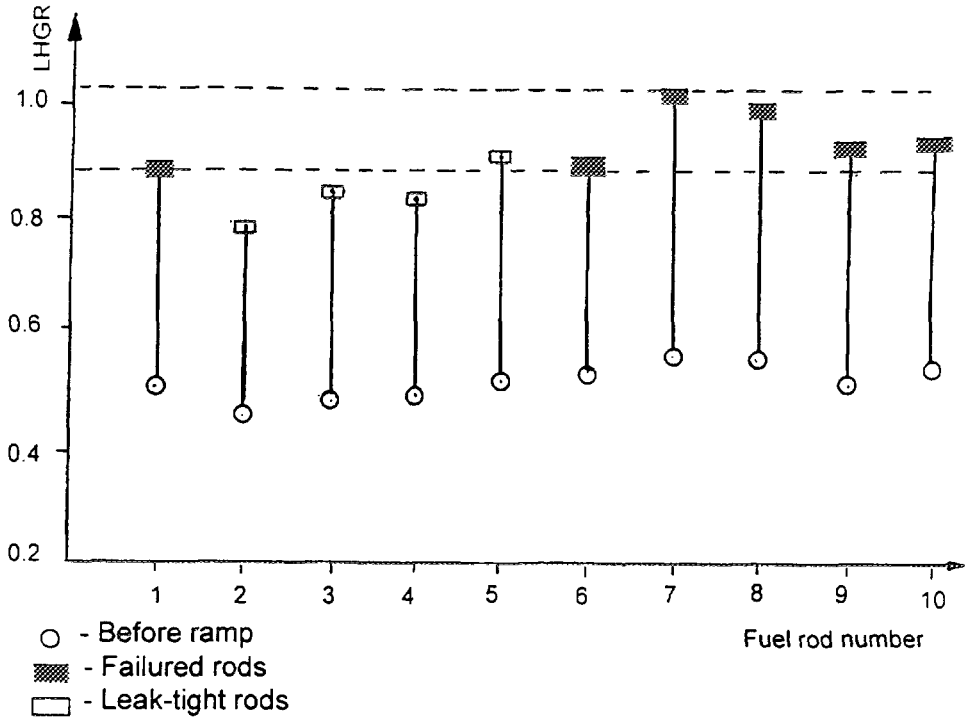

Fig. 3. Maximum LHGR before and after power ramp at a moment of rod failures appearance

3.4 FEATURES OF INTERPRETATIONS OF R-3 RESULTS

These figures illustrate two methods for acquiring results when several fuel rods are being tested simultaneously. The first one considered the LHGR at crack locations, whereas the second one took into account the maximum LHGR only. So far as crack appearance depends upon the whole number of factors which weight is sometimes hard to determine, the second method is closer to probabilistic approach. This assumption is confirmed by the fact that damage locations do not always agree with the maximum LHGR defined by gamma-scanning on Zr-95 activity. For example, Fig. 4 shows the distribution of Zr-95 along the height of one of the fuel rods together with the crack position. Both methods took into consideration the failed fuel rods only which have exactly exhibited cracks or evident depletion of Cs-137. The fuel rod selection for analysis can be refined after subsequent post irradiation examinations (PIE) when the damage type, its position and the cause of damage occurrence will be found out.

The fact that interpretation of the results may be different can be seen in Fig.2 and 3 . The scope of LHGR for evaluating the limiting heat load is greater by a factor of 2 for the first mode (LHGR at evident crack locations and at locations of crack suspicion of failed fuel rods No. 6,7,8,10) than for the second one (maximum LHGR).

The values of average arithmetical mean differ by 8 W/cm. Later on, in order to define the selection of LHGR, subsequent analysis by one of these methods must be utilized after carrying out the full cycle of non-destructive examinations (NDE) and PIE, elucidating the damage locations and the amount of failed fuel rods.

It should be noted, that several failed fuel rods subjected to the different LHGR may appear, the possibility of defining the limiting LHGR is maintained, because, as a rule, some of the fuel rods left keep their tightness. In R-3 peaks of coolant activity at the channel outlet were registered just after reaching the power maximum, but a general amount of peaks noted was in agreement with a quantity of failed rods

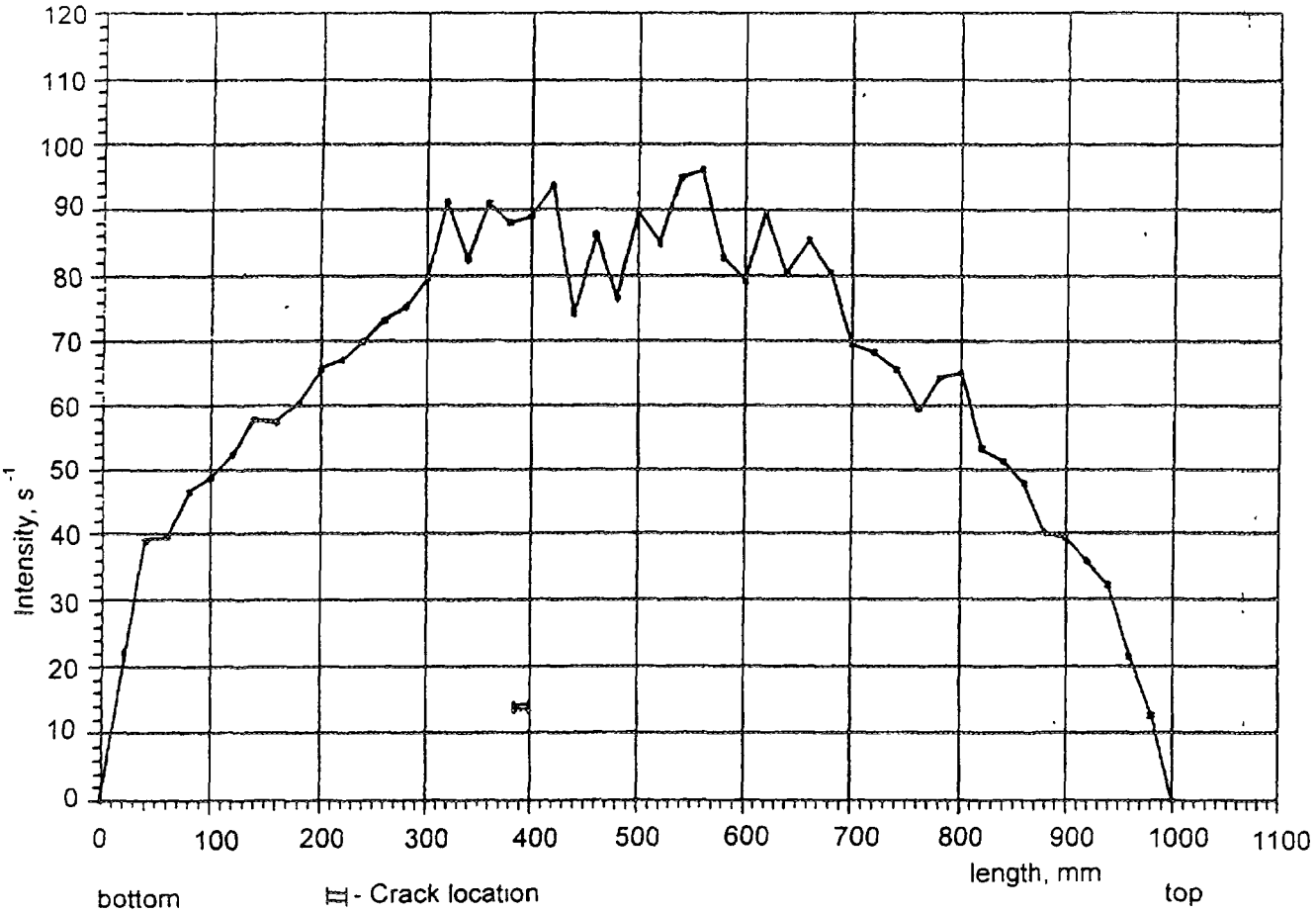

Fig. 4. Z-95 activity distribution along the fuel rod No 7

revealed. Duration of the peak activity scope was 7 min, time of fission products lifting to the activity sensor was about 20 sec. During subsequent irradiation no peak was observed down to the reactor power decrease. The information of such type can also be utilized for evaluating the time of fuel rods operation until their loss of integrity.

4. INFORMATION ACQUIRED

As a whole, the following information received during the test or after NDE and PIE completion can also be used for checking up the different calculational codes. This includes:

- LHGR distribution during the test;
- fission products distribution along the length of fuel rods (Xe,I,Ba,La,Cs...);
- time until coolant activity rise and its kinetics;
- dimensions and crack location;
- changes of fuel rod size (diameter, length, bending);
- gaseous fission products yield;
- fuel swelling and fuel pellet stack elongation, appearance of a gap between pellets, diameter of a centre hole;
- maximum fuel temperature and its radial changes being determined by the dimensions of the specific zones of a pellet cross-section.

n some cases, an additional selective examination can be conducted to find out the state of cladding material (hydrogening, strength properties, phase content, pellet-cladding interaction zone), crack surface features, elementary content of PCI zone, etc.

5. CONCLUSION

The range of LHGR inherent in fuel rod failures may be sufficiently large even in the case of almost equal values of burnup, when carrying out the power ramping experiments with the fuel rods at high burnup (refabricated rods), in order to refine this range the statistical tests can be done with the appropriate method of the result processing, and also a special careful examinations and calculational analysis are needed to be performed aimed at revealing factors which are responsible for the difference in fuel rod resistance when they being subjected to the power ramp.

REFERENCES

[1] Research Reactors of RIAR and their Experimental Possibilities, G.I. Gadziev, A.F. Grachev et.al., RIAR Report, 1993.

SESSION 2
FUEL THERMAL PERFORMANCE

THERMAL CONDUCTIVITY OF FULLY DENSE UNIRRADIATED UO_2: A NEW FORMULATION FROM EXPERIMENTAL RESULTS BETWEEN 100°C AND 2500°C, AND ASSOCIATED FUNDAMENTAL PROPERTIES.

G. DELETTE, M. CHARLES
Commissariat à l'énergie atomique,
Grenoble, France

Abstract

The various contributions to the thermal conductivity of UO_2 are first reviewed: *contribution from phonons* is preponderant up to 1600°C; radiative contribution is negligible in the case of a polycrystalline sample, and is unable to account for the increase in conductivity observed above 1600°C; *electronic contribution*, which seems patently to be responsible for this increase, is efficient from 1400°C (electron-hole pairs treated as small polarons). Given the lack of decisive arguments on their actual efficiency, it was decided that, for temperatures above 2400°C, neither a possible decrease in the electronic contribution due to vacancies, nor an additional possible contribution from Frenkel pairs would be described. We do not therefore go beyond the above-mentioned electronic contribution. In the light of these considerations, the law established by CEA for the thermal conductivity of unirradiated UO_2, on the basis of a homogeneous set of measurements between 100°C and 2500°C, has been revised. A least-square method applied to the above measurements was used to derive simultaneously the four adjustable constants of the law which is henceforth proposed:

$$\lambda = \frac{1}{A + BT} + \frac{C}{T^2}\exp\left(-\frac{W}{kT}\right)$$

The values of A, B, C, and W obtained, have the advantage of giving a better account of the high temperature results compared to the Martin recommendation (which has, by the way, the same physical form as above). Furthermore, this new law allows an extrapolation towards the melting point which is better founded than the earlier CEA law, while still respecting the value of the integrated thermal conductivity up to melting. Finally, various burnup effects (impurities, stoichiometry, etc.) can be formulated in physical terms. Moreover, the values of various fundamental properties connected with the derived constants have been determined: Debye temperature, Grüneisen parameter, Mott-Hubbard energy, electrical conductivity. These values are discussed and compared with published data.

PRESENTATION

In this document the question of the components of the thermal conductivity of UO_2 is restated, in order to account for the measurements already published by the CEA up to high temperatures (2500 °C). The case of stoichiometric, totally dense and non-irradiated UO_2 is treated.

The first part is a discussion of the mechanisms involved and of their formulation. The second part uses the results obtained by the CEA to formulate the various contributions considered, and the values of the corresponding parameters are compared with published data.

1. MODELLING OF THE THERMAL CONDUCTIVITY OF URANIUM DIOXIDE

1.1 GENERAL CONSIDERATIONS

The change in thermal conductivity of UO_2 in relation to temperature is well known between 600 and 2500°C (Figure 1 according to [1]): starting from 4 to 5 $W.m^{-1}.K^{-1}$, a hyperbolic reduction occurs first of all, followed by a minimum at around 1600°C and finally a rise until the melting point.

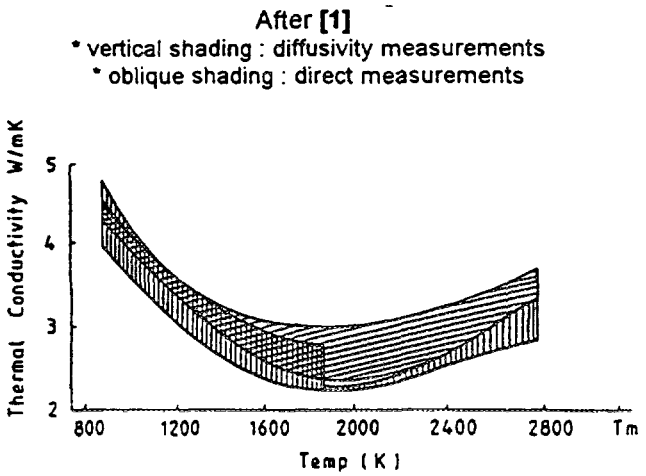

FIG. 1 Thermal conductivity of UO_2 at various temperatures

1.2 LATTICE CONTRIBUTION λ_{ph}

1.2.1 Basic relation

The phonons of the acoustic branch give:

$$\lambda_{ph} = 1/3\ C_v \ell\ v$$

- C_v: heat capacity per unit volume,
- ℓ : mean free path of the phonons (collision process with "Umklapp" - cf [2]),
- v : mean velocity of the phonons (~ speed of sound in the solid).

Considering a variation in ℓ in 1/T, and the presence of impurities and lattice defects, the following relation applies for a temperature T significantly higher than the Debye temperature $(\Theta)_D$ of the crystal [3]

$$\lambda_{ph} = \frac{1}{A + BT} \qquad (1)$$

B is the *intrinsic* parameter and A the *extrinsic* parameter. It is important to note that the relation (1) is valid only if the quantity of defects is such that $A < \frac{1}{3} BT$ [3].

Existing experimental determinations give [1]:

- *intrinsic* parameter:

$$2.12 \times 10^{-4}\ \text{m.W}^{-1} < B < 2.24 \times 10^{-4}\ \text{m.W}^{-1} \qquad (2)$$

- *extrinsic* parameter (stoichiometric fuel in early life), with **T in K**:

$$2.466 \times 10^{-2}\ \text{m.K.W}^{-1} < A < 5.746 \times 10^{-2}\ \text{m.K.W}^{-1} \qquad (3)$$

1.2.2 Expression of the intrinsic parameter B

Consideration will be given to the following formula proposed in [4]:

$$B = G \times \frac{\gamma^2 n^{2/3}}{\delta \Theta_D^3 \overline{M}} (in\ cm.W^{-1}) \qquad (4)$$

G is given by:

$$G = 4.118 \times 10^7 \times (1 - 0.514\gamma^{-1} + 0.228\gamma^{-2}) \qquad (5)$$

$\gamma = \left(\frac{\delta \ln \Theta_D}{\delta \ln V} \right)_T$ is the Grüneisen parameter of the solid.

n is the number of atoms of the unit cell (n = 3 for UO_2).
δ^3 is the mean atomic volume, at ambient temperature (in $Å^3$ per atom)

$\overline{M}$ is the mean molar mass (in grams per atom)

There is important dispersion of published values of γ (from 1.6 to 2.0) and especially of Θ_D (from 183 to 377 K). The following approach is adopted:

*to determine γ the well-known expression is used: $\gamma = \frac{\alpha V}{\beta_a C_p}$, where α is the volume thermal expansion coefficient, V the molar volume, β_a the adiabatic coefficient of compressibility, and C_p the specific heat at constant pressure. Reference [5] gives a value of 1.9 ± 0.1.

*to determine Θ_D the *Willis's neutron diffraction* studies [6] are used. They give $\Theta_D = 377 \pm 10$ K

From the above values, the following relation is found:

1.75×10^{-4} m.W^{-1} < B < 2.58×10^{-4} m. W^{-1}, which is compatible with (2).

1.2.3 Molecular dynamics calculations

References [7] and [8] give the calculation of the lattice contribution by molecular dynamics, with a Born-Mayer-Huggins potential, and Green-Kubo relationships between the macroscopic charge and energy fluxes, and the corresponding local gradients. The authors have highlighted another contribution above 1700°C (electronic contribution).

1.3 RADIATIVE CONTRIBUTION λ_r

Energy conservation with radiative fluxes gives an integral-differential equation. The equivalent radiative conductivity, λ_r is not expressed in analytical form, unless the mean free path of the photons is low compared with the dimensions of the sample (Rosseland approximation). This is the case for a sample of UO_2 exceeding one centimetre in size. The following expression can then be defined:

$$\lambda_R = \propto T^3$$

In reality ([9], [10]), radiation is highly diffused by charged carriers of thermally activated creation, which leads to a significant reduction in λ_R.

Moreover [11], if the whole problem is resolved without the Rosseland approximation, it is found that λ_r in fact increases more slowly than T^3.

The case of fuel pellets

For UO_2 a radiative conductivity at melting point of a few ten % of total conductivity has been estimated. However, this value, which concerns a non-irradiated dense single crystal, must be considerably reduced for a fuel pellet because of the *grain boundaries* [12] and the *porosity* of the matrix [13]. Finally, λ_r may be considered to be negligible [1], [14].

At melting point, the radiative contribution λ_r represents a maximum of 0.1% of total thermal conductivity.

1.4 ELECTRONIC CONTRIBUTION λ_e

This is a heat transfer mode that is directly linked to the *electrical conductivity* of UO_2, based on the existence of typical electron excitations.

UO_2 should be considered as a Mott-Hubbard-type insulator rather than a classic semiconductor [1], [15]. Below a temperature of about 1400°C, an *extrinsic* conduction regime is set up which is governed by stoichiometric deviations or by the doping agent concentration [16], [17].

Above this temperature the regime is *intrinsic*, associated with the following reaction:

$$2\,U^{4+} \rightarrow U^{3+} + U^{5+} \qquad (6)$$

This regime is characterised by the creation of carriers (electrons on U^{3+} and holes on U^{5+}). This breakage of the insulating state requires additional U energy (*Mott-Hubbard energy*). The carriers created are described, by associating them with induced lattice deformations caused by their presence, as *small polarons* [2]. These carriers therefore migrate by hopping from site to site.

Expression of the electronic contribution

Wiedemann-Franz's law which is applied to a conventional semi-conductor is not applicable in this particular case. For UO_2, allowance must be made for the simultaneous diffusion of matched carriers according to the following scheme: thermally activated creation of electron-hole pairs, migration of both carriers by hopping in a thermal gradient, recombination of the pair in a cold zone.

The expression for λ_e is then [15]:

$$\lambda_e = \left(\frac{k}{e}\right)^2 T \frac{\sigma_n \sigma_p}{\sigma_n + \sigma_p} \left(\frac{U}{kT}\right)^2$$

- k is Boltzmann's constant,
- e is the electron charge,
- T is the temperature (in K),
- σ_n and σ_p describe the electrical conductivity of electrons and holes respectively,
- U is the Mott-Hubbard energy.

If $\zeta = \frac{\sigma_n}{\sigma_p}$ and $\sigma = \sigma_n + \sigma_p$, the following expression is obtained:

$$\lambda_e = \left(\frac{k}{e}\right)^2 T \frac{\sigma\zeta}{(1+\zeta)^2} \left(\frac{U}{kT}\right)^2 \qquad (7)$$

⇒ **Estimation of the ratio** $\zeta = \frac{\sigma_n}{\sigma_p}$

The measurements taken by Killeen [16] show that Seebeck's coefficient for UO_2 becomes independent of temperature above 1400°C. Winter [15] indicates that this is consistent with the assumption $\zeta = 1$.

The relation (7) then becomes:

$$\lambda_e = \frac{1}{4}\left(\frac{U}{e}\right)^2 \frac{\sigma(T)}{T} \tag{8}$$

⇒ **Expression of the electrical conductivity σ(T) for T > 1400°C**

Let $\bar{n}$ and $\bar{p}$ be the respective fractions of electrons and holes, the mobility of which is given by μ_n and μ_p. For stoichiometric UO_2: $\bar{n} = \bar{p}$. The equality established above ($\sigma_n = \sigma_p$) then leads to:

$$\mu_n(T) = \mu_p(T) = \mu(T)$$

The total electrical conductivity can then be written:

$$\sigma(T) = 2\, e\, N_u\, \bar{n}\, \mu(T) \tag{9}$$

- N_u is the density of uranium atoms
- $\bar{n}$ is deduced from the law of mass action associated with the reaction (6). According to the formulation given by Harding [18]:

$$\bar{n}^2 = a \exp\left(-\frac{U}{kT}\right) \tag{10}$$

where a is a constant.

The *mobility*, for the mechanism considered, takes the following form [17], [18]:

$$\mu(T) = \frac{F}{T} \exp\left(-\frac{V}{kT}\right)$$

where V is the migration energy of the carriers.

According to (9), we have thus:

$$\sigma(T) = \frac{2\, e\, N_u\, a\, F}{T} \exp\left(-\frac{W}{kT}\right)$$

of the form:

$$\sigma(T) = \frac{D}{T} \exp\left(-\frac{W}{kT}\right) \tag{11}$$

with:

$$D = 2\, e\, N_u\, a\, F \tag{12}$$

and

$$W = \frac{U}{2} + V \tag{13}$$

From relations (8) and (11) the final expression of the electronic contribution is deduced, for the stoichiometric oxide in an *intrinsic* regime:

$$\lambda_e = \frac{C}{T^2} \exp\left(- \frac{W}{kT} \right) \tag{14}$$

with:

$$C = \frac{1}{4} \left(\frac{U}{e} \right)^2 D \tag{15}$$

The various published values of U and V, and the corresponding values of W, are listed in Table I.

1.5 VALUES ABOVE 2400°C

1.5.1 Attenuation of the electronic contribution?

Weilbacher [19] considers a reduction in the electronic contribution due to trapping of carriers by oxygen vacancies, with an activation energy (3.29 eV) of the order of magnitude of the formation energy of defects in UO_2.

However, this reduction can be called into question [1] in view of the important relative uncertainty (about 8%) on the values of C_p used to deduce λ from diffusivity measurements.

1.5.2 Additional contribution beyond 2400°C (existence of a super-ionic state)?

The values of C_p at high temperatures in fact give rise to another problem [23].

The curve used by Weilbacher is obtained by differentiating a unique high-temperature enthalpy law. But Dworkin and Bredig [24] have shown that there is an order-disorder type transition in the anionic

Tableau 1 : **creation energy of charged carriers U, migration energy V, and activation energy of electrical conductivity W (various authors).**

Auteurs	U (eV) (Mott-Hubbard energy)	V (eV) (carrier migration energy)	W (eV) $(= \frac{U}{2} + V)$
Hyland [1]	1.86	0.24	1 17
Young [9]	2.30	-	-
Winter [15]	2.00	0.30	1.30
Dudney [17]	2.40	0.20	1.40
Harding [18]	2.52	0.15	1.41
Weilbacher [19]	2.26	-	-
Killeen [20]	2.30	0.14	1.29
Hampton [21]	2.40	0.12	1.32
Aronson [22]	-	0.30	-

sub-lattice of certain fluorite-type compounds ($SrCl_2$, CaF_2, PbF_2). This transition requires the use of two different enthalpy laws to obtain a more satisfactory fit. A peak value for C_p is thus obtained centred on a temperature of $0.8T_m$. On this basis, Williams [25] proposes for $SrCl_2$ a Frenkel pair diffusion model, and calculates a contribution λ_{fp} which has the same order of magnitude as the increase in conductivity observed in this body for $T > 0.8T_m$.

⇒ **Case of UO_2**

The situation is not so clear [23].

On one hand, Ralph [26], has used the UO_2 enthalpy measurements taken by Hein [27], to develop a numerical treatment which highlights a peak in the C_p curve around 2400°C. Other indications suggest the existence of a Bredig-type transition.

In addition, the rare experimental results available at the temperatures considered [19] do not indicate any particular increase in thermal conductivity. However, these results have been established from diffusivity values, *using a C_p law which does not have a peak at 0. 8 T_m*

Moreover, the parameters coming into play in the calculation of λ_{fp} are not well known [25].

1.5.3 Attitude adopted

For lack of sufficient information, no description will be given of the attenuation of the electronic contribution nor of the increase due to the Bredig transition. Indeed, it is worth noting that the two terms have opposite signs and thus compensate for each other, at least in part.

These terms could possibly be introduced once they are better known.

1.6 SUMMARY

- The thermal conductivity up to about 1500°C can be described in a satisfactory manner by a lattice contribution.
- The noticeable transparency observed in the infrared for UO_2 single crystals no longer exists in fuel pellets (effect of porosity and grain boundaries).
- The existence of intrinsic electrical conduction above 1400°C gives rise to a contribution to thermal conductivity, attributed to the electron-hole pairs treated as small polarons, which would explain the increase in thermal conductivity in this zone.
- Above 2400°C the situation is not so clear-cut: the Frenkel pairs could take part in heat transfer and, in parallel by trapping the carriers, the vacancies could attenuate the electronic contribution. Given the lack of experimental and theoretical data it is not possible to formulate these effects (which in fact should compensate each other, at least partially).

2. THE CEA LAW: A NEW FORMULATION

2.1 THE CURRENT CEA LAW

2.1.1 Results

Two series of experimental points, one going up to 2300 °C [28], and the other up to 2500 °C [29] were obtained by the same direct measurement method, described in [29], for stoichiometric fuel in early life.

In the phonon conduction field, the conductivity is described by a classic law of the type $(A+BT)^{-1}$ then, to make allowance for the rise in the curve at high temperatures, a T^m term was considered .

For an oxide of density 10.65 g.cm^{-3}, the law is written [30]:

$$\lambda(T) = \frac{1}{0.10449 + 2.27 \times 10^{-4} T} + 3.4125 \times 10^{-17} T^{4,94}$$

In this relation, ***T is given in*** *°C*, and λ is given in W.m^{-1}K^{-1}.

2.1.2 Comparison with Harding and Martin's law (often known as Martin's law)

Harding [18] expresses the thermal conductivity of UO_2 as the sum of a lattice contribution and an electronic contribution:

$$= \frac{1}{0.0375 + 2.165 \times 10^{-4} T} + \frac{4.715 \times 10^{9}}{T^2} \exp\left[- \frac{1}{} \right. \qquad (16)$$

In this relation, T is the temperature in K, and λ is in W.m^{-1}K^{-1}.

Harding reports good agreement between this law and Brandt's compilation of experimental values [31]. The manner in which this law was constructed is recalled below :

→ for the *lattice contribution*, the authors use the values of A and B taken from an unpublished report by Killeen (cf [32]).
→ for the electronic *contribution*, they based their calculations on the electrical conductivity law (11):

$$\sigma(T) = \frac{D}{T} \exp\left(- \frac{W}{kT} \right)$$

They determine D and W by adjusting this formula to measurements taken by Bates [33]. They found: D = 2.97 × 10^{9} K.(W.m)$^{-1}$ and W = 1.41 eV.

By taking V = 0.20 eV (Dudney value [17]), the relation (13) gives:

U = 2.42eV

However, by considering the *integral of thermal conductivity between 500 °C and the melting point*, they preferred to use U = 2.52 eV, and thus V = 0.15 eV, leading to the following recommended values

V = 0.15 eV
U = 2.52 eV

Both laws (CEA and Martin) are plotted on **Figure 2**, together with the experimental points of the CEA, reduced to zero porosity according to the correction of [34]. Excellent agreement is found up to 1800°C, with an increasing deviation at higher temperatures. Towards the melting point, the central temperature calculated with Martin's law would be about 80°C higher than the value given by the CEA law, for the same linear power.

2.2 NEW FORMULATION OF THE CEA LAW

The fitting of the CEA experimental points was reviewed, considering a law of the form:

$$\lambda(T) = \frac{1}{A + BT} + \frac{C}{T^2} \exp\left(- \frac{W}{kT} \right)$$

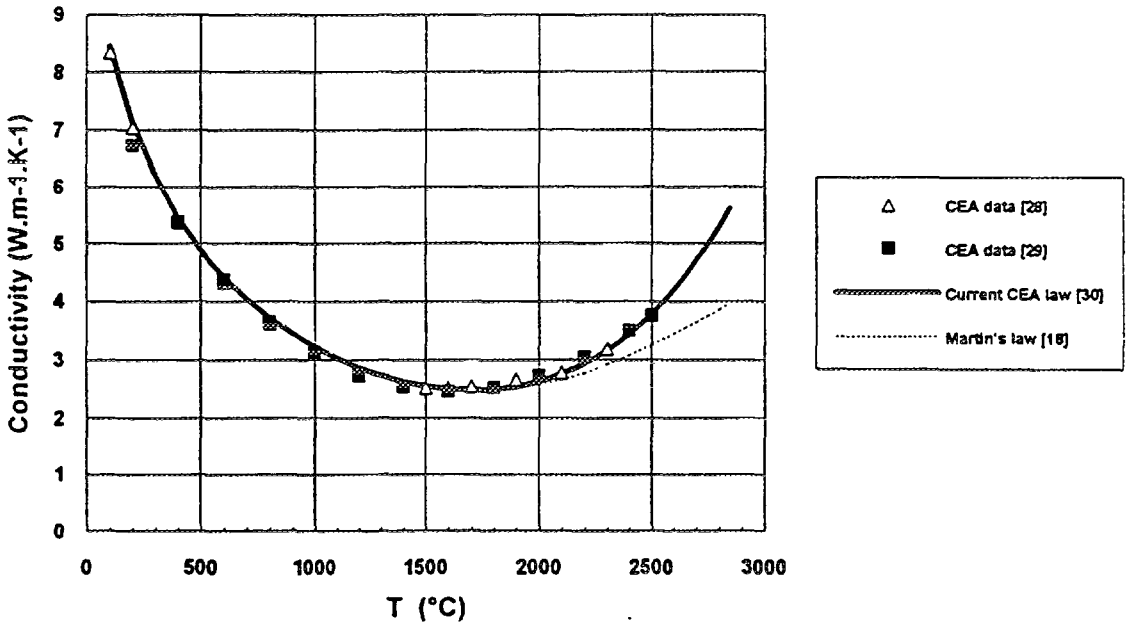

FIG. 2 Thermal conductivity of UO_2 - Current CEA law

By simultaneously determining the four parameters A, B, C, and W, the following expression is obtained for dense UO_2:

$$\frac{1}{.034944 + 2.2430 \times 10^{-4} T} + \frac{6.157 \times 10^{9}}{T^2} \exp\left[-\frac{1.41 \times}{}\right. \qquad (17)$$

(*T in K*, λ en $W.m^{-1}.K^{-1}$)

2.3 DISCUSSION

2.3.1 Values of A and B

According to the relation (17), we have:

$$A = 3.4944 \times 10^{-2}\ m.K.W^{-1} \quad \text{and} \quad B = 2.2430 \times 10^{-4}\ m.W^{-1}$$

* the value of A is compatible with (3)

* according to (4) and (5), the experimental value of B is found with $1.88 < \gamma < 2.00$ and $367\ K < \Theta_D < 384\ K$. The agreement with the theory is thus satisfactory.

2.3.2 Activation energy W

The activation energy obtained (1.41 eV) is identical to that found by Harding [(16)] and in agreement with other published values. These values generally result from electrical conductivity measurements. The coherence observed characterises the mechanism responsible for this conductivity.

2. 3. 3 Parameter C and integral of the conductivity at melting point

The value of C obtained in (17) is about 30% higher than the value indicated by Harding [(16)]. To appreciate this deviation, Figure 3 shows the two laws and the experimental points. The central temperatures estimated near melting point would differ by about 60°C.

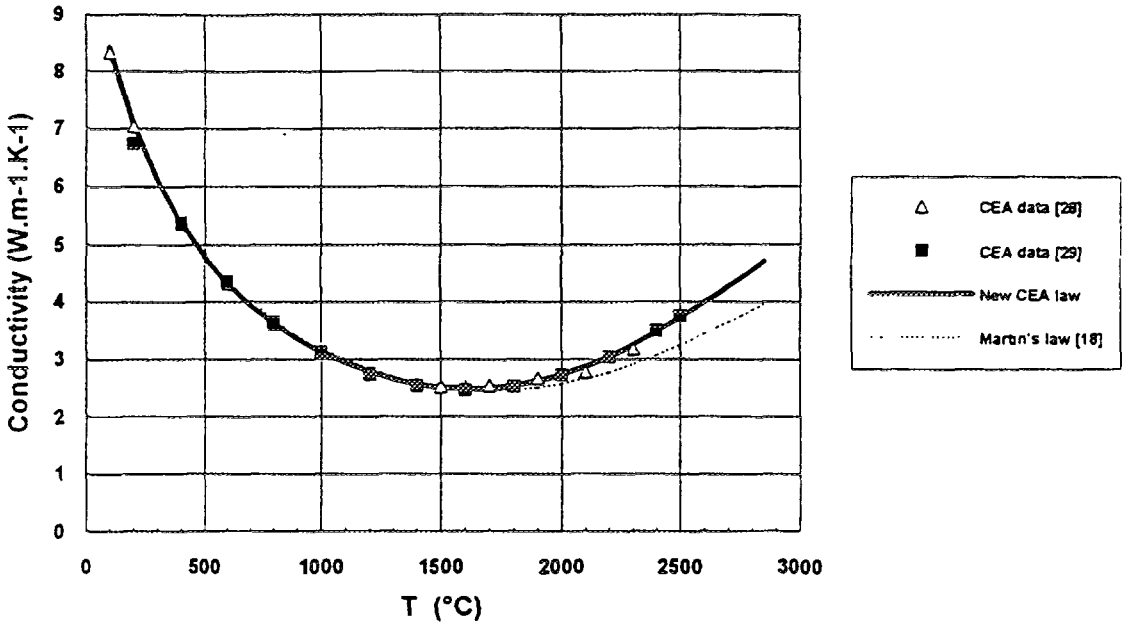

FIG. 3 Thermal conductivity of UO_2 - New CEA law

* The new CEA formulation lowers the integral of thermal conductivity at high temperature compared to the previous law. However, this drop must be compensated for by taking a higher T_m value (2847°C instead of 2800°C) and, between 500°C and melting point, the same value is found to within 3.5×10^{-3}.

* Moreover, Harding has adjusted his law to obtain Marchandise's integral value at melting point [35]. His procedure raises two problems:

- [35] gives $I_m = \int_{773}^{T_m} \lambda \, dT = 6.8$ kW.m^{-1} for a 5% initial porosity, taking $T_m = 3073$ K, and considering that, in practice, as from 2000°C, the porosity drops to 1%. Harding adjusted C in order to obtain the same value for I_m, but with $T_m = 3120$ K, and considering zero porosity as from 1700°C.

- the reference value concerns in-pile fuel for which it is known that, at least at high temperature, the conductivity is lower than that of out-of-pile fuel [30].

All this contributes to envisaging a higher value of C in Harding's work, with care being taken when attempts are made to refit a thermal conductivity law to the integral of the conductivity at melting point.

2.3.4 Electrical conductivity and Mott-Hubbard free energy

A special interest is taken here for σ in relation to the laws proposed by Bates [33] and Killeen [16]. Having deduced C from the λ measurements, the value of V is that proposed in [17] (0.20 eV). U is then fixed (2.42 eV) taking into account W (1.41 eV). Expressions (15) and (11) then give:

$$\sigma(T) = \frac{4.205 \times 10^{9}}{T} \exp\left(- \frac{1.41 \times 1.6 \times 10^{-19}}{kT} \right) \quad (\Omega.m)^{-1}$$

Figure 4 can be used to compare this σ(T) law with the measurements taken by Bates, and with the Harding adjustment:

$$\sigma_M(T) = \frac{2.970 \times 10^9}{T} \exp\left(-\frac{1.41 \times 1.6 \times 10^{-19}}{kT} \right) \quad (\Omega.m)^{-1}$$

and with Killeen's law (resulting from measurements up to 2000 K):

$$\sigma_K = 2600 \times \exp\left(\frac{-1.07 \times 1.6 \times 10^{-19}}{kT} \right) \quad (\Omega.m)^{-1}$$

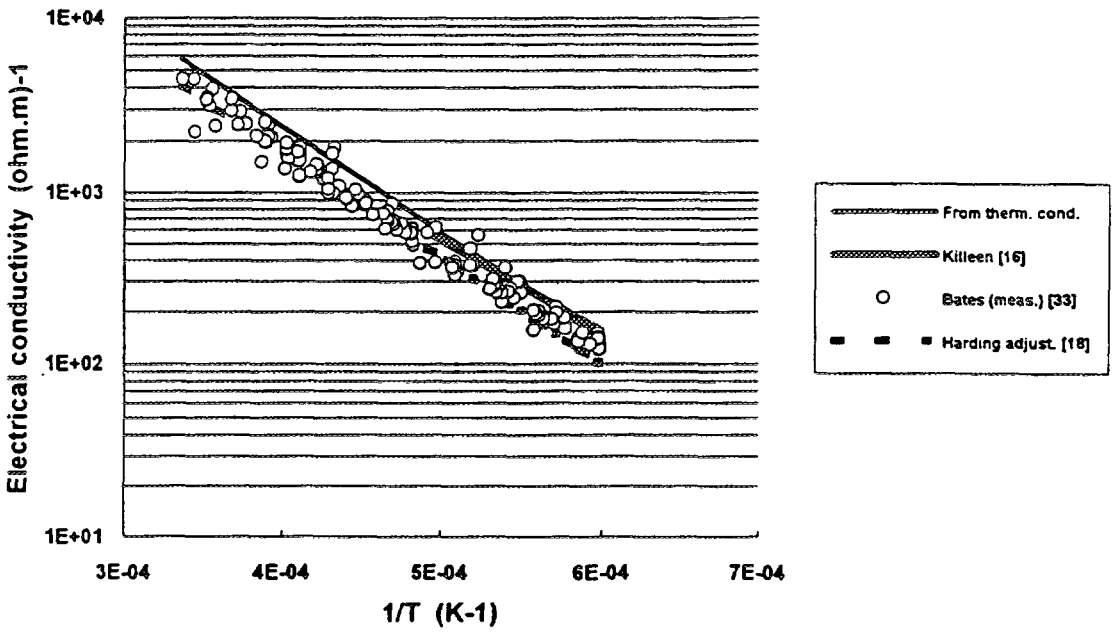

FIG. 4 Electrical conductivity of UO_2

σ_M is close to the lower limit of Bates' measurement interval σ is at the upper limit of this interval, but in good agreement with σ_K.

If the value suggested in [17] (0.0554 $m^2.V^{-1}.s^{-1}$) is taken for F above 1400 °C, the relations (15) and (12) give a value of a = 9.71.

Physical sense of a

The mass action law associated with (6) is written as follows:

$$\frac{\bar{n}^2}{(1 - 2\bar{n})} = \exp\left(-\frac{G}{kT} \right) \tag{18}$$

where G = U-TS, with S *being the variation in entropy associated with rupture of the insulating state.* Assuming 1-2n ˜ 1, then the relation (10) is found with:

$$a = \exp\left(\frac{S}{2k} \right)$$

This corresponds to $S = 4.5\,k$. According to [15], S ~ 2k. There is thus a $\sigma \leftrightarrow \mu$ coherence problem. Note that Harding's work leads to values of a = 6.9 and S = 3.9.

[36] indicates that: $\mu = \frac{G}{T}(1-2\bar{n})\exp\left(-\frac{V}{kT}\right)$ and [15] gives an electrical conductivity in the following form:

$$\sigma(T) = \frac{K}{T}\bar{n}(1-2\bar{n})\exp\left(-\frac{W}{kT}\right)$$

With (18), we find:

$$\sigma(T) = \frac{K}{T}\frac{\exp\left(\frac{S}{2k}\right)}{\left(1+2\exp\left(\frac{S}{2k}\right)\exp\left(-\frac{U}{2kT}\right)\right)}\exp\left(-\frac{U}{2kT}\right)\exp\left(-\frac{V}{kT}\right)$$

Taking V = 0.20 eV, and by fitting this relation to the Bates' measurements by a least-squares method, the following values are obtained:

U = 2.41 eV $\qquad$ $S = 1.77k$ $\qquad$ K = 1.332 x 10^9 $(W.m)^{-1}.K^2$

Applied to λ, this formalism was found to have no major advantage which could compensate for its complexity. But it is worth noting that it confirms the value of W, and above all, *it enables the value of S to be defined*, by confirming the order of magnitude (2k) that Winter indicated as being consistent with Killeen's Seebeck coefficient measurements [151.

Nevertheless, the mobility (pre-exponential factor) has to be studied in further detail.

3. CONCLUSIONS

3.1 The experimental points of the CEA up to 2500°C have been fitted to a new thermal conductivity law, including the contribution of phonons and the electronic contribution at high temperatures:

$$\lambda(T) = \frac{1}{0.034944 + 2.2430\times10^{-4}\,T} + \frac{6.157\times10^{9}}{T^2}\exp\left[-\frac{1.41\times1.6\times10^{-19}}{kT}\right]$$

(*T in K*, l in $W.m^{-1}.K^{-1}$)

The value of B (intrinsic parameter of the contribution of phonons) is in agreement with the theoretical estimate, using γ values between 1.88 and 2.00 and Θ_D values between 367 and 384 K. The values of C and W indicate a good compatibility with Bates and Killeen's laws (electrical conductivity) by taking S = 1.8 k, V = 0.20 eV and U = 2.42 eV.

3.2 This new CEA formulation has the advantage of being based on better physical grounds than the previous law for extrapolations to the melting point, without calling into question the integral of the conductivity at melting point. Moreover, it is closer to Martin's law at high temperatures, while at the same time giving a better account of the measurements above 1800°C.

3.3 The analysis performed should, in the near future, provide the means to take more detailed account of the effects of irradiation (over-stoichiometry, presence of impurities), whether at the level of term A of the lattice contribution or with respect to the electronic contribution [151

REFERENCES

[1] HYLAND, G.J., Thermal Conductivity of Solid UO_2: critique and recommendation, J. Nucl.Mat., 113 (1983) 125-132.

[2] KITTEL, C., Introduction à la physique de l'état solide, Dunod Université, (1972).

[3] KLEMENS, P.G., Theory of heat conduction in nonstoichiometric oxides and carbides, High Temp.-High Press., 17 (1985), 41-45.b

[4] SLACK, G.A., The Thermal Conductivity of Nonmetallic Crystals, Sol. State Phys., 34 (1979) 3-71.

[5] MOMIN, A.C., KARKHANAVALA, M.D., Temperature Dependence of the Grüneisen Parameter and Lattice Vibrational Frequencies of UO_2 and ThO_2 in the Range 298-2300 °K, High Temp. Science, 10 (1978) 45-52.

[6] WILLIS, B.T.M., Neutron diffraction studies of the actinide oxides - II. Thermal motions of the atoms in uranium dioxide and thorium dioxide between room temperature and 1100°C, Proc. Roy. Soc. A, 274 (1963) 134 (part II).

[7] GILLAN, M.J., The Molecular Dynamics Calculation of Transport Coefficients, Physica Scripta, T39 (1991) 362.

[8] LINDAN, P.J.D., GILLAN, M.J., A molecular dynamics study of the thermal conductivity of CaF_2 and UO_2, J. Phys.: Condens. Matter, 3 (1991) 3929.

[9] YOUNG, R.A., Model for the Electronic Contribution to the Thermal and Transport Properties of ThO_2, UO_2 and PuO_2 in the Solid and Liquid Phase, J. Nucl. Mat. 87 (1979) 283.

[10] BOBER, M., Spectral Reflectivity and Emissivity of Solid and Liquid UO_2 as a Function of Wavelength, Angle of Incidence and Polarization, High Temp., High Pressure 12 (1980) 297.

[11] VISKANTA, R., Influence of Internal Thermal Radiation on Heat Transfer in UO_2 Fuel Elements, Nucl. Sci. Eng. 21 (1965) 13.

[12] ANDERSON, E.E., Radiative Heat Transfer in Molten UO_2 based on the Rosseland Diffusion Method, Nucl. Technol. 30 (1976) 65.

[13] HAYES, S.L., PEDDICORD, K.L., Radiative heat transfer in porous uranium dioxide, J. Nucl. Mat., 202 (1993) 87.

[14] BROWNING, P., On the Relative Importance of the Electronic and Radiative Contributions to the Thermal Conductivity of Uranium Dioxide, J. Nucl. Mat., 92 (1980) 33.

[15] WINTER, P.W., The electronic transport properties of UO_2, J. Nucl. Mat. 161 (1989) 38.

[16] KILLEEN, J.C., The effect of Niobium oxide additions on the electrical conductivity of UO_2 J. Nucl. Mat. 88 (1980) 185.

[17] DUDNEY, N.J., COBLE, R.L., TULLER, H.L., Electrical Conductivity of Pure and Yttria-Doped Uranium Dioxide, J. Am. Ceram. Soc. 64 n°11 (1981) 627.

[18] HARDING, J.H., MARTIN, D.G., A recommendation for the thermal conductivity of UO_2, J. Nucl. Mat., 166 (1989) 223-226.

[19] WEILBACHER, J.C., Diffusivité thermique de l'oxyde d'uranium et de l'oxyde de thorium à haute température, High Temp.-High Press., 4 (1972) 431-438.

[20] KILLEEN, J.C., The measurement of the electron to hole mobility ratio in UO_2 and its effect on thermal conductivity, J. Nucl. Mat. 92 (1980) 136.

[21] HAMPTON, R.N., SAUNDERS, G.A., The electrical impedance of single crystal urania at elevated temperature, J. Nucl. Mat. 154 (1988) 245.

[22] ARONSON, S., RULLI, J.E., SCHANER, B.E., Electrical Properties of Nonstoichiometric Uranium Dioxide, Chem. Phys. 35 (1961) 1382.

[23] RALPH, J., Recent developments in the study of the high temperature thermophysical properties of UO_2, Nucl. Energy 26 n°4 (1987) 259.

[24] DWORKIN, A.S., BREDIG, M.A., Diffuse Transition and Melting in Fluorite and AntiFluorite - Type of Compounds: Heat Content of Potassium Sulfide from 298 to 1260 K, J. Phys. Chem. 72 (4) (1968) 1277.

[25] WILLIAMS, R.K., Enhanced thermal conductivity associated with formation of the superionic state, Phys. Rev. B 26 (10) (1982) 5983.

[26] RALPH, J., HYLAND, G.J., Empirical Confirmation of a Bredig Transition in UO_2, J. Nucl. Mat. 132 (1985) 76.
[27] HEIN, R.A., SJODAHL, L.H., SZWARC, R., Heat Content of Uranium Dioxide from 1200 to 3100 K, J. Nucl. Mat. 25 (1968) 99.
[28] CONWAY, J.B., FEITH, A.D., An interim report on a round-robin experimental program to measure the thermal conductivity of stoichiometric uranium dioxide, GEMP 715 (1969)
[29] STORA, J.P., et al., Conductibilité thermique de l'oxyde d'uranium fritté dans les conditions d'utilisation en pile, Rapport CEA R 2586 (1964).
[30] BARBIER, Y., BRUET, M., Modelling of the fuel-cladding heat transfer, IAEA Specialists" Meeting on Water Reactor Fuel Element Performance Computer Modelling, Blackpool (1978)
[31] BRANDT, R., et al., Thermal Conductivity and Emittance of Solid UO_2, CINDAS Purdue University, West Lafayette, Indiana (1976)
[32] MARTIN, D.G., A Re-appraisal of the Thermal Conductivity of UO_2 and mixed (U,Pu) Oxide Fuels, J. Nucl. Mat., 110 (1982) 73-94.
[33] BATES, J.L., Electrical Conductivity of UO_2, Pacific North West Laboratory Report, BNWL-296 Pt2 (1967).
[34] VAN CRAYENEST, J.C., STORA, J.P., Effet de la porosité sur la variation de conductibilité thermique du bioxyde d'uranium en fonction de la température, J. Nucl. Mat., 37 (1970) 153
[35] MARCHANDISE, H., Conductibilité thermique du bioxyde d'uranium, Commission des Communautés Européennes, Rapport EUR 4568 f (1970)
[36] TULLER, H.L., NOWICK, A.S., Small polaron electron transport in reduced CeO_2 single crystals, J.Phys.Chem.Solids, 38 (1977) 859-867

THERMAL CONDUCTIVITY OF HYPERSTOICHIOMETRIC SIMFUEL

P.G. LUCUTA, R.A. VERRALL
Chalk River Laboratories,
AECL Research,
Chalk River, Ontario, Canada

H. MATZKE
CEC Joint Research Centre,
Karlsruhe, Germany

Abstract

At extended burnup, reduction in fuel thermal conductivity occurs as fission-gas bubble, solid fission-product (dissolved and precipitated) build-up, and the oxygen-to-uranium ratio (O/U) possibly increases. The effects of solid fission products and the deviation from stoichiometry can be investigated using SIMFUEL (SIMulated high-burnup UO_2 FUEL). The reduction in fuel conductivity due to solid fission products was assessed and reported previously. In this paper, thermal conductivity measurements on hyperstoichiometric SIMFUEL and UO_{2+x} investigating the effect of the excess of oxygen on fuel thermal properties, are reported. The thermal diffusivity, specific heat and density of hyperstoichiometric SIMFUEL and UO_{2+x}, annealed at the same oxygen potential, were measured to obtain thermal conductivity. The excess of oxygen lowered the thermal diffusivity, but did not significantly affect the specific heat. The thermal conductivity of UO_{2+x} (no fission products present) decreases with an increasing O/U ratio; a reduction of 15%, 37% and 56% at 600°C, and 11%, 23% and 33% at 1500°C, was found for O/U ratios of 2.007, 2.035 and 2.084, respectively. For the SIMFUEL annealed at ΔGo_2 = -245 kJ/mol (corresponding to $UO_{2.007}$), the thermal conductivity was practically unchanged, although for the higher oxygen potentials ($\Delta Go_2 \geq$ - 205 kJ/mol) a reduction in thermal conductivity of the same order as in UO_{2+x} w as measured. For SIMFUEL, annealed in reducing conditions, the fission products lowered thermal conductivity significantly. However, for high oxygen potentials ($\Delta Go_2 \geq$ -205 kJ/mol), the thermal conductivities of UO_{2+x} and SIMFUEL were found to be approximately equal in the temperature range of 600 to 1500°C. Consequently, excess oxygen is the dominant factor contributing to thermal conductivity degradation at high oxygen potentials.

1. INTRODUCTION

Thermal conductivity of UO_2 is an important property, because it controls the fuel operating temperature and therefore influences almost all important processes (gas release, swelling, grain growth) and limits the linear power. Changes in thermal conductivity occur during irradiation as fission-gas bubbles form, fission products build up and the oxygen-to-metal ratio (O/M) possibly increases.

Simulated high-burnup fuel, termed SIMFUEL, provides a convenient way to investigate intrinsic fuel thermal properties. We have previously reported on the fabrication procedure and characterization of SIMFUEL [1-3] that demonstrated the equivalence of the microstructure and phase structure to irradiated high-burnup fuel. All classes of fission products-dissolved oxides, metallic precipitates and perovskites (except for the gases and volatiles)-were present in SIMFUEL [2,3].

Thermal conductivities of SIMFUEL, determined from thermal diffusivity, specific heat and density measurements, decrease with simulated burnup increase [4-7]. The influence of simulated fission products on thermal conductivity was analysed considering the precipitated phases and the dissolved oxides in the UO_2 fluorite matrix. The degree of phonon scattering by the solute fission products in the UQ - which determines the reduction in thermal conductivity - was also calculated for the various simulated burnups [8,9].

Besides the dissolved fission products, the possible deviation from fuel stoichiometry (an increase in the oxygen-to-uranium (O/U) ratio) in irradiated fuel can also affect thermal conductivity and fission-product mobility. For O/U ratios between 2.00 to 2.11, Goldsmith and Douglas [10] reported a

degradation in the thermal conductivity of "pure" UO_{2+x} over the temperature range of 500-1000°C. They found a reduction in thermal conductivity of 28% at 1000°C and 39% at 500°C for an O/U ratio of 2.05.

The effect of porosity and stoichiometry on UO_2 thermal conductivity was also investigated by Hobson et al. [11]. They have measured thermal diffusivities by laser flash on 93 and 96% theoretical density (TD) specimens with a deviation from stoichiometry of 0.006, 0.03 and 0.06, respectively. The results showed a reduction in thermal conductivity with increasing temperature and deviation from stoichiometry. For $UO_{2.06}$ they found a change in the slope at 500°C. Above this temperature they reported practically no changes in thermal conductivity.

In our study, the effect of excess oxygen (deviation from stoichiometry) on fuel thermal conductivity was investigated using SIMFUEL with equivalent simulated burnups of 3 and 8 at %[1]. The thermal diffusivity and specific heat were measured on specimens annealed in controlled oxidizing conditions and combined to obtain the thermal conductivity values. Microstructural changes and the actual measurements of the deviation from stoichiometry of hyperstoichiometric UO_2 and SIMFUEL were discussed and described elsewhere [12].

2. EXPERIMENTAL TECHNIQUES

2.1 HYPERSTOICHIOMETRIC SIMFUEL

Excess oxygen is generated in irradiated fuel as many fission products have a lower valence than uranium. From the fission yields and valence states of the fission products, the excess of oxygen per atom percent burnup can be estimated: the result is that *one atomic percent burnup causes a change from 2.000 to 2.009* in the O/M ratio. However, in practice, the excess oxygen is thought to migrate to and react with the Zircaloy sheath, so no net oxidation of the fuel should be observed. Recently, it has been questioned whether the CANLUB coating on the inside of the Zircaloy sheath in CANDU fuel was inhibiting ZrO_2 formation at high burnup [13], in which case the excess of oxygen may remain in the fuel.

Excess oxygen was introduced in SIMFUEL and UO_2 by annealing the specimens in an oxidizing atmosphere (CO_2/CO mixture). An appropriate ratio of the gas mixture and the annealing temperature determines the oxygen potential, which is linked to the O/U ratio [12]. The relationship is known for unirradiated UO_2, but is *unknown* for irradiated nuclear fuel and SIMFUEL.

The O/U ratios of 2.0069, 2.035 and 2.084 were measured using the coulometric-titration technique [12] for the hyperstoichiometric UO_{2+x} samples, prepared in CO_2/CO atmospheres of 9/1 and 99/1 at different annealing temperatures (Table 1). The oxygen pressure of the annealing atmosphere was measured and recorded upstream and downstream of the hot zone by two zirconia oxygen sensors. To avoid the precipitation of U_4O_9 at low temperatures, the specimens were quenched to room temperature. The measured values of the O/U ratio are lower than those predicted from the experimental conditions (Table 1) due to oxygen loss during cooling down [12]. SIMFUEL specimens were prepared under identical conditions, having been exposed to the same oxygen potential. However, the O/U ratio in SIMFUEL is different, due to the oxidation of the metallic precipitates (Mo and Ru) and different initial stoichiometry, as well as the changes in the valence of some dissolved additives.

2.2 THERMAL DIFFUSIVITY AND SPECIFIC HEAT MEASUREMENTS

For thermal diffusivity measurements, disks of 12 mm diameter and about 1 mm thick were sliced from the pellets. The surfaces were polished to be parallel within 0.01 mm. Smaller specimens, about 6 mm in diameter and 2-3 mm thick, were used for specific heat measurements. All specimens were first annealed at 1500°C in reducing conditions to remove mechanical damage, before the final anneal in

[1] 1 at% burnup ≡ 225 MW h/kg U = 9.38 MWd/kg U.

TABLE I Stoichiometric deviations and corresponding oxygen potentials of hyperstoichiometric specimens and the experimental conditions for preparation.

Measured O/U	Final ΔGo_2 (kJ/mol)	Annealing Conditions			Predicted O/U
		Gas mixture	Temp. (°C)	ΔGo_2(kJ/mol)	
2.000	-540	4%H_2/Ar	1700	-550	2.000
2.007	-245	CO_2/CO=9	1310	-232	2.010
2.035	-205	CO_2/CO=99	1220	-190	2.045
2.084	-160	CO_2/CO=99	1380	-150	2.100

oxidizing atmosphere. Disks free of cracks and fissures were selected for the thermal diffusivity measurements. Density was measured by immersion for the thermal diffusivity specimens and was found to be around 98% TD.

Thermal diffusivity was measured by the laser-flash method from room temperature to 1500°C. The thermal diffusivity was determined from the rear-surface temperature rise, after the front surface of the sample was heated by the laser beam at various temperatures obtained by heating the sample in a graphite furnace, and the results were checked during the cooling cycle. The measurements were performed in vacuum (10^{-6} torr). No major changes in the oxidation state (O/U ratio) of the specimens were detected using the coulometric titration technique after the thermal diffusivity measurements.

he specific heat of SIMFUEL was measured between 25 and 1500°C using a differential scanning calorimeter (DSC) with sapphire as a reference material. The standard and sample, both encapsulated in pans, were subjected to the same heat flux, and the differential power required to heat the sample at the same rate was recorded. The specific heat of SIMFUEL specimens was computed from the mass of the sapphire standard, the differential power and the known specific heat of the sapphire.

The thermal conductivity (λ) was calculated from the thermal diffusivity (α), specific heat (c_p) and density (ρ), using the standard expression [7]:

$$\lambda = \alpha \cdot C_p \cdot \rho \qquad (1)$$

Density was corrected for temperature (T) using the thermal expansion coefficient of the UO_2 [14].

The thermal conductivity results were normalized to 95% and 100% of the TD, applying corrections for the porosity using the Loeb equation:

$$\lambda = \lambda_{TD} (1 - \beta \cdot P)$$

where P is the pore volume fraction ($P = 1 - \rho/\rho_{TD}$), β is a constant, and the subscript TD refers to a 100% theoretical density sample. The value for β, including its temperature dependence, reported by Notley and McEwan [15] ($2.58 - 0.58 10^{-3} T$), was used.

3. RESULTS AND DISCUSSION

Thermal diffusivity values of hyperstoichiometric UO_2, normalized to the same density, were lower than those of the stoichiometric specimens. The measured thermal diffusivity values showed low scatter and good reproducibility during heating and cooling of the specimen. Thermal diffusivities of

SIMFUEL were lower than that of the UO_2 for the specimens annealed under the same oxygen potential, with the difference especially marked at low temperatures. The specific heat of SIMFUEL was found to be slightly but systematically higher than for the pure UO_2, for each deviation from stoichiometry. For example, the difference in the specific heat between 3 at% simulated burnup SIMFUEL and UO_2 amounts to less than 2%, for an experimental error of 1% in the data measured using DSC. Specific heat also slightly increases with the deviation from stoichiometry for each simulated burnup.

The thermal conductivity of UO_{2+x} (100% of TD) decreases with an increasing O/U ratio (Figure 1); a reduction of 13%, 37% and 56% at 600°C and 11%, 23% and 33% at 1500°C was found for O/U ratios of 2.007, 2.035 and 2.084, respectively.

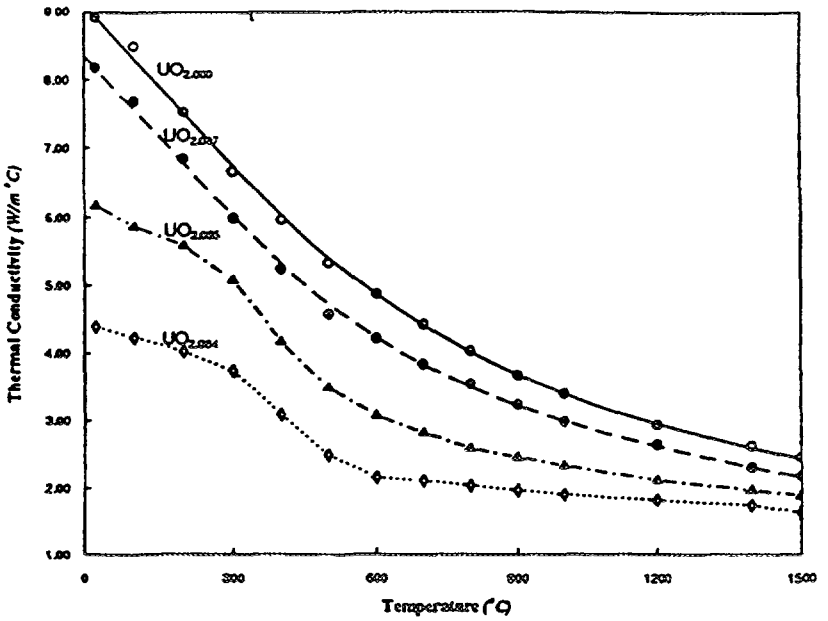

FIG. 1. *Thermal conductivities, normalized to 100% of TD, for stoichiometric UO_2 and hyperstoichiometric UO_{2+x} in the 25 to 1500 °C temperature range.*

Between 400 and 600°C, a change in the slope of the thermal conductivity variation curve of the UO_{2+x} occurred for deviations from stoichiometry of 0.035 and 0.084. This discontinuity in the thermal conductivity variation with the temperature is associated with the phase change from U_4O_9 to UO_{2+x}. Precipitation of the U_4O_9 phase, identified by X-ray diffraction (XRD) [12], could not be avoided, despite the careful preparation of the UO_{2+x} specimens. The same behaviour for the UO_{2+x} thermal conductivity due to the U_4O_9 resolution in the fluorite lattice has been reported previously by other researchers [10, 11].

The reduction measured by us in the thermal conductivity of hyperstoichiometric UO_{2+x} is in good agreement with the previously reported results; for example, our values for $UO_{2.035}$ match well those obtained by Goldsmith and Douglas [10] for $UO_{2.04}$ between 400°C and 1000°C.

The thermal conductivity results from hyperstoichiometric SIMFUEL with an equivalent burnup of 3 and 8 at% decrease also with the temperature; these variations are shown in Figures 2 and 3.

The thermal conductivity values obtained from hyperstoichiometric SIMFUEL also decrease with temperature for each simulated burnup and oxygen potential. In general, the thermal conductivities of hyperstoichiometric SIMFUEL were lower than those measured on the specimens annealed in reducing

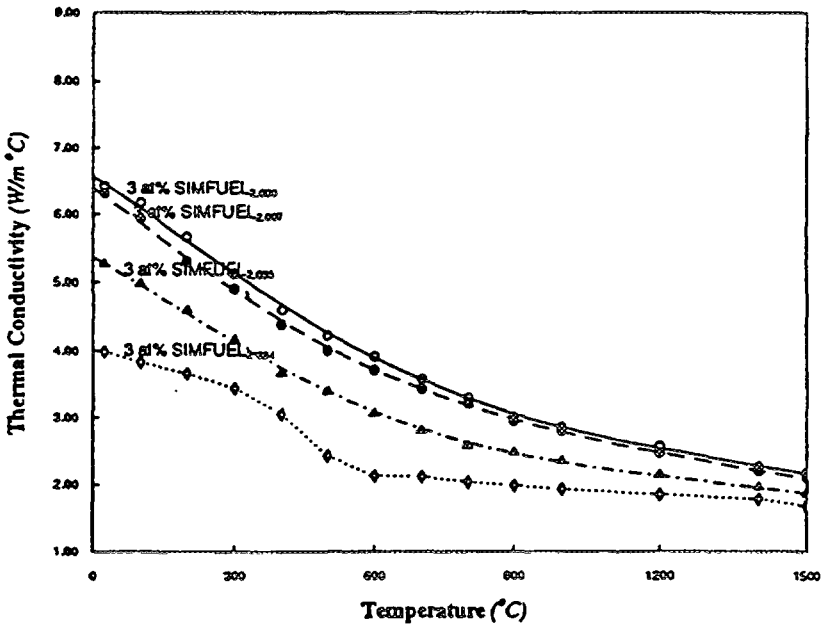

FIG. 2. *Thermal conductivities of 3 at% burnup SIMFUEL (ΔGo_2 = -550, -245, -205 and -160 kJ/mol - 100% TD) as a function of temperature. The label indicates the equivalent deviation from stoichiometry measured in the reference UO_2.*

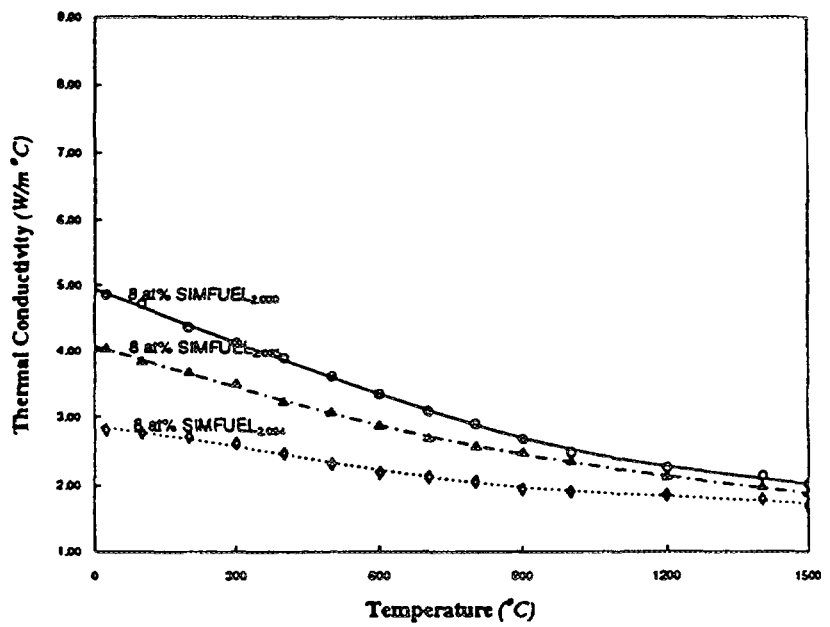

FIG. 3. *Thermal conductivities of 8 at% burnup SIMFUEL normalized to 100% TD as a function of temperature for ΔGo_2 of -540, -205, and -160 kJ/mol.*

conditions (-540 kJ/mol), except for the lower oxygen potential of -245 kJ/mol (x = 0.007 in UO_{2+x}), for which the change in thermal conductivity was practically nil at 3 at% burnup (Figure 2). At higher oxygen potential, similar reduction to that observed for UO_{2+x} was found for SIMFUEL (Figures 2 and 3).

The discontinuity in the thermal conductivity variation observed in $UO_{2.035}$ and $UO_{2.084}$ does not occur for 8 at% simulated burnup SIMFUEL, and for the lower oxygen potentials for the 3 at% SIMFUEL; in both cases, U_4O_9 could not be detected by XRD. These differences can be related to a different oxidation behaviour of SIMFUEL compared with UO_2 [15]. Figures 4 and 5 show the effect of the burnup for a given oxygen potential: ΔGo_2 = -205 kJ/mol (corresponding to $UO_{2.035}$), and ΔGo_2 = -160 kJ/mol ($UO_{2.084}$).

The effect of the burnup becomes less significant with increasing oxygen potential. For an oxygen potential of ΔGo_2 = -245 kJ/mol O_2 (corresponding to $UO_{2.007}$), there is a small reduction of about 10% at 700°C, 6% at 1000°C and 3% at 1500°C for 3 at% burnup SIMFUEL compared to UO_{2+x}. For an oxygen potential of ΔGo_2 = -205 kJ/mol ($UO_{2.035}$) or higher, and temperatures above 600°C, the simulated burnup does not affect the thermal conductivity; practically the same thermal conductivity values were obtained for UO_{2+x} and SIMFUEL (Figures 4 and 5).

The thermal resistivity (R = $1/\lambda$) of UO_{2+x} and hyperstoichiometric 3 at% SIMFUEL showed a nearly linear variation with temperature for the temperature range of 600 to 1500°C, for which the excess of oxygen is dissolved in the fluorite lattice (Figures 8 and 9). This variation shows the hyperbolic term to be predominant in the analytical expression of SIMFUEL thermal conductivity. Consequently, we can fit our data as well with the equation used by Hobson et al. [11]:

$$\lambda = (A(\beta) + B(\beta)\cdot T)^{-1} + C(\beta)\cdot T^3$$

where the coefficients can be burnup-dependent. In the investigated temperature range, the electronic conductivity contribution is nil (C=0). The coefficients of the best-fit line for the linear variation of the thermal resitivity with temperature, at various burnups and stoichiometry, are listed in Table 2.

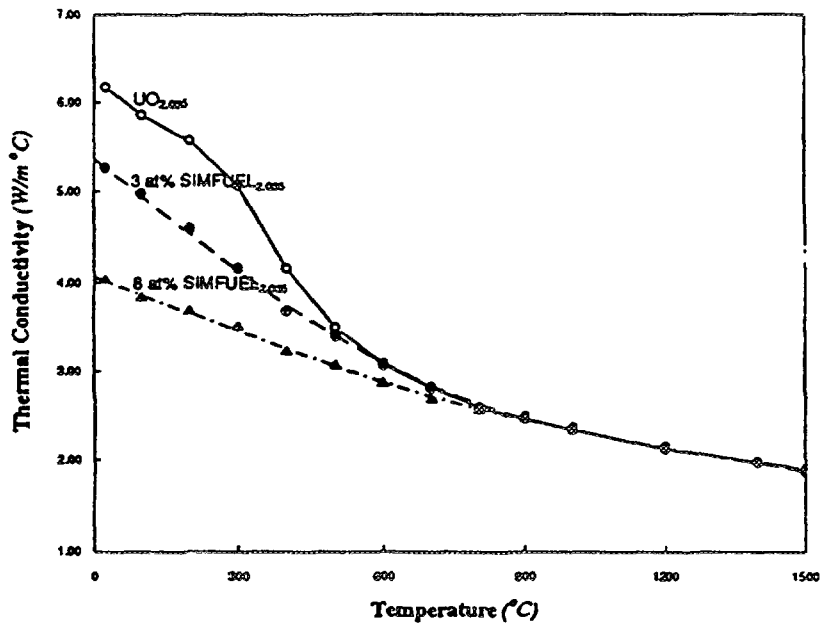

FIG. 4. Thermal conductivities of $UO_{2.035}$ and SIMFUEL (ΔGo_2 = -205 kJ/mol, labelled as 2.035) normalized to 100% TD as a function of temperature.

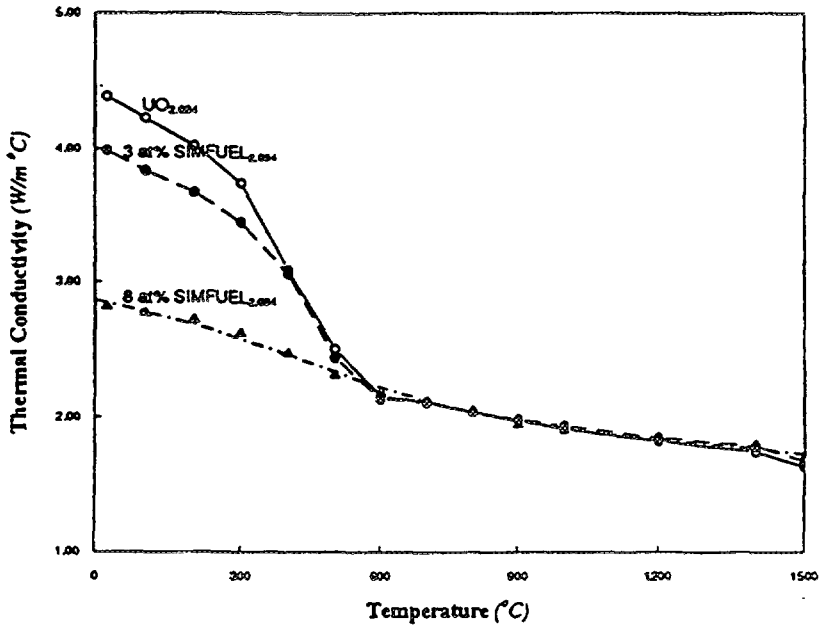

FIG. 5. *Thermal conductivities of $UO_{2.084}$ and SIMFUEL (at ΔGo_2 = -160 kJ/mol, labelled 2.084) normalized to 100% TD as a function of temperature.*

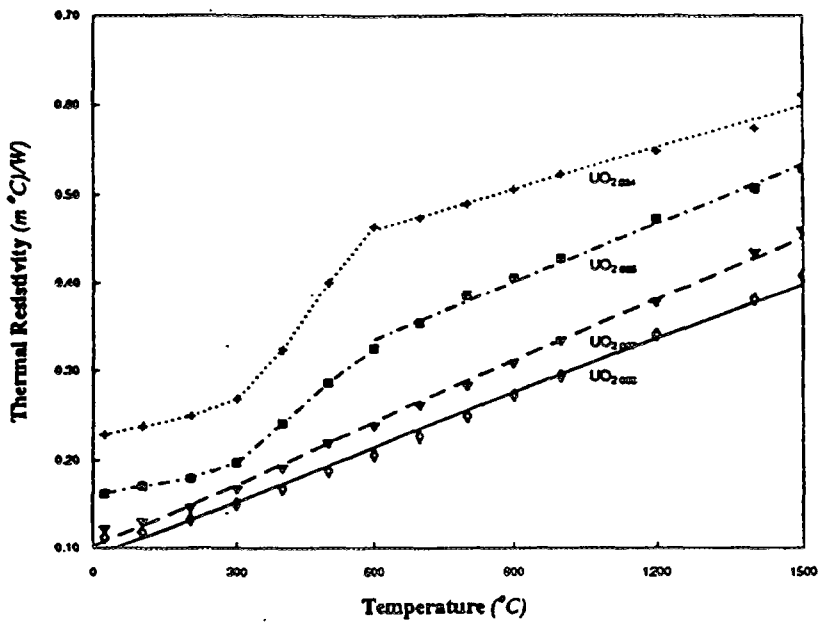

FIG. 6. *Thermal resistivity of UO_{2+x} normalized to 100% TD as a function of temperature.*

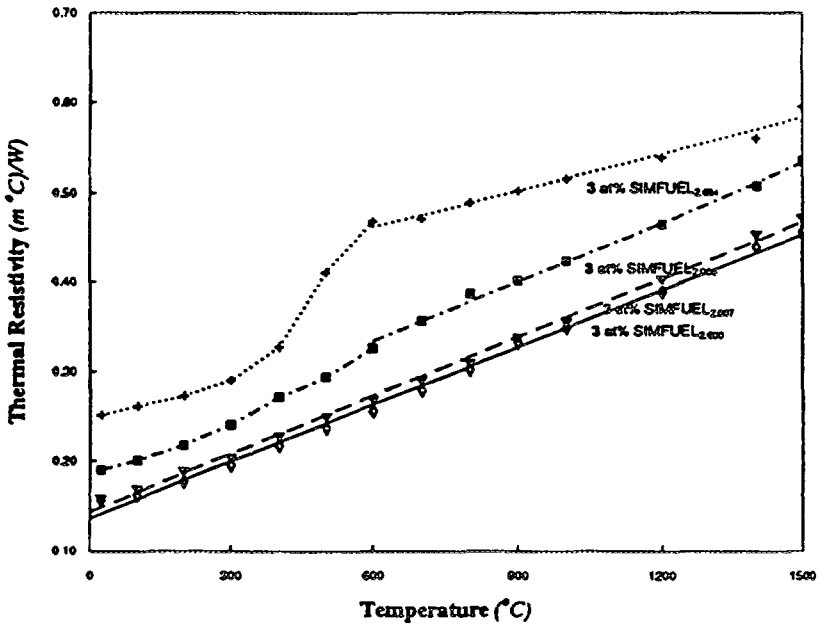

FIG. 7. *Thermal resistivity of hyperstoichiometric 3 at% burnup SIMFUEL normalized to 100% TD as a function of temperature.*

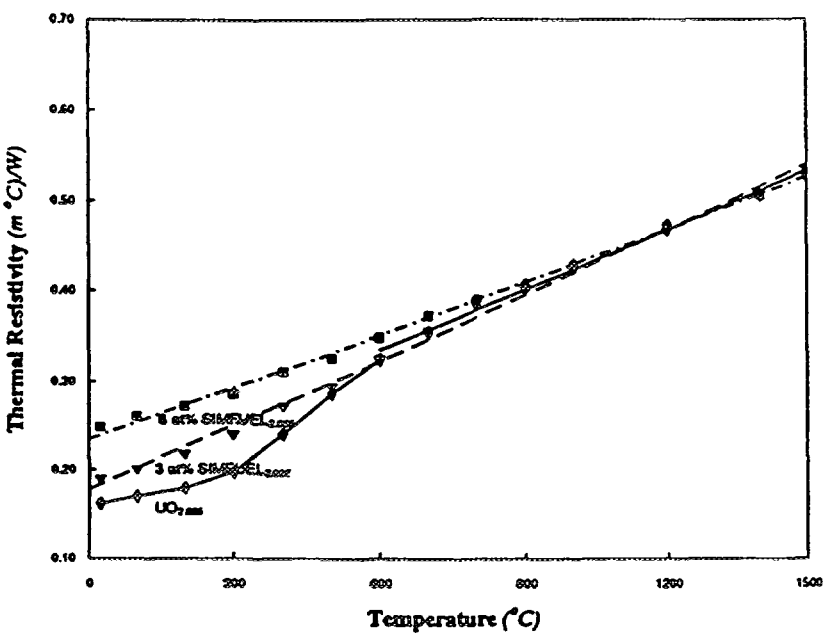

FIG. 8. *Thermal resistivities of $UO_{2.035}$ and SIMFUEL, equivalent burnups of 3 and 8 at% (ΔGo_2 = -205 kJ/mol O_2) as a function of temperature. The values were normalized to 100% TD.*

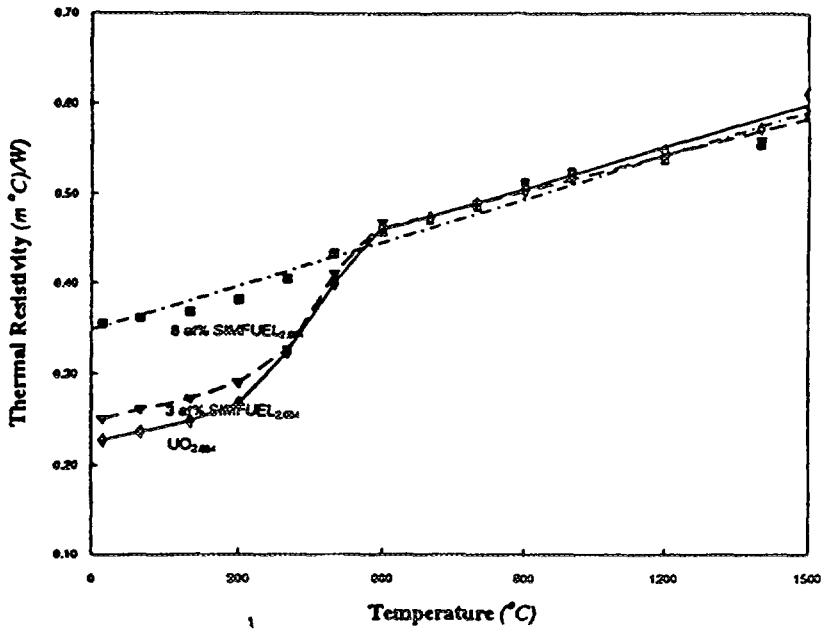

FIG. 9. *Thermal resistivities of $UO_{2.084}$ and SIMFUEL (ΔGo_2 = -160 kJ/mol O_2) normalized to 100% TD as a function of temperature.*

TABLE II **Coefficients of the best-fit line, $\lambda = (A+BT)^{-1}$ for UO_{2+x} and hyperstoichiometric SIMFUEL with equivalent burnups of 3 and 8 at%.**

ΔGo_2 kJ/mol	x UO_{2+x}	A			$B \cdot 10^{-3}$		
		0 at%	3 at%	8 at%	0 at%	3 at%	8 at%
-540	0.000	0.0911	0.1362	0.1858	0.235	0.212	0.205
-245	0.007	0.1022	0.1433	---	0.233	0.217	---
-205	0.035	0.2031	0.1997	0.2346	0.220	0.223	0.195
-160	0.084	0.3669	0.3819	0.3844	0.155	0.134	0.134

The negligible effect of the simulated burnup obtained for the high oxygen potentials is shown as well for thermal resistivity variation with temperature. Figures 8 and 9, for the two oxygen potentials of -205 kJ/mol O_2 and -160 kJ/mol O_2 illustrate that in the fuel-operating temperature range, the thermal resistivity of SIMFUEL is not affected by increasing burnup.

Increased point-defect scattering in the fluorite lattice can account for the degradation in thermal conductivity of hyperstoichiometric UO_{2+x}. For small deviations from stoichiometry ($UO_{2.007}$), the scattering from oxygen interstitials appears to be smaller in SIMFUEL. For high oxygen potentials, the phonon scattering by the oxygen sublattice defects appears to be dominant, and a saturation in the number of defects could explain the same values obtained for UO_{2+x} and SIMFUEL.

4. CONCLUSIONS

Based on these results:

- Thermal conductivities of hyperstoichiometric UO_{2+x} were lower than those measured on stoichiometric specimens.

- The thermal conductivity of hyperstoichiometric SIMFUEL was reduced compared to the samples annealed in reducing conditions for high oxygen potentials.

- Simulated burnup does not play any major role at high oxygen potentials, or alternatively, excess oxygen is the dominant factor contributing to thermal conductivity degradation at high oxygen potentials.

An obvious immediate application is to insert the measured conductivities into fuel performance models, and evaluate the effect on central temperature and fission-gas release. The predictions of the improved models could then be compared with data from irradiated high-burnup fuel. Our earlier results on the effect of simulated burnup on fuel thermal conductivity were incorporated in the actual fuel codes, and gave better agreement with the measured data.

ACKNOWLEDGEMENT

The financial support of CANDU Owners Group (COG) for this work is gratefully acknowledged.

REFERENCES

[1] LUCUTA P.G., PALMER B.J.F., MATZKE HJ., and HARTWIG D.S., "Preparation and Characterization of SIMFUEL: Simulated CANDU High-Burnup Nuclear :Fuel," Proc. of Second Int. Conference on CANDU Fuel, Ed. I.J. Hastings, CNS Toronto (1989) 132-146; also AECL report, AECL-10117 (1989).

[2] LUCUTA P.G., VERRALL R.A., MATZKE HJ., and PALMER B.J.F., "Microstructural Features of SIMFUEL - Simulated High-Burnup UO_2-Based Nuclear Fuel," J. Nucl. Mater. 178 (1990) 48-60.

[3] MATZKE HJ., LUCUTA P.G., and VERRALL R.A. "Formation and Behaviour of Barium Silicate in UO_2-Based SIMFUEL," J. Nucl. Mater. 185 (1991) 292-296.

[4] LUCUTA P.G. MATZKE HJ., VERRALL R.A., and TASMAN H.A., "Thermal Conductivity of SIMFUEL," J. Nucl. Mater. 188 (1992) 198.

[5] LUCUTA P.G. MATZKE HJ., VERRALL R.A. and HASTINGS I.J., "Thermal Conductivity and Gas Release from SIMFUEL," IAEA Technical Committee Meeting on Fission Gas Release and Fuel Rod Chemistry Related to Extended Burnup, Pembroke, Ontario, Canada, 1992 April 28-May 1, IAEA-TECDOC-697.

[6] MATZKE HJ., LUCUTA P.G., VERRALL R.A and HIERNAUT J.P., "Thermophysical Properties of UO_2 and SIMFUEL - Simulated High-Burnup Fuel," Proc. 22nd International Conference on Thermal Conductivity, November 7-10, Tempe, Arizona (1993).

[7] LUCUTA P.G. MATZKE HJ., VERRALL R.A. and HASTINGS I.J.,, "Characterization and Thermal Properties of Hyperstoichiometric SIMFUEL," Third Int. Conf. CANDU Fuel, Pembroke, Ontario, Canada, October (1992) 2-61.

[8] LUCUTA P.G. MATZKE HJ., VERRALL R.A., and KLEMENS P.G., "Analysis of SIMFUEL Thermal Conductivity," Proc. 22nd International Conference on Thermal Conductivity, November 7-10, Tempe, Arizona (1993).

[9] LUCUTA P.G. MATZKE HJ., VERRALL R.A.,, "Modelling of UO_2-Based SIMFUEL Thermal Conductivity," to be published in J. Nucl. Mater.

[10] GOLDSMITH L.A., and DOUGLAS J.A.M., "Measurements on Thermal Conductivity of Uranium Dioxide at 670 -1270 K," UKAEA report TGR 2103(w), (1971).

[11] HOBSON I.C., TAYLOR R., and AINSCOUGH J.B. "Effect of Porosity and Stoichiometry on the Thermal Conductivity of Uranium Dioxide," J. Phys. D: Appl. Phys. 7, (1974), 1003-1015.

[12] LUCUTA P.G. MATZKE HJ., VERRALL R.A., "Microstructural Features of Hyperstoichiometric SIMFUEL," 13th. IUPAC Conference on Chemical Thermodynamics, Clermont-Ferrand, France, July 17-22, 1994 - to be published.

[13] FLOYD M., NOVAK J., and TRUANT P.T., "Fission-Gas Release in Fuel Performing to Extended Burnups in Ontario Hydro Nuclear Generating Stations," IAEA Technical Committee Meeting on Fission Gas Release and Fuel Rod Chemistry Related to Extended Burnup, Pembroke, Ontario, Canada, 1992 April 28-May 1, IAEA-TECDOC697, also AECL report, AECL-10636 (1992).

[14] MATPRO - A Handbook of Materials Properties for Use in the Analysis of Light Water Reactor Fuel Rod Behaviour, TREE-NUREG-1005, EG&G Idaho, Inc. (1989).

[15] NOTLEY M.J.F. and McEWAN J.R. Nucl. Appl. Technol., 2 (1966) 117-122.

A PROPOSAL FOR A UNIFIED FUEL THERMAL CONDUCTIVITY MODEL AVAILABLE FOR UO_2, $(U\text{-}PU)O_2$ AND $UO_2\text{-}GD_2O_3$ PWR FUEL

D. BARON
Electricité de France,
Moret-sur-Loing

J.C. COUTY
Electricité de France,
Villeurbanne

France

Abstract

In order to cope with the current fuel management targets which are focussed on higher discharge burnups, initial ^{235}U fuel enrichments have been increased from 3.25 % to 4 %. To avoid an increase in boron concentration in the primary circuit, Gadolinium is used as a burnable poison, spread in the uranium oxide matrix of selected rods, in order to absorb the initial reactivity excess. Obviously, fuel thermal conductivity is affected when introducing any stranger element. Previously, the EDF thermomechanical code provided two different models to simulate the fuel thermal conductivity: one available for UO_2 and $(U\text{-}Pu)O_2$ fuels, the other for Gadolinia fuels, depending on the calculations to be done. No effect of the initial fuel stoichiometry was taken into account in the second model. That situation suggested the development of a unified model available for any fuels presently loaded in the EDF PWR reactors. This paper deals with the choice of the formulation, the data base used and the methodology applied for parameter fitting. Results in terms of measured versus predicted evaluation are then discussed.

1. INTRODUCTION

In order to cope with the current fuel management targets which are focussed on higher discharge burnups, initial ^{235}U fuel enrichments have been increased from 3.2 % to 4 %. To avoid an increase in boron concentration in the primary circuit, Gadolinium is used as a burnable poison, spread in the uranium oxide matrix of selected rods, in order to absorb the initial reactivity excess.

Concerning the fuel thermomechanical behaviour, an addition of gadolinium in uranium dioxide sharply decreases the fuel thermal conductivity in the range of temperatures representative of standard operating conditions. This physical property tends to be more or less affected with regard to the quantity of added Gd_2O_3 powder introduced during the manufacturing process. This is mainly due to:

- a change in the vacancies proportion in the oxygen sub-lattice
- a difference in atomic masses between Uranium and Gadolinium which adds an anharmonic component of crystal vibrations.

Previously, the EDF thermomechanical code provided two different models: one available for UO_2 and $(U\text{-}Pu)O_2$ fuels, the other for Gadolinia fuels, depending on the calculations to be done. No effect of the initial fuel stoichiometry was taken into account in the second model. That situation suggested the development of a unified model available for any fuels presently loaded in the EDF PWR reactors.

2. THEORETICAL ASPECT

2.1 FUEL THERMAL CONDUCTIVITY MODELLING

Two phenomena are responsible for the thermal transfer through a solid: the propagation of atoms vibrations around their lattice site and the electronic transport, corresponding to the kinetic energy carried by free electrons at high temperatures. The solid thermal conductivity can therefore be written as the sum of two components:

$$K(T) = K_s(T) + K_e(T)$$

2.1.1 Phonon component

Thermal transfer in a solid is mainly due to atomic oscillation in the crystal lattice. The thermal conductivity of an ionic solid such as Uranium dioxide can be derived by assuming the solid to consist of an ideal gas in which the quasi-particles are phonons [1]. The problem is then solved by using the equations of the elementary kinetic theory. Phonon gas can be considered as isotropic as long as the particles are continuously colliding with each other.

Assuming particles move for example in the "x" direction, the energy yield by the particles which corresponds to a temperature variation ΔT is given by:

$$E_{th} = C\,\Delta T$$

where "C" is the average heat capacity associated to the particles. If v_x is their average rate, and τ the elapsed time between two collisions, these particles have crossed the temperature gradient ΔT such as

$$\Delta T = v_x\,\tau\,dT/dx$$

If "n" is the number of particles per unit volume, the flux in the x direction is $n\,v_x$. The thermal heat flux by surface unit is then:

$$J = -n\,\langle v_x^2\rangle\,C\,\tau\,dT/dx$$

Because the phonon gas can be assumed isotropic, J becomes:

$$J = -1/3\,n\,v_m^2\,C\,\tau\,dT/dx$$

where v_m is the average phonon speed. Assuming now that λ is the phonon mean free path,

$$\lambda = v_m\,\tau$$

then it becomes:

$$J = -1/3\,n\,C\,v_m\,\lambda\,dT/dz = -\,ks(T)\,dT/dz$$

ks(T) is the solid thermal conductivity which is finally given by:

$$ks(T) = 1/3\,n\,C\,v_m\,\lambda$$

The fuel conductivity is therefore proportional to the phonon mean free path. The value of this parameter is related to two main phenomena: the geometric diffusion and the phonon-phonon scattering.

a) geometric diffusion

The first one depends on the number of crystal defects, whatever the local temperature is. However, at very low temperature, in a solid free of defects, the mean free path can be equivalent to the sample width. The thermal conductivity becomes in such a case a function of the sample dimensions.

b) phonon-phonon scattering

If interatomic strength were purely harmonic, phonon-phonon scattering should be enabled and the mean particles free path would be only limited by the crystal boundaries or by the crystal defects. In

the uranium dioxide phonon-phonon scattering results of the anharmonic components of the crystal vibrations.

In an ionic crystal, lattice anharmonicity indeed increases with the mass difference between anions and cations. In UO_2 or PUO_2 oxides, this mass difference is much greater than in all others common oxides. For that reason, the thermal conductivity of such actinide oxides are considerably lower than most of the crystalline oxides.

The kinetic theory of gases shows that the collision mean free path is given by the reprocical of the product of the collision cross section and the density of scatterers. At temperatures well above the Debye temperature, the phonon density is proportional to the local absolute temperature T.

From the above considerations, the thermal conductivity of the fuel oxide is then usually formulated as follows:

$$k_s = \frac{1}{R_i + R_u(T)}$$

$\mathbf{R_i}$ represents the thermal resistance related to the phonon-lattice defects interactions. These defects can be either vacancies or interstitial atoms. R_i can be evaluated using the Ambegaokar formula [2]:

$$R_i = \frac{4\pi^2 \overline{V}\, \theta_D}{v_m^2 h} \sum_n \Gamma_n$$

v_m	: average phonon celerity	$\overline{V}$	: Average atomic volume
h	: Plack constant	θ_D	: Debye temperature

Γn : Diffusion section for defects type n. This parameter depends on the defect type n mass, the environnal binding energy and the difference between the defects size and the lattice normal sites. Abeles gives for Γn the following formula [2]:

$$\Gamma_n = \frac{x}{12}\left|\left(\frac{M_n - M}{M}\right)^2 + \eta\left(\frac{r_n - r}{r}\right)^2\right|$$

η	= 32(1+1.6 γ)2	x	: Atomic fraction of the type defect n
M	: Ion mass in normal sites	Mn	: mass of the type n defect
r	: atomic radius of the ion in normal site	rn	: atomic radius of the type n defect

$\mathbf{R_u(T)}$ is the intrinsic thermal resistance of the lattice, resulting of phonon-phonon scattering, due as said above to the lattice anharmonicities. It can be estimated from the base material properties, using the Leibfried-Schlömann formula [2]:

$$R_u(T) = \frac{\gamma^2 T}{3.81\left[\frac{k}{h}\right]^3 \overline{M}\overline{V}^{\frac{1}{3}}\, \theta_D^3}$$

γ	: Grüneisen constant	M	: Average atom mass
h	: Planck constant	$\overline{V}$	: Average atomic volume
k	: Boltzman constant	θ_D	: Debye temperature
T	: Absolute temperature		

2.1.2 Free particles component

The above component is described by a continuous decreasing function of the local temperature. However, it can be observed at high temperatures (> 2000 °C), that the fuel thermal conductivity is improving again. This next component is representative of an improvement of the energy transportation by free electrons at high temperatures. Free electrons population increases faster and faster when temperature increases. This often leads to describe this component as proportional to the temperature at the third power:

$$Ke(T) = C\,T^3$$

Finally the thermal conductivity can be empirically simulated by a formula of the following type:

$$K(T) = (A+BT)^{-1} + C\,T^3$$

2.2 EFFECT OF A STOICHIOMETRY DEVIATION

In the fuel oxide the stoichiometry is the ratio of the number of oxygen atoms to the number of metallic atoms: O/M. In stoichiometric UO_2 fuel or PuO_2 fuel, the O/M value is 2. A deviation of this ratio corresponds to the creation of either vacancies or oxygen interstitials in the oxygen sub-lattice. Whatever the deviation is, the consequence is an increase in the defects population. It will affect the R_i function which is the "A" parameter in the above formula.

One can assume that the increase in defects population and its effect on fuel diffusivity can be roughly considered as a linear function of the stoichiometry deviation "x". "A" can then be written:

$$A = A_0 + A_1\,x$$

2.3 EFFECT OF PLUTONIUM

The Plutonium isotope masses present values close to that of the 238 Uranium isotope (less than half a percent difference). For this reason, a Plutonium presence in some lattice Uranium sites should not affect theoretically the fuel thermal conductivity.

The existence of an eventual effect is however widely debated in the open literature. This difference of appreciation can perhaps be explained by the difficulty in properly controlling the O/M ratio during the experiment. Most of written data concerns high plutonium content fuels. These fuels are systematically under-stoichiometric because PuO is a more stable oxide. The effect of a stoichiometry deviation is then more likely to explain the reported thermal conductivity degradation.

Nevertheless, even if Pu had a slight effect, it should be minimized by the non-homogeneity of the final product. The fuel is indeed obtained by mixing together UO_2 and PuO_2 powders. Even if the mixing methodology is improved, this leads to a non-homogeneous distribution of the plutonium, gathered in clusters within the UO_2 matrix.

The present PWR MOX fuels have a maximum plutonium content of 10 %. Actual manufacturing allows the production of stoichiometric oxides. The French experience on non-irradiated MOX fuel, including several manufacturing processes, outlined a fuel thermal conductivity very similar to UO_2 fuel. This is consistent with the Phillipponneau's recommendations in the European catalogue on RNR MOX fuel [3].

Taking into account the above considerations, the uncertainties on fuel conductivity measurements, the discrepancy observed on all the results obtained on fuel conductivity measurements and the low contents used in PWR MOX fuels, it seems reasonable to disregard an eventual effect of the Plutonium content.

2.4 EFFECT OF GADOLINIUM

Even if Gadolinium is homogeneously mixed with Uranium, the Gd_2O_3 motifs are much more complex than that of UO_2. Gd_2O_3 natural structure is built on a cubic body-centered lattice with a mesh parameter equal to 10.818 Å (with 16 molecules by unit cell) against 5.4682 Å for the UO_2 cubic face-centered lattice (with 4 molecules by unit cell) [4]. The presence of Gadolinium means a strong distortion the UO_2 lattice in its surrounding and results in an increase of the defects population.

Furthermore, the Gadolinium is a trivalent atom. The consequence of that trivalent state is a modification of the oxygen sub-lattice even if an apparent stoichiometry is obtained in manufacture. These two aspects lead to a strong influence of the gadolinium content on the Ri parameter (A parameter) described above. It can be assumed that the number of defects increases faster and faster as gadolinium content is increasing. For this reason, if "g" is the gadolinium weight content, Ri(g) can be described as a polynomial function of second order.

On the other hand, the Gadolinium modifies also phonon-phonon scattering because of its different mass (157 g against 238 g for Uranium). This property will influence the Ru parameter (B parameter). This justifies an empirical fitting of that parameter in the K(T) formula.

3. FUEL CONDUCTIVITY MODEL

3.1 METHODOLOGY AND FORMULATION PROPOSED

The major problem when developing such a model is to use an homogeneous data base. In the framework of the NFIR program [5] [6], a base of fuel conductivity measurements have been collected for UO_2-Gd_2O_3 fuels with a reference on UQ samples. For each gadolinium content, several initial stoichiometries have been tested.

Our confidence on this data base is related to its homogeneity, a good characterization of samples and the use of a flash laser technic for diffusivity measurements. In order to fit the parameters of the law, we have then voluntarily limited the experimental data base to this NFIR data. The domain investigated by this data base will define the validity domain of the law:

Fuel temperature :	250 to 1800 °K
Gadolinium Content:	0 to 12 %
Fuel stoichiometry :	1,995 to 2,045

All the data base has been firstly reduced to a reference fuel density value of 95 % TD, using the LOEB and ROESS porosity correction [7] on the experimental thermal conductivities. A+BT can be considered as the fuel thermal resistivity due to phonon energy transportation. After a fitting of the C parameter, one can evaluate from the measured fuel conductivity K_{ms}: $R_{ph} = 1/(K_{ms} - CT^3) = A+BT$. The A and B parameters can then be easily fitted.

This job led to the following formula for **non-irradiated fuels at 95 %TD density**:

$$K(T) = [(A+B\,T)^{-1} + C\,T^3] * D(T)$$
$$A = A_0 + A_1\,x + A_2\,g + A_3\,g^2$$
$$B = B_0 + B_1\,g + B2\,g^2$$

Parameters

$A_0 = 0.0524$ $A_1 = 4.0$ $A_2 = 0.3079$ $A_3 = 12.2031$
$B_0 = 2.553\ 10^{-4}$ $B_1 = 8.606\ 10^{-4}$ $B_2 = -0{,}0154$

K(T) thermal conductivity (W/m/°K)
T local temperature (°C)
g gadolinium content
x absolute value of (2 - O/M) (-)

Porosity correction (LOEB and ROESS law [7])

$D(T) = (1 - por\ \alpha(T)) / (1 - 0.05\ \alpha(T))$
$\alpha(T) = 2.7384 - 0{,}58\ 10^{-3}\ T \qquad T < 1273.15\ °C$
$\alpha(T) = 2. \qquad T \geq 1273.15\ °C$

Burnup correction

Indeed, this formula is available for non-irradiated fuel. It must be corrected with burnup when operating in reactors, to take into account the thermal transfer degradation due to the progressive physical and chemical fuel modification. These phenomena are consecutive to the redistribution of the solid and gaseous fission products and to irradiation damages. The correction used by EDF is the formulation proposed a long time ago by LOKKEN and COURTRIGHT [8]. The E parameter is used as a code fitting factor:

$$K(T,Bu) = (1/K(T) + E\ BU/T)^{-1}$$

T fuel local temperature (°K)
BU fuel local burnup (MWd/tU)
K(T) fresh fuel thermal conductivity (W/m/°K)
E fitting factor

3.2 QUALIFICATION AND DISCUSSION

The qualification conducted on EDF data base for UO_2, $(U\text{-}Pu)O_2$ and $UO_2\text{-}Gd_2O_3$ fuels shows a relatively good adequation of such a law for the fuel performance analysis. The confrontation of the model against experimental data is presented in Figures 1 to 5.

Figures 1A, 1B and 1C illustrate the model prediction for UO_2 fuel for three different initial stoichiometries: 2.000, 2.005, 2.010 against the NFIR data.

Figures 2A, 2B show the model prediction against the NFIR data for $UO_2\text{-}Gd_2O_3$ fuel with an initial stoichiometry equal to 2.000 and a gadolinium weight content respectively 4 and 8 % .

Figures 3A, 3B and 3C are a comparison against NFIR data for a gadolinium content of 12 % and different initial stoichiometries: 1.995, 2.005 and 2.013.

Concerning model predictions for $(U\text{-}Pu)O_2$, the model comparison is presented in Figure 4A and 4B against the best estimate law developed by PHILIPPONEAU on standard RNR MOX fuels, for two stoichiometry values: 2.000 and 1.98. The Philipponeau law and the model proposed are very close but outline a divergence above 2000 °K. This is due to a different value adopted for the C parameter. This parameter is a best estimate value obtained from the NFIR data base which nevertheless have no measurements above 1800 °K. Obviously it will be necessary to ascertain this value on higher temperature measurements if the law is to be used out of the predefined domain. One can assume the present value to be conservative.

As shown in Figure 5, a qualification on open literature is more difficult because of a great discrepancy of all the measurements reported [9-11]. This discrepancy could be explained by a non-homogeneity of the methodologies, a misunderstanding on the control of certain parameters such as fuel

densities, pore spectrum or a non-control the fuel chemistry in certain experimental conditions. As an example, an evolution of fuel chemistry during high temperature diffusivity measurements could be responsible for the drift observed in Figure 3A above 1500 °K.

FIGURE 1A
O/M = 2.000

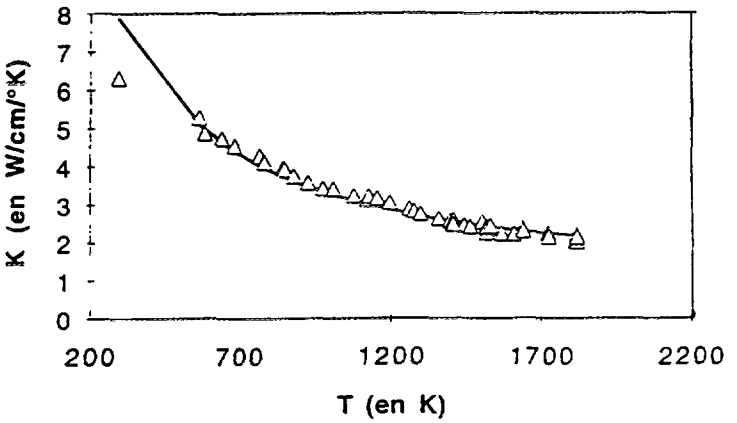

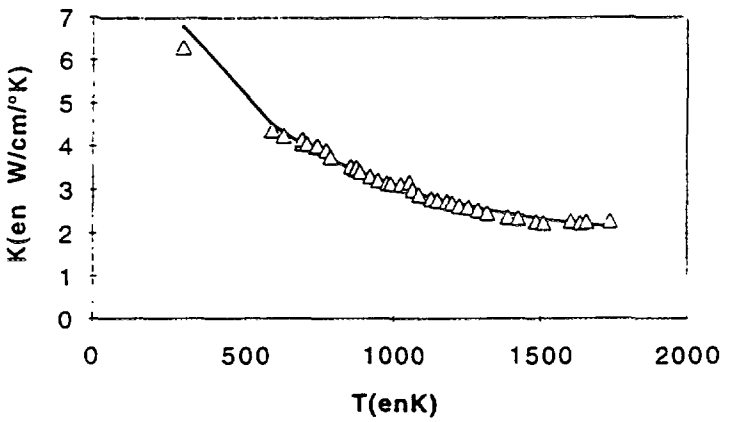

FIGURE 1B
O/M = 2.005

FIGURE 1C
O/M = 2.010

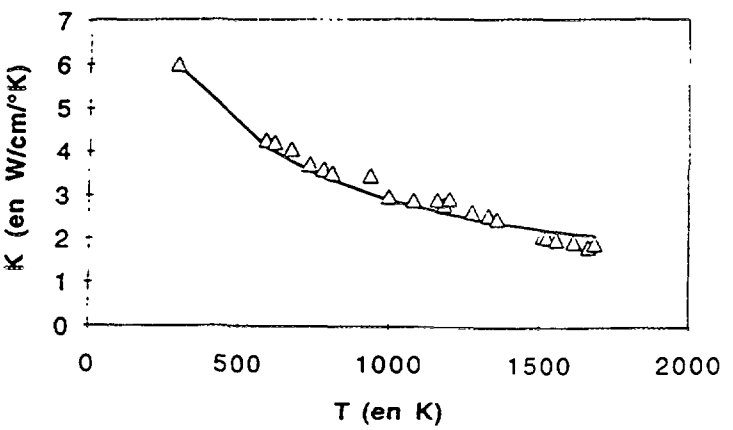

FIG. 1 *Model qualification on NFIR data UO_2 - 95% TD*
a) O/M = 2.000
b) O/M = 2.005
c) O/M = 2.010

Δ NFIR data

Model prediction

FIGURE 2A

Gd = 4 % - O/M = 2.000

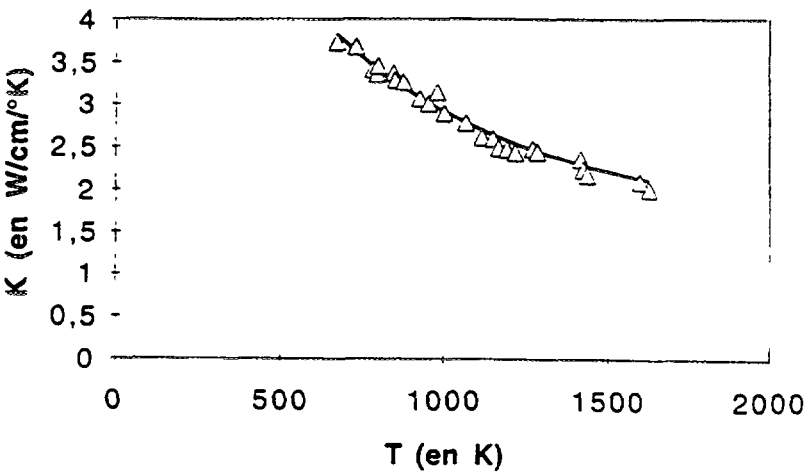

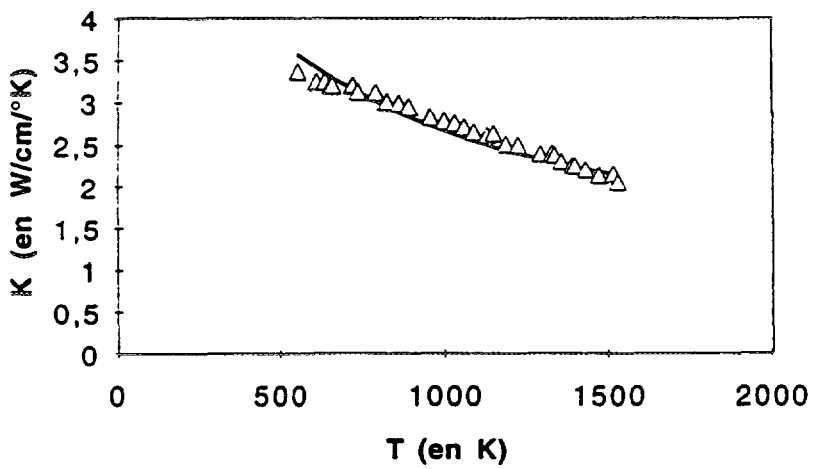

FIGURE 2B

Gd = 8 % - O/M = 2.00

FIG. 2 *Model qualification on NFIR data UO_2 - Gd_2O_3 - 95%TD*

a) *Gd = 4% - O/M = 2.000*

b) *Gd = 8% - O/M = 2.00*

Δ NFIR data

—— Model prediction

FIGURE 3A

Gd = 12 % - O/M = 1.995

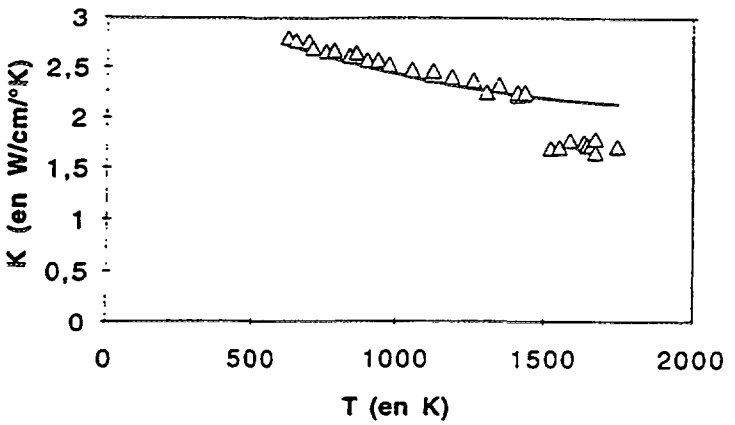

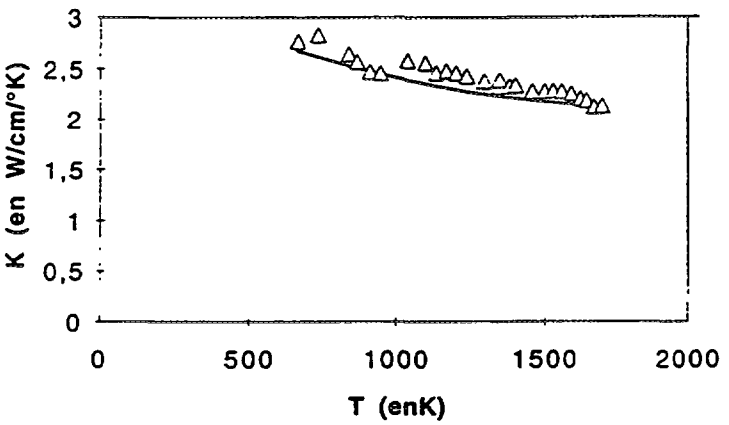

FIGURE 3B

Gd = 12 % - O/M = 2.005

FIGURE 3C

Gd = 12 % - O/M = 2.013

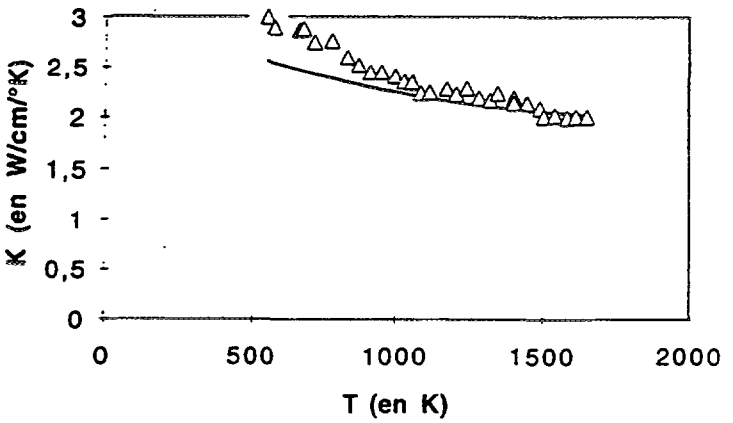

FIG. 3 *Model qualification on NFIR data UO_2 - Gd_2O_3 - 95%TD*

a) Gd = 12% - O/M = 1.995

b) Gd = 12% - O/M = 2.005

c) Gd = 12% - O/M = 2.013

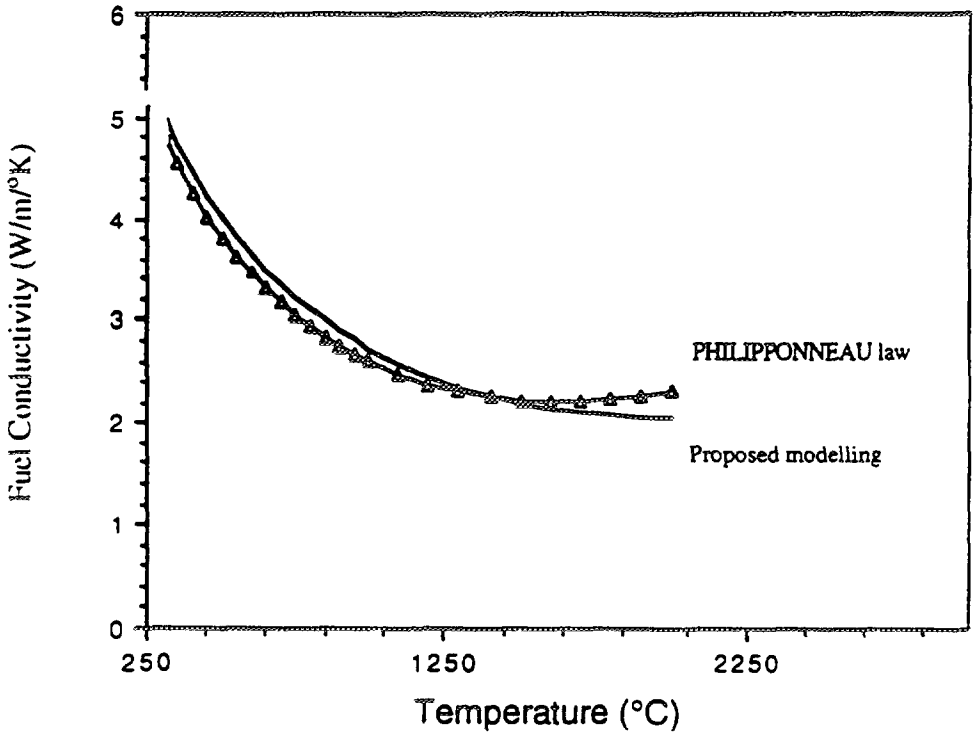

FIGURE 4A

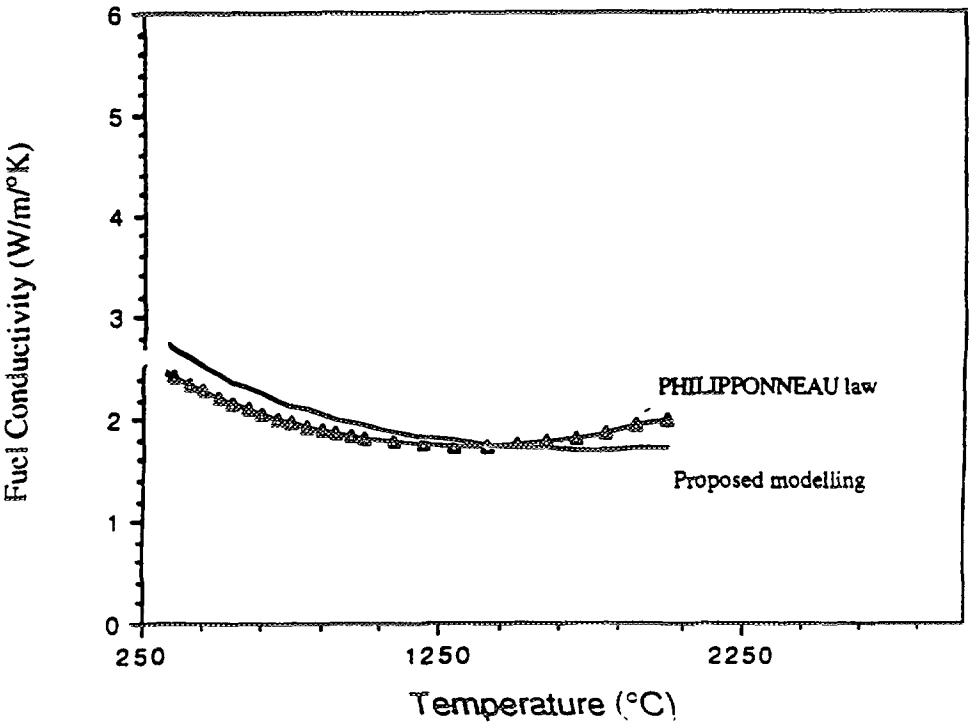

FIGURE 4B

FIG. 4 *Fuel thermal conductivity*
a) O/M = 2 - 95%TD - 0%Gd - BU = 0
b) O/M = 1.96 - 95%TD - 0%Gd - BU = 0

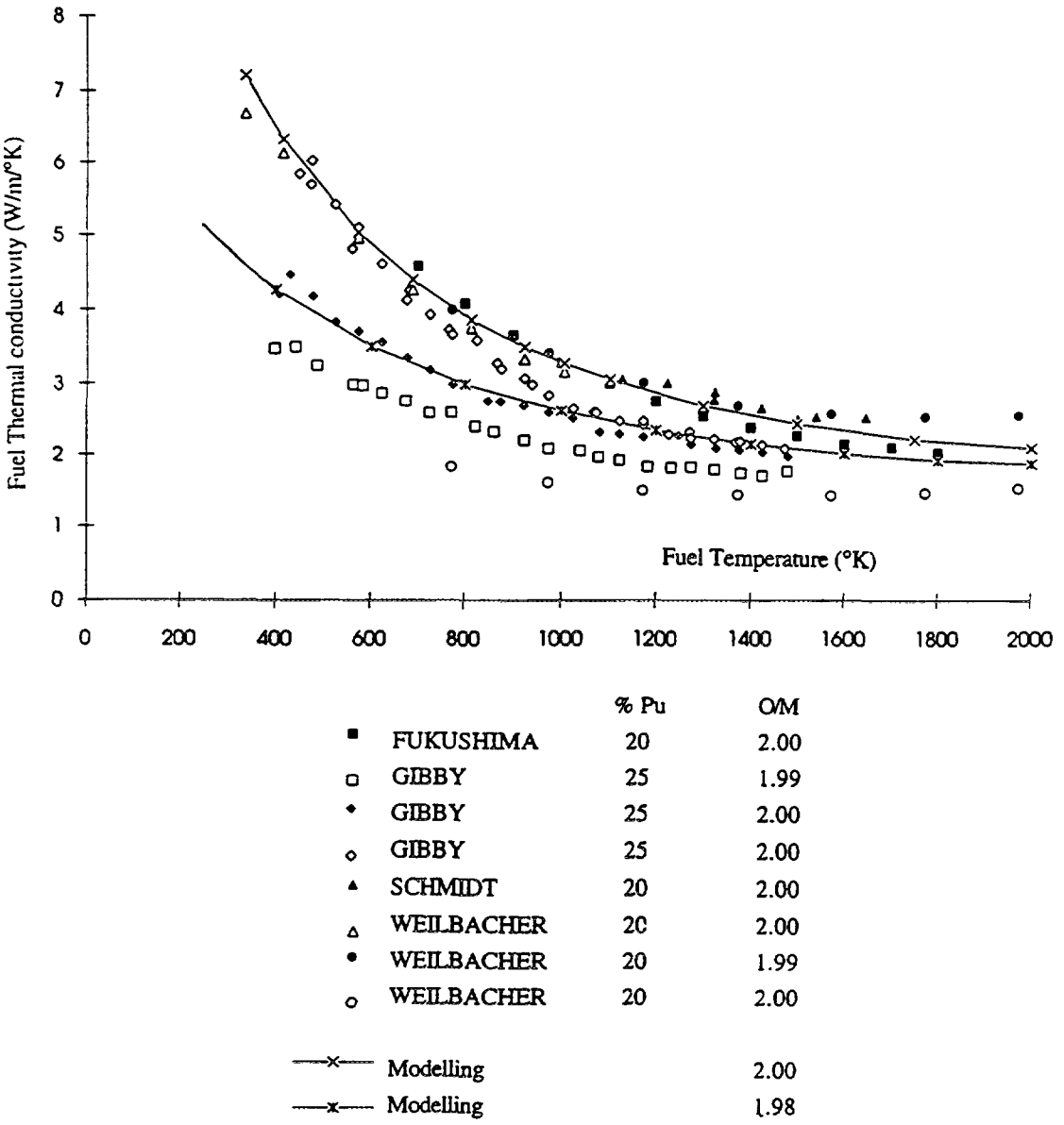

FIG. 5 *Model qualification against $(U\text{-}Pu)O_2$ database for stoichiometries ≥ 1.98*

4. CONCLUSIONS

The diversity of the nuclear fuels loaded in the PWR reactors leads the designer to improve modelling in the fuel thermomechanical behaviour codes. The use of unified formulas, taking into account the specificities of each kind of fuel is always more convenient for the simulation. The fuel thermal conductivity model proposed in this communication is not revolutionary but allows one to meet such a need.

A short presentation of the theoretical aspect allows one to understand the choices made in term of model formulation. The law so obtained is usable in class 1 and class 2 safety analysis for standard UO_2, $(U\text{-}Pu)O_2$ and $UO_2\text{-}Gd_2O_3$ fuels presently loaded in the EDF power plants. The input parameters are the local temperature, the fuel porosity, the fuel stoichiometry and the gadolinia weight content. It as been shown that the effect of the plutonium content can be neglected for PWR MOX fuels.

The validation of such formulation is always very delicate when looking at the wide discrepancy of all the reported data in the open literature. For this reason it would be presumptuous to insure a perfect prediction of such a model. However, the validation against an homogeneous data base outlined a suitable behaviour for non-irradiated fuel thermal conductivity simulation.

A burnup correction is to be added for irradiated fuels. EDF presently associates the LOKKEN and COURTRIGHT correction with this formulation, in which the single parameter is a code fitting coefficient. Further works have to be done to control the law margins for temperatures above 2000 °C.

REFERENCES

[1] OLANDER,Donald R., "Fundamental Aspect of Nuclear Reactor Fuel Element, chapter 10", Department of Nuclear Energy, BERKELEY, CA - USA, TID - 26711-P1, 1976.

[2] GIBBY,R.L., "The effect of the Plutonium Content on the Thermal Conductivity of (U,Pu)O2 Solid Solutions", Journal of Nuclear Materials, 38 163-177, 1971.

[3] PHILIPPONEAU, Y., "Thermal Conductivity of Mixed Oxide Fuel review and recommendations", Fast Reactor European Collaboration Data Sheet, AGT 010101/P14.

[4] TAYLOR, A., KAGLE,B.J., "Crystallographic Data on Metal and Alloy Structures", Westinghouse Research Laboratories, S1013 - Dover Publications New York, 1962.

[5] BUSH,R.A.MACHIELS, A.J. "Properties of the Urania-Gadolinia System (Part 1), Final Report", NFIR-RP-03-06D, December 1986.

[6] WATSON, R.H. MACHIELS, A.J. "Properties of the Urania-Gadolinia System (Part 2), Final Report", NFIR-RP-03-05D, NP-5862-LD June 1988.

[7] LOEB, A.L.,Journal of American Ceramic Society, 37:96 , 1954.

[8] LOKKEN, R.O.COURTRIGHT, E.L. "Review of the Effects of Burnup on the Thermal Conductivity of UO2", BNWL-2270, 1976.

[9] GIBBY,R.L. "The Thermal Diffusivity and Thermal Conductivity of stoichiometric $(U_{0.8},P_{\omega 0.2})O2$ ", BNWL-UC-25, Metal,s Ceramics and Materials, 1968.

[10] HETSLER, F.J. et al, "The Thermal Conductivity of Uranium and Uranium-Plutonium Oxides", GEAP-4879, AEC Research and Development Report, August 1967.

[11] FUKUSHIMA, S. et al, Journal of Nuclear Materials 116, p73, 1983

FIRST STEPS TOWARDS MODELLING HIGH BURNUP EFFECTS IN UO_2 FUEL

C. O'CARROLL, K. LASSMANN,
J. VAN DE LAAR, C.T. WALKER
CEC Joint Research Centre,
Karlsruhe, Germany

Abstract

High burnup initiates a process that can lead to major microstructural changes near the edge of the fuel: formation of subgrains, the loss of matrix fission gas and an increase in porosity. A consequence of this, is a decrease of thermal conductivity near the edge of the fuel which may have major implications for the performance of LWR fuels at higher burnup. The mechanism for the changes in grain structure, the apparent depletion of Xe and increase in porosity is associated with the high fission density at the fuel periphery. This is in turn due to the preferential capture of epithermal neutrons in the resonances of ^{238}U. The new model *TUBRNP* predicts the radial burnup profile as a function of time together with the radial profile of plutonium. The model has been validated with data from LWR UO_2 fuels with enrichments in the range 2 to 8.25% and burnups between 21 to 75 Gwd/t. It has been reported that at high burnup EPMA measures a sharp decrease in the concentration of Xe near the fuel surface. This loss of Xe is interpreted as a signal that the gas has been swept out of the original grains into pores: this "missing" Xe has been measured by XRF. It has been noted experimentally that the restructuring (Xe depletion and changes in grain structure) have an onset threshold local burnup in the region of 70 to 80 GWd/t: a specific value was taken for use in the model. For a given fuel *TUBRNP* predicts the local burnup profile, and the depth corresponding to the threshold value is taken to be the thickness of the Xe depleted region. The theoretical predictions have been compared with experimental data. The results are presented and should be seen as a first step in the development of a more detailed model of this phenomenon.

1. INTRODUCTION

In recent years a great deal of interest has been shown in high burnup (>40 GWd/t) related phenomena at the rim of UO_2 fuels [1-11]. This phenomenon at the edge of the fuel, often called the "Rim Effect", can be divided into four processes [8]:

plutonium and burnup increase
increased porosity
reduction in grain size
athermal release of fission gas from the grains

It is believed that the high burnup in the rim due to increased Pu production initiates a restructuring of the fuel grains. This restructuring includes an increase in porosity, formation of subgrains and a loss of Xe from the UO_2 matrix. In reference [11] the clear relationship between Xe depletion from the grains and increased porosity is demonstrated. The loss of Xe can be interpreted as a signal that the gas has migrated to pores in the so called cauliflower structure [2], due to the formation of subgrains. However, there is no conclusive evidence to show that, in all cases, the the Xe depletion depth and the depth of fuel subgrain formation are the same.

Various models have been developed to explain these microstructural changes [12-17]. The atomistic model of Rest and Hofman treats the problem in terms of irradiation induced formation and restructuring of defects [14,15]. This results in a formula which gives the critical fission density (threshold burnup) for the onset of restructuring. This critical value is dependent on both temperature and fission rate

(enrichment). Lemekhov's model [16] gives a value for the threshold burnup which is a function of temperature and independent of enrichment. The values predicted by Lemekhov are in reasonably good agreement with experiment. However, the critical values predicted by these models do not have a radial dependence and thus must be used in conjunction with a radial burnup relation to determine the penetration depth. The model developed by Kameyama et al. [19] combines the radial burnup profile calculated by the ANRB code with a threshold burnup value to estimate this depth. The scope of this paper is to analyse experimental data on the depth of the Xe depleted zone, as measured by EPMA, with the *TUBRNP* model.

2. DESCRIPTION OF MODEL

The *TUBRNP* (TRANSURANUS burnup) model predicts the radial power density distribution as a function of burnup (and hence the radial burnup profile as a function of time) together with the radial profiles of the uranium and plutonium isotopes [18]. In the present context, of particular interest, is the marked increase in the concentration of plutonium near the fuel surface at high burnup. This is a result of the capture of epithermal neutrons in the resonances of ^{238}U to form ^{239}Pu. This in turn leads to high local burnups at the edge of the pellet which is the first step in the process leading to the restructuring of the fuel at the rim.

The model has been verified against a large database of UO_2 spent fuel measurements for enrichments in the range 2% to 8.25% and for burnups between 21 GWd/t and 75 GWd/t. For example, comparisons between the model predictions of the plutonium and burnup profiles with experimental results (UO_2 fuel) are illustrated in Figs. 1 and 2: as can be seen the agreement is excellent. Note that there are no free parameters in the model: the input data are the fuel geometry (r_{in}, r_{out}), porosity, enrichment, initial concentration of plutonium isotopes and average burnup.

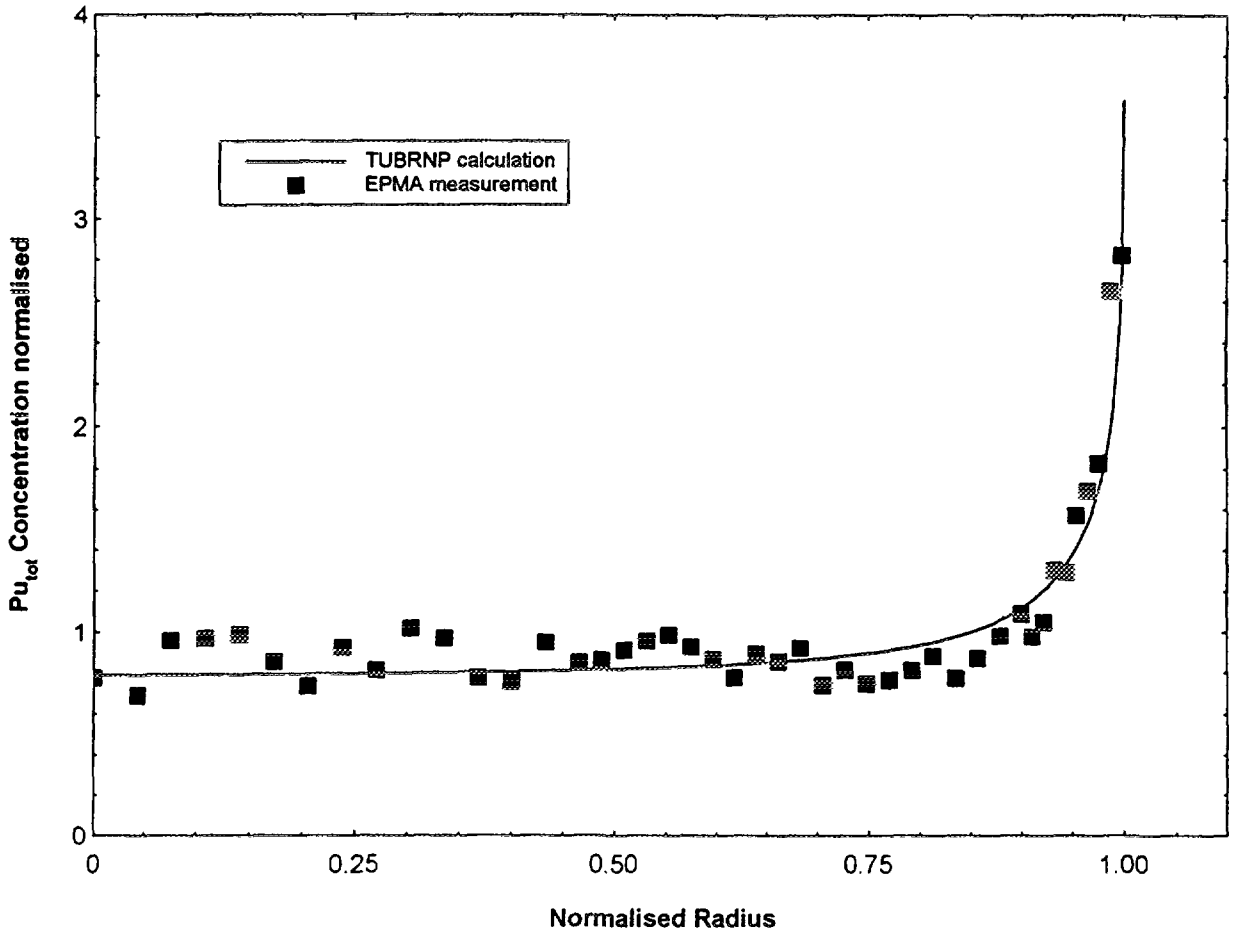

Fig. 1 Total plutonium concentration as a function of the fuel radius measured by EPMA. The solid line is the TUBRNP model prediction.

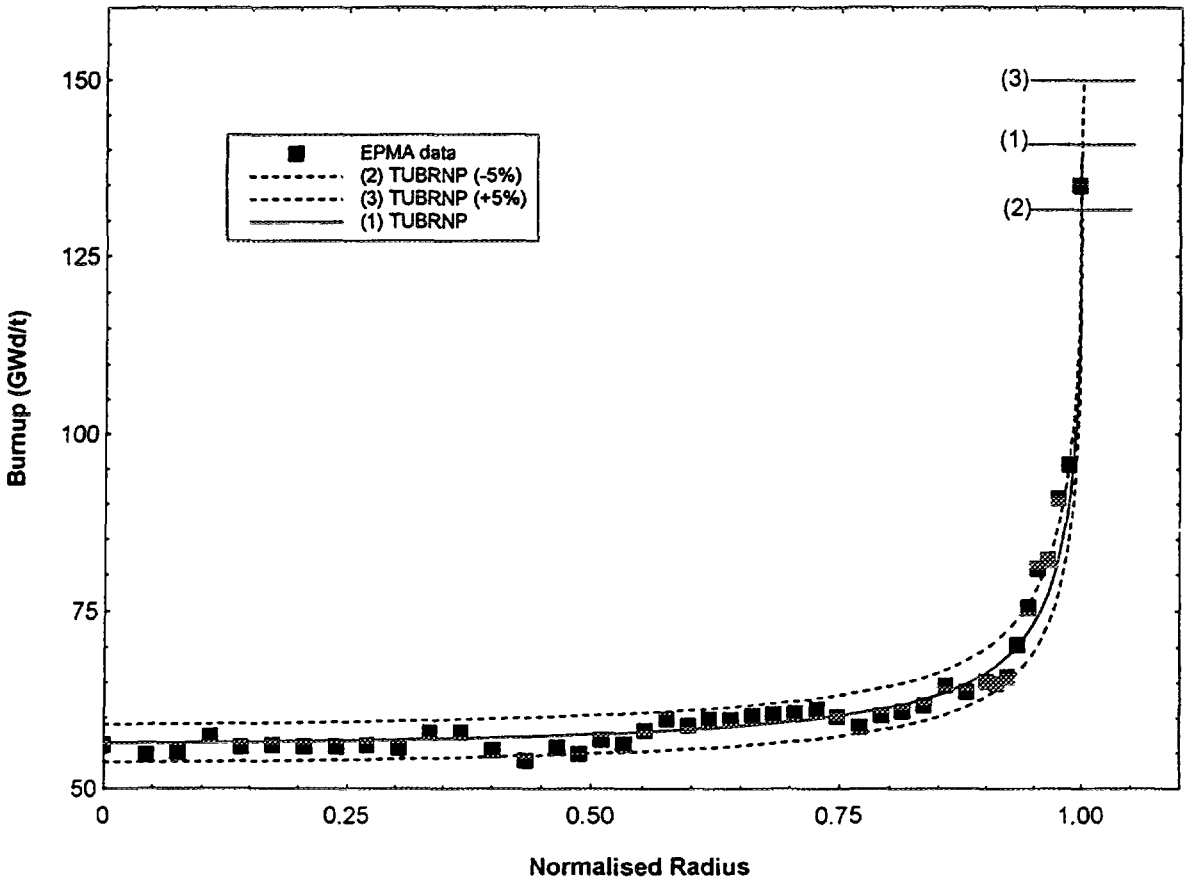

Fig. 2 Burnup as a function of fuel radius as measured by EPMA. The solid line (1) and dashed lines, (2) and (3), are the TUBRNP model predictions at nominal burnup $<B>$ and $<B> \pm 5\%$, respectively.

2.1 APPLICATION TO FUEL RESTRUCTURING AT THE RIM

It has been noted experimentally that the Xe depletion has an onset threshold local burnup in the range 70 to 80 GWd/t [4,19]. This is the same range as the threshold for subgrain formation. Given a value for this threshold, τ_b say, *TUBRNP* predicts the local burnup profile and the depth which corresponds to τ_b is taken to be the thickness of the Xe depleted zone.

3. EXPERIMENTAL DATA

The dataset analysed consisted of high burnup UO_2 fuel with enrichments from 2 to 8.25% and burnups between 40 and 75 GWd/t, see Table I. The Xe, plutonium and burnup profiles were produced by EPMA measurements. The EPMA data was used to estimate the depth (δ_{EPMA}) to which Xe depletion in the UO_2 matrix was observed, see Fig. 3. Most of released Xe is retained in pores as has been shown by x-ray fluorescence measurements (XRF) [5,11].

3.1 ELECTRON PROBE MICROANALYSIS

Quantitative analysis was carried out at an electron acceleration potential of 25 keV with beam currents of 250 and 100 nA. The conventional microprobe correction procedure was made using the Institute's QUAD2 program of Farthing et al. [20] which is based on the Quadrilateral Model of Scott and

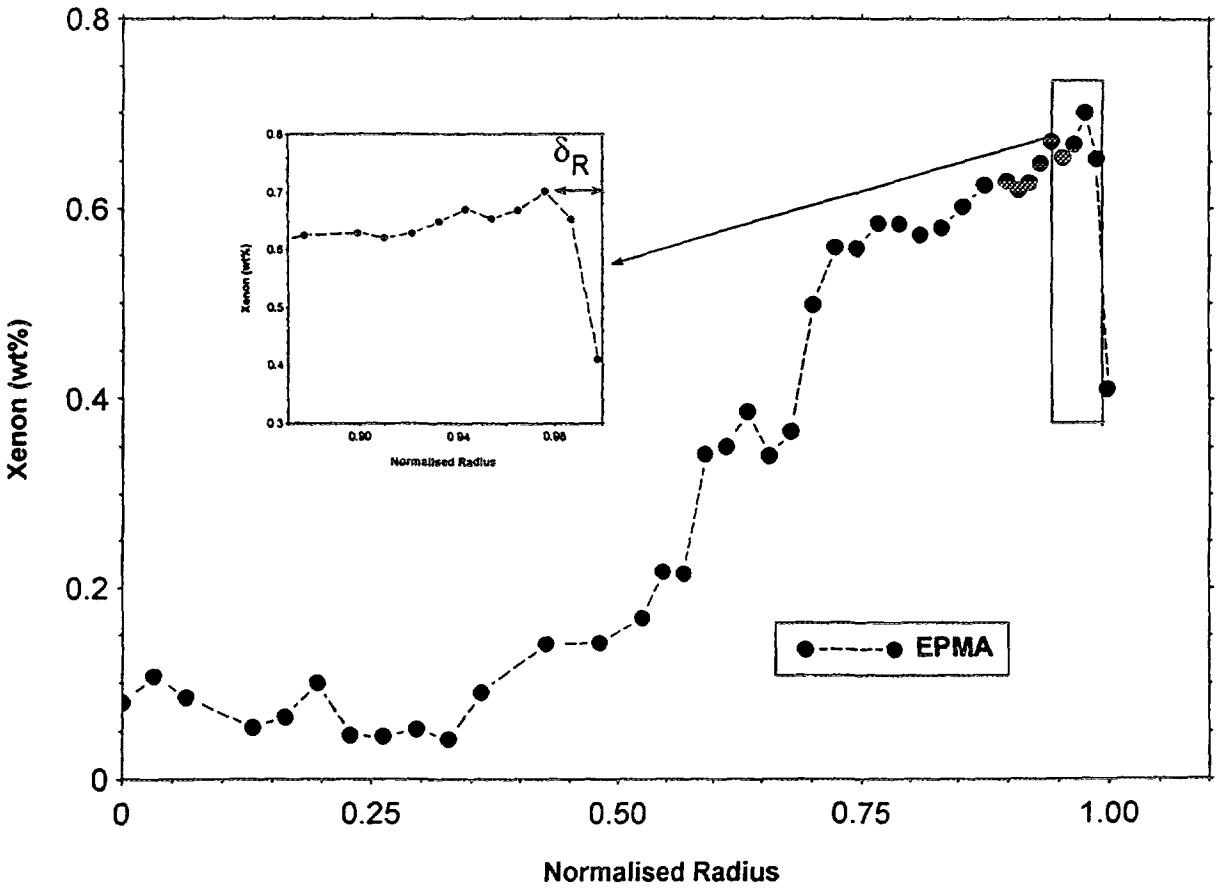

Fig. 3 The Xe concentration as a function of radius measured by EPMA. Details near the edge are shown in the insert: the depth of the Xe depletion zone is denoted by d_{EPMA}. Note that the error in the measured Xe concentration is about 5%.

TABLE I. RANGE OF PELLET AND PIN CHARACTERISTICS.

pellet radius (mm)	4-6
pellet density (%TD)	94-96
^{235}U (wt%)	2-8
burnup (GWd/t)	40-75

Love [21]. Radial concentration profiles were obtained by point analysis along the fuel radius at intervals of 50 to 150 μm. At each location six measurements were made. These were up to 10 mm apart and were placed to avoid pores, large gas bubbles and cracks. The specimen current image (absorbed electron current) was used to obtain information about the disposition of the pores and gas bubbles in the location where point analysis was performed.

Plutonium was analysed using the M_β X-ray line and a quartz [1011] diffracting crystal. A PuO_2 standard was used. The intensity of the plutonium M_β line was corrected for X-ray contributions from the neighbouring U $M_{\lambda 2}$ line as described elsewhere [18]. The confidence interval on a measured plutonium concentration of 2.0 wt% is around 10% relative at a significance level of 99%. This uncertainty is due solely to the statistics of X-ray counting. After correction for the use of a compound standard and after accounting for interference from the U $M_{\lambda 2}$ line the confidence interval is of the order of 20% relative.

Xenon was analysed using the approach developed at the Institute for Transuranium Elements [22]. The confidence interval on the measured Xe concentrations at a significance level of 99% is about 5% relative at a concentration of 0.5 wt% and 10-20% relative at 0.05 wt%. For Cs and Nd, similar levels of uncertainty are expected. Xenon depletion in the UO_2 matrix was assessed with reference to the Xe concentration given by the local burn-up which in turn was calculated from the measured local concentration of neodymium.

4. ANALYSIS OF DATA

The *TUBRNP* model calculates the depth to which the burnup is greater than the threshold burnup, τ_b, as a function of fuel geometry, porosity, enrichment and average burnup. The notation δ_R is used for this calculated depth. It is dependent on the fuel geometry since, for a fixed average burnup, the local burnup profile will vary with the fuel outer radius (and inner radius if there is a central void). Calculations showed a slight increase in δ_R with outer radius. Dependence on the fuel porosity was found to be negligible in the range studied (4 to 6%). In the following the calculated depth, δ_R, is compared with the measured depth, δ_{EPMA}.

To understand completely the dependence of δ_R on the enrichment and burnup it is helpful to plot the results of calculations in 3D. In Figs. 4 to 6 the values of δ_R for the standard case, see Table II, are plotted as a surface: the measured data is included for comparison. The use of the term "restructured zone" is used as a general term to include Xe depletion, burnup increase, reduction in grain size and increased porosity. Here the predicted depth with local burnup greater than τ_b is compared with the measured Xe depletion depth. It is clear that the threshold burnup τ_b=60 GWd/t underpredicts whereas τ_b=80 GWd/t overpredicts the actual depth of Xe depletion. A value of τ_b=70 GWd/t gives reasonable agreement, Fig. 5. On closer examination of Figs. 4 to 6 it can be seen that the model predicts a variation of δ_R with enrichment. This variation changes both with the average burnup *and* with the value of the threshold burnup, τ_b. The model calculations predict that, at fixed average burnup below the threshold burnup (or at least close to it), δ_R decreases with increasing enrichment. Above the threshold burnup δ_R increases sharply with enrichment. This can be clearly seen in Fig. 5 where the value at average burnup $<B>$ =70 GWd/t serves as a line of demarcation between these two types of variation with enrichment.

In order to provide a detailed analysis of the experimental data the value of δ_R was evaluated with *TUBRNP* for each case. The quantity is a well defined number derived from the input parameters. The fuel geometry and enrichment are also well defined. However, there may be errors in the given values for the nominal average burnup. Therefore calculations were done for the nominal average burnup value $<B>$ and at $<B> \pm 5\%$ to take such errors into account. An example of the change in burnup profile can be seen in Fig. 2. This of course will influence the depth to which the burnup profile extends with values greater than τ_b. In Figs. 7 to 9 the values of δ_R are plotted as a function of average burnup along with the measured values derived from the Xe profile. The errors in estimating the edge of the Xe depleted zone are also displayed. For convenience the values of δ_R are displayed only at nominal average burnup. It can be concluded from these three graphs that τ_b=60 and 80 GWd/t are lower and upper limits for the threshold burnup. The values of δ_R calculated at τ_b=70 GWd/t are in reasonable agreement with the Xe measurements.

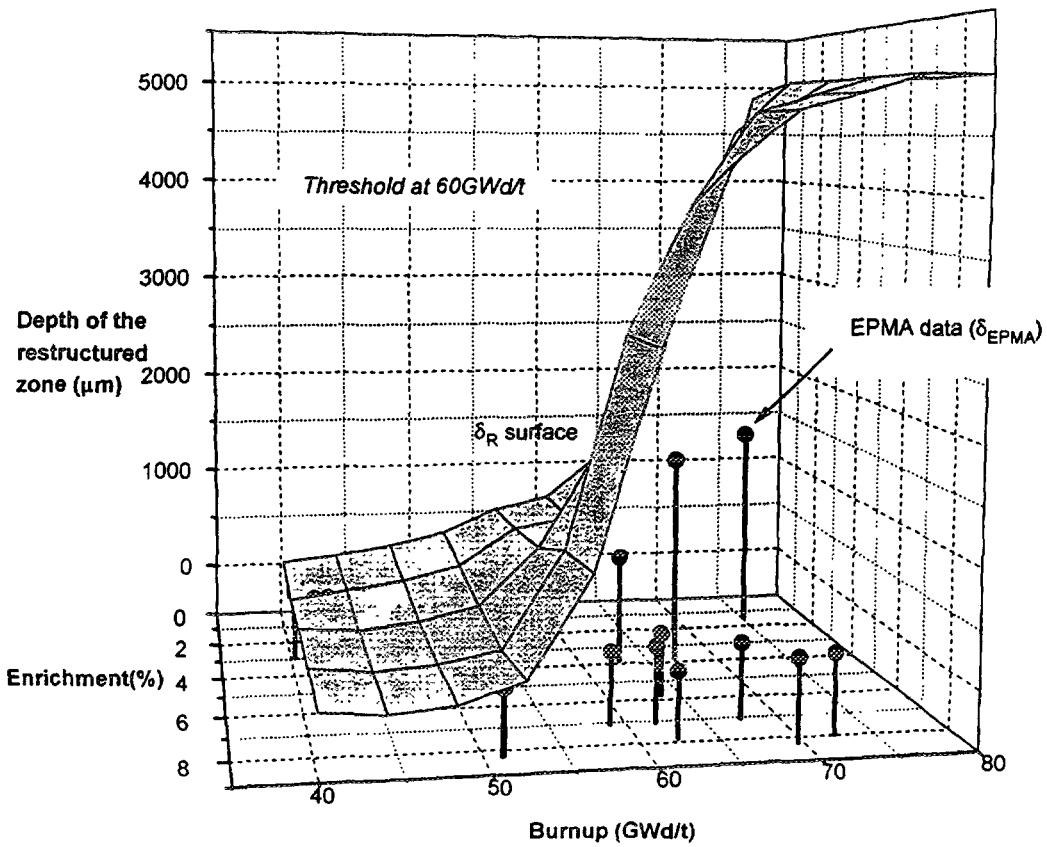

Fig. 4 The depth of the restructured zone as a function of enrichment and average burnup. The surface is the prediction (d_R) of the TUBRNP model for the standard case, see Table II, with a threshold value of t_b=60 GWd/t. The points are the values of the depth of this zone derived from the Xe profiles (d_{EPMA}).

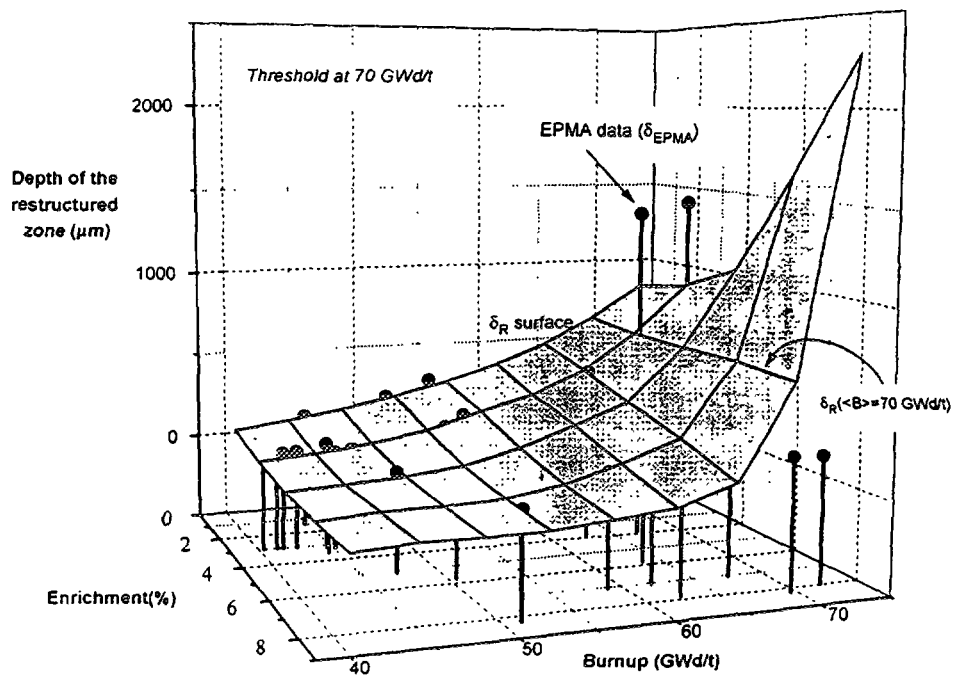

Figure 5

Fig. 5 The depth of the restructured zone as a function of enrichment and average burnup. The surface is the prediction (d_R) of the TUBRNP model for the standard case, see Table II, with a threshold value of t_b=70 GWd/t. The points are the values of the depth of this zone derived from the Xe profiles (d_{EPMA}).

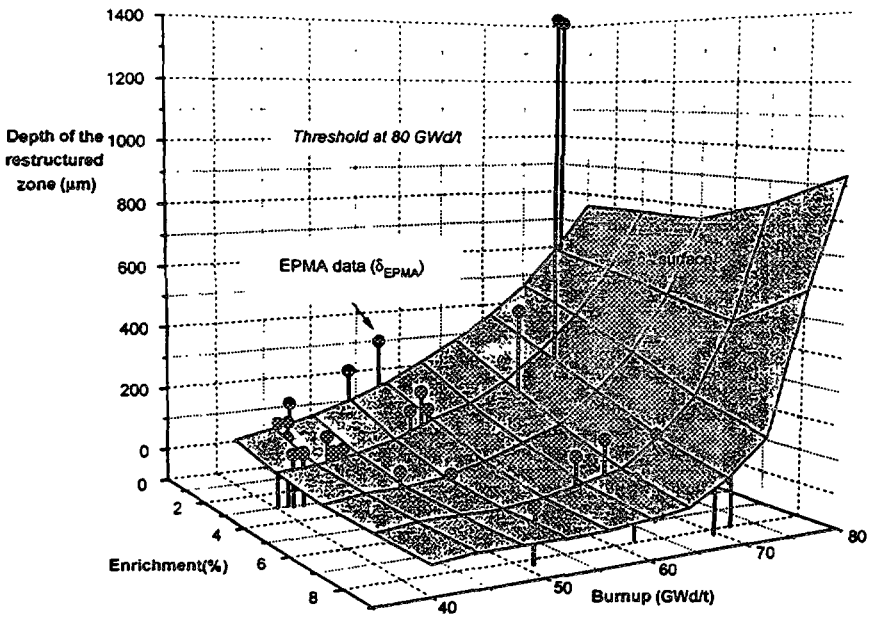

Fig. 6 The depth of the restructured zone as a function of enrichment and average burnup. The surface is the prediction (d_R) of the TUBRNP model for the standard case, see Table II, with a threshold value of t_b=80 GWd/t. The points are the values of the depth of this zone derived from the Xe profiles (d_{EPMA}).

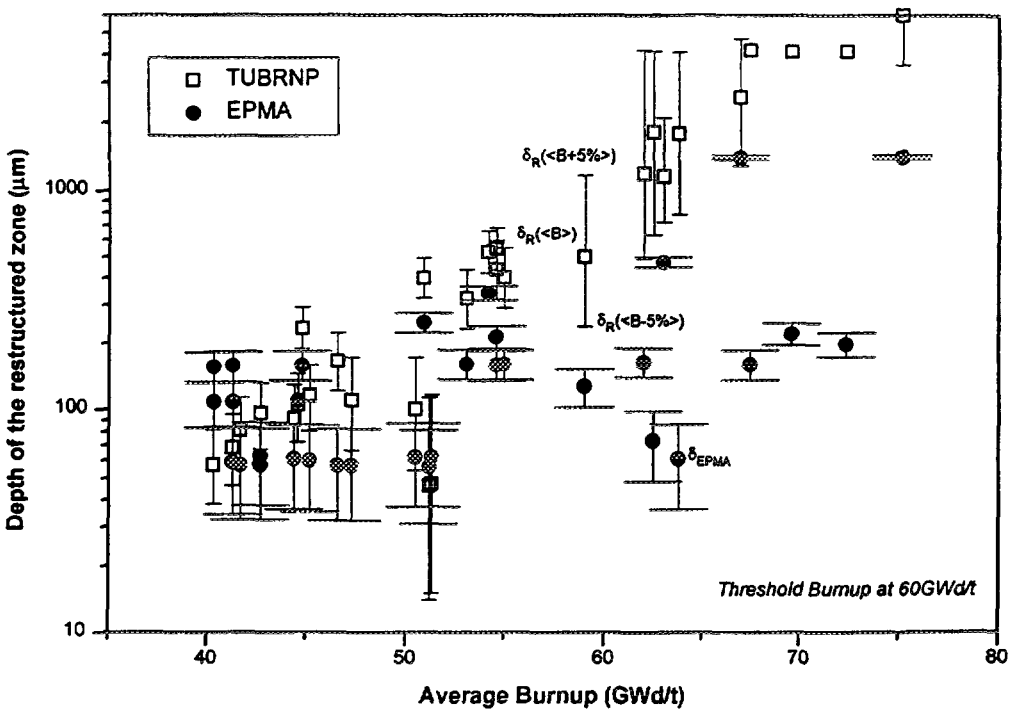

Fig. 7 Log-log plot of the depth of the restructured zone as a function of the average burnup. The predicted values are calculated at the nominal burnup <B> and at <B> ±5% for a threshold burnup of 60 GWd/t. The upper and lower values of d_R (<B> ±5%) are plotted at <B> for convenience. The points are the values of the depth (with errors) of this zone derived from the Xe profiles (d_{EPMA}).

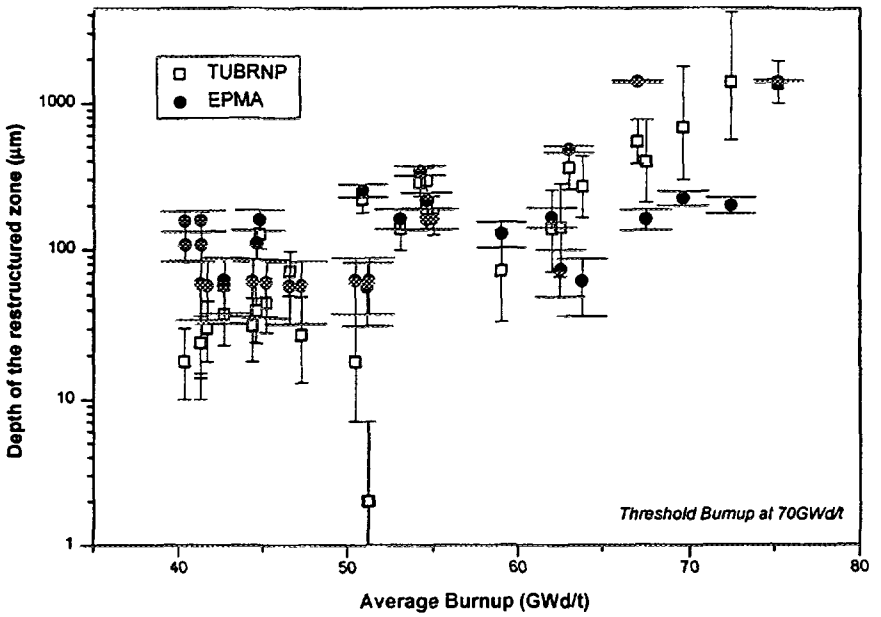

Fig. 8 Log-log plot of the depth of the restructured zone as a function of the average burnup. The predicted values are calculated at the nominal burnup <B> and at <B> ±5% for a threshold burnup of 70 GWd/t. The upper and lower values of d_R (<B> ±5%) are plotted at <B> for convenience. The points are the values of the depth (with errors) of this zone derived from the Xe profiles (d_{EPMA}).

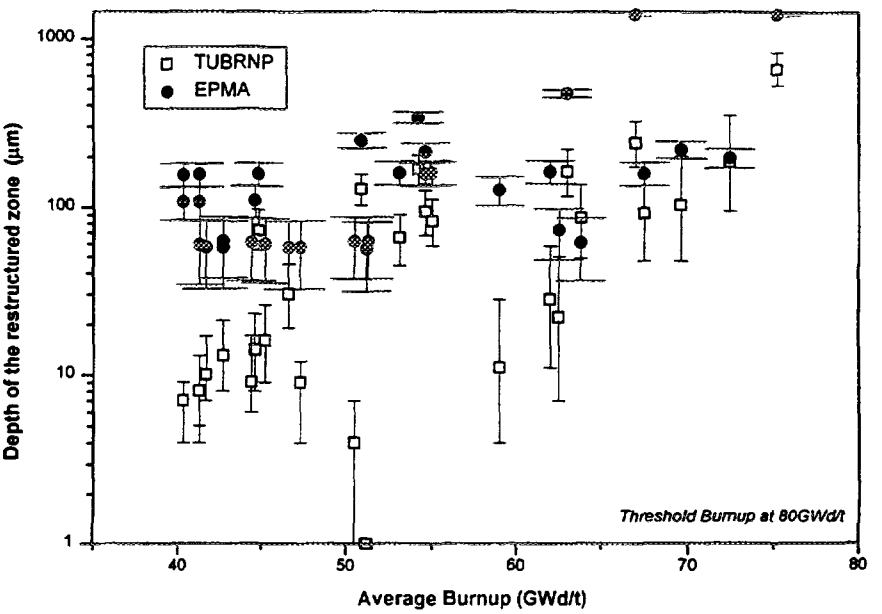

Fig. 9 Log-log plot of the depth of the restructured zone as a function of the average burnup. The predicted values are calculated at the nominal burnup <B> and at <B> ±5% for a threshold burnup of 80 GWd/t. The upper and lower values of d_R (<B> ±5%) are plotted at <B> for convenience. The points are the values of the depth (with errors) of this zone derived from the Xe profiles (d_{EPMA}).

TABLE II PARAMATERS USED FOR STANDARD CALCULATION.

pellet radius (mm)	5
pellet density (%TD)	95
^{235}U (wt%)	2-8
burnup (GWd/t)	40-75

5. SUMMARY

Change in the structure of high burnup fuels (average burnup greater than 40 GWd/t) is a complex phenomenon which results in the formation of subgrains, the loss of matrix fission gas and an increase in porosity. The basic process that causes this to occur is the high value of local burnup at the fuel edge due to increased production of ^{239}Pu from resonance capture in ^{238}U. The *TUBRNP* model was developed to describe this phenomenon in UO_2. Its predictions for the depth of the Xe depleted zone, as derived from EPMA measurements, are in reasonable agreement with experiment even though such other parameters such as temperature are not included: this is in progress. Therefore the model should be seen as a first step in the modelling of high burnup phenomena in UO_2 fuel.

ACKNOWLEDGEMENTS

The authors would like to thank Hj. Matzke for stimulating discussions

REFERENCES

[1] WALKER C.T. and COQUERELLE M., Correlation between microstructure and fission gas release in high burnup UO_2 and MOX fuel, Proceedings International Topical Meeting On Light Water Reactor Fuel Performance, Avignon, April, 21-24 (1991) 506.

[2] MATZKE Hj., BLANK H., COQUERELLE M., LASSMANN K., RAY I.L.F., RONCHI C. and WALKER C.T., Oxide Fuel Transients, J. Nucl. Mater., 166 (1989) 165.

[3] MANZEL R. and EBERLE R., Fission gas release at high burnup and the influence of the pellet rim, Proceedings International Topical Meeting On Light Water Reactor Fuel Performance, Avignon, April, 21-24 (1991) 528.

[4] WALKER C.T., KAMEYAMA T., KITAJIMA S. and KINOSHITA M., Concerning the microstructure changes that occur at the surface of UO_2 pellets on irradiation to high burnup, J. Nucl. Mater., 188 (1992) 73.

[5] CUNNINGHAM M.E., FRESHLEY M.D. and LANNING D.D., Development and characteristics of the rim region in high-burnup UO_2 fuel pellets, J. Nucl. Mater. 188 (1992) 19.

[6] UNE K., NOGITA K., KASHIBE S. and IMAMURA M., Microstructural change and its influence on fission gas release in high burnup UO_2 Fuel, J. Nucl. Mater., 188 (1992) 65.

[7] THOMAS L.E., BEYER C.E. and CHARLOT L.A., Microstructural analysis of LWR spent fuels at high burnup, J. Nuc. Mater., 188 (1992) 85.

[8] MATZKE Hj., On the rim effect in high burnup UO_2 LWR fuels, J. Nucl. Mater. 189 (1992) 141.

[9] MATZKE Hj., Oxygen potential in the rim region of high burnup UO_2 fuel, J. Nucl. Mater. 208 (1994) 18.

[10] MATZKE Hj., TUROS A. and LINKER G., Polygonization of single crystals of the flourite-type oxide UO_2 due to high dose ion implantation, Nuc. Instr. and Meth. in Phys. Res., B91 (1994) 294.

[11] BAGGER C., MOGENSEN M. and WALKER C.T., Temperature measurements in high burnup UO_2 nuclear fuel: implications for thermal conductivity, grain growth and gas release, J. Nuc. Mater., 211 (1994) 11.

[12] BIRON J.P., BORDIN B., GEOFFROY G., MAUNIER C. and BARON D., Fuel Microstructure and Rim Effect at High Burn-up, Proceedings International Topical Meeting On Light Water Reactor Fuel Performance, West Palm Beach, April, 17-21 (1994) 321.

[13] KJAER-PEDERSON N., Rim effect observations from the third Risø fission gas project, IAEA IWGFPT Technical Meeting on Fission-Gas Release and Fuel-Rod Chemistry Related to Extended Burnup, Pembroke, April 28 - May 1 (1992) .

[14] REST J. and HOFMAN G.L., Kinetics of recrystallization and fission-gas-induced swelling in high burnup UO_2 and U Si nuclear fuels, Fundamental Aspects of Inert Gases in Solids, (DONNELLY S.E and EVAN J.H. eds.), Plenum Press, New York (1991) 443.

[15] REST J. and HOFMAN G.L., Dynamics of irradiation-induced grain subdivision and swelling in U_3Si_2 and UO_2 fuels, J. Nucl. Mater., 210 (1994) 187.

[16] KAMEYAMA T., MATSUMURA T. and KINOSHITA M., Numerical analysis for microstructure change of a light water reactor fuel pellet at high burnup, Nuc. Tech., 106 (1994) 334.

[17] LEMEKHOV S.E., Computer code ASFAD: Status, resent developments and applications, Proceedings International Topical Meeting On Light Water Reactor Fuel Performance, West Palm Beach, April, 17-21 (1994) 162.

[18] LASSMANN K., O'CARROLL C., VAN DE LAAR J. and WALKER C.T., The radial distribution of plutonium in high burnup UO_2 fuels, J. Nucl. Mater. 208 (1994) 223.

[19] KAMEYAMA T., MATSUMURA T. and KINOSHITA M., Analysis of Rim Structure Formation in Battelle High Burnup Effects Program, Proceedings International Topical Meeting On Light Water Reactor Fuel Performance, Avignon, April, 21-24 (1991) 620.

[20] FARTHING I., LOVE G., SCOTT V.D. and WALKER C.T., Electron Beam Microanalysis, (BOEKSTEIN A. and PAVICEVIC M.K. eds.), Mikrochim. Acta, 12 (1993) 117.

[21] SCOTT V.D. and LOVE G., X-ray Spectrom. 21 (1992) 27.

[22] WALKER C.T., J. Nucl. Mater. 80 (1979) 190.

MODELLING OF SOME HIGH BURNUP PHENOMENA IN NUCLEAR FUEL

K. FORSBERG, F LINDSTRÖM, A.R. MASSIH
ABB Atom,
Västerås, Sweden

Abstract

In this paper the results of some modelling efforts carried out by ABB Atom to describe certain light water reactor fuel high burnup effects are presented. In particular the degradation of fuel thermal conductivity with burnup and its impact on fuel temperature is briefly discussed. The formation of a porous rim and its effect on athermal fission gas release has been modelled and the model has been used to predict the release of pressurized water reactor fuel rods that were operated at low power densities. furthermore, a mathematical model which combines the diffusion and re-solution controlled thermal release with grain boundary movement has been briefly described. The model is used to compare release with diffusion only and release caused by diffusion and grain boundary sweeping (due to grain growth). Finally, analytical expressions are obtained for the calculation of fuel stoichiometry as a function of burnup.

1. Introduction

The steady increase in the discharge burnup of fuel in light water reactors (LWR) in parallel with many investigations that are carried out on high burnup fuel have generated a wealth of experimental data which are ready for quantitative evaluations. The results of the evaluations are culminated in terms of mathematical models which can be implemented in fuel performance computer codes. These models are then used in the analysis for further extension of burnup and in licensing of the fuel to a desired target burnup.

In this paper we present the results of some modelling efforts, related to high burnup effects, carried out in ABB Atom in the past few years. One important issue has been the degradation of fuel thermal conductivity with burnup and its effect on fuel thermal behaviour. Measurements performed by Lucuta et al on SIMFUEL [1] show that the UO_2 fuel thermal conductivity decreases steadily with burnup (≈ 17 % in 30 MWd/kgU at 550 °C). Similarly thermal conductivity data deduced from fuel centerline measurements performed in the Halden reactor [2] indicate a conductivity degradation of about 2 Km/kW/(MWd/kgUO_2), i.e., 18% in 30 MWd/kgUO_2 at 550 °C.

An important observation made on high burnup fuel is the formation of a porous outer ring in fuel pellet with a thickness of 100 to 200 μm [3, 4]. In this region, the local burnup is significantly increased due to formation of plutonium through the resonance absorption of neutrons. Recent investigations by Cunnigham et al [3] indicate that the rim region holds

the potential for enhanced athermal fission gas release observed in low power density rods in LWRs at high burnups. In this paper we attempt to model the thermal conductivity degradation of UO_2 fuel with burnup and the rim release using the experimental data available on these phenomena. Simple microburnup physics models have been utilized to calculate the burnup distribution across the pellet as a function of irradiation time which is needed to model these effects.

Another issue of interest at high burnups is the thermal-mechanical behaviour of fuel during power transients. Measurements show [5] that during power ramps, the UO_2 grains undergo growth in fuel pellet regions where the temperature is sufficienly high. Grain growth causes grain boundary sweeping of fission product gases thus enhancing the release process. A physically based model describing diffusion of fission gases in a growing grain with boundary sweeping has been formulated, and has been outlined here.

A high burnup fuel phenomenon which influences fuel thermal behaviour is the variation of fuel stoichiometry with fuel burnup. Oxygen-to-metal ratio (O/M) affects both fuel thermal conductivity and fission gas diffusion coefficient. Following Lassmann [6] a diffusion model for oxygen vacancy under thermal gradient is considered and approximative analytical solutions are derived for both steady-state and transient conditions. The oxygen distribution model has been used to predict the radial profile of O/M across the pellet at different burnups for the steady-state condition. The time constant for the transient solution of the diffusion equation for the oxygen excess has been calculated and then its dependence on temperature and concentration has been studied.

2. Fuel Thermal Conductivity and Temperature

The fuel pellet temperature is described by the heat conduction equation given by

$$C_p\rho\frac{\partial T}{\partial t} = \nabla.(k\nabla T) + q''' \tag{1}$$

where $T = T(r,t)$ is the fuel temperature at position r and time t, C_p the heat capacity at constant pressure [J/kg K], ρ the fuel density [kg/m^3], $k = k(T,u)$ the thermal conductivity which is a function of temperature and burnup u, $q''' = q'''(r,t,u)$ the power density [W/m^3], $\nabla.= \frac{1}{r}\frac{\partial}{\partial r}$ and $\nabla = r\frac{\partial}{\partial r}$ given in cylindrical geometry.

The temperature boundary conditions are $\left.\frac{\partial T}{\partial r}\right|_{r=0} = 0$ and $T(r_{out},t) = T_s(t)$ where r_{out} is the fuel pellet radius and T_s is the pellet surface temperature.

In a steady-state situation, T is independent of time and Eq. (1) can be integrated to give

$$\int k(T,u)dT = -\int_0^{r_{out}} \frac{\int_0^r q'''(r',u)r'dr'}{r} dr \tag{2}$$

The power density q''' in the pellet is expressed as

$$q''' = \bar{q}''' \sum_j \alpha \sigma_{f,j} N_j(r,u)\phi(r) \tag{3}$$

where $\bar{q}'''$ is the pellet average power density, $\sigma_{f,j}$ is the microscopic fission cross section for isotope j, $N_j(r,u)$ is the concentration of isotope j at position r and burnup u, $\phi(r)$ is the thermal flux, and α is the proportionality factor. If monoenergetic (one-group) diffusion theory of neutrons is assumed, ϕ obeys [7]

$$\nabla^2\phi - \kappa^2\phi = 0 \tag{4}$$

with boundary condition $d\phi/dr|_{r=r_i} = 0$. Here $\kappa^2 = \Sigma_{a,t}/D_n$ where $\Sigma_{a,t}$ is the total macroscopic absorption cross section and D_n is the neutron diffusion coefficient and κ is the inverse neutron diffusion length. The concentration of isotopes obey depletion equation, see for example Lassmann et al [8]. The solution of Eq. (4) can be expressed in terms of the modified Bessel function, e.g., for the solid cylinder $\phi = I_1(\kappa r)$. A subroutine based on the Lassmann et al model has been used to calculate the burnup distribution across the fuel pellet.

The thermal conductivity of UO_2 fuel consists of the sum of two contributions: the conduction through lattice vibrations (phonons) and conduction by electronic process. The phonon contribution is a dominating term to the thermal conduction process for temperatures below 1900 K. The average thermal conductivity of UO_2 as a function of burnup has been obtained from thermal diffusivity measurements by Lucuta et al [1]. Using the phonon term of the correlation provided by Reymann in MATPRO [9] plus the burnup dependence data of Lucuta et al we have:

$$k(T,u) = \frac{1}{k_0 + k_1 u + (k_2 - k_3 u)T} \qquad [\mathrm{W/mK}] \tag{5}$$

where

k_o = 0.047
k_1 = 1.73×10^{-3}
k_2 = 2.5×10^{-4}
k_3 = 5.41×10^{-8}
T = fuel temperature [K]
u = fuel burnup [MWd / kg U]

As an example fuel temperature as a function of burnup is calculated for a BWR rod with the dimensions given in Table 1 and a given power history with and without the burnup term using Eq. (5) in the fuel performance code STAV. The results are presented in Figs. 1 and 2.

Table 1 Nominal Fuel Rod Data for the SVEA-96/100 Design

Rod diameter	mm	9.62
Clad wall thickness	mm	0.63
Pellet diameter	mm	8.19
Number of rods per assembly		96/100
Fuel pellet density	g/cm^3	10.47

2. Fission Gas Release

Fission product gas release is an important phenomenon for the performance of LWR fuel rods. The gas released to the pellet-clad gap region of fuel rod degrades the thermal conductance of the gas gap which leads to higher fuel temperature and further enhancement of the release rate. The fission gas release will also increase the rod internal pressure. As such the prediction of the amount of fission gas release as a function of burnup is an essential part of fuel rod design. The fission gas release process in UO_2 fuel is considered to consist of two mechanisms: an athermal release and thermal release. The athermal release accounts for the contribution of release caused by *direct recoil* of fission fragments within a layer equal to the range of the fission fragments in the fuel (≈ 10 μm), and by the *knockout* mechanism which is an elastic collision between fission fragments and fission product gas atoms in the fuel.

Athermal release is primarily fission rate dependent and in LWRs it is almost a linear function of burnup up to the burnup of around 40

Figure 1a

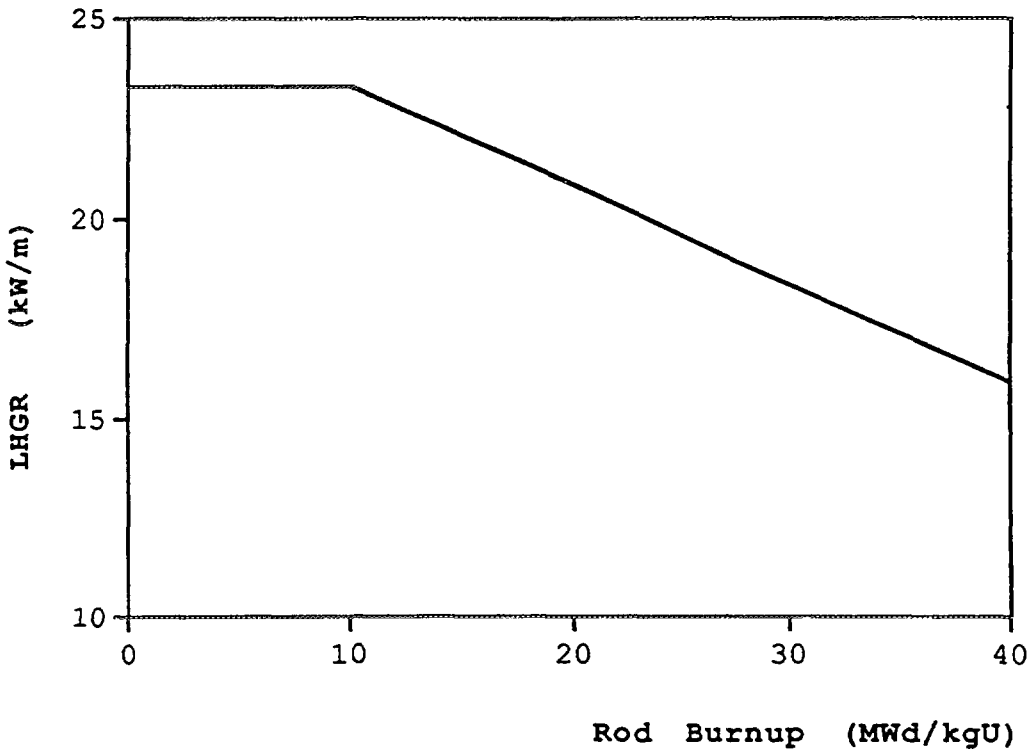

Figure 1b

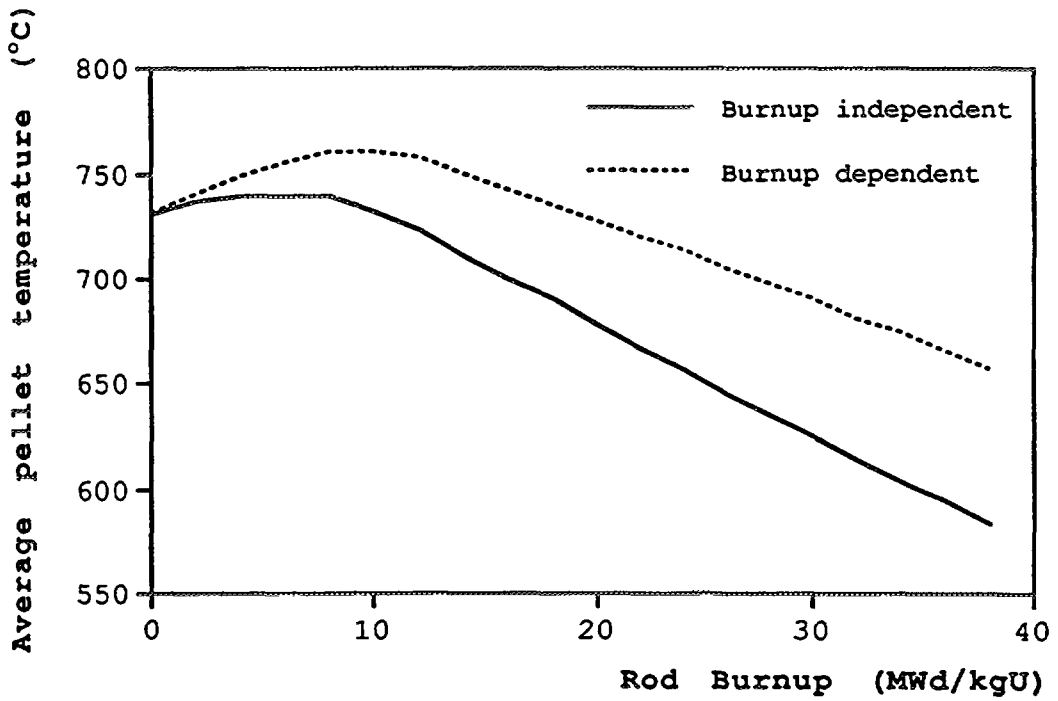

Figure 1 (a) Linear heat generation rate versus burnup used in this calculation. (b) Fuel pellet average temperature as a function of burnup with and without burnup dependent thermal conductivity.

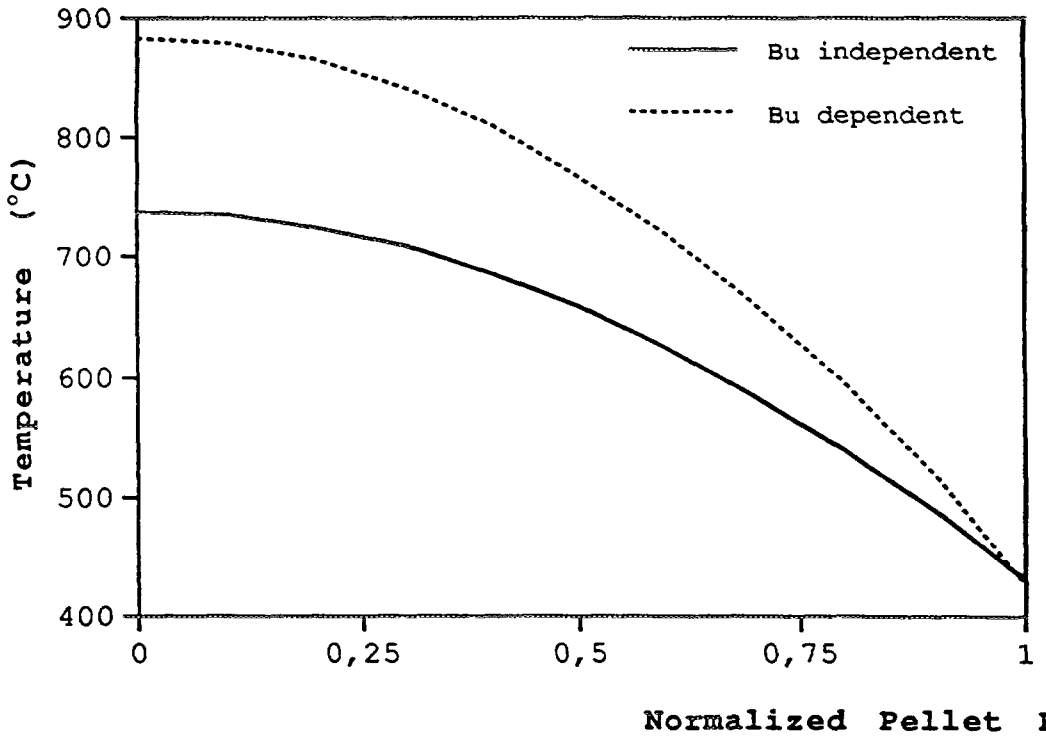

Figure 2 Fuel pellet temperature profile at a rod burnup of 40 MWd/kg U with and without burnup dependent thermal conductivity.

MWd/kgU. More specifically the rate of the number of gas atoms released by athermal process can be written as: $dN_r / dt \approx N_g \dot{f}$ where N_g is the number of gas atoms generated per unit volume of fuel, $N_g = \dot{f} t y$, y is the fission yield, $\dot{f}$ the fission rate and t is the irradiation of time. The release fraction $\mathcal{F}_{ath} = N_r / N_g \sim \dot{f} t = Cu$ where u is the fuel burnup [MWd/kg U] and C is a constant of proportionality. For example Lorenz [10] has provided such a linear correlation with $C = 8.5 \times 10^{-5}$.

The thermal release is highly temperature dependent and is driven by thermal processes in irradiated fuel. These include gas diffusion to grain boundaries, grain growth, and gas bubble migrations. In this section we focus our attention to the modelling aspects of two particular effects: the athermal release due to the so called "rim effect" and the thermal release caused by gas diffusion and grain growth.

2.1 Athermal Release and Rim Effect

As mentioned earlier recent data obtained from LWR fuel rods operating at low powers show that athermal release accelerates at burnups of around 45 MWd/kgU. The fraction of athermal release is roughly under 1% for rod burnups below 45 MWd/kgU. High burnup fuel data show that this release accelerates to roughly 3 % when rod burnup level reaches up to around 60 MWd/kgU. Furthermore, recent measurements show at

burnup of about 45 MWd/kgU a porous outer ring in the fuel pellet forms. The typical thickness of this ring is about 100 to 200 μm. In this region the local burnup is greatly increased because of Pu production by resonance absorption of epithermal neutrons. Hence, it is expected that the porous rim of LWR fuel is associated with increase in fission rate and local burnup, caused by Pu-generation. Moreover, it is anticipated that the enhanced athermal release, observed in low power density rods, emanates from the rim region.

More specifically, electron probe microanalysis and x-ray fluorescence (XRF) measurements performed by Cunnigham et al [3] on UO_2 fuel irradiated to high burnups show that there is a threshold pellet-edge burnup (~ 65 MWd/kg) at which the rim region's fractional depletion of xenon occurs. Hence, although a great amount of gas is retained in the fuel porosity, the recoil and knockout process also enhance the release rate from the outer edge region. Cunnigham et al have provided an empirical correlation based on curve fitting of measured data for rim region release as a function of burnup. This correlation (or the data) constitutes the basis of the rim region athermal release model presented here.

In our model the fraction of athermal fission gas release in the rim region is calculated via:

$$\mathcal{F}_{rim} = \frac{\int_{r_{in}}^{r_{out}} F\{u(r)\}u_n(r)rdr}{\int_{r_{in}}^{r_{out}} rdr} \tag{6}$$

where the functional $F\{u(r)\}$ is the fraction of depletion of fission gas release in the rim region, and $u_n(r)$ is the normalised local burnup, i.e., $u_n(r) = u(r) / \bar{u}$ where $\bar{u}$ is the mean pellet burnup. Since F is zero for $u<u_{rim}$, we suppose that F has a step function form:

$$F\{u(r)\} = \begin{cases} 0 & u < u_{rim} \\ F_{rim} & u \geq u_{rim} \end{cases} \tag{7}$$

where u_{rim} is the threshold burnup for rim release and F_{rim} is assumed to be constant. This is prima facie an adhoc assumption. However, it is made with the aposteriori justification by the success of predicting the experimental athermal release fraction as a function of pellet average burnup.

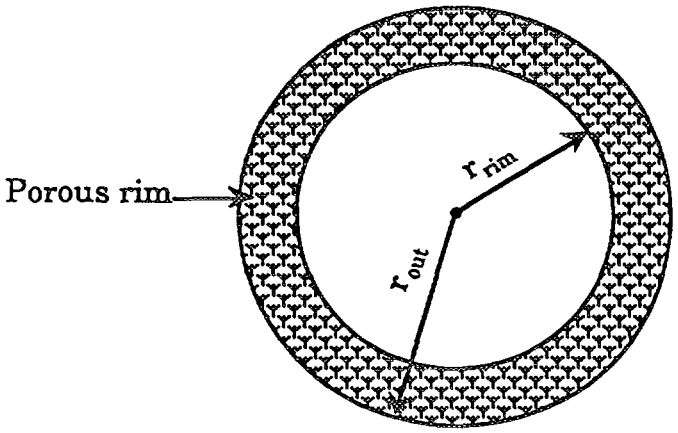

Geometry of a pellet with a porous rim

If we insert (7) into (6) we readily find

$$\mathcal{F}_{rim} = F_{rim}\frac{\int_{r_{rim}}^{r_{out}} u(r)rdr}{\overline{u}\int_{r_{in}}^{r_{out}} rdr} = \frac{F_{rim}}{\mathcal{A}}\frac{\int_{r_{rim}}^{r_{out}} u(r)rdr}{\overline{u}} \tag{8}$$

where r_{rim} is the rim edge inner radius (see the drawing above), $\mathcal{A} = \left(r_{out}^2 - r_{in}^2\right)/2$ and

$$\overline{u} = \mathcal{A}^{-1}\int_{r_{in}}^{r_{out}} u(r)\,rdr \tag{9}$$

The rim radius is calculated via

$$r_{rim} = r_i + \frac{u_{rim} - u_i}{u_{i+1} - u_i}\left(r_{i+1} - r_i\right) \qquad \text{for } r_{i+1} = r_{out}$$

$$r_{rim} = r_i + \frac{u_{rim} - u_i}{u_{i+1} - u_i}\left(r_{i+1} - r_i\right) + \frac{u_{rim} - u_i}{u_{i+2} - u_i}\frac{u_{rim} - u_{i+1}}{u_{i+2} - u_{i+1}}\left(r_{i+2} - r_i\right) - \frac{u_{rim} - u_i}{u_{i+1} - u_i}\frac{u_{rim} - u_{i+1}}{u_{i+2} - u_{i+1}}\left(r_{i+1} - r_i\right) \qquad \text{for } r_{i+1} < r_{out} \tag{10}$$

The values of u_i are calculated from a microburnup subroutine mentioned earlier (section 2). It should be noted that since u_i varies with local burnup so does r_{rim} and that in turn affects the fraction of athermal release in the rim region. The values for the two constants u_{rim} and F_{rim} are chosen such that $\mathcal{F}_{rim}$ matches the empirical correlation reported by Cunnigham et al. We have used this model to calculate rim region's

athermal release as a function of burnup for a BWR UO_2 fuel pellet with diameter 8.19 mm, density 10.46 g/cm^3 and ^{235}U enrichment of 3.6 %. The results are plotted in Fig. 3 along with the data of Cunnigham et al.[3] We have also calculated the fraction of rim area as a function of average pellet burnup (see Fig. 4).

The athermal fission gas release fraction is then

$$\mathcal{F}_{ath} = \mathcal{F}_{av}^{ath} + \mathcal{F}_{rim} \tag{11}$$

where $\mathcal{F}_{av}^{ath}$ is the pellet average athermal release which is assumed to be a linear function of burnup. The model presented above has been used to predict the release of some low-powered PWR rods as a function rod burnup. Figure 5 shows release data for these rods along with the calculated curve. It is seen that the enhancement of release is captured aptly by the present model.

2.2 Thermal Release: gas diffusion and grain growth

An outstanding problem in LWR fuel modelling is the accurate description of release of fission product gases while UO_2 grains are undergoing grain growth. The problem is relevant in the case where fuel experiences power ramps leading to a raise in fuel temperature. The increase in fuel temperature enhances volume diffusion of gas atoms to

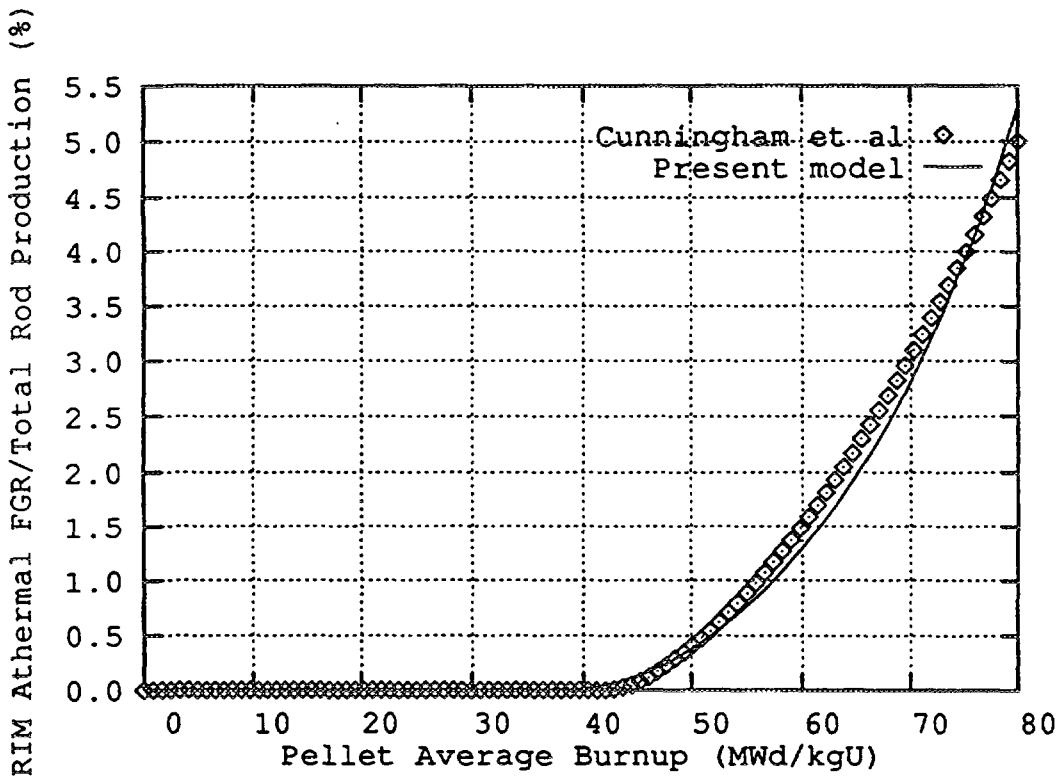

Figure 3 Rim region fission gas release (in percent) versus burnup.

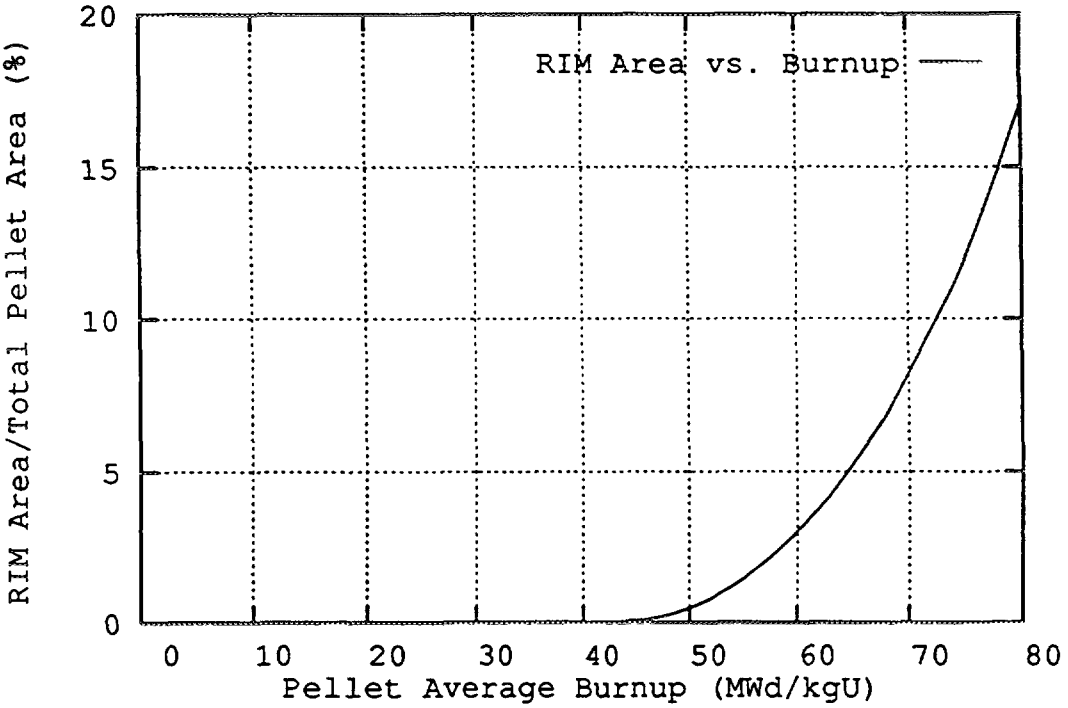

Figure 4 Fraction of rim area versus pellet average burnup.

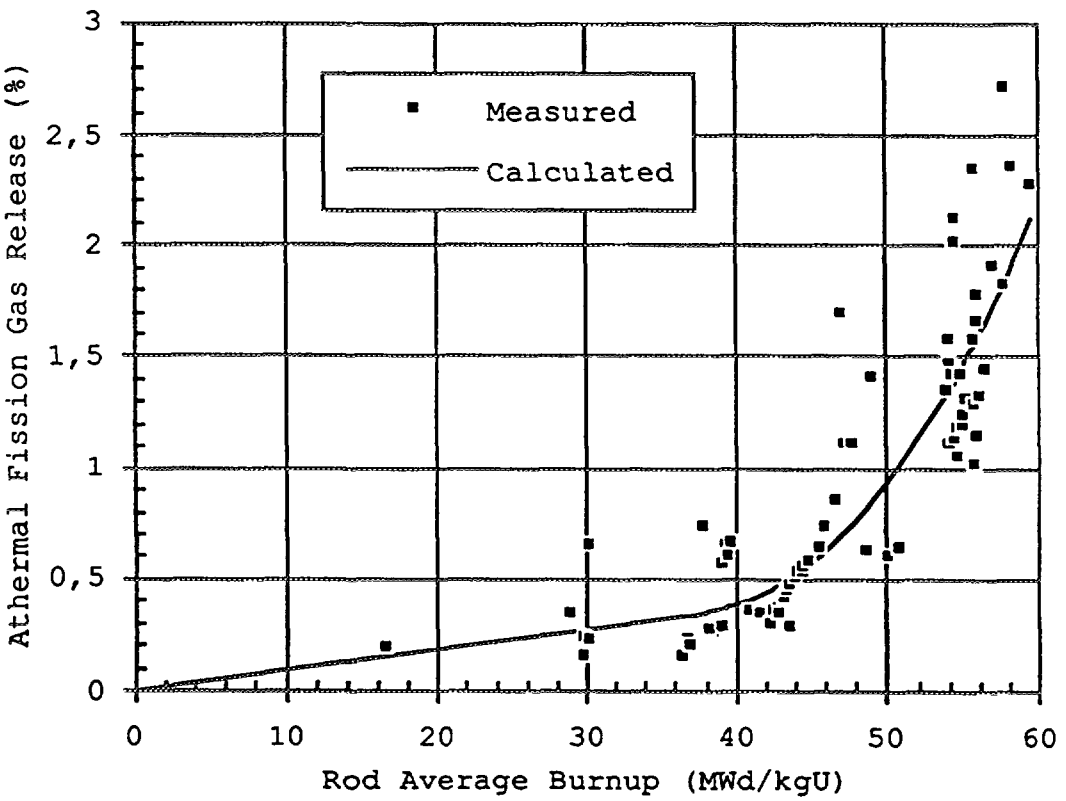

Figure 5 Athermal fission gas release as a function of rod average burnup. The symbols are the measured data obtained from different PWRs.

the grain boundaries, and causes grain growth which sweeps the gases to grain boundaries. Upon saturation of grain boundaries with gases, release to the "void" volume of fuel rod will occur. The concept of grain boundary movement as a mechanism for gas sweeping and release was appearently first applied by Hargreaves and Collins [11].

We attempt to model this process by supposing that UO_2 consists of spherical grains of equal size, i.e., the equivalent sphere model [12,13]. The fission product gases are produced at a rate $\beta(t)$ in a grain with radius $R(t)$. The gases migrate to grain boundaries by diffusion coefficient $D(t)$. The gas atoms reaching the boundary precipitate into intergranular bubbles where the local areal density is denoted by $N(t)$ with the grain boundary re-solution rate, $B(t)=b\lambda$ (b is the grain boundary re-solution probability and λ the re-solution depth from grain face). Note that all the considered variables are time dependent and hence mathematical treatment of the problem warrants special consideration.

The governing equation for concentration of gas atoms at position r in the UO_2 grain at time t is given by

$$\frac{\partial C(r,t)}{\partial t} = D(t)\left(\frac{\partial^2}{\partial r^2} + \frac{2}{r}\frac{\partial}{\partial r}\right)C(r,t) + \beta(t) \qquad \text{for } 0 < r < R(t) \tag{12}$$

Subject to the boundary conditions

$$\frac{\partial}{\partial r}C(0,t) = 0 \tag{13}$$

and

$$C(R,t) = \frac{B(t)N(t)}{D(t)} \tag{14}$$

Since the gas diffusion and grain growth can occur simultaneously, Eq. (12) can be transformed to the equivalent equation of the form

$$\frac{\partial}{\partial \tau}C(x,\tau) = \frac{\partial^2}{\partial x^2}C(x,\tau) + \left[\frac{2}{x} + \frac{\mathcal{R}_\tau}{\mathcal{R}}x\right]\frac{\partial C(x,\tau)}{\partial x} + \mathcal{P}(\tau) \tag{15}$$

where

$$x \equiv \frac{r}{R(t)} \quad , \quad \tau \equiv \int_0^t \frac{D(s)}{R^2(s)}ds \quad , \tag{16}$$

$$\mathcal{R}_\tau \equiv \frac{\partial \mathcal{R}}{\partial \tau}\,, \tag{17}$$

$$\mathcal{P}(\tau(t)) = \frac{R^2(t)}{D(t)}\beta(t), \tag{18}$$

and the transformed re-solution rate:

$$\mathcal{B}(\tau(t)) = \frac{R(t)}{D(t)}B(t)\,, \tag{19}$$

The boundary condition (13) is transformed to

$$\frac{\partial C(0,\tau)}{\partial x} = 0, \tag{20}$$

At the boundary $r = R(t)$, i.e., $x = 1$. We note that (15) includes explicitly the rate of grain radius $\mathcal{R}_\tau = d\mathcal{R}/d\tau$. Note that a different font is used for the variables in τ-space as compared to t-space.

The total amount of gas $G(t)$ per unit volume in a grain of radius R is

$$\begin{aligned} G(t) &= \frac{2\pi R^2 N + \int_0^R 4\pi r^2 C(r,t)dr}{4\pi R^3/3} \\ &= \frac{3D(t)C(R,t)}{2RB} + \frac{3\int_0^R r^2 C(r,t)dr}{R^3} \end{aligned} \tag{21}$$

Here the first term on the right hand side of (21) expresses the amount of gas situated in the grain boundary in equilibrium with the gas inside the grain, while the second term represents the amount of gas inside the grain whose distribution is governed by the diffusion equation.

As long as no gas is released we have

$$G(t) = \int_0^t \beta(s)\,ds, \tag{22}$$

Now if we let $\mathcal{G}(\tau(t)) = G(t)$ and employ the definitions in (16), equation (21) can be rewritten as

$$\frac{\mathcal{G}(\tau)}{3} = \frac{C(1,\tau)}{2B} + \int_0^1 x^2 C(x,\tau)dx, \tag{23}$$

Here we can note that $\mathcal{G}(\tau)$ can also be computed by

$$\mathcal{G}(\tau) = \int_0^{\tau} P(s)ds, \tag{24}$$

The grain growth kinetics of irradiated UO_2 material has been described by Ainscough et al [14] via

$$\frac{\partial R}{\partial t} = \mathcal{A}_1\left(\frac{R_m - R}{2RR_m}\right) \tag{25}$$

where R_m is the limiting radius of the grain at which grain growth ceases, expressed as $R_m = 1.115\times10^{-3}\exp(-7620/RT)$, [m] and $\mathcal{A}_1$ is an Arrehenius type factor given as $\mathcal{A}_1 = 5.24\times10^{-5}\ \exp(-267000/RT)$, [m²/h]. When the concentration of gas at the grain boundary reaches a certain level the saturation value is defined by

$$C_{max}\ (t) = \frac{B\,(t)\,N_s\,(t)}{D\,(t)} \tag{26}$$

then gas release will occur. The gas atom density per unit area of grain boundary at saturation N_s can be calculated through the gas equation of state [15]. In the computations we have assumed first that $C_{max}(t)$ is linear in t, and then upon grain saturation, only a fraction x of the intergranular gas is released. This means that upon release the concentration at grain boundary will be dropped to a value of $(1-x)C_{max}$.

The boundary value problem presented by Eqs. (14)-(24) is amenable to numerical treatments. Since the numerical treatment of the problem gives rise to a stiff set of equations [16] the traditional Crank-Nicholson or explicit time integration technique is hardly suitable for this problem. Hence a finite difference method with a Rosenbrock type time integration scheme [16, 17] has been utilized to solve this boundary value problem, that is to calculate fission gas release as a function of time. The details of this calculation will be presented elsewhere. For the purpose of this paper we have compared, using this model, predictions of fission gas release with grain growth (i.e. with grain boundary sweeping) and the case when the grain radius is constant. The correlations we have used for gas production, diffusion coefficient, grain boundary saturation are the same as in Ref. [18] and are listed in the appendix for completeness. The results of the computations are presented in Fig. 6. In these computations the temperature history consists of a step function, 1000 °C for 2000 h and then a ramp to 1600 °C held for 200 h. It is seen that the amount of gas release

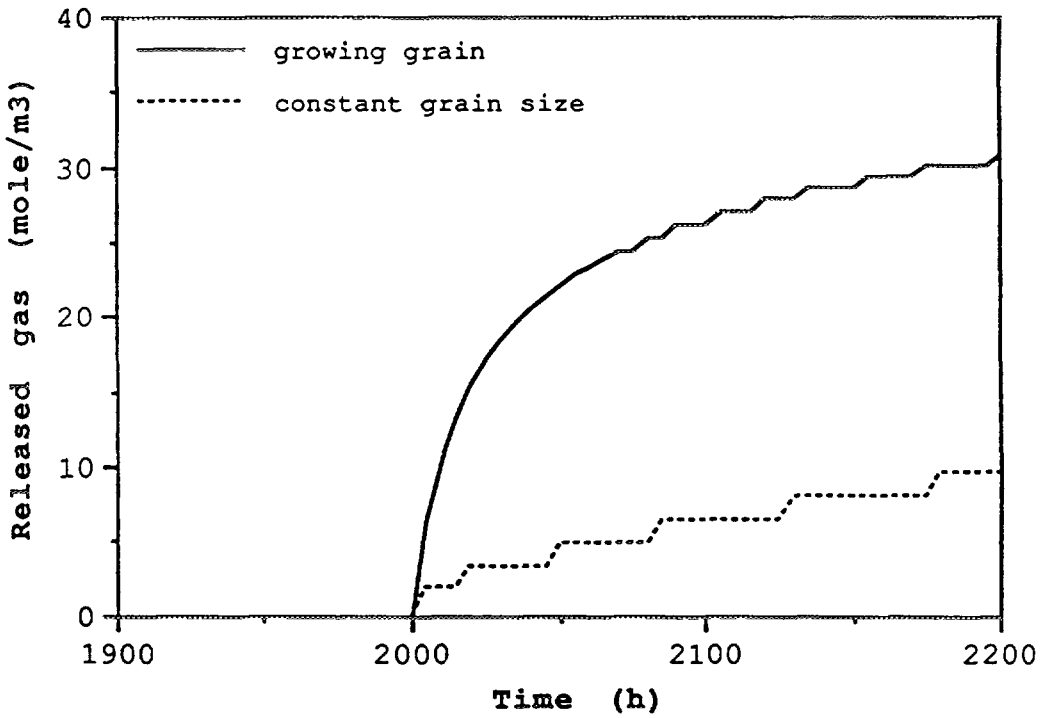

Figure 6 Fission gas release as a function of time after a discontinuous raise in fuel temperature (ramp) to 1600 °C.

is about five times larger with grain growth than without grain growth. After 200 h the grain radius is increased from 5 μm to 11.2 μm.

The Rosenbrock method provides an accurate solution of the boundary value problem considered here, however, its implementation in a fuel performance code (used for many routine analyses) leads to excessive computer storage and CPU time, which makes its usage impractical.

We have developed a semi-analytic solution of the boundary value problem which provides a fast algorithm for calculation of the release in fuel performance codes. This algorithm has been verified against the full numerical solution, details of which will be presented elsewhere. Nevertheless, this approach is outlined below.

The process of thermal gas release by diffusion and grain growth may be divided into two regimes; the diffusion dominating regime when $D/R^2 \geq \mathscr{C} R_t/R$, and the grain growth dominating regime when $D/R^2 < \mathscr{C} R_t/R$. where $\mathscr{C}$ is a constant. In the diffusion dominating regime the boundary value problem, Eqs. (15)-(24), is solved by a truncated series method and the solutions are obtained in terms of products of polynomials and trigonometric functions.

In the grain growth regime, i.e., when grain boundary sweeping is the sole mechanism for thermal release, we can derive the governing

equation by calling on the expression for the average concentration of gas atoms in a grain of radius R:

$$\overline{C} = \frac{3\int_0^R r^2 C(r,t)dr}{R^3} \tag{27}$$

If we differentiate both sides of Eq. (27) with respect to time we find

$$\frac{\partial \overline{C}}{\partial t} = \frac{3}{R}\left[-\overline{C} + \frac{B}{D}N\right]\frac{\partial R}{\partial t} + \beta(t) \tag{28}$$

where we have employed Eq. (14). Equation (28) describes the kinetics of grain boundary sweeping with the re-solution effect. In case of no re-solution and no gas production, i.e., B=0 and β=0, the solution of (28) is $\overline{C} = C_0 (R / R_0)^3$ where R_0 and C_0 are the grain radius and gas concentration at time t=0.

When the grain boundary re-solution effect is accounted for, two situations are considered: either that no gas release has yet taken place, or that gas release has occured. In the latter case Eq. (28) is solved for a given N with solution:

$$\overline{C} = C_0\left(\frac{R_0}{R}\right)^3 + \frac{BN}{D}\left[1 - \left(\frac{R_0}{R}\right)^3\right] + \frac{1}{R^3}\int R^3(t)\beta(t)dt \tag{29}$$

If no gas has yet been released, N in Eq. (28) is replaced by the condition (21) in the form of

$$N = \frac{2R}{3}\left(G - \overline{C}\right) \tag{30}$$

and then it is solved for $\overline{C}$ for a given $G(r)$, yielding:

$$\overline{C} = G_0 + (C_0 - G_0)\left(\frac{R_0}{R}\right)^3 e^{\frac{2B}{D}(R_0 - R)} - \frac{3e^{\frac{-2BR}{D}}}{R^3}\int_{R_0}^{R} r^2 e^{\frac{2B}{D}r} G(r)dr \tag{31}$$

We should emphasize that the formalism outlined here is for grains of equal size. It has been shown by El-Said and Olander [19] that the single-grain size models overpredict the fractional gas release and hence the grain size distribution effect needs to be taken into account. This effect can be included in the above formalism.

3. Oxygen Redistribution in Fuel

The oxygen in LWR fuel will increase from its initial oxygen-to-metal ratio (O/M) of 2.00 during irradiation. In addition, due to the presence of a large temperature gradient across the fuel pellet, a redistribution of oxygen is expected. In this section some theoretical aspects of the oxygen redistribution model will be discussed.

The oxygen vacancies or oxygen atom solutes in oxide fuels in the presence of a thermal gradient and within the dilute solution limit is expressed by the following diffusion equation [6]:

$$\frac{\partial w}{\partial t} = \nabla.\left(D_w \nabla w + \frac{\mathcal{K}}{\eta} w \right) \tag{32}$$

where w is the deviation from stoichiometry (w=O/M–2.00), D_w is the diffusion coefficient for oxygen vacancies or interstitials, $\mathcal{K}= \nabla T(r,t)$ is the temperature gradient across the fuel pellet, and $\eta^{-1}=Q(w)/RT^2$ with $Q(w)$ being the effective heat of transport which is concentration dependent and R the gas constant. The material properties of oxygen in oxide fuels are given by Lassmann [6] and thus are not repeated here.

If we assume an axial symmetry and neglect the axial temperature gradient, Eq. (32) in cylindrical coordinates becomes

$$\frac{\partial w}{\partial t} = \frac{1}{r}\frac{\partial}{\partial r}\left[r D_w \left(\frac{\partial w}{\partial r} - w \frac{Q(w)}{R} \frac{\partial (1/T)}{\partial r} \right) \right] \tag{33}$$

The boundary condition imposed on Eq. (33) is a Neumann boundary condition which demands that the flux of oxygen vacancies or interstitials are prescribed at the boundary, i.e., at the pellet inner and outer radii: $r=r_{in}$ and $r=r_{out}$. Supposing a quasi-equilibrium situation this boundary condition can be written as

$$\frac{\partial w}{\partial r} = \frac{w Q(w)}{R} \frac{\partial (1/T)}{\partial r} \qquad r = r_{in} \tag{34a}$$

$$\frac{\partial w}{\partial r} = \frac{w Q(w)}{R} \frac{\partial (1/T)}{\partial r} \qquad r = r_{out} \tag{34b}$$

A full numerical solution of this boundary value problem has been evaluated by Lassmann [6]. We shall here focus on some analytical properties of these equations.

3.1 Steady-State Condition

Let us first analyze the steady-state solution of (33) defined as $w = \tilde{w}_0$, i.e., we have

$$\frac{\partial \tilde{w}_0}{\partial r} = \tilde{w}_0 \frac{Q(\tilde{w}_0)}{R} \frac{\partial (1/T)}{\partial r} \tag{35}$$

If we assume that, in the first approximation that $Q(\tilde{w}_0)$ is constant, i.e., $Q(\tilde{w}_0)=Q_0$ then the solution to Eq. (35) is

$$\tilde{w}_0(r) \approx \tilde{w}_0(0) e^{\frac{Q_0}{R}\left[\frac{1}{T(0)} - \frac{1}{T(r)}\right]} \tag{36}$$

In the second approximation we assume that Q is a linear function of $\tilde{w}_0$. This approximation is valid so long as $\tilde{w}_0<0.0065$, i.e., we have:

$$Q \approx Q_0(1-h\tilde{w}_0) \tag{37}$$

With this assumption the analytical solution is given by

$$\tilde{w}_0 \approx \frac{1}{h + a_1 e^{-Q_0/RT(r)}} \tag{38}$$

where a_1 is a constant determined by the boundary condition:

$$a_1 = \left(\frac{1}{\tilde{w}_0(0)} - h\right) e^{+Q_0/RT(0)} \tag{39}$$

For the "best" explicit approximation (Padé approximant) we have

$$Q \approx Q_0 \frac{1-h\tilde{w}_0/2}{1+h\tilde{w}_0/2} \tag{40}$$

The solution in this case is

$$\tilde{w}_0 = \frac{2}{h}\left[1 - \frac{2}{1+\sqrt{1+a_2 e^{Q_0/RT(r)}}}\right] \tag{41}$$

where a_2 is a constant given by:

$$a_2 = \frac{2h\tilde{w}_0(0) e^{-Q_0/RT(0)}}{\left[1-h\tilde{w}_0(0)/2\right]^2} \tag{42}$$

The exact solution of Eq. (33) for any $Q(\tilde{w}_0)$ can be written in terms of the exponential integral:

$$Ei(h\tilde{w}_0) = a_3 + Q_0 / RT \tag{43}$$

where

$$Ei(x) = -\int_{-x}^{\infty} \frac{e^{-t}}{t} dt \tag{44}$$

and

$$a_3 = Ei(h\, w_0(0)) - Q_0/(RT(0)) \tag{45}$$

The solutions presented in this section can be used as a basis for an algorithm for the computation of the oxygen redistribution in oxide fuels in fuel performance codes.

Sample Calculations

Let us for the sake of illustration evaluate the oxygen-to-metal ratio across fuel pellet, utilizing some of the approximations presented here. For this purpose we need the temperature distribution across pellet. The code STAV has been run for a given power history using the fuel rod data listed in Table 1. The fuel central temperature and the pellet surface temperature calculated at two different burnups are listed in the table below:

Rod burnup [MWd/kgU]	Power density [kW/m]	$T(0)$ [°C]	$T(r_{out})$ [°C]
20	21	921	459
40	16	739	422

The temperature data are fitted to a parabolic equation as a function of pellet radius:

$$T(r) = T(0) + (r/r_{out})^2 [\, T(r_{out}) - T(0)] \tag{46}$$

Equation (46) together with the data in the above table have been utilized to calculate the oxygen-to-metal ratio as a function of pellet radius for several approximations presented above. The shift in stoichiometry in LWR is assumed to be $\Delta(O/M) = 1.39 \times 10^{-4} / (\mathrm{MWd/kgU})$, [6]. The results are plotted in Figs. 7 and 8. It can be seen that the Padé

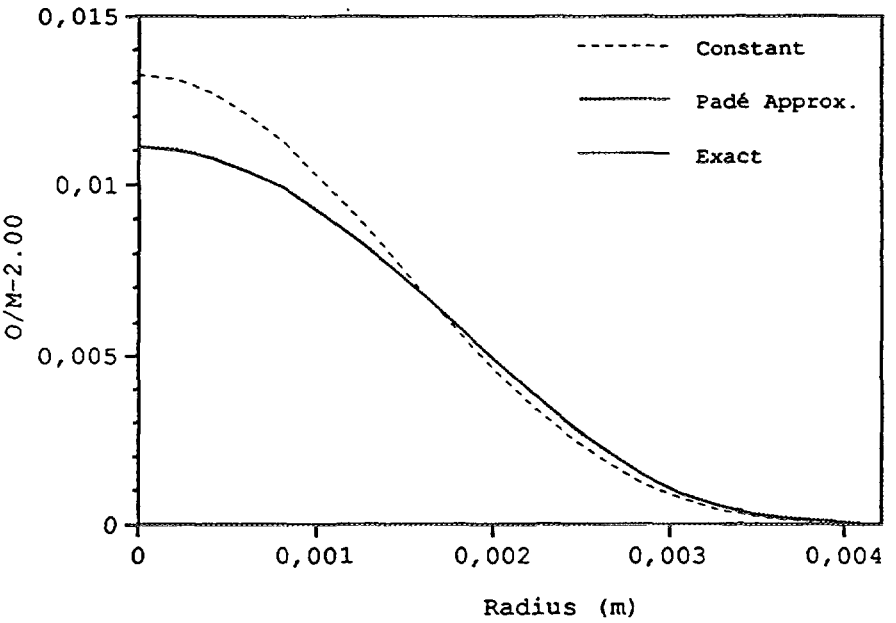

Figure 7 Deviation from stoichiometry for UO_2 fuel as a function of the pellet radius at 20 MWd/kg U for different solutions of the equilibrium Eq. (35). The Q approx. refers to the Padé approximant solution of Eq. (40). The results of the Padé approximant solution and the exact solution are indistinguishable.

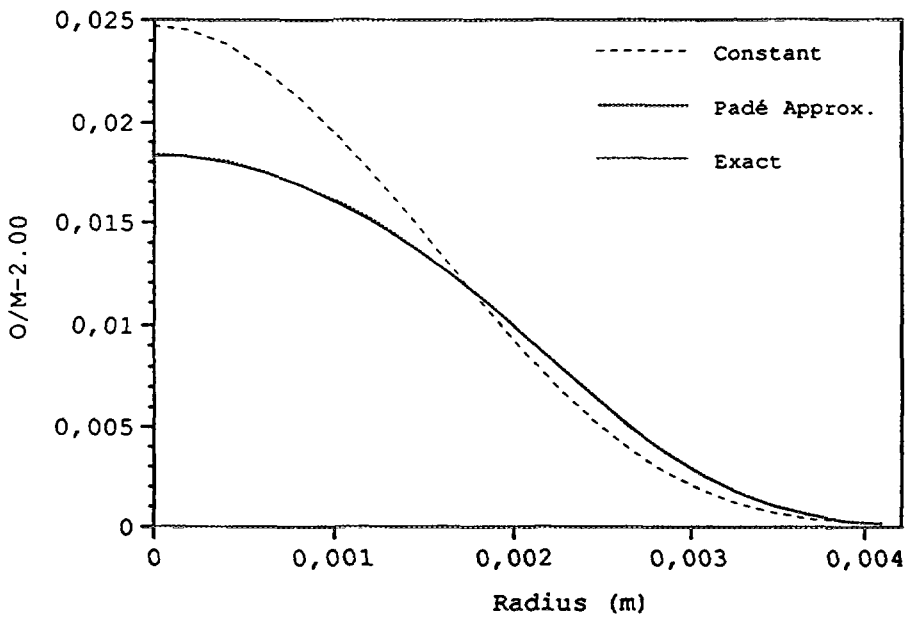

Figure 8 Deviation from stoichiometry for UO_2 fuel as a function of the pellet radius at 40 MWd/kg U for different solutions of Eq. (35). The Q approx. refers to the Padé approximant solution Eq. (40). The results of the Padé approximant solution and the exact solution are indistinguishable.

approximation is as good as the exact solution which is solved numerically.

3.2 Transient Condition

Equation (6) can be anlayzed using a perturbation technique. We can start by writing

$$w = \tilde{w}_0 + \sum_{i=1}^{\infty} \varepsilon^i w_i \tag{47}$$

where ε^i is a perturbation parameter assumed to be small ($\varepsilon^i < 1$) and in the quasi-static condition $\tilde{w}_0$ is assumed to be weakly time dependent.

Substituting (47) into (33) and considering the first term

$$\frac{\partial \tilde{w}_0}{\partial t} = -\frac{\partial w_1}{\partial t} + \frac{1}{r}\frac{\partial}{\partial r}\left[rD_w\left(\frac{\partial w_1}{\partial r} - w_1\tilde{g}\right)\right] \tag{48}$$

where

$$\tilde{g} \equiv \frac{[Q(\tilde{w}_0) + \tilde{w}_0 Q'(\tilde{w}_0)]}{\mathrm{R}} \cdot \frac{\partial(1/T)}{\partial t} \tag{49}$$

and utilizing the approximation: $Q(w) \approx Q(\tilde{w}_0) + \varepsilon w_1 Q'$.

Expanding w_1 in terms of orthogonal functions $\tilde{e}_k$

$$w_1(r,t) = \sum_{k=0}^{\infty} \alpha_k(t)\tilde{e}_k(r,t) \tag{50}$$

with

$$\frac{\partial \alpha_k(t)}{\partial t} = -\tilde{\lambda}_k(t)\alpha_k(t) - \tilde{\psi}_k(t) \tag{51}$$

and substituting in (48) we find

$$\frac{\partial \tilde{w}_0}{\partial t} - \sum_{k=0}^{\infty} \tilde{\psi}_k \tilde{e}_k = \sum_{k=0}^{\infty} \alpha_k \left\{\tilde{\lambda}_k \tilde{e}_k + \frac{1}{r}\frac{\partial}{\partial r}\left[rD\left(\frac{\partial \tilde{e}_k}{\partial r} - \tilde{e}_k\tilde{g}\right)\right]\right\} \tag{52}$$

If we equate the left-hand side to zero and the right-hand side termwise to zero we obtain

$$\tilde{\lambda}_k \tilde{e}_k r e^{-\mathscr{I}} = -\frac{\partial}{\partial r}\left(Dre^{-\mathscr{I}}\frac{\partial \tilde{e}_k}{\partial r}\right) + \tilde{e}_k e^{-\mathscr{I}}\frac{\partial(Dr\tilde{g})}{\partial r} \tag{53}$$

where

$$\mathscr{I} = \int \tilde{g} dr$$

Equation (53) can be simplified to

$$\tilde{\lambda}_k \tilde{f}_k r e^{\mathscr{A}} = \frac{\partial}{\partial r}\left(D r e^{\mathscr{A}} \frac{\partial \tilde{f}_k}{\partial r} \right) \tag{54}$$

where

$$\tilde{f}_k \equiv e^{-\mathscr{A}} \tilde{e}_k \tag{55}$$

The Neumann boundary condition in terms of $\tilde{f}_k$ is written as

$$\frac{\partial \tilde{f}_k}{\partial r} = 0 \qquad \text{at} \quad r = 0, \quad r = r_{out} \tag{56}$$

The eigenvalue problem described by Eqs. (55)-(56) has been solved numerically by discretizing Eq. (55) to an eigenvalue problem in terms of a tridiagonal matrix [20]. The first nonzero eigenvalue can be identified as the time constant, $\tilde{\lambda}_1 \sim 1/\tau$, for the approximate solution given by Lassmann [6]:

$$w(r,t) = \tilde{w}_0 + \left[w(r,0) - \tilde{w}_0 \right] e^{-(t-t_0)/\tau} \tag{57}$$

Using this method we have calculated the normalized time constant or its inverse $\left(\lambda r_{out}^2 / D_{av}\right)$ versus temperature (Figure 9) and versus $w(= O/M - 2)$ (Figure 10). The average diffusion coefficient is defined as $D_{av} = D_w(T_{av})$ where T_{av} is the harmonic average of the inner and outer temperatures, i.e., $1/T_{av} = \left(1/T(0) + 1/T(r_{out})\right)/2$.

4. Concluding Remarks

Analytical models presented in this report provide some detailed understanding for the complex processes that nuclear fuel endures during irradiation. These models also offer the theoretical bases for the computational tools used to predict fuel behaviour at high burnups. In this paper we only presented an overview and some applications of these models. The mathematical details for these models will be presented elsewhere.

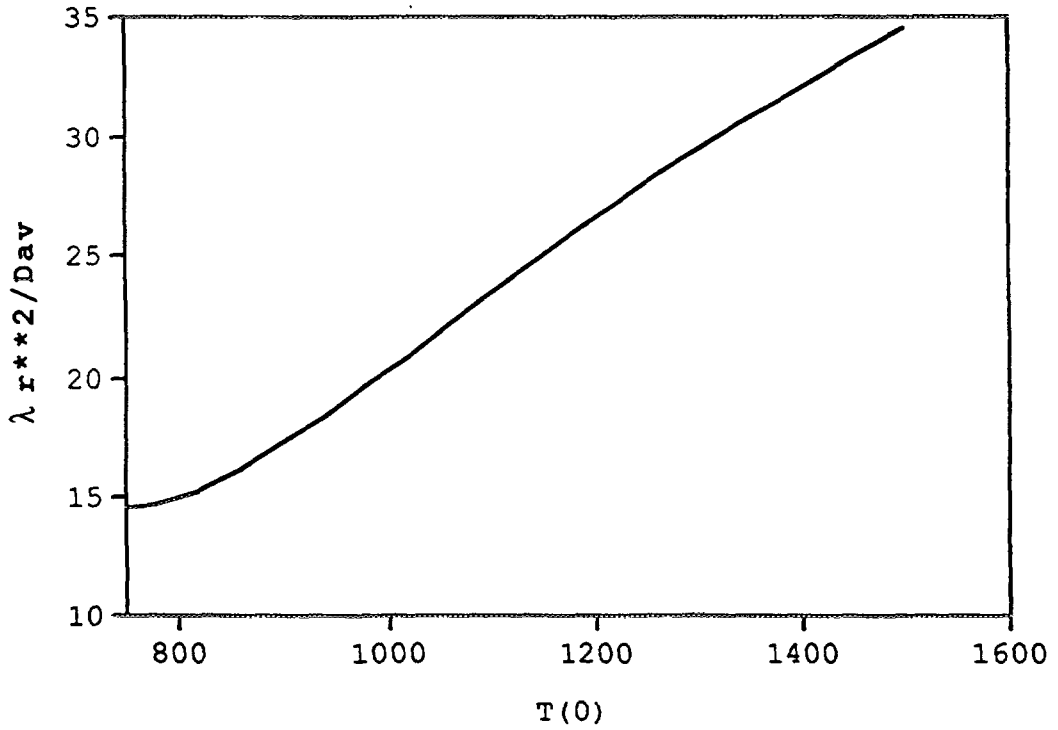

Figure 9 Inverse of the dimensionless time constant $\lambda^2 r_{out}^2 / D_{av}$ versus centerline temperature for constant surface temperature of 695 K.

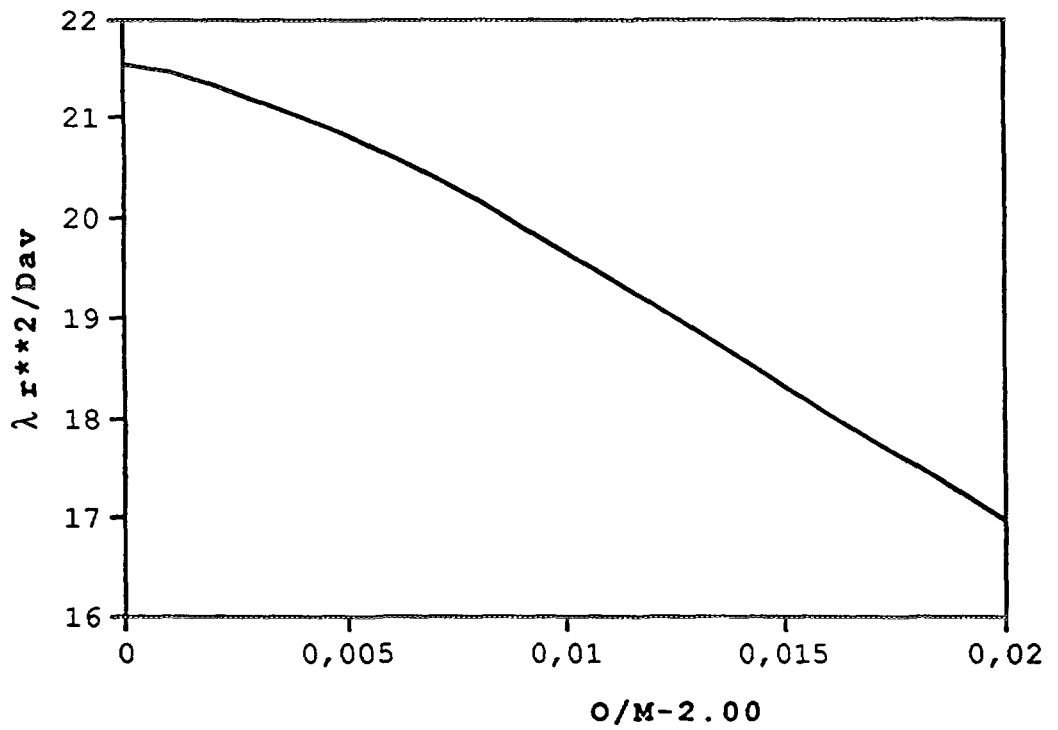

Figure 10 Inverse of the dimensionless time constant $\lambda^2 r_{out}^2 / D_{av}$ versus w $(= 0/M - 2.00)$ for a fixed centerline temperature of $T(0) = 1012$ K and average concentration $\tilde{w} = 0.0056$.

Acknowledgement:

We thank Gunnar Hedé for computations underlying the plots in Figure 6 of this report, and Anette Medin for the graphics.

References

[1] P. G. Lucuta, Hj. Matzke, R. A. Verall and H. A. Tasman J. Nucl. Mater., 188 (1992) 198-204.

[2] E. Kolstad and C. Vitanza, J. Nucl. Mater., 188 (1992) 104-112.

[3] M. E. Cunnigham, M. D. Freshley and D. D. Lanning, J. Nucl. Mater., 188 (1992) 19-27.

[4] Hj. Matzke, J. Nucl. Mater., 189 (1992) 141-148.

[5] D. Schrire and G. Lysell, International Topical Meeting on LWR Fuel Performance, Avignon-France, April 21-24, 1991.

[6] K. Lassmann, J. Nucl. Mater., 150 (1987) 10-16.

[7] A. M. Weinberg and E. P. Wigner, *The Physical Theory of Neutron Chain Reactors*, University of Chicago Press, 1958.

[8] K. Lassmann, C. O'Carroll, J. van der Laar and C. T. Walker, J. Nucl. Mater., 208 (1994) 223-231.

[9] D. L. Hagrman and G. A. Reymann, MATPRO-version 11, NURGER/CR-0497, 1979.

[10] R. A. Lorenz, ANS Topical Meeting on LWR Fuel Performance, Portland, Oregon, April 29 - May 3, 1979.

[11] R. Hargreaves and D. Collins, J. Br. Nucl. Energy Soc., 15 (1976) 311-318.

[12] M. V. Speight, Nucl. Sci. & Eng., 37 (1969) 180-185.

[13] K. Forsberg and A. R. Massih, J. Nucl. Mater., 135 (1985) 140-148.

[14] J. B. Ainscough, B. W. Oldfield and J. O. Ware, J. Nucl. Mater., 49 (1973/74) 117-128.

[15] R. J. White and M. O. Tucker, J. Nucl. Mater., 118 (1983) 1-38.

[16] W. H. Press, S. A. Teukolsky, W. T. Vetterling, B. P. Flannery, *Numerical Recipes in FORTRAN Second Edition*, Cambridge University Press, 1992.

[17] L. F. Shampine, ACM Trans. Math. Software, 8 (1982) 93-113.

[18] K. Forsberg, A. R. Massih and K. Andersson, Enlarged Halden Programme Group Meeting on Fuel Performance Experiments and Analysis, Sanderstolen, Norway, 2-7 March, 1986.

[19] V. M. El-Saied and D. R. Olander, J. Nucl. Mater., 207 (1993) 313-326.

[20] J. Stoer and R Bulirsch, *Introduction to Numerical Analysis*, Springer Verlag, New York, 1980.

Appendix Correlations for Re-solution Rate, Gas Diffusion Coefficient and Gas Production Rate in UO_2 Fuel

The resolution rate is given by

$B = 1.84\times10^{-14}$ [m/s]

The gas diffusion coefficient is expressed as

$$D = \begin{cases} 1.09\times10^{-17}\exp(-6614/T) & T > 1650\,K \\ 2.14\times10^{-13}\exp(-22884/T) & 1381 < T < 1650\,K \\ 1.51\times10^{-17}\exp(-9508/T) & T < 1381\,K \end{cases}$$

R_0 = The initial grain radius = 5 μm

β = Generation rate of fission gas atoms =

$$= 2.9\times10^{16}\left(2.606 + \frac{0.6386}{1 + 375E/W_R}\right)W_R, \text{ atom/m}^3\text{s}$$

where W_R is the rating (W/g) and E is the enrichment taken to be:

$E = 0.03$

W_R is assumed to be dependent on the temperature in accordance to the table below.

For the computation of N_s we have used:

a = The average bubble radius = 0.5 μm
γ = Bubble surface tension = 0.6 J/m^2
2θ = The angle where two free surfaces meet at a grain boundary = 100°
f_b = Fractional coverage of grain boundaries at saturation = 0.25

Thus the density of the intergranular gas at saturation is

$$N_s = 1.382\times10^{-2}\frac{1}{T}\ \left(\text{mole/m}^2\right)$$

Numerical Values for Power Density and Gas Production Rate

Temperature (°C)	Rating (W/g)	Production rate (mole/m^3 s)
1000	29.8	4.4×10^{-6}
1100	34.1	5.1×10^{-6}
1200	38.3	5.7×10^{-6}
1300	42.4	6.4×10^{-6}
1400	46.6	7.2×10^{-6}
1500	50.8	7.7×10^{-6}
1600	55.0	8.3×10^{-6}

COMPARISON OF THE ENIGMA CODE WITH EXPERIMENTAL DATA ON THERMAL PERFORMANCE, STABLE FISSION GAS AND IODINE RELEASE AT HIGH BURNUP

J.C. KILLEEN
Nuclear Electric plc,
Barnwood, United Kingdom

Abstract

The predictions of the ENIGMA code have been compared with data from high burn-up fuel experiments from the Halden and RISO reactors. The experiments modelled were IFA-504 and IFA-558 from Halden and the test II-5 from the RISO power bump test series. The code has well modelled the fuel thermal performance and has provided a good measure of iodine release from pre-interlinked fuel. After interlinkage the iodine predictions remain a good fit for one experiment, but there is significant overprediction for a second experiment (IFA-558). Stable fission gas release is also well modelled and the predictions are within the expected uncertainty band throughout the burn-up range. This report presents code predictions for stable fission gas release to 40GWd/tU, iodine release measurements to 50GWd/tU and thermal performance (fuel centre temperature) to 55GWd/tU. Fuel ratings of up to 38kW/m were were modelled at the high burn-up levels. The code is shown to accurately or conservatively predict all these parameters.

1. INTRODUCTION

The fuel performance code ENIGMA, version 5.2, is used for PWR applications in the United Kingdom. The present paper presents code predictions against high burn-up data for thermal performance, fission gas and iodine release. The version of the code used here has a new transient iodine release model, and the iodine release predictions presented here are the equilibrium values from the new model.

2. DATA BASE

The data base used in this code comparison exercise contains three experiments, each of which comprises thermocoupled fuel assemblies. Two of these experiments are from the Halden HBWR, (IFA-504 and IFA-558) and the third experiment is a ramp test on refabricated fuel tested in the RISO reactor (II-5).

The iodine release relies on recent data from the Halden HBWR gas flow rigs, IFA-504 and IFA-558.

2.1 IFA-504.

IFA 504 is a gas flow rig with a high level of instrumentation. The rig consists of 4 rods, each with two centre thermocouples and two pressure transducers. All the rods had 100μm initial radial gaps, but differed in terms of the fuel pellet characteristics as follows:

Rod 1: 6μm grain size, solid, dished pellets.
Rod 2: Large grain size, solid, flat ended pellets.
Rod 3: 0.35%Nb doped 26μm grain size, solid, dished pellets.
Rod 4: 6μm grain size, hollow, dished pellets.

Fuel temperatures were measured as functions of local power during start-up ramps with fill gases of helium, argon and xenon. In addition temperatures (normalised to 20kW/m) are available throughout life with the rods filled with helium, and at different times with the rods filled with argon.

The present data uses measurements made on IFA 504 to a burn-up of 55GWd/tU.

2.2 IFA-558

IFA 558 was a UK sponsored assembly comprising 6 geometrically identical rods equipped with gas flow lines, pressure transducers and fuel centre thermocouples. The difference between the rods lay in the operational helium filling pressure. Rods 1 and 2 were held at 40 bar pressure, rods 3 and 4 at 2 bar pressure and rods 5 and 6 at 20 bar. The rods used BNFL fuel.

The present data uses measurements to just over 40GWd/tU. In the later stages of the irradiation, the pressure conditions within the rods were relaxed, and the thermal data reported here have been normalised to 30kW/m and 1.8 bar pressure.

2.3 RISO III Project

This report considers one experiment from the RISO series of power bump tests on refabricated fuel rodlets. The test, II-5, was carried out on fuel that had been pre-irradiated to a burn-up of 52.5GWd/tU in IFA 161 at Halden. Details of the RISO tests can be found in Ref [1].

3. RESULTS

3.1 THERMAL BEHAVIOUR

3.1.1 IFA-504

Figure 1 shows the ENIGMA 5.2 predictions for the four rods of the IFA-504 gas flow experiment. The predictions have been made for a linear heat rating of 20kW/m throughout life and the measured data points have been extracted from the experimental data base.

The Figure shows that the code correctly represents the gradual rise in fuel centre temperature with burn-up, with an overall rise of approximately 150°C at 50GWd/tU.

There is considerable scatter within the data measurements, which is best noted for rod 4, where both rod thermocouples have survived to 50GWd/tU. These two thermocouples can vary by as much as 90°C (at 35GWd/tU) and provide a severe test of the code, which is only making a single prediction for the rod. It is considered therefore, that the predictions, which typically lie within the scatter band of the data, are an excellent representation of the data throughout the life of the experiment.

3.1.2 IFA-558

Figure 2 shows the thermal behaviour of five of the IFA-558 rods throughout life to just over 40GWd/tU. There are no data for rod 4, where both rod thermocouples failed at start of life. The data in these figures have been normalised to a linear power of 30kW/m. The design of IFA-558 was similar to IFA-504, but this gas flow rig was run with a simpler gas exchange history. The result is that there is less scatter in the measurements, and the two thermocouples in a rod are typically measuring temperatures less than 30°C apart. However, this scatter will still provide a limit to the accuracy that can be expected from the code predictions, which only give a single prediction for each rod. Where the two thermocouples give consistently differing temperatures throughout life (e.g. rod 5) there may well be systematic differences in history between the two ends of the rod that are not modelled in the present case.

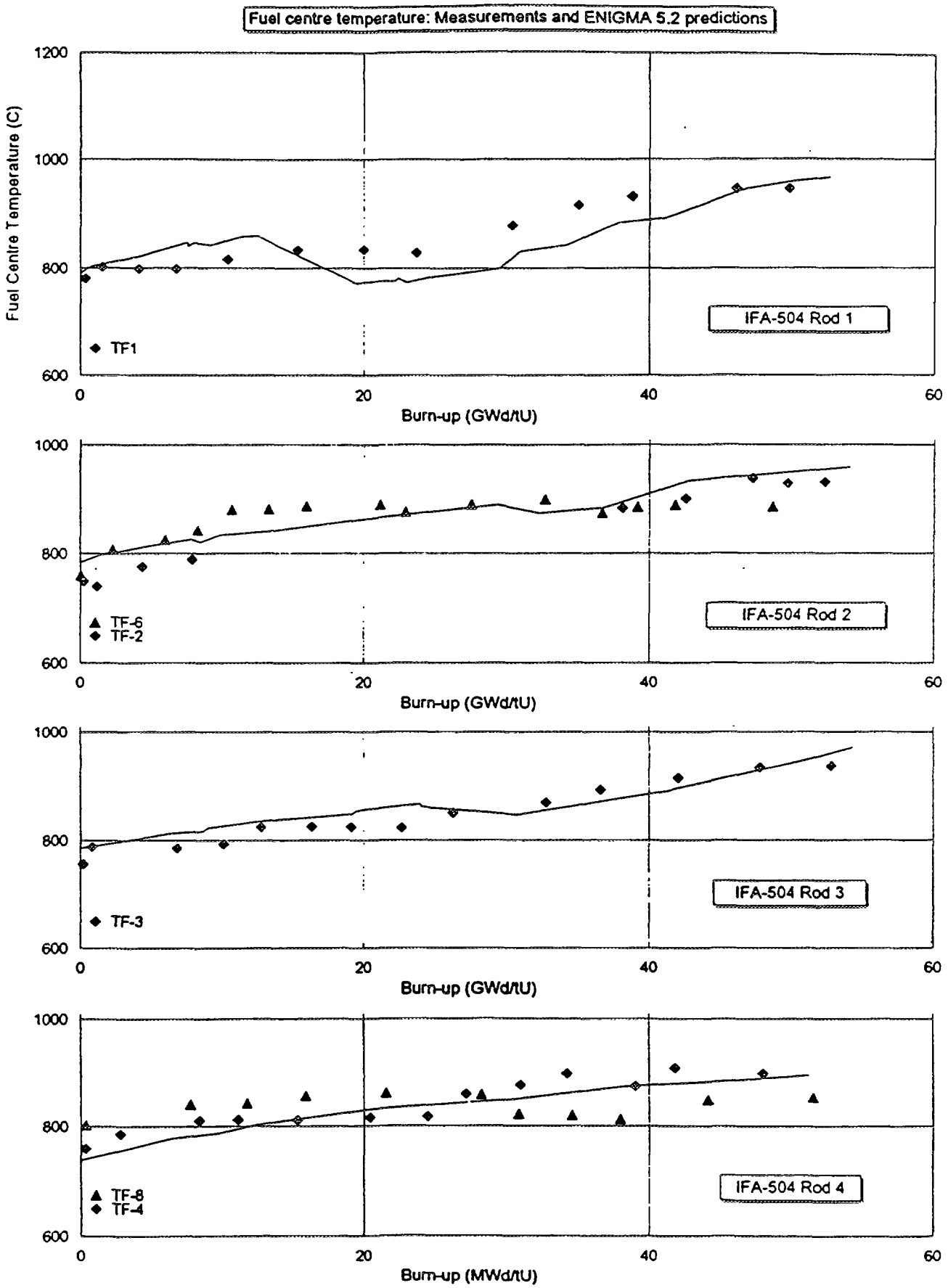

FIG. 1. *ENIGMA 5.2: Predictions of fuel centre temperature for IFA-504 throughout life normalised to 20kW/m.*

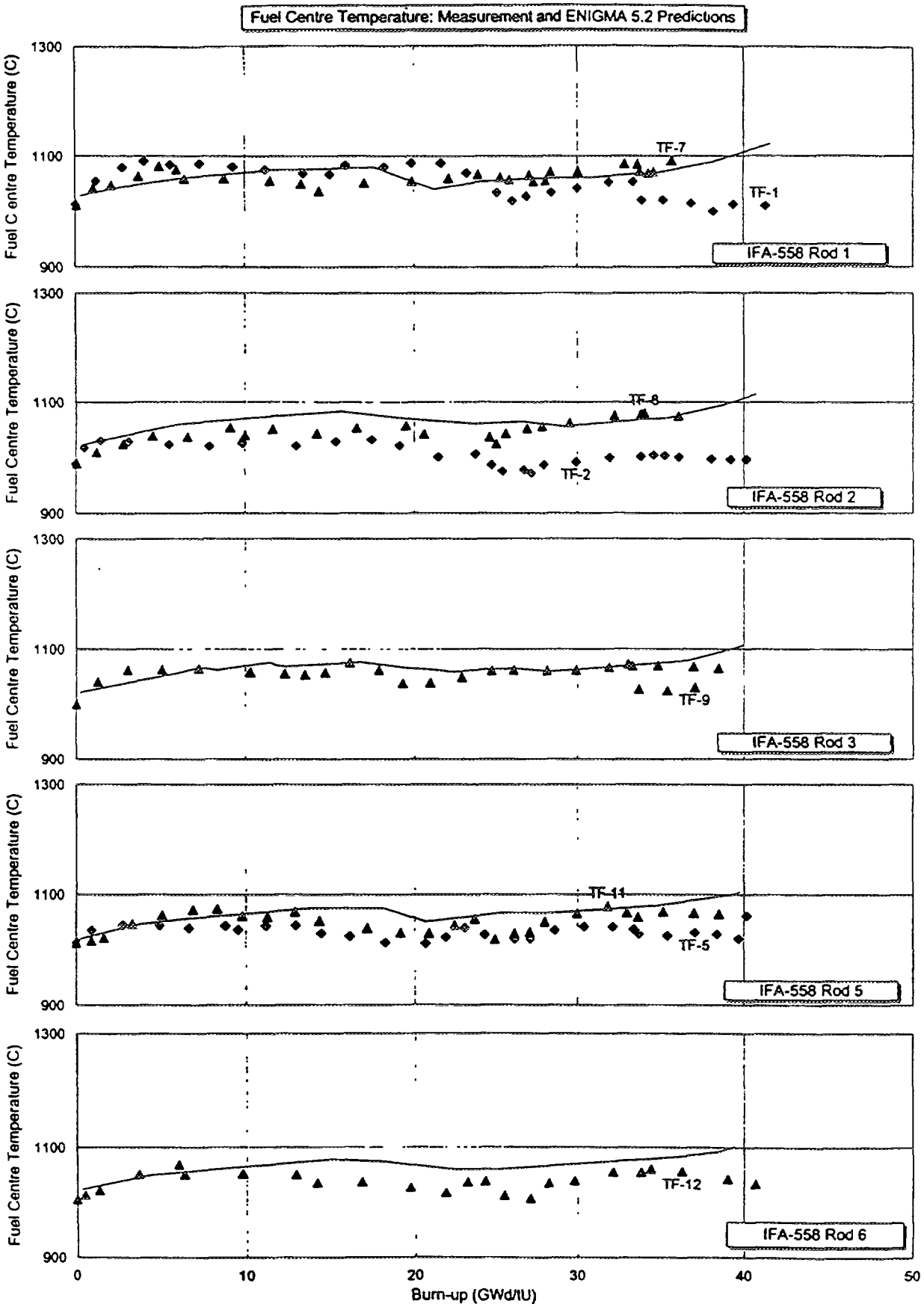

FIG. 2. *ENIGMA 5.2: Predictions of fuel centre temperature for IFA-558 throughout life normalised to 30kW/m.*

There is one further feature of the measurements that is worthy of note. In rods 1 and 2, where both thermocouples have survived throughout life, there has been a change in the measurements at around 25GWd/tU. At this burn up the measurement from the lower numbered thermocouple (at the bottom of each rod) has dropped relative to the higher numbered thermocouple. This change is not noticeable in rod 5, and the bottom thermocouples are not available for the other rods. It is known that such a shift could arise from failure of a single neutron detector in the assembly which would provide inaccurate power measurements in a restricted region of the assembly and hence the derived constant power centre temperatures would also be in error.

Figure 2 also gives the ENIGMA 5.2 predictions of the fuel centre temperature at 30kW/m. It can be seen that the code gives an excellent prediction of the data, with the exception of the lower numbered thermocouples from rods 1 and 2 at high burn-up (discussed in the previous paragraph) and slight over-prediction of rod 6 by typically 25°C, which is still within the scatter band discussed earlier.

The ENIGMA 5.2 code allows for the input file to split the total fuel porosity into three components, each of which is treated separately within the code. The first is fine porosity which is considered capable of sintering. The second component is reserved for large diameter porosity, $> 1\mu m$, which can also sinter. The third component is for artificially large porosity introduced during manufacture. The first two components of porosity have an identical effect on the fuel thermal conductivity with respect to their volume fraction, with the conductivity proportional to a factor of $(1\text{-porosity})^{2.5}$. The same is not true of large porosity which is assumed to have a smaller effect of volume fraction on fuel thermal conductivity with a correction factor of $(1\text{-porosity})^{1.0}$.

The present understanding of the effect of porosity is that the 2.5 exponent is apropriate to all porosity therefore in the present analysis all the porosity was assumed to lie in the 'sinterable' components. It is clear that this treatment, where the thermal effect of porosity is considered in a consistent manner, provides an excellent fit to the data.

3.1.1 RISO Ramp Test

The RISO II-5 bump-test measurements are shown in Figure 3. The ENIGMA 5.2 predictions have been performed using the two options within the code for gas mixing in the fuel-cladding gap. Figure 3 shows the code predictions for instantaneous gas mixing, whilst Fig. 12 shows the code response to slower gas mixing as the rod power was cycled. The code over-predicts the measured temperatures by around 100°C at the highest rating (38kW/m) in the experiment, with the instantaneous gas mixing model providing a closer fit to the data.

3.2 IODINE RELEASE.

3.2.1 IFA-504

Figure 4 shows the comparison between the ENIGMA 5.2 predictions for iodine release and the measurements made on the four rods of IFA-504. The code predictions have been made for the same power conditions as pertained during the experimental measurements and as the experimental measurements were designed to measure the equilibrium iodine release it is the equilibrium code predictions presented here. There is good agreement between the measurements and predictions, with a small tendency for the code to overpredict.

Figure 5 shows the comparison between the ENIGMA 5.2 predictions for iodine release and the measurements made on the six rods of IFA-558. The code predictions have been made for the same power conditions as pertained during the experimental measurements. In all cases the code significantly overpredicts the iodine release following interlinkage at around 20GWd/tU, and the tendency for

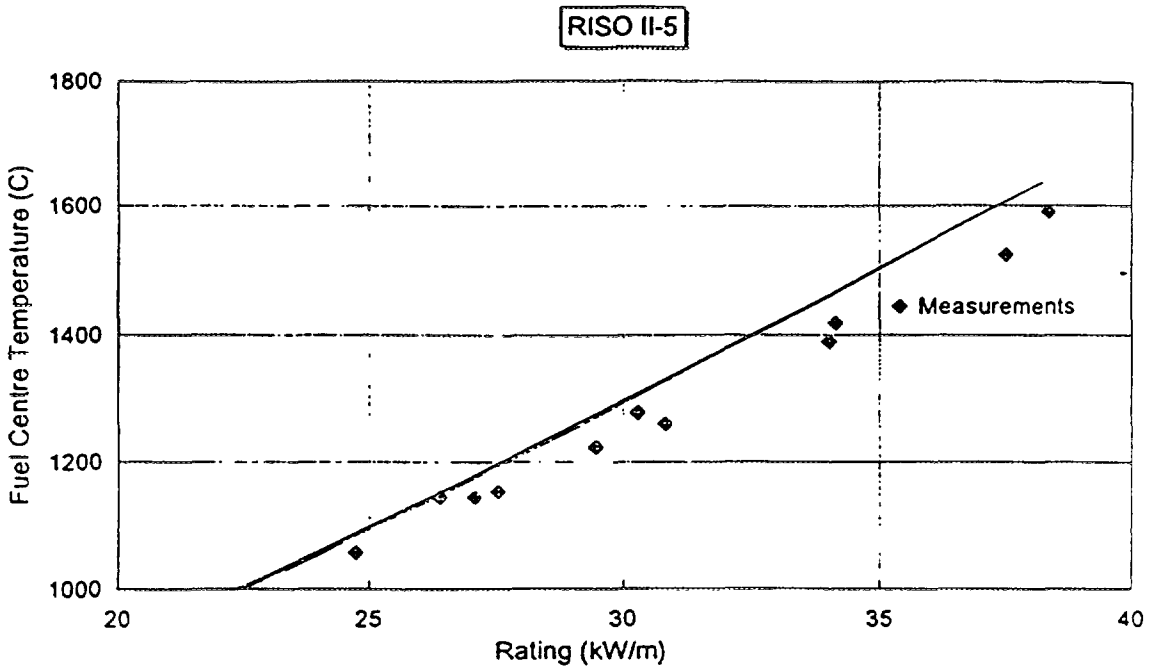

FIG. 3(a). *ENIGMA 5.2: Predictions of fuel centre temperature for RISO II-5. Instantaneous gas mixing model.*

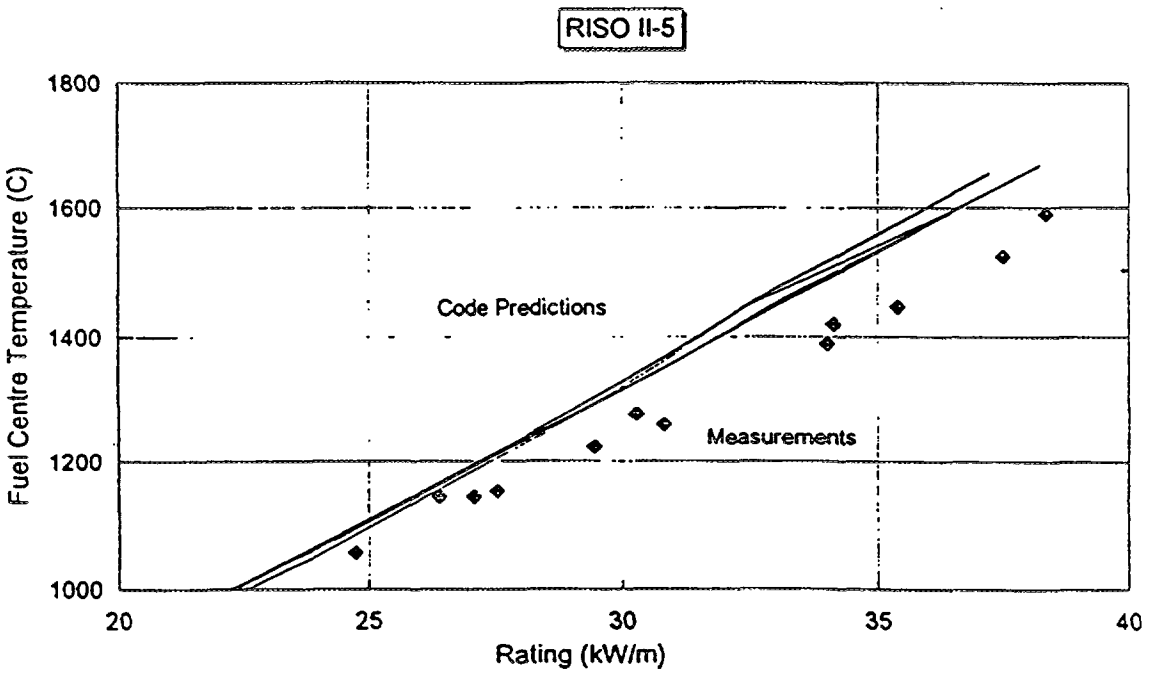

FIG. 3(b). *ENIGMA 5.2: Predictions of fuel centre temperature for RISO II-5. Slow gas mixing model.*

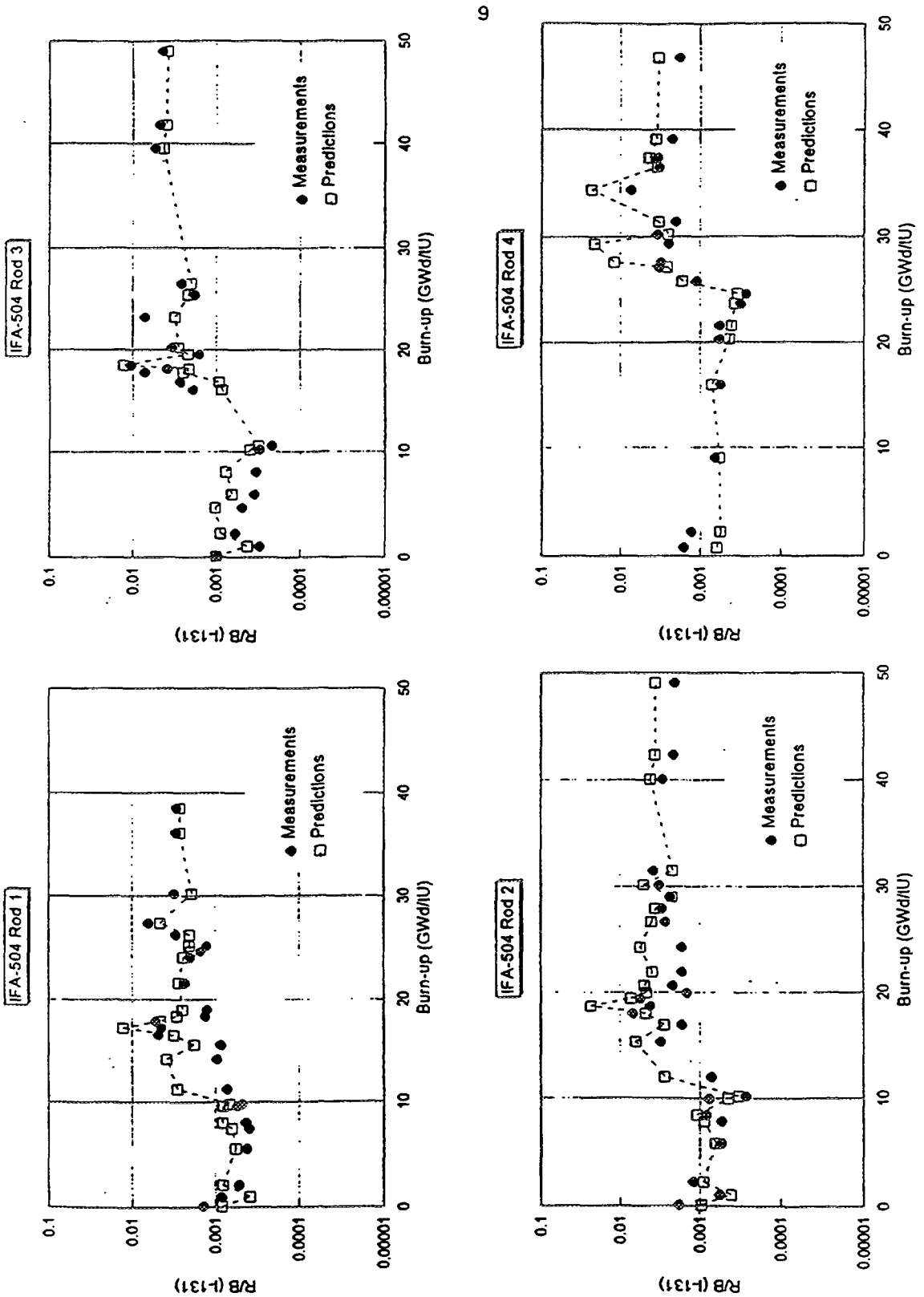

FIG. 4. *ENIGMA 5.2: Predictions of iodine release for IFA-504. The predictions have been made for equilibrium release at the rod power when the experimental measurement was made.*

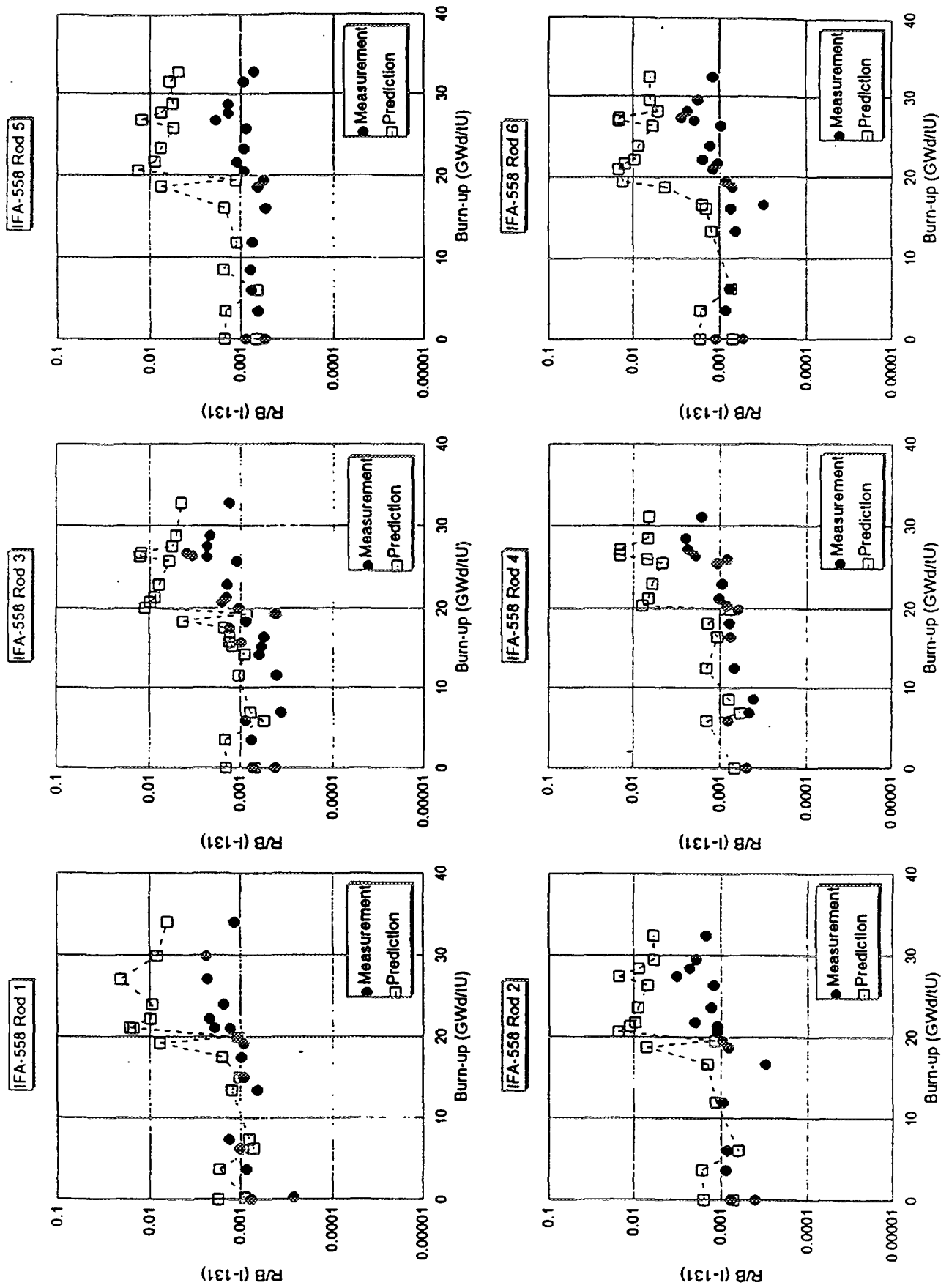

FIG. 5. *ENIGMA 5.2: Predictions of iodine release for IFA-558. The predictions have been made for equilibrium release at the rod power when the experimental measurement was made.*

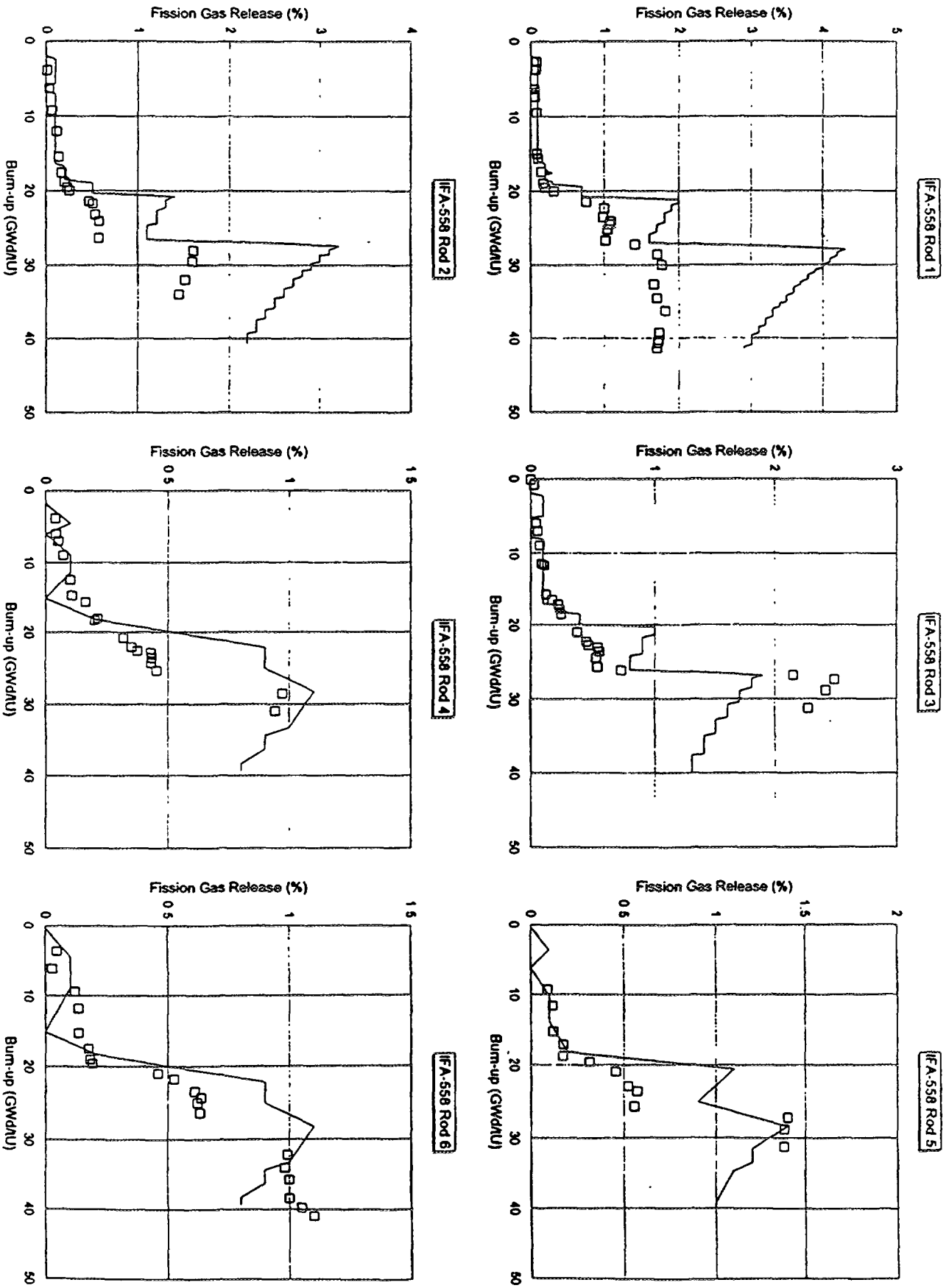

FIG. 6. *ENIGMA 5.2: Predictions of stable gas release for IFA-558. Experimental measurements are also shown.*

overprediction at lower burn-up is much more marked than for the IFA-504 data. The high burn-up overprediction is typically just under an order of magnitude (x7).

3.3 STABLE FISSION GAS RELEASE FROM IFA-558

Throughout the operation of IFA-558 attempts were made to collect all the krypton-85 that was released from the six rods. These measurements can be used to provide a data set to test the stable gas predictions of the ENIGMA 5.2 code. Figure 6 gives the comparison between the measurements and the code predictions for each of the six rods.

The figure shows that ENIGMA 5.2 tends to overpredict the release of stable gas during the period of interlinkage, typically at around 20-25GWd/tU in these tests. At the higher burn-up towards the end-of-life, the code predictions are in good agreement with the data and are always within a scatter band of $\times/\div 2$, which is within the uncertainty band of power, rod parameters and fuel thermal conductivity.

4. DISCUSSION

The thermal performance of the high burn-up experiments considered have been well predicted by the ENIGMA 5.2 code. The predictive capability is within the scatter of the data, and the long term trends in fuel centre temperature are well modelled.

The only areas of uncertainty were in the prediction of the ramp behaviour of the RISO II-5 test where the code over-predicted the temperatures, and the high numbered thermocouples in rods 1 and 2 of IFA-558 where there is a suspicion that the data might be in error, particularly in the light of the measurements from other thermocouples in the same rods which are well modelled.

The iodine predictions for the IFA-558 measurements at high burn-up show considerable overprediction following interlinkage at around 20GWd/tU. The comparison with the IFA-504 rod 4 measurements are interesting as this rod was hollow, as are the IFA-558 rods. The code predictions for IFA-504 rod 4, which are similar to the IFA-558 predictions, are by contrast a good fit to the data both before and after interlinkage.

The stable gas release measurements show a similar picture of overprediction at interlinkage for IFA-558, but the code predictions are always within a factor of two of the data.

The low release of iodine from the IFA-558 rods is mirrored by other fission gas release data from this assembly, where the increase in release rate of the short lived isotopes on interlinkage was much less than for the equivalent IFA-504 experience. The difference may well lie in the fuel type, as IFA-504 used a variety of special fuels, whilst IFA-558 used modern BNFL controlled porosity fuel. The more modern fuel has benefited from significant improvements in sinterability over older fuel types. It is suggested that there is more sintering of this fuel following interlinkage and hence a reduced surface area for the release of short lived fission products. A second possibility lies in the higher powers experienced by IFA-558, where there is some evidence that the measurements might be affected by retention in the fuel-clad gap.

It is worth noting that the code is conservative where the differences between the predictions and measurement are significant, in particular for the post-interlinkage iodine releases from IFA-558 and the temperature predictions for the RISO bump test.

5. CONCLUSIONS

The predictions of the code ENIGMA 5.2 have been compared with data from high burn-up fuel experiments to extend the range of validation.

The code has well modelled the fuel thermal performance and has provided a good measure of iodine release from pre-interlinked fuel. After interlinkage, the iodine predictions remain a good fit to the data for one experiment, but significantly overpredict the release for IFA-558. This shows that the release of short lived iodine and fission gas is likely to be conservatively estimated by ENIGMA 5.2.

This report provides a comparison of fuel centreline temperatures and radioactive fission product release and demonstrates that ENIGMA 5.2 gives good agreement for these parameters up to 50GWd/tU and in the case of fuel temperatures to a rating of 38kW/m at this burn-up.

This report demonstrates that the ENIGMA 5.2 code accurately predicts or conservatively predicts fuel temperatures and radioactive fission product release up to a burn-up of 50GWd/tU and stable fission gas release to 40GWd/tU. The code can therefore be considered to be highly suitable for use up to these burn-ups.

REFERENCES

[1] BAGGER C., MOGENSEN M., AND WALKER C T., Temperature measurements in high burn-up fuel: Implications for thermal conductivity, grain growth and gas release. J. Nucl. Mater. 211 (1994) 11-29.

MOX FUEL IRRADIATION BEHAVIOUR IN STEADY STATE (IRRADIATION TEST IN HBWR)

S. KOHNO, K. KAMIMURA
Power Reactor and Nuclear Fuel
Development Corporation,
Naka-gun, Ibaraki-ken,
Japan

Abstract

Two rigs of plutonium-uranium mixed oxide(MOX) fuel rods have been irradiated in Halden boiling water reactor (HBWR) to investigate high burnup MOX fuel behavior for thermal reactor. The objective of irradiation tests is to investigate fuel behavior as influenced by pellet shape, pellet surface treatment, pellet-cladding gap size and MOX fuel powder preparation process. The two rigs have instrumentations for in-pile measurements of the fuel center-line temperature, plenum pressure, cladding elongation and fuel stack length change. The data, taken through in-operation instrumentation, have been analysed and compared with those from post-irradiation examination. The following observations are made: 1) PNC MOX fuels have achieved high burn-up as 59GWd/tMOX (67GWd/tM) at pellet peak without failure; 2) there was no significant difference in fission gas release fraction between PNC MOX fuels and UO_2 fuels; 3) fission gas release from the co-converted fuel was lower than that from the mechanically blended fuel; 4) gap conductance was evaluated to decrease gradually with burn-up and to get stable in high burn-up region. 5) no evident difference of onset LHR for PCMI in experimental parameters (pellet shape and pellet-cladding gap size) was observed, but it decreased with burn-up.

1. INTRODUCTION

The Power Reactor and Nuclear Fuel Development Corporation (PNC) has been developing plutonium-uranium mixed oxide (MOX) fuel for fast breeder reactor (FBR), light water reactor (LWR) and the advanced thermal reactor (ATR). [1]

The purpose of this paper is to present the thermal and mechanical behaviour of MOX fuel for thermal reactors obtained by both in-pile and as part of post irradiation examination (PIE). The analysis deals with the internal pressure, fission gas release, fuel temperature and PCMI behaviour on each experimental parameters (pellet shape, pellet surface treatment, pellet-cladding gap size and MOX fuel powder preparation method).

Two instrumented irradiation rigs in HBWR were occupied for the experiments.

One is named IFA-514 of which the irradiation started since July, 1979 and ended in November, 1988, having achieved the maximum burn-up of 49 GWd/tMOX(56GWd/tM) at pellet peak without failure. PIE had been carried out in Kjeller Laboratory until 1990. Three of six rods in IFA-514 rig have continued to be irradiated as a new rig(IFA-565). The irradiation started in November 1990 and ended in October 1993. The maximum burn-up was 59GWd/tMOX(67GWd/tM) at pellet peak. PIE is now carried out in Kjeller Laboratory.

The other is named IFA-529 of which the irradiation was performed from July 1980 to October 1986 having achieved the maximum burn-up of 33GWd/tMOX(38GWd/tM) at pellet peak. PIE had been carried out also in Kjeller Laboratory until February,1988.

The experimental parameters are pellet shape (hollow/solid) and pellet surface treatment (ground/as-sintered) for IFA-514/565 experiment, and pellet-cladding gap size and MOX fuel powder preparation method, i.e., direct co-conversion from mixed plutonium-uranium nitrate solution with microwave heating (MH Method) [2] and mechanically powder blending for IFA-529 experiment.

The experiments of IFA-514/565 and 529 are carried out as a part of joint research program between PNC and Japan Atomic Energy Research Institute (JAERI) with the participation in the OECD Halden Reactor Project.

2. FUEL DESIGNS AND IRRADIATION CONDITIONS

2.1 DESIGN OF RIG

IFA-514/565

A simplified configuration of instrumentation and experimented parameters is shown in Figure 1. The fuel rods have the same fuel stack length of 1380mm.

After non destructive post irradiation examination for six fuel rods of IFA514 were performed, three of them were reassembled to IFA-565. The design of the clusters is similar to that of IFA-514.

IFA-529

IFA-529 fuel assembly consists of two clusters which have six short MOX fuel rods respectively. All twelve rods are equipped with instruments in either or both ends. The pellet-cladding diametral gap size and MOX pellet fabrication process are experimental parameters. The configuration of instrumentation and experimental parameters is shown in Figure 2. The fuel stack length is about 550mm.

2.2 FUEL ROD SPECIFICATION

IFA-514/565

The fabrication data of IFA-514/565 fuel rods are given in Table 1. The six fuel rods have the same cladding dimensions as those of BWR 8 x 8 fuel assembly. The fuel pellets are sintered of 5.8%PuO_2-Nat.UO_2 mechanically blended powder, 94% theoretical density, chamfered, and 10mm long. Pellet-cladding diametral gap size is in the range of 220mm to 260mm.

IFA-529

The fabrication data of IFA-529 fuel rods are given in Table 1. The pellets are enriched to 8.3%PuO_2-Nat.UO_2 and have 94% theoretical density. Pellet-cladding diametral gap size is in the range of 160mm to 340mm. The difference of MOX pellet fabrication process is shown in Figure 3.

2.3 IRRADIATION CONDITIONS

IFA-514/565

IFA-514 was irradiated for about 9.3 years. The six rods in IFA-514 experienced almost same linear heat rating(LHR) except the rods loaded with hollow pellets. The maximum LHR of the rods loaded with solid pellets was 5 lKW/m. The mean LHR averaged for burn-up was 24KW/m. The pellet peak burn-up was nearly 49GWd/tMOX(56GWd/tM).

IFA-565 was irradiated for about 12.2 years. The mean LHR averaged for burnup was 23KW/m. The pellet peak burn-up was nearly 59GWd/tMOX(67GWd/tM).

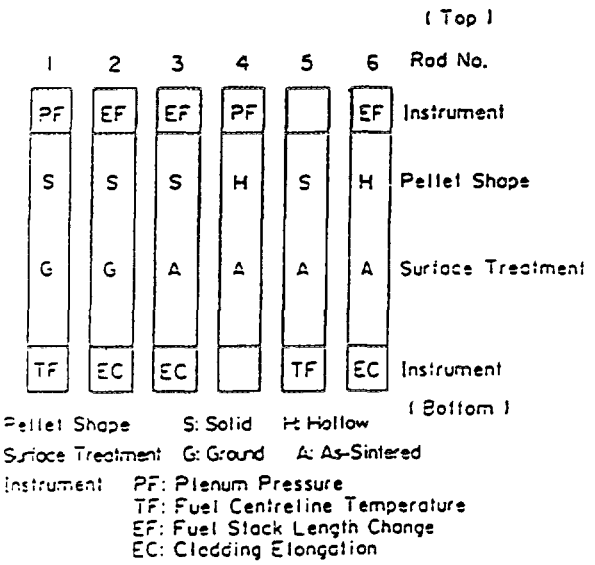

FIG. 1. *Simplified configuration of instrumentation and experimental parameters in IFA-514 (IFA-565 consists of rod nos. 3,4 and 6).*

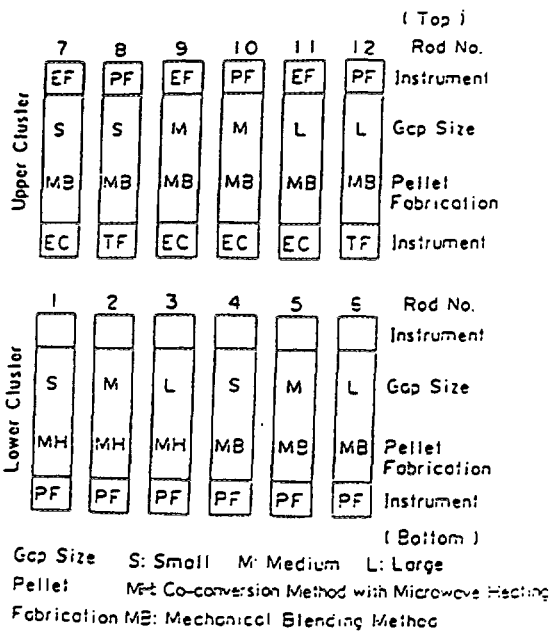

FIG. 2. *Simplified configuration of instrumentation and experimental parameters in IFA-529.*

TABLE 1. SPECIFICATION DATA OF IFA-514/565 AND IBA-529

	IFA-514/565	IFA－529
Pellet		
Fabrication Method	MB＊1	MH＊2／MB
Shape	Solid／Hollow	Solid
Surface Treatment	Ground／As＊3	As
Outer Diameter (㎜)	10.56	10.47～10.64
Inner Diameter (㎜)	3.5＊4	－
Density (%T.D.)	94	94
PuO_2 Concentration (wt%)	5.8	8.3
U－235 Enrich (wt%)	Nat.U	Nat.U
Cladding		
Material	Zry－2	Zry－2
Outer Diameter (㎜)	12.53	12.53
Inner Diameter (㎜)	10.80	10.80
Fuel Rod		
Fuel Stack Length (㎜)	1380	550
Pellet－Clad Gap (㎛ Dia)	220～250	160～340
Filling Gas	He	He
Filling Pressure	1 atm	1 atm
Assembly		
Number of Fuel Rods	6	12 (Upper Cluster 6, Lower Cluster 5)

＊1 Mechanical Blending Method

＊2 Co－conversion Method with Microwave Heating

＊3 As－Sintered Pellet

＊4 only for Hollow Pellet

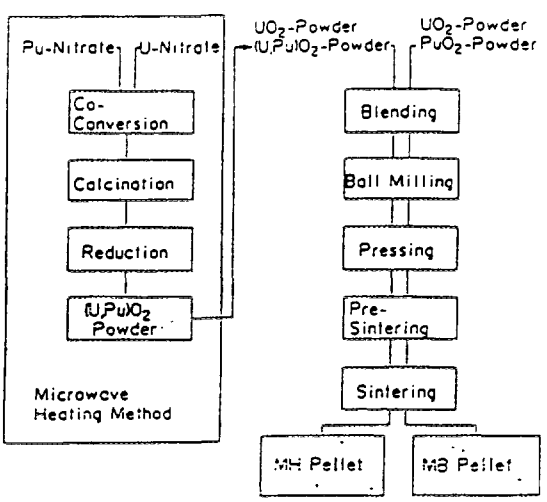

FIG. 3. *Flow chart of MOX fuel manufacturing process.*

IFA-529

IFA-529 was irradiated for about 6.3 years. The maximum LHR was 50KW/m. The pellet peak burn-up of lower cluster was nearly 31 GWd/tMOX(35GWd/tM).

The irradiation conditions of two rigs are summarized in Table 2.

3. EXPERIMENTAL RESULTS AND DISCUSSIONS

3.1 TYPICAL PIE RESULTS OF IFA-514/565 AND IFA-529

The PIE results of non-destructive test for IFA-565 rod No.3,4,6 are summarized in Table 3. It can be seen in Table 3 that PNC MOX fuels have achieved high burn-up of 59GWd/tMOX at pellet peak without failure.

Fig. 4 shows the alpha auto-radiograph pictures of irradiated IFA-514 and IFA529. Comparing PIE results of IFA-514 and IFA-529, it is seen that the alpha intensity near the rim of pellet for high irradiated IFA-514 is higher than IFA-529 pellet. It might be caused by Rim Effect. We plan to analyse the Rim Effect in detail by following PIE of IFA-565.

TABLE 2. IRRADIATION DATA OF IFA-514/565 AND 529

		MAX.Pellet Peak LHR (KW/m)	Ave. LHR (Rod_Ave.) (KW/m)	Pellet Peak Burn-up (GWd/tMOX)	Average Burn-up (GWd/tMOX)	Irradiation*1 Time (Year)
IFA-514/565	Sollid Pellet Rod	51	24 (23)	49 (58)	40 (49)	9.3 (12.2)
	Hollow Pellet Rod	48	21 (21)	48 (59)	39 (50)	9.3 (12.2)
IFA-529	Upper Cluster	50	22	33	25	6.3
	Lower Cluster	50	24	31	28	6.3

*1 Irradiation time is definded by the time that the rig is in the reactor.
*2 ( ) including IFA-565 as of October1993.

TABLE 3. PIE RESULTS OF IFA-565 ROD NO. 3/4/6

Visual Examination	The pellet/pellet interfaces were visible. No other characteristic effects were observed.
Dimensional Measurements	The maximum increase of diameter : 75-125μm. The maximum bow of the rod : 0.2-1mm.
Eddy Current Testing	Two major eddy current bulges could be seen at the contact areas of the spacer/canning due to a oxide layer (30- 60μm) No other characterisuc effects were observed
Gamma Scanning	The regular activity drop corresponding to the pellet/pellet gap could be clearly seen.
Neutron Radiography	Fuel pellets : Remarkable crack, break off of pellet and disorder of fuel stack were not observed. Inter-pellet gap : The gap for each rod was below about 25μm. Canning : Nothing to be seen

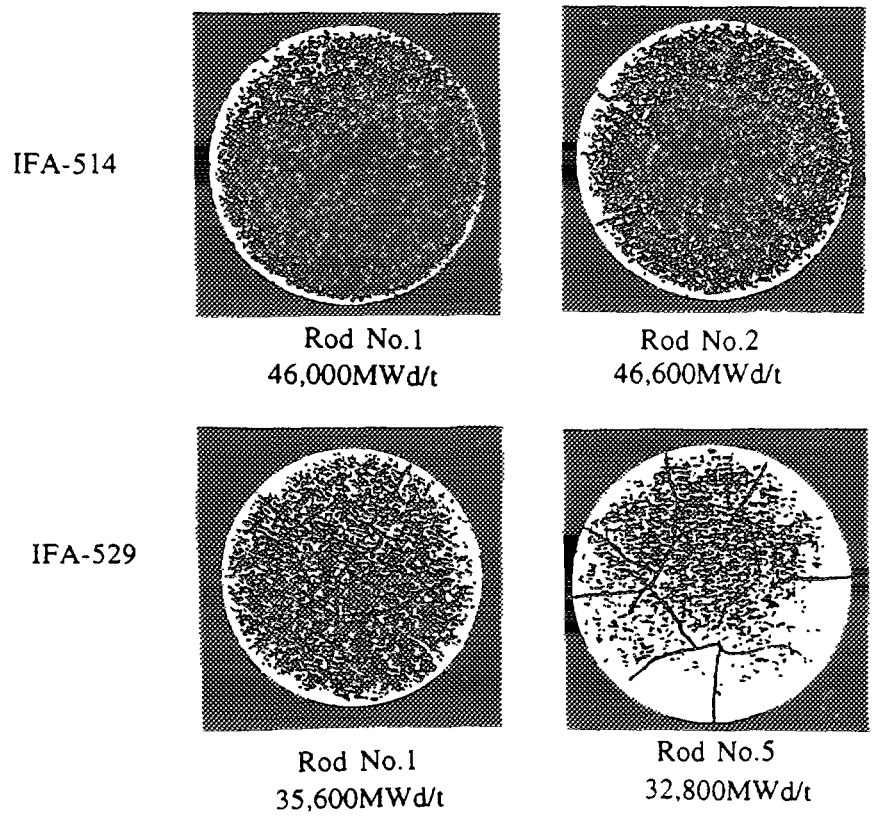

FIG. 4. Alpha auto-radiograph pictures of irradiated IFA-514 and IFA-529.

3.2 INTERNAL PRESSURE OF FUEL ROD

IFA-514/565

Figure 5 shows the comparison of internal pressure between Rod-1 and Rod-4 in IFA-514. There is no significant difference of fabrication specifications between Rod-1 and Rod-4 except the central hole. The data are normalized in the condition of zero power and 240 °C. It is seen in Figure 5 that the rod internal pressure in Rod-1 (solid pellet) is much higher than that of Rod-4 (hollow pellet). Even though considering that the average LHR of Rod-1 is relatively higher than that of Rod-4 (3KW/m), the internal pressure of Rod-4 (hollow pellet) might be still lower than that of Rod-1 (solid pellet). It might be caused by the difference of fuel temperature and free volume between two rods [3] [11].

IFA -529

The internal pressures of the six fuel rods in the lower cluster of IFA-529 are plotted as a function of burn-up in Figure 6. As those fuel rods are installed in the same lower cluster, the rod average powers are supposed to be approximately equal. It is seen that the internal pressures of Rods 1, 2 and 3 loaded with MH pellets are lower than those of Rods 4, 5 and 6 loaded with MB pellets. Figure 6 also shows that except Rod-6, the smaller the pellet-cladding gap size, the lower the internal pressure is. This phenomenon might be explained by taking account of gap conductance dependence upon gap size [3] [5].

3.3 FISSION GAS RELEASE

Figure 7 shows the comparison of fission gas release between Rod-1 of IFA-514 and Rod-4 of IFA-514/565. The fission gas release is remarkable from 15GWd/tMOX. It is seen that the fission gas release fraction of Rod-1 increases until the end of life up to 23% at the burn-up of 40GWd/tMOX.

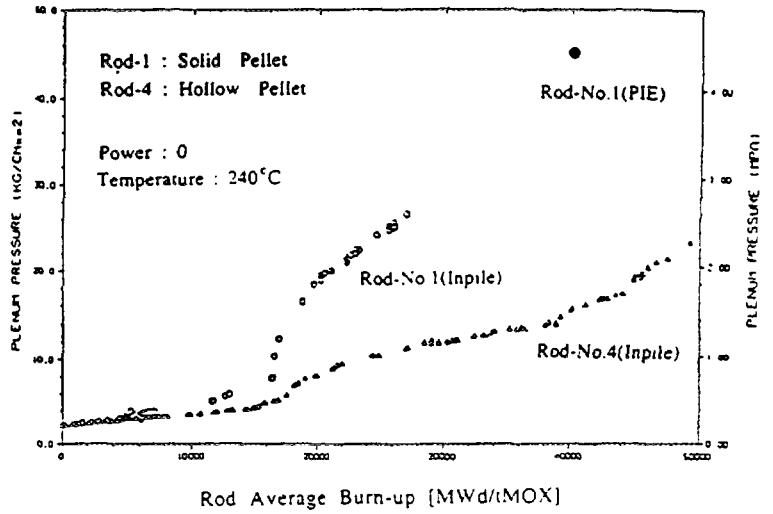

FIG. 5. Plenum pressure of IFA-514 as a function of burnup.

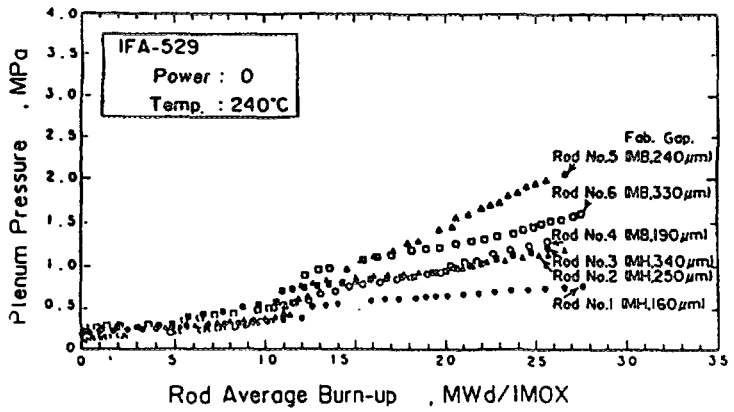

FIG. 6. Plenum pressure in IFA-529 at zero power as a function of burnup.

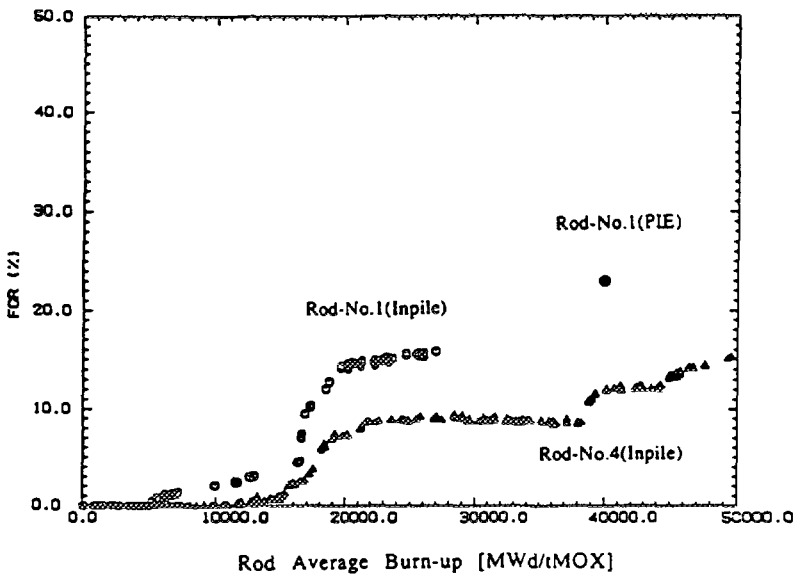

FIG. 7. Fission gas release fraction of IFA-514/565.

On the contrary, the fission gas release fraction of Rod-4 decreases slightly to reach 9% at the end of IFA-514 life. But, at the beginning of the re-irradiation in IFA-565, the fission gas release fraction of Rod-4 increased slightly to reach 10%.

The fission gas release fraction of Rod-1 is much higher than that of Rod-4 at 40GWd/tMOX. Even taking into account the difference of LHR (3KW/m), it seems the fission gas release fraction of Rod-1 (solid pellet) is larger than that of Rod-4 (hollow pellet). But it is necessary to confirm the in-pile data by using PIE data which are to be obtained.

Figure 8 shows the burn-up dependency of fission gas release fraction for BWR UO_2 fuels. The data of PNC MOX fuels for ATR and BWR are also plotted in Figure 8. The scattered region of PNC MOX fuel fission gas release fraction data is within that of UO_2 fuel. Fission gas release fraction in-pile and PIE data of Rod-1 (solid pellet) and in-pile data of Rod-4 (hollow pellet) of IFA-514/565 are drawn in the same figure. Those two lines are also located in the scattered region of UO_2 fission gas release fraction data [3]-[6].

To compare the fission gas release fraction between different type of fuels, it is necessary to compare at the same linear heat rating.

Generally, fission gas release occurs above 10GWd/tM of burn-up, and the maximum linear heat rating experienced above 10GWd/tM is most effective on fission gas release fraction. A. Ohuchi et al. [7] made an analysis of measured UO_2 fission gas release fraction as a function of maximum linear heat rating(210GWd/tM). The result is depicted in Figure 9. In this figure, data of PNC MOX-fuels irradiation experiments are also plotted. It is seen that fission gas release fraction data of PNC MOX fuels are located in the band of UO_2 [11].

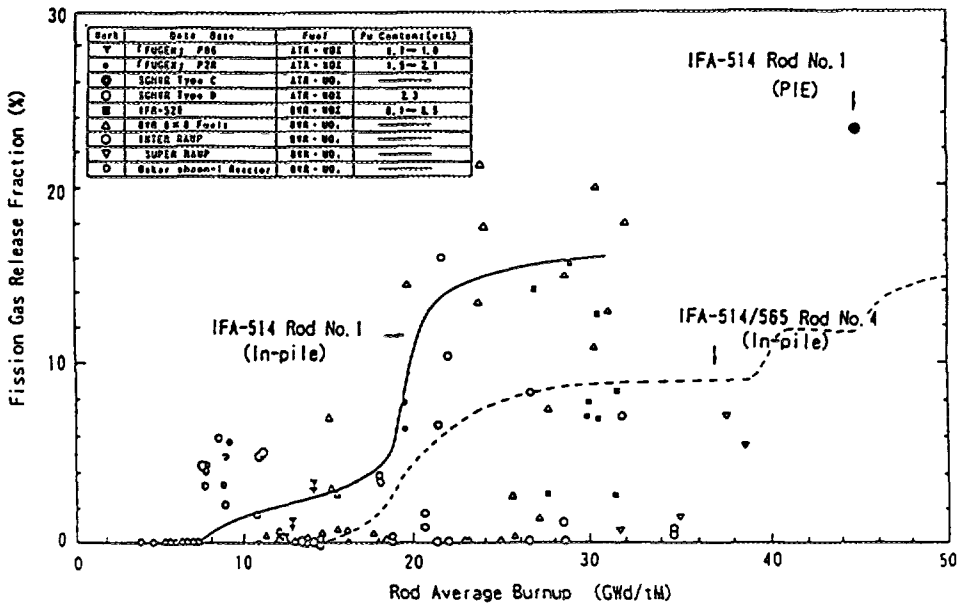

FIG. 8. Fission gas release fraction of UO_2 and MOX fuels as a function of burnup.

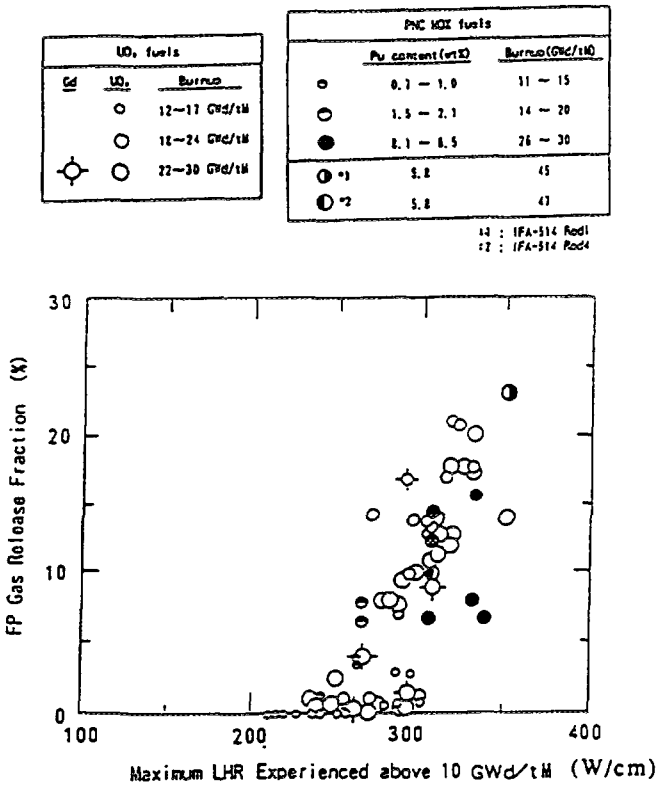

FIG. 9. *Fission gas release fraction of UO_2 and MOX fuels as a function of maximum LHR experienced above 10 GWd/tM.*

3.4 FUEL TEMPERATURE

In each two fuel rods of IFA-514 and 529, thermocouples were inserted to measure fuel centerline temperature directly. Considering that fuel temperature depends on LHR, the temperature data corresponding to the LHRs of 10, 20 and 30KW/m were picked up for analysis. Figure 10 shows the temperature change of Rods-1 and 5 in IFA-514. Although there was a little difference between them up to the burn-up of 16GWd/tMOX, both temperatures become almost same value after the burn-up of 16GWd/tMOX. No significant difference in pellet surface treatment is observed.

In general, gap conductance increases according to LHR because of decrease of gap width. Calculations of gap conductance at various fuel burn-ups were made along the LHR of 20KW/m and based on data sets of both coolant temperature and fuel centerline temperature. Results of the calculations are shown in Figure 11. It is seen that gap conductance gradually decreases with burn-up, however in high burn-up region it becomes rather steady [8].

3.5 PCMI BEHAVIOUR

In-pile PCMI behaviour was analysed using cladding extensometers of the fuel rods in IFA-514 and 529. In general, cladding elongates according to increase of power due to its thermal expansion. When hard contact between pellets and cladding occurs, cladding makes an abrupt elongation because cladding is dragged out by elongated fuel stack. For example, a relation between cladding elongation and LHR for Rod-3 in IFA-514 is shown in Figure 12. The LHR at which cladding makes an abrupt elongation is called "onset LHR for PCMI". It is a good indicator to evaluate easily how PCMI occurs. Figure 13 shows a dependence of the onset LHR for PCMI on burn-up for Rods 2, 3 and 6 in IFA-514. The onset LHR for PCMI gradually decreases with burnup. The onset LHR for PCMI of Rod-6 (hollow pellet) is slightly higher than that of other rods until 5GWd/tMOX. However, no manifest difference in pellet shapes and pellet surface treatments is observed concerning PCMI behaviour .

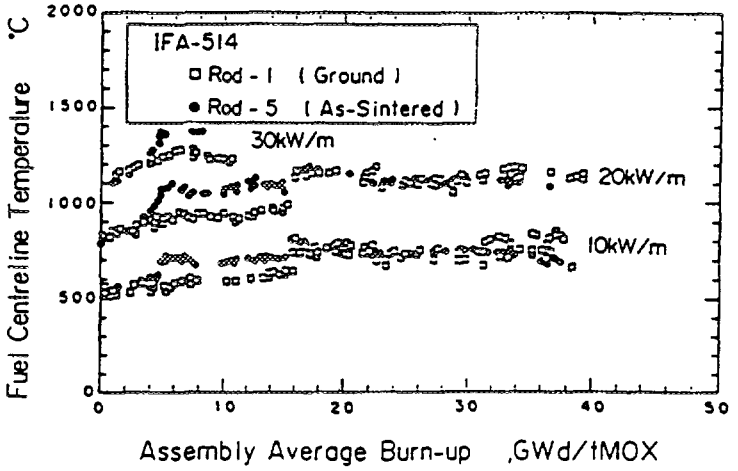

FIG. 10. Fuel centreline temperature at T/C position in IFA-514.

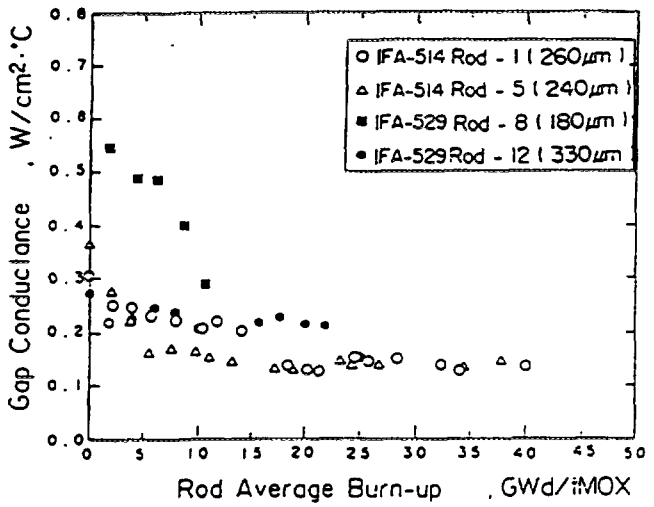

FIG. 11. Gap conductance as a function of burnup at a 20 kW/m.

Figure 14 also shows a dependence of the onset LHR for PCMI on burn-up for Rods 7, 9, 10 significant PCMI is observed for any fuel rods. The dependence of the onset LHR for PCMI on burn-up in IFA-529 is similar to that in IFA-514. No significant dependence on pellet-cladding gap size is observed in IFA-529 [5] [8] [10] [12] [13].

Figure 15 shows the longitudinal metallography pictures of IFA-529 rod 7 and 11 after irradiation. It is seen that the initial pellet-cladding gap size is closed on two rods. Initial gap size and remained gap after irradiation are not correlated. This result also shows that the onset LHR for PCMI does not depend on pellet-cladding gap size.

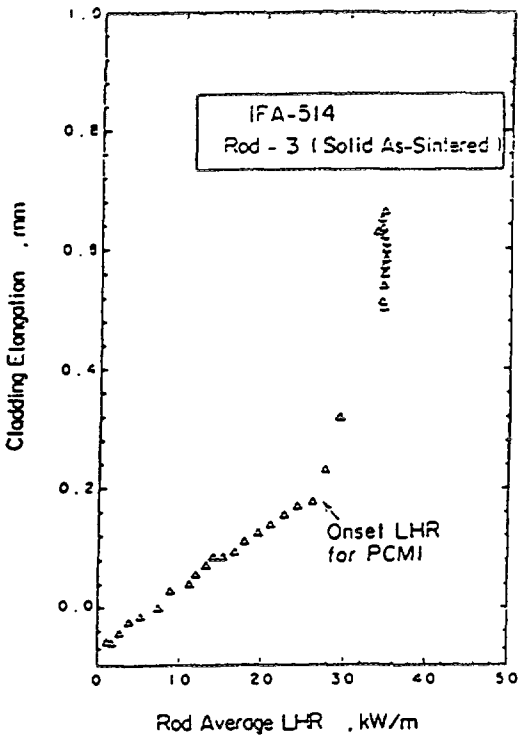

FIG. 12. Example of dependence of cladding elongation on LHR.

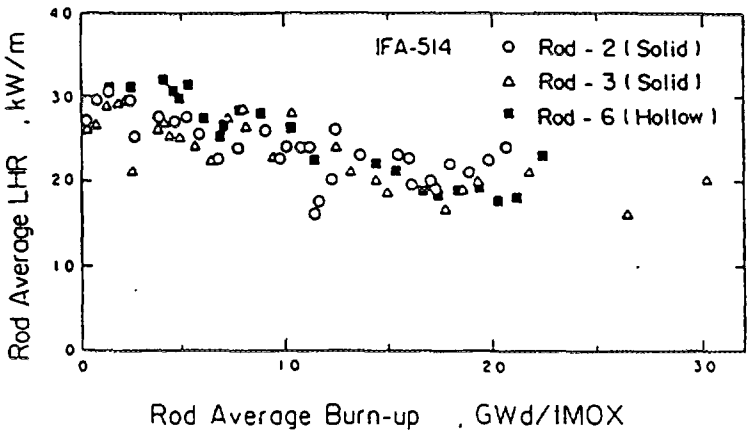

FIG. 13. Onset LHR for PCMI in IFA-514 as a function of burnup.

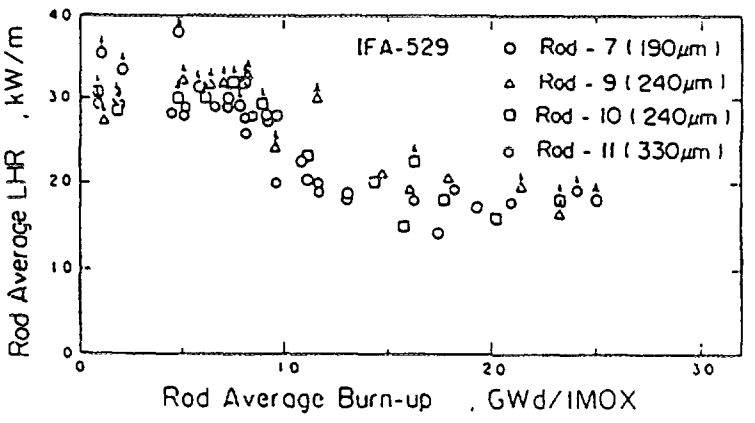

FIG. 14. Onset LHR for PCMI in IFA-529 as a function of burnup.

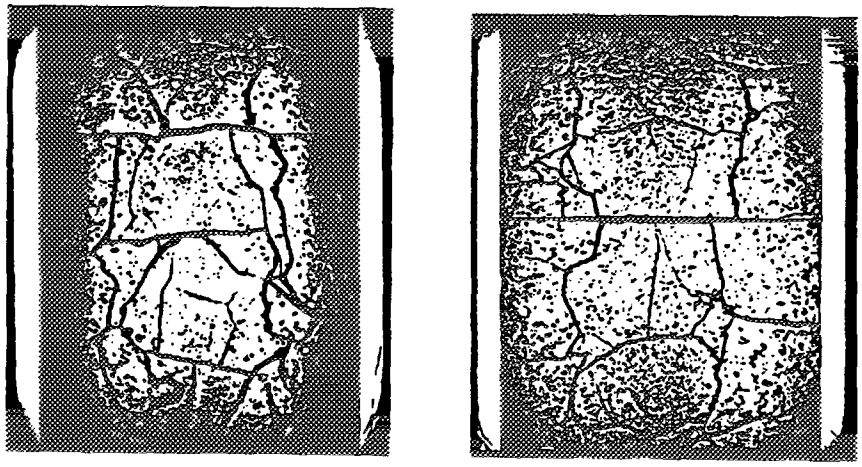

Rod No.7
(Initial gap: 190μm)

Rod No.11
(Initial gap: 330μm)

FIG. 15. Longitudinal metallography pictures of irradiated IFA-529.

4. CONCLUSIONS

Some conclusions derived from the data obtained by the instrumentations and the PIE are as follows.

(I) PNC MOX fuels have achieved high burn-up as 59GWd/tMOX (67GWdltM) at pellet peak without failure.

(2) There was no significant differences in fission gas release fraction between PNC MOX fuels and UO_2 fuels.

(3) Fission gas release from the co-converted fuel was lower than that from the mechanically blended fuel.

(4) Gap conductance was evaluated to decrease gradually with burn-up and to get stable in high burn-up region.

(5) No evident difference of onset LHR for PCMI in experimental parameters (pellet shape and pellet-cladding gap size) was observed, but it decreased with burn-up.

REFERENCES

[1] MISHIMA Y., Japanese Fuel Study Related to Extended Burn-up and Plutonium Recycling, IAEA Specialists' Meeting on Improved Utilization of Water Reactor Fuel with Special Emphasis on Extended Burnups and Plutonium Recycling, Mol , 1984.

[2] KOIZUMI M., OHTSUKA K., ISAGAWA H., AKIYAMA H., and TODOKORO A., Development of Process for the co-conversion of Pu-U Nitrate Mixed Solutions to Mixed-Oxide Powder Using a Microwave Heating Method, Nuclear Technology 61,55 (1983)

[3] KAMIMURA K., ABE T., and YOKOUCHI Y., Fission Gas Release Behaviour of MOX Fuel(IFA-514 and IFA-529), Workshop Meeting on Fission Product Release, Halden, 19-20 September, 1985.

[4] VITANZA C., KOLSTAD E., and GRAZIANI U., Fission Gas Release from U O 2 Pellet Fuel at High Burn-up, ANS Topical Meeting on Light Water Reactor Fuel Performance, Portland, 1979.

[5] ABE T., KANEDA K., UEMATSU S. and SHIKAKURA S., Thermal and Mechanical Behaviours of MOX Fuel Rods in IFA-529, Enlarged Halden Programme Group Meeting, Leon, 8- 13 May, 1988.

[6] SAIRANEN R., VITANZA C., KELPPE S., and RANTA-PUSKA K., Steady State Fission Gas Release from IFA-505 Data Evaluation Comparison with Release Models, HWR- 157 (1986).
[7] OHUCHI A. et al, Behaviour of Gaseous and Volatile Fission Products in BWR Fuel Rods, IAEA Specialists' Meeting on Post Irradiation Examination and Experience, Tokyo, Japan 26-30 Nov. 1984.
[8] MISHIMA T., KAMIMURA K., and TANAKA K., Thermal and Mechanical Behaviours of MOX Fuel Rods, IAEA Technical Committee Meeting on Recycling of Pu and U in Water Reactor Fuels, Cadarache, France, Nov. 13-16, 1989.
[9] KAMIMURA K., MAEDA S., MISHIMA T., Irradiation Test of MOX Fuel Rods for Water Reactor(I)-Thermal Behaviours of IFA-529 Fuel Rods., Atomic Energy Society of Japan, Apr. 2-4, 1990.
[10] MAEDA S., KAMIMURA K., MATSUMOTO M., Irradiation Test of MOX Fuel Rods for Water Reactor(2)-Mechanical Behaviours of IFA-529 Fuel Rods., Atomic Energy Society of Japan, Apr. 2-4, 1990.
[11] KAMIMURA K., FP Gas Release Behaviour of High Burn-up MOX Fuel for Thermal Reactors., IAEA Technical Committee Meeting on Fission Gas Release and Fuel Rod Chemistry Related to Extended Burnup., Pembroke, Canada, Apr. 27-May 1, 1992.
[12] KIKUCHI K., NAKAIIMA Y., and MATSUMOTO M.,Post Irradiation Examination of MOX Fuel Rods., Atomic Energy Society of Japan, Mar. 2729, 1993.
[13] KOHNO, S., KAMIMURA, K., "MOX Fuel Irradiation Behavior in Steady State " , ANS Topical Meeting, April 17-21, 1994.

A SIMULATION OF THE TEMPERATURE OVERSHOOT OBSERVED AT HIGH BURNUP IN ANNULAR FUEL PELLETS

D. BARON
Electricité de France,
Moret-sur-Loing

J.C. COUTY
Electricité de France,
Villeurbanne

France

Abstract

Instrumented experiments have been carried out in recent years to calibrate and improve temperature calculations at high burnup in PWR nuclear fuel rods. The introduction of a thermocouple in the fuel stack allows the experimenter to record the centre-line temperature all along the irradiation or re-irradiation. Power history is predefined to obtain a relation between local power levels and centre-line temperatures. The results obtained on fresh fuel have not revealed any abnormal behaviour as have observations done on high burnup rods. In this case, a sudden overshoot has been recorded on the thermocouple temperature above an average power threshold. Several hypotheses have been suggested. Only two seem to be acceptable: one in relation to an effect of grain decohesion, another based on a modification of fuel chemistry. The apparent reversibility of the phenomenon when power decreases led us to prefer the first explanation. Indeed, the introduction of a thermocouple means that annular fuel pellets must be used. These are either initially manufactured with a central hole or drilled after base irradiation, using the "RISOE" technique. One must bear in mind that the use of such annular pellets drastically changes the crack pattern as irradiation proceeds. This is due to a different stress field which, combined with a weakening of the grain binding energy, leads to a partial grain decohesion on the inner face of the annular pellet. Modification of the grain binding energy is related to the presence of an increasing local population of gas bubbles and metallic precipitates at grain boundaries. as swelling creates intergranular local stresses which also could probably enhance the grain decohesion process. This grain decohesion concerns a 250 to 350 μm depth and shows a narrow cracks network through which released fission gas can flow, temporarly pushing the resident helium gas out. The low conductivity of these gaseous fission products and the numerous gas layers created this way could partly explain the unexpected temperatures measured in high burnup fuels. The purpose of this paper is to present a simulation of such a phenomenon and the parametric study conducted to reinforce this hypothesis. This approach is also convenient to explain why the fission gas release level measured after re-irradiation is not in agreement with centerline temperatures recorded. One can also assume a reversibility of the phenomenon as soon as the fission gas release process stabilizes, and suggest a methodology in order to avoid such problems when undertaking similar experiments in the future.

1. INTRODUCTION

Because temperature is the most influential parameter in most of the phenomena induced in a nuclear fuel rod under irradiation, the mastership of the radial temperature gradient must be continuously improved in the thermomechanical behaviour codes. This improvement is particularly needed for the fuel rod simulation at high burnup to insure conservatism in safety calculations. One can only evaluate the margins if uncertainties are well known. For fresh fuel rods, the discrepancy level on the fuel centre-line temperature is never less than several percents. It is due mainly to the power history uncertainties. A better accuracy can however be achieved in experimental irradiations, using in-pool gamma calibrations as is done in the CEA pools [1].

rain growth and fission gas relesase are currently used to evaluate temperature predictions in high burnup fuel rods. However, using grain growth as temperature marker, assumes that growth mechanism is not modified by fuel chemichal and physical modifications. On the other hand, using the fission gas release level does not allow the designer to calibrate thermal and fission gas release models separately. An eventual drift on one model with burnup must be counterbalanced by the others. In this configuration one model cannot be easily changed for another.

To solve such a problem, as has been done for fresh rods, instrumented experiments have been carried out in the framework of the High Burnup Chemistry program (HBC program, managed by the Belgonucleaire Company). The introduction of a thermocouple in the fuel stack (similar to CONTACT experiments [2] [3] [4]) allows the experimenter to record the centre-line temperature all along the re-irradiation. Power history is predefined to obtain a relationship between local power levels and centre-line temperatures.

Indeed, the introduction of a thermocouple means that annular fuel pellets must be used. These are either initially manufactured with a central hole or drilled after base irradiation, using the "RISOE" technique. Central hole diameter is minimum 1.5 mm due to thermocouple size.

For the HBC program, in order to avoid pellets drilling in high burnup fuel, annular pellets already irradiated at consequent burnup, with a standard initial hole about 2.5 mm diameter, have been proposed. Indeed, one must bear in mind that the use of such annular pellets drastically changes the crack pattern as irradiation proceeds. But no one thought of the effect of an induced grain decohesion at the inner surface. This could be an explanation of the abnormal thermocouple temperatures measured during power transients.

The purpose of this paper is to present a simulation of such a phenomenon and the parametric study conducted to reinforce this hypothesis to explain abnormal temperatures. We will see that this approach is convenient to explain why the fission gas release level measured after re-irradiation is most in agreement with the temperatures expected than with the centre-line temperatures recorded.

2. ASSUMED MECHANISMS

2.1 OBSERVATIONS AND DISCUSSION

All the similar experiments reported on fresh fuel have not revealed any abnormal behaviour as have observations done on the 45000 MWd/tU fuel rod examined. In this case, a sudden overshoot has been recorded on the thermocouple temperature above an average power threshold.

Several hypotheses have been suggested. Only two seem to be acceptable: one in relation to an effect of grain decohesion, another based on a modification of fuel chemistry. The apparent reversibility of the phenomenon when power decreases led us to prefer the first explanation.

Several points should be made:

- the rod power was rised step by step, one step lasted a few hours, enough to reach temperature steady state but not fission gas release stability,
- power level during base irradiation up to 45000 MWd/tU was low enough to avoid any strong fission gas release. For this reason, all the gaseous and volatile fission gas products are retained in the fuel matrix before the experiment (in a fresh rod the amount of retained gas is negligible),
- post irradiation examinations showed a 250 to 350 μm zone at the inner surface where grain decohesion occurs (figure 1),
- when power decreases under the power threshold identified, the thermocouple temperature level is back to expected values.
- cumulative time at maximum power does not exceed 8,5 hours,

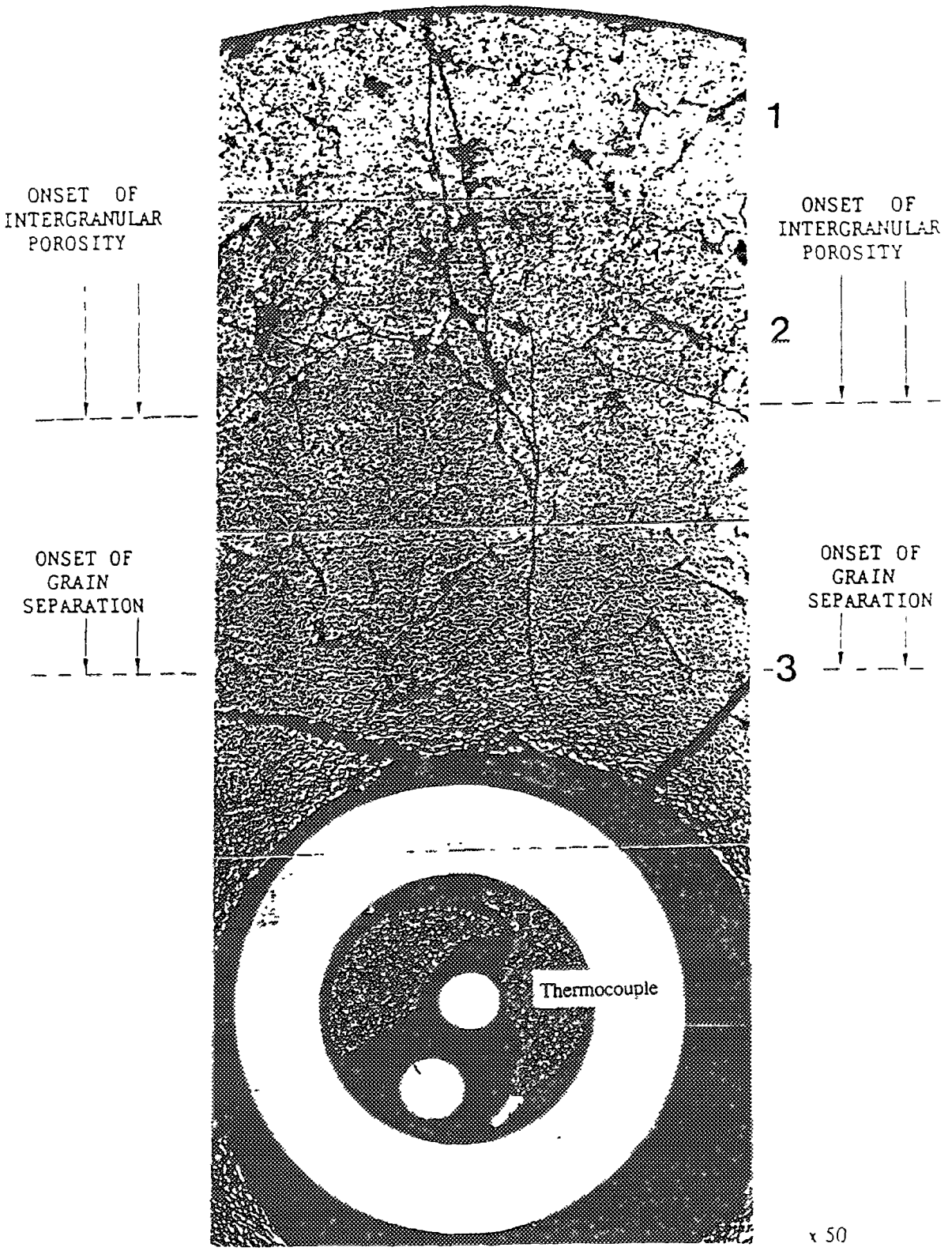

FIG. 1. Post-Irradiation Fuel Ceramography

- the end of life fission gas release fraction measured is consistent with code evaluation but not consistent with the thermocouple temperatures,
- the temperature drift kinetic seems to be consistent with fission gas migration kinetic,
- the maximum Gamma power deposit in the thermocouple components is evaluated to a level of 1.6 W/cm.

Thermal fission gas release is a threshold phenomenon. The release temperature threshold is related to saturations effects allowing progressive gas percolation in grain boundaries. It must not be confused with the diffusion temperature threshold within the grains representative of an activation energy level.

Simplifying, the release temperature threshold is a parameter decreasing with the local average fuel burnup. This means that, at high burnup, when the power level is high enough for more than 40 hours - time for which fission gas release steady state is reached (High Burnup Effect Program [5]) - , fission gas release fraction can be roughly evaluated by the ratio between the fuel volume above the temperature threshold and the total fuel volume. This is due to the fact that the remaining amount of gas trapped in the matrix is negligible in comparison to the amount of gas created.

For that reason, if the fission gas release level is roughly as expected by the codes, it means that the radial temperature gradient is properly evaluated from the pellet surface to the fission gas release transition zone or that the position of the transition zone is certainly properly simulated. That leads us to conclude that if something abnormal occurs, it must be between the transition zone and the thermocouple.

2.2 SCENARIO PROPOSED

Power is increased step by step. As long as the thermal fission gas release is not activated by the fuel local temperature, the thermocouple temperature is as expected. When the fission gas release temperature threshold is reached and passed over in the pellet central zone, bubble gas diffusion starts. Most of the gas migrates towards the grain boundaries, building a bubble chain all along the grain boundaries, paticularly in triple intergranular sites.

A minimum of time is required to accumulate enough gases to allow percolation along grain boundaries and gas to flow outside the fuel. During this period, pressure rises in intergranular bubbles inducing stresses between grains.

This situation, combined with a weakening of the grain binding energy, can lead to a partial grain decohesion on the inner face of the annular pellet. Modification of the grain binding energy is related to the presence of an increasing local population of gas bubbles and metallic precipitates at grain boundaries. In a plain pellet, because of different limit conditions in the center of the pellet, compressive stresses probably enable such a grain decohesion or limit this decohesion to a fine network of microcracks as observed in the HATAC experiment rods [6] [7].

This grain decohesion concerns a 250 to 350 μm depth and shows a narrow cracks network through which released fission gas can flow, temporarily pushing the resident helium gas out. Interlayer gas mixture during this period can be assumed to be constituted of nearly 100 % of fission gases (Xenon and Krypton isotopes).

The low conductivity of these gaseous fission products, combined with the grat number of gas layers degrade in this region the fuel average apparent thermal conductivity. We propose to evaluate such an effect in the next chapter.

The reversibility of the phenomenon can be explained by a gas re-mixing during the power decrease. This re-mixing can be activated by a natural convection flow monitored by temperature gradients. If that occurs, the gas mixture thermal conductivity is strongly improved by Helium which represents more than 95 % of the mixture.

When power is back to the highest level, gas flow starts again and fuel thermal conductivity is degraded again. However because fuel gas content is decreasing, interlayer gas flow will also decrease progressively until total possible fission gas release is achieved. The consequence would certainly have been a decrease of the thermocouple temperature if the highest power could have been maintained long enough.

3. SIMULATION

3.1 MODELLING

Fuel decohesion has been simulated in an unidimensional thermal calculation by an alternation of fuel zones and gas layers where gas mixture can be modified (figure 2). Fuel zones thickness is representative of grain diameters. Effect of Gas composition, gas layers thickness and decohesion zone thickness were studied.

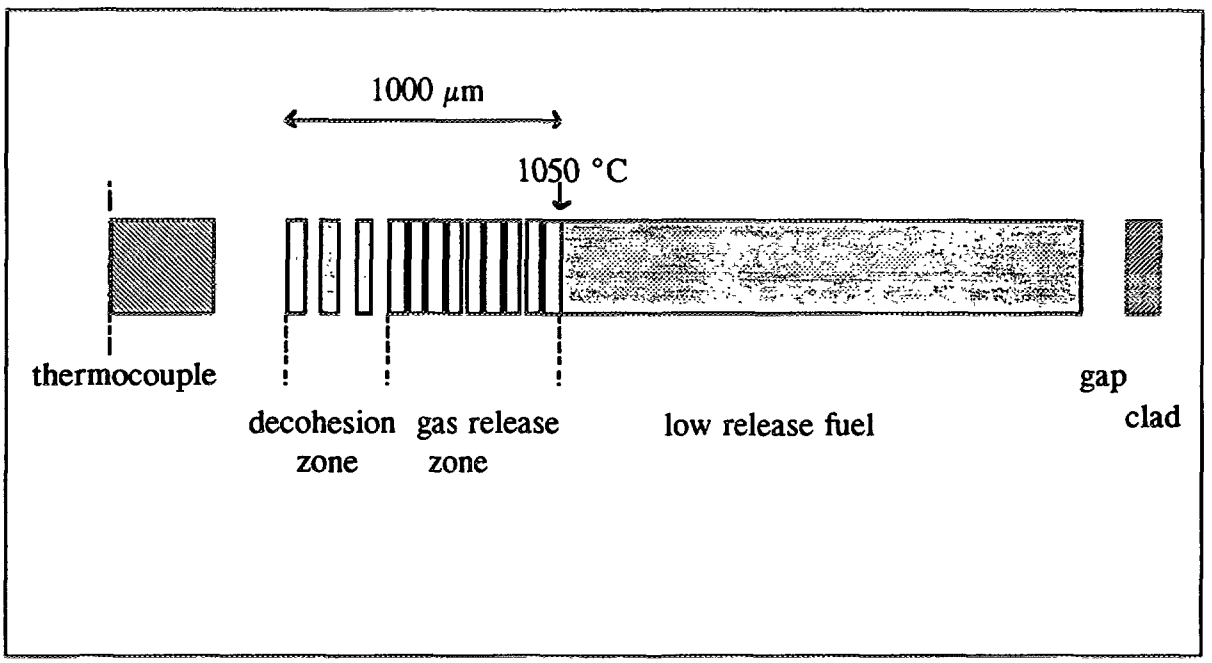

Because an assumption was made on a non-modification of the transition zone position, calculation is made from this isothermal line towards the center with a specific code using the thermal standard subroutine of the EDF fuel rod thermomechanical code. Temperature threshold at the transition zone was assumed at 1050°C, which is consistent with the lowest bound evaluated for a 45000 MWd/tU burnup [5].

Power sources are distributed in the fuel and take into account the radial depression due to plutonium build up in the pellet "rim". Average power level is assumed as 340 W/cm. A maximum value of 1.6 W/cm for the gamma power deposit in the thermocouple components is assumed.

Three zones are to be considered:

a) fuel part without grain decohesion

Even if grain decohesion doesn't occur within this zone, fission gas diffusion is activated by the local temperature. Gas bubbles are then present in the grain boundaries, filled by Xenon. This bubble decoration is assumed to create thermal bridges at each grain boundary because of the fission gas low

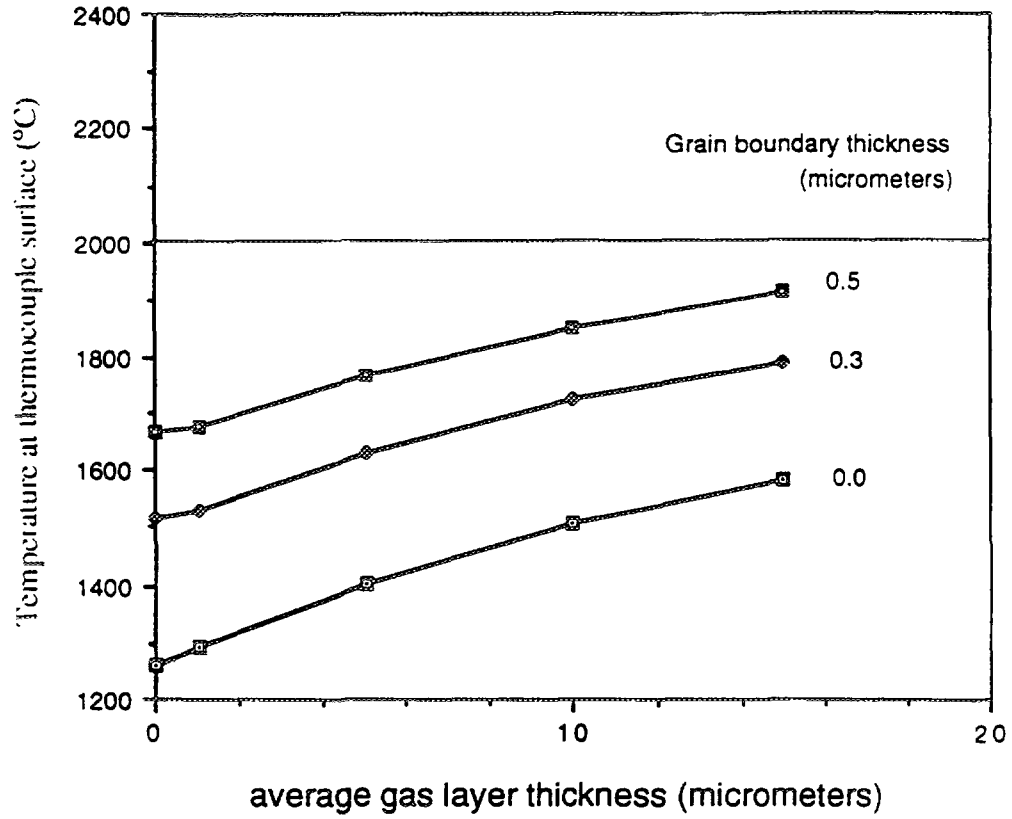

FIG. 2a. Decohesion Zone width = 190 micrometers

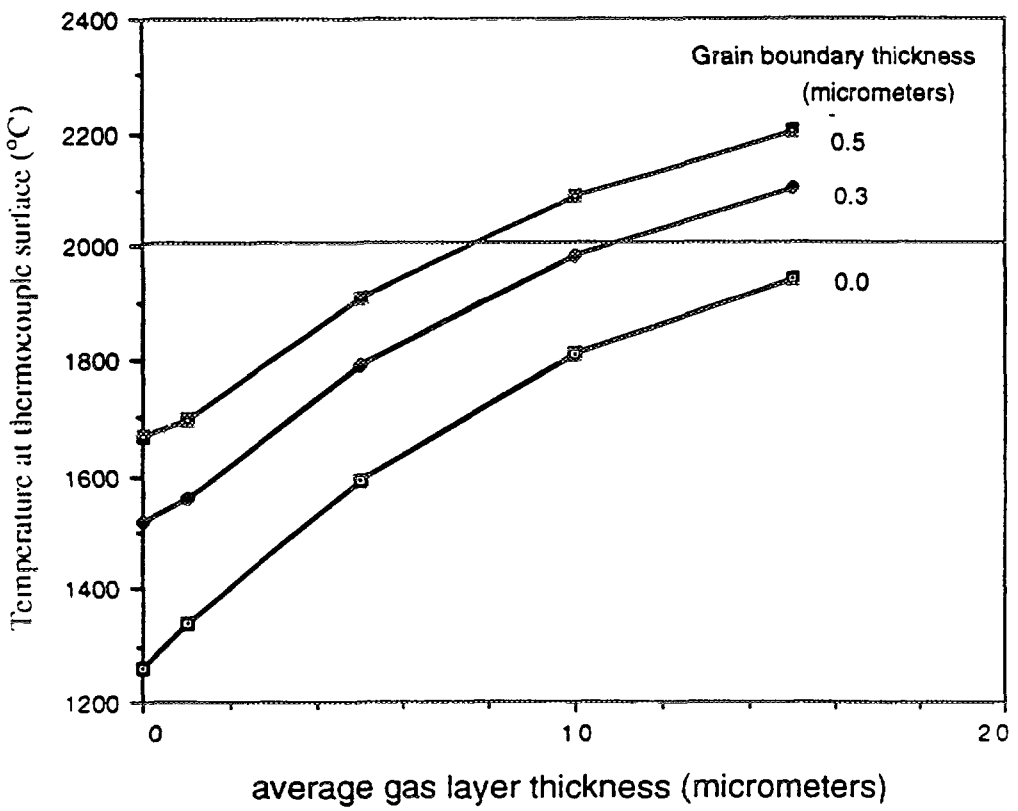

FIG. 2b. Decohesion Zone width = 290 micrometers

conductivity. The average fuel thermal conductivity degradation is indeed certainly stronger in comparison with the same amount of porosities spread within the fuel matrix. Average bubble size in the grain boundaries is 2 μm. Because bubbles are distributed discontinuously along the grain boundaries the simulation takes into account an equivalent maximum grain boundary thickness of 0,5 μm which is the quarter of the bubble average diameter.

b) fuel part concerned by grain decohesion

The thickness of each fuel zone in the decohesion area is assumed equivalent to the average grain size: 12 μm. Measurements on post-irradiation ceramographies show a grain decohesion zone width evaluated from 250 to 350 μm and an average inner radius decreased of 60 μm. The fuel zone concerned by grain decohesion is then between 190 to 290 μm.

c) gap between the fuel and the thermocouple envelope

The gap between the inner fuel surface and the thermocouple envelope is assumed to be filled by fission gases. Thermal transfer proceeds by convection through the gas but also by a radiative transfer which limits strongly the temperature drop through the gap. In spite of what is observable on the fuel ceramography, the thermocouple has been assumed to be centred in the pellet hole.

In all the following results gas mixtures in grain boundaries bubbles, in gas layers and in the fuel to thermocouple gap, are assumed to be 100 % Xenon. However, other calculations have also been done to evaluate the mixture influence but are not reported here.

3.2 RESULTS AND DISCUSSIONS

The simulation results are reported in Table 1 and Table 2 for two respective width (190 and 290 μm) for the decohesion zone. For each case, temperatures are given for the pellet inner surface and the thermocouple outer surface.

In the decohesion zone, the calculation is done for different values of the average gas layer thickness: 1, 5, 10 and 15 μm.

In the high fission gas release zone, the effect of an equivalent gas film at grain boundaries is given for several average values of the thickness: 0, 0.1, 0.2, 0.3, 0.4 and 0.5 μm.

Figures 2A and 2B give a graphic representation of the influence of the parameters upon the maximum temperatures at thermocouple outer diameter. They show that a 2000 °C can be easily reached in spite of the quite low fuel power (340 W/cm). This is consistent with the results obtained for the instrumented rod. The temperature drop between the fuel and the thermocouple is always within 10 to 60 °C.

Figure 3 gives a good idea of the thermal gradient to which such a simulation leads. This gradient is not parabolic any more and only a few fuel volume, corresponding to the decohesion zone, achieve really more than 1400 °C. Because decohesion occurs probably during the first minutes at power or during the transient, grain growth is unlikely. Indeed, no evidence of grain growth was observable on post irradiation fuel ceramographies.

Nevertheless, back to the temperatures obtained, the simulation assumes the worst conditions corresponding to the first hours at power: all grain decohesion is achieved, fission gas release is underway with a high release rate (gas mixture being essentially fission gases). After this period, grains are providing with less and less fission gases and so, fission gas release rate decreases; the gas mixture in the gas interlayers improve their conductance by an homogeneisation with Helium. This means that, if the power level is maintained more than 30 to 40 hours, the temperature as measured by the thermocouple will drop down to a value more consistent with the codes evaluations.

TABLE I

CALCULATION FOR A DECOHESION ZONE WIDTH OF 190 μm

	Average gas layer thickness in the decohesion zone			
grain boundary thickness (μm)	1	5	10	15
0	1236 (1293)	1356 (1404)	1468 (1509)	1551 (1585)
0,1	1326 (1377)	1440 (1483)	1546 (1583)	1625 (1656)
0,2	1412 (1457)	1520 (1559)	1621 (1655)	1695 (1725)
0,3	1492 (1533)	1595 (1631)	1692 (1723)	1763 (1790)
0,4	1568 (1605)	1667 (1700)	1760 (1789)	1827 (1853)
0,5	1642 (1676)	1738 (1768)	1826 (1853)	1891 (1915)

T1 (T2):
T1 temperature at pellet inner surface (°C)
T2 temperature at thermocouple outer surface (°C)
pellet average power: 340 W/cm
reference from standard calculations: 1202 (1263)

TABLE II

CALCULATION FOR A DECOHESION ZONE WIDTH OF 290 μm

	Average gas layer thickness in the decohesion zone			
grain boundary thickness(μm)	1	5	10	15
0	1286 (1340)	1556 (1593)	1782 (1808)	1930 (1941)
0,11370 (1418)	1628 (1661)	1844 (1868)	1986 (1996)	
0,2	1449 (1492)	1696 (1727)	1904 (1927)	2040 (2050)
0,3	1524 (1563)	1762 (1791)	1962 (1984)	2093 (2103)
0,4	1594 (1631)	1824 (1851)	2018 (2039)	2144 (2153)
0,5	1662 (1696)	1884 (1910)	2072 (2091)	2193 (2202)

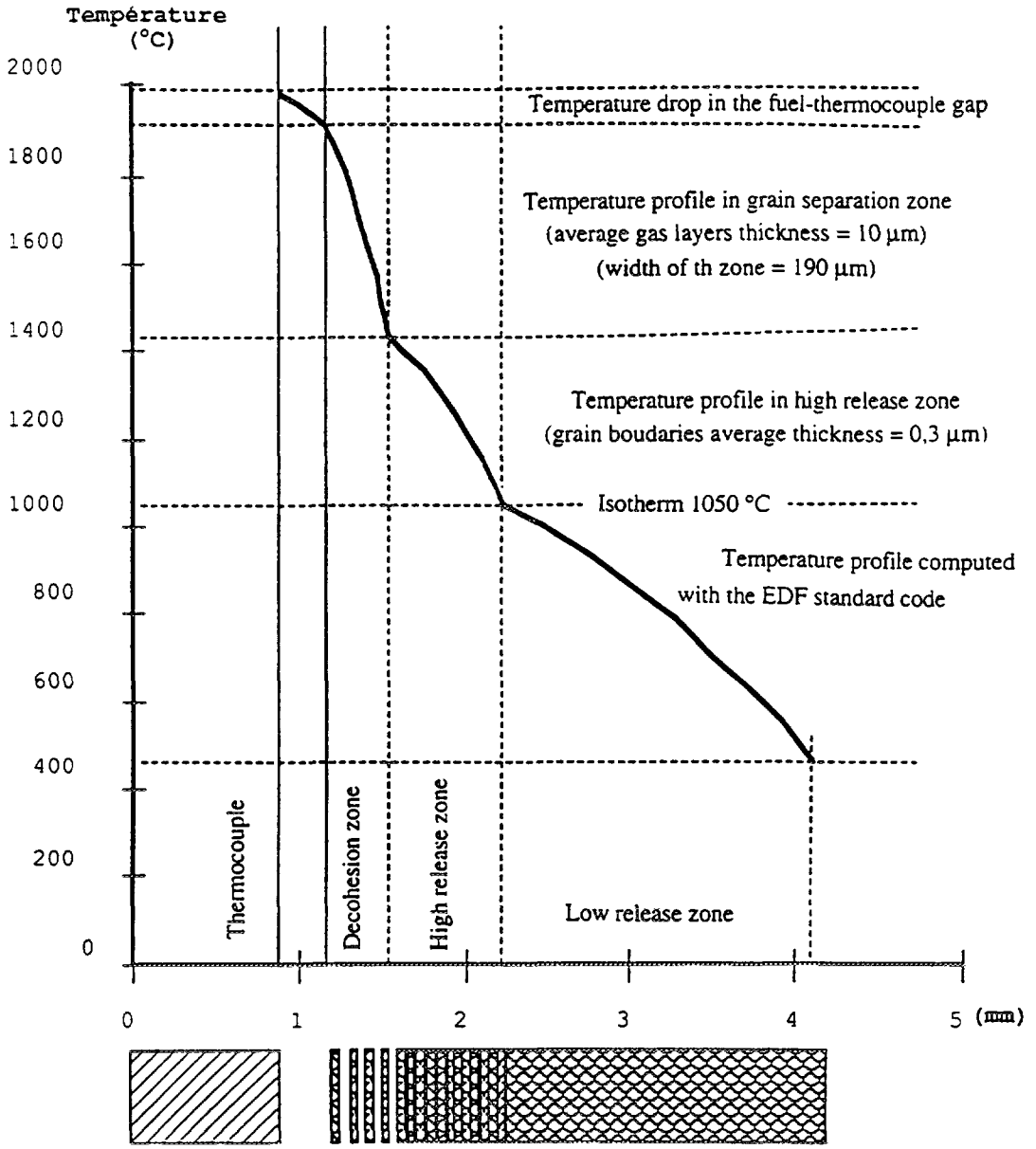

FIG. 3. Radial Profile in the Fuel Pellet

However, in the zone not concerned by grain decohesion, the effect of the bubbles, still remaining in the grain boundaries, should certainly degrade slightly more than expected the fuel central temperature just because the modellings used in our codes assume the porosities to be always spread homogeneously in the fuel matrix. This effect cumulated with the residual effect of the decohesion zone with a majority of Helium in the interlayers leads to a non-total but partial reversibility of the phenomenon as described.

If this scenario is to be retained, that leads to conclude that such a phenomenon could be avoided when undertaking a similar experiment just using smaller power steps and longer holding times at each step. Surely, one can expect that even operating in such a manner, fuel grain decohesion will still occur. However, these operating conditions will give time for gases to be released progressively, zone by zone, and so limit the effect on the average thermal transfer. Such an experiment could also confirm the scenario proposed.

4. CONCLUSION

Instrumented experiments have been carried out in recent years to calibrate and improve temperature calculations at high burnup in PWR nuclear fuel rods. The introduction of a thermocouple in the fuel stack allows the experimenter to record the centre-line temperature all along the irradiation or re-irradiation but impose the use of annular pellets.

The results obtained on fresh fuel have not revealed any abnormal behaviour as have observations done on high burnup rods. In this case, a sudden overshoot has been recorded on the thermocouple temperature above an average power threshold.

The scenario proposed in this communication shows that an overshoot on the fuel central temperature in an annular pellet can be explained by the effect of a fuel grain decohesion and the possibility for the fission gases to flow through the cracking network so generated. The fuel thermal behaviour is then strongly correlated with the fission gas release kinetic. However, it has also been shown that, in this simulation, the temperature overshoot has almost no influence on the total fission gas release level within the fuel rod.

This scenario is very consistent with all the observations done during post irradiation exams on the concerned experimental fuel rod. It assumes a partial reversibility of the phenomenon as soon as the fission gas release process stabilizes. A methodology has been suggested in order to avoid such problems when undertaking similar experiments in the future.

AKNOWLEDGMENTS

The authors aknowledge the valuable works done by the CEN/SCK and Belgonuclaire within the High Burnup Chemistry programme. The post irradiation examinations and the following discussions have particularly helped in the interpretations and the simulation presented above. They would also like to thank Christophe DUBARRY and Benoît LEVALLOIS who performed the calculations and wrote the two reports from which these results are extracted.

REFERENCES

[1] FRIBOULET,C., ROCHE,M., "Irradiation Facilities of the CEA/DERPE for Power Ramping and Power Cycling Experiments", IAEA TCM on Power Ramping, Cycling and Load Following Behaviour of Water Reactor Fuel, May 18-21, 1987, LYON (FRANCE)

[2] CHARLES, M., ABASSIN, J.J., BARON, D., BRUET, M., MELIN, M., "Utilization of CONTACT Experiemnts to Improve the Fission Gas Release Knowledge in PWR Fuel Rods", IAEA Specialist Meeting on Water Fuel Element Performance Computer Modelling, March 14-19, 1982, PRESTON (UK).

[3] BRUET, M., DODELIER, J. MELIN, P. POINTUD, M.L., "Contact 1 and 2 Experiments: Behaviour of PWR Fuel Rod up to 15 000 MWD/TU", IAEA Specialist Meeting on Water Fuel Element Performance Computer Modelling, March 17-21, 1980, BLACKPOOL (UK).

[4] CHARLES, M., BRUET, M., "Gap Conductance in Fuel Rod, Modelling of Furet and CONTACT Results", IAEA Specialist Meeting on Water Fuel Element Performance Computer Modelling, April 9-13, 1984, BOWNESS-ON-WINDERMERE (UK).

[5] BARNER, J.O., CUNNINGHAM, M.E., FRESHLEY, M.D., "High Burnup Effect Program -Final Report", DOE/NE/34046-1, HBEP 61(3P27), UC-523.

[6] PORROT, E., CHARLES, M., HAIRION, JP., LEMAIGNAN, C., FORAT, C., MONTAGNON, F., "Fission Gas Release during Power Transients at High Burnup", ANS-ENS International Topical Meeting on LWR Fuel Performance, APRIL 21-24, 1987, AVIGNON (FRANCE).

[7] LEMAIGNAN, C., RAYBAUD, A., BARON, D., "Fission Gas Release during Power Transients at High Burnup", IAEA TCM on Power Ramping, Cycling and Load Following Behaviour of Water Reactor Fuel, May 18-21, 1987, LYON (FRANCE).

VALIDATION OF THE TUBRNP MODEL WITH THE RADIAL DISTRIBUTION OF PLUTONIUM IN MOX FUEL MEASURED BY SIMS AND EPMA

C. O'CARROLL, J. VAN DE LAAR, C.T. WALKER
CEC Joint Research Centre,
Karlsruhe, Germany

Abstract

The prediction of fuel rod behaviour in a Light Water Reactor at high burnup is difficult because the thermal and mechanical analyses depend strongly on complex material behaviour that changes with burnup. In particular the radial power density distribution in fuel rods is non-uniform and is a function of burnup. At the beginning of irradiation, i.e. at low burnup, the concentration of fissile material is constant that means that the radial power exhibits only a small variation across the fuel radius. At high burnup there is a change in this concentration with a marked increase in the ^{239}Pu concentration near the fuel surface. The variation can be explained as follows: owing to the capture of epithermal neutrons in the resonances of ^{238}U (with a high absorption cross-section) there is a large build-up of plutonium near the pellet surface. Consequently, the power density profile that is proportional to the neutron flux and the concentration of fissile material exhibits a steep rise near the pellet surface at high burnup. The new model *TUBRNP* (TRANSURANUS burnup) predicts the radial power density distribution as a function of burnup (and hence the radial burnup profile as a function of time) together with the radial profile of plutonium. Comparisons between measurements and the predictions of the *TUBRNP* model have been made for UO_2 LWR fuels: they were found to be in excellent agreement and it is seen that *TUBRNP* is a marked improvement on previous models. A powerful technique for the characterisation of irradiated fuel is Electron Probe Microanalysis (EPMA). Uranium, plutonium and fission product distributions can be analysed quantitatively. A complement, providing isotopic information with a lateral resolution comparable to EPMA, is secondary ion mass spectrometry (SIMS). Recently, the technique has been successfully applied for the measurement of the radial distribution of plutonium isotopes in irradiated nuclear fuel pins. The extension of the *TUBRNP* model to mixed oxide fuels seems to be the natural step to take. In MOX fuels the picture is greatly complicated by the presence of the (U, Pu)O_2 agglomerates. The rim effect referred to above may be masked by the high concentrations of plutonium in the bulk of the fuel. A detailed investigation of a number of MOX fuel samples has been made using the *TUBRNP* model. Results are presented for a range of fuels with different enrichment and burnup. Through its participation in the PRIMO and DOMO programmes, PSI in conjunction with the Institute for Transuranium Elements had the opportunity to validate the new theoretical model *TUBRNP*. The authors wish therefore to express their thanks to the organizers and to the numerous European and Japanese organizations which have supported these two international programmes on MOX fuel behaviour.

1. INTRODUCTION

Increasing interest is being shown in mixed oxide fuels as a means of utilising plutonium produced from UO_2 fuels and for the transformation of weapons plutonium to a more proliferation resistant form. It is therefore important to understand the behaviour of plutonium in such fuels. Standard codes such as ORIGEN [1] can predict the buildup of the various isotopes as a function of burnup. However, they give only the average concentrations of the isotopes with no indication of how the isotopes are spatially distributed. In real fuels, plutonium is not distributed homogeneously across the fuel radius. Each isotope has its own characteristic radial profile. In particular, due to epithermal neutron capture, the concentration of plutonium increases near the edge of the fuel.

In a recent paper [2] a model was proposed to describe the buildup of plutonium in high burnup UO_2 fuels due to epithermal neutron capture. This is an extension of the well known RADAR (RAting Depression Analysis Routine) of Palmer et al [3]. It has been incorporated into the fuel performance code

TRANSURANUS [4] and is called *TUBRNP* (TRANSURANUS burnup). It was shown that it could accurately predict the radial distribution of plutonium over a wide range of burnups and enrichments. The logical step is to extend this model to include MOX fuels.

MOX fuels consist of uranium oxide with (U, Pu)O_2 agglomerates typically of the order of 100 microns in diameter. The following factors, however, must be considered:

(a) further resonance effects,
(b) MOX thermal neutron spectrum,
(c) MOX capture and absorption cross-sections.

In its present form the model treats only (a) and (b): improvements that will fully include (b) and (c) are in progress.

The results of SIMS and EPMA analysis from the Paul Scherrer Institute (PSI) provide detailed results for the total and radial dependent values for burnup and isotopic composition [5]. These measurements make manifest new results concerning resonance effects. In Fig. 1, it is evident from the radial distributions of ^{240}Pu and ^{241}Pu that there is a resonance absorption process for ^{240}Pu similar to that for ^{238}U. This was verified upon examination of the (n, γ) cross-sections for ^{240}Pu and the model has been extended to include this effect. The model was validated against a variety of PWR and BWR MOX fuel data: different neutron cross-sections for the BWR cases were used.

2. DESCRIPTION OF THE MODEL

We can write down the following general equations for the rate of change of concentration of the relevant isotopes:

$$\frac{dN_{235}}{dt} = -\sigma_{a,235}\bar{N}_{235}\phi, \tag{1a}$$

$$\frac{d\bar{N}_{238}}{dt} = -\sigma_{a,238}\bar{N}_{238}\phi, \tag{1b}$$

$$\frac{d\bar{N}_j}{dt} = -\sigma_{a,j}N_j\phi + \sigma_{c,j-1}\bar{N}_{j-1}\phi, \tag{1c}$$

where $\bar{N}$ is the number of atoms per unit volume, σ_a the absorption cross-section, σ_c the capture cross-section, ϕ the neutron flux and the subscript j represents the isotopes ^{239}Pu, ^{240}Pu, ^{241}Pu, ^{242}Pu. For convenience the time variable is transformed to a burnup increment ($\phi\Delta t \rightarrow \Delta bu$):

$$\Delta bu = \frac{q'''\Delta t}{\rho_{fuel}} = \frac{\alpha}{\rho_{fuel}}\sum_k \sigma_{f,k}\bar{N}_k\phi\Delta t, \tag{2}$$

where q''' is the power density, ρ_{fuel} the fuel density, $\sigma_{f,k}$ the fission cross-section of isotope k and α is a conversion factor ($=3.8\times10^{-16}$). The quantity $\Sigma_k\sigma_{f,k}\bar{N}_k\phi$ is the number of fissions per unit volume per unit time. The basic equations can be written as,

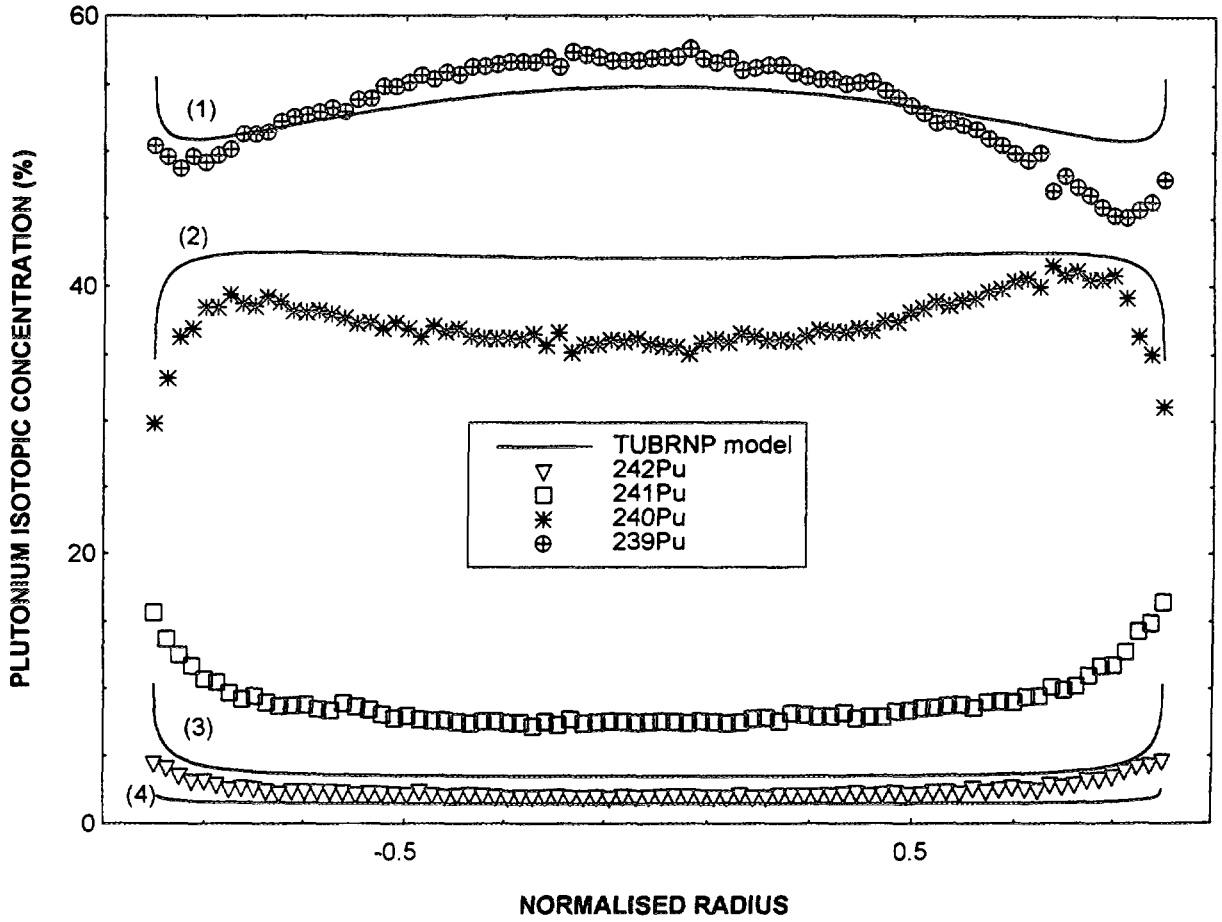

Fig. 1. The isotopic plutonium composition plotted as a function of fuel radius as determined by SIMS (PWR) and predicted by TUBRNP. The curves labelled 1 to 4 correspond to the predictions for the isotopes 239 to 242.

$$\frac{d\bar{N}_{235}}{dbu} = -\sigma_{a,235}\bar{N}_{235}A, \tag{3a}$$

$$\frac{d\bar{N}_{238}}{dbu} = -\sigma_{a,238}\bar{N}_{238}A, \tag{3b}$$

$$\frac{d\bar{N}_{j}}{dbu} = -\sigma_{a,j}\bar{N}_{j}A + \sigma_{c,j-1}\bar{N}_{j-1}A, \tag{3c}$$

where

$$A = 0.8815\,\frac{\rho_{fuel}}{\alpha\sum_{k}\sigma_{f,k}\bar{N}_{k}}$$

Note that the cross-sections in the equations above are to be considered average effective cross-sections valid for a specific reactor type: here we are interested in PWR and BWR conditions.

2.1 LOCAL CONCENTRATIONS AND RADIAL PROFILE

The fuel cross-section is divided into 500 radial zones and the plutonium concentration in each zone is obtained from the distribution of the thermal neutron capture and resonance absorption: these are treated separately. The former is just the radial thermal neutron flux. The contributions of resonance absorption effects (in ^{238}U and ^{240}Pu) are modelled by distributing the plutonium isotopes ^{239}Pu and ^{241}Pu according to given functions (form factors). To derive local concentrations the following set of equations is used,

$$\frac{dN_{235}(r)}{dbu} = -\sigma_{a,235} N_{235}(r) A, \tag{4a}$$

$$\frac{dN_{238}(r)}{dbu} = -\sigma_{a,238} \bar{N}_{238} f_1(r) A, \tag{4b}$$

$$\frac{N_{239}(r)}{dbu} = -\sigma_{a,239} N_{239}(r) A + \sigma_{c,238} \bar{N}_{238} f_1(r) \tag{4c}$$

$$\frac{N_{240}(r)}{dbu} = -\sigma_{a,240} \bar{N}_{240} f_2(r) A + \sigma_{c,239} N_{239}(r) \tag{4d}$$

$$\frac{N_{241}(r)}{dbu} = -\sigma_{a,241} N_{241}(r) A + \sigma_{c,240} \bar{N}_{240} f_2(r) \tag{4e}$$

$$\frac{dN_{242}(r)}{dbu} = -\sigma_{a,242} N_{242}(r) A + \sigma_{c,241} N_{241}(r) A \tag{4f}$$

The local concentrations of ^{238}U and ^{240} Pu, $N_{238}(r)$ and $N_{240}(r)$, are written as $\bar{N}_{238} f_1(r)$ and $\bar{N}_{240} f_2(r)$ where $f_i(r)$, i = 1,2 are radial shape functions with normalisation factors defined by,

$$\frac{\int_{r_{in}}^{r_{out}} f_i(r)\, r dr}{r_{out}^2 - r_{in}^2} = 1 \qquad i = 1,2 \tag{5}$$

where r_{in} and r_{out} are the inner and outer fuel radii. The shape functions take into account the resonance absorption in ^{238}U and ^{240}Pu that lead to the formation of ^{239}Pu and ^{241}Pu, respectively. These distribution functions can be interpreted as the combination of a constant production of ^{239,241}Pu from thermal neutron capture plus a highly non-linear term for production due to resonance absorption.

The local power density q'''(r) which is needed for the thermal analysis is proportional to the neutron flux and the macroscopic cross-section for fission,

$$q'''(r) \propto \sum_k \sigma_{f,k} N_k \Phi \tag{6}$$

In order to determine ϕ, thermal flux diffusion theory can be applied and the resulting solutions of the differential equation are,

$$\phi(r) \propto I_0(\kappa r) \qquad \text{for a solid cylinder,} \tag{7a}$$

$$\phi(r) \propto I_0(\kappa r) + \frac{I_1(\kappa r_{f,out})}{K_1(\kappa r_{f,out})} K_0(\kappa r) \quad \text{for a hollow cylinder.} \tag{7b}$$

where I and K are the modified Bessel functions. The inverse diffusion length, κ, is given by,

$$\kappa = \sqrt{\frac{\Sigma_{a,tot}}{D}},$$

where $\Sigma_{a,tot} \approx \sum_k \sigma_{a,k} \overline{N}_k$, $D = \frac{1}{3\Sigma_s} = \frac{1}{3\sigma_s \overline{N}_{tot}}$; $\overline{N}_k$ and $\overline{N}_{to}$ are the averaged values.

For the non-linear part of the distribution function, due to resonance absorption, the following function is used,

$$_i \propto 1 + p_1 \exp\left(-p_2 (r_{out} - r)^{p3}\right) \qquad i = 1, \tag{9}$$

where p_1, p_2 and p_3 are constants. This is based on the empirical radial shape function of Palmer et al. [3]. The values of the parameters used for MOX data are the same as those for UO_2 fuels. This model has been successfully applied to the case of UO_2 fuels (both PWR and BWR) with burnups between 21 and 64 GWd/t and enrichments in the range 2.9 to 8.25% [2].

3. EXPERIMENTAL DATA

The dataset used to test the validity of the model has been taken from a number of sources. The MOX fuel specimens were fabricated by different processes and were cut from rods of different design (PWR and BWR). The pellet and pin design characteristics were in the range given in Table I. The quantitative radial and local Pu distributions in the irradiated fuel samples were evaluated at PSI by secondary ion mass spectrometry (SIMS) and electron probe microanalysis (EPMA).

3.1 MEASUREMENT OF THE RADIAL PU DISTRIBUTION

To determine the relative Pu isotopic distribution and the burnup across MOX fuel pellet cross-sections a modified, shielded A-DIDA-SIMS [6] has been used. Measurements were made according to the method developed at PSI [5].

Before mounting and transferring the samples to the SIMS machine the selected fuel sections were prepared by grinding and polishing to a thickness of about 1 mm. Under UHV an O_2^+ primary beam of 12 keV energy at a beam current of 200 nA and a spot size of about 50 μm were used for operation. This beam was scanned over an area of about 0.1 0.1 mm in order to average out local inhomogeneities in composition and surface texture. Point analysis at step intervals of 0.1 mm along five parallel line scans over the diameter was performed. Secondary ions of the MO^+ type were normally monitored because the count rates for these are higher. A normalisation procedure was applied to minimize the geometrical, physical and chemical effects on the secondary ion count rates [5]. The relative count rates were

Table I **Range of relevant pellet and pin design characteristics**

pellet radius (mm)	4.00 - 5.53
pellet density (%TD)	94.0 - 95.6
^{235}U (wt%)	.23 - .72
Pu/(U+Pu) (wt%)	2.8 - 11.5
burnup (GWd/tM)	15 - 55

transformed into local isotopic compositions using radiochemical analysis results carried out on adjacent fuel samples.

The acquisition time (range: 1-20s) was set to give a statistical error of 3% for the accumulated counts of the isotope with the lowest secondary ion intensity. The overall error for an individual isotopic concentration was calculated to be better than 4%. Because of the instrumental arrangement inherent measurement errors were observed at larger pellet diameters, leading to systematic tilts for the radial isotopic distribution of ^{235}U and the burnup. This was compensated by linear regression correction around the central points. For most of the peripheral points in the burnup distribution the relative corrections made are significant and can reach about 10%. This possibly leads to an overall uncertainty of around 5%. It is pointed out that the burnup has been calculated from the measured ^{148}Nd concentration and includes estimates of the secondary ion yields in the normalisation and the unknown contribution of ^{148}Sm in the SIMS count rate. These are of minor influence however, hence the error limits for the burnup at the rim are estimated to lie between 5 and 10%. Generally the effects of cracks, pores, the cold gap and different zones of surface finish are not included in the error estimation. This can also cause local systematic deviations in the measured relative count rates.

Additional information was obtained with the electron probe microanalyser (Camebax SXR/SX50; WDS-EPMA) which is normally used to make quantitative elemental point measurements. Using the beam scanning mode an attempt was made to determine the radial Pu concentration distribution. However, the size of the area that can be scanned is limited by the geometry of the diffracting crystal. Also, the loss of counts due to the imperfect surface state (presence of pores and cracks) introduces uncertainties in the measured concentrations. Therefore, point analysis was used and the analysed area was about 10 times smaller than that in the SIMS analysis. This means that EPMA was more susceptible to local Pu inhomogeneities and as a result a smooth radial Pu profile could not be obtained.

In the rim zone uncertainties exist due to the poor positioning capabilities of the ion beam in SIMS which leads to undesired contributions from the fuel/cladding gap. Here, the capacity of EPMA to provide local Pu concentration is an advantage. The relative error for EPMA with reference to the radiochemically determined value lies between 6% and 11% for the chosen conditions (HV 20 keV, 170 nA, 50 s counting time).

4. ANALYSIS OF DATA

Analysis was done using results from the techniques described above with PWR and BWR data. Values for the neutron absorption and capture cross-sections were altered for the BWR model. Note that there are no free parameters in the model: the only input parameters are the fuel geometry (r_m, r_{out}), percentage porosity, enrichment, average burnup, initial concentrations of ^{235}U and the plutonium isotopes.

4.1 PWR DATA

The *TUBRNP* model was used to predict the final amount of plutonium and its isotopic composition for the samples studied. Comparisons between the results of radiochemical analysis and *TUBRNP* calculations gave good agreement, especially for the total final plutonium content. The predictions by *TUBRNP* differed from the measured values by at most 12%, see Table II for two examples. The ORIGEN code (ORIGEN2 version 2.1 for the PC [7] using a MOX cross-section library) was also used to predict the final total and isotopic plutonium concentrations. The results of *TUBRNP* and ORIGEN are comparable, see Table II, demonstrating that the simpler *TUBRNP* model is sufficiently detailed to model the complicated processes of the formation and destruction of plutonium isotopes in MOX fuel. Moreover, the *TUBRNP* model provides the radial dependence of these concentrations which cannot be done by ORIGEN.

In Figs. 1 to 4 the plutonium isotopic composition, as determined by SIMS, is plotted as a function of fuel radius. The solid curves are the *TUBRNP* model predictions. The agreement is good except for the over and under prediction of the ^{240}Pu and ^{241}Pu concentrations, respectively. This can be seen in greater detail in Table II where the percentage difference between the model predictions and experiment are given (note that the absolute values for $^{241,242}Pu$ are relatively small, a few percent). This can be ameliorated by improving the values for the cross-sections (in progress).

In Fig. 5, an example of the burnup profile (from SIMS ^{148}Nd measurements) along with the *TUBRNP* prediction is given. Given the spread of the data it is difficult to draw any definite conclusions. Nonetheless the agreement is reasonable: results were similar for the other cases.

4.2 BWR DATA

The *TUBRNP* model was used with the introduction of new cross-sections for the BWR. The model was successful in providing very good predictions for the total plutonium content (see Table III, example 1 and Fig. 6) and its isotopic composition (Figs. 7 and 8) in each of the cases studied, see also Table III. In Fig. 6 the total amounts of plutonium, as determined by SIMS, EPMA and the *TUBRNP*

Table II **Percentage deviation of the predictions of *TUBRNP* and ORIGEN from the results of radiochemical analysis for two PWR samples (note that the indicate over and under prediction). The ORIGEN calculations were done with the latest ORIGEN 2.1 PC version.**

	Example 1		Example 2	
	TUBRNP	ORIGEN	TUBRNP	ORIGEN
Total Pu	-11.98	-7.69	+7.45	+11.63
^{239}Pu	-0.59	-1.61	+1.84	+3.42
^{240}Pu	+11.7	-0.99	+9.95	-3.06
^{241}Pu	-40.7	+32.6	-13.46	+17.78
^{242}Pu	-20.8	-5.0	-9.28	-7.23

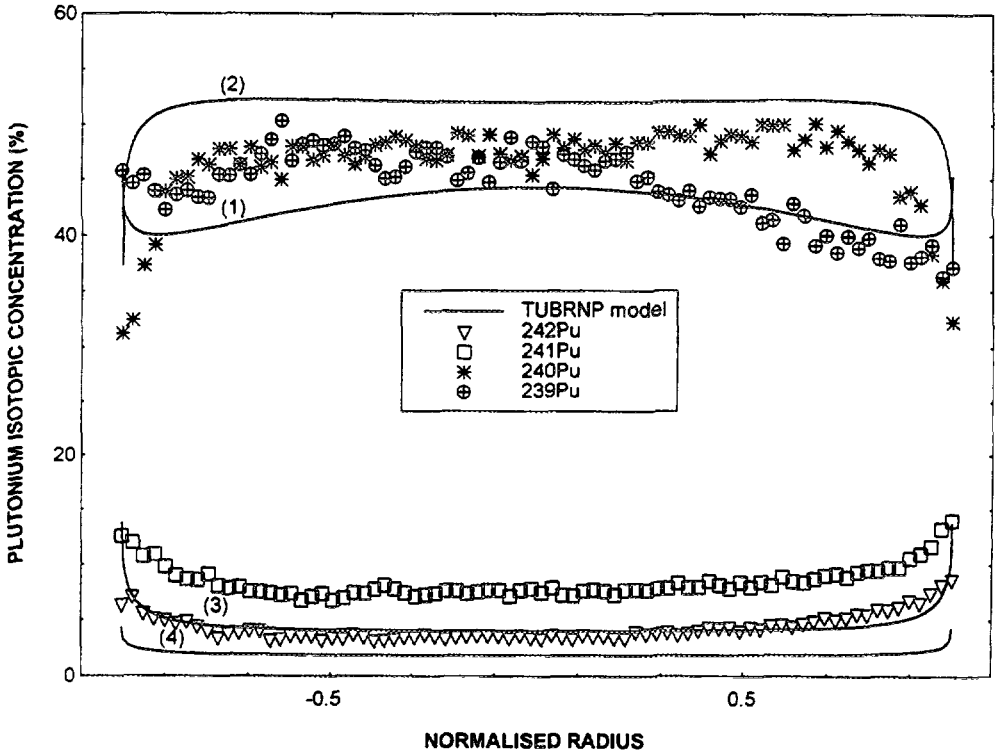

Fig. 2. The isotopic plutonium composition plotted as a function of fuel radius as determined by SIMS (PWR) and predicted by TUBRNP. The curves labelled 1 to 4 correspond to the predictions for the isotopes 239 to 242.

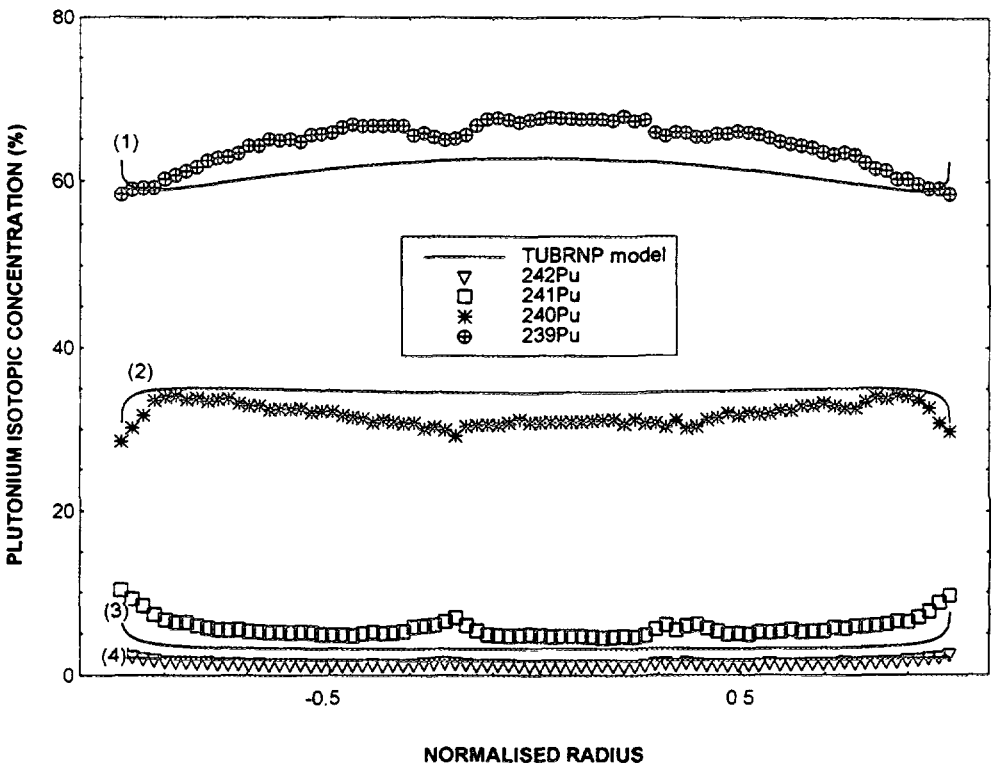

Fig. 3. The isotopic plutonium composition plotted as a function of fuel radius as determined by SIMS (PWR) and predicted by TUBRNP. The curves labelled 1 to 4 correspond to the predictions for the isotopes 239 to 242.

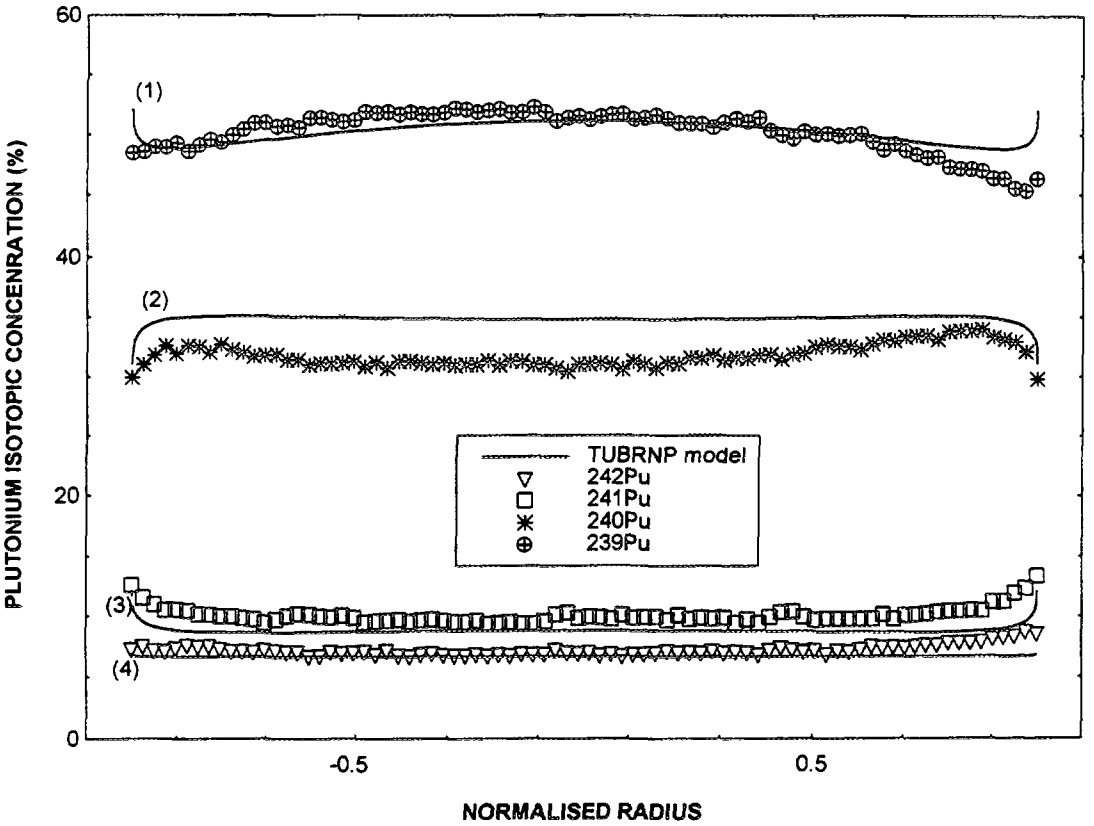

Fig. 4. The isotopic plutonium composition plotted as a function of fuel radius as determined by SIMS (PWR) and predicted by TUBRNP. The curves labelled 1 to 4 correspond to the predictions for the isotopes 239 to 242.

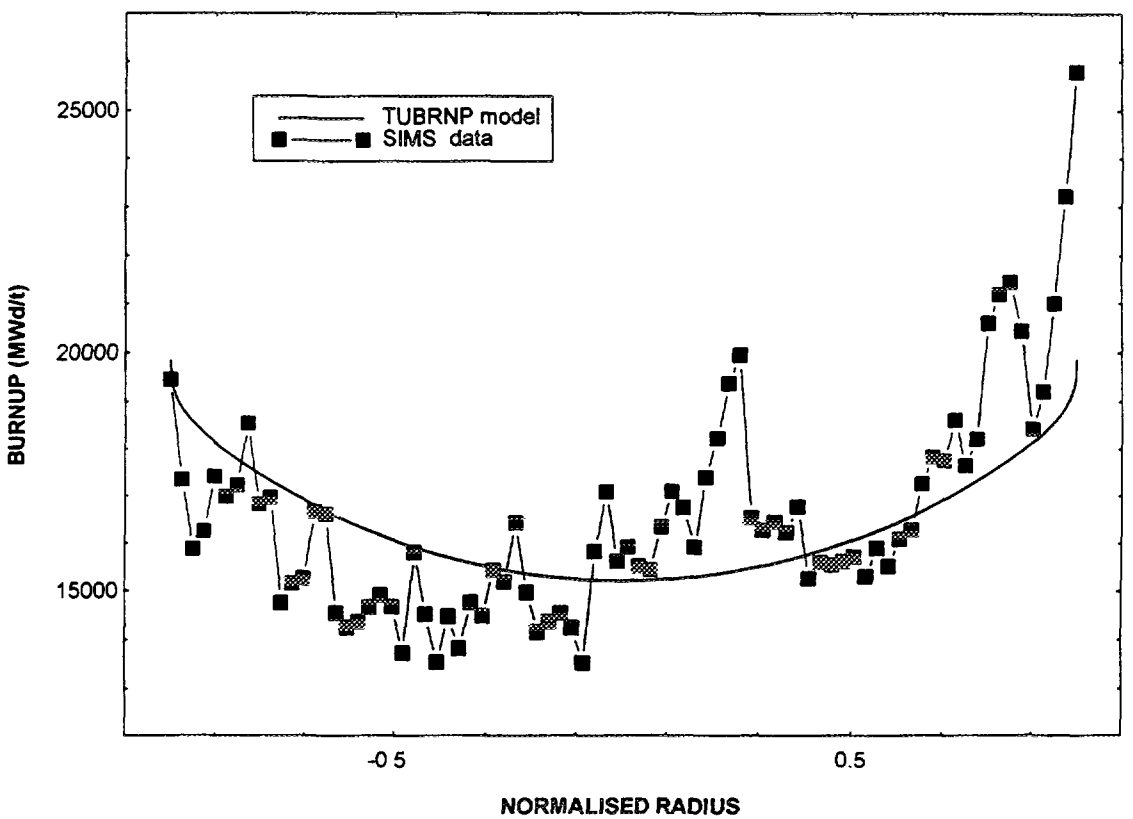

Fig. 5. The burnup (MWd/t) plotted as a function of radius as determined from SIMS ^{148}Nd measurements (PWR) and the TUBRNP prediction.

Table III **Percentage deviation of the predictions of *TUBRNP* and ORIGEN from the results of radiochemical analysis for two BWR samples (note that the indicate over and under prediction). The ORIGEN calculations were done with the latest ORIGEN 2.1 PC version.**

	Example 1		Example 2	
	TUBRNP	ORIGEN	TUBRNP	ORIGEN
Total Pu	-2.38	+10.59	-5.05	+4.17
^{239}Pu	+10.1	-2.05	+6.71	+5.71
^{240}Pu	+11.75	-10.81	+13.2	+0.74
^{241}Pu	-38.69	+58.6	-31.9	+4.16
^{242}Pu	-28.32	+16.77	-23.0	-10.34

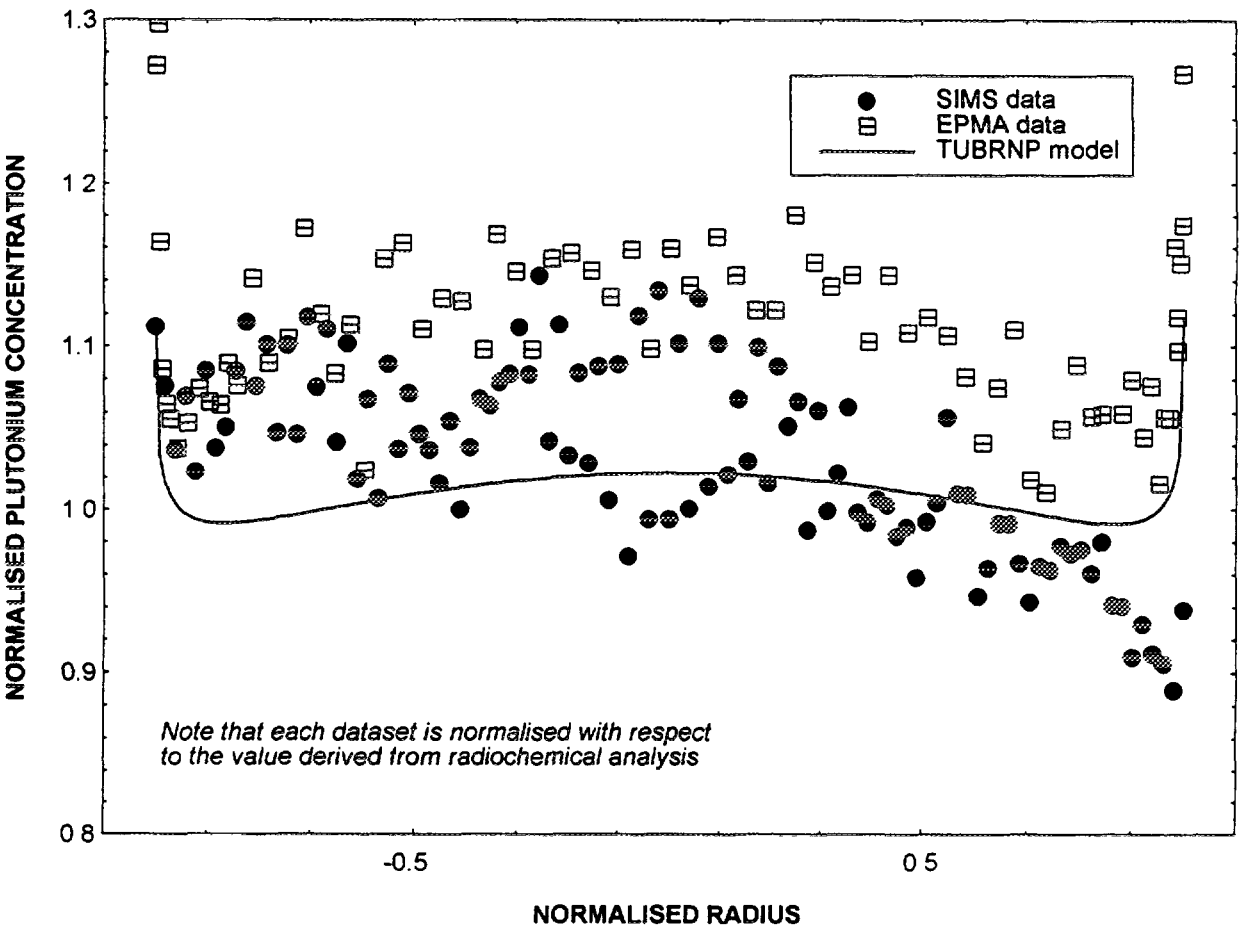

Fig. 6. Total plutonium content as predicted by TUBRNP and measured by SIMS and EPMA plotted a function of radius for a BWR sample. The data is normalised to the total plutonium content as determined by radiochemical analysis.

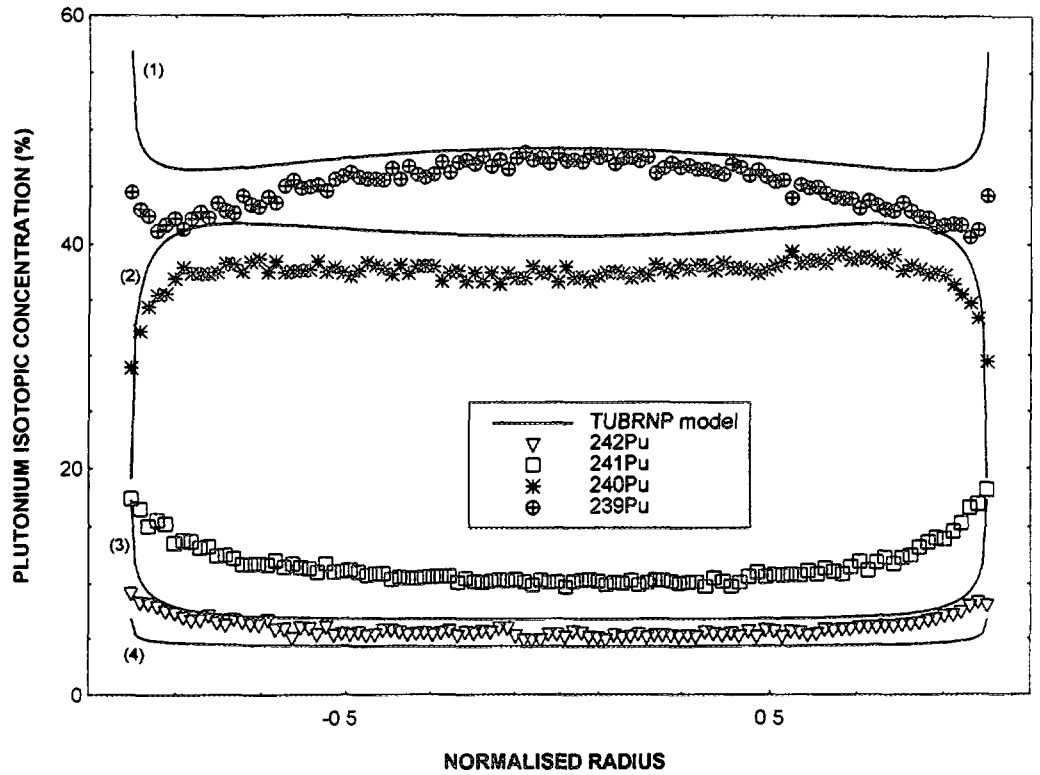

Fig. 7. The isotopic plutonium composition plotted as a function of fuel radius as determined by SIMS (BWR) and predicted by TUBRNP. The curves labelled 1 to 4 correspond to the predictions for the isotopes 239 to 242.

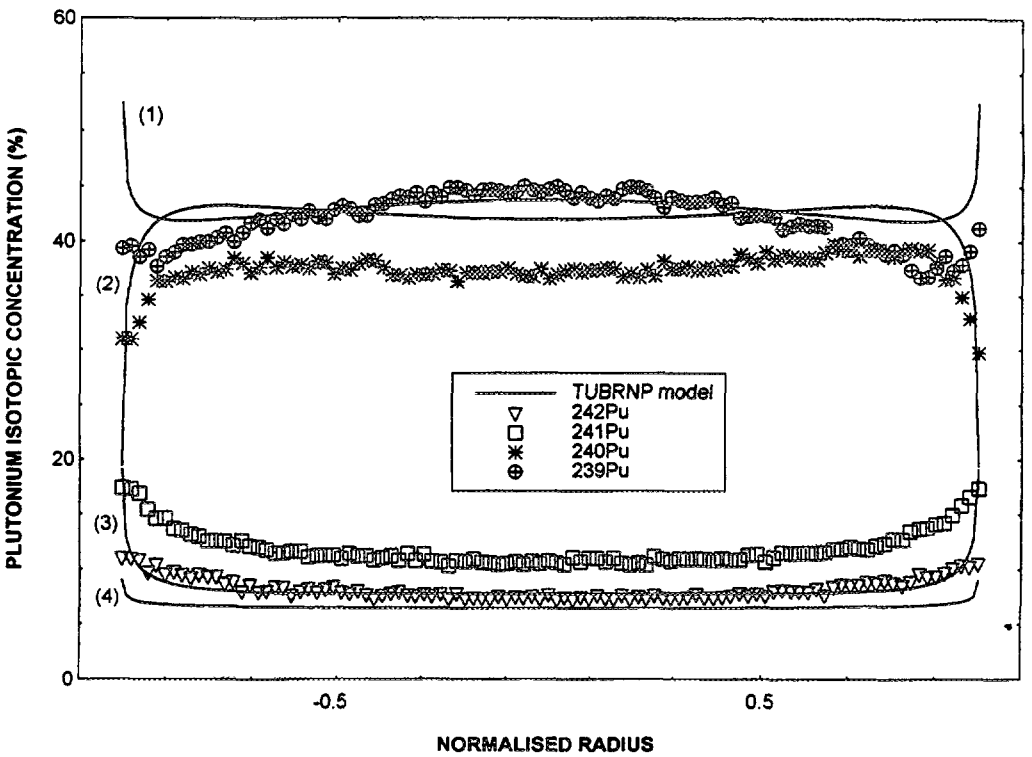

Fig. 8. The isotopic plutonium composition plotted as a function of fuel radius as determined by SIMS (BWR) and predicted by TUBRNP. The curves labelled 1 to 4 correspond to the predictions for the isotopes 239 to 242.

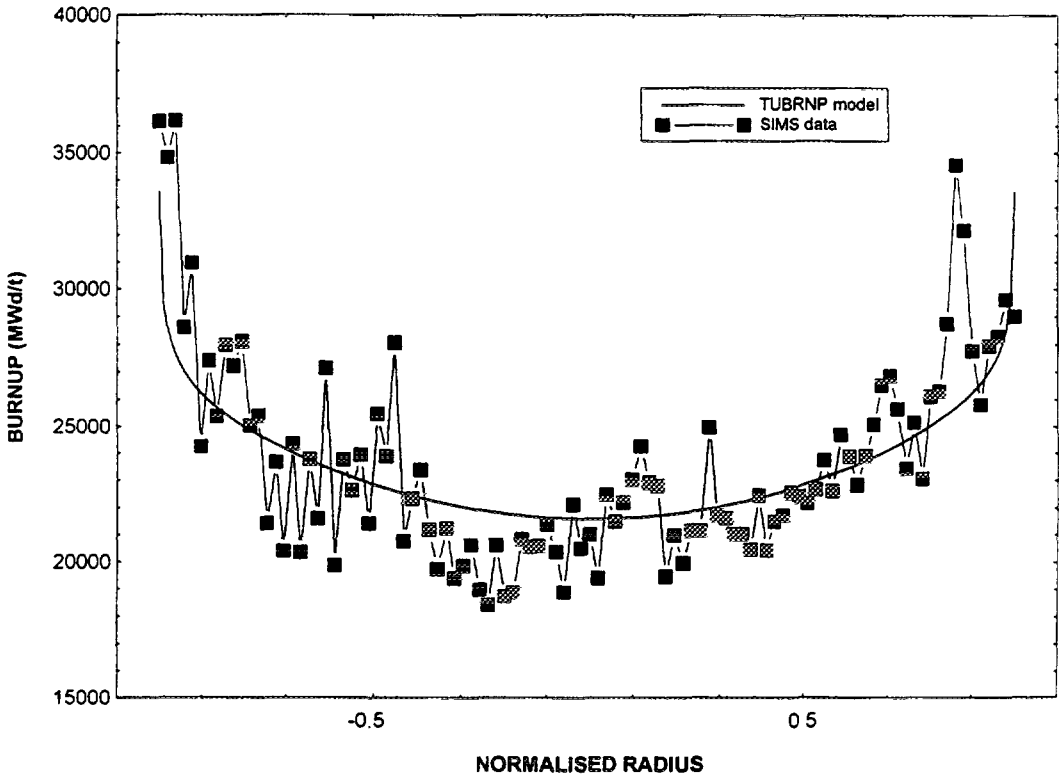

Fig. 9. The burnup (MWd/t) plotted as a function of radius as determined from SIMS ^{148}Nd measurements (BWR) and the TUBRNP prediction.

model are plotted as a function of fuel radius. All of the data is normalised to the value derived from radiochemical analysis. As can be seen the *TUBRNP* (MOX version) predictions show good agreement with experiment. In particular the buildup of plutonium near the surface is correctly modelled. This increased Pu production near the edge of the fuel is small when compared with the marked increase for UO_2 fuels [2]. There are two reasons for this; first, the MOX agglomerates reduce this effect by decreasing the amount of available ^{238}U at the pellet surface. Second, the high plutonium concentrations in the agglomerates mask any increase of plutonium in the matrix. The predictions for the isotopic composition profiles are also very good, Table III and Figs. 7, 8. Calculations with ORIGEN showed comparable results and in some cases the *TUBRNP* predictions were closer to the measured values. The predicted burnup profile in Fig. 9 is in good agreement with the measured data.

5. SUMMARY

A new version of the *TUBRNP* model has been developed in order to predict the buildup of plutonium and its isotope in MOX fuels. In its present form it includes the buildup of $^{239,241}Pu$ near the edge of the fuel due to resonance capture in ^{238}U and ^{240}Pu. New cross-sections have been introduced for the BWR case. The model predictions are in good agreement with the radiochemical results for total Pu content and with SIMS and EPMA measurements of the radial profiles. Comparisons with ORIGEN predictions showed similar results. Work on improving the model by using better values for the cross-sections and treating the flux depression is in progress. Given the complexity of MOX fuels, the model, even in its present form, is a valuable tool for the analysis of mixed oxide fuel data.

ACKNOWLEDGEMENTS

The authors would like to thank K. Lassmann for many productive discussions.

REFERENCES

[1] BELL M.J., "ORIGEN-The ORNL Isotope Generation and Depletion Code", ORNL-4628 (1973).

[2] LASSMANN K., O'CARROLL C., VAN DE LAAR J. and WALKER C.T., The radial distribution of plutonium in high burnup UO_2 fuels, J. Nuc. Mater. 208 (1994) 223.

[3] PALMER I.D., HESKETH K.W. and JACKSON P.A., Water Reactor Fuel Element Performance Computer Modelling, (GITTUS J. ed), Applied Science, UK (1983) 321.

[4] K. LASSMANN, TRANSURANUS: a fuel rod analysis code ready for use, J. Nuc. Mater. 188 (1992) 295.

[5] H.U. ZWICKY, E.T. AERNE, A. HERMANN, H.A. THOMI and M. LIPPENS, Radial plutonium and fission product isotope profiles in mixed oxide fuel pins evaluated by secondary ion mass spectrometry, J. Nuc. Mater. 202 (1993) 65.

[6] G. BART, AERNE T., FLÜCKIGER U. and SPRUNGER E., Modification of a secondary ion mass spectrometer to allow the examination of highly radioactive specimens, Nuclear Instr. and Meth. 180 (1981) 109.

[7] OAK RIDGE NATIONAL LABORATORY, ORIGEN 2.1: Isotope generation and depletion code--matrix exponential method, internal report CCC-371 (1991).

SESSION 3
CLAD CORROSION/PCI AND TRANSIENT MODELLING

MODELLING THE WATERSIDE CORROSION OF PWR FUEL RODS

XA9744809

T.J. ABRAM
Fuel Engineering Department,
British Nuclear Fuels plc,
Salwick, Preston,
United Kingdom

Abstract

The mechanism of zirconium alloy cladding corrosion in PWRs is briefly reviewed, and an engineering corrosion model is proposed. The basic model is intended to produce a best-estimate fit to circumferentially-averaged oxide thickness measurements obtained from inter-span positions, away from the effects of structural or flow mixing grids. The model comprises an initial pre-transition weight gain expression which follows cubic rate kinetics. On reaching a critical oxide thickness, a transition to linear rate kinetics occurs. The post-transition corrosion rate includes a term which is dependent on fast neutron flux, and an Arrhenius thermal corrosion rate which has been fitted to isothermal ex-reactor data. This thermal corrosion rate is enhanced by the presence of lithium in the coolant, and by the concentration of hydrogen in the cladding. Different cladding materials are accounted for in the selection of the model constants, and results for standard Zircaloy-4, low tin (or "optimized") Zircaloy-4, and the Westinghouse advanced alloy ZIRLO™ are presented. A method of accounting for the effects of grids is described, and the application of the model within the ENIGMA-B and ZROX codes is discussed.

1. INTRODUCTION

Alloys of zirconium and tin, known as the Zircaloys, were developed by Westinghouse in the 1950s for use as fuel cladding in pressurized water reactors. Since that time, trends towards flexible fuel management and higher discharge burnups in modern commercial PWR plant have led to increasingly demanding fuel duties, which have challenged the corrosion resistance of established Zircaloy-4 cladding materials. As a result, the waterside corrosion of PWR fuel rods, and the associated accumulation of hydrogen within the cladding, are currently regarded as amongst the factors which are most likely to limit fuel duties.

The purpose of this paper is to outline the development of a new engineering corrosion model, which aims to encompass the mechanisms which govern the corrosion of zirconium alloys in PWRs, whilst retaining a format suitable for incorporation into general fuel modelling codes. The scope of the model is limited to corrosion in predominantly single phase aqueous environments, over the temperature range 550-700 K. The mechanisms thought to govern the corrosion of zirconium-based alloys are briefly reviewed in Section 2, and a format for the model is proposed. The application of the model is described in Section 3, and its validation is summarized in Section 4.

2. THE CORROSION OF ZIRCONIUM-BASED ALLOYS IN PWR ENVIRONMENTS

2.1 ISOTHERMAL EX-REACTOR CORROSION.

The isothermal corrosion of zirconium alloys is often conveniently divided into pre-transition and post-transition regimes, each characterised by its reaction rate.

2.1.1 Pre-Transition Corrosion

The pre-transition corrosion kinetics observed for Zircaloy-4 typically follow a cubic rate law [1]. The proposed model is based on the data of Dyce [2] and Stehle [3], and follows the form proposed by Garzarolli, Garde *et al* [4] :

$$\frac{dw}{dt} = \frac{A}{\delta_{OX}^2} \cdot \exp\left(\frac{-Q_{PRE}}{R \cdot T} \right) \quad (1)$$

where dw/dt is the weight gain rate in $mgO_2/dm^2/day$; T is the metal-oxide interface temperature in K; δ_{OX} is the local oxide thickness in m; A is a constant with units of mgO_2/day; Q_{PRE} is an activation energy term in kJ/kmol; and R is the universal gas constant (8.3144 kJ/kmol/K).

The constants A and Q_{PRE} have been derived using the pre-transition measurements in [2] and [3], although A has been allowed to vary slightly in order to improve the fit statistics.

2.1.2 Post-Transition Corrosion

Beyond a characteristic thickness, the corrosion rate increases to an approximately linear relation with time. For Zircaloy-4, this transition from cubic to linear kinetics occurs at a clearly defined point on a plot of weight gain against time. Garzarolli *et al* [4] have suggested that the transition thickness is a function of metal-oxide interface temperature, and over the temperature range of interest for PWR cladding, this corresponds to a transition thickness of 2-2.5μm. A constant value of 2.2μm has been assumed for the current model.

The post-transition oxide layer is known to develop a cracked and porous structure, and the presence of microcracks is thought to provide a more direct route for oxygen migration than diffusion along crystallite boundaries. However, it is thought that neither the cracks nor the pores extend completely to the oxide-metal interface, and therefore that a thin "barrier" layer of impervious oxide is always present. A linear oxidation rate would then be approached when the rate of formation of the "barrier" layer and the rate of porosity generation reach an equilibrium. The linear post-transition corrosion rate adopted for standard Zircaloy-4 in the present model is illustrated in Fig. 1, and follows a similar form to eqn. (1), but without the inverse dependence on oxide thickness. Similar models proposed by Garzarolli *et al* [4], Hillner [5], and McDonald *et al* [6] are included in Fig. 1 for comparison. The model for low tin Zircaloy-4 uses the same activation energy term as the standard Zircaloy-4 model, but with a modified pre-exponential frequency factor. The model used for ZIRLO™ is taken from Ref. [7].

The out-of-pile corrosion tests which are used to define the pre- and post-transition corrosion rates are performed in autoclaves. Such tests are relatively inexpensive, but do posses certain limitations.

(a) The absence of a heat flux precludes any mechanisms which depend on a thermal gradient, notably the increase in metal-oxide interface temperature, but also the diffusion of reactants within the oxide layer, and the re-distribution of mobile species such as hydrogen and lithium.

(b) The absence of radiation precludes vacancy formation due to fast neutron damage, and localized radiolysis of the coolant.

(c) The practicalities of maintaining test conditions for extended periods limits the oxide thicknesses achievable.

These limitations result in significant differences between corrosion rates obtained from isothermal autoclave tests, and those inferred from measurements on irradiated fuel cladding. These differences are accounted for by the application of enhancement or acceleration factors, which are described in the following Sections.

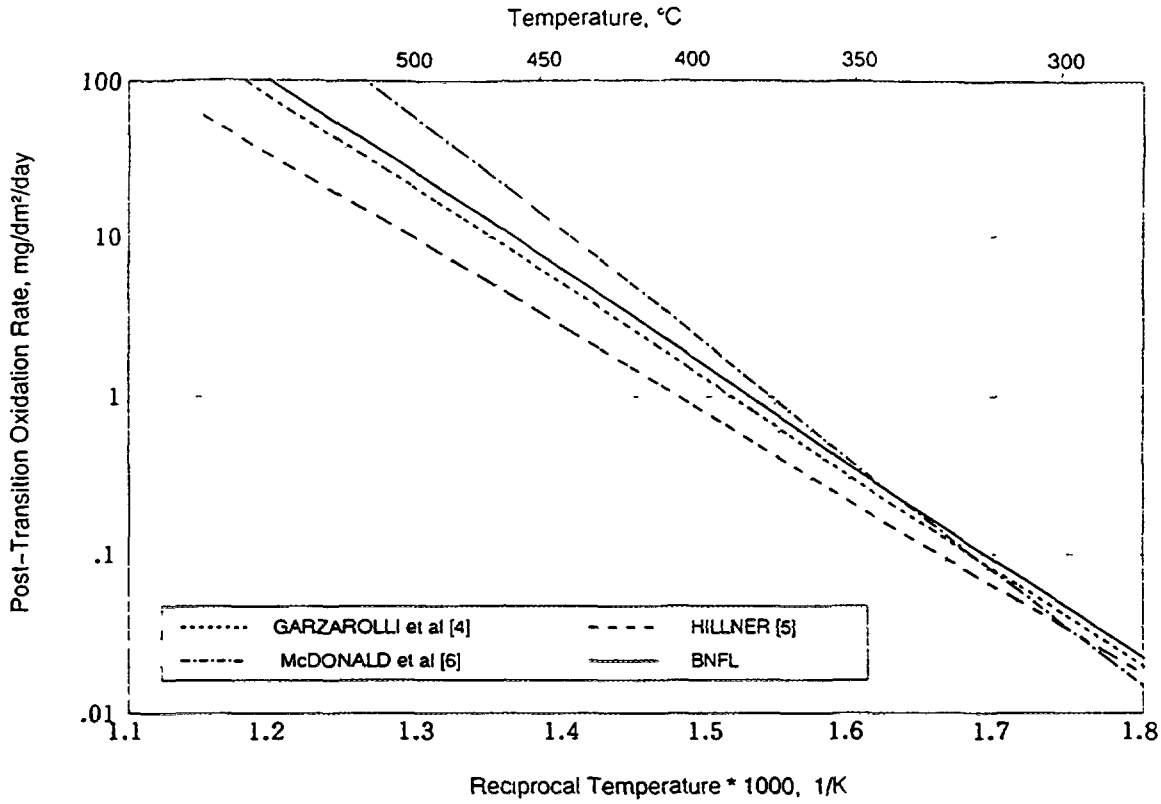

FIG. 1. Post-Transition Arrhenius Expressions for Standard Zr-4

2.2 HEAT FLUX EFFECTS

The principal effect of a heat flux is to increase the temperature at the interface between the oxide and the underlying metal, due to temperature drop across the existing oxide layer. Since the calculated interface temperature will be strongly influenced by the value of oxide thermal conductivity assumed, a review of available conductivity data has been undertaken.

The data of Kingery [8], with a mean value of 1.8 W/m/K, are usually cited as being typical of fully-dense, unirradiated oxide. This value, which is independent of temperature in the range 300-450°C, is considered to be an appropriate for thin, pre-transition oxide layers. As the thickness of the oxide layer increases, its morphology changes from an impervious film to a cracked, porous structure. The cracking pattern, which will be affected by the geometry of the specimen, is likely to influence the oxide conductivity. Therefore, only measurements obtained from specimens of typical fuel rod geometry have been included in this review.

Garzarolli *et al* [4] suggest that the conductivity of irradiated specimens is somewhat lower than oxide films grown in autoclaves, but that the effective conductivity of the oxide is largely independent of temperature over the region of interest. They also report that the conductivity appears to decrease with increasing oxide thickness, and this is supported by the data of Gilchrist, who has reported the results of measurements on unirradiated specimens obtained using a laser flash method [9,10]. Further recent data on irradiated oxide has been obtained from reactor A, where the mean conductivity of a 60μm oxide layer is reported to be around 1.1 W/m/K.

All of these data have been plotted in Fig. 2, together with various recommendations made in recent years. Using this data, the following model for the effective thermal conductivity of the oxide layer k_{ox} (in kW/m/K) has been developed.

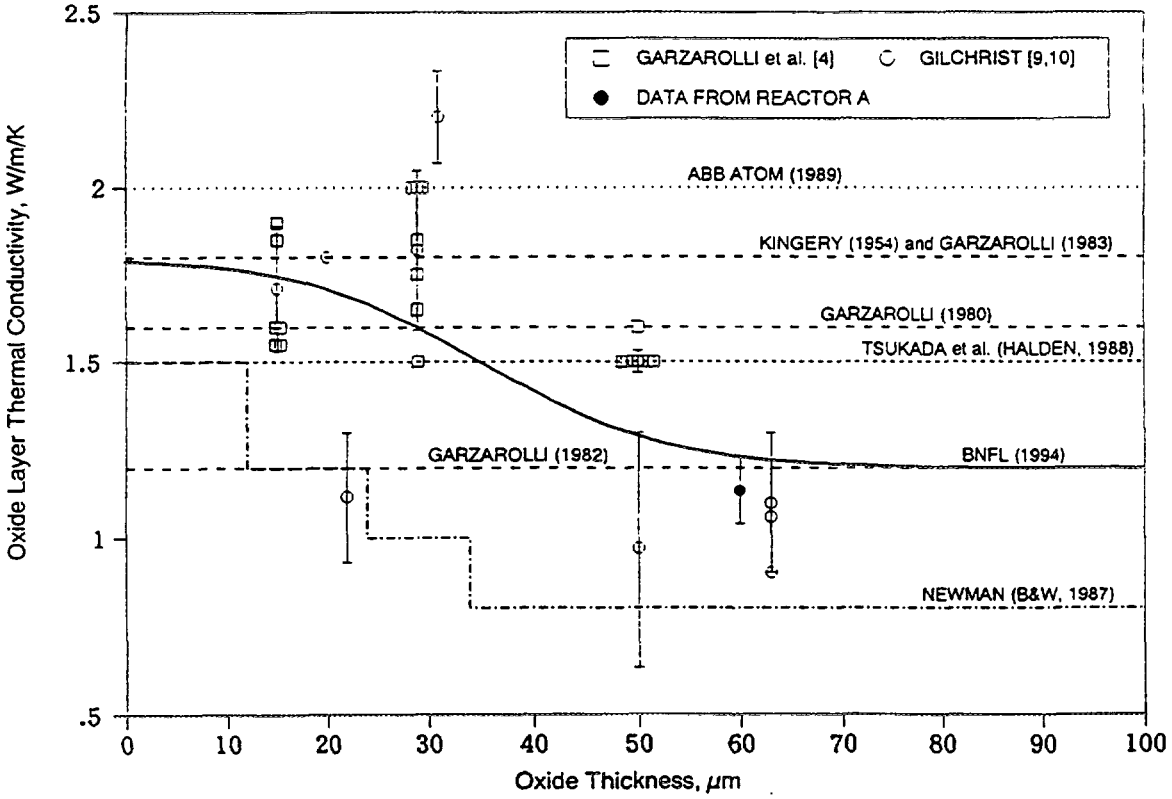

FIG. 2. Zirconium Oxide Thermal Conductivity vs. Oxide Thickness: Published recommendations and data

$$k_{OX} = 0.5 \cdot \{ (k_{MAX} + k_{MIN}) - (k_{MAX} - k_{MIN}) \cdot \tanh(U\delta_{OX} - V) \} \quad (2)$$

where: $U = 4. / (\delta_{MIN} - \delta_{MAX})$, $V = 0.5 \cdot (\delta_{MIN} + \delta_{MAX})$

and k_{MAX} and k_{MIN} are the upper and lower values of thermal conductivity (1.8 and 1.2 W/m/K); δ_{OX} is the local average oxide thicknesses in m; and δ_{MAX} and δ_{MIN} are the oxide thicknesses at which k_{OX} is within 5% of k_{MAX} and k_{MIN} respectively (70 and 0 μm).

The smooth reduction is conductivity with thickness is considered to be more realistic than a piecewise linear model, and is considered to be in good agreement with the available data.

2.3 NEUTRON FLUX EFFECTS

Several mechanisms for corrosion enhancement due to a fast neutron flux have been proposed:

(a) The neutron flux creates additional defects in the oxide lattice, which can open new diffusion pathways for oxygen.

(b) Lattice damage may reduce the thermal conductivity of the oxide layer.

(c) Lithium is continually being formed in the coolant by the nuclear reaction $^{10}B(n,\alpha)^{7}Li$. Billot *et al* [12] have suggested that some of this lithium could enter the oxide as a result of recoil energy, and high lithium contents in the oxide layer have been associated with enhanced corrosion rates.

(d) Localized radiolysis of the coolant may concentrate oxidizing species inside cracks in the oxide.

These radiation effects would be expected to result in different corrosion rates for irradiated specimens, although the differences in corrosion rate reported by previous workers range from little or no observed effect [13], to a factor of 1.5 due to Dickson *et al* [14], a factor of between 2 and 2.5 due to

Hillner [15], and a factor of around 4 from an EPRI study. The EPRI model suggested by Garzarolli *et al* contains the following dependence on fast flux :-

$$\frac{dw}{dt} = \{C_o + U\cdot(M\cdot\phi)^{0.24}\}\exp\left(\frac{-Q}{R\cdot T}\right) \quad (3)$$

where ϕ is the fast neutron flux (E > 1. MeV) in n/m^2/s, and C_o, U and M are constants which are adjusted to fit the corrosion database.

Many corrosion models include the effects of irradiation as multiplicative factors on the thermally-induced corrosion rate. Although a multiplicative factor conveniently allows an overall enhancement factor to be defined, it suggests that the effects of temperature and irradiation are cumulative, whereas evidence from corrosion experiments carried out in non-aqueous environments [1] suggest that the irradiation effects reduce with increasing temperature, and become small above 400°C. The results of these experiments may not be directly applicable to aqueous environments, since mechanisms (c) and (d) above were presumably not represented; however, it does seem reasonable that solid-state damage may anneal out at elevated temperatures, and that the effects of irradiation should be assumed to be independent of temperature. This implies an additive irradiation effect, as proposed by Cox [16,17]. The model described in this paper includes an additive effect, but one which retains the form of the EPRI model:

$$\frac{dw}{dt} = C\cdot\phi^{0.24} + F\cdot\exp\left(\frac{-Q}{R\cdot T}\right) \quad (4)$$

2.4 CLADDING HYDROGEN UPTAKE AND ITS EFFECTS

Zirconium has a strong affinity for hydrogen, and readily absorbs it into a solid solution. In PWRs, several potential sources of hydrogen exist:

(a) Zircaloy cladding typically contains around 20μg/g of hydrogen in the as-manufactured condition.
(b) Hydrogen may be generated or released from within the fuel pellet.
(c) A hydrogen overpressure is maintained in the primary circuit to ensure a reducing environment.
(d) Hydrogen is liberated from the water as a result of the oxidation of the cladding.
(e) Radiolytic decomposition of the coolant results in an increase in available H^+ ions.

Modern manufacturing methods avoid high pellet moisture contents, and UO_2 pellet specifications typically limit individual pellet hydrogen contents to < 1 μg/g. Although hydrogen is dissolved in the coolant, evidence from experiments conducted using a tritium as a tracer in a T_2O/H_2O mixture shows that hydrogen isotopes which enter the metal do so as an integral part of the corrosion reaction, and not by reaction with any dissolved hydrogen in the water [1]. This situation persists until hydrogen overpressures of tens of MPa are present [18].

Therefore, to a good approximation, the hydrogen content of the cladding may be assumed to be due entirely to the initial as-manufactured content, plus that which arises from the oxidation of the cladding. Studies [18] have shown that the volume-averaged hydrogen content of a cladding sample from a particular axial location is linearly related to the average oxide thickness over the sample. This indicates that a constant fraction of the hydrogen liberated from the corrosion reaction is absorbed by the cladding. This is known as the pickup fraction, and varies with cladding chemical composition and metallurgy. Using the pickup fraction, a direct calculation of the radially and circumferentially averaged hydrogen content from the average oxide thickness is possible:

$$H = H_o + \frac{27100\cdot F_p\cdot\delta_{OX}}{WALL_o - \delta_{OX}/\lambda} \quad (5)$$

where H is the average local hydrogen content in μg/g; H_0 is the as-manufactured hydrogen content in μg/g; F_P is the hydrogen pickup fraction; $WALL_0$ is the initial cladding wall thickness in m; and λ is the Pilling-Bedworth ratio (1.56 for ZrO_2).

With increasing concentration or decreasing temperature, the terminal solid solubility of precipitation (TSSP) is reached, and one or more of the hydride phases in the Zr-H system is precipitated. The TSSP for Zircaloys has been measured by Slattery [19], and is given by the following relation :

$$TSSP = 41100 \cdot \exp\left(\frac{-28002}{R \cdot T}\right) \tag{6}$$

For cladding temperatures in the range 325-375°C, the TSSP for hydrides is in the range 150-230 μg/g.

Hydrogen in solid solution is mobile within the cladding, and migrates down temperature gradients to concentrate in cooler regions; for example at inter-pellet gaps in the longitudinal direction and towards the cladding surface in the radial direction. Thus, local hydrogen concentrations can exceed the TSSP whilst the average concentration remains considerably less than this limit. Recent experiments conducted by Garde [20] and by NDC [21] on hydrogen charged cladding samples indicate that localized hydriding may result in an enhanced post-transition corrosion rates. Garde has suggested that this is due to hydride-initiated fractures in the metal substrate, which destroy the coherency of the protective oxide sub-layer and allow the oxidation front to advance into the metal. The enhancement factor F_{HYD} calculated from the NDC experiments is a function of local hydrogen concentration H_{LOCAL}:

$$F_{HYD} = \text{MAX}\{\ 1.0,\ \alpha - \beta \log[\ H_{LOCAL}\ ]\ \} \tag{7}$$

The local hydrogen content may be found by solving the transport equation for hydrogen, but this is computationally demanding and is not considered suitable for incorporation into a clad corrosion or fuel performance code. Instead, a simple linear factor is used to convert the average hydrogen contents given by eqn. (5) to the local values used in eqn. (7).

2.5 CLADDING METALLURGY EFFECTS

The typical chemical composition of standard and low tin Zircaloy-4 and ZIRLO™ cladding is given in Table 1. In addition to the alloying additions, impurities of oxygen, carbon and nitrogen are also present. The effects of variations in these alloying elements and impurities have been widely studied, although it is not always clear that the observed effects are due solely to chemistry variations, since differences in cladding heat treatment and microstructure can also have a significant impact on corrosion resistance. Nevertheless, it is possible to draw some general conclusions from the data available in the literature.

Table 1 ***Comparison Between Chemical Composition for Standard Zircaloy-4, Low Tin Zircaloy-4 and ZIRLO™ Cladding Material***

element	*Standard Zr-4*	*Low Tin Zr-4*	*ZIRLO™*	*units*
Nb	< 0.01	< 0.01	1.0	weight %
Sn	1.2-1.45	1.2-1.35	1.0	weight %
Fe	0.2	0.2	0.1	weight %
Cr	0.1	0.1	-	weight %
Si	100	100	100	μg/g
Zr + impurities	balance	balance	balance	--

For Zircaloy-4 alloys, there is strong evidence that decreasing the tin content results in improved corrosion resistance [22,23,24]. Reduced carbon content also appears to have a beneficial effect [22,23]. However, it has been shown that for a given set of annealing parameters, the percentage of recrystallization increases with reducing carbon content, and it may be this which is responsible for the improved corrosion resistance. A relatively high silicon content has been linked with good corrosion resistance by Siemens [23], and also in a recent NFI investigation [25].

The recrystallized fraction in the cladding is determined by the temperature and duration of the final stress-relief anneal. Post-transition corrosion rates have been obtained from 360°C autoclave tests on Zircaloy-4 samples with different recrystallized fractions RX_F, and a regression fit to this data has been calculated. This has been used to define a rate factor F_{RXA}, which describes the isothermal ex-reactor post transition corrosion rate of recrystallized material relative to material with negligible recrystallization:

$$F_{RXA} = 1. - 0.341 RX_F \quad (8)$$

The size and distribution of second phase particles have also been shown to have a significant effect on Zircaloy-4 corrosion rates. For most production processes, where the material undergoes intermediate to fast β-quenching followed by a series of α-anneals (below 800°C, where Fe, Cr and Ni are insoluble), the size and distribution of the second phase particles is closely related to the cumulative annealing parameter ΣA. Siemens have observed a sharp decrease in corrosion resistance below ΣA values of around $3x10^{-18}$ hours, but little dependence on ΣA in the range $5x10^{-18}$ to 10E-16 hours [23].

2.6 WATER CHEMISTRY AND VOID FRACTION EFFECTS

During PWR operation, boric acid is used to control excess reactivity throughout the cycle. If used alone this would result in a corrosive environment due to lowering of the coolant pH, so an alkalizing agent is added to increase pH levels. Lithium hydroxide is used in Western PWRs since it has a low capture cross section, does not produce radioactive species, and is supplemented by lithium produced by the $^{10}B(n,\alpha)^{7}Li$ reaction. Eastern VVERs use either potassium hydroxide or hydrazine. Coolant pH levels are maintained at slightly alkaline values, typically at or above $pH_{300°C}$ 6.9, in order to minimize crud deposition in the core, and hence reduce the production of soluble activation products. This requires careful control of the lithium and boron concentrations, and since the early 1980's most Western PWRs have followed a co-ordinated lithium-boron control strategy. Examples of such strategies are listed below, and are illustrated in Fig. 3.

(a) *Co-ordinated $pH_{300°C}$ 6.9 Chemistry*. The boron and lithium follow a co-ordinated control band which maintains the average hot (300°C) pH at 6.9.

(b) *Modified Chemistry Control Strategy*. Li concentration is held at 2.05 ± 0.15 μg/g until the $pH_{300°C}$ reaches either 7.2 or 7.4, after which the Li and B are co-ordinated to maintain the same $pH_{300°C}$.

(c) *Elevated Lithium Chemistry Control Strategy*. Similar to (b) above, except that the initial Li concentration is held at 3.35 ± 0.15 μg/g until the $pH_{300°C}$ reaches either 7.2 or 7.4.

Although increasing the coolant pH has been shown to result in reduced operator doses, high lithium levels have also been shown to promote IGSCC in Inconel 600 SG tubing, and may enhance corrosion of Zircaloy components. The corrosion of zirconium alloys in lithiated water has been widely studied over many years, and some of the principal results obtained are briefly summarised below.

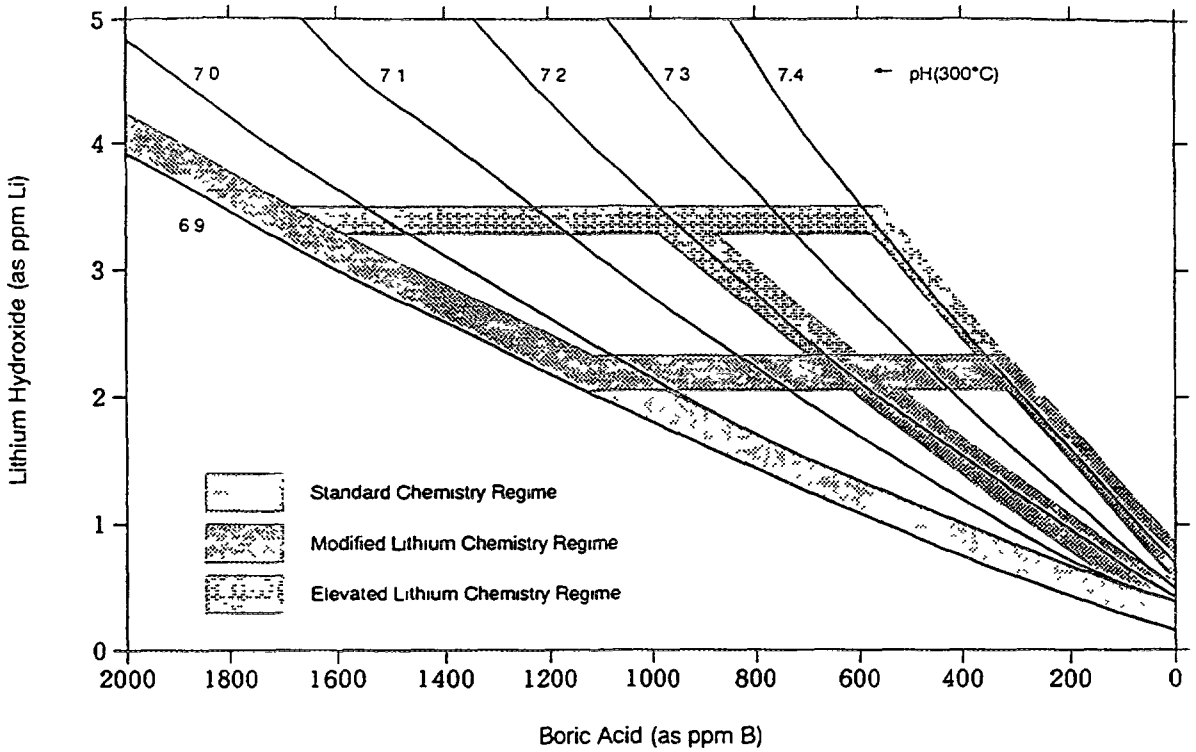

FIG. 3. Examples of co-ordinated Li-B coolant chemistry regimes

2.6.1 Isothermal Autoclave studies

Early work by Hillner and Chirigos [26] and Kass [27] concluded that lithium could significantly enhance Zircaloy corrosion rates, but that this enhancement usually occurred above pH 11.3, unless lithium concentration occurred in crevices. A similar study was conducted by McDonald *et al* [6], where significant enhancement was observed for coolant lithium levels greater than around 100-200 μg/g. Although such concentrations are higher than those typically encountered in PWR coolant, it was suggested that localized nucleate boiling could concentrate lithium in thick, porous oxide layers.

2.6.2 Autoclave and Heat Flux Rig Tests in Li/B

AEA workers have investigated the combined effects lithium and boron on corrosion rate, using isothermal autoclave tests to establish trends and then confirming some of the results using a heat flux rig [28]. The tests were conducted using 220 μg/g lithium in order to simulate the concentrating "hideout" mechanism, and with various concentrations of boron. The results indicate that the presence of as little as 50 μg/g boron has a significant ameliorating effect on the corrosion rate, compared to tests without boron.

2.6.3 CEA data from the CIRENE heat flux loop.

Several experiments have been conducted by the CEA using the CIRENE heat flux loop [29]. A range of conditions have been studied, including void fractions of $0 \leq \alpha \leq 40\%$, lithium concentrations of $0 \leq$ [Li] ≤ 350 μg/g, and boron concentrations of $0 \leq$ [B] ≤ 1000 μg/g. An additional range of tests have been performed in identical pH conditions, but in the presence of KOH instead of LiOH. The results of these tests show that the presence of lithium does enhance post-transition corrosion rates, and that boron has a marked ameliorating effect at concentrations above 200 μg/g. Void fractions $> 5\%$ have been found to enhance corrosion rates in LiOH, with the gross enhancement observed for $\alpha > 10\%$. However, if the same pH values are obtained using KOH instead of LiOH, no evidence of enhanced corrosion is observed.

SIMS analyses of the oxide films have confirmed that lithium is concentrated in the film grown in LiOH, but that no equivalent potassium concentration is observed for films grown in KOH. It is concluded that the effect of void fraction is due to lithium concentration in the oxide film, and that the difference in ionic radii is responsible for the difference in metal ion uptake.

2.6.4 Halden IFA-568 Experiment

In this experiment four PWR rod segments were tested under single phase and nucleate boiling conditions [30]. The coolant contained 3.8-4.5 μg/g lithium and 940-1069 μg/g boron. Evaluations of the lithium effect have been made by comparing measured oxide thicknesses to predicted thicknesses obtained using the EPRI corrosion model. No evidence for a corrosion enhancement was found.

2.6.5 Commercial PWR Experience

Several PWRs have operated for at least part of one cycle with elevated lithium chemistry, although none of these plants has continued with this strategy, due to problems with IGSCC of steam generator tubes and control rod drive mechanism penetrations. Available data is reviewed below, and is summarized in Table 2.

An EPRI sponsored programme has been conducted at Millstone Unit 3 to investigate the effects of elevated lithium on cladding corrosion and plant radiation fields [31]. Plant cycles 2 and 3 were of 18-month duration, and followed elevated lithium chemistry. Comparisons with data from a similar plant (North Anna 1) indicate a slight lithium enhancement of around 15%, but high variability is evident between measurements from the same assemblies. At present, it seems likely that the enhancement factor lies somewhere between 1.0 and 1.15.

Ringhals units 2, 3, and 4 operated elevated lithium chemistry for several 12-month cycles. Oxide thickness measurements have been reviewed by Nuclear Electric [31], and no evidence for enhanced corrosion has been found.

St Lucie unit 1 operated for 8 months out of an 18-month cycle with elevated lithium chemistry [31]. Oxide thicknesses were measured on 102 rods from 9 assemblies, and the results were normalized using the MATPRO corrosion model. It has been concluded that the increase in the MATPRO "corrosion parameter" required to fit the results would result in a 10-15% increase in end of life oxide thickness, and that this result is significant at the 95% confidence level.

Oconee unit 2 operated for one 12-month cycle with elevated lithium [32]. Oxide measurements were then conducted on fuel which had been irradiated for 1, 2, 3 and 4 cycles. No effect was observed for the once and twice-burnt fuel, but high measurements were obtained for the three and four-cycle fuel. A lack of reliable measurements from previous campaigns prevented any firm conclusions from being drawn, although a lithium enhancement in the thick oxide layers was suspected.

Calvert Cliffs units 1 and 2 operated with elevated lithium during 220 efpd of one 24-month cycle [31]. Oxide measurements were assessed by CE to be typical of those expected for the fuel duty, and therefore no lithium effect was concluded.

Table 2 Summary of Reported Commercial PWR Experience with Elevated Lithium

Plant	Elevated lithium exposure	Corrosion enhancement
Oconee	one 12-month cycle	20-50% for 3 & 4 cycle rods
St Lucie 1	8 months at 3.2-3.5μg/g Li	10-15%
Ringhals 2, 3 and 4	~3 months at 3.2-3.5μg/g Li	none
Millstone 3	2x~8 months at 3.2-3.5μg/g Li	approx. 15%
Calvert Cliffs 1 and 2	7 months at 2.2-3.2μg/g Li	none

Based on the experimental and operational evidence available, it is concluded that some enhancement in corrosion rates does occur in the presence of lithium, but that a characteristic oxide thickness is required before any effect is evident. The data also suggest that, for a given lithium concentration, an upper-limit to the corrosion enhancement is approached, again after the accumulation of a second characteristic oxide thickness. The thicknesses at which both the onset and the saturation of the lithium enhancement occur seem to be dependent on the lithium concentration in the bulk fluid. This is supported by the post-transition corrosion rate data of Hillner and McDonald *et al*, which have been obtained at different concentrations of LiOH. This data is plotted in Fig. 4 in the form of weight gain rate at zero LiOH concentration (as predicted by the equation illustrated in Fig. 1) against the enhancement factor required to reproduce the data in the presence of LiOH, in the manner employed by Evans *et al* [22]. This plot shows the relative enhancement factors obtained for various lithium concentrations, together with the enhancement onset and plateau values. This behaviour is expected to be reproduced in-reactor, although the initiating and plateau values of oxide thickness, together with the magnitude of the enhancement, are expected to be altered by the presence of boron in the coolant and by the thermal gradient and neutron damage in the oxide layer.

Boron has been found to have a significant ameliorating effect on the lithium enhancement above concentrations of 50-100 μg/g. In most fuel management schemes, the boron concentration is maintained above 50 μg/g for around 95% of the cycle length, so, to a good approximation, a combined Li-B effect can be assumed, and correlated with lithium concentration. The evidence reviewed above suggests that a cumulative lithium term is required, such that an appropriate enhancement factor, ranging from unity to some upper value, can be applied to the corrosion rate, depending on the accumulated lithium exposure. The following expression for a corrosion rate enhancement factor is proposed, based on a transition from a factor of unity to an upper value, according to the accumulated "lithium-days" exposure :

$$F_{LITHIUM} = MAX\left(1.0,\ MIN\left\{ \sum_{i=1}^{n} (C_1 \cdot [Li]_i \cdot t_i),\ F_{Li\ -\ MAX} \right\} \right) \qquad (9)$$

where $F_{LITHIUM}$ is the dimensionless enhancement in corrosion rate due to lithium; $F_{Li\text{-}MAX}$ is the maximum lithium enhancement; $[Li]_i$ is the lithium concentration in the coolant over time step i ; t_i is the duration of timestep i ; n is the current timestep number, and C_1 is a constant.

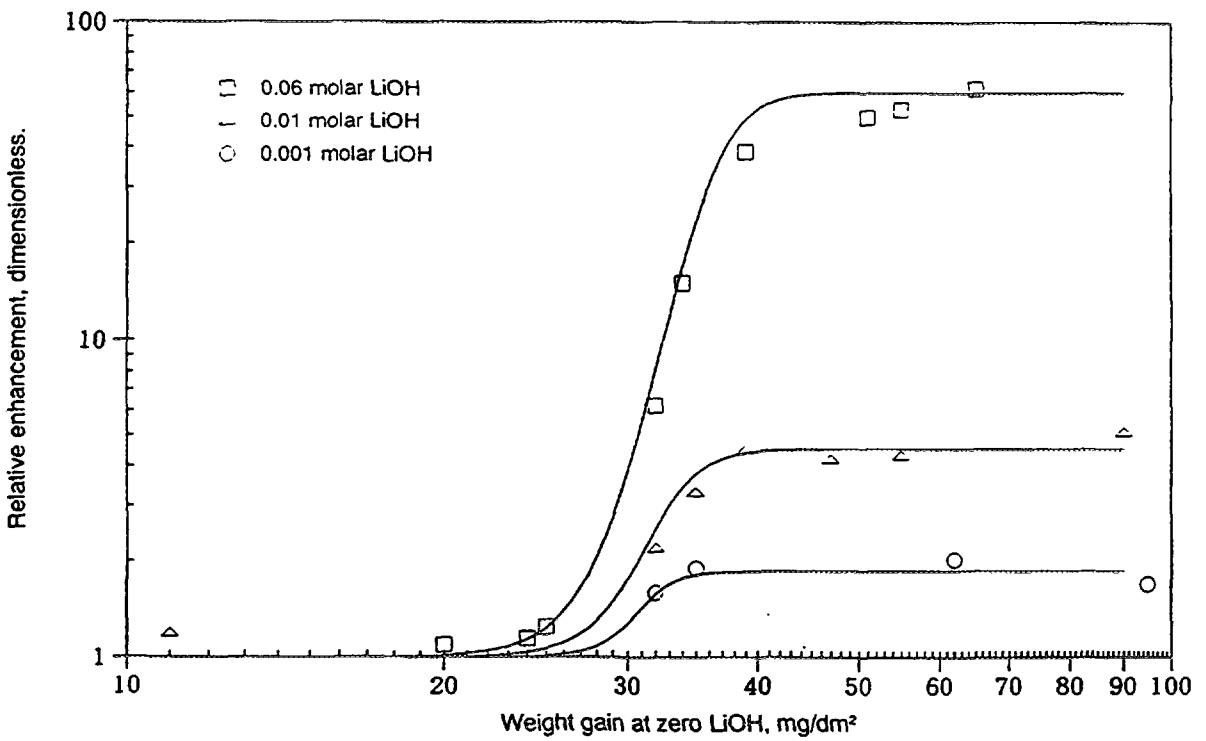

FIG. 4. Relative effect of LiOH concentration on post-transition weight gain

3. CORROSION MODEL IMPLEMENTATION

3.1 DIFFERENT MODEL TYPES

As described in Section 2, the isothermal ex-reactor corrosion rates of Zircaloy-4, low tin Zircaloy-4 and ZIRLO™ materials are significantly different. It is therefore appropriate to consider these materials as separate populations, for which separate sets of model constants must be derived.

Cladding oxide thickness varies considerably, both at the localized and macroscopic levels, and in both axial and circumferential directions. Furthermore, the increase in thickness with axial height along the rod is not monotonic, but follows a "saw tooth" profile, with the local depressions in oxide thickness corresponding to grid locations. It is necessary to decide how to treat these variations in thickness, and which values are the most appropriate to use for each application:

(a) For fuel design purposes, it is usually necessary to calculate the maximum value of local oxide thickness resulting from a given fuel duty.

(b) For calculating cladding average hydrogen contents, the maximum value of circumferentially-averaged oxide thickness is appropriate, since the hydrogen content measurements used to determine the pick-up fraction are usually volume-averaged values obtained from short axial segments of cladding.

(c) For general fuel modelling applications, where the fuel rod is often represented by axial segments which are greater than ~½ a grid span in length, a value of oxide thickness averaged over the entire grid span is often appropriate.

The approach adopted here is to fit two sets of corrosion model constants for each of the standard Zircaloy-4, low tin (optimized) Zircaloy-4, and ZIRLO™ materials. One set of constants is fitted to measurements obtained from inter-span locations, away from the effects of structural and/or flow mixer grids. This model is the basis for applications (a) and (b) above. The second set of constants is selected to obtain a least-squares fit to corrosion measurements from all axial locations, and corresponds to application (c). Circumferential variations in oxide thickness are conservatively accounted for by increasing the best-estimate oxide thickness according to:

$$\text{max. local oxide} = C_{MAX1} \cdot (\text{best-estimate oxide}) + C_{MAX2}$$

such that at least 95% of the azimuthal maximum measurements are bounded.

3.3 ANALYSIS OF GRID EFFECTS

As mentioned previously, structural and flow mixer grids are known to cause local reductions in oxide layer thickness, with the range of observable effects typically extending from a few millimetres upstream of the grid to around 20 effective sub-channel diameters downstream (around 200-250 mm). This reduction is thought to be due to a combination of:

(i) a reduction in local power and fast flux at the grid location, due to parasitic neutron capture by the grids and to the displacement of the moderator;

(ii) the hydraulic disturbance introduced by the grid, which enhances turbulent mixing between sub-channels and reduces the thickness of the thermal boundary layer.

An examination of axial power profiles suggests that Inconel structural grids result in a local power reduction in the range 5 to 10%. Calculations performed using the best-estimate inter-span model (described in Section 3.2) suggest that the predicted reduction in local oxide thickness at grid locations is insufficient to account for the observed reduction. Therefore, a method of accounting for the effects of enhanced turbulence on the heat transfer process close to grid locations has been developed.

The principal effect of grid-induced turbulence is the enhancement in coolant film heat transfer coefficient, resulting from a reduction in the thickness of the thermal boundary layer. To a first approximation, the enhancement in film heat transfer coefficient may be considered to begin either at, or

slightly upstream of, the leading edge of the grid, and to decay in an exponential manner downstream of the grid, such that its effects become negligible at some characteristic distance downstream of the trailing edge (usually around 20 effective sub-channel diameters). Such a model has been suggested in Ref. [4], but this only includes the downstream effects of the grid, whereas the data suggest that an upstream effect is also present, although with a reduced range. Therefore, a similar model to that given in [4] has been developed, but including both an upstream and downstream effect:

$$h_x = h_\infty \cdot MIN\left\{G_1 \cdot \left(\frac{x}{De}\right)^{G2}, G_3\right\} \tag{10}$$

where h_x is the local heat transfer coefficient (subject to a minimum of h_∞) at a distance x from the nearest grid in kW/m^2/K; h_∞ is the fully developed heat transfer coefficient in kW/m^2/K; and De is the sub-channel effective diameter, based on the heated perimeter, in m.

Values for the constants G_1, G_3, and upstream and downstream values of G_2 have been obtained by optimizing the fit to data from the North Anna Advanced Alloy Demonstration Programme, described in Section 4. Examples of the predictions made using this model are illustrated in Fig. 5, where, at each axial location, the average of all measurements made on 2-cycle low tin Zircaloy-4 rods is plotted against the corresponding average of all predictions.

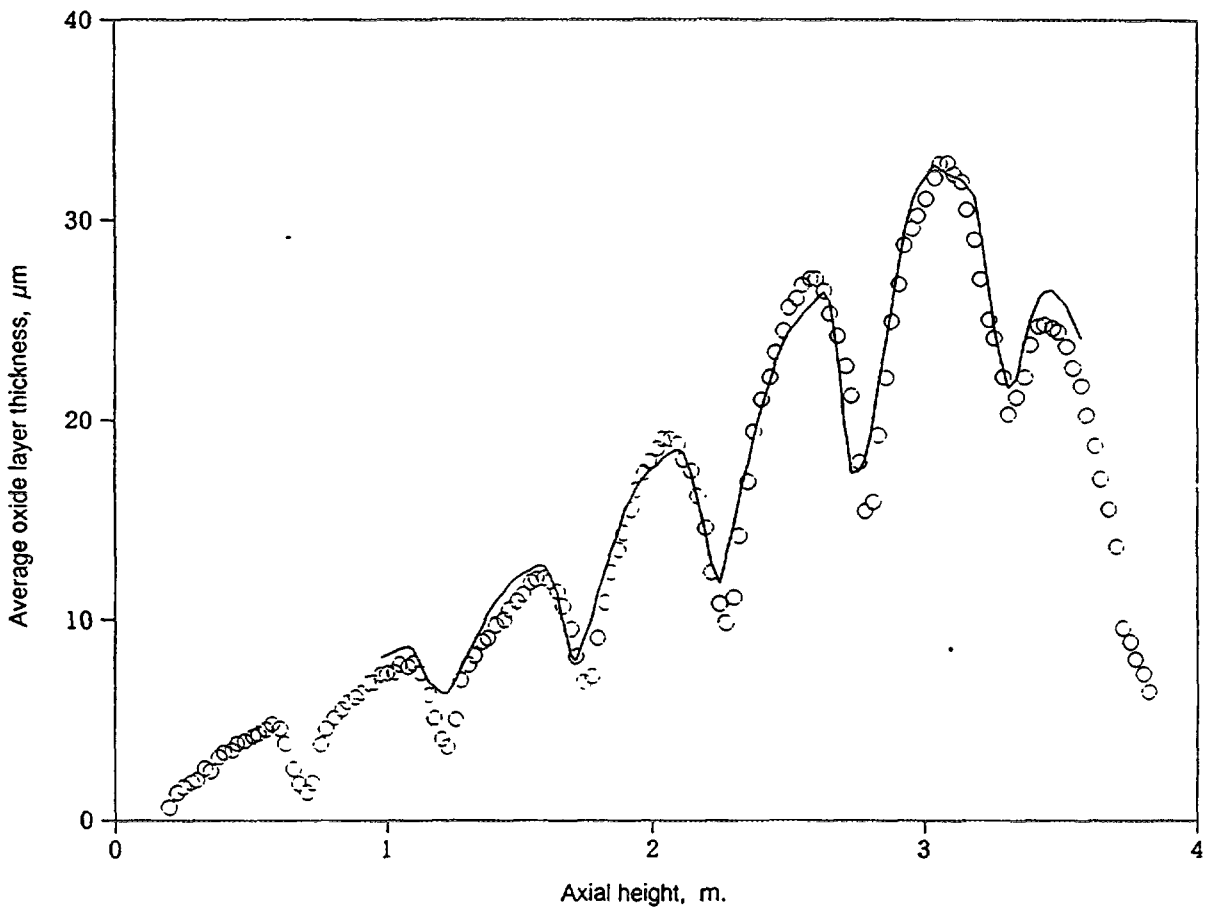

FIG. 5. North Anna 1 optimized Zr-4 rods after 2 x 18 month cycles: Predictions using the grid effects model

4. CORROSION MODEL VALIDATION

Corrosion data from the following programmes in commercial PWR plants has been used to calibrate and validate the corrosion model:

(a) *The North Anna Advanced Alloy Demonstration Program.*
This programme was initiated by Westinghouse with the aim of comparing the in-reactor performance of standard Zircaloy-4, improved (low tin) Zircaloy-4 and ZIRLO™ cladding materials [34]. North Anna Unit 1 is a Westinghouse three-loop plant utilising 17x17 fuel, and was selected because it operated 18-month cycles with relatively high coolant temperatures and power density. Plant data are summarised in Table 3. Corrosion measurements obtained using the eddy current technique (ECT) are available after one and two 18-month cycles (rod average burnups of 23 and 41 MWd/kgU respectively).

(b) *The North Anna High Burnup Program.*
The aim of this programme was to obtain standard Zircaloy-4 corrosion data from high burnup fuel irradiated in a relatively high temperature PWR [35]. *In situ* ECT measurements were obtained using single linear traces on 24 two-cycle peripheral fuel rods from Region 8A, and 24 peripheral fuel rods from Region 6 after three and four cycles.

(c) *Data from Commercial PWR B.*
Reactor B is a high power density, high temperature plant, utilising a 15x15 fuel design and operating 12-month cycles. Plant data are summarised in Table 3. Data from standard Zircaloy-4 and low tin Zircaloy-4 materials are available after each of four reactor cycles. Spiral trace ECT oxide thickness measurements were obtained, and detailed records of reactor power and water chemistry histories are available.

The approach adopted has been to arbitrarily divide databases (a) and (c) into two groups. One group is used to calibrate the model constants, whilst the second group is used to provide validation of the model. Database (b) has been used only for validation.

The predictions obtained using the best-estimate circumferential average oxide thickness model, including the grid effects model, are plotted against measured data from each of the three cladding types in Fig. 6. Also included in each of these plots is an indication of the measurement accuracy associated with the ECT ($\pm 5\mu$m).

Reasonable agreement can be seen for the standard Zircaloy-4 data, although some scatter is evident, beyond that which could result from measurement inaccuracy alone. Analysis of the errors does

Table 3 ***Commercial PWR Plant Data Summary***

	North Anna 1#	*Reactor B*
Plant design	3-loop	3-loop
Fuel design	17x17	15x15
Core average power, kW/m	18.74	23.06
Inlet temperature, °C	290	292.9
Outlet temperature, °C	329	326.9
% of heat generated in fuel	97.4	98.1
cladding outer diameter, mm	9.5	10.75
active fuel length, m.	3.66	3.4

- after uprating

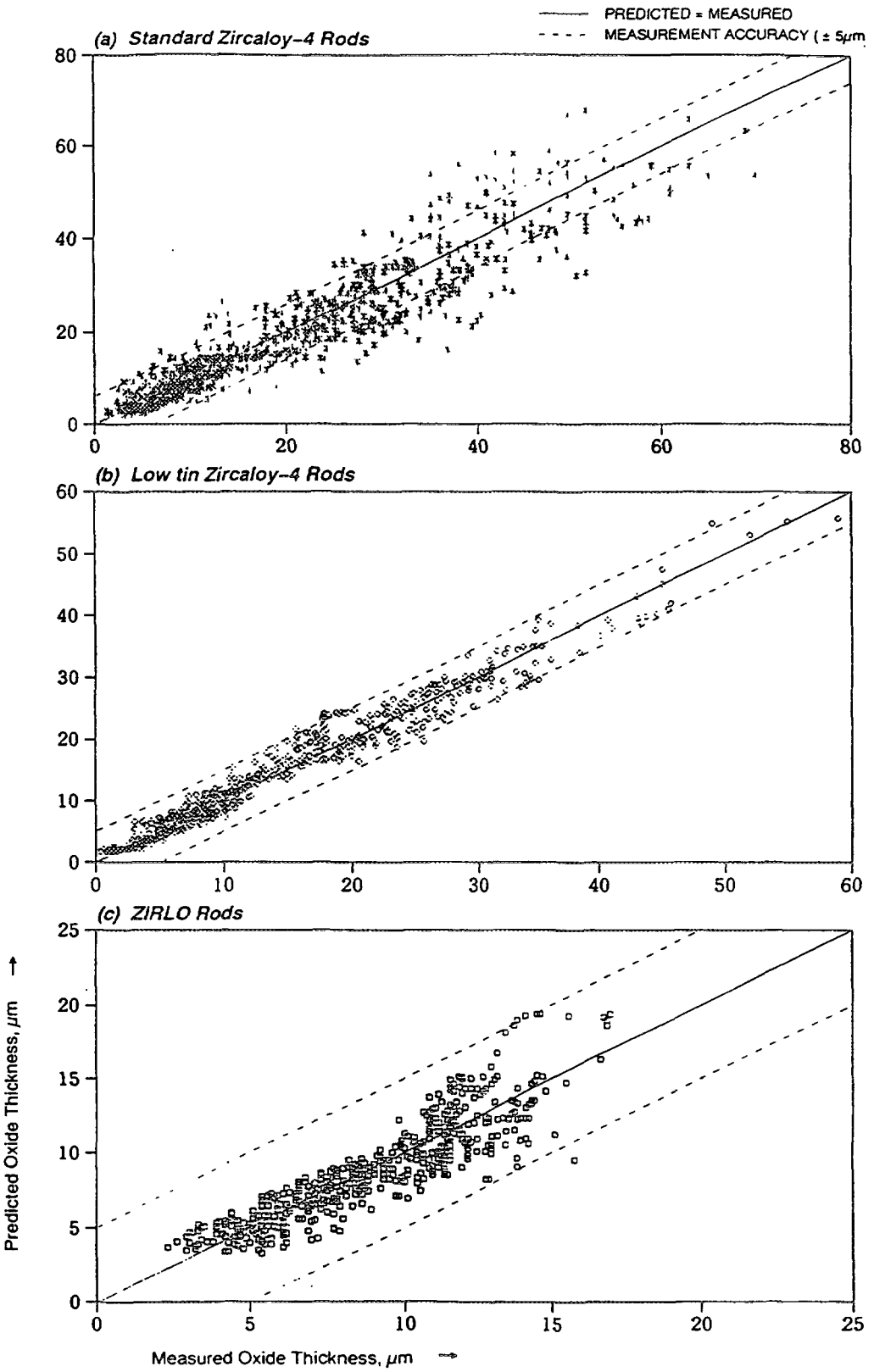

FIG. 6. Circumferential average oxide measurements vs. predictions

not reveal any bias with reactor, local burnup or axial elevation, so it is assumed that the scatter is due to a combination of chemical and/or metallurgical variations between cladding lots, uncertainties in reactor power levels and axial shape factors, uncertainties in the calculation of rod surface temperatures, and random error.

Good agreement is seen for the low tin Zircaloy-4 and ZIRLO™ models, with most of the scatter being confined within the measurement uncertainty bands.

5. CONCLUSIONS

5.1

The corrosion of Zircaloy-4 and ZIRLO™ alloys in PWR environments has been reviewed. An engineering corrosion model of the following form has been proposed :-

for oxide thicknesses $\leq 2.2\ \mu m$:-

$$\frac{dw}{dt} = \frac{A}{\delta_{OX}^2} \cdot \exp\left(\frac{-B}{T}\right)$$

for oxide thicknesses $> 2.2\mu m$:-

$$\frac{dw}{dt} = C \cdot \phi^D + E \cdot F_{HYD} \cdot F_{LITH} \cdot F_{RXA} \cdot \exp\left(\frac{-G}{T}\right)$$

where: A, B, C, D, E, and G are constants
F_{HYD} , F_{LITH} and F_{RXA} are dimensionless factors to account for the effects of hydrogen concentration, lithium concentration, and cladding recrystallized fraction.

5.2

The model has been calibrated and validated using in-reactor data from standard and low tin Zircaloy-4, and from ZIRLO™. The model has been found to give reasonably good predictions of the validation data base.

A method of accounting for the thermal-hydraulic effects of grids on corrosion thickness has been described. The method has been shown to give reasonably good agreement with measurements obtained from North Anna Unit 1.

REFERENCES

[1] INTERNATIONAL ATOMIC ENERGY AGENCYCorrosion of Zirconium Alloys in Nuclear Power Plants., IAEA TECDOC-684 January 1993.

[2] DYCE, I. H., "Corrosion of Zircaloy fuel cladding - the influence of high heat fluxes", Nuclear Engineering, **9**, 1964.

[3] STEHLE, H., KADEN, W., & MANZEL, R., "External Corrosion of Cladding in PWRs", Nuclear Engineering and Design, **33**, 1975.

[4] GARZAROLLI, F., GARDE, A. M., et al., Waterside Corrosion of Zircaloy Fuel Rods, Electric Power Research Institute report EPRI NP-2789, December 1982.

[5] HILLNER, E., "Corrosion of zirconium-base alloys - an overview", Zirc. in the Nuclear Industry, 3rd Int. Symp., ASTM STP 633. 1977.

[6] McDONALD, S. G., SABOL, G. P., & SHEPPARD, K. D., "Effect of lithium hydroxide on the corrosion behaviour of Zircaloy-4", Zirc. in the Nuclear Industry, 6th Int.Symp., ASTM STP 824, 1984, pp. 519-530.

[7] SABOL, G. P., KILP, G. R., BALFOUR, M. G. & ROBERTS, E, "Development of a cladding alloy for high burnup", Zirc. in the Nuclear Industry, 8th Int. Symp. ASTM STP 1023, 1989.

[8] KINGERY, W. D., FRANCL, J., COBLE, R. L., & VASILOS, T., "Thermal conductivity: X, data for several pure oxide materials corrected to zero porosity", J. American Chem. Soc., **37** (2), February 1954, pp. 107-111.

[9] GILCHRIST, K. E., "Thermal property measurements on Zircaloy-2 and associated oxide layers up to 1200°C", J. Nucl. Materials, **62**, 1976, pp. 257-264.

[10] GILCHRIST, K. E., "Thermal conductivity of oxide deposited on Zircaloy fuel tube material - a continuation of previous work", J. Nucl. Materials, **82**, 1979, pp. 193-194.

[11] BILLOT, Ph., & ROBIN, J. C., "Mechanistic understanding of Zircaloy corrosion in PWRs through a corrosion model", IAEA Tech. Comm. meeting on Fundamental Aspects of Corrosion on Zirconium Base Alloys in Water Reactor Environments, 1989. IWGFPT/34.

[12] BILLOT, Ph., BESLU, P., & ROBIN, J. C., "Consequences of lithium incorporation in oxide films due to irradiation effect", ANS/ENS Topical Meeting on LWR Fuel Performance, Avignon, France, April 1991.

[13] KAISER, R. S., MILLER, R. S., MOON, J. E. & PISANO, N. A., "Westinghouse High Burnup Experience at Farley 1 and Point Beach 2", ANS/ENS Topical Meeting on LWR Fuel Performance. Avignon, France. April 1991.

[14] DICKSON, I. K., EVANS, H. E. & JONES, K. W., J. Nuclear Materials, **80**. 1979.

[15] HILLNER, E., Zirconium in Nuclear Applications, ASTM STP 754, 1982.

[16] COX, B., Assessment of PWR Waterside Corrosion Models and Data, Electric Power Research Institute report EPRI NP-4287, 1985.

[17] COX, B. "A new model for the in-reactor corrosion of zirconium alloys", IAEA Tech. Com. Meeting on Influence of Water Chemistry on Fuel Cladding Behaviour, Rez, Czech Republic, 1993.

[18] HILLNER, E., "Hydrogen absorbtion in Zircaloy during aqueous corrosion: effects of environment", Westinghouse report WAPD-TM-411. Bettis Atomic Power Laboratory, 1964.

[19] SLATTERY, G. F., J. Inst. Metals, **95**, 1967.

[20] GARDE, A. M., "Enhancement of Aqueous Corrosion of Zircaloy-4 due to Hydride Precipitation at the Metal-Oxide Interface". Zirc. in the Nuclear Industry, 9th Int. Symp. ASTM STP 1132, 1991.

[21] KIDO, T., "A study on enhancement of uniform corrosion of Zircaloy-4 cladding under high burnup operation in PWRs", EPRI Workshop on PWR Fuel Corrosion, CHENG, B., (ed.), Washington DC, July 1993.

[22] EVANS, H. E., BALE, M. G. & POLLEY, M. V., A Review of the NFIR-1 Zircaloy Corrosion Projects, Volume 2: Evaluation of the Corrosion Data, Electric Power Research Institute report EPRI NP-7320, August 1991.

[23] GARZAROLLI, F. & HOLZER, R., "Waterside corrosion performance of light water power reactor fuel", Nuclear Energy, **31** (1), February 1992, pp. 65-86.

[24] EUCKEN, C., et al, "Influence of chemical composition on uniform corrosion of zirconium-base alloys in autoclave tests", Zirc. in the Nuclear Industry, 8th Int. Symp. ASTM STP 1023, 1989.

[25] INOUE, S., MORI, K., MURATA, T. & KOBAYASHI, S., "PWR Fuel rod corrosion in Japan", IAEA Tech. Com. Meeting on Influence of Water Chemistry on Fuel Cladding Behaviour, Rez, Czech Republic, 1993.

[26] HILLNER, E. & CHRIGOS, J. N., "The effects of lithium hydroxide and related solutions on the corrosion rate of Zircaloy in 680°F water", Westinghouse report WAPD-TM-307, August 1962.

[27] KASS, S., "Corrosion and hydrogen pickup of Zircaloy in concentrated lithium hydroxide solutions", Corrosion, **25** (1), January 1969.

[28] BRAMWELL, I. L., PARSONS, P. D. & TICE, D. R., "Corrosion of Zircaloy-4 PWR cladding in lithiated and borated water environments", Zirc. in the Nuclear Industry, 9th Int. Symp. ASTM STP 1132, 1991, pp. 628-642.

[29] PECHEUR, D., GIORDANO, A., PICARD, E, BILLOT, Ph. & THOMAZET, J., "Effect of elevated lithium on the waterside corrosion of Zircaloy-4: experimental and predictive studies", IAEA Tech. Com. Meeting on Influence of Water Chemistry on Fuel Cladding Behaviour, Rez, Czech Republic, 1993.

[30] KARLSEN, T., GUNNERUD, P. & VITANZA, C., "Light water reactor materials and water chemistry studies at Halden", 6th Int. Conf. on Water Chemistry of Nuclear Reactor Systems, Vol. 1, BNES, October 1992.

[31] EVANS, H. E. & POLLEY, M. V., "A review of the effect of lithium on PWR fuel rod waterside corrosion", 6th Int. Conf. on Water Chemistry of Nuclear Reactor Systems, Vol. 1, BNES, 1992.

[32] CHURCH, K., "Effect of elevated pH/LiOH on fuel rod corrosion at Oconee-1", EPRI Workshop on PWR Fuel Corrosion, CHENG, B., (ed.), Washington DC, July 1993.

[33] WEISMAN, J. & TONG, L. S., Thermal Analysis of Pressurized Water Reactors, ANS, 1970.

[34] SABOL, G. P., et al, "In-reactor corrosion performance of the ZIRLO™ alloy and Zircaloy-4 and related corrosion modelling", ANS Topical Meeting on LWR Fuel Performance, West Palm Beach, Florida, USA, April 1994.

[35] KILP, G. R., et al, "Corrosion experience with Zircaloy and ZIRLO™ in operating PWRs", ANS/ENS Topical Meeting on LWR Fuel Performance, Avignon, France, April 1991.

MODELLING THE GAS TRANSPORT AND CHEMICAL PROCESSES RELATED TO CLAD OXIDATION AND HYDRIDING

R.O. MONTGOMERY, Y.R. RASHID
ANATECH Research Corporation,
San Diego, California,
United States of America

Abstract

Models are developed for the gas transport and chemical processes associated with the ingress of steam into a LWR fuel rod through a small defect. These models are used to determine the cladding regions in a defective fuel rod which are susceptible to massive hydriding and the creation of sunburst hydrides. The brittle nature of zirconium hydrides (ZrH_2) in these susceptible regions produces weak spots in the cladding which can act as initiation sites for cladding cracks under certain cladding stress conditions caused by fuel cladding mechanical interaction. The modeling of the axial gas transport is based on gaseous bimolar diffusion coupled with convective mass transport using the mass continuity equation. Hydrogen production is considered from steam reaction with cladding inner surface, fission products and internal components. Eventually, the production of hydrogen and its diffusion along the length results in high hydrogen concentration in locations remote from the primary defect. Under these conditions, the hydrogen can attack the cladding inner surface and breakdown the protective ZrO_2 layer locally, initiating massive localized hydriding leading to sunburst hydrides. The developed hydrogen evolution model is combined with a general purpose fuel behavior program to integrate the effects of power and burnup into the hydriding kinetics. Only in this manner can the behavior of a defected fuel rod be modeled to determine the conditions that result in fuel rod degradation.

1. INTRODUCTION

In earlier fuel rod designs, the presence of hydrogenous contaminants produced internal hydriding in initially undefected fuel rods [1]. Internal clad hydriding leading to primary defection of a fuel rod (primary hydriding) has been essentially eliminated by improvements in manufacturing procedures. In contrast, secondary hydriding occurs as a consequence of steam in the fuel rod that has entered through a primary defect. Secondary hydriding remain a problem in LWR fuel rods as long as primary failures continue to occur from such sources as manufacturing flows or debris fretting.

Under the appropriate conditions, the hydrogen produced by the reaction of steam with the fuel rod components will be absorbed into the Zircaloy cladding. The absorption of hydrogen by the cladding can occur in three different modes, expected because of corrosion, accelerated, and massive [2]. Expected hydrogen absorption results from the hydrogen pickup during the formation of zirconium oxide (ZrO_2) by corrosion. Accelerated hydriding is defined as hydrogen absorption in excess of the nominal pickup fraction expected from corrosion.

Massive hydriding is the formation of localized regions of δ-phase zirconium hydride un the cladding caused by grossly accelerated hydrogen absorption. It is the massive hydriding combined with Fuel-Cladding Mechanical Interaction (FCMI) that leads to the large failures recently experienced.

Locke has reviewed the operation of fuel rods with primary defects [3]. He concluded that the occurrence of fuel rod degradation and excessive fission product release was caused by massive hydriding of the zirconium alloy cladding. From the review, Locke developed a relationship between the time to failure (excessive fission product release) after primary defection and surface heat flux (operating power).

The relationship indicates that hydriding induced failure required long incubation periods at low power. As fuel rod power increases, the incubation period becomes shorter, and at high power levels, hydriding induced failure is immediate. Since cladding deterioration is usually a combination of massive localized hydriding and stresses in the cladding induced by FCMI, the Locke relationship between time and average power does not consider all the various factors that influence fuel rod behavior, such as, rod geometry and type, burnup, power history, and power changes.

There has been only a limited number of experimental studies on the zirconium alloy hydriding process, especially in the area of localized massive hydrides. Out-of-pile experiments have been conducted to determine the reaction kinetics leading to zirconium hydrides (ZrH_2). The effects of temperature and hydrogen pressure on the reaction rate has been investigated by Marshall and Une [4,5]. At low pressures ($< .2$ atm), the absorption rate exhibited dependence on the hydrogen pressure. However, at pressures approaching 1 atm, the absorption rate was insensitive to hydrogen pressure due to saturation of the sample surfaces. The entire samples were converted to zirconium hydride at the completion of the test in the experiments by Une. In these experiments, the hydrogen source was unlimited and the maximum pressure used in the experiments was 1.2 atm. These conditions do not directly simulate the hydriding conditions in an LWR fuel rod. In this case, the hydrogen supply is limited and the pressure is significantly higher.

Lunde evaluated the surface conditions leading to either localized sunburst hydrides or uniform hydrogen absorption using closed-end Zircaloy-2 tubes containing hydrogen at 2-4 atm [6]. The tubes had sandblasted or pickled inside surfaces and were tested as received, with local fluoride contaminations, as autoclaved, and autoclaved with scratches. Localized hydriding leading to sunburst formation was only observed in samples containing local fluoride contamination. Uniform absorption occurred in the as-received tube samples, and, no hydrogen absorption was observed in the autoclaved samples at exposures to 48 hours. Lunde did not report that the localized hydriding behavior depended on the hydrogen pressure.

All the investigators reported either no absorption or a delay time in hydrogen absorption depending on the surface oxide thickness on the test samples. Delay times as long as 8 hours were measured by Une for surface oxide thicknesses of 1.6 μm. Lunde used a standard steam autoclave treatment for 3 days at 400 C which resulted in an oxide thickness of ~2 μm, and, observed no appreciable hydrogen absorption in the autoclaved samples at 48 hours of exposure.

The results of these experiments can be summarized as follows: the formation of sunburst hydrides is produced only when the zirconium alloy surface has been broken locally, allowing for a high surface flux of hydrogen into the material; and the absorption rate is independent of pressure at high pressures, i.e., the absorption reaction is controlled by hydrogen diffusion in the Zircaloy.

1.1. BEHAVIOR OF A FUEL ROD WITH A PRIMARY DEFECT

Although PCI related defects have been reduced to an acceptable statistically low level, debris fretting and undetected fabrication flaws remain as primary defect sources in LWR fuel rods. These can eventually develop into through-wall primary defects and admit coolant which immediately flashes to steam, reaching equilibrium in a short time. This step establishes the initial conditions for an incubation period during which the steam in the fuel-cladding gap reacts with the fuel rod internal components resulting in hydrogen production. Figure 1 is a schematic of a fuel rod which displays the different active processes in a defected fuel rod. First, the inner surface of the cladding begins to oxidize by reaction with steam, producing zirconium oxide (solid) and hydrogen (gas). This reaction is common to all Zircaloy cladding types, although the oxidation rate is several times faster for zirconium liner cladding. A fraction of the hydrogen is absorbed by the Zircaloy material and the remainder mixes with the steam in the gap. The steam in the gap also undergoes radiolytic decomposition through interaction with the fission fragments released from the fuel surface. Interaction with the fission products decomposes the water molecule into hydrogen peroxide and hydrogen gases. Also, the hydrogen peroxide can react with the fuel material,

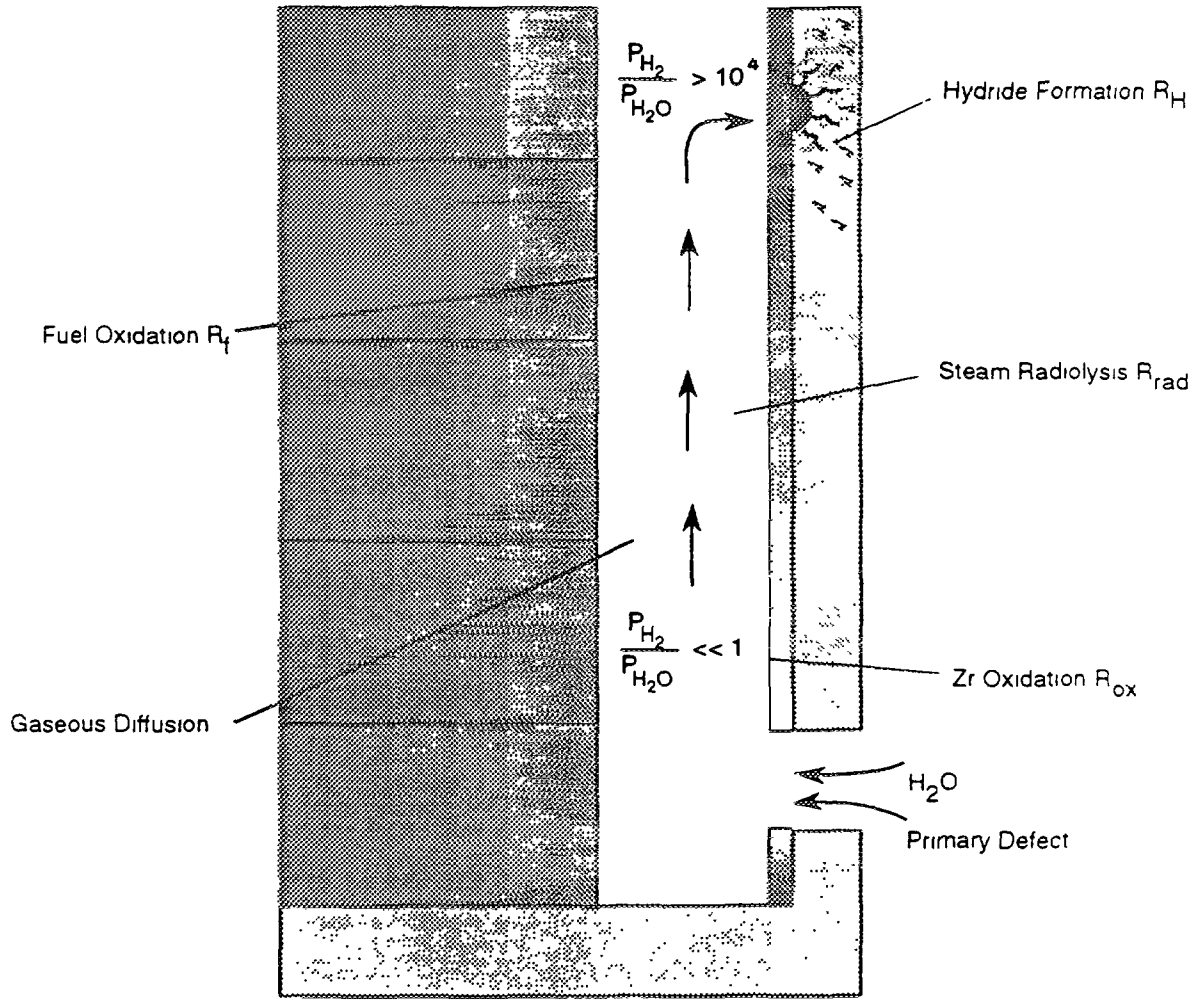

FIG. 1 Schematic of Chemical and Diffusional Processes in a Defective Fuel Rod

oxidizing the pellet, even in the presence of a reducing hydrogen atmosphere. The direct or indirect reaction of water molecules with the fuel and cladding results in a concentration gradient of gases in the fuel-cladding gap with the concentration of steam decreasing at locations remote from the primary defect. The variation in concentration causes steam to diffuse away from the primary defect toward the hydrogen-rich regions and hydrogen to diffuse towards the primary defect. Provided the incubation time and diffusion distances are long enough, oxygen starvation will occur some distance away from the primary defect. The condition of oxygen starvation can persist for extended periods unless interrupted by a large power reduction or reactor shutdown which would cause the gap to open and transport additional steam into the hydrogen-rich regions. Eventually the protective oxide layer begins to breakdown locally, either by oxygen depletion from the zirconium oxide or by the tensile stresses produced by FCMI, creating a porous structure. At the location of oxide breakdown, the high absorption rate of hydrogen results in saturation of the Zircaloy surface and the formation and growth of sunburst hydrides.

2. MODELING APPROACH

The processes described above are combined in a hydrogen evolution model which has been incorporated into the FREY fuel behavior program. The effects of burnup, power level, and power changes on the fuel-cladding gap are then integrated into the model. FREY is a general 2-dimensional

axisymmetric fuel behavior program which models the time dependent thermo-mechanical behavior of a LWR fuel rod. The fuel-cladding gap size and fuel rod temperatures are provided by FREY as functions of axial position and time. For conditions where gap closure occur, a minimum effective diameter for gas transport is employed that represents the partial relocation of the gap volume into the fuel cracks and the mismatch between the pellet and cladding contact. A value of 20 μm is used based on experimental gas flow measurements in the Halden Facility [8].

2.1 AXIAL GAS TRANSPORT IN THE FUEL ROD VOID VOLUME

The axial gas transport model utilizes the mass continuity equation for a gaseous medium undergoing bimolar diffusion to determine the molar concentrations of hydrogen and steam in the fuel-cladding gap. The continuity equation for one gaseous species (hydrogen) assuming a constant pressure is given by [9];

$$C_t \frac{\delta x}{\delta t} = C_t D \nabla^2 x + \nabla \cdot J_t \, x + R \tag{2-1}$$

where x is the mole fraction of hydrogen, D is the steam/hydrogen diffusion coefficient, R is the production rate of hydrogen, and J_t is the total convective flux induced by mass imbalances. For a bimolar system, the mole fraction of steam (q) is simply (1-x). The molar density, C_t, is determined using the ideal gas law,

$$C_t = \frac{P}{R_u T} \tag{2-2}$$

where P is the internal pressure, T is the local temperature of the gas, and R_u is the universal gas constant. The diffusion coefficient, D, for a steam/hydrogen mixture is given by,

$$D = \frac{(PD)_o}{P} \left(\frac{T}{T_o} \right)^{1.68} \tag{2-3}$$

where $(PD)_o$ is equal to 0.27 MPa-cm^2/s and T_o is a reference temperature.

The model assumes that the internal pressure remains equal to the coolant pressure during the oxidation and hydriding process. Because of this assumption, a mass balance approach can be used to determine the influx of steam through the primary defect as a result of material losses by absorption at remote locations in the fuel rod. Using this approach, the total flux, J_t, at axial location z, some distance away from the primary defect, is given by the integral of all absorption process between z and the fuel rod end Z_{pl};

$$J_t(z) = \pm \frac{1}{\Delta g} \int_z^{z_{pl}} F_{abs} \, dz \tag{2-4}$$

where F_{abs} is the net absorption flux out of the gap and Δg is the fuel-cladding gap thickness. The sign of the integral depends on the relative location of the primary defect and the axial location z. At the primary defect, the total mass flux is the summation of all absorption processes within the fuel rod.

2.1.1 Hydrogen Production

The fuel rod is separated into three different regions for modeling the hydrogen production terms in the gas transport model: lower plenum, upper plenum, and fuel-cladding gap. The sources of hydrogen are as follows:

Lower Plenum: $R = R_{ox}$
Upper Plenum: $R = R_{ox} + R_g$
Fuel-Cladding Gap: $R = R_{ox} + R_{rad}$

The cladding inner surface oxidation, R_{ox} , results because of the steam-zirconium reaction,

$$Zr + 2H_2O \rightarrow ZrO_2 + 2H_2 \tag{2-5}$$

The process in Equation 2-5 consumes steam, produces zirconium oxide at the cladding inner surface and releases hydrogen. The reaction rate is dependent on the temperature, the material composition, and the amount of the reactive species in the gap. The corrosion rate of zirconium alloys used in the methodology is expressed in terms of an Arrhenius function of temperature by the equation,

$$w = A_1 \exp\left(-\frac{B_1}{T_c}\right) \tag{2-6}$$

where A_1 and B_1 are experimental constants, T_c is the cladding inner surface temperature and w is the rate of oxide formation. The constants A_1 and B_1 are determined for each of the different zirconium alloys using out-of-pile measurements and PIE data. Zircaloy oxidation kinetics has been studied in both steam and water environments and is well established for the conditions on the outer cladding surface. Traditionally, waterside corrosion of Zircaloy depends on the ZrO_2 thickness with oxide accumulation being cubic with time at low oxide thickness and linear at higher thickness [10]. A linear oxide buildup is used in the current model to represent the inner surface oxidation. The availability of experimental data for Zr oxidation under in-reactor conditions is limited. However, the oxidation rate for pure zirconium is faster than Zircaloy because less alloying impurities are present in the material to inhibit the oxidation process. Although limited, data for Zr indicate that the oxidation rate is not dependent on the oxide thickness.

The rate of hydrogen production from the steam Zirconium reaction is proportional to the inner surface oxidation and is given by

$$R_{ox} = \alpha w S V (1-f) q^{0.01} \tag{2-7}$$

where α is a conversion factor between oxide formation and hydrogen production, S is the surface area of oxidation, and V is the volume of the gap. The additional empirical factor $q^{0.01}$ has been applied to represent the effect of oxygen starvation where q is the mole fraction of steam in the gap. For $q < 10^{-3}$, the oxidation process, and thus, the hydrogen production is shut off due to oxygen starvation. During the oxidation process, a fraction of the hydrogen produced is picked up by the Zircaloy material and the remainder is released into the gap. The pickup fraction (f) is dependent on several factors, including the type of oxide formed, the pre-oxide Zircaloy composition, and temperature and can vary from 100% during the initial oxidation to 5%, with the average being 10-20% for both Zircaloy-2 and Zircaloy-4 [2]. The model uses a pickup fraction of 10% based on the PIE data of hydrided cladding material.

The hydrogen getter oxidation, R_g, is activated only if a getter is present in either plena. Getter oxidation proceeds by the same reaction given in Equation 2-5 and is represented in the model using Equation 2-6 with different reaction rate constants A_1 and B_1. Oxidation of the getter material initiates immediately on introduction of steam in the fuel rod. The process is much more rapid then inner surface oxidation and is complete in 3 to 4 days, depending on the amount and the type of getter material. Because of the rapid reaction rate, the getter oxidation is an important source of hydrogen during the initial stages of defective fuel rod operation.

Ionizing fission products released from the fuel pellet surface interact with the gas in the fuel-cladding gap, decomposing the steam into hydrogen and hydrogen peroxide. Radiolysis of steam in the gap depends on the fission product flux from the fuel surface, the linear energy transfer (LET) between the steam and the fission products, the G value for the reaction and the gap geometry. Olander has

determine the volumetric hydrogen peroxide production rate for typical fuel rod conditions [10]. Since hydrogen is produced during the radiolytic decomposition of steam at the same rate as the hydrogen preoxide, the value derived by Olander for representative fuel rod conditions is used in the model for R_{rad}.

The above reactions replace the steam with hydrogen in the fuel rod void volume as a function of the local temperature, material composition, the amount of steam present, and the local geometry. The hydrogen concentration increases at locations remote form the primary defect, and, it is at these locations that the criterion for hydrogen absorption can be achieved.

2.1.2 Massive Hydrogen Absorption

Zirconium hydride (ZrH_2) formation in Zircaloy cladding results from the rapid absorption of hydrogen from the fuel-cladding gap. Before massive hydriding can develop, two important criterion much be satisfied: oxygen starvation and localized ZrO_2 breakdown. Oxygen starvation is required before massive hydrogen absorption can occur since any oxygen (steam) will react with the zirconium and form an oxide layer which prevents hydrogen absorption. A steam partial pressure ratio of 10 is used in the model as the criterion for oxygen starvation. Steam pressures below this value are insufficient to react with the zirconium and form ZrO_2. Clayton has reviewed several out-of-pile zirconium coupon hydriding experiments to determine the critical steam partial pressure for massive hydriding [2]. The data indicate that the critical steam partial pressure ratio for massive hydriding is between 10^{-3} and 10^{-4} for defective fuel rod conditions.

A ZrO_2 layer between the hydrogen atmosphere and the Zircaloy inhibits the absorption process. The protective nature of the oxide layer is a function of the thickness, and for thin layers exposure to hydrogen, can result in localized penetration and subsequent absorption [6]. In addition, fuel-cladding interaction can produce microcracks in the oxide layer, compromising the protectiveness of the layer. As mentioned in Section 1.1, Une observed delay times in hydrogen absorption which depended on the oxide thickness [5]. Even though the data presented by Une is limited, the data indicates that an increase in delay time was not linear with an increase in oxide thickness. An exponential fit to the data by Une shows good agreement as displayed in Fig 2. The trend suggests that very long delay times can result for oxide thicknesses approaching 5 μm. A minimum protective oxide thickness criterion of 5 μm is used in the model to prevent hydrogen absorption at cladding surfaces that contain an oxide film.

For regions in the fuel-cladding gap where both criteria are satisfied, hydrogen absorption is initiated at a rate sufficient to saturate the absorption surface. In addition, the characteristic shape of sunburst hydrides suggest that the absorption surface area is considerably less than the apparent size of a sunburst as observed in a micrograph. Therefore, an effective absorption surface area of 2000 μm^2 is used in the model to represent the local hydrogen absorption site.

2.2 SUNBURST HYDRIDE FORMATION

Hydrogen absorbed at the inner surface of the cladding diffuses towards the outer surface because of both the hydrogen concentration gradient and the temperature gradient. This redistribution of hydrogen results in sunburst hydride growth as the hydrogen concentration exceeds the terminal solubility at distances away from the absorption surface. As long as the surface flux continues to supply hydrogen, the sunburst hydride will grow towards the outer surface.

2.2.1 Hydrogen Diffusion and Precipitation

The diffusion of hydrogen and precipitation of zirconium hydride (ZrH_2) is governed by the atomic diffusion of hydrogen coupled with the hydrogen terminal solubility in Zircaloy. The hydrogen diffusion and sunburst hydride growth model is based on the approach described by Sawatzky [11]. For the thermal diffusion in a two-phase region, the following assumptions are used:

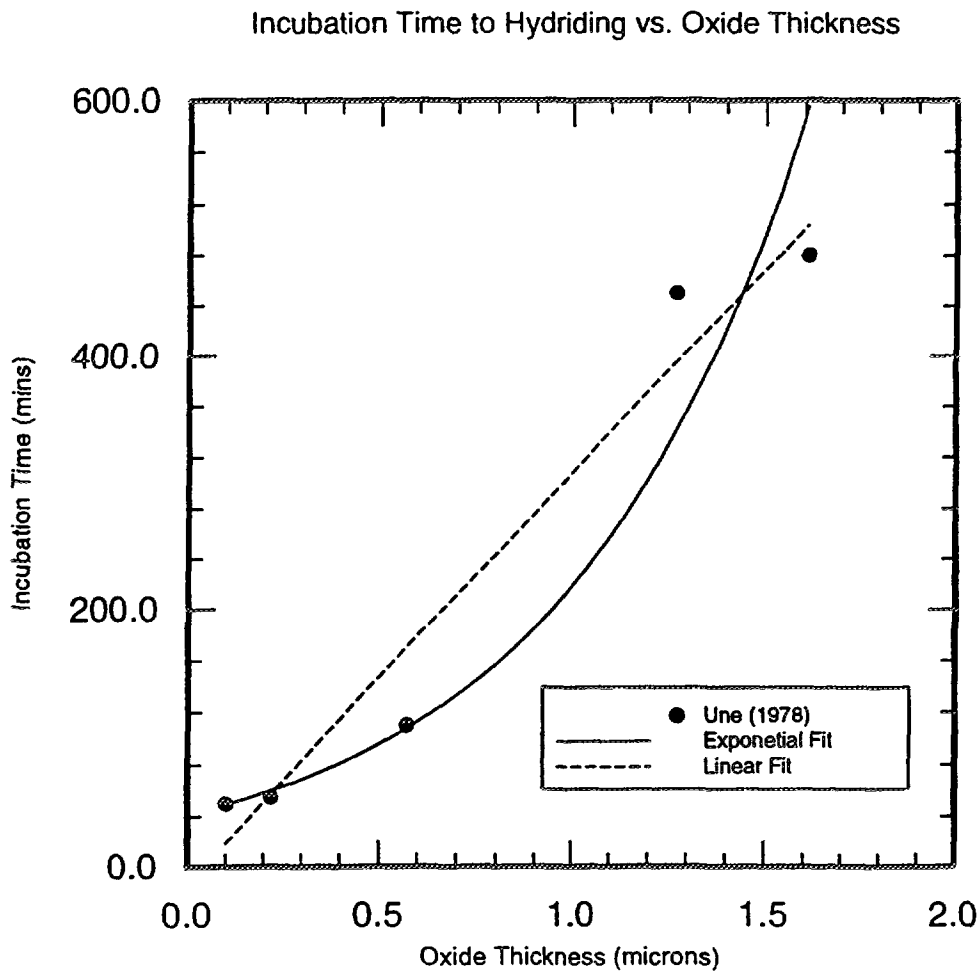

FIG. 2 Incubation Time to Hydrogen Absorption Versus Oxide Thickness

(a) Hydrogen is the only component diffusing.

(b) The hydride is in equilibrium with the solid solution in the two-phase region.

(c) Diffusion is predominately in the solid-solution (alpha) phase. The precipitation and resolution from the hydride acts as a source or sink of hydrogen.

Using these assumptions, a hydrogen diffusion model can be described that determines the amount of hydrogen (α-phase) and the amount of zirconium hydride (δ-phase) as a function of radial position in the cladding. The hydrogen diffusional flux, J_h in the α-phase is given by,

$$J_h = -D_h \frac{\delta C}{\delta R} - \frac{Q^* D_h C}{RT^2} \frac{dT}{dr} \qquad (2\text{-}8)$$

where D_h is the hydrogen-Zircaloy diffusion coefficient, C is the hydrogen concentration, T is the temperature, R is the gas constant, and Q^* is the heat of transport. Expressions derived by Sawatzky using out-of-pile experiments are used for the diffusion coefficient and the heat of transport. Applying the mass continuity equation, the time variation of the hydrogen concentration can be written as,

$$\frac{\delta C}{\delta t} = -\nabla \cdot J_h - R_p \qquad (2\text{-}9)$$

where R_p is the precipitation or resolution rate for zirconium hydrides. Kammenzind has conducted laboratory experiments on hydrogen diffusion and hydride precipitation and has determined that R_p can be represented by [12],

$$R = \sigma^2 (C - C_{max}) \tag{2-10}$$

where σ is an experimental coefficient which is a function of temperature and C_{max} is the terminal solubility. By using Equation 2-10, the precipitation of hydrides in the model is not instantaneous, but occurs at a rate that is temperature dependent. The expression by Kearns is used in the model for the hydrogen terminal solubility in Zircaloy [13]. Equation 2-10 is applied only when the concentration, C, exceeds the terminal solubility. Finally, the incremental increase in the zirconium hydride concentration is determined by,

$$\nabla C_{ZrH2} = \sigma^2 (C - C_{max}) \nabla t \tag{2-11}$$

The approach above is applied using a finite difference method with the cladding thickness divided into several radial rings. Surface boundary conditions can be either a hydrogen flux or concentration. Hydrogen thermal diffusion experiments conducted by Sawatzky were used to benchmark the model [11]. In these tests, a Zircaloy-2 bar containing a uniform hydrogen concentration was placed in a temperature gradient for an extended period to induce thermal diffusion. The temperature gradient was selected so that the initial hydrogen concentration in part of the specimen exceeded the terminal solubility, forming hydrides. Upon completion of the test, the specimens were sectioned into thin discs and the total hydrogen content in each disc was analyzed using the hot-vacuum extraction method.

A comparison of the model predictions is shown in Fig 3 for two tests conducted by Sawatzky. The model predicts well the hydriding boundary indicated by the large increase in hydrogen concentration. Both the total hydrogen and the α-phase hydrogen content predicted by the model are shown for comparison. An interesting observation from the model predictions is the significant amount of supersaturation in the α-phase hydrogen. Kammenzind mentions the possibility of supersaturation before hydride precipitation, but no experimental data is provided to quantify the effect. Further work is required to determine the validity of the supersaturation effect since the hot-vacuum extraction method only measures the total hydrogen content and cannot separate between the two different phases.

2.2.2 Sunburst Hydride Growth

The hemispherical shape of a sunburst hydride indicates that the hydrogen diffusion emanates from a point source at the cladding inner surface. As an approximate method to represent the effect of volume on the sunburst hydride growth, the diffusion model described above is applied in spherical coordinates with the origin at the inner cladding surface. An equivalent sphere with a maximum radius equal to the cladding thickness is used as the geometric model. A schematic of the model representation is shown in Fig 4.

As mentioned in Section 1.1, the hydrogen conditions in the fuel-cladding gap will produce immediate saturation of the absorption surface when massive hydriding is initiated. Therefore, the inner surface boundary condition will be a surface concentration at the saturation value (16200 ppm H), representing a point source of hydrogen, as long as the absorption process is active. As the sunburst hydride grows, the saturation surface will diffusion from the point source and migrate across the cladding. For locations less than r_b, the hydrogen content is equal to the saturation value. A zero flux boundary condition is employed at the outer cladding surface.

The hydrogen flux, F_{abs}, across the cladding inner surface is required to interact with the axial gas transport model. F_{abs} is the hydrogen loss rate from the gap into the cladding and is necessary to maintain the hydrogen saturation at the inner cladding surface. The hydrogen flux from the gap can be computed

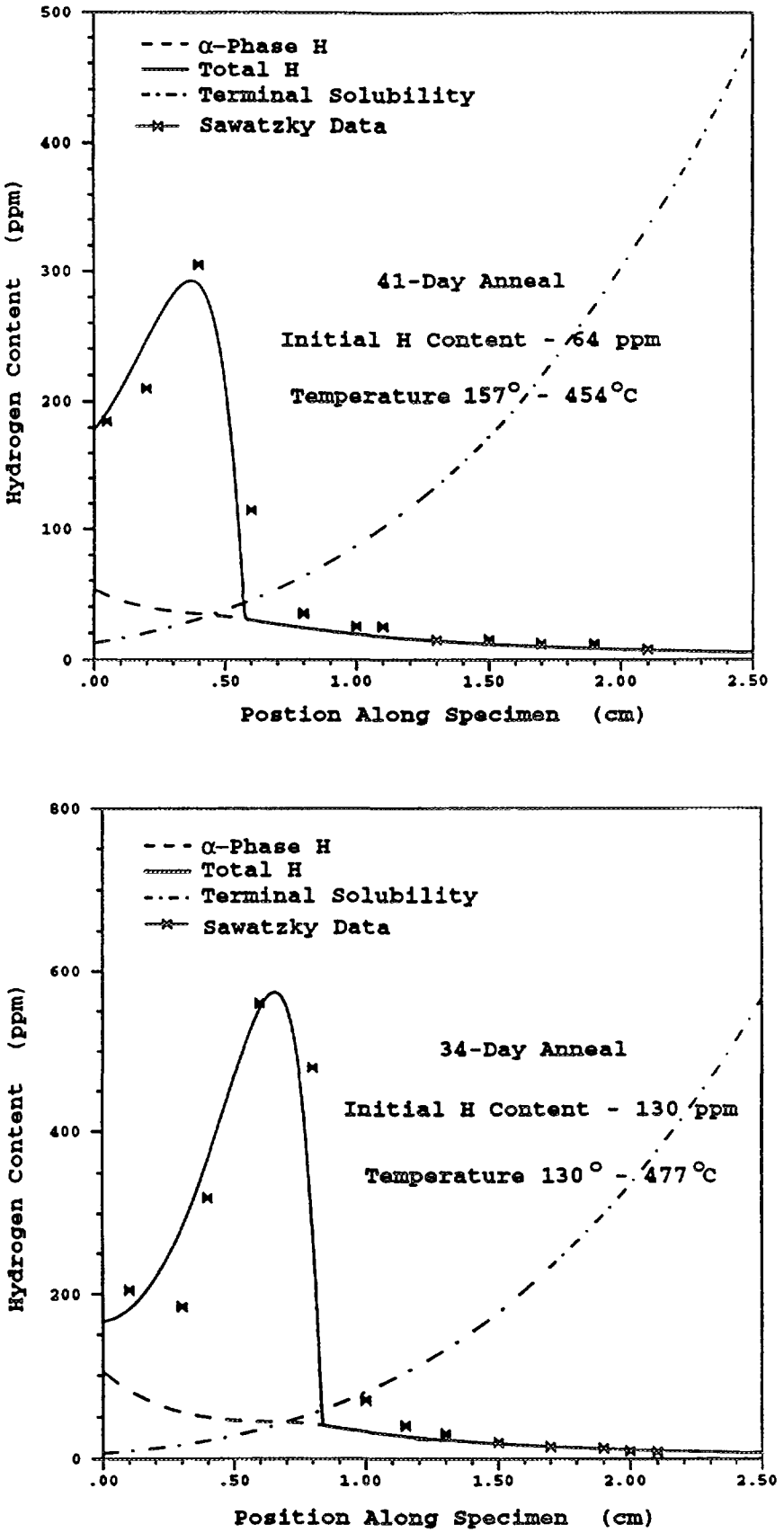

FIG. 3 Comparison of Hydrogen Diffusion Model with Sawatzky Experiments

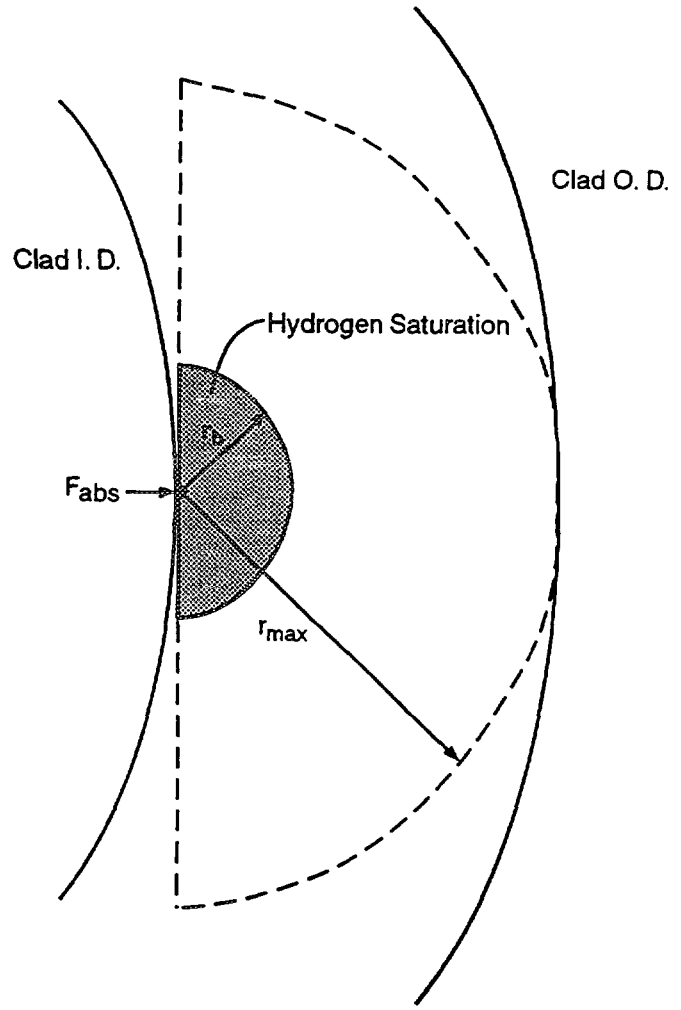

FIG. 4 Sunburst Hydride Model Representation

by determining the diffusional flux in the cladding at the saturation boundary r_b. At the saturation boundary, the hydrogen flux is given by Equation 2-9 evaluated at r_b, or

$$F_{abs} = -D_h \frac{\delta C}{\delta r}\Big|_b - \frac{Q^* D_h C}{RT^2} \frac{dT}{dr}\Big|_b \qquad (2\text{-}12)$$

As long as the conditions in the fuel-cladding gap are conducive for hydrogen absorption, the hydrogen loss from the fuel-cladding can be represent by this approach.

3. MODEL VERIFICATION

The power reactor rod Hatch 1 Rod F4 was analyzed with the hydrogen evolution model to determine the fuel rod behavior resulting from operation with a primary defect. Rod F4 is a BWR fuel rod with barrier cladding which operated for 2 cycles, obtaining a discharge average exposure of 17 GWd/MTU. A primary defect developed in the upper plenum location during the initial portion of the second cycle of operation. The rod operated without significant physical deterioration for approximately 8 months, at which time, an increase in activity level was observed after a local power change. Post-irradiation examinations revealed a considerable amount of hydride formations in the lower third of

the fuel rod. An axial crack in this region was also observed. Additional information, including a discussion of the operational characteristics, is provided in Reference [14].

Two analyses are presented to demonstrate the dependence of clad oxidation and hydriding behavior on the oxidation rate of the cladding inner surface. In the base analysis, an oxidation rate, which was twenty times that of Zircaloy-2, is used to represent the oxidation kinetics of the zirconium liner in steam. A second analysis is presented that uses a Zircaloy-2 oxidation rate. This second analysis provides information for a "non-lined" rod operating under identical power conditions. Rod parameters that described the irradiated condition of the fuel rod were used to initialize the analysis, including the gap thickness, cladding strains, and the internal gas composition. The primary defect was introduced at the time indicated from the coolant activity, and the location determined from the PIE information was used. For both cases, the axial profile of the predicted hydrogen concentration in the fuel-cladding gap and the inner surface oxide thickness are shown in Fig. 5 at the end of eight months of operation. Each case analyzed developed hydrogen rich regions in the fuel rod gap. However, the axial extent is considerably more for the high oxidation rate case, producing conditions in the gap that effectively shut off the inner surface oxidation in the lower third of the fuel rod. As a consequence, the oxide thickness in the lower third remains low ($< 5\mu m$). Based on the oxide thickness criterion presented in Section 2.1.2, the lower one third of the fuel rod is susceptible to sunburst hydride formation. This agrees well with the PIE observations summarized in Fig 6. The ratio of hydrogen content to inner surface oxide thickness is presented in Fig 6 as determined from the PIE measurements. For expected hydrogen pickup from corrosion, this ratio is constant at ~2 ppm/μm. The ratio increases dramatically for massive hydriding conditions since the hydrogen absorption is independent of oxide thickness. The predicted axial zone corresponds well with the PIE results which shows ratios exceeding 3 ppm/μm in the lower one third of the fuel rod.

In contrast, the hydrogen rich zone for the Zircaloy-2 oxidation case develops slowly and allows for continued oxide formation. Therefore, a protective layer of oxide exists over the entire fuel rod length, as shown in Fig. 5. The only region susceptible for hydriding is the lower 50 cm. The difference in oxide thickness in the upper region between the two cases can be attributed to the oxidation rate.

4. CONCLUSIONS

A hydrogen evolution model for LWR fuel rods operating with a primary defect has been developed for use in the FREY fuel behavior program. The axial gas transport and the chemical reactions associated with the steam in the fuel-cladding gap are represented in the model. To include the effects of hydrogen on the cladding, the approach contains a hydrogen absorption and diffusion model that considers the initiation and growth of sunburst hydrides. A unique method is used to relate the hydrogen transport in the fuel-cladding gap to the absorption of hydrogen by the cladding. By using the hydrogen evolution model on actual power reactor rods that have operated with primary defects, a relationship between the hydrogen concentration in the gap and the inner cladding oxide thickness has been identified which when satisfied will induce massive hydriding. Once complete, the hydrogen evolution model will be able to determine the effects of operational procedures and fuel design changes on the oxidation and hydriding kinetics of LWR fuel rods operating with a primary defect.

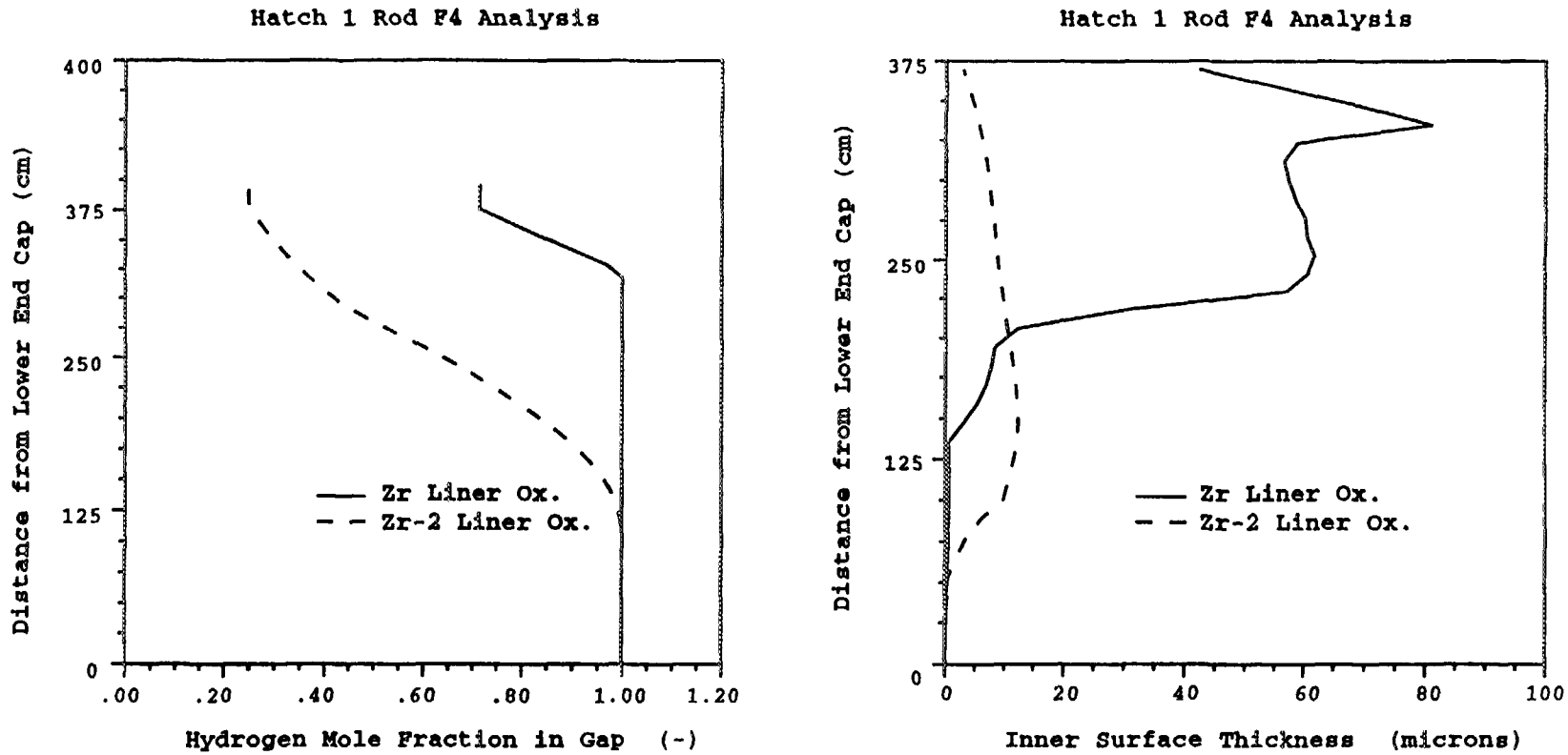

FIG. 5 Hydrogen Concentration in Gap and Inner Surface Oxide Thickness Profiles After 8 Months of Operation for Hatch 1 Rod F4

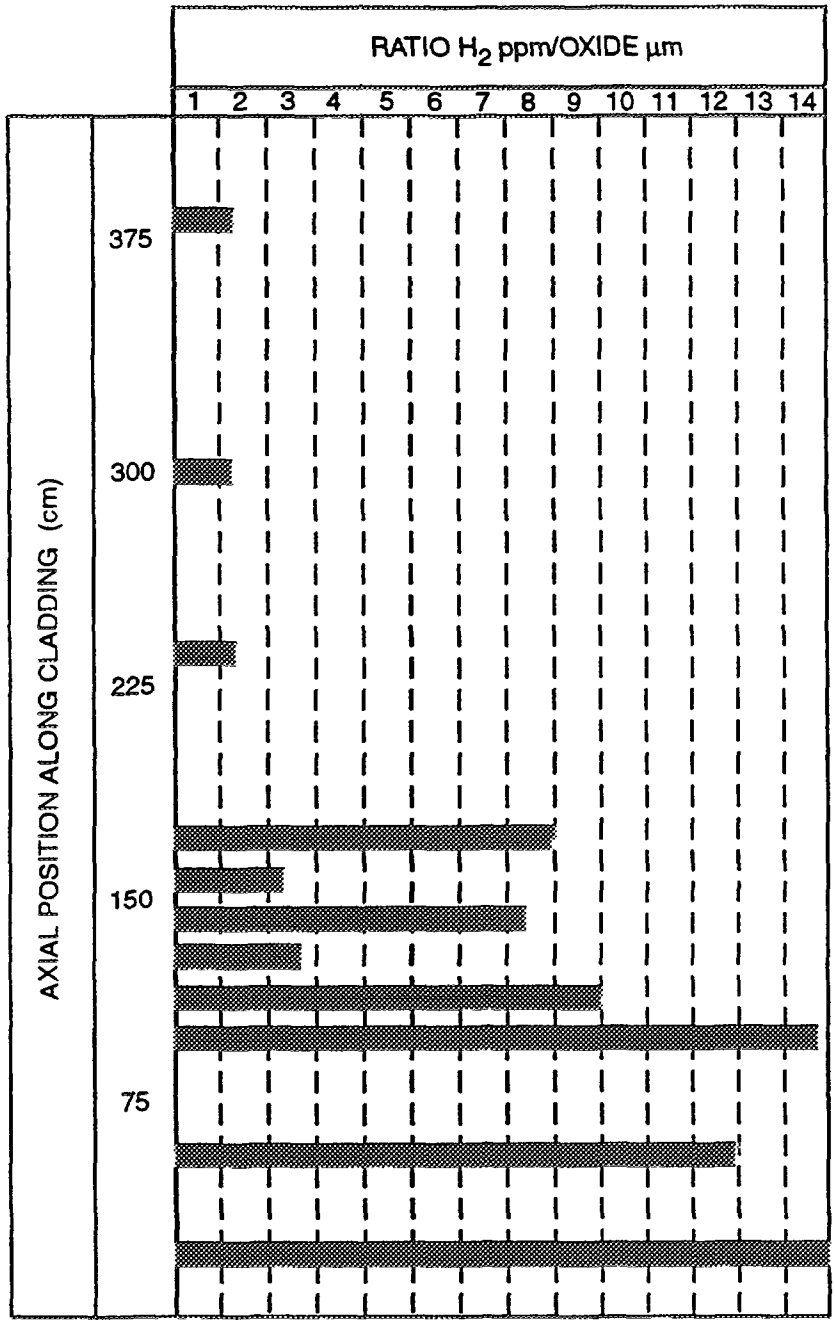

FIG. 6 Ratio of Cladding Hydrogen Content to Inner Surface Oxide Thickness Determined from PIE Measurements [14]

REFERENCES

[1] PICKMAN, D.O., "International Cladding Corrosion Effects", Nucl. Eng. and Design, 33, 141 (1975).

[2] CLAYTON, J.H., "International Hydriding In Irradiated Defected Zircaloy Fuel Rods", Zirconium in the Nuclear Industry: Eight International Symposium, ASTM STP 1023, American Society for Testing and Material, Philadelphia, (1989) pp 266-288.

[3] LOCKE, D.H., "The Behavior of Defective Reactor Fuel," Nuc. Eng. and Design 21, (1972) 318-330.

[4] MARSHALL, R.P., "Absorption of Gaseous Hydrogen by Zircaloy 2," J. Less-Common Metals, 13, (1967) 45-54.
[5] UNE, K., "Kinetics of Reaction of Zirconium Alloy with Hydrogen," J. Less-Common Metals, 57, (1978) 93-101.
[6] LUNDE, L., "Localized or Uniform Hydriding of Zircaloy: Some Observations on the Effect of Surface Conditions; J. Nuc. Mat.44 (1972) 241-245.
[7] RASHID, Y.R., et al., "FREY-01: Fuel Rod Evaluation System, "Volume 14, EPRI NP-3277, February 1993.
[8] Halden Memorandum, "Diffusional Mixing in LWR Fuel Rods", FNOTE 357,1992-06-09, 1992.
[9] BIRD, R.B., et al., Transportation Phenomena, Wiley & Sons, New York, New York (1960), p.557.
[10] OLANDAR, D.R., VAKNIN, S. "Secondary Hydriding of Defected Zircaloy-Clad Fuel Rods," EPRI TR-101773, January 1993.
[11] SAWATZKY, A., "Hydrogen in Zircaloy-2: Its Distribution and Heat Transport," J. Nuc. Mat.2, No.4 (1960) 321-328.
[12] KAMMENZIND, B.F., et al., "Hydrogen Pickup and Redistribution in Alpha-Annealed Zircaloy-4," WAPD-T-3010, July 1993.
[13] KEARNS, J.J., J. Nucl. Mater., 22, (1967) 292-303.
[14] ARMIJO, S., "Performance of Failed BWR Fuel," Proceedings ANS International Topical Meeting on LWR Fuel Performance, West Palm Beach, FL, April 1994.

INTEGRITY: A SEMI-MECHANISTIC MODEL FOR STRESS CORROSION CRACKING OF FUEL

M. TAYAL, K. HALLGRIMSON, J. MACQUARRIE, P. ALAVI
Atomic Energy of Canada Ltd,
Mississauga, Ontario,
Canada

S. SATO, Y. KINOSHITA, T. NISHIMURA
Electric Power Development Company Ltd,
Tokyo, Japan

Abstract

In this paper we describe the features, validation, and illustrative applications of a semi-mechanistic model, INTEGRITY, which calculates the probability of fuel defects due to stress corrosion cracking. The model expresses the defect probability in terms of fundamental parameters such as local stresses, local strains, and fission product concentration. The assessments of defect probability continue to reflect the influences of conventional parameters like ramped power, power-ramp, burnup and Canlub coating. In addition, the INTEGRITY model provides a mechanism to account for the impacts of additional factors involving detailed fuel design and reactor operation. Some examples of the latter include pellet density, pellet shape and size, sheath diameter and thickness, pellet/sheath clearance, coolant temperature and pressure, etc. The model has been fitted to a database of 554 power-ramp irradiations of CANDU fuel with and without Canlub. For this database the INTEGRITY model calculates 75 defects vs 75 actual defects. Similarly good agreements were noted in the different sub-groups of the data involving non-Canlub, thin-Canlub, and thick-Canlub fuel. Moreover, the shapes and the locations of the defect thresholds were consistent with all the above defects as well as with additional 14 ripple defects that were not in the above database. Two illustrative examples demonstrate how the defect thresholds are influenced by changes in the internal design of the fuel element and by extended burnup.

1. INTRODUCTION

The performance record of CANDU[1] fuel is excellent, with fuel bundle integrity exceeding 99.9%[1]. Most of the defects occurred during identifiable departures from the norm, and helped improve our understanding of the nature and level of defect probabilities. Previous surveys of the defects have shown that in these small number of defects, stress corrosion cracking (SCC) is an important mechanism for fuel failures [1].

At present empirical correlations [2,3,4] are available to define the limits of powers and of power-ramps within which CANDU fuel can be operated without risk of failure from SCC under normal operating conditions. Their use is generally recommended within the ranges of their respective databases. Often fuel engineers also need to assess the impact of operating fuel under conditions beyond the existing database, for example: extended burnups; mixed oxide (MOX) fuel; slightly enriched (SEU) fuel; manufacturing variations/flaws; variations in pellet density; diametral/axial clearances; pellet length and shape; element diameter; etc. These applications generally fall outside the range of the existing databases of the empirical correlations. To help assess the likelihood of SCC under such conditions, a semi-mechanistic approach for SCC, called INTEGRITY [5], was developed in 1990.

This paper presents an evolution of the above concept and contains improved equations that increase the accuracy of the INTEGRITY model. The improved model - called INTEGRITY-2 - has been

---

[1] CANDU: CANada Deuterium Uranium

based on and compared to a database of 554 power-ramp irradiations and 14 ripple defects of CANDU fuel. The results are presented here.

At this time the applicability of INTEGRITY-2 is limited to stress corrosion cracking at circumferential ridges due to single power-ramps with dwell periods of 2.5h or longer.

In this paper we first provide some technical background relevant to SCC, followed by a discussion of the mechanistic equations and their validation. Two illustrative examples show how the defect thresholds are influenced by changes in the internal deign of the fuel element and by extended burnup.

Figure 1 defines some of the terms used in this paper. The nomenclature is given towards the end.

2. BACKGROUND

SCC of fuel element cladding occurs when the irradiation-embrittled sheath experiences high tensile stresses/strains in the presence of a corrosive internal environment provided by the fission products. It may also be influenced by hydrides, which can provide sites for crack initiation and which can also blunt the growth of cracks [6,7].

The high tensile stresses occur mostly due to pellet expansion because of power-ramps. These result from on-power fuelling and/or from changes in reactor power. Tensile stresses can also potentially be caused by excessive pressure of fission gas. Thus SCC assessments are important because collapsible sheaths experience higher stresses/strains, and because the comparatively higher operating powers of CANDU fuel lead to higher fission gas release.

About 80 - 90% of the defects during SCC-excursions so far in commercial CANDU reactors have occurred at circumferential ridges and were caused by power-ramps. Therefore the focus of this paper is on SCC defects at circumferential ridges caused by power-ramps.

Most of the remaining SCC defects have occurred at the re-entrant corner near the sheath/endcap weld, and were also caused by power-ramps. A few isolated SCC defects have also occurred due to excessive gas pressures at high burnups. At a later date we expect to expand INTEGRITY-2 to also cover the latter two subsets of SCC defects.

Both the locations noted above (circumferential ridge, endcap weld) are locations of stress/strain concentrations.

Many factors contribute to SCC in CANDU fuel. There is convincing evidence [6,7,8] that the likelihood of SCC is influenced by the following factors: the local tensile stresses and strains; the local concentration of corrodants at the crack tip; the duration of tensile stresses/strains; and the influences of microstructure, of hydrides and of irradiation on the resistance of Zircaloy to SCC. The studies to-date have focused on iodine, on cesium, and on cadmium as the likely corrodants.

We call these the mechanistic parameters pertinent to SCC. The mechanistic parameters, in turn, are affected by a number of operational and design parameters. For example, the effects of ramped power, of power-ramp, of burnup, of dwell time, and of Canlub have been documented extensively [2,6,8].

In addition, in the area of ridge stresses/strains, IRDMR[2] experiments have demonstrated that ridge strains are increased by higher density of UO_2, by faster ramp-rates, and by increased burnups [9].

---

[2] IRDMR: In-Reactor Diameter Measurement Rig

Similarly, Carter has shown that longer pellets also increase the ridge strain [10]. A study of 1988 Pickering defects has suggested [11] that fuel containing long dense pellets is more susceptible to SCC.

Likewise, in the area of corrosive internal environment, enrichment changes the heat generation rate profile within the fuel element. This changes the pellet temperature and hence the fission gas release. Previous reviews have suggested that enriched CANDU fuel power-ramped in research reactors (NRU/NRX) is more susceptible to SCC than natural-uranium fuel ramped in commercial CANDU reactors [2]. Also, gamma-radiography has demonstrated that some fission products tend to concentrate at the interfaces between neighbouring pellets [12]. For example, Lysell and Schrire report that the concentrations of I-131, I-133, Cs-134, and Cs-137 are a factor of 4 to 14 higher at the pellet interfaces compared to the mid-pellet positions [12]. This means that the number of pellets in the stack can also affect the local concentration of corrosives.

IRDMR measurements show that repeated power cycles give persistent strain cycles [13]. This can lead to a combination of SCC and corrosion-assisted fatigue [14]. Similarly, multiple ramps in power have been noted to fail fuel more easily, via the effect of unrelaxed stresses from previous ramps.

In the past, empirical correlations [2,3,4] have been developed to assess the likelihood of SCC failures. Two analytically-based models [5,15] have also been developed.

he empirical correlations generally express the defect probability as a function of: power-ramp (ΔP); ramped power (P_{max}); and burnup (ω). Sometimes the effects of dwell time and of graphite thickness are also considered.

In these, the power-ramp represents the stresses and the strains in the sheath at the ridge. The combination of ramped power, burnup, and graphite thickness represents the concentration of corrosive fission products at the inner surface of the sheath. The resistance of the sheath to SCC is represented by burnup.

As noted earlier, in addition to the operational parameters such as power ramp, ramped power, and burnup that are covered explicitly in the empirical correlations, SCC is also influenced by several design parameters such as pellet density, clearances, pellet shape, etc. The INTEGRITY model is being developed to address factors like these.

3. DATA COLLECTION

A considerable database was compiled for this study, including out-reactor tests and in-reactor ramps.

3.1 OUT-REACTOR DATA

We used Lunde and Videm's out-reactor measurements [16] on irradiated Zircaloy to quantify the effect of fluence (burnup) on the threshold stress for SCC. The data covers burnups up to 800 MW.h/kgU - see Figure 2a. The figure exhibits the expected trend that for a given hold period and corrodant concentration, the threshold stress for SCC generally decreases with burnup.

Figure 2a also shows that for a given fluence (burnup), the threshold stress for SCC depends on the concentration of the corrodant at the sheath surface. With higher concentration of the corrodant, failure threshold is reached at lower stresses for any given burnup. Thus there is a threshold combination of stress and corrodant concentration for a given burnup. This means that for each burnup one can expect a series of threshold ramped powers (ΔPs), each corresponding to a different maximum power (P_{max}). This is illustrated further in the next section.

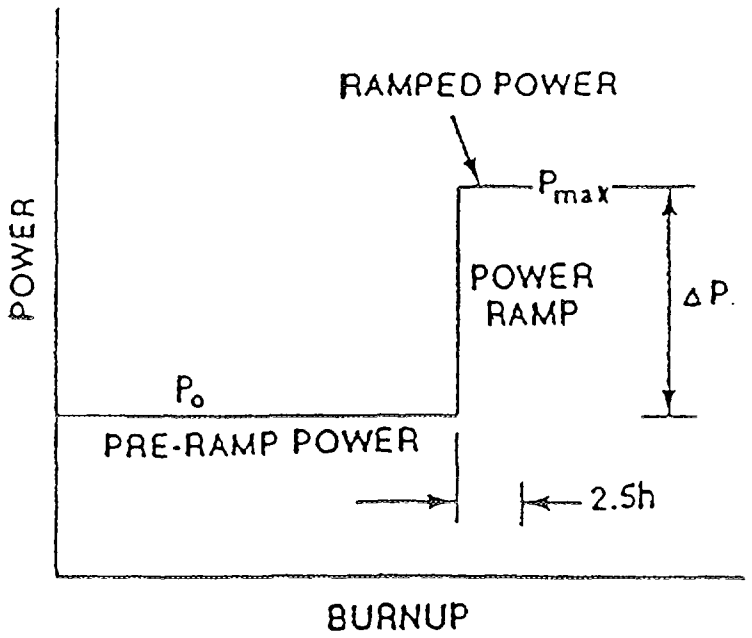

(a) POWER HISTORY

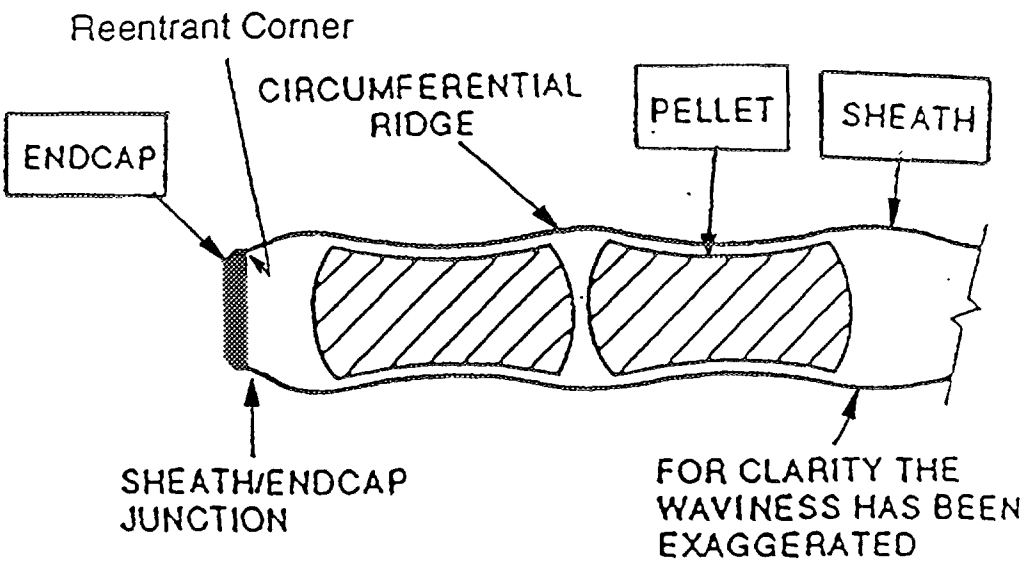

(b) FUEL ELEMENT

FIG. 1. Definitions of Terms

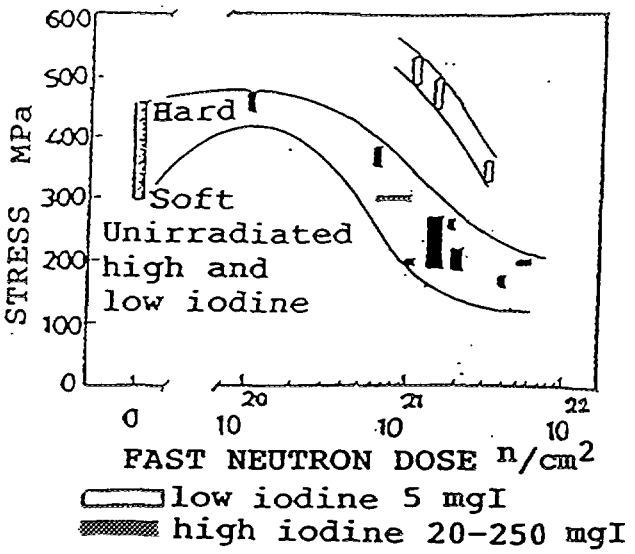

(a) Failure stress for SCC in 1-3 h.
(Reproduced from Lunde and Videm, 1980)

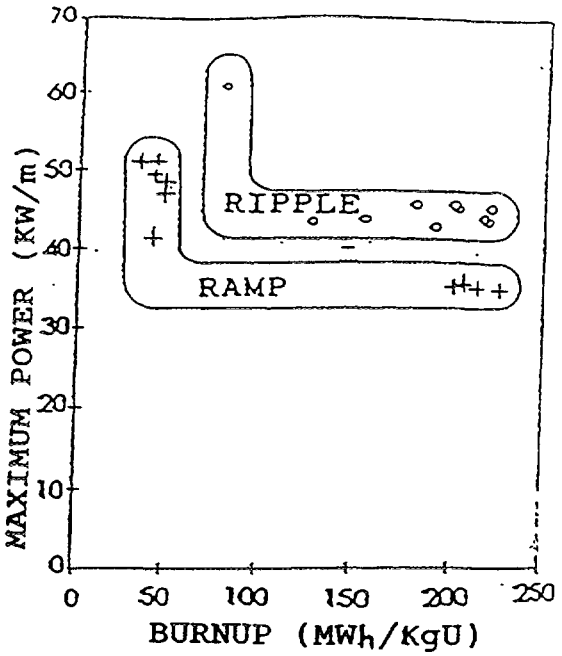

(b) Non-Canlub defects near the maximum power thresholds

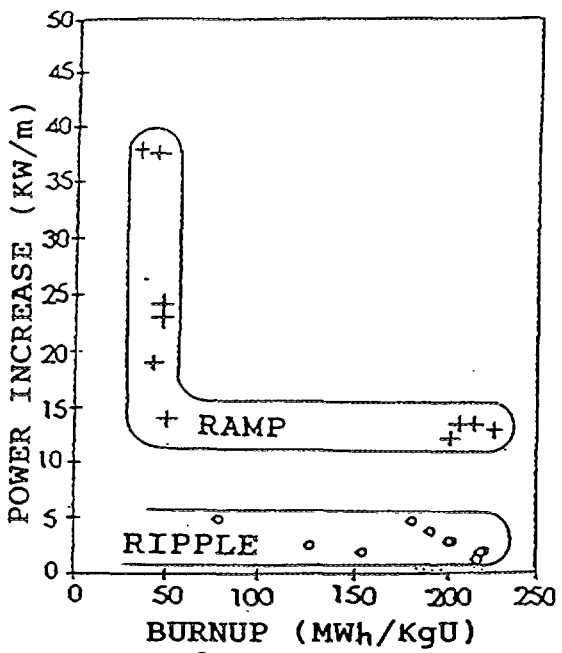

(c) Non-Canlub defects near the power increase thresholds

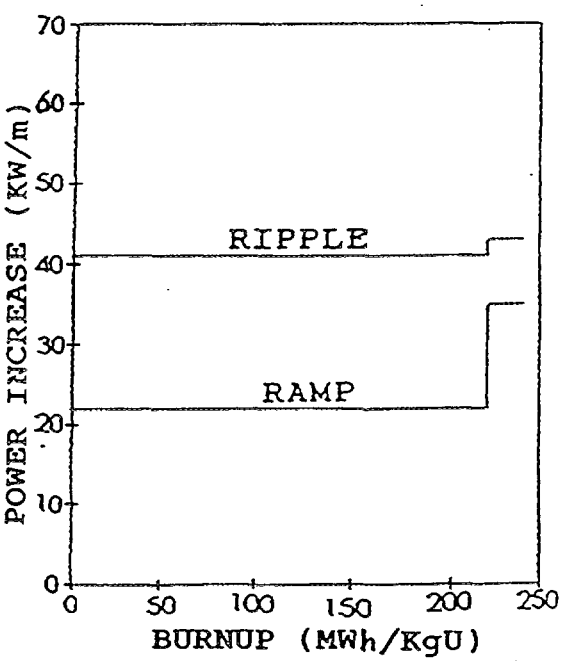

(d) Idealized power histories for ramps and ripples

FIG. 2. Data for Failure Thresholds

3.2 IN-REACTOR DATA

We also compiled a database of 568 power-increases involving 89 SCC defects at circumferential ridges under conditions of long dwell periods. They cover information from CANDU power reactors as well as from research reactors (NRU/NRX).

The data covers the following ranges:

- Ramped powers: 28 to 92 kW/m
- Power ramps: 6 to 60 kW/m
- Burnups: up to 742 MWh/kgU

The above data can be divided into the following four categories:

- Non-Canlub Ramps: 50 defects in 410 ramps;
- Non-Canlub Ripples: 14 defects. No information is readily available for intact fuel in this category;
- Thin-Canlub Ramps: 8 defects in 21 ramps;
- Thick-Canlub Ramps: 17 defects in 123 ramps.

Thus the defect probability can be calculated for the ramp data, providing a total of 75 defects in 554 irradiations. The ripple data provides 14 additional irradiations which can help locate defect thresholds but do not quantify defect probabilities.

We checked if the ramp and ripple defects come from the same population. For this purpose, we reviewed the non-Canlub defects that are close to the defect thresholds. The results are shown in Figures 2b to 2d. The ramp and ripple thresholds seem to form separate populations for maximum power as well as for power-increase - see Figures 2b and 2c.

Compared to the ramps, the ripples are generally associated with higher maximum power (Figure 2b) and lower power-ramps (Figure 2c). This can be related to the generally higher initial powers involved in the ripple data. This is further illustrated in Figure 2d, which shows idealized power histories for typical ramp and ripple defects at ~220 MW.h/kgU. It is clear that the ripple defects operated at initial powers higher than the maximum power threshold for the ramp defects. Thus they had higher amounts of fission products and required comparatively small power-ramps for the defects.

This is similar to the effect of iodine noted earlier from the independent data of Lunde and Videm [16] - see figure 2a - where higher amount of iodine lowered the threshold stress for SCC.

From this we conclude that the thresholds for maximum power and for power-ramp are mutually dependent on each other.

We note that at this time the defect data is available in terms of bundle defects for 89 ramps/568 irradiations, and in terms of element defects for only 39 ramps/158 irradiations. Our mechanistic model uses the bundle-defect data so that the model can benefit from the much larger database.

4. DEFINITIONS OF MECHANISTIC TERMS

Following Reference 5, we based our mechanistic model on fission product concentration, work density, and SCC-resistance. In this section we give their definitions.

The fission product concentration, f, represents the corrodant concentration at the inside surface of the sheath at the ridge.

The work density, u, is the area under the stress-strain curve. It is calculated by using the following equation:

$$u = \int \sigma_{11}\, d\epsilon_{11} + \int \sigma_{22} + \int \sigma_{33}\, d\epsilon_{33} + \int \sigma_{13}\, d\epsilon_{13}$$

where the integral is taken over the power-ramp. The symbols "σ" and "ϵ" represent the local stresses and strains respectively, and the subscripts 1, 2, 3 represent the radial, circumferential, and axial directions respectively. Thus the work density represents the combined influences of the radial, hoop, axial, and shear components of the elastic-plastic stresses and strains. It is equal to the work done, or energy imparted to the sheath by the expanding pellet.

The SCC-resistance measures Zircaloy's inherent resistance to failure via SCC. We define it as the work density required to fail Zircaloy via SCC at a given burnup and fission product concentration. The mathematical details of the model are given in the next section.

5. MATHEMATICAL FORMULATIONS

a. The shape of the curve for SCC-resistance was derived from the out-reactor data of Lunde and Videm [16]. As noted earlier, the above data is valid up to 800 MW.h/kgU. The equation of this shape is given by:

$$u_s = 2.358 \times 10^{12}\, F^{-0.6056} \qquad (1)$$

where

$$F = 7.58 \times 10^{18} \omega \qquad (2)$$

b. Next, we calculated the work densities for the 568 power increases described in the previous section. This was done by using the ELESTRES code [17] to calculate the incremental pellet displacements during the ramp, and the FEAST code [18] to calculate the resulting stresses, strains, and work densities at the inner surface of the sheath at the ridge. The FEAST calculations considered elastic-plastic effects. To account for the effects of local stress/strain concentrations at the circumferential ridge, a graded mesh of about 300 axisymmetric finite elements was used [17]. The SHEATH code was used to automate the calculations. Thus the work density reflects the influences of parameters like the size of the power-ramp, pellet density, diametral clearance, pellet shape (e.g. length, chamfer size, land width, dish depth), coolant pressure, etc., on the stresses and strains in the sheath.

c. The above work density was expressed in non-dimensional form by defining the work density ratio (W) as follows:

$$W = u/u_s \qquad (3)$$

Thus the work density ratio incorporates the shape of threshold stresses measured by Lunde and Videm.

d. Then we used ELESTRES to calculate the fission gas released to the pellet-sheath gap. For this calculation, we used a dwell time of 2.5 h[2] and calculated the average fission gas in the gap during the above hold after the ramp.

This was converted to fission product factor in the gap as follows - please see the nomenclature given at the end:

$$g = \frac{VD}{2\pi\ell\,(n+1)} \tag{4}$$

The above equation reflects the experimental evidence on I-131 noted earlier, in that it allows the corrosive fraction of the fission products to concentrate in narrow rings at inter-pellet interfaces. The fission product factor in the gap, g, is a function of the operating conditions and fuel design. It covers the combined influences of parameters such as ramped power, burnup, sheath diameter, number of pellets, pellet density, initial power and coolant temperature, on the amount of fission products at the inner surface of the sheath.

e. We next calculated the fission product concentration at the inside surface of the sheath at the ridge, f. To do this we subtracted the protection provided by Canlub, c, from the fission product concentration in the gap, g:

$$f = g - c \tag{5}$$

In equation (5) the net effect of Canlub is considered equivalent to a net reduction in the amount of fission products that reach the surface of the sheath.

f. The protection provided by Canlub, c, was considered proportional to the mass of Canlub for high values of fission product release. At low values of fission product release, the protection was considered to also depend on the concentration of the fission gas in the gap. Thus, based on a statistical analysis, 'c' was defined as follows:

$$c = \text{minimum of } \{g, \text{ or } [1 - \exp(-\sqrt{(qm)})]\, g, \text{ or } vm\} \tag{6}$$

Here, "m" is the mass of graphite at the ridge and is calculated from:

$$m = 2\pi r\ell tp \tag{7}$$

Thus thicker Canlub is considered to provide greater protection against SCC. In INTEGRITY the effect of Canlub is treated as a continuous function of graphite thickness rather than a series of separate curves for no-, thin-, or thick-Canlub.

g. A "Damage Index" d was defined to assess the combined influences of the work density ratio and the fission product concentration as follows:

$$d = aW^x f^y \tag{8}$$

This form of the damage index ensures that zero damage is assigned if either the work density or the fission product concentration is zero.

h. From this, a defect probability "p" was defined as [3,4]:

$$p = \frac{1}{1 + \exp\{-(d-z)\}} \tag{9}$$

i. The six empirical coefficients, a, q, v, x, y and z, were found by a least-squares regression analysis to fit the actual number of defects observed in the previous database. The methodology outlined by R. daSilva was used [4]. Four of the coefficients, a, x, y, and z, define the influences of work density ratio and of fission product concentration on the defect probability. For these trends the most reliable statistical guidance is provided by the non-Canlub ramp data because it is the most numerous. Hence this data was given the highest weight in determining these four coefficients. The thick-Canlub data was used mainly to quantify the effect of Canlub, viz. coefficients q and m. The thin-Canlub data was not used to obtain the coefficients because it contains only 21 irradiations, hence it was considered too small for statistical purposes. The non-Canlub ripple data was also not used because for that set we do not have data on intact fuel at this time, hence the defect probabilities cannot be quantified for them. Nevertheless, the final correlation was tested for consistency against all four sets of data.

In obtaining the least squares fit, we set the defect probability to 1% [2] for the non-Canlub ramp defect with the lowest value of the damage parameter.

6. GOODNESS OF FIT

The goodness of fit was checked by six separate methods: **i)** Number of observed vs calculated defects; **ii)** Shapes of calculated defect thresholds vs. data; **iii)** Distribution of defects in risk groups; **iv)** Distribution of defects on the basis of defect probability; **v)** Distribution of defect probability; and **vi)** Discrimination of defects/intacts. These are described in the following paragraphs.

i) Number of Observed vs Calculated Defects

We used the model to calculate the expected number of defects in the 3 sets of data for which the defect/intact statistics are available (i.e., excluding non-Canlub ripples). The following results were obtained: In the 410 non-Canlub ramps, the model calculated 50 defects vs. the actual number of 50. In the 21 thin-Canlub ramps, the model calculated 8 defects vs. the actual 8. In the 123 thick-Canlub ramps, the model calculated 17 defects vs. the actual 17. Thus in all, for the 554 ramps, the model calculated a total of 75 defects which is the same as the actual number (also 75).

The above information is displayed in Figure 3. The calculated numbers match the observed defects well.

ii) Shapes of Calculated Defect Thresholds vs. Data

Figures 4a and 4b show typical shapes of calculated defect thresholds vs data. Note from Figure 4a that the calculated shape of the ΔP threshold changes its curvature sharply at ~ 100 MW.h/KgU. This is very similar to the actual data. Figure 4b shows that the calculated thresholds for the non-Canlub ripple defects are consistent with the actual data, even though this data was not used in the derivation of the coefficients.

iii) Distribution of Defects in Risk Groups

This comparison follows the suggestions made by R. daSilva in Reference 14. Accordingly, the data were arranged in ascending order (smallest to highest) of the damage index. They were then split into ten groups, each containing similar number of ramps, to form deciles of risk tables. For each decile, the calculated number of defects were compared to the actual defects. Typical results are shown in Figure 4c. The trends of the calculations generally agree well with the observations.

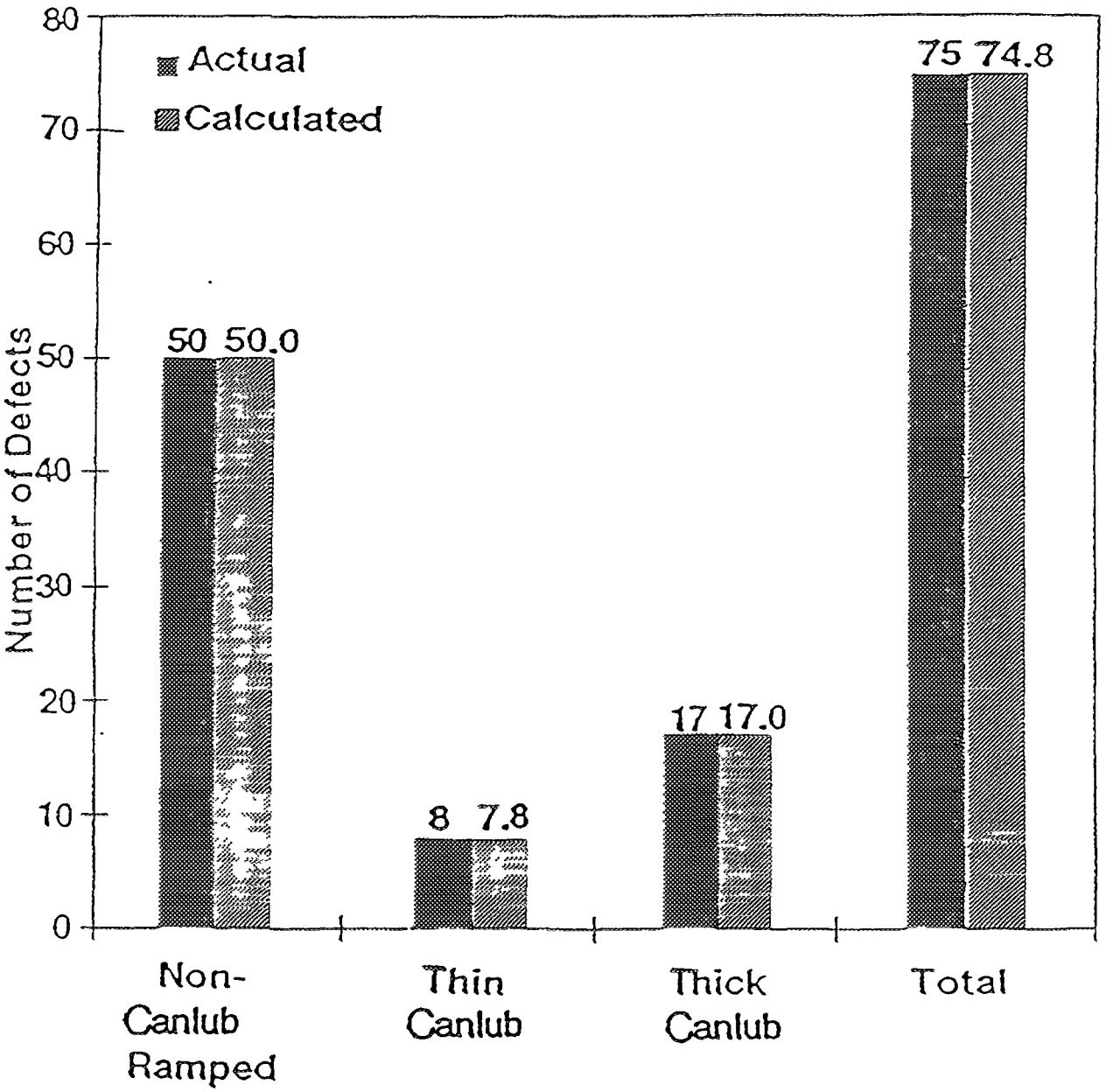

FIG. 3. *Number of Defects - Actual Versus Calculated*

iv) Distribution of Defects on the Basis of Defect Probability

This is an alternate method of examining the detailed distribution of defect probabilities, and can be used for correlations which do not explicitly quantify the risk below the defect threshold (e.g. Fuelograms [2]). Although our model does define a damage index, we are nevertheless providing this additional information for comparison and for consistency with past results. In this method, the data is grouped into ten sets depending on the calculated defect probability, for example defect probability of 0-10%, 10-20%, etc. For each set, the actual defect probability is compared with the calculated. Typical results are shown in Figure 4d. The two numbers beside each point in Figure 4d specify the number of actual defects and the total number of irradiations in that set, respectively. For example, the set representing 0-10% calculated defect probability contains 20 actual defects in 314 irradiations. The comparison is tenuous in regions where the statistics are small. Overall, our model is in reasonable agreement with data.

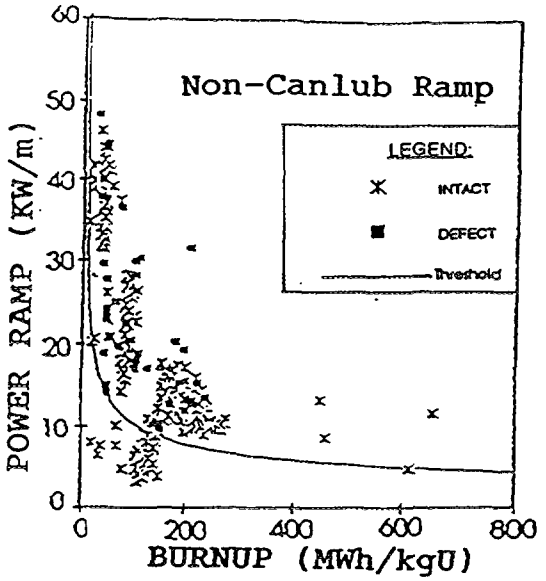

(a) Shape of the calculated Non-Canlub ramp defect threshold vs. data

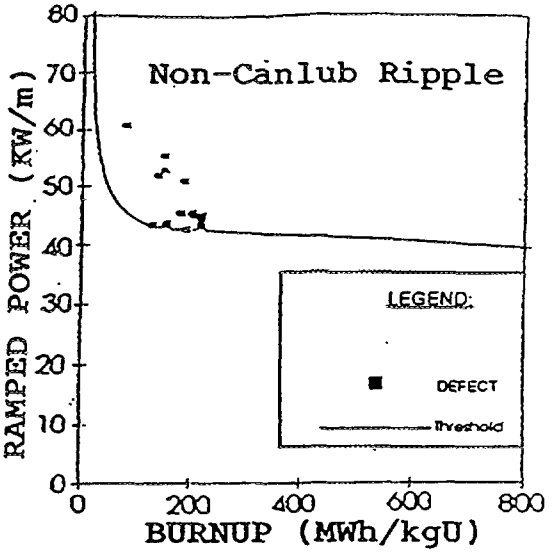

(b) Shape of the calculated Non-canlub ripple defect threshold vs. data

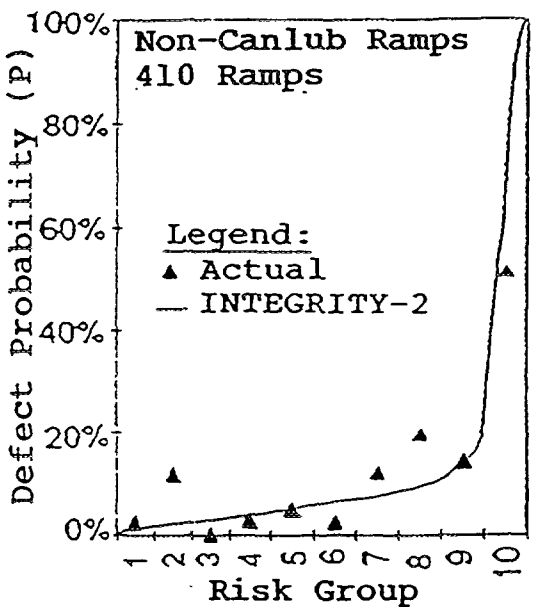

(c) Distribution of defects in risk groups

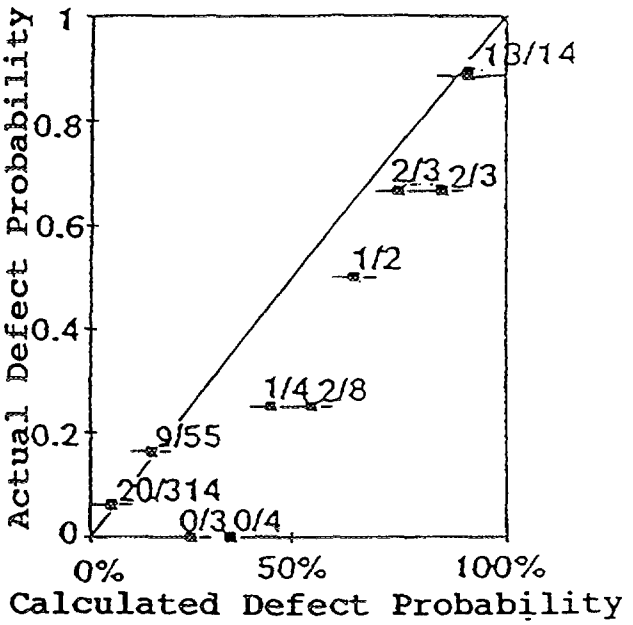

(d) Distribution of defects on the basis of defect probability

FIG. 4. Distributions of Defects - Actual Versus Calculated

v) Distribution of Defect Probability

Figure 5 shows how the defect probability is influenced by the damage index for all four sets of data. The expected s-shaped curve is clearly visible. Also, if the model were good, the density of defects should get progressively higher with increasing damage index. This is indeed exhibited by the data. Further, for the model to be good, all the defects should have a calculated defect probability of 1% or higher. This too is exhibited by the data, including the ripple defects.

vi) Discrimination of Defects/Intacts

Figure 6 checks how well the defect thresholds mark the onset of failures for all four sets of data (i.e. including the non-Canlub ripple defects). All the actual defects lie above the calculated 1% defect threshold, indicating that the calculated thresholds are consistent with the actual data.

In Figure 6, the non-Canlub ripple defects generally lie at the highest fission product concentrations. This reflects their comparatively high pre-ramp powers.

Canlub prevents some of the fission gas in the gap from reaching the sheath surface. Thus the Canlub failures occur for lower values of fission product concentration and correspondingly higher values of work density ratio. This effect is more pronounced in thick Canlub fuel, and is also visible in Figure 6.

7. FEATURES OF THE MODEL

- The shape of the defect threshold is based on out-reactor tests which define a basic, continuously-varying material property (SCC threshold). Hence the accuracy of the shape is not subject to the comparatively larger uncertainty expected in defect thresholds derived solely from a limited number of yes/no type of in-reactor defects. Thus the model is usable in the range of the database of the above out-reactor tests.

- Although the shapes of the defect thresholds are derived from out-reactor data, they do match quite well with the available in-reactor data on 568 power-increases. Also, the calculated number and distribution of defects agree well with the actual data.

- One set of equations correlates well with four different sets of data, i.e., non-Canlub ramps; non-Canlub ripples; thin-Canlub ramps; and thick-Canlub ramps. This provides confidence that the pertinent trends are captured well.

- The defect probability curves show continuous variations with operational parameters like ΔP and P_{max}. Thus some of the unnatural jumps and plateaux exhibited by a previous empirical correlation have been eliminated.

- The principles of statistics are followed rigorously. This has eliminated a weakness of a previous empirical correlation.

- The model recognizes the interdependence of P_{max} and ΔP in determining the defect thresholds. This makes it consistent with the observed differences in ramp and ripple defect thresholds, as well as with the differences in stress thresholds observed by Lunde and Videm for different corrodant concentrations.

- The model incorporates the influence of operational parameters such as power-ramps, ramped powers, coolant temperature, and coolant pressure; and of design variables such as Canlub mass, pellet density, clearances and pellet shape, etc.

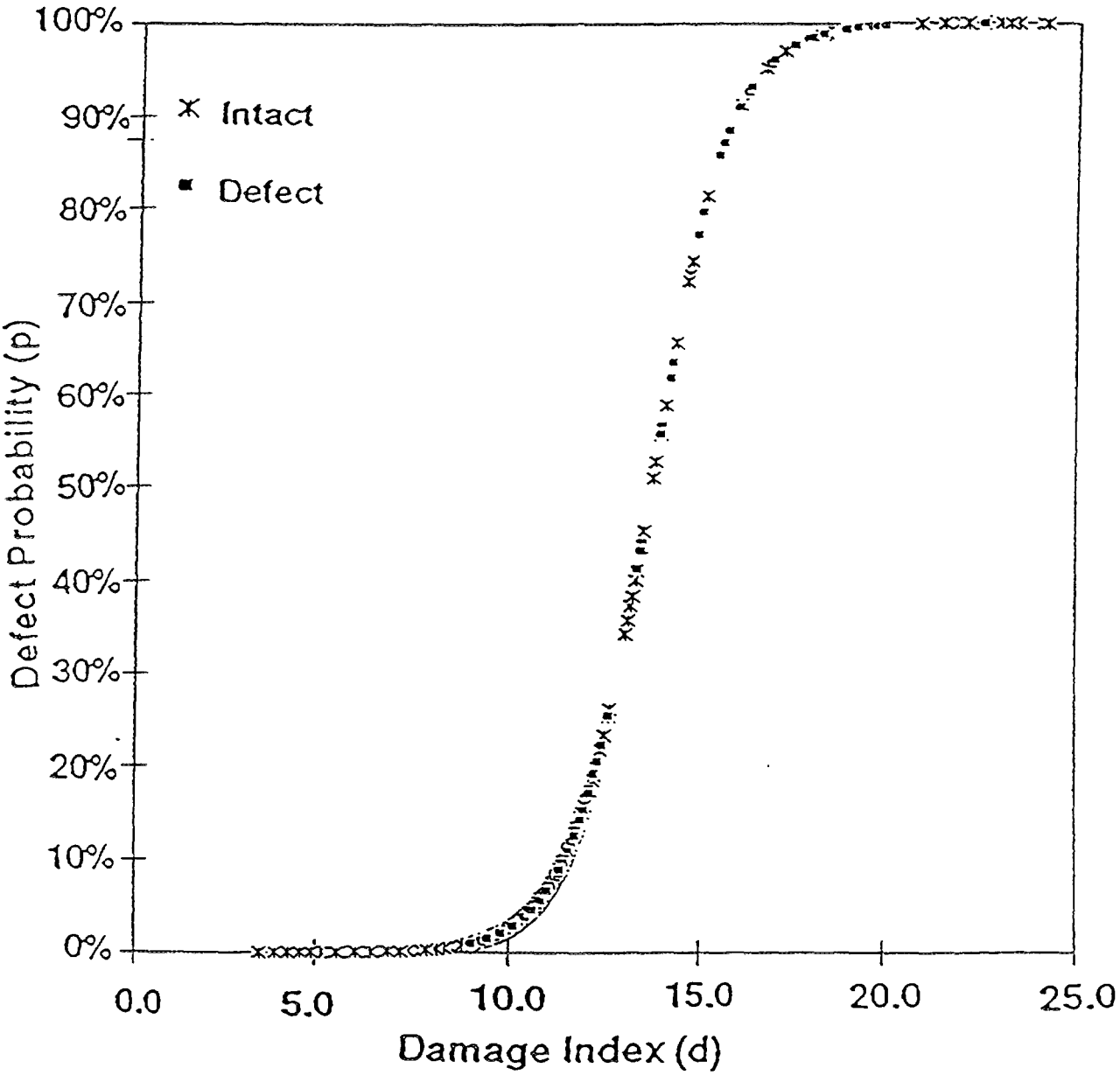

FIG. 5. Defect Probability Versus Damage Index - All Data

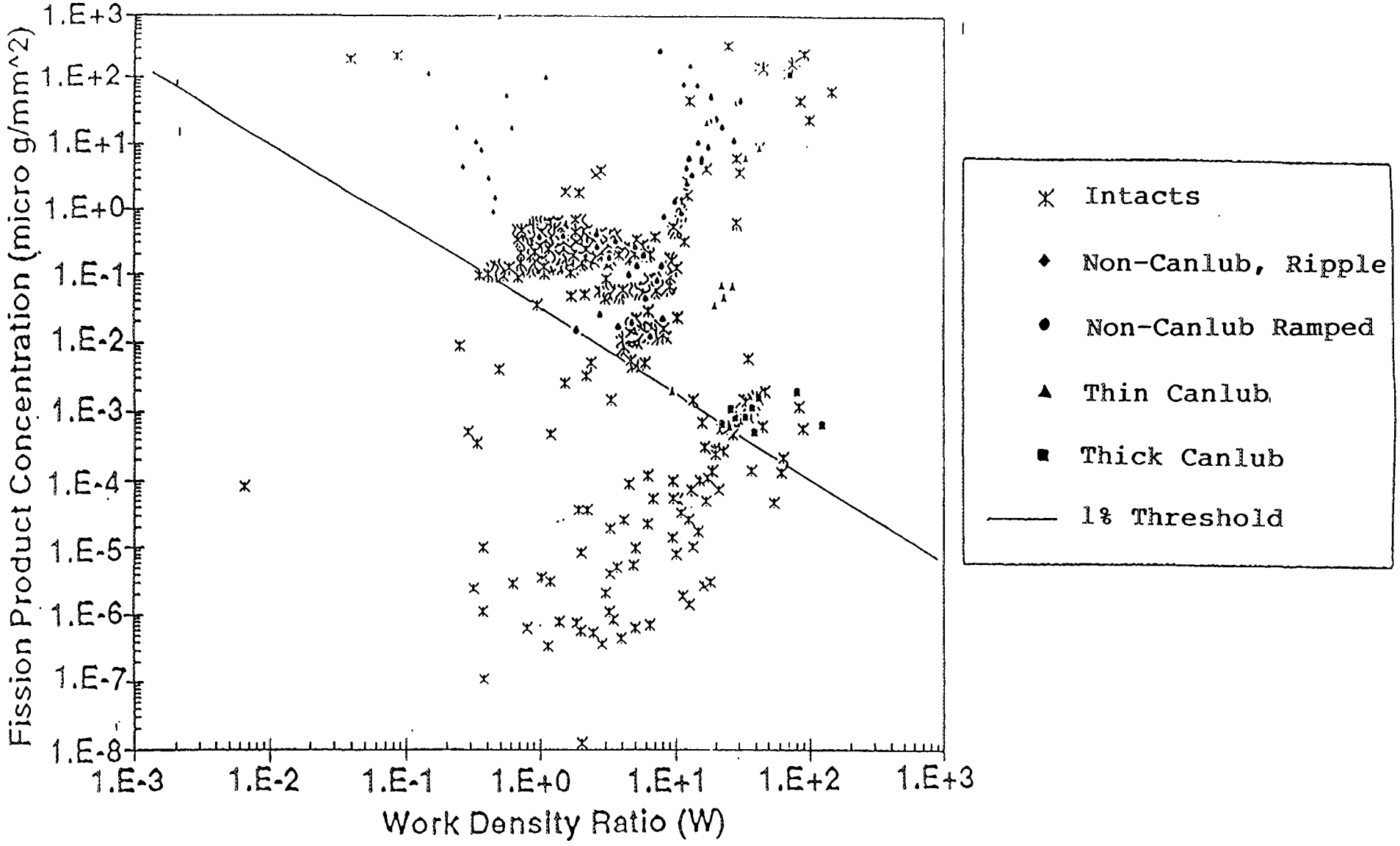

FIG. 6. Defect Threshold for All Data

The model is considered valid for burnups up to 800 MW.h/kgU; infinite dwell times (longer than 2.5 h); and single ramps in power. The model is limited to estimates of defect probability due to stress corrosion cracking at circumferential ridges.

The next two sections provide illustrative examples on the use of the INTEGRITY model.

8. ILLUSTRATIVE EXAMPLE #1: PELLET DENSITY

As an illustrative example, we assessed the influence of pellet density on the defect probability of 37-element CANDU fuel. Figure 7a shows the power history considered, consisting of a ramp of 35 kW/m to a maximum power of 56 kW/m at 100 MW.h/kgU. Figure 7b shows the calculated trends of the damage index, and demonstrate the opposing effects of density, pellet temperature and porosity. At low densities, increasing the density decreases pellet temperatures which decreases the damage index. At higher densities, the low porosity in high-density fuel causes higher expansion of the pellet, which increases the damage index. For this power history the defect probability stays below 1% for pellet densities less than 10.8 g/cc.

9. ILLUSTRATIVE EXAMPLE #2: HIGH BURNUP

As another illustrative example, we assessed the influence of extended burnup - about 700 MW.h/kgU - on the integrity of a fuel element of reduced diameter containing slightly enriched uranium fuel. An optimized pellet shape was considered featuring short pellets, big chamfers, big land, and reduced density [19]. Figure 7c shows the combinations of power-ramps/ramped-powers considered. The ramped powers range from 25 to 56 kW/m, and the power-ramps from 1 to 40 kW/m. Figure 7d shows the calculated damage index. Again, the calculated trends look reasonable. The defect probabilities reflect a balance between higher fission gas release due to enrichment, lower volume of fission gas release due to smaller diameter, tendency for higher concentration of fission products due to reduced diameter, and lower stresses/strains due to the optimized shape and density of the pellet.

10. DISCUSSION

The INTEGRITY model discussed here does not replace the empirical correlations now in use. Rather, it provides a means of extending the range of applicability of the correlations, to conditions that are either not covered by the existing data base or are sparsely represented.

The INTEGRITY model continues to reflect the influences of operational parameters that are currently used in existing empirical correlations for defect thresholds/probabilities, viz: power-ramp, ramped power, and burnup. In addition, it provides a vehicle to account for the impacts of detailed fuel design parameters such as pellet density, pellet shape and size, sheath diameter and thickness, pellet/sheath clearances, etc. Additional operational parameters can also be covered, for example coolant temperature and pressure, etc. As noted earlier, previous experiments and irradiations have already demonstrated that combinations of the above features can have considerable impacts on factors such as stresses, strains, and fission gas releases, and hence on SCC defects.

The examples discussed above demonstrate how INTEGRITY can be applied to obtain first-order estimates of defect thresholds and probabilities in situations where sufficient empirical data may not exist to provide reliable guidance. With further evolution, some specific applications of the preceding concepts could include the following:

10.1 GUIDE THE ACCEPTANCE/LOADING OF NEW FUEL

Sometimes the as-fabricated fuel contains combinations of tolerances that are not sufficiently covered by the previous well-characterized database on ramp testing. One example is fuel of high mass,

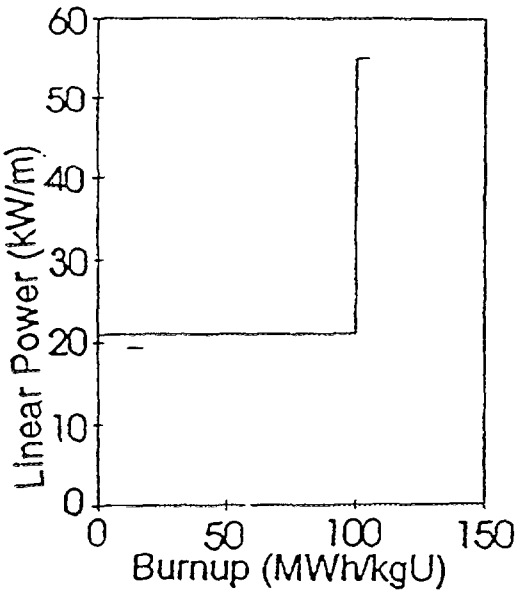

(a) Power Ramp Data
(Illustrative Example #1)

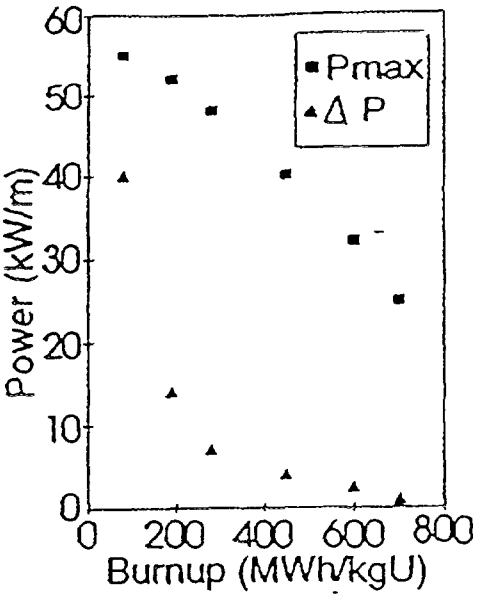

(c) Power History for
ALS CANDU Reactor
(Illustrative Example #2)

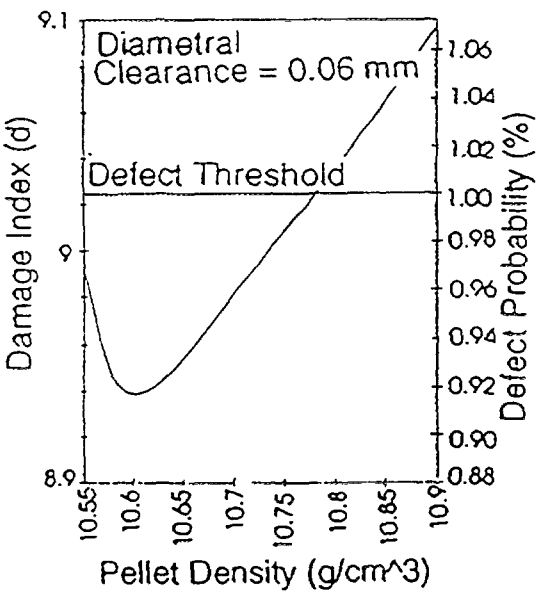

(b) Effect of Density
(Illustrative Example #1)

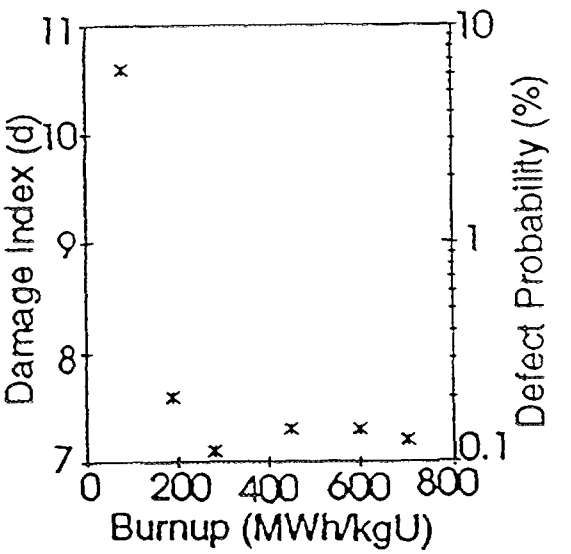

(d) Damage Index and
Defect Probability
(Illustrative Example #2)

FIG. 7. Illustrative Examples

including high UO_2 density and low clearances. Or, the fuel may contain manufacturing flaws whose impact is unknown from previous tests. The approach outlined here can help provide an interim guidance about the expected performance of such fuel.

10.2 AID FUEL SPECIFICATIONS

The model can be used to define the sensitivity of SCC defects for combinations of fuel fabrication parameters like pellet density, pellet shape, pellet/sheath clearances, etc. This can help confirm that the limits in fuel specifications reflect only the safe combinations of above and related parameters.

10.3 GUIDE REACTOR OPERATION

Similarly, the approach can help guide reactor operation in new areas of operation, e.g., effects of power cycles, extended burnups, non-routine startups, non-routine fuelling, etc.

10.4 AID EVOLUTION OF FUEL DESIGN

Some specific fuel evolution activities currently underway include[1]: High Burnup Fuel, Slightly Enriched Uranium Fuel, Fuel for Highly Advanced Core, Low Void Reactivity Bundle, Mixed Oxide (MOX) Fuel, and DUPIC (Direct Use of PWR Fuel in CANDU). Again, the approach outlined above can be applied in these evolutions.

11. CONCLUSIONS

a. Two independent sets of data suggest that defect thresholds for maximum power (fission products) and for power-ramp (stresses/strains) are mutually dependent on each other.

b. A mechanistic model called INTEGRITY-2 has been developed for assessing SCC at ridges. It accounts for fuel design as well as operational parameters in calculating SCC. Its applicability extends to burnups of 800 MW.h/kgU.

c. The model shows excellent fit with defect statistics in 554 ramps. In particular, checks show:

- 50 calculated defects vs. 50 actual defects in 410 non-Canlub ramps;
- 8 calculated vs. 8 actual defects in 21 thin-Canlub ramps; and
- 17 calculated vs. 17 actual defects in 123 thick-Canlub ramps.

d. The shapes of the defect threshold curves are consistent with the distributions of the actual data noted above, and with 14 additional defects involving power ripples in non-Canlub fuel. The calculated distributions of the defects in different risk regions are also consistent with actual data.

e. The model contains a term for the mass of Canlub, so any thickness of Canlub can be assessed.

f. An illustrative example shows that the pellet density first decreases, then increases, the defect probability. This is due to the competing influences of pellet temperature and pellet porosity. Another illustrative example suggests that fuel integrity can be enhanced by optimizing the shape and density of the pellet.

ACKNOWLEDGEMENTS

We thank Mr. T. Tanaka (EPDC), J.W. Love (AECL), R. Sejnoha (AECL), I.E. Oldaker (AECL), T. Carter (AECL), M. Floyd (AECL), P. Chan (AECL), W. Richmond (AECL), D.E. Teed

(GEC), M. Hoare (Zircatec), and J. Lawless (Univ. of Waterloo), for valuable technical discussions and help during this project. We also thank L. Lunde (Norway), K. Videm (Norway), and Journal of Nuclear Materials for permission to reproduce Figure 2a. Financial support by Electric Power Development Company Limited, Japan, is also gratefully acknowledged.

LIST OF SYMBOLS

a	empirical coefficient
c	empirical coefficient for the effect of Canlub on fission product concentration
d	damage index
D	density of free gas
f	fission product concentration at the sheath inner surface at the ridge ($\mu g/mm^2$)
F	fast neutron fluence ($>$ 1 Mev) (n/cm^2)
g	fission product factor in the gap ($\mu g/mm^2$)
ℓ	width of the ring over which the fission products concentrate at the circumferential ridge (mm)
m	mass of Canlub (,ug)
n	number of pellets in the fuel element
ΔP	power-ramp (kW/m)
P_{max}	ramped power (kW/m)
p	defect probability (fraction)
q	empirical coefficient
r	inner radius of the sheath (mm)
t	thickness of Canlub (μm)
u	work density (MPa)
v	empirical coefficient
V	volume of released fission gas
W	work density ratio
x, y, z	empirical coefficients

Greek Symbols

ϵ	strain
ρ	density of Canlub
σ	stress
ω	burnup (MW.h/kgU)

Subscript

s	shape of threshold

REFERENCES

[1] GACESA M., BOCZAR P.G., LAU J.H.K., TRUANT P.T., MACICI N., YOUNG E.G., "Canadian Fuel Development Program", Third International Conference on CANDU Fuel, Canadian Nuclear Society, Pembroke, Canada, 1992 October 04-08.

[2] PENN W.J., LO R.K., AND WOOD J.C., "CANDU Fuel - Power Ramp Performance Criteria", Nuclear Technology, 34 (1977), pp. 249-268.

[3] HAINS A.J. , DASILVA R.L. AND TRUANT P.T., "Ontario Hydro Fuel Performance Experience and Development Program", International Conference on CANDU Fuel, Canadian Nuclear Society, Chalk River, 1986 October 06-08.

[4] DASILVA R.L., "CAFE - A Probabilistic Model for Predicting CANDU Fuel SCC Power Ramp Failures", Third International Conference on CANDU Fuel, Pembroke, Canadian Nuclear Society, 1992 October 04-08.

[5] TAYAL M., MILLEN E., SEJNOHA R., VALLI G., "A Semi-Mechanistic Approach to Calculate the Probability of Fuel Defects", AECL Report AECL-10642, 1992 October.

[6] COX B., "Pellet Clad Interaction (PCI) Failures of Zirconium Alloy Fuel Cladding - A Review", Journal of Nuclear Materials, 1990 August, Vol. 172, Issue -3, pp. 249-292.

[7] COX B., "Environmentally Induced Cracking of Zirconium Alloys - A Review", Journal of Nuclear Materials, 1990 January, Vol. 170, Issue -1, p 1-23.

[8] COX B., WOOD J.C., "Iodine Induced Cracking of Zircaloy Fuel Cladding - A Review", Atomic Energy of Canada Limited, Report AECL-4936, 1974.

[9] FEHRENBACH P.J., MOREL P.A., SAGE R.D., "In-Reactor Measurement of Cladding Strain: Fuel Density and Relocation Effects", Nuclear Technology, Volume 56, 1982, pp. 112-119.

[10] CARTER T.J., "Experimental Investigation of Various Pellet Geometries to Reduce Strains in Zirconium Alloy Cladding", Nuclear Technology, Volume 45, 1979, pp. 166-176.

[11] FLOYD M.R., CHENIER R.J. LEACH D.A., ELDER, R.R. "An Overview of the Examination of Fuel as a Follow-up to the 1988 November Overpower Transient in Pickering NGS-A Unit 1", Third International Conference on CANDU Fuel, Canadian Nuclear Society, Pembroke, Canada, 1992 October 04-08.

[12] LYSELL G., SCHRIRE D. "Fission Product Distribution at Different Power Levels", IAEA Meeting on Fuel Performance at High Burnup for Water Reactors, Studsvik, Sweden, 1990 June 05-08, IWGFPT/36, pp. 132-139.

[13] FEHRENBACH P.J., MOREL P.A. "In-Reactor Measurement of Clad Strain: Effect of Power History", AECL Report AECL-6686, 1980.

[14] TAYAL M., MANZER A.M., SEJNOHA R., KINOSHITA Y., HAINS A.J., "The Integrity of CANDU Fuel during Load Following", AECL Report AECL-9797, 1989.

[15] NOTLEY M.J.F., "PRAMP - A Model for Calculating the Probability of Fuel Defects", Third International Conference on CANDU Fuel, Canadian Nuclear Society, Chalk River, Canada, 1992 October 4-8, pp 5-11 to 5-20.

[16] LUNDE L., VIDEM K. "The Influence of Testing Conditions and Irradiation on the Stress Corrosion Cracking Susceptibility of Zircaloy", Journal of Nuclear Materials, 95 (1980), pp. 210-218.

[17] TAYAL M., "Modelling CANDU Fuel Under Normal Operating Conditions: ELESTRES Code Description", Atomic Energy of Canada Limited, Report AECL-9331, 1987.

[18] TAYAL M., "FEAST: A Two-Dimensional Non-Linear Finite Element Code for Calculating Stresses", Seventh Annual Conference, Canadian Nuclear Society, 1986. Also Report AECL-8763.

[19] TAYAL M., RANGER A., SINGH P.N., HASTINGS I.J., HAINS A.J., KINOSHITA Y., "The Integrity of CNADU Fuel at Extended Burnups", Canadian Nuclear Society, Second International Conference on CANDU Fuel, Pembroke, Canada, 1989 October 1-5, pp 413-428.

TRANSIENT FUEL ROD BEHAVIOUR PREDICTION WITH RODEX-3/SIERRA

M.R. BILLAUX, S.H. SHANN, L.F. VAN SWAM
Siemens Power Corporation,
Richland, Washington,
United States of America

Abstract

This paper discusses some aspects of the fuel performance code SIERRA (SIEmens Rod Response Analysis). SIERRA, the latest version of the code RODEX-3, has been developed to improve the fuel performance prediction capabilities of the code, both at high burnup and during transient reactor conditions. The paper emphasizes the importance of the mechanical models of the cracked pellet and of the cladding, in the prediction of the transient response of the fuel rod to power changes. These models are discussed in detail. Other aspects of the modeling of high burnup effects are also presented, in particular the modeling of the rim effect and the way it affects the fuel temperature.

1. INTRODUCTION

During the last three years, considerable effort has been devoted at Siemens Power Corporation (SPC) to upgrade the fuel performance code RODEX-3 [1-2]. The objective was to derive a code for PWR and BWR applications, integrating the knowledge gained in the recent years from Siemens internal and international research programs, and meeting modern Quality Assurance standards. A modular structure was adopted to facilitate the introduction and testing of new models, and to simplify the comparison of new models with the old ones. British units were changed to S.I. units. New iterative and convergence techniques were introduced to prevent unpredictable numerical instabilities.

All the individual models of the code were reviewed, tested and redesigned where necessary, so as to improve the code capability to predict the fuel rod behavior at high burnup and during transient conditions. The physical properties of UO_2, zircaloy, noble gases and water have also been updated. Special attention has been devoted to the burnup dependence of fuel thermal conductivity. The latter point is not discussed further in the present paper.

2. MECHANICAL MODELS OF THE FUEL PELLET AND OF THE CLADDING

A weak point of most fuel performance codes is their mechanical models. Whereas a lot of effort has been devoted in the last twenty years to the development of sophisticated fission gas release models, the mechanics of the cracked pellet and of the anisotropic cladding are generally rather primitive. This situation is paradoxical, because many more fuel rods fail from pellet-cladding mechanical interaction (PCMI) than from gas overpressure. This paradoxical situation comes perhaps from the fact that it is relatively easy to puncture an irradiated fuel rod, measure the gas pressure and analyze the punctured gas, whereas nobody has ever been able to measure a hoop (circumferential) stress at the cladding inner surface during reactor operation. Another explanation is that the theory of elasticity was developed at the beginning of the century and is assumed to be easy, whereas fission gas release is based on concepts more recently developed within the domain of solid state physics. The latter is therefore more attractive to the physicist. An attempt has been made here to define the minimum requirements for a reliable fuel rod mechanical model.

In the present paper, the transient mechanical models are defined as being those based upon a stress-strain analysis of the fuel pellet and of the cladding. An essential condition is that the total strains, used in the "compatibility equations", include the elastic strains. The stresses, compatible with the elastic deformations, are then used to calculate the fuel swelling and hot pressing, the creep of fuel and cladding, and the other stress dependent deformations during a time step. All the other models give steady state or asymptotic solutions of the equations of the mechanics. They are called here steady state models. According to these definitions, the mechanical models of the reference version of RODEX-3 [3] were steady state models, since the elastic strains were not integrated in the stress strain analysis.

2.1 MECHANICAL MODEL OF THE CLADDING

In SIERRA, the mechanical model of the cladding is one-dimensional, with plane strain and axisymmetry approximations. The total axial deformation is uniform along the radius. The total deformation includes the thermal expansion, an elastic term and the non-elastic deformation (creep, plasticity, growth,etc.). This model is a generalization of the CRASH model [4], to account for the anisotropic properties of the cladding. It includes:

- the anisotropic creep of the zircaloy cladding
- anisotropic thermal expansion
- temperature dependent anisotropic growth
- geometrical changes resulting from the waterside corrosion.

The theory of the elasticity is used to calculate the stresses and the elastic deformations of the cladding. The problem consists of solving a system of seven equations:

- 3 Hooke's equations
- 1 equilibrium equation
- 3 compatibility equations

Assuming that the elastic modulus and the Poisson's ratio are uniform along the cladding thickness, the radial deformation, obtained by solving these equations, is given by the relation:

$$u = \frac{1-2\mu}{2(1-\mu)}\left[\frac{1}{r}\int_a^r r(\epsilon_{r\,cr}+\epsilon_{\theta\,cr})\,dr + r\int_a^r \frac{\epsilon_{r\,cr}-\epsilon_{\theta\,cr}}{r}\,dr\right]$$

$$+\frac{1+\mu}{1-\mu}\frac{1}{r}\int_a^r \bar{\alpha}\Delta T r dr + \frac{1}{2}\left(\frac{1-2\mu}{1-\mu}\right) r\int_a^r (\alpha_r-\alpha_\theta)\Delta T\,\frac{1}{r}\,dr + C_1 r + \frac{C_2}{r}$$

$$\bar{\alpha} = \frac{\alpha_r + \alpha_\theta + 2\mu\alpha_z}{2(1+\mu)}$$

$$\Delta T = T - T_{ref}$$

a	: cladding inner radius
T	: temperature
T_{ref}	: reference temperature
μ	: Poisson's ratio
$\alpha_r, \alpha_\theta, \alpha_z$	: average thermal expansion coefficients along the principal directions
$\epsilon_{r\,cr}, \epsilon_{\theta cr}, \epsilon_{z\,cr}$	: permanent strains along the principal directions

The constants C_1 and C_2 are integration constants and are calculated from the boundary conditions.

The compatibility equations assure coupling between the thermal strains, the elastic strains and the non-elastic strains:

$$\epsilon_{r\,th} + \epsilon_{r\,el} + \epsilon_{r\,cr} = \frac{du}{dr}$$

$$\epsilon_{\theta\,th} + \epsilon_{\theta\,el} + \epsilon_{\theta\,cr} = \frac{u}{r}$$

$$\epsilon_{z\,th} + \epsilon_{z\,el} + \epsilon_{z\,cr} = C$$

ϵ_{th} : thermal strain elastic strain
ϵ_{el} : elastic strain
ϵ_{cr} : non-elastic strain

If variations over time of the thermal and elastic strains are neglected, the derivation of the above equations gives:

$$\dot{\epsilon}_{r\,cr} = \frac{d\dot{u}}{dr}$$

$$\dot{\epsilon}_{\theta\,cr} = \frac{\dot{u}}{r}$$

$$\dot{\epsilon}_{z\,cr} = \dot{C}$$

A system of nine equations can now be solved:

- 1 equilibrium equation
- 3 compatibility equations
- the definition of the generalized stress used in the creep correlation
- the creep correlation
- 3 flow rule equations

The calculation of the stresses is now decoupled from that of the thermal and elastic strains. The stresses do not depend any more on the strains, but on the strain rates. This model gives a steady state solution of the equations of the mechanics, i.e. after the relaxation of the transient stresses. The latter model was used in RODEX-3 (reference version).

It is interesting to compare the responses of the two models to a power ramp. This is illustrated in Figures 1 and 2, which show, for a Super-Ramp test, the hoop stress distributions through the cladding wall, at a pellet-to-pellet interface, obtained at the maximum of a power ramp, and after twelve hours of operation at ramp terminal level. The two models predict nearly identical average hoop stresses over the cladding thickness. But the distributions are rather different. At the maximum of the ramp, the hoop stress at the cladding inner surface increases from 265 MPa calculated by RODEX-3 to 380 MPa calculated by SIERRA. As expected, after twelve hours of operation at high power level, the difference between the two predictions is much smaller.

A thorough knowledge of the elastic and the creep properties of the zircaloy cladding is important to correctly predict the stress level in the cladding. The average hoop stress in the cladding, calculated

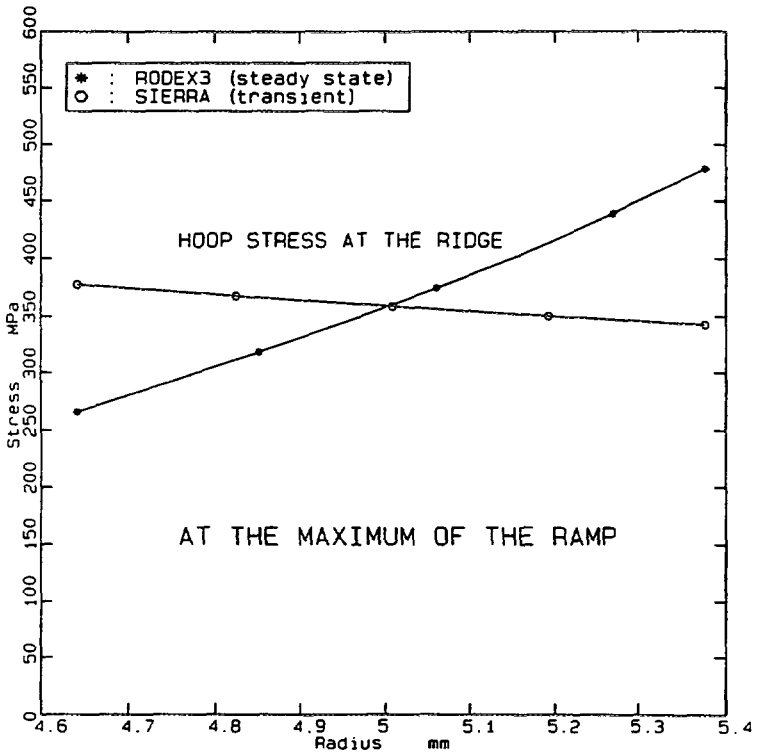

FIG. 1 *Super-Ramp PK2/1 (ramp test)*
Hoop stress distribution in the cladding comparison of RODEX-3 and SIERRA

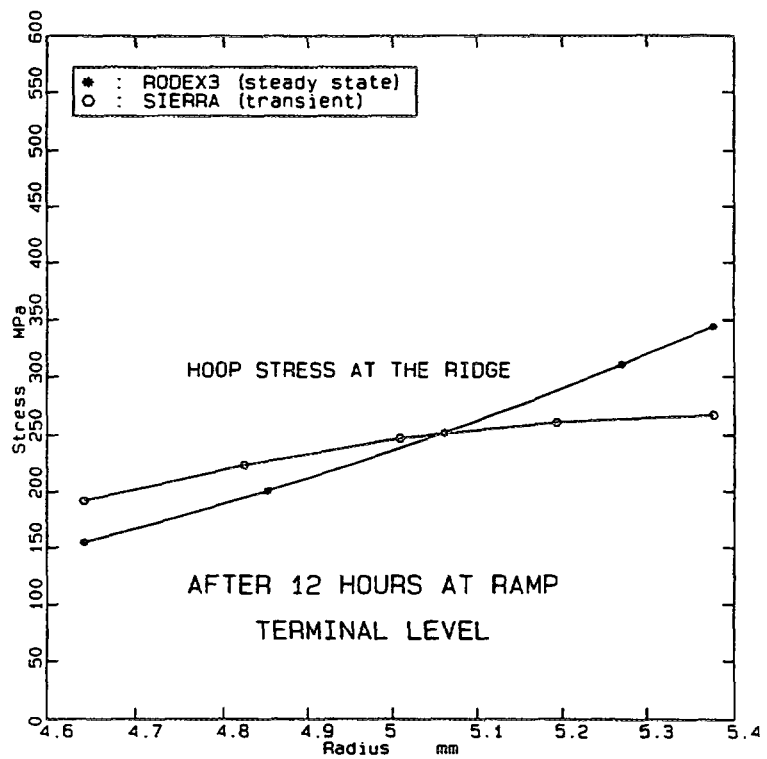

FIG. 2 *Super-Ramp PK2/1 (ramp test)*
Hoop stress distribution in the cladding comparison of RODEX-3 and SIERRA

at the maximum of a fast power ramp, is roughly proportional to the elastic modulus used in the calculation. The fuel pellet imposes its deformation onto the cladding. In the MATPRO handbook [5] it is suggested that the latter depends on the effective cold work of the zircaloy tube. The effective cold work takes into consideration the annealing effect of any subsequent heat treatment. At 400 C, 50% effective cold work of an unirradiated zircaloy cladding tube would decrease the elastic modulus by about 18%. The reality of this effect is highly questionable. Opposite trends have been reported [5]. According to the authors of MATPRO, that effect was "tentatively" included in their model. Nevertheless this single change contributes to a decrease of the calculated average hoop stress in the cladding, at the maximum of a fast power ramp, by about 16%.

After a transient mechanical interaction between the fuel pellets and the cladding, the stresses in the cladding relax. The relaxation kinetics depends on the creep properties of both the fuel pellet and the cladding. The creep of the cladding is the sum of two components: the thermal creep and the irradiation induced creep. The irradiation induced creep rate of the zircaloy seems to be largely unaffected by the fast neutron fluence. In contrast, out-of-pile tests, performed on irradiated pieces of cladding, have shown great sensitivity of the thermal creep to the fast neutron fluence [6]. Zircaloy hardening and loss of ductility are observed as the result of fast neutron irradiation. That effect is considered both in RODEX-3 [7] and in SIERRA.

2.2 MECHANICAL MODEL OF THE PELLET

In SIERRA, the mechanical model of the cracked fuel pellet is consistent with that of the cladding. The model is one-dimensional and is based on the following assumptions:

1. the axisymmetry approximation is justified
2. from the beginning of the irradiation, the pellet is cracked into wedge shaped segments
3. the segment pattern is always the most compact one (no radial relocation); the fragments are in contact with each other; the radial ring, where contact occurs, is called "bridging annulus"
4. in an average axial plane, the axial stress, resulting from the axial force, is uniform over the cross section;
5. in any radial rings, where the radial cracks are open, the hoop stress is equal to the gas inner pressure.

The axisymmetry assumption means that the model considers an infinite number of infinitely thin cracks.

The stresses and the elastic strains in the pellet are derived from the theory of the elasticity. This implies the resolution of a system of seven equations:

- 3 Hooke's equations
- 1 equilibrium equation
- 3 compatibility equations

The pellet is radially subdivided into a number of concentric rings. The calculation of the stresses and of the elastic strains is performed in two steps:

- the calculation of the radial crack profile in the radially unrestrained pellet
- the stress-strain analysis of the restrained pellet

The radially unrestrained pellet is by definition a pellet that is not subjected to any radial force from pellet-cladding mechanical interaction (PCMI). In that case, the radial and axial stresses are equal, uniform, and equal to the gas inner pressure. This is a consequence of the cracking assumption.

The calculation of the deformations of the radially unrestrained pellet is performed to predict how the radial cracks will close under the effect of radial pressure. When the radial pressure increases, the bridging annulus widens. The cracks close in several radial rings, creating sometimes several bridging annuli. The order of the rings, in which the cracks will successively close, is later referred to as "closure sequence". It depends on the radially unrestrained crack profile. This profile in turn depends on the distributions of thermal expansion, swelling, creep and hot pressing. The model, presented here, is valid for any arbitrary crack profile.

The unrestrained cracking profile is calculated by solving, first the three Hooke's equations to obtain the elastic strains resulting from the axial forces, then the first two compatibility equations:

$$\epsilon_{r\,th} + \epsilon_{r\,el} + \epsilon_{r\,cr} = \frac{du}{dr}$$

$$\epsilon_{\theta\,th} + \epsilon_{\theta\,el} + \epsilon_{\theta\,cr} + \epsilon_{\theta\,crack} = \frac{u}{r}$$

$\epsilon_{\theta\,crack}$: hoop strain resulting from the opening of radial cracks

An integration constant appears in the solution. It is the "radial relocation constant". It is determined by the compact fuel segment pattern assumption.

The second step of the calculation, is the stress-strain analysis of the restrained pellet.

An initial stress and strain calculation is performed assuming that the bridging annulus is reduced to one ring. The pellet/cladding contact pressure is then equilibrated by the hoop stress in that ring. The equilibrium equation is used to calculate the radial stress distribution and the hoop stress in the bridge. Hooke's equations give the elastic strain distributions, and the compatibility equations give the crack radial profile. The change of the crack width is estimated in terms of a displacement.

A second stress and strain calculation is performed, assuming that the cracks are elastically closed in a second ring, the next one in the ring closure sequence, and that the contact pressure is equilibrated by that single ring. The calculation is then repeated for the next rings of the closure sequence.

As the equations of elasticity are linear, the solution of the stress and strain calculation, when the bridging annulus extends to several rings (adjacent or not), is a linear combination of the solutions of these partial problems. After each calculation the program calculates the elastic response of the pellet in each ring, in terms of crack displacement, to a unit hoop stress in the bridging ring. A matrix is built in that way, which can be inverted. The elastic calculation is limited to the rings where the cracks are closed. The elastic hoop displacements, necessary to close the cracks, are known. They are equal to the opposite of the hoop displacements associated with the cracking of the radially unrestrained pellet. The only unknowns are the hoop stresses in each ring of the bridge(s) and the relocation constant. An additional equation is needed to determine the latter. It is obtained by integrating the equilibrium equation along the radius:

$$\int_{r_i}^{r_o} \sigma_\theta\, dr = -P r_o$$

The extent of the bridging annulus is not known a priori. What is known, is that, all along the contact zone between wedge shaped fragments, the hoop stress must be negative (the compressive stress must be larger than the gas inner pressure). So the calculation is first performed assuming that the contact zone is limited to one ring, then to two rings, and so on. The final results with a negative hoop stress all along the contact zone, is the physical solution of the problem. The rest is numerical analysis.

In the reference version of RODEX-3 the stresses are calculated by means of a correlation based on the hoop strain resulting from cracking in the unrestrained pellet [3]:

$$\sigma_\theta = \frac{-F_{eq} \cdot E_{eff}}{[1 + C \cdot \varepsilon_{\theta crack}]}$$

F_{eq} : normalization factor to satisfy the integrated equilibrium equation
E_{eff} : effective elastic modulus
C : parameter determined by benchmarking

The elastic strains are not calculated. The elastic modulus is artificially reduced at high temperature and the parameter C is adjusted, so that the correlation gives a hoop stress distribution qualitatively similar to a steady state distribution, i.e. after significant fuel creep has occurred in the pellet center and the stresses have relaxed. The responses of the two models to a power ramp is illustrated in Figures 3 and 4. Figures 3 and 4 show the radial distribution of the radial and axial stresses respectively, obtained at the maximum of a power ramp in a Super-Ramp test. The distributions calculated by the two models are very different. In SIERRA the whole contact pressure is equilibrated by the radial and hoop stresses in the central part of the pellet. In RODEX-3 the larger part of the contact pressure is equilibrated by the hoop stress in the rigid outer part of the pellet. The latter result implies large creep in the central part of the pellet and the closure of the cracks up to the pellet rim. This can only be attained after a very long time in steady state operation.

3. RIM EFFECT AND TRANSIENT ATHERMAL FISSION GAS RELEASE

Owing to the radial thermal flux depression in the fuel pellet and the plutonium build-up at the pellet rim, the local burnup in the reaches values typically twice as large as the average pellet burnup. Above a threshold local burnup the microstructure of the ceramic fuel pellet changes into what has been termed a "cauliflower" structure. This structure is characterized by the formation of small grains, 0.5 to 1μm in diameter, a high fraction of porosity (up to 30%) and a low fission gas concentration within the grains.

The rim effect can significantly affect the fuel performance at high burnup. First the high porosity region acts as an efficient thermal barrier, which contributes to an increase in fuel temperature all along the pellet radius. Secondly the high fraction of fission gas in the pores and on the grain boundaries in the rim is the source of potential athermal fission gas release during power transients. Athermal fission gas release as high as 7% has been observed during transient testing of several fuel rods in the Third Risø Fission Gas Project [8]. There is some evidence that the gas was released at power levels below 17 kW/m. The experience with this type of fission gas release however is limited, and it has not been possible to characterize it without some speculation. The athermal transient fission gas release could be function of physical parameters like the burnup, the grain size, the porosity and the power ramp rate. More transient tests on high burnup fuel rods are necessary, especially at low power level to correlate this effect.

The effect of high porosity at the pellet rim on fuel conductivity and on temperature distribution is better understood. A new model has been introduced into SIERRA. The outer radial region of the pellet has been subdivided into two subregions, the outer one being the rim region. Two parameters have to be calculated: the width of the rim region and its average density. It is not necessary to develop a mechanistic model of the rim region, when simple empirical correlations give more reliable results. So the width of the rim region is determined by means of a correlation linear with the burnup:

$$w_{rim} = w_o (-150 + 2.5\, BU)$$

w_{rim} : width of the rim in μm

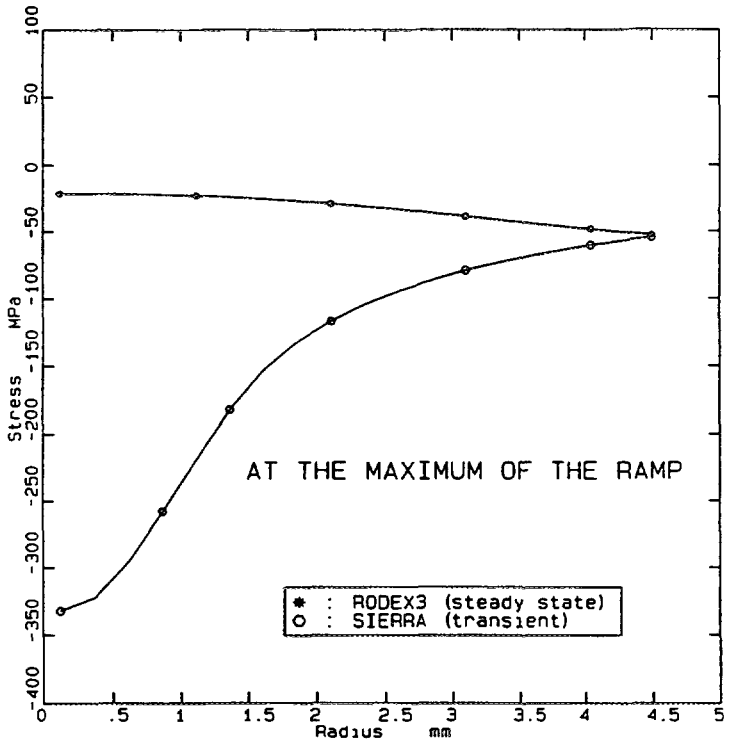

FIG. 3 *Super-Ramp PK2/1*
Hoop stress distribution in the pellet comparison of RODEX-3 and SIERRA

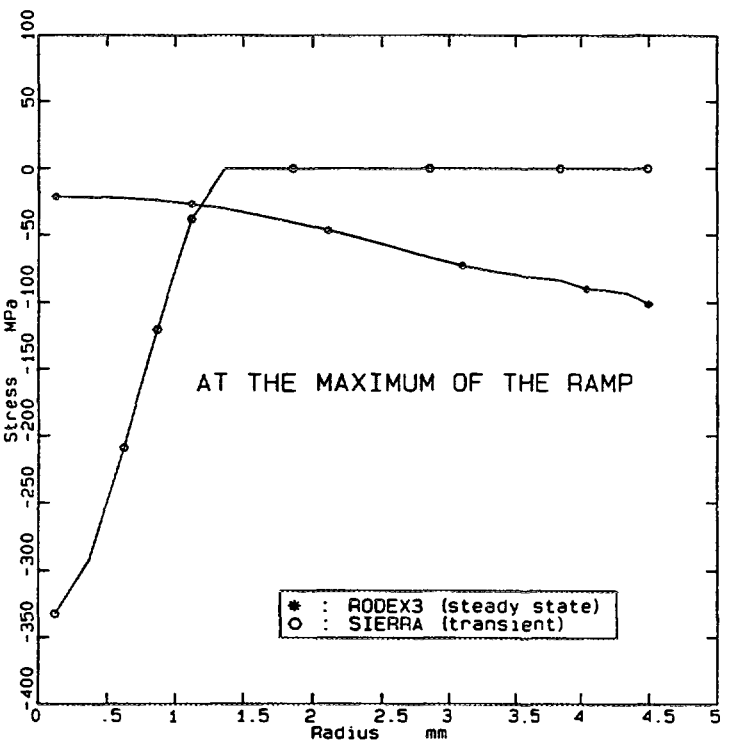

FIG. 4 *Super-Ramp PK2/1*
Hoop stress distribution in the pellet comparison of RODEX-3 and SIERRA

w_0 : constant = 1μm
BU : local burnup at the pellet rim in MWd/kgU

This correlation is based on the experimental results presented in Reference [9]. The average porosity in the rim region is tentatively determined by the following correlation:

$$p = 0.25 - 0.15\, e^{-\frac{BU-60}{20}}$$

The asymptotic value of 25% is consistent with the high fraction of porosity (up to 30% [10]) observed at the pellet rim. The fuel conductivity correlation used in SIERRA includes a burnup effect consistent with the observations performed at Risø (Third Risø Fission Gas Project) and at Halden [11]. The burnup used in the correlation is the local burnup in the considered radial region of the pellet. Thus, for the rim region, it is the burnup in the rim region. The porosity correction factor is that proposed by K.L.Peddicord [12]:

$$f(p) = e^{-2.14p}$$

supposed to be valid up to 30% porosity.

Figure 5 shows the effect of the rim model on the centerline temperature at power peak in a PWR 14 x 14 fuel rod irradiated at a constant peak pellet power of 25 kW/m. The Figure shows that, in high burnup fuels, that effect cannot be neglected. At power ramp conditions, at high burnup, the presence of a porous pellet rim region is expected to enhance both athermal fission gas release from the rim region, and thermal fission gas release owing to the temperature effect. The increased pellet thermal expansion will also affect the pellet-cladding mechanical interaction. With our limited experience in that matter, it is really difficult to assess the validity of the rim model. There is a urgent need for more experimental results on high burnup rods.

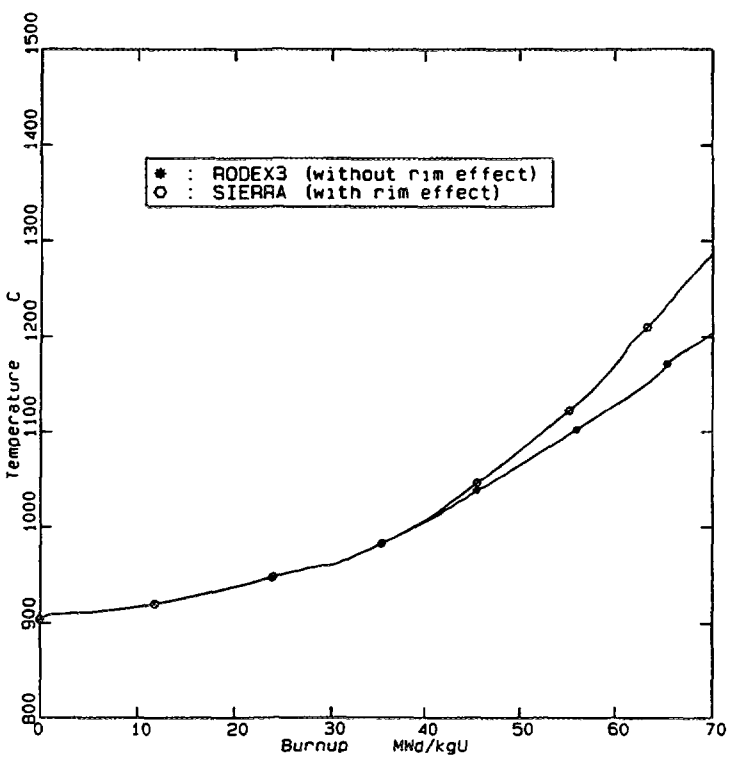

FIG. 5 *Rim Effect*
PWR 14 x 14 Fuel Rod irradiated at 250 W/cm
Fuel centerline temperature vs burnup comparison of RODEX-3 and SIERRA

4. CONCLUSIONS

The SIERRA code has been developed as a versatile modular code for PWR and BWR fuel performance applications, meeting modern Quality Assurance standards. This new generation code has improved fuel performance prediction capabilities, especially at high burnup and during transient reactor conditions. At high burnup, typically above 55 MWd/tU, the reliability of the models is limited by the experimental data available.

REFERENCES

[1] SHANN, S.H., MERCKX, K.R., LINDENMEIER, C.W., LEE, C.C., ROBINSON, A.H., "A Two Group Radial Power Distribution Prediction Model", ANS/ENS International Topical Meeting on LWR Fuel Performance, Avignon, France, April 21-24, 1991.

[2] SHANN, S.H., VAN SWAM, L.F. "Fuel Performance Modeling of High Burnup Fuel", IAEA Technical Committee Meeting on Fission Gas Release and Fuel Rod Chemistry Related to Extended Burnup, Pembroke, Ontario, Canada,28 April-1 May 1992,1AEA-TECDOC-697.

[3] MERCKX, K.R. "Mechanical Deformation Models Based on Segment Mechanics", IAEA Specialists' Meeting on Water Reactor Fuel Element Performance Modelling, Preston, UK, September 19-22, 1988.

[4] GUYETTE, M., "CRASH - A Computer Program for the Evaluation of the Creep and Plastic Behavior of Fuel Pin Sheaths", Nucl. Appl. & Techn. 9 (1970) 60-69.

[5] SCDAP/RELAP5/MOD2 Code Manual, Volume 4: "MATPRO - A Library of Materials Properties for Light-Water-Reactor Accident Analysis", NUREG/CR-5273, EGG-2555, Vol.4., February 1990.

[6] PAPAZOGLOU, T.P., DAVIS H.H., "EPRI/B&W Cooperative Program on PWR Fuel Rod Performance", EPRI report NP-2848, March 1983.

[7] HOPPE, N.E., "Engineering Model for Zircaloy Creep and Growth", International Topical Meeting on LWR Fuel Performance, Avignon (France), April 21-24, 1991.

[8] BILLAUX, M.R., SHANN, S.H., VAN SWAM, L.F., "Effect of Grain Size on the Fission Gas Release from the Rim of High Burnup Fuel Pellets", ANS International Topical Meeting on Light Water Reactor Fuel Performance", West Palm Beach, Florida, April 16-21, 1994.

[9] CUNNINGHAM, M.E., FRESHLEY, M.D., LANNING, D.D., "Development and characteristics of the rim region in high burnup UO_2 fuel pellets", J.Nucl.Mater.188 (1992) 19-27.

[10] MATZKE, H.-J., "On the rim effect in high burnup UO_2 LWR fuels", J.Nucl.Mater. 189 (1992) 141-148.

[11] KOLSTAD, E., VITANZA, C., "Fuel rod and core materials investigations related to LWR extended burnup operation", J.Nucl.Mater. 188 (1992) 104-112.

[12] PEDDICORD, K.L., CUNNINGHAM, M.E., TRIPATHI, A.,"Porosity Correction to Thermal Conductivity Based on Analytical Temperature Solutions", Trans.Am.Nucl.Soc.,Vol.28 (1978) 548.

THE ELASTIC MODEL FOR ARBITRARY RADIALLY CRACKED FUEL IMPLEMENTED IN COMETHE-4D

S. SHIHAB
Belgonucleaire S.A.,
Brussels, Belgium

Abstract

Among high burnup effects, the swelling occurring in the pellet rim is such that the fuel presents a radial bridging in its periphery. This secondary bridging has an important effect on the mechanical reaction of the fuel in case of PCI. The present paper describes the elastic mechanical model of the fuel to be implemented in COMETHE-4D which alleviates problems encountered with the previous model which assumed such bridging to occur solely in the central part of the fuel.

1. INTRODUCTION

As a consequence of the growing demand for high burnup fuel modelling, the COMETHE programme has been enhanced with new modules that can support such modelling [1]. Among these, the neutronique module IRIS 12] calculates the actinides, fission products and the radial power profile evolutions along the irradiation history. A particular high burnup effect has lead to the need for reviewing the mechanical modelling of the cracked pellet; this is the increasing differential swelling in the rim. It is due to the increasing radial depression of the fission rate with burnup, which tends to be much higher in the pellet rim (the pellet surface burnup can be as much as 2 to 3 times the average pellet burnup). The associated swelling will eventually close the radial cracks and yields to the need of calculating the pellet mechanical reaction for arbitrary radially cracked pellets.

In the COMETHE mechanical model it is assumed that the fuel cannot sustain tensile stress occurring with differential thermal expansion due to the temperature gradient and various swelling mechanisms. As a result, a radial dependent cracks ratio f is introduced as the unfilled fraction of the perimeter at a given radial location. It can be understood by figuring that the perimeter, at a given initial location R, expands linearly with a strain ϵ_θ (due to the thermal expansion and the local swelling) whereas its enclosed surface expands at a different rate yielding a hot radius r. Thus the cracks fraction is defined as:

$$f(r) = \frac{2\pi r - 2\pi R(1+\epsilon_\theta)}{2\pi r} \qquad (1)$$

Without PCI, this cracks fraction is always positive. The fuel is assumed to crack freely and its fragments to relocate outwardly. When PCI develops, the cracks widths are reduced and some are eventually closed, reflecting a tangential compressive stress. This yields to a negative cracks fraction. Actually, the cracks fraction can be figured as an image of the tangential stress state of the fuel along its radius.

The mechanical model used in COMETHE-IIIL is described in [3]. It had provision to deal with crack filling in case of PCI but implicitly assumed that cracks are open outwardly. As a result, when bridging occurred in the periphery (null cracks at the pellet outer radius, i.e. the pivot is located at the pellet surface) the method considered a filled core and over-estimated the fuel overall (effective) stiffness.

A temptative work was performed to solve this general case in 1972 [4],[5] but was abandoned because the existing analytical solution was fast and accurate enough for the moderate burnups considered then.

The present paper addresses this problem and presents a method based on modelling the fuel as a set of adjacent rings being either cracked or plain tangentially and in mutual elastic interaction. The cracks width profile is assumed to vary linearly within each ring. An iterative schema is used to seek the mechanical equilibrium with the clad by solving the mechanical constitutive equations and updating the radial cracks profile.

The method assumes a plane stress/strain state for a given axial slice of the fuel. Axial effects are considered in other parts of code COMETHE [6] and are reflected through the local strains and the elastic/plastic state of the fuel along the radius. However, the later two effects are considered in this model.

2. RADIAL RINGS STRESS/STRAIN EQUATIONS

As stated, the pellet is radially subdivided into concentric rings. Each ring can be either fully cracked or either radially closed. A further subdivision is performed whenever a ring has a local bridging in order to have one of these two types of rings. Hereafter, the stress/strain equations are derived for both types of rings.

2.1 UNCRACKED OR CLOSED RING CONSTITUTIVE EQUATIONS

A ring is considered to be closed if the calculated crack profile is negative along its width. It is a dynamic, through iterations, state. As the ring is not cracked, a compressive tangential stress may occur and is thus considered. The fuel properties are radius dependent through temperature, porosity, burnup and foreign elements [7]. The derived equations are the classical ones applicable to elastic tubes [8] except for the tangential continuity condition.

The elastic state equations read

$$\epsilon_r = \frac{1}{E}(\sigma_r - \nu\sigma_\theta) \tag{2}$$

$$\epsilon_\theta = \frac{1}{E}(\sigma_\theta - \nu\sigma_r) \tag{3}$$

Local radial and hoop stresses are related through the radial equilibrium condition:

$$\frac{\delta\sigma_r}{\delta r} + \frac{\sigma_r - \sigma_\theta}{r} = 0 \tag{4}$$

And the radial continuity condition is

$$\epsilon_r = \frac{\delta u}{\delta r} \tag{5}$$

The tangential continuity condition is obtained by calculating the relative tangential displacement of a cracked circumference (note that the ring can be closed when constrained but initially open). Before deformation, the circumference length is $2\pi r(1 - f)$; after a radial deformation u and crack closure, this length becomes $2\pi(r + u)$. The tangential strain reads:

$$\epsilon_\theta = \frac{2\pi(r + u) - 2\pi r(1 - f)}{2\pi r(1 - f)}$$
$$= \frac{u}{r} + f + \frac{f}{1 - f}\left(\frac{u}{r} + f\right) \tag{6}$$
$$\approx \frac{u}{r} + f$$

(the last term of the right side equation is of second order magnitude and is neglected). If prior to deformation, the ring was closed ($f = 0$), the latter condition reduces to the normal plain ring tangential continuity condition ($\epsilon_\theta = u/r$).

2.2 CRACKED RING CONSTITUTIVE EQUATIONS

For cracked rings the tangential stress is set to zero and the crack profile has to be accounted for in writing the continuity equation of the radial stress. Thus the elasticity equations read:

$$\epsilon_r = \frac{1}{E}\sigma_r \tag{7}$$

$$\epsilon_\theta = -\frac{v}{E}\sigma_r \tag{8}$$

The radial equilibrium is obtained by equating the forces applied on an elementary cracked layer:

$$\frac{\delta r\sigma_r(1 - f)}{\delta r} = 0 \tag{9}$$

where the cracks width rf is assumed to vary linearly within the ring.

Radial continuity constrains the radial strain

$$\epsilon_r = \frac{\delta u}{\delta r}, \tag{10}$$

whereas no condition is needed for the tangential strain ϵ_θ.

3. PELLET STRESS/STRAIN EQUATIONS

The previous constitutive equations are solved in order to relate the stresses and displacements of the rings from outer to inner radii (increasing index). They can be written as:

$$T_{i+1} = A_i T_i + B_i \tag{11}$$

where $T_i = (\sigma_r(r_i), u(r_i))^T$ - noted $(\sigma_i, u_i)^T$ for simplification - are node related quantities and the matrices A_i and B_i have different expressions following the ring geometry:

Uncracked rings:

$$A_i^{uncracked} = \begin{pmatrix} (1 + (1 - v_i)S_i)\frac{E_{i+1}}{E_i} & -S_i\frac{E_{i+1}}{r_i} \\ -(1 - v_i^2)S_i\frac{r_i+1}{E_i} & (1 + (1 + v_i)S_i)\frac{r_i+1}{r_i} \end{pmatrix} \tag{12}$$

$$B_i^{uncracked} = \begin{pmatrix} -E_{i+1}(x_i + y_i) \\ -r_{i+1}[x_i - y_i - v_i(x_i + y_i)] \end{pmatrix} \quad (13)$$

Cracked rings:

$$A_i^{cracked} = \begin{pmatrix} \frac{r_i c_c - a_c}{r_{i+1} c_c} \frac{E_{i+1}}{E_i} & 0 \\ -\frac{r_i c_c a_c}{c_c} \ln\left(\frac{r_i c_c a_c}{r_{i+1} c_c a_c}\right) \frac{1}{E_i} & 1 \end{pmatrix} \quad (14)$$

$$B_i^{cracked} = \begin{pmatrix} 0 \\ 0 \end{pmatrix} \quad (15)$$

where v_i is the ring average Poisson ratio and S_i, x_i, y_i, a_c, c_c are integration constants defined for each ring:

$$S_i = \frac{1}{2}\left(\frac{r_i^2}{r_{i+1}^2} - 1\right),$$

$$a_c = r_i f_i - (r_{i+1} f_{i+1} - r_1 f_1)\frac{r_i}{r_{i+1} + r_i},$$

$$c_c = 1 - \frac{(r_{i+1} f_{i+1} - r_i f_i)}{r_{i+1} - r_i},$$

$$x_i = -\frac{a_c}{2}\left(\frac{1}{r_i} - \frac{1}{r_{i+1}}\right) + \frac{1 - c_c}{2} \ln\left(\frac{r_i}{r_{i+1}}\right),$$

$$y_i = \frac{a_c}{2r_{i+1}^2}(r_i - r_{i+1}) + \frac{1 - c_c}{4r_{i+1}^2}(r_i^2 - r_{i+1}^2).$$

If a ring presents a combined cracked and uncracked pattern, the associated matrices are deduced by subdividing the ring into a cracked portion and an uncracked one. The limit of the two subdivisions is set at radius r_c for which the crack width is null. This requires calculating the crack width profile using the ring constitutive equations.

Combining these ring inward stress/strain relations, one has the following relation between the fuel outer surface stress and displacement values to innermost ring values:

$$T_{m+1} = \left(\prod_{i=1}^{m} A_i\right) T_1 + \sum_{i=1}^{m}\left(\prod_{j=i+1}^{m} A_j\right) B_i = AT_1 + B \quad (16)$$

defining the pellet surface to pellet centre stress/strain transfer matrices. The independent term B can be figured as the necessary stress/strain needed to close the cracks. The B_i term is null for an initially closed ring.

4. FUEL AND CLAD BOUNDARY CONDITIONS

Two conditions are needed in order to determine the stress/strain state. They are fixed by the boundary conditions on both the fuel and the clad.

4.1 FUEL BOUNDARY CONDITIONS

The fuel outer stress is related to the contact pressure following:

$$\sigma_1 = -\frac{P_c}{1 - f_1} \tag{17}$$

obtained by noting that the contact pressure P_c applies radially only on the filled surface.

At the fuel centre, the boundary condition depends on the geometry and the fuel mechanical state:

4.1.1 Elastic fuel core

The radial stress at the inner surface is null (compression of the fuel by the rod inner pressure P_{in} is neglected):

$$\sigma_{m+1} = a_{11}\sigma_1 + a_{12}u_1 + b_1 = 0 \tag{18}$$

(a_{ij} and b_i denote the elements of transfer matrices A and B). If the central radius is null, which is untractable with the current formulation, a fictitious small central radius (i.e. 1 μm) is assumed without any incidence on the results precision.

4.1.2 Plastic fuel core

In case of a plastic core, the fuel is treated as two concentric regions; an inner flowing plastic one and an outer elastic one. Suppose that the plastic maximum radial extend r_p falls in ring index i ($r_{i+1} \le r_p < r_i$) then the elastic modelling of the fuel is limited to radius r_i. At this radius the radial stress can be expressed as before:

$$\sigma_p = a_{11}\sigma_1 + a_{12}u_1 + b_1 \tag{19}$$

(a and b are the coefficients of the transfer matrices A and B calculated from r_1 to r_p).

This stress is determined considering two cases; either there is enough room (void) in the centre for an inward displacement or not. In the latter case, a filled plastic core is formed which limits the inward displacement by a hydrostatic reaction. Denoting the radius of this filled plastic core as r_L, the maximum inward displacement $u_L < 0$ at the plasticity radius r_p that can be achieved without stress (free flowing plasticity) is:

$$u_L = r_L - r_p. \tag{20}$$

If the elastic displacement u_p at radius r_p is lower than u_L ,the local radial stress is null:

$$\sigma_p = 0 \tag{21}$$

Otherwise, the formed plastic core responds elastically by a hydrostatic compressive stress to the displacement in excess of u_L:

$$\sigma_p = \frac{E}{1 - \nu}\frac{u_p - u_L}{r_L} \tag{22}$$

(here E and ν denote average values in the plasticity region). Recalling that the displacement $u_p = a_{21}\sigma_1 + a_{22}u_1 + b_2$, one has (using equation (19)):

$$\frac{E}{\nu)r_L}a_{21})\sigma_1 + (a_{12} - \frac{E}{(1 - \nu)r_L}a_{22})u_1 + b_1 - \frac{E}{(1 - \nu)r_L}(b \tag{23}$$

Depending on the fuel centre state, equations (18), (21) or (23) constitute the first boundary condition.

4.2 CLAD BOUNDARY CONDITIONS

The outer surface of the clad is subject to the coolant pressure P_{out} and the inner surface is subject to the fuel/clad contact pressure P_c and inner gas pressure P_{in}. The inner radial displacement of the clad can be written as:

$$u_g = W_c (P_c + P_{in}) - W_{co} P_{out} \tag{24}$$

with the following expressions for the clad flexibilities W:

$$W_c = \frac{r_g}{E_g}\frac{r_g^2(1 - \nu_g) + r_h^2(1 + \nu_g)}{r_h^2 - r_g^2} \tag{25}$$

$$W_{co} = \frac{r_g}{E_g}\frac{2r_h^2}{r_h^2 - r_g^2} \tag{26}$$

E_g is the clad's mean Young elastic module, ν_g its Poisson ratio and r_g, r_h are respectively the inner and outer clad radii. (Note that as the aim of the method is to calculate the pellet radial flexibility, the anisotropy and creep features of the clad need not to be treated here).

Finally, the pellet-clad interference $\delta = r_g - r_l$ should be cancelled by the inward and outward displacements of respectively the fuel outer radius and clad inner radius, that is:

$$u_1 = \delta + u_g = \delta + W_c (P_c + P_{in}) - W_{co} P_{out} \tag{27}$$

This is the second condition needed to solve the mechanical state of the fuel.

5. CONTACT PRESSURE AND FUEL MECHANICAL STATE

Substituting the expressions of δ_1, u_1 (equations (17) and (27)) into equations (18), (21) or (23), one has the following expression for the contact pressure:

$$P_c = \frac{-a_{12}\delta - b_1 + a_{12}(W_{co}P_{out} - W_c P_{in})}{a_{12}W_c - a_{11}/(1 - f_1)} \tag{28}$$

where the expressions for a_{12}, a_{11} and b_1 depend on the inner fuel state:

- fully elastic fuel: coefficients of equation (18),
- hollow plastic centre: coefficients of equation (19) with condition (21),

- plastic core: they correspond to the factors of σ_1 , u_1 and the independent term of equation (23), respectively.

As σ_1 and u_1 can be calculated, equation (11) permits to deduce all the stresses and displacements in the pellet. So, the new pattern of cracks can be estimated along the radius. For closed rings, the tangential stress is used to define the negative (closed) new (provisional) crack widths:

$$(rf)^* = r\frac{\sigma_\theta}{E} \tag{29}$$

$$= r\left(\frac{u}{r} + f + \frac{v}{E}\sigma_r\right) \tag{30}$$

For cracked rings, the new crack width is obtained considering the deformation of a perimeter at a given radius r. Prior to deformation, the length of the filled portion was $2\pi r(1 - f)$ and after deformation it is $2\pi r(1 - f)(1 + \epsilon_\theta)$, whereas the perimeter length is $2\pi(r + u)$. The difference between the two last values is the new crack width:

$$2\pi(rf)^* = 2\pi(r + u) - 2\pi r(1 - f)(1 + \epsilon_\theta) \tag{31}$$

$$= 2\pi r\left(\frac{u}{r} + f + \frac{v}{E}\sigma_r(1 - f)\right) \tag{32}$$

(where ϵ_θ was replaced with its expression (8)).

This updated profile of crack widths is used to determine whether the rings are closed or open after deformation, depending on their sign. It is used in section 3 to determine the limit of the cracked zone within a ring. The whole process is repeated with the updated crack profiles and convergence is achieved within few (3 - 5) iterations.

6. EXAMPLES

Results are illustrated for a standard PWR rod with an average burnup of about 55 GWd/tM. COMETHE computed the radial crack width profile as shown in figure 1 for both the free and constrained pellet. The free pellet growth is governed by the single rim tangential bridging or pivot. For the constrained pellet, the mechanical equilibrium imposes two bridging adding one at the centre. This shows that the pivot concept is not valid for modelling high burnup fuel. Figure 2 shows the results of a parametric study when varying the pellet-clad interference. The fuel effective pellet stiffness exhibits clear non linear behaviour regarding the interference.

The model was validated using COMETHE data base. Three comparisons with TRIBULATION ([9]) rod diameters deformations are shown in figures 3 and 4. They clearly show the benefit of the new COMETHE pellet mechanical model.

7. CONCLUSIONS

The COMETHE-4D proves to be accurate in modelling the clad diametral deformations for high burnup fuel (above 50 GWd/tM). It is interesting to note that inward cracks (outward bridging) can reduce the contact pressure by a factor of 3 when compared with a plane pellet and for small pellet-clad interferences. This solves the mechanical problem encountered with the so called "Rim Effect".

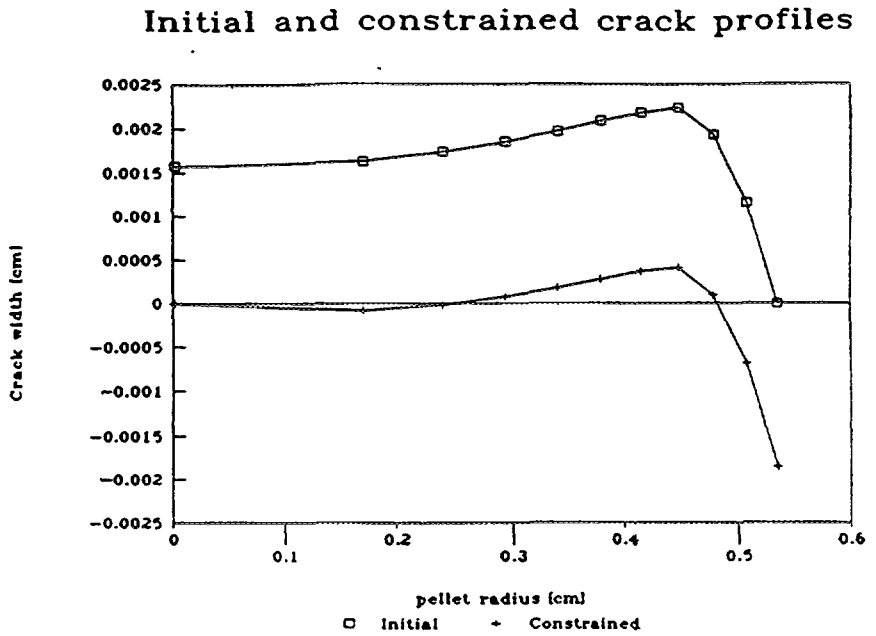

FIG. 1 A sample initial crack profile compared with that obtained after interaction. The bridging occurs in the rim which has a local burnup above 90 GWd/tM. Note that the constrained fuel presents two bridging.

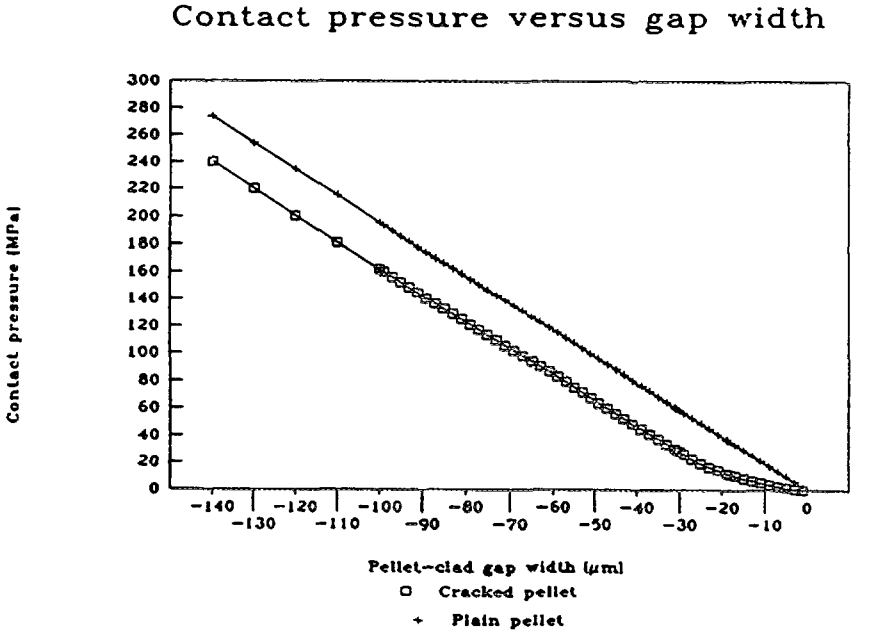

FIG. 2 Effect of the pellet/clad interference width on the contact pressure. The figure compares the computed contact pressure for a plain pellet with that obtained with a cracked pellet. The latter has a crack profile illustrated in Figure 1. The contact pressure is noticeably lower for the cracked fuel at low interferences. It shows that the cracked pellet effective stiffness is non linear.

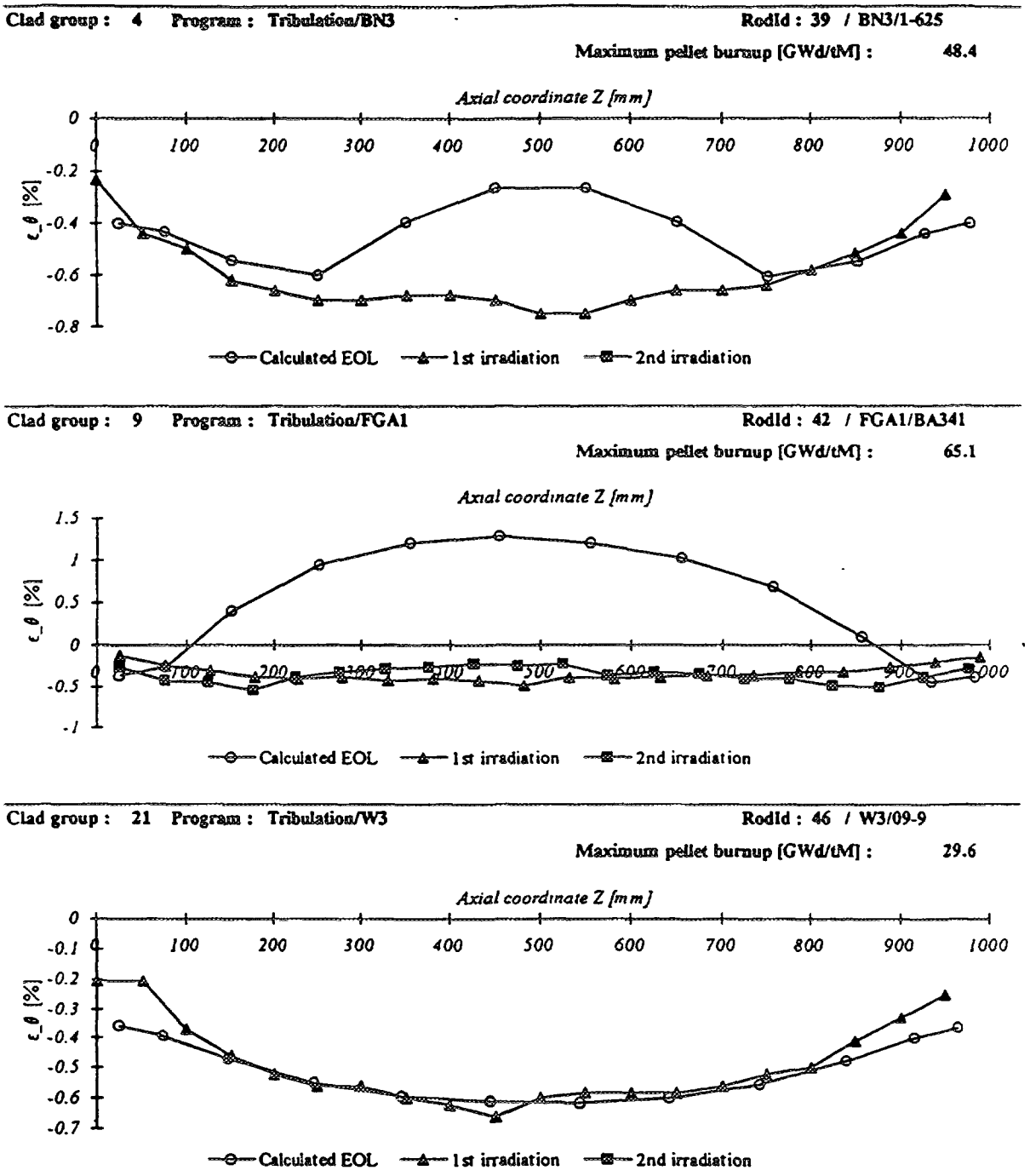

FIG. 3 Comparison of the previous COMETHE pellet mechanical model results with experimental data from 3 TRIBULATION rod deformations. Note the excessive calculated clad creep out in the central portion of the fuel column due to the rim bridging effect for the first 2 rods (high burnup). The matching is good for the third rod (moderate burnup). Plain symbols denote the measured values.

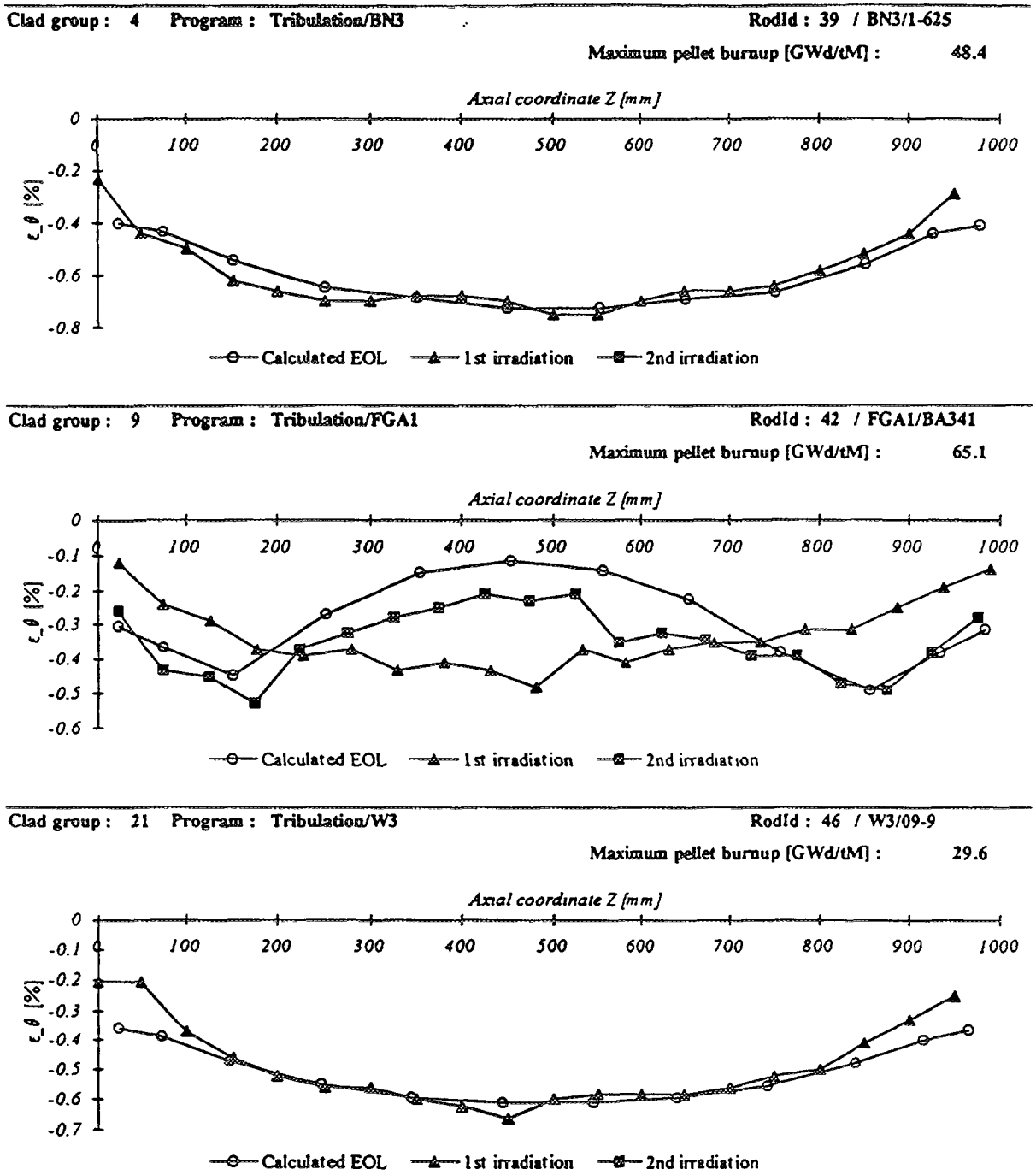

FIG. 4 Comparison of the new COMETHE pellet mechanical model results with experimental data of the same TRIBULATION rods. Input data has not been changed. The rim bridging effect has no noticeable effect on the clad deformation. Plain symbols denote the measured values.

Further development will introduce a fuel creep law, specially needed for narrow bridging layers. This can be achieved simply as the stress/strain state of the fuel is known. Axial effects will be included by rewriting the constitutive equations for a tri-axial stress state.

REFERENCES

[1] HAAS D., BILLAUX M., FALLA A., Mechanisms Affecting PCI/SCC at High Burnup. IAEA-TC-657/2.5 Preston, England (September 1988).

[2] BILLAUX M., LIPPENS M., BOULANGER D., Production of Helium in U02 - Pu02 Mixed Oxide Fuel IAEA-TC-657/3.6 Preston, England (September 1988).

[3] HOPPE N., BILLAUX M., VAN VLIET J., COMETHE IIIL - General Description BELGONUCLEAIRE (February 1982)

[4] HOPPE N., COMETHE-4 Modele d'Expansion du Combustible BN-134/ni/899, BELGONUCLEAIRE, (March 1972).

[5] DUPONT O., & HOPPE N.,COMETHE-4 Organigramme de Calcul pour une Tranche Axiale. BN-134/ni/902, BELGONUCLEAIRE, (July 1972).

[6] BELGONUCLEAIRE - COMETHE-4D Volume 1- General Description (September 1993)

[7] BELGONUCLEAIRE - COMETHE-4D - Volume 2 - Material Properties

[8] FEODOSSIEV V. F., Résistance des matériaux, Editions MIR, Moscou.

[9] LIPPENS M., BOULANGER D., TRIBULATION Final Report, TR 89/79, BELGONUCLEAIRE, (September 1989).

BI/TRI-DIMENSIONAL EFFECTS OBSERVED IN PWR FUEL DURING TRANSIENT CONDITIONS AND THEIR NUMERICAL SIMULATION

B. LINET, N. HOURDEQUIN
Departement de Mecanique et Technologie,
CEA Centre d'Etudes Nucleaires de Saclay,
Gif-sur-Yvette,
France

Abstract

TOUTATIS is the modular program (both modules 2D and 3D are included) from the METEOR project developed by the French Atomic Energy Commission " CEA " The model allows the user to calculate the deformations connected to the pellet-clad system, and hence the Pellet-Cladding Interactions " PCI" induced by unilateral contact.Furthermore TOUTATIS provides sufficient versatility to allow the simulation of almost any phenomena, from creep and plasticity to the stress corrosion (residual stresses, dish filling of the pellets from the center, thermo-mechanical feedback) or fuel cracking (3D). The general approach provides a unique capability for understanding different phenomena, some of which remain still unexplained. The first example is related to rod bending, since this phenomenon has been observed in some experimental reactors.Several possible explanations have been put forward, such as flux dipping, buckling or thermohydraulic perturbations... Indeed a spatial parabolic distribution of the flux induces a shift of the isopower area in the pellets, but its effect decreases progressively as the distance from the center of the pellet is increased.So the variations on the clad temperature are just a few degrees and cannot produce the stated rod bending.The second hypothesis was based on a thermohydraulic perturbation.Both chosen configurations (azymutal area/small spot), which induced a thermal perturbation (corroborated by shift of the bubble area), are nevertheless insufficient to bring about the recorded strains.Lastly the calculations performed with the 3D model showed clearly that this rod bending was caused by single buckling induced itself by the immobilization of the rod in experimental channel. The second example concerns the RIM effects: indeed the characteristics of this area are more and more different from those of the pellet, as the burn-up increases.These thermal, mechanical and physico-chemical differences induce varied effects depending on whether the regime is steady-state or transient.This study is currently in progress. The results of the analysis confirm the accuracy of the component models in TOUTATIS.In addition, the mutual interest of the modeling, numerical simulation and experimentation should be emphasized in order to evaluate more accurately some feedbacks and laws. ROD BENDING: The bowing of the fuel element has been observed during some irradiations.Simulations have been carried out with TOUTATIS code in order to determine the origin of this phenomenon.This bowing could be produced by the following reasons: radial and/or azimuthal redistribution of power; thermohydraulic anomaly on the external surface of the fuel rod; lock up of the thermal dilatation in the rod holder inside the reactor. The two first hypothesis induce a radial temperature gap between the front-and backside rod (relatively to the core). and therefore the thermal differential dilatation could activate the strain mode of the fuel element and finally its bowing.The last hypothesis can cause the bowing of the rod and its buckling.

1. RADIAL/AZIMUTHAL POWER REDISTRIBUTION DUE TO HIGHER NEUTRONIC FLUX IN FRONT OF THE CORE

The distribution of localized volumic power is assumed to be 5% higher on the inner surface of the rod (closer to the core) and 5% decreased on the outer side, as shown by the experimental conditions (see chart N° 1). The calculations have established that the eccentricity of the isothermal curves (see chart N° 2) and hence the thermal differential dilation can not only account for this bowing (see chart N° 3).

This result can be proved by the following assessment: the gradient of temperature on the peripheral area i.s too low to activate a mode of strain in bending (10° C on the outer side of the pellet. 2°C on the inner side and equal temperature on the outer side of the clad due to boundary conditions).

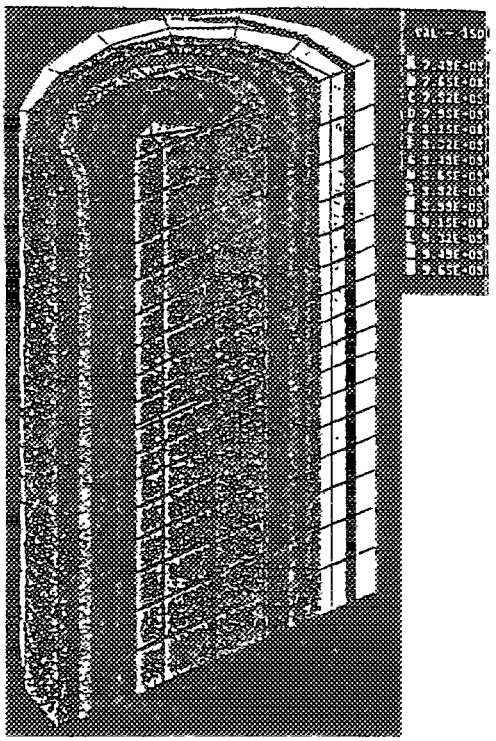

FIG. 1. *Isovalues of volumic power (W/m^3) of the pellets*

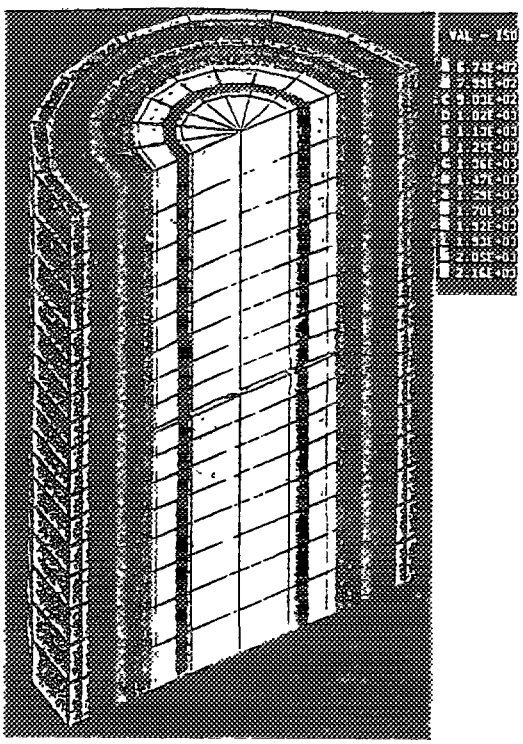

FIG. 2. *Isothermal values (K) of the simulated rod*

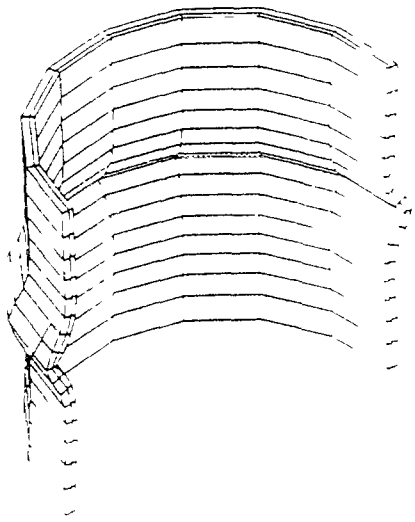

FIG. 3. Magnification (×50) clad deformation

2. THERMOHYDRAULIC ANOMALY ON THE OUTER SURFACE OF THE FUEL ROD

The simulated fuel rod is composed of two half pellets which have been presumably irradiated (modifications of the size due to creep and swelling). A power ramp up to 460 W/cm according two different sets of boundary conditions in temperature is simulated hereafter.

2.1 AZIMUTHAL GRADIENT OF TEMPERATURE ALONG THE ROD

A sector of the outer surface of the clad (90°) is overheated of 20°C and 300°C - see chart N°4. The bowing of the rod is pointed out constant (circular strain), then its total deflection can be expressed as a function of the calculated parameters of the simulated rod deflection and rotation angle of its section see chart N° 5.

$$F = \frac{1 - \cos\frac{n\delta}{2}}{1 - \cos\delta} f$$

A deflection of 0,70 mm is obtained, corresponding to a temperature gap of 20°C, respectively 6.43 mm and 300°C. Noticing the linearity of the relation leads to find a minimal value of its azimuthal temperature gradient higher than 250°C on the total length of the rod, in agreement with the experimental bowing of 5.05 mm. This result seems unrealistic and therefore the previous hypothesis can not account for this bowing.

2.2 LOCALIZED TEMPERATURE GAP

This gap could be due to the rod holder. This last one could modify the nature of the flow of the coolant fluid, change the cooling and favor the formation of a dry vapor bubble, which could then overheat the surface in close contact with it. This area is modeled by a 90°sector (7mm high and 5cm^2 square surface) overheated of the intermediate (250°C) and ultimate (600°C) ΔT temperature gap - see chart N° 6.

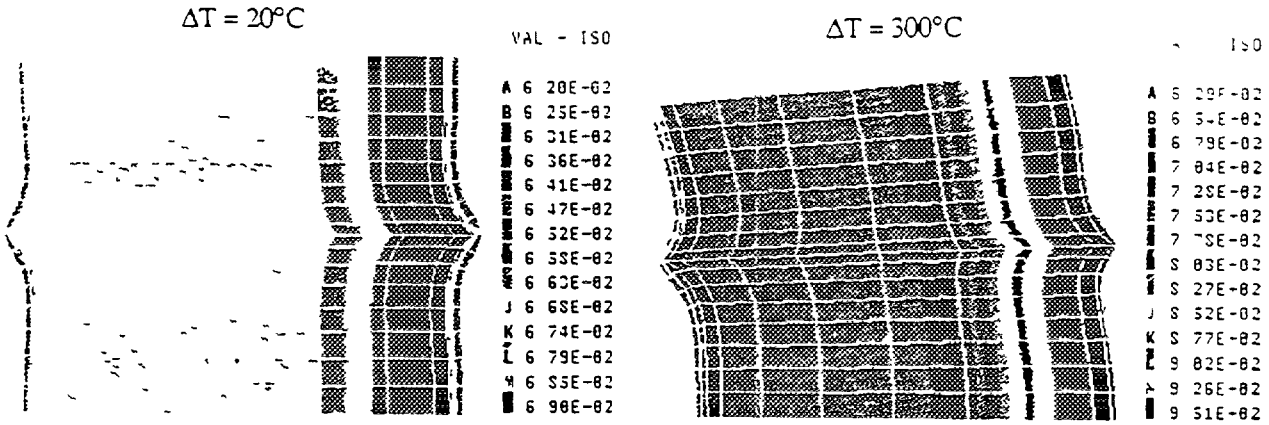

FIG. 4. *Magnification (×50) clad deformation, seen on the axial plane through the rod axis, in which occurs the curvature (temperature)*

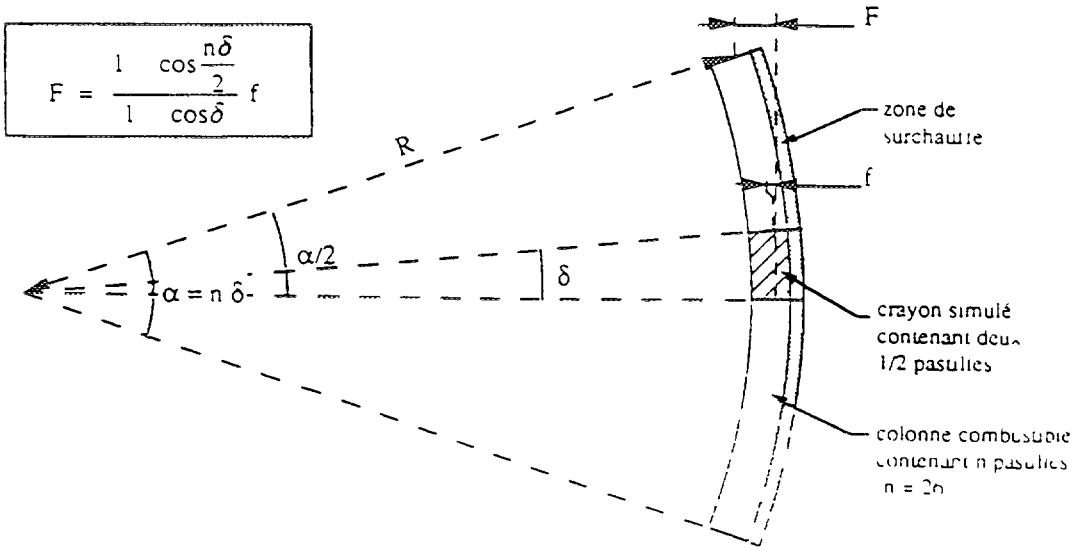

FIG. 5. *Extrapolation from the simulated column to the total rod in the case of a constant radius rod.*

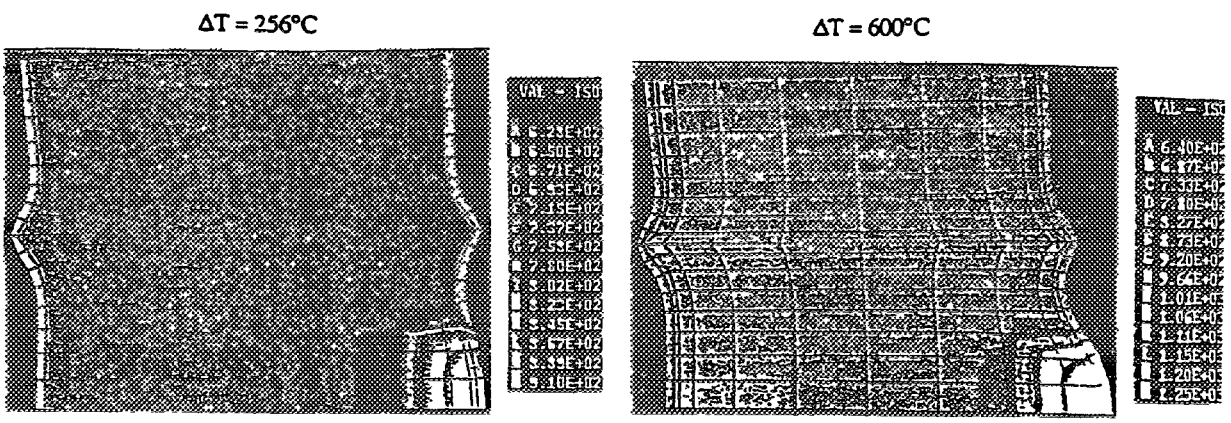

FIG. 6. *Magnification (×50) of the cladding seen on the axial plane through the rod axis in which occurs the curvature (temperature)*

Assuming that only the area of the rod closer to the overheated zone undergoes deformation, the deflection of the complete fuel rod is defined as a function of its length L and some calculated parameters (length 1, deflection f and rotation angle of its section d) see chart N° 7.

$$F = f + (L/2 - l) \operatorname{tg} \delta$$

For areas overheated of 250°C and 600°C, the deflections are respectively 0.25 mm and 0,375 mm. Although more realistic than the previous one, this hypothesis of thermohydraulic anomaly can not induce the bowing observed experimentally, in regard to usual localized temperature increases.

So we can conclude that this thermohydraulic anomaly is just a consequence of the bowing of the fuel rod and that the bowed rods undergo overheating. This is confirmed by the pretty good agreement between the experimental and simulated eccentricity of the isothermal curves - see macrography N°8 and 9 respectively. The boundary between the darker internal and brighter intermediate zones corresponds to an isothermal curve of about 1330 °C.

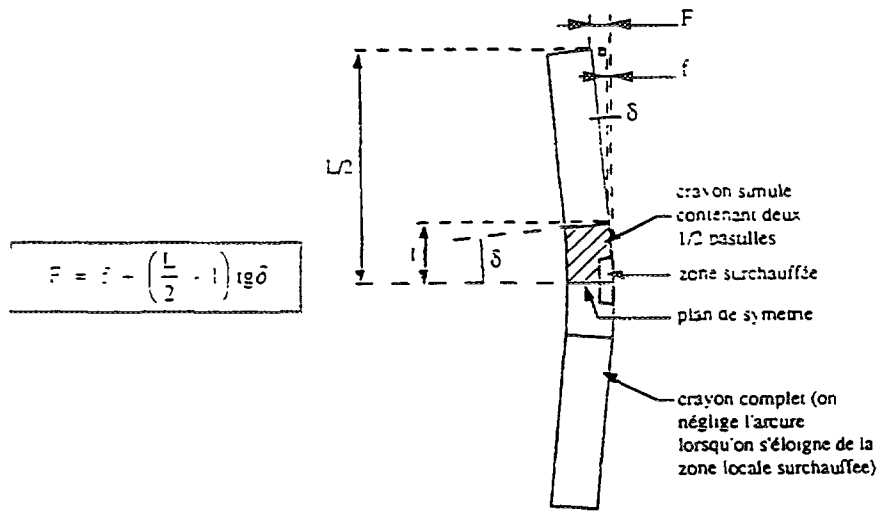

FIG. 7. Modelling of the total rod in the case of specific bowing related to the overheated area.

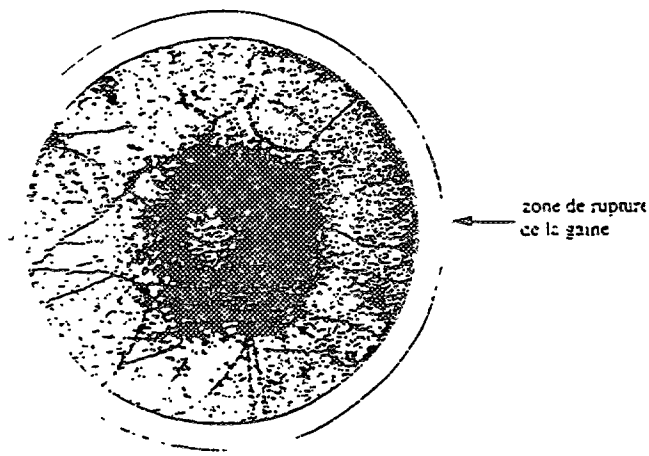

FIG. 8. Macrographic view of the cross section of the rod. Off-centering of the central dark zone (towards the clad rupture area: thermal heterogeneity)

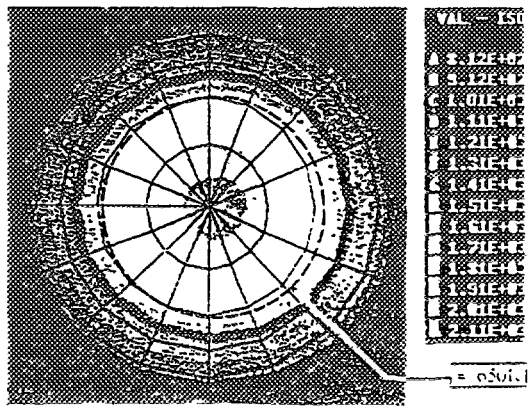

FIG. 9. *Isothermal values on the cross section of the simulated rod. Their off-centering towards the overheated area (on the right, periphery view) is similar to the one observed in the macrographic view (FIG.8)*

3. ROD BUCKLING BY BECK UP THE LONGITUDINAL THERMAL DILATATION.

The buckling can induce a large amplitude bowing, if a longitudinal loading is transmitted to the rod through its holder and reaches the critical Euler's value (for which the rod is laterally unstable). The first condition is met because an interaction of the rod with its holder has been observed experimentally. The second condition is checked by simulating the buckling with two simplified models which encompass the rigidity of the actual rod (whose description is complex).

3.1 CALCULATIONS WITH THE MODEL MINORING THE ROD RIGIDITY

Let's consider a rod with open radial gap and without pellet-clad interaction. The rigidity only has to be taken into account in the buckling, the fuel rod and the clad being not interacting (the stiffness of the spring assuring the load of the pellets is neglected). Therefore the rod is simulated by a cylinder with the characteristics of the clad, and some different interfaces rod-holder are considered (see chart N°10):

1) 2 balls-and-socket joints,
2) 1 ball-and-socket joint and 1 embedding,
3) 2 embeddings

Assuming the anchor of the rod in its holder, we take too into account the differential thermal dilatation of the rod-holder. Within the experimental conditions, the dilatation of the modeled rod (cylinder) due to the thermal loading, which is assumed homogeneous in the thickness and equal to outer surface temperature of the clad (344°C), is impeded by the nature of its contact with the holder, which transmits a longitudinal loading F of about 550 N. The critical Euler's load of buckling Fc in each system (simulated rod, contacts) is also computed:

$$Fc = \mathbf{k}\, \pi^2 EI/l^2$$

where **E** is the Young's modulus of the structure, **I** the moment of inertia of its section, l its free length of buckling and **k** a parameter characterizing its mechanical boundary conditions. Then each critical buckling loading Fc is compared to the axial loading F - see chart N° 10.

$$\lambda = F_C/F$$

Under this load the only less rigid interfaces allow the buckling of the simulated rod with a minored rigidity ($\lambda < 1$). In these conditions, the critical load is equal 524 N . On the other side, according to the Euler's theory, the following equation is verified:

$$F_{c3}\,(2114\ N) = 2\,F_{c2}\,(1076\ N) = 4\,F_{c1}\,(524\ N)$$

3.2 CALCULATIONS WITH THE MODEL MAJORING THE ROD RIGIDITY

Let's consider a rod with closed radial gap and a strong pellet-clad interaction, modelled by coupling of the pellets and the clad together. This last hypothesis seems to be confirmed experimentally by comparable elongations (about 1%) of clad and fuel.

So the rigidities of the fuel and clad (considered parallel on the total free length of buckling) and the hypothesis of anchoring (different from anchoring of the fuel rod to its support) contribute to increase the rigidity of the actual fuel. A segment of the rod (2 pellets high), embedded at its base and free at the other end is modelled. By symmetry with regard to its basic plane, this system is equivalent to a fuel rod which is 4 pellets high and which is joined at its ends (see the first contact, §3.2).

Within this configuration (modelling the 4 pellets rods) and the experimental conditions, the critical loading of buckling F_{c4}, and the axial loading F due to the lock up of the thermal dilatation of the rod - see chart N° 11- are computed:

$$\lambda = F_{c4}/F = 1.87$$

In the same configuration of interface (2 ball-and-socket joints), the critical Euler's load in the complete rod contact (n pellets) is calculated from the Euler's equation of F_{c4}, seeing that the free length of buckling (expressed as a function of the pellet size h) is the only one variable parameter:

$$F_{c4} = k\,\pi^2 EI/(4h^2)\ ;\ F_{cn} = k\,\pi^2 EI/(nh^2) \Longrightarrow F_{cn}/F_{c4} = (4/n)^2$$

Considering a discontinued stack of pellets (and hence with a discontinued rigidity) induces an error by extrapolating the free length of buckling. This one has been checked less than 5% with a "beam model" of a rod (with discontinuous rigidity). Since the thermal field in the complete rod is in good agreement with the actual thermal field in the simulated rod, the differential thermal dilations and then the axial loadings F are identical.

$$F = 41\,000\ N$$

This value is much higher than the one related to the rod with minored rigidity because in this last case only the temperature in the clad was taken into account.
So the result for the complete rod is expressed as:

$$Fcn/F_{c4} = (4/n)^2\ (F_{cn}/F) = (4/n)^2.(F_{c4}/F)\quad (F_{cn}/F) = (4/n)^2\lambda 4$$

For the configuration of interfaces with 2 balls-and-socket joints and with the following set of data ($\lambda = 1.87$ and $n=36$), it is obtained:

$$F_{cn}/F = 0.023 < 1 \Longrightarrow \text{BUCKLING}$$

$$F_{cn} = 946\ N$$

The critical loadings for the other configurations of interface can also be determined:
(2) 1 joint and 1 embedding: Fc = 2 x 946 = 1886 N
(3) 2 embeddings: Fc = 4 x 946 = 3776 N

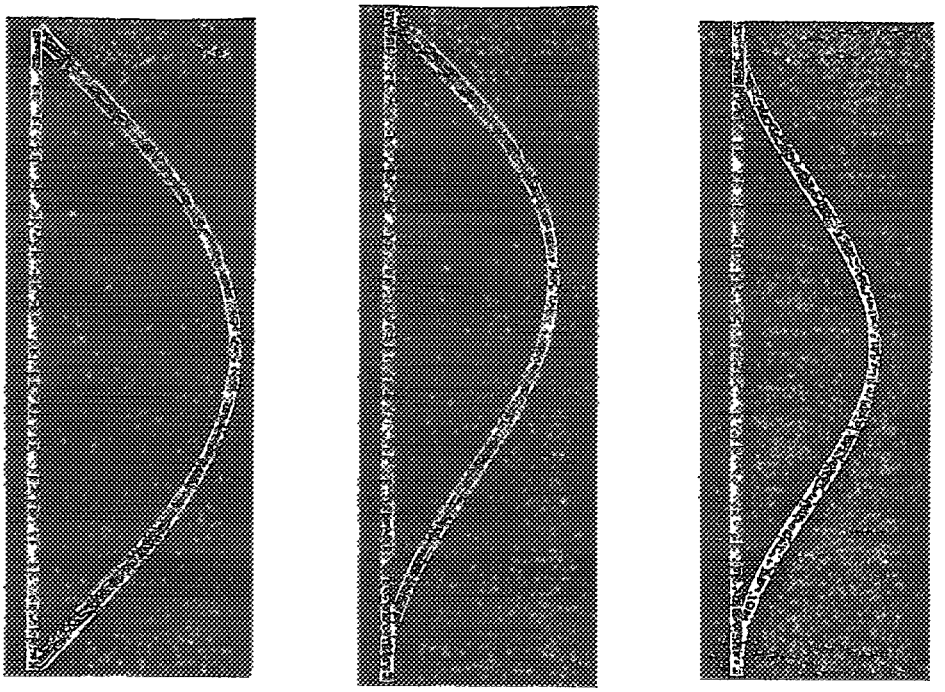

(1) 2 articulations
$\lambda = 0,95 < 1 \Rightarrow$ *Flambage*

(2) 1 articulation+1 encastrement
$\lambda = 1,93 > 1 \Rightarrow$ *pas flambage*

(3) 2 encastrements
$\lambda = 3,76 > 1 \Rightarrow$ *pas flambage*

FIG. 10. ***Rod's buckling calculation (with reduced stiffness) in each considered configuration of the connection system***

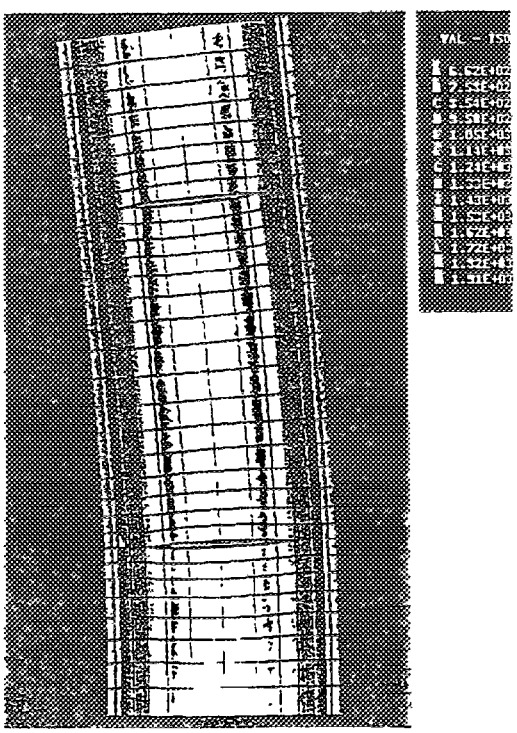

FIG. 11 ***Calculation of the buckling of the simulated rod (4 pellets) with an increased stiffness jointed to its extremities (metric system: model of the upper ½rod): $\lambda_4 = 1,87$***

So we notice that the critical loading of the rod with majored rigidity remains lower than the axial loading (# 41000 N), which implies its buckling in all the configurations of interfaces.

4. CONCLUSION

The most realistic modeling of loading is the one with majored rigidity (and actual thermal field of the rod). Since that the rigidity of the actual rod is lower than in the model, it can be concluded that the bowing is certainly due to buckling. In the case of non anchoring but slippage of the rod inside its holder, the hypothesis of buckling remains valid if the friction factor is high enough to transmit one tenth of the axial loading (41000/10 = 4100 > 3772 ===> buckling).

RIM EFFECT

The modeling of all phenomena connected to the pellet (and hence to the clad) is necessary to insure the integrity of the clad. One of these phenomena is the RIM EFFECT.

The characteristics of this area are more and more different from those of the pellet, as the burn-up increases. The burn-up, the porosity, the rate of Pu strongly increase and a non negligible part of the radioactivity is included within this zone despite its low thickness. Its peripheral location induce varied effects:

** amplification of the consequences of a clad breaking. An accurate knowledge of the stress field is needed.

** direct relation to the stresses within the clad because:

*** the important porosity induces a decreasing of the local thermal conductivity. So it can be assumed that the rim is a thermal screen between the pellet and the clad, which implies increasing of the central temperature of the pellet, of its dilatation and hence of the stresses of the clad.

*** the mechanical characteristics decrease and should let the stresses decrease in opposition with the effects of the temperature.

This brief analysis emphasizes the interest on parametric studies in order to evaluate more accurately the effects on the stresses within the clad. A first-step of the process is to let the thermal conductivity K of this specific area change, then its mechanical characteristics (E) and finally both of them simultaneously. Calculations have been performed with the code TOUTATIS.

1. DECREASING OF THE YOUNG'S MODULUS.

Clad ridges and thickness of the RIM are respectively about 15 and 100μ. So a strong decrease of the Young's modulus (80%) was presumably assumed to deteriorate the value of both ridges and strains of the clad.

The results of the calculation however show a low variation of the radial strain (less than 1μ), as the E/E_{rim} ratio increases from 1 to 10. These calculations have been benchmarked with a 2D analytical model (which does not take into account the axial effects).

If the range $1 < E/E_{rim} < 10$, the U_{rim} can be expressed as following - see chart 13

" $1 < E/E_{rim} < 10000$ " " " " " " 14

" " " $\sigma\theta\theta$ " " " " " " 15

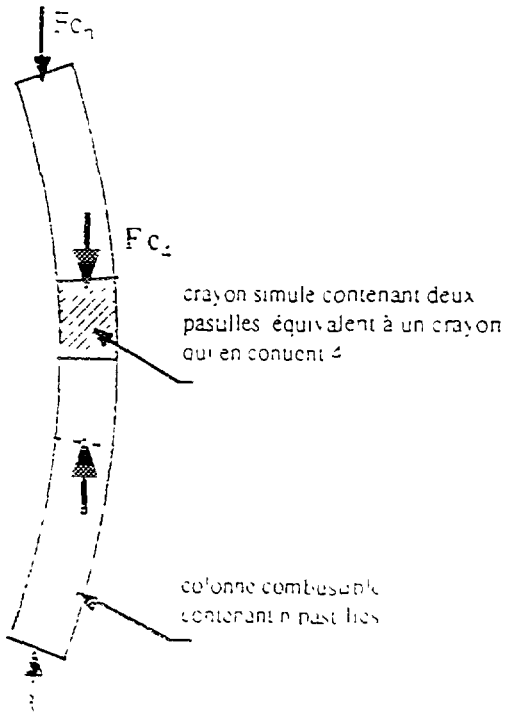

FIG. 12. *Calculation of the critical load for the total rod by extrapolation of the critical load of the simulated rod: $\lambda_n = (4/n)^2 \lambda_4 = 0{,}023 < 1$ buckling*

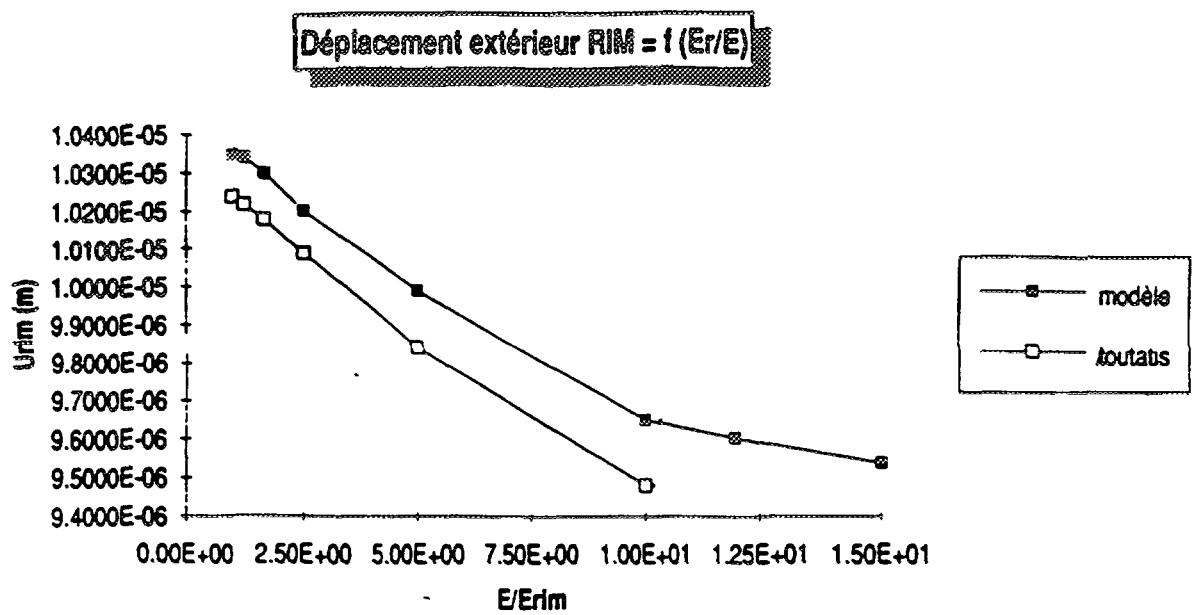

FIG. 13. *External moving RIM = f(Er/E)*

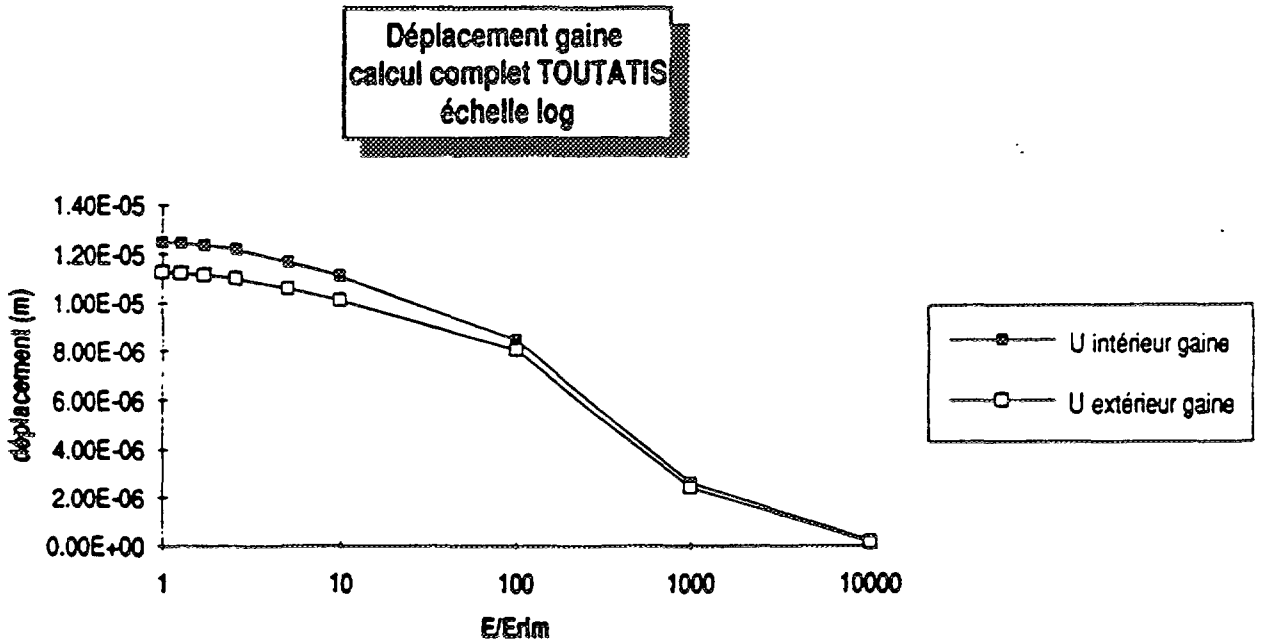

FIG. 14. Clad moving total calculation TOUTATIS (log scale)

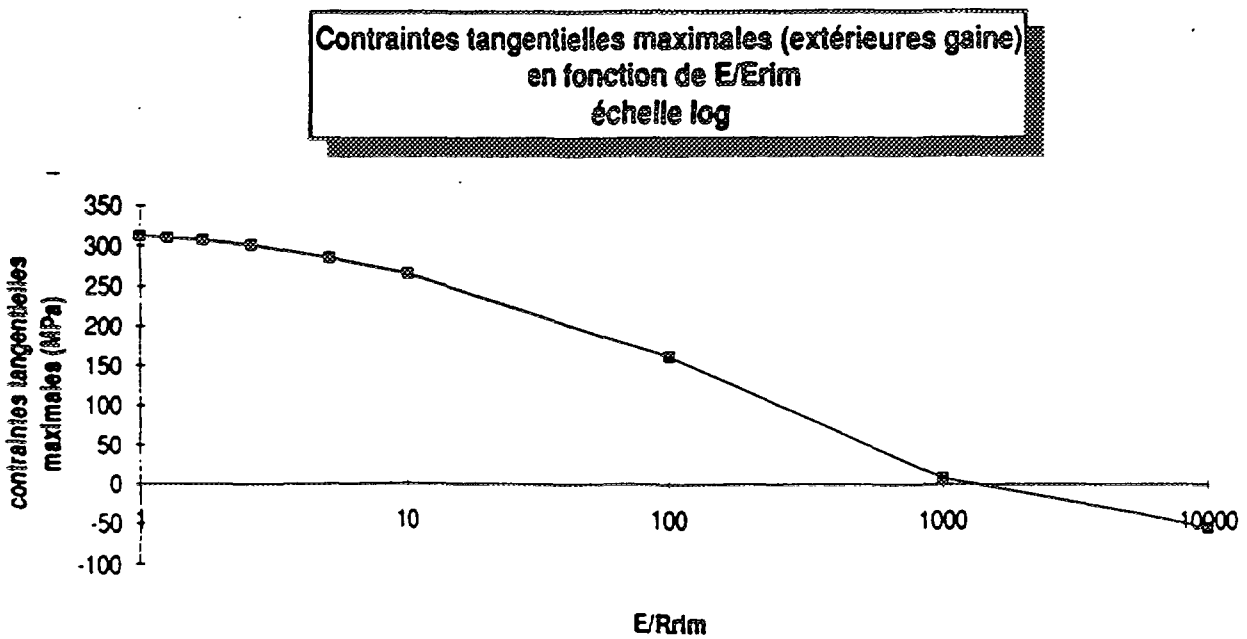

FIG. 15. Maximum tangential stress (external part of the cladding)versus E/Erim (log scale)

2. DECREASING OF THE THERMAL CONDUCTIVITY

Calculations have been carried out with the same set of data as previously, except the ratio K_{rim}/K whose values vary from 1.0 to 0.4. It is well known that K_{rim} is lower than K and decrease with the porosity, and the RIM is assumed to be more porous than the rest of the pellet. So the decrease of the thermal conductivity in the pellet periphery - as a thermal screen - induces an increase of the central temperature of the pellet - see charts N°s 16, 17.

This effect is important: it goes from 1346 K to 1596 K as the ratio changes up to 2.5. Given that the temperature is the key parameter in irradiation modeling, its strong correlation to the value of K is an important factor (creep, fission gas release...)

If the range $1 < K/K_{rim} < 2.5$, the U_{rim} can be expressed as following - see chart 18

" " " " ÓθΘ " " " " " 19

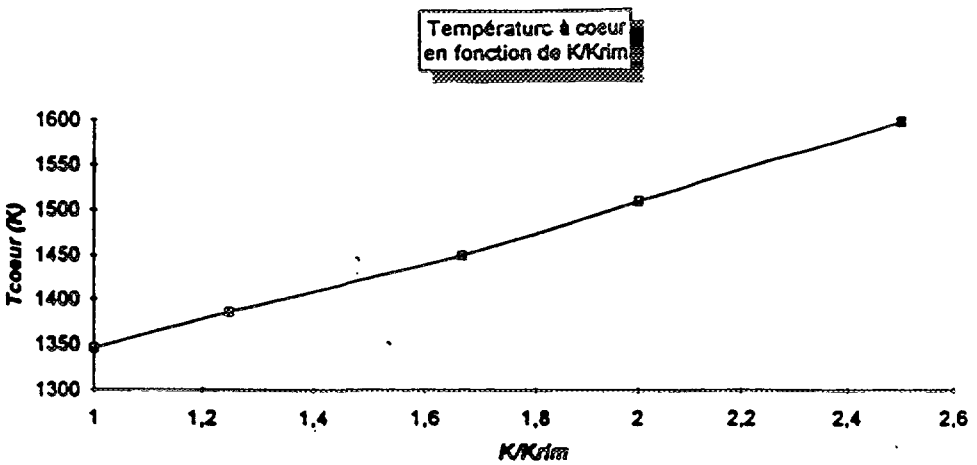

FIG. 16. Core temperature versus K/Krim

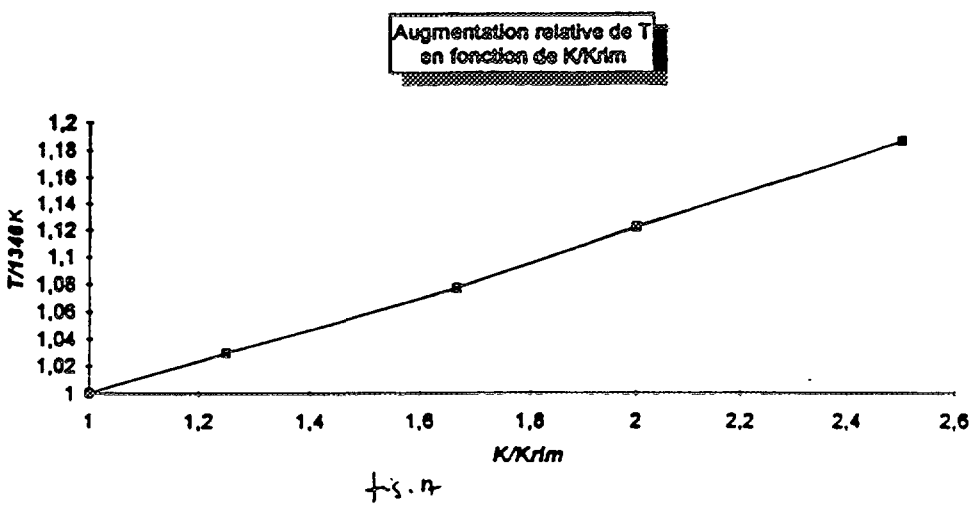

FIG. 17. Relative increase of T versus K/Krim

3. THERMO-MECHANICAL COUPLING

Calculations with the following set of data (E/E_{rim} = 10 and K/K_{rim} = 2) have been carried out in order to estimate the coupling between the decreasing of the Young's modulus and thermal conductivity. The list below allows the reader to compare these results to those with E and K decreasing separately (effect number one and number two).

	T coeur	$\Gamma\theta\theta$ max	$\Gamma\pi$ max	U
(0) absence de RIM	1346	312	-235.3	12.31
(1) E/Erim = 10 et K/Krim = 1	1325	264.4	-161.9	11.31
(2) E/Erim = 1 et K/Krim = 2	1510	435.4	-266.4	19.57
Superposition de (1) et (2)	1489	387.8	-192.9	18.57
E/Erim = 10 et K/Krim = 2	1489	395	-185.4	18.05

There is a pretty good agreement between these results obtained from the first set of data and those corresponding to the superposition of the effect number one and number two. Moreover the list shows clearly the non thermal coupling between the decreasing of E and K. The hypothesis of superposition of the strains due to the thermal dilation of the RIM and due to the loadings seems justified "a posteriori".

CONCLUSION

The first parametric rim calculations confirm the non-impact of the decrease of the Young's modulus (localized in the rim area with realistic ratio such as E/E_{rim} = S) on the numerical results of the simulation. For higher values of the ratio, both stresses and strains of the clad are noticeably reduced, but such a degradation of the mechanical properties during commercial use of the rods has never been highlighted.

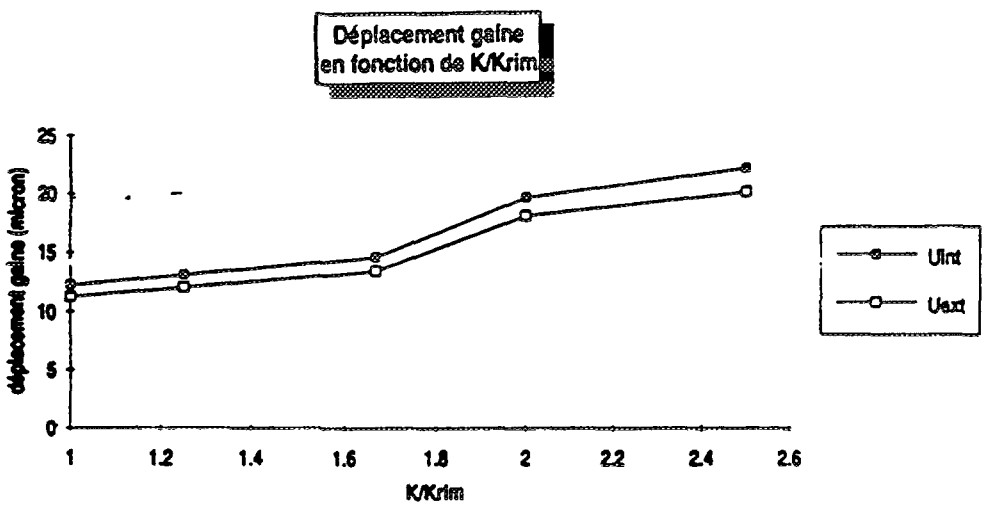

FIG. 18. Clad displacement versus K/Krim

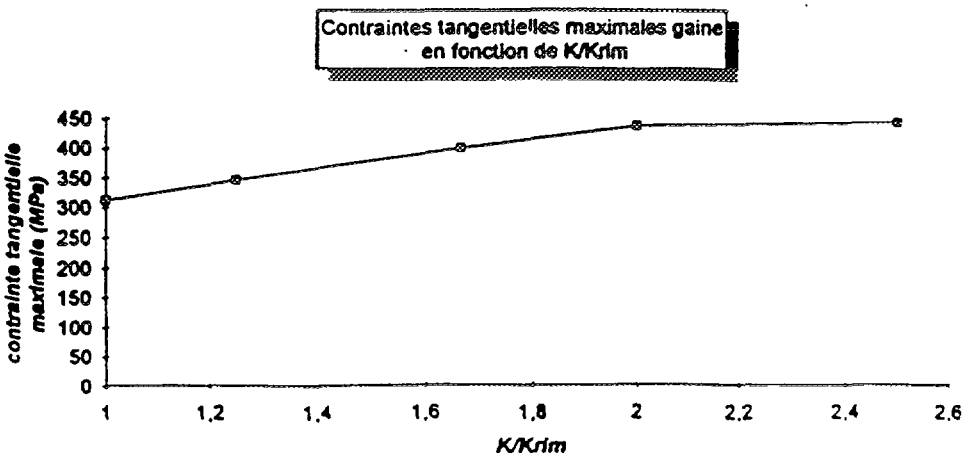

FIG. 19. Maximum tangential stresses of the cladding versus K/Krim

Related to the thermal studies, the relative increase of the central temperature and of the strains and stresses of the clad is approximately as important as the K decrease. So the impact of K/K_{rim} is much higher (> 10) than the one of E/E_{rim} for values ratio lower 25. Furthermore calculations have clearly showed that there is no significant coupling between the degradation of K and E parameters in the RIM area.

However some other parameters have to be taken into account, specifically from the thermo-mechanical point of view. All these first results are just preliminary.

SESSION 4
FISSION GAS RELEASE

EQUI-AXED AND COLUMNAR GRAIN GROWTH IN UO_2

R.J. WHITE
Berkely Technology Centre,
Nuclear Electric plc,
Berkeley, United Kingdom

Abstract

The grain size of UO_2 is an important parameter in the actual performance and the modelling of the performance of reactor fuel elements. Many processes depend critically on the grain size, for example, the degree of initial densification, the evolution rate of stable fission gases, the release rates of radiologically hazardous fission products, the fission gas bubble swelling rates and the fuel creep. Many of these processes are thermally activated and further impact on the fuel thermal behaviour thus creating complex feedback processes. In order to model the fuel performance accurately it is necessary to model the evolution of the fuel grain radius. When UO_2 is irradiated, the fission gases xenon and krypton are created from the fissioning uranium nucleus. At high temperatures these gases diffuse rapidly to the grain boundaries where they nucleate immobile lenticular shaped fission gas bubbles. In this paper the Hillert grain growth model is adapted to account for the inhibiting "Zener" effects of grain boundary fission gas porosity on grain boundary mobility and hence grain growth. It is shown that normal grain growth ceases at relatively low levels of irradiation. At high burnups, high temperatures and in regions of high temperature gradients, columnar grain growth is often observed, in some cases extending over more than fifty percent of the fuel radius. The model is further extended to account for the de-pinning of grains in the radial direction by the thermal gradient induced force on a fission gas grain boundary bubble. The observed columnar / equi-axed boundary is in fair agreement with the predictions of an evaporation / condensation model. The grain growth model described in this paper requires information concerning the scale of grain boundary porosity, the local fuel temperature and the local temperature gradient. The model is currently used in the Nuclear Electric version of the ENIGMA fuel modelling code.

1. INTRODUCTION

In the absence of an understanding of the thermal performance of irradiated UO_2, fuel modelling rapidly degenerates into the realms of empirical speculation. Since the thermal behaviour is critically dependent on many thermally activated processes, there exist a multitude of feedback loops in the fuel modelling process, some positive, like fission gas contamination of the fill gap, and some negative, like the gap closure effects of fuel swelling. It is therefore clear that effective fuel thermal modelling requires knowledge of many diverse factors. An example of this is the study of grain growth in UO_2.

The grain size of UO_2 is an important determining parameter for fuel densification, fission gas release, fission gas swelling and fuel creep. These parameters can influence the fuel thermal behaviour and, hence, fuel grain growth. Since, to a first approximation, fission gas release depends on the inverse grain size, an inadequacy in grain growth modelling is rapidly reflected in inaccuracies in calculated fission gas inventories. An acceptable fission gas release model should predict fission gas releases to within a *times or divide by two* criterion. Deficiencies in grain growth modelling can easily render this target unattainable.

Grain growth results in a net reduction in grain boundary area and hence a reduction in grain boundary free energy. The problem is similar to the growth of second phase particles in a metallic matrix

and invariably results in similar kinetic behaviour. The differences, however, are not simply due to the fact that the grains occupy all space, that is the volume fraction of precipitate is one hundred percent, but are related to the possibility that the grain boundaries may be inhibited from moving by the presence of impurities, precipitates or bubbles. It is the presence of an irradiation induced grain growth retarding mechanism which complicates the modelling of grain growth.

2. THEORETICAL CONSIDERATIONS

2.1 BASIC CONCEPTS

The inward force, **F**, on an element of grain boundary is inversely proportional to its radius of curvature. Thus, $F \alpha \gamma_{gb}/D_g$ where γ_{gb} is the grain boundary energy per unit area and D_g is the grain diameter. The velocity, **v**, of the boundary is given by the Nernst-Einstein relation and is

$$v = \frac{dD_g}{dt} \alpha \frac{D}{kT} \frac{\gamma_{gb}}{D_g}$$

where **D** is the diffusion coefficient of the boundary. This relation yields a simple parabolic growth law. Most out-of-pile studies of UO_2 grain growth indicate that the growth rate varies more as D_g^a where n is between 2 and 3 suggesting that the derivation given above is overly simplistic.

Ainscough et al [1] have proposed that grain growth may be retarded or even terminated by an array of deposits of fission products, either solid precipitates or gas filled pores. They proposed that the grain growth law may be written in the following way to reflect the limiting grain size, D_{max}

$$\frac{dD_g}{dt} \approx k^1 \left(\frac{1}{D_g} - \frac{1}{D_{max}} \right)$$

In a more detailed study, Hillert [2] uses the standard Lifshitz and Slyozov [3] & Wagner [4] (LSW) techniques for particle coarsening applied to the growth of an array of grains in the presence of a dispersion of second phase particles and suggests that the grain growth is more accurately modelled by the following equation.

$$\frac{dD_g}{dt} = \frac{k^1}{D_g} \left(1 - \frac{D_g}{D_{max}} \right)^2 \qquad (1)$$

In addition, Hillert adapts Zener's [5] calculation to relate the limiting grain size to the size and density of the population of second phase particles. For a uniform dispersion of particles of radius, **r**, and volume fraction, **f**, the net retarding stress, **S**, on the grain boundary resulting from those particles residing in close proximity to the boundary is $S = 4f\gamma_{gb}/3r$ and the limiting grain diameter is given by

$$D_{max} = \frac{\gamma_{gb}}{S} \qquad (2)$$

2.2 EXTENSION OF MODEL TO INTERGRANULAR POROSITY

The methods developed by Zener [5] and Hillert [2] apply to a uniform dispersion of precipitates. In the case of irradiated UO_2 the main retarding influence will be the development of fission gas porosity on the grain boundaries. The fission gas release model [6] in the ENIGMA fuel modelling code [7] specifically addresses the issue of porosity development and the following ideas are an extension of the ENIGMA model.

It is assumed that the lenticular 'bubbles' which form on the grain faces are not equilibrium bubbles but highly overpressurised and can best be described as quasi-crystallites with a packing density of ϵ, where $\epsilon = 0.15$. The reasons for this behaviour are obscure and may be related to the non-equilibrium situation engendered by the presence of irradiation induced resolution of gas atoms from the cavities. This may also be accompanied by an irradiation induced vacancy depletion process and may lead to overpressurised bubbles.

During the early stages of the irradiation, gas will accumulate on the boundaries and precipitate into lenticular shaped cavities. Those cavities close to grain edges - regions of threefold symmetry - will move onto the edges and take up a triangulated cigar shape. Because of the geometrics of grain face and grain edge bubbles a continuous tunnel will form along the grain edges when the fractional coverage of the face has reached 40%. For light irradiations the bubbles will be so small that the resulting edge tunnel will be unstable against collapse by surface tension forces and the process will begin anew, this time with slightly larger grain face bubbles.

In the gas release calculation, the important factor is the concentration of gas on the grain boundaries, the size of the bubbles being relatively unimportant. Furthermore, it is also assumed that the grain face coverage is always 40%, an approximation of minor importance to gas release calculations but of significance to the grain growth model. In the calculation of limiting grain size the calculation is refined so that the incubation is treated more correctly as a pre-interlinkage period in which the bubble size is fixed at a small but constant value and the fractional coverage builds up to 40% followed by an approach to saturation in which the coverage is fixed at 40% and the grain face bubble radius can grow.

2.3 PRE-INTERLINKAGE PERIOD

In this regime it is assumed that the bubble radius of curvature, $\mathbf{r_p}$, is constant and that the accumulation of fission gas atoms results in a progressive increase of the fractional coverage from zero to 40%. Because the specific free energy, γ_{gb} of the UO_2/UO_2 interface (gb = grain boundary) differs from the specific free energy, γ_{fs} of the UO_2/Vacuum interface (fs = free surface), the cavities are of a lenticular shape with a semi-dihedral angle θ and a projected radius on the grain face of $\mathbf{r_p}$. (Note that $\gamma_{fs} = \gamma_{gb}/2\cos\theta$ and $r_f = r_p\sin\theta$). In these circumstances the restraining force on the grain boundary is given by

$$F = \pi\gamma_{fs} r_p \sin\theta = \frac{\pi\gamma_{gb} r_p \tan\theta}{2} \qquad (3)$$

If it is further assumed that each lenticular bubble resides inside a circular cell of radius R_c - this implies that the fractional coverage $F_c = r_p^2/R_c^2$ - the stress on the grain boundary arising from this force averaged over its cell is

$$S = \frac{r_p \gamma_{gb} \tan\theta}{4R_c^2} \qquad (4)$$

and it should be noted that each cell is shared between two grains and the effective area of grain boundary is $2\pi R_c^2$.

The relationship between bubble size and grain boundary areal gas concentration, N_f is given by the ENIGMA gas release model [6] as,

$$r_p = \frac{10bN_f}{\epsilon} \qquad (5)$$

where **b** is the Van der Waal's constant for xenon and ϵ is the gas atom packing fraction in the cavity. For $F_c < 40\%$ we can write

$$F_c = \left(\frac{r_p^o}{R_c} \right)^2 \tag{6}$$

and similarly

$$N_f = \frac{F_c \epsilon r_p^o}{4b} \tag{7}$$

where r_p^o is the grain face bubble radius in the pre-interlinkage region. Substituting from Eqns. 6 & 7 for R_c into Eqns. 2 & 4 yields

$$D_{max}^{irr} = \frac{\epsilon r_p^{02} \cot\theta}{bN_f} = \frac{K^{irr}}{N_f} \tag{8}$$

2.4 STEADY STATE INTERLINKAGE PERIOD

This regime is characterized by a fixed fractional coverage of grain boundaries of $F_c = 0.4$ and with the additional gas release contributing to bubble growth and progressive edge interlinkage rather than increased coverage. Under these conditions it is clear that $R_c^2 = 2.5r_p^2$ and that r_p is given by Eqn. 5. Substituting into Eqns. 2 & 4 gives

$$D_{max}^{irr} = \frac{100 bN_f \cot\theta}{\epsilon} \tag{9}$$

This result arises from the fact that the maximum grain size is inversely proportional to the average stress over the lenticular cell and that once the grain faces are saturated, ie $F_c = 40\%$, all additional gas contributes to increasing the size of the bubbles. However, the cell size is proportional to the bubble size and since the force only increases with the bubble radius while the area it acts upon increases as the square of the bubble size, the actual retarding stress decreases with increasing bubble size, hence the maximum grain size increases with grain boundary gas concentration once the saturation average of 40% is reached. It should be noted, however, that for all practical grain boundary gas concentrations, Equation 9 acts as a bar to any further grain growth.

3. EXTENSION TO COLUMNAR GRAIN GROWTH

The analysis in §2 indicates that grain growth is rapidly terminated as soon as an appreciable fraction of fission gas is deposited on the grain boundaries. In fact, most of the equiaxed grain growth must occur before the fractional coverage reaches 40%. However, at high temperatures columnar grain growth occurs suggesting that the pinning effect of bubbles is mitigated by some external agency, usually assumed to be associated with the steep temperature gradients in the fuel. The most likely transport mechanism under these circumstances is the evaporation of UO_2 species from the hot side of a bubble and its deposition on the cold side. In this way the bubble appears to migrate up the temperature gradient whereas the flux of UO_2 is in the opposite direction. The effective force on a bubble in a temperature gradient is [8]

$$F = - \frac{V_b}{\Omega} \frac{Q_s^* \nabla T}{T} \tag{10}$$

where V_b is the volume of the lenticular bubble, Ω is the 'atomic' volume of the UO_2 species, Q_s^* is the latent heat of vaporisation, T is the absolute temperature and ∇T is the temperature gradient.

The criterion as to whether or not columnar grain growth occurs depends on the relative magnitudes of the pinning force of the bubble, Eqn. 3, and the de-pinning force, Eqn. 10. That is, if the force on a bubble in a temperature gradient exceeds the force holding that bubble to the grain boundary, then bubble migration and hence grain growth can occur. Two points are important here, firstly, since the temperature gradient is radial, grain growth will only occur in the radial direction resulting in columnar grains. Secondly, Equations 3 & 10 define the forces on, rather than the velocities of, grains or bubbles. For this latter calculation we require a grain boundary mobility and in the absence of either experimental measurements of columnar grain velocity or good theoretical models it would seem sensible to use the same grain mobility as pertains in equi-axed growth extrapolated to the higher temperatures at which columnar grain growth occurs.

Equating Eqns. 3 & 10 and noting that the volume of a lenticular bubble [9] is

$$V_b = \frac{4\pi r_p^3 f_f(\theta)}{3\sin^3\theta} \quad where \quad f_f(\theta) = 1 - \frac{3\cos\theta}{2} + \frac{\cos^3\theta}{2} \tag{11}$$

the criterion for the onset of columnar grain growth in UO_2 where the semi-dihedral angle, $\theta = 50°$ [10] may be written as

$$r_p^2 \frac{\nabla T}{T} > \frac{1.19\gamma_{gb}\Omega}{Q_s^*} \tag{12}$$

4. EXPERIMENTAL DATA

4.1 OUT-OF-PILE GRAIN GROWTH

Equation 1 has been used to analyse of out-of-pile data originating from Ainscough data [1], Singh [11] and Watson et al [12]. The derived rate constants and limiting grain sizes are shown in Figs. 1 & 2 and the solid lines on these Figures are given by

$$k^1 = 3.735 \times 10^{-8} \exp\left(-\frac{27100}{T}\right) \; m^2 s^{-1}$$

and

$$D_{max} = D_0 + D_{max}^{th} \quad with \quad D_{max}^{th} = 4.275 \times 10^{-3} \exp\left(-\frac{9000}{T}\right) \; m$$

where **T** is the absolute temperature and $\mathbf{D_0}$ is the initial grain size.

4.2 IN-PILE EQUI-AXED GRAIN GROWTH

From the analysis in §4.1 it would appear that the grain size has a maximum value in out-of-pile situations. It is possible that this is a result of as-fabricated porosity and impurities and the temperature dependence of the limiting grain size may be a result of possible sintering of as-fabricated pores during the grain-growth anneal. Whether the limiting in-pile grain size should also be temperature dependent clearly depends on whether the value of grain face bubble radius for interlinkage, i.e. $\mathbf{r_p^0}$, is temperature dependent. Analysis of fission gas release from out-of-pile anneals [13] suggests that this radius is temperature independent so one might expect the irradiation component of the limiting grain size should also be temperature independent. A reasonable form for the limiting in-pile grain size might be

$$D_{max}^{i-p} = D_0 + \frac{D_{max}^{th} D_{max}^{irr}}{D_{max}^{th} + D_{max}^{irr}} \tag{13}$$

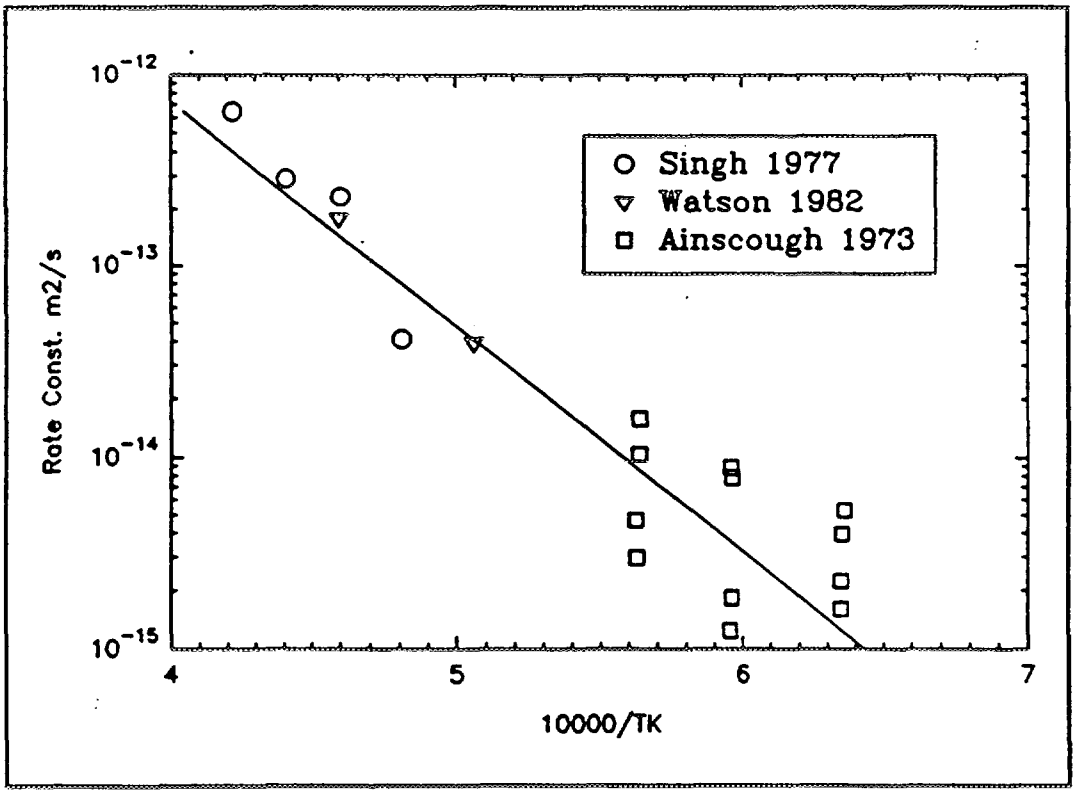

1. *Grain growth rate constant obtained from fits to the Hillert equation applied to average grain sizes for three sets of out-of-pile growth data.*

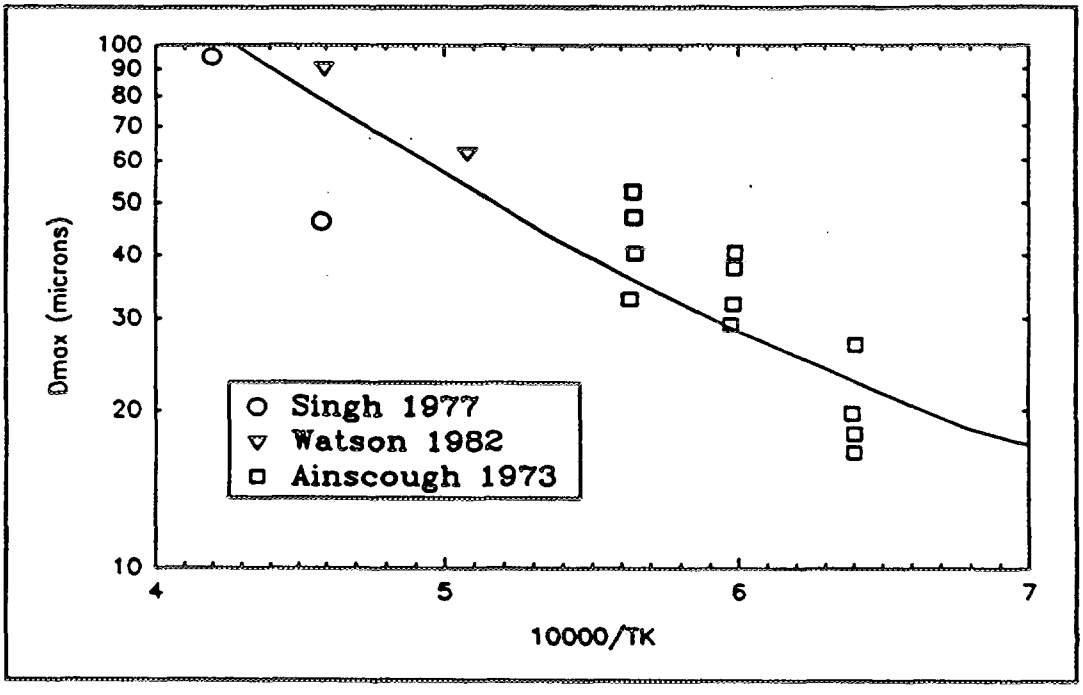

2. *Maximum grain size (average) deduced from fits to Hillert grain growth equation applied to three sets of out-of-pile grain growth data.*

where D_{max}^{irr} and D_{max}^{th} are the irradiation and thermal maximum grain sizes given above. Initial runs with ENIGMA on a limited database suggest that reasonable correspondence may be obtained with a bubble radius of 0.12 μm which is itself equivalent to a grain boundary gas atom concentration of ~2.0 x 10^{19} m^{-2}. It would thus seem unlikely that the gas atom concentration could ever rise to such a value that Eqn. 9 could define a sufficiently large limiting grain diameter to permit further grain growth after Eqn. 8 had terminated grain growth.

4.3 COLUMNAR GRAIN GROWTH

Using the ENIGMA calculation for bubble radius yields the following criterion for the transition from equi-axed to columnar grain growth

$$\Phi = 100\frac{\nabla T}{T}\left(\frac{bN_f}{\epsilon}\right)^2 > \frac{1.19\gamma_{gb}\Omega}{Q_s^*} \qquad (14)$$

ENIGMA [7] has been modified to print out the 'peak-in-time' value of this parameter during the course of irradiation of three Halden rods [14] in which columnar grains were observed in PIE. The radial extent of columnar grains is shown in Table I along with the required value of the columnar grain parameter, Φ at that radial point.

The radial variation of Φ can be seen in more detail in Figure 3 in which the ENIGMA calculation is plotted for the three rods. Note that because of the symmetry of the temperature profile the parameter tends towards zero at the centre of a solid rod. This implies that the force on the cavities will be zero and hence there should be a region of equi-axed grains in the centre of a solid rod. This is not observed in practice possibly due to the fact that radial pellet cracking occurs, thus destroying the perfect radial symmetry. Another possible reason for the absence of the equi-axed core is that as the cavity is driven up the temperature gradient it collects gas atoms by a sweeping process and grows in radius thus requiring a smaller thermal gradient to keep it moving than was initially required to set it in motion.

5. DISCUSSION AND CONCLUSIONS

In the previous sections an outline model for UO_2 grain growth has been presented. This model uses the Hillert [2] treatment for grain growth when growth is inhibited by the dragging effect of precipitates and/or porosity. Columnar grain growth can occur when the force on lenticular porosity in a temperature gradient exceeds the pinning force of the porosity to the grain boundary. In reality the situation will be more gradual than presented here and it is clearly possible to define the maximum possible grain size in the radial direction as a balance of the thermal and mechanical stresses so that it becomes a continuous function of temperature gradient and bubble radius. However, because of the steep variation of the columnar grain parameter, Φ, with pellet radius, it is unlikely that this approach would yield any better results than the present simplistic approach.

An estimate of the columnar grain parameter, Φ can be obtained from Eqn. 14. The value of γ_{gb} used in ENIGMA is 0.32 J/m^2 and Ω is 4.1 x 10^{-29}. Olander [8] quotes a value of 415 kJ/mole for Q_s^* which produces a value of Φ = 2.26 x 10^{-11}. This value should be compared with the values quoted in the Table I. The agreement is particularly good when it is considered that the criterion depends on such factors as bubble radius and that this is calculated on the basis of an, as yet, unproven assertion that the grain face bubbles behave more as quasi-crystallites than equilibrium bubbles.

TABLE I: **Extent of Columnar Grain Growth and ENIGMA Calculation of Columnar Grain Growth Parameter.**

Rod	Radial Extent of Columnar Grains	ENIGMA Calculation for Φ (x 10^{-11})
A	45%	3.4
B	50%	2.2
C	20% - 25%	3.5 - 2.9

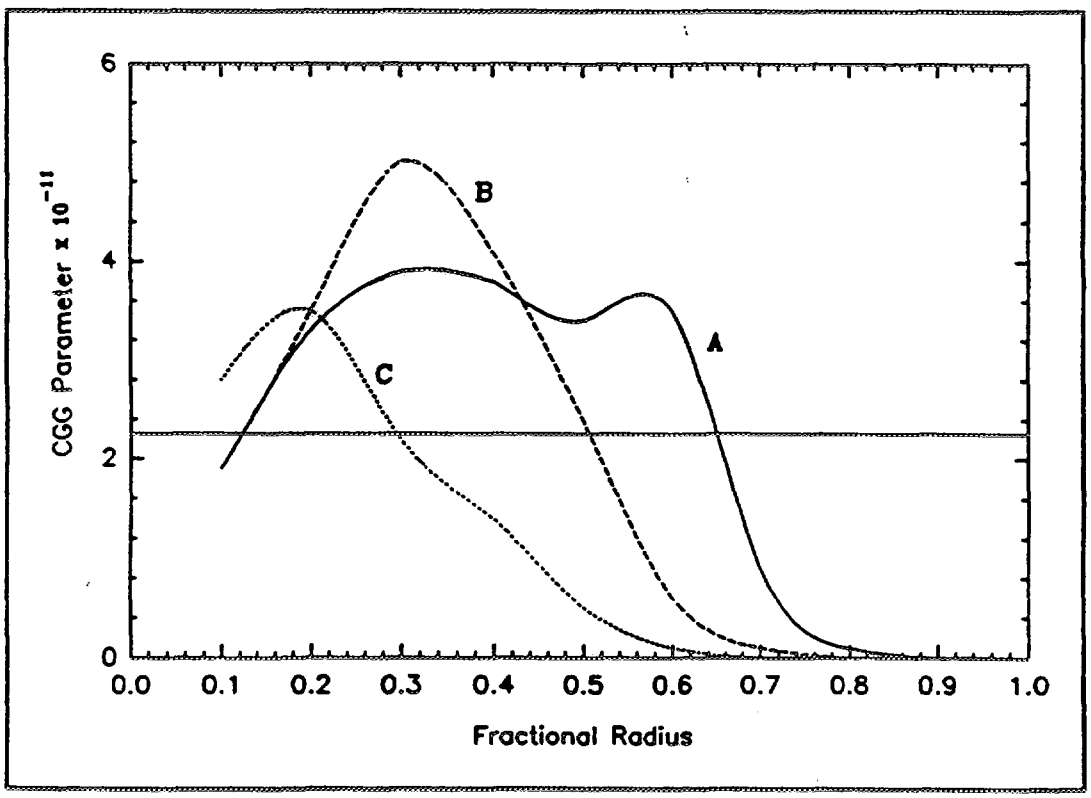

3. ENIGMA calculation of columnar grain growth parameter as a function of radial position across the pellet for three Halden fuel rods. The solid line shows the theoretical estimate of the parameter. Note 0.0 is pellet centre.

ACKNOWLEDGEMENT

This paper is published by permission of Nuclear Electric. Thanks are due to the Halden Project for permission to use PIE information on extent of columnar grain growth.

REFERENCES

[1] AINSCOUGH J B, OLDFIELD B W AND WARE J 0: Isothermal Grain Growth Kinetics in Sintered UO_2 Pellets, 1. Nuclear Materials, 49, 117, 1973/74.

[2] HILLERT M: On the Theory of Normal and Abnormal Grain Growth, Acta Metall. 13, 227, 1965.
[3] LIFSHITZ I M AND SLYOZOV V V: Zh. Eksp. Teor. Fiz. 35, 479, 1958.
[4] WAGNER C: Z. Electrochemie 65, 581, 1961.
[5] ZENER C: (Priv. Comm. to C S Smith) in Trans. Am. Inst. Mining (metall) Engrs. 175, 15, 1949.
[6] WHITE R J: A New Mechanistic Model for the Calculation of Fission Gas Release. Paper presented at the ANS/IAEA International Topical Meeting on Light Water Reactor Fuel Performance held at West Palm Beach, Florida, USA, April 17-21, 1994.
[7] KILGOUR W J, TURNBULL J A, WHITE R J, BULL A J, JACKSON P A & PALMER I D,: Capabilities and Validation of the ENIGMA Fuel Performance Code. ANS/ENS Topical Meeting on LWR Fuel Performance held at Avignon, France, April 21-24, 1991.
[8] OLANDER D R: Fundamental Aspects of Nuclear Reactor Fuel Elements. TID-26711-P1, 1976.
[9] CLEMM P J & FISHER J C, Acta Metall. 3, 70, 1955.
[10] REYNOLDS G L, BEERE W & SAWBRIDGE P T: J. Nucl. Mater. 41, 112, 1971.
[11] SINGH R N: J. Nucl. Mater. 64, 174, 1977.
[12] WATSON R H, HOWARD R J and WOOD G A: Paper presented to the UO_2 Basic Properties Committee, 1981.
[13] White R J & Wood P: Paper to be presented at the BNES Conference on Fuel Management and Fuel Handling, Edinburgh, Scotland, 20-22 March 1995.
[14] Sairanen R, On the Effect of Irradiation Conditions on Fuel Structural Changes, Halden Project Report, June 1984.

BEHAVIOUR OF LARGE GRAIN UO_2 PELLET BY NEW ADU POWDER

Y. HARADA
Nuclear Development Corporation,
Tokai, Ibaraki

S. DOI
Mitsubishi Atomic Power Industries Inc.,
Kobe

S. ABETA
Mitsubishi Heavy Industries Ltd,
Yokohama

K. YAMATE
Kansai Electric Power Corporation Inc.,
Osaka

Japan

Abstract

In Japan, high burnup PWR fuel is being developed for assembly discharge burnups from 48 to 55GWd/t. As the pressure in the rods due to fission gas release from the pellets during the long burnup period is an important issue, some kinds of large grain pellets are being investigated in order to reduce fission gas release assuming their behaviour will be as predicted by the simple diffusion mode. One kind of large grain pellet is manufactured from the highly sinterable powder produced by the new ADU (ammonium diuranate) process for converting UF_6 gas to UO_{2+x} powder. Firstly, we checked the difference in the characteristics of the new active powder and the one in current use by investigating its pelletizing (pressing and sintering), densification, grain growth and microstructure (pore and grain structure). Secondly, we measured the thermal creep, thermal expansion and thermal conductivity of the large grain pellet, in out-of-pile tests. As a result, it was found that the thermal properties of the large grain pellet are the same as those of the current ADU pellet except for thermal densification and creep behaviour. Thirdly, irradiation experiments were performed in the Halden test reactor and the pressure and fuel stack length change in the rods were monitored at power. After irradiation up to about 20GWd/t, PIE has been carried out. It was confirmed that the fission gas release of the large grain pellet is lower and the in-pile densification is smaller than for pellets in current use. The reduction due to the large grain size is lower than expected from the Booth model because the fission gas release rate is very small and the effect of recoil/knockout is comparable to that of diffusion for a low linear heat rate. This paper compares the microstructure of the new pellet with its large grains and pores produced by a poreformer and a current pellet with normal sized grains and intrinsic pores. It also describes how this comparison relates the in-pile behaviour of the large grain pellets to the results of the out-of-pile tests.

1. INTRODUCTION

In Japan, high burnup PWR fuel is being developed in order to increase discharge burnups from 48 to 55GWd/t (Assembly).

The criterion for the pressure in the fuel rods is that the pellet/clad gap must never reopen due to fission gas release from the UO_2 pellets during the high burnup period.

From the above view point, our design calculation shows that the need of the reduction of the fission gas release rate is set to be one third of that of the current UO_2 fuel pellets.

Therefore some kinds of large grain pellets are being investigated to reduce fission gas release assuming they behave as predicted by a simple diffusion model that is the Booth model [1].

We are investigating three kinds of large grain pellets as follows.

(1) the large grain pellet doped with niobia [2, 3] or chromia [4] as a sintering aid in our new fabrication process

(2) the large grain UO_2 pellet sintered in the oxidative atmosphere using our three stage-sintering method at a low temperature for a short period [5, 6, 7].

(3) the large grain pellet that is manufactured from the highly sinterable powder produced by the new ADU (ammonium diuranate) method of converting [8] from UF_6 gas to UO_{2+x} powder.

This paper describes how the in and out-of-pile densification depends on pore structure and the fission gas release depends on the grain structure for the large and normal sized grain pellets made from new and current ADU powders respectively.

2. EXPERIMENTAL PROCEDURES

2.1 OUT-OF-PILE UO_2 PELLET CHARACTERIZATION

The new ADU conversion process has been reported [8]. The difference between the current and the new process is the change from room-temperature to pyrohydrolysis in other words, from wet to dry hydrolysis.

The ordinary chatacteristics of the current and modified UO_{2+x} powder were measured to investigate the effects on pressing and simerability as shown in Table 1. The density increase caused by tapping the current powder is higher than that of the modified powder. For sinterability, the specific surface area of the modified powder is higher than that of the current one due to the roughness of the morphology [3] and fine primary particles. This shows that the modified powder can be sintered easily. Both types of green pellets were pressed using a double cycle (slug and green pellet) after the addition of U_3O_8 to the currently used powder and a poreformer to the modified powder in order to keep the specified sintered density. Lubricant was added to both granules. Under the same conditions, the density of the green pellet made from the current powder was higher than that from the modified powder.

Both types of UO_2 pellets were sintered under normal conditions at 1750°C in wet hydrogen gas.

The dimensions and immersion density of the sintered and resintered UO_2 pellets were measured. The pore and grain structure of the sintered and resintered pellets were investigated by ceramography and quantitative image analysis. The same method was also used on irradiated pellets after the in-pile tests.

The UO_2 pellets used in this study are the type used 17 x 17 PWR fuel and their characteristics are shown in Table 2.

2.2 THERMAL PROPERTIES MEASUREMENTS

The thermal expansion of the large and normal grain UO_2 pellet was measured using the differential dilatometer (Rigaku Denki Co.,LF/TCM-FA8510B). The strain difference of the test sample and a known reference sample (Y_2O_3) was measured up to 1 500°C in a mixture of wet hydrogen and argon gas.

The thermal diffusivity of both UO_2 pellets was measured by using the laser flash method (Rigaku Denki Co.,CN8098). The samples were 2mm thick disks, sliced from the UO_2 pellets. The temperature

Table 1 **ADU UO_{2+x} powder Characterization**

Item	Modified	Current
Hydrolysis of Conversion	Dry/Pyro	Wet/RoomTemp.
Morphology	Rough	Flat
Apparent Density (g/cc)	1.4	1.4
Tap Density (g/cc)	2.1	3.5
Fischer Average Particle Size (μm)	0.9 ~ 1.9	0.8 ~ 1.2
BET Specific Surface Area (m^2/g)	9.8 ~ 13.6	1.2 ~ 2.5

Table 2 **ADU UO_2 pellet Characterization**

Item	Large Grain	Normal Grain
U_3O_8 Addition (wt%)	none	20
Poreformer Addition (wt%)	0.7 ~ 1.0	none
Sintering Atmosphere	Wet hydrogen	Wet hydrogen
Sintering Temperature (°C)	1750	1750
Average Grain Size (μm)	23	8
Density (%TD)	94.1	95.3
Density Change during Resintering at 1700°C for 24h (%TD)	0.19	1.08

change on the reverse side of the sample during laser irradiation of the face side was measured up to 1000°C at intervals of 200°C in a vacuum. In principle, the thermal diffusivity α (cm^2s^{-1}) is calculated by the following equation assuming one dimensional thermal diffusion

$$\alpha = 0.1388L^2/t_{1/2} \quad (1)$$

where L (cm) is the sample thickness and $t_{1/2}$ (s) is the time taken to reach a temperature equal to half of the maximum temperature change. In our measurement, the logarithmic method [9] was applied for the data reduction.

The thermal conductivity k ($Wm^{-1}K^{-1}$) is calculated according to Eq. (2)

$$k = \alpha \rho C_p \quad (2)$$

where ρ (gcm^{-3}) is the measured density and C_p ($WK^{-1}g^{-1}$) is the heat capacity taken from reference data [10].

The thermal creep rate of both UO_2 pellets was measured using the controlled-atmosphere constant-stress creep apparatus (Toshin Kogyo Co.,HCT-3000). The steady state creep rate was measured after the initial transient creep had occurred. The data was taken between 1100°C and 1600°C at intervals of 100°C with axial compression stresses between 1.0 and 20kg/mm^2. The tests were done in argon gas lo keep the stoichiometry of the samples.

2.3 IRRADIATION TESTS AND PIE PROCEDURES

The characteristics of the large and normal grain UO_2 pellet supplied for the irradiation tests and PIE are shown in Table 2. The average grain size of the large grain UO_2 pellet is three times larger than that of the normal one because our aim is to reduce the fission gas release to one third and the Booth model gives Eq. (3)

$$FGR \propto 1/d \tag{3}$$

where FGR (%) is the fission gas release rate and d (μm) is the average grain size. The sintered density of both pellets is the same, but the density change during resintering of the large grain UO_2 pellet is one fifth of that of the normal grain sized pellet.

The test fuel rods were irradiated in the Halden HBWR. The enrichment of the U^{235} is 9.0wt.%. The fuel stack length is 350mm and the fuel rods were initially filled with He to a pressure of 1 bar.

The irradiation data were recorded and included the power history, fuel center temperature, fuel stack length change and pressure change for both rods.

After the irradiation to about 20GWd/t, PIE was done on the puncture test and ceramography.

3. RESULTS

3.1 MICROSTRUCTURE OF SINTERED UO_2 PELLETS

The pore and grain structure of the large and normal grain UO_2 pellets are shown in Fig. 1 and 2. The figures show of the ceramographs of the polished and chemically-etched surfaces, respectively. The pore and grain size distributions of the large and normal grain pellets that were measured using quantitative image analysis are shown in Fig. 3 and 4. The volumetric pore size distribution was obtained from the measured pore diameters and the pore area. The result was converted to a volumetric distribution by normalizing by the total porosity given by pellet density.

The pore structure of the normal grain pellet consists of intrinsic pores that are smaller than about 10 μm as a poreformer was not used. The pore structure of the large grain pellet consists of large pores (mainly > 10 μm) that are formed by adding a poreformer. The grain size distribution of the large grain pellet has a broader range than that of the normal pellet.

3.2 THERMAL EXPANSION

The thermal expansion coefficients of the large and normal grain UO_2 pellets are the same, as can be seen in Fig. 5. This shows that the thermal expansion is independent of the differences in the microstructure of the two pellets.

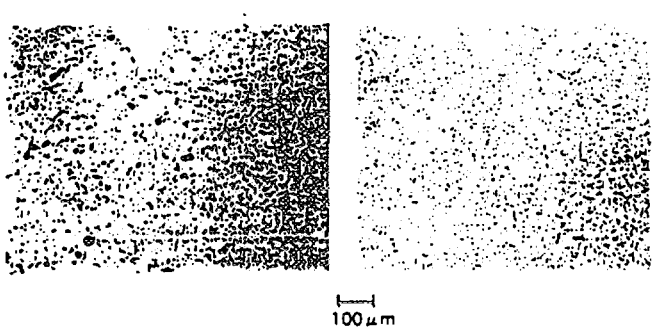

FIG. 1 Ceramograph of Pore Structure of sintered UO_2 pellets

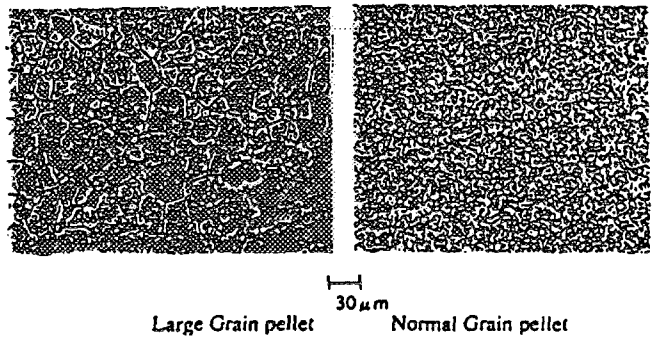

FIG. 2 Ceramograph of Grain Structure of sintered UO_2 pellets

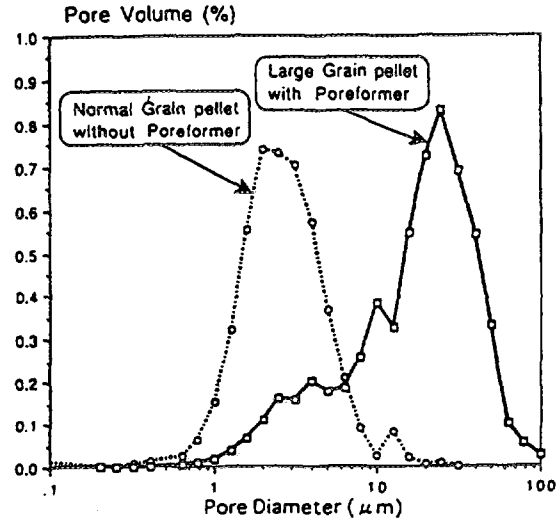

FIG. 3 Pore Size Distribution of sintered UO_2 pellets

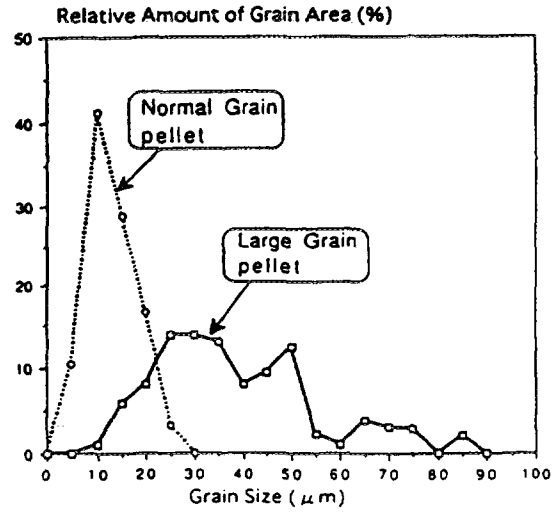

FIG. 4 Grain Size Distribution of sintered UO_2 pellets

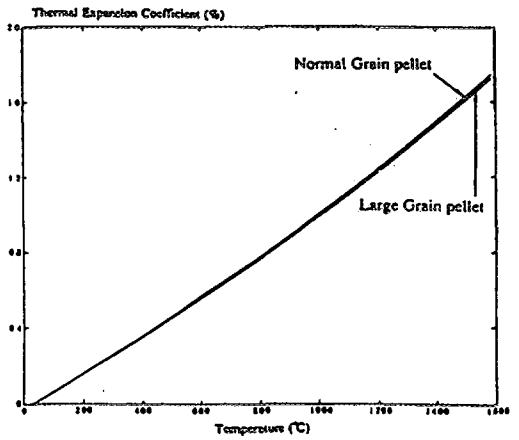

FIG. 5 Comparison of Thermal Expansion Coefficients

3.3 THERMAL CONDUCTIVITY

The thermal conductivities of the large and normal grain UO_2 pellets are estimated to be the same based on the reproducibility of ± 2% shown in Fig. 6. This shows that the thermal conductivity is independent of the differences in the microstructure, particularly the pore structure, of the two pellets. The equation for the measured thermal conductivity is given below

$$k = 1/(A+BT) \quad (4)$$

where	constant	large grain pellet	normal grain pellet
	A	2.31×10^{-2}	3.40×10^{-2}
	B	2.53×10^{-4}	2.30×10^{-4}

and T (K) is the temperature.

3.4 THERMAL CREEP

The relation between the thermal steady state creep rate and stress is shown in Fig. 7 and 8 at 1200 and 1500°C respectively. The stress dependence in the high stress region is stronger than that in the low stress region. It is clear that the creep rate of the large grain pellet is lower than that of the normal one in the low stress region. The Arrhenius plot of creep rate is shown in Fig. 9. The temperature dependences in the high and low stress regions for the large and normal grain pellets are not identical. It is not clear that the creep rate of the large grain pellet is lower than that of the normal one in the low stress region above 1600°C. The formula for our experimental creep rate $\dot{\varepsilon}$ (h^{-1}) is given by Eq. (5)

$$\dot{\varepsilon} = A\,\sigma^{n} \exp(-Q/RT) \quad (5)$$

where			large grain pellet	normal grain pellet
	low stress region	A	3.30×10^{8}	1.03×10^{3}
		n	2.92	1.57
		Q (kcal/mol)	110.0	56.2
	high stress region	A	3.58×10^{5}	7.43×10^{1}
		n	7.03	8.53
		Q (kcal/mol)	104.6	84.6

and σ is the stress in kg/mm^2.

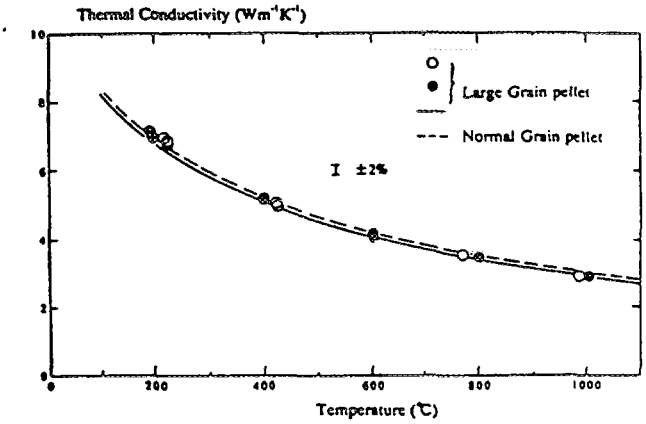

FIG. 6 Comparison of Thermal Conductivities

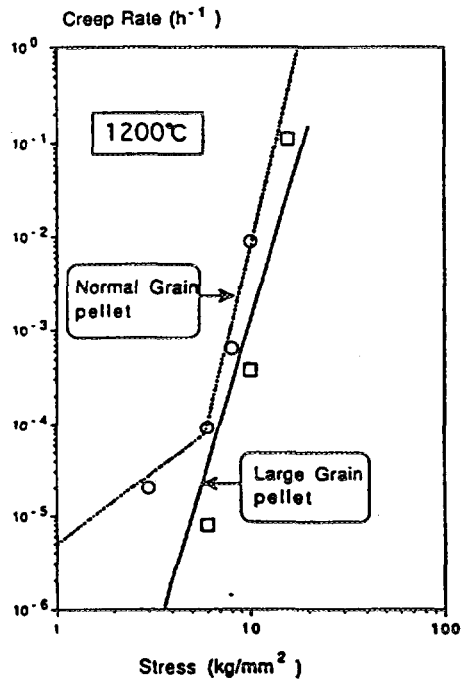

FIG. 7 Thermal Steady State Creep Rate of UO_2 vs Stress

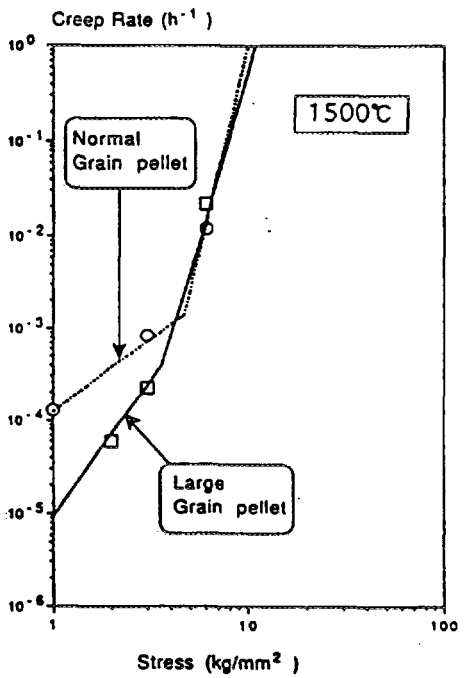

FIG. 8 Thermal Steady State Creep Rate of UO_2 vs Stress

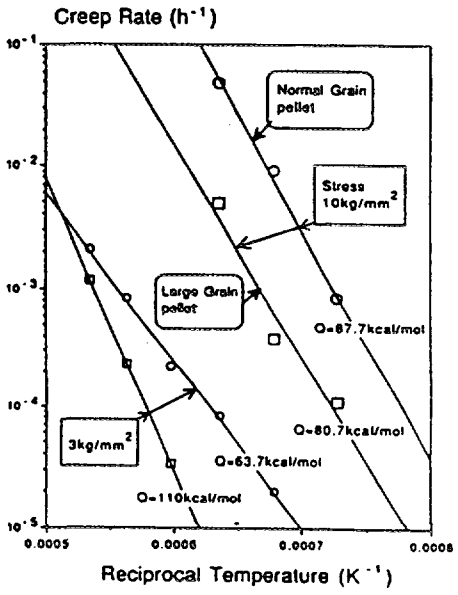

FIG. 9 Arrhenius Plot of Creep Rate for Large and Normal Grain UO_2 pellet

The transition stress [11, 12] at which diffusion creep under low stress changes to dislocation creep under high stress for the large grain pellet is from about 3 to 4kg/mm^2 between 1100 and 1600°C. The transition stress for the normal pellet is from about 7 to 4kg/mm^2.

3.5 FUEL CENTER TEMPERATURE AND STACK LENGTH CHANGE

The linear heat rate and pellet center temperature during burnup of the large and normal grain UO_2 pellet fuel rods are shown in Fig. 10 and 11. The total burnups at the end of the irradiation were 21.0 and 20.1GWd/t respectively. The temperature of the large grain rod was anomalous due to a malfunction of the W/Re thermocouple measuring pellet temperature. The rod average linear heat rate of both rods was below about 30kW/m.

The fuel stack length change with burnup is shown in Fig. 12. The in-pile densification of the large grain rod is smaller than that of the normal one. But, the swelling behaviour following densification cannot be clearly determined from these fuel stack length change trends.

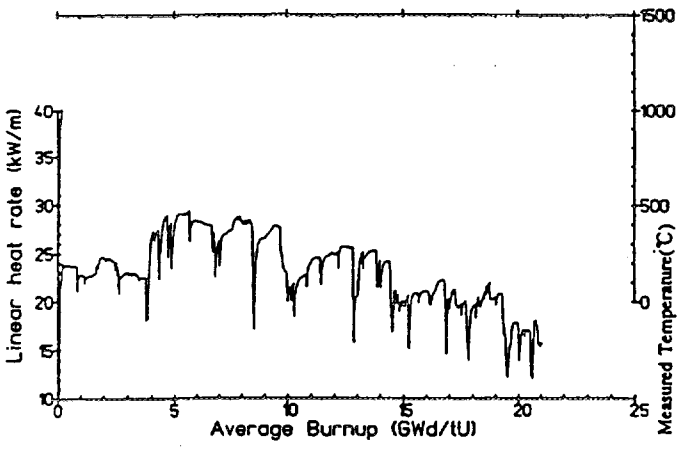

FIG. 10 Linear Heat Rate and Fuel Temperature vs. Burnup for Large Grain Pellet Fuel Rod

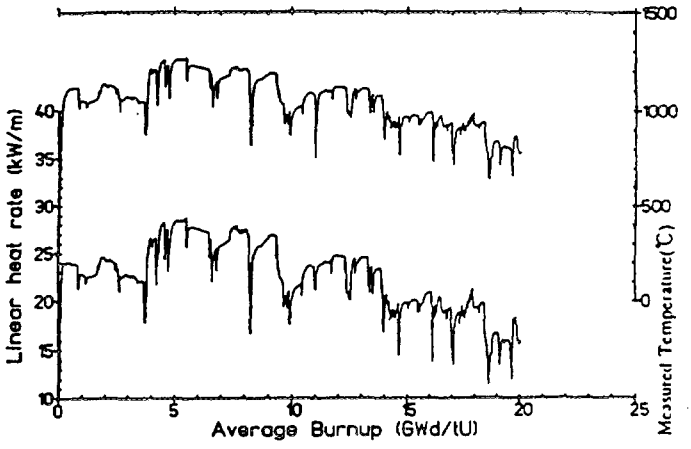

FIG. 11 Linear Heat Rate and Fuel Temperature vs. Burnup for Normal Grain Pellet Fuel Rod

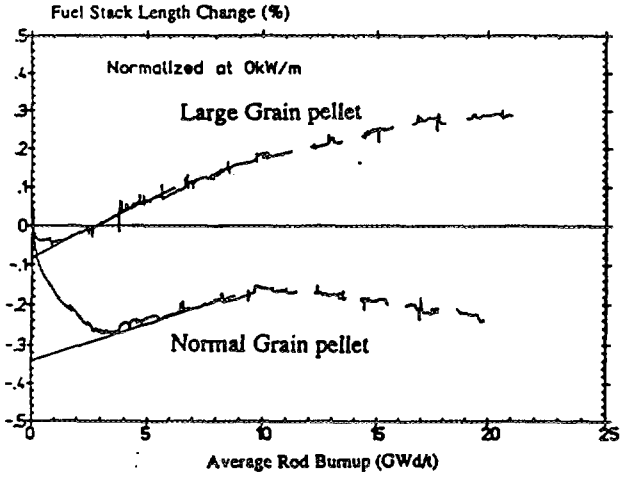

FIG. 12 Fuel Stack Length during Irradiation

3.6 PRESSURE IN THE RODS AND FISSION GAS RELEASE

The measured pressures in the fuel rods versus the rod average burnup are shown in Fig. 14. The internal pressure increase of the large grain rod is slightly less than that of the normal one. However, the free volume of the large grain rod is smaller than that of the normal one because of the smaller densification of the large grain pellets and because there was no free cladding creep down during the test.

The results of the puncture test showed that the fission gas release rates of the large and normal grain rods are 2.27% and 2.90% respectively. The change in the free volume of the rods during irradiation is from 4.1 to 3.7cm^3 and from 4.0 to 3.8cm^3 for the large and normal grain rods respectively.

4. DISCUSSION

4.1 FUEL TEMPERATURE AND PCMI

It was not able to compare the fuel temperatures of the large and normal grain rod. As mentioned above, it is considered that the thermal expansion and thermal conductivity of both UO_2 pellets are the same. But Fig.12 shows that the pellet/clad gap of the large grain rod is smaller than that of the normal

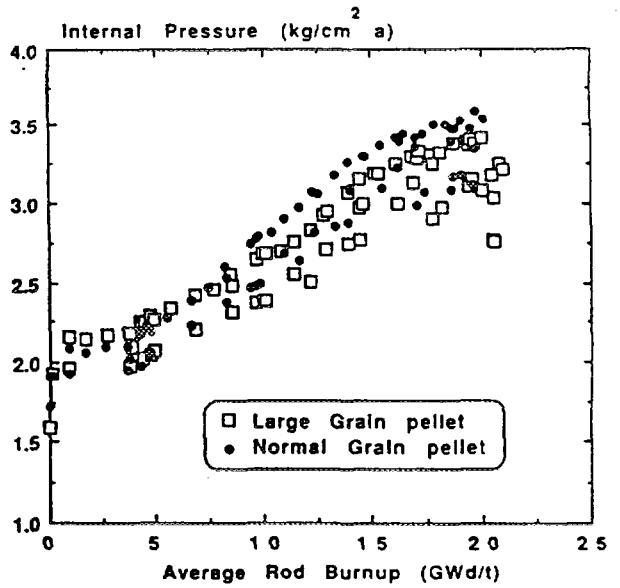

FIG. 13 Comparison of Pressure Changes in Fuel rods

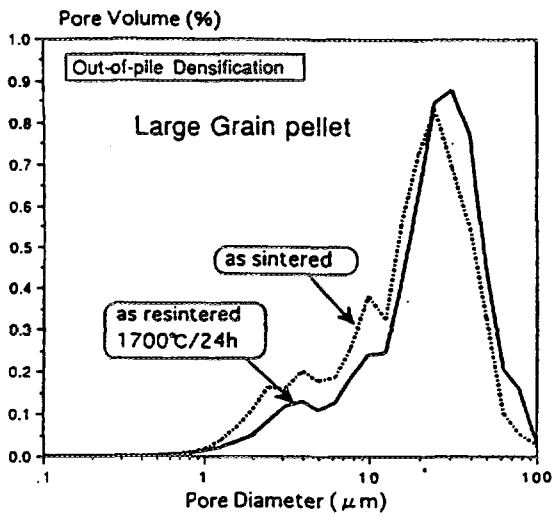

FIG. 14 Pore Size Distribution before and after Resintering

one at low burnup due to the large grain pellet's smaller densification and therefore the pellet/clad gap conductance of the large grain rod is estimated to be higher than that of the normal one. On the other hand, the creep down of the zircalloy-4 cladding is negligible because the primary system pressure and temperature of the HBWR are 34bar and 240°C respectively which are lower than these of a PWR. Therefore it is expected to remeasure the fuel center temperature for the two rods.

The effect of the difference of diffusion creep under low stress of the UO_2 pellet on the PCMI under the base irradiation and ramp test, cannot be clearly determined from this HBWR irradiation test and therefore it is planned to make another irradiation test up to a high burnup in PWR and ramp tests.

4.2 IN-PILE AND OUT-OF-PILE DENSIFICATION DEPENDENCE ON PORE STRUCTURE

The pore size distribution before and after the thermal resintering at 1700°C for 24h and the irradiation to about 20GWd/t is shown in Fig. 14~17 for the large and normal grain UO_2 pellet.

The total porosity after irradiation is determined from the extrapolation back to 0GWd/t as shown in Fig. 12. The variation in the densification as measured is about ± 0.2%TD as shown in Fig.18.

It is considered that both the in-pile and out-of-pile densification occur due to the disappearance [13] or the coalescence of small pores. The in-pile densification behaviour can be guessed from the out-of-pile densification and the change in pellet pore size distribution which occurs during resintering [14].

4.3 FISSION GAS RELEASE DEPENDENCE ON GRAIN STRUCTURE

The average grain size during the irradiation did not change. For the large grain pellet the size before the test was 23 μm and afterwards was 23 μm. For the normal grain size, the corresponding figures was 8 μm and 9 μm. The FGR reduction rate R (%) considering the grain size distribution of the sintered pellet is calculated according to Eq. (6)

$$R = FGR_{Large}/FGR_{Normal} = \Sigma\, a_i(1/d_i)(1/D_{Normal}) \quad (6)$$

where d_i (μm) is an average grain size in a class interval of 5μm, a_i is the relative grain area for that class is given in Fig. 4 and $D_{Normal} = \Sigma\, a_i d_i$. The result of R = 35% is obtained for the large sized grains.

The FGR consists of the recoil/knock-out and diffusion release. The FGR that escapes without being trapped will make a significant contribution on account of the low power level during the test and can be estimated [15] by Eq. (7)

$$FGR_{Recoil/knock\text{-}out} = \exp(-6920/T_{Fuel} + 33.95 - 0.338\,\rho) \quad (7)$$

where T_{Fuel}(K) is the average fuel temperature 1100 [$\fallingdotseq(1500_{Centre} + 800_{Surface})/2$] and ρ (%TD) is the pellet density. The equation gives $FGR_{Recoil/knock\text{-}out}$ = 1.17% for both pellets. Therefore the reduction in the FGR due to diffusion is:

$$R = 100 \times (2.27 - 1.17)/(2.90 - 1.17) = 66\%$$

The internal pressure predicted using the actual power history that the power level of the large grain rod was slightly higher than that of the normal one, can be matched with the measured data if it is that R is about 40%[16]. It can be seen that the FGR of the large grain pellet is less than that of the norrnal one, but lower than would expected from the Booth's model .

5. CONCLUSIONS

The following are the main conclusions of this study on out-of-pile and in-pile behaviours of the large and normal grain UO_2 pellet made from the modified and current ADU powder respectively.

(1) The thermal expansion coefficients and thermal conductivities of the two pellets are to be estimated to be the same. This shows that these thermal properties are independent of the differences in the microstructure.

(2) The thermal steady creep rate of the large grain pellet is lower than that of the normal one in the low stress region of diffusion creep.

(3) The out-of-pile densification of the large grain pellet is one fifth of that of the normal one.

(4) Both the in-pile and out-of-pile densification occur due to the disappearance or the coalescence of small pores in the variation of ± 0.2%TD can be guessed for the two pellets.

(5) The fission gas release of the large grain rod is less than that of the normal one considering diffusion release and the actual power history at about 20GWd/t.

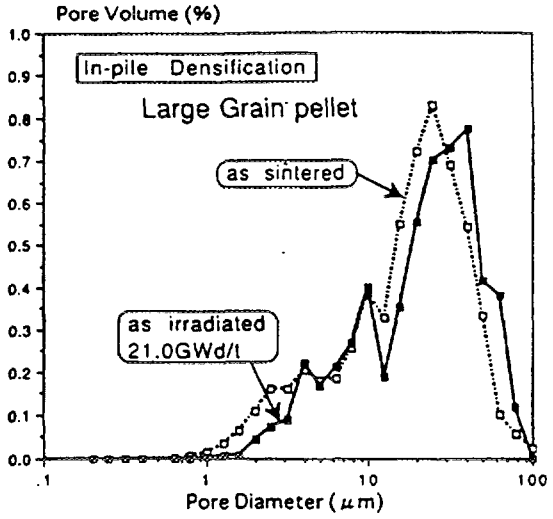

FIG. 15 Pore Size Distribution before and after Irradiation

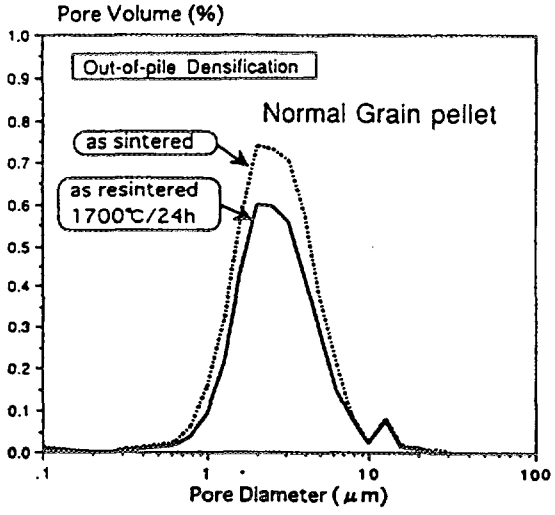

FIG. 16 Pore Size Distribution before and after Resintering

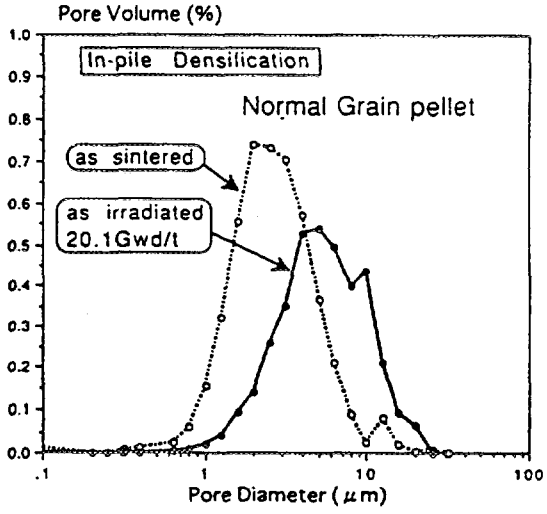

FIG. 17 Pore Size Distribution before and after Irradiation

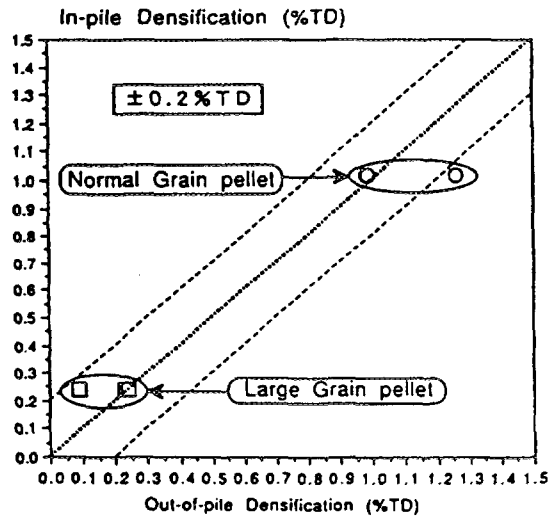

FIG. 18 Comparison of IN/Out-of-pile Densification

ACKNOWLEDGEMENTS

The thermal properties measurements and irradiation experiments were conducted jointly with the Hokkaido, Shikoku and Kyushu Electric Power Companies and Japan Atomic Power Co. Inc. The authors wish to express their appreciation for the cooperation given by these power companies and for the assistance and help of Yuji Kosaka (NDC).

REFERENCES

[1] BOOTH, A. H., AECL Report No.496 (1957)
[2] HARADA, Y. et. al., JP 2-182653 A (1990)
[3] DOI, S., ABETA, S. AND HARADA Y., IAEA TCM, Nykoping, Sweden (1990)
[4] HARADA, Y. et. al., JP 62-185408 A (1987)
[5] HARADA, Y. et. al., JP 62-179986 A (1987)
[6] HARADA, Y. et. al., JP 63-134299 A (1988)
[7] HARADA, Y. et. al., JP 63-52716 A (1988)
[8] ONOUE, T., ,YATO, T., TANAKA, H., Trans. ANS 56,90 (1988)
[9] TAKAHASHI, Y., YARNAMOTO, K., OHSATO, T., TERAI, T. ,The ninth Japan Symposium on Thermophysical Properties, 175-178 (1988)
[10] FINK, J. K., CHASANOV, M. G., LEIBOWITZ, L., J. Nucl. Mater. 102 ,17-25 (1981)
[11] BURTON, B., REYNOLDS, G. L., Acta Met. 21,1073-1078 (1973)
[12] BUNON, B., REYNOLDS, G. L., BARNS, J. P., J. Mater. Sci., 8,1690-1694 (1973)
[13] FERRARI, H. M., ROBERTS, E., SCOTT, J., BNES Nuclear Fuel Perforrnance Conference, London, 52, (1973)
[14] MAIER, G., ASSMANN, H., DORR, W., J. Nucl. Mater., 153,213-220 (1988)
[15] MACDONALD, P. E. et. al., MATPRO-Ver.9, TREE-NUREG-1005 (1976)
[16] SUZUKI, S., MURAKARNI, K., TAKAHASHI, T., International Topical Meeting On Light Water Reactor Fuel Performance, West Palm Beach, USA, 352-359 (1994)

EXPERIMENTS TO INVESTIGATE THE EFFECTS OF SMALL CHANGES IN FUEL STOICHIOMETRY ON FISSION GAS RELEASE

P.S. COPELAND, R.C. SMITH
Windscale Laboratory,
AEA Technology,
Seascale, Cumbria,
United Kingdom

Abstract

Fuel pin failure in-reactor leads to fission product and in the case of a PWR fuel debris release to the coolant. For economic reasons immediate shutdown and discharge of failed fuel needs to be avoided but this needs to be counter-balanced against the increasing dose to operators. Currently, AGR fuel is discharged soon after detection of a failure. PWR practice is to continue running with failed rods, monitoring coolant activity, and only shutting down the reactor and discharging the fuel when circuit activity levels become unacceptable. The rate of fission product release under failed fuel conditions is of key importance and considerable effort has been directed towards establishing the dependency of release on temperature, heating rate, burn-up, and also the extent of fuel oxidation. As a precursor to a possible wider investigation of this area, a small programme was mounted during 1992/1993 to confirm whether small changes in the oxidation state of the fuel, for example those caused by minor cladding defects, would significantly effect fuel behaviour during postulated design basis faults. The objective of the programme was to determine the effects of small departures from stoichiometric fuel composition on fission gas release, and to compare the results with the current methodology for calculating releases under fault conditions. A total of eight experiments was performed. Two were intended as baseline tests to provide a reference with which to compare the effect of oxidation state influenced behaviour with that of thermal effects. It was found that small changes in stoichiometry of ~1 x 10^{-6} had little or no effect on release but that changes of ~1 x 10^{-4} were observed to increase the diffusion coefficient, for ^{85}Kr, by up to an order of magnitude and hence greatly increase the release rate. The stoichiometry of the samples used in these tests was, for convenience, adjusted using $He/H_2/H_2O$ atmospheres. Although the current recommendations are based on experiments conducted in CO_2/CO atmospheres, reasonable agreement was found between effective diffusion coefficients calculated for these new experimental data and those calculated using current recommendations.

1. INTRODUCTION

Fuel pin failure in-reactor leads to fission product and in the case of a PWR fuel debris release to the coolant. For economic reasons immediate shutdown and discharge of failed fuel needs to be avoided but this needs to be counter-balanced against the increasing dose to operators. Currently, AGR fuel is discharged soon after detection of a failure. PWR practice is to continue running with failed rods, monitoring coolant activity, and only shutting down the reactor and discharging the fuel when circuit activity levels become unacceptable.

The rate of fission product release under failed fuel conditions is of key importance and considerable effort has been directed towards establishing the dependency of release on temperature, heating rate, burn-up, and also the extent of fuel oxidation.

The objective of the work programme described here is to determine the effects of small departures from stoichiometric composition on the diffusion coefficient and hence fission gas release of irradiated UO_{2+x} and to compare the results with the current methodology for calculating releases.

The experimental programme is designed to extend the observations made during recent experiments [1], which has indicated that a small change in oxygen potential, corresponding to a change in stoichiometric state of the fuel of $x < 10^{-3}$, produced a significant effect on release of fission gas.

The equipment used in these experiments is based on that developed by Small [2], but has been modified and improved in design to provide better control of the experimental conditions [1]. This has included the introduction of controlled amounts of moisture to vary the oxidation potential of the sweep gas, and hence equilibrium oxygen to metal (O/M) values. It allows small (< 100mg) samples of irradiated UO_2 to be heated to temperatures up to 2500°C at controlled heating rates up to 200°C s^{-1}. Fission gas release is measured by the on-line measurement of the long lived ^{85}Kr isotope using a beta scintillation counter. An outline description of the equipment is given, although a more detailed description is available in Reference [3].

2. EXPERIMENTAL

2.1 FUEL ORIGIN

All the specimens were in the form of 3mm diameter discs of ~0.5mm thickness: these were prepared from slices of the parent fuel pin by an ultrasonic trepanning technique.

Stringer B4180 (4V35) was loaded into Hinkley Point R4 on 20 November 1977 and discharged on 16 May 1983. The specimens were removed from Pin 19 (outer ring) of Element 4. The burn-up was measured as 17.9 GWd $t^{-1}U$ by radiochemical analysis of adjacent fuel pellets cut from the pin. The grain size of the fuel was measured, using the mean linear intercept (mli) method, as 5.6 μm.

2.2 THE MK2 TRANSIENT FISSION GAS RELEASE RIG

The Mk2 Transient Fission Gas Release rig was designed to operate in the temperature range 1000-2500°C, at ramp rates between 0.1 and 200°C s^{-1}, providing a greater range of temperature and heating conditions than previous equipment. A wide range of sweep gas conditions can be employed, operating at ~ 1bar pressure, including He/H_2, $He/H_2/H_2O$ and CO_2/CO mixtures, allowing experiments to be conducted under oxidising, reducing or inert conditions.

A 6kW RF induction furnace is provided for the heating of specimens. An 'H' section susceptor and support rod are made of either tantalum, or iridium if an oxidising sweep gas is to be used. The specimen is loaded into the upper recess of the susceptor. Temperature measurement and control are achieved using a fibre-optic pyrometer sighting onto the top surface of the specimen. The light signal is transmitted from the lens to a detector/amplifier, and finally through to a Eurotherm type 818 processor/controller, via a fibre-optic cable. The Eurotherm 818 can be programmed to produce temperature history profiles comprising up to eight steps. Each step may include a linear ramp between two set points and/or a dwell at a fixed temperature.

The pyrometer is calibrated against Pt/Pt13%Rh and W5%Re/W26%Re thermocouples.

2.3 SWEEP GAS CIRCUIT

The general layout of the sweep gas system is illustrated in Figure 1. Gas is supplied either directly from a cylinder or through a moisture control unit, passing through a flow controller and instruments to measure the pressure, oxygen potential and moisture content before entering the furnace. The gas returns from the furnace through pressure, flow, oxygen, and moisture meters and into the beta scintillation counter. Alternatively, the sweep gas can be routed through a specimen crushing jig and a fuel dissolution tube (see Section 2.5), if analysis of retained fission gas is required.

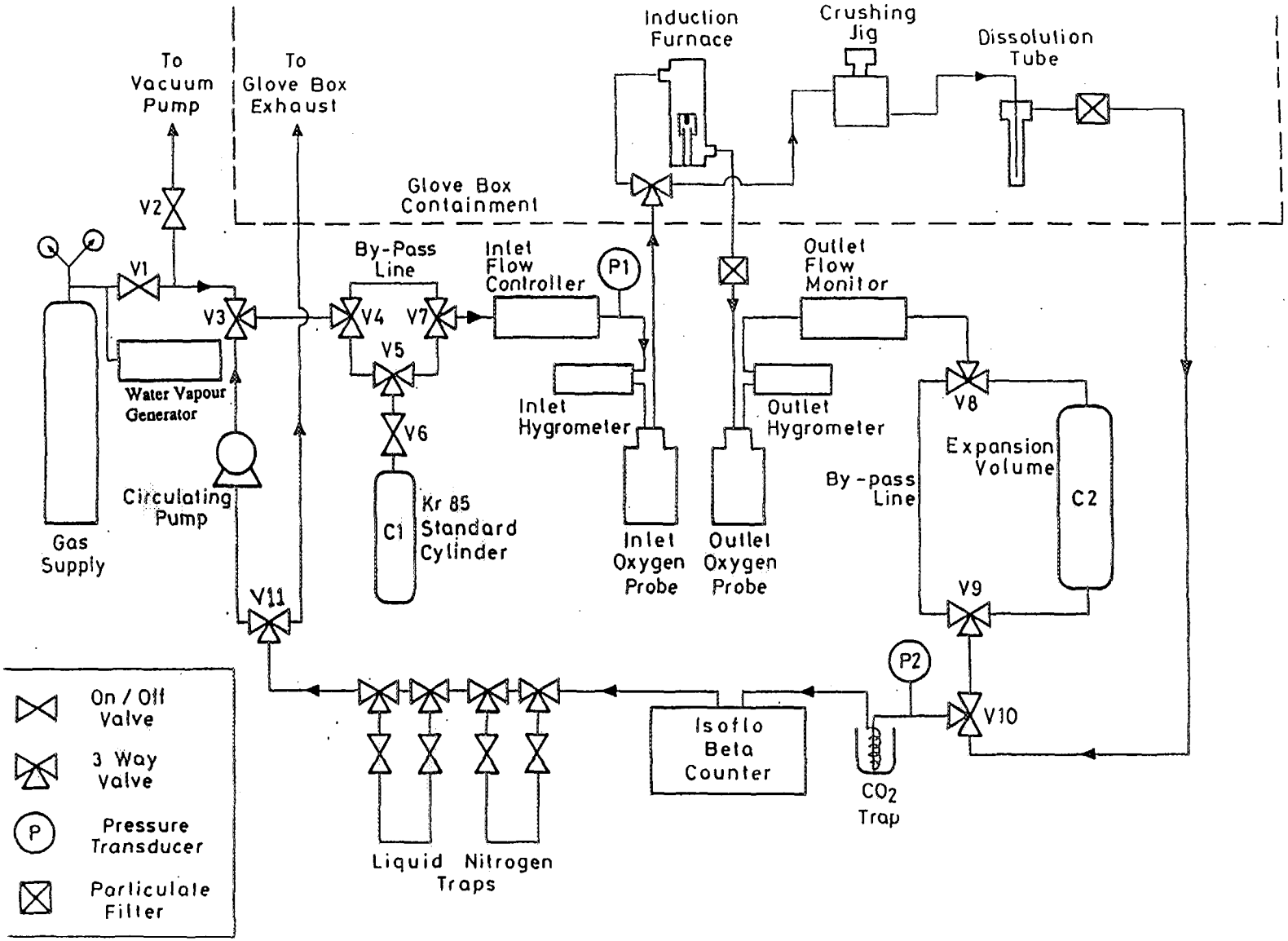

FIG. 1 *Schematic layout of the sweep gas circuit*

2.3.1 Oxygen Potential measurement

The oxygen potential of the sweep gas is measured by a pair of Kent Z-FG series oxygen analysers situated in the rig sweep gas loop on either side of the transient furnace. However, readings are reliable only for oxygen potentials above about -450kJ mol^{-1} as below this the Seebeck effect [4] becomes significant. The measurements from these instruments were not used in the analysis of the results presented in this report; the base line oxygen potential required during these experiments was at the limit of the instruments' range and the readings were therefore considered to be unreliable. Control and measurement of oxygen potentials during these tests was achieved using values calculated from the hygrometer readings (Section 2.3.2). Under the most oxidising conditions studied here, there was reasonable agreement between calculated and measured oxygen potentials. However, it was noted that under more 'reducing' conditions (i.e. more negative oxygen potential values) the discrepancy between calculated and measured values increased. It is unclear whether this discrepancy at low oxygen potentials arises as a function of the oxygen probe or the use of the Wheeler and Jones [5] equation in the extreme range.

2.3.2 Water Vapour generation and measurement

A water vapour generator is provided in order to introduce controlled levels of moisture into the sweep gas. It employs a technique whereby the sweep gas is routed either through columns of hydrated ferrous sulphate or through a by-pass, after which the flow is recombined to provide a specified percentage of the maximum water vapour concentration available. Four two way valves allow a total of fourteen intermediate concentrations. The maximum concentration is controlled by the temperature of the ferrous sulphate, which is contained in a heated and thermostatically controlled chamber. The temperature of the chamber is adjustable, allowing fine adjustment of the water vapour concentration. The unit supplies the sweep gas stream with water vapour at constant vapour pressure at a given temperature. The unit is supplied with an individual calibration giving the delivered specified percentages of the maximum.

Water vapour pressure is measured by a pair of Michell Series 2000 hygrometers. These measure changes in capacitance of an alumina film as it adsorbs and releases water vapour. These measurements allow oxygen potentials, at the relevant specimen temperatures, to be calculated using the HWOXPOT code, compiled by P K Mason, AEA Technology, and based on Wheeler and Jones [5].

The HWOXPOT code has been validated against SOLGASMIX [6]. It was found that the SOLGASMIX calculations resulted in oxygen potential figures that were consistently -5.7kJ mol^{-1} more reducing than those obtained from the same data with HWOXPOT. However, when the equilibrium O/U ratios, derived from the oxygen potentials calculated by both methods are compared, it is seen that they agree to within 2.6×10^{-3} for the most oxidising conditions studied (-221kJ mol^{-1}), and to within 1.0×10^{-6} for the baseline runs ($\sim$ -600kJ mol^{-1}).

2.4 FUEL DISSOLUTION FURNACE AND CRUSHING JIG

The ^{85}Kr inventory of the samples is determined by dissolving them in a mixture of sodium and potassium salts and passing the released gas through the beta scintillation counter. From this a calibration factor is derived, expressed as counts/mg, enabling the fractional releases from experiments to be calculated. The total release during an experiment is derived by integrating the instantaneous release over time. Fractional fission gas release is then calculated using the calibration factor with reference to the specimen mass.

A facility is also provided for crushing specimens to powder, of the order of the grain size, to release gas stored in grain boundary porosity.

These techniques enable the fraction of ^{85}Kr retained on grain boundaries, and the fractional release during transient heating tests, to be determined independently.

2.5 BETA ACTIVITY DETECTION

The activity of the sweep gas is measured using an ISOFLO beta scintillation counter. Background radiation is excluded by housing the flow cell in a light tight chamber shielded by lead.

The data are logged with an IBM compatible PC based system using data acquisition software to control a 16 channel data acquisition card.

3. TEST PROGRAMME

The test programme comprised eight tests. In all the tests performed small specimens (<60mg) of fuel were washed and weighed in a standardised procedure before loading into an iridium susceptor assembly.

For the first four tests the furnace was ramped to its final temperature under either He/2%H_2 or He/500vpmH_2 with no added moisture. On reaching the required temperature the moisture generator output was adjusted to give stepped changes in oxygen potential. The figures obtained for each test are shown in Table 1. For tests FUP10-1 and 2 the furnace was ramped to 1800°C in He/2%H_2 to pre-condition the specimens to give a fully interlinked grain boundary porosity structure. The fully interlinked specimens were then subjected to ramps to 1600°C again under He/2%H_2. Upon reaching this temperature moisture was added to the flowing gas stream.

For the final four tests the sweep gas composition was maintained throughout the tests with the temperature of the specimen being adjusted to give a stepped change in stoichiometry. The first two tests of this group were baseline runs with no moisture added, one specimen ramped as received, the other having an interlinked grain boundary porosity structure appropriate to tests FUP10-1 and 2. The specimens were first ramped to their initial temperature of 1200°C. After ~1800s the temperature of the specimen was increased by 100°C and again held at temperature. This procedure was repeated until a final temperature of 1700°C was achieved.

The errors were associated with fission gas release fractions are considered to be $< \pm 10\%$.

4. RESULTS

4.1 RELEASE EXPERIMENTS

Figures 2a and 3a show typical plots of temperature, release rate and dewpoint against elapsed time whilst figures 2b and 3b show plots of cumulative fractional release and temperature. The results from each test expressed in terms of stoichiometry, calculated using the equations of deFranco and Gatesoupe [7], are shown in Table 1. During all of the tests performed where significant moisture was added secondary release fractions were observed as a result of a change in the stoichiometry of the fuel.

4.2 DIFFUSION COEFFICIENTS

Since the release after the initial burst appear to show diffusional kinetics the results were analysed to obtain an effective diffusion coefficient according to Booth [8].

Predicted diffusion coefficients were also calculated using the Killeen and Turnbull model [9], which calculates the effective diffusion coefficient, D_{eff}. This model suggests that D_{eff} is the sum of three components D_1, D_2 and D_3:

Table 1. Step changes in sweep gas conditions and stoichiometry.

Test Identity	Temp (K)	Step	Dewpoint (°C)	Moisture (ppm(V) H_2O)	Calculated Oxygen Potential ($kJmol^{-1}$)	Equivalent Stoichiometry
FUP10 - 1	1873	a	-41.3	110	-333	2.000584
		b	-20.1	1000	-264	2.005155
		c	-15.0	1650	-249	2.008328
		d	-5.6	4000	-221	2.018789
		e	-14.4	1750	-247	2.008805
FUP10 - 2	1873	a	-43.1	90	-339	2.000478
		b	-26.5	520	-284	2.002723
		c	-14.8	1680	-248	2.008472
		d	-10.5	2600	-235	2.012738
FUP10 - 3	2073	a	-42.2	100	-317	2.001113
		b	-21.0	920	-241	2.009662
FUP10 - 4	1873	a	-48.1	50	-358	2.000266
		b	-26.6	520	-285	2.002723
		c	-21.5	900	-268	2.004655
		d	-12.3	2100	-241	2.010450
FUP10 - 5	1473	a	-83.9	0.28	-605	2.000000
	1573	b			-612	2.000000
	1673	c			-619	2.000000
	1773	d			-626	2.000000
	1873	e			-633	2.000000
	1973	f			-639	2.000000
FUP10 - 6	1473	a	-83.4	0.31	-603	2.000000
	1573	b			-609	2.000000
	1673	c			-616	2.000000
	1773	d			-622	2.000000
	1873	e			-629	2.000000
	1973	f			-635	2.000000
FUP10 - 7	1473	a	-52.7	28.0	-493	2.000001
	1573	b			-492	2.000001
	1673	c			-491	2.000002
	1773	d			-490	2.000003
	1873	e			-489	2.000004
	1973	f			-487	2.000006
FUP10 - 8	1473	a	-43.1	71.0	-381	2.000049
	1573	b			-372	2.000089
	1673	c			-364	2.000152
	1773	d			-355	2.000246
	1873	e			-347	2.000378
	1973	f			-338	2.000557

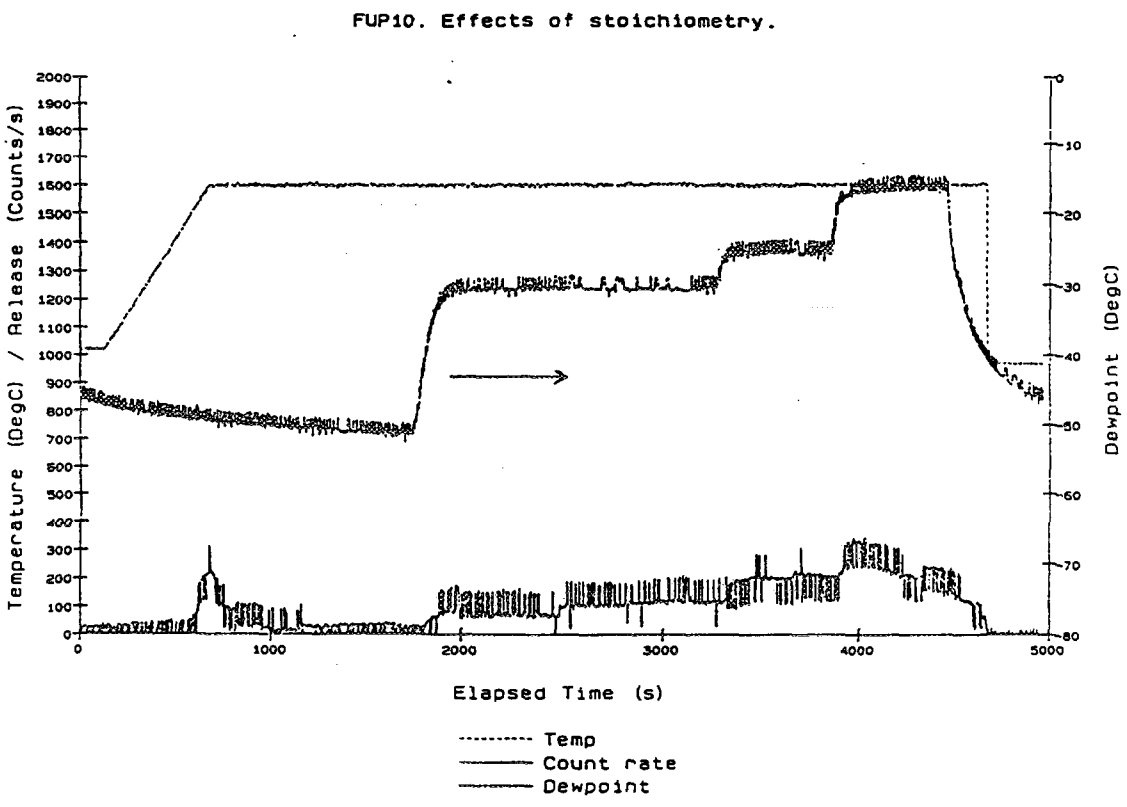

FIG. 2a *Graph showing effect of change in dewpoint on release rate (FUP10-4)*

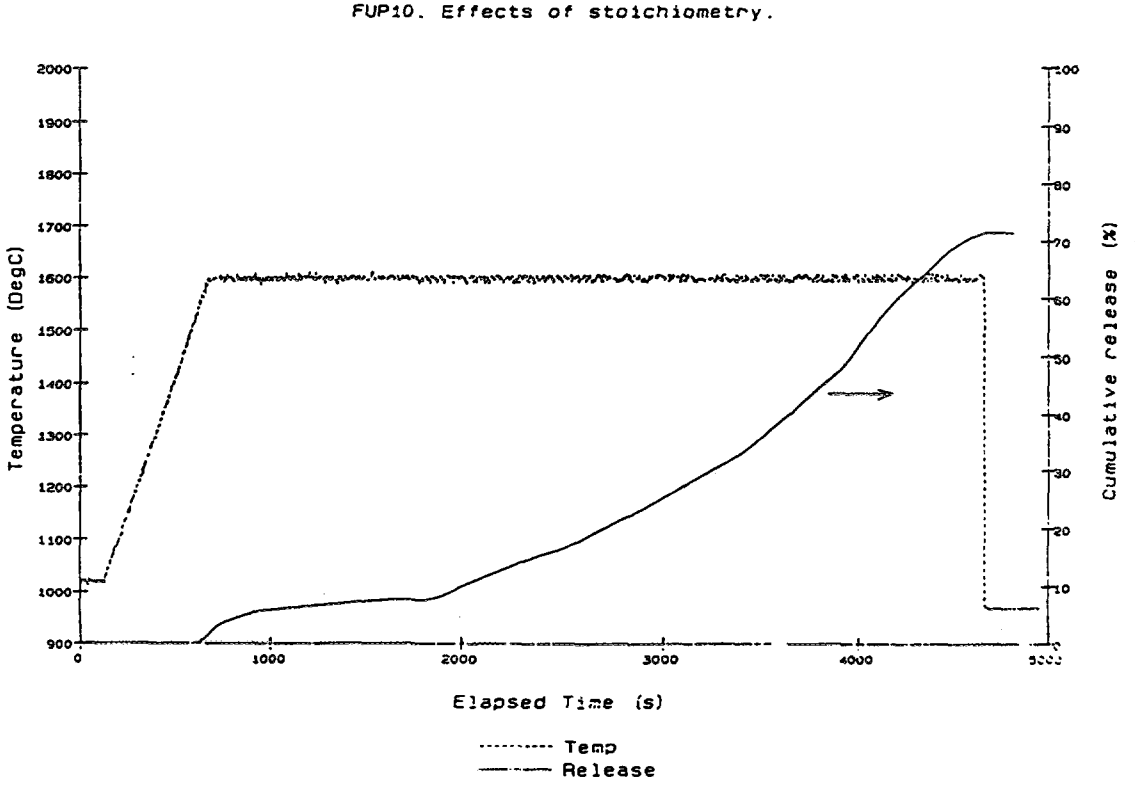

FIG. 2b *Graph showing cumulative release (FUP10-4)*

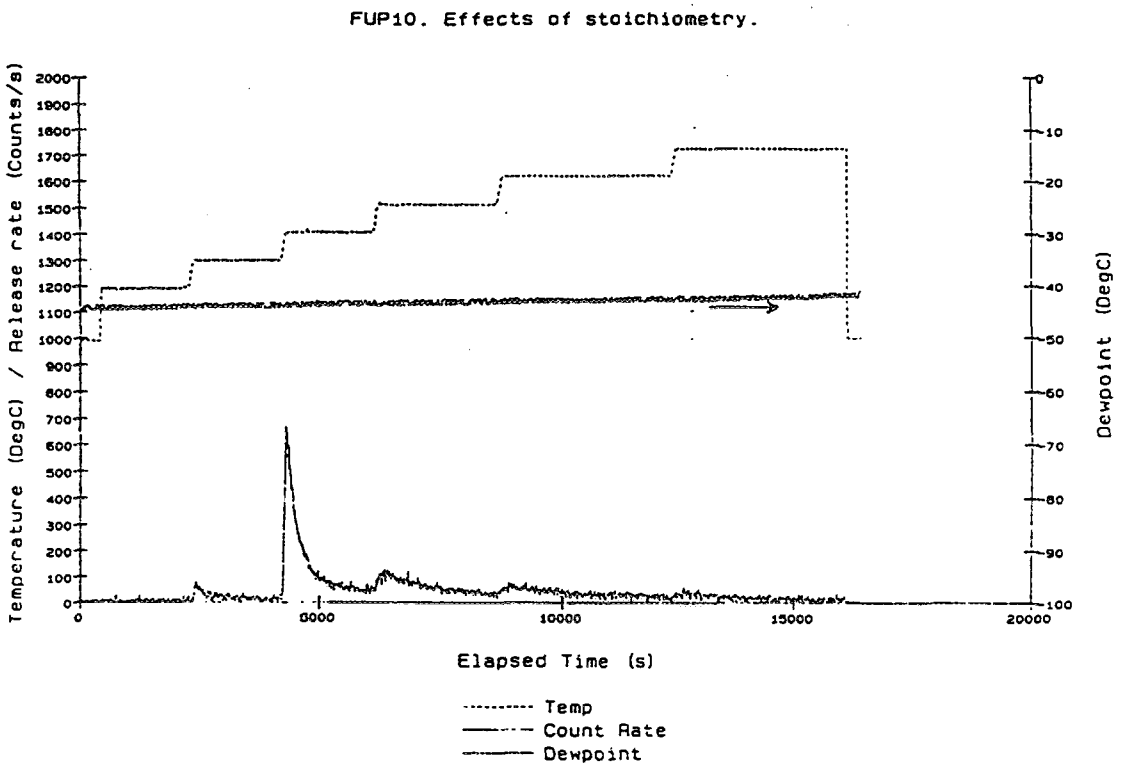

FIG. 3a *Graph showing effect of change in dewpoint on release rate (FUP10-8)*

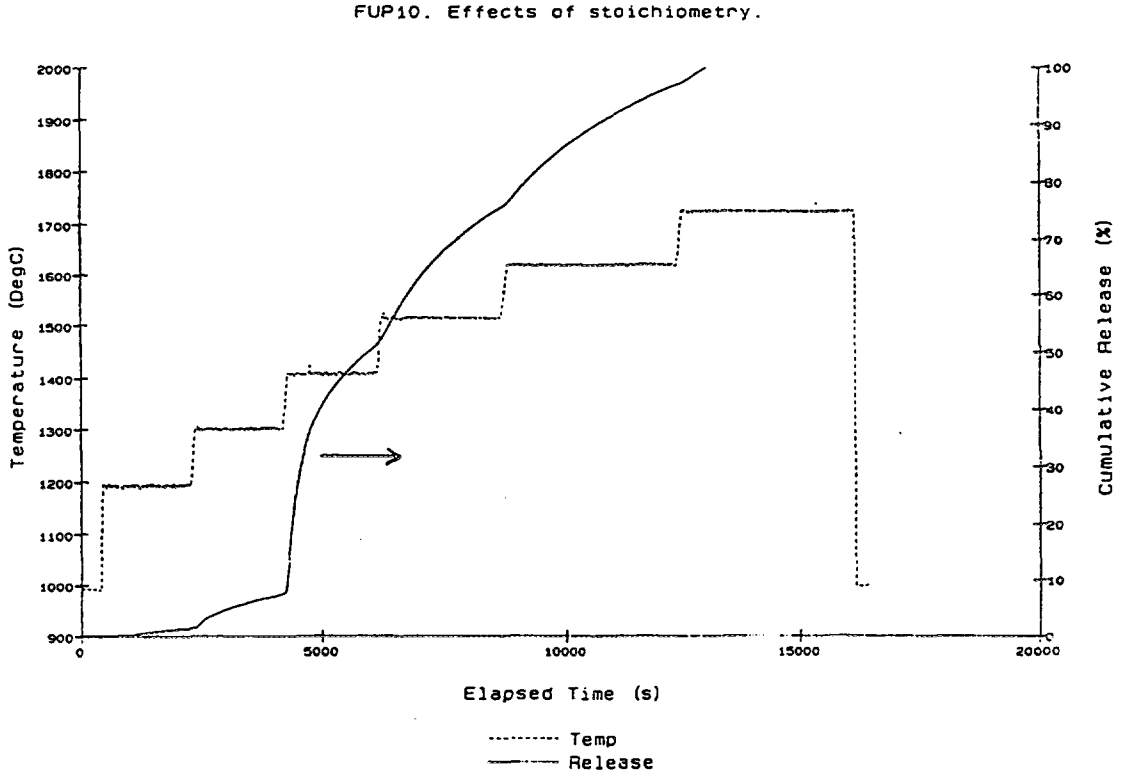

FIG. 3b *Graph showing cumulative release (FUP10-8)*

(i) Intrinsic diffusion represented by the results of Davies and Long [10].

$$D_1 = 7.6E\text{-}10 \exp(-35000/T) \quad (1)$$

where T is the temperature in K.

(ii) Vacancy assisted diffusion.

$$D_2 = s^2 j_v (v + v_u) \quad (2)$$

where s is the atomic jump distance in metres
j_v is the uranium vacancy jump rate in s^{-1}
v is the extrinsic vacancy concentration supported by irradiation damage to the cation lattice
and v_u is the thermodynamic vacancy concentration per atom.

(iii) Irradiation enhanced athermal diffusion.

$$D_3 = 2E\text{-}40.\phi \quad (3)$$

where ϕ is the fission density in fissions m^{-3} s^{-1}.

4.2.1 Allowance for Oxidation Kinetics

In addition recent work by Nuclear Electric [11] has suggested that a fourth term, should be included to allow for D_{eff} to change as a function of oxidation kinetics. This term has been derived from fission gas release data generated in CO_2/CO atmospheres in the temperature range 1100-1350°C.

Although it is recommended that this enhanced diffusional release term should only be applied to atmospheres of CO_2/1%CO in the temperature range 1100-1350°C, it was felt that it may be of some benefit to investigate its use in less oxidising atmospheres such as those examined here. It should be noted however, that caution is advisable when using the term outside its limit of applicability as it is likely to overpredict releases and therefore diffusion coefficients.

It can be seen from equation (3) above, that in the absence of fission D_3 becomes zero. The results of the predicted diffusion coefficients shown in Figures 4a and 4b consequently include only D_1 and D_2 in the first case, and D_1, D_2 and the enhanced diffusional release term in the second case.

5. DISCUSSION

For the purposes of this study the results obtained from the test carried out at 1800°C can be discounted. This is due to the fact that at high temperatures thermal properties will dominate allowing no meaningful measurements to be gathered on oxidation state influenced diffusion rates.

Experiments clearly showed a large effect on release due to a small change in stoichiometry. A change in stoichiometry of ~1 x 10^{-6} (FUP10-7), as compared with the baseline test FUP10-5, was observed to have little or no effect on release but a change of ~1 x 10^{-4} (FUP10-8) had a large effect on release and diffusion coefficient, increasing the diffusion coefficient by approximately an order of magnitude.

Plotting the results on a graph (Figure 4a) with the predictions made from the Killeen and Turnbull model [9], shows the diffusion coefficients, for $x > 0.00001$, reported here to have consistently higher values than otherwise may have been predicted. If, however, the results are plotted on a graph with the

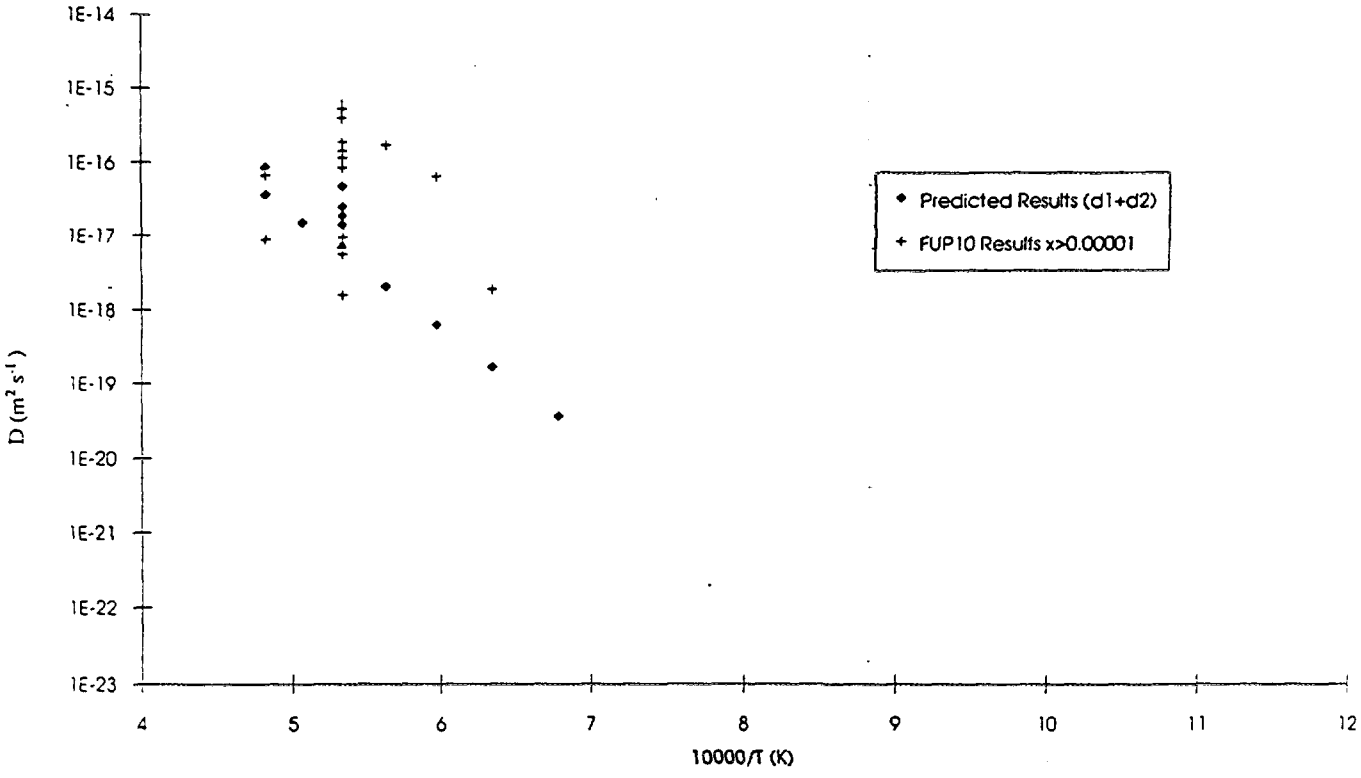

FIG. 4a *Results and predicted diffusion coefficients without enhanced diffusional release term.*

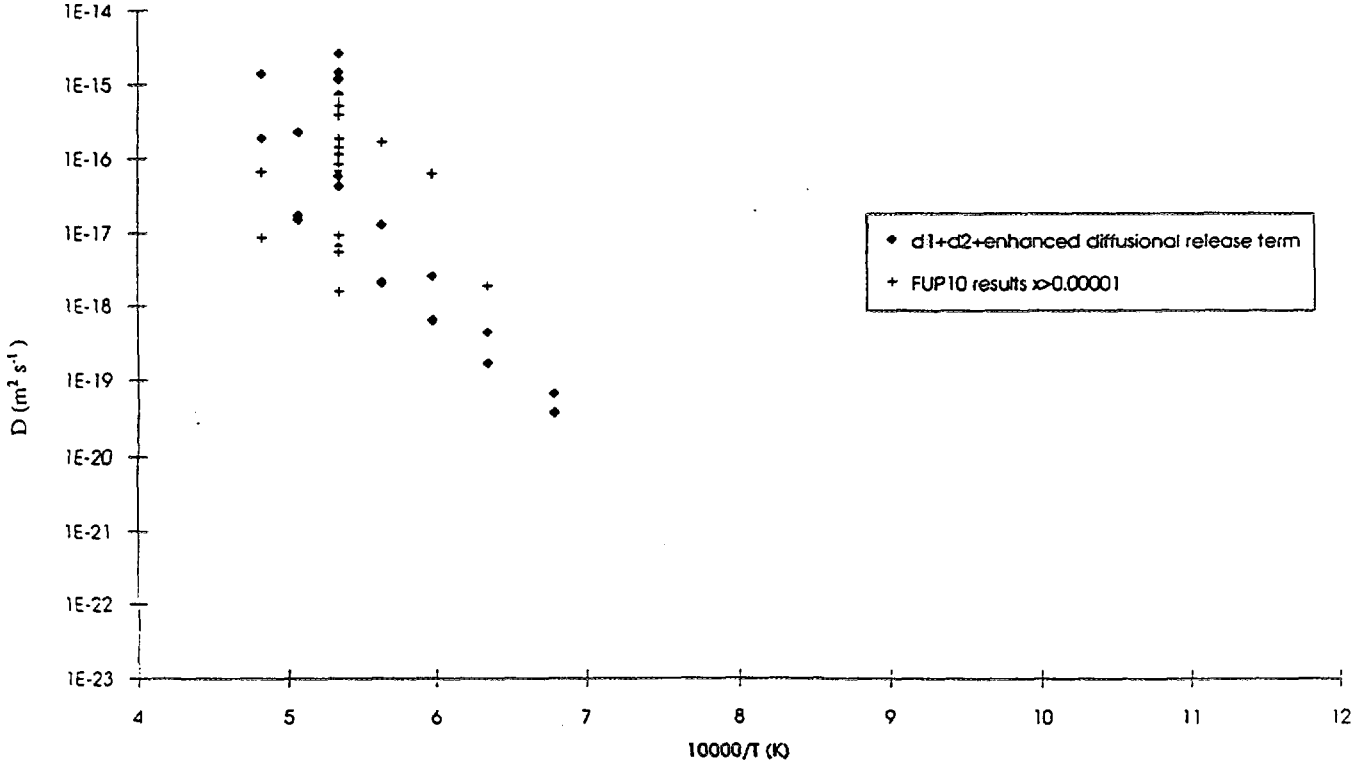

FIG. 4b *Results and predicted diffusion coefficients with enhanced diffusional release term.*

predictions from the Killeen and Turnbull model taking into account the enhanced diffusional release term for oxidation kinetics, it can be seen from Figure 4b that the results are in much greater agreement. This indicates that the term may be applicable to conditions other than the current range of validation. However, because this is based on evidence primarily at 1600°C, further work at lower temperatures (1200-1500°C) would be needed to make any firm conclusions.

6. CONCLUSIONS

The primary conclusions of this study are:

i) A change in stoichiometry of ~1 x 10^{-6} was observed to have little or no effect on release whilst a change of ~1 x 10^{-4} was observed to increase the diffusion coefficient by up to an order of magnitude and hence greatly increase the release rate.

ii) Diffusion coefficients calculated from the experimental data obtained in these tests are notably higher than would be expected using the Killeen and Turnbull model for all tests that produced hyperstoichiometric compositions greater than 2.00001.

iii) If the effective diffusion coefficients for these data are predicted using the Killeen and Turnbull model with the addition of the enhanced diffusional release term the experimental results are in much greater agreement. This could imply that the term when allied to the Killeen and Turnbull model may have a much wider range of application than was first thought, including use in $He/H_2/H_2O$ atmospheres applicable to PWR operation. To assess this fully, more data would be required in the temperature range 1200-1600°C, with stoichiometric values of between 0.00001 and 0.1.

ACKNOWLEDGEMENTS

The authors wish to acknowledge the financial support of the United Kingdom Health and Safety Executive.

REFERENCES

[1] SMITH, R.C. & COPELAND, P.S. "Scoping tests to investigate the influence of fuel stoichiometry on fission gas release" AEA-RS-2084 (1992).

[2] SMALL, G.J. "Transient gas release from irradiated U02: specimen characterisation and experimental methods" AERE-R11773 (1987).

[3] SMITH, R.C., SMALL, G.J. & COPELAND, P.S., "A rig for measuring fission gas release during rapid transients to high temperatures". AEA-TRS-2025 (1991).

[4] BULLOCK, B.R., Private communication, (1989).

[5] WHEELER, V.J. & JONES, I.G., "Thermodynamic and ccompositional changes in $UO_{2\pm x}$ ($x < 0.005$) at 1950K". J. Nucl. Mat. 42 (1972) 117-121.

[6] ERIKSSON, G., "Thermodynamic studies of high temperature equilibrium - XII. SOLGASMIX - a computer program for calculation of equilibrium composition in multi-phase systems", Chem Scr 8 (1975) 100.

[7] deFRANCO, M. & GATESOUPE, J.P., "The thermodynamic properties of (U,Pu)O2+x described by a cluster model.". Plutonium and other Actinides, 1976, Page 133.

[8] BOOTH, A.H., "A method of calculating fission gas diffusion from UO_2 fuel and its application to the X-2-f loop test.". AECL-496. CRDC(1958)721.

[9] KILLEEN, J. C. & TURNBULL, J.A., "An experimental and theoretical treatment of the release of ^{85}Kr from hyperstoichiometric uranium dioxide". Proc. Symp. on Chemical Reactivity of Oxide Fuel and Fission Product Release, Berkeley, Glos, England, April 7-9, 1987. (ed SIMPSON, K. A. & WOOD, P.), Pages 387-404.

[10] DAVIES, D. & LONG, G., "The emission of xenon-133 from lightly irradiated uranium dioxide spheroids and powders." AERE-R-4347 (1963).

[11] BRADFORD, M.R. Nuclear Electric, Internal Use Only document (1991).

A FISSION GAS RELEASE MODEL

A. DENIS, R. PIOTRKOWSKI
Argentine Atomic Energy Commission,
Buenos Aires, Argentina

Abstract

The fission gases produced by irradiated nuclear fuels affect in different manners the fuel performance. On the one hand they diminish the heat transfer between fuel and cladding causing an increase in the rod temperature. On the other hand, the increase in the internal rod pressure may lead to cladding failure and to the consequent release of fission products to the atmosphere. It is therefore essential to be able to predict the amount of gas produced during operation, especially under high burnup conditions. The hypothesis contained in the model developed in this work are as follows. The UO_2 is considered as a collection of spherical grains. Nuclear reactions produce fission gases, mainly Xe and Kr, within the grains. Due to the very low solubility of these gases in UO_2, intragranular bubbles are formed, of a few nanometres in size. The bubbles are assumed to be immobile and to act as traps which capture gas atoms. Free atoms diffuse towards the grain boundaries, where they give origin to intergranular, lenticular bubbles, of the order of microns. The gas atoms in bubbles, either inter or intragranular, can re-enter the matrix through the mechanism of resolution induced by fission fragment impact. The amount of gas stored in intergranular bubbles grows up to a saturation value. Once saturation is reached, intergranular bubbles inter-connect and the gas in excess is released through different channels to the external surface of the fuel. The resolution of intergranular bubbles particularly affects the region of the grain adjacent to the grain boundary. During grain growth, the grain boundary traps the gas atoms, either free or in intragranular bubbles, contained in the swept volume. The grain boundary is considered as a perfect sink, ie the gas concentration is zero at that surface of the grain. Due to the spherical symmetry of the problem, the concentration gradient is null at the centre of the grain. The diffusion equation was solved using the implicit finite difference method. The initial solution was analytically obtained by the Laplace transform. The calculations were performed at different constant temperatures and were compared with experimental results. They show the asymptotic growth of the grain radius as a function of burnup, the gas distribution within the grain at every instant, the growth of the gas content at the grain boundary up to the saturation value and the fraction of gas released by the fuel element referred to the total gas generated, as a function of burnup.

1. INTRODUCTION

Among the many fission products generated in a nuclear fuel, the noble gases Xe and Kr play a special role due to their virtually complete insolubility in the fuel matrix. The rejected gases either are released from the fuel and contribute to the gaseous atmosphere in the fuel pin or they precipitate forming bubbles within the fuel. Irradiation can cause bubbles destruction and thus, the fraction of gas held in bubbles is reduced while that of atoms dispersed in the matrix is increased. A nonzero dynamical solubility of noble gases appears since complete precipitation in bubbles is impossible because of kinetic reasons [1].

The fission gases produced by irradiated nuclear fuels affect in different manners the fuel performance. On the one hand they diminish the heat transfer between fuel and cladding causing an increase in the rod temperature. On the other hand, the increase in the internal rod pressure may lead to cladding failure and to the consequent release of fission products to the atmosphere. It is therefore essential to be able to predict the amount of gas produced during operation, especially under high burnup conditions.

2. OUTLINE OF THE MODEL

The hypotheses contained in the model developed in this work are as follows [2]. The UO_2 is considered as a collection of spherical grains. Nuclear reactions produce fission gases, mainly Xe and Kr, within the grains. Due to the very low solubility of these gases in UO_2, intragranular bubbles are formed of a few nanometers in size. The bubbles are considered to be immobile and to act as traps which capture gas atoms. Part of the free atoms diffuse towards the grain boundaries, where they give origin to intergranular, lenticular bubbles of the order of microns. The gas atoms in bubbles, either inter or intragranular, can re-enter the matrix through the mechanism of resolution induced by fission fragment impact. The amount of gas stored in the intergranular bubbles grows up to a saturation value. Once saturation is reached, intergranular bubbles interconnect and the gas in excess is released through different channels to the external surface of the fuel. The resolution of intergranular bubbles particularly affects the region of the grain adjacent to the grain boundary. During grain growth the grain boundary traps the gas atoms, either free or in intragranular bubbles, contained in the swept volume. The grain boundary is considered as a perfect sink, i.e. the gas concentration is zero at that surface of the grain. Due to the spherical symmetry of the problem, the concentration gradient is null at the center of the grain.

3. DIFFUSION WITH TRAPPING AND RESOLUTION

The diffusion equation in a spherical grain of radius a, which includes also trapping and resolution by intragranular bubbles, is

$$\frac{\delta c}{\delta t} = D\left(\frac{\delta^2 c}{\delta r^2} + \frac{2}{r}\frac{\delta c}{\delta r}\right) - gc + bm + \beta \qquad (1)$$

where c represents the concentration of dissolved gas atoms (atoms/ m^3), m the concentration of gas atoms trapped in intragranular bubbles (atoms/m^3), β the gas production rate per unit volume (atoms/ m^3/s), D the single gas atom diffusion coefficient (m^2/s), g the probability of a dissolved gas atom of being captured by a trap (s^{-1}) and b the probability of a gas atom trapped in a bubble of being redissolved per unit time (s^{-1}).

The balance equation for the trapped atoms is

$$\frac{\delta m}{\delta t} = gc - bm \qquad (2)$$

The total concentration of gas within a grain is

$$\Psi = c + m \qquad (3)$$

and obeys the equation

$$\frac{\delta \Psi}{\delta t} = D\left(\frac{\delta^2 c}{\delta r^2} + \frac{2}{r}\frac{\delta c}{\delta r}\right) + \beta \qquad (4)$$

Under stationary trapping conditions, the amount of trapped gas m, remains unchanged and equations (2) and (3) become

$$gc = bm \qquad \text{and}$$

$$\Psi = c\left(1 + \frac{g}{b}\right) \qquad (5)$$

Using relation (5), equation (4) transforms into

$$\frac{\delta\Psi}{\delta t} = D'\left(\frac{\delta^2\Psi}{\delta r^2} + \frac{2}{r}\frac{\delta\Psi}{\delta r}\right) + \beta \qquad (6)$$

where D′ is the effective diffusion coefficient within a grain under equilibrium trapping conditions [3] and is related to D by

$$D' = \frac{Db}{b + g} \qquad (7)$$

4. GAS ATOM DIFFUSION COEFFICIENT

According to White and Tucker [3] and Turnbull et al. [4] the diffusion process is controlled in different temperature ranges by at least one of three distinct mechanisms.

i) At the highest temperatures it seems likely that diffusion proceeds through the cation lattice by means of thermally activated vacancies and is expressed by

$$D_1 = 7.6 \times 10^{-10}\exp(-7 \times 10^4/RT) \quad [m^2/s]$$

where R = 1.987 cal/mol K and T is the absolute temperature.

ii) Below 1400°C diffusion is assumed to occur by means of vacancies produced by the irradiation process. Interstitials are also produced and in equal numbers as vacancies. Both defects have a certain probability of mutual recombination. Sinks like bubbles, grain boundaries and dislocations also capture vacancies. The balance equation for vacancies (V) and interstitials (I) is

$$\frac{dC_\gamma}{dt} = K - D_\gamma C_\gamma k_\gamma^2 - \alpha C_I C_V \quad \text{with} \quad \gamma = I, V$$

where K is the irradiation damage rate, i.e., the displacement rate of atoms from their lattice sites during irradiation, k_γ is the vacancy or interstitial sink strength and D_γ is the vacancy or interstitial mobility. The last term describes the mutual annihilation of vacancies and interstitials with $\alpha = ZD_I/S^2$, where S is the atomic jump distance equal to $\Omega^{1/3}$, $\Omega = 4.09 \times 10^{-30} m^3$ is the atomic volume and Z is the number of sites around a defect from which mutual recombination is inevitable.

In the steady state situation, i.e. $dC_\gamma/dt = 0$, and considering that bubbles are the dominant, unbiased sinks ($\mu = k_I = k_V = 10^{15}\ m^{-2}$), the vacancies concentration is given by

$$V = \frac{\mu S^2 + ZV_0}{2Z}\left[\sqrt{1 + \frac{4KZ}{j_V(\mu S^2 + ZV^0)^2}} - 1\right]$$

where the vacancy jump frequency is $j_V = 10^{13}V_0\ s^{-1}$ and $D_V = S^2 j_V$, with $V_0 = \exp(-5.52/RT)$. The resulting contribution to the diffusion coefficient of the fission gas is

$$D_2 = S^2 j_V V$$

According to Turnbull [4] every fission event produces between 10^4 and 5×10^5 defects. If the fission rate is F $(m^{-3} s^{-1})$, the damage rate is in the range

$$10^4 F\Omega \leq K \leq 5 \times 10^5 F\Omega$$

Following [2], we have chosen $K = 10^4 F\Omega$ with $F = 10^{19}$ $m^{-3}s^{-1}$ and Z = 2.

iii) No conclusion has been reached as for the mechanism of the low temperature, athermal diffusion tail. A term proportional to the fission rate F, scaled to agree with experimental results reported by Turnbull et al. [4], is taken to represent this region

$$D_3 = 2 \times 10^{-40} F \qquad [m^2/s]$$

The composite expression for the diffusion coefficient over the whole temperature range is [3]

$$D = D_1 + D_2 + D_3$$

5. BUBBLES SIZE AND CONCENTRATION

Several authors [3,4] propose that bubbles are nucleated along the track of the energetic fission fragments. Every fission event gives rise to two fission fragments and each of these nucleate α bubbles. Therefore, 2α bubbles are created for each fission and the creation rate of bubbles is $2\alpha F$. On the other hand, a fission fragment travels a distance $l_f = 6 \times 10^{-6}$ m before loosing its energy and destroys the bubbles along its path. Turnbull [4] assumes that a fission fragment has a range of influence about its path of $Z_0 \approx 10^{-9} m$ and that a single collision or graze is sufficient to destroy totally a bubble. All the bubbles of radius R at a distance $\leq R + Z_0$ of the center of the fission fragment path are destroyed. Then, the destruction rate of bubbles is $2\pi F l_f (R+Z_0)^2 C_B$, where C_B represents the bubbles density. In summary, we have

$$\frac{dC_B}{dt} = 2\alpha F - 2\pi F l_f (R + Z_0)^2 C_B$$

After a short period of irradiation the intragranular bubble population stabilizes both in size and density [3]. The saturation value of the bubble concentration is $(dC_B/dt = 0)$

$$C_B = \frac{\alpha}{\pi l_f (R + Z_0)^2}$$

Considerations on the bubble size distribution lead to a correction of this last expression

$$C_B = \frac{1.52\alpha}{\pi l_f (\bar{R} + Z_0)^2}$$

where $\bar{R}$ is the mean radius of bubbles. Different expressions are reported for $\bar{R}$. According to White et al. [3] it is given by

$$\bar{R} = 5 \times 10^{-10} [1 + 106 \exp(-0.75/kT)] \quad [m] \quad \text{with} \quad k = 8.618 \times 10^{-5} eV/K$$

Several values are found in the literature for the parameter α. According to Turnbull [4], it must be in the range 5 to 10; White et al. [3] and Nakajima [2] propose $\alpha = 24 \pm 2$.

6. TRAPPING PARAMETERS

The capture rate at bubbles, g, is given by White et al. [3] and Nakajima [2] as

$$g = 4\pi \bar{R} D C_B \qquad [s^{-1}]$$

To obtain the expression of the resolution rate of trapped gas atoms back into solution, b, the bubble size distribution has to be taken into account. b is given by [2,3]

$$b = 3.03 F \pi l_f (R + Z_0)^2 \qquad [s^{-1}]$$

The effective diffusion coefficient D' can then be evaluated by means of equation (7).

7. GAS PRODUCTION RATE

Irradiation is assumed to produce an homogeneous distribution of fissions within the grain at a rate F. There exists a certain probability per fission of directly forming a particular nuclide. But these isotopes are radioactive and transmute to other elements. The overall yield, y, of a given nuclide includes the contribution due to beta decay of the precursors in the mass chain in addition to the independent yield of the nuclide. Thus, the uniform gas generation rate is yF.

The net rate of gas accumulation in grain boundaries is reduced by bubble resolution. This process provides an additional source of gas atoms which penetrate into the grain specially in a thin layer adjacent to the grain boundary following a distribution function $h(r)$ with a maximum at $r = a\text{-}\lambda$, with $\lambda \ll a$. $h(r)$ is also assumed to be zero at $r = a$ and at $r = a - 2\lambda$. If at a given time there are N gas atoms per unit area of the grain boundary, the source term arising from resolution must be such that the volume integral of the distribution function verifies

$$\int_{a-2\lambda}^{a} h(r) 4\pi r^2 dr = 4\pi a^2 \frac{bN}{2}$$

where the factor $1/2$ indicates that half of the atoms penetrate each of the neighboring grains. Therefore, the gas generation rate term, β, of equation (6) is given by

$$\beta = \begin{cases} yF & \text{for } 0 \le r \le a - 2\lambda \\ yF + h(r) & \text{for } a - 2\lambda < r \le a \end{cases} \qquad (8)$$

For the fission gases Xe and Kr, $y \approx 0.3$. The value of λ is expected to be about 2×10^{-8} m [6].

8. EQUIAXED GRAIN GROWTH

The equiaxed grain growth is expressed by the Ainscough model [5] modified by Ito et al.[6]:

$$\frac{da}{dt} = k \left(\frac{1}{a} - \frac{f}{a_m}\right)$$

where

$$k = 3.64 \times 10^{-9} \exp(-63800[cal/mol]/RT)$$

with $R = 1.987$ $cal/mol\ K$ and

$$a_m = 1.1 \times 10^{-3} \exp(-7620/T) \qquad [m]$$

$$f = 1 + \eta \frac{N}{N_s}$$

N is the number of gas atoms per unit area of the grain boundary and Ns its saturation value. η is taken as 0.5.

9. SATURATION LEVEL AT GRAIN BOUNDARY

The intergranular bubbles are considered to be lenticular and sized in the micrometer range. When the grain faces are covered up to a fraction F_s, it is considered that the interlinkage of the bubbles takes place and any new fission gas atom is released.

If r_f is the curvature radius of a bubble and θ its semidihedral angle, then it covers a circular area with radius $r_f sin\ (\theta)$ on the grain boundary. The volume of each bubble is given by

$$V_b = \frac{4}{3}\pi r_f^3 f_f\ (\theta)$$

with

$$f_f\ (\theta) = 1 - \frac{3}{2}\cos\theta + \frac{1}{2}\cos^3\theta$$

The number of intergranular bubbles per unit area is

$$\frac{F_s}{\pi r_f^2 \sin^2\theta}$$

If the ideal gas law is considered valid, the total number of gas atoms at the grain boundary in saturation conditions is given by

$$N_s = (2\lambda + r_f P_{ext}) \times \frac{4wF_s}{3kT}$$

where $k = 1.380658 \times 10^{-23}\ J/K$, $r = 0.626\ J/m^2$, $r_f = 5 \times 10^{-7}\ m$, $P_{ext} = 0$, $w = f_f\ (\theta)/\sin^2\ (\theta)$. With $\theta = 50°$, as considered by different authors (e.g.[6]), w = 0.287. F_s is considered equal to 0.5, according to [2,6] although other authors refer a value of 0.25 [3].

The temperature dependence of the saturation level is such that it diminishes in two orders of magnitude from T = 500 K to T = 3000 K. P_{ext} can be used as a parameter to adjust the fission gas release during cooling transients, when it can be required to take negative values.

10. FISSION GAS RELEASE

The number of fission gas atoms contained in the grain at the time t_k is determined by

$$C_k = 4\pi \int_0^{a_k} r^2 \Psi_k dr$$

Before saturation, the gas content per unit area of the grain boundary at the time t_k, N_k, is determined by a balance equation which considers:

i) the gas content of the grain and grain boundary at the instant k - 1

$$C_{k-1} + 4\pi a_{k-1}^2 \frac{N_{k-1}}{2}$$

ii) the amount of gas generated by fission during Δt_k

$$\frac{4}{3}\pi a_k^3 yF\Delta t_k .$$

iii) the amount of gas incorporated to the grain and grain boundary by sweeping of the grain boundary

$$C_{k-1}\frac{a_k^3 - a_{k-1}^3}{a_{k-1}^3} + 4\pi a_{k-1}^2 \frac{N_{k-1}}{2}\frac{a_k^3 - a_{k-1}^3}{a_{k-1}^3}$$

These quantities balance with the gas content of the grain and grain boundary at t_k

$$C_k + 4\pi a_k^2 \frac{N_k}{2}$$

and the following expression is obtained

$$C_{k-1}\left(\frac{a_k}{a_{k-1}}\right)^3 + \frac{4}{3}\pi a_k^3 yF\Delta t_k + 4\pi a_{k-1}^2 \frac{N_{k-1}}{2}\left(\frac{a_k}{a_{k-1}}\right)^3 \qquad (9)$$

with the initial conditions ($t = 0$, $k = 0$) $C_0 = 0$ and $N_0 = 0$. Then, for $k = 1$ and $t = \mathfrak{t} = \Delta\mathfrak{t}$, we have

$$\frac{4}{3}a_1^3 yFt_1 = C_1 + 4\pi a_1^2 \frac{N_1}{2} \qquad (10)$$

from where N_1 is calculated if C_1 is obtained from the analytical solution Ψ_1 at $t = \Delta t_1$. Using equation (9) for $k = 2$, where $t_2 = t_1 + \Delta t_2$, together with equation (10) we obtain

$$\frac{4}{3}a_2^3 yFt_2 = C_2 + 4\pi a_2^2 \frac{N_2}{2}$$

from where N_2 is easily calculated. In a similar manner we determine N_k at every instant t_k by means of

$$\frac{4}{3}a_k^3 yFt_k = C_k + 4\pi a_k^2 \frac{N_k}{2}$$

which express that the total number of gas atoms generated by fissions since the beginning of irradiation are distributed between the interior of the grain, either as dissolved atoms or in intragranular bubbles, and the grain boundary.

Once the saturation level is reached, the fission gases are released. The release at a given time t_k is given by R_k

$$R_k = \frac{4\pi a_k^2}{2}\max\left[N_k - N_{s,k},\ 0\right]$$

where $4\pi a_k^2 N_k$ represents all the atoms not contained within the grain. When saturation has not yet been achieved they are all allocated in the grain boundary. Otherwise, they are distributed between the grain boundary, $4\pi a_k^2 N_s$, and the free volume of the fuel pin, $4\pi a_k^2 (N_k - N_s)$.

The fractional release F_k from the fuel with volume V, at the end of the k-th time step is given by

$$F_k = \frac{R_k}{\frac{4}{3}\pi a_k^3 yFt_k}$$

This expression is valid both for one grain and for the whole fuel, since if n_k grains are present the generation and the release are multiplied by the same factor.

11. THE CALCULATION PROCEDURE

The diffusion equation (6) is solved by means of the implicit finite difference method [7]. The initial solution of the diffusion equation was calculated using the Laplace transformation.

At $r = 0$, and because of symmetry, the boundary condition $\delta\Psi/\delta r = 0$ must be satisfied. At r = a, the condition of perfect sink of the grain boundary implies $\Psi = 0$.

12. RESULTS

Table 1 shows the values of the parameters in the SI used in our calculations taken from the referenced papers.

TABLE 1

t_0	=	10^3	initial time
Ω	=	4.09×10^{-29}	atomic volume
μ	=	10^{15}	sink strength of bubbles
Z	=	2	number of sites around a point defect
K	=	10^4	rate of defect production per atom
y	=	0.3	number of gas atoms created per fission event
λ	=	2×10^{-8}	half-width of the distribution of re-entered atoms
a	=	1×10^{-5}	initial grain radius
η	=	0.5	parameter to calculate the maximum grain size
γ	=	0.626	surface stress of the bubbles
r_f	=	5×10^{-7}	radius of curvature of the lenticular bubbles
P_{ext}	=	0	external pressure on the grain boundary bubbles
θ	=	50	half-angle between the surfaces of a lenticular bubble
F_s	=	0.5	fraction of grain boundary surface occupied by bubbles
Z_0	=	10^{-9}	range of influence of a fission fragment
l_f	=	6×10^{-6}	range of a fission fragment before coming to rest
α	=	24	number of intragranular bubbles nucleated per fission fragment
F	=	3.1×10^{19}	fission rate
Δx	=	$\lambda/4$	grid spacing used in the numerical calculation

Figures 1 - 4 display our results together with those obtained by Zimmermann [8] in isothermal experiments at 1250, 1500, 1750 and 2000 K labelled as *a*. The curves labelled *b* were calculated using the normal parameters listed in Table 1. In the calculations for curves labelled *c* and *d* some parameters were modified in order to investigate their influence on the fitting between calculated and measured results. For *c* the diffusion coefficient was multiplied by 8. For *d* the low temperature term of the diffusion coefficient, D_2, was changed to 4.6×10^{-39} F and the resolution rate parameter, *b*, was multiplied by 3. The search for better parameters was attempted because many of them are yet poorly determined.

13. CONCLUSIONS

The model, based on physical principles, considers the atomic diffusion with trapping of the fission gases Xe and Kr generated during irradiation of the nuclear fuel UO_2, the precipitation of gas in intra and intergranular bubbles, its resolution due to impact of energetic fission fragments, the interconnection of grain boundary bubbles and the sweeping of gas by the grain boundary movement.

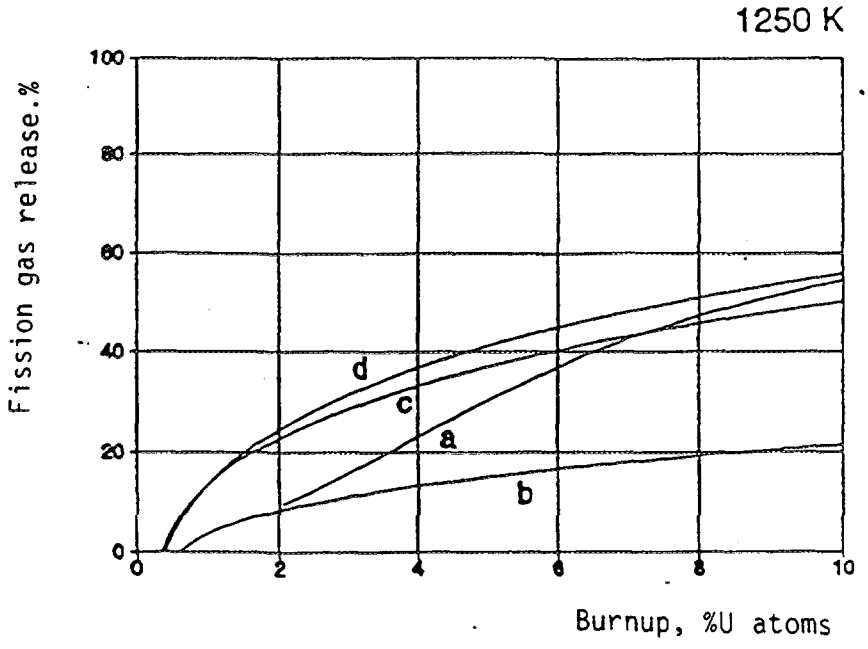

Figure 1

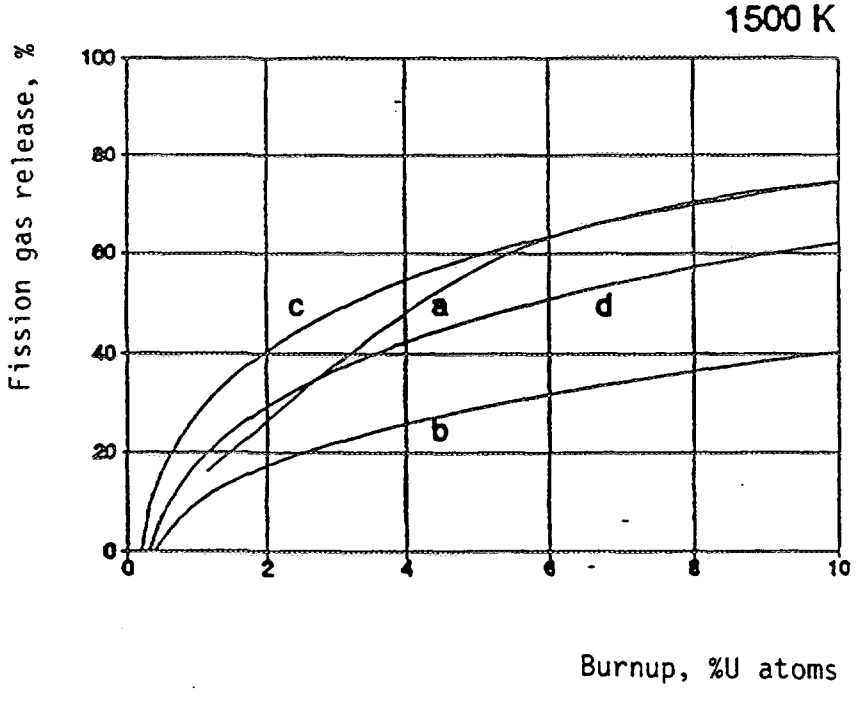

Figure 2

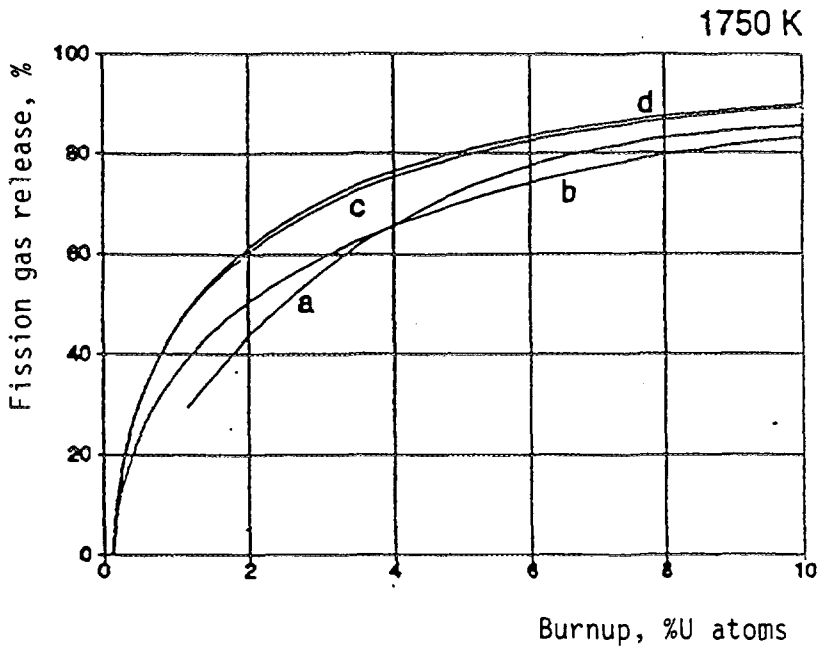

Figure 3

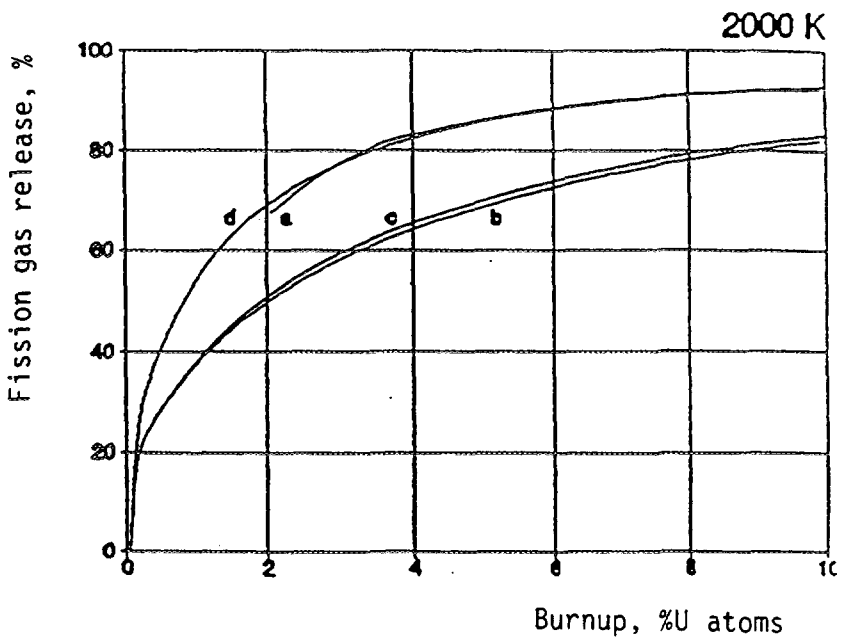

Figure 4

The calculation code is able to simulate numerically the grain growth, the amount of gas dissolved in the fuel matrix and accumulated in bubbles, either intragranular or intergranular, the saturation of the latter and the consequent release of gas to the free volume of the fuel pin. The calculation time is sufficiently short as to make this code a good tool to be incorporated to other more general performance code.

The results of the isothermal calculations were compared with experimental data reported in the literature. The agreement between both families of results is quite good and it can be improved if a more adequate set of parameters is found.

ACKNOWLEDGEMENTS

The authors wish to acknowledge *Dr. E.J. Savino, Ing. H. Nassini and Dr. E.A.García* for their suggestions in the development of the model.

REFERENCES

[1] OLANDER, D., Fundamental Aspects of Nuclear Reactor Fuel Elements, Technical Information Center, U.S. Department of Energy, 1976

[2] NAKAJIMA, T., AND SAITO, H., A comparison between fission gas release data and FEMAXI-IV code calculations, Nuclear Engineering and Design 101 (1987) 267-279.

[3] WHITE, R. AND TUCKER, M., A new fission-gas release model, Journal of Nuclear Materials 118 (1983) 1-38.

[4] TURNBULL, J., FRISKENEY, C., FINDLAY, J., JOHNSON, F. AND WALTER, A., The diffusion coefficients of gaseous and volatile species during the irradiation of uranium dioxide, Journal of Nuclear Materials 107 (1982) 168-184.

[5] AINSCOUGH, J.B., OIDFIELD, B.W. AND WARE, J.O., J. Nucl. Mater. 49(1973/1974)117-128.

[6] ITO, K., IWASAKI, R. AND IWANO, Y., Finite element model for analysis of fission gas release from UO_2 fuel, Journal of Nuclear Science and Technology 22 [2] (1985) 1~9-138.

[7] DENIS, A. AND GARCÍA, E.A.;Simulation with the HITO code of the interaction of Zircaloy with uranium dioxide and steam at high temperatures, Journal of Nuclear Materials 185 (1991) 96-113.

[8] ZIMMERMANN, H., Investigations on swelling and fission gas behaviour in uranium dioxide, Journal of Nuclear Materials 75 (1978) 154-161.

FISSION GAS RELEASE DURING POST IRRADIATION ANNEALING OF LARGE GRAIN SIZE FUELS FROM HINKLEY POINT B

J.C KILLEEN
Nuclear Electric plc,
Barnwood, United Kingdom

Abstract

A series of post-irradiation anneals has been carried out on fuel taken from an experimental stringer from Hinkley Point B AGR. The stringer was part of an experimental programme in the reactor to study the effect of large grain size fuel. Three differing fuel types were present in separate pins in the stringer. One variant of large grain size fuel had been prepared by using an MgO dopant during fuel manufacture, a second by high temperature sintering of standard fuel and the third was a reference, 12μm grain size fuel. Both large grain size variants had similar grain sizes around 35μm.

The present experiments took fuel samples from highly rated pins from the stringer with local burn-up in excess of 25GWd/tU and annealed these to temperatures of up to 1535°C under reducing conditions to allow a comparison of fission gas behaviour at high release levels. The results demonstrate the beneficial effect of large grain size on release rate of ^{85}Kr following interlinkage. At low temperatures and release rates there was no difference between the fuel types, but at temperatures in excess of 1400°C the release rate was found to be inversely dependent on the fuel grain size. The experiments showed some differences between the doped and undoped large grain size fuel in that the former became interlinked at a lower temperature, releasing fission gas at an increased rate at this temperature. At higher temperatures the grain size effect was dominant.

The temperature dependence for fission gas release was determined over a narrow range of temperature and found to be similar for all three fuel types and for both pre-interlinkage and post-interlinkage releases, the difference between the release rates is then seen to be controlled by grain size.

1. INTRODUCTION

During normal operation the fuel grain size has little influence on the release of fission products. However, following a period of high temperature operation or extended burn-up, where the grain boundaries have become saturated with fission gas so that interlinkage of porosity and enhanced fission product release has been initiated, then it is expected that the grain size will determine the rate of release of fission products. This effect is due to the reduced grain boundary surface area and the longer diffusion distance to the grain boundary within a larger grain.

In order to evaluate large grain size fuel in a commercial reactor, an experimental stringer was loaded into Hinkley Point B reactor. This stringer contained pins filled with standard fuel as a reference and two types of large grain sized fuel pins, one with MgO doped fuel and the other with a high temperature sinter fuel. The mean grain size of both variants was greater than 30 microns, whilst the standard fuel had a normal grain size of around 12 microns. The pins examined had burn-ups in excess of 25GWd/tU.

The PIE fission gas release measurements made on the large grain size pins confirmed that they had behaved normally during the irradiation, and the fission gas releases were similar to those found in the standard pins (around 0.15%). The stringer had not been subjected to high temperatures in the reactor, and on discharge none of the fuel was found to have significant grain boundary porosity.

The present report describes post-irradiation annealing experiments carried out on this fuel, to determine if the expected reduction in fission gas release rate does occur in these large grain size fuel

samples during high temperature anneals. The release rate of the long lived rare gas isotope ^{85}Kr was monitored from the samples during the anneals. The release rate of this isotope is assumed to be representative of the stable inert gases released during the experiments.

2. EXPERIMENTAL

2.1 SAMPLES

The samples were taken from three pins irradiated in Element 3 of a CAGR stringer, comprising a large grain size pin, a standard pin and a doped pin respectively. Each sample was a randomly shaped, pellet fragment, each had a similar weight and came from a random radial position of the appropriate pellet. The burn-up of all the samples was 25.1GWd/tU. Table I gives details of the samples used and the an indication of the initial anneal of each.

2.2 ANNEALS

The anneals were carried out using a shielded furnace capable of reaching 1700°C under controlled atmospheres. The furnace is described in more detail in Reference [1]. The anneals were carried out in a flowing atmosphere of 2% hydrogen in helium to ensure that the samples were close to stoichiometric composition throughout the anneals.

The purpose of the present experiments was to determine the difference in release behaviour of large and small grain size fuel, so the anneal temperatures were chosen to give significant gas release during an initial experimental period of a few hours. Initial tests indicated that a temperature of 1410°C was suitable, but it should be noted that this temperature is lower than that found for similar releases in previous work with stoichiometric UO_2 [1].

2.2.1 Atmosphere determination

During the experiments on-line measurements were made of the oxygen potential of the exit gas using a solid state, yttria stabilised zirconia oxygen probe operating at 820°C. This device gave a measurement of -460kJ throughout the experiments, with no significant variations observed during the tests. However, because of the low temperature at which fission gas release occurred, gas chromatography was carried out on the flow gas used in the experiments and an impurity level of 20-30 vpm of oxygen was found. This value for the oxygen impurity level was in agreement with the on-line measurements of the exit gas oxygen potential. With this atmosphere the sample stoichiometry will not rise above 2.0001 during the experiments and oxidation is not believed to be significant.

2.2.2 Temperature determination

The sample temperature was monitored using two Pt/Pt-13%Rh thermocouples located in the sample support tube with the tips approximately 4mm from the sample. The sample was annealed in the centre of the furnace hot zone which is approximately 90mm long. The furnace temperature was controlled from a separate W/WRe thermocouple in the windings. Some of the initial experiments experienced problems with the temperature controller, and the sample hold temperatures fluctuated, by typically 15°C, around the nominal setting. Later experiments in the series were under manual control and the temperature variation was reduced to around 5°C.

2.2.3 Sample anneals

In order to determine the behaviour of the differing fuel types, two different series of anneals were undertaken. For the first the samples were ramped to around 1410°C at 0.1°C/sec and held at this

temperature for several hours. Subsequently these samples were further annealed at higher temperatures and in some cases annealed in an oxidising atmosphere of 1%CO/CO_2, to try to achieve 100% gas release to enable accurate calibration of the gas release during the earlier anneals. The second series of anneals were carried out using a ramp and hold technique, with steps of around 50°C and hold times of an hour. The intention of these anneals was to see if there was any differences in the initiation of gas release between the fuel types. Full details of the anneals are given in Table II.

One final experiment was carried out on sample B4, following a prolonged isothermal anneal after the ramp experiment. At this time the sample was releasing gas at a reasonably constant rate, so the temperature was reduced in 50°C steps to determine the rate of release as a function of temperature. The

Table I: Sample details, including base irradiation fission gas release measurement.

Sample identity	Initial Anneal	Weight (mg)	Type	Gas release (%)	Density ($Mg.m^3$)	Grain size (μm)
A1	to 1410°C	416.26	High temperature sinter	0.158	10.76	35 - 40
A2	to 1420°C	470.24				
A3	Ramp test	353.97				
B0	CO_2	427.50	Standard grain size fuel	0.107	10.65	11 - 14
B1	to 1410°C	243.85				
B2	to 1410°C	263.76				
B3	Ramp test	397.80				
B4	Ramp test	369.94				
C1	to 1400°C	397.55	MgO doped fuel	0.229	10.54	35 - 50
C3	Ramp test	428.90				

Table II: Sample anneals and ^{85}Kr releases.

Sample	Atmosphere	Temperature (°C)	Hold time (hours)	Incremental ^{85}Kr release (%)	Cumulative ^{85}Kr release (%)
A1	2%H_2	1410	1.5	10	10
A2	2%H_2	1420	62	52	52
	2%H_2	1502	2.5	1	53
	1%CO/CO_2	1230	15	10	54
	1%CO/CO_2	1300	27	18	82
	1%CO/CO_2	1340	20	10	92
B0	2%H_2	1670	5	61	61
	1%CO/CO_2	1350	24	61	92
B1	2%H_2	1410	60	82	82
B2	2%H_2	1410	12.5	72	72
	2%H_2	1515	42	10	82
C1	2%H_2	1390	15	12	12
	2%H_2	1450	3	2	14
	2%H_2	1506	15	11	25
A3	2%H_2	Ramp			6
B3	2%H_2	Ramp			22
B4	2%H_2	Ramp			50
	2%H_2	Ramp down			50
C3	2%H_2	Ramp			6

temperature hold periods were short and the cumulative release of gas during the experimental period was small, so that the fission gas profile in the sample is not believed to have changed significantly during the test.

2.3 BETA COUNTING

Continuous beta counting of the released ^{85}Kr was carried out by monitoring the furnace exit gas. The system was calibrated by two methods, the first was to pass a known volume of standard ^{85}Kr through the system and record the cumulative counts for the known quantity of gas. The second method was to record the cumulative counts for two samples which were annealed at high temperatures in $1\%CO/CO_2$ to give total release fractions approaching 100%. To compare the two methods, the total ^{85}Kr content of the samples was calculated from the irradiation history at the time of the annealing experiments ($4.85mCi/gmUO_2$). The two calibrations techniques were found to be in agreement to within 10% for samples B0 and A2 which were calculated to have released in excess of 90% during the annealing experiments.

Two further calibrations were carried out during each experiment. One was to ensure that the gas flow, and hence dilution of the released fission gas, was constant. A fixed flow rate of 15ml/min was used. The second important calibration was to periodically measure the background counts in the counter during the experiments. The latter was carried out by switching the gas flows so that clean argon was passed through the counter whilst the active gas was carried through a bypass line. The background was found to vary considerably throughout the experiments with the background rising following large releases of fission gas. The regular monitoring of the background permitted an accurate estimate of the true count rate to be made throughout the experiments.

The count rates are integrated to give the cumulative release fractions shown in this paper, and a reasonable estimate of the integrating error due to the background is 20%. This error will be greater for long anneals with low release rates, and will be a random error. The other major error source, due to calibration of the system, will be systematic and all the tests will be biased by this error in a similar manner. The systematic errors are expected to lie within 20%, but will not affect comparative measurements between the different experiments.

3. RESULTS

3.1 RAMP AND HOLD ANNEALS

The initial phase of these experiments was a ramp to temperature at a rate of 0.1°C followed by a prolonged hold. The cumulative releases for the first few hours of the anneals for all of the ramp and hold samples are given in Fig. 1, which compares the results for the standard and large grain size samples. The corresponding temperature histories are given in Fig. 2. The figures show that gas release is first detected as the temperature of each sample reaches 1280°C, and that by the time the temperature has reached 1400°C the samples are releasing a considerable fraction of their gas content. The cumulative releases observed at the end of the long term hold anneals are shown in Table II.

The major result is that the release from the standard fuel is typically three times the level seen for the large grain size samples. However the results do not permit discrimination between the release from sample C1, the doped fuel, and the other large grain size samples, A1 and A2. This is because there were small temperature differences (approx 15°C) between these three samples, with the highest temperature giving the highest release.

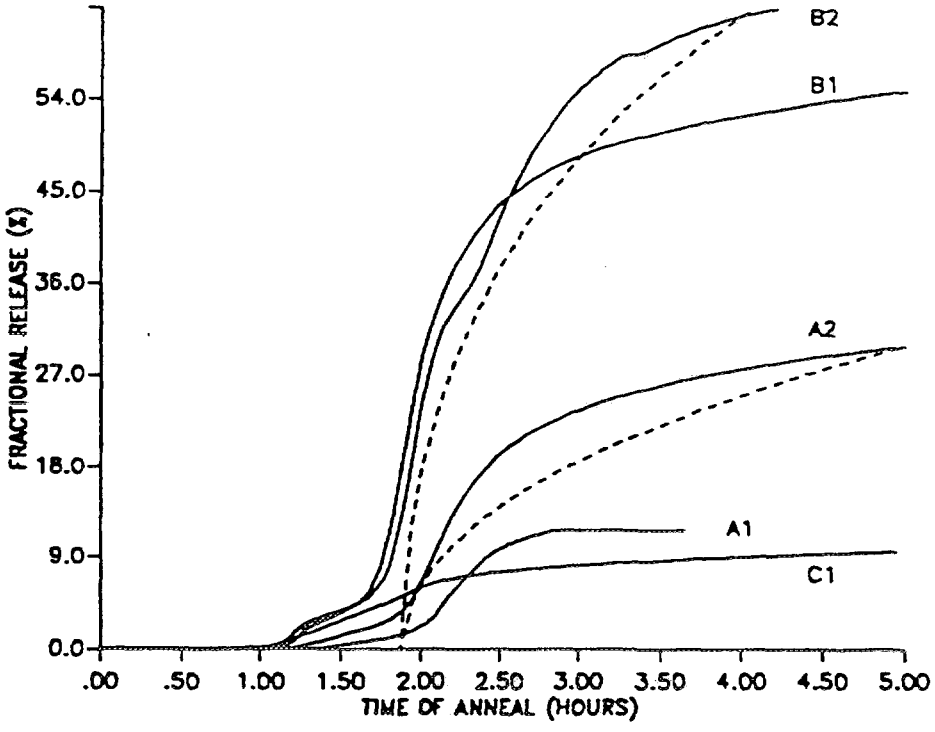

FIG. 1. ***Fractional release as a function of time.*** *The figure shows the cumulative release for the first five hours of the "Ramp and Hold" anneals. The dashed lines are a simple diffusive model with grain sizes of 12μm and 35μm. The diffusion coefficient, D, is taken as 6.5x10 $^{17} m^2 s^{-1}$.*

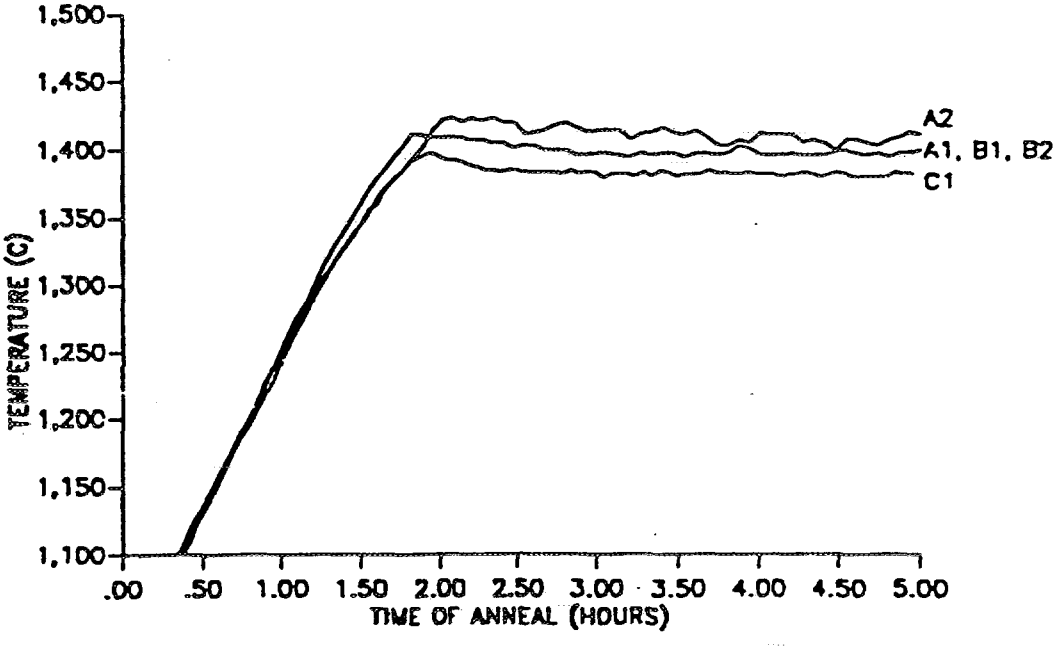

FIG. 2. ***Annealing temperatures.*** *The figure shows the annealing temperatures of the samples A1, A2, B1, B2, and C1 for the first five hours of the anneals. The origin of the timing is the attainment of 1000°C during the ramp to temperature.*

A simple way to analyse the data is to use the diffusive model due to Booth [2], which gives the fractional release, F, during post-irradiation annealing as:

$$F = \frac{6}{\sqrt{\pi}} \sqrt{\left(\frac{Dt}{a^2}\right)} - \frac{3Dt}{a^2} \qquad for \quad F < 0.77 \tag{1}$$

$$F = 1 - \frac{6}{\pi^2} \exp\left(-\pi^2 \frac{Dt}{a^2}\right) \qquad for \quad F \geq 0.77 \tag{2}$$

where D is the diffusion coefficient, t is the anneal duration and a is the radius of a spherical diffusion volume. For the present case the radius, a, is taken as 0.75 x the mean linear intercept grain size. Figure 1 also shows Booth release curves calculated for 12μm and 35μm fuel, utilising a nominal diffusion coefficient selected to approximate to the data. It is clear that the releases are approximated by the model, which does not include effects of changing temperatures and interlinkage, and it does demonstrate the magnitude of the expected grain size effect which is comparable to the effect observed. At the longer annealing times (Table II) the effect of grain size remained, with the large grain size fuel having released significantly less fission gas than the standard fuel.

3.1.1 Step ramp anneals

The onset of fission gas release was seen to occur at temperatures below the hold temperature for the long term anneals, so a ramp and hold sequence of anneals was undertaken to allow measurement of the initial release mechanism. The same temperature ramp rate of 0.1°C/sec was used in these tests, but hold periods of one hour were used at approximately 50°C steps. The hold sequence was initiated at 1000°C and the samples were held at 1280°C, following five temperature steps, for 16 hours overnight before the ramp and hold sequence was restarted. The second part of the temperature cycle is shown for samples A3, B3 and C3 in Fig. 3. A longer hold was carried out at 1440°C, for two hours, as the release rate was seen to increase significantly during this hold.

No fission gas release was observed during the initial ramps, nor during the overnight hold at 1280°C for the A3 and B3 samples, whilst the C3 (MgO doped sample) did give a small burst of release at around 1100°C. Continuous release of fission gas was initiated for all three samples on heating to 1330°C and the rate of release increased at each subsequent temperature rise. The release rate curves for these three samples are given in Fig. 4. It can be seen that the samples all gave similar releases at the start of the ramp sequence. The MgO doped fuel sample was the first sample to show signs of interlinkage as an increasing release rate was observed during the second and third hold periods. Similar increasing release rates were also observed for the other samples during subsequent, higher temperature hold periods. These increases in release rate at constant temperature are due to an increase in the fuel surface to volume (S/V) ratio as the fission gas causes interlinkage of grain boundary porosity. Table II notes the cumulative fractional release from the three samples at the end of the step ramp sequence, and it is worthy of note that the cumulative releases are lower than would be anticipated from the results of the long term anneals described in the previous section.

3.1.2 Fission gas release rates during controlled cooling

Sample B4 was held at temperatures in excess of 1500°C for over 20 hours following the step ramp test. By this time the release fraction was around 50% and the release rate of fission gas was falling slowly. It was decided to try to estimate the activation energy of the release process by altering the temperature and following the change in release rate.

The final experiment was carried out with the sample temperature first raised to 1535°C, held for 4 hours and then reduced in four steps of half hour hold duration, to 1350°C at which temperature there was no further measurable release of fission gas. The integrated release during the lower temperature holds was less than would have been released during an extra 20 minutes at 1535°C. The rate of change of release at the higher temperature was around 5% per hour, so the change in gas concentration within

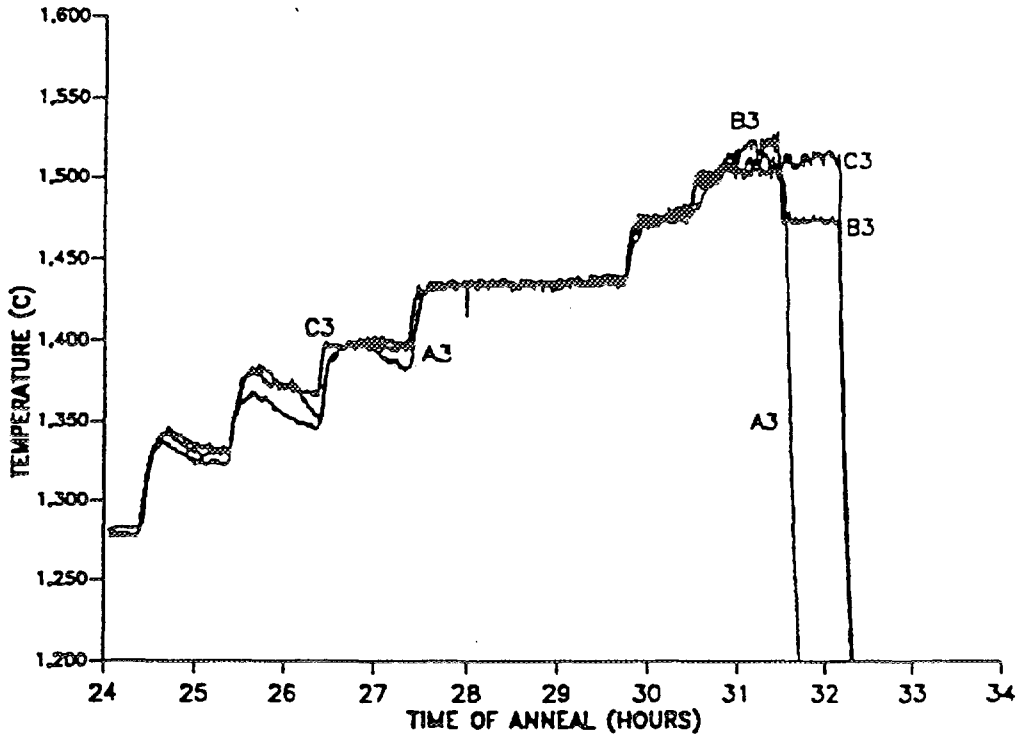

FIG. 3. ***Temperature of samples A3, B3, and C3.*** *The hold times were usually 1 hour duration and the ramp rate 0.1°C/s^{-1}. The samples had already been ramped to 1280°C and held for 16 hours.*

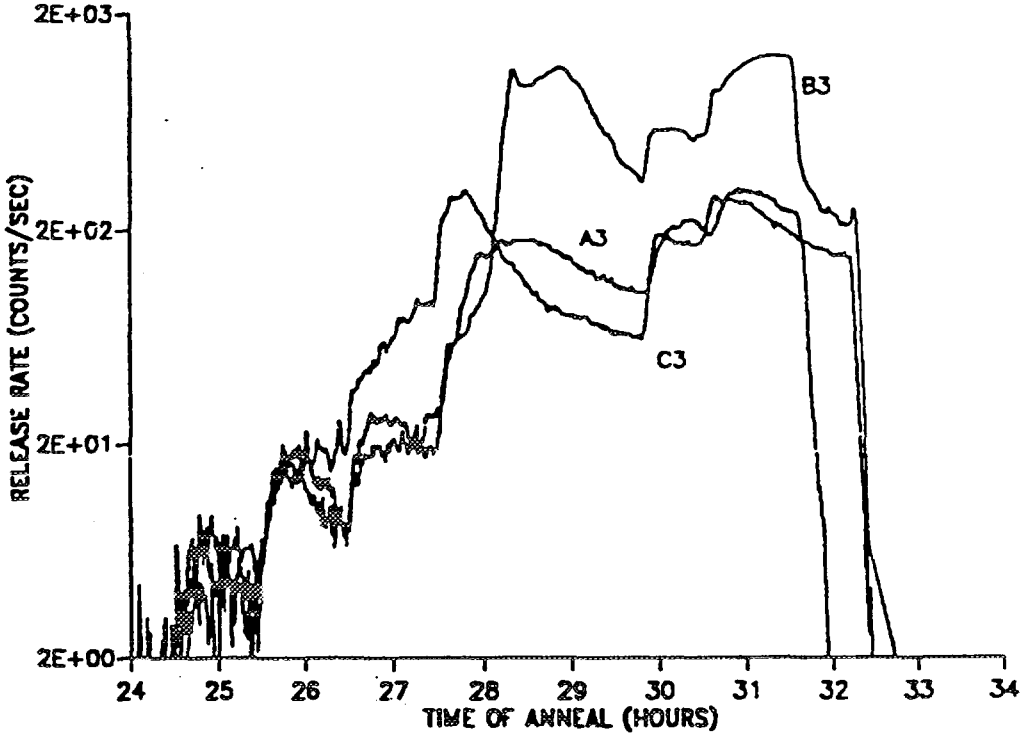

FIG. 4. *Count rate of the A3, B3, and C3 samples during the ramp anneals.*

the sample is expected to have changed by less than 2% during the latter part of the anneal. The results of the experiment are shown as an Arrhenius plot in Fig. 5 where an extra point has been added to the diagram by extrapolating the release rate measured at 1515°C.

4. DISCUSSION

4.1 GENERAL CONSIDERATIONS

As noted in the previous section, the releases found from these samples are larger than those found in similar previous experiments [1]. The enhancement is not only seen in the quantity of gas released, but the onset of release is also observed to occur at a lower temperature. Typically the temperature for onset of significant fission gas release under reducing conditions had been found to be around 1500°C compared with the onset temperature of 1410°C observed in the present experiments. One possible reason for higher gas release would be oxidation of the sample [3], but in the present experiments the use of a flow gas containing 2% hydrogen which was continually monitored would seem to eliminate this possibility during the anneals, despite the low level of oxygen impurity found. It remains possible that the samples were affected during the ramp to temperature by the oxygen impurity but the equilibrium atmosphere at temperature will have been strongly reducing to UO_2, and no gas release was observed at temperatures below 1000°C due to oxidation.

A second possible cause is the effect of burn-up on fission gas release. Such an effect has been observed for fuel with burn-up in excess of 20GWd/tU, for both reducing and oxidising anneal atmospheres. The present fuel has a burn-up of 25GWd/tU which is a high burn-up for CAGR fuel, and it is possible that this has influenced the results. One further influence on the release could well be the thermal history of the post-irradiation anneal. In these experiments there was rather less release from the samples from the 'step ramp' series of tests. For these tests the main difference was a long hold (16 hours) at 1280°C, a temperature just below that at which release occurred.

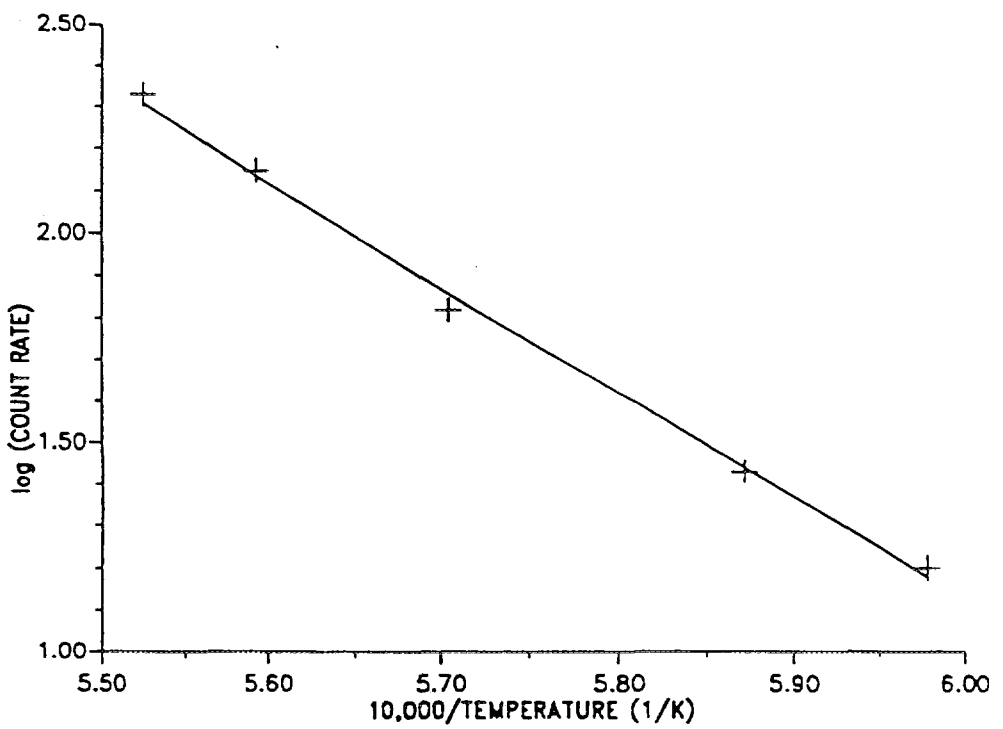

FIG. 5. ***Release rate as a function of reciprocal temperature for the down ramp. The figure shows the logarithmic release rate during the final stages of the B4 anneal. The fitted line has a slope of 460kJ/mol.***

The post-irradiation annealing of UO_2 is best carried out as a comparative study, and as there is no reference sample of lower burn-up nor an oxidation comparison, it is not possible to further examine the possible cause of the high releases seen. However the comparisons made between the differing samples within the study are not expected to be influenced by any such consideration.

4.2 RELEASE MECHANISMS

The results from the 'ramp and hold' tests were presented in Fig 1 as cumulative release plots with a superimposed fitting of a Booth diffusive release model. It is clear that this model does not adequately describe the release rates observed in these experiments and attempts to model the total releases with a single diffusion coefficient were not successful.
The reason for the model failure, particularly the high early release, could be due to release of gas previously deposited on grain boundaries as the fuel interlinked or be due to a high burn-up effect. Whatever the reason, the important feature of the results is that there is a consistent and significant difference in the release rates of the standard and large grain size samples. The difference in release levels between the two sample types can be well described by a function that is proportional to the inverse grain size, as would be predicted by a diffusion based model. This result will be independent of all systematic errors in the calculation of cumulative release, and the comparative values will be accurate to the level of the statistical counting errors and errors due to the differing burn-ups of the samples. These errors are believed to be less than 20%.

4.3 STEP RAMP ANNEALS

The problems with analysis of the ramp and hold experiments led to isochronal type experiments being undertaken. The analysis of the release is again based on a diffusion model, and utilises the approximate Booth release formula, (Eqn (1)), rearranged to give Dt/a^2 as a function of F for $F <$ 0.77.

$$\frac{Dt}{a^2} = \left(\frac{1}{\sqrt{\pi}} - \sqrt{\frac{1}{\pi} - \frac{F}{3}} \right)^2 \tag{3}$$

For values of $F < 0.1$ eqn (3) can be simplified to give

$$\frac{Dt}{a^2} = \frac{\pi}{36} F^2 \tag{4}$$

Figure 6 shows a plot of F^2 against time for the early stages of the A3 and B3 anneals. The slope of the straight line regions of the plot were measured as were the straight line portions of similar plots for the other samples and temperatures. The full equation (3) was used in the analysis of samples B3 and B4 when the release was above 10%, and the right hand side of Eqn (3) was plotted against time. Values of Dt/a^2 are derived from the least squares fits and are shown in Table III.

The results in Table III are given only for regions where there was no significant curvature in the plots, such as arose for sample C3 during interlinkage at around 1400°C and the early part of the 1430°C anneal of sample B3. These values of the effective diffusion coefficient, D/a^2, are plotted in Fig 7.

Examination of Figure 7 shows that the data fall into three roughly parallel sets and the figure gives an indication of the slope of the data with lines of slope 75,000K superimposed on the data. The first set is at temperatures below 1400°C where there is no difference between the large and small grain size samples. The other two data sets show a clear distinction between the different grain sizes. The explanation is due to the interlinkage phenomenon, and the low temperature release comes from a small surface area of the fuel and is not affected by grain size or dopant. Following interlinkage the effect of the grain size is seen and the effective diffusion coefficient is an order of magnitude larger for the small grain size samples.

Table III: Effective diffusion coefficient calculated from ^{85}Kr release curves.

Temperature (°C)	Calculated value of D/a^2 from measured slope of F^2 against time ($10^{-10}sec^{-1}$)			
	A3	B3	C3	B4
1325	-	0.23	-	-
1335	0.303	-	0.90	-
1355	-	0.803	-	0.17
1370	1.06	-	not linear	-
1390	2.30	2.43	not linear	-
1400	-	-	-	560
1430	93	1500	85	1500
1475	243	1960	190	3600
1500	510	4800 (Eqn 3)	390	4500 (Eqn 3)
1475	-	2050 (Eqn 3)	-	-

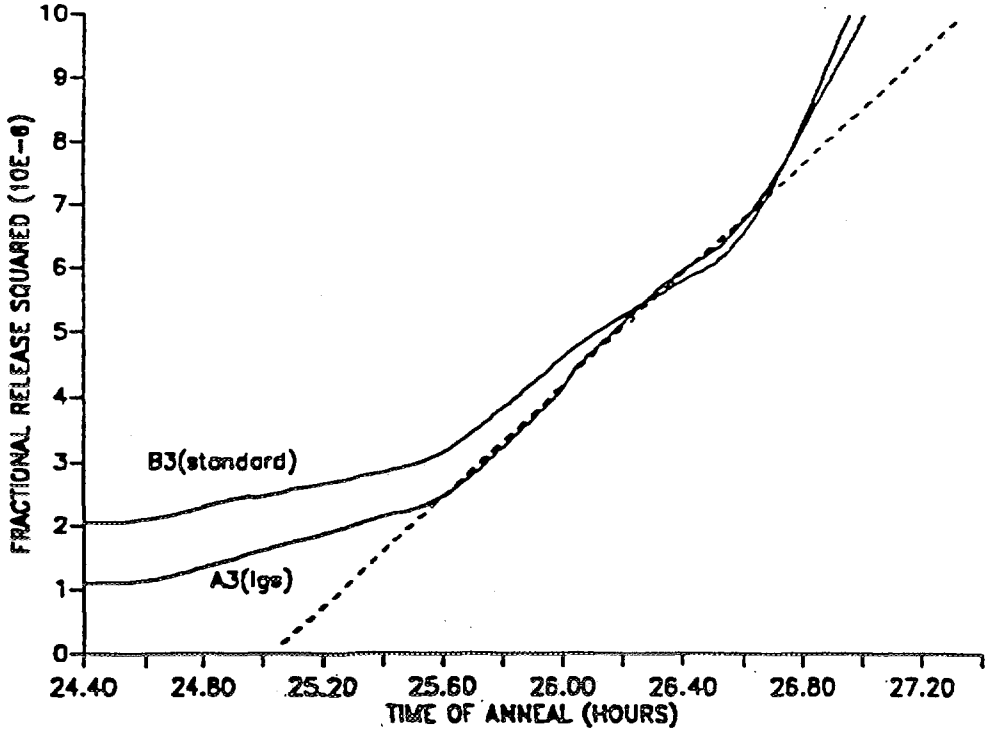

FIG. 6. ***Squared cumulative release from samples A3 and B3.*** *The squared cumulative release is shown for three hold periods. The dotted line is a least squares fit to the hold period at 1370°C for sample A3.*

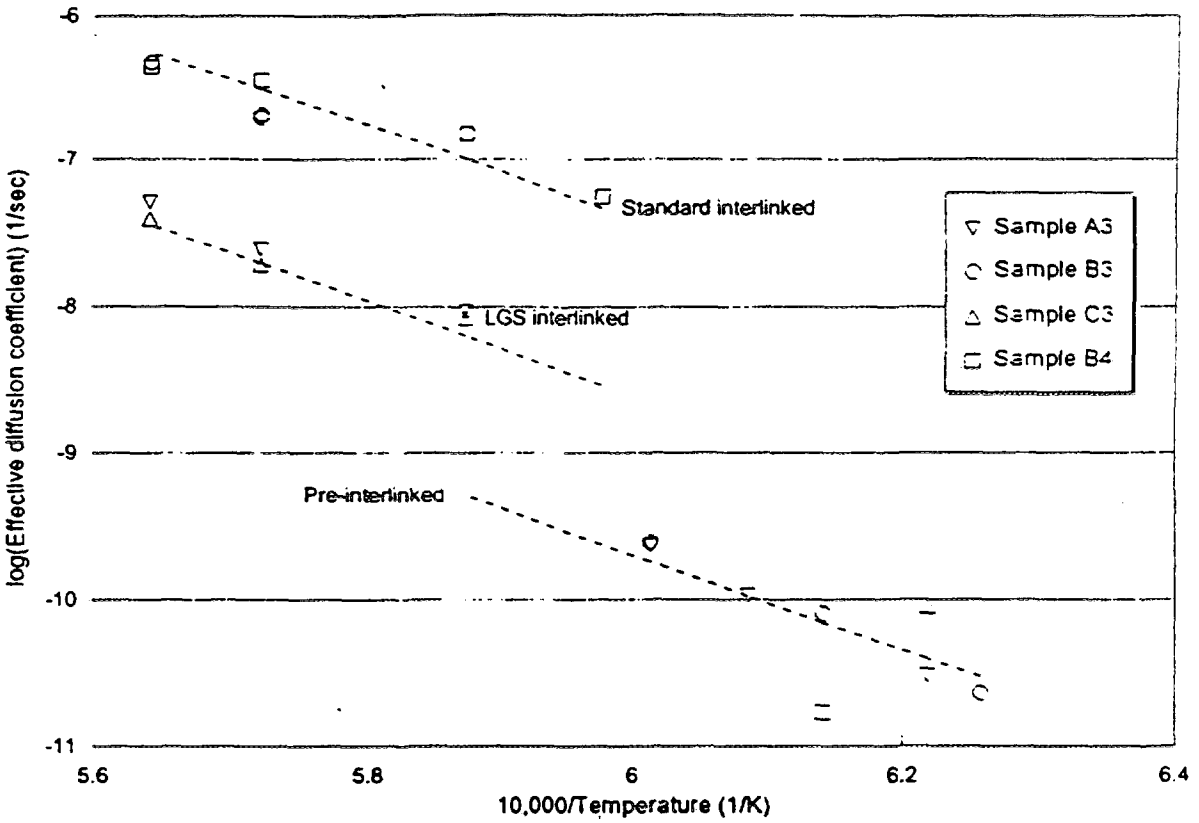

FIG. 7. ***Effective diffusion coefficient as a function of reciprocal temperature.*** *The figure shows the effective diffusion coefficient (D/a^2) calculated from the fits to the squared cumulative release curves of the step ramped samples. The dotted lines have a slope equivalent to an activation energy of 640kJ/mol.*

Despite the comparatively small temperature range available it is possible to measure the activation energy of the effective diffusion coefficient if the data from the large grain samples are grouped together at high temperatures and all the samples are grouped at the lower temperatures. The results give high values for the activation energies, which are presented as equivalent temperatures. For the pre-interlinked data the best fit is given as 85,000K, at the higher temperature the large grain size sample fit is 60,000K and 50,000K for the standard grain size samples.

4.4 FISSION GAS RELEASE ON COOLING

The final experiment of the series measured the fission gas release rate during a step cooling ramp. The basis for the analysis is the diffusion equation:

$$J = - D \nabla C \qquad (5)$$

where J is the flux of gas atoms across the surface of the diffusion volume and C is the concentration of gas atoms within the volume. The experimental measurements of release rate at 1535°C show a change of less than 2% within the time scale of the experiment. The assumption is therefore made that ∇C is constant during the cooling time. With this assumption the release rate is then proportional to the diffusion coefficient and the temperature dependence of D can be determined from Fig 5. The best estimate of the activation temperature from the figure is 55,000K.

5. EFFECT OF GRAIN SIZE ON RELEASE OF 85-KRYPTON

The results of the experiments carried out on the large grain size samples, whether doped or not, show a reduced release rate of fission gas compared to the standard material once interlinkage has taken place. Long term isothermal anneals show cumulative releases that are one third of those observed from standard fuel, and measurements of the effective diffusion coefficient between 1400°C and 1500°C show an inverse dependence on grain size, with no difference in activation energy. The best estimate of the activation temperature for diffusion in this temperature range obtained from all the data is 55,000K with an uncertainty of 10,000K.

There is no effect of grain size on the release rate at temperatures below 1300°C where release is arising from the geometric sample surface area and interlinkage has not occurred.

There is a difference in the behaviour of the MgO doped fuel during the ramp anneals. This sample started to show signs of interlinkage, as shown by the increasing release rate at constant temperature, at lower temperatures than the two undoped samples. At intermediate temperatures around 1350°C the doped sample was releasing gas at the highest rate. Similar early interlinkage and lower final release of fission gas has been observed previously with chromia doped fuel during irradiation [4].

The high temperature sinter samples did not show this early interlinkage, and the onset of enhanced release was seen at the same temperature as the standard sample. The difference between this sample type and the standard reference seems to be solely one of grain size.

5.1 EFFECT OF MEASUREMENT ERRORS ON THE ANALYSIS

A major problem with post-irradiation annealing experiments is the calculation of absolute release values from integrated release rate measurements. Calibration of the counting system is a source of possibly serious systematic error and long annealing times with low release rates can be vulnerable to small errors in the background determination. For the present experiments the maximum release measured is 92% following an anneal at high temperatures in an oxidising atmosphere. This result limits the maximum underprediction error in the measurements to around 10%, but overprediction error is harder to establish and could be greater. The analysis is based on finding the slope of a function of F^2, which will double any measurement error in the determination of a diffusion coefficient.

A further problem arises when a burst of gas is released due to some non-diffusive mechanism, for example sample cracking. The consequent cumulative fractional release will be systematically in error by an additive constant. An example of this problem is seen in the low temperature measurement of the effective diffusion coefficient of sample C3. This sample gave a small burst of release during heating but gave releases identical to the other samples at 1330°C. The inclusion of the burst release fraction has given rise to an effective diffusion coefficient x3 higher than the other samples, as shown in Figure 20. This problem becomes less significant as the cumulative release rises.

Fortunately, despite the potentially large errors in the determination of absolute values for the effective diffusion coefficients, the technique of post-irradiation annealing is capable of accurate determination of relative values. The systematic errors drop out of the determination of activation energies (relative temperature measurements) and the effect of grain size (relative release rate measurements). The reliability of the comparative measurements in this paper are therefore limited only by the small random errors of the counting system and other random errors in the determination of the physical properties used, for example mass, burn-up and grain size. These errors are calculated to be below 20%.

6. CONCLUSIONS

The release of fission gas from high burn-up CAGR type fuel is inversely proportional to the grain size once interlinkage has been established. This dependence, derived from a diffusion based model of gas release, holds even when the releases cannot be simply explained by a single diffusion coefficient.

The temperature dependence of release rate is the same for the three sample types within the experimental errors and is found to be 55,000K for interlinked fuel, corresponding to an activation energy of 460kJ/mole. The temperature range for which this activation temperature was found is 1535-1400°C for the reference fuel and 1430-1500°C for the large grain size fuel.

Before interlinkage had been established in the fuel the releases of fission gas from three fuel types were indistinguishable.

The MgO doped fuel interlinked at a lower temperature than either the reference fuel or the high temperature sinter fuel. There is therefore a range of conditions for which this fuel type releases gas at a higher rate than standard fuel.

REFERENCES

[1] BAKER, C. and KILLEEN, J C., Fission gas release during post irradiation annealing of UO2. Materials for nuclear reactor core applications, BNES, London. 198

[2] BOOTH, A. H., AECL Report CRDC 521. 1957.

[3] KILLEEN, J. C., and TURNBULL, J. A., An experimental and theoretical treatment of the release of ^{85}Kr from hyperstoichiometric uranium dioxide. Workshop on chemical reactivity of oxide fuel and fission product release, Berkeley, UK. 1987.

[4] KILLEEN, J. C., Fission gas release and swelling in UO2 doped with Cr_2O_3. J. Nucl. Mater. 88 (1980) 177.

SESSION 5
ADVANCED METHODS

FUEL ROD ANALYSIS TO RESPOND TO HIGH BURNUP AND DEMANDING LOADING REQUIREMENTS

Probabilistic methodology recovers design margins narrowed by degrading fuel thermal conductivity and progressing FGR

R. EBERLE, L. HEINS, F. SONTHEIMER
Siemens AG,
Unternehmensbereich KWU,
Erlangen, Germany

Abstract

The proof that fuel rods will safely withstand all loads arising from inpile service conditions is generally achieved through the assessment of a number of design criteria by using a conservative analysis methodology in conjunction with design limits "on the safe side". The classical approach is the application of a fuel rod code to the Worst Case which is defined by the combination of most unfavorable conditions and assumptions with respect to the criterion under consideration. As it is evident that the deterministic construction of such Worst Cases imply an (unknown but) intuitively very high degree of conservatism, it is not surprising that this will develop to cause problems the more demanding fuel insertion conditions have to be anticipated (increased burnup, high efficiency loading schemes etc.). A certain relief can be gained from cautious revisions of single design limits based on grown performance experience. But this increase of knowledge allows as well to change the established deterministic "go/no-go" conception into a better differentiating assessment methodology by which the quantification of the implied conservatism and the remaining design margins is possible: the Probabilistic Design Methodology (PDM). Principles and elements of the PDM are described. An essential prerequisite is a best-estimate fuel rod code which incorporates the latest state of knowledge about potential performance limiting phenomena (e.g. burnup degradation of fuel oxide thermal conductivity) as *Siemens/KWU's CARO-E* does. An example is given how input distributions for rod data and model parameters transfer into a frequency distribution of maximum rod internal pressure, and indications are given how this is to be interpreted in view of a probabilistically re-formulated design criterion. The PDM provides a realistic conservative assessment of design criteria and will thus recover design margins for increasingly aggravated loading conditions.

1. PRINCIPLES AND ELEMENTS OF CLASSICAL FUEL ROD DESIGN ANALYSES

An essential part of the engineering work in the field of designing fuel rods for insertion in commercial power plants is the assessment that the rods will safely withstand all mechanical and thermal loads arising from the foreseen and to some extent also postulated inpile conditions. The common components of this type of analyses are

- a set of design quantities (parameters) which have to be analyzed,
- a set of corresponding design limits for the design parameters,
- a fuel rod analysis code,
- a set of corresponding directives for the conservative application of the code in view of the parameters to be assessed.

The design parameters and corresponding limits are generally referred to as design criteria; the complete system constitutes the design methodology, within which the particular components are strongly interrelated and interdependent and can normally not be simply exchanged without interfering with the consistence of the whole methodology.

The dominant principle within such a design methodology is to demonstrate that the design limits are not violated even for the rod which will experience the severest insertion conditions (in terms of power history and/or burnup) including the fiction that within this particular rod most unfavorable combinations of fabrication tolerances and performance bounds will meet (Worst Case assessment). In [1] it is explained that an approach like this needs a specific selection of such combinations for each design criterion under consideration and that an uncorrelated mere piling-up of all unfavorable thinkable assumptions could result in highly hypothetic performance predictions beyond technical reality. This can be mitigated through integral Worst Case validations and a correlated combination of conservative input selections which still maintains the conservative coverage of a design criterion; a respective method is also described in [1].

In Fig. 1 the essential elements of a design methodology which follows the just outlined approach (and which is referred to from now on as "deterministic") are schematically put together. (The sketched curves do not mean something specific; but the reader may think e.g. of the development of rod internal pressure with insertion time.) Whereas the most probable result for a design parameter may experience a moderate evolution in time, burnup etc., the conservative analysis predicts a much more pronounced increase considerably deviating from the best-estimate value and coming much closer to the design limit for the analyzed quantity. The still existing distance to the design limit is the design margin.

It is clear that assumptions being most unfavorable for one design criterion are not necessarily the most unfavorable ones for the others. Therefore a complete design analysis consists of a whole system of those Worst Cases, each one specific for the assessment of one design criterion. In this approach the applied code should be a best-estimate code in the sense, that its predictions represent always the most likely results for the particular input data selection. Conservatism is thus handled via the conservatism contained in the input data set itself.

A further contribution to the total conservatism in this approach stems from the stipulation of the design limit itself (which needs not always to be a constant figure but may also vary - normally degrade - with progressing burnup) which is established well below a real failure limit or a region where technical risks cannot any longer be excluded. Admittedly, especially (but not only) in the early days of nuclear

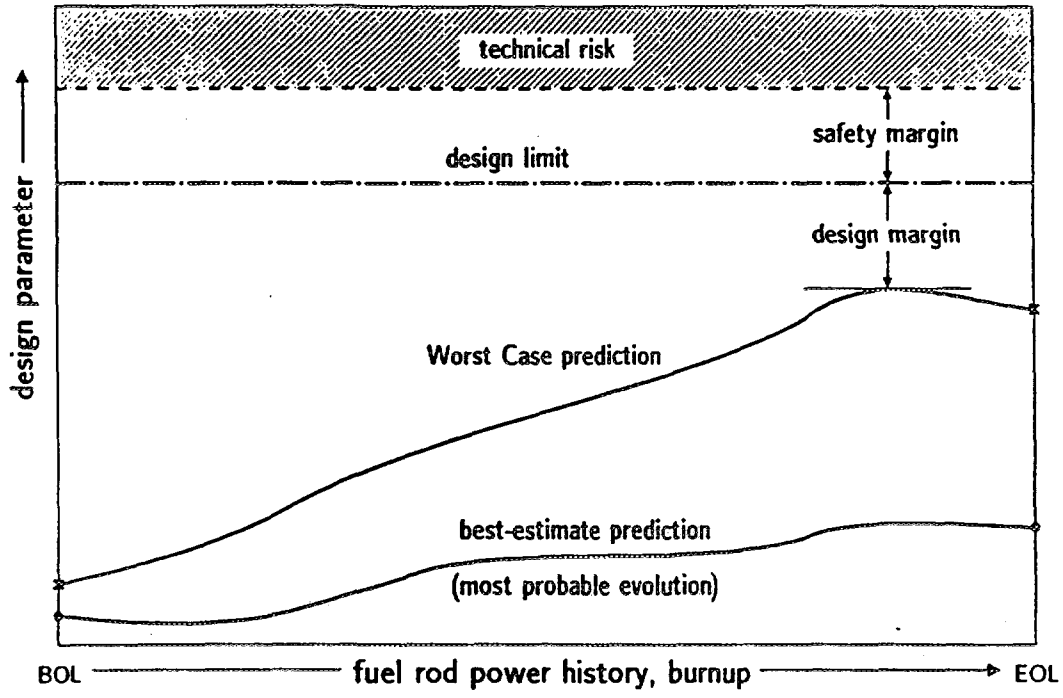

1. Principles of Deterministic Design Analyses

engineering these safety margins on top of the design margins could often not be quantified very precisely, and therefore the design limits were cautiously set on the safe side, i.e. "generously" off the risk limits defined by engineering judgement. This generosity was also stimulated by the awareness that fuel rod behavior controlling mechanisms were not always modelled reliably enough in the available codes or even not addressed - since they were not yet known.

2. INCREASING DEMANDS AND GROWING EXPERIENCE: CAUTIOUS REVISIONS OF CRITERIA WHILE KEEPING THE GENERAL METHODOLOGY

For a long time the just described methodology including its generously stipulated criteria was no severe limitation for the design engineer as the fuel was operated in a way that even under most unfavorable assumptions one did normally not come into conflict with the design limits. But then - mainly in the 1980's - things had developed into a direction where designing within the existing limits became increasingly tougher as the former comfortable margins to these limits narrowed down considerably. This happened mainly for two reasons: The fuel rod insertion conditions became more and more demanding and the rod designs themselves became more and more ambitious. Characteristics for the first are higher burnup, high efficiency loading patterns ("low leakage") and plant upratings; for the second the trend to an increased amount of UO_2 (or MOX) in the rods may be mentioned which is generally to the debit of the rod internal free volume.

On the other hand operating experience and knowledge gained from experimental programs had also grown; this led to both a firmer basis for the assessment of technical limits as well as upgraded fuel rod analysis codes (model improvements and broader validation data bases) with an increased reliability in their predictive capabilities. From there it was possible in particular cases to cautiously revise design criteria so that they gave again room for some margin without a higher technical risk as this could now more reliably be estimated. An example for such a redefined design criterion within an other vise unchanged methodology was the transition from the coolant pressure being the limit for the maximum rod internal pressure, to the clad "non-lift-off" criterion which demands that the pellet-to-clad gap must not re-open or widen due to an internal overpressure [2].

3. FURTHER CHALLENGES: INCREASINGLY DOMINANT MECHANISMS AND NEW PHENOMENA

Burnup extension is still an ongoing process which normally comes along with higher rated (and hence higher enriched) fuel. Parallel investigations and experimental programs have accompanied this process, and knowledge has increased about potential performance affecting phenomena associated with increasing burnup and thermo-mechanical loads of the fuel rods. Two of the currently most frequently addressed phenomena in this respect are fission gas release (FGR) and fuel oxide thermal conductivity (FTC).

3.1 FISSION GAS RELEASE AT EXTENDED BURNUP

While the discussion about the nature of the release mechanisms beyond a certain burnup range and their contribution to total FGR still goes on, there is at least consensus that higher rated fuel will release more fission gas at the same burnup as compared with more moderately operated, and that the fractional FGR rate experiences a more pronounced progression when entering burnup ranges above 55-60 MWd/kgU; Fig. 2 (out of [3]) clearly demonstrates this. Together with the fact that the amount of generated fission gas increases practically linearly with burnup, it becomes evident that FGR may develop into a major challenge for designing fuel rods for further extended burnup and accordingly enriched fuel. (E.g. in a 17x17 fuel rod 7 % FGR at a burnup of 60 MWd/kgU increase the free gas inventory by roughly half of the amount of the initial fill gas!)

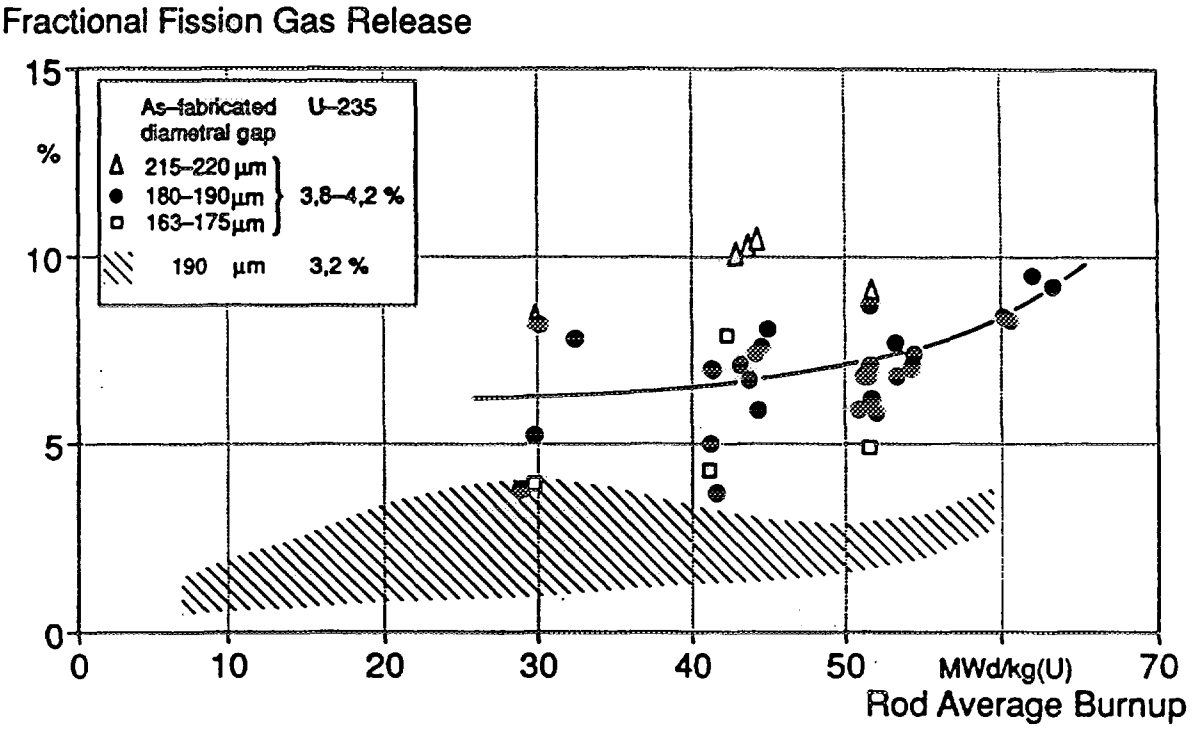

2. Fractional Fission Gas Release of Higher Enriched PWR Fuel Rods up to High Burnups [3].

3.2 BURNUP DEPENDENT FUEL OXIDE THERMAL CONDUCTIVITY

Fig. 2 also conveys clear evidence that FGR is a strongly temperature controlled mechanism. In this respect at least one contribution to FGR progression with increasing burnup (despite closing pellet-to-clad gap and normally decreasing rating) could be a degradation of FTC with burnup. Investigations into this phenomenon have been intensified within the last years [4], and they indeed revealed a steady decrease of the FTC with progressing burnup. This degradation is observed for the whole temperature range but differs quantitatively for different temperatures: the higher the oxide temperature the less pronounced the degradation in FTC.

Siemens/KWU performed own research and analyses in this field. Based on the evaluation of a series of Halden experiments and other experiments with well characterized temperature instrumented rodlets, this burnup dependence could very consistently be introduced by an additional term in the phonon contribution to the overall heat conductance mechanism as already described by van Vliet [5]. For 95 %T.D. the *Siemens/KWU* evaluation yields

$$k_{phonon} = 1/(A + B \cdot T + F \cdot \text{burnup})$$

with A,B = constants for fresh fuel

T = abs. Temperature

F = $0.0019(W/K\ m)^{-1}\ (MWd/kgU)^{-1}$.

For T = 1000 K the resulting decrease of k_{95} (the total FTC) with burnup is given in Fig. 3 together with a prediction derived from thermal diffusivity measurements on SIMFUEL, a UO_2 material which is "artificially burned" through appropriate homogeneous additions of solid fission product oxides [6]. The

SIMFUEL related curve can be regarded as a good confirmation of the described approach as the small difference can be attributed to effects in the real fuel behavior in addition to the contamination with fission products, e.g. sub-microscopic fission gas bubbles and microcracks. Fig. 4 finally demonstrates the already mentioned variation of the burnup effect for different oxide temperatures.

3.3 CARO-E, A FUEL ROD CODE TO BE APPLIED IN ANALYSES UP TO HIGH BURNUP

Siemens/KWU's fuel rod code CARO undergoes a continuous development on the basis of the company's growing experience in in-pile fuel rod behavior. Among many others the just discussed high burnup relevant items are incorporated in the newest level CARO-E which is currently in the final release procedure for routine design analysis work. As an example in Table I the FGR validation data base of CARO-E is compiled. It also contains the highest burnup points of Fig. 2; together with others they represent the high burnup data base reaching up to a fuel rod average value of 78 MWd/kgU. An essential feature of the code is of course the modeling of the burnup dependent FTC as discussed.

CARO-E is a best-estimate code in the sense as described in chpt. 1. The most recent benchmark of the code for FGR predictions against the data base of Table I is graphically represented in Figs. 5 and 6, which show the comparison of predicted vs. measured FGR and the scatter of predicted over measured values along the burnup., resp. Not only the high predictive capabilities of the code can be emphasized but also the broad validation base (both with respect of number of data as well as of parameter ranges) make CARO-E a reliable tool for fuel rod design analysis including the high burnup regime.

4. LIMITATIONS OF THE DETERMINISTIC DESIGN METHODOLOGIES: What is a realistic Worst Case and how likely is it to occur?

Applying a code with features just described for CARO-E in deterministic Worst Case analyses for fuel under modern highly demanding service conditions will obviously result in predictions which may again come very close to - if not already beyond - the established classical design limits, and this the more when extension of burnup is aimed for. The design engineer will of course counteract this tightness by optimizing the rod design accordingly; and the vastly grown experience and data bases in all fields of fuel

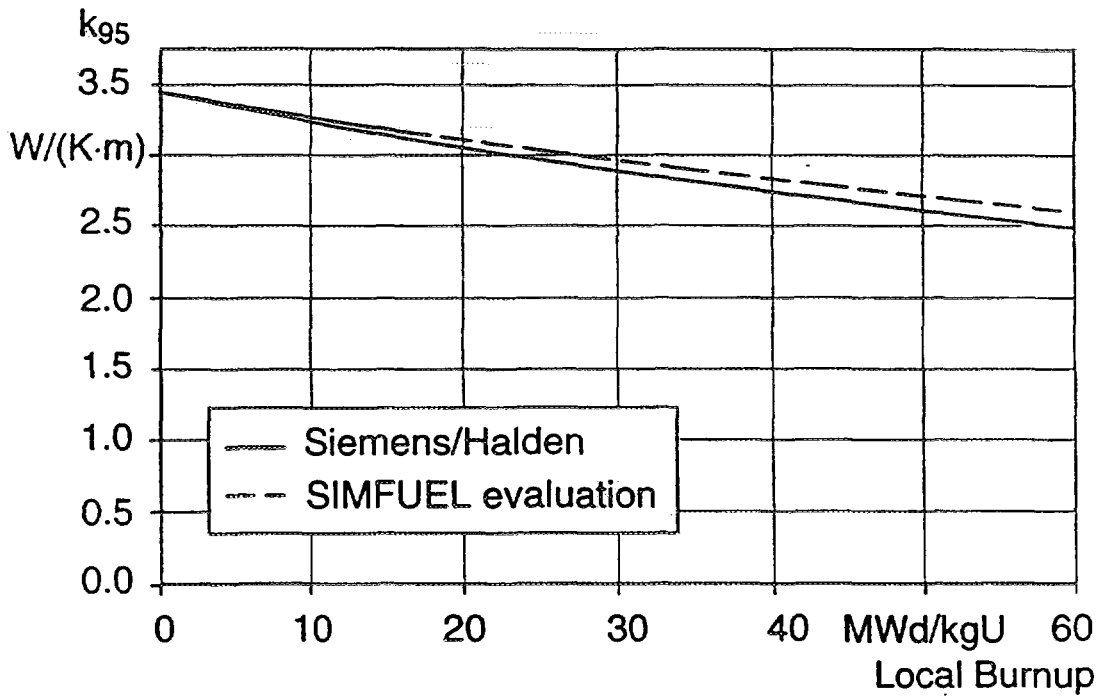

3. Burnup Dependence of Fuel Oxide Thermal Conductivity at 1000K

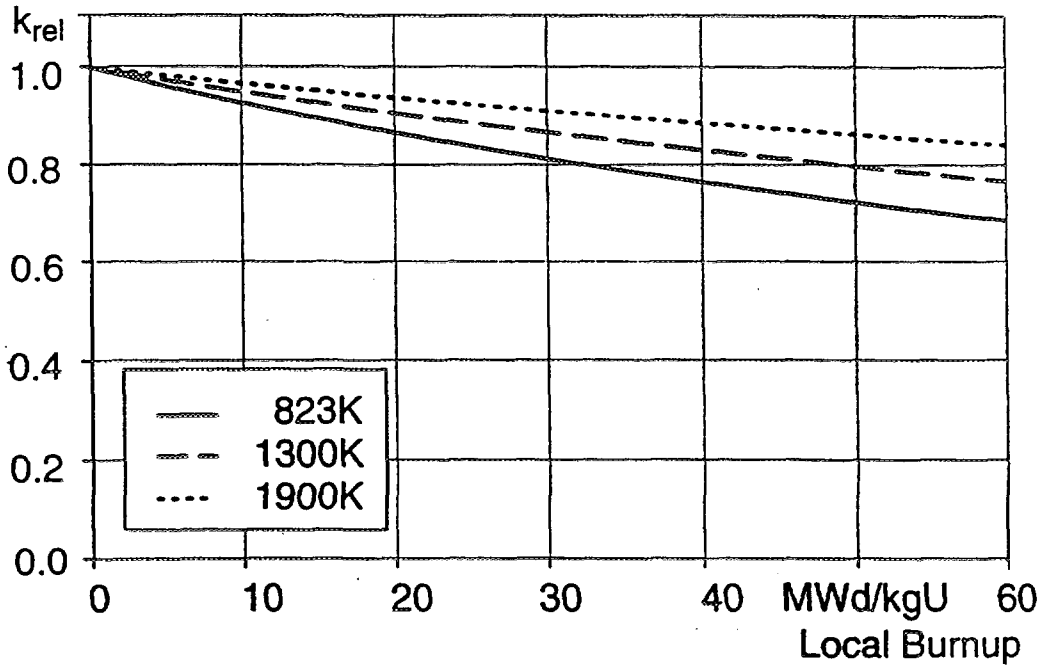

4. Relative Change of Fuel Oxide Thermal Conductivity with Burnup for Different Temperatures

Table 1 CARO-E Validation Data Base for Fission Gas Release

predominant type of release	no. of rods in burnup range [MWd/kgM] <30	30 _ 60	>60	rod type full length	segment	max. LHGR [W/cm]
steady-state	61	112	4	139	38	315*
transient (≤3 h)	1	8	–	–	9	440†
transient (>3 h)	53	49	–	21	81	620†

*cycle and rod averaged
†peak value

- total number of FGR data points: 288
  (pre-characterized rods with known individual power histories)
- comprises data from PWR and BWR
- UO_2, UO_2/Gd_2O_3 and MOX of different fabrication

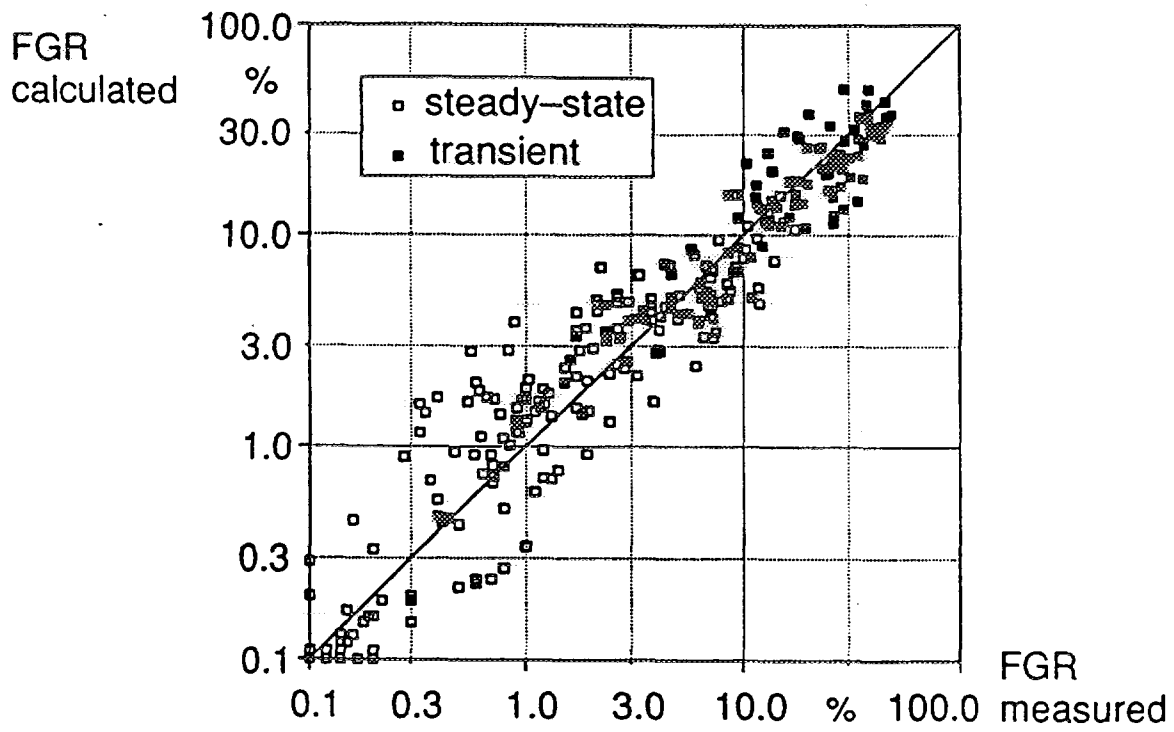

5. CARO-E Validation: Calculated (Best-Estimate) vs Measured Fission Gas Release

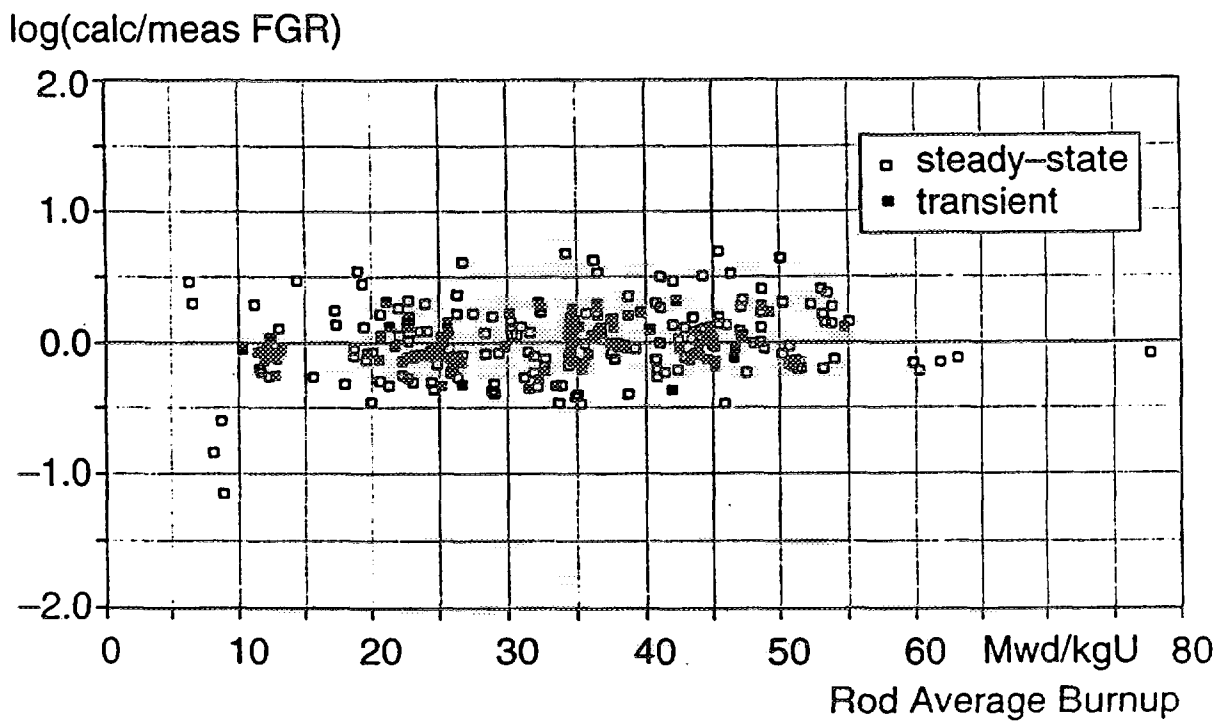

6. CARO-E Validation: Scatter of Predicted/Measured Fission Gas Release as a Function of Burnup

rod in-pile performance will also help him to do this much more efficiently than in the past. But nevertheless the former (and in some cases intermediately revised) margins will soon be consumed and cannot be recovered without design adaptations which imply economic drawbacks.

Now, before again looking out for potential revisions of design criteria, the general question should be asked whether the classical deterministic methodology is still an adequate approach. Any revision of an existing design criterion can only be justified through the meantime grown knowledge and experience, which comprise both the quantitative aspect of accumulated data bases as well as the general observation, that modern LWR fuel could and still can reliably and safely be operated under continuously growing technical and economic demands. Having this in mind one can argue just as well, that a new design analysis method should be established which makes adequate use of the high level of quantitative and qualitative experience gained in all the years since the early days, when lack of knowledge and scarce experience was compensated by conservative surcharges even for the Worst Case.

And the Worst Case itself: an agglomerate of thinkable unfavorable combinations of fabrication and performance model parameters, imputed to the full axial extension of the rod, and prevailing during its whole insertion time under most severe operating conditions! It is generally recognized, that this is a fiction which is intuitively extremely unlikely to happen in reality. The question is: what is a "realistic" Worst Case?

The main drawback of the deterministic "go/no go" Worst Case approach is also addressable in the following way: The analysis results are conservative, but there is no way to quantify the degree of conservatism, because neither the probability of the existence of the Worst Case nor the number of cases close to it but with other extreme parameter combinations, can be predicted. On the other hand this is what is needed for the assessment of a reload design and its real technical limits or margins: the distribution of the critical design parameters in the neighborhood of the design limits, which for themselves have in many cases also not necessarily to be sharp thresholds.

5. THE PROBABILISTIC DESIGN METHODOLOGY (PDM)

5.1 FREQUENCY DISTRIBUTIONS INSTEAD OF ISOLATED RESULTS

The requirements formulated in the last paragraph can be met by a *Probabilistic Design Methodology*. Its basic principles can easily be explained by referring again to the standard deterministic method as described in chpt. 1: That approach was based on calculations using well-aimed selections of (for the particular design parameter under consideration) most unfavorable combinations of the input quantities - fabrication parameters, model assumptions - and the severest power history (cf. Fig. 7). For the PDM the single Worst Case runs of the same best-estimate fuel rod code are replaced by a whole series of different runs, each using a different combination of possible input data, whereby each input quantity is randomly selected out of its individual distribution. Such a technique is long known as the Monte Carlo (MC) method, but only now after the introduction of powerful workstations the capability of this method can routinely be used on an economically and technically acceptable level. (To make the MC simulation more efficient the so-called Latin Hypercube Sampling [7] for the random input selection can be used.)

From each run with the code the results are recorded. The superposition of all output values for one design parameter finally generates a frequency distribution for each design parameter. (Fig. 8 gives a schematic representation of this procedure.) If the calculations are adequately performed, the thus obtained distributions can be regarded as representative samples of the values which the particular parameters can obtain in the fuel rods in the reactor core.

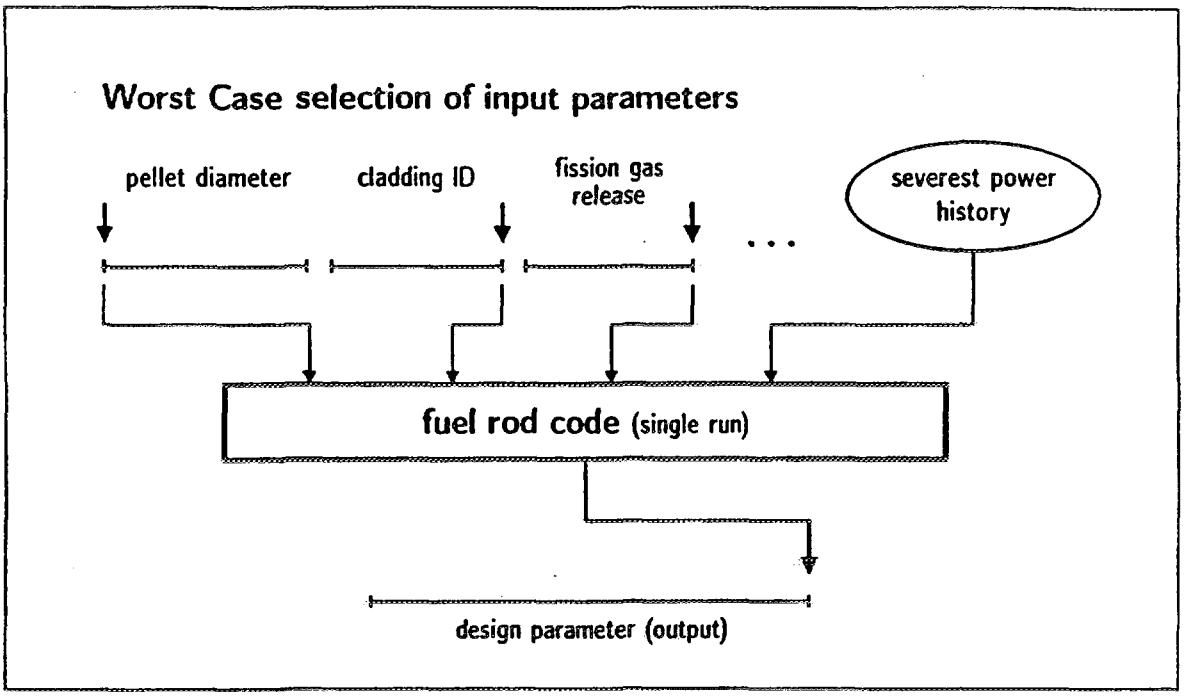

7. Standard Deterministic Methodology: Selection of Worst Case Input Set for One Design Criterion

5.2 NEED FOR A NEW FORMULATION OF DESIGN CRITERIA

The different design criteria are no longer addressed through individual (normally one another excluding) Worst Cases but by statements derived from the evaluation of the frequency distributions of the respective parameters, all resulting from the same series of MC runs.

Statements based on finite statistical samples should take into account the underlying statistical uncertainty. Therefore they should be formulated accordingly. E.g. for the rod internal pressure this could read as follows: With a statistical certainty of 95 % the pressure values of at least 95 % of the fuel rods in the core are below xxx bar. It is obvious that then the formulation of the corresponding design limit has usually also to be accommodated to reflect the statistical character of the results.

5.3 THE ELEMENTS OF THE PDM IN DETAIL

From the just described principles the following essential elements of the new methodology can be summarized [8]:

- a best-estimate fuel rod analysis code,
- a set of adequately formulated design criteria to be observed,
- statistical distributions for the relevant input quantities, which belong to two different classes as
  - rod fabrication data [9],
  - parameters for the rod behavior controlling mechanisms (model parameters; e.g. FGR model parameter distribution to reflect the calculated/ measured scatter of Fig. 5),

- a sufficiently large set of power histories, representative for all (at least for all relevant) power histories in the core,
- a conception for a sufficient number of MC runs with the fuel rod code on the just said distributions,
- generation of frequency distributions for the design (output) parameter of interest,
- analysis of the statistical uncertainty.

It should be recognized that those are the components of a full statistical analysis. For a routine application a somewhat simplified approach may be used which relies on a set of generic probabilistic analyses and demonstrates that a specific reload design is still within the bounds of the respective generic frequency distributions.

6. EXAMPLE FOR A PDM ANALYSIS: Assessment of maximum rod internal pressure

An example is presented in which a given fuel rod design is statistically analysed on a set of 2904 power histories out of a particular fuel management scheme. This set comprises all 3 and 4 cycle power histories in the core (equilibrium cycles, quarter core reload, part low leakage loading pattern). The example addresses the maximum rod internal pressure; the code used was CARO-E.

For comparison, the results of the corresponding deterministic design analysis performed with the yet used code version CARO-D5.S (for deterministic analyses) are given: Out of the set of the 2904 power histories, the limiting one for the rod internal pressure yields the following values:

- result of the most conservative input (Worst Case) 170 bar
- result of the nominal/best-estimate input 107 bar
- design limit (conservative against lift-off) 186 bar

The first value is the result which is stated in a *Siemens/KWU* standard fuel rod design report up to now; it is accepted since it is below the design limit.

In Table II results of the CARO-E MC analysis performed in the described way are summarized. In a first approach each power history out of the above mentioned set of 2904 had been combined with one random input data set of the fabrication data and modeling parameters. The random data set had been selected from the specific distributions of the input variables.

In the first 6 lines of Table II mean values and standard deviations are given for 6 such calculation series. From the very similar distributions it can be realized, that the results are already very stable. In the next steps the number N of runs per series had been increased by taking each of the power histories twice and four times, resp. The results are also given in Table II; the frequency distribution of the final series with N = 4 x 2904 = 11,616 runs is presented in Fig. 9. As can be seen from Table II and Fig. 9, even the extreme values of the output distributions are well below the classical deterministic result of 170 bar.

All distributions show a similar shape with a smooth continuously decreasing high value tail without any indications of lumps or irregular agglomerations. An approximation of the distribution by a log-normal probability density function seems quite reasonable.

With respect of design analysis results, statements on the tails of the distribution are important. To generate such results independently of single extreme values, statements in terms of quantiles and statistical certainties are appropriate. These statements are necessary to relate the results to the probabilistic design criterion which has to be formulated according to chpt. 5.2. Different quantiles are listed in Table II, columns 5 through 7; they are calculated with a statistical certainty of 95 %. (Standard textbook formulae are used to evaluate the quantiles as functions of the statistical uncertainty.)

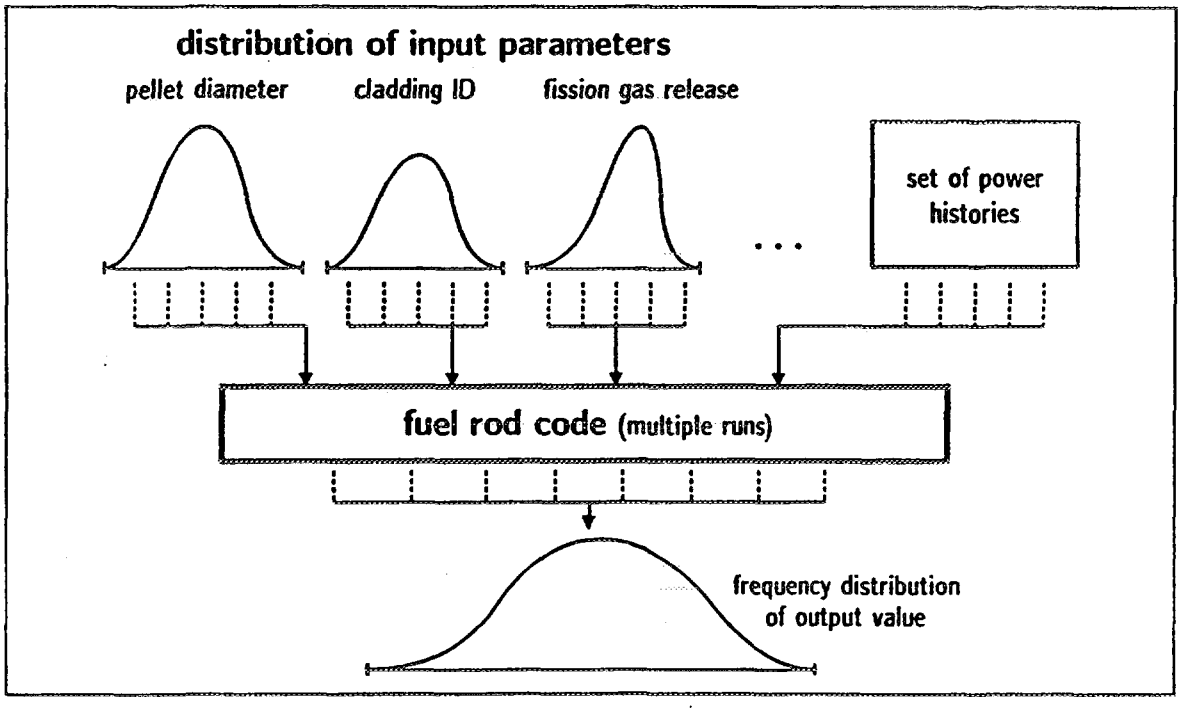

8. *Probabilistic Design Methodology: Monte Carlo Calculations to Generate Distribution of Performance Predictions*

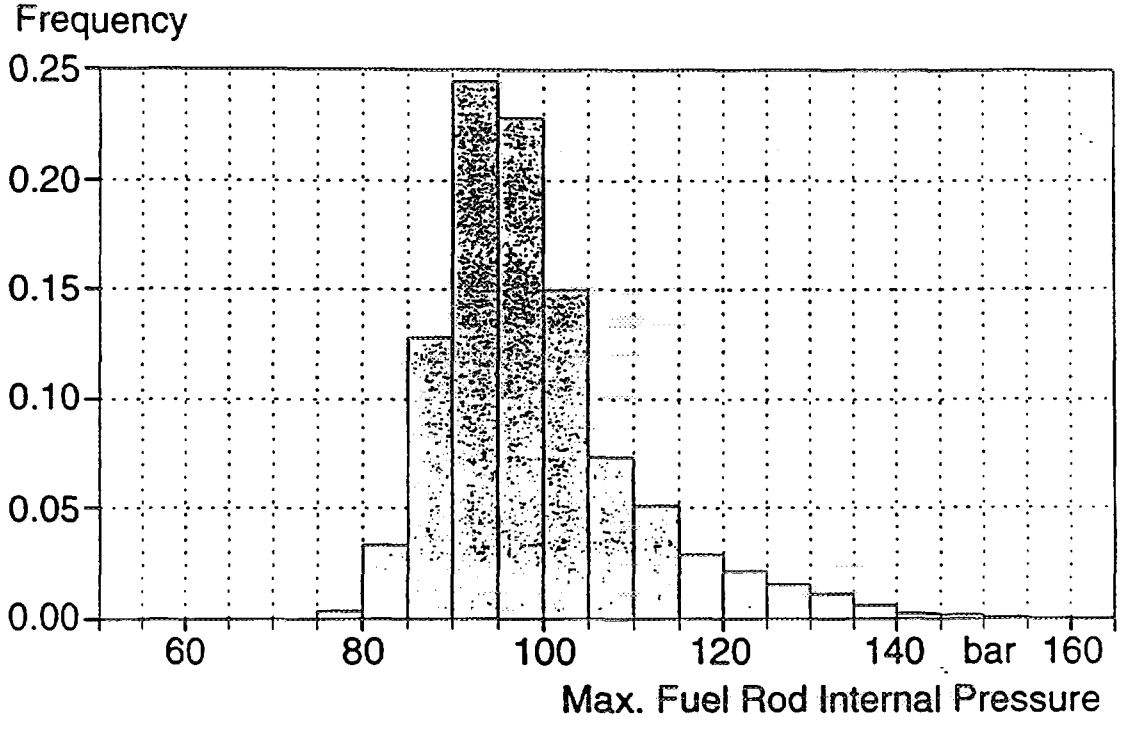

9. *Frequency Distributions of Maximum Rod Internal Pressure (N = 11,616 Runs)*

Table II Example Results of CARO-E Monte Carlo Calculation: Maximum Rod Internal Pressure

number of runs	series no.	mean value [bar]	standard deviation [bar]	95% quantile [bar]	99% quantile [bar]	99.9% quantile [bar]
2904	1	99.2	11.2	123.3	140.1	
	2	99.2	10.9	123.7	137.7	
	3	99.2	11.3	124.5	140.5	
	4	99.2	11.2	123.5	138.1	
	5	99.1	11.0	123.5	140.2	
	6	99.1	11.0	123.4	140.7	
5808	1	99.2	11.2	123.4	139.6	
11,616	1	99.2	11.1	122.3	138.9	154.1
	2	99.2	11.1	122.6	137.6	156.0

all quantiles are calculated for a statistical certainty of 95%

Based on the largest number (N = 11,616) of CARO-E runs, probabilistic statements on the high value tail of the distribution are possible; e.g.

(a) With a statistical certainty of 95 % the maximum internal pressure of at least 99 % (99.9 %) of all 3 and 4 cycle rods do not exceed 139 (156) bar.

(b) With a statistical certainty of 95 % the number of fuel rods with an internal pressure higher than 164 bar is less than 3.

In order to also quantify the influence of fabrication parameters, another series of MC calculations was performed during which as an example the cladding inner diameter was kept constant at its unfavorable (upper) tolerance limit; the result was that the 95 %/95 %-value had increased by only less than 5 bar [8].

7. CONCLUSIONS

Worst Case assessments in combination with conservative "go/no-go" design limits were for a long time adequate methods in fuel rod design analyses. Since in the meantime both the fuel insertion conditions became more and more demanding as well as knowledge about potential performance affecting mechanisms and experience data bases had considerably increased, time has come to replace the classical deterministic method by a probabilistic one which provides more, especially more differentiated information about a reload design.

An essential prerequisite is the availability of a high quality best-estimate fuel rod performance code which is validated against a sufficiently large and broadranging representative data base and which incorporates the newest perceptions of phenomena coming along with modern highly demanding insertion conditions.

The Probabilistic Design Methodology - applicable to any design criterion - is a powerful tool to realistically assess the behavior of the fuel rods in a reactor core. It has also the capability of characterizing the degree of conservatism within a reload design analysis through the statistical investigations of numbers of rods coming close to a design limit or by making statements about the statistical certainty for the actual occurrence of extreme cases. Thus real margins to design limits can be quantified, an important precondition if the fuel is to be operated into extended burnup regimes.

REFERENCES

[1] EBERLE, R., et al., How to Make a Fuel Rod Modelling Code Meet the Requirements of Design Applications, Nucl. Eng. Des. 101 (1987) 207--212

[2] EBERLE, R., et al., Fuel Rod Analysis in High Burnup Loading Schemes, IAEAIWGFPT/36, Proc. Techn. Comm. Meeting on Fuel Performance at High Burnup for Water Reactors, Studsvik/Sweden (1990) 172-180

[3] MANZEL, R., et al., Fuel Rod Behaviour at Extended Burnup, Proc. (ANS) 1994 Int. Topical Meeting on Light Water Reactor Fuel Performance, West Palm Beach/Florida (1994) 335-342

[4] TURNBULL, J.A., WHITE, R.J., The Effect of Burnup on Fuel Thermal Conductivity, HPR 333/3, Halden Project Seminar on High Bum-up Fuel Performance Topics, Fredrikstad/Norway (1987)

[5] Van VLIET, J., HAAS, D., Influence of Fission Products on UO2 Thermal Conductivity, 6th Post SMiRT Seminar on Mathematical/Mechanical Modelling of Reactor Fuel Elements, Kippel/Switzerland (1987)

[6] LUCATA, P.G., et al., Thermal Conductivity of SIMFUEL, J. Nucl. Mat. 188 (1992) 198-204

[7] McCAY, M.D., et al., A Comparison of Three Methods for Selecting Values of Input Variables in the Analysis of Output from a Computer Code, Technometrics 21 (1979) 239-245

[8] HEINS, L., SCHIEDEL, R., Probabilistic Fuel Rod Design Applied to Maximum Rod Internal Pressure Criterion of PWR Fuel Rods, Proc. (KTG) Annual Meeting on Nuclear Technology, Stuttgart/Gerrnany (1994) 319--322

[9] HEINS, L., et al., Statistical Analysis of QC Data and Estimation of Fuel Rod Behaviour, J. Nucl. Mat. 178 (1991) 287--295

PROBABILISTIC FUEL ROD ANALYSES USING THE TRANSURANUS CODE

K. LASSMANN, C. O'CARROLL, J. VAN DE LAAR
CEC Joint Research Centre,
Karlsruhe, Germany

Abstract

After more than 25 years of fuel rod modelling research, the basic concepts are well established and the limitations of the specific approaches are known. However, the widely used mechanistic approach leads in many cases to discrepancies between theoretical predictions and experimental evidence indicating that models are not exact and that some of the physical processes encountered are of stochastic nature. To better understand uncertainties and their consequences, the mechanistic approach must therefore be augmented by statistical analyses. In the present paper the basic probabilistic methods are briefly discussed. Two such probabilistic approaches are included in the fuel rod performance code TRANSURANUS: the Monte Carlo method and the Numerical Noise Analysis. These two techniques are compared and their capabilities are demonstrated.

1. INTRODUCTION

The safety of nuclear reactors is largely determined by the safe and reliable performance of fuel rods in which the radioactive fission products are generated and maintained. Besides many other measures to further increase the high safety standard of fuel rods, (such as material selection, control of fabrication processes, quality control and detailed irradiation experiments), fuel rod performance codes are used extensively in research, by manufacturers and licensing authorities to improve the design and to better understand and evaluate the fuel rod behaviour.

After more than 25 years of research of fuel rod modelling, the basic concepts are well established and the limitations of the specific approaches are known. However, the widely used mechanistic approach leads in many cases to discrepancies between theoretical predictions and experimental evidence indicating that most of the physical processes encountered are not sufficiently understood and cannot be modelled exactly. Some of these processes may even be of stochastic nature. Generally, the material behaviour is far too complex to be characterised by models or correlations consisting of a few parameters. Therefore, for a better understanding of the uncertainties involved and their technological consequences, the influence of the various parameters needs to be investigated which is best done by probabilistic methods.

In the present paper the basic probabilistic methods are briefly discussed. Two such probabilistic approaches are included in the fuel rod performance code TRANSURANUS [1, 2]: the Monte Carlo method and the Numerical Noise Analysis. These two techniques are compared and their capabilities are demonstrated.

2. GENERAL PROBABILISTIC METHODS

Probabilistic standard techniques are sensitivity methodologies, response surface techniques and Monte Carlo methods.

Sensitivity methodologies range from the multiple running of a problem, in which input data or model parameters are varied up to a rigorous mathematical treatment based on general perturbation theory.

Cady and Kenton [3, 4] developed an importance theory for a non-linear lumped parameter system formulated as a set of non-linear differential equations which allows the calculation of

a) the sensitivity of a response function to any physical or design parameter,
b) the importance of any parameter and
c) the variance of the response function caused by the variances and covariances of all parameters.

The importance theory provides more information than an ordinary system integration. However, this method has never been used in fuel rod modelling, probably because the mathematical effort would be too great to formulate the many local, highly non-linear phenomena such as fission gas release in the form of the basic differential equations needed.

The response surface technique has first been used in the fuel rod performance code FRAP by Peck [5]. This code allows an uncertainty analysis of the steady-state and transient behaviour of LWR fuel rods. Sengpiel [6] extended this methodology to the analysis of events with low probability in a loss of coolant accident. The construction of a response surface is based upon a careful combination of variations of parameters called the experimental design (sampling). One standard technique is the Latin hypercube sampling. The problem is that one has to decide in advance what parameter should be selected and how fine the variation of each parameter should be performed.

The Monte Carlo method is simple and straightforward. Its main drawbacks are:

a) high computer costs,
b) it does not provide any information between the variation of parameters and the variations of the results and
c) it gives no information about the relative contribution of specific parameters to the overall uncertainty.

The Monte Carlo method is based upon random sampling with the consequence that "clustering" cannot be avoided. Clustering means that very similar combinations of parameters are calculated which increase the numerical expenditure but do not increase the overall accuracy. Instead of random sampling quasi-random sequences are recommended [7] which fill the space more uniformly than uncorrelated random numbers. Usage of quasi-random sequences leads to Quasi-Monte Carlo methods which may be considered as a combination of the variation of parameters in response surface techniques with its experimental design and the standard Monte Carlo technique. Quasi-Monte Carlo methods should increase the accuracy since the error is proportional to $1/n$ compared with a $1/\sqrt{n}$ dependence for the standard Monte Carlo method where n is the number of computer runs. In other words the application of a Quasi-Monte Carlo method should result in a reduction of runs.

Probabilistic methods have not been used frequently until now and there are only few publications (for instance Ref. 8-12). However, with the advent of cheap and fast workstations the situation will certainly change.

3. PROBABILISTIC OPTIONS OF THE TRANSURANUS CODE

The fuel rod performance code TRANSURANUS offers as standard probabilistic option a Monte Carlo technique which is fully justified in view of the achievements reached by modern hard- and software improvements of computer technology as well as the progress made in numerical methods. This technique avoids the problems encountered with sensitivity methodologies and response surface techniques in finding the relevant parameters and in doing a correct sampling. The second technique employed in the TRANSURANUS code is the Numerical Noise Analysis [12] which offers the advantage that the computational costs are approximately identical with a deterministic analysis.

In the following both probabilistic approaches are compared in order to demonstrate the probabilistic capabilities of the TRANSURANUS code.

3.1 MONTE CARLO METHOD

The applied simple Monte Carlo technique is straightforward. The following quantities are treated as statistical (random) variables, i.e. are varied in each Monte Carlo run:

a) Geometry of the fuel rod (fuel and cladding)
b) Specific models, e.g. the gap conductance
c) All material properties in fuel, cladding and coolant (thermal conductivity, thermal strain etc.)
d) All prescribed quantities (linear rating, mass flow rate, boundary conditions etc.)

The computational costs depend on the number of Monte Carlo runs. In practise 100 to 500 runs turned out to be sufficient, which means that the costs of such a statistical Monte-Carlo analysis increase by a factor of 100 to 500 compared with a deterministic analysis.

3.2 OUTLINE OF NUMERICAL NOISE ANALYSIS MODEL

The fundamental idea underlying this approach is the following: analogous to standard noise analysis of measured quantities the most important parameters of the fuel rod model are varied slightly on a Monte-Carlo basis in each time interval $\Delta t = t_{n+1} - t_n$. These changes of model parameters result in changes of the different resulting quantities (such as for instance centre line temperatures) which can be

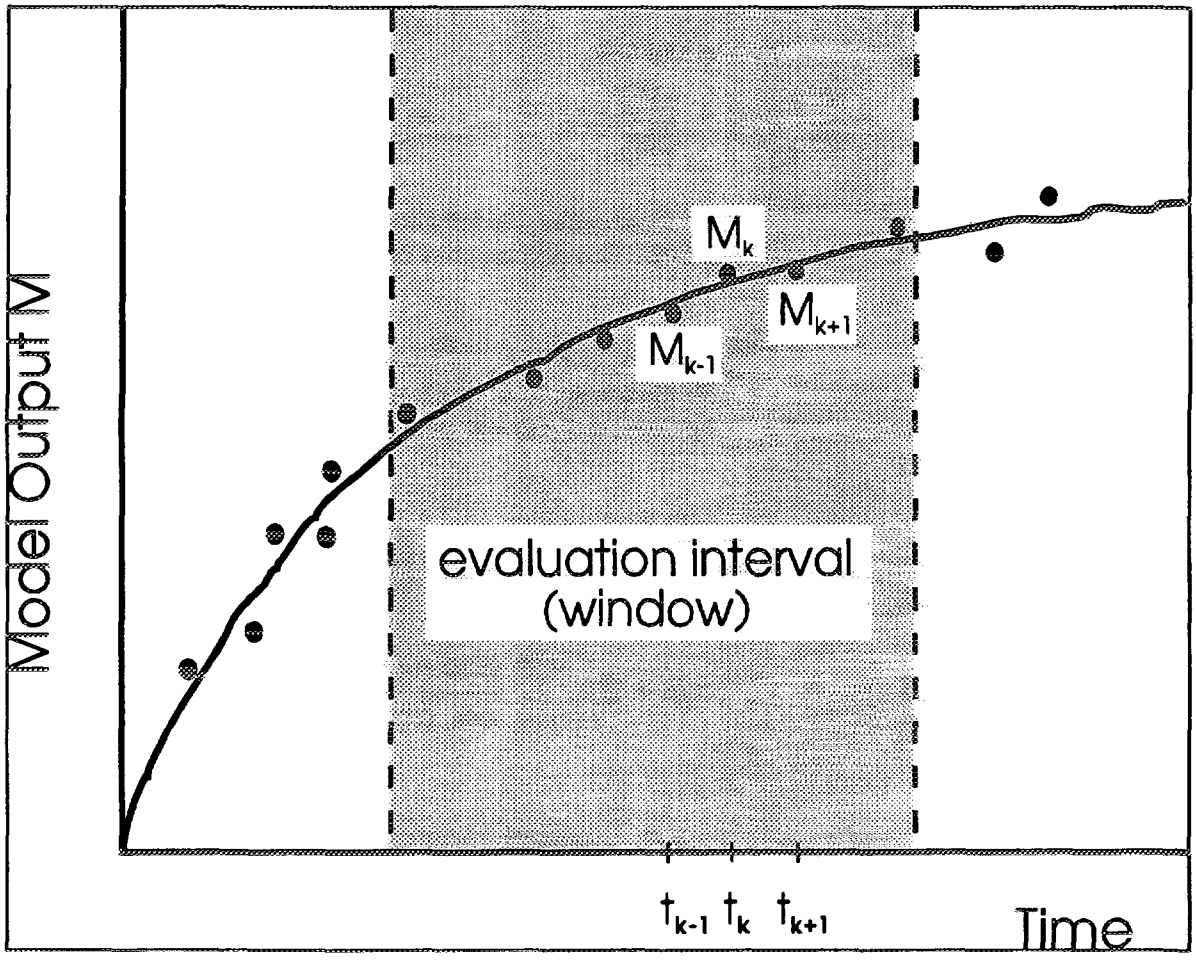

Basic principle of the Numerical Noise Analysis: definition of the evaluation interval or window

regarded as artificially produced "numerical noise". The known variation of model parameters and the resulting variation of the model results allow the analysis of the sensitivity of the model with respect to its parameters. Two limitations become apparent:

1. The changes of the parameters during a time interval may influence the unperturbed numerical solution only slightly, roughly within the numerical accuracy. This requirement is easy to meet since modern compilers have a possibility to automatically increase the accuracy. If a certain accuracy is sufficient for the unperturbed solution the perturbed computer model can be calculated with greater accuracy in such a way that perturbations will not influence the solutions in their previous accuracy, but further digits will be available for evaluation of the influence parameters. Of course, the numerical accuracy of an iterative solution is only increased if the limits of convergence are reduced correspondingly.

2. The numerical noise analysis can only be applied over several time steps (the evaluation interval or window, see schematic Figure below) with the condition that the number of time steps m is larger then the number ℓ of unknown parameters.

The general equations are derived as follows: consider any prediction of a model that depends on parameters α_i ($i = 1, 2, \ldots, \ell$). The sensitivity coefficients, $\partial M/\partial_i \alpha$, of the model prediction can be obtained from known variations $\Delta\alpha_i^k$ defined by

$$(1)\quad \Delta\alpha_i^k = \alpha_i(t = t_k) - \alpha_i(t = t_{k-1})$$

and known variations ΔM_k in the evaluation interval:

$$(2)\quad \Delta M_k = M_k - M_{k-1} = \frac{\partial M}{\partial \alpha_1}\Delta\alpha_1^k + \frac{\partial M}{\partial \alpha_2}\Delta\alpha_2^k + \ldots, \qquad k = 2, m+1 \qquad m > \ell$$

where m is the number of subintervals in the whole evaluation interval. In order to obtain the variations of the parameters α_i they are randomly disturbed. This process may be considered as the introduction of numerical noise.

Equation (2) constitutes an overdetermined system of equations, $\mathbf{a}\,\mathbf{x} = \mathbf{b}$, which is solved in a least square sense by multiplying the equation with the transpose $\mathbf{a}^T$ of the matrix $\mathbf{a}$. The resulting matrix $\mathbf{a}^T\mathbf{a}$ of the system of equations is symmetrical and positive definite and can be solved effectively by a Cholesky algorithm without pivoting.

The predicted M is considered as function of the random variables α_i and all the appropriate statistical techniques may be used. From the sensitivity coefficients, $\delta M/\delta\alpha_i$, the uncertainty of the model prediction is given by the variance of M

$$(3a)\quad var\ M = \sum_{i=1}^{\ell}\left(\frac{\partial M}{\partial \alpha_i}\right)^2 var(\alpha_i) + 2\sum_{i=1}^{\ell}\sum_{j=1}^{j<\ell}\frac{\partial M}{\partial \alpha_i}\frac{\partial M}{\partial \alpha_j}\ covar\ (\alpha_i,\alpha_j)$$

or

$$(3b)\quad \sigma_M^2 = \sum_{i=1}^{\ell}\left(\frac{\partial M}{\partial \alpha_i}\right)^2 \sigma_{\alpha_i}^2 + 2\sum_{i=1}^{\ell}\sum_{j=1}^{j<\ell}\frac{\partial M}{\partial \alpha_i}\frac{\partial M}{\partial \alpha_j}\rho_{ij}\sigma_{\alpha_i}\sigma_{\alpha j}$$

where σ_{α_i} is the standard deviation of the parameter α_i and $\rho_{i,j}$ the correlation coefficient between the parameters α_i and α_j.

The equations given above have some aspects in common with general sensitivity methods, however, they must be considered as a special case. At present this method is applied within the TRANSURANUS code to three relevant parameters: linear rating q', gap conductance h_{gap} and thermal conductivity λ_{fuel} of the fuel. The analyses provide the uncertainty of the centre line temperature, $\vartheta_{c,fuel}$, the integral fission gas release f, and the inner pin pressure p_i. Details of these analyses are given in the subsequent sections.

3.3 FUEL ROD MODEL

The sensitivity coefficients of the fuel centre line temperature $\vartheta_{c,fuel}$ at a specific axial position can be estimated from the approximate analytic solution

$$(4) \qquad \vartheta_{c,fuel} \approx \vartheta_{cool} + \frac{q'}{2\pi}\left(\frac{1}{r_{clad}^{outer} h_{clad-cool}} + \frac{s_{clad}}{r_{clad}^{av} \lambda_{clad}} + \frac{1}{r_{fuel}^{outer} h_{gap}} + \frac{1}{2\lambda_{fuel}} \right)$$

where the linear rating q', the gap conductance h_{gap} and the thermal conductivity of the fuel, λ_{fuel}, are considered as random variables; r is the radius and s the thickness. Eq (4) gives in an analytic form the relevant dependencies from which the sensitivity coefficients of the fuel centre temperature with respect to linear rating, gap conductance and thermal conductivity can be approximated:

$$(5a) \qquad \frac{\delta \vartheta_{c,fuel}}{\delta q'} = c_1$$

$$(5b) \qquad \frac{\delta \vartheta_{c,fuel}}{\delta h_{gap}} = c_2 \frac{q'}{h_{gap}^2}$$

$$(5c) \qquad \frac{\delta \vartheta_{c,fuel}}{\delta \lambda_{fuel}} = c_3 \frac{q'}{\lambda_{fuel}^2}$$

The constants c_1, c_2 and c_3 are the unknowns to be fitted. In comparison to eq (4) they take - when fitted to a detailed fuel rod model - the behaviour of a realistic fuel rod into account. The uncertainty of the centre temperature, σ_ϑ, is given by eq. (3).

Fission gas release is a highly nonlinear, local and time dependent process which can only roughly be approximated by a simple, incremental point model. We assume that the fission gas release rate $\dot{c}_{rel}$ is given by

$$(6) \qquad \dot{c}_{rel} = c_4 \left(\overline{\vartheta}_{c,fuel}^{rod} - \vartheta_0 \right) \left(c_{grain} + c_{gb} \right)$$

where $\overline{\vartheta}_{c,fuel}^{rod}$ is the average fuel rod centre temperature, c_{grain} and c_{gb} is the total amount of fission gas in the grains and at grain boundaries, all quantities taken at time t. The term $\left(\overline{\vartheta}_{c,fuel}^{rod} - \vartheta_0 \right)$ accounts for the nonlinearity of fission gas release with temperature; ϑ_0 is a model parameter (typically 1000 °C) that can be considered as a threshold for fission gas release. The uncertainty of the fission gas released during a time step $\Delta t = t_{n+1} - t_n$ is

(7) $$\Delta\sigma_{c_{rel}} = c_4\left(c_{grain} + c_{gb}\right)\bar{\sigma}_{\vartheta}^{rod}\Delta t$$

where $\bar{\sigma}_{\vartheta}^{rod}$ is the uncertainty of the average fuel rod centre temperature. $\bar{\sigma}_{\vartheta}^{rod}$ is obtained by applying eqs. (3 and 5) to all sections or slices of the fuel rod.

The uncertainty of the total fission gas released is

(8) $$\sigma_{c_{rel}}\left(t = t_{n+1}\right) = \sigma_{c_{rel}}\left(t = t_n\right) + \Delta\sigma_{c_{rel}}$$

where c_{gas} is the total gas inside the fuel pin (fillgas and fission gas released c_{rel}). The inner gas pressure p_i is approximated by

(9) $$p_i = c_5 c_{gas}\bar{\vartheta}_{c,fuel}^{rod} + c_6 c_{gas}\vartheta_{cool,out}$$

with the uncertainty

(10) $$\sigma_{Pi} = c_5\ \sigma_{c_{rel}}\bar{\vartheta}_{c,fuel}^{rod} + c_6\ \sigma_{c_{rel}}\vartheta_{cool,out}$$

4. RESULTS OF PROBABILISTIC TRANSURANUS ANALYSES

Exact solutions are available for many specific problems in fuel rod structural analysis. Here, the simplest case of a thermal analysis shall be used. Making the assumptions a) cylindrical, solid fuel geometry, b) steady state c) constant radial power density and d) constant thermal conductivity λ, the centre temperature $\vartheta_{c,fuel}$ in the fuel is given by

(11) $$\vartheta^* = \frac{q'}{4\pi\lambda}$$

where $\vartheta^* = \vartheta_{c,fuel} - \vartheta_{outer}$

To test the two statistical packages of the TRANSURANUS code two cases are investigated. In the first case only the linear rating q' is treated as a continuous random variable with a Gaussian probability density distribution, characterised by a mean linear rating $\bar{q}'$ and a standard deviation σ_q. The resulting probability density function of the centre temperature of the fuel, f_ϑ , is

(12) $$f_\vartheta(\vartheta^*) = \frac{4\pi\lambda}{\sigma_q\sqrt{2\pi}} e^{-\frac{\left(\vartheta^* - \frac{\bar{q}'}{4\pi\lambda}\right)^2}{2\left(\frac{\sigma q}{4\pi\lambda}\right)^2}}$$

Note that in Eq. (12) the thermal conductivity λ is considered as constant.

In the second case both, q' and the thermal conductivity λ are considered as random variables. Equation (11) is written as $\vartheta^* = x / \lambda$ where

$$x = \frac{q'}{4\pi} \quad ; \quad \bar{x} = \frac{\bar{q}'}{4\pi} \quad and \quad \sigma_x = \frac{\sigma_q}{4\pi}$$

The resulting probability density function of the centre temperature of the fuel, f_ϑ, is

$$(13) \qquad f_\vartheta(\vartheta^*) = \frac{e^{\frac{b^2}{2a} - \frac{c}{2}}}{\pi a \sigma_x \sigma_\lambda}\left[e^{-\frac{b^2}{2a}} + b\sqrt{\frac{\pi}{2a}}\,erf\left(\frac{b}{\sqrt{2a}}\right)\right]$$

where

$$a = \left(\frac{\vartheta^*}{\sigma_x}\right)^2 + \frac{1}{\sigma_\lambda^2} \quad ; \quad b = \frac{\vartheta^*\bar{x}}{\sigma_x^2} + \frac{\bar{\lambda}}{\sigma_\lambda^2} \quad ; \quad c = \left(\frac{\bar{x}}{\sigma_x}\right)^2 + \left(\frac{\bar{\lambda}}{\sigma_\lambda}\right)$$

Figures 1 and 2 show the excellent agreement between the exact solution, the Monte-Carlo technique and the Numerical Noise analysis. Mean values and standard deviations are compared in Tables I and II. Figure 3 shows an example where the centre line temperature is given as a function of time. Compared are the exact error and the errors according to the Numerical Noise analysis.

The FUMEX case 2 may serve as an example of a probabilistic analysis for a real fuel irradiation which took place in the Halden reactor. Fig. 4 shows the fission gas release as a function of time. Here the agreement is only reasonable.

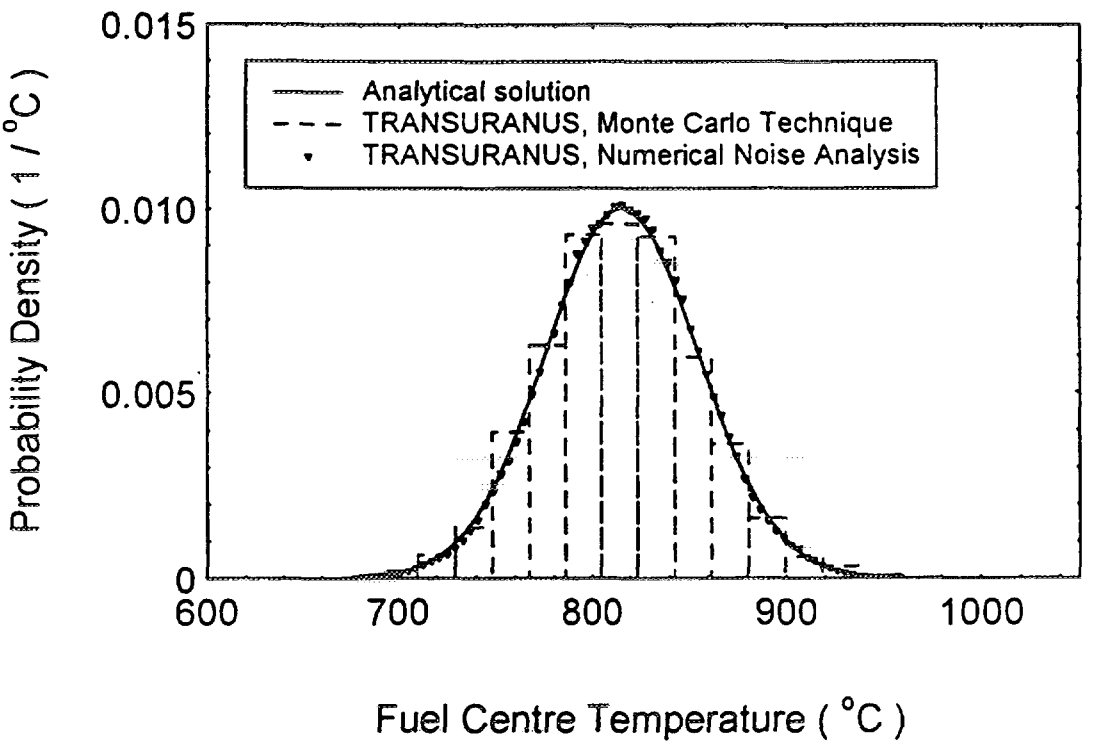

FIG. 1. *Probability density function of the fuel centre temperature; Comparison between the exact solution, the Monte Carlo technique and the Numerical Noise Analysis according to the TRANSURANUS code for case 1 in which the linear rating q' was treated as continuous random variable.*

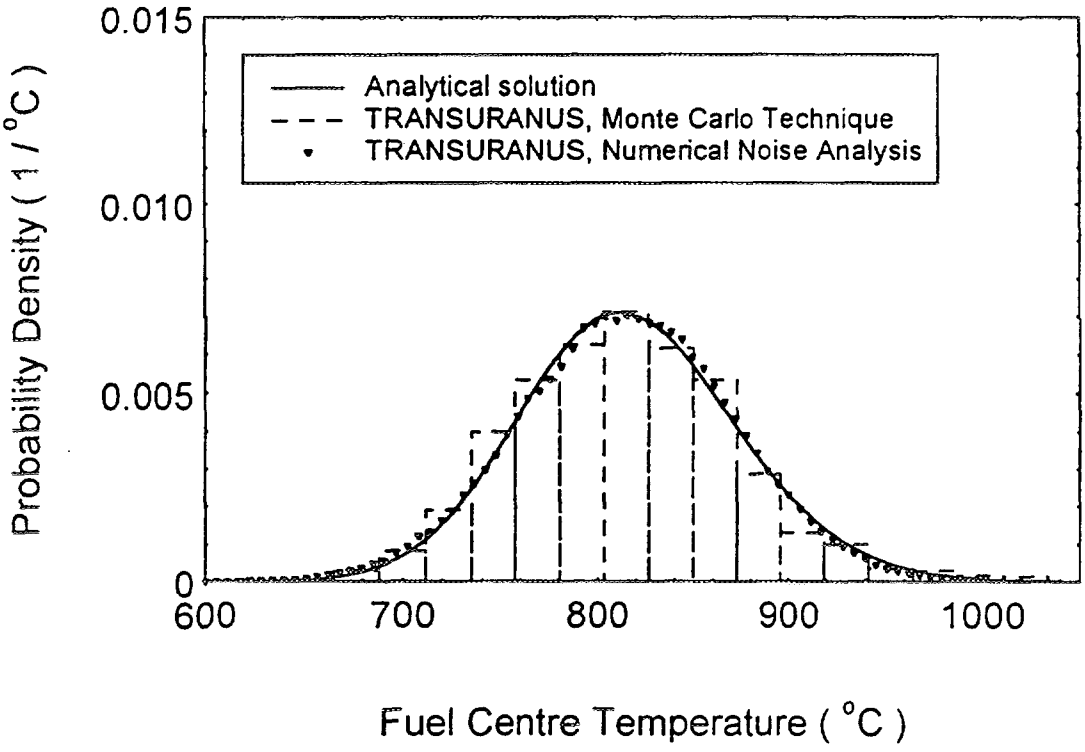

FIG. 2. *Probability density function of the fuel centre temperature; Comparison between the exact solution, the Monte Carlo technique and the Numerical Noise Analysis according to the TRANSURANUS code for case 2 in which the linear rating q' and the thermal conductivity l were treated as continuous random variables.*

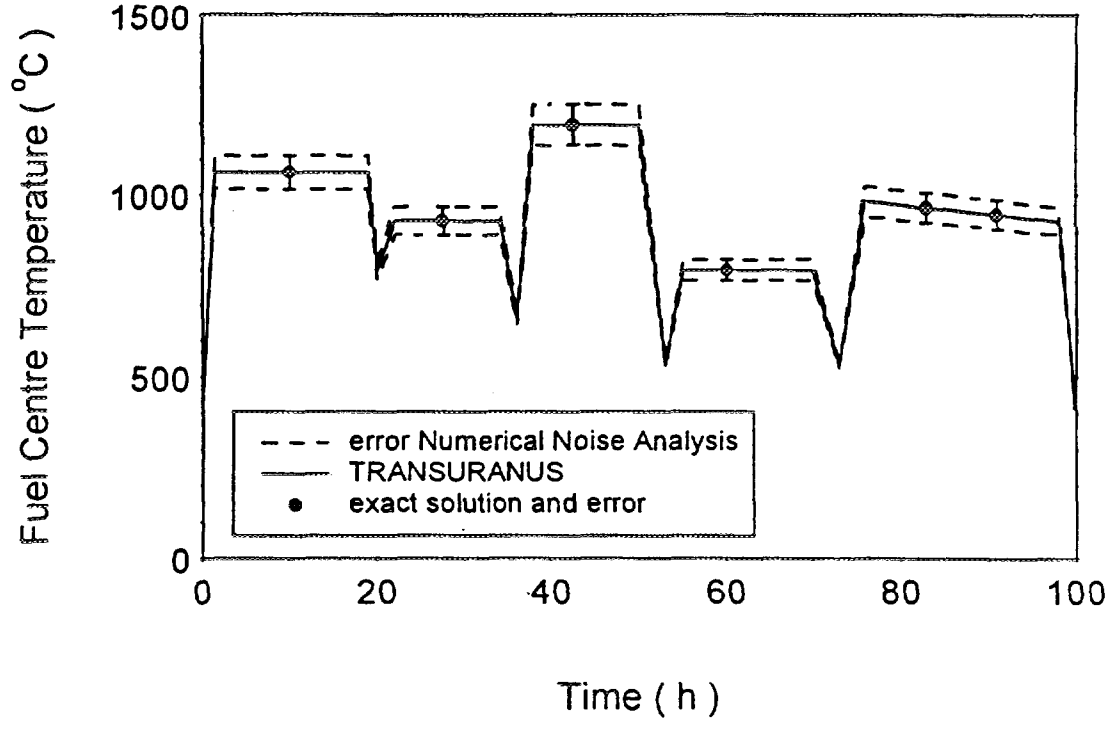

FIG. 3. *Fuel centre temperature as a function of time: Comparison between the exact solution and the Numerical Noise Analysis according to the TRANSURANUS code; the linear rating q' and the thermal conductivity l of the fuel were treated as continuous random variables.*

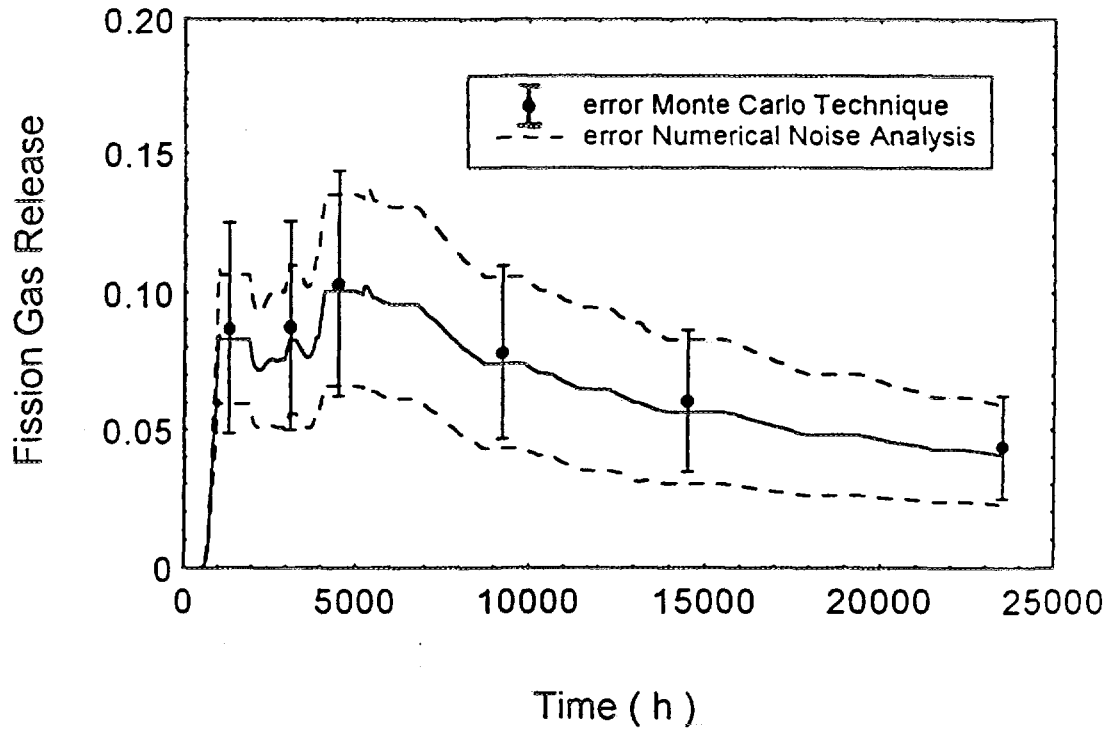

FIG. 4. *Fission gas release as a function of time: Comparison between the exact solution and the Numerical Noise Analysis according to the TRANSURANUS code; the linear rating q' and the thermal conductivity l of the fuel were treated as continuous random variables.*

Table I: Comparison between exact solutions, the Monte Carlo method and the Numerical Noise analysis; the linear rating q' was treated as random variable

Exact solution	$\overline{\vartheta}_{c,fuel} = 815,775$	$\sigma_{\vartheta} = 39,789$
TRANSURANUS Monte Carlo technique	$\overline{\vartheta}_{c,fuel} = 816,399$	$\sigma_{\vartheta} = 39,725$
TRANSURANUS Numerical Noise Analysis	$\overline{\vartheta}_{c,fuel} = 815,630$	$\sigma_{\vartheta} = 39,025$

Table II: Comparison between exact solutions, the Monte Carlo method and the Numerical Noise analysis; the linear rating q' and the thermal conductivity λ were treated as random variables

Exact solution	$\overline{\vartheta}_{c,fuel} = 817,779^{a)}$	$\sigma_{\vartheta} = 56,66^{a)}$
TRANSURANUS Monte Carlo technique	$\overline{\vartheta}_{c,fuel} = 816,399$	$\sigma_{\vartheta} = 58,21$
TRANSURANUS Numerical Noise Analysis	$\overline{\vartheta}_{c,fuel} = 815,630$	$\sigma_{\vartheta} = 55,99$

a) The mean of the centre temperature $\overline{\vartheta}_{c,fuel}$ and the standard deviation σ_{ϑ} can only be derived numerically.

5. CONCLUSIONS

Probabilistic methods have not been used frequently until now and there are only a few publications in the area of modelling the fuel rod behaviour. However, with the advent of cheap and fast workstations now available, the situation will certainly change. The fuel rod performance code TRANSURANUS includes two such probabilistic approaches : the Monte Carlo method and the Numerical Noise Analysis. The Monte Carlo method must be considered as a very flexible, general approach whereas the Numerical Noise Analysis is more specific and limited. At present this method is applied within the TRANSURANUS code to three relevant parameters which dominate the fuel rod behaviour: linear rating q', gap conductance h_{gap} and thermal conductivity λ_{fuel} of the fuel. The analyses provide the uncertainty of the centre line temperature $\vartheta_{c,fuel}$, the integral fission gas release f, and the inner pin pressure p_i. The main advantage of the Numerical Noise Analysis is that by considering these relevant parameters as random variables a fairly good probabilistic analysis can be performed at the expense of approximately only one single deterministic analysis.

REFERENCES

[1] LASSMANN, K., BLANK, H., Modelling of Fuel Rod Behaviour and Recent Advances of the TRANSURANUS Code, Nucl. Eng. Design, 106 (1988), 291-313

[2] LASSMANN, K., TRANSURANUS: A Fuel Rod Analysis Code Ready for Use, Journal of Nuclear Materials, 188 (1992) 295-302

[3] KENTON, M.A., A general sensitivity theory for simulations of non-linear time-dependent systems, PhD thesis CURL-58, Cornell University, Nuclear Reactor Laborator , Ithaka, New York (1981)

[4] CADY K.B., KENTON, M.A. An Importance theory for lumped parameter systems, Transactions of the American Nuclear Society, TANSAO 38 (1981), 331

[5] PECK, S.O. , Automated uncertainty analysis methods in the FRAP computer codes, IAEA Specialist's Meeting on Fuel Element Performance Computer Modelling, Blackpool, U.K. (1980)

[6] SENGPIEL, W., Probabilistische Untersuchungen des Brennstabverhaltens in einem Brennelement eines Druckwasserreaktors bei einem hypothetischen Kühlmittelverluststörfall, Kernforschungszentrum Karlsruhe, KfK 2965 (1980)

[7] PRESS, W.H. et al., Numerical Recipes in FORTRAN: The Art of Scientific Computing, Cambridge University Press, ISBN 0-521-43064-X (1992)

[8] PALMER, I.D., Probabilistic performance analysis using the SLEUTH fuel modelling code, IAEA Specialists' Meeting on Water Reactor Fuel Element Performance Computer Modelling, Bowness-on-Windermere, UK (1984) IAEA-IWGFPT/19, 166

[9] ROSSI, J., SAIRANEN, R., Uncertainty analysis of fuel rod steady-state thermal behaviour by the probabilistic response surface method, IAEA Specialists' Meeting on Water Reactor Fuel Element Performance Computer Modelling, Bowness-on-Windermere, UK (1984) IAEA-IWGFPT/19, 179

[10] BULL, A.J., A probabilistic analysis of PWR and BWR fuel rod performance using the code CASINO-Sleuth, Nucl. Eng. and Design 101 (1987) 213

[11] HEINS, L. et al., Statistical analysis of QC data and estimation of fuel rod behaviour, Journal of Nuclear Materials 178 (1991) 287

[12] LASSMANN, K., Numerical Noise Analysis: A New Probabilistic Technique, Computer Methods in Applied Mechanics and Engineering 40 (1983), 111-119

MODELLING CHEMICAL BEHAVIOUR OF WATER REACTOR FUEL

R.G.J. BALL, J. HENSHAW, P.K. MASON, M.A. MIGNANELLI
AEA Technology,
Harwell, Didcot, Oxfordshire,
United Kingdom

Abstract

For many applications, large computer codes have been developed which use correlation's, simplifications and approximations in order to describe the complex situations which may occur during the operation of nuclear plant or during fault scenarios. However, it is important to have a firm physical basis for simplifications and approximations in such codes and, therefore, there has been an emphasis on modelling the behaviour of materials and processes on a more detailed or fundamental basis. The application of fundamental modelling techniques to simulate various chemical phenomena in thermal reactor fuel systems are described in this paper. These methods include thermochemical modelling, kinetic and mass transfer modelling and atomistic simulation and examples of each approach are presented. In each of these applications a summary of the methods are discussed together with the assessment process adopted to provide the fundamental parameters which form the basis of the calculation.

1. INTRODUCTION

Much effort has been put into the development of modelling techniques for studying chemical processes relevant to nuclear power generation, reflecting the difficulties inherent in studying such processes experimentally. For many applications, large computer codes have been developed which use correlation's, simplifications and approximations in order to describe the complex situations which may occur during the operation of nuclear plant or during fault scenarios. However, it is important to have a firm physical basis for the simplifications and approximations in such codes and, therefore, there has also been an emphasis on modelling the behaviour of materials and processes on a more detailed or fundamental basis.

Among the fundamental modelling techniques, some make no assumptions about the microscopic nature of the materials whereas others describe behaviour on an atomic level. In the former category, thermochemical modelling has long played a role in helping to understand the complex multi-phase and multi-component chemical equilibria that occur in a reactor system. For example, thermochemical modelling has been used to investigate the chemical constitution of the fuel-clad gap in a fuel rod in order to determine the conditions under which corrosion of the cladding may be expected during normal operating conditions (e.g. iodine-induced stress corrosion cracking of the cladding in a PWR rod) [1].

The modelling of chemical kinetics and mass-flow problems has also been extensively applied to the nuclear field. For example, recent advances have been made in modelling the effect of radiation on the chemical form of vapour phase species generated within a fuel rod [1]. In addition to vapour phase radiation chemistry, studies have also been made of the aqueous phase. Thus, calculations have been made on the yield of oxidising or reducing species in the coolant of a reactor, due to the effect of radiation, which could cause corrosion of reactor components and limit their life-time [2,3].

Other fundamental techniques attempt to model the microscopic behaviour of nuclear materials. Atomistic simulation methods, for example, have been applied to the study of the migration of volatile fission products within a fuel grain. Such studies have elucidated the likely solution sites, charge states and mechanisms of diffusion of these species under a range of oxidising conditions leading to an improved understanding of fission product release processes [4,5,6].

In Section 2 of this paper, the modelling and simulation techniques applied to reactor chemistry problems will be described in more detail. In Section 3, examples will be given of recent work performed by AEA Technology, using these techniques. Although the emphasis of this paper is on modelling techniques, experimental studies play an integral part in many investigations, providing many of the data which are required for the calculations. In AEA Technology, this synergy between experiments and modelling is fully recognised and many work programmes involve a combination of the two.

2. MODELLING TECHNIQUES

2.1 THERMOCHEMICAL MODELLING

Thermochemical modelling techniques are frequently employed for investigating the chemical constitution of systems under various conditions. The central problem in the calculation of thermodynamic equilibria is to obtain a representation of the Gibbs energy of the total system as a function of temperature, pressure and composition. The total Gibbs energy of the system is simply given by the weighted sum of the Gibbs energies of the individual phases present at equilibrium. The equilibrium state is then obtained by minimising the total Gibbs energy with respect to the amount and composition of the phases under various conditions.

If the phase is a pure substance then the Gibbs energy can usually be obtained from standard sources of thermochemical data. The Gibbs energies for solution phases are more complicated to express. An important parameter for a solution phase is the Gibbs energy of mixing, ΔG^{mix}, which is the change in Gibbs energy accompanying the formation of the solution from its constituents. For an ideal solution, ΔG^{mix} is simply given by the temperature multiplied by the configurational entropy change on forming the solution. In a non-ideal solution, however, ΔG^{mix} will be given by the ideal configurational contribution plus an excess Gibbs energy term, G^{ex}. The modelling of multi-component systems is concerned with deriving suitable representations for G^{ex} which reproduce the experimental phase relationships of a particular system. In some cases, this can be achieved by using a polynomial in composition to describe the binary and higher order interactions between the components. However, for some solution phases, more complex models are required.

Having derived models and data to represent the Gibbs energies of all the phases in a system, the equilibrium state can then be determined by minimising the total Gibbs energy. A widely used tool for this is MTDATA [7], which is an integrated software package incorporating modules for the management and retrieval of thermodynamic data, the processing of those data to determine the equilibrium composition under specified conditions, and the graphical or tabular presentation of the results.

2.2 KINETIC MODELLING

When attainment of thermodynamic equilibrium is slow, or when phenomena perturb the system from thermodynamic equilibrium (such as the presence of a radiation field) chemical kinetics have to be employed to understand the behaviour of a system. The development of kinetics models usually involves three decisions: what reference frame to use when fluid flow is important; what conservation equations need to be solved; and what is the chemical reaction scheme appropriate to the system. Once these decisions have been made the time dependent equations describing the problem can be defined and the equations integrated subject to certain boundary conditions. For some models, several hundred equations may be required to simulate the system adequately and the integrations must usually be carried out using a computer package. In much of our work the computer code, FACSIMILE [8], developed by AEA Technology, is employed for this task.

Typical input data for a kinetic model include: (i) diffusion constants and flow velocities, to describe mass transport; and (ii) chemical rate constants, thermodynamic data and, when radiation is

present, G-values (the number of species produced from 100 eV of radiation energy absorbed), to describe the chemistry. The results from the calculations normally consist of species concentrations as a function of position and time. A variety of techniques can then be used to analyse how the results from the model may depend on the input parameters for the conditions of interest and if any of the equations being solved are redundant (for instance a particular chemical pathway is not active).

2.3 ATOMISTIC SIMULATION

The computer simulation of solids is a very active field and has led to the development of techniques for investigating the structural, thermodynamic and transport properties of a wide range of materials. Such methods include energy minimisation for perfect or defective lattices, molecular dynamics and Monte Carlo methods. In addition to these simulation techniques, many calculations of defect properties have employed quantum mechanical techniques which attempt to solve the Schr÷dinger equation to some suitable degree of approximation.

In the Section 3.3, the application of static lattice simulation techniques to understanding fission product behaviour within the uranium oxide lattice is described. Briefly, the methods are based on the minimisation of the energy of a lattice of ions. For the perfect crystal, the full periodicity of the lattice is used in order to calculate the lattice energy, lattice parameter and other physical properties for the relaxed structure. On introducing a defect, however, the periodicity is disrupted and so a two-region approach is adopted in which the relaxation of a portion of the lattice (region I) immediately surrounding the defect is calculated explicitly, whereas the remaining crystal is treated as a dielectric continuum. In this way, it is possible to calculate the energy either to incorporate an interstitial atom or ion into the crystal, or to remove a lattice ion to create a vacancy. By combining such calculations, a range of phenomena may be investigated at a mechanistic level, such as intrinsic crystal disorder, nonstoichiometry and the behaviour of impurities (such as fission products) in the lattice. A number of computer codes have been developed by AEA Technology for carrying out lattice simulations, including HADES [9] and CASCADE [10].

In contrast to the quantum mechanical techniques alluded to above, at the heart of any computer simulation is the interatomic potential, which seeks mathematically to represent the potential energy of the system as a function of particle coordinates. All of the information that is calculated is contained within the interatomic potential and its first and second derivatives and so its derivation must be undertaken with care. For ionic systems, the main physical interactions that must be included are the Coulombic electrostatic interactions and the short-range repulsive interactions. Whilst empirical potentials are generally the most reliable, they depend on having sufficient crystal data available to fit the various parameters. This is not the case when considering volatile fission product behaviour in the uranium oxides for various nuclear applications and so theoretical techniques, such as the electron-gas method, have to be adopted. A major benefit of the use of electron-gas potentials is the consistency that they introduce into calculations on a wide range of systems.

3. MODELLING EXAMPLES

The methods described in Section 2 have been used to examine a range of problems relevant to the nuclear industry. Three specific examples are presented in this section which demonstrate the application of thermodynamic, kinetic and atomistic modelling methods. Section 3.1 describes the application of thermodynamic methods to calculate the phase equilibria of UO_2, U,GdO_2, U,PuO_2 and U,Gd,PuO_2 fuels to provide an understanding of the fuel behaviour during fabrication and irradiation, in particular melting behaviour during fuel transients. The second example, given in Section 3.2, describes how thermodynamic and kinetic methods have been used to predict the chemical behaviour of the volatile fission products in the fuel-clad gap in order to determine the conditions under which corrosion of the cladding may be expected under normal operating conditions. The third example, in Section 3.3, describes

the atomistic modelling of the migration behaviour of fission products in oxidised fuel to elucidate the release mechanisms of these species from the grains.

3.1 MODELLING OF THE PHASE RELATIONSHIPS IN THERMAL REACTOR FUELS

An understanding of the phase relationships of thermal reactor fuels for the likely conditions to be encountered during the fuel cycle is an important factor in the prediction of the chemical behaviour of such fuels. These include uranium dioxide, mixed uranium-plutonium dioxide and uranium-gadolinium dioxide. Work has been performed, therefore, to develop a model for the thermodynamics and phase relationships of the fluorite phase in the U-Pu-Gd-O system in order to predict more precisely the behaviour of fuel during fabrication, reactor operation and reprocessing. Particular applications, such as the conditions of temperature and gas compositions required for sintering or the influence of the irradiation conditions on the variation of the solidus temperature with time, could be treated using the model.

A considerable amount of experimental data are available on the thermodynamic properties for the U-O, Pu-O, U-Pu-O (MOX) and U-Gd-O systems and these have been optimised to provide a description of the phase relationships. From the combination of the detailed assessments of the two ternary systems U-Pu-O and U-Gd-O, the data can also be used to predict the properties of the quaternary system MOX-Gd_2O_3. Similarly the basic model can be extended to include the main fission products in solution in the fuel lattice to predict the effects of burn-up on these properties. The models developed at present are preliminary. Further optimisation of the interaction parameters between the components are still required in order to reproduce specific details of the phase diagrams.

3.1.1 U-UO_2-UO_3 System

In modelling the high temperature behaviour of urania a good thermodynamic description of the U-UO_3 system has been obtained using a model in which both the liquid and fluorite phases are represented as simple Redlich-Kister solutions with U, UO_2 and UO_3 as components [11,12,13]. The important phases U_4O_9 and U_3O_8 have been included in the assessment, but only as stoichiometric compounds. Since the oxygen potential data close to the stoichiometric composition are not well defined, no data between $1.98 < O/U < 2.02$ were used in the assessment. The phase diagram for the U-UO_3 system, calculated from the selected values, is shown in Fig. 1, together with some of the many experimental data points.

3.1.2 Modelling of Pu additions to urania

A suitable associate model for the fluorite phase of the U-Pu-O system involves the addition of at least two species to the model described above, PuO_2 and a species with $O/Pu < 2$. Besmann and Lindemer [14,15] have shown that the oxygen potential data, and to a lesser extent, the phase diagram in the region of PuO_2, can be reproduced using a model of the fluorite phase with the species $Pu_{4/3}O_2$ and PuO_2. However their model for urania cannot satisfactorily reproduce the phase behaviour in equilibrium with the liquid. In the extension to the ternary system, the model adopted here for the fluorite phase is given by, (U, UO_2, UO_3, $PuO_{1.5}$, PuO_2) and so a total of six new interaction terms, in principle, have to be defined. As a first estimate only the two interactions with the major species, UO_2, would be set different from zero, although a negative interaction between $PuO_{1.5}$ and UO_3 may be appropriate. Using approximate values for these interactions and ideal interactions for the other terms, Fig. 2 shows the calculated oxygen potentials for a mixed oxide $U_{0.9}Pu_{0.1}O_{2\pm x}$ as a function of temperature.

3.1.3 Modelling of Gd additions to urania

Models which exist for the $(U,Gd)O_{2\pm x}$ fluorite phase involve ternary species comprising U(V) or U(VI) and postulate the presence of Gd^{+3}-U^{+5} complexes to describe the variation of oxygen potential with composition. If one chooses to add $GdO_{1.5}$ or a similar binary trivalent species, the Gd, which cannot change valency, acts merely as an inert diluent and the sharp change in oxygen potential in the $(U,Gd)O_{2\pm x}$

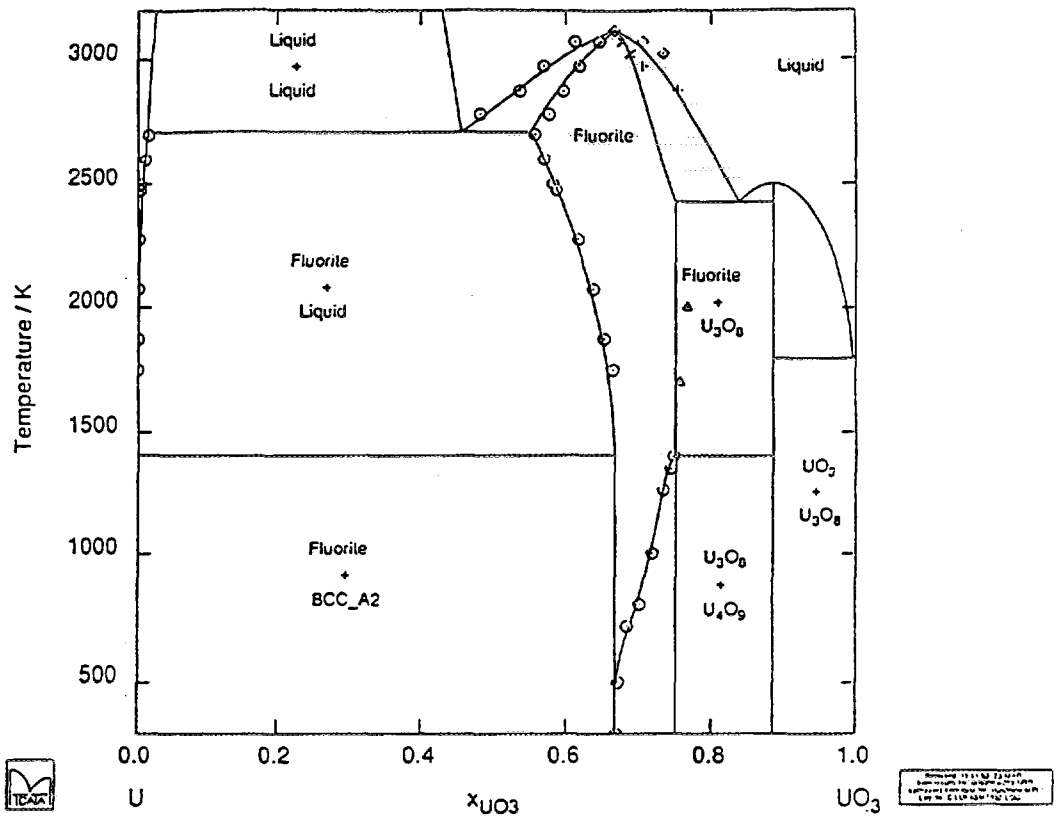

1. Calculated U-UO_3 Diagram

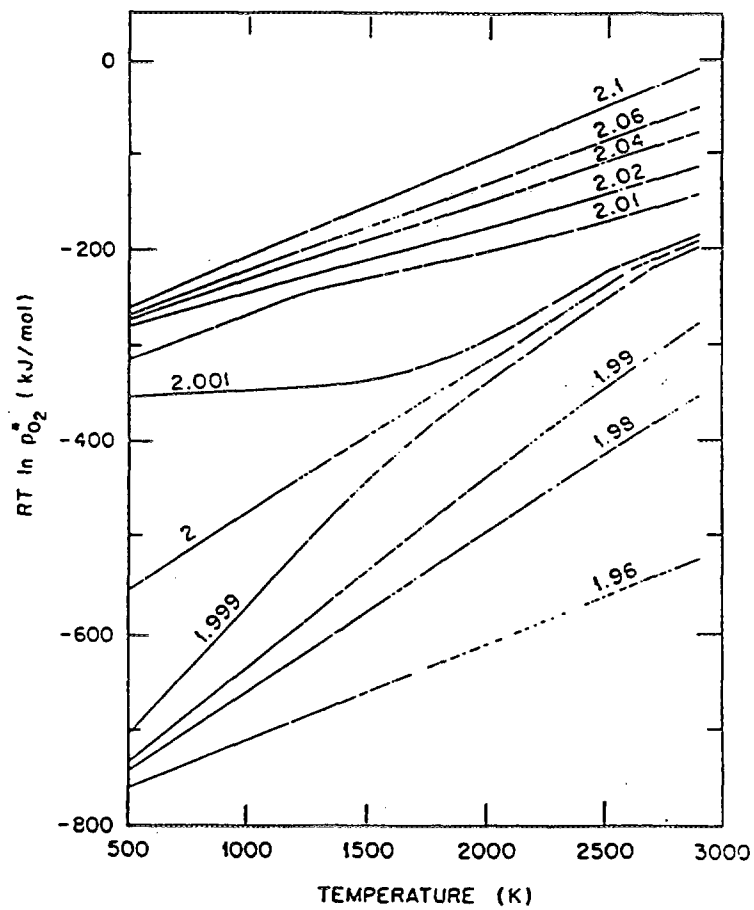

2. Oxygen Potentials in $(U,Pu)O_{2\pm x}$ [4]

fluorite phase occurs when the O/U ratio passes through 2.0; that is at an overall O/M < 2.0 (M= U+Gd). However, for most of the lanthanide elements (except Eu, which can become divalent), the sharp change in oxygen potential occurs as the O/M passes through 2.0 [16]. This is a consequence of the fact that the formation of interstitial defects in the fluorite phase requires much less energy than the formation of oxygen vacancies. As Lindemer and Brynestad [17] have shown, this behaviour can be modelled by using $Gd_{4/3}O_2$ and Gd_2UO_6, to fit the oxygen potential data in this system. In this work, the model used for urania has UO_2 and UO_3 as the important species in hyperstoichiometric phases and the composition of the ternary U-Gd-O species to be used as a component of the fluorite solid solution must be determined by trial optimisations. Scoping calculations have been made using the species $GdO_{1.5}$ and $GdUO_4$. The oxygen potentials for the fluorite phase $(U_{0.831}Gd_{0.169})O_{2\pm x}$ at 1573 K calculated using this model are compared with the measured values [18] in Fig. 3.

3.1.4 Modelling of Pu and Gd additions to urania

The final synthesis of the separate models considered above will yield a model for the fluorite $(U,Pu,Gd)O_{2\pm x}$ phase, except for the interactions between the Pu-containing and Gd-containing species. However, for compositions of MOX-Gd_2O_3 fuel with relatively small amounts of Pu and Gd present, such interactions should not have a large effect on the predicted oxygen potentials. For higher levels of additions, these interactions could be noticeable, and some consideration of the Pu-Gd-O system may be required, particularly for the hypostoichiometric compositions. Purely as an illustration of the type of information that would result from a detailed optimisation, the oxygen potentials at 1773 K of the phases $(U_{1-y-z}Pu_yGd_z)O_{2\pm x}$ have been calculated as a function of x, using the parameters discussed in the sections above. The results are shown in Fig. 4 for different compositions. The results are in no way quantitatively significant, but the marked increase in oxygen potentials as the percentages of Pu and Gd are increased is quite clear.

These calculations provide an indication that a realistic model could be developed to represent the thermodynamic behaviour of the U-Pu-Gd-O system. A similar approach to expand the model to include soluble fission products could also be developed to predict the behaviour of irradiated mixed oxide fuel.

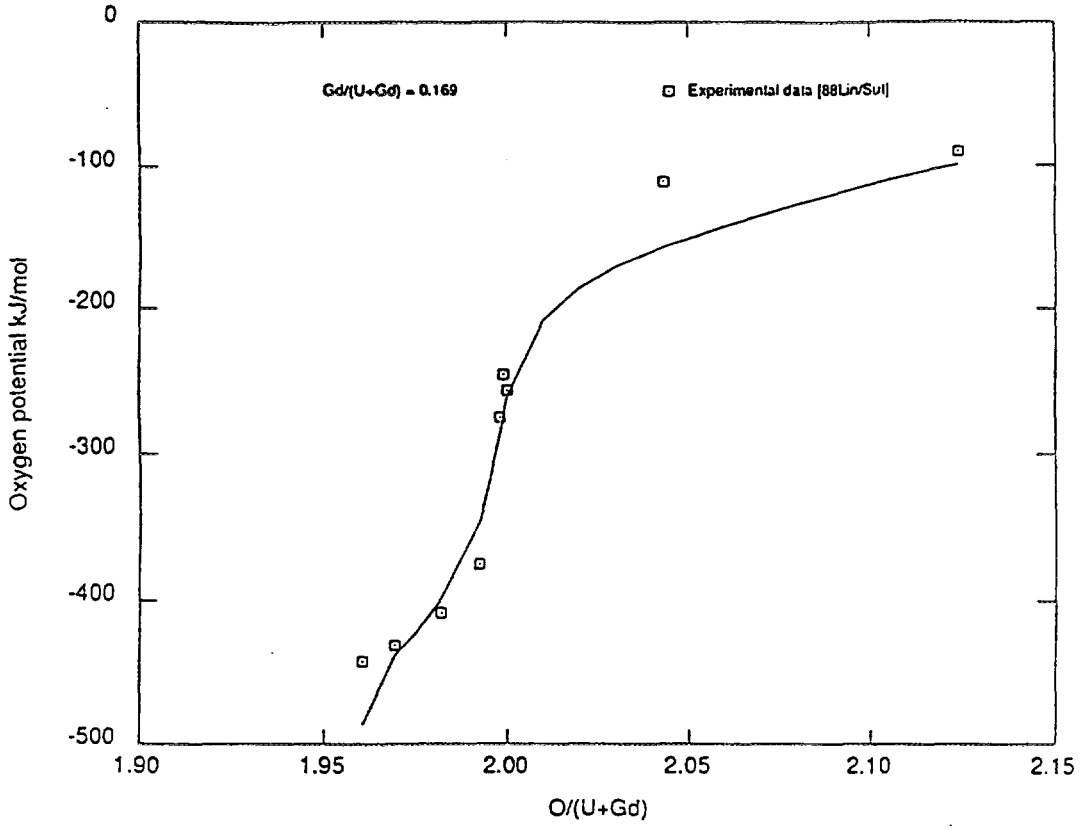

3. Scoping Calculations: Oxygen Potentials in $(U,Gd)O_2$

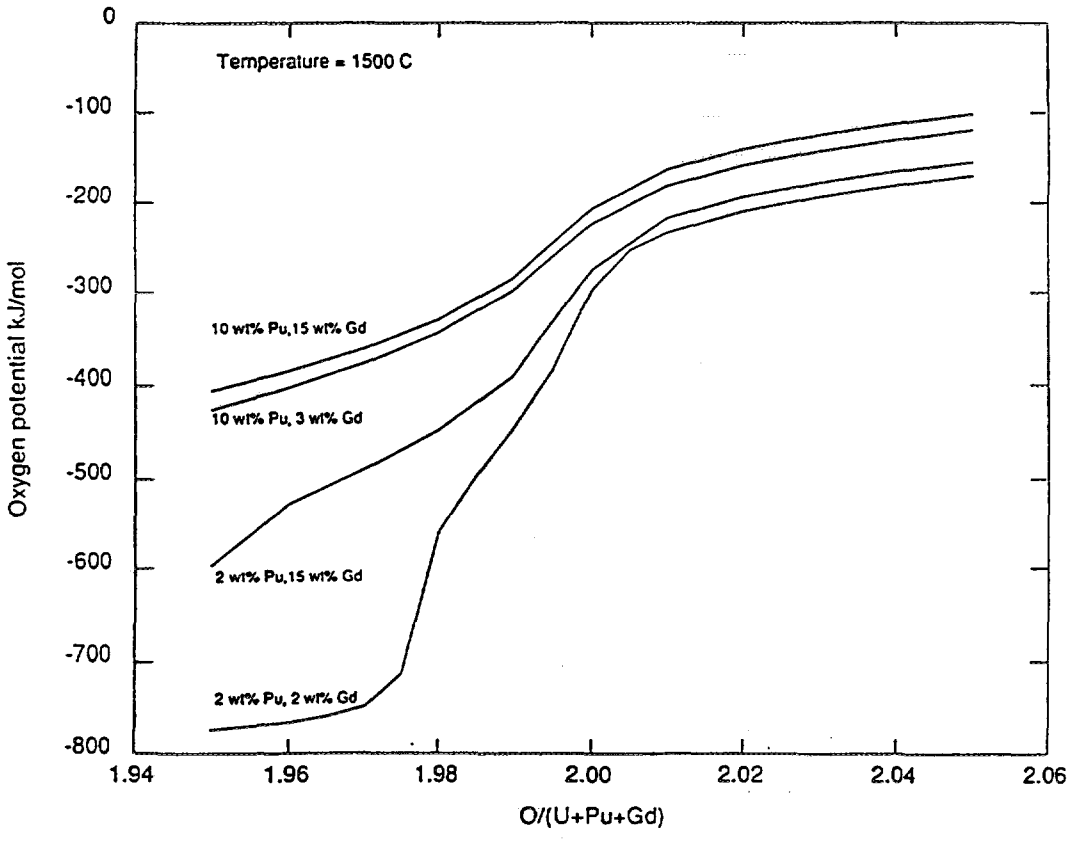

4. Scoping Calculations: Oxygen Potentials in $(U,Gd)O_2$

3.2 CALCULATING THE CHEMICAL CONSTITUTION OF THE FUEL-CLAD GAP IN OXIDE FUEL PINS

An important part of any attempt to predict the operational performance of nuclear fuel pins is to possess an understanding of the likely mechanisms of failure of their cladding. In the PWR system, iodine-induced stress corrosion cracking (SCC) has frequently been invoked as a mechanism of failure of the zircaloy cladding. In order to elucidate the mechanisms of failure of a chemical nature, it is necessary to have a thorough knowledge of the chemical phenomena which could occur within the gap between the fuel and the cladding. The following example demonstrates how thermodynamic and kinetic methods can be used together to investigate this problem.

Enclosed in the PWR fuel rod are pellets of uranium dioxide, or uranium-plutonium dioxide fuel which are clad in zircaloy. Factors which influence the chemical state of the condensed phases and the nature and presence of the gas phase species include the temperature within the gap, the oxygen potential of the fuel and the availability of fission product elements. The effect of irradiation within the gap also has to be considered. The approach taken in this study was to calculate first the chemical constitution of the condensed phases within the gap at appropriate temperatures for the normal operation of the fuel. The chemical equilibria for a range of oxygen potentials has been calculated using suitable input values for the predominant gas phase species within the gap.

Under reactor conditions the concentrations of the gaseous species are expected to be different from those at thermal equilibrium because the large continuous input of radiation, largely in the form of fission fragment radiation, tends to dissociate molecules into neutral atoms or ions. For the perturbation

of the gas phase equilibria due to irradiation by fission fragments, the kinetics of the reactions have been considered between the excited and ionised atoms of the rare gases He, Kr, and Xe with the gaseous molecules CsI and Cs_2Te. The data for the rate constants for these reactions have been obtained from published information or from estimates by analogy. The necessary differential equations in species concentrations with respect to time were solved numerically by using the FACSIMILE program.

3.2.1 Thermodynamic equilibria

It is important to have a detailed understanding of the relationship between oxygen potential and the various parameters of operating fuel (for example, rating and burn-up of the fissile atoms) because the oxygen potential can so markedly influence the transport properties of the oxide lattice. In this assessment the influence of the changes in oxygen potential with burn-up have been simulated by simply examining the effects of successive addition of small quantities of oxygen to the chosen components within the gap. Also in this assessment the effect of the fission product Mo on the chemical constitution has been considered. This element can be volatile under some conditions and can be transported to the gap either as $Cs_2MoO_4(g)$ or, at higher oxygen potentials, particularly at high burn-up, as $MoO_3(g)$. The effects of allowing a small quantity of Zr from the cladding to react with the fission product elements Cs, I and Te has also been studied.

In the calculations described here, the fission product inventory was based on a fuel burn-up of 2.9% and a 1% release into the gap. The calculation of the constitution within the gap has been carried out with and without the inclusion of Mo and Zr and the cases studied are shown in Table 1. The condensed phases which are present for the four cases depend on which elements participate in the reactions. Particular phases will buffer the oxygen potential over a range of added oxygen and the changes in the phase assemblages with the amount of added oxygen will alter the amounts of species in the gas phase. The variation of the pressures of the predominant gas phase species with oxygen potential for the cases considered are shown in Figs. 5 and 6. The calculations were performed up to oxygen potentials as high as -250 $kJ.mol^{-1}$.

Experiments quoted by Konashi et al [19] indicated that at cladding temperatures from 573 to 1000 K the threshold partial pressure of I required for SCC rises from ca 10^{-14} bar at 573 K to ca 10^{-6} bar at 1000 K. The logarithm of the partial pressure falls approximately linearly as 1/T increases, where T is the absolute temperature in Kelvin. At a temperature of 650 K, as used in this assessment, the threshold partial pressure of I is predicted to be ca 10^{-12} bar. It can be seen by comparing Fig. 5 (Case 1 - without Mo) and Fig. 6. (Case 4 - with Mo) that the pressure of the elemental iodine species increases with increasing oxygen potential, more so for Case 4 with Mo present, as recognised by Goetzmann [20]. It can be inferred from Fig. 6 that if Mo is present, the threshold for SCC may be exceeded at higher oxygen potentials. Goetzmann considered that reactions of CsI with Mo containing species to form Cs_2MoO_4 are

Table 1

Cases for calculation of the fuel-clad gap constitution of a PWR fuel pin.

Case	Amount per gram of original oxide fuel (mol)						
	He	Cs	I	Te	U	Mo	Cladding Zr
1	1.31×10^{-5}	2.07×10^{-7}	1.21×10^{-8}	3.18×10^{-8}	3.68×10^{-3}	0	0
2	1.31×10^{-5}	2.07×10^{-7}	1.21×10^{-8}	3.18×10^{-8}	3.68×10^{-3}	2.52×10^{-7}	0
3	1.31×10^{-5}	2.07×10^{-7}	1.21×10^{-8}	3.18×10^{-8}	3.68×10^{-3}	0	2.51×10^{-9}
4	1.31×10^{-5}	2.07×10^{-7}	1.21×10^{-8}	3.18×10^{-8}	3.68×10^{-3}	2.52×10^{-7}	2.51×10^{-9}

Temperature 650 K; burn-up 2.9%; amount of fission product element is 1% of inventory in pin; free volume in pin is 1.393×10^{-5} dm^3

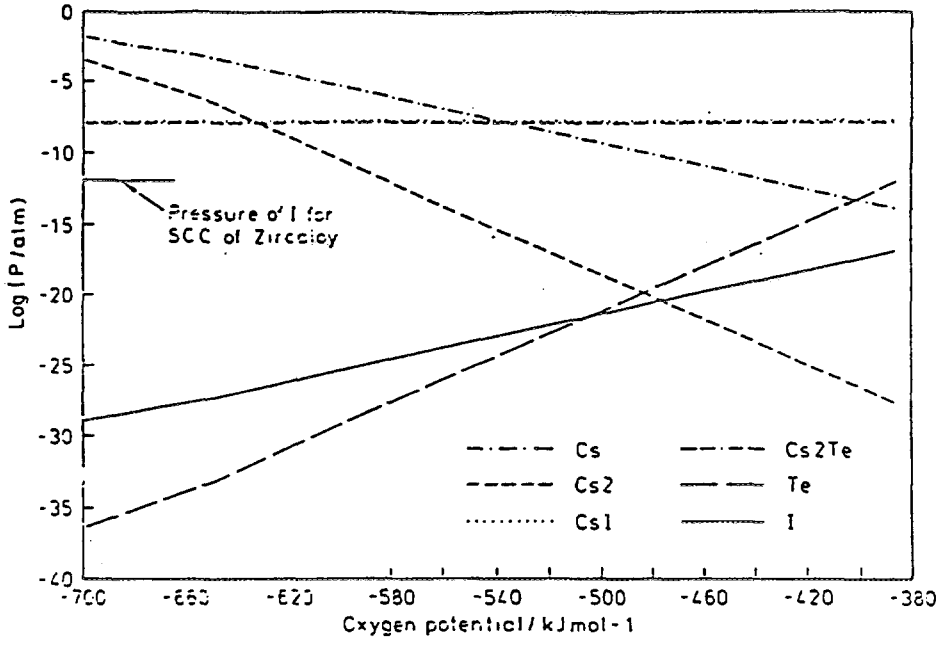

5. *Variation of the pressures of the predominant gas phase species with oxygen for Case 1 (table 1) of the PWR calculations*

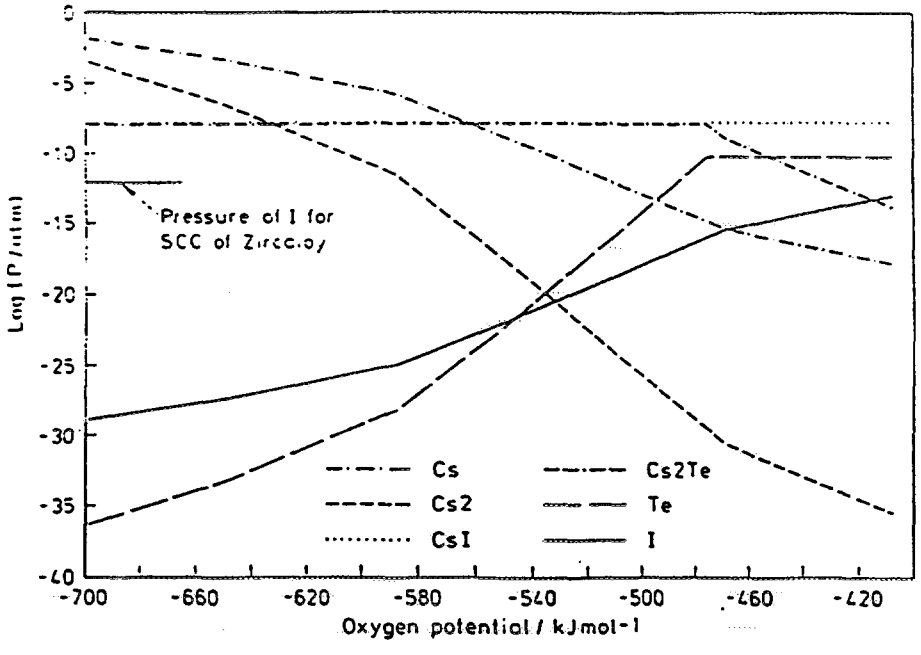

6. *Variation of the pressures of the predominant gas phase species with oxygen for Case 4 (table 1) of the PWR calculations*

important in increasing the iodine activity to that appropriate to SCC. However, the calculations performed during this assessment did not support evidence for any such reactions occurring with CsI under the chosen conditions.

3.2.2 Kinetic modelling: Perturbation of the thermal equilibria by radiation effects

The radiation fuel pins are exposed to under normal operation can lead to the perturbation of the gas phase equilibria in the fuel-clad gap due to irradiation by fission fragments. The combined effect of all the reactions that will occur is to cause a new dynamic equilibrium to be established quickly, for which the steady state concentrations of atoms are expected to be greater than in the absence of radiation.

The kinetic simulation of the chemistry was simplified by assuming that all the He+ ions recombine with electrons efficiently to form excited metastable atoms. In addition, the concentrations of CsI, Cs and Cs_2Te in the gaseous phase were assumed to be constant since there is, for the case considered, a supply of condensed CsI and Cs_2Te to replenish any lost from the gaseous state by dissociation.

For Case 1 in which Mo and Zr are not involved in the reactions within the gaps, the effect of radiation of the gas phase has been examined at 650 K. The results are shown in Table 2. It should be noted that there is an increase in the pressures of I, I_2, Te and Te$_2$ when the thermal equilibria are perturbed by radiation. For the case at the higher value of oxygen potential, the pressure of I and I_2 are not influenced by the use of a second or third order rate constant for the recombination of Cs and I. For the lower values of oxygen potential however, the use of a third order rate constant gives lower pressures for I than I_2 than when a second order rate constant is used in the assessment of the influence of radiation.

For the cases that do not include Mo, the thermal equilibria alone are not sufficient to provide high enough iodine potential for SCC. However, it can be seen from Table 2 that the partial pressure of iodine is substantially enhanced in the presence of radiation and at higher oxygen potentials well exceeds the SCC threshold.

3.3. MODELLING THE BEHAVIOUR OF VOLATILE FISSION PRODUCTS WITHIN FUEL

The detailed behaviour of fission product atoms within the fuel matrix is complex and involves a combination of steps, which include the diffusion of gas atoms through the unperturbed lattice, the trapping of the atoms in vacancy clusters and radiation damage sites and the precipitation of gas bubbles within the grain [21]. The subsequent diffusion of the fission products to the grain boundaries then relies on the movement of these bubbles or the re-solution (normally radiation-induced) of the atoms from these bubbles. Once in the grain boundaries, the fission product atoms may react chemically with other species or travel to the fuel rod plenum or to the fuel-clad gap. In the work reported here, only fission product diffusion in the bulk oxide lattice is considered. Although this represents a somewhat idealised situation, bulk diffusion is often identified as a rate-determining process which therefore controls the overall release of the fission products from the fuel matrix. Attention has also been focused on the question of the influence of fuel oxidation on the behaviour of the fission products. The major product of oxidation of UO_2 fuel in air or in other suitably oxidising atmospheres is U_3O_8. Such conditions may be encountered in the event of accidents, occurring during fuel handling, fuel storage or transport.

Atomistic simulation techniques have been applied extensively in recent years to the study of volatile fission product behaviour in both $UO_{2\pm x}$ [4,6] and $U_3O_{8\pm z}$ [5,6]. Experimental studies of fission product diffusion in uranium oxides provide some basic data but necessitate performing experiments on irradiated fuel. Ion implantation is a technique commonly used to study fission product behaviour at an atomic level but it can damage the host lattice and so prevent the study of gas behaviour within a perfect lattice environment. Thus, computer simulation methods offer a valuable complement to experimental techniques. In this section, we shall briefly describe just one part of this work, namely the behaviour of Xe in U_3O_{8-z}, and show how the atomistic simulations have clarified conflicting experimental results for this system.

Table 2

The effect of radiation on the pressures of the gaseous species in the fuel-clad gap of PWR fuel pin at 650 K. Case 1 (Table 1).

Condensed phases CsI, CsI_2Te

Partial pressures (bar)						
CsI	Cs	I	I_2	Cs_2Te	Te	Te_2
$\overline{G}_{O_2}$ = -698 kJ.mol^{-1}						
Thermal equilibrium						
1.8×10^{-8}	1.6×10^{-2}	1.2×10^{-29}	1.6×10^{-52}	1.3×10^{-8}	5.8×10^{-37}	1.8×10^{-57}
With radiation						
1.8×10^{-8}	1.6×10^{-2}	1.8×10^{-15}	2.6×10^{-31}	1.3×10^{-8}	2.2×10^{-17}	3.9×10^{-35} a)
1.8×10^{-8}	1.6×10^{-2}	2.5×10^{-17}	1.0×10^{-34}	1.3×10^{-8}	2.2×10^{-17}	3.9×10^{-39} b)
$\overline{G}_{O_2}$ = -400 kJ.mol^{-1}						
Thermal equilibrium						
1.8×10^{-8}	4.6×10^{-14}	4.3×10^{-18}	1.2×10^{-28}	1.3×10^{-8}	6.9×10^{-14}	2.6×10^{-11}
With radiation						
1.8×10^{-8}	4.6×10^{-14}	8.5×10^{-8}	2.6×10^{-6}	1.3×10^{-8}	1×10^{-5}	3.5×10^{-2} c)

a) With 2nd order rate constants for reaction: Cs + I + He → CsI + He
b) With 3rd order rate constants for reaction: Cs + I + He → CsI + He
c) With 2nd and 3rd order rate constants for reaction: Cs + I + He → CsI + He

In the U_3O_8 structure there are two types of oxygen ion: those in the U-O planes and those in -U-O-U-O- chains running perpendicular to the planes (see Fig. 7). Atomistic defect calculations have shown that it is ca. 2 eV (i.e. ca. 193 kJ.mol^{-1}) more difficult to form a chain oxygen vacancy than a plane oxygen vacancy [22]. This correlates well with the observed bond strengths (i.e. vibrational stretching frequencies), which are greatest along the -U-O-U-O- chains. Further calculations on the migration of oxygen vacancies in U_3O_8 indicate that vacancy migration within the planes is easy (the activation energy is ca. 0.3 eV), as it is in UO_2. However, if a metastable population of chain oxygen vacancies is formed, say through radiation damage, then the calculations show that the activation energy required to anneal out those oxygen vacancies (through migration of the vacancy from the chain site to a plane site) is large (ca. 2 eV). Therefore, such a population of chain oxygen vacancies would be relatively stable to annealing out. This correlates well with the observed ready amorphisation of U_3O_8 under rather low radiation doses.

In considering the behaviour of fission product Xe within the U_3O_8 lattice, we are concerned both with the sites at which the Xe atoms will be trapped (solution sites) and the mechanisms and activation energies for their migration between these sites. A number of possible solution sites have been considered, including interstitial sites, oxygen vacancy sites and combination vacancy/interstitial sites. In stoichiometric U_3O_8, the solution of Xe is predicted to occur at a 9-coordinated site (illustrated in Fig. 8), which lies centrally above the triangle of oxygen ions defined by O(4)-O(4)-O(3) in Fig. 7. This site is larger than the alternative, trigonal bipyramidal interstitial sites which lie above each of the oxygen ions

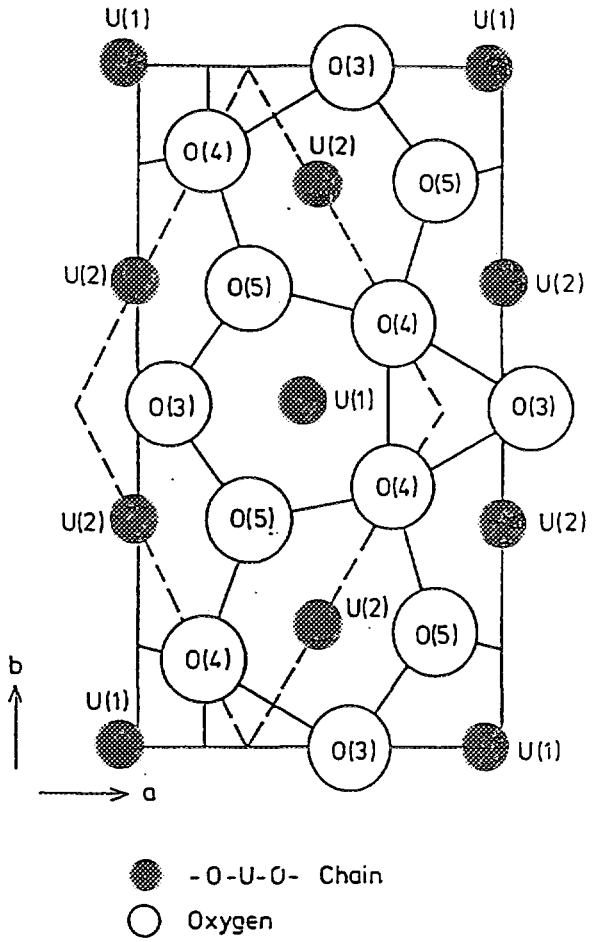

7. *The structure of α-U_3O_8(z=O plane). Chains of uranium-oxygen-uranium atoms run parallel to the z axis*

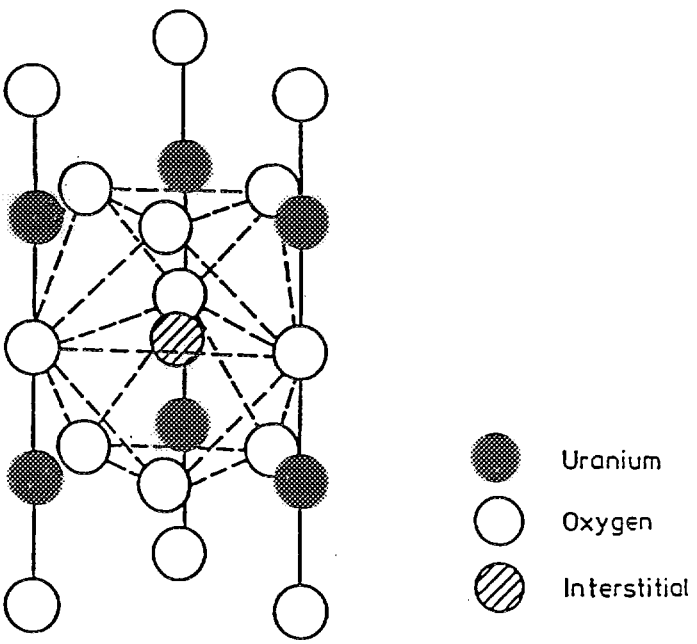

8. *Nine-coordinated interstitial site in U_3O_8*

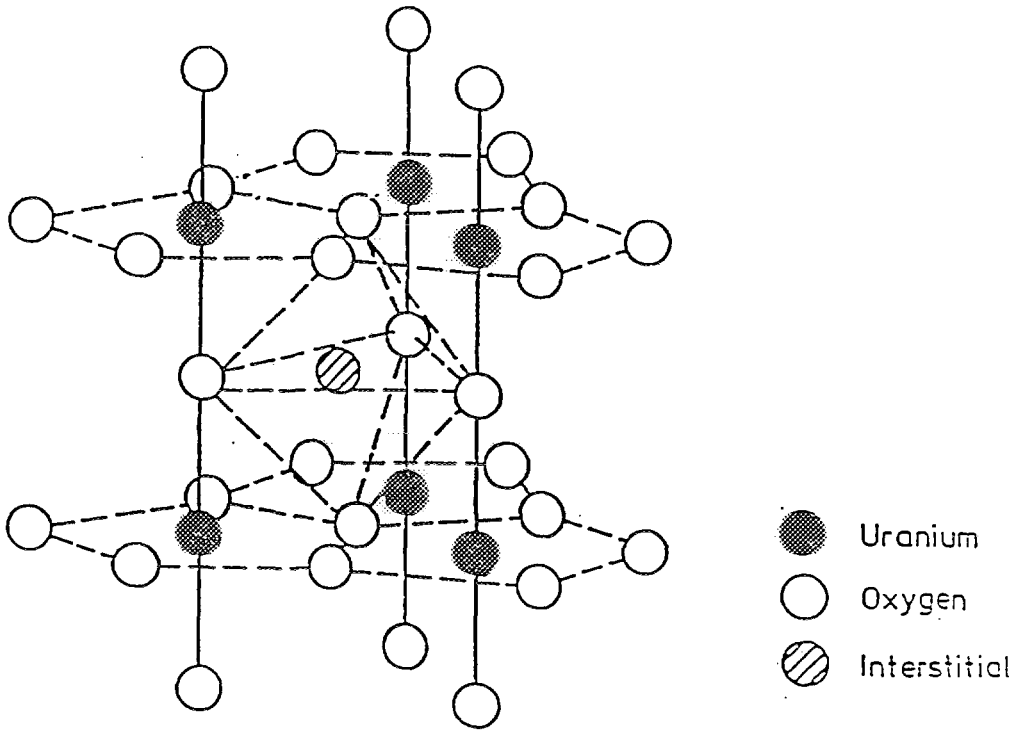

9. Trigonal bipyramidal interstitial in U_3O_8

in the planes (illustrated in Fig. 9). In U_3O_{8-z}, the solution of Xe is predicted to be most favourable in combination interstitial/vacancy sites. Although there are 19 such combinations, inspection of the fully relaxed coordinates of the gas atoms show that they occupy only five distinct crystallographic sites, labelled α, β, γ, δ and ϵ [5]. At equilibrium, the gas atoms occupy the γ or δ sites (an interstitial site adjacent to an O(3) or O(4) plane oxygen vacancy). In the presence of a metastable population of anion vacancies in the -O-U-O-U-O- chains of the U_3O_8 structure, the gas atoms will occupy the α or β sites, in which the gas atom sits adjacent to the chain oxygen vacancy.

For the migration of Xe in stoichiometric U_3O_8, we must consider the movement of the gas atoms between the 9-coordinated interstitial solution sites. The highest energy for such a step is encountered as the gas atom moves through the trigonal bipyramidal interstitial site above the O(5) oxygen ions and the total activation energy for migration of Xe between 9-coordinated solution sites is calculated to be 4.3 eV. This is comparable to the calculated activation energy for interstitial migration of Xe in UO_2. At thermal equilibrium in U_3O_{8-z}, the Xe atoms occupy the γ or δ combination interstitial/vacancy sites, situated above the triangle of oxygens defined by O(4)-O(4)-O(3) in Fig. 7. Between each such triangle lies a higher energy ϵ site, associated with an O(5) trigonal bipyramidal interstitial site, through which the Xe atom must pass during migration between its solution sites. In considering the migration of the gas atoms, a number of mechanisms have been envisaged, with the lowest energy route having a calculated activation energy of 3.8 eV.

A significant component of the activation energy for Xe migration in both U3O8 and U_3O_{8-z} are the repulsive interactions between the gas atom and the chain oxygen ions as it moves through the pillared-layer structure. These interactions are minimised when the gas atom occupies the 9-coordinated interstitial, γ or δ positions and are greatest as it passes through the O(5) interstitial or ϵ site. One way of reducing these energies would be to introduce a chain oxygen vacancy. Such vacancies could be formed through radiation damage and it was suggested earlier that once they had been created, they would be relatively stable with respect to annealing out by oxygen ion diffusion. In the presence of a metastable

population of chain oxygen vacancies the Xe atoms would be trapped at the associated α or β sites rather than at the 9-coordinated interstitial, γ or δ sites expected for thermal equilibrium. The calculated activation energy for migration of Xe between the α and β sites is only 1.3 eV and so if chain oxygen vacancies are present, the Xe atoms would take advantage of them in migrating through the lattice.

Experimentally, two measurements of Xe migration in U_3O_{8-z} have been made [23,24,25]. In irradiated samples of U_3O_{8-z}, the measured activation energy for Xe is 0.85 eV, which is in reasonable accord with our radiation damage-assisted mechanism. However, in ion implantation studies that have employed a low radiation dose, the activation energy for Xe was found to be much higher, 3.9 ± 0.2 eV, which is in agreement with our calculated value for Xe migration under equilibrium conditions. Thus, the simulations suggest that the material used in the experiments on irradiated samples would have had a significant population of metastable chain oxygen vacancies as a consequence of radiation damage. This would lead to a relatively low activation energy for migration of the Xe atoms. However, in the ion-implantation studies, employing a low radiation dose, the lattice damage would have been kept to a minimum and the Xe migration would then have been via a higher activation energy mechanism involving the thermally-generated plane oxygen vacancies.

4. CONCLUSIONS

Described in this paper are three examples of the development and applications of models to simulate, from a fundamental basis, a range of phenomena important in the nuclear industry. The examples included:

1. The calculation of the phase equilibria of UO_2, U,GdO_2, U,PuO_2 and U,Pu,GdO_2 fuels to provide an understanding of the fuel behaviour during fabrication and irradiation, particularly melting behaviour during transients;

2. The application of thermodynamic and kinetic modelling techniques to predict the behaviour of the volatile fission products in the fuel-clad gap in a PWR to determine the conditions under which corrosion of the cladding may occur under normal operation;

3. The development of models to simulate the basic properties of irradiated fuel to provide an understanding of fission product release processes.

A valuable aspect of the development of fundamental models is that they can serve as a test of our understanding of key processes. If our best estimate fundamental model cannot reproduce an experimental observation to within an acceptable margin then our understanding of the process is likely to be inadequate or incorrect. Fundamental and empirical models both have a role to play but if a fundamental model is able to describe a process then this implies a sound understanding which is particularly important in safety related applications. Although the emphasis of this paper has been on fundamental modelling techniques, it is recognised that experimental studies play an integral part in the understanding of important phenomena. Both the fundamental modelling and experimental studies can provide a physical basis for simplifications and approximations made in a number of applications in the nuclear industry.

ACKNOWLEDGEMENTS

Some of the work described in this paper has been carried out as part of the Corporate Research programme of AEA Technology. The authors wish to acknowledge the work of Dr M H Rand in performing some of the thermodynamic calculations reported here. The authors are also grateful to the Royal Institution of Great Britain with whom we have collaborated on various aspects of the atomistic modelling work.

REFERENCES

[1] BALL, R.G.J, BURNS, W.G., HENSHAW, J., MIGNANELLI, M.A., POTTER, P.E., J. Nucl. Mater. 167 (1989) 191

[2] RUIZ, C.P., LIN, C.C., ROBINSON, R., BURNS, W.G., CURTIS, A.R., "Model calculations of water radiolysis in BWR primary coolant". Water chemistry of nuclear reactor systems 4, BNES, 131-140 (1989)

[3] RUIZ, C.P., LIN, C.C., ROBINSON, R., BURNS, W.G., HENSHAW, J., "Model calculations of water radiolysis and electrochemical potentials in BWR primary coolant II". Water chemistry of nuclear reactor systems 6, BNES, 141-153 (1992)

[4] BALL, R.G.J., GRIMES, R.W., J. Chem. Soc., Faraday Trans. II 86 (1990) 1257

[5] BALL, R.G.J., GRIMES, R.W., Phil. Mag. 66 (1992) 473

[6] BALL, R.G.J., GRIMES, R.W., J. Nucl. Mater. 188 (1992) 216

[7] DAVIES, R.H., DINSDALE, A.T., HODSON, S.M., GISBY, J.A., PUGH, N.J., BARRY, T.I., CHART, T.G., 'User Aspects of Phase Diagrams', Ed. F H Hayes, Institute of Materials, London (1991) 140

[8] MALLESON, A.M., KELLET, H.M., MYHILL, R.G., SWEETENHAM, W.P., AEA Harwell Report AERE-R13729 (1990)

[9] NORGETT, M.J., AEA Harwell Report AERE-R7650 (1974)

[10] LESLIE, M., SERC Daresbury Laboratory Report, DL/SCI/TM31T (1982)

[11] RAND M.H., ACKERMANN R.J., GRONVOLD F., OETTING F.L., PATTORET A., Rev. Int. Hautes Temper. RΘfract. 15 (1978) 355-365

[12] LINDEMER T.B., BESMANN T.M., J. Nucl. Mater. 130 (1985) 473-488

[13] NAKAMURA A., FUJINO T., J. Nucl. Mater. 110 (1987) 215-222

[14] BESMANN T.M., LINDEMER T.B., J. Nucl. Mater. 130 (1985) 489-504

[15] BESMANN T.M., LINDEMER T.B., J. Nucl. Mater. 130 (1986) 292-293

[16] UNE K., OGUMA M., J. Nucl. Mater. 118 (1983)189-194

[17] LINDEMER T.B., BRYNESTAD J., J. Amer. Ceram. Soc. 69 (1986) 867-876

[18] LINDEMER T.B., SUTTON A.L., J. Amer. Ceram. Soc. 71 (1986) 553-561

[19] KONASHI, K., KAMIMURA, K., YOKOUCHI, Y., J. Nucl. Mater. 125 (1984) 244

[20] GOETZMANN, O., J. Nucl. Mater. 107 (1982) 185

[21] MATZKE, Hj., Rad. Effects 53 (1980) 219-242

[22] BALL, R.G.J., DICKENS, P.G., J. Mater. Chem. 1(1) (1991) 105

[23] LINDNER, R., MATZKE, Hj., Z. Naturforschg. 14a (1959) 582-584

[24] MATZKE, Hj., J. Mat. Sci. 2 (1967) 444-456

[25] MATZKE, Hj., Rad. Effects 28 (1976) 249-25

A MODEL FOR THE OXYGEN POTENTIAL OF OXIDE FUELS AT HIGH BURNUP

P. GARCIA, J.P. PIRON
CEA Centre D'études de Cadarache,
Saint-Paul-lez-Durance

D. BARON
Direction des études et recherches,
Electricité de France,
Moret-dur-Loing

France

Abstract

The recent drive towards extending the average burnup of nuclear oxide fuels has lead to the need to assess the chemical state of fission products in highly irradiated rods. Modelling of fuel chemistry is indeed essential in order to shed light on mechanisms such as those that lead to cladding failure or the effect on conductivity of the O/M ratio. Using Lindemer's analysis as a starting point, a comprehensive description of the chemical state of the fluorite fuel matrix along with the most abundant fission products has been developed. The model was then implemented within the framework of an upgraded version of the SOLGASMIX program known as SAGE. In addition to approximately seventy solid compounds, three different mixture phases are modelled. The first one is the gaseous phase and comprises roughly sixty different compounds. The second is made up of noble metals such as Mo, Ru, Tc, Pd. The third mixture phase is a representation of the fluorite fuel matrix. Since SAGE is a code which calculates chemical equilibria by minimising the Gibbs energy of the system, it is essential that reliable free energies of formation be used as data. This is relatively straightforward with regard to most compounds and thermochemical data are readily available in the open literature. As regards the fluorite phase however, the basic hypothesis is that it is possible to model the effect of defects such as interstitials (in the hyperstoichiometric phase) and vacancies (in the hypostoichiometric phase) by assuming the existence of hypothetical solute compounds such as $U_2O_{4.5}$ that stabilise the hyperstoichiometric phase. As rare earths (Re) of valence two or three are dissolved in the matrix, the hypothetical compounds $Re_{4/3}O_2$ and URe_2O_6 are chosen to reflect the behaviour of the ternary system. This description accurately predicts the hypostoichiometric region of the phase diagram but underestimates the increase in oxygen potential in the hyperstoichiometric region. This can be interpreted as resulting from the fact that rare earths of valence two or three have an effective negative charge in the crystal lattice. Following Olander's analysis, this results in a reduction of the number of sites available to oxygen interstitials, hence an increase of the oxygen potential as compared to pure UO_2. The novelty lies in the implementation of this concept within the framework of a fairly straightforward program. Two sets of calculations were performed. The first was aimed at reproducing oxygen potential measurements performed on unirradiated fluorite matrices such as $UO_{2\pm x}$, $U_yPu_{1-y}O_{2\pm x}$, $U_yRe_{1-y}O_{2\pm x}$. The results of the second set of calculations were then compared to oxygen potential measurements of irradiated specimens or specimens with a simulated burnup.

1. INTRODUCTION

There is still very much uncertainty as to the actual oxygen potential and oxygen over metal ratio (O/M) of irradiated L.W.R. fuels. Generally speaking, the thermochemical state of the irradiated fluorite matrix and fission products is a question still very much open to debate. Modelling is made all the more difficult as the average burnup of fuel rods increases. Local phenomena such as the RIM effect (e.g. [1]) are also possible.

The substantial increase in burnup associated with this phenomenon is bound to affect the O/M ratio and hence the thermal behaviour of the fuel. The O/M ratio of the fuel is the result of a complicated balance between fission products (such as rare earths) and plutonium atoms dissolved in the fluorite matrix, oxygen atoms liberated by the fission of U235 or Pu239, and other elements found in relatively large quantities such as noble metals, zirconium from the cladding, or volatile fission products (Cs, I, Te). These could form separate oxide phases. Although these phases have not been observed under normal operating conditions, it is rather interesting to be able to ascertain whether their presence is at least thermodynamically possible. In addition, any mechanistic approach to stress corrosion cracking should include a comprehensive thermochemical assessment of what occurs at the fuel-cladding interface.

In this paper, we present the work which has been carried out using the programme SAGE. The programme, which calculates chemical equilibria based on free energies of reactions, has been used to perform calculations which are then compared to the measured oxygen potential of fluorite phases such as $U_{1-y}Gd_yO_{2+x}$ in both the hypostoichiometric and hyperstoichiometric regions of the ternary phase diagram. After initial adjustments the model was used to calculate the oxygen potential of simulated high burn-up fuels [3,4]. Lastly, an attempt was made at estimating the chemical state of a highly irradiated fuel rod. Results were compared to measurements performed by Matzke [5].

2. MODELLING THE $U_yRE_{1-y}O_{2\pm x}$ FLUORITE PHASE

2.1 INTRODUCTION

It is assumed that the irradiated oxide fuel may be described as comprising several phases in thermodynamic equilibrium. The first phase represents the fluorite matrix which contains a proportion of dissolved plutonium atoms along with fission products which are known to have a tendency to remain in the original matrix. The gaseous phase is modelled as an ideal mixture phase containing approximately 60 compounds. A separate noble metal phase is included to account for the possible presence of metal inclusions. Finally, around seventy separate solid compounds are modelled. The general approach is very similar to that presented by Ball et al. [6] and it is fairly straightforward to account for the gaseous mixture phase and the solid compounds. Indeed, the calculations are performed using the SAGE programme [7] which minimises the Gibbs energy of the system. Hence the main difficulty lies in establishing a reliable set of thermodynamic data [8].

However, one of the main stumbling blocks regards the oxygen potential modelling of the fluorite phase. This phase was first represented by Lindemer et al. using an ideal solution model [9]. The representation we have chosen is largely inspired by this work, but we have introduced additional hypotheses which somewhat improve the modelling in the hyperstoichiometric region of the phase diagrams.

2.2 BASIC ASSUMPTIONS OF LINDEMER'S APPROACH

The starting point of the analysis is that UO_{2+x} crystallises in a fluorite phase which can accommodate relatively large deviations from stoichiometry. The UO_{2+x} phase is reported to be stable for O/M ratios ranging from 2 to 2.25 at temperatures above 940°C [10]. The stability of the UO_{2+x} phase is usually ascribed to the propensity of uranium atoms to acquire a valency greater than 4, i.e. 5 or 6. Simply speaking, the interstitial oxygen atoms are stabilized by an increase in valency of a proportion of uranium atoms. Lindemer's analysis of experimental values [9], available in the open literature, shows that oxygen potential measurements are accurately reproduced using simple chemical equilibria, by assuming that the fictitious solute compounds $U_2O_{4.5}$ and U_3O_7 form an ideal solution with the UO_2 species as solvent. Lindemer derives a value of the Gibbs free energy of formation for these two hypothetical solute compounds. The stability of the hypostoichiometric phase $U_yPu_{1-y}O_{2-x}$ is modelled in much the same way. That is to say that the solute compound $Pu_{4/3}O_2$ in equilibrium with PuO_2 and UO_2 accounts for the

presence of oxygen vacancies for O/M values below 2. The results obtained using this model are on the whole quite satisfactory. We refer the reader to Lindemer's original papers for further details [9,11].

In a similar way, for the ternary $<U_yRe_{1-y}O_{2+/-x}>$ system, where Re represents a trivalent rare earth, Lindemer and Brynestad [12] use the following equilibrium to account for the variations of the oxygen potential wilh the O/M ratio:

$$2UO_2 + 3Re_{4/3}O_2 + O_2 \Leftrightarrow 2URe_2O_6$$

The latter compound is the association of a rare earth atom of valence three with a uranium atom in an oxidised state. Its role is to stabilize the $<U_yRe_{1-y}O_{2+/-x}>$ fluorite phase at an oxygen potential lower than what it would be, were the rare earth atoms present in a separate sesquioxide phase.

It is important to note that by applying Gibbs' rule of phases to these systems, be it UO_{2+x}, $U_yPu_{1-y}O_{2+x}$ or $U_yRe_{1-y}O_{2+/-x}$, one shows that the oxygen potential is a function of temperature, oxygen over metal ratio, and rare earth or plutonium content only. This justifies assessing the validity of the models used by comparing measured and calculated oxygen potential values.

The results of calculations performed using $U_2O_{4.5}$ and U_3O_7 as the hyperstoichiometric species along with the fictitious compounds $Gd_{4/3}O_2$ and UGd_2O_6 are shown in Figure 1. The results are compared to oxygen potential measurements carried out by Une et al. [13,14] for an oxide containing 14% gadolinium at 1273K. Values for pure urania and an 11% plutonium mixed oxide, taken from [13,14] and [15], are also reported. The characteristic oxygen potential transition around an O/M value of 2 is properly reproduced for both the U-Pu-O and U-Gd-O systems. Although calculated values are satisfactory in the hypostoichiometric region, the increase in oxygen potential for the hyperstoichiometric Gd solid solution is underestimated by about 100kJ/mol as the value of O/M approaches 2. The model presented in the following section is based on oxygen potential measurements for Gd doped urania although Gd has a fairly low fission yield. However, Gd is known to be representative of other trivalent rare earths and oxygen potential measurements for the $U_yGd_{1-y}O_{2+/-x}$ system have been performed over a wide range of temperatures, deviations from stoichiometry and rare earth contents because of the possible use of Gd as a burnable poison in LWR fuels.

At this stage two important questions need to be examined. The first one regards the actual reason behind the increase in oxygen potential of oxides containing trivalent rare earths. The second one relates to the reason why a simple model gives results which show no substantial increase of the oxygen potential in the hyperstoichiometric region.

2.3 MODELLING THE HYPERSTOICHIOMETRIC PHASE.

2.3.1 Introduction

Many authors have attempted to address the first issue (e.g. [16]). Olander's analysis seems to offer the most simple and probable scenario. Indeed, if one assumes the valency of gadolinium atoms to remain at 3, then their effective charge in the fluorite matrix is negative and is worth -1. Hence, rare earth atoms will tend to repel oxygen atoms thus reducing the number of sites available to them, in turn increasing the effective oxygen activity and potential. Answering the second question open to debate is now fairly straightforward. In the hyperstoichiometric region of the $\overline{\Delta G(O_2)}$ vs. O/M diagram, Lindemer's model predicts that out of the two fictitious compounds UGd_2O_6 and $Gd_{4/3}O_2$, UGd_2O_6 is by far the more stable. In this model, the oxygen potential is therefore the result of the activity of the $U_2O_{4.5}$ species and the following equilibrium:

$$8UO_2 + O_2 \Leftrightarrow 4U_2O_{4.5}$$

In terms of free energies of formation and activities, this equates to:

(1) $$\overline{\Delta G(O_2)} = 4\Delta G^{\circ}(U_2O_{4.5}) - 8\Delta G^{\circ}(UO_2) + RT\ln\left(\frac{a^4_{U_2O_{4.5}}}{a^8_{UO_2}}\right)$$

According to ideal thermodynamics, the activity of a species which enters into the composition of an ideal solid solution is equal to its molar fraction. Hence, if gadolinium is introduced in moderate quantities, and supposing the O/M ratio of the solution is close to stoichiometry, then the activity of the UO_2 species is more or less unchanged. Since the molar fraction of $U_2O_{4.5}$ is in effect an indication of deviation from stoichiometry, equation (1) predicts that the oxygen potential of the fluorite solution with or without gadolinium should remain almost the same.

Using SAGE to compute chemical equilibria requires the use of Gibbs free energies. It seemed therefore natural to us to turn to Wadier's work regarding the behaviour of neodymium doped urania [17]. Trivalent rare earths in a UO_{2+x} fluorite structure, are known to occupy the same positions as any ordinary uranium atom. Generally speaking, there are five basic possible configurations, each corresponding (for all but pure urania) to the substitution of one or more uranium atoms for an equal number of rare earth atoms. Let E_f^i $(o \le i \le 4)$ be the energy of formation of the hyperstoichiometric defect for the i-th configuration and E_f their average value. E_f can easily be expressed as a function of E_f^i and y the proportion of rare earth:

(2) $$E_f = \sum_{i=0}^{4} C_4^i . E_f^i . y^i . (1 - y)^{4-i}$$

In our representation of the fluorite matrix, we take the free energies of formation of both hyperstoichiometric species $U_2O_{4.5}$ and U_3O_7 to be given by equation (2). However, since our aim is to model solid solutions containing much less than 30% rare earths, the analysis was performed, using only the first three terms in equation (2). Equation (2) thus becomes:

(2a) $$_f = E_f^{\circ}(T).(1 - y)^4 + 4E_f^1(T).y.(1 - y)^3 + 6E_f^2(T).y^2.(1 - y)$$

In the above equation, E_f° is taken to be the free energy of formation of the hyperstoichiometric defect in pure urania. The problem now consists in computing values for E_f^i $(1 \le i \le 2)$ based on measurements performed at different temperatures and for different values of y.

2.3.2 Exact stoichiometry

Our aim here is to briefly outline the method employed both to obtain values for E_f^i and to ascertain the validity of the model. Firstly we need to establish the basic equations which govern the system. Let X1, X2, X3, X4, X5 be the respective molar fractions of the following compounds: UO_2, $U_2O_{4.5}$, U_3O_7, $Gd_{4/3}O_2$, and UGd_2O_6. Conservation of mass, gadolinium and oxygen yields three independent mass balance equations:

(3) $$X1 + X2 + X3 + X4 + X5 = 1$$

(4) $$\frac{(4/3)X4 + 2X5}{X1 + 2X2 + 3X3 + (4/3)X4 + 3X5} = y$$

(5) $$\frac{2X1 + 4.5X2 + 7X3 + 2X4 + 6X5}{X1 + 2X2 + 3X3 + (4/3)X4 + 3X5} = 2$$

Three more independent equations may be obtained by expressing the equilibrium between the relevant compounds. This yields:

(6) $$2\Delta G^{\circ f}(uo_2) + 2RTln(X1) + \frac{1}{4}\overline{\Delta G(o_2)} = \Delta G^{\circ f}(u_2o_{4.5}) + RTln(X2)$$

(7) $$2\Delta G^{\circ f}(u_2o_{4.5}) + 2RTln(X2) = \Delta G^{\circ f}(u_3o_7) + RTln(X3) + \Delta G^{\circ f}(uo_2) + RTln(X1)$$

(8) $$3\Delta G^{\circ f}(Gd_{4/3}O_2) + 2\Delta G^{\circ f}(uo_2) + \overline{\Delta G(o_2)} - 2\Delta G^{\circ f}(UGd_2O_6) = RTln(\frac{x5^2}{x1^2.x3^3})$$

This adds up to 6 independent equations. However, the problem lies in computing values for ΔG^{of} ($U_2O_{4.5}$) and $\Delta G^{of}(U_3O_7)$ from measured oxygen potentials, for a given proportion of gadolinium and at a certain temperature. Since $\overline{\Delta G(O_2)}$ is known, there are 7 unknown quantities, i.e. X1 through X5, and the Gibbs free energies for both supposed hyperstoichiometric defects. One more equation is therefore needed. In equation (7), the oxygen potential does not appear explicitly, hence it is in principle true whatever value of y. We therefore postulate that $2\Delta G^{\circ f}(U_2O_{4.5}) - \Delta G^{\circ f}(U_3O_7)$ is independent of y which finally yields the elusive seventh equation necessary to entirely solve the problem:

(9) $$2\Delta G^{\circ f}(u_2o_{4.5})[y,T] - \Delta G^{\circ f}(u_3o_7)[y,T] = 2\Delta G^{\circ f}(u_2o_{4.5})[y=0,T] - \Delta G^{\circ f}(u_3o_7)[y = 0,T]$$

Measured oxygen potential values were taken from those reported by Lindemer [18] and Une & Oguma [13,14]. Around 20 different values of $\Delta G^{\circ f}(U_2O_{4.5})$ and $\Delta G^{\circ f}(U_3O_7)$ were thus computed, over an 800K temperature range (from approximately 1000.K to 1800.K) with y ranging from 4 to 30%. At a given composition and whenever possible, a linear regression was used to extend values of $\Delta G^{\circ f}(U_2O_{4.5})$ and $\Delta G^{\circ f}(U_3O_7)$ to all temperatures. Using equation (2a) and values obtained from experimental results at a given temperature, a second order least squares fit is performed to yield values for $E_f^1(T)$ and $E_f^2(T)$. A linear regression with respect to temperature, using seven values for each $E_f^i(T)$, eventually yields:

$$E_f^1(T) = -1704.6 + 0.2187T$$

- for $U_2O_{4.5}$:

$$E_f^2(T) = -3304.3 + 0.6028T$$

$$E_f^1(T) = -2366.4 + 0.2149T$$

- for U_3O_7:

$$E_f^2(T) = -5132.1 + 0.9684T$$

where $E_f^i(T)$ are expressed in kJ/mol and T in K.

2.3.3 Deviation from stoichiometry

The approach chosen for the hyperstoichiometric region is essentially the same. That is to say that only equation (5) is modified to give:

$$(11) \qquad \frac{2X1 + 4.5X2 + 7X3 + 2X4 + 6X5}{X1 + 2X2 + 3X3 + (4/3)X4 + 3X5} = 2 + x$$

where x represents deviation from stoichiometry.
Not surprisingly, applying the analysis described in the previous section to values of x strictly positive, yields a different set of results for each $E_f^i(T)$ and for each defect. Hence we define the function f(x,T), a priori independent of y, as:

$$f(x,T) = \frac{\Delta G^{\circ f}(U_aO_b)(y,x,T) - \Delta G^{\circ f}(U_aO_b)(y = 0, x = 0,T)}{\Delta G^{\circ f}(U_aO_b)(y,x = 0,T) - \Delta G^{\circ f}(U_aO_b)(y = 0, x = 0,T)}$$

Figure 1 shows that as the O/M ratio increases, the oxygen potential of a solid solution containing some proportion of gadolinium approaches that of pure urania. This is a general tendency. Hence, one may expect f to decrease with increasing values of x. The simplest form f may take is a polynomial function of x, e.g.: $f(x, T) = 1 - a(T)x^{b(T)}$. At a given temperature, $\Delta G^{\circ}f(U_aO_b)(y, x, T)$ is computed as detailed in the previous section for as many values of x as possible. The function ln(1-f(x,1273.)) (computed from values taken from [13,14,18]) is plotted against ln(x) in figure 2 for the $U_2O_{4.5}$ species to substantiate the underlying assumptions of the model. Several comments are in order. Firstly, the assumed expression for f is apparently well suited. Secondly, as foreseen, f is indeed independent of y. Values of a and b are then calculated by performing a logarithmic regression with respect to x.

Performing the above exercise at various temperatures enables us to plot a(T) and b(T). A quadratic temperature dependency for a and b was found to be quite satisfactory. The results regarding the $U_2O_{4.5}$ species are shown in figure 3.

2.3.4 Discussion

Establishing a range of temperatures, gadolinium concentrations and deviations from stoichiometry over which one may be sure of the results the model yields is a rather arduous task. Experimental results may differ according to the technique employed, e.g. thermogravimetric (TGA) or solid electrolyte galvanic cell (EMF) measurements. Most authors though (e.g. [14]) agree that the error in measuring the O/M ratio is roughly ± 0.001 to ± 0.002 at 1273K. However, such an error will lead to a greater uncertainty in terms of oxygen potential, especially close to exact stoichiometry. So strictly speaking, the error made when announcing an oxygen potential value is a complex function of y, x, T, and the experimental technique. Roughly speaking though, it is reasonable to assume that the oxygen potential of the fluorite matrix is known to within 50kJ/mol for an O/M value approaching 2.

Figures 4 through 6b illustrate results obtained using this model and an adequately modified version of SAGE at various gadolinium concentrations, temperatures and O/M values. The calculated and

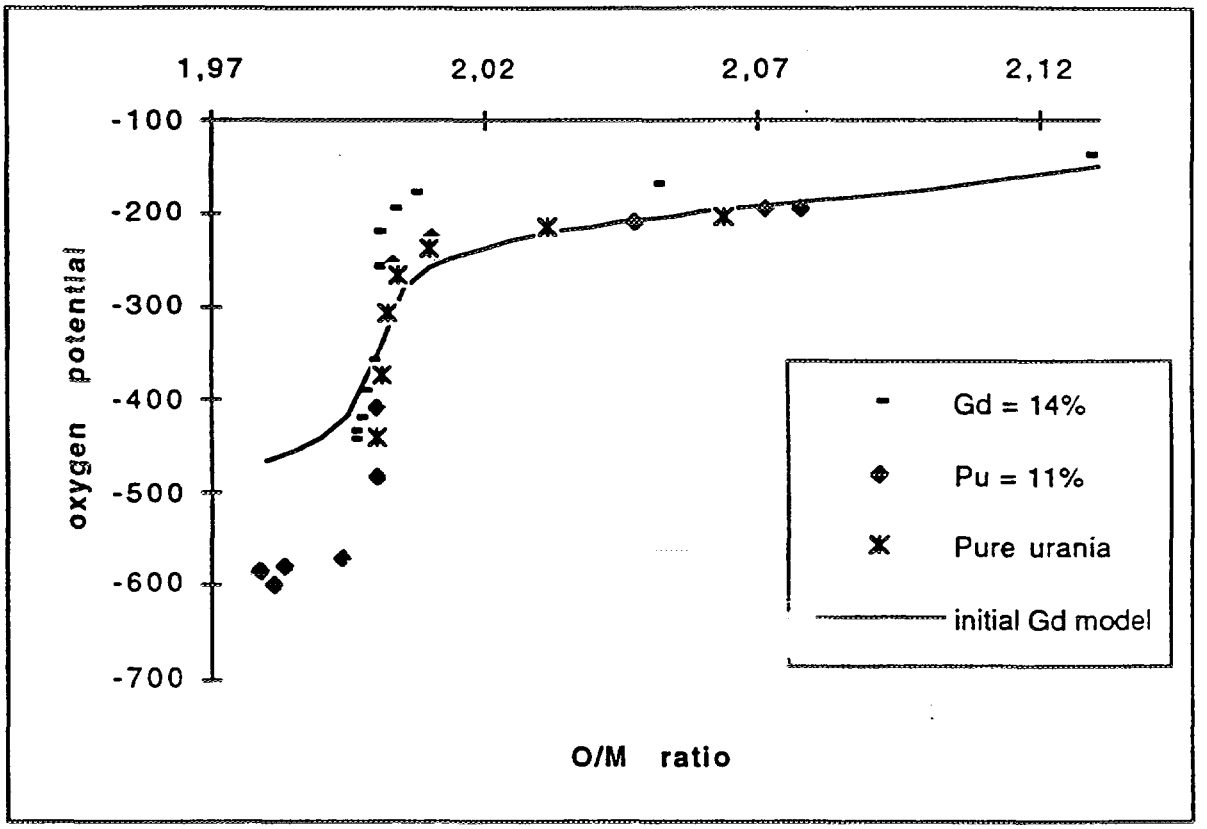

FIG. 1. *Oxygen potentials of Gd doped urania, 11% Pu mixed oxide, pure urania T # 1273K*

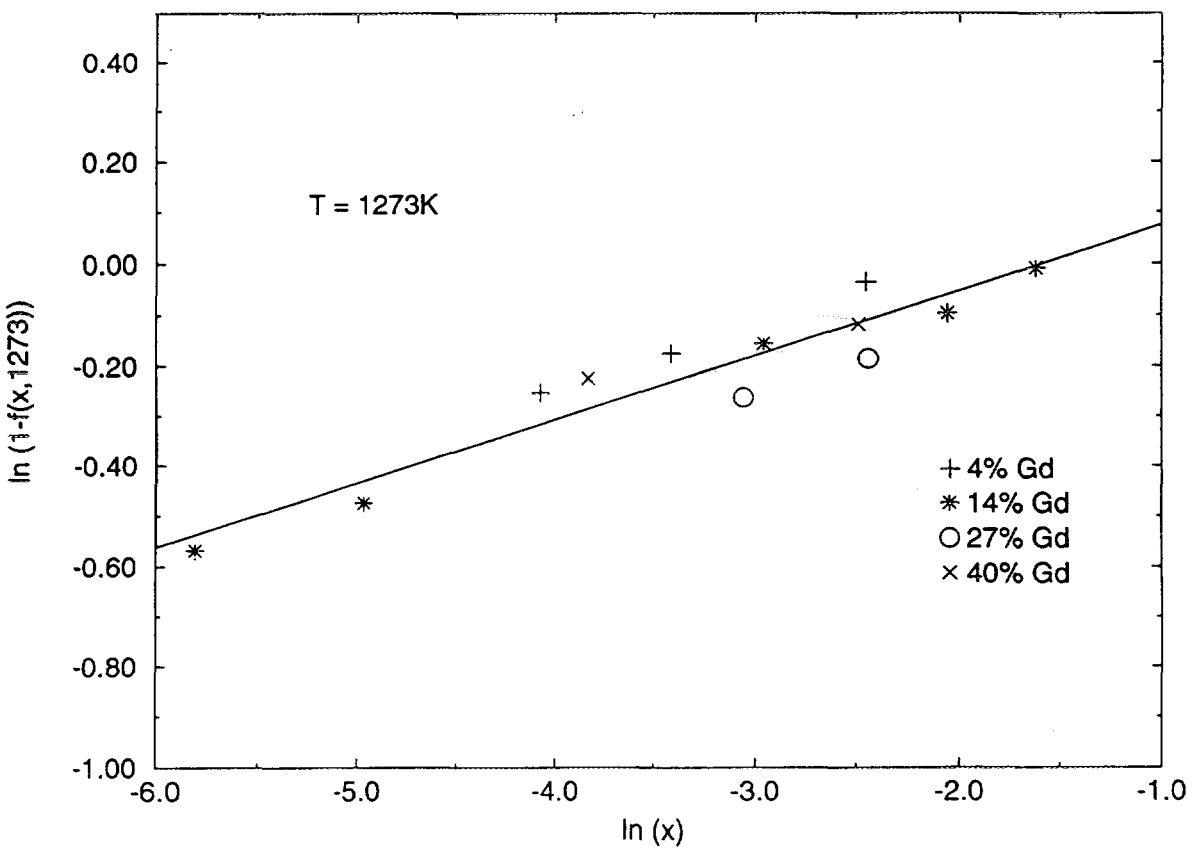

FIG. 2. *Hyperstoichiometric U-Gd-O solid solution behaviour*

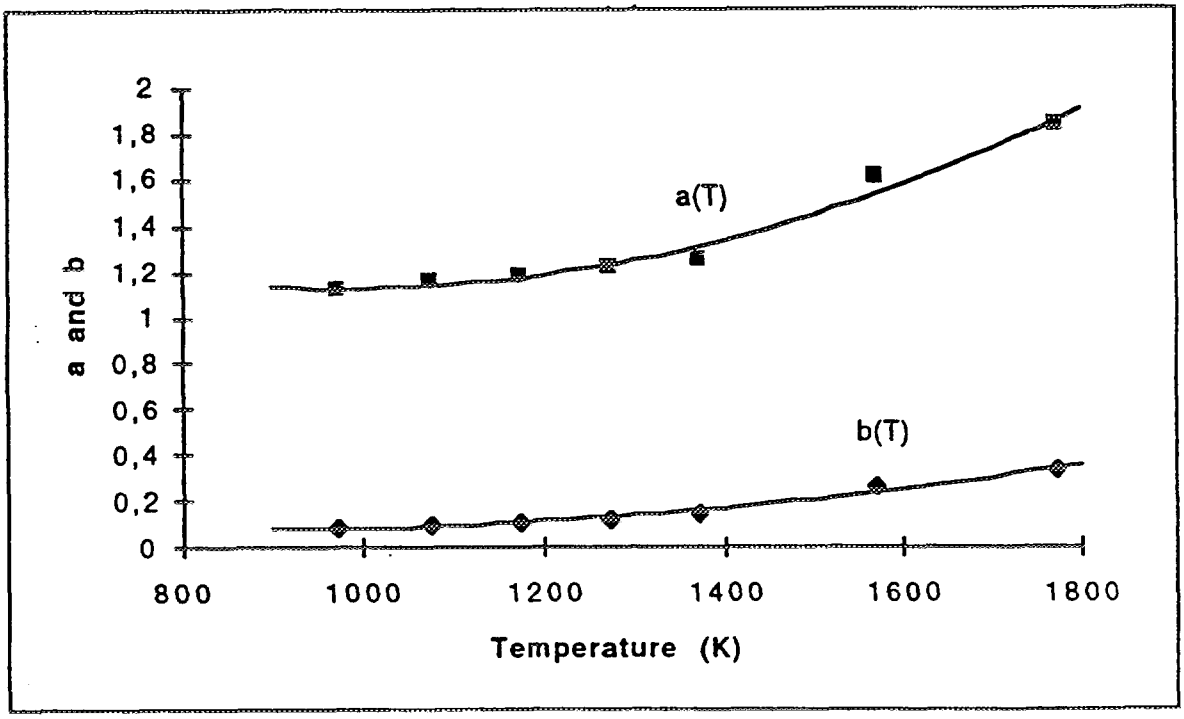

FIG. 3. *a(T) and b(T) for U204.5 species*

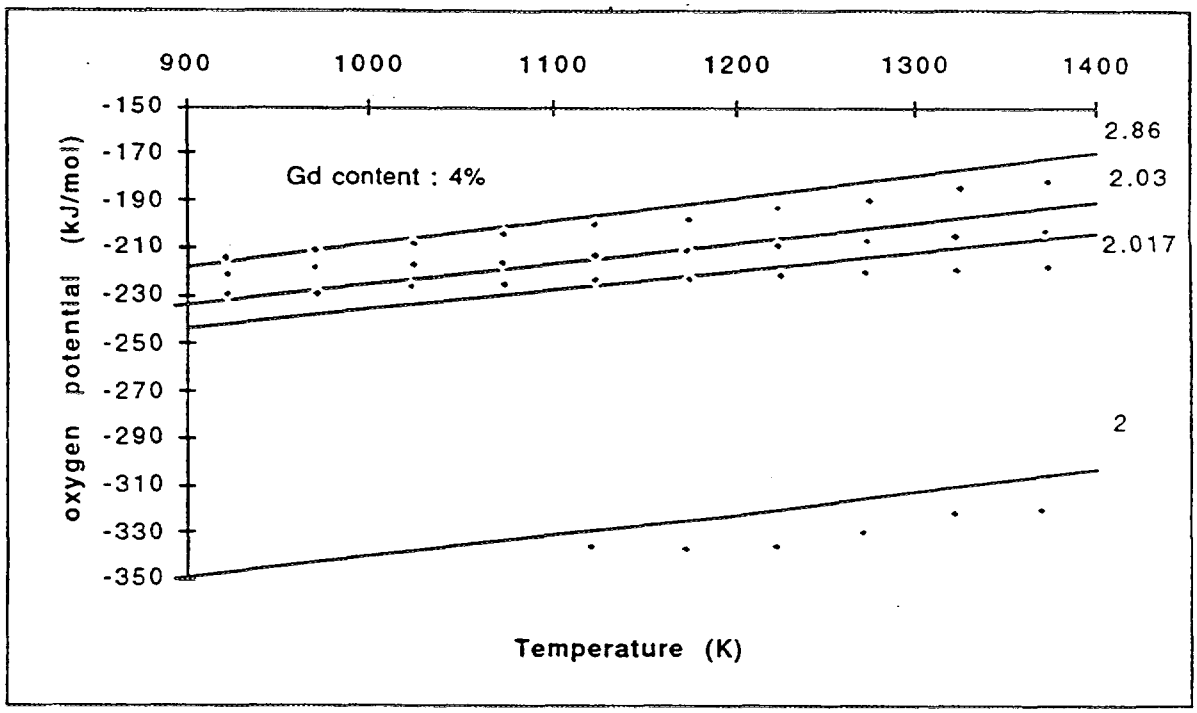

FIG. 4. *Comparison of model calculations (straight lines) and experimental data points*

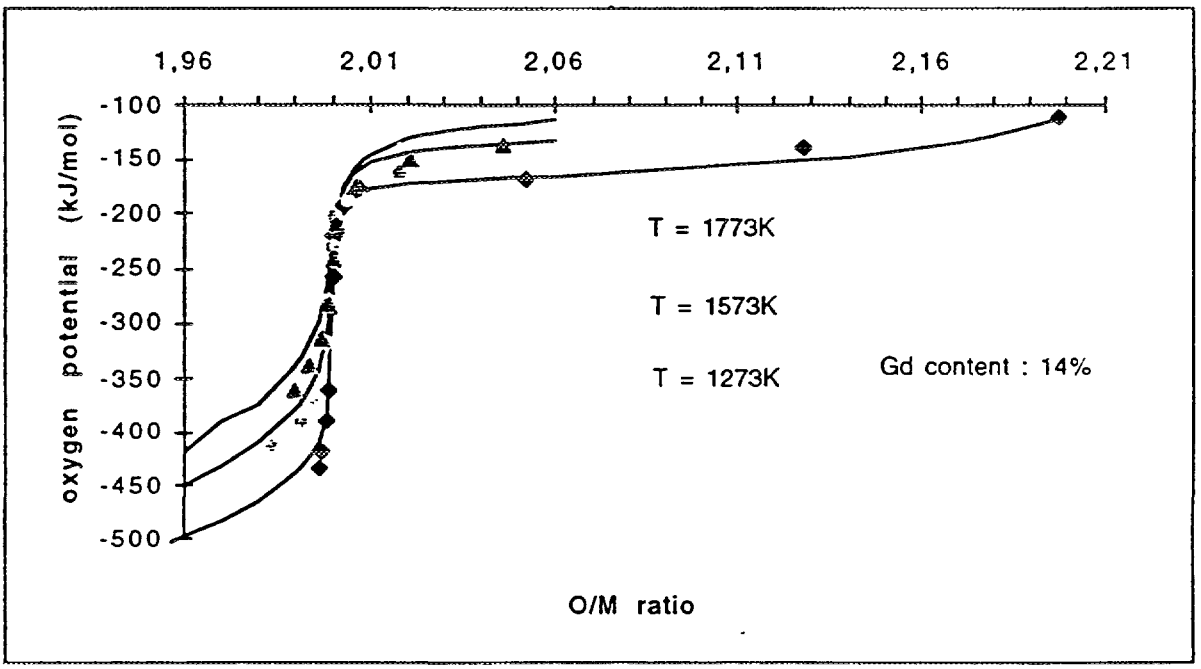

FIG. 5. *Comparison of model calculations (solid curves) and experimental data points*

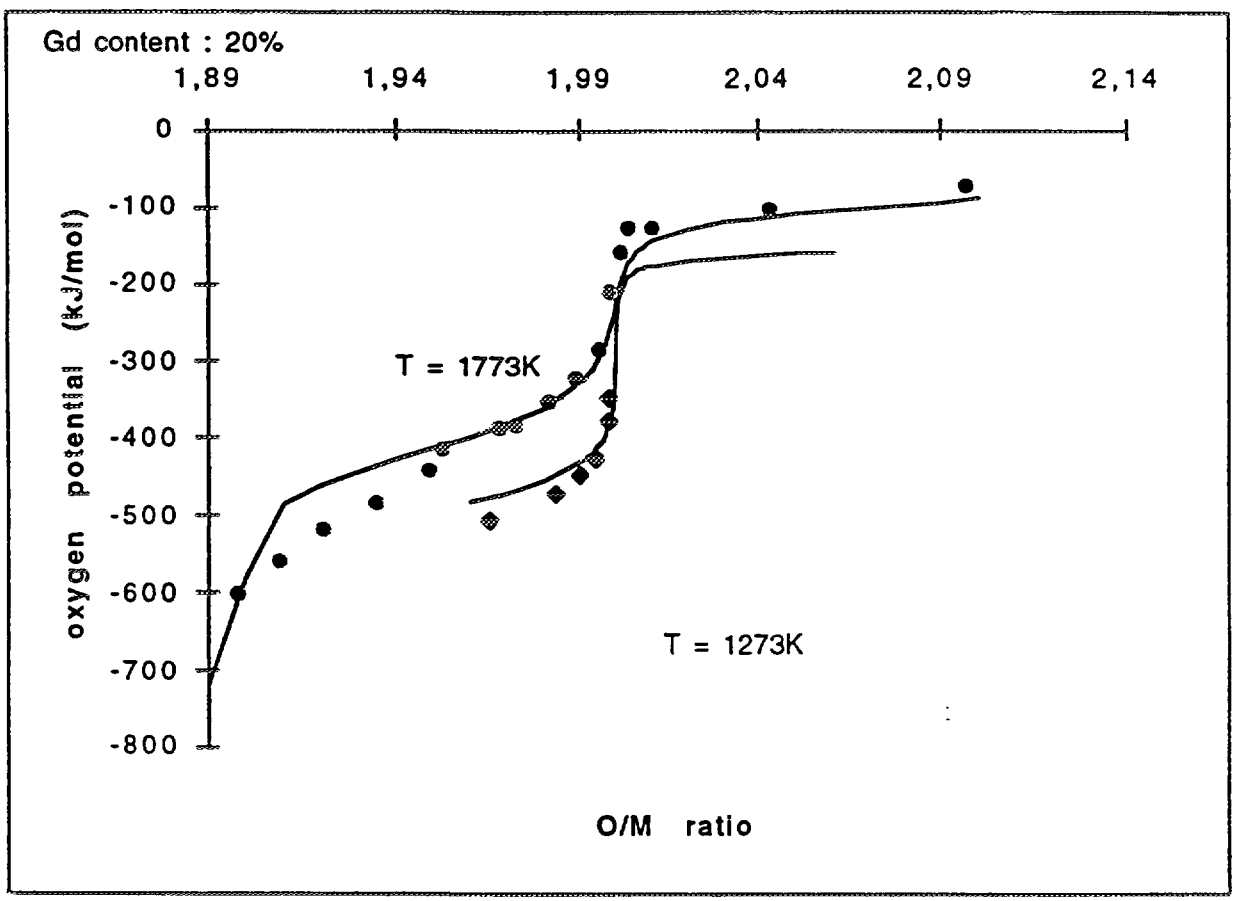

FIG. 6a. *Comparison of model calculations (solid curves) and experimental data points*

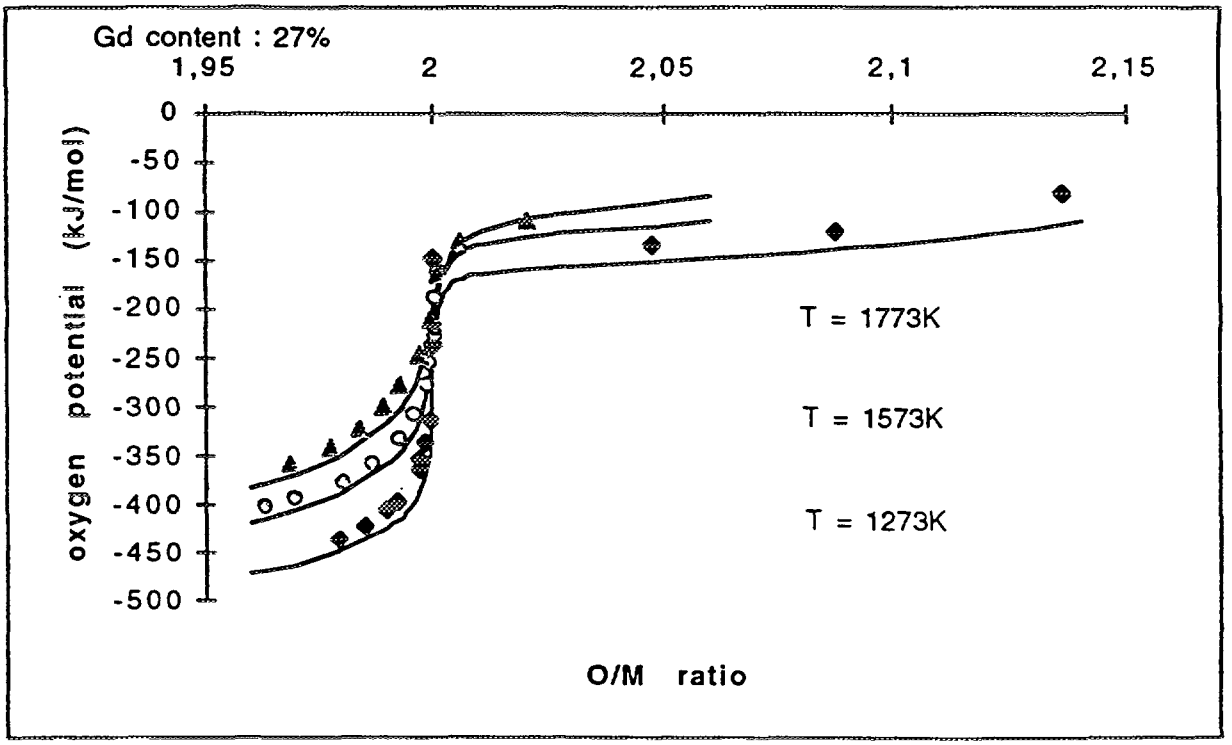

FIG. 6b. Comparison of model calculations (solid curves) and experimental data points

experimental results seem to be in very good agreement. This, one could say, is hardly surprising since the model was adjusted to fit these measurements. However, one may take heart from the fact the model produces equally good results at low (4%) or high (27%) gadolinium concentrations. It is interesting to note that most calculated values fall well within 20kJ/mol of the corresponding experimental value. A maximum discrepancy of about 50kJ/mol is seen for a temperature of 1273K, a 27% gadolinium concentration and an O/M ratio of about 2 (fig.6b). More importantly though, the main tendencies are properly reproduced, i.e.:

- sudden increase in oxygen potential for an O/M ratio of 2
- increase in oxygen potential with temperature for a given gadolinium content
- at a given temperature, increase in oxygen potential with increasing values of y.

It is however rather difficult to give a physical meaning to the values of the various free energies of formation that appear in the model. None the less the fact that f decreases with increasing values of x corroborates the physical interpretation according to which, as the number of interstitial atoms increases, they eventually become oblivious to the presence of trivalent rare earth atoms.

One must bear in mind the fact that the model has been adjusted to suit the results of experiments whose temperatures (between 1000K and 1800K), O/M ratios (up to 2.2) and gadolinium contents (between 4% and 30%) are somewhat out of focus with the desired application range (i.e.: $700K < T < 1500K$, O/M around 2, $0 < y < 5\%$).

3. CALCULATING SIMFUELS AND IRRADIATED OXIDES

3.1 INTRODUCTION

For completeness, a word needs to be said about the way other dissolved fission products are treated. As regards trivalent rare earths for instance, it is widely known (e.g. [19]) that the U-Nd-O

system shows striking thermodynamic similarities to the U-Gd-O system. We thus model Nd and Gd in exactly the same way. The equivalent lanthanum (La) system however shows a greater propensity to increase the oxygen potential of the fluorite phase [20]. The element is nevertheless modelled according to the same principles as Gd and Nd. Since very little data regarding yttrium (Y) is available, the modelling chosen is the same as that for La. The works of Hagemark [20] in the hyperstoichiometric region support this choice.

Europium (Eu) and Samarium (Sm) are both known to take on a divalent or trivalent state. They are both modelled in the same way. Cerium (Ce) is represented by a trivalent ($Ce_{4/3}O_2$) and tetravalent (CeO2) species, the energy of formation of which is adjusted to fit results from [26]. Ba and Sr are modelled as forming monoxides which may remain soluble in the fluorite matrix.

As for Zr which is a relatively abundant fission product, our modelling is largely inspired by Ball and presented by Potter [21].

3.2 MODEL CALCULATIONS OF WOODLEY'S AND UNE & OGUMA'S SIMULATED HIGH BURNUP FUELS

Measurements performed by Woodley [3] and Une & Oguma [4] are of great significance if we are to check the validity of the approach described in the previous sections, the ultimate aim of which is to predict the thermochemical state of an irradiated uranium-plutonium oxide matrix. Woodley's measurements pertain to $U_{0.75}Pu_{0.25}O_{2-x}$ solid solutions whose burnup is simulated by adding various rare earths and zirconium in proportion to their fission yields. The simulated burnup ranged from 0 to 10 at%. Figure 7 is a plot of measured vs. calculated points for all of Woodley's results. Figure 8 compares model calculations to oxygen potential values as a function of burnup, for various O/M ratios and at 1373K.

The discrepancy between measured and calculated oxygen potentials at 0 at% burnup remains largely unchanged at 10 at%. The most important deviation seen at 1173K ranges from around 50kJ/mol to 80kJ/mol. Although calculations seem to systematically overestimate experimental values, agreement is generally satisfactory. That is to say that the most important feature is properly reproduced, i.e. a nearly linear increase with burnup of the oxygen potential. Differences observed are in any case very much in line with Woodley's own account of the accuracy of the O/M measurements which is thought to be roughly $\pm$ 0.002.

It is also rather interesting to compute the oxygen potential of solid solutions as prepared by Une & Oguma which contrary to Woodley's are hyperstoichiometric and contain no plutonium.

Figure 9 shows a comparison of model calculations and experimental data points taken from [4] at a temperature of 1573K. Again the agreement between the model and experimental results is excellent, except maybe for O/M values very close to 2 i.e. $x<0.002$. This value of x is within the range of accuracy reported by Une et al., i.e. $\pm$ 0.00 1.

Hence both Woodley's and Une's results purport to show that our modelling of the oxygen potential of the fluorite phase is reasonable.

3.3 OXYGEN POTENTIALS OF HIGHLY IRRADIATED FUELS

3.3.1 Possible buffering reactions

We have no intention of presenting here an exhaustive account of buffering reactions which may occur in a highly irradiated fuel rod. We refer the reader to e.g. [6,22] for a more comprehensive account. Nevertheless, in classifying fission products, some appear to belong to two categories at a time. Molybdenum (Mo) and zirconium (Zr) show such a behaviour. If the oxygen potential is high enough, Mo may oxidise to MoO_2 or Cs_2MoO_4 thus depleting the metallic inclusions it usually makes up along with Pd, Rh, Ru, Tc. Zr too may either be dissolved in the matrix or form a separate oxide. These two

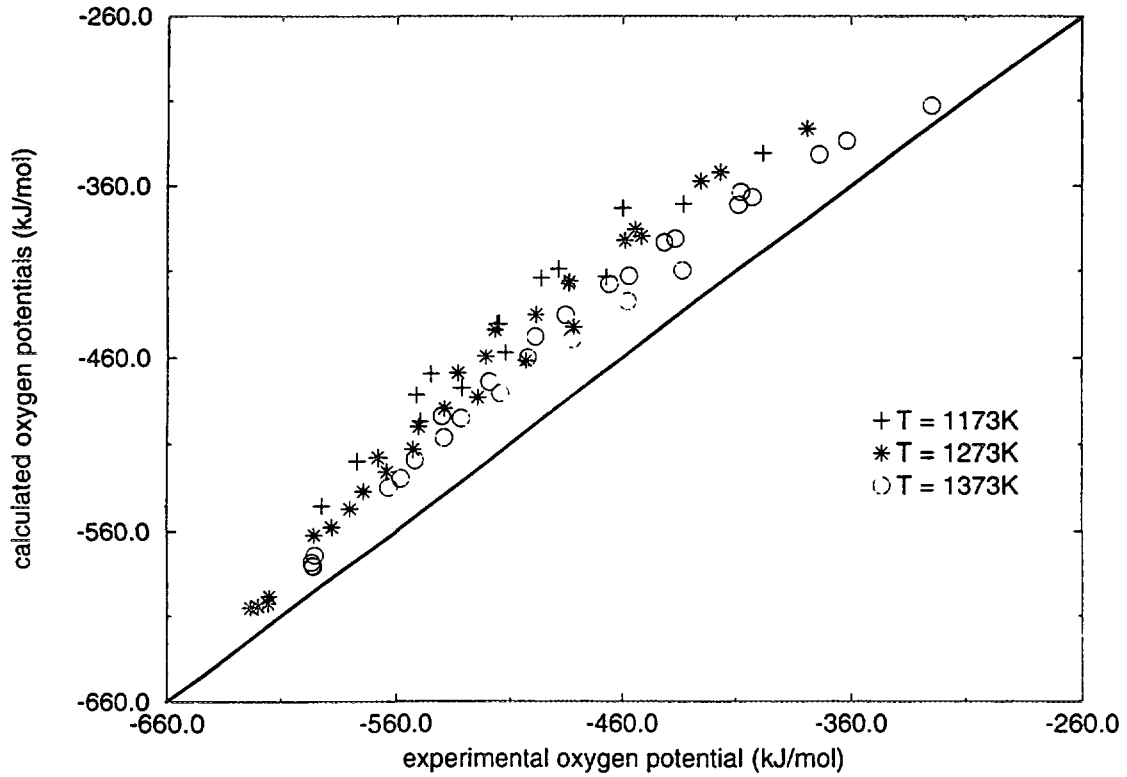

FIG. 7. *Calculated vs. experimental oxygen potentials (Woodley)*

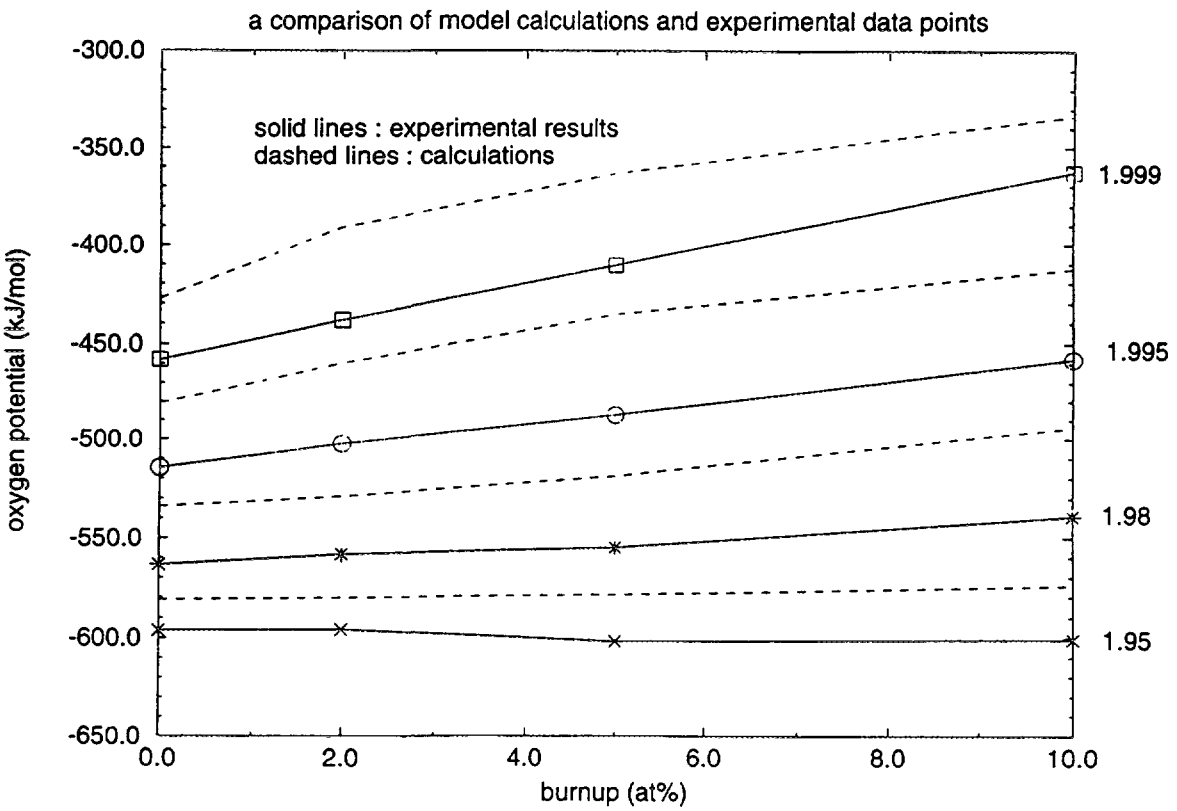

FIG. 8. *Oxygen potential vs. simulated burnup - T = 1373K*

elements therefore appear to play a key role with respect to our general assessment. Other possible reactions which have been accounted for are those which lead to the formation of caesium uranates. Most of the thermodynamic data used concerning separate oxide phases and gaseous species was either taken from [6] or [8]. Noble metal inclusions are treated simply on the basis of results obtained by Yamawaki et al. and presented in [23]. A more general approach could however be implemented following Gürler and Pratt's contributions in this field [24,25].

3.3.2 High burnup calculations

Finally, calculations were performed at burnups ranging from 0 to 200 GWd/tM. The increase in Pu concentration due to the RIM effect was accounted for on the basis of results taken from [2]. Concentrations for calculating points at 150 and 200 GWd/tM were 1.5 and 3% of initial heavy metal atoms respectively. These figures are in line with Matzke's assessment [5]. Table I gives the quantities of fission products and plutonium used in the calculation. These quantities are taken to be characteristic of L.W.R.

Although several calculations were performed only two are reported here. Figure 10 shows the calculated change in oxygen potential as a function of burnup at a temperature of 750°C. Both sets of calculations are reported. In the first case, Mo is allowed to oxidise. However we assume that at that temperature, Cs, Mo and Ba are not mobile enough to form caesium molybdates in important quantities. Molybdates are hence not permitted to form. Detailed results show that in this instance caesium uranates become stable. The second calculation was performed assuming that no Mo whatsoever oxidizes. In the first case, the O/M ratio decreased linearly with burnup from an initial value of 2 to just above 1.992 at 200 GWd/tM. Conversely, assuming no Mo oxidizes leads an increase of the O/M ratio and eventually a slightly hyperstoichiometric fuel. Results from [5] also appear in figure 10. These suggest that an efficient oxygen sink is at work. For the first set of calculations, after an initial rapid rise, the oxygen potential stabilises at roughly -410kJ/mol. The oxygen potential values and the O/M ratios are both very much in line with [5].

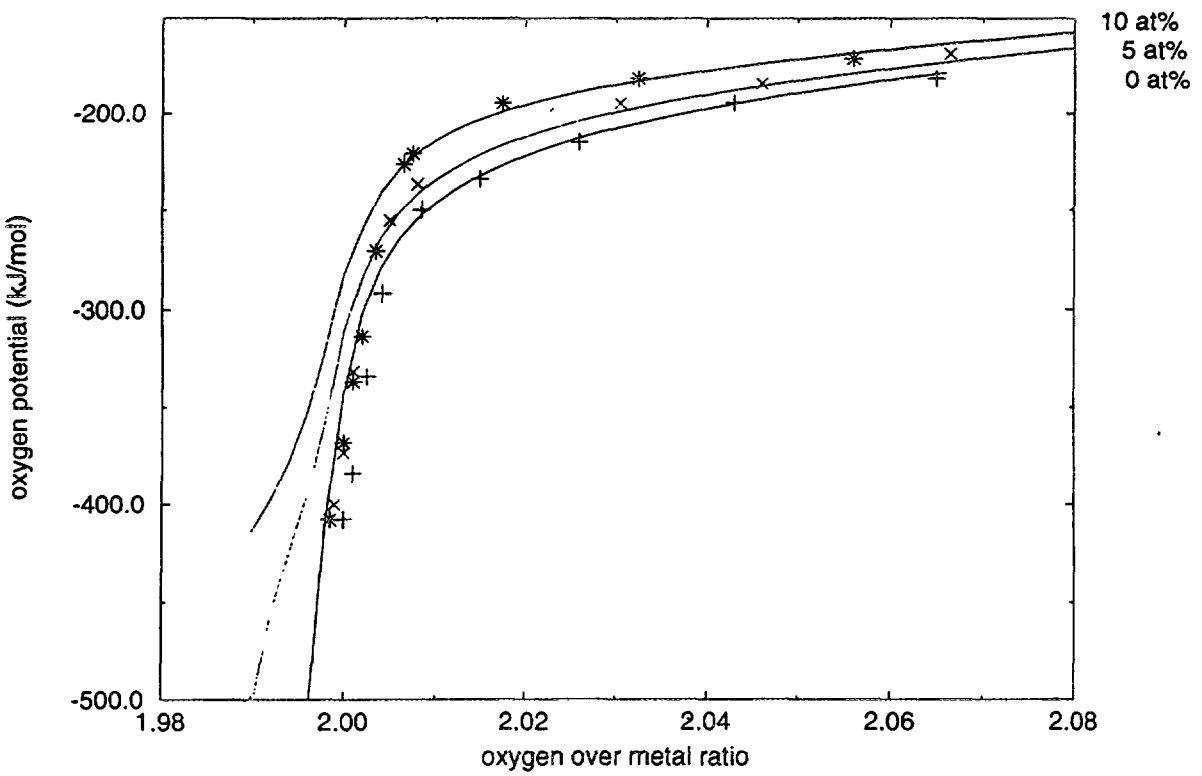

FIG. 9. Oxygen potential of simulated high burnup fuels T = 1573K

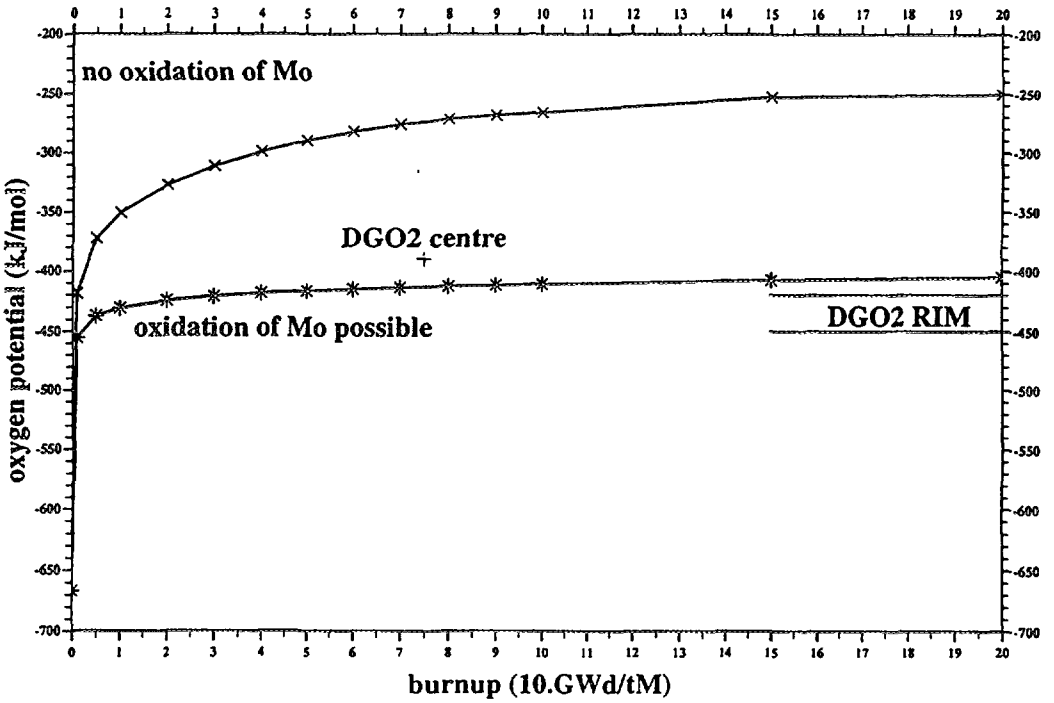

FIG. 10. DGO2 vs. burnup (1023K)

If one accounts for a reasonable amount of oxygen to be transferred to the zircalloy cladding (in line with experimental observations), a greater quantity of Mo is found in metallic inclusions (approximately 65% of the total amount of Mo). More importantly though, neither the oxygen potential of the fuel nor its O/M ratio fundamentally change. In short, measurements taken from [5] are properly reproduced if either Mo or Mo and Zr from the cladding are allowed to oxidise. A majority of Mo is found in the noble metal phase.

A comprehensive model describing the chemical behaviour of the fuel rod should be capable of calculating oxygen transfer. Oxygen is known to migrate in a temperature gradient, but an extra driving force for oxygen migration may arise as a result of cladding oxidation. The situation is somewhat complicated by kinetic considerations. Indeed, it is quite probable that the cladding will only act as an efficient sink if the fuel cladding gap is closed.

4. CONCLUSION

A model has been developed using the SAGE programme to assess the thermochemical state of irradiated fuels containing a wide range of dissolved fission products (essentially rare earths). The model has been used to compute the oxygen potential of Gd doped urania over a wide range of stoichiometries (1.9-2.1) and temperatures (800K-1800K). Having extended the model to account for the presence of other soluble fission products, on the basis of known experimental results, its validity was successfully checked by calculating the oxygen potentials of simulated high burnup fuels. Finally, using readily available thermochemical data, a general assessment of the chemical state of irradiated LWR fuels was attempted. Calculations have revealed that some form of oxidation, either Mo or Zr, has to occur to fall within the range of oxygen potential measurements reported by Matzke. The overall O/M ratio of the fuel decreases linearly with burnup and the oxygen potential is rapidly stabilized. The fuel is thus seen to become slightly hypostoichiometric (1.992 at 200 GWd/tM).

table 1 : quantities of chemical elements considered in the calculations.

Bu (GWd/tM)	1	10	40	80	90	100	150	200
U	0.998548	0.985933	0.9496	0.9061	0.8953	0.8845	0.8350	0.77
O_2	1.	1.	1.	1.	1.	1.	1.	1.
Pu+Pr	$5.10\ 10^{-4}$	$4.646\ 10^{-3}$	$1.27\ 10^{-2}$	$1.85\ 10^{-2}$	$1.99\ 10^{-2}$	$2.13\ 10^{-2}$	$2.37\ 10^{-2}$	$4.16\ 10^{-2}$
Nd+Gd+Pm	$1.97\ 10^{-4}$	$1.968\ 10^{-3}$	$7.9\ 10^{-3}$	$1.57\ 10^{-2}$	$1.77\ 10^{-2}$	$1.97\ 10^{-2}$	$2.95\ 10^{-2}$	$3.94\ 10^{-2}$
Y+La	$7.3\ 10^{-5}$	$7.35\ 10^{-4}$	$2.9\ 10^{-3}$	$5.8\ 10^{-3}$	$6.6\ 10^{-3}$	$7.3\ 10^{-3}$	$1.13\ 10^{-2}$	$1.51\ 10^{-2}$
Ce	$1.28\ 10^{-4}$	$1.282\ 10^{-3}$	$6.4\ 10^{-3}$	$1.03\ 10^{-2}$	$1.15\ 10^{-2}$	$1.28\ 10^{-2}$	$1.92\ 10^{-2}$	$2.56\ 10^{-2}$
.m.:Eu+Sm	$4\ 6\ 10^{-5}$	$4.64\ 10^{-4}$	$1.9\ 10^{-3}$	$3.7\ 10^{-3}$	$4.2\ 10^{-3}$	$4.6\ 10^{-3}$	$7.0\ 10^{-3}$	$9.3\ 10^{-3}$
Zr+Nb	$2.76\ 10^{-4}$	$2.761\ 10^{-3}$	$1.10\ 10^{-2}$	$2.21\ 10^{-2}$	$2.48\ 10^{-2}$	$2.76\ 10^{-2}$	$4.15\ 10^{-2}$	$5.53\ 10^{-2}$
Ba+Sr	$1\ 41\ 10^{-4}$	$1.405\ 10^{-3}$	$5.6\ 10^{-3}$	$1.12\ 10^{-2}$	$1.26\ 10^{-2}$	$1.41\ 10^{-2}$	$2.11\ 10^{-2}$	$2.81\ 10^{-2}$
Cs	$1.53\ 10^{-4}$	$1.530\ 10^{-3}$	$6.1\ 10^{-3}$	$1.22\ 10^{-2}$	$1.37\ 10^{-2}$	$1.53\ 10^{-2}$	$2.30\ 10^{-2}$	$3.06\ 10^{-2}$
Te	$3.3\ 10^{-5}$	$3.29\ 10^{-4}$	$1.3\ 10^{-3}$	$2.6\ 10^{-3}$	$3.0\ 10^{-3}$	$3.3\ 10^{-3}$	$4.9\ 10^{-3}$	$6.6\ 10^{-3}$
I	$1.5\ 10^{-5}$	$1.54\ 10^{-4}$	$6\ 10^{-4}$	$1.2\ 10^{-3}$	$1.4\ 10^{-3}$	$1.5\ 10^{-3}$	$2.3\ 10^{-3}$	$3.1\ 10^{-3}$
Mo	$2.46\ 10^{-4}$	$2.455\ 10^{-3}$	$9.8\ 10^{-3}$	$1.96\ 10^{-2}$	$2.21\ 10^{-2}$	$2.46\ 10^{-2}$	$3.68\ 10^{-2}$	$4.91\ 10^{-2}$
Pd	$8.5\ 10^{-5}$	$8.55\ 10^{-4}$	$3.4\ 10^{-3}$	$6.8\ 10^{-3}$	$7.7\ 10^{-3}$	$8.5\ 10^{-3}$	$1.28\ 10^{-2}$	$1.71\ 10^{-2}$
Ru+Tc+Rh	$2.28\ 10^{-4}$	$2.282\ 10^{-3}$	$9.1\ 10^{-3}$	$1.83\ 10^{-2}$	$2.05\ 10^{-2}$	$2.28\ 10^{-2}$	$3\ 42\ 10^{-2}$	$4.56\ 10^{-2}$

However, any conclusive account will need to encompass a realistic description of the mobility of fission products and oxygen in a temperature gradient. Also the chemical state of Zr in the cladding must be properly modelled if progress is to be made, as should the state of fission products which are generally regarded as insoluble. Little for instance is known of the position Cs atoms occupy in the irradiated fluorite lattice (or the energy of formation of their associated defects). Furthermore, SAGE only performs equilibrium calculations which take for granted the availability of chemical species. However it is by no means certain that an equilibrium situation is reached, especially in the RIM area. It is also still unclear what effect an irradiation environment has on the system. One must therefore remain cautious in extrapolating the calculations presented in this paper to an in pile situation.

ACKNOWLEDGEMENTS

The authors are pleased to express their gratitude to T.B. Lindemer for having supplied the experimental data base much of this work is based on. Electricite de France and Framatome are also thanked for their financial support.

REFERENCES

[1] MATZKE, Hj., "On the rim effect in high burnup UO_2 LWR fuels", J.N.M. 189 (1992) 141-148.

[2] GUEDENEY, P., TROTABAS, M., BOSCHIERO, M., FORAT, C., BLANPAIN, P., "Fragema fuel rod behaviour characterization at high burnup", International topical meeting on LWR fuel performance, Avignon (April 1991).

[3] WOODLEY, R.E., "Variation in the oxygen potential of a mixed-oxide Fuel with Simulated Burnup", JNM 74 (1978) 29()-296.
[4] UNE, K., OGUMA, M., "Oxygen potentials of UO_2 fuel simulating high burnup", Journal of Nuclear Science and Technology, 2n (1983) 844-851.
[5] MATZKE, Hj., "Oxygen potential in the rim region of high burnup UO_2 fuel", J.N.M. 2()8 (1993) 18-26.
[6] BALL, R.G.J., BURN.S, W.G., HENSHAW, J., MIGNANELLI, M.A., POTTER, P.E., "The chemical constitution of the fuel-clad gap in oxide fuel pins for nuclear reactors", J.N.M. 167 (1989) 191 -204.
[7] ERIKSSON, G., Chem. Scripta 8 (1975) 100.
[8] CORDFUNKE, E.H.P., KONINGS, R.J.M., "Thermochemical data for reactor materials and fission products", Elsevier Science Publishers (1990)
[9] LINDEMER, T.B., BESMANN, T.M., "Chemical thermodynamic representations of $UO_{2\pm x}$", J.N.M. 130 (1985) 473-488.
[10] SCHANER, B.E., Metallographic Determination of the U02-U409 Phase Diagram, JNM 2 (1960) 110-120.
[11] LINDEMER, T.B., BESMANN, T.M., "Chemical thermodynamic representation of $<PuO_{2-x}>$ and $<U_{1-z}Pu_zO_w>$, J.N.M. 130) (1985) 489-504.
[12] LINDEMER, T.B., BRYNESTAD, J., "Review and chemical thermodynamic representation of $<U_{1-z}Ce_zO_{2\pm x}>$ and $<U_{1-z}Ln_z0_{2\pm x}>$;Ln=Y,La,Nd,Gd", J. Am. Ceram. Soc. 69 (1986) 867-876.
[13] UNE, K., OGUMA, M., "Thermodynamic properties of non stoichiometric urania-gadolinia solid solutions in the temperature range 700 - 1100°C", J.N.M. 110 (1982) 215-222.
[14] UNE, K., OGUMA, M., "Oxygen potentials of $(U,Gd)O_{2\pm x}$ solid solutions in the temperature range 1000 - 1500°C", J.N.M. 115 (1983) 84-90.
[15] MARKIN, T.L., MCIVER, E.J., "Proceedings of the third international conference on plutonium", Chapman and Hall, London (1967) 845-857.
[16] OLANDER, D.R., PARK, K., "Defect models for the oxygen potential of gadolinium and europium-doped urania", J.N.M., 187 (1992) 89-96.
[17] WADIER, J-F., "Diagramme de phase et propriétés thermodynamiques du système uranium-néodyme-oxygène", Thèse, Université Paris VI, 1973.
[18] LINDEMER, T.B., SUTTON, A.L., "Study of nonstoichiometry of $<U_{1-z}Gd_zO_{2\pm x}>$, J. Am. Ceram. Soc. 71 (1988) 553-561.
[19] UNE, K., OGUMA, M., "Oxygen potentials of $(U,Nd)0_{2\pm X}$ solid solutions in the temperature range 1000 -1500°C", JNM 118 (1983) 189-194.
[20] HAGEMARK, K., BROLI, M., "Equilibrium oxygen pressures over solid solutions of urania-yttria and urania-lanthana 1100°C to 1400°C", J. Am. Ceram. Soc. 50 (1967) 563-567.
[21] POTTER, P.E., "The chemical constitution of irradiated nuclear fuels", Thermochemistry and chemical processing (Proc. Symp. Sundaram, 1989), 107-129.
[22] KLEYKAMP, H., "The chemical state of fission products in oxide fuels", JNM 131 (1985) 221-246.
[23] YAMAWAKI, M., NAGAI, Y., KOGAI, T., KANNO, M., "Thermodynamic studies on molybdenum/noble-metal alloys", Thermodynamics of nuclear materials (Proc. Int. Symp.Jülich, 1979), Vol. 1, IAEA, Vienna (1980), 249-261.
[24] GÜRLER, R., PRATT, J.N., "A computer assessment of the ternary Ru-Rh-Pd system", JNM 199 (1992) 22-28.
[25] GÜRLER, R., PRATT, J.N., "A computer calculation of the ternary Mo-Pd-Rh phase diagram", JNM 200 (1993) 16-23.
[26] DUCROUX, R., JEAN BAPTISTE, Ph., "Mesure du Potentiel d'Oxygène dans le Système $U_{0.7}Ce_{0.3}O_{2\pm x}$ à l'aide d' une Minisonde à Electrolyte Solide", JNM 97 (1981) 333-336.

BORON NITRIDE COATED URANIUM DIOXIDE AND URANIUM DIOXIDE-GADOLINIUM OXIDE FUELS

G. GÜNDÜZ
Department of Chemical Engineering,
Middle East Technical University

I. USLU, C. TORE, E. TANKER
Turkiye Atom Enerjisi Kurumu

Ankara, Turkey

Abstract

Pure urania and urania-gadolinia (5 and 10%) fuels were produced by sol-gel technique. The sintered fuel pellets were then coated with boron nitride (BN). This is achieved through chemical vapor deposition (CVD) using boron trichloride and ammonia. The coated samples were sintered at 1600 K. The analyses under scanning electron microscope (SEM) showed a variety of BN structures, mainly platelike and rodlike structures were observed. Burnup calculations by using WIMSD4 showed that BN coated and gadolinia containing fuels have larger burnups than other fuels. The calculations were repeated at different pitch distances. The change of the radius of the fuel pellet or the moderator/fuel ratio showed that BN coated fuel gives the highest burnups at the present design values of a PWR. Key words: burnable absorber, boron nitride, gadolinia, CVD, nuclear fuel.

INTRODUCTION

The use of boron compounds and especially boron carbide as burnable absorber in nuclear reactors resulted in some residual poison problems due to the low neutron absorption cross section (~760 b) of boron and in the last decade there has been serious attempts to shift to gadolinium (~ 49000 b). Gadolinium can be incorporated into urania (UO_2) in the form of gadolinia (Gd_2O_3) by powder mixing or sol-gel technique. The high amount of gadolinia in the fuel results in significant decrease in thermal conductivity, and some complexities in nuclear design. The full review of information about the use of gadolinia has been given in a recent work [1].

An alternative to gadolinia is the use of zirconium diboride (ZrB_2) coating, so called integral fuel burnable absorber [2-4]. The coating is achieved by sputtering method. However there are technical difficulties in fabrication technique, quality control of the layer, and dissolution of unreacted ZrB_2. In addition, the moderator temperature coefficient control is not very satisfactory in a reactor core having ZrB_2 coated fuel.

The physical and chemical problems associated with ZrB_2 fuel can be overcome by using boron nitride (BN) coating. It can be coated also on urania-gadolinia fuel so that lower amounts of gadolinia can be used in the fuel, hence a relative improvement is achieved in thermal conductivity. In this research work pure urania and urania-gadolinia fuel pellets were coated by BN. So it unifies the nuclear advantages of both gadolinium and boron.

BN COATING

BN prepared by CVD has been extensively investigated in the last decade in surface coating, production of synthetic abrasives, and manufacturing integral circuits in solid state electronics. The process consists of reducing or decomposing a volatile compound at high temperature onto a substrate at relatively low temperature. Low pressure CVD and plasma enhanced CVD processes are also getting important applications. Various chemical substances have been used to deposit BN. The major ones are; (a) reactions of ammonia (NH_3) with boron compounds, such as B_2H_6, BCl_3, BF_3 $B(OCH_3)_3$, H_3BO_3, and

$B_{10}H_{14}$ [5-23]; (b) thermal decomposition of borazoles such as $B_3Cl_3N_3H_3$ and $B_3N_3Cl_6$ [24], and borazines such as $BH_3HN(CH_3)_2$, $BHN(C_2H_5)_3$, and $B_3N_3H_3(CH_3)_3$ [25-27].

Among those B_2H_6 and BCl_3 are the most widely used boron compounds, the latter is preferred for its lower price and relatively low handling problems. The addition of boron three chloride (BCl_3) to NH_3 shows a complex pathway [28] with the overall reaction,

$$BCl_3 + 3NH_3 \rightarrow BN(s) + 3HCl\ (g)$$

EXPERIMENTS

In the experiments three different fuels were coated by BN. These fuels are,

i) pure urania
ii) urania-gadolinia (5%)
iii) urania-gadolinia (10%)

Each fuel was produced by sol-gel technique. The method of production and the effects of production parameters on the properties of these fuels were explained elsewhere [29].

The fuel pellets were coated by BN in a tube furnace which is shown in Fig. 1.

BCl_3 vapor introduced through a capillary was purged into the furnace by argon gas. NH_3 gas diluted with H_2 was introduced from a different tube, and mixing and chemical reaction take place in the hot zone of the furnace at a temperature around 875 K. The fuel pellets were located at the exit of the alumina tube where the temperature is between 450 and 500 K. BN powder formed under these conditions can be easily scratched, and rubbed off, but it is sticky. Its surface area determined by BET nitrogen absorption technique was found to be 2.38 m^2/g.

In Fig. 2 three pellets partially coated with white BN were shown. X-ray diffraction and infrared spectrum analyses of BN powder were found to be in agreement with the ones given in the literature [30,31].

The pellets were then sintered at 1600 K and 1900 K for 2 hrs. The white BN powder turned into hard glassy material with negligible porosity.

An examination of the surfaces of fuel pellets coated by BN was done by using a scanning electron microscope (SEM) (JSM, Model:6400). Figures 3 and 4 show the coatings on pure UO_2 fuel. A leaflike BN is found to form on UO_2 fuel as seen in Fig. 3. However this is not very common and smooth platelike coating was obtained as in Fig.4. UO_2 grains could be barely seen under the coating.

In Figs. 5 and 6 coatings on UO_2-Gd_2O_3 (5%) were shown. In Fig. 5 a completely formed BN plate is seen on the right upper part while the rest of the surface is coated with granular BN. In Fig. 6 the fuel surface is completely covered with BN. The coating in this figure is so thin that electron penetration is sufficient to show also the coated surfaces of $UO_2Gd_2O_3$ (10%) fuel.

In Fig. 7 rodlike BN coating is seen. In Fig. 8 the increased thickness caused cracks on the BN coating. In Figs. 9 and 10 the side views of the coatings were shown in pure UO_2 and UO_2- Gd_2O_3 (10%) specimens. The phase on the right hand side is BN which forms only on the surface with no penetration into the fuel in either case.

Rapid heating to 1900 K for sintering usually caused large losses from BN coating. So the proper sintering temperature should not exceed 1600K. Once BN coating is achieved further heating to 1900 K did not change the physical properties of the coating.

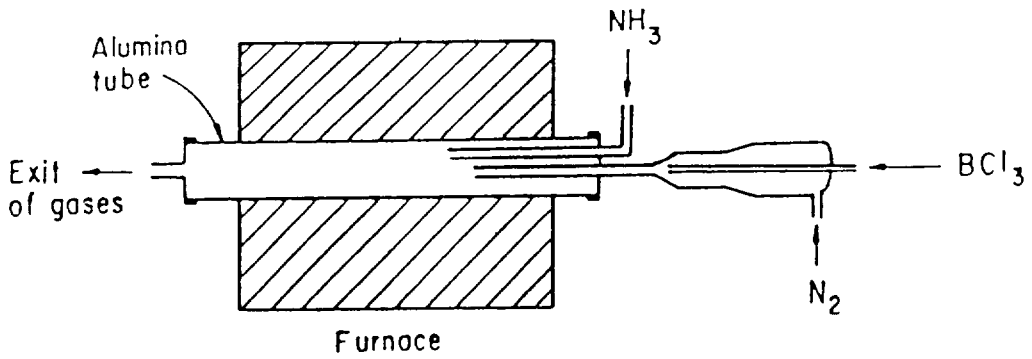

FIG 1 *Furnace for BN Coating*

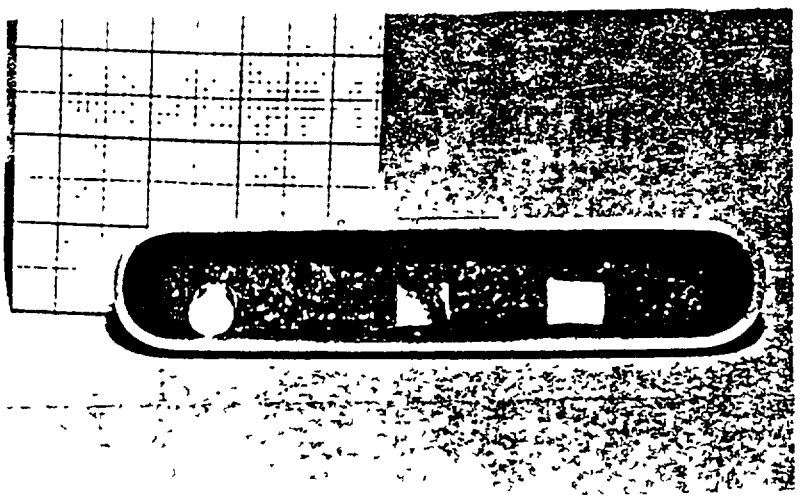

FIG. 2 *BN coated fuel pellets (not sintered)*

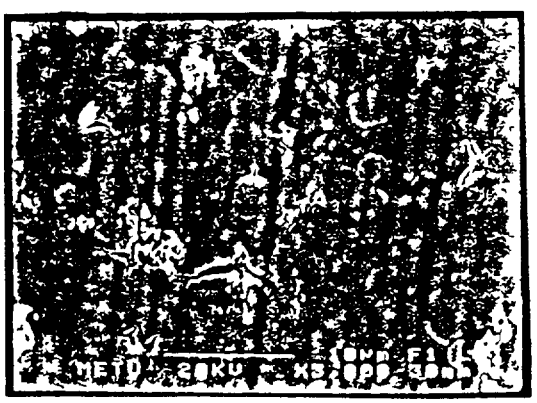

FIG. 3 *Leaflike BN formation*

FIG. 4 *BN coated urania fuel*

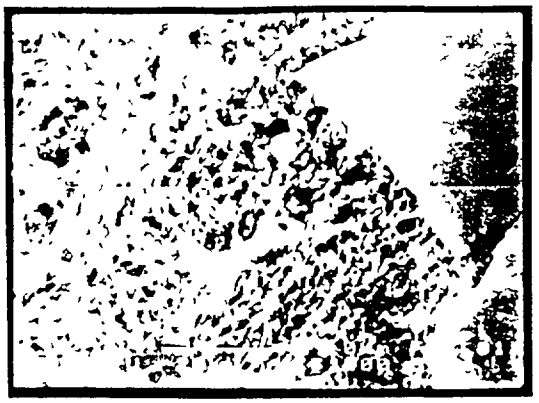

FIG. 5 *BN plate formation*

FIG. 6 *Thin BN coating*

FIG. 7 *Rodlike BN coating*

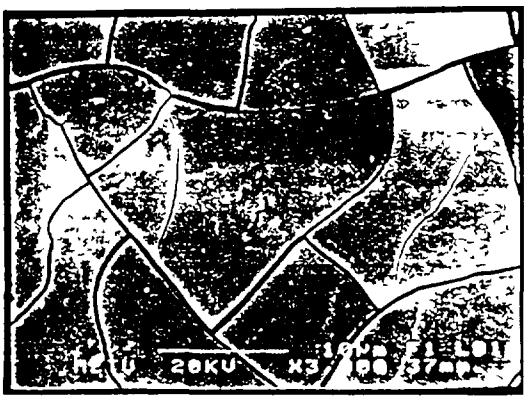

FIG. 8 *Cracks on BN coating*

COMPUTER CALCULATIONS

The performance of the fuels in a PWR core were studied by using cluster option of the WIMSD4 code [33]. The calculations were done on about 1/16 th of a KWU assembly where the pitch distance was 1.27 cm. The small matrix used in calculations makes a 5 x 5 assembly. Guide thimbles, instrumentation tube, grids etc. were not considered, and there was no boron in water. The fuel element which contains gadolinia was located at the center, and all fuel elements had their fuel pellets coated with BN. However some calculations were also done with no BN and/or no gadolinia. The enrichment of fuel was 5%, and gadolinia was changed as 0, 5, and 10 %. Two different BN coating thicknesses were considered as 30μm and 70μm. In calculations two different cases were considered. In the first case the fuel diameter was kept constant and the pitch distance was changed by changing the number of fuel elements in an assembly. Hence the ratio of cross sectional area of the total number of rods to the cross sectional area of the moderator changed. In the second case the radius of fuel elements were increased, but the total area of the moderator and the number of fuel rods in an assembly were kept constant so the ratio of the total cross sectional area of the fuel elements to the cross sectional area of the moderator changed.

Figure 11 shows a typical change of k_{eff} values at different pitch distances. The energy produced when $k_{eff} = 1$ was shown in Fig. 12 for all the fuels. It is seen that the linearity of the curve is lost at pitch

distances below 1.27 cm. A similar behavior of curves was observed when the change of burnup with respect to the ratio of moderator to fuel area was plotted.

In the second case, when the radius of fuel pellet was increased the difference in burnups disappeared for 30μm and 70μm BN coatings at 1.27 cm pitch distance. The further increase in the pitch distance decreases the closest distance between fuel elements resulting in lower moderation of neutrons. This in turn decreases the burnup in either case as seen from Fig.14. The fuel with 70μm BN coating resulted in lower burnup than 30μm BN coating. In fact as the radius of the fuel pellet increases for a constant BN coating thickness, the fuel with larger diameter contains relatively larger quantities of BN. The pitch distance used in normally operating reactors (e.g. 1.27 cm) seems to be also the best value for BN coated fuels. As the amount of gadolinia and/or the thickness of BN coating increases the burnup also increases as seen from Fig.14. The dependence of burnup on gadolinia content is not linear.

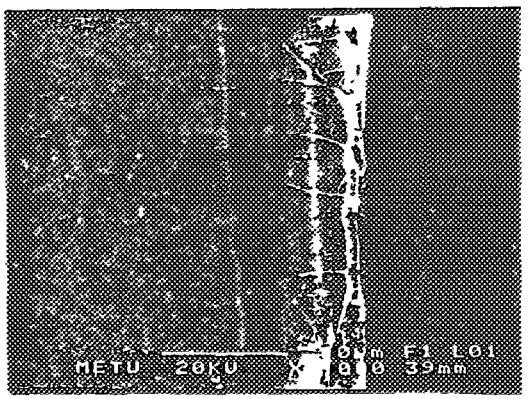

FIG. 9 *Side view of BN coating*

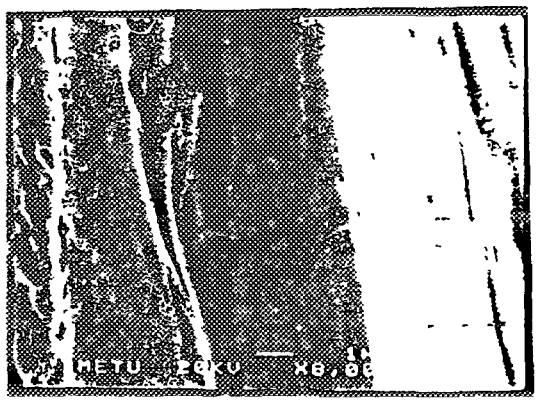

FIG. 10 *Another side view*

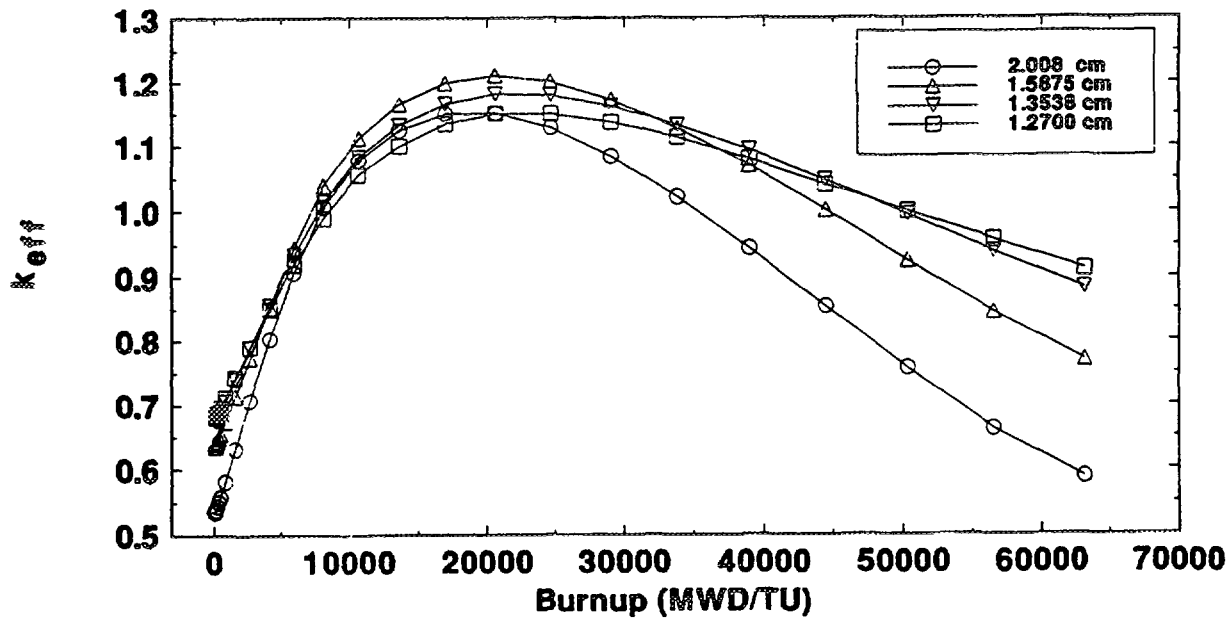

FIG. 11 *k_{eff} values at different burnups (enr: 5%, BN: 70 μm)*

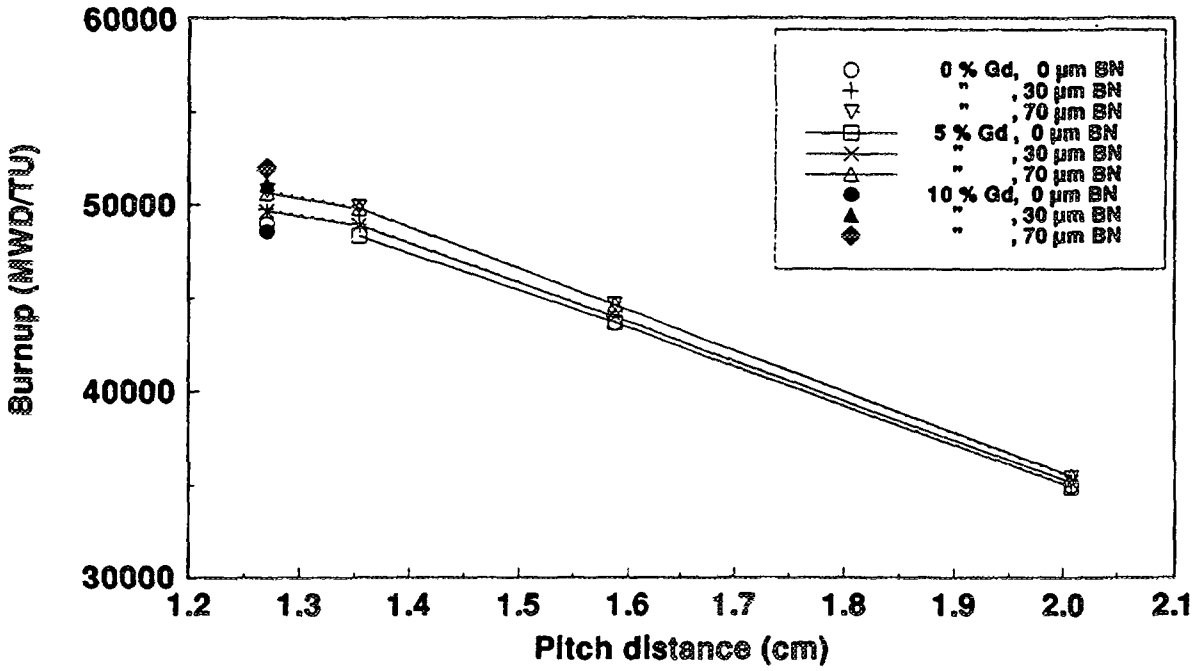

FIG. 12 *Change of burnup*

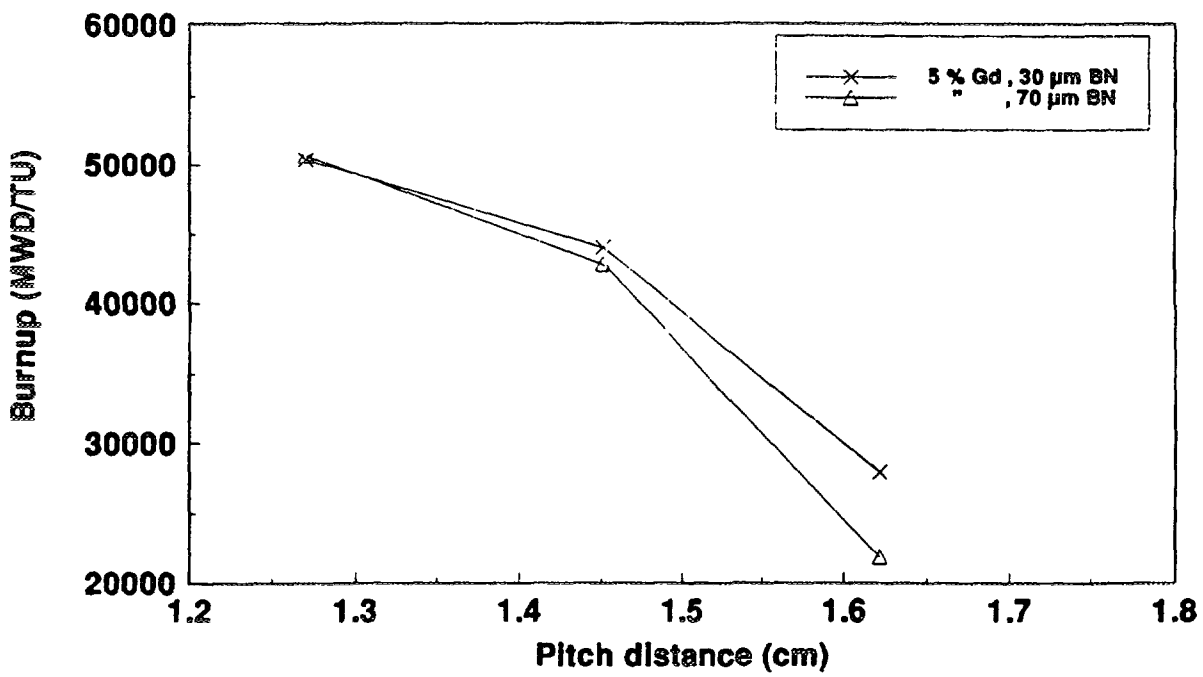

FIG. 13 *Change of burnup*

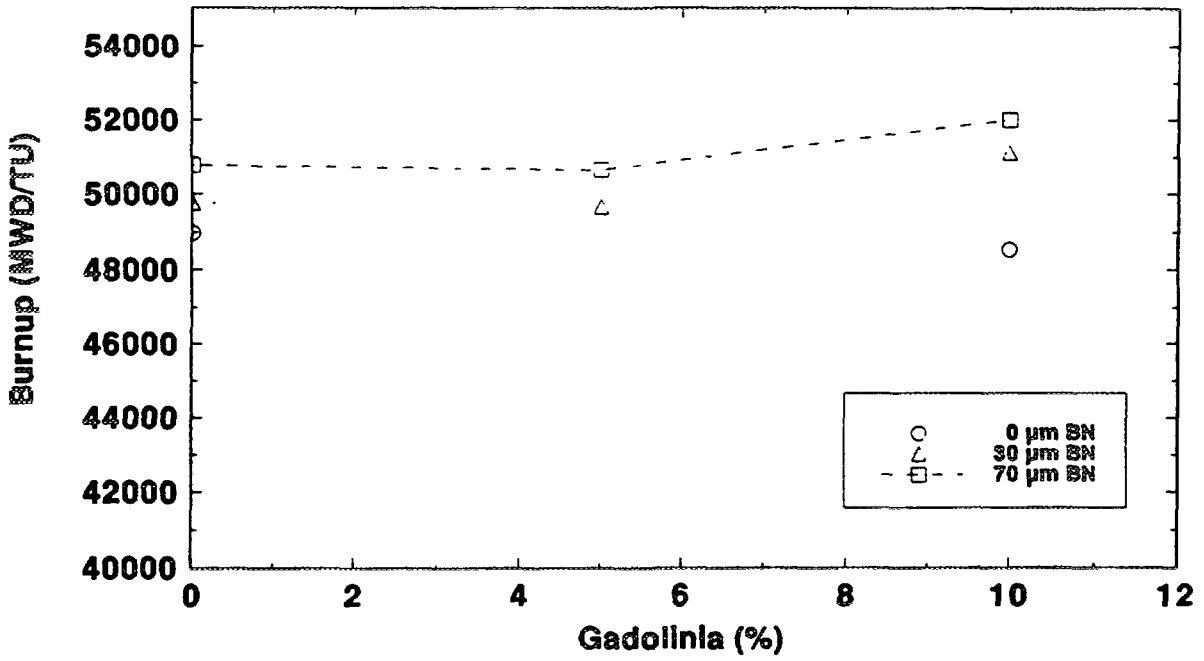

FIG. 14 Change of burnup with gadolinia

CONCLUSIONS

1. BN coating of nuclear fuels by CVD was accomplished.
2. Platelike and rodlike BN layers formed on fuel pellets.
3. Computer calculations showed that BN coating improved the fuel burnup of uraniagadolinia fuel.
4. The highest burnup was achieved at the present design specifications of a PWR

ACKNOWLEDGEMENT

This work was partly supported by International Atomic Energy Agency under the contract IAEA:5977 RB2. We realize that this work could not be accomplished without this very valuable support, and we appreciate it.

REFERENCES

[1] INTERNATIONAL ATOMIC ENERGY AGENCY: Burnable Absorber Fuel, Final Report on the Co-ordinated Research Programme on Burnable Absorber Fuel, IAEA-TECDOC, 1993.
[2] SIMMONS, R.L. et.al., Nucl. Tec. 80 (1988).
[3] PRITCHETT, J.E. et:al, Operating Experience with ZrB2 Integral Fuel Burnable Absorbers, ANS 1987 Winter Meeting Proc., 117-118 (1987).
[4] SRINILTA, S. et.al., A Comparison of Gd and ZrB2 as Integral Fuel Burnable Absorbers in PWRs, ANS 1987 Winter Meeting Proc (1987)., 124-126.

[5] RAND, M. J.and ROBERTS, M. J., Electrochem. Soc., 115, 23 (1968).
[6] MURARKA, M. J., CHANG, C.C., WANG, D.N.K., and SMITH,T.E., J.Electrochem. Soc., 126, 1951 (1979).
[7] HIRAYAMA, M. and K. SHOHNO, J. Electrochem. Soc., 122, 1671 (1975).
[8] STEELE, S.R., FEIST, W. and GETTY, W. "Research On Thin Film Tunnel Cathodes, Recombination Cathodes and Similar Cold Cathodes", Final Rep., (Contract DA 28-043-AMC-0035(E)), (September, 1966).
[9] STEELE, S.R., PAPPIS, J., SCHILLING, H. and SIMPSON, J. "Chemical Vapor Deposited Materials For Electron Tubes". lst.Triannu.Rep., (Contract DAA 1307-68C-0156) (June 1986).
[10] BARONIAN,W., Mater. Res. Bull., 7, 119 (1972).
[11] SANO, M. and AOKI, M., Thin Solid Films, 83, 247 (1981).
[12] MOTOJIMA, S., TAMURA, Y., Thin Solid Films, 88, 269 (1982).
[13] TAKAHASHI, T., ITOH, H., TAKEUCHI, A., J. Cryst. Growth, 47, 245 (1979).
[14] TAKAHASHI, T., ITOH, H., KURDODA, M., J. Cryst. Growth, 53, 418 (1981).
[15] GEBHARDT, J.J., Proc. 4th. Int. Conf. on"Chemical Vapor Deposition", Boston, MA, Electrochemical Society, Princeton, NJ, 460 (1973).
[16] CLERC, G., GERLACH, P., Proc. 5th. Int. Cof. on "Chemical Vapor Deposition", Slough,. Electrochemical Society, Princeton, NJ., 777 (1975).
[17] ZUNGER, A., KATZIR, A., HALPERIN, A., Phys. Rev. B, 13, 5560 (1976).
[18] POWELL, C.F., OXYLEY, J.H., BLOCHER, J.M., "Vapor Deposition", Wiley, New York, 663, (1966).
[19] HANIGOFSKY, J.A., ,et al., J. Am. Ceram.Soc.74[2], 301-305 (1991).
[20] LEE, W.Y., et al., J. Am. Ceram. Soc., 74[9], 2136-40 (1991).
[21] MATSUDA, T., et al., J. Mater. Sci., 21, 649-658 (1986).
[22] PIERSON, H.O., J. Compos. Mater., 9, 228 (1975).
[23] NASLAIN, R., et al., J. Am. Ceram. Soc., 74 [10], 2482-88 (1991).
[24] CONSTANT, G., FEURER, R., J. Less-Common Met., 82, 113 (1981).
[25] SCHMOLLA,W., and. HARTNAGEL, H.L., Solid State Electronics, 26, 10, 931939 (1983).
[26] PACIOREK, K.J.L., et al., Inorg. Chem. 27, 2432-2436 (1988).
[27] MAYA, L., and RICHARDS, H.L., J. Am. Ceram. Soc., 74, [2] 406-409 (1991).
[28] GAFRI, O., GRILL, A., and ITZHAK, D., Thin Solid Films, 72, 523-527 (1980).
[29] GUNDUZ, G.., Uranium-Gadolinium Oxide Fuel Production Sol-Gel Technique, Final Report, IAEA Vienna (1992).
[30] TAINE R.T and NARULA C.K., Chem. Review 90, 73 (1990).
[31] LEE W.Y., LACKEY W.J., J. Am. Ceram. Soc., 74, 2642 (1991).
[32] ROTH M.J., MACDOUGALL J.D., KEMSHELL P.B., The Preparation of Input Data for WIMS, AEW-R 538, (1967).

A MODEL FOR THE DESCRIPTION OF THE EVOLUTION OF PU AGGLOMERATES IN MOX FUELS

E. FEDERICI
CEA Centre D'études de Cadarache,
Saint-Paul-lez-Durance

P.BLANPAIN
FRAMATOME,
Lyon

P. PERMEZEL
Electricité de France,
Moret-dur-Loing

France

Abstract

In order to describe the irradiation behaviour of Pu agglomerates under LWR steady state conditions in MIMAS MOX fuels, a model including the neutronic evolution of the heavy atoms and their diffusion processes between the agglomerates and the matrix has been developed. It leads to the calculations of Pu enrichment in the two phases and of the agglomerates size evolution during irradiation. The calculated distribution of the fission in the fuel gives access to the local power and burnup heterogeneity factor. Electron probe microanalyses (EPMA) have been carried out on fuels irradiated up to 45000 MWd/tM. Diametral and local distribution of Pu are used to calculate the enrichments of the agglomerates and the matrix, which are then compared to the results of the model. During irradiation, the Pu concentration falls markedly in the agglomerates and increases steadily in the matrix, leading to a homogenization of the fuel on a microstructural scale. Heterogeneity factors give an estimate of the deviation from homogeneity. Knowing the local fission rate and burnup in the agglomerates and the matrix enables the calculation of local fission gas concentrations, which are compared to the xenon EPMA diametral distribution. Comparison with the calculated matrix xenon concentration at the edge of the pellet where there is no gas release, shows that some fission gas atoms which originated from the agglomerates, have been dissolved in the matrix by recoil. The calculated gas concentrations give an estimate of the quantity of gas dissolved. This work has been performed with the intent to improve fuel rod performance code estimates of fission gas concentrations retained or released in both the matrix and the agglomerates.

1. INTRODUCTION

In MIMAS (MIcronized MASter blend) MOX fuels, fabrication route induces an heterogeneous microstructure characterized by high Pu-content agglomerates - favouring high burnup values during irradiation - dispersed in a low Pu-content matrix.

Differences between these two phases are clearly revealed by post-irradiation examinations (PIE) and show a fission product accumulation, and an important porosity development in the agglomerates.

However, the fuel tends towards homogeneity as irradiation proceeds, due to heavy atom neutronic and diffusion processes, which favour the equalization of Pu in the matrix and in the agglomerates, and an implantation in the matrix of fission gas created in the agglomerates.

A heterogeneity model has been developed in order to (i) calculate and predict the fuel microstructure after base irradiation in order to compare the results with PIE, essentially electron-probe microanalyses (EPMA), (ii) estimate quantitatively the fission gas concentrations both in the agglomerates and the matrix for a coupling with fission gas release model of fuel rod performance code.

2. PU AGGLOMERATES EVOLUTION MECHANISMS

2.1 NEUTRONIC EVOLUTION

Neutron flux induces a neutronic evolution of the heavy atoms in the fuel. A simplified neutronic chain including U and Pu isotopes has been used (Fig. 1). One group cross-sections have been deduced from results obtained by the CEA 99 group neutronic code APOLLO, for a normal irradiation of a MOX fuel in a LWR. For each nuclide, an absorption cross-section (σ_a) and for fission atoms, a fission and a capture cross-section (σ_f and σ_c) are used. The evolution of the concentrations c_i can then be written as:

$$\frac{dc_i}{dt} = A_i - B_i$$

where A_i is the creation rate of the nuclide (worth 0 for U235, U238 and Pu238)$_i$ and B is the disappearance rate.

For example, the A and B terms for Pu241, deduced from the neutronic chain are:

$$A_{Pu241} = \sigma_{aPu240}\, c_{Pu240}\, \Phi$$

$$B_{PU241} = \sigma_{aPu241}\, c_{Pu241}\, \Phi - \lambda_{Pu241}\, c_{Pu241}$$

where σ_{aPu240}, σ_{aPu241} are the absorption cross-sections for Pu240 and Pu241, Φ is the neutron flux and $\lambda_{Pu241} = \ln(2)/T_{pu241}$, T_{Pu241} for the Pu241 period.

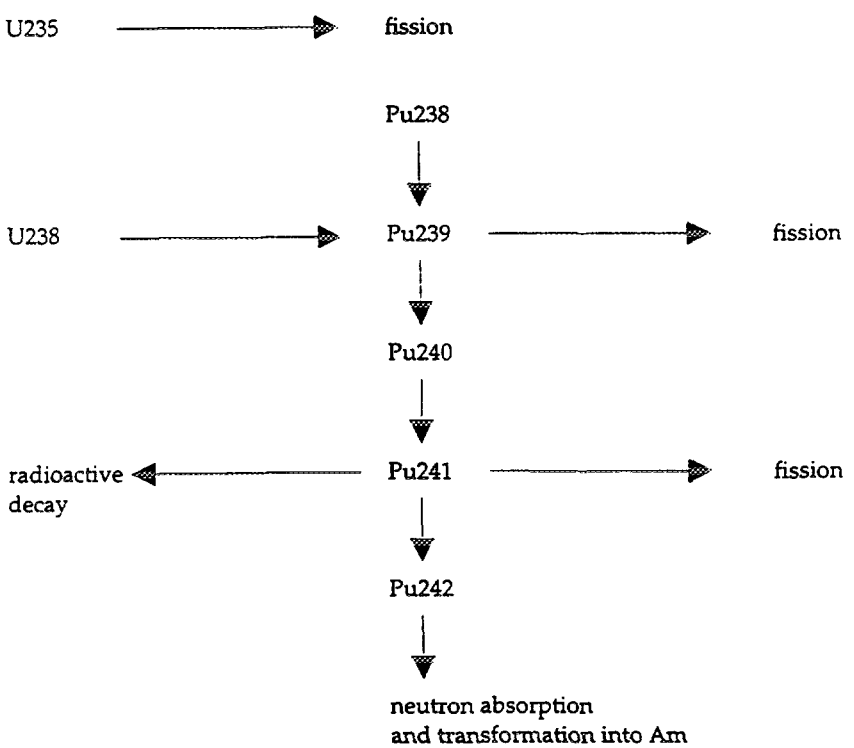

FIG. 1 Neutronic chain used in the heterogeneity model

2.2 DIFFUSION

Thermal and irradiation-enhanced metal diffusion of U and Pu occur during irradiation. For normal conditions, fuel temperature does not exceed 1300°C. Below this temperature, the diffusion coefficient is athermal and doesn't depend on Pu content. It can be described by:

$$D = k\dot{F}$$

where $\dot{F}$ is the fission rate (fissions. cm^{-3}. s^{-1}), and k is a constant equal to 1.2 10^{-29} cm^5 [1].

Note that for off-normal conditions, thermal diffusion could be added without major modifications.

The agglomerates are considered as spherical. Concentrations depend on radius (r), the centre of the agglomerate being chosen as the origin of coordinates (r = 0). Diffusion equation in spherical coordinates is used:

$$\frac{\delta c_i}{\delta t} = \frac{1}{r^2}\frac{\delta}{\delta r}\left(r^2 D \frac{\delta c_i}{\delta r}\right)$$

2.3 COUPLING NEUTRONIC AND DIFFUSION

The change with respect to time of concentrations is the sum of the neutronic and diffusion evolution defined in the last two sections. The equations are coupled via the neutronic terms which mix the concentrations, and the system to be resolved is non linear, due to the fact that the diffusion coefficient depend on the fission atom concentrations.

The numerical resolution is performed as follows: knowing the heavy atoms concentrations are function of radius at time step t_n, one wishes to calculate them at time step t_{n+1}. First, the neutron flux Φ is calculated from the power history of the rod, then the diffusivity is calculated according to:

$$D_{n+1} = k\Phi(\sigma_{fU235} c^n_{U235} + \sigma_{fPu239} c^n_{Pu239} + \sigma_{fPu241} c^n_{Pu241}$$

The concentrations are then calculated using a finite difference resolution scheme.

3. COMPARISON WITH EXPERIMENTAL RESULTS

3.1 FUEL CHARACTERISTICS

Fuel rods used for comparison with model calculations are part of the Saint-Laurent-B1 program [2]. A total of 16 rods fabricated using the MIMAS process have been thoroughly examined in hot cells in CEA Saclay and CEA Cadarache with careful attention being given to the fuel microstructure obtained by EPMA.

The MIMAS process is known to produce a heterogeneous distribution of Pu in agglomerates on a microscopic scale. Their Pu content is close to the master-mix enrichment (# 30 wt% Pu), and they are dispersed in a low-Pu content matrix [3].

Three mean pellet plutonium contents are used within an assembly: 2.88, 4.36 and 5.57 wt% Pu in the present case. Typical average agglomerate diameter, as measured by alpha-autoradiography, is close to 20 μm.

The heterogeneity model is applied to a class of agglomerates defined by its average radius and average enrichment, dispersed in a Pu-free matrix. With this hypothesis, the initial agglomerate volumetric fraction is:

$$F_V = \frac{e_{pell.}}{e_{aggl.}}$$

where $e_{pell.}$ is the average pellet Pu enrichment and $e_{aggl.}$ is the agglomerate Pu content. For the three zones, F_V = 9.6 (low Pu-content), 14.5 (medium Pu-content) and 18.6 (high Pu-content) vol%.

Fuel rods have been extracted after one, two and three irradiation cycles. Their highest mean (resp. peak) burnup is 41000 (resp. 46500) MWd/tM, and their linear power falls in the range 150 to 220 W/cm.

3.2 HEAVY ATOM EVOLUTION

Typical calculated evolution of Pu concentration in the agglomerates and in the matrix is shown in figure 2 after one, two and three irradiation cycles.

Neutronic evolution leads to a decrease in Pu concentration in the agglomerates and an increase in the matrix. Their value tends towards the mean Pu concentration, which can be calculated supposing the fuel to be homogeneous. Slight diffusion of Pu in the matrix occurs on a length lower than 5 μm.

Deviation from homogeneity can be estimated by heterogeneity factors. The power (resp. burnup) heterogeneity factor is defined as the ratio of the agglomerates or matrix power (resp. burn-up) versus their mean pellet value. Their initial value is close to the ratio of initial Pu concentration in the agglomerate or the matrix against mean Pu enrichment, i. e. nearly null for the matrix and 10.4 (low Pu content), 6.9 (medium Pu content) and 5.4 (high Pu content) for the agglomerates. They tend towards 1 as the irradiation proceeds. An example of their evolution versus burnup is shown in figure 3.

These results have been checked against EPMA, which enables the measurement of Pu concentration in the agglomerates and the matrix. Local analyses with a resolution of 2 μm clearly show

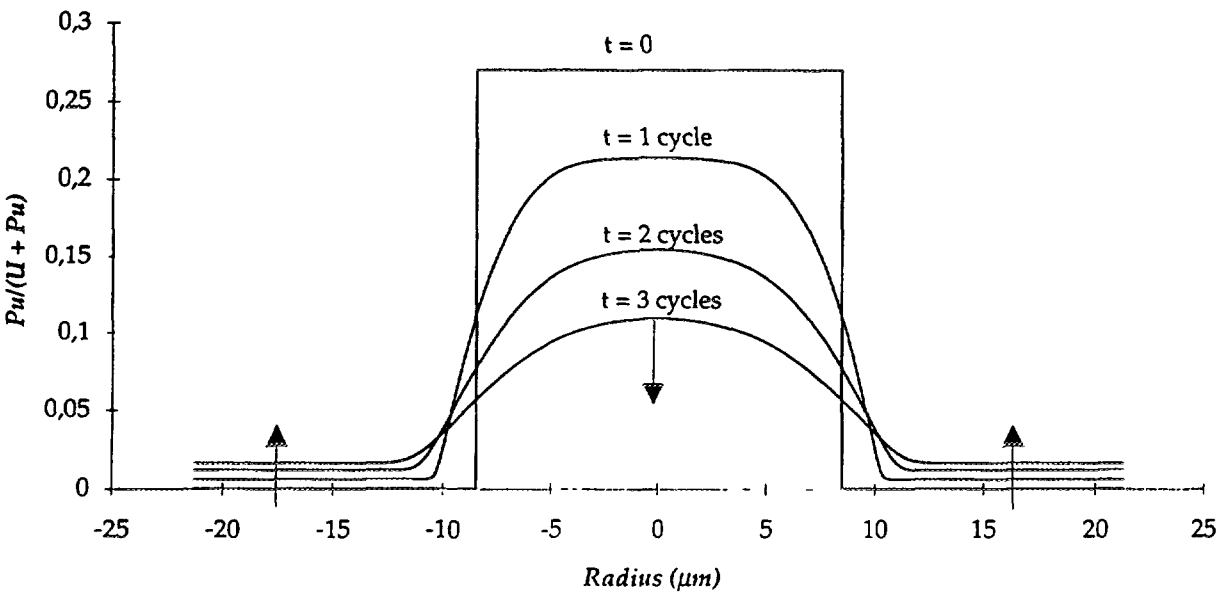

FIG. 2 Pu profile evolution during irradiation

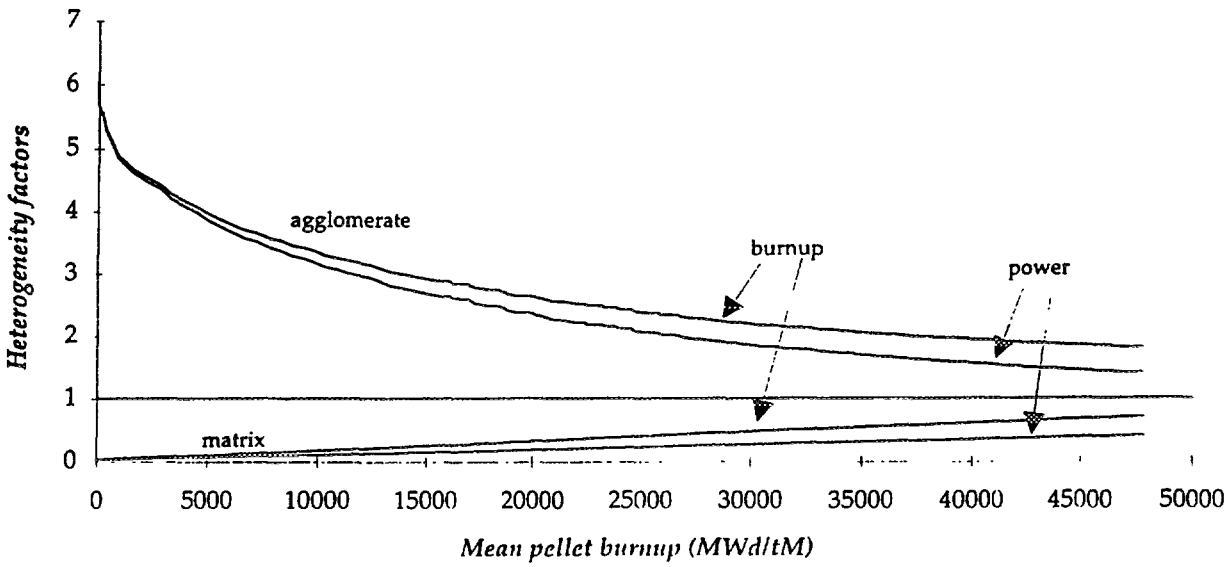

FIG. 3 Power and burnup heterogeneity factors of agglomerates and matrix versus mean pellet burnup

the agglomerate structure and particularly the Pu enrichment; diametral measurements enable the calculation of the matrix content. They are shown in figure 4 together with model calculations for the intermediate Pu-content zone.

3.3 FISSION GAS REPARTITION

Fission gases are created for a large part in the agglomerates where most of the fissions occur. The rates of birth of Xe and Kr for MOX fuels under normal conditions have been calculated using the APOLLO code and are used with the heterogeneity factors to calculate the gas distribution between the agglomerates and the matrix.

Another important phenomenon is taken into account: a significant amount of the gas atoms created within the agglomerates is implanted in the surrounding matrix by recoil. Gas atoms which are concerned must have been created in the range of fission fragment (i. e. of the order of 10 μm) from the agglomerate surface. A parameter named f_d, representing the fraction of fission gas created in the agglomerates and dissolved in the matrix has been introduced. The expressions for the gas concentrations are then:

$$GC_a^{aggl.} = GC^{aggl.}(1 - f_d)$$

$$GC_a^{mat.} = GC^{mat.} + GC^{aggl.} f_d \frac{x_{aggl.}}{1 - x_{aggl.}}$$

where $GC_a^{aggl.}, GC_a^{mat}$ (resp $GC^{aggl.}$ $GC^{mat.}$) are the created fission gas concentrations after (resp. before) implantation in the matrix and $x_{aggl.}$ is the agglomerate volumetric fraction.

Note that:

$$x_{aggl.} GC_a^{aggl.} + (1 - x_{aggl.}) GC_a^{mat.} = x_{aggl.} GC^{aggl.} + (1 - x_{aggl.}) GC^{mat.} = GC^{pell}$$

where GC^{pell} is the average pellet fission gas concentration.

This approach could also be used in case of an initial distribution of agglomerate diameter, to take into account the as-fabricated fuel microstructure. The f_d factor should then be written to show explicitly its proportionality with the free surface of agglomerates.

The diametral Xe EPMA of fuel rod pellets from the three Pu content zones, various power histories and burnups have been used to adjust the f_d parameter. A value of 25 % has been found to reproduce correctly xenon measurements in the matrix near the edges of the pellet where no fission gas release occurred (Fig 5, 6 and 7). As the burnup increases, fission gases remaining in the agglomerates accumulate in bubbles and are less visible with EPMA.

The value obtained for f_d is slightly lower but close to the one calculated by Walker and al. [4] (33 %) on MOX fuels whose fabrication process is similar to MIMAS.

In figure 7, thermal release of Xe from the matrix is seen at the centre of the pellet, due to a high power level reached by the rod on its third irradiation cycle (# 220 W/cm).

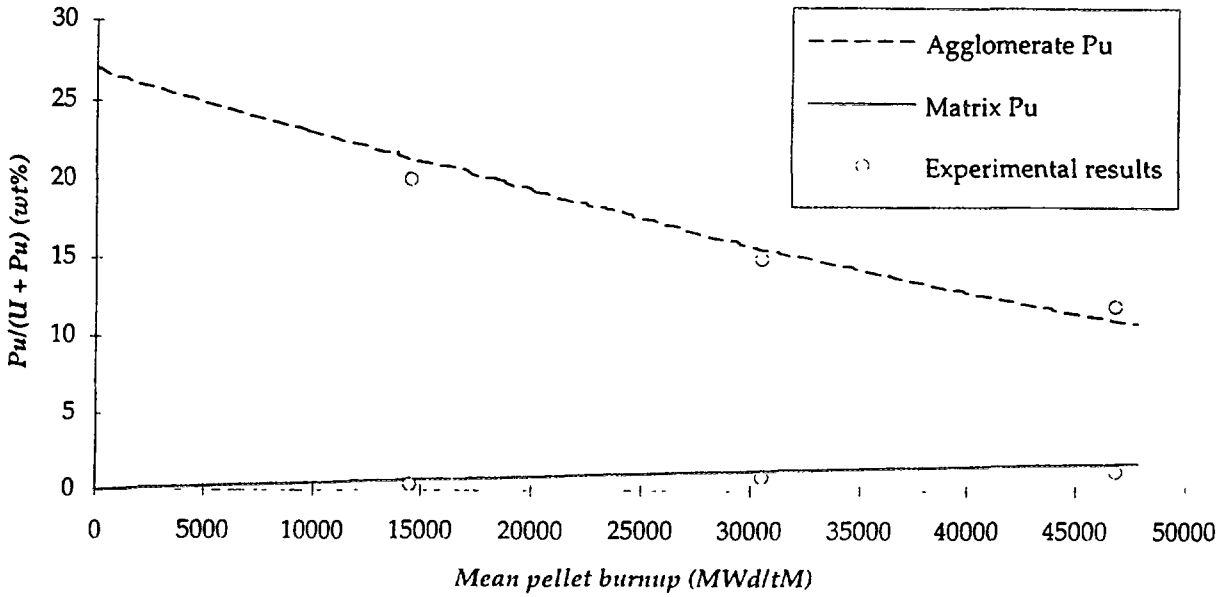

FIG. 4 Calculated andmeasured Pu content in the agglomerates and the matrix

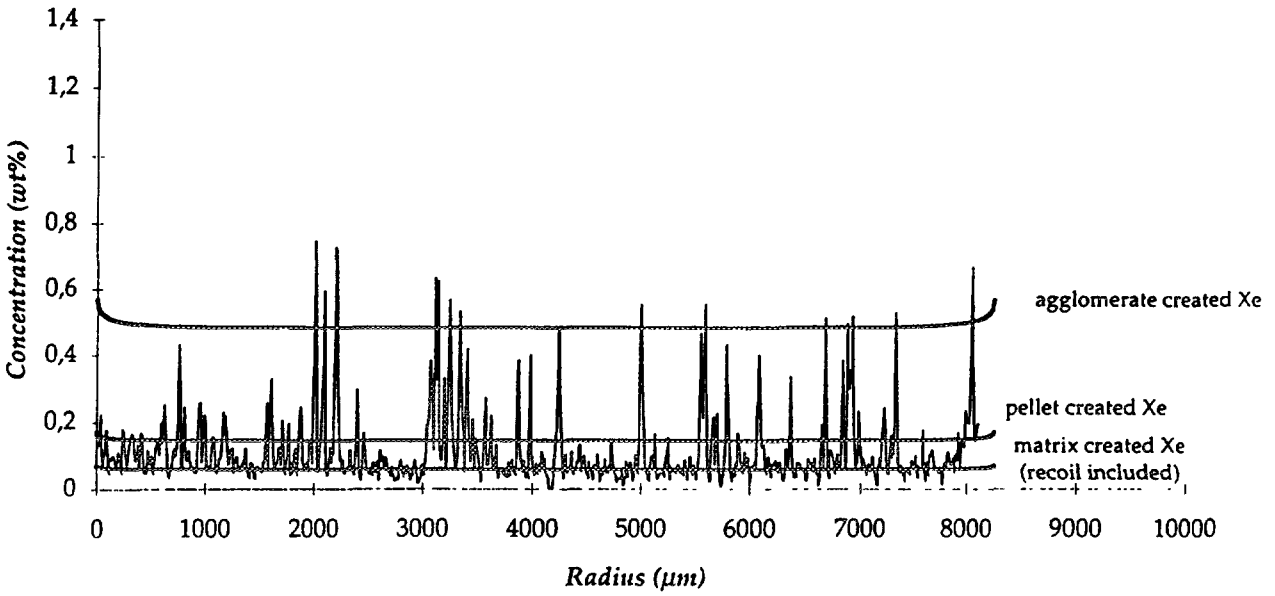

FIG. 5 Xenon diametral distribution - 1 irradiation cycle

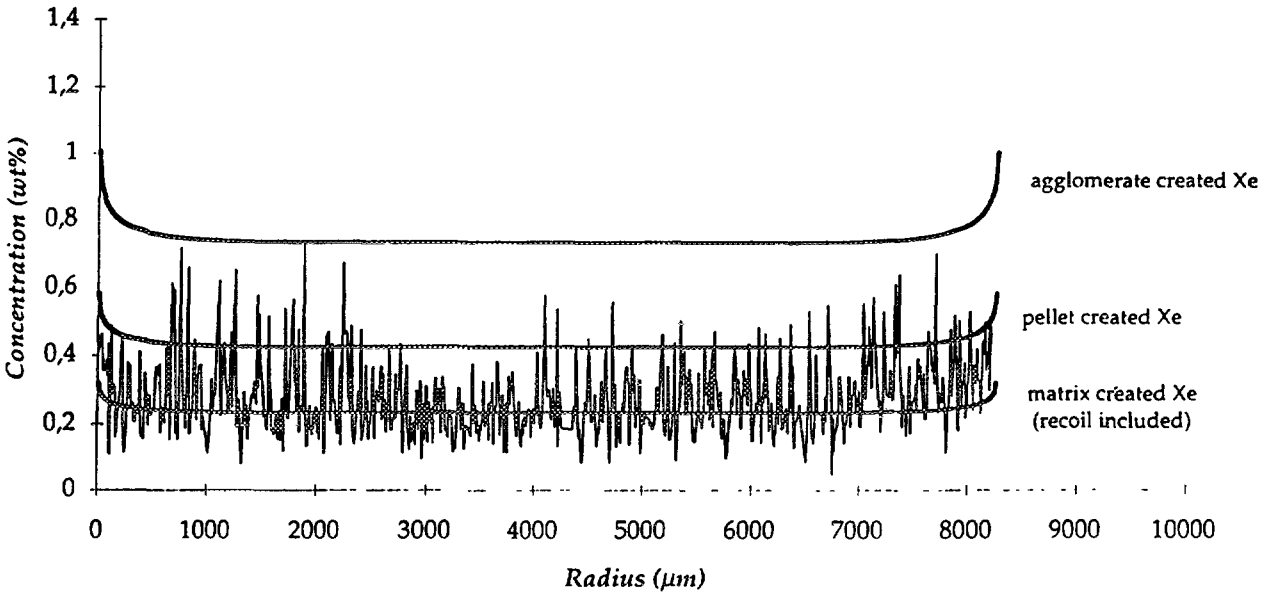

FIG. 6 Xenon diametral distribution - 2 irradiation cycles

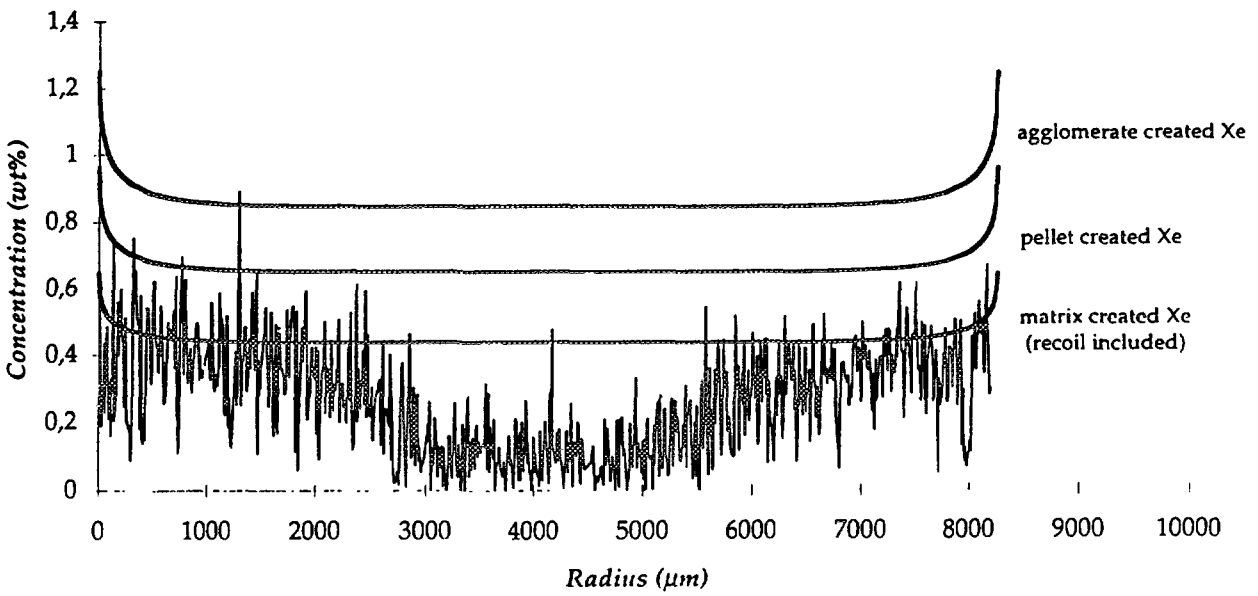

FIG. 7 Xenon diametral distribution - 3 irradiation cycles

4. CONCLUSION

MIMAS MOX fuels could be qualified as "moderately heterogeneous". Indeed, the Pu enrichment of the as-fabricated fuel is limited by the master-mix step to about 30 wt% Pu and the irradiation tends to homogenize the fuel microstructure mainly through neutronic processes, which overcome diffusion in normal conditions, and by a decrease of fission gas overconcentrations in the agglomerates due to recoil in the matrix.

The developed heterogeneity model yields quantitative estimates of the heavy atom and fission gas concentrations both in the agglomerates and the matrix.

Complementary results for as-fabricated MOX fuels are underway at Cadarache and should give more information on size and Pu enrichment distribution in the agglomerates. High burn-up effects in the agglomerates (fission gas release, precipitation of metallic fission products, ...) should also be included in the model whose results should confirm and explain the behaviour of MIMAS MOX fuels in normal conditions. The concentrations calculated by the model should also be used as initial conditions for fuel behaviour studies under off-normal conditions.

REFERENCES

[1] MATZKE, Hj., "Diffusion in ceramic oxide systems", Advances in Ceramics, 17 (1986) 1-54

[2] BLANPAIN, P., THIBAULT, X., TROTABAS, M., "MOX fuel experience in French power plant", International topical meeting on light water reactor fuel performance, West Palm Beach, Florida (April 1994)

[3] LIPPENS, M., VAN LOON, C., KETELS, J., "Ceramographic techniques and electron probe microanalyses applied to uranium-plutonium oxides", Technical committee on properties of materials for water reactor fuel elements and methods of measurements", IAEA, Vienna (October 1986)

[4] WALKER, C. T., COQUERELLE, M., GOLL, W., MANZEL, R., "Irradiation behaviour of MOX fuels: results of an EPMA investigation", Nuclear Engineering and Design, 131(1991) 1-16

LIST OF PARTICPANTS

ARGENTINA

Denis, A.	Argentine Atomic Energy Commission, Av. del Libertador 8250, 1429 Buenos Aires
Marino, A.C.	Argentine Atomic Energy Commission, Av. del Libertador 8250, 1429 Buenos Aires

BELGIUM

Bairiot, H.	F E X, Lijsterdreef 24, B-2400 Mol
Shihab, S.	Belgonucléaire SA, Avenue Ariane 4, B-1200 Brussels

BULGARIA

Stefanova, S.	Institute for Nuclear Research and Nuclear Energy, Blvd, Tzarigradsko Chausse 72, Sofia 1784
Vitkova, M.	Institute for Nuclear Research and Nuclear Energy, Blvd, Tzarigradsko Chausse 72, Sofia 1784

CANADA

Lucuta, P.G.	Chalk River Laboratories, Atomic Energy of Canada Ltd, Chalk River Ontario, KOJ 1JO
Tayal, M.	Design Analysis (Fuel Branch), AECL- CANDU, 2251 Speakman Drive, Mississauga, Ontario L5K IB2

CHINA

Shishun, Zhang	China Institute of Atomic Energy, P.O. Box 275 (64), Beijing 102413
Yingchao, Zhang	China Institute of Atomic Energy P.O. Box 275 (64), Beijing 102413

CZECH REPUBLIC

Svoboda, R.	Nuclear Research Institute Řež plc, 250 68 Řež

FINLAND

Kelppe, S.	VTT Energy, P.O. Box 1604, FIN-02044 Jyvaeskylae

Ranta-Puska, K.	VTT Energy, P.O. Box 1604, FIN-02044 Jyvaeskylae

FRANCE

Baron, D.	Direction des études et recherches, Electricité de France, B.P. 1, F-77250 Moret-sur-Loing,
Bernaudat, C.	EDF/SEPTEN, 12/14 avenue Dutriévoz, F-69828 Villeurbanne Cedex
Blanpain, P.	FRAMATOME, 10 rue Juliette Récamier, F-69456 Lyon Cedex
Charles, M.	Commissariat à l'énergie atomique, CEA/Grenbole - DTP/SECC/LRMC, 17 rue des Martyrs, F-38054 Grenoble Cedex
Federici, E.	DRN/CEN Cadarache, F-13108 Saint-Paul-lez-Durance
Garcia, Ph.	DRN/CEN Cadarache, F-13108 Saint-Paul-lez-Durance
Linet, B.	Commissariat à l'énergie Atomique, DRN/DMT/SETIC, Bâtiment 460, F-91191 Gif-sur-Yvette

GERMANY

Eberle, R.	Siemens AG Unternehmensbereich KWU, P.O. Box 3220, D-91050 Erlangen

INDIA

Das, M.	Nuclear Power Corporation, Vikram Sarabhai Bhavan, Anushaktinagar, Mumbai 400094
Dutta, B.K.	Reactor Engineering Division, Bhabha Atomic Research Centre, Hall - 7, BARC, Trombay, Mumbai

JAPAN

Harada, Y.	Nuclear Development Corporation, 622 12 Funaishikawa, Tokai-mura, Ibaraki-ken, 319-11
Ichikawa, M.	Japan Atomic Energy Research Institute, Tokai-mura, Naka-gun, Ibaraki-ken, 319-11
Ishida, M.	Nippon Nuclear Fuel Development Co. Ltd, 2163 Narita-cho, Oarai-machi Higashi-ibaraki-gun, Ibaraki-ken, 311-13

Kitajima, S.	Central Research Institute of Electric Power Industry, 11-1 Iwato kita 2 Chome, Tokyo 201
Kohno, S.	Power Reactor and Nuclear Fuel Development Corporation, 4-33 Muramatsu, Tokai-mura, Naka-gun, Ibaraki-ken, 319-11

NORWAY

Wiesenack, W.	Institutt for Energiteknikk, OECD Halden Reactor Project, Os Allé 13, P.O. Box 173, N-1751 Halden

ROMANIA

Horhoianu, G.	Institute for Nuclear Research, P.O. Box 78, R-0300 Pitesti

RUSSIAN FEDERATION

Bobrov, S.	Research Institute of Atomic Reactors, 433510, Dimitrovgrad-10, Ulyanovsk region
Medvedev, A.V.	All Union Scientific and Research, Institute of Inorganic Materials, AUSRIIM, St. Rogov 5, 123060 Moscow

SLOVAKIA

Petényi, V.	Nuclear Regulatory Authority of Slovak Republic, Okružná 5, 918 64 Trnava

SPAIN

Quecedo, M.	Uranio S.A. (ENUSA), Empresa Nacional de Santiago Rusinol 12, SP-28040 Madrid
Vicente, C.	Institute of Nuclear Technology, CIEMAT, Madrid

SWEDEN

Forsberg, K.	ABB Atom AB, S-721 63 Västerås
Grounes, M.	Studsvik Nuclearr AB, S-611 82 Nyköping
Massih, A.R.	ABB Atom AB, S-721 63 Västerås

SWITZERLAND

Ott, Ch.	Fuel Behaviour Modelling, 27 PSI CH, Paul Scherrer Institute, CH-5232 Villigen PSI

TURKEY

Gündüz, G.	Department of Chemical Engineering, Middle East Technical University (ODTÜ), 06531 Ankara

UNITED KINGDOM

Abram, T.J.	Fuel Engineering Department, BNFL Springfields, Salwick, Preston PR4 OXJ
Aldred, K.	Springfields Works, British Nuclear Fuels plc, Preston, Lancashire PR4 OXJ
Copeland, P.S.	Fuel Evaluation Department, Windscale Laboratory, AEA Technology, Seascale, Cumbria CA20 IPF
Councill, D.N.	Springfields Works, British Nuclear Fuels plc, Preston, Lancashire PR4 OXJ
Ellis, W.E.	Windscale Laboratory, AEA Technology, Seascale, Cumbria CA20 IPF
Hargreaves, R.	Windscale Laboratory, AEA Technology, Seascale, Cumbria CA20 IPF
Harrison, F.	Springfields Works, British Nuclear Fuels plc, Preston, Lancashire PR4 OXJ
Killeen, J.C.	Nuclear Electric plc, Barnett Way, Barnwood, Glos. GL4 7RS
Mason, P.	AEA Technology, 540.1 Harwell, Didcot, Oxfordshire OX11 0RA
Peebles, D.	Springfields Works, British Nuclear Fuels plc, Preston, Lancashire PR4 OXJ
Rothwell, J.P.	Nuclear Installations Inspectorate, St. Peters House, Stanley Precinct, Bootle, Merseyside L20 3LZ
Tempest, P.	Berkeley Technology Centre, Nuclear Electric plc., Berkeley, Glos. 13 9PB
Tissington, D.	Springfields Works, British Nuclear Fuels plc, Preston, Lancashire PR4 OXJ
Turnbul, A.	Cherry-Lyn, The Green, Tockington, Bristol BS12 4NJ
White, R.J.	Berkeley Technology Centre, Nuclear Electric plc., Berkeley, Glos. 13 9PB

UNITED STATES OF AMERICA

Billaux, R.	Nuclear Division, Engineering and Manufacturing Facility, Siemens Power Corporation, 2101 Horn Rapids Road, P.O. Box 130, Richland, WA 99352-0130
Rashid, Y.R.	Anatech Research Corporation, 5435 Oberlin Drive, San Diego, California 92121
Montgomery, R.	Anatech Research Corporation, 5435 Oberlin Drive, San Diego, California 92121

CEC

O'Carroll, C.	Institute for Transuranium Elements, CEC Joint Research Centre, Postfach 2340, D-19322 Karlsruhe, Germany
Lassmann, K.	Institute for Transuranium Elements, CEC Joint Research Centre, Postfach 2340, D-19322 Karlsruhe, Germany

OECD

Sartori, E.	OECD/NEA, Le Seine St-Germain, 12 Boulevard des Îles, F-92130 Issy-les-Moulineaux, France

IAEA

Chantoin, P. *(Scientific Secretary)*	Division of Nuclear Power and the Fuel Cycle, Wagramerstrasse 5, P.O. Box 100, A-1400 Vienna, Austria